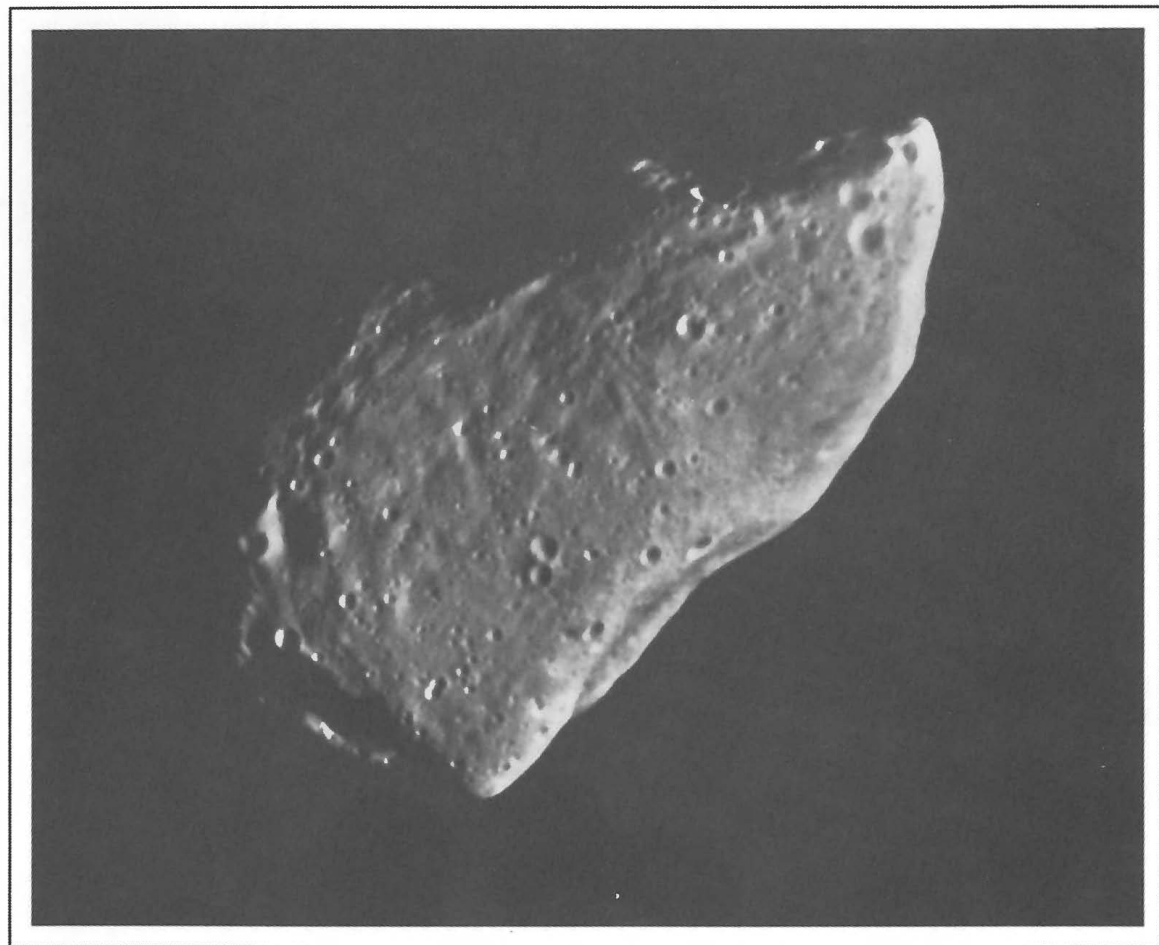


Asteroids, Comets, Meteors 1991



Edited by Alan W. Harris and Edward Bowell

Asteroids, Comets, Meteors 1991

*Published by the Lunar and Planetary Institute,
3600 Bay Area Boulevard, Houston TX 77058-1113, USA.*

Copyright Lunar and Planetary Institute 1992.

Printed in the United States of America.

Library of Congress Cataloging-in-Publication Data applied for.

ISBN 0-942862-07-04 Softcover.

Cover Photo: (951) Gaspra, imaged by the Galileo spacecraft from a range of 5300 km on October 29, 1991, is an irregular S-type asteroid $19 \times 12 \times 11$ km in size. The resolution of 54 m/pixel is the highest for the Gaspra encounter. The Sun is shining from the right, and the phase angle is 50° . Gaspra's north pole is at upper left (in reference to frame of photograph); it rotates in the prograde sense with a 7.09-hr period.

Gaspra is much more heavily cratered than previously studied bodies of comparable size such as Phobos and Deimos. The asteroid's very irregular shape suggests that it was collisionally derived from a larger body. Consistent with such a history are groovelike lineaments, thought to be related to fractures, that are 100 to 300 m wide and tens of meters deep. The lineaments form two intersecting groups of differing morphology, one group being wider and more pitted than the other. Such features have hitherto only been seen on Phobos, but were predicted for asteroids as well. Gaspra also exhibits a variety of enigmatic curved depressions and ridges in the terminator region at left. Image courtesy of Jet Propulsion Laboratory.

Asteroids, Comets, Meteors 1991

Edited by Alan W. Harris and Edward Bowell



Proceedings of the international conference held at Northern Arizona University, Flagstaff, USA June 24-28, 1991



Picnic lunch in the Inner Basin of the San Francisco Peaks



*Mildred Matthews with Gareth Williams,
recoverer of long-lost asteroid Mildred*



Dorothy and Paul Barringer

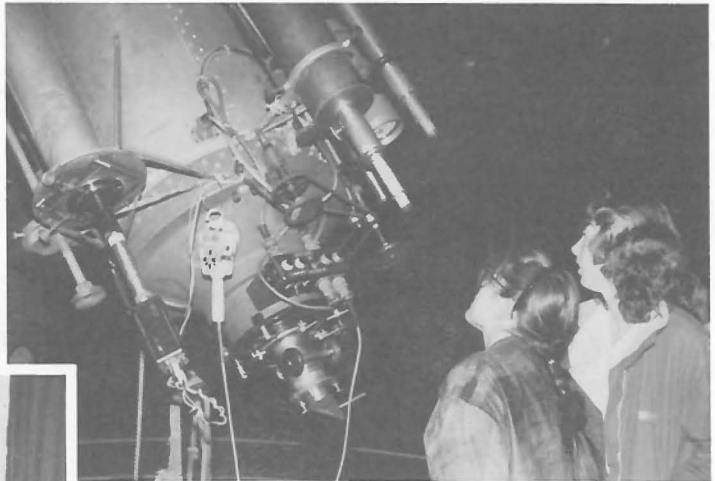


At Meteor Crater, a recent asteroid impact

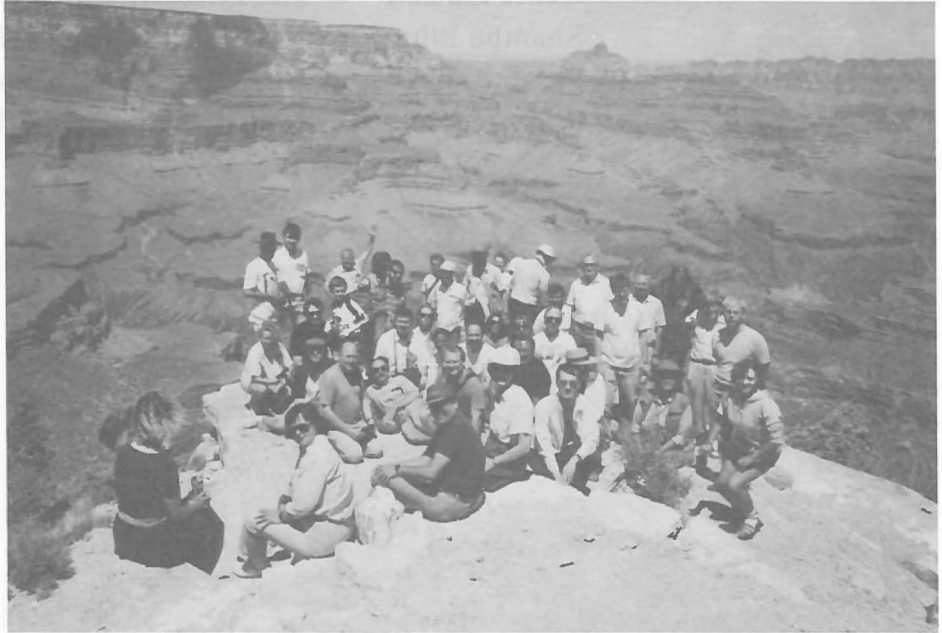


(Left) Pam Jones still smiling after working so hard

(Below) At Lowell Observatory's historic 24-inch reflector



(Left) Organizational matters (left to right: Clark Chapman, Al Harris, Ted Bowell)



(Right) Geology lesson on the South Rim of Grand Canyon

EDITORS

Alan W. Harris
Edward Bowell

SCIENTIFIC ORGANIZING COMMITTEE

Michael F. A'Hearn	Jürgen H. Rahe
Edward Bowell (Co-Chairman)	Hans Rickman
Clark R. Chapman	Hans Scholl
Michel C. Festou	Edward M. Shoemaker
Alan W. Harris (Co-Chairman)	Edward F. Tedesco
Ľubor Kresák	Giovanni M. Valsecchi
Claes-Ingvar Lagerkvist	Iwan P. Williams
Dmitrij F. Lupishko	Vincenzo Zappalà

LPI PROGRAM SERVICES

Pamela Jones
Cathy Fischer

LPI PUBLICATIONS SERVICES

Susan Boatright	Ronna Hurd
Renee Dotson	Christy Owens
Shantha Elluru	Linda Tanner
Sarah Enticknap	Pam Thompson
Mary Heye	Stephanie Tindell
Stephen L. Hokanson	

Preface

The international conference Asteroids, Comets, Meteors 1991 (“ACM ’91”), was held on the campus of Northern Arizona University in Flagstaff, Arizona, USA, June 24–28, 1991. Similar meetings were held in Uppsala, Sweden, in 1983, 1985, and 1989, and a sequel meeting is scheduled for June 14–18, 1993, in Belgirate, Italy. The sequence of meetings has seen rapid growth. The first had 76 participants, almost exclusively from Europe (including several Eastern European participants). The second meeting grew to 131 participants, with 41 from North America and 3 from Japan. The third meeting had 158 participants, with attendees from South America and Australia, in addition to the countries represented at previous meetings. So it was with great pleasure, but also some surprise, that we welcomed 307 registrants to the meeting in Flagstaff. Just over half (176) were from North America, with 89 from Western Europe, 28 from Eastern Europe and Central Asia, 5 from Japan, 1 from India, 6 from Australia and New Zealand, and 2 from South America. We are gratified to note that in holding the meeting in North America, the number participating from other countries did not diminish.

The style of ACM meetings has continued to evolve, in part driven by the increase in size and number of papers presented. In Flagstaff, a plenary session devoted to invited papers and short contributed papers of broad interest was held each morning. Afternoons were set aside for a variety of activities run in parallel, including longer and/or more specialized contributed paper sessions, workshops and committee meetings, and poster displays. On Wednesday afternoon, June 26, we had a field trip to Meteor Crater, where participants were able to examine the result of an asteroidal collision close up. This proceedings volume comprises written accounts of the papers presented, including both invited and contributed papers, and poster as well as oral presentations. We have not included summary reports of the various workshops, although a few of the papers were presented in such workshops.

In these proceedings, we have not sorted papers by topic (asteroids, comets, meteors), as was done in past volumes. Instead, all papers have been ordered alphabetically by first author, and indexes for topics, objects, and all authors are given. In the topical index, we have retained separation by asteroids, comets, and meteors; if appropriate, however, any given paper may be referred to in more than one of these major divisions.

The papers submitted to this proceedings were each critically reviewed by one of a cadre of referees; about 20% of papers were sent to two or more referees. About half the 171 papers received were returned to their authors for suggested revisions. This process, while substantially improving the quality of the volume, has been labor intensive and time consuming, especially in cases where communication with authors (such as those in Eastern Europe) has been difficult. We were assisted principally by Mike A’Hearn, Rick Binzel, Jack Brandt, Anita Cochran, Bo Gustafson, Dave Schleicher, and Don Yeomans. We thank them and other reviewers for giving generously of their time and expertise.

Sponsors of ACM ’91 were very important to the meeting. We are most grateful for a grant from the Barringer Crater Company, without which it would have been impossible for most of the Eastern European participants to attend, and financial support from the Planetary Astronomy Program of the National Aeronautics and Space Administration, which helped pay for conference facilities and provided a number of small grants for student participants. We also gratefully acknowledge the underwriting of a reception by Lowell Observatory, and defrayment of part of the cost of the conference banquet by Meteor Crater Enterprises, Incorporated.

It is also a pleasure to thank the many individuals who worked hard to make the meeting a success and to produce this volume. Most of the members of the Scientific Organizing Committee were pressed into service on many occasions. In particular, Mike A'Hearn, Clark Chapman, Michel Festou, Gene Shoemaker, and Ed Tedesco helped us put the scientific program together. We especially thank Pam Jones and Cathy Fischer of the Program Services Department of the Lunar and Planetary Institute for their skilled help in organizing the meeting. Renee Dotson, Stephanie Tindell, and other members of the Publications Services Department of the LPI were responsible for the production of this volume and the abstract volume. Anne-Marie Malotki designed and drafted an engaging meeting logo. At Northern Arizona University, we were assisted by Marcy Biesemeyer, Louise Brown, and Linda Jones of the du Bois Conference Center; Matt Tallarovic provided audio-visual expertise. Help projecting slides and viewgraphs was provided by Bobby Bus, Clifford Cunningham, Flavio Mendez, Michelle Olmstead, Brian Skiff, and Leslie Zimmerman. Helen Horstman assisted at the registration and information desks.

We are especially appreciative of the help and cooperation of those who made possible the memorable social events and field trips. We thank Gary Shoemaker and the staff of Meteor Crater Enterprises, Incorporated, for hosting the field trip and banquet at Meteor Crater; Gene Shoemaker (no relation) and Dave Roddy of the U.S. Geological Survey for conducting tours into Meteor Crater; George Billingsley (USGS) and Gene Shoemaker for their geologic descriptions at the rim of the Grand Canyon; Anne-Marie Malotki for conducting a tour to Sunset Crater and Wupatki Indian ruins; Bob Millis, Mary Lou Evans, and the staff of Lowell Observatory for hosting the reception at the observatory; and Wayne and Judy Hite, of The Arboretum at Flagstaff, who were instrumental in allowing us to host a reception there for Eastern European participants.

*Alan Harris
Pasadena, California*

*Edward Bowell
Flagstaff, Arizona*

LIST OF PARTICIPANTS

- Michael F. A'Hearn**
*University of Maryland
 Astronomy Program
 College Park MD 20742, USA
 Phone: 301-454-6076*
- James Abraham**
*Saturday Evening Post
 4825 North Arlington Avenue
 Indianapolis IN 46226, USA
 Phone: 317-226-3860*
- Thomas J. Ahrens**
*California Institute of Technology
 Seismological Laboratory
 Mail Code 252-21
 Pasadena CA 91125, USA
 Phone: 818-356-6906*
- Elena V. Alfimova**
*Shternberg State Astronomical Institute
 Department of Celestial Mechanics
 Moscow 119899, RUSSIA
 Phone: 0893764*
- Judith H. Allton**
*Lockheed Engineering & Sciences
 2400 NASA Road 1
 Mail Code C23
 Houston TX 77058, USA
 Phone: 713-483-5766*
- E. Alvarez del Castillo**
*University of Arizona
 Steward Observatory
 Tucson AZ 85721, USA*
- Claude Arpigny**
*Institut d'Astrophysique
 Université de Liège
 Avenue de Cointe, 5
 B-4200 Liège, BELGIUM*
- Angelo Atzei**
*ESTEC
 Postbus 299
 2200 AG Noordwijk
 THE NETHERLANDS
 Phone: 31-1719-83418*
- Pulat B. Babadzhanov**
*Institute of Astrophysics
 Tajik Academy of Sciences
 22 Sviridenko Str.
 Dushanbe 734670, TAJIKISTAN
 Phone: 8-3772-27-46-14*
- Jack W. Baggaley**
*University of Canterbury
 Physics Department
 Christchurch, NEW ZEALAND
 Phone: 64-3-667001*
- Philippe Baille**
*Royal Military College
 Math Department
 Kingston, Ontario, K7K 5LO, CANADA
 Phone: 613-541-6095*
- Antonio G. Baratta**
*Osservatorio Astrofisico
 Citta' Universitaria
 Viale A. Doria 6
 95125 Catania, ITALY
 Phone: 39-95-330533*
- Patricia Barnes-Svarney**
*2603 Smith Drive
 Endwell NY 13760, USA
 Phone: 607-748-0892*
- J. Paul and Dorothy Barringer**
*Barringer Crater Company
 20 Nassau Street Box 672
 Princeton NJ 08542, USA
 Phone: 609-924-4660*
- M. Antonietta Barucci**
*Observatoire de Paris
 5, Place J. Janssen
 92195 Meudon
 Principal Cedex, FRANCE
 Phone: 1-4507-7539*
- Annick Bec-Borsenberger**
*Bureau des Longitudes
 77 Av. Denfert-Rochereau
 F-75014 Paris, FRANCE
 Phone: 16-1-4052-2273*
- Oleg I. Belkovich**
*Engelhardt Astronomical Observatory
 Observatory Station
 Kazan SU-422526, RUSSIA
 Phone: 32-48-27*
- Michael J. Belton**
*Kitt Peak National Observatory
 950 N. Cherry Ave.
 Tucson AZ 85719, USA
 Phone: 602-327-5511*
- Philippe Bendjoya**
*O.C.A. Observatoire de Nice
 BP 139
 06003 Nice Cedex, FRANCE
 Phone: 92-00-31-59*
- Gretchen K. Benedix**
*California Space Institute
 Mail Code O216
 La Jolla CA 92093-0216, USA
 Phone: 619-534-5827*
- Daniel Benest**
*O.C.A. Observatoire de Nice
 BP 139
 06003 Nice Cedex, FRANCE
 Phone: 92-00-31-08*
- Jean Bénit**
*KFA
 Julich, GERMANY
 Phone: 492661616152*
- Lance Benner**
*Washington University
 Department of Earth and
 Planetary Sciences
 One Brookings Dr., Box 1169
 St. Louis MO 63130, USA
 Phone: 314-889-5744*
- A. C. Beresford**
*Flinders University
 School of Physics
 Box 2100
 Adelaide 5001, AUSTRALIA
 Phone: 6182012679*
- Richard P. Binzel**
*Massachusetts Institute of Technology
 Department of Earth, Atmospheric and
 Planetary Sciences
 54-426
 Cambridge MA 02139, USA
 Phone: 617-253-6486*
- D. F. Blake**
*NASA Ames Research Center
 Mail Stop 239-4
 Moffett Field CA 94035-1000, USA
 Phone: 415-604-4816*
- Dominique Bockelée-Morvan**
*Observatoire de Paris
 5, Place J. Janssen
 92195 Meudon
 Principal Cedex, FRANCE*
- Hermann Boehnhardt**
*ESOC/MBP
 Wilhelm-Glaessing-Strasse 31
 W-6100 Darmstadt, GERMANY
 Phone: 49-6151902810*
- Daniel C. Boice**
*Southwest Research Institute
 Space Sciences Division
 6220 Culebra Rd.
 San Antonio TX 78228-0510, USA
 Phone: 512-522-3782*
- James Boswell**
*University of Sheffield
 Department of Physics
 Sheffield, S3 7RH, UNITED KINGDOM
 Phone: 0742-768555*

Edward Bowell <i>Lowell Observatory 1400 W. Mars Hill Road Flagstaff AZ 86001, USA Phone: 602-774-3358</i>	Luke Burke <i>University of Florida 211 SSRB Gainesville FL 32611, USA Phone: 904-392-2058</i>	Bertrand Chauvineau <i>OCA/CERGA Avenue Copernic 06130 Grasse, FRANCE Phone: 33-93-36-58-49</i>
John C. Brandt <i>University of Colorado LASP Campus Box 392 Boulder CO 80309, USA Phone: 303-492-3215</i>	Robert Burnham <i>Astronomy Magazine P. O. Box 1612 Circle Waukesha WI 53187, USA Phone: 414-7968776 x572</i>	Galina P. Chernova <i>Institute of Astrophysics Dushanbe 734670, TAJIKISTAN Phone: 27-37-93</i>
Daniel Britt <i>University of Arizona Lunar and Planetary Laboratory Tucson AZ 85721, USA Phone: 602-621-8805</i>	Bobby Bus <i>Massachusetts Institute of Technology Department of Earth, Atmospheric and Planetary Sciences Cambridge MA 02139, USA</i>	Nikolai S. Chernykh <i>Crimean Astrophysical Observatory Nauchnyj 334413, CRIMEA</i>
C. Leigh Broadhurst <i>NASA Goddard Space Flight Center Code 693 Greenbelt MD 20771, USA Phone: 301-286-2563</i>	George Busenberg <i>472 Greensboro Ct. Claremont CA 91711, USA Phone: 714-626-5037</i>	Klim I. Churyumov <i>Astronomical Observatory of Kiev University Observatornaya Street, 3 Kiev 252053, UKRAINE Phone: 216-19-94</i>
Michael Brown <i>University of California/Berkeley Department of Astronomy Berkeley CA 94720, USA Phone: 415-643-8594</i>	Humberto Campins <i>University of Florida Department of Astronomy 211 SSRB Gainesville FL 32611, USA Phone: 904-392-3066</i>	Jacques Clairemidi <i>Observatoire Besancon BP 1615 25000 Besancon Cedex, FRANCE Phone: 33-81-66-69-15</i>
Peter Brown <i>International Meteor Organization 181 Sifton Avenue Fort McMurray, Alberta T9H 4V7, CANADA Phone: 403-743-8625</i>	Mario Carpino <i>Osservatorio Astron. de Brera Via Brera, 28 20121 Milano, ITALY</i>	Anita Cochran <i>The University of Texas McDonald Observatory Austin TX 78712-1083, USA Phone: 512-471-1471</i>
Donald Brownlee <i>University of Washington Department of Astronomy Physics Hall Seattle WA 98195, USA Phone: 206-543-8575</i>	Uri Carsenty <i>D.L.R., Oberpfaffenhofen OE-PE 8031 Wessling, GERMANY Phone: 49-8153-281328</i>	William Cochran <i>The University of Texas McDonald Observatory RLM 15.308 Austin TX 78712, USA Phone: 512-471-6474</i>
Scott Alan Budzien <i>Johns Hopkins University Department of Physics and Astronomy Baltimore MD 21218, USA Phone: 301-338-8485</i>	Claudio Casacci <i>Via Adau 12 10080 S. Abenigo Canauese Torino, ITALY Phone: 39-11-725089</i>	Michael R. Combi <i>University of Michigan Space Physics Research Lab. 2455 Hayward Street Ann Arbor MI 48109, USA Phone: 313-764-7226</i>
Marc W. Buie <i>Lowell Observatory 1400 W. Mars Hill Road Flagstaff AZ 86001, USA</i>	Alberto Cellino <i>Observatorio Astronomino di Torino Strada Observatorio 20 10025 Pino Torinese (70), ITALY Phone: 39-11-841067</i>	Angioletta Coradini <i>CNR Reparto Planetologia Viale dell'Università 00185 Rome, ITALY Phone: 39-6-4456951</i>
Bonnie Buratti <i>Jet Propulsion Laboratory Mail Stop 183-501 4800 Oak Grove Drive Pasadena CA 91109, USA Phone: 818-354-7427</i>	Zdenek Ceplecha <i>Ondrejov Observatory 251 65 Ondrejov, CZECHOSLOVAKIA Phone: 42-20485201</i>	Marcello Coradini <i>European Space Agency 8-10 Rue Mario Nikis 75738 Paris Cedex 15, FRANCE Phone: 33-1-42737555</i>
Roberto Burchi <i>Osservatorio Astronomico di Collurania 64100 Teramo, ITALY Phone: 39-861-210490</i>	Clark R. Chapman <i>Planetary Science Institute 2421 East 6th Street Tucson AZ 85719, USA Phone: 602-881-0332</i>	Jacques Crovisier <i>Observatoire de Meudon F-92195 Meudon, FRANCE Phone: 1 45 07 75 99</i>
		Clifford Cunningham <i>250 Frederick St. Apt. 1707 Kitchener, Ontario N2H 2N1, CANADA Phone: 519-578-9597</i>

- Mats Dahlgren**
*Astronomical Observatory
 Box 515
 75 120 Uppsala, SWEDEN
 Phone: 4618525724*
- John Davies**
*Royal Observatory
 Blackford Hill
 Edinburgh EH93HJ
 UNITED KINGDOM
 Phone: 44 31 668 8299*
- Paul Davies**
*Lowell Observatory
 1400 W. Mars Hill Road
 Flagstaff AZ 86001, USA*
- Donald R. Davis**
*Planetary Science Institute
 2421 E. 6th Street
 Tucson AZ 85719, USA
 Phone: 602-881-0332*
- Colette M. de la Barre**
*1741 Granville Avenue #102
 Los Angeles CA 90025, USA
 Phone: 213-820-7137*
- Magda Delva**
*Space Research Institute
 INFFELDG. 12
 A-8010 Graz, AUSTRIA
 Phone: 03768737444*
- Stanley F. Dermott**
*University of Florida
 Department of Astronomy
 SSRB 224
 Gainesville FL 32611, USA
 Phone: 904-392-3748*
- Michael A. Disanti**
*NASA Goddard Space Flight Center
 Mail Code 693
 Greenbelt MD 20771, USA
 Phone: 301-286-7036*
- Neil Divine**
*Jet Propulsion Laboratory
 Mail Stop 301-460
 4800 Oak Grove Drive
 Pasadena CA 91109, USA
 Phone: 818-354-4992*
- Luke Dones**
*CITA
 University of Toronto
 60 St. George St.
 Toronto, Ontario M5S 1A1, CANADA
 Phone: 416-978-3863*
- François V. Dossin**
*Institut d'Astrophysique
 Université de Liège
 Avenue de Cointe, 5
 B-4200 Liège, BELGIUM
 Phone: 41-373584*
- Edward M. Drobyshevski**
*Russian Academy of Sciences
 A.F. Ioffe Physico-Tech. Inst.
 19402 St. Petersburg K-21, RUSSIA*
- David F. Dudek**
*615 Esplanade Unit 712
 Redondo Beach CA 90277-4140, USA
 Phone: 213-316-2646*
- David W. Dunham**
*Computer Sciences Corp.
 10110 Aerospace Road
 Lanham MD 20706, USA
 Phone: 301-794-1392*
- Daniel D. Durda**
*University of Florida
 Department of Astronomy
 211 Space Sciences Research Bldg.
 Gainesville FL 32611, USA
 Phone: 904-392-2052*
- Peter Eberhardt**
*University of Bern
 Physikalisches Institut
 Sidlerstrasse 5
 CH-3012 Bern, SWITZERLAND
 Phone: 4131654404*
- Eric W. Elst**
*Royal Observatory at Uccle
 Ringlaan 3
 B-1180 Uccle, BELGIUM
 Phone: 02-3730309*
- Steffi Engel**
*University of Arizona
 Lunar and Planetary Laboratory
 Tucson AZ 85721, USA
 Phone: 602-621-4655*
- Sylvie Espinasse**
*CNR-Reparto Planetologia
 Viale dell' Università, 11
 001855 Rome, ITALY
 Phone: 06/4456951*
- Paolo Farinella**
*Università di Pisa
 Dipartimento di Matematica
 Via Buonarroti
 I-56127 Pisa, ITALY
 Phone: 50 599554*
- Costanzo Federico**
*CNR-Reparto Planetologia
 Viale dell' Università, 11
 00185 Rome, ITALY
 Phone: 075-4693223*
- Paul D. Feldman**
*Johns Hopkins University
 Department of Physics and Astronomy
 Baltimore MD 21218, USA
 Phone: 301-338-7339*
- Ignacio Ferrin**
*Universidad de los Andes
 Facultad de Ciencias-Grupo
 Apartado 700
 Merida 5101, VENEZUELA*
- Anthony J. Ferro**
*Arizona State University
 Physics Department
 Astronomy Group
 Tempe AZ 85287-1504, USA
 Phone: 602-465-7719*
- Michel Festou**
*Observatoire de Midi-Pyrénées
 URA 285 du CNRS
 14 Ave. E. Belin
 31400, FRANCE
 Phone: 33-61-33-29-29*
- Uwe Fink**
*University of Arizona
 Lunar and Planetary Laboratory
 Tucson AZ 85721, USA
 Phone: 602-745-0155*
- Alan Fitzsimmons**
*Queen's University of Belfast
 APS Division
 Department of Pure and Applied Physics
 Belfast BT7 1NN, UNITED KINGDOM
 Phone: 0232 245133*
- George J. Flynn**
*SUNY at Plattsburgh
 Department of Physics
 Plattsburgh NY 12901, USA
 Phone: 518-564-3156*
- Marina Fomenkova**
*California Space Institute O216
 La Jolla CA 92093-0216, USA
 Phone: 619-534-5827*
- Space Research Institute**
*Profsoyuznaya 84/32
 Moscow 117810, RUSSIA
 Phone: 619-534-5827*
- Otto Franz**
*Lowell Observatory
 1400 W. Mars Hill Road
 Flagstaff AZ 86701, USA*
- Christiane Froeschlé**
*O.C.A. Observatoire de Nice
 BP 139
 06003 Nice Cedex, FRANCE
 Phone: 9200-3011*
- Claude Froeschlé**
*O.C.A. Observatoire de Nice
 BP 139
 06003 Nice Cedex, FRANCE
 Phone: 93017985*

- Marcello Fulchignoni**
*Rome University
 Istituto Astronomico
 Via Lancisi 29
 00161 Rome, ITALY
 Phone: 39-4403734*
- Michael J. Gaffey**
*Rensselaer Polytechnic Institute
 Geology Department, West Hall
 Troy NY 12181-3590, USA
 Phone: 518-276-6300*
- Henry L. Giclas**
*120 E. Elm Avenue
 Flagstaff AZ 86001, USA
 Phone: 602-774-4769*
- Raymond Goldstein**
*Jet Propulsion Laboratory
 Mail Stop 169-506
 4800 Oak Grove Drive
 Pasadena CA 91109, USA
 Phone: 818-354-0241*
- Ed Grayzeck**
*University of Maryland
 Astronomy Program
 College Park MD 20742, USA
 Phone: 301-405-1539*
- Jacklyn Green**
*Jet Propulsion Laboratory
 Mail Stop 183-501
 4800 Oak Grove Drive
 Pasadena CA 91109, USA*
- Manfred G. Grensemann**
*European Space Agency
 SCI/SP, ESTEC
 Noordwijk, THE NETHERLANDS
 Phone: 31-171983551*
- Eberhard Grün**
*Max-Planck-Institut für Kernphysik
 Postfach 103980
 6900 Heidelberg 1, GERMANY
 Phone: 49-6221-516-478*
- William Grundy**
*University of Arizona
 Lunar and Planetary Laboratory
 Department of Planetary Science
 Tucson AZ 85721, USA
 Phone: 602-621-2692*
- Bo Å. S. Gustafson**
*University of Florida
 211 SSRB
 Astronomy Department
 Gainesville FL 32611, USA
 Phone: 904-392-7677*
- Gerhard Hahn**
*Astronomiska Observatoriet
 Box 515
 S-751-20 Uppsala, SWEDEN
 Phone: 46-18113522*
- Michael E. Haken**
*University of Maryland
 Astronomy Program
 College Park MD 20742, USA
 Phone: 301-405-1504*
- Alan Hale**
*New Mexico State University
 Department of Astronomy
 P.O. Box 4500
 Las Cruces NM 88003, USA
 Phone: 505-646-3409*
- Douglas P. Hamilton**
*Cornell University
 408 Space Sciences Bldg.
 Ithaca NY 14853-6801, USA
 Phone: 607-255-6307*
- Alan W. Harris**
*Jet Propulsion Laboratory
 Mail Stop 183-501
 4800 Oak Grove Drive
 Pasadena CA 91109, USA
 Phone: 818-354-6741*
- Jack B. Hartung**
*Solar System Associates
 600 East 5th Street
 Des Moines IA 50309, USA
 Phone: 319-335-1575*
- Hitoshi Hasegawa**
*ASTEC, Inc.
 BR Ichigaya
 6 Minamicho Shinjuku
 Tokyo 162, JAPAN
 Phone: 81352615974*
- Robert Hawkes**
*Mount Allison University
 Physics Department
 Sackville NB, E0A 3C0, CANADA
 Phone: 506-364-2582*
- Martin Hechler**
*ESA/ESOC
 Robert-Bosch-STR5
 61 Darmstadt, GERMANY
 Phone: 49-6151-902291*
- Eleanor F. Helin**
*Jet Propulsion Laboratory
 Mail Stop 183-501
 4800 Oak Grove Drive
 Pasadena CA 91109, USA
 Phone: 818-354-4606*
- Rod Heyd**
*Arizona State University
 Department of Physics and Astronomy
 Tempe AZ 85287-1504, USA
 Phone: 602-965-1986*
- Michael Hicks**
*University of Arizona
 Lunar and Planetary Laboratory
 Tucson AZ 85721, USA
 Phone: 602-621-2692*
- Susan Hoban**
*NASA Goddard Space Flight Center
 Code 693
 Greenbelt MD 20771, USA
 Phone: 301-286-3840*
- Martin Hoffmann**
*Observatorium Hoher List
 D-5568 Daun, GERMANY
 Phone: 49-6592-2937*
- Henry E. Holt**
*Northern Arizona University
 2036 N. Crescent Drive
 Flagstaff AZ 86001, USA
 Phone: 602-527-7000*
- Ellen S. Howell**
*University of Arizona
 Lunar and Planetary Laboratory
 Tucson AZ 85721, USA
 Phone: 602-621-6950*
- Walter Huebner**
*Southwest Research Institute
 Space Sciences Division
 6220 Culebra Road
 San Antonio TX 78228-0510, USA
 Phone: 512-522-3385*
- Wesley T. Huntress Jr.**
*NASA Headquarters
 Code SL
 Washington DC 20546, USA
 Phone: 202-453-1588*
- Kimmo Innanen**
*York University
 Physics Department
 4700 Keele Street
 North York, Ont. M3J 1P3, CANADA
 Phone: 416-736-5051*
- Violeta Ivanova**
*Bulgarian Academy of Sciences
 Department of Astronomy
 Blvd. Lenin 72
 Sofia 1784, BULGARIA
 Phone: 74-311 (559)*
- Albert A. Jackson**
*Lockheed Engineering and Sciences Co.
 2400 NASA Road 1, Code C23
 Houston TX 77058, USA
 Phone: 713-333-7679*
- William M. Jackson**
*University of California
 Department of Chemistry
 Davis CA 95616, USA
 Phone: 916-752-6310*

- Peter Jenniskens**
*Leiden Observatory
 Niels Bohrweg 2
 2333 CA Leiden, THE NETHERLANDS
 Phone: 71-275850*
- David Jewitt**
*Institute for Astronomy
 2680 Woodlawn Drive
 Honolulu HI 96822, USA
 Phone: 808-948-6664*
- Klaus Jockers**
*Max-Planck-Institut für Aeronomie
 D-3411
 Katlenburg-Lindau 3, GERMANY
 Phone: 5556-401-293*
- James Jones**
*University of Western Ontario
 Physics Department
 London, Ontario N7A 3K7, CANADA
 Phone: 519-661-3283*
- William Jones**
*University of Sheffield
 Department of Physics
 Sheffield S3 7RH, UNITED KINGDOM
 Phone: 0742 768555 x 4279*
- William H. Julian**
*New Mexico State University
 Department of Mathematical Sciences
 Las Cruces NM 88003, USA*
- Mikko Kaasalainen**
*University of Helsinki
 Observatory and Astrophys. Lab.
 Tahtitorinmaki
 SF-00130 Helsinki, FINLAND
 Phone: 358-1912944*
- Colin Keay**
*University of Newcastle
 Physics Department
 Newcastle NSW 2308, AUSTRALIA
 Phone: 61-49-215451*
- H. Uwe Keller**
*Max Planck Institut für Aeronomie
 D-3411 Katlenburg-Lindau, GERMANY
 Phone: 49-5556-401419*
- Sang J. Kim**
*University of Maryland
 Astronomy Program
 College Park MD 20742, USA
 Phone: 301-405-1546*
- Tina King**
*U. S. Geological Survey
 2255 N. Gemini Drive
 Flagstaff AZ 86001, USA*
- Nicolai N. Kiselev**
*Institute of Astrophysics
 Tajik Academy of Sciences
 22 Sviridenko Str.
 Dushanbe 734670, TAJIKISTAN
 Phone: 8-3772-27-46-14*
- James Jay Klevett**
*University of Maryland
 Astronomy Program
 College Park MD 20742, USA
 Phone: 301-593-1876*
- Marvin Kleine**
*Arizona State University
 Department of Physics and Astronomy
 Tempe AZ 85287-1504, USA
 Phone: 602-965-1986*
- Jurgen Klinger**
*Laboratoire de Glaciologie
 B.P. No. 96
 F-38402 St. Martin d'Heres
 Cedex, FRANCE
 Phone: 33-76425872*
- Zoran Knežević**
*Astronomska Opservatorija
 Volgina 7
 11050 Beograd, SERBIA
 Phone: 38 11 404 513*
- Hermann Kochan**
*DLR - RS
 P. O. Box 906058
 D-5000 Kohn 90, GERMANY
 Phone: 49/2203/601-2667*
- Harald Kohl**
*Max-Planck-Inst. für Kernphysik
 P.O. Box 103980
 D-6900 Heidelberg, GERMANY
 Phone: 6221-516543*
- Gabriele Kölzer**
*Abteilung Nuklearchemie
 am Institut für Biocchemie
 zulpicher Str. 47
 5000 Köln 1, GERMANY
 Phone: 492214702682*
- Norbert Kömle**
*Osterreichische Akademie der
 Wissenschaften, Inst. Weltraum.
 A-8042 Graz
 Lustbuhelstrasse 46, AUSTRIA
 Phone: 0316 41 3 32/13*
- Detlef Koschny**
*Technische Universität München
 Lehrstuhl für Raumfahrttechnik
 Richard-Wagner-Str. 18,
 D-8000 München 2, GERMANY
 Phone: 89-2105-2578*
- Akira Kouchi**
*LAF Huygens Lab.
 University of Leiden
 Leiden, THE NETHERLANDS
 Phone: 071-275943*
- Ekkehard Kührt**
*Max Planck Institut für Aeronomie
 D-3411 Katlenburg-Lindau, GERMANY*
- Ravi Kulkarni**
*University of Maryland
 Astronomy Program
 College Park MD 20742, USA
 Phone: 301 405-1560*
- George Kurkhuli**
*Abastumani Astrophysical Observatory
 Mt. Kanobili 383762, GEORGIA
 Phone: 37-52-26*
- Yves Langevin**
*Inst. de' Astrophysique Spatiale
 Batiment 120
 Campus d'Orsay
 F-91405 Orsay Cedex, FRANCE
 Phone: 33-1-69858681*
- Stephen Larson**
*University of Arizona
 Lunar and Planetary Laboratory
 Tucson AZ 85721, USA
 Phone: 602-621-4973*
- Kevin Lawler**
*U. S. Geological Survey
 2255 N. Gemini Drive
 Flagstaff AZ 86001, USA*
- Mark Lawler**
*University of Washington
 Astronomy Department, FM-20
 Seattle WA 98195, USA*
- Pascal Lee**
*Cornell University
 404 Space Sciences Bldg.
 Ithaca NY 14853-6801, USA
 Phone: 607-255-6546*
- Anny-Chantal Levasseur-Regourd**
*Université Paris
 Service d'Aeronomie
 BP3
 91371 Verrières, FRANCE
 Phone: 33 164474293*
- Harold Levison**
*USNO
 OM Department
 Washington DC 20392, USA
 Phone: 202-653-1568*
- David H. Levy**
*120 William Carey St.
 Tucson AZ 85747, USA
 Phone: 602-762-5638*

David J. Lien <i>Bucknell University Department of Physics Lewisburg PA 17837, USA Phone: 717-524-3767</i>	Clifford Matthews <i>1010 Twelfth Street Wilmette IL 60091, USA Phone: 312-996-5393</i>	Sylvia Miller <i>Jet Propulsion Laboratory 4800 Oak Grove Dr. Pasadena CA 91109, USA Phone: 818-354-2947</i>
Bertil A. Lindblad <i>Lund Observatory Box 43 S 22100 Lund, SWEDEN Phone: 4646107301</i>	Mildred Matthews <i>University of Arizona Lunar and Planetary Laboratory Tucson AZ 85721, USA Phone: 6020621-2902</i>	Robert L. Millis <i>Lowell Observatory 1400 W. Mars Hill Road Flagstaff, AZ 86001, USA Phone: 602-774-3358</i>
Mats Lindgren <i>Astronomiska Observatoriet Box 515 S-751 20 Uppsala, SWEDEN Phone: 461852S724</i>	Alain Maury <i>Telescope de Schmidt 06460 Clauzelles, FRANCE Phone: 011-33-93426270</i>	Alice Monet <i>U. S. Naval Observatory Flagstaff Station P.O. Box 1149 Flagstaff AZ 86002, USA Phone: 602-779-5132</i>
Carey Lisse <i>ST Systems, Inc. NASA Goddard Space Flight Center Code 685 Greenbelt MD 20771, USA Phone: 301-286-4559</i>	Neil McBride <i>University of Sheffield Department of Physics Sheffield, S3 7RH, UNITED KINGDOM Phone: 0742-768S55 x4284</i>	Guy Moreels <i>Observatoire de Bisançon 41 bis Ave. de L'Observatoire 25000 Bisançon, FRANCE Phone: 81 666900</i>
Jane Luu <i>Center for Astrophysics 60 Garden Street Cambridge MA 02138, USA Phone: 808-988-2199</i>	Tony McDonnell <i>Canterbury U. K. Unit Space Sciences Canterbury CTZ 7NR, UNITED KINGDOM Phone: 44 227 459616</i>	Thomas Morgan <i>NASA Headquarters Code ELC Washington DC 20546, USA Phone: FTS 453-1616</i>
Per Magnusson <i>Queen Mary & Westfield College School of Mathematical Sciences Mile End Road London E1 4NS, UNITED KINGDOM Phone: 44 71 975 5484</i>	Lucy Ann McFadden <i>University of Maryland Astronomy Program College Park MD 20742, USA</i>	Esther Morrow <i>California Space Institute O216 La Jolla CA 92093-0216, USA Phone: 619-534-5827</i>
Allesandro Manara <i>Osservatorio Astron. di Brera Via Brera, 28 I-20121 Milano, ITALY Phone: 39-2875555</i>	William McKinnon <i>Washington University Department of Earth and Planetary Sciences One Brookings Drive St. Louis MO 63130, USA Phone: 314-889-5604</i>	Stefano Mottola <i>D.L.R. Oberpfaffenhofen Plan. Remote Sensing Section 8031 Wessling, GERMANY Phone: 0049-8153-28595</i>
Robert Marcialis <i>Jet Propulsion Laboratory Mail Stop 183-501 4800 Oak Grove Drive Pasadena CA 91109, USA Phone: 818-584-2922</i>	Roland Meier <i>University of Bern Physik. Inst. Sidlerstr. 5 3012 Bern, SWITZERLAND Phone: 31-65-44-28</i>	Beatrice E. A. Mueller <i>Kitt Peak National Observatory 950 N. Cherry Avenue Tucson AZ 85719, USA Phone: 602-325-9220</i>
Brian G. Marsden <i>Harvard-Smithsonian Center for Astrophysics 60 Garden St. Cambridge MA 02138, USA Phone: 617-495-7244</i>	Flavio Mendez <i>Lowell Observatory 1400 W. Mars Hill Road Flagstaff AZ 86001, USA Phone: 602-774-3358</i>	Jean Mueller <i>Palomar Observatory Palomar Mountain CA 92060, USA Phone: 619-742-3808</i>
John J. Matese <i>University of Southwest Louisiana Physics Department Box 44210 Lafayette LA 70504, USA Phone: 318-0231-6697</i>	Tadeusz Michałowski <i>Adam Mickiewicz University Astronomical Observatory Słoneczna 36 60-286 Poznań, POLAND Phone: (0-61) 679-670</i>	Karri Muinonen <i>Lowell Observatory 1400 W. Mars Hill Road Flagstaff AZ 86001, USA Phone: 602-774-3358</i>
	Andrea Milani <i>University of Pisa Via Buonarroti 2 56127 Pisa, ITALY Phone: 3950599557</i>	Michael Mumma <i>NASA Goddard Space Flight Center Code 693 Infrared and Radio Astronomy Branch Greenbelt MD 20771, USA Phone: 301-286-6994</i>

- Carl D. Murray**
*Queen Mary & Westfield College
 Mile End Road
 Astronomy Unit
 London E1 4NS, UNITED KINGDOM
 Phone: 44-1-075-5456*
- Tsuko Nakamura**
*National Astronomical Observatory
 2-21-1 Osawa
 Mitaka
 Tokyo 181, JAPAN
 Phone: 0422-41-3628*
- Orlando A. Naranjo**
*Universidad de los Andes
 Facultad de Ciencias-Grupo
 Apartado 690
 Merida 5101, VENEZUELA
 Phone: 058 074 401330*
- Michael Nolan**
*University of Arizona
 Lunar and Planetary Laboratory
 325 Space Science #92
 Tucson AZ 85721, USA
 Phone: 602-621-4655*
- Pascal Oberti**
*Observatoire de la Cote D'Azur
 Avenue N. Copernic
 F-06130 Grasse, FRANCE
 Phone: 33/93 36 58 99*
- Michelle Olmstead**
*Lowell Observatory
 1400 W. Mars Hill Road
 Flagstaff AZ 86001, USA
 Phone: 602-774-3358*
- Ronald Oriti**
*Santa Rosa Jr. College
 Planitarium Director
 1501 Medocino Avenue
 Santa Rosa CA 95401, USA
 Phone: 707-823-1605*
- David J. Osip**
*University of Florida
 Department of Astronomy
 SSRB 224
 Gainesville FL 32611, USA
 Phone: 904-392-3748*
- Steven J. Ostro**
*Jet Propulsion Laboratory
 Mail Stop 300-233
 4800 Oak Grove Drive
 Pasadena CA 91109, USA
 Phone: 818-354-3173*
- M. Ottink**
*Bongweg 2gG.
 3192 NE
 Hooguliet
 Rotterdam, THE NETHERLANDS
 Phone: 3110-4166224*
- Patrick Palmer**
*University of Chicago
 Department of Astronomy and Astrophysics
 5640 S. Ellis Ave.
 Chicago IL 60637, USA
 Phone: 312-702-7972*
- Paolo Paolicchi**
*Dipartimento di Fisica
 Università di Pisa
 56100 Pisa, ITALY*
- Thierry Pauwels**
*Koninklijke Sterrenwacht
 van Belgie
 Ringlaan 3 B-1180
 Brussels, BELGIUM
 Phone: 32-2-3730225*
- Stanton J. Peale**
*University California
 Department of Physics
 Santa Barbara CA 93106, USA
 Phone: 805-961-2977*
- Carolyn C. Petersen**
*University of Colorado
 LASP
 Campus Box 392
 Boulder CO 80309-0392, USA
 Phone: 303-492-8208*
- Eduard M. Pittich**
*Astron. Inst. of the Slovak
 Academy of Sciences
 Dubravská cesta 9
 842 28 Bratislava, CZECHOSLOVAKIA
 Phone: 42-7-375157*
- C. Debi Prasad**
*Max-Planck-Institut für Aeronomie
 Postfach 20
 Max-Planck-Strasse 2
 D-3411 Katlenburg-Lindau, GERMANY
 Phone: 49-5556-401 343*
- David L. Rabinowitz**
*University of Arizona
 Lunar and Planetary Laboratory
 Tucson AZ 85721, USA
 Phone: 602-621-2774*
- Jurgen Rahe**
*NASA Headquarters
 Code SL
 Washington DC 20546, USA
 Phone: 202-453-1597*
- R. Rajamohan**
*Indian Inst. of Astrophysics
 Koramangala
 Bangalore 560034, INDIA
 Phone: 530672 to 530676*
- Cora E. Randall**
*University of Colorado
 LASP
 Campus Box 392
 Boulder CO 80309-0392, USA
 Phone: 303-492-8208*
- Gibson Reaves**
*University of Southern California
 Department of Astronomy
 Los Angeles CA 90089-1342, USA
 Phone: 213-740-6330*
- Russell Redman**
*N. R. C. of Canada
 100 Sussex Drive
 Ottawa, Ontario, K1A 0R6, CANADA
 Phone: 613-991-5837*
- David Reitzel**
*1230 West 29th Street #16
 Los Angeles CA 90007, USA
 Phone: 213-749-2613*
- Jurgen Rendtel**
*International Meteor Organization
 Gontardstr. 11
 Potsdam 1570, GERMANY
 Phone: (03733) 310219*
- Terrence W. Rettig**
*University of Notre Dame
 Department Physics
 Notre Dame IN 46556, USA
 Phone: 219-272-8146*
- Dennis C. Reuter**
*NASA Goddard Space Flight Center
 Code 693
 Greenbelt MD 20771, USA
 Phone: 301-286-2042*
- Hans Rickman**
*Astronomiska Observatoriet
 Box 515
 S-751-20 Uppsala, SWEDEN
 Phone: 46-18113522*
- Frans Rietmeijer**
*University of New Mexico
 Department of Geology
 Albuquerque NM 87131, USA
 Phone: 505-277-2035*
- Elizabeth Roemer**
*University of Arizona
 Lunar and Planetary Laboratory
 Tucson AZ 85721, USA
 Phone: 602-621-2897*
- Elizabeth E. Roettger**
*NASA Goddard Space Flight Center
 Planetary Systems Branch
 Code 693
 Greenbelt MD 20771, USA
 Phone: 301-338-8378*

Alessandra Rotundi
*Rome University
Istituto Astronomico
University d'Roma
Via Lancisi 29
00161 Rome, ITALY*

Philippe Rousselot
*Observatoire de Besancon
BP 1615
25010 Besancon Cedex, FRANCE
Phone: 81666915*

Ken Russell
*Anglo Australian Observatory
Private Bag
Coonabarabran, NSW, AUSTRALIA
Phone: 068 421 622*

Nalin Samarasinha
*University of Maryland
Astronomy Program
College Park MD 20742, USA
Phone: 301-4051544*

Takehiko Satoh
*Science University of Tokyo
1-3 Kagurazaka
Shinjuku-ku
Tokyo 162, JAPAN
Phone: 81332604271*

Linda M. Sauter
*Massachusetts Institute of Technology
Department of Earth,
Atmospheric and Planetary Sciences
54-426
Cambridge MA 02139, USA
Phone: 617-253-6486*

David Schleicher
*Lowell Observatory
1400 W. Mars Hill Road
Flagstaff AZ 86001, USA
Phone: 602-774-3358*

F. Peter Schloerb
*University of Massachusetts
Astronomy Lederle
Grad. Res. Tower B
Amherst MA 01003, USA
Phone: 413-545-4303*

Hans Scholl
*Observatoire de Nice
B.P. 139
06003 Nice, Cedex FRANCE
Phone: 92003041*

Rita Schulz
*Ruhr-Universität Bochum
Astronomisches Institut
Postfach 102148
D-4630 Bochum 1, GERMANY
Phone: 234-7003388*

Gerhard H. Schwehm
*European Space Agency
Space Science Department of ESA
ESTEC, Postbus 299
2200 AG Noordwijk, THE NETHERLANDS
Phone: 31-1719 83539*

James Vernon Scotti
*University of Arizona
Lunar and Planetary Laboratory
Tucson AZ 85721, USA
Phone: 602-621-2717*

Zdenek Sekanina
*Jet Propulsion Laboratory
Mail Stop 183-401
4800 Oak Grove Drive
Pasadena CA 91109, USA
Phone: 818-354-7589*

Carolyn Shoemaker
*U.S. Geological Survey
2255 N. Gemini Drive
Flagstaff AZ 86001, USA
Phone: 602-527-7181*

Eugene M. Shoemaker
*U.S. Geological Survey
2255 N. Gemini Drive
Flagstaff AZ 86001, USA
Phone: 602-527-7003*

George G. Shoemaker
*Meteor Crater Enterprises, Inc.
603 N. Beaver, Suite C
Flagstaff AZ 86001, USA
Phone: 602-774-8350*

Viktor A. Shor
*Institute of Theoretical Astronomy
Naberezhnaya Kutuzova, 10
St. Petersburg, 191187, RUSSIA
Phone: 278-88-24*

Milos Šimek
*Astronomical Institute
251 65 Ondrejov, CZECHOSLOVAKIA
Phone: 02 724525*

Grzegorz Sitarski
*Space Research Center
Bartycka 18
00-716 Warsaw, POLAND
Phone: 4822-41-00-41*

Brian Skiff
*Lowell Observatory
1400 W. Mars Hill Road
Flagstaff AZ 86001, USA
Phone: 602-774-3358*

Andrej Sokolsky
*Institute of Theoretical Astron.
Naberezhnaya Kutuzova, 10
St. Petersburg, 191187, RUSSIA*

Nina A. Solovaya
*Sternberg State Astronomical Institute
University Prospect 13
119899 Moscow V-234, RUSSIA
Phone: 709593977346*

Hyron Spinrad
*University of California
Department of Astronomy
Berkeley CA 94720, USA
Phone: 415-642-2078*

Duncan Steel
*Anglo-Australian Observatory
Private Bag
Coonabarabran, NSW 2357, AUSTRALIA
Phone: 61-68-426238*

S. Alan Stern
*Southwest Research Institute
Space Sciences Division
6220 Culebra Road
San Antonio TX 78228-0150, USA
Phone: 512-522-5127*

Jason Stiffler
*1837 Rosemount Avenue
Claremont CA 91711, USA
Phone: 714-626-5624*

Jan Štohl
*Slovak Academy of Science
Astronomical Institute
84228 Bratislava, CZECHOSLOVAKIA
Phone: 042-7-357157*

Ronald Stone
*U. S. Naval Observatory
Flagstaff Station
P.O. Box 1149
Flagstaff AZ 86002, USA
Phone: 602-779-5132*

Alex Storrs
*University of Texas
Astronomy Department
RLM 15.308
Austin TX 78712-1083, USA
Phone: 512-471-1473*

Timothy Swindle
*University of Arizona
Lunar and Planetary Laboratory
Tucson AZ 85721, USA
Phone: 602-621-4128*

Mark V. Sykes
*University of Arizona
Steward Observatory
Tucson AZ 85721, USA
Phone: 602-621-2054*

Ślawomira Szutowicz
*Space Research Centre
Ul. Bartycka 18
00-716 Warsaw, POLAND
Phone: 41-00-41 w.50*

<p>Yasuhiko Takagi <i>Department of Earth Sciences Nagoya University Chikusa-ku Nagoya, 464-01, JAPAN Phone: 81-52-783-0659</i></p>	<p>Vladimir Vanysek <i>Charles University Department of Astronomy 15000 Praha 5, CZECHOSLOVAKIA</i></p>	<p>Daniel P. Whitmire <i>University of Southwestern Louisiana Department of Physics 44210 Lafayette LA 70504, USA Phone: 318-231-6185</i></p>
<p>Gonzalo Tancredi <i>Astronomiska Observatoriet Box 515 S-75120 Uppsala, SWEDEN Phone: 018-113522</i></p>	<p>Glenn Veeder <i>Jet Propulsion Laboratory Mail Stop 183-501 4800 Oak Grove Drive Pasadena CA 91109, USA</i></p>	<p>Gareth Williams <i>Smithsonian Astrophysical Observatory 60 Garden Street Cambridge MA 02139, USA Phone: 617-495-7444</i></p>
<p>Andrew Taylor <i>University of Canterbury Physics Department Christchurch, NEW ZEALAND Phone: 6403667001</i></p>	<p>Russell G. Walker <i>Jamieson Science & Engineering 5321 Scotts Valley Drive #204 Scotts Valley CA 95066, USA</i></p>	<p>James G. Williams <i>Jet Propulsion Laboratory Mail Stop 238-332 4800 Oak Grove Drive Pasadena CA 91109, USA Phone: 818-354-6466</i></p>
<p>Edward F. Tedesco <i>Mission Research Corp. One Tara Blvd., Suite 302 Nashua NH 03062-0070, USA Phone: 603-891-0070</i></p>	<p>Lawrence Wasserman <i>Lowell Observatory 1400 W. Mars Hill Road Flagstaff AZ 86001, USA Phone: 602-774-3358</i></p>	<p>Wieslaw Wisniewski <i>University of Arizona Lunar and Planetary Laboratory Space Sciences Building Tucson AZ 85721, USA Phone: 602-621-6956</i></p>
<p>Stephen C. Tegler <i>University of Florida Department of Astronomy 212 Space Sciences Bldg. Gainesville FL 32611, USA Phone: 904-392-2052</i></p>	<p>Jun-ichi Watanabe <i>National Astronomical Observatory Osawa Mitaka, 181 Tokyo, JAPAN</i></p>	<p>Andrew Woszczyk <i>Institute of Astronomy Nicolaus Copernicus University Chopini 12/18 PL-87-100 Torun, POLAND Phone: 48 56 26037</i></p>
<p>David Tholen <i>University of Hawaii Institute for Astronomy 2680 Woodlawn Drive Honolulu HI 96822, USA Phone: 808-948-6930</i></p>	<p>Hal Weaver <i>Space Telescope Science Institute 3700 San Martin Drive Baltimore MD 21215, USA</i></p>	<p>Robert Wu <i>University of Southern California Space Sciences Center Stauffer Hall of Science 274 Los Angeles CA 90089-1341, USA Phone: 213-740-6332</i></p>
<p>Donald T. Thompson <i>Lowell Observatory 1400 W. Mars Hill Road Flagstaff AZ 86001, USA Phone: 602-774-3358</i></p>	<p>Stuart Weidenschilling <i>Planetary Science Institute 2421 East 6th Street Tucson AZ 85719, USA Phone: 602-881-0332</i></p>	<p>Zidian Wu <i>University of London Queen Mary and Westfield College Astronomy Unit, Mile End Road London E1 4NS, UNITED KINGDOM Phone: 081-983-1528</i></p>
<p>Bozenna Todorovic-Juchniewic <i>Space Research Center Bartnicka 18 00-716 Warsaw, POLAND</i></p>	<p>Paul Weissman <i>Jet Propulsion Laboratory Mail Stop 183-601 4800 Oak Grove Drive Pasadena CA 91109, USA</i></p>	<p>Susan Wyckoff <i>Arizona State University Department of Physics Tempe AZ 85287, USA Phone: 602-965-2223</i></p>
<p>Giau Paolo Tozzi <i>Oss. di Arcetri Largo E. Fermi, 5 50125 Firenze, ITALY</i></p>	<p>Randii Wesson <i>3285 Florecita Drive Altadena CA 91001, USA</i></p>	<p>Xingfa Xie <i>NASA Goddard Space Flight Center Lab for Extraterrestrial Physics Code 693 Greenbelt MD 20771, USA Phone: 301-286-3829</i></p>
<p>Paul Travis <i>P.O. Box 233 Ashland OR 97520, USA</i></p>	<p>George W. Wetherill <i>DTM-Carnegie Institution 5241 Broad Branch Road NW Washington DC 20015, USA Phone: 202-686-4375</i></p>	<p>Zhang-fan Xing <i>LAF Huygens Laboratorium Niels Bohrweg 2, Postbus 9504 2300 R.A. Leiden, THE NETHERLANDS Phone: 071275892</i></p>
<p>Bob Turner <i>30033 20 Place S.W. Federal Way WA 98023, USA</i></p>	<p>Fred L. Whipple <i>Smithsonian Astrophysical Observatory 60 Garden Street Cambridge MA 02138, USA Phone: 617-864-7383</i></p>	
<p>Thomas Van Flandern <i>META Research 6327 Western Avenue, N.W. Washington DC 20015, USA</i></p>		

Eleonora Yagudina
Institute of Applied Astronomy
8 Zhdanov Street
37042 St. Petersburg, RUSSIA

Donald K. Yeomans
Jet Propulsion Laboratory
Mail Stop 301-150
4800 Oak Grove Drive
Pasadena CA 91109, USA
Phone: 818-354-2127

James W. Young
Table Mountain Observatory
P.O. Box 367
Wrightwood CA 92397, USA
Phone: 619-249-3551

Vincenzo Zappalá
Astronomical Observatory
10025 Pino Torinese, ITALY
Phone: 39-11-842040

Ben H. Zellner
Space Telescope Science Institute
3700 San Martin Drive
Baltimore MD 21218, USA
Phone: 301-338-4729

Leslie Zimmerman
Lowell Observatory
1400 W. Mars Hill Road
Flagstaff AZ 86001, USA
Phone: 602-774-3358

Krzysztof Ziolkowski
Space Research Center
ul. Bartycka 18
00-716 Warsaw, POLAND
Phone: 22 410041

Harry Zscheeg
Bieths - Str. 1
6900 Heidelberg, GERMANY

CONTENTS

<i>Light Curve and Fan-Shaped Coma of Comet P/Tempel 2 in 1988-89</i>	
H. Akisawa, M. Tsumura, A. Nakamura, and J. Watanabe	1
<i>About Distribution and Origin of the Peculiar Group of Sporadic Meteors</i>	
V. V. Andreev	5
<i>Phobos and Deimos are Sources of Meteoroids</i>	
V. V. Andreev and O. I. Belkovich	9
<i>Determination of Meteor Flux Distribution Over the Celestial Sphere</i>	
V. V. Andreev, O. I. Belkovich, T. K. Filimonova, and V. V. Sidirov	17
<i>Fragmentation and Densities of Meteoroids</i>	
P. B. Babadzhanov	23
<i>P/Machholz 1986 VIII and Quadrantid Meteoroid Stream. Orbital Evolution and Relationship</i>	
P. B. Babadzhanov and Yu. V. Obrubov	27
<i>Radar Meteor Orbital Structure of Southern Hemisphere Cometary Dust Streams</i>	
W. J. Baggaley and A. D. Taylor	33
<i>A Southern Hemisphere Radar Meteor Orbit Survey</i>	
W. J. Baggaley, D. I. Steel, and A. D. Taylor	37
<i>Ion Produced Cometary Organic Crust</i>	
G. A. Baratta and G. Strazzulla	41
<i>Asteroids with Unusual Lightcurves: 14 Irene and 51 Nemausa</i>	
I. N. Belskaya and A. N. Dovgopol	45
<i>Low Cost Missions to Explore the Diversity of Near Earth Objects</i>	
M. J. S. Belton and A. Delamere	49
<i>Simulated Families: A Test for Different Methods of Family Identification</i>	
Ph. Bendjoya, A. Cellino, Cl. Froeschlé, and V. Zappalá	57
<i>The Use of the Wavelet Cluster Analysis for Asteroid Family Determination</i>	
Ph. Bendjoya, E. Slezak, and Cl. Froeschlé	61
<i>Bias Correction Factors for Near-Earth Asteroids</i>	
G. K. Benedix, L. A. McFadden, E. M. Morrow, and M. N. Fomenkova	65
<i>Stochasticity of Comet P/Slaughter-Burnham</i>	
D. Benest and R. Gonczi	69
<i>Observations of OH in Comet Levy with the Nançay Radio Telescope</i>	
D. Bockelée-Morvan, P. Colom, J. Crovisier, E. Gérard, and G. Bourgois	73
<i>Comet P/Tempel—Some Highlights and Conclusions from the 1988 Apparition</i>	
H. Boehnhardt, A. Bär, and L. Massonne	77
<i>Coma Imaging of Comet P/Brorsen-Metcalf at Calar Alto in Late July to Mid August 1989</i>	
H. Boehnhardt, V. Vanysek, K. Birkle, and U. Hopp	81
<i>A Preliminary Model of the Coma of 2060 Chiron</i>	
D. C. Boice, I. Konno, S. A. Stern, and W. F. Huebner	85

<i>CCD Imaging of the Inner Coma Jets of Comet P/Halley</i>	89
J. Boswell and D. W. Hughes	
<i>Initial Overview of Disconnection Events in Halley's Comet 1986</i>	93
J. C. Brandt, C. E. Randall, Y. Yi, and M. Snow	
<i>High-Resolution Observations of the Spatial and Velocity Distribution of Cometary Hydrogen</i>	97
M. E. Brown and H. Spinrad	
<i>Debris About Asteroids: Where and How Much?</i>	101
J. A. Burns and D. P. Hamilton	
<i>Gross-Fragmentation of Meteoroids and Bulk Density of Geminids from Photographic Fireball Records</i>	109
Z. Ceplecha and R. E. McCrosky	
<i>Lifetime of Binary Asteroids vs. Gravitational Encounters and Collisions</i>	113
B. Chauvineau, P. Farinella, and F. Mignard	
<i>The First Identification of C_2 Emission Bands in Comet Scorichenko-George (1989e_J) Spectrum</i>	117
K. I. Churyumov and G. F. Chorny	
<i>Influence of Solar Activity Upon Light Curves of Comets P/Halley (1986 III) and P/Churyumov-Gerasimenko (1982 VIII)</i>	121
K. I. Churyumov and V. S. Filonenko	
<i>Plasma-Beam Instabilities in Cometary Ionospheres</i>	125
K. I. Churyumov, N. Ya. Kotsarenko, G. V. Lizunov, and O. P. Verkhoglyadova	
<i>Dust and Gas Jets. Evidence for a Diffuse Source in the Halley's Coma</i>	129
J. Clairemidi, P. Roussetot, F. Vernotte, and G. Moreels	
<i>Observations of Cometary Parent Molecules with the IRAM Radio Telescope</i>	133
P. Colom, D. Despois, G. Paubert, D. Bockelée-Morvan, and J. Crovisier	
<i>Radio Spectroscopy of Comets: Recent Results and Future Prospects</i>	137
J. Crovisier	
<i>The Great Asteroid Nomenclature Controversy of 1801</i>	141
C. J. Cunningham	
<i>The Orbital Evolution of Real Asteroids Near the 4:1 Mean-Motion Resonance with Jupiter</i>	145
M. Dahlgren, G. Hahn, C.-I. Lagerkvist, and M. Lundström	
<i>Interplanetary Magnetic Field Changes and Condensations in Comet Halley's Plasma Tail</i>	149
M. Delva and K. Schwingenschuh	
<i>The Origin and Evolution of the Zodiacal Dust Cloud</i>	153
S. F. Dermott, D. D. Durda, B. Å. S. Gustafson, S. Jayaraman, Y. L. Xu, R. S. Gomes, and P. D. Nicholson	
<i>A Photometric Survey of Outer Belt Asteroids</i>	157
M. Di Martino, M. Gonano-Beurer, S. Mottola, and G. Neukum	

<i>Modeling of Asteroidal Dust Production Rates</i>	
D. D. Durda, S. F. Dermott, and B. Å. S. Gustafson	161
<i>From Asteroid Clusters to Families: A Proposal for a New Nomenclature</i>	
P. Farinella, D. R. Davis, A. Cellino, and V. Zappalá	165
<i>Injecting Asteroid Fragments into Resonances</i>	
P. Farinella, R. Gonczi, Ch. Froeschlé, and Cl. Froeschlé	167
<i>IUE Observations of Periodic Comets Tempel-2, Kopff and Tempel-1</i>	
P. D. Feldman and M. C. Festou	171
<i>Water and Dust Production Rates in Comet P/Halley Derived from Ultraviolet and Optical Observations</i>	
M. C. Festou	175
<i>The Gas Production Rate of Periodic Comet d'Arrest</i>	
M. C. Festou, P. D. Feldman, and M. F. A'Hearn	177
<i>Production Rates for Comet P/Tempel 2 from Long Slit CCD Spectroscopy</i>	
U. Fink and M. Hicks	183
<i>P/Halley: Spatial Distribution and Scale Lengths for C₂, CN, NH₂, and H₂O</i>	
U. Fink, M. Combi, and M. A. DiSanti	187
<i>Spectroscopy of D-Type Asteroids</i>	
A. Fitzsimmons, M. Dahlgren, C.-I. Lagerkvist, P. Magnusson, and I. P. Williams	191
<i>Atmospheric Entry Survival of Large Micrometeorites: Implications for Their Sources and for the Cometary Contribution to the Zodiacal Cloud</i>	
G. J. Flynn	195
<i>Polynomial Approximations of Poincaré Maps for Hamiltonian Systems</i>	
C. Froeschlé and J.-M. Petit	201
<i>The Effect of Secular Resonances in the Asteroid Region Between 2.1 and 2.4 AU</i>	
Ch. Froeschlé and H. Scholl	205
<i>A Strong 3.4 μm Emission Feature in Comet Austin 1989c1</i>	
S. F. Green, J. K. Davies, T. R. Geballe, T. Brooke, and A. T. Tokunaga	211
<i>Deimos: A Reddish, D-Type Asteroid Spectrum</i>	
W. M. Grundy and U. Fink	215
<i>Did Earth-Approaching Asteroids 3551, 3908, or 4055 Produce Meteorites?</i>	
B. Å. S. Gustafson and I. P. Williams	219
<i>Collisional and Dynamic Evolution of Dust from the Asteroid Belt</i>	
B. Å. S. Gustafson, E. Grün, S. F. Dermott, and D. D. Durda	223
<i>Long-Term Evolution of 1991 DA: A Dynamically Evolved Extinct Halley-type Comet</i>	
G. Hahn and M. E. Bailey	227
<i>Lightcurve of Comet Austin (1989c1) and Its Dust Mantle Development</i>	
H. Hasegawa and J. Watanabe	231
<i>Palomar Planet-Crossing Asteroid Survey (PCAs): Recent Discovery Rate</i>	
E. F. Helin	235

<i>Spectroscopic Observations of Comet Austin (1989c)</i>	
R. Heyd, S. Wyckoff, P. Wehinger, and P. Mack	237
<i>Metallic Atoms and Ions in Comets: Comet Halley 1986 III</i>	
S. Ibadov	241
<i>Asteroid-type Orbit Evolution Near the 5:2 Resonance</i>	
S. I. Ipatov	245
<i>Formation of Ions and Radicals from Icy Grains in Comets</i>	
W. M. Jackson	249
<i>Cometary Implications of Recent Laboratory Experiments on the Photochemistry of the C₂H and C₃H₂ Radicals</i>	
W. M. Jackson, Y. Bao, R. S. Urdahl, X. Song, J. Gosine, and C. Lu	253
<i>H₂O⁺ Structures in the Inner Plasma Tail of Comet Austin</i>	
K. Jockers, T. Bonev, and E. H. Geyer	257
<i>First Images of a Possible CO⁺-Tail of Comet P/Schwassmann-Wachmann 1 Observed Against the Dust Coma Background</i>	
K. Jockers, T. Bonev, V. Ivanova, and H. Rauer	261
<i>Doppler Velocities in the Ion Tail of Comet Levy 1990c</i>	
K. Jockers, H. Rauer, C. D. Prasad, and E. H. Geyer	265
<i>Evolution of the Quadrantid Meteor Stream</i>	
J. Jones and W. Jones	269
<i>Forward-Scatter Radiant Mapping</i>	
J. Jones and A. R. Webster	273
<i>Effect of the Geomagnetic Field on the Diffusion of Meteor Trains</i>	
W. Jones and J. Jones	277
<i>Observation of Meteors by MST Radar</i>	
W. Jones and S. P. Kingsley	281
<i>The Correlation Between Water Production Rates and Visual Magnitudes in Comets</i>	
L. Jorda, J. Crovisier, and D. W. E. Green	285
<i>Inversion Methods for Interpretation of Asteroid Lightcurves</i>	
M. Kaasalainen, L. Lamberg, and K. Lumme	289
<i>Modification of Primordial Ices by Cosmic Rays as Simulated by Cyclotron Irradiation</i>	
R. I. Kaiser and K. Roessler	293
<i>Meteor Fireball Sounds Identified</i>	
C. Keay	297
<i>On the Asteroidal Jet-Stream Flora A</i>	
J. Klačka	301
<i>Asteroid Proper Elements and Secular Resonances: Progress Report</i>	
Z. Knežević and A. Milani	305
<i>Integrated Software Package "STAMP" for Minor Planets</i>	
O. M. Kochetova and V. A. Shor	309

<i>Particle Emission from Artificial Cometary Materials</i>	313
G. Kölzer, H. Kochan, and K. Thiel	
<i>The Effect of a Non-Volatile Dust Mantle on the Energy Balance of Cometary Surface Layers</i>	317
N. I. Kömle and G. Steiner	
<i>Disturbances of Both Cometary and Earth's Magnetospheres Excited by Single Solar Flares</i>	321
I. Konno, T. Saito, Y. Kozuka, K. Nishioka, M. Saito, and T. Takahashi	
<i>A New Measurement of Thermal Conductivity of Amorphous Ice and Its Implications for the Thermal Evolution of Comets</i>	325
A. Kouchi, J. M. Greenberg, T. Yamamoto, T. Mukai, and Z. F. Xing	
<i>The Solar Wind Structure that Caused a Large-Scale Disturbance of the Plasma Tail of Comet Austin</i>	329
Y. Kozuka, I. Konno, T. Saito, and S. Numazawa	
<i>Spin Vector and Shape of 532 Herculina</i>	333
T. Kwiatkowski and T. Michalowski	
<i>Evaluating Some Computer Enhancement Algorithms that Improve the Visibility of Cometary Morphology</i>	337
S. M. Larson and C. D. Slaughter	
<i>Heliocentric Distance Dependencies of the C₂ Lifetime and C₂ Parent Production Rate in Comet P/Brorsen-Metcalf (1989o)</i>	345
M. Lazzarin, G. P. Tozzi, C. Barbieri, and M. C. Festou	
<i>Polarimetric Observations of Comet Levy 1990c and of Other Comets: Some Clues to the Evolution of Cometary Dust</i>	349
A. Ch. Levasseur-Regourd, J. B. Renard, and E. Hadamcik	
<i>The State of Knowledge Concerning the Kuiper Belt</i>	353
H. F. Levison	
<i>Numerical Simulations of Cometary Dust</i>	359
D. J. Lien	
<i>A Computer Search for Asteroid Families</i>	363
B. A. Lindblad	
<i>Activity of the Lyrid Meteor Stream</i>	367
B. A. Lindblad and V. Porubčan	
<i>Dynamical Timescales in the Jupiter Family</i>	371
M. Lindgren	
<i>Activity in Distant Comets</i>	375
J. X. Luu	
<i>Philosophy and Updating of the Asteroid Photometric Catalogue</i>	379
P. Magnusson, M. A. Barucci, M. T. Capria, M. Dahlgren, M. Fulchignoni, and C.-I. Lagerkvist	
<i>Cometary Orbital Evolution in the Outer Planetary Region</i>	381
A. Manara and G. B. Valsecchi	

<i>The Eleven Observations of Comets Recorded Between 678AD and 1114AD Recorded in the Anglo-Saxon Chronicles</i>	E. G. Mardon, A. A. Mardon, and J. Williams	385
<i>The Recovery of Asteroids After Two Observations</i>	B. G. Marsden	395
<i>Comet Nongravitational Forces and Meteoritic Impacts</i>	J. J. Matese, P. G. Whitman, and D. P. Whitmire	399
<i>The Spatial Distribution of Large Cometary Meteoroids in the Inner Solar System</i>	N. McBride and D. W. Hughes	403
<i>The Geocentric Particulate Distribution: Cometary, Asteroidal or Space Debris?</i>	J. A. M. McDonnell and P. R. Ratcliff	407
<i>Near Infrared Reflectance Spectra: Applications to Problems in Asteroids-Meteorite Relationships</i>	L. A. McFadden and A. B. Chamberlin	413
<i>Spin Vectors of Asteroids 21 Lutetia, 196 Philomela, 250 Bettina, 337 Devosa and 804 Hispania</i>	T. Michalowski	417
<i>Ground-based Observations of 951 Gaspra: CCD Lightcurves and Spectrophotometry with the Galileo Filters</i>	S. Mottola, M. Di Martino, M. Gonano-Beurer, H. Hoffmann, and G. Neukum	421
<i>CCD-Photometry of Comets at Large Heliocentric Distances</i>	B. E. A. Mueller	425
<i>Asteroid Orbital Error Analysis: Theory and Application</i>	K. Muinonen and E. Bowell	429
<i>Long-Term Orbital Evolution of Short-Period Comets Found in Project "Cosmo-Dice"</i>	T. Nakamura and M. Yoshikawa	433
<i>Rotational Behavior of Comet Nuclei Under Gravitational Perturbations</i>	P. Oberti, E. Bois, and C. Froeschlé	439
<i>15 Years of Comet Photometry: A Comparative Analysis of 80 Comets</i>	D. J. Osip, D. G. Schleicher, R. L. Millis, M. F. A'Hearn, and P. V. Birch	443
<i>The Shape of Asteroid 1917 Cuyo</i>	S. J. Ostro and W. Z. Wisniewski	447
<i>The Importance of Guiding on the Motion of a Comet in Astrometric Observations</i>	Th. Pauwels	451
<i>A New Method for Astrometric Observations of Asteroids</i>	Th. Pauwels	455
<i>On LAMs and SAMs for Halley's Rotation</i>	S. J. Peale	459
<i>Burst of the 1969 Leonids and 1982 Lyrids</i>	V. Porubčan and J. Štohl	469

<i>On Associations of Apollo Asteroids with Meteor Streams</i>	473
V. Porubčan, J. Štohl, and R. Vaňa	473
<i>Observations of Comet Levy 1990c in the [OI] 6300-Å Line with an Imaging Fabry-Perot</i>	
C. D. Prasad, K. Jockers, H. Rauer, and E. H. Geyer	477
<i>The Flux of Small Asteroids Near the Earth</i>	
D. L. Rabinowitz	481
<i>Narrow Band Photometry of Selected Asteroids</i>	
R. Rajamohan and S. G. Bhargavi	487
<i>The Disconnection Event of 16.0 March 1986 in Comet Halley</i>	
C. E. Randall, J. C. Brandt, Y. Yi, and M. Snow	493
<i>Laboratory Studies on Cometary Crust Formation: The Importance of Sintering</i>	
L. Ratke, H. Kochan, and H. Thomas	497
<i>Visual Data of Minor Meteor Showers—Limits of the Method</i>	
J. Rendtel and R. Koschack	501
<i>Long Slit Spectroscopy of NH₂ in Comets Halley, Wilson and Nishikawa-Takamizawa-Tago</i>	
T. W. Rettig, S. C. Tegler, S. Wyckoff, R. Heyd, R. Stathakis, and D. A. Ramsay	505
<i>Twentieth Century Light Curves and the Nucleus of Comet P/Tempel 2</i>	
H. Rickman, M. C. Festou, G. Tancredi, and L. Kamél	509
<i>Carbon Petrology in Cometary Dust</i>	
F. J. M. Rietmeijer	513
<i>Wake in Faint Television Meteors</i>	
M. C. Robertson and R. L. Hawkes	517
<i>Chemical and Physical Effects in the Bulk of Cometary Analogs</i>	
K. Roessler, F. Bénit, and M. Sauer	521
<i>Evolution of Near UV Halley's Spectrum in the Inner Coma</i>	
P. Rousselot, J. Clairemidi, F. Vernotte, and G. Moreels	525
<i>Mosaic CCD Method: A New Technique for Observing Dynamics of Cometary Magnetospheres</i>	
T. Saito, H. Takeuchi, Y. Kozuka, S. Okamura, I. Konno, M. Hamabe, T. Aoki, S. Minami, and S. Isobe	529
<i>Submillimeter Molecular Line Observations of Comet Levy (1990c)</i>	
F. P. Schloerb and W. Ge	533
<i>Spatial and Temporal Variations in the Column Density Distribution of Comet Halley's CN Coma</i>	
R. Schultz, W. Schlosser, W. Meisser, P. Koczet, and W. E. Celnik	537
<i>Automated Detection of Asteroids in Real-Time with the Spacewatch Telescope</i>	
J. V. Scotti, T. Gehrels, and D. L. Rabinowitz	541
<i>Sublimation Rates of Carbon Monoxide and Carbon Dioxide from Comets at Large Heliocentric Distances</i>	
Z. Sekanina	545

<i>Interpreting Asteroid Photometry and Polarimetry Using a Model of Shadowing and Coherent Backscattering</i>	
Yu. G. Shkuratov and K. Muinonen	549
<i>On the Distribution of Minor Planet Inclinations</i>	
V. A. Shor and E. I. Yagudina	553
<i>Diurnal Variation of Overdense Meteor Echo Duration and Ozone</i>	
M. Šimek	557
<i>Melting, Vaporization, and Energy Partitioning for Impacts on Asteroidal and Planetary Objects</i>	
C. L. Smither and T. J. Ahrens	561
<i>3-D Orbital Evolution Model of Outer Asteroid Belt</i>	
N. A. Solovaya, I. A. Gerasimov, and E. M. Pittich	565
<i>The Tapanui Region of New Zealand: Site of a 'Tunguska' Around 800 Years Ago?</i>	
D. Steel and P. Snow	569
<i>1991 DA: An Asteroid in a Bizarre Orbit</i>	
D. Steel, R. H. McNaught, and D. Asher	573
<i>A CCD Search for Distant Satellites of Asteroids 3 Juno and 146 Lucina</i>	
S. A. Stern and E. S. Barker	577
<i>Cartography of Asteroids and Comet Nuclei from Low Resolution Data</i>	
P. J. Stooke	583
<i>The Nature of Comet Nuclei</i>	
M. V. Sykes and R. G. Walker	587
<i>Forced Precession of the Cometary Nucleus with Randomly Placed Active Regions</i>	
S. Szutowicz	593
<i>Velocity Distribution of Fragments of Catastrophic Impacts</i>	
Y. Takagi, M. Kato, and H. Mizutani	597
<i>The Vicinity of Jupiter: A Region to Look for Comets</i>	
G. Tancredi and M. Lindgren	601
<i>Determination of Orbits of Comets: P/Kearns-Kwee, P/Gunn, Including Nongravitational Effects in the Comets' Motion</i>	
B. Todorovic-Juchniewicz and G. Sitarski	605
<i>Minor Satellites and the Gaspra Encounter</i>	
T. Van Flandern	609
<i>The Role of Organic Polymers in the Structure of Cometary Dust</i>	
V. Vanysek, H. Boehnhardt, and H. Fechtig	613
<i>High Resolution Images of P/Tempel 1 and P/Tempel 2 Constructed from IRAS Survey Data</i>	
R. G. Walker, H. Campins, and M. Schlapfer	617
<i>Rotation of Split Cometary Nuclei</i>	
J. Watanabe	621
<i>Meteor Radiant Mapping with MU Radar</i>	
J. Watanabe, T. Nakamura, T. Tsuda, M. Tsutsumi, A. Miyashita, and M. Yoshikawa	625

<i>The Comet Rendezvous Asteroid Flyby Mission: A Status Report</i>	629
P. Weissman and M. Neugebauer	
<i>A New Activity Index for Comets</i>	633
F. A. Whipple	
<i>The Mass of (1) Ceres from Perturbations on (348) May</i>	641
G. V. Williams	
<i>Gaspra and Ida in Families</i>	645
J. G. Williams	
<i>What Makes a Family Reliable?</i>	649
J. G. Williams	
<i>The Unusual Lightcurve of 1990 TR</i>	653
W. Z. Wisniewski	
<i>Velocity Distributions of H and OH Produced Through Solar Photodissociation of H₂O</i>	657
C. Y. R. Wu, F. Z. Chen, and D. L. Judge	
<i>Formation of The Leonid Meteor Stream and Storm</i>	661
Z. Wu and I. P. Williams	
<i>The Contribution of Electron Collisions to Rotational Excitations of Cometary Water</i>	667
X. Xie and M. J. Mumma	
<i>On the Dynamical Structure of the Trojan Group of Asteroids</i>	671
R. V. Zagretdinov, I. P. Williams, and M. Yoshikawa	
<i>A Comparison Between Families Obtained from Different Proper Elements</i>	675
V. Zappalá, A. Cellino, and P. Farinella	
<i>A Candidate for the Parent Body of the Taurid Complex and its Search Ephemeris</i>	679
K. Ziolkowski	
<i>CoMA-A High Resolution Time-of-Flight Secondary Ion Mass Spectrometer (TOF-SIMS) for In Situ Analysis of Cometary Matter</i>	683
H. Zscheeg, J. Kissel, and Gh. Natour	
<i>Author Index</i>	689
<i>Subject Index</i>	691

LIGHT CURVE AND FAN-SHAPED COMA OF COMET P/TEMPEL 2 IN 1988-89

Hiroki Akisawa¹, Mitsunori Tsumura², Akimasa Nakamura¹ and Junichi Watanabe³

¹ Hoshi-no-Hiroba; 8-13-607, Shiroyama 3-chome, Odawara-shi, 250 Japan

² Wakayama City Children's Science Center, & Hoshi-no-Hiroba

³ National Astronomical Observatory of Japan

ABSTRACT. Visual and Photographic Monitoring observations of comet P/Tempe1 2 were carried out by a Japanese amateur group "Hoshi-no-Hiroba" in 1988 – 1989. We analyzed the light curve and the time variation of the fan-shaped coma. The light curve was asymmetric to the perihelion passage. The fan angle in September – October was wider than that in December. The direction of the fan generally coincided with Sekanina's prediction (1988).

Introduction

It is important to monitor the activity of comets which are potential targets of future missions. Comet P/Tempe1 2 was a candidate of the CRAF mission (Nausebauer, 1987). The monitoring observations of this comet was carried out by a Japanese amateur group "Hoshi-no-Hiroba" in 1988 – 1989 apparition. The observations were divided into two categories. One is the visual observations of total magnitude of this comet. The other is the photographic observations of the fan-shaped coma in order to know its time variation. In this paper, we report some results obtained by these observations.

Observations of total magnitude

Visual observations of comet P/Tempe1 2 were performed by many members in the "Hoshi-no-Hiroba". The original charts for standard comparison stars were supplied to all the observers in advance. We obtained 87 total magnitude data in 1988.

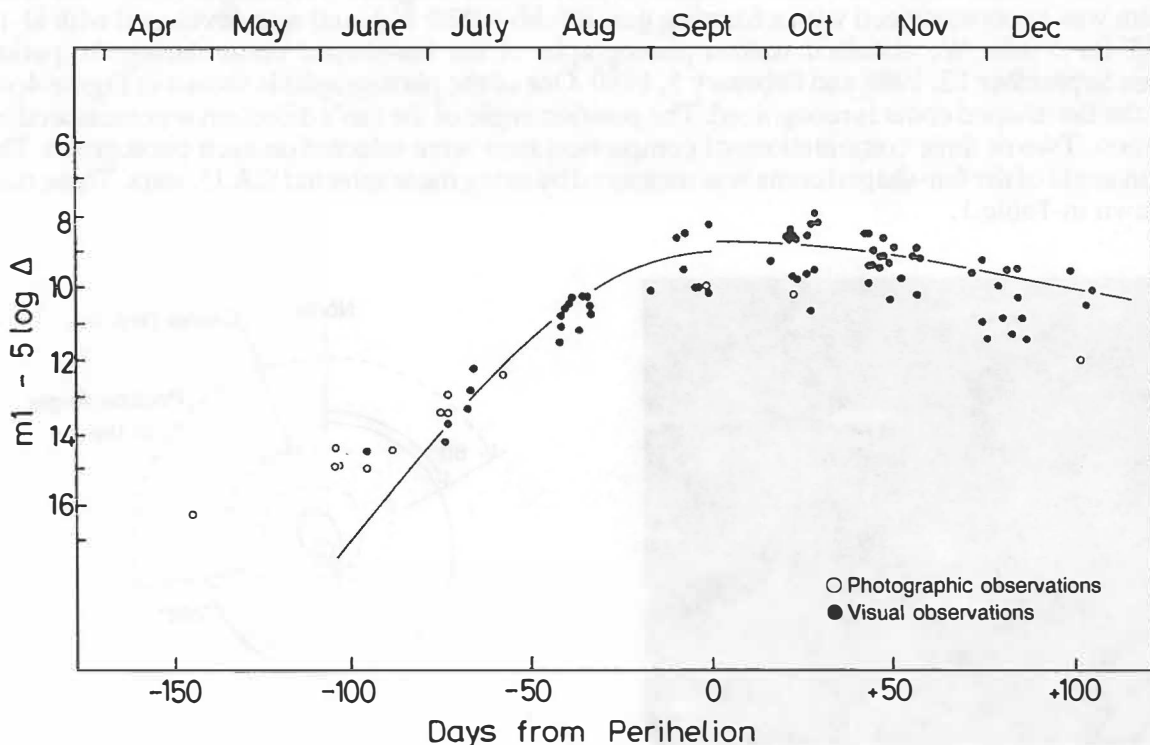


Figure 1. The light curve of comet P/Tempe1 2

Figure 1 shows the light curve, which is clearly asymmetric to the perihelion passage. The obtained equations of the light curve are follows.

$$m_1 = -2.38 (\pm 0.99) + 5 \log \Delta + 81.83 (\pm 5.95) \log r \text{ (pre-perihelion)}$$

$$m_1 = +6.86 (\pm 0.54) + 5 \log \Delta + 14.04 (\pm 3.11) \log r \text{ (post-perihelion)}$$

The regressions of these light curves are shown in Figures 2 and 3, respectively.

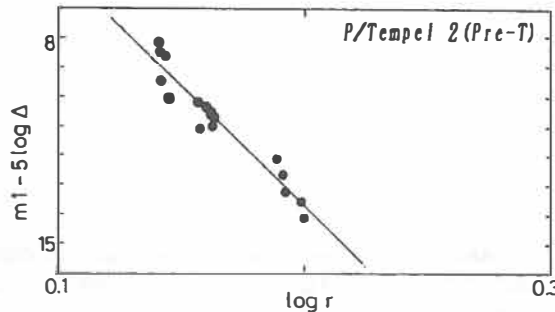


Figure 2. The light curve in pre-perihelion

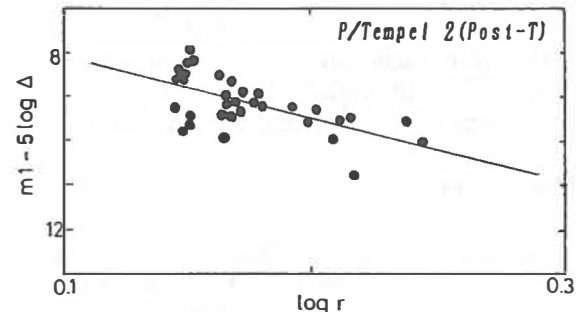


Figure 3. The light curve in post-perihelion

Observations of the fan-shaped coma

The photographic observations of the fan-shaped coma were performed by 31 cm reflector (f.l. 1650 mm) with focal reducer (for F4.2, f.l. 1290 mm) in Oishi observatory. The site is located on the Wakayama prefecture in Japan ($E=135^{\circ}20'23''$, $N=34^{\circ}07'57''$, $H=340\text{m}$ above sea level). We used the emulsion Kodak TP2415, which is sensitive over a wide range of wavelength (300 – 700 nm). The film was hypersensitized with a forming gas (8% H₂ + 92% N₂), and was developed with D-19 at 20°C for 5 min. We obtained sixteen photographs of the fan-shaped coma during the period between September 12, 1988 and February 5, 1989. One of the photographs is shown in Figure 4, on which the fan-shaped coma is recognized. The position angle of the fan's direction was measured by inspection. Two or three combinations of comparison stars were selected on each photograph. The position angle of the fan-shaped coma was measured by using these selected S.A.O. stars. These data are shown in Table 1.

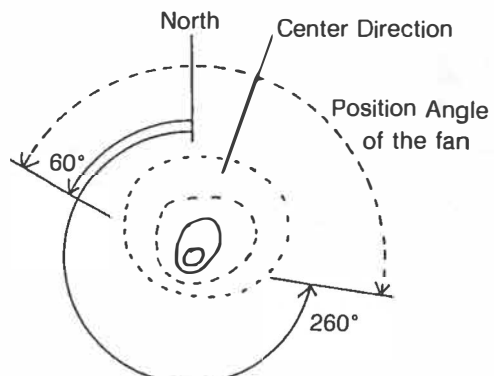
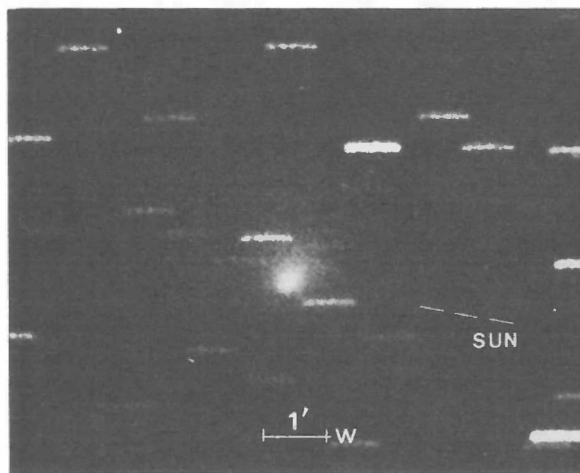


Figure 4. The observed fan-shaped coma of comet P/Tempel on Oct. 31.43, 1988 (No. 6)

Table 1. Observational data of fan-shaped coma

No.	Date (UT)	Oishi Obs. Plate No.	Exposure	Position Angle of the fan	Center Direction	Dia.	D.C.
1	Sept. 12.46, 1988	6673	5	220° – 60°	320°	4.0'	4
2	Sept. 13.47, 1988	6686	20	210° – 60°	315°	3.0'	4
3	Sept. 15.48, 1988	6710	15	275° – 35°	335°	2.0'	4
4	Oct. 3.44, 1988	6752	20	280° – 30°	335°	3.0'	3
5	Oct. 14.48, 1988	6798	10	280° – 20°	330°	2.0'	4
6	Oct. 31.43, 1988	6831	20	260° – 60°	340°	2.5'	4
7	Nov. 8.44, 1988	6846	15	275° – 45°	340°	2.0'	4
8	Nov. 12.47, 1988	6897	15	300° – 45°	352°.5	2.0'	4
9	Nov. 30.42, 1988	6912	15	320° – 70°	15°	1.5'	3
10	Dec. 1.45, 1988	6916	14	300° – 70°	5°	1.5'	2
11	Dec. 6.41, 1988	6925	15	310° – 70°	10°	1.5'	3
12	Dec. 8.45, 1988	6969	15	290° – 70°	0°	1.5'	3
13	Dec. 12.49, 1988	6972	15	280° – 60°	350°	1.2'	2
14	Dec. 27.47, 1988	6989	16	Uncertainty	about 20°	0.8'	2
15	Jan. 2.41, 1989	7000	15	330° – 70°	20°	0.7'	3
16	Feb. 5.43, 1989	7053	15	Uncertainty	about 20°	0.7'	0

Sekanina (1987a, b) analyzed the rotation axis and the surface structure of nucleus of comet P/Tempel 2 by applying the spin-vector model to the fan-shaped coma observed in 1899 – 1972. On the basis of his model, Sekanina (1988) predicted the direction and shape of the fan of this comet in 1988 – 1989 apparition. The comparison between Sekanina's prediction and our observations is shown in Figure 5. The observed center of the direction of the fan agrees with his prediction. On the other hand, the fan angle in September – October was wider than that in December. This is an opposite sense to the Sekanina's prediction.

Concluding Remarks

Visual and Photographic Monitoring observations of comet P/Tempel 2 were carried out by a Japanese amateur group "Hoshi-no-Hiroba" in 1988 – 1989. The photographic observations show the developed fan-shaped coma which generally coincides with Sekanina's prediction (1988). This suggests that the CRAF mission can be based on the Sekanina's model (1987a, b) for the nucleus of this comet. The result of the visual observations shows the strong asymmetry in the light curve to the perihelion passage. This may be due to a seasonal effect of the cometary nucleus (Weissman, 1987). Visual magnitude observations give us useful information on the global activities of comets even if each estimate is less accurate than the photometry. More than 300 members in the "Hoshi-no-Hiroba" have great potential for contributing to such monitoring observations of the mission targets.

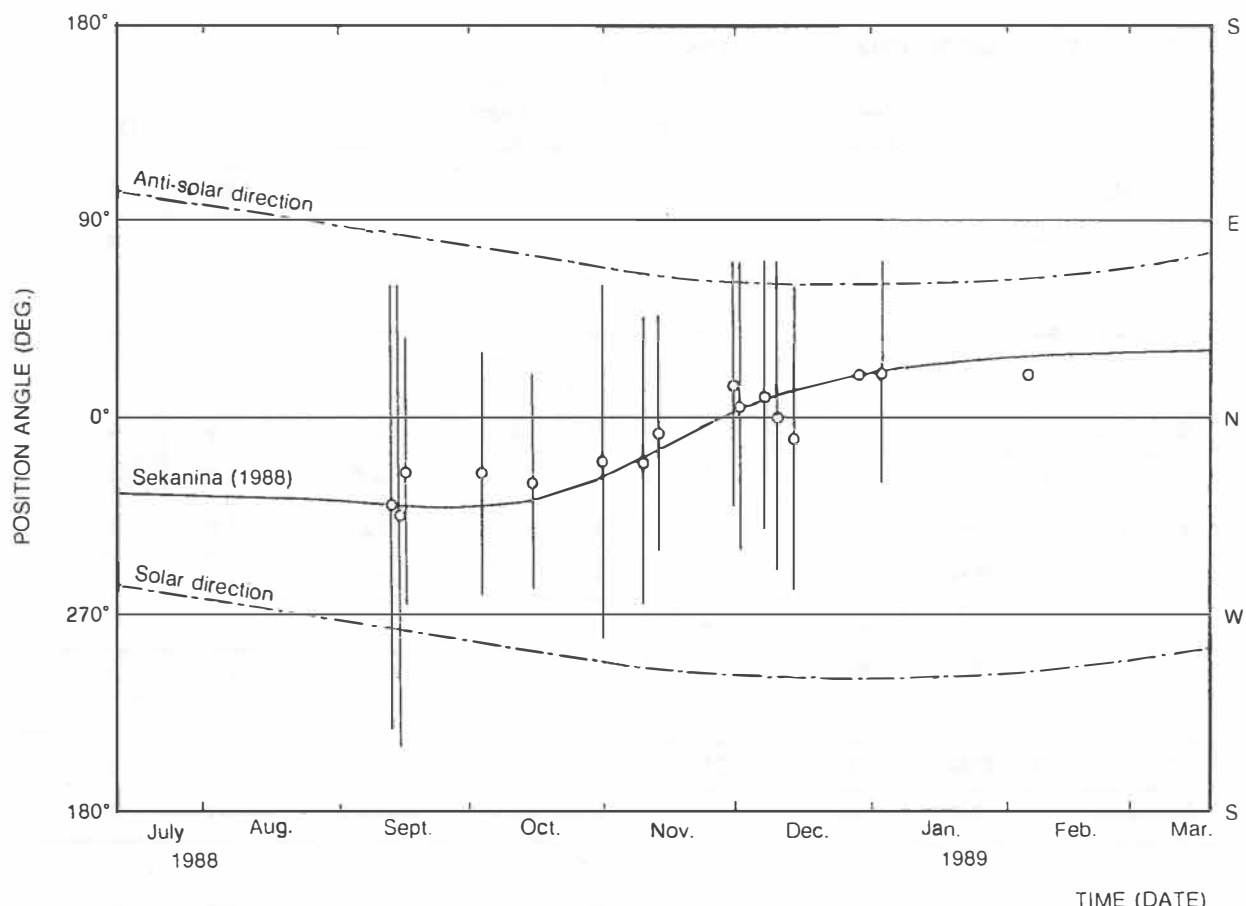


Figure 5. The observed direction of the fan-shaped coma and the comparison with the Sekanina's prediction.

References

- Neugebauer M. (1987) The comet rendezvous asteroid flyby mission. In Proc. Symposium on the Diversity and Similarity of Comets, pp.517–522, ESA SP-278.
- Sekanina Z. (1987a) Anisotropic emission from comets: Fans versus jets — I. Concept and modeling. In Proc. Symposium on the Diversity and Similarity of Comets, pp.315–322, ESA SP-278.
- Sekanina Z. (1987b) Anisotropic emission from comets: Fans versus jets — II. Periodic Comet Tempel 2, In Proc. Symposium on the Diversity and Similarity of Comets, pp.323–336, ESA SP-278.
- Sekanina Z. (1988) Comet P/Tempel 2. In IAU Circular, 4624 (8 July 1988).
- Weissman P.R. (1987) Post-perihelion brightening of comet P/Halley: Springtime for Halley. Astron. Astrophys., 187, 873–878.

ABOUT DISTRIBUTION AND ORIGIN OF THE PECULIAR GROUP OF SPORADIC METEORS

V.V. ANDREEV

Kazan University, Engelhardt Astronomical Observatory, 422526,
Kazan, USSR

ABSTRACT

A particular group of sporadic meteors are picked out from analysis of meteor catalogues derived from results of radar observations in Mogadisho and Kharkov. The semi-major axes are equal or more than 1.73 AU and inclinations of orbits are equal or more than 90° for these meteors. The distributions of radiants, velocities and elements of orbits were derived. The probable source of meteor bodies of this peculiar group is the long-period comets, in particular, the comets of the Kreutz's group.

INTRODUCTION

The multi-mode character of the distributions of heliocentric radiants and velocities of sporadic meteoroids follows from analysis of meteor observational data (Andreev, Belkovich, 1987). This fact points to a complicated structure of the sporadic meteoroid complex. It in turn is the consequence of the plurality of parent bodies and origin mechanisms of meteoroids. The perturbing action of the planet and nongravitational forces influence on the structure of meteoroid complex. The analysis also shows presence of the meteoroids at orbits which have not analogues among another Solar system bodies.

METHOD OF REDUCTION OF OBSERVATIONAL DATA

Let us try to take into account these facts at least roughly and for large meteoroids (Andreev, 1988).

In the present time comets and asteroids are considered as main sources of meteoroids. The difference in point of views on the problem consists in the estimation of the relative contribution these sources (Kresak, 1967). Jupiter is the main perturbing body in the Solar system. The circular restricted three-body problem is the simplest dynamical framework allowing to take into account the principal perturbational influence of Jupiter. In our case that is the system of three bodies: Sun, Jupiter and a particle (Kresak, 1969, 1972, 1979).

On this base we represent the whole sporadic meteoroid complex as the aggregate of several groups of meteoroids. Every group is determined by the value of Tisserand's invariant

$$T = a^{-1} + 2 \cdot A_J^{-3/2} \cdot \sqrt{[a \cdot (1 - e^2)]} \cdot \cos i,$$

and the inclination of the meteoroid orbit i to the ecliptic. In the equation A_J is the Jupiter's semi-major axis, a and e is meteoroid semi-major axis and eccentricity respectively.

Groups of meteoroids are determined as follows:

- | | |
|--|--|
| Group I : $T < T_o$ | - meteoroid orbits are similar to comet ones, |
| group II : $T \geq T_o, i < 90^\circ$ | - meteoroid orbits are similar to asteroid ones, |
| group III: $T \geq T_o, i \geq 90^\circ$ | - this type of orbit absents among the orbits of small bodies. |

Where T_o is equal to 0.5767.

From investigation of the comet orbit distribution on value of T from Marsden's catalogue for 1979 year it follows that almost all long-period and parabolic comets have $T < 0.36$. This value of T have been taken for determination of two components of group I. Meteoroids whith $T_o > T \geq 0.36$ are related to subgroup Ib. And meteoroids whith $T < 0.36$ are related to subgroup Ia.

Let us to carry out the analysis of the meteoroid orbits of the third group. The semi-major axes are less than 1.73 AU and inclinations are large than 90° for meteoroid orbits from this group.

The investigation of the similar orbits had been carried out by Jones et al (1985) from television observations of meteors.

RESULTS

The reduction of 12 catalogues available on magnetic tapes of Lund Data Center shows that the number of such meteors increase then the masses of the meteoroids decrease.

Table 1. Data on catalogues and number of meteors with peculiar orbits

	Name of catalogue	N tot.	N III	n
1	HARPHOT	1006	2	0.199
2	MCROSKY	1989	15	0.754
3	FIREBAL	359	0	0.000
4	SOVPHOT	551	11	2.00
5	TVJONES	434	53	12.2
6	HAR6165	18453	2127	11.5
7	HAR6869	19219	1773	9.23
8	OBNINSK	8424	1553	18.4
9	KHARKOV	5114	1622	31.7
10	ADE6061	2040	87	4.26
11	ADE6869	1414	146	10.3
12	MOGADIS	5180	845	16.3

$$\Sigma = 8234$$

In the table N_{tot} . is the number of sporadic meteors in the catalogue, N_{III} is the number of meteors of the third group in the catalogue, Σ is the total number of meteors of the third group in all catalogues, $n = N_{III} / N_{tot}$, for the catalogue, per cent.

The catalogue of the sporadic meteors is a result of extraction of meteors of six meteor showers: Lirids, η -Aquarids, Perseids, Orionids, Leonids and Geminids. The value of D is equal or less than 0.2 is the criterion of belonging to a meteor shower (Southworth, Hawkins 1967).

Catalogues with the numbers from six to eleven will be considered only in the analysis because of sufficient quantity of the third group meteors.

Data on meteoroids with the smaller masses are presented in the KHARKOV catalogue and meteoroids with the greatest masses are in the MOGADIS catalogue. It follows from the comparision of the distributions of pre-atmospheric velocities, heliocentric velocities and radiants, Tisserand's invariants, and orbital elements a, e, q, and i for these two catalogues that character of semi-major axis and eccentricity distributions depends on meteoroid masses. The dependence corresponds to the scheme of the Pointing-Robertson effect. In this point of view one can note that this effect does not influence on orbital inclination and the distributions of inclination angles have practically similar shape for the meteoroids of the third group in all catalogues.

Analisis of the observational bias due to intersection probability of the Earth's orbit by meteoroids with orbits satisfied to conditions

$$a \cdot (1 - e) \leq 1 \text{ AU} \leq a \cdot (1 + e).$$

had been carried out.

In the present time we do not know the evolutional mechanisms drastically changing orbital inclinations except close encounters with the major planets. Therefore it is naturally to look for the parent bodies for these meteoroids among small bodies already moving on orbits with inclinations greater than 90° . These small bodies known now are comets.

Mechanism of the origin of meteoroids is the desintegration process of comets during their perihelion passage. According to Whipple's model of comet nucleus velocities of ejected meteoroids are the large the less masses of particles. It is evidently that the larger velocities of ejected particles the larger deviations of meteoroid orbits from comet's one. These deviations only can form orbits with small semi-major axes similar to ones for considered meteoroids.

CONCLUSION

Analisis of desintegration processes during perihelion passage on Sekanina's scheme (Sekanina, 1967) shows that the third group meteoroids can be formed by desintegration of nucleus of

long-period and parabolic comets with very small perihelion distances. The Kreutz' group comets are likely the main contributor.

REFERENCES

- Andreev V.V. and Belkovich O.I. (1987) Models of sporadic meteor body distributions. Handbook for MAP, 25, 298-304.
- Andreev V.V. (1988) Modelling of the sporadic meteoroid complex. Second GLOBMET Symposium: Abstracts, 17.
- Kresak L. (1969) The discrimination between cometary and asteroidal meteors. I. Orbital criteria. Bull. Astron. Inst. Czechosl., 20, 177-188.
- Kresak L. (1972) Jacobian integral as a classification and evolutionary parameter of interplanetary bodies. Bull. Astron. Inst. Czechosl., 23, 1-34.
- Kresak L. (1979) Dynamical interrelations among comets and asteroids. In Asteroids (T.Gehrels, ed.), pp. 289-309, Univ. Arizona Press, Tucson.
- Jones J., Sarma T., and Ceplecha Z. (1985) Double-station observations of 454 TV meteors. III. Populations. Bull. Astron. Inst. Czechosl., 36, 116-122.
- Sekanina Z. (1967) Problems of origin and evolutions of the Kreutz family of Sun-grazing comets. Acta Univ. Carolinae., No. 2, 33-84.
- Southworth R.B. and Hawkins G.S. (1963) Statistics of meteor streams. Smithson. Contr. Astrophys., 7, 261-285.

PHOBOS AND DEIMOS ARE SOURCES OF METEOROIDS

V.V.Andreev, O.I.Belkovich

Engelhardt Astronomical Observatory, SU-422526, Kazan, USSR

ABSTRACT

Data of Pioneer 10 meteoroid penetration detectors were revised taking into account the orientation of detectors and the spacecraft velocity relative to the sporadic meteor flux. The meteor flux density increases as an exponent to the orbit of Mars for two times for the particles with masses greater than 10^{-6} g and six times for the particles with masses greater than 10^{-9} g then decreases after the orbit. Ejections of secondary meteoroid particles from surfaces of Phobos and Deimos are possible explanation of the increase the meteoroid flux.

INTRODUCTION

One source of our knowledge on distribution of meteor matter in the interplanetary space is data obtained *in situ* from space probes. Beyond of the Earth's orbit progress has been made by space probes Mariner 4 and Pioneer 10 experimental. It is a pity the number of registered events is scanty. In this case a correct interpretation of experimet results is very important.

INTERPRETATION OF EXPERIMENTAL RESULTS

The problem has been discussed in detail by many authors, for example, Humes et al, 1974. For the interpretation of observational data one must consider the orientation of the collecting area relative to flux of the sporadic meteoroids and equipment selectivity. The solution of the problem is simplified in the case of the isotropic sporadic flux density. But it is not the case since we have a very unisotropic distribution of the sporadic flux density over the celestial sphere (Andreev and Belkovich, 1987). The flux density $Q(V, \epsilon, \psi)$ is determined as

$$Q \cdot P(V, \epsilon, \psi) = Q P_{\epsilon, \psi}(V) P(\epsilon, \psi),$$

Q is the total flux density of meteoroids with masses greater than some value m coming from all celestial sphere, intersecting for unit time unit area normal to the velocity vector; $P(V, \epsilon, \psi)$ is the three-dimensional distribution of a meteoriod velocity V and

coordinates of meteor radiant ϵ, ψ ; $P_{\epsilon, \psi}(V)$ is the conditional distribution of velocities for a radiant direction ϵ, ψ and $P(\epsilon, \psi)$ is the two-dimensional distribution of meteor radiants. The mathematical model of $Q(V, \epsilon, \psi)$ in the vicinity of the Earth's orbit for sporadic meteoroids with masses greater than 10^{-6} g in heliocentric system of coordinates has been derived from radar meteor observations (Andreev and Belkovich, 1987).

A number of events (registrations) N in unit of time is

$$N = Q_0 \Phi$$

where

$$\Phi = \int \int \int F(V_1, \epsilon_1, \psi_1) P(V_1, \epsilon_1, \psi_1) \sin \epsilon_1 d\epsilon_1 d\psi_1 dV_1,$$

$F(V_1, \epsilon_1, \psi_1)$ is a selectivity function that takes into account radiant coordinates relative to a collecting area and the physical conditions of registration. In the last equation the reference system V_1, ϵ_1, ψ_1 is related to the space probe. The transformation of the flux density from the heliocentric reference system to the space probe frame of reference is carried out by the next equation

$$Q(V_1, \epsilon_1, \psi_1) = Q(V, \epsilon, \psi) (V_1/V)^{\frac{3}{2}} (\sin \epsilon_1 / \sin \epsilon)$$

(Andreev and Belkovich, 1987).

Two kinds of equipment were installed on board of Pioneer 10 for registration of meteoroids. The first was the meteoroid penetration detectors and the second was the asteroid/meteoroid detector (AMD) or Sisyphus. In the case of the penetration detectors the orientation of the collected area has very important role due to their small field-of-view. The line of vision was directed opposite to the Earth's direction during the whole mission and parallel to spacecraft spin axis. In contrast to this its field of view of the AMD experiment was much greater due to the rotation of the spacecraft and the optical subsystem was pointed at an angle of 45° relative to the spacecraft spin axis (Soberman et al, 1977).

RESULTS AND DISCUSSION

For the part of orbit of Pioneer 10 from 1 AU to 2 AU values of the function Φ have been calculated. The function F for penetration detectors has been taken on the base of results of Humes et al, 1974. For the Sisyphus experiment the collecting area has been taken into account. The variations of the function Φ versus heliocentric distance for the two experiments are shown in Fig. 1. As pointed out earlier the variations of the function are greater for the penetration experiment due to orientation of collecting area.

The relative variations the flux density in the heliocentric

frame of reference versus heliocentric distances are shown in Fig. 2. The flux density is normalized so that it is equal to 1 at the Earth's orbit. Data for the experiment carried out at the space probe Mariner IV are also shown without correction on observational bias because of the absence of information about the orbit and equipment of the probe. This correction is negligible in the case of the random orientation of the collecting area. Both sets of the data show similar exponential increase of meteor flux density to the Mars orbit. The exponential decay of the flux density one can see after the maxima. The slight difference of the maxima position may be attributed to experimental uncertainties. The function of the relative flux density variation R between the Earth's and Mars orbits for the meteoroid masses $10^{-12} - 10^{-9}$ g is

$$R = \exp [a(r-1)]$$

where a is equal to 4.3 for this meteoroid masses.

Interpretation of Sisyphus experiment results have been made in the assumption of similarity of the function R for meteoroid with masses greater than 10^{-6} g at heliocentric distances 1.0 - 1.4 AU. We have assumed also that $R = 0.96$ for the heliocentric distances 1.4 - 2.0 AU. The function R fits best of all to the experimental data for a equal to 1.8.

Table 1. Observed (N_{obs}) and calculated (N_{cal}) number of registrations of AMD experiments

r_1	r_2	N_{obs}	N_{cal}
1.04	- 1.2	32	31.9
1.2	- 1.4	32	32.0
1.4	- 1.6	15	15.7
1.6	- 1.8	15	15.1
1.8	- 2.0	15	15.1

N_{cal} is taken proportional to

$$\frac{r_2}{r_1} \int \exp [a(r-1)] dt$$

where t is the time of flight of the spaceprobe.

The value of a becomes greater if the maximum of the R function corresponds to the distance from the Sun less than 1.4.

CONCLUSION

Thus the correct interpretation of the Pioneer 10 and Mariner IV data on the sporadic meteoroid flux density at the heliocentric distances 1.0 - 2.0 AU lead us to the conclusion that the flux maximum corresponds to the vicinity of the martian orbit. But the

escape velocity from the planet surface is greater than one for the satellites of Mars. Phobos and Deimos are most possible sources of meteoroids.

REFERENCES

Andreev V.V. and Belkovich O.I. (1987) Models of sporadic meteor body distributions. Handbook for MAP, 25, 298-304.

Humes D.H., Alvarez J.M., O'Neal R.L., and Kinard W.H. (1974) The interplanetary and near-Jupiter meteoroidal environments. J. Geophys. Res., 79, 3677-3684.

Soberman R.K., Neste S.L., and Lichtenfeld K. (1977) Results of the asteroid - meteoroid particle experiment on Pioneer 11. Space Res., 17, 559-564.

Captions for Figures

Fig. 1. Variations of the Φ functions vs heliocentric distances.

Fig. 2. Relative flux density at the heliocentric distances from 1.0 to 2.0 AU. Dashed line is the flux density for the AMD experiment.

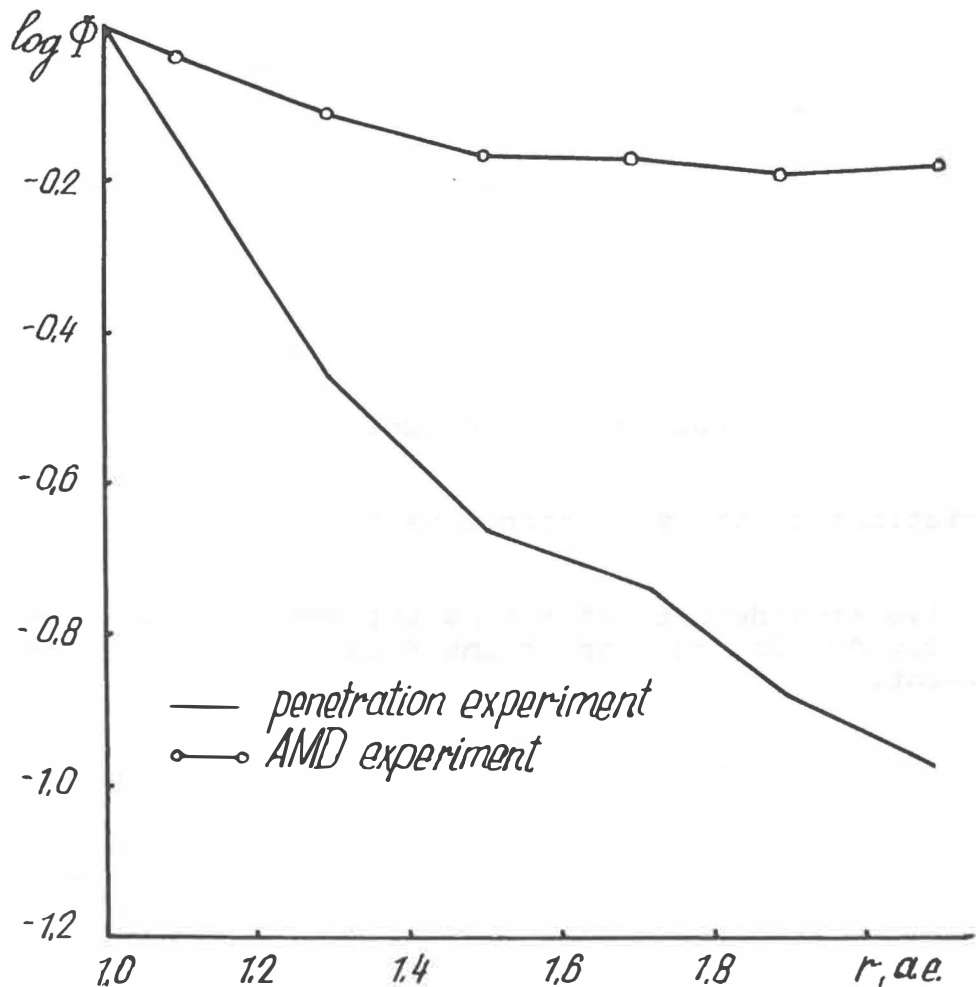


FIGURE 1.

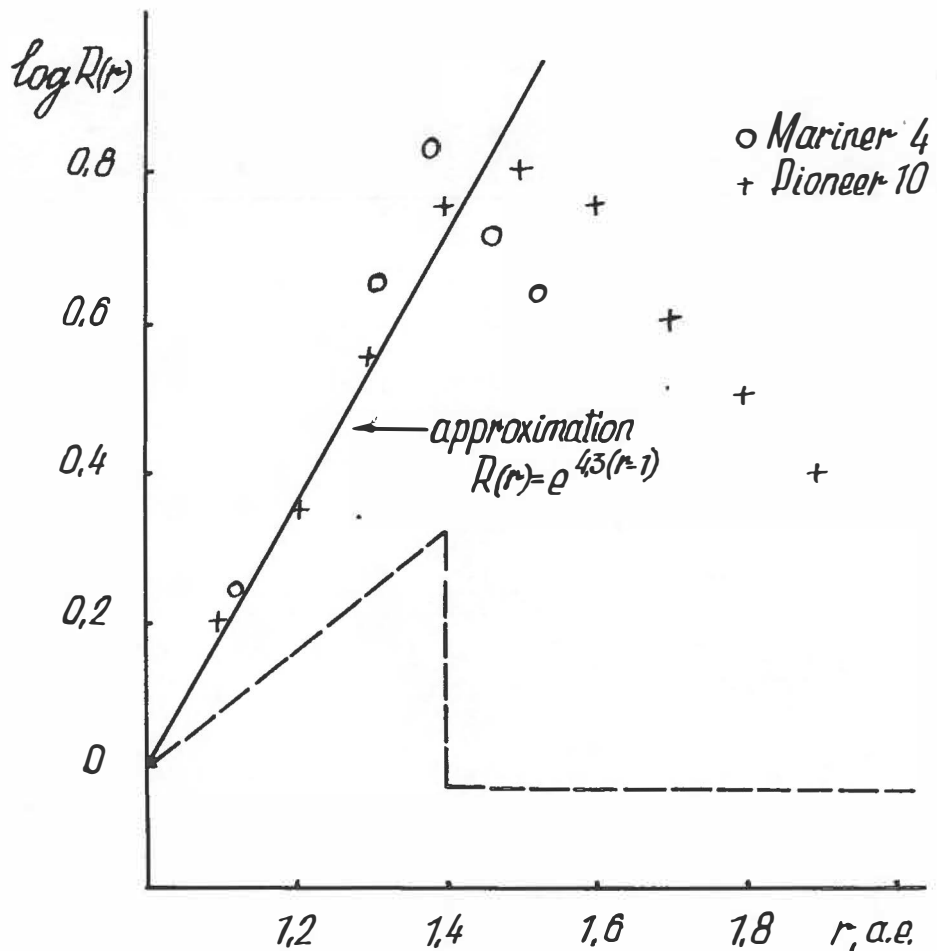


FIGURE 2.

DETERMINATION OF METEOR FLUX DISTRIBUTION OVER THE CELESTIAL SPHERE

V.V.Andreev, O.I.Belkovich
Engelhardt Astronomical Observatory, SU-422526, Kazan, USSR

T.K.Filimonova, V.V.Sidorov
Kazan State University, Lenin st. 18, SU-420008, Kazan, USSR

ABSTRACT

A new method of determination of meteor flux density distribution over the celestial sphere is discussed. The flux density was derived from observations by radar together with measurements of angles of arrival of radio waves reflected from meteor trails. The role of small meteor showers over the sporadic background is shown.

INTRODUCTION

Morton and Jones (1981) proposed a method of determination of radiant distribution from observations by a single radar with a measurement of arrival angles of signals reflecting from meteor trails. The method was realized for shower meteors only. A new method was worked out in Kazan to derive meteor flux density distribution over the celestial sphere. Observations were carried out by the radar with the aerial turning every 15 minutes successively in four directions: North, East, South, West. So all meteor radiants above the horizon were observed for an hour. The radar has operated according to the GLOBMET program therefore observations of velocities of meteor trail drifts due to winds were carried out simultaneously.

DESCRIPTION OF THE METHOD

The celestial sphere was divided into 578 areas $\Delta\omega = 10^\circ \times 10^\circ$ each in spherical frame of reference ϵ, ψ , where ϵ is the elongation from the apex and $\epsilon = 90^\circ$, $\psi = 0$ is the direction relative to the Sun. If we know the direction to the reflecting point at a meteor trail then a position of the meteor radiant must be at the radiant line above the horizon. A radiant line is an arc of a great circle formed by intersection of a plane normal to the direction to the reflecting point and the celestial sphere. In this case the radiant line intersects some number of areas $\Delta\omega_i$. The probability P_i that the radiant is inside the area $\Delta\omega_i$ is

$$P_i = \frac{Q_i \Delta\omega_i \Delta S_i \Delta l_i}{\sum Q_i \Delta\omega_i \Delta S_i \Delta l_i}$$

Q_i is the flux of sporadic meteor bodies inside the area $\Delta\omega_i$, ΔS_i is the effective collecting area in the echo plane for the direction to the reflecting point, Δl_i is the radiant line length in the limits of the area. One can take $Q_i = 1$ as the first approximation and for every hour of observations and distribute all registered meteors to the areas by parts equal to P_i . So for every hour one can count hourly rate for every area N_{ki} . Meteor activity of every area can be represented as a point (shower) radiant with a flux

$$Q'_{ki} = Q_{ki} \Delta\omega_i.$$

The flux density Q'_{ki} for shower meteors can be calculated from known hour rate N_{ki} and position of the radiant relative to the radar aerial. Q_{ki} can be found from the previous formula. Then the mean values

$$Q_i = n_i^{-1} \sum_{(k)} Q'_{ki}$$

is calculated for every area $\Delta\omega_i$ and for the entire interval of observation. n_i is the number of hours of observation. These values of Q_i are used for a second approximation, etc. The iteration process is repeated until the solution becomes stable.

RESULTS

The method permits us to obtain meteor flux density distribution over the celestial hemisphere for a diurnal interval of observation. An example of the distribution is given in Fig.1. Several picks are evident on the plot and they are apparently small meteor showers acting for a period from several hours to several days. In the last case one can trace them at successive diurnal distributions.

Radar observations for 1988 year have been used to get an averaged geocentric flux density distribution of meteor bodies with masses greater than some value. The ionisation coefficient was taken by V.Tokhtashev (Andreev et al, 1976)

$$\beta = \beta_0 (V/V_0 - 0.2)^{3.5}$$

where β and β_0 are the coefficients for meteoroid velocities V and

V_0 respectively, $V_0 = 40 \text{ km s}^{-1}$. The model of the velocity distribution was taken from Andreev and Belkovich (1987). The annual distribution of the meteor flux density is shown in Fig.2.

REFERENCES

- Andreev V.V. and Belkovich O.I. (1987) Models of sporadic meteor body distributions. Handbook for MAP, 25, 298-304.
- Andreev V.V., Belkovich O.I., and Tokhtashev V.S. (1976) The heliocentric distribution of the meteor bodies at the vicinity of the Earth's orbit. Lecture Notes in Physics, (H. Elsasser, H. Fechtig, eds.), Springer-Verlag, 48, 383-384.
- Morton J.D. and Jones J. (1981) A method for imaging radio meteor radiant distributions. Mon. Not. Roy. Astron. Soc., 198, 739-746.

Captions for Figures

Fig. 1. The distribution of meteor flux density over the celestial sphere, October 9, 1988.

Fig. 2. The annual distribution of flux density of meteoroids with masses greater than 10^{-5} g over the celestial sphere, 1988.

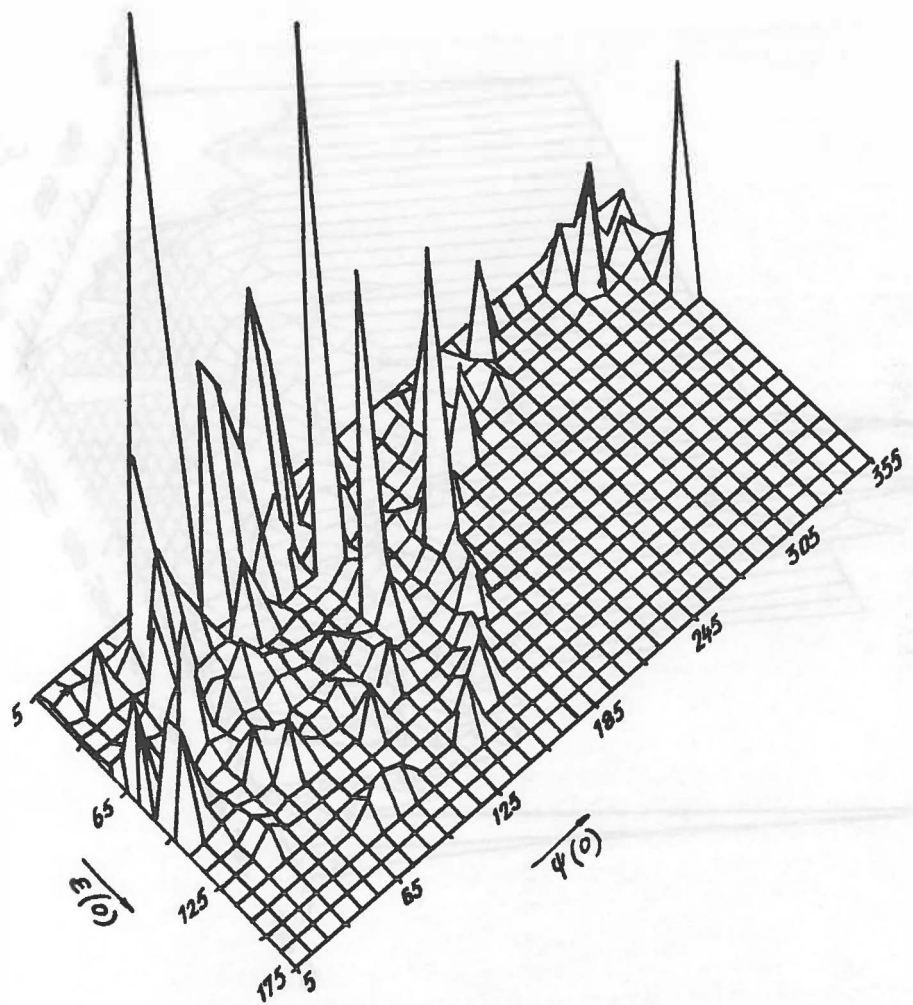


FIGURE 1.

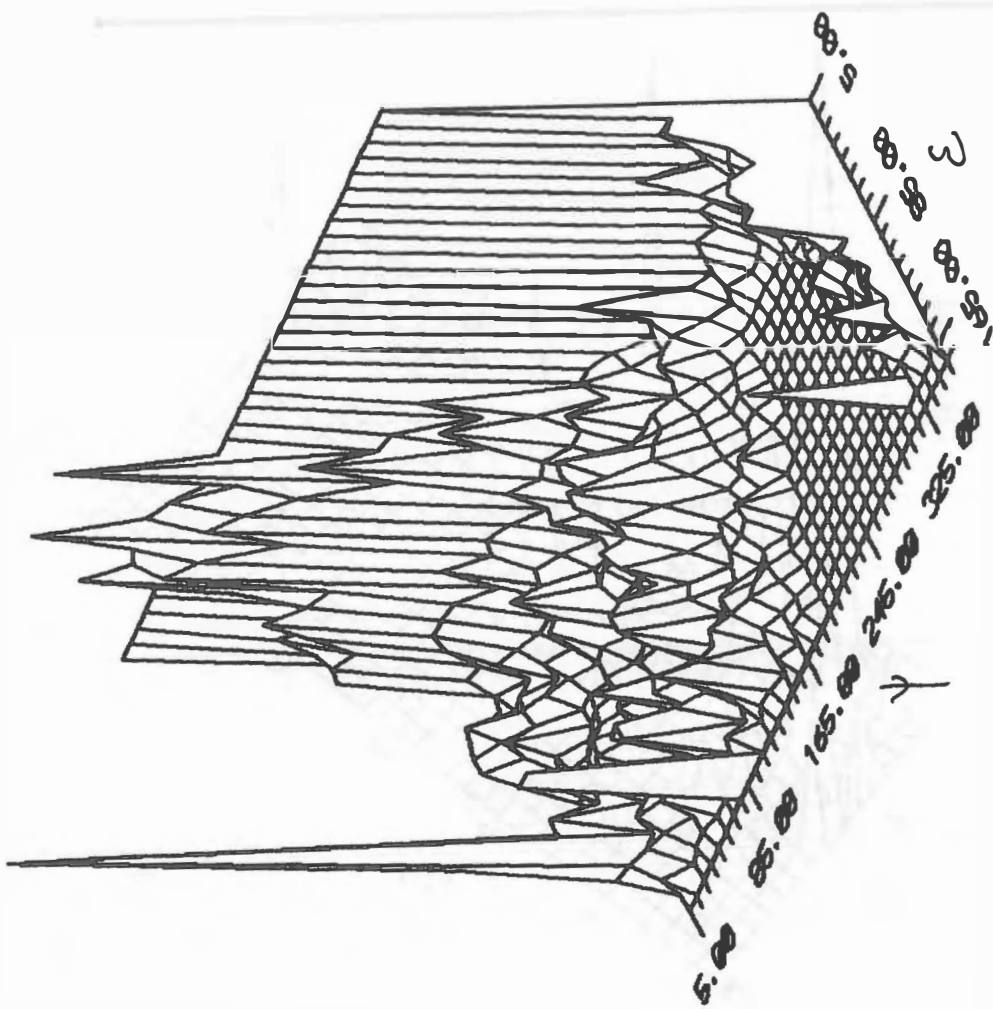


FIGURE 2.

FRAGMENTATION AND DENSITIES OF METEOROIDS

P.B.Babadzhanov, *Institute of Astrophysics, Dushanbe, 734670, USSR*

Abstract. Photographic observations of meteors carried out in Dushanbe by the method of instantaneous exposure have shown clearly that meteoroids entering the Earth's atmosphere are subjected to different types of fragmentation. The quasi-continuous fragmentation of meteoroids is mostly widespread. Using the physical theory of meteors which takes into account the quasi-continuous fragmentation of meteoroids and on the basis of light curves of meteors the densities of meteoroids of different streams have been determined. The results enable to conclude that the densities of meteoroids are over an order of magnitude higher than they have been assumed before. Moreover they are close to the densities of carbonaceous and ordinary chondrites.

Introduction

The majority of meteoroids are products of desintegration of cometary nuclei. Thus the investigation of meteoroids' physical parameters is important not only for meteor astronomy but is of great interest for understanding of physical features of cometary nuclei. An oppinion on low values of meteoroid ensities is widely spread till the recent time. This oppinion is based on the Verniani's (1969) results deduced from photographic observations of meteors using Super-Schmidt cameras. According to these results the average density of sporadic or stream meteoroids is equal to 0.3 g/cm^3 . The same values were obtained from photographic observation of bright meteors in Dushanbe using small cameras (Babadzhanov and Khaimov 1972). McCrosky (1968) estimated the average density of fireball-producing bodies to be 0.4 g/cm^3 , i.e almost the same as for more small bodies. Recently Halliday (1988) estimated the densities of Geminid meteoroids as from 0.7 to 1.3 g/cm^3 . However, in these works meteoroid fragmentation in the atmosphere was insufficiently taken into account or totally ignored. These results contradict Ceplecha's (1975) conclusion that the average meteoroid density varies in the range from 0.2 to 3.7 g/cm^3 .

Analysing the data on photographic observations of meteors Levin (1961) distinguished four main forms of meteoroid's fragmentation: 1) the decay of a meteoroid into comparable large nonfragmenting debris; 2) the progressive disintegration of the original meteoroids into fragments, at which each fragment continue to crumble into smaller fragments; 3) the instantaneous spray of a large number of small particles that gives rise to meteor flares; 4) the quasi-continuous fragmentation-a gradual release of smallest fragments from surface of a parent meteoroid and their subsequent evaporation.

Quite probably that in the atmosphere a meteoroid may undergo the different combination of these fragmentation forms (Babadzhanov et al. 1989).

Quasi-continuous fragmentation of meteoroids

Unique meteor photographs obtained in Dushanbe by the method of instantaneous exposure (Babadzhanov 1983) with exposure of $5.6 \times 10^{-5} \text{ s}$ show clearly the effects of different types of meteoroid's fragmentation. But the most common type is the quasi-continuous fragmentation forming the shortlivingmeteor wakes of up to several ten metres in length. Instantaneous images of such meteors have a drop-like shape.

A theory of quasi-continuous fragmentation developed during last decade

(Lebedinets 1980; Novikov et al. 1984; Babadzhanov et al. 1984, 1988) allow to estimate both the masses of separated fragments and the density of meteoroids. According to this theory the meteor luminosity $I(\rho)$ at the height where the atmospheric density is equal to ρ depends on the main parameters of a meteoroid in the following way (Novikov et al. 1984; Babadzhanov et al. 1984, 1988):

$$(1) \quad I(\rho) = \frac{9\tau_v M_0 V_0^3 \cos Z_R}{2H(R_o R_1)^3} \left\{ F_1(\rho) \theta(a-\rho) + F_2^3(\rho) \theta(\rho-a) \theta(b-\rho) + \frac{1}{30} F_3(\rho) \theta(\rho-b) \theta(\rho_e-\rho) \right\},$$

where

$$(2) \quad F_1(\rho) = \rho \left\{ \frac{1}{3} (\rho_e - \rho)^2 \left[R_1^3 - (a - \rho)^3 \right] - \frac{1}{2} (\rho_e - \rho) \left[R_1^4 - (a - \rho)^4 \right] + \frac{1}{5} \left[R_1^5 - (a - \rho)^5 \right] \right\},$$

$$(3) \quad F_2(\rho) = \rho \left\{ \frac{1}{3} (\rho_e - \rho)^2 - \frac{1}{2} R_1 (\rho_e - \rho) + \frac{1}{5} R_1^2 \right\},$$

$$(4) \quad F_3(\rho) = \rho (\rho_e - \rho)^5,$$

$$(5) \quad a = \rho_e - R_o, \quad b = \rho_e - R_1,$$

τ_v , M_0 , V_0 are the luminous efficiency, preatmospheric meteoroid mass and velocity; H - the scale height; Z_R - the zenith distance of meteor radiant; ρ_e - atmospheric density in the arbitrary point of the meteor trajectory; a - the atmospheric density at the height of complete evaporation of fragments released at the moment of fragmentation beginning; b - the atmospheric density at the height of the end of fragmentation; R_o and R_1 - the parameters determining the quasi-continuous fragmentation:

$$(6) \quad R_o = \frac{6Q_f M_0^{1/3} \delta^{2/3} \cos Z_R}{\Lambda A H V_0^2}, \quad R_1 = \frac{6(Q-Q_f) M_0^{1/3} \delta^{2/3} \cos Z_R}{\Lambda' A' H V_0^2},$$

Q_f - the specific energy of meteoroid fragmentation; $Q=8 \times 10^{10}$ erg/g - the specific energy of heating and evaporation of meteoric matter; Λ, A, δ - the heat transfer coefficient, the shape factor and the meteoroid density respectively; Λ', A' - the same values for the fragments. $\theta(x)$ - Heavyside's function: $\theta(x)=1$ at $x>1$ and $\theta(x)=0$ at $x \leq 0$.

Meteoroid densities

Using the observed values of M_0 , V_0 , Z_R and the light curves of meteors by the method of successive approximations we determined such values of the parameters R_o and R_1 of equation (1) for which the theoretical and observed meteor light curves would coincide in the best way.

The meteoroid density and mass of fragments may be estimated from derived values of R_o and R_1 if the values of Λ , Λ' , A , A' , Q_f and δ are known apriori. According to Lebedinets (1991) for large meteoroids of mass between 0.01 and 10 g the heat transfer coefficient depends on mass M_0 as

$$(7) \quad \Lambda = \Lambda_0 + (1 - \Lambda_0) \exp(-kM_0),$$

where $\Lambda_0 = 0.03$, $k = 0.25 \text{ g}^{-1}$. It is assumed that $A=1.5$, $A'=1.21$, $H=6 \text{ km}$, $\Lambda'=1$, $\delta=3.5 \text{ g/cm}^3$. From the data of Lebedinets (1987) paper the dependence of fragmentation energy on density may be approximated as

$$(10) \quad Q_f * 10^{-10} = 0.10 + 0.180 \text{ g}_0.$$

Simulation of the meteor light curves was carried out for meteoroid densities between 0 and 10 g/cm^3 and mass of fragments between 10^{-10} and 10^{-9} g . As an example, Fig. 1 shows the results of simulation of two meteor light curves where the absolute meteor magnitude M is plotted against the altitude. As it seen, the observed light curves of examined meteors (marked by "X") correspond to theoretical ones calculated taking account of the quasi-continu-

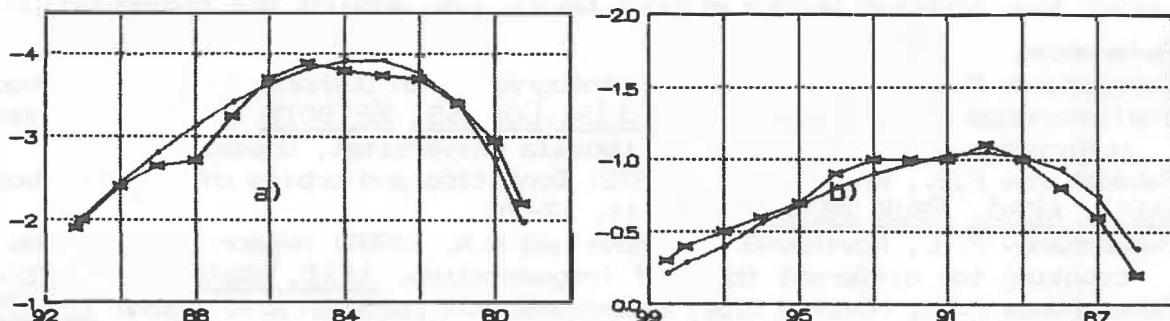


Fig. 1. Observed (X) and theoretical light curves of the meteors: a) Sporadic, $M_0 = 2.1 \text{ g}$, $V_0 = 43.1 \text{ km/s}$, $\cos Z_R = 0.794$; b) Geminid, $M_0 = 0.54 \text{ g}$, $V_0 = 36.1 \text{ km/s}$, $\cos Z_R = 0.800$

Table 2. Meteoroid densities

Shower	Parent body	Numbers of meteoroids of different densities (g/cm^3)					Mean All density g/cm^3	
		<1	1-2	2-3	3-5	5-8		
Perseids	P/Swift-Tuttle	2	4	5	27	8	46	3.8
Leonids	P/Tempel-Tuttle	1	5	1	2	1	10	2.5
Geminids	Phaethon	-	-	1	2	6	9	5.9
δ Cygnids	?	-	-	1	-	1	2	5.0
Quadrantids	P/Machholz	-	2	-	1	1	4	3.3
δ Aquarids	P/Machholz	-	-	1	4	5	10	5.3
Taurids	P/Encke	1	-	-	3	-	4	3.7
Sporadic		2	1	3	11	7	24	4.1

ous fragmentation. The results of determination of densities of meteoroids belonging to different streams are given in Table 2. An analysis of results shows that light curves of 109 out of 361 bright meteors photographed in Dushanbe are described sufficiently well by the theory of quasi-continuous fragmentation. That is about 30% of total number of investigated meteors. About 70% of the meteoroids probably exposed to other types of fragmentations. Out of 79 meteors, which light curves are described satisfactorily by the theory of quasi-continuous fragmentation, 18 meteors were produced by the

dense stony or chondrite type or iron meteoroids, 12 meteors - by the carbonaceous chondrites C2 and C1, and 18 meteors - by the carbonaceous chondrites C0 or dustballs.

Conclusion

So taking into account the quasi-continuous fragmentation, as a result of mathematical simulation of meteor light curves it is revealed that both among stream's and sporadic meteoroids the particles of quite different densities are found. It should be noted that on the average Perseid and Leonid meteoroids are considerable less dense than Geminids or Δ-Aquarids. Apparently this difference is caused by closeness of Geminid's and Δ-Aquarid's perihelion to the Sun (accordingly 0.14 and 0.07 A.U.). Perihelion of the Perseids and Leonids are close to 1 A.U. These results are in accordance with the estimates of meteoroid densities derived by the Lebedinets (1987) on the basis of meteor accelerations. On the average the densities of meteoroids are of 1-1.5 order larger than proposed before without taking into account the fragmentation.

References

- Babadzhanov P.B. (1983) Fireballs photographed in Dushanbe by the method of instantaneous exposure. In Asteroids, Comets, Meteors (C.-I. Lagerkvist and H. Rickman, eds.), pp. 439-445, Uppsala universitet, Uppsala.
- Babadzhanov P.B., Khaimov I.M. (1972) Densities and orbits of meteor bodies. Dokl. Akad. Nauk Tajik. SSR, 14, 17-21
- Babadzhanov P.B., Novikov G.G., Konovalova N.A. (1989) Meteor light curves accounting the different forms of fragmentation. Astr. Vestnik, 23, 277-281
- Babadzhanov P.B., Novikov G.G., Lebedinets V.N., Blokhin A.V. (1984) Theory of quasi-continuous fragmentation of meteor bodies accounting deceleration. Preprint of Physical Technology Institute, No 919, Leningrad, 55 pp.
- Babadzhanov P.B., Novikov G.G., Lebedinets V.N., Blokhin A.V. (1988) Procedure of interpretation of meteors' observations accounting fragmentation. Astron. Vestnik, 22, 71-78
- Bronshtein V.A. (1981) Physics of meteor phenomena, Nauka, Moscow, 416 pp.
- Ceplecha Zd. (1975) Ablation and shape-density coefficients. Bull. Astron. Inst. Czecho-Slov., 26, 242-248
- Jacchia L.G. (1955) The physical theory of meteors VIII. Fragmentation as the cause of the faint-meteor anomaly. Astrophys. Journ., 121, 521-527
- Halliday I. (1988) Geminid fireballs and the peculiar asteroid 3200 Phaethon. Icarus, 76, 279-294
- Lebedinets V.N. (1980) Dust in the high atmosphere and space, Meteors. Gydrometeoizdat, Leningrad, 247 pp.
- Lebedinets V.N. (1987) On the peculiarity of meteoroid density distributions in different meteor streams. Astron. Vestnik, 21, 262-271
- Lebedinets V.N. (1991) On the fraction of interplanetary solid bodies generating meteorites. Astron. Vestnik, 25, 200-207
- Levin B.Yu. (1962) Fragmentation of meteor bodies and estimates of the density of the atmosphere. Bull. Komissii po kometam i meteoram, 6, 3-10.
- McCrosky R.E. (1968) Orbits of photographic meteors. In Physics and Dynamics of Meteors, (L.Kresak and P.Millman, eds.), Reidel, Holland, pp. 265-279.
- Novikov G.G., Lebedinets V.N., and Blokhin A.V. (1984) On the fragmentation of meteoroids. Quasi-continuous fragmentation. Pisma v AJ, 10, 71-76
- Verniani F. (1969) Structure and fragmentation of meteoroids. Space Sci. Rev., 10, 230-261

P/MACHHOLZ 1986 VIII AND QUADRANTID METEOROID STREAM. ORBITAL
EVOLUTION AND RELATIONSHIP; *P.B.Babadzhanov and Yu.V.Obrubov,*
Astrophysical Institute, Dushanbe, 734670, USSR

Abstract. The evolution of the P/Machholz's meteoroid stream was simulated. It shows, that this stream may produce eight meteor showers. There are the known observed meteor showers such as the Quadrantids, Ursids, Northern and Southern Δ-Aquarids, Daytime Arietids and Α-Cetids. A satisfactory agreement of the theoretical and observed geocentric radiants and orbits allows to conclude, that the above showers could have been resulted from the decay of the P/Machholz nucleus. The age of the stream is estimated to be 7.5 millennia.

Introduction

The Quadrantids are one of the most interesting major meteor showers. The high activity and short duration of the Quadrantids imply the existence of a parent comet. The Quadrantid meteoroid stream is of great interest in respect to dynamics too. It is one of few meteoroid streams which can produce eight related meteor showers. Six of eight meteor showers such as the Northern and Southern Δ-Aquarids, Daytime Arietids, Ursids, Α-Cetids and Quadrantids are well-known from observations (Babadzhanov and Obrubov 1987, 1989).

In May 1986 D.Machholz discovered a new comet, which had got the designation 1986 VIII. This comet may be a unique object for investigations of the cometary nucleus evolution due to the short orbital period (5.25 yr) and small perihelion distance (0.127 AU). The fact that the comet Machholz was not discovered before 1986 is of interest as well. It seems more surprising since according to Sekanina (1990) 75 % of comet's returns to the Sun were favourable for observations. Sekanina (1990) and Green et al. (1990) assume the comet Machholz to be dormant for a long time till 1986.

Evolution of P/Machholz's orbit

McIntosh (1990) followed the evolution of P/Machholz's orbit over a period of 4 millennia. He found large variations in orbital inclination (from 12 to 80°) and in perihelion distance (from 0.05 AU or even less to about 1 AU) and pointed to the surprising coincidence in orbital variation of P/Machholz with that of the Quadrantids. However, McIntosh did not find a similarity in their orbits at some fixed moment, that could have confirmed on the possible genetic relationship. McIntosh consider the main reason to be in the time shift in variations of e , q , i . Green et al. (1990) have also followed the evolution of P/Machholz's orbit. Although they used more precise orbit, but the results did not differ from those of McIntosh. They did not find any close encounter with the Jupiter either.

It is known that the orbital element determining the body's position in the Keplerian orbit is calculated rather roughly. Thus, the body's position in its orbit becomes uncertain after hundreds or even tens of orbital revolutions. Therefore, it is necessary to study the motion of the comet (or test particles) at different initial positions. We have integrated the equations of the perturbed motion of the comet and three test particles back in time. The starting orbit was taken from Green et al. (1990). The starting eccentric

anomalies E of test particles were taken to be equal to 90° , 180° and 270° , while for the comet $E=0^\circ$ at the time of perihelion passage in 1986. The integration was carried out by the Runge-Kutta method of the fourth order with the self-adjusting step length at the time interval of about 8 millennia. The perturbations from the Jupiter and Saturn were taken into account, but their motions were supposed to be unperturbed. It is turned out that the motion of two of three test particles suffered a number of close encounters with the Jupiter at the distances Δj less than 0.3 AU. The data on these encounters for the last two millennia are given in the Table 1, where T - the year of encounter, and Δj - the value of encounters in AU.

Table 1. Encounters of P/Machholz's test particles with the Jupiter.

T	Δj	a	e	i	T	Δj	a	e	i
$E=180^\circ$									
976	0.260	3.184	0.615	81.0°	538	0.209	3.068	0.647	82.2°
692	0.258	3.178	0.567	82.1°	360	0.194	3.101	0.649	81.2°
16	0.296	3.200	0.618	82.5°	253	0.162	3.060	0.699	82.8°
					206	0.267	3.006	0.743	81.4°
$E=270^\circ$									

As seen from Table 1, the encounters do not lead to the catastrophic changes in orbits. The data of Table 1 allowed to conclude that P/Machholz had not any close encounters with the Jupiter at least after 976 AD. This confirms the fact that the comet was dormant for a long time till 1986.

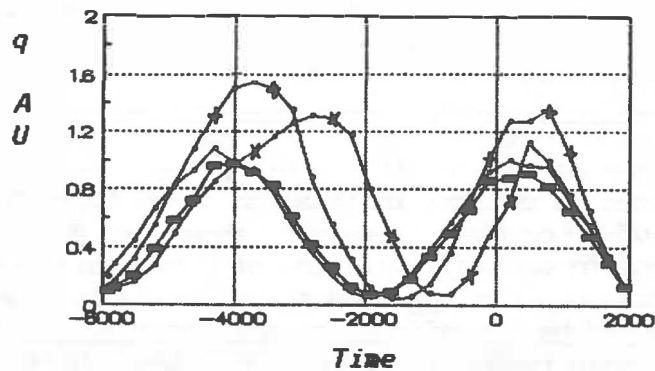


Fig.1. Variations of perihelion distances of P/Machholz - ■, and three test particles:
 • - $E=90^\circ$, + - $E=180^\circ$,
 x - $E=270^\circ$. Time in yrs.

Fig.1 presents the variations in perihelion distances of the comet and test particles. As seen, the periods and the ranges of variations have some scatter caused by the different starting positions. This occurs at variations in e and i too. The same results were obtained when the evolution of the Quadrantid meteoroid stream was studied (Williams et al. 1979; Babadzhanyan et al. 1991).

The model of the P/Machholz meteoroid stream

It seems very likely that P/Machholz was an active comet in the past. Hence, the meteoroids were being ejected from comet's rotating nucleus at different directions and velocities. To model the meteoroid stream evolution one should choose the initial time moment and give the distribution of meteoroids

orbits. The starting time is taken to be 4500 BC under two reasons:

1. Near this moment we have found the most similarity between P/Machholz and mean Quadrantid's osculating orbits, i.e. the D-criterion is equal to 0.14;
2. The radius-vector to the ascending node of the comet's orbit is close to the Jupiter's orbit.

The first reason was chosen because it requires the least ejection velocities responsible for the Quadrantid shower formation. The second because of the likelihood of the capture of the comet by Jupiter into a short-period orbit. It is known, that the meteoroids' orbits in the same stream differ strongly from the comet's orbit by their semimajor axes and eccentricities. Thus, the initial distribution of the meteoroid orbits was taken to be:

$a=2.70$ AU	$e=0.691$	$E^0 = 30^\circ, 270^\circ$;
$a=2.80$ AU	$e=0.702$	$E^0 = 10^\circ, 70^\circ, 130^\circ, 190^\circ, 250^\circ, 310^\circ$;
$a=3.03$ AU	$e=0.725$	$E^0 = 0^\circ, 60^\circ, 120^\circ, 180^\circ, 240^\circ, 300^\circ$;
$a=3.20$ AU	$e=0.740$	$E^0 = 20^\circ, 80^\circ, 140^\circ, 200^\circ, 260^\circ, 320^\circ$.

For all orbits we took $q=0.834$ AU, $i=69^\circ$, $\Omega=283^\circ.3$, and $\omega=170^\circ.7$. According to our calculation the comet Machholz had such elements in 4500 BC. This distribution, except of the eccentric anomaly E , corresponds to the meteoroid ejection velocities of up to 300 m/s along and opposite the comet motion in the perihelion, and represents a young flat meteoroid stream.

Then, for all particles we have calculated the perturbations from the Jupiter and Saturn beginning from 4500 BC till 3000 AD. By the way all intersections of particles' orbits with the Earth's orbit were fixed. The Earth-crossing orbits can be divided into two groups: the first group includes the orbits with high inclinations (from 67° to 80°) and perihelion distances from 0.9 to 1.0 AU; the second group - the orbits with moderate inclinations (from 19 to 40°) and small perihelion distances - from 0.03 to 0.12 AU.

Each group may be divided into four subgroups according to their perihelion arguments. In the first group the perihelion arguments cluster around the $\omega = 0^\circ \pm 5^\circ$ and $180^\circ \pm 6^\circ$, and in the second group - around $\omega = 0^\circ \pm 26^\circ$ and $180^\circ \pm 30^\circ$. So there are eight subgroups of the Earth-crossing orbits, i.e. eight meteor showers, which could be produced by P/Machholz. The names and ranges of orbital elements and geocentric radiants for these eight showers are given in Table 2.

The difference between the simulated Quadrantids and Ursids as well as the Carinids and δ -Velids seems to be rather relative because there is no clear line neither among their orbits nor the radiants. In order to distinguish these showers we used some additional dynamical criterion. The orbits with $\omega < 180^\circ$ were thought to belong to the Quadrantids and with $\omega > 180^\circ$ to the Ursids respectively. For the Carinids - $\omega < 360^\circ$ and for the δ -Velids - $\omega > 0^\circ$. This distinction allows us to determine the direction of secular variations of radii-vectors to the orbital nodes. Moreover, the Quadrantid and Carinid meteoroids collide with the Earth after the perihelion, but the Ursid and δ -Velid meteoroids - before the perihelion. Table 2 presents the observed orbital elements and geocentric radiants for six of the eight meteor showers according to the data of different authors. A satisfactory agreement of the theoretical and observed radiants and orbits confirms the possible genetical relationship of all these showers with the comet Machholz.

Table 2. Theoretical (T) and observed (O) ranges of orbital elements of the P/Machholz's meteor showers.

	q min max	e	i	Ω	ω	α	δ	v_g min max	
Quadrantids									
T	.92-1.02	.65-.72	67-72	278-290	159-180	223-243	+42-+54	38-43	
O	.97-0.98	.65-.70	69-73	280-283	167-170	219-232	+48-+55	40-43	
Ursids									
T	.92-1.02	.66-.72	68-73	271-282	180-198	215-227	+48-+60	38-45	
O	.94-0.95	.64-.85	54-67	260-283	187-206	190-226	+58-+76	33-40	
Carinids									
T	.92-1.02	.66-.71	72-80	86-109	344-360	149-164	-64-+46	41-49	
O				Will be recognised ?					
Δ -Velids									
T	.92-1.02	.68-.71	74-80	99-109	0-16	142-160	-61-+50	41-49	
O				Will be recognised ?					
Northern δ -Aquarids									
T	.04-.11	.96-.99	19-40	104-136	326-340	316-340	-10-+2	40-44	
O	.06-.12	.95-.98	14-21	128-143	323-334	337-346	-5-+3	40-42	
Southern δ -Aquarids									
T	.03-.12	.96-.99	20-40	296-322	141-160	334-351	-18-13	39-44	
O	.07-.14	.96-.99	23-32	304-322	139-152	337-351	-19-14	40-44	
Daytime Arietids									
T	.03-.12	.96-.99	20-40	72-87	20-37	42-50	+22-+25	40-44	
O	.04-.10	.94-.98	18-46	77-89	19-30	43-50	+22-+26	39-44	
α -Cetids									
T	.04-.12	.96-.99	19-36	249-263	203-216	39-53	+8-+13	39-44	
O	.06-.18	.89-.99	20-31	255-269	194-214	44-53	+6-+12	37-39	

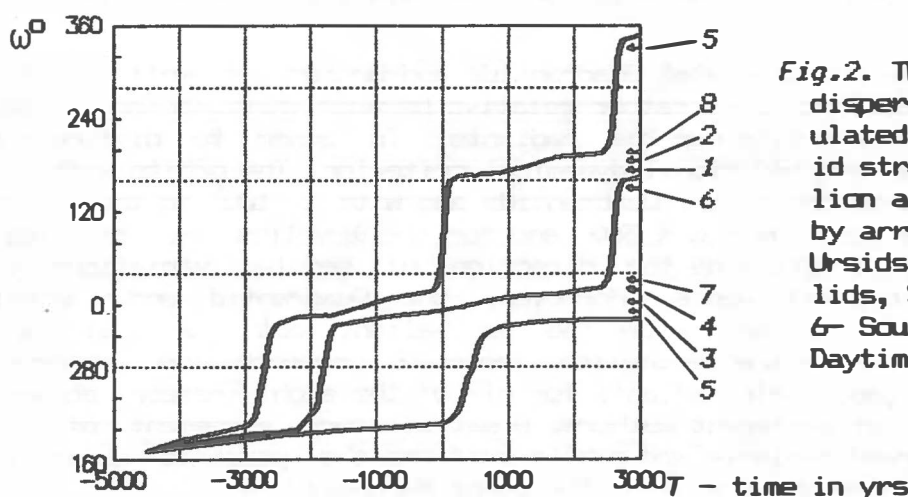


Fig.2. The increase of the dispersion of ω in the simulated P/Machholz's meteoroid stream. The shower perihelion arguments are indicated by arrows: 1- Quadrantids, 2- Ursids, 3- Carinids, 4- Δ -Velids, 5- Northern δ -Aquarids, 6- Southern δ -Aquarids, 7- Daytime Arietids, 8- α -Cetids

Simultaneous activity of meteor showers produced by the same parent body is possible if the dispersion of particles' perihelion arguments embraces those of the showers. Fig.2 shows the increase in the dispersion of the perihelion arguments under planetary perturbations for the simulated P/Machholz's meteoroid stream. As seen 7.5 millennia later after meteoroid ejection the dispersion becomes more than 360° (Fig.2). By this moment all the eight meteor showers must manifest their activity. This time interval may be considered to be an evaluation of the P/Machholz stream age. The real stream age might be even less if the initial dispersion in the semimajor axes is assumed to be greater.

Discussion

The simulation of the P/Machholz's meteoroid stream shows clearly that this comet can produce eight meteor showers. At present at least six of eight meteor showers are known from observations and show high activity. Earlier this result was obtained when studing only the Quadrantid meteoroid stream evolution (Babadzhanov and Obrubov 1987, 1989; Babadzhanov et al. 1991). Now we have come to the conclusion that the parent comet of the above six meteor showers is found. It is the comet Machholz 1986 VIII.

A possibility of the relationship of P/Machholz with Daytime Arietids and Delta-Aquarids was investigated by McIntosh (1990) too. However, he had doubts about their genetic relationship and about our results concerned the possible interrelations of the observed showers. His doubts are based on the time shift in the orbital variations of the P/Machholz and Quadrantids and on the differences in the directions to perihelia of the meteor shower current orbits.

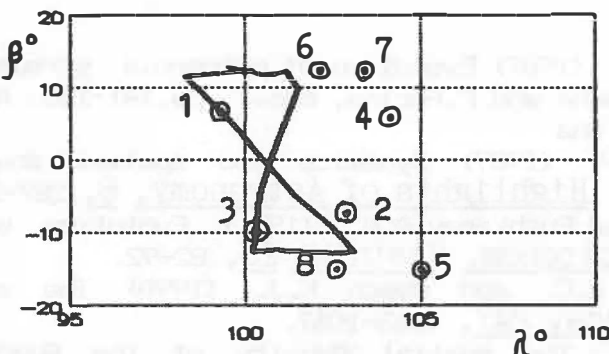


Fig.3. Evolution of the perihelion position of P/Machholz's orbit. Current perihelion positions of the related meteor showers are marked by numbers as in Fig.2.

The observed differences among the meteor shower orbits and in the comet's orbit may have resulted from the differential planetary perturbations. Fig.3 gives the variations in the perihelion position of P/Machholz's orbit during one period of the perihelion argument variation. As seen, this position changes from -15° to 15° in ecliptic latitude β and from 98° to 103° in ecliptic longitude λ , painting the curve like "eight". Since the dispersion of ω in the meteoroid stream reaches 360° with time, then all directions seem to be possible within these ranges. For all simulated Earth-crossing meteoroid orbits the positions of perihelia are approximately in bounds from -20° to $+20^\circ$.

in β and from 88° to 109° in λ . There are also the observed and theoretical perihelion positions of the P/Machholz meteor showers in Fig.3. As seen, the planetary perturbations explain the dispersion of perihelion positions very well.

According to Babadzhanov et al. (1991) to ensure the observed activity of six meteor showers the comet Machholz must have maximum initial mass of 1.4×10^{18} g, that corresponds to the radius about 7 km if the mean density of the cometary nucleus of 0.8 g/cm^3 . For comparison McBride and Hughes (1990) obtained the radius of 1 km under assumption that P/Machholz had produced the Quadrantid meteor shower only. According to Sekanina (1990) the current radius of the P/Machholz nucleus do not exceed 2.7 km. If assume the comet to be inside the Jupiter's orbit during 7-8 millennia, then taking into account small perihelion distance, it is not difficult to explain the decrease of its radius from 7 to 2.7 km or even less.

Conclusions

The investigation of P/Machholz orbital evolution gives an evidence that during the nearest 500 yrs the cometary orbit will intersect the Earth's orbit at the place of appearance of the Daytime Arietids and later - at the place of appearance of the Northern Delta-Aquarids. Thus, one may expect the increase in the activity of these showers.

The best confirmation of our results would have been a discovery of the Carinid and Delta-Velid meteor showers. Taking into account the radiant positions of these showers in the Southern hemisphere, we asked prof. W.J.Baggaley (New Zealand) to carry out special showers searches with his new meteor radar and received his kind consent.

References

- Babadzhanov P.B. and Obrubov Yu.V. (1987) Evolution of meteoroid streams. In Interplanetary Matter (Z.Ceplecha and P.Pecina, eds.), pp.141-150. Astron. Institute of Czechoslovakia, Praha
- Babadzhanov P.B. and Obrubov Yu.V. (1989) Dynamics and spatial shape of short-period meteoroid streams. Highlights of Astronomy, 8, 287-293.
- Babadzhanov P.B., Obrubov Yu.V. and Pushkarev A.N. (1991) Evolution of the Quadrantid meteoroid stream. Astronom. Vestnik, 25, 82-92.
- Green D.W.E., Rickman H., Porter A.C. and Meech K.J. (1990) The strange periodic comet Machholz. Science, 247, 1063-1067.
- McBride N. and Hughes D.W. (1990) The spatial density of the Quadrantid meteoroid stream - a clue to the decay of the parent comet. In Asteroids, Comets, Meteors III (C.I.Lagerkvist, H.Rickman, B.A.Lindblad, and M.Lindgren, eds.), pp. 555-558, Uppsala universitet, Uppsala
- McIntosh B.A. (1990), Comet P/Machholz and the Quadrantid Meteor Stream. Icarus, 86, 299-304.
- Sekanina Z. (1990) Periodic comet Machholz and its idiosyncrasies. Astron. J., 99, 1268-1278.
- Williams I.P., Murray C.D. and Hughes D.W. (1979) The long-term orbital evolution of the Quadrantid meteor stream. Month. Not. Roy. Astron. Soc., 189, 483-492.

RADAR METEOR ORBITAL STRUCTURE OF SOUTHERN HEMISPHERE COMETARY DUST STREAMS

W J Baggaley, A D Taylor,
Physics Department, University of Canterbury, Christchurch, New Zealand

The Christchurch, New Zealand meteor orbit radar (AMOR) with its high precision and sensitivity, permits studies of the orbital fine structure of cometary streams. PC generated graphics are presented of data on some Southern Hemisphere Streams. Such data can be related to the formation phase and subsequent dynamical processes of dust streams.

INTRODUCTION

The AMOR 8 km baseline facility has been in routine operation since April 1990 and to June 1991 1.32×10^5 meteoroid orbits have been obtained. The limiting sensitivity corresponds to radar meteor magnitude + 13 with orbital precision 2 degrees in angular elements and 10% in $(1/a)$ (Baggaley et al 1992).

An outstanding feature of the facility is the radar signal processing routines and orbit reduction and graphics packages which permit rapid presentation and analyses of a large number of orbits. Such comprehensive data sets will permit the study of the structure and related dynamics of cometary dust streams. The orbital properties of four short-period cometary streams observed in 1990-1 are here presented for the Eta Aquarids, Alpha Scorpids, South delta Aquarids, Alpha Capricornids. AMOR achieves a high data rate: for example the number of high precision orbits for the Eta Aquarids, is 361, compared with the 5 of Lindblad (1989) and 1 of Cook (1972).

THE DATA

We have several methods of analysing and presenting data. For illustration two types of presentation are given. Right ascension - declination plots ($40^\circ \times 14^\circ$) of meteor radiant points of (i) all meteors and (ii) those meteors identified as cometary stream members by employing the modified D criterion of Drummond (1979). The DD criterion gives a measure of the distance between points in a five parameter orbit phase space. The procedure was a serial search employing a seed orbit (from Cook 1972 or a mean from an AMOR direct D test) and subsequent membership requiring at least two orbits with $DD < 0.04$. The other presentation is of the orbital distributions and mean values of those meteors selected from the serial search.

Work has also been carried out on the density profiles of streams: achieved by fixing four elements while varying the fifth across the range of interest.

Examples of the PC-generated graphics available from the AMOR system are shown in Fig 1 giving celestial coordinate plots of corrected meteor radiants for the Eta Aquarid shower 1990 and Fig 2 showing distributions of orbital elements for the Southern Delta Aquarid shower 1990. Fig 1 illustrates the daily radiant motion (L being the solar longitude) and stream member selection resulting from the operation of the DD criterion. From the

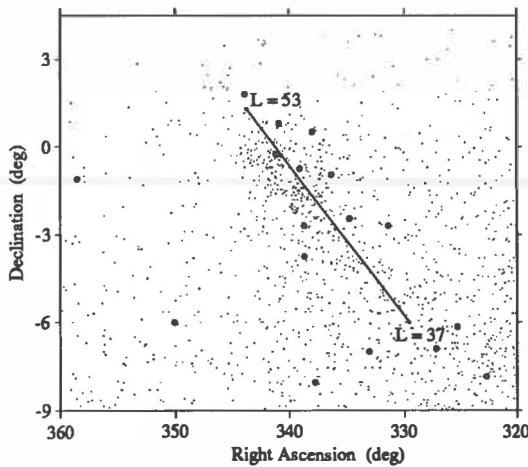


Figure 1(a): Daily motion of the eta Aquarid mean orbit is overlaid on the corrected geocentric radiants 1990 April 28 - May 18. L is the solar longitude. Large dots correspond to meteors brighter than +5 mag.

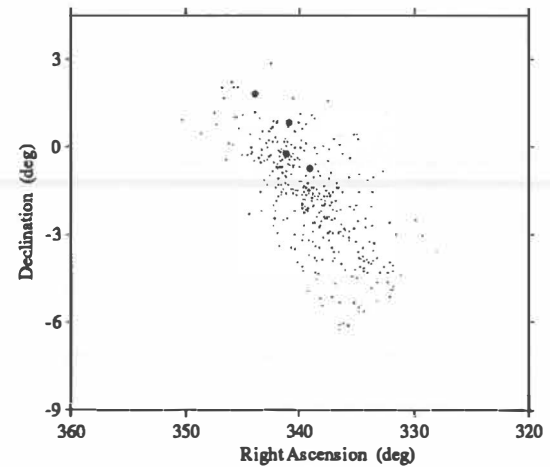


Figure 1(c): Radiants of 361 meteors selected by a RA-Dec box parallel to the daily motion of the radiant.

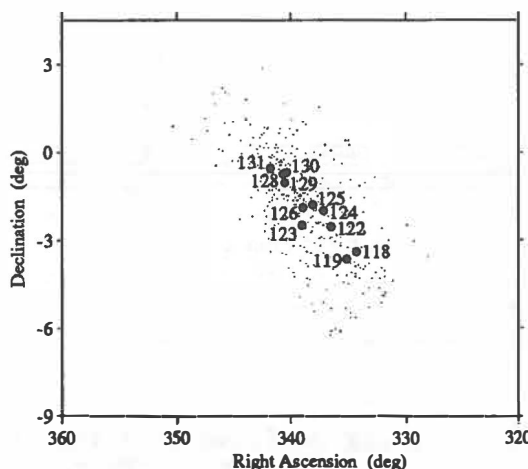


Figure 1(b): Mean position of the radiant points for shower meteors detected on each day number as the Earth moves through the stream.

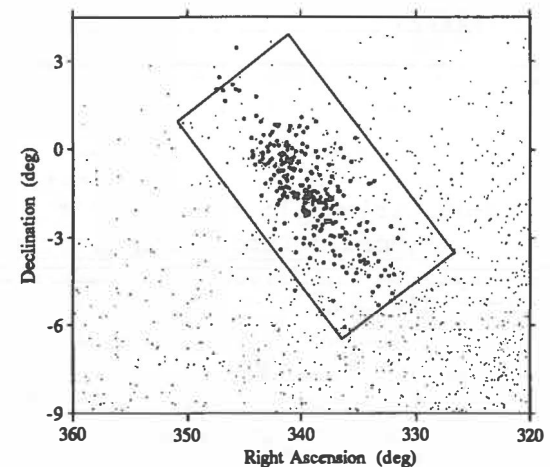


Figure 1(d): Radiants of stream meteors identified using a D criterion serial search plotted as larger spots. The mean stream orbit from (c) is used to seed the group and membership requires two parent sponsors within $DD < 0.04$ of the proposed orbit.

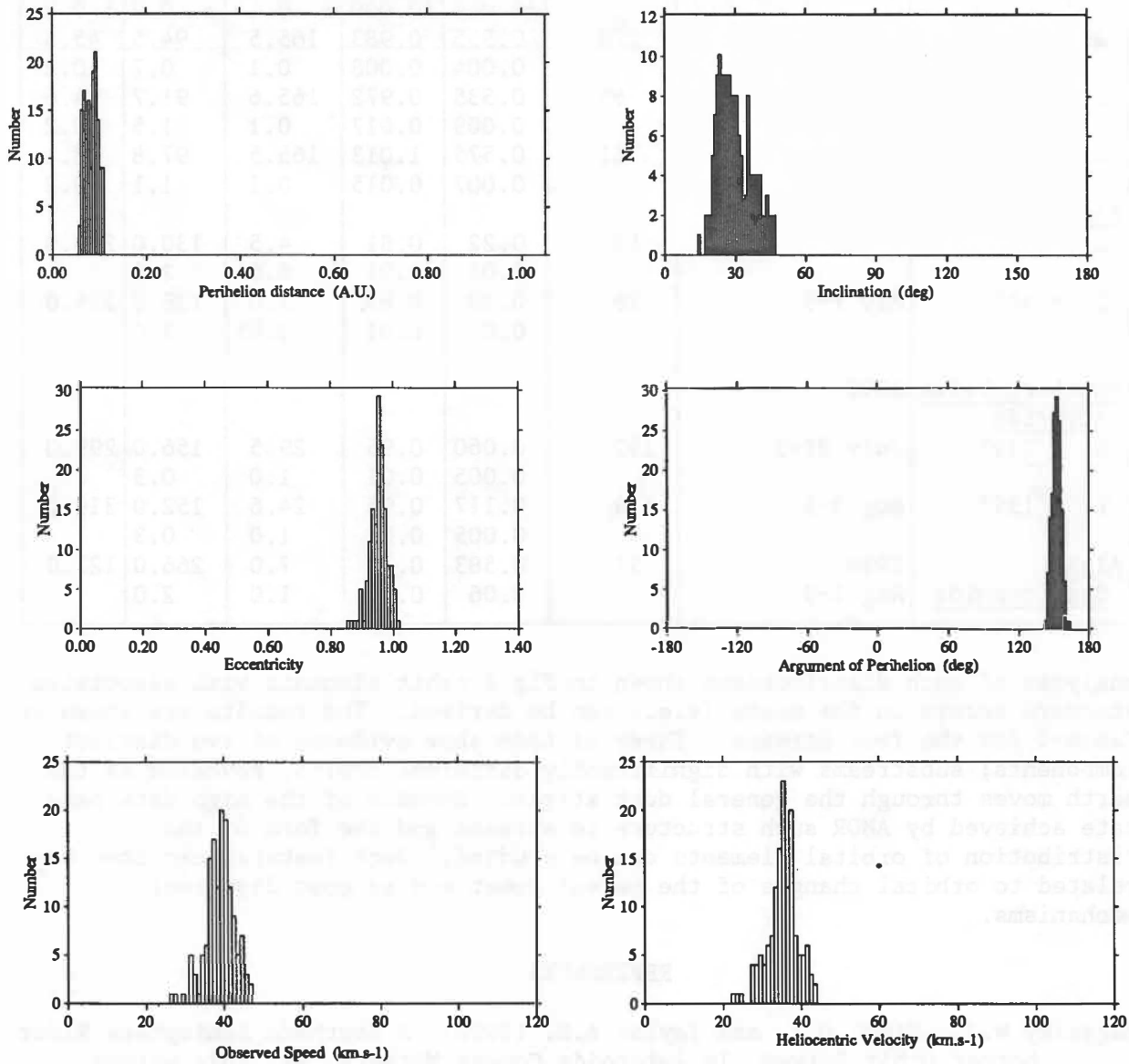


Figure 2: Southern Delta Aquarids. Distribution of orbital elements for 144 stream meteors detected 1990 August 3,4 and 5.

TABLE 1. MEAN ORBITAL ELEMENTS

Stream	Dates	Number	q	e	i	w	Ω_{1950}
<u>Eta Aquarids</u>	1990						
radiant box	April 28-May 18	361	0.566 ±0.006	0.969 ±0.009	165.8 ±0.1	95.4 ±0.9	45.8 ±0.2
serial search		270	0.555 0.004	0.983 0.008	165.5 0.1	94.5 0.7	45.5 0.2
L = 49		65	0.535 0.009	0.972 0.017	165.6 0.1	91.7 1.5	44.6 0.2
L = 45		61	0.575 0.007	1.013 0.015	165.5 0.1	97.8 1.1	48.1 0.2
<u>Alpha Scorpid</u> s	1991						
L = 38°	April 27-9	53	0.22 0.01	0.81 0.01	4.5 0.05	130.0 2.0	218.0
L = 46°	May 7-9	38	0.20 0.01	0.85 0.01	3.0 0.05	136.0 2.0	226.0
<u>Southern Delta Aquarids</u>	1990						
L = 119°	July 21-3	152	0.060 0.005	0.95 0.01	29.5 1.0	156.0 0.3	299.0
L = 139°	Aug 3-5	139	0.117 0.005	0.96 0.01	24.6 1.0	152.0 0.3	319.0
<u>Alpha Capricornids</u>	1990	57	0.583 0.06	0.70 0.01	7.0 1.0	266.0 2.0	127.0
	Aug 1-3						

analysis of such distributions shown in Fig 2 orbit elements with associated standard errors in the means (s.e.) can be derived. The results are shown in Table 1 for the four streams. Three of them show evidence of two distinct components; substreams with significantly different orbits, revealed as the earth moves through the general dust stream. Because of the high data rate achieved by AMOR such structure in streams and the form of the distribution of orbital elements can be studied. Such features can then be related to orbital changes of the parent comet and to dust dispersal mechanisms.

REFERENCES

- Baggaley W.J., Steel D.I. and Taylor A.D. (1992) A Southern Hemisphere Radar Meteor Orbit Survey In Asteroids Comets Meteors '91, this volume.
- Cook A.F. (1972) A working list of meteor streams Meteor Research Program NASA CR-2109 Smithsonian Astrophysical Observatory Washington DC.
- Drummond J.D. (1979) On the meteor-comet orbital discriminant D. Proc Southwest Reg Conf Astron Astrophys, 5, 83-6.
- Lindblad B.A. (1989) The orbit of the Eta Aquarid meteor stream in Third International Symposium Asteroids, Comets, Meteors. (C. I. Lagerkvist, P. Magnusson, H. Rickmann, eds.), Uppsala, Sweden.

A SOUTHERN HEMISPHERE RADAR METEOR ORBIT SURVEY

W.J. Baggaley, D.I. Steel[†] and A.D. Taylor[‡]

Department of Physics, University of Canterbury, Christchurch, New Zealand.

Abstract: A meteor radar system has been operated on a routine basis near Christchurch, New Zealand, to determine the orbits of Earth-impacting interplanetary dust and meteoroids. The system sensitivity is +13 visual magnitude, corresponding to $\sim 100 \mu\text{m}$ sized meteoroids. With an orbital precision of 2° in angular elements and 10% in orbital energy ($1/a$), the operation yields an average of 1500 orbits daily with a total to date in excess of 10^5 .

The use of pc's and automated data reduction permit the large orbital data sets we collect to be routinely reduced. Some illustrative examples are presented of the signal formats/processing and the results of data reduction, giving the individual orbital elements and hence the overall distributions. Current studies include the distribution of dust in the inner solar system; the influx of meteoroids associated with near-Earth asteroids; and the orbital structure existing in comet-produced streams.

THE RADAR SYSTEM AND DATA COLLECTION

After some years of construction a meteor orbit radar (AMOR) was commissioned for routine determination of the heliocentric orbits of Earth-impacting dust in 1990 February (Steel and Baggaley, 1985; Taylor, 1991). The facility (acronym AMOR being one type of near-Earth asteroid of interest in dust studies) is situated at geographic coordinates $172^\circ 41' \text{ East}$, $43^\circ 49' \text{ South}$ near Christchurch, New Zealand. The transmitter provides 20 kW peak pulse power at 26.2 MHz, with a pulse interval of 2.64 ms (giving a sampling frequency of 379 s^{-1}), fed into a horizontal stack of eight rhombic antennas providing a south-directed beam about 30° above the horizon: this means that most detected meteors have radiants close to and south of the equator. Meteor echoes are received by an array of three antennas with spacing N-S and E-W of $\sim 8 \text{ km}$, each antenna being a collinear array of length 12λ . FM radio links transmit signals from each outstation to the central site. Echo elevation is measured using a radio interferometer consisting of two antennas having a ground separation of 5λ providing signals in phase quadrature. Echo timing between the three antenna arrays provides N-S and E-W meteoroid velocity components which together with the echo elevation located within the narrow ($\sim 2^\circ$ azimuth) transmitter beam permits each meteor radiant point and its velocity to be determined; for more details of this and previous radar meteor orbit determination techniques see Steel and Baggaley (1985) and references therein. This technique has an advantage over previous orbit radars using Fresnel diffraction patterns to determine velocities in that the resulting number of successful orbit determinations is about an order of magnitude greater (because of the paucity of recorded diffraction patterns). The system limiting sensitivity corresponds to radio meteor magnitudes of about +13 [approximately $100 \mu\text{m}$ -sized dust particles; this is similar to the limiting magnitude of the Harvard Radar Meteor Project (Cook *et al.*, 1972), although most meteors detected therein were rather brighter (larger meteoroids)].

To facilitate interfacing to a portable pc the facility uses a five channel meteor logger, consisting of timing control, signal duplexing using transfer via direct memory access to the computer, and linear 8-bit conversion to digitize the incoming analogue radar signals. The interface to the pc permits the logging of three amplitude channels (from the spaced antenna locations named Home, Nutt and Spit) and two phase channels (triangular sine and cosine: Tin and Tos), all with $40\mu\text{s}$

[†]Present address: Anglo-Australian Observatory, Private Bag, Coonabarabran, NSW 2357, Australia.

[‡]Present address: Unit for Space Sciences, University of Kent, Canterbury, CT2 7NR, England, U.K.

sampling, which renders 66 range bins each of width 6 km in every radar sweep. The echo recognition program records a half-second of data straddling each meteor, identifies enduring echoes, and discriminates against interfering signals.

Raw echo data from the 30 Mbyte pc disk are transferred to the institution's VAX mainframe where programs operate on the data using various digital signal processing routines in order to reject echoes affected by ionospheric scatter and broadcast interference and those yielding ambiguous parameters; suppression of random transient signals etc. is also carried out. Time intervals

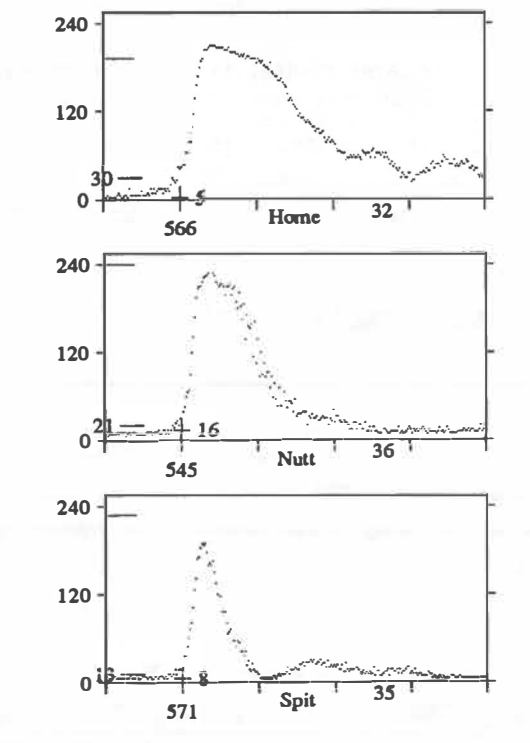


Figure 1: An example of a raw meteor observation record where no Fresnel oscillations are detected, as is most often the case.
Ordinate: Radar pulse number (spacing 2.64 ms).
Abscissa: Relative amplitudes (8-bit digital).

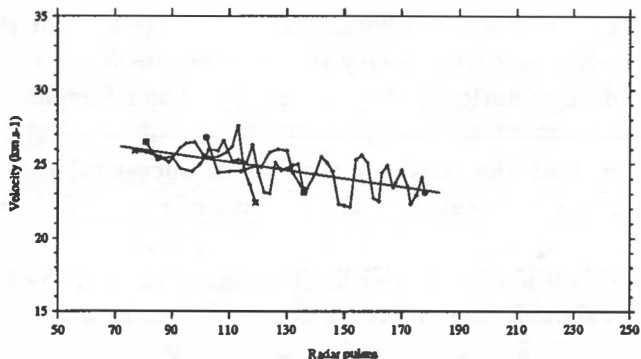
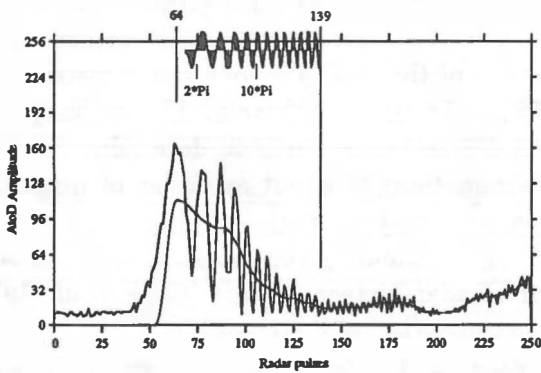
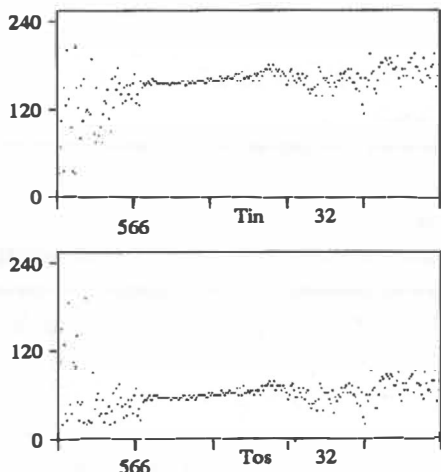


Figure 2: An example of a meteor echo showing a Fresnel pattern and the deduced deceleration.
Left: Diagnostic output from routines establishing the relative phase of pulse amplitudes: the deceleration can thus be determined from this record only, in principle.
Right: Velocity data from simultaneous Fresnel patterns at the three receiving sites allow a cross-check; in addition the deceleration may vary at different points in the meteoroid trajectory (different altitudes). The measured atmospheric deceleration was 10.6 km sec^{-2} .

between echoes are defined by the instant of the maximum gradient in the rising edge of the signal (corresponding to the specular reflection condition in the leading edge of the Fresnel diffraction pattern of the echo). Those echoes with well-defined diffraction patterns in at least one channel, about 10% of the total, provide an independent velocity calibration: algorithms to extract the sinusoidal component and hence derive a velocity are applied, whilst the analysis of subsections of either one oscillating profile or overlapping subsections from multiple stations yield meteoroid decelerations. Such information permits accurate estimates of pre-atmospheric velocities for these dust particles. Example of meteor echo records are shown in Figures 1 and 2.

Reduction programs calculate the heliocentric orbital elements after standard corrections for diurnal aberration, zenith attraction and the Earth's orbital motion with several coordinate transformations. The overall system resolution is about 2° in angular elements (due mainly to the antenna beam widths) and 10% in $1/a$ (due mainly to the echo timing uncertainties).

METEOR ORBIT SURVEY DATA

There are two unique features of the AMOR facility. One is the rapid reduction of on-site radar signal recordings to provide orbital element data sets amounting to approximately 1500 meteor orbits daily: this allows in principle an almost continuous survey, the limitation being the stamina of the staff. Secondly, the data processing software and graphics permit the comprehensive display of all desired orbital information. The provision of such facilities allows the full exploitation of the incoming data in near-real time, whereas the volume of data tended to strangle the surveys carried out in the 1960's. For example, the equipment of the Harvard Radar Meteor Project (Cook *et al.*, 1972) was run generally for only the first five minutes in each hour; the available technology has advanced sufficiently to allow powerful radars such as AMOR to now provide in a manageable form very extensive data sets pertaining to the distribution of meteoroids and dust in the inner solar system, and thus the origin (NEA's? SP Comets? LP Comets?) and evolution of these particles to be better understood (*cf.* Baggaley and Taylor, these proceedings).

The computer software and hardware mentioned above allow the efficient presentation of many characteristics of the data; for example radiant plots (R.A *vs.* Dec), orbital element distributions, ecliptic velocity projections (yielding direction of arrival in geocentric or heliocentric frames), or two-dimensional plots (*e.g.* semi-major axis *vs.* eccentricity). Examples are presented in Figure 3 for the whole data set collected between 1990 April and 1991 June; these are unweighted data, with no allowance having been made for the meteoroid collision probability with the Earth, detection probability in the atmosphere, and other selection effects which distort the detected distributions from the true distributions in space.

To the time of writing 132,996 individual meteor orbits have been determined with AMOR, compared to the total of about 68,000 determined by radar, photographic and TV techniques from the U.S.A., the U.S.S.R., Somalia, Australia and Canada and stored at the IAU Meteor Data Center in Lund, Sweden. Thus not only have we almost doubled mankind's inventory of meteor orbits with AMOR, but we have also increased the number of southern hemisphere meteor orbits by an even larger factor. The only previous radar orbit set-up south of the equator was operated from Adelaide, South Australia, in the 1960's, and produced less than 4,000 orbits to sizes of ~ 1 mm (see Olsson-Steel, 1988, and original references therein); the Soviets built a radar near Mogadisho in Somalia in the 1960's giving orbits for southern radiants but these are of dubious quality. As this program enters the detailed analysis stage, with much stream-searching and so on to be carried out amongst the currently-available data set, we plan to continue operations so as to increase the available archive of meteor orbits from the southern hemisphere further still, with particular emphasis upon deep southern radiants.

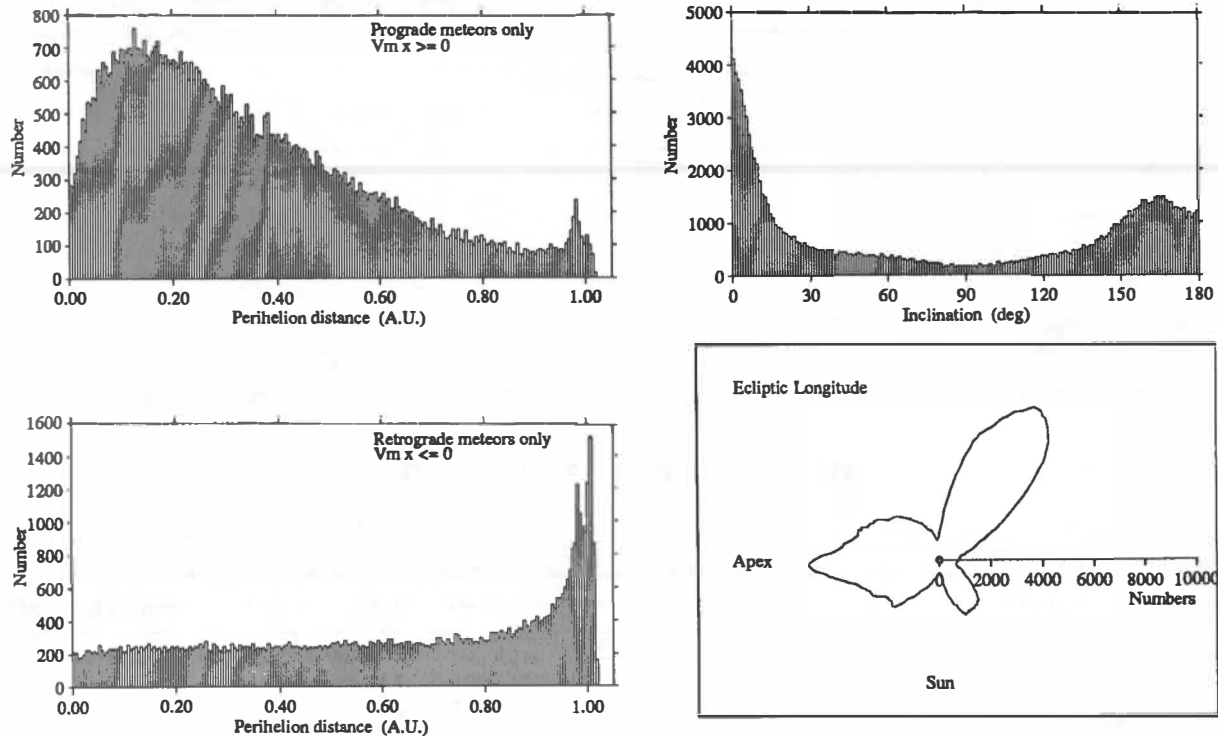


Figure 3: Examples of orbital element distributions for 132,996 meteors detected between 1990 March and 1991 June. At top right the inclination distribution indicates that there are many meteoroids of low inclination and an increase in the number at $i > 120^\circ$, although this is mainly due to the higher collision probabilities (low and high i) and higher incoming velocities (high i) of such orbits. At left are shown the distributions of perihelion distances separately for the prograde and retrograde meteoroids, showing that most prograde meteoroids are detected well-away from perihelion, most retrograde meteoroids close to perihelion; again impact probability considerations mean that these should not be viewed as being true distributions in space. (Note that the twin peaks near $q = 1$ AU in the plots allow an independent assessment of the eccentricity of the Earth's orbit to be made!). The polar plot of the corrected (Earth's motion removed) ecliptic radiants shows the three-lobed shape characteristic of the same distributions from other surveys. For comparative plots see, for example, Olsson-Steel (1988).

References

- Cook, A.F., Flannery, M.R., Levy, H., McCrosky, R.E., Sekanina, Z., Shao, C.-Y., Southworth, R.B., and Williams, J.T. (1972). NASA Contractor Report 2109.
- Olsson-Steel, D. (1988). Identification of meteoroid streams associated with Apollo asteroids in the Adelaide radar orbit surveys. *Icarus*, 75, 64–96.
- Steel, D.I. and Baggaley, W.J. (1985). Meteoroid orbits determined by southern hemisphere radar. In *Properties and Interactions of Interplanetary Dust, IAU Coll. 85* (R.H. Giese and Ph. Lamy, eds.), pp. 299–303. Reidel, Dordrecht, Holland.
- Taylor, A.D. (1991). Ph.D. Dissertation, Department of Physics, University of Canterbury, N.Z.

ION PRODUCED COMETARY ORGANIC CRUST

G.A. Baratta

Osservatorio Astrofisico, Città' Universitaria I-95125 Catania, Italy

G. Strazzulla

Istituto di Astronomia, Città' Universitaria I-95125 Catania, Italy

ABSTRACT

For several years many experimental results have been obtained on the chemical and physical changes induced by ion and electron irradiation of materials with a view to their Astrophysical relevance (Foti et al., 1984; Johnson et al., 1984; Andronico et al., 1987; Lanzerotti et al., 1987; Strazzulla et al., 1991a; Strazzulla and Johnson, 1991). Among the studied effects, one of particular interest is the formation of an organic refractory residue left over after ion irradiation and warming-up at room temperature. We call this residue IPHAC (Ion Produced Hydrogenated Amorphous Carbon). Although "in situ" infrared spectroscopy points out the formation of new molecular species during bombardment at low temperature (Strazzulla & Baratta, 1991) it is not clear if IPHAC is already formed or if its formation is triggered by temperature increase during warming-up of the irradiated target. Being Raman Spectroscopy a technique particularly suitable for the analysis of carbonaceous materials, we have thought and build-up an experimental apparatus to obtain Raman Spectra of frozen hydrocarbons during ion irradiation (Spinella et al., 1991). The present experimental results point out clearly to the formation of IPHAC already at low T and low energy deposition (\simeq few eV/C-atom).

EXPERIMENTAL RESULTS

Raman spectroscopy gives valuable information on the effects induced by ions impinging on solids at low temperature. Indeed this technique has both the ability to distinguish between chemical species and can provide valuable evidence to the structural properties of materials and, in particular, of carbonaceous materials (Robertson et al., 1986). Raman spectroscopy has been in fact used to get insight in the structural lattice damage of solids resulting from ion bombardment (Wright et al., 1976).

Details on the experimental set-up we have used have been given elsewhere (Spinella et al. 1991). A scattering chamber was faced through KBr windows, to a Raman SPEX 1488 double monochromator equipped with two holographic gratings (1800 grooves/mm) to which an OMA III intensified reticon or a cooled photomultiplier were faced as detectors. We used a 90 degrees scattering geometry where the direction of incident and collected light, as well as the direction of the ion-beam, are mutually perpendicular. Vacuum was better than 10^{-7} mbar. Frosts were accreted onto a silicon crystal (111) substratum put in thermal contact with a closed-cycle Helium cryostat (10-300 K) by admitting gas into the chamber, through a needle valve. The cold finger has been designed to avoid that the laser (Argon ion gas laser) light, reflected in the specular direction, could be collected by the monochromator collimating lenses. After or during condensation, ices were bombarded by 3 keV He^+ ions. The beam produces a $2 \times 2 cm^2$ spot on the target. Currents were in the range of few μ -ampere/cm² or less in order to avoid a macroscopic heating.

In a particular experiment, a benzene (C_6H_6) film, (about $2 \mu m$ thick) obtained by slow rate deposition ($\approx 0.11 \mu m/min$) on the substratum ($T= 77 K$), was irradiated with $3 \text{ keV } He^+$ ions. Some spectra are reported in Fig. 1: (from top to bottom) as deposited, after 30 eV/C-atom and after warming-up at room temperature. All of the spectra in the figure were obtained by using the 514 nm Argon laser line, with an output power less than $\approx 40 \text{ mW}$. The incident light was with the electric vector orthogonal to the plane of scattering; the scattered light polarization was not analyzed. The entrance slit width was 0.1 mm , corresponding to a resolution of about 5 cm^{-1} and the exposure time was $3 \text{ sec} \times 30 \text{ scan}$ in each spectral region. It is interesting to note that, in the irradiated sample, a newly formed broad band at $\approx 1600 \text{ cm}^{-1}$, typical of amorphous carbon or hydrogenated amorphous carbon (Robertson, 1986; Yoshiwawa et al., 1988), appears in addition to the benzene ones. The appearance of such a structure points-out that IPHAC has been already formed during bombardment at low temperature.

Analogous results have been obtained by irradiating frozen butane (C_4H_{10}). A butane film (about $2 \mu m$ thick), accreted on the silicon substratum ($T=10 K$) at a rate deposition as above, was irradiated with $3 \text{ keV } He^+$ ions. The spectra were obtained by using a cooled photomultiplier as detector. Some spectra are reported in Fig. 2: (from top to bottom) as deposited, after 1.5 eV/C-atom and after 21 eV/C-atom ; the last spectrum was obtained for the organic residue at $10 K$. The slits width was 0.2 mm , corresponding to a resolution of about 10 cm^{-1} and the exposure time was 0.3 sec (with a sampling step of 2 cm^{-1}). All of the remaining parameter concerning the laser and the scattering geometry were the same as for the benzene experiment. Also in this case the newly formed broad band at $\approx 1600 \text{ cm}^{-1}$ appears in addition to the butane ones. The appearance of the structure even in an aliphatic (single bonds) compound like butane, testifies for the generality of the process concerning the formation, at low temperature, of IPHAC, i.e. of a complex mixture of ring molecules linked together by linear chains (Strazzulla & Baratta, 1991).

CONCLUSIONS

These results may have relevant astrophysical applications, in particular for cometary physics. In fact, the outer layers of a comet, the comet's mantle, is altered by cosmic-ray particle processing of the ices and organics during the comet's $4.6 * 10^9$ years residence time in the Oort cloud (Donn, 1976; Wipple, 1977; Strazzulla, 1986; Johnson et al., 1987).

It has been suggested (Johnson et al., 1987; Strazzulla & Johnson, 1991; Strazzulla et al., 1991b) that a comet exposed to background particle radiation in the Oort cloud obtains an outer web of non-volatile material which will lead to the formation of a substantial "crust". The results presented here support the hypothesis that the cometary organic crust can be already formed during the long stay in the Oort cloud and its development does not require a first passage (heating) in the inner Solar System.

When a new comet enters the inner Solar System there will be early activity, initial fissures in the crust and the break-off of unstable pieces of the crust, due to warming of sub surface species. If this comet enters a periodic orbit in the inner Solar System the remaining mantle should be continuously hardened due to thermal processes (Fanale & Salvail, 1984; Prialnik & Bar-Nun, 1988).

ACKNOWLEDGEMENTS

This research has been supported by the Italian Space Agency (ASI).

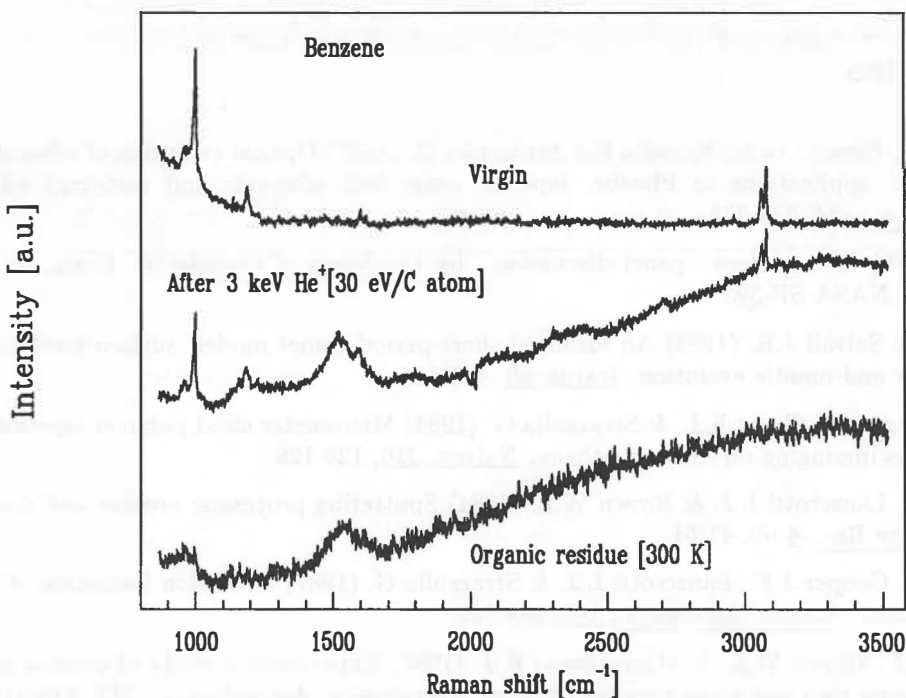


Fig.1 Raman spectra of frozen benzene: as deposited (77 K), during irradiation with 3 keV He ions (77 K) and of the organic residue (300 K) left over after ion irradiation.

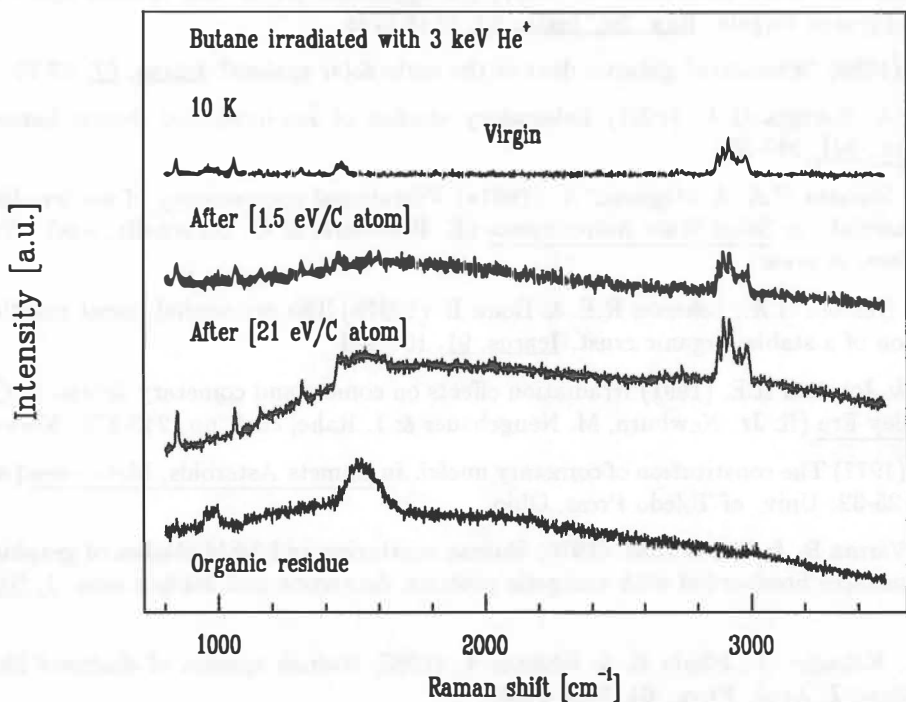


Fig.2 Raman spectra of frozen butane: as deposited (10 K), during irradiation with 3 keV He ions (10 K) and of the organic residue (10 K) left over ion irradiation.

REFERENCES

- Andronico G., Baratta G.A., Spinella F.& Strazzulla G. (1987) Optical evolution of laboratory-produced organics: applications to Phoebe, Iapetus, outer belt asteroids and cometary nuclei. *Astron. Astrophys.*, **184**, 333-336
- Donn B. (1976) The nucleus: panel discussion. in *The Study of Comets* (B. Donn, et al., eds), pp. 611-621. NASA SP-393
- Fanale F.R. & Salvail J.R. (1984) An idealized short-period comet model: surface insolation, H_2O flux, dust flux and mantle evolution. *Icarus*, **60**, 476-511
- Foti G., Calcagno L., Sheng K.L. & Strazzulla G. (1984) Micrometer sized polymer layers synthesized by MeV ions impinging on frozen methane. *Nature*, **310**, 126-128
- Johnson R.E., Lanzerotti L.J. & Brown W.L. (1984) Sputtering processes: erosion and chemical change. *Adv. Space Res.*, **4 n9**, 41-51
- Johnson R.E., Cooper J.F., Lanzerotti L.J. & Strazzulla G. (1987) Radiation formation of a non-volatile comet crust. *Astron. Astrophys.*, **187**, 889-892
- Lanzerotti L.J., Brown W.L. & Marcantonio K.J. (1987) Experimental study of erosion of methane ice by energetic ions and some consideration for astrophysics. *Astrophys. J.*, **313**, 910-919
- Prialnik D., & Bar-nun A. (1988) The formation of a permanent dust mantle and its effects on cometary activity. *Icarus*, **74**, 272-283
- Robertson J. (1986) Amorphous carbon. *Adv. in Phys.*, **35**, 317-374
- Spinella F., Baratta G.A., Strazzulla G. (1991) An apparatus for in situ Raman spectroscopy of ion irradiated frozen targets. *Rew. Sc. Instr.*, **62**, 1743-1745
- Strazzulla G. (1986) "Primitive" galactic dust in the early solar system? *Icarus*, **67**, 63-70
- Strazzulla G. & Baratta G.A. (1991) Laboratory studies of ion-irradiated frozen benzene. *Astron. Astrophys.*, **241**, 310-316
- Strazzulla G., Baratta G.A. & Magazzu' A. (1991a) Vibrational spectroscopy of ion-irradiated carbonaceous material. in *Solid State Astrophysics* (E. Bussoletti & G. Strazzulla, eds). North-Holland, Amsterdam, in press
- Strazzulla G., Baratta G.A., Johnson R.E. & Donn B. (1991b) The primordial comet mantle: Irradiation production of a stable, organic crust. *Icarus*, **91**, 101-104
- Strazzulla G. & Johnson R.E. (1991) Irradiation effects on comets and cometary debris. in *Comets in the Post-Halley Era* (R. Jr. Newburn, M. Neugebauer & J. Rahe, eds), pp. 243-275. Kluwer, Dordrecht
- Whipple F.L. (1977) The constitution of cometary nuclei. in *Comets Asteroids, Meteorites* (A.H. Delsemme, ed), pp. 25-32. Univ. of Toledo Press, Ohio
- Wright R.B., Varma R. & Gruen D.M. (1976) Raman scattering and SEM studies of graphite and silicon carbide surfaces bombarded with energetic protons, deuterons and lithium ions. *J. Nucl. Mat.*, **63**, 415-421
- Yoshikawa M., Katagiri G., Ishida H. & Ishitani A. (1988) Raman spectra of diamond like amorphous carbon films. *J. Appl. Phys.*, **64**, 6464-6468

ASTEROIDS WITH UNUSUAL LIGHTCURVES: 14 IRENE AND 51 NEMAUSA

Belskaya I.N.* and Dovgopol A.N.[†]

* Astronomical Observatory of Kharkov University, Sumskaya str.
35, Kharkov 310022, USSR

[†] The Main Astronomical Observatory of Ukrainian Academy of Sciences, Goloseevo, Kiev 252127, USSR

INTRODUCTION

Some asteroids with peculiar lightcurves have been chosen for more detail investigation. We present the first results of that study. Observations were obtained in 1989 and 1990 using the 70-cm telescope of Kharkov Observatory; the 40-cm telescope of Abastumani Observatory (Georgia) and the 60-cm telescope of the Main Astronomical Observatory of Ukrainian Academy of Sciences (mount. Majdanak, Middle Asia). Observations and their reduction were carried out in standard way. The aspect data, absolute magnitude of primary maximum and lightcurve amplitude are given in Table. The last column of the Table refers to the observation sites.

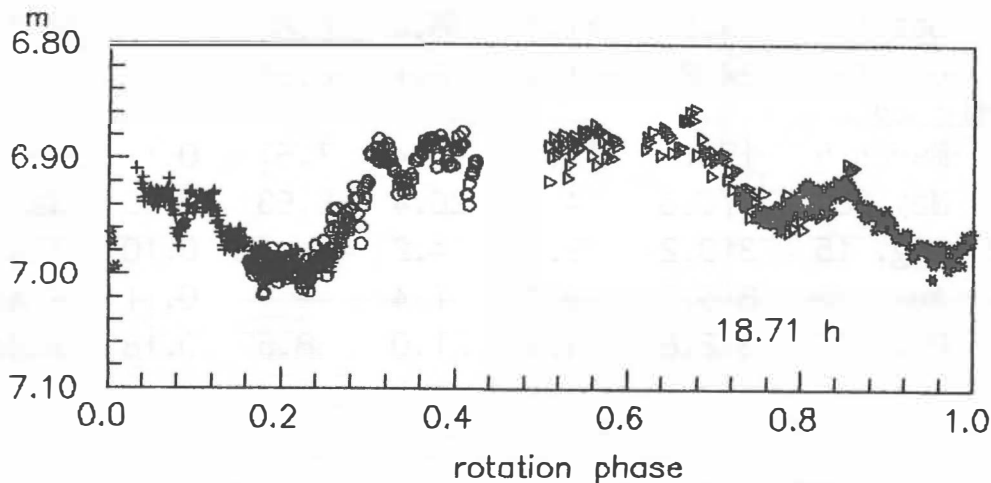
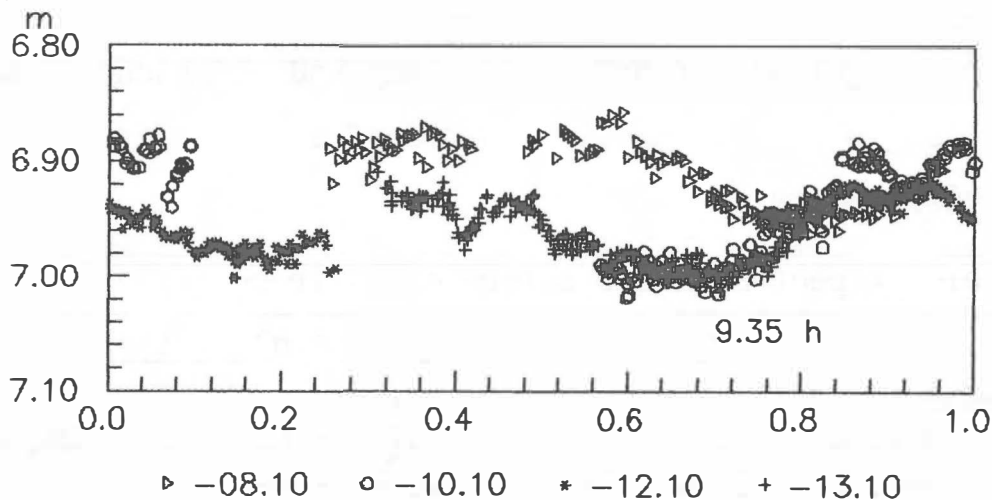
Table. Aspect data for asteroids 14 Irene and 51 Nemausa

	Date	λ	β	α	$V_0(1,\alpha)$	ΔV	
<u>14 Irene</u>							
1990	Oct. 8	35.3	-11.4	7.7	6.89	0.12	Majdanak
	Oct. 10	34.9	-11.4	7.1	6.86	-	" -
	Oct. 12	34.5	-11.4	6.4	6.85	-	" -
	Oct. 13	34.2	-11.4	6.1	6.86	-	" -
<u>51 Nemausa</u>							
1989	March 5	176.6	-1.3	5.4	7.67	0.11	Abastumani
	May 28	170.6	4.6	26.4	8.63	0.13	Majdanak
1990	Aug. 15	319.2	9.8	4.2	-	0.10	Kharkov
	Aug. 26	316.5	9.0	7.4	-	0.11	Kharkov
	Oct. 10	312.8	4.9	21.0	8.52	0.18	Majdanak

ASTEROID 14 IRENE

This asteroid was called "puzzling" since numerous observations during 5 apparitions didn't give an unambiguous result of its rotation period. Two possible values of Irene's period had been determined: $9^{\text{h}}35$ and $18^{\text{h}}71$ (Scaltriti et al. 1981).

Our observations of 14 Irene were carried out during 4 nights in the 1990 apparition when the lightcurve amplitude was about $0^{\text{m}}12$. Fig.1 shows the composite lightcurves obtained with each of two values of rotation period. As one can see "short" period contradict to our observations. Two times longer value of Irene's rotation period $P=18^{\text{h}}71 \pm 0^{\text{h}}01$ satisfies to new observations and previously published data. But in that case lightcurve of 14 Irene displays strange asymmetric shape. To our mind the determining rotation period may be only half of true value.



ASTEROID 51 NEMAUSA

Lightcurves of asteroid Nemausa display unusual shape with at least three pairs of extrema. The previous lightcurves were obtained during 6 apparitions. Our observations were carried out in 1989 at small (6°) and large (26°) values of phase angle (Fig.2). As one can see the amplitude and shape of lightcurves are considerably changed. The next 1990 apparition of Nemausa our purpose was to study the lightcurve dependence on phase angle more detail. Fig.2 shows the lightcurves obtained in 1990 at phase angle 4° , 7° and 21° . The lightcurve shape changes in similar way as in 1989 while the ecliptic longitude difference between the apparitions is nearly 140° . Rotation phases in Fig.2 have been computed using the same zero moment and corrected for aspect changes. The pole coordinates are assumed to be equal $\lambda=330^\circ$ and $\beta=-80^\circ$; $P_{\text{sid}}=0^d324290 \pm 0^d000001$ with retrograde sense of rotation. These values have been obtained by the method of photometric astrometry using available data (Gaamelgaard and Kristensen, 1986) and our observations. But the pole coordinates have been obtained with great uncertainty since their values depend on chosen extremum. It is necessary to take into account the lightcurve peculiarities which may be caused by albedo "spots" (Hahn et al., 1986). We try to model Nemausa surface by ellipsoid with different "spots" but any acceptable result haven't been obtained.

References

- Gaamelgaard P., Kristensen L.K., 1986, in: Asteroids, Comets and Meteors II, eds. Lagerkvist et al., Uppsala Observatory, p.77.
Hahn G., Lagerkvist C-I., Magnusson P., Rickman H., ibid., p.93.,
Scaltriti F., Zappala V. et al., 1981, Astron. Astroph. 100, p.326.

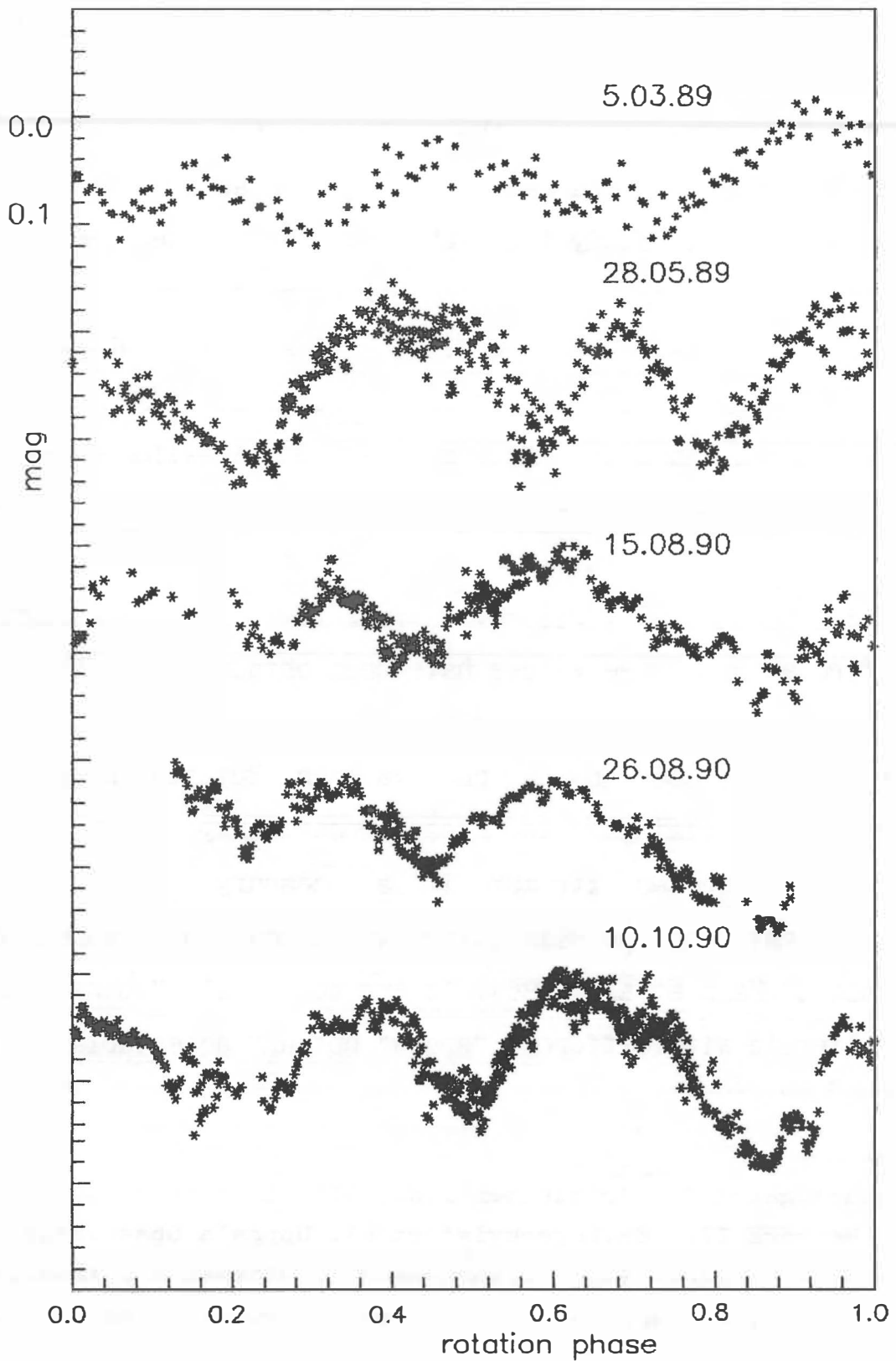


Fig.2. Composite lightcurves of 51 Nemausa

LOW COST MISSIONS TO EXPLORE THE DIVERSITY OF NEAR EARTH OBJECTS

Michael J.S. Belton

National Optical Astronomy Observatories, Tucson, AZ, 85711

Alan Delamere

Ball Aerospace, Boulder, CO, 80306

ABSTRACT

We propose a series of low-cost flyby missions to perform a *reconnaissance* of near-Earth cometary nuclei and asteroids. The primary scientific goal is to study the physical and chemical *diversity* in these objects. The mission concept is based on the Pegasus launch vehicle. Mission costs, *inclusive* of launch, development, mission operations and analysis, are expected to be near \$50M per mission. Launch opportunities occur in all years. The benefits of this reconnaissance to society are stressed.

A RECONNAISSANCE OF NEAR EARTH OBJECTS

In their *Strategy for the Exploration of Primitive Solar-System Bodies - Asteroids, Comets and Meteoroids: 1980-1990* the Committee on Planetary Exploration of the Space Science Board (COMPLEX, 1980) noted that "In order to realize the further goal of understanding the factors that produce diversity in the population of comets, a balanced and economical program of cometary exploration could include flyby as well as rendezvous-mode investigations."

In this paper we propose a series of small, innovative, low-cost flyby missions to make a reconnaissance of near-Earth objects (NEOs) which includes a selection of asteroids as well as cometary nuclei.

NEOs are derived from the main-belt asteroids and periodic comets, and thought to be a collection of collisional fragments, primitive objects, and extinct or dormant cometary nuclei. In addition, many active periodic comets enter near-Earth space and we include them in this population. NEOs are the primary source population of large objects that strike the Earth. The inevitable probability that they have been responsible for cataclysmic impacts on the Earth (Chapman and Morrison, 1989) and the indisputable certainty that these will occur in the future has renewed general interest in these objects to such an extent that the American Institute for Aeronautics and Astronautics (AIAA, 1990) has proposed that they be seriously studied so that ways can be found to protect society from future threats. NEOs also represent the most convenient source of materials needed for future utilization and exploitation of space (Swindle *et al.*, 1991). The interiors of extinct comet nuclei may still be composed of water which makes them important candidates as future base sites for human deep space exploration.

Knowledge of the properties of these objects is sparse (McFadden *et al.*, 1989). Approximately 150 objects are known and about a dozen new objects are discovered each year. The total population is expected to exceed several thousands (Shoemaker *et al.*, 1979). Weissman *et al.* (1989) have surveyed the known population and found that 29 of the objects could be cometary nuclei. Yeomans (1991) finds that the asteroids Icarus and Apollo are

possibly nearly-extinct cometary nuclei since their orbital motion appears to be affected by non-gravitational reaction forces.

Low transfer energy ($C_3 < 5 \text{ km}^2/\text{sec}^2$) mission opportunities to these objects are very frequent and small spacecraft with innovative payloads could be delivered to them with short flight times (<1 year) from very low-cost launch vehicles.

Given the combination of wide social interest in these objects with an exceedingly weak scientific understanding of their physical and chemical properties, we propose that the initial reconnaissance of the solar system, so ably undertaken by NASA to the primary planets and satellites of the solar system, *now be extended to NEOs with a series of low-cost flyby missions.*

OTHER REQUIREMENTS

Flagship missions like CRAF, Rosetta, Cassini, Galileo are *absolutely* essential to satisfy the scientific goals of planetary exploration even though they are expensive, complex, and time-consuming endeavors. However, there is also a need for small, low-cost, rapidly completed missions to provide frequent flight opportunities. Flight mission are needed to provide vehicles for the development and testing of innovative instrumentation, mechanisms, communications, systems, and flight software. Opportunities are needed for the training and inspiration of young engineering and scientific talent (Allen, 1990; Coleman, 1990). The United States Senate Appropriations Subcommittee (US, 1991) has recently recognized these problems and has directed NASA to "prepare, with input from the scientific community, a plan to stimulate and develop small planetary or other space science projects...."

In our opinion, the proposed reconnaissance of NEOs will go far to satisfy these demands. Missions could be as frequent as 1-2 per year at all-inclusive costs of roughly \$50M per mission. Over the span of an individuals "professional lifetime" there would be the order of 10 to 20 flight opportunities. The total costs of the reconnaissance program, stretched over two decades, would be comparable with the cost of a single flagship mission.

INTERPLANETARY CAPABILITY OF PEGASUS AND COSTS

To constrain total mission costs to around \$50M per flight and to provide frequent launch opportunities it is necessary to find a launch vehicle that is in itself inexpensive but has flexible launch characteristics and enough performance and injection accuracy to place small ($\sim 10 \text{ kg}$) instrument payloads on intercept trajectories to a wide selection of NEOs. This requires injection of approximately 100kg with C_3 of $5 \text{ km}^2/\text{sec}^2$. The *Pegasus* launch vehicle (Anon, 1989), which was recently selected by NASA and the U.S. Air Force as their "small" launch vehicle (Anon, 1991), meets these requirements. The expected performance is $> 85 \text{ kg}$ injected mass for $C_3 < 5 \text{ km}^2/\text{sec}^2$ using a STAR 20A solid rocket motor upper stage (Barnett, 1991). Substantial enhancements of this performance are expected with planned upgrades for the *Pegasus* series (Schade, 1991), and, in some low C_3 missions, a lunar swingby (Uphoff, 1990) will improve the performance significantly.

The cost of a *Pegasus* launch (including integration and launch operations) is expected to be about \$10M. In Table 1 we show our estimates of the cost and mass apportionments that we expect to be appropriate to small NEO flyby missions.

Table 1: Apportionment of Costs and Mass for a Small NEO Flyby Mission

Mass (kg):	Costs (\$M):		
Kick stage adaptors etc.	20	Instrument	10
Spacecraft and systems	40	Spacecraft development	20
Instrument payload	10	Flight Operations	10
		Pegasus launch	10
Total	70kg	Total	\$50M

There already exists much experience with small spacecraft designs that fall within these mass and cost constraints and 3-axis stabilized, spinner, and dual-spin configurations are all feasible. In our concept we would expect that the payload would be fully integrated with the spacecraft and provide essential flight functions (terminal guidance, self-sequencing, etc). Communications requirements would be minimized by the use of massive onboard solid-state memory.

MISSION OPPORTUNITIES

In Table 2 we list some low-energy flight opportunities, discovered by Sauer and Yeomans (1990), that occur in the last half of the 1990's and which could be flown by a small spacecraft launched with Pegasus.

Table 2: A Selection of NEO Flyby Opportunities			
Object	C ₃ (km/sec) ²	Flight time (yrs)	Launch year
Eros	1.892	0.80	1995
Oljato	1.377	0.56	1995
P/Honda-Mrkos-Pad.	3.316	0.72	1995
P/Churyumov-Ger.	4.078	0.67	1995
Dionysius	0.074	0.77	1996
1980 PA	1.272	0.28	1996
Quetzalcoatl	1.549	0.86	1996
Bacchus	1.939	0.78	1996
P/Hartley 2	2.155	1.02	1996
P/Wirtanen	4.000	1.07	1996
1983 RD	1.148	0.86	1997
P/Giacobini-Zinner	1.335	0.97	1997
Geographos	2.018	0.99	1997
1981 ET3	2.333	1.02	1997
Lick	4.481	0.80	1997
Sisyphus	0.752	0.59	1998
McAuliffe	2.287	0.48	1998
Oljato	3.212	0.52	1999

Opportunities of particular interest are Eros (the largest known near-Earth asteroid), Geographos (the most elongated nucleus known), Oljato (possibly a "nearly-extinct" comet), and P/Giacobini-Zinner whose interaction with the solar wind was earlier explored by the International Cometary Explorer (ICE).

All of the above opportunities are to a single object and have short (*i.e.* low-cost) flight missions. Low-energy missions to multiple NEO targets are thought to exist and extended mission scenarios may be possible.

SCIENTIFIC OBJECTIVES AND MEASUREMENT GOALS

To quantify the concept of *diversity*, we have developed a series of scientific questions appropriate to a program of small flyby missions (Table 3). They serve to illustrate the breadth of significant scientific problems that a series of small flyby reconnaissance missions can elucidate:

Table 3: Some High-level Goals for Flyby Missions to near-Earth Objects

Near-Earth Cometary Nuclei:

- Do Cometary nuclei, in fact, have diverse physical properties?
- Are cometary nuclei chemically inhomogeneous on global scales?
- Are major structural differences evident in the surface layers of different comets?
- Is the carbon chemistry the same in all comets?
- How well can we assess the availability of H₂O on "extinct" or "dormant" comets?
- What evolutionary processes are reflected in the appearance of the surfaces of comets?
- How does the nature of the interaction with the solar-wind depend on the nature of the comet?

Near-Earth Asteroids:

- What evidence is there for collisional formation?
- What evidence is there for differentiated objects?
- What evidence for post-collisional evolution?
- How does the taxonomic classification compare with the physical and chemical properties of their surfaces?

These goals can easily be translated in to a series of measurement objectives (Table 4) appropriate for flyby missions which identifies the kind of payloads that need to be considered:

Table 4: Measurement Goals and Instrument Packages

Surface Composition	Near-Infrared Camera/Spectrometer
Physiographic Units	High-resolution Camera
Global Properties	Near-Infrared Camera
Surface Morphology	High-resolution Camera
Magnetism and Volatiles	High-resolution Camera
Dust Composition	Particles and Fields Package
Dust Density and Size Distribution	Ultra-violet Spectrometer
Solar wind Interactions/Coma Aeronomy	Dust Analyzer
	A "smart" Counter
	Particle and Fields Package
	Ultra-violet Spectrometer

For the proposed reconnaissance a set of about six generic instrument payloads are needed. Many of these instruments already exist, but are too heavy to fly together on a single mission. Micro-technology could reduce instrument size but this path is expensive and, if taken to extremes, could undermine the basic concept of small low-cost missions. We advocate an innovative approach to instrumentation with some miniaturization but maintaining highly focussed measurement goals. In our concept the instrument is merely an extension of the spacecraft itself and would provide many of the functions necessary for supporting the mission. Thus a camera system would provide "lock-on" terminal guidance and might be self-sequencing. We expect that some missions would be focussed entirely on imaging science while others would focus on either aeronomical, particle and fields, or solar-wind interactions.

PROGRAMMATICS

Our experience with previous missions indicates that a four year project cycle should be appropriate. Each mission should be run as a guaranteed design-to-cost project and a short definition phase will be required to ensure that all key areas are clearly defined. The hardware development phase would take approximately 24 months and represents the bulk of the expenditures up to the time of launch. The last phase of the program would be flight operations and data analysis which we estimate would be completed by launch plus 12 months in most cases. This indicates that a reconnaissance program could be supported at an average level of about \$25M per year (all-inclusive costs) with a new mission initiated every two years. Current accounting practices in the NASA Solar System Exploration Program separate out the costs for development, launch, and flight operations. The development cost of a series of flyby missions (a new mission start every two years) would average out at about \$15M per year to the Solar System Program. This is an unusually low number for flight programs in planetary exploration.

In order to maintain low-costs it is not only necessary to have short missions with highly focussed scientific objectives but experience shows that the development, budgetary, and flight operations responsibilities should be primarily entrusted to a small and dedicated research team. For this reason we advocate that individual missions be carried out by small research groups in university, industrial, or NASA research settings. Overall *program* development, which would encompass the phasing of missions, mission selection, project and budgetary oversight, etc. would be the responsibility of a NASA center. Launch operations would be provided directly by industry.

Finally, on an aggressive note, we believe that expansion of this concept to an international program would foster competition in technical innovation while simultaneously maintaining a healthy cooperation on scientific questions. In many ways the proposed reconnaissance has already begun on the international scene. ICE, flown by the United States to P/Giacobini-Zinner, was the beginning and was closely followed by the Giotto/VEGA/Suisei/Sakigaki flybys to P/Halley. A continuance is certain with the retargeting of the Giotto spacecraft to a future flyby of P/Grigg-Skjellerup and an extension is implicit with already planned future flybys of main-belt asteroids by Galileo (Gaspra and Ida), CRAF (Mandeville), and Cassini (1989 UR1).

BENEFITS TO SOCIETY

The proposed reconnaissance of NEOs offers several benefits to society. It provides frequent access to space for innovative research and experimentation by small university, industry, and government research groups. It therefore provides an enormous increase in the opportunities for young scientists in the formative stage of their careers to participate in the development of space technology and exploration. It helps lay a basis for the utilization of NEOs as space resources in the future human exploration of space. Finally, the scientific exploration of these objects, which at some future time could threaten the earth, will make

them familiar to engineers and scientists and better understood by ordinary people who will have to cope with such traumatic events.

Acknowledgements We would like to acknowledge many inputs and much help during the development of the ideas expressed in this paper. We are particularly indebted to the encouragement of our colleagues W. Eckstrom, C. Uphoff, D. K. Yeomans, C. Sauer, R. Boain, J. Beckman, C. Elachi, R. Jones, C. Chapman, and J. Veverka.

References

- AIAA (1990) Dealing with the treat of an Asteroid striking the Earth. American Institute of Aeronautics and Astronautics Position Paper, Washington, D.C., April 1990.
- Allen, L. (1990) Quoted in Face To Face. In Aerospace America, 10-11, June Issue.
- Anon, (1989) Pegasus Rolls Out. Aviation Week and Space Technology, pp. 36-41, August 14 Issue.
- Anon, (1991) In News Breaks. Aviation Week and Space Technology, p. 17, April 22 Issue.
- Barnett, P. M. (1991) Launch Vehicle Overview. Talk presented at the Workshop on Microspacecraft for Planetary Exploration. The Planetary Society, Pasadena.
- Chapman, C.R., and Morrison, D. (1989) Cosmic Catastrophes. Plenum Press, New York. 302pp.
- Coleman, P. (1990) We Need More Small Space Missions. In USRA Quarterly, p. 19, Fall Issue.
- COMPLEX (1980) Strategy for the Exploration of Primitive Bodies - Asteroids, Comets, and Meteoroids: 1980 - 1990. National Academy of Sciences, Washington, D.C. 83pp.
- McFadden, L. A., Tholen, D. J., and Veeder, G. J. (1989). Physical Properties of Aten, Apollo, and Amor Asteroids. In Asteroids II (R.P. Binzel, T. Gehrels, and M.S. Mathews, Eds.), pp.442-467. The University of Arizona Press, Tucson.
- Sauer, C. D., and Yeomans, D. K. (1990). Private communication, April 12, 1991.
- Schade, C. C. (1991). Presentation at Workshop on Microspacecraft for Planetary Exploration. The Planetary Society, Pasadena.
- Shoemaker, E. M., Williams, J.G., Helin, E.F., Wolfe, R. F. (1979). Earth-crossing asteroids: Orbital classes, collision rates with Earth and origin. In Asteroids (T. Gehrels Ed.), University of Arizona Press, Tucson
- Swindle, T.D., Lewis, J. S., and McFadden, L. A. (1991). The case for Planetary Sample Return Missions: 4. Asteroids and the History of Planetary Formation. EOS, in press.
- Uphoff, C. (1990). Potential Improvements in PEGASUS Performance for Deep Space Mis-

sions with $0 < C_3 < 30 \text{ km}^2/\text{sec}^2$. Ball Aerospace Internal Memorandum, May 12, 1990.

US, (1991). US Senate Appropriations Subcommittee on VA, HUD, and Independent Agencies. Language from their Report of July 10, 1991.

Weissman, P. R., A'Hearn, M. F., McFadden, L. A., and Rickman, H. (1989). Evolution of Comets into Asteroids. In Asteroids II (R. P. Binzel, T. Gehrels, and M. S. Mathews, Eds.), pp. 880-920. The University of Arizona Press, Tucson.

Yeomans, D. K. (1991) A Comet among the Near-Earth Asteroids. Astron. J., 101, 1920-1928.

SIMULATED FAMILIES: A TEST FOR DIFFERENT METHODS OF FAMILY IDENTIFICATION

Bendjoya Ph.* , Cellino A.+ , Froeschlé Cl.* , Zappalá V.+

* O.C.A BP 139 06003 Nice cedex France

+ O.A.T I-10025 Pino Torinese (Torino) Italia

ABSTRACT

A set of families generated in fictitious impact events (leading to a wide range of "structures" in the orbital element space have been superimposed to various backgrounds of different densities in order to investigate the efficiency and the limitations of the methods used by Zappalá et al. (1990) and by Bendjoya et al. (1990) for identifying asteroid families. In addition an evaluation of the expected interlopers at different significance levels and the possibility of improving the definition of the level of maximum significance of a given family were analyzed.

INTRODUCTION

The asteroid family determination has appeared for a longtime as an analysis method dependent problem. For the first time two different methods have given a good agreement between the families defined by each method. These two methods are the hierarchical single linkage clustering method used by Zappala et al. (1990) and the wavelet transform cluster analysis used by Bendjoya et al. (1990).

The purpose of this paper is to show how the efficiency of both method has been tested in a situation which is 'a priori' known. The idea is to "create" in the osculating element space a family the members of which are known. Both methods have been tested with respect to some physical parameters of the families and with respect to the background.

Part two will introduce the way the artificial families have been generated and the chosen parameters will be presented. Part three will briefly remind both clustering methods and the fourth part will give comparative results in which the number of interlopers has been computed for each cases.

SIMULATED FAMILIES

The origin of asteroid families is commonly admitted to be due to a collisional event. Dynamical families have been artificially generated by giving to the family members a typical ejection velocity following a power law. Since the definition of families is based on purely dynamical arguments, the power law for the ejection velocity can be justified by laboratory fragmentation experiments.

The number of fragments dN with a mean ejection velocity between V and $V + dV$ is given by:

$$dN = 0 \text{ if } V < V_{\min}$$

$$dN = CV^\alpha dV \text{ if } V \geq V_{\min}$$

V_{\min} is the minimum ejection velocity; C is a constant. The histogram for the ejection velocity at infinity is given fig 1 with the power law fitting it. From laboratory fragmentation experiments α has been taken equal to 3.25. The diameter of the parent body has been chosen equal to 100 km. A family of 50 members has been generated for the following cases: $V_{\min} = 50$ m/s, 100 m/s, 150 m/s and 200 m/s. Each family has been respectively plunged in a background (BG) of 300, 600, 900 asteroids. Fig. 2 shows three examples of simulated families in different backgrounds in the (a, e) and (a, i) planes where a , e , i are respectively the semi major axis, the eccentricity and the inclination of the asteroids.

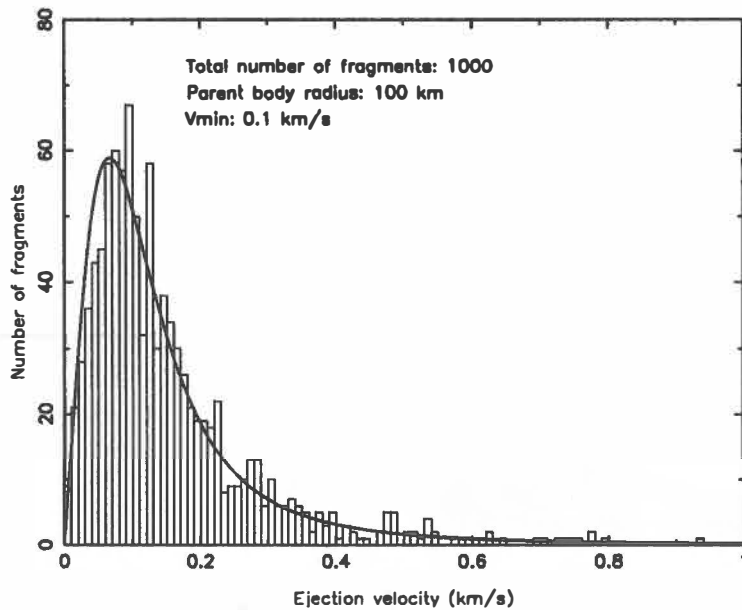


fig. 1 Ejection velocity distribution at infinity

In order to test the reliability of such artificial families, the density of the simulations has been compared to the family densities in the 6 studied zones (see Zappala et al., 1990) of the asteroid main belt. It appears that, except for zone 2 which is the Flora region, most of the real families have to be compared to the simulation with 50 members in a background of 300 asteroids.

THE TWO CLUSTERING METHODS

(i). The single linkage hierarchical clustering method is a grouping method that consists in agglomerating successively the closest clusters. Being given a distance the dimension of which is a velocity one, for the problem we are interested on, the two closest objects are identified and agglomerated in order to be replaced by a unique object. All the distances are then updated and the same rule is played again as long as two objects survive. It is then possible to built a dendrogram giving for any threshold of the distance the number of clusters existing at this value of the distance. Families are then defined by comparing this dendrogram with a similar one derived from a quasi random distribution of elements matching the large scale structures of the real distribution (see Zappala et al., 1990).

(ii). The wavelet transform cluster analysis is a density method based on the computation of a wavelet coefficient on each node of a network superimposed to the set of data. The wavelet coefficient can be seen as an indicator of proximity. The wavelet transform acts as a zoom and point out structures which have the same size as the studied scale. By applying the wavelet transform on a quasi random distribution, defined as above, it is possible to define a threshold that quantify the risk that a detected structure is due to chance. The analysis is performed for a set of scale and structures appear to fit into each other from small scales to large ones. A criterion based on the philosophy of the wavelet transform is then apply in order to cut the hierarchy and to define families (see Bendjoya et al. 1990 and Bendjoya et al. in this proceedings).

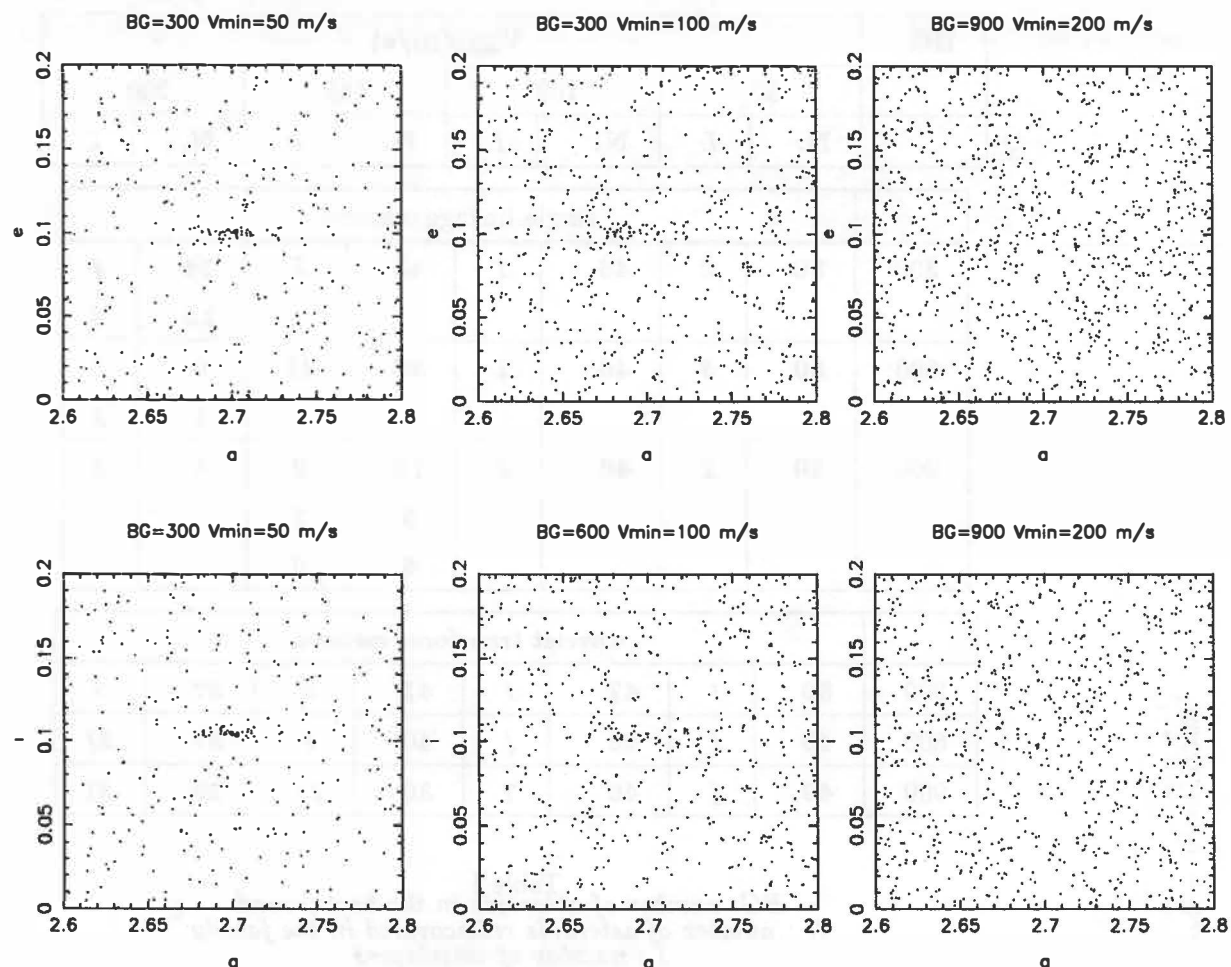


fig. 2 Three examples of simulated families
in the (a', e') and (a', i') planes
BG: the number of asteroids in the background

THE RESULTS

Table I presents the results obtained by the two methods. In each case the number of interlopers, i.e. the asteroids which are not original members but the relative velocity of which includes them in a computed family. In this table N represents the number of asteroids originally belonging to the family that are identified by the methods as belonging to a family, I represents the number of interlopers.

CONCLUSION

This work allows to believe 'a posteriori' in the reliability of the previous analysis made on the real families of the asteroid main belt since the density of most of these families is comparable to the easier cases that is 50 objects in a background of 300 asteroids. For the more difficult cases (such as for the Flora region) this analysis on the simulated families permits to point out the need for making a distinction between clusters and families and for having a new nomenclature. Finally the cluster analysis on simulated families could appear as a tool for testing very rapidly a part of the reliability of a new method of proper element computation in the sense that the cluster analysis on an artificial family made both in the osculating element space and in the proper element space must give very close results.

BG	V_{min}(m/s)							
	50		100		150		200	
	N.	I.	N.	I.	N.	I.	N.	I.
single linkage method								
300	50	2	46	1	45	5	14	4
							15	3
600	50	3	46	4	36	11	9	2
							5	2
900	50	2	46	2	19	2	8	2
					5	2		
					5	0		
wavelet transform method								
300	50	1	47	1	41	3	37	9
600	49	4	46	4	40	9	37	24
900	49	4	46	7	36	11	29	27

Table I
BG: number of asteroids in the background
N : number of asteroids rediscovered in the family
I : number of interlopers

References

- Bendjoya Ph., Slezak E., Froehlé Cl. (1990) The wavelet transform a new tool for asteroid family determination.
Astron. and Astroph. (in press)
- Zappala V., Cellino A., Farinella P., Knezevic, Z. (1990) Asteroid families: identification by hierarchical clustering and reliability assessment.
Astron. J., 100, 2030-2046

THE USE OF THE WAVELET CLUSTER ANALYSIS FOR ASTEROID FAMILY DETERMINATION

Bendjoya Ph., Slezak E., Froeschlé Cl.
O.C.A BP 139 06003 Nice cedex France

ABSTRACT

The asteroid family determination has been for a longtime analysis method dependent. A new cluster analysis based on the wavelet transform has allowed an automatic definition of families with a degree of significance versus randomness. Actually this method is rather general and can be applied to any kind of structural analysis. We will rather concentrate on the main features of the method. The analysis has been performed on the set of 4100 asteroid proper elements computed by Milani and Knézévic (see Milani and Knézévic 1990). Twenty one families have been found and influence of the chosen metric has been tested. The results have been compared to Zappala et al.'s ones (see Zappala et al 1990) obtained by the use of a completely different method applied to the same set of data. For the first time, a good overlapping has been found between the both method results, not only for the big well known families but also for the smallest ones.

INTRODUCTION

The purpose of this paper is to introduce a new method of cluster analysis based on the wavelet transform in order to determine asteroid families. The mathematical basis of the wavelet transform will be briefly presented and we will rather insist on the way it has been used. Then it will be shown how this method has been performed on a set of proper elements computed by Milani and Knezevic (version 4.2) (see Milani and Knezevic 1990) and how the families have been defined with a degree of significance versus randomness. Finally the results will be compared to those found by a complete different method used by Zappala et al. (see Zappala et al. 1990).

THE WAVELET TRANSFORM

Among many fields of applications the wavelet transform appears to be well suited for signal processing purpose since it enables one to get informations on a signal both in frequencies and space. The wavelet transform of a signal can be seen as a decomposition of this signal onto a base of functions defined from dilatations and translations of a unique function called the analyzing wavelet.

Let the one-dimensional signal $f(x)$, and the analyzing wavelet $\psi(x)$, belong to $L^2(\mathbb{R})$. The wavelet transform of $f(x)$ depends on the scale σ and the location b according to the expression:

$$C(\sigma, b) = \sigma^{-\frac{1}{2}} \int_{-\infty}^{+\infty} f(x)\psi^*(\frac{x-b}{\sigma})dx \quad (1)$$

where $\sigma^{-\frac{1}{2}}$ is a $L^2(\mathbb{R})$ normalization factor and * denotes the complex conjugate. The wavelet transform can be seen as a mathematical zoom which is able to extract the σ -sized features from the signal around the location b . In fact when σ decreases thinner and thinner details can be extracted and finally $f(x)$ can be seen as the sum of all its details at different scales.

In order to be an analyzing wavelet the function $\psi(x)$ must satisfy certain conditions. The admissibility condition (see Meyer 1990) can be written for a regular function as:

$$\int_{-\infty}^{+\infty} \psi(x)dx = 0 \quad (2)$$

Moreover $\psi(x)$ must nearly compact supported for numerical reasons and smooth both in the real and Fourier spaces in order to give a good localization of an event in both spaces.

These three conditions present the "mexican hat function" as a good candidate for being an analyzing wavelet (see fig.1). This function comes from the second derivative function of a Gaussian function and is defined, for isotropic analysis by:

$$\psi_\sigma(r) = \left(n - \frac{r^2}{\sigma^2}\right) \exp\left(-\frac{r^2}{2\sigma^2}\right) \quad (3)$$

where r is the distance defined in the space in which the signal is defined and n its dimension.

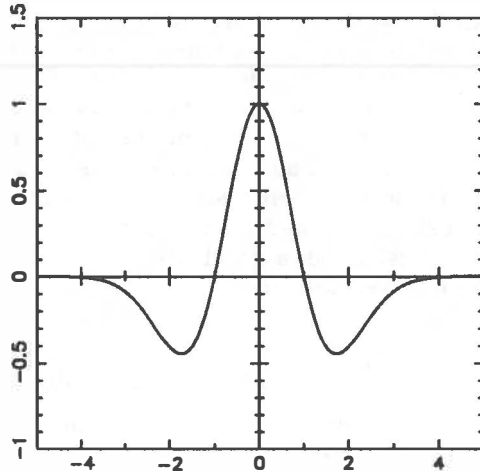


Fig 1. The 1D mexican hat function

THE WAVELET CLUSTER ANALYSIS METHOD

In the case of asteroid family determination, the signal under study is a discrete one: it is a set of point in the proper element space. As this signal can be modelled by a set of Dirac functions the integral in the wavelet transform definition (eq. 1) is replaced by a discrete sum. Because of the use of a computer the wavelet transform of the signal is computed for each node of a network and we will rather speak of a wavelet coefficient at a considered point \vec{b}_i of the network. This coefficient is then discrete sum of the weights, w_j , of the N data points.

$$C(\sigma, \vec{b}_i) = \sum_{j=1}^N w_j \quad (4)$$

where:

$$w_j = \left(n - \frac{r_{ij}^2}{\sigma^2}\right) \exp\left(-\frac{r_{ij}^2}{2\sigma^2}\right) \quad (5)$$

where r_{ij} is the distance between the node \vec{b}_i and the j^{th} data point.

It is obvious that for a node located in uniformly populated area the size of which is large compared to the studied scale, and because of eq.2, the wavelet coefficient will be near 0 since the positive weights will be compensated by the negative ones. On the other hand, for a node centered on an area which is a cluster of points the size of which is about the studied scale, the wavelet coefficient will be positive and negative if this area is a hole of the same size. The discret wavelet transform of a set of points yield to a map of coefficients, for a given scale, where high positive values point out structures of about the same size. The advantage of the wavelet transform over other cluster analysis method is to enable one to get informations both on the location and the size of the structures within the signal.

The major problem however is to distinguish the physical structures from structures due to chance. A threshold has to be introduced in the wavelet coefficients in order to quantify the chance. The idea is to build a pseudo random distribution in the sense that: being given a certain number of boxes in the original distribution of points, the pseudo random distribution is built in putting randomly the same number of points in each equivalent box in order to keep the same local density of points. The wavelet map of coefficients is then computed on each distribution of points. An histogram of the wavelet coefficients coming from a pseudo random distribution is made. The value of the coefficient for which 99.5% of the other coefficients have a lower value than this one, defines the threshold. There are indeed 5 chances over 1000 to find a higher valued coefficient. By reporting the threshold, averaged over many pseudo random distribution realisations, in the wavelet coefficient map of the original distribution and by keeping only the coefficients higher than this threshold, it is obvious that the structures associated to these wavelet coefficients have less than 5 over 1000 risks to be due to chance. It is then possible to extract the structures at the studied scale by superimposing the grid with the conserved coefficients over the original set of data.

The next step is to choose a metric well fitted to the studied problem in order to compute the wavelet coefficients. Because of the break-up origin of the families, a metric with the dimension of a velocity has been chosen. From the Gauss equations and by substituting the proper elements to the osculating ones and after having averaged these equations over the fast variables, we obtain a relative velocity δv between the points of the set of proper elements:

$$\delta v = n a' \sqrt{k_1 \left(\frac{\delta a'}{a'} \right)^2 + k_2 (\delta e')^2 + k_3 (\delta i')^2} \quad (6)$$

n is the mean motion, a' , e' , i' are respectively the proper semi-major axis, the proper eccentricity and the proper inclination.

k_1, k_2, k_3 is a set of arbitrary coefficients that has been chosen equal to $\{\frac{5}{4}, 2, 2\}$.

The wavelet analysis is so performed on the same set of data for several scales with the fitted networks and structures are pointed out for each scale with the same degree of significance versus chance. The ultimate problem is to cut the hierarchy in order to define the families. A criterion based on the philosophy of the wavelet transform has been chosen. This criterion is based on the additional information got from one scale to the successive one. The largest scale to consider in order to define families is the one for which the number of added asteroids is either 0 or for which the next scale brings obviously too much new asteroids. The first case indicates that the families are well isolated, the second one shows that structures are merging and bridges are made between structures.

THE RESULTS

Twenty one families have been defined from this analysis. All the well-known big families have been found again (Eunomia, Koronis, Eos and Themis). For the other smaller and much more debated families, the results have been compared with those obtained by Zappala et al. (see Zappala et al. 1990) with a complete different method and from the same set of data. It has been pleasant to constat that the overlapping of the results of both methods was good even for small families. Table I. presents the names of the twenty one families, the number of members of each families, the percentage of asteroids found in the same family by both methods and the number of asteroid found by the wavelet transform clustering method and not itemized by the hierarchical single linkage clustering method. In 'Flora' region the comparison is less good than for the other zones (defined by the mean motion resonances), but this can be explained by two reasons at least. First it seems that Zappala et al. have been a little severe in the way of cutting their hierarchy in this region and this explained by the very dense background of this zone. Secondly the poor quality code of the proper elements given by Milani and Knezevic (see Milani and Knezevic 1990) in this region has not been taken into account.

On the other hand the percentage of same results for Themis can grows up to 87% by cutting the hierarchy of Zappala et al. at a lower level.

Nevertheless the good agreement of the whole between the two different methods permits to be more confident in the existence of the families.

zones	names of families	number of members	scale (m/s)	comparison idem (%)	number of added asteroids
zone 2	Lucretia	6	110		
	Berolina	114	450		
	Auravictrix	26	230		
	Iduberga	5	110		
zone 3	Vesta	5	110	71.4	0
	Amalasuntha	6	80	75	0
	Leonce	5	80	100	0
	Polona	20	230	0	20
	1969UN	19	320	63	7
	Tinchen	7	110	50	1
zone 4	Eunomia	114	450	95.6	31
	Adeona	17	160	100	2
	Leto	37	450	100	15
	Lydia	22	320	100	16
	Maria	34	320	94	4
	Dora	18	320	100	2
	Agnia	12	320	86	6
zone 5	Koronis	125	320	91	1
zone 6	Eos	172	230	87	0
zone 7	Themis	117	160	51	0
	Veritas	6	110	86	0

CONCLUSION

The wavelet transform is a powerfull tool in a lot of domains. It has successfully been applied in a cluster analysis method in order to point out dynamical families in the asteroid proper element space. This first incursion in the celestial mechanic field has permit to get a certain coherence about the family definition by the comparison with results obtained by a complete different method.

References :

- Bendjoya Ph., Slezak E., Froeschlé (1990) The wavelet transform a new tool for asteroid family determination.
Astronomy and Astrophysic J. (in press)
- Meyer,Y.: 1989, Orthonormal wavelets in Wavelets, time-frequency methods and phase space, (J.M. Combes, A. Grossmann, Ph. Tchamitchian Eds.), Springer-Verlag
- Milani,A. and Knežević,Z. : 1990, Celestial Mechanic 4, 347-412
- Zappalà,V.,Cellino,A.,Farinella,P.,Knežević,Z.: 1990, Astron. J. 100, 2030

Bias Correction Factors for Near-Earth Asteroids

G. K. Benedix (AMES Dept., UCSD; California Space Institute 0216, UCSD, La Jolla, CA 92093-0216)

L. A. McFadden (California Space Institute, UCSD, La Jolla, CA 92093-0216)

E. M. Morrow (AMES Dept., UCSD; California Space Institute 0216, UCSD, La Jolla CA 92093-0216)

M. N. Fomenkova (California Space Institute 0216, UCSD, La Jolla, CA 92093-0216; Space Research Institute, Profsoyuznaya 84/32, Moscow 117810, USSR)

ABSTRACT

Knowledge of the population size and physical characteristics (albedo, size, rotation rate) of near-Earth asteroids (NEAs) is biased by observational selection effects which are functions of the population's intrinsic properties and the size of the telescope, detector sensitivity, and search strategy used. The NEA population is modeled in terms of orbital and physical elements: a , e , i , ω , Ω , M , albedo, and diameter and an asteroid search program is simulated using actual telescope pointings of right ascension, declination, date, and time. The position of each object in the model population is calculated at the date and time of each telescope pointing. The program tests to see if that object is within the field of view ($FOV = 8.75^\circ$) of the telescope and above the limiting magnitude ($V=+16.5$) of the film. The effect of the starting population on the outcome of the simulation's discoveries is compared to the actual discoveries in order to define a most probable starting population.

INTRODUCTION

The near-Earth asteroids (NEAs) are a population whose orbits approach or cross the orbit of Earth. Their proximity to Earth makes them a subject of curiosity and they may provide information about the origin and evolution of our solar system and perhaps life on Earth.

Where were the NEAs formed? How did they come to be in the region of space that they now occupy? Are they main belt asteroids, extinct comets, or a combination? What are they made of? How large is the true population? What is their true distribution of size and albedo? Do they contain carbon, water, and/or other life-forming elements?

The questions which motivate this study are dependent on accurate knowledge of the orbits, physical characteristics, and size of the true population. The term true population is defined as the total population of objects including the ones that have not yet been discovered or characterized. The term discovered population is used to refer to the approximately 200 NEAs with known orbital elements and some known physical properties (McFadden, et al., 1989). The nature and character of the true population is unknown because of biases due to observational selection effects, which have not been fully addressed. There are two types of biases, those intrinsic to the physical properties of the population, size, albedo and orbit, and those controlled by the parameters of the observing program. The relative availability of asteroids for discovery was addressed by (Shoemaker, et al., 1990), and (Luu and Jewitt , 1989) have demonstrated the existence of bias through study of the contribution of phase effects. The objective of this project is to define and quantify the bias factors that are associated with determining a true population of NEAs accounting for contributions from one of the search programs.

Our approach consists of creating different populations of NEAs with different orbital elements and physical characteristics and replicating the ground-based telescopic search program of the Palomar Asteroid Comet Survey (PACS) using the actual telescope pointings and an ephemeris program applied to our model population. The modeled discoveries are then compared to the

number of real NEA discoveries, thus revealing a numerical bias correcting factor. In the process of determining bias factors, we are also studying the likelihood that various population characteristics might be real. This paper will serve as a progress report through August, 1991.

THE MODEL

Our model population consists of 2000 asteroids. This number was chosen in order to incorporate an estimate made by (Shoemaker et al., 1990) based on the cratering rates of asteroids with Earth. We doubled his estimate for a starting point. An asteroid is defined by eight parameters: six orbital elements, and two physical characteristics: albedo and H magnitude. Each parameter is represented by a random value generated in accordance with statistics given in Table 1. The diameter is derived from magnitude and albedo by the following equation:

$$D = 10^{(3.1295 - 0.5 \log(p) - 0.2H)} \quad (1)$$

where p is albedo, H is absolute magnitude, and 3.1295 is a constant which is dependent on wavelength. This equation is modified from (Bowell and Lumme 1979).

TABLE 1 Statistics of known NEAs on which model population is based.

Parameter	Mean	S	Distribution
a	1.92	0.66	Gaussian
e	0.50	0.16	Gaussian
i	0.00	19.60	Half-Gaussian
Ω	182.19	98.56	Uniform
ω	176.88	107.11	Uniform
M	167.85	106.52	Uniform
H	16.76	2.00	Power Law
p	0.14	0.08	Gaussian

Search Simulation

A computer program, called Search by D. Tholen, takes as input the position in the sky (right ascension and declination) and the date and time that an area of sky was searched. The limits of the telescope (field of view, limiting magnitude) are also specified. The program searches through a model population. The telescope pointings from the Palomar Asteroid Comet Survey (PACS) for the years 1984-1988 are used as input. Eugene and Carolyn Shoemaker use the 48 cm Schmidt telescope at Mt. Palomar for this program. To simulate the telescope and plate film, a limiting magnitude of 16.5 and a field of view of 8.75° are included as input parameters. The program takes each of the telescope pointings and determines if a modeled asteroid is in the field of view and below the limiting magnitude of the telescope at that time. If an asteroid is there, the program writes the "discovery" to an output file.

DISCUSSION and FUTURE DIRECTIONS

Table 2 shows the discoveries from 1984-1988 for both the real (column labeled NEA) and modeled populations for each model thus far created. The sky coverage for the 1986 telescope pointings is only half complete because the telescope was in exclusive use for another program. Model 1 and 2 are based on uniform distributions for all orbital elements with the difference between the two being the seed used to initiate the random number generator. The limiting magnitude is 18.0 in models 1-3. Models 3 and 4 use Gaussian distributions for a, e, i, p, and H, and uniform distributions for ω , Ω , and M. In model 4, we lowered the limiting magnitude to 16.5 and generated correlated distributions of a and e, and H and p. The number of simulated

discoveries was reduced. In model 5, H and p are not correlated, H is expressed by a power law distribution, and p is Gaussian. Figures 1 and 2 show a versus e for the discovered and model 5 populations, respectively.

TABLE 2. Comparison of discovered asteroids: Real and modeled

Year	NEA	Model 1	Model 2	Model 3	Model 4	Model 5
1984	3	117	109	129	47	134
1985	5	152	162	140	98	67
1986	9	197	192	168	38	45
1987	11	145	151	114	47	52
1988	8	-	-	-	-	27

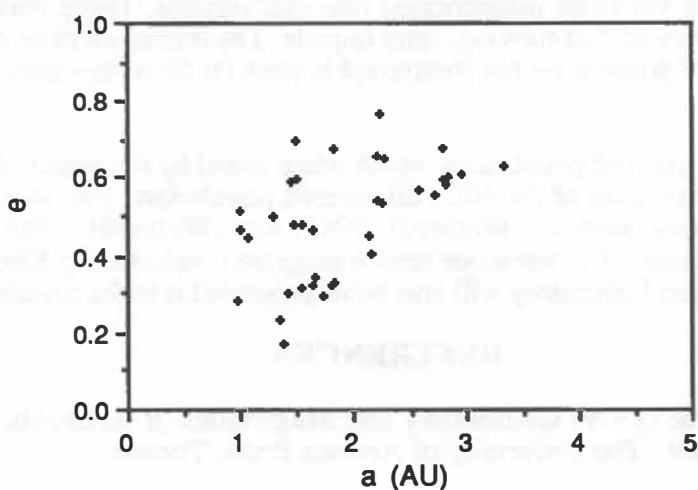


Figure 1. Semi-major axis (a) versus eccentricity (e) for the NEA population 1984-1988

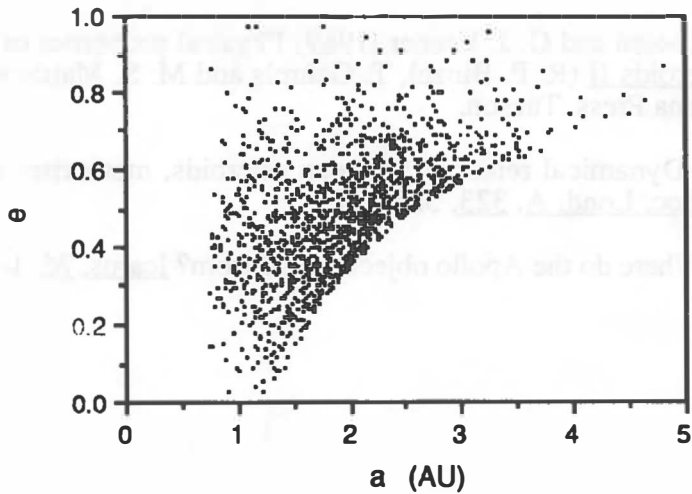


Figure 2. Semi-major axis (a) versus eccentricity (e) for model 5 population.

We believe that the number of simulated discoveries is much larger than the number of real ones because of two main reasons. First, albedos and magnitudes in our models are, on average, too high. The true population of NEA's is, probably, much darker. This indicates that the NEA's are not predominantly derived from the inner edge of the main belt which is dominated by bright

asteroids. Rather they originated from the center or outer main belt where 60% of those asteroids >50 km are dark, or from comet nuclei, which are known to have very low albedos. Discovered NEA's are biased towards brighter objects that are easier to discover. Secondly, almost one hundred of the real NEA's were discovered before 1984. But as we don't have telescope pointings for the period of time earlier than 1984, those "already known" discoveries have not been accounted for in our model. This is a significant factor which we have not yet estimated.

We have concentrated on improving the accuracy of the physical model of the population and the constraints on the observing program. The starting populations based on diameters and albedo distributions rather than on albedo and magnitude distributions seems to be better connected with the existing hypothesis about the NEA's population and, hence, to provide better physical basis for our simulation. We should try two-dimensional Maxwellian distribution to simulate inclinations (as was suggested by J. Williams and J. Bhattacharyya). The effect of relative motion and film sensitivity have yet to be incorporated into calculations. These parameters combined select against the discovery of fast-moving, faint objects. The impact of plate edge effects, focus variations as a function of position on the photographic plate on discovery rates is minor, but have to be assessed.

We plan to create model asteroid populations which when tested by the search simulation program results in the best approximation of the NEA discovered population. Previously defined models of population distributions, such as (Wetherill, 1987) and (Wetherill, 1988) will also be run through the search simulation. The telescope search program conducted by Eleonor Helin and her colleagues at Jet Propulsion Laboratory will also be incorporated into the simulation.

REFERENCES

- E. Bowell and K. Lumme (1979) Colorimetry and Magnitudes of Asteroids. In Asteroids (T. Gehrels, ed.), pp. 132-169. The University of Arizona Press, Tucson.
- J. Luu and D. Jewitt (1989) On the relative numbers of C-types and S-types among near-Earth asteroids. Astron. J., **98**, 1905-1911.
- L.-A. McFadden, D. J. Tholen and G. J. Veeder (1989) Physical properties of Aten, Apollo and Amor asteroids. In Asteroids II (R. P. Binzel, T. Gehrels and M. S. Matthews, eds.), pp. 442-467. University of Arizona Press, Tucson.
- G. W. Wetherill (1987) Dynamical relations between asteroids, meteorites and Apollo-Amor objects. Phil. Trans. R. Soc. Lond. A, **323**, 323-337.
- G. W. Wetherill (1988) Where do the Apollo objects come from? Icarus, **76**, 1-18.

STOCHASTICITY OF COMET P/SLAUGHTER-BURNHAM

D.Benest and R.Gonczi
O.C.A. Observatoire de Nice
B.P. 139, F-06003 NICE Cedex, FRANCE

ABSTRACT

Three comets are now known to be at or near the 1/1 resonance with Jupiter: P/Slaughter-Burnham, P/Boethin and the newly discovered P/Ge-Wang. Although details of the individual orbits differ, the three comets have very similar general dynamical behaviour: their orbits show many transitions between the different types of resonant motion (satellite libration, anti-satellite libration and circulating motion).

The stochastic character of such cometary orbits, mainly due to encounters with Jupiter, is investigated using Lyapunov Characteristic Indicators. For each comet of the group, we study the influences on the stochasticity of initial eccentricity, inclination, longitude of node and $l - l_J$ (mean longitude of comet minus mean longitude of Jupiter).

We present here our first results for P/Slaughter-Burnham.

INTRODUCTION

Three comets are now known to be at or near the 1/1 resonance with Jupiter, namely their heliocentric period is the same as Jupiter's: P/Slaughter-Burnham (1981 XVIII), P/Boethin (1986 I) and P/Ge-Wang (1988 VIII). In a previous paper (Benest, 1990), their orbital evolutions were compared, using the classical elliptic three-dimensional restricted three-body model Sun - Jupiter - comet. Although details of the individual orbits differ, the three comets have very similar general dynamical behaviour, which confirms that they obviously belong to the same family.

The three cometary orbits show many transitions between the different types of resonant motion, classically named according to the evolution versus time of the simple argument $l - l_J$ (difference of mean longitudes between the comet and Jupiter): libration and circulation. *Libration* corresponds to an oscillation of $l - l_J$ around a given value l_0 ; when $l_0 = 0^\circ$, we have a *satellite libration*, i.e. the comet is thus considered as a remote satellite of Jupiter, at least temporarily (as is P/Boethin now). A libration around $l_0 = 180^\circ$ is an *anti-satellite libration*, as P/Slaughter-Burnham now is. Any other kind of libration may occur, as $l - l_J$ may oscillate around any given value of L_0 , as examples $\pm 60^\circ$ (the well-known Trojans). *Circulation* corresponds to a monotonous variation of $l - l_J$, as do P/Ge-Wang nowadays (see Benest, 1990, for a detailed bibliography).

Generally speaking, low amplitude of libration prevent close encounters with Jupiter; on the other hand, when the amplitude of the libration becomes high enough, or during circulation, a close encounter with Jupiter will occur sooner or later, which is known to induce a more or less drastic change in the cometary orbital elements. As is now well-known, such close encounter with a planet introduces generally stochasticity in the

long-term dynamical behaviour of the cometary orbit: namely, two orbits with very close initial conditions diverge exponentially and have very different ultimate fates.

Our aim now is to study the stochasticity of the orbits of the three comets known to be at or near the 1/1 resonance with Jupiter, P/Slaughter-Burnham, P/Boethin and P/Ge-Wang. For this purpose, we compute quantities related to the theory of Lyapunov Characteristic Exponents.

Two orbits initially close diverge either linearly or exponentially depending on whether the initial points lie in an integrable or in a stochastic region of the phase space. This classical property has been extensively used as an indicator of stochasticity, and theoretically developed by Lyapunov, whose Characteristic Exponents (hereafter called LCE) indicate quantitatively how fast nearby orbits diverge and thus the degree of unpredictability of such orbits. But as the LCE's are *stricto sensu* limiting values at $t \rightarrow \infty$, they are evidently impossible to compute practically. We then define the Lyapunov Characteristic Indicators (LCI's) as the truncated values of the LCE's for a finite time; these LCI's provide however a fairly good quantitative measure of the stochasticity for a given orbit (for more details, see e.g. Gonczi and Froeschlé, 1981).

Our dynamical model is the classical elliptic three-dimensional restricted three-body problem (Sun - Jupiter - comet). The equations of motion are integrated during 10^5 years, using a Bulirsch-Stoer method with variable step size. LCI's are computed every three steps. We plan to study both the evolution of the orbital elements and the LCI's for our three comets; thereafter, we will try to evaluate the respective influences of the initial eccentricity and the initial inclination of the cometary orbit and of the initial value of $l - l_J$ on the stochasticity of the orbits. Finally, we will undertake more precise studies, which could take into account other perturbations (e.g. from the other planets, or even the so-called non-gravitational forces known to act often on comets). We present here our first results for P/Slaughter-Burnham (hereafter called P/SB).

RESULTS

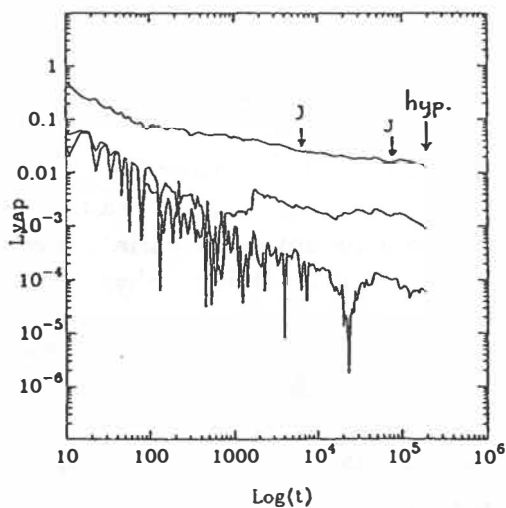


Figure 1. Evolution versus time of the 3 main LCI's (whose limits are identified with the LCE's) for comet P/SB;
"J" = close approach with Jupiter;
"hyp" = hyperbolic escape.

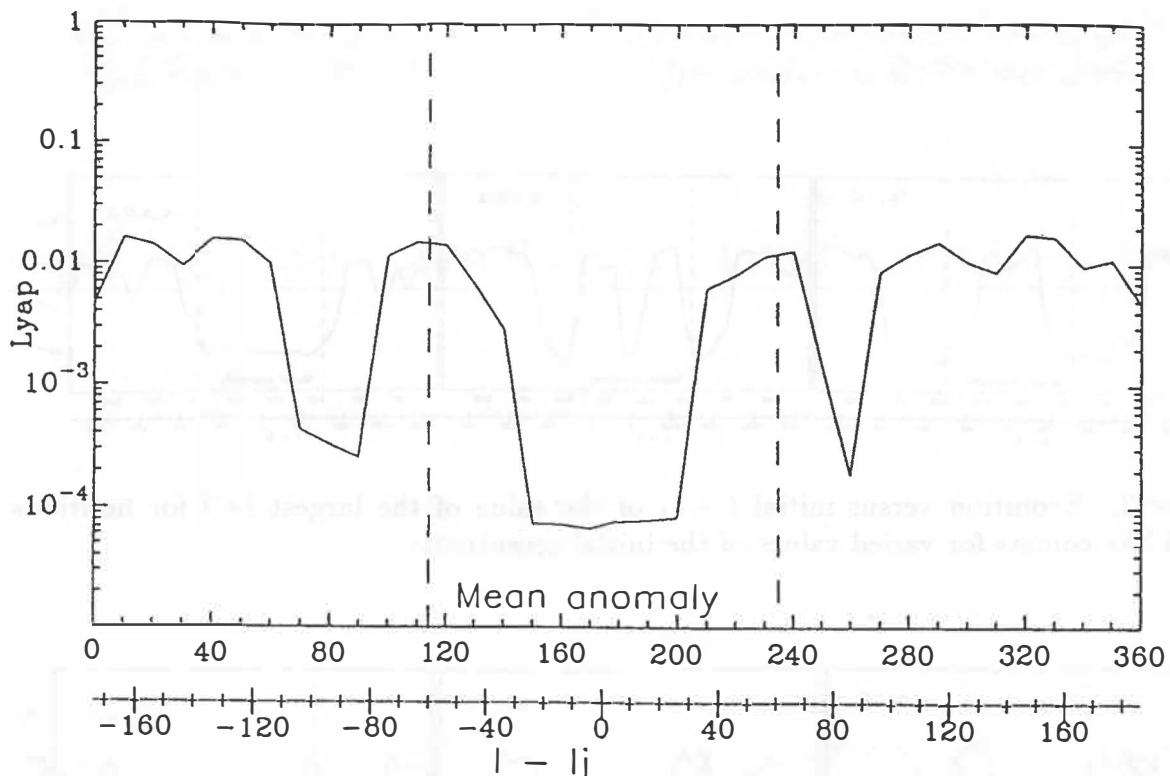


Figure 2. Evolution versus initial $l - l_J$ of the value of the largest LCI for fictitious P/SB-like comets.

Figure 1 shows that, as expected, the orbit of P/SB is stochastic. Now, all other elements remaining equal to those of the actual comet, we vary the initial value of $l - l_J$, i.e. we vary the initial value of M (the mean anomaly of the comet) from 0° to 360° every 10° ; figure 2 shows the evolution versus $l - l_J$ of the value of the largest LCI at 10^5 years for these fictitious comets ("P/SB-like comets") together with the actual comet P/SB (which has initial $l - l_J = 186.16^\circ$, i.e. $M = 0^\circ$); such a curve needs a mean computing time of 50 CPU hours on a SUN 4 at the Observatory of Nice. The curve reveals an interval of stability (i.e. for "Lyap" $< 10^{-4}$) between $l - l_J = -20^\circ$ and $l - l_J = +20^\circ$.

How does this curve evolve when we vary the other elements? Therefore we have varied independently (and again all other elements remaining equal to those of the actual comet) the initial eccentricity, inclination, longitude of node and longitude of perihelion; and for each such set of elements for fictitious P/SB-like comet, we vary $l - l_J$ as before.

We vary the initial eccentricity e from 0 to 0.9 every 0.1; for $e=0$, we observe two intervals of stability around $l - l_J = -60^\circ$ and $l - l_J = +60^\circ$, which correspond to the triangular points L_4 and L_5 (the Trojans); when e increases, these two intervals progressively shrink while the central interval appears and grows (see fig.2, where $e=0.50395$) up to $e=0.8$; for $e=0.9$, the curve is much more irregular and the orbits are probably all stochastic (see fig.3).

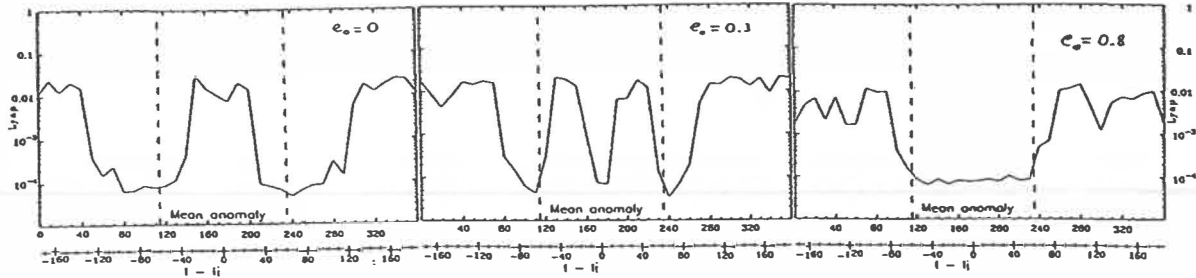


Figure 3. Evolution versus initial $l - l_J$ of the value of the largest LCI for fictitious P/SB-like comets for varied values of the initial eccentricity e .

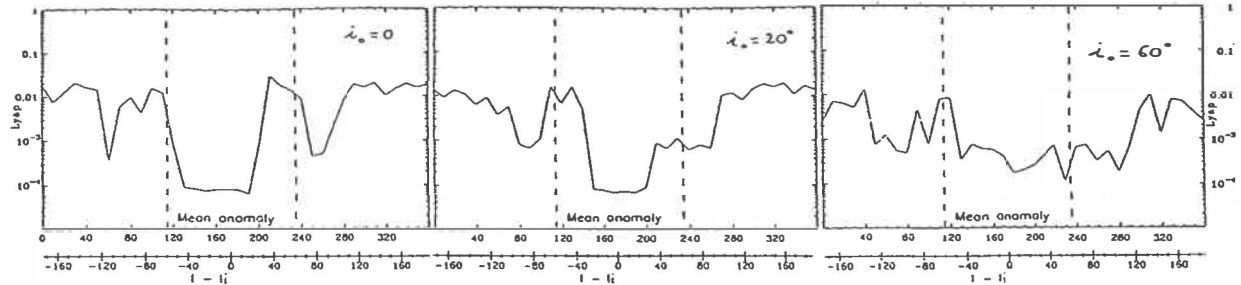


Figure 4. Evolution versus initial $l - l_J$ of the value of the largest LCI for fictitious P/SB-like comets for varied values of the initial inclination i .

We vary the initial inclination i from 0^0 to 90^0 every 10^0 ; between $i=0^0$ and $i=40^0$, the curve looks roughly like fig.2 (where $i=8.1531^0$), although becoming more and more irregular; for $i \geq 50^0$, the curve is completely irregular and the orbits are all stochastic (see fig.4).

When we vary the initial longitudes of node and of perihelion, we observe as expected only a shift of the curve.

We have now to do the same job for the two other comets (P/Boethin and P/Ge-Wang) and to compare the results in order to explain their dynamical behaviour.

REFERENCES

Benest, D. (1990) P/Ge-Wang joins P/Slaughter-Burnham and P/Boethin in the club of comets in 1/1 resonance with Jupiter. *Celest. Mech.*, 47, 361-374.

Gonczi, R., Froeschlé, C. (1981) The Lyapunov Characteristic Exponents as indicators of stochasticity in the Three Body Restricted Problem. *Celest. Mech.*, 25, 271-280.

OBSERVATIONS OF OH IN COMET LEVY WITH THE NANÇAY RADIO TELESCOPE

D. Bockelée-Morvan, P. Colom, J. Crovisier, E. Gérard, G. Bourgois

Observatoire de Paris, Section de Meudon, F-92195 Meudon, France

Abstract. Due to extremely favourable excitation conditions, comet Levy (1990c) exhibited in August-September 1990 the strongest OH 18-cm signal ever recorded in a comet at the Nançay radio telescope. This unique opportunity was used to measure the OH satellite lines at 1612 and 1721 MHz, to perform extensive mapping of the OH radio emission and to make a sensitive evaluation of the cometary magnetic field, of the H₂O outflow velocity and of the OH production rate.

OBSERVATIONS

Comet Levy (1990c) was monitored almost daily, one hour per day, from June 16 to September 30 1990, simultaneously in the 1667 and 1665 MHz main lines of the OH ground state Λ -doublet (Fig. 2a), both in right and left circular polarizations. The general observing procedure is detailed in Gérard *et al* (1989). As shown in Fig. 1, the signal was most of the time notably larger than that recorded in comet Halley at Nançay, and exhibited a strong enhancement at the beginning of September. This can be explained from the combination of favourable geometry and excellent excitation conditions (Table 1), in particular the crossing of the galactic plane by the comet on September 5. Indeed, this resulted in the amplification by the OH maser lines of a continuum background notably larger than the 2.7 K cosmic background. We took advantage of the strong signal to measure, on Sept. 3 and 4, the satellite OH lines at 1612 and 1721 MHz. Both satellite lines, which were predicted to be 9 times weaker than the 1667 MHz main line, were detected with a signal-to-noise ratio of about 8 (Fig. 2b, c). To our knowledge, the only reported attempt to observe the satellite lines in a comet was made at Nançay in comet Meier 1978 XXI (Despois *et al* 1979): the lines were detected at a 5-sigma level after nearly one month of observations. From Aug. 21 to Sept. 1 and Sept. 7 to 18, we spent part of the daily integration time with the beam aimed at offset positions with respect to the comet centre. The offsets were $\pm 7^\circ$, $\pm 10.5^\circ$ and $\pm 14^\circ$ in right ascension, corresponding to 2, 3 and 4 beams. The signal was more intense in the anti-Sun side.

Figure 1 : Line area of the 1667 MHz OH line in comet Levy (1990c) as a function of heliocentric distance. Daily values are displayed. The arrow shows the maximum intensity recorded at Nançay for P/Halley.

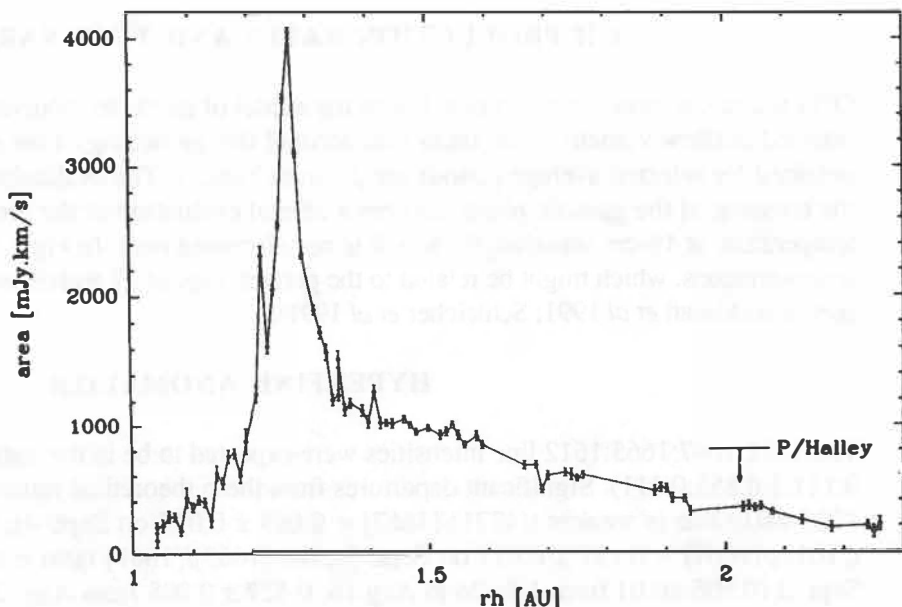


Table 1 : Parameters of the OH spectra of comet Levy (1990c) and inferred OH production rates.

date	Δ AU	r_h AU	V_h^a km s ⁻¹	inv ^b	line area ^c mJy.km s ⁻¹	Bs ^d km s ⁻¹	Q[OH] ^e 10 ²⁸ s ⁻¹	Q[OH] ^f 10 ²⁸ s ⁻¹
00616-900627	2.20	2.20	-21.5	0.50	202±11	1.62±0.09	9.5±0.7	12.0±0.9
00701-900705	1.85	2.05	-21.7	0.49	322±08	1.65±0.04	14.0±0.6	16.1±0.7
00712-900717	1.48	1.91	-21.7	0.49	419±11	1.56±0.04	14.5±0.5	16.8±0.5
00726-900729	1.08	1.75	-21.7	0.49	571±13	1.58±0.04	15.4±0.4	16.7±0.4
00731-900803	0.92	1.68	-21.6	0.49	597±12	1.66±0.04	14.7±0.3	15.0±0.3
00809-900814	0.65	1.56	-21.3	0.50	893±13	1.75±0.03	21.2±0.3	16.0±0.2
00815-900819	0.51	1.48	-20.9	0.50	961±12	1.74±0.02	16.1±0.2	13.6±0.1
00820-900824	0.44	1.41	-20.6	0.50	1046±17	1.80±0.04	17.2±0.2	13.1±0.2
00825-900901	0.45	1.34	-19.9	0.50	1355±21	1.77±0.03	21.5±0.3	17.0±0.2
00902-900904	0.51	1.29	-19.3	0.48	2860±38	1.82±0.03		
00905-900909	0.58	1.25	-18.8	0.46	2558±29	1.82±0.03		
00910-900913	0.70	1.19	-17.8	0.42	860±32	2.09±0.09		
00914-900918	0.80	1.15	-16.8	0.38	569±20	1.83±0.08	22.3±0.7	16.6±0.5
00919-900923	0.92	1.10	-15.5	0.32	329±14	1.79±0.09	16.2±0.8	13.5±0.6
00925-900929	1.07	1.05	-13.6	0.22	232±15	2.05±0.14	24.2±1.6	17.5±1.1

a : comet heliocentric velocity ; b : OH maser inversion from Despois *et al* (1981) ; c and d : area and half larger base of the best trapezia ; e : OH production rate computed according to Bockelée-Morvan *et al* (1990) (see text) ; f : OH production rate computed using the OH density model 1986a, i.e. OH and OH-parent scalelengths of $1.4 \cdot 10^5$ and $6 \cdot 10^4$ km respectively, OH radial velocity of 1.4 km s^{-1} , collisional quenching not being included.

H₂O OUTFLOW VELOCITY

Following Bockelée-Morvan *et al* (1990a), we applied trapezoidal fitting in order to remove the contribution of the OH ejection velocity v_d in the OH line shapes and determine the H₂O outflow velocity v_p . The results of the fits, in particular the half larger base Bs of the best trapezia which should be close to $v_p + v_d$, are displayed in Table 1. Assuming $v_d = 0.9 \text{ km s}^{-1}$, the inferred velocities range from 0.6 km s^{-1} to 1.1 km s^{-1} and confirm the global increase of the outflow velocity with decreasing heliocentric distance observed in other comets (Bockelée-Morvan *et al* 1990a, b).

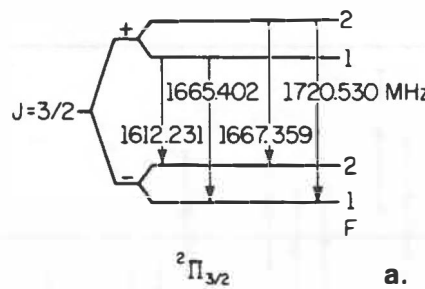
OH PRODUCTION RATES AND TIME VARIABILITY

OH production rates were computed with the model of Bockelée-Morvan *et al* (1990a), which uses the inferred outflow velocities and takes into account the quenching of the maser by collisions. The results obtained for selected average periods are given in Table 1. The evaluation of the production rates during the crossing of the galactic plane requires a careful evaluation of the continuum background brightness temperature at 18-cm wavelength, which is not discussed here. In Fig.1, the OH emission exhibits short term variations, which might be related to the periodicities of 17 and 19 hours seen in UV and visible light curves (Feldman *et al* 1991; Schleicher *et al* 1991).

HYPERFINE ANOMALIES

The 1721:1667:1665:1612 line intensities were expected to be in the statistical weight ratios 1:9:5:1 (i.e. 0.111:1:0.555:0.111). Significant departures from these theoretical ratios are present in comet Levy: the 1721 MHz line is weaker ($[1721]/[1667] = 0.069 \pm 0.012$ on Sept. 4); the 1612 MHz line is stronger ($[1612]/[1667] = 0.137 \pm 0.015$ on Sept. 3); the $[1665]/[1667]$ ratio is below the nominal value before Sept. 3 (0.506 ± 0.01 from July 26 to Aug. 16; 0.527 ± 0.008 from Aug. 24 to Sept. 2) and above it after

(0.582 ± 0.008 for Sept. 5-6). [1665]/[1667] anomalous ratios are also present in other comets, with a systematic trend for enhanced ratios at negative inversions of the OH Λ -doublet. UV pumping by the Sun, which is the main excitation mechanism of the OH cometary radio lines, tends to establish normal hyperfine ratios (Despois *et al* 1981). Departures from normal ratios should occur if the optical depths are not negligible. The line intensity is $\propto (\exp(-\tau) - 1)$, the optical depth τ having the opposite sign of the inversion (Despois *et al* 1981). Therefore, for positive inversions, the 1667 MHz line should be enhanced with respect to the 1665 MHz line, and the main lines should be enhanced with respect to the satellite lines. This is in contradiction with what is observed in comet Levy. On the other hand, the relative line intensities are well explained by a net population transfer from $F=2$ to $F=1$, occurring within both the upper and lower levels of the Λ -doublet (Fig. 2a). Sub-normal values of the [1665]/[1667] ratio suggest a more efficient transfer inside the lower level than in the upper level, while values above the theoretical value indicate the opposite. A possible explanation for this redistribution of the hyperfine populations might be inelastic collisions.



a.

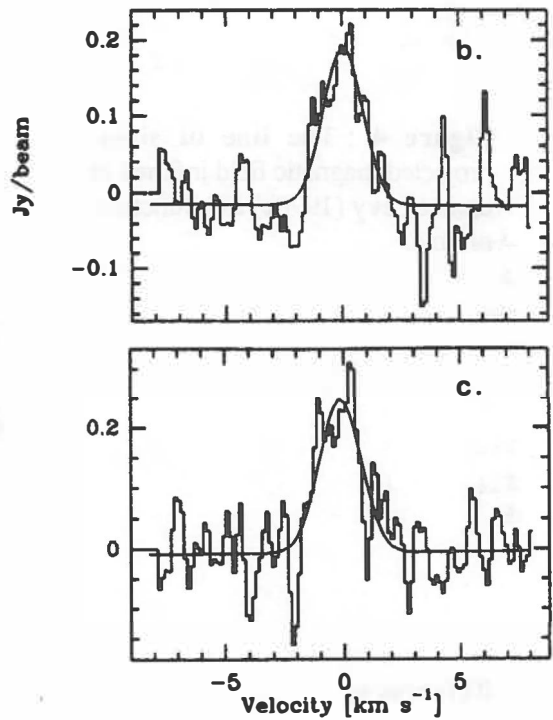


Figure 2 : a . The Λ -doublet of the OH ground state. Hyperfine splitting has been exaggerated for clarity; **b.** The 1721 MHz line detected in comet Levy on Sept. 4, 1990; **c.** The 1612 MHz line detected on Sept. 3. The OH Doppler velocities are referred to the nucleus.

ZEEMAN EFFECT AND COMETARY MAGNETIC FIELD

The Zeeman effect (i.e. the frequency difference between the left and right circular polarization components) of the OH 18-cm lines is proportional to the projection of the magnetic field on the line of sight, averaged over the line-of-sight and over the beam. Gérard (1985) measured the Zeeman effect in the OH lines of comet Austin 1982 VI and obtained a tentative detection of the projected magnetic field $\langle B_p \rangle = 50 \pm 21$ nT for Aug. 6-12, 1982. In P/Halley, outside the magnetic cavity where the field was nil, *Giotto* measured total field values of several 10 nT (Neubauer *et al* 1987). As shown in Fig. 3, the Zeeman effect was clearly detected in comet Levy at the end of August. From Fig. 4, which shows the evolution of $\langle B_p \rangle$ for individual days, one can see that $\langle B_p \rangle$ was nearly constant over the period Aug. 31 to Sept. 6, with a mean value of -22 ± 3 nT from Aug. 31 to Sept. 2, the negative sign indicating a magnetic field directed towards the observer. The averages made over several days before August 31 show that $\langle B_p \rangle$ was, in this period, less intense. It is interesting to note that the viewing conditions were rapidly varying at the end of August.

Figure 3 : Average 1667-1665 MHz spectrum of Levy on Aug. 31 to Sept. 3 in right-handed (thick line) and left-handed (dotted line) circular polarization. The frequency shift from left to right-handed polarization corresponds to a line of sight magnetic field of 22 ± 3 nT towards the observer.

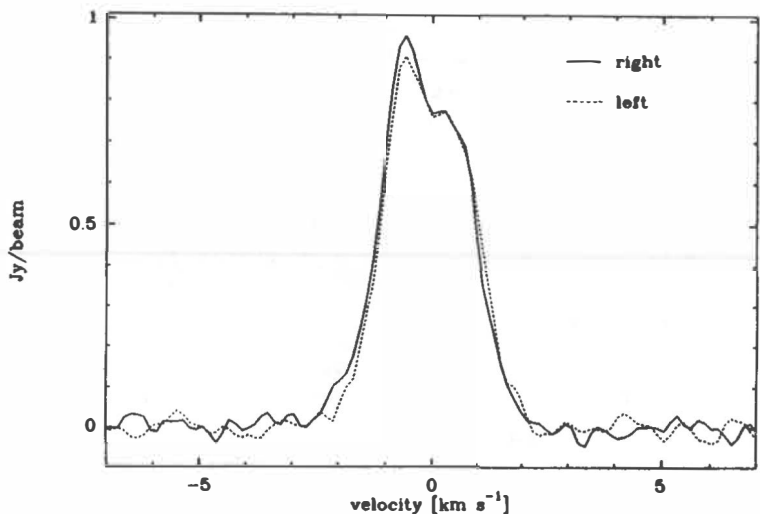
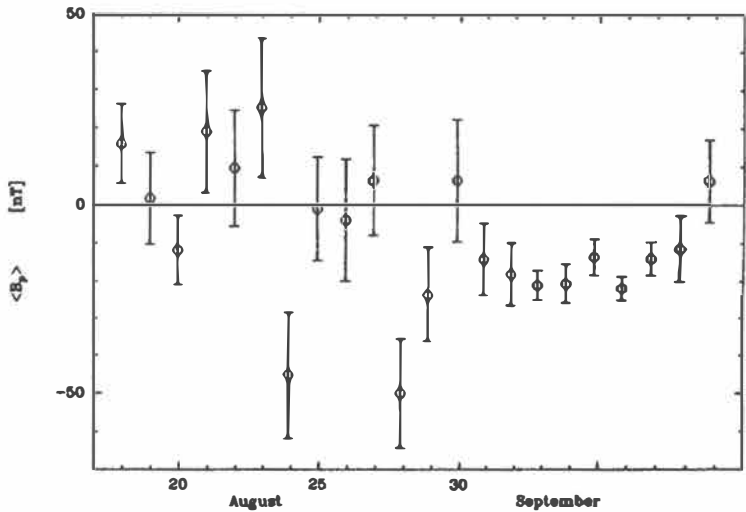


Figure 4 : The line of sight projected magnetic field inferred in comet Levy (1990c) as a function of time.



References

- Bockelée-Morvan D., Crovisier J. and Gérard E. (1990a) Retrieving the coma gas expansion velocity in P/Halley, Wilson 1987 VII and several other comets from the 18-cm OH line shapes. *Astron. Astrophys.*, **238**, 382-400
- Bockelée-Morvan D., Crovisier J., Gérard E. and Bourgois G. (1990b) OH radio observations of comets P/Brorsen-Metcalf (1989o), Okazaki-Levy-Rudenko (1989r), AArseth-Brewington (1989a1) and Austin (1989c1) at the Nançay Radio Telescope. In *Workshop on Observations of Recent Comets* (Huebner *et al.*, eds), pp. 75-79. Southwest Research Institute, San Antonio.
- Despois D., Gérard E., Crovisier J. and Kazès I. (1979) IAU General Assembly, Commission 15, Montreal
- Despois D., Gérard E., Crovisier J. and Kazès I. (1981) The OH radical in comets : observation and analysis of the hyperfine transitions at 1667 MHz and 1665 MHz. *Astron. Astrophys.*, **99**, 320-340
- Feldman P.D., Budzien S.A., A'Hearn M.F., Festou M.C. and Tozzi G.P. (1991) Ultraviolet and visible variability of the coma of comet Levy (1990c). This conference.
- Gérard E. (1985) An estimate of the magnetic field strength in the OH coma of comet Austin 1982 VI . *Astron. Astrophys.*, **146**, 1-10
- Gérard E., Bockelée-Morvan D., Bourgois G., Colom P. and Crovisier J. (1989) Observations of the OH radio lines in comet P/Halley 1986 III. *Astron. Astrophys. Suppl.*, **77**, 379-410
- Neubauer F.M. (1987) Giotto magnetic-field results on the boundaries of the pile-up region and the magnetic cavity. *Astron. Astrophys.*, **187**, 73-79
- Schleicher D.G., Millis R.L., Osip D.J. and Birch P.V. (1991) Comet Levy (1990c): Groundbased photometric results. This conference.

COMET P/TEMPEL - SOME HIGHLIGHTS AND CONCLUSIONS FROM THE 1988 APPARITION *

H. Boehnhardt, (*Dr.-Remeis Sternwarte, Bamberg, and
mbp Software & Systems, Dortmund*)

A. Bär, (*Dr.-Remeis Sternwarte, Bamberg*)

L. Massonne (*mbp Software & Systems, Dortmund*)

* based in part on observations obtained at the European
Southern Observatory ESO, La Silla/Chile.

Abstract: From the brightness development and a sequence of imaging observations of the coma activity onset of comet P/Tempel 2 in 1988, it is concluded that there might have happened eruptive events of strong dust and gas outbursts during May and June 1988. A comparison of dust coma modelling calculations with CCD observations of the coma widely confirms Sekanina's nucleus model for the comet.

1. Introduction

During the 1988 apparition of comet P/Tempel 2 a series of observations were performed by a team of the Bamberg observatory and some external collaborators (in total 11 team members). The team work was supplemented by amateur observers who contributed the visual brightness estimations of the comet. The scientific aims of the observations were to estimate the nucleus size, to monitor the coma activity and its morphology, to derive some characteristic values of the gas productions of C₂, C₃ and CN together with basic data on molecular physics of C₂ and to provide position measurements for an improved orbit determination of the comet. The results of this research project on P/Tempel 2 (except the astrometry) are published in Boehnhardt et al. (1990).

In this paper we present some further conclusions on possible eruptive events during the preperihelion activity phase of P/Tempel 2 and a comparison of the coma imaging observations with dust coma model calculations of the comet.

2. Eruptive events in the lightcurve and the coma development

From the published imaging and photometry of comet P/Tempel 2 during the transition phase of marginal to significant coma activity (see Jewitt and Luu, 1990: 9-15/4/88 = probably no coma; Boehnhardt et al., 1990: 4/5/88 = no coma; Wisniewski, 1990: 8-9/5/88 = faint coma; West, 1988: 17/5/88 = significant coma) we conclude that the onset of major gas and dust production of the cometary nucleus took place between 135 to 131 days before perihelion, i.e. at the rather close solar distance

of 1.9 AU. At similar solar distances most comets have already developed prominent comae. At the same time interval preperihelion the visual lightcurve of the comet showed an instantaneous increase of about 3 magnitudes (from 16.5 mag nuclear to 13.5 mag coma brightness; see Weiss, 1989). The temporal coincidence of both phenomena could have been caused by an eruptive onset of gas and dust emission from a large and highly active surface area of the nucleus. The weak gas emission of P/Tempel 2 observed by Cochran (1991) from February 1988 onwards may therefore resemble either the moderate outgassing of the inactive surface of the nucleus or it may indicate the eventual "smoke" of the activity centre of the May eruption. Before early May 1988 this active region seemed to have been protected against sunlight (either by a surface crust or by shadowing effects due to surface geometry). After the activity onset in May 1988 the cometary brightness remained constant for about 50 days. Thereafter, a second rapid brightness increase can be seen in the reported lightcurve (Boehnhardt et al., 1990). A similar behaviour of P/Tempel 2, i.e. a brightness plateau with a successive eruptive brightness increase, can also be inferred from the 1967 lightcurve of the comet (Weiss, 1989). It would be interesting to look for similar features of eruptive events and for their temporal repetition or non-repetition during the forthcoming apparitions of P/Tempel 2.

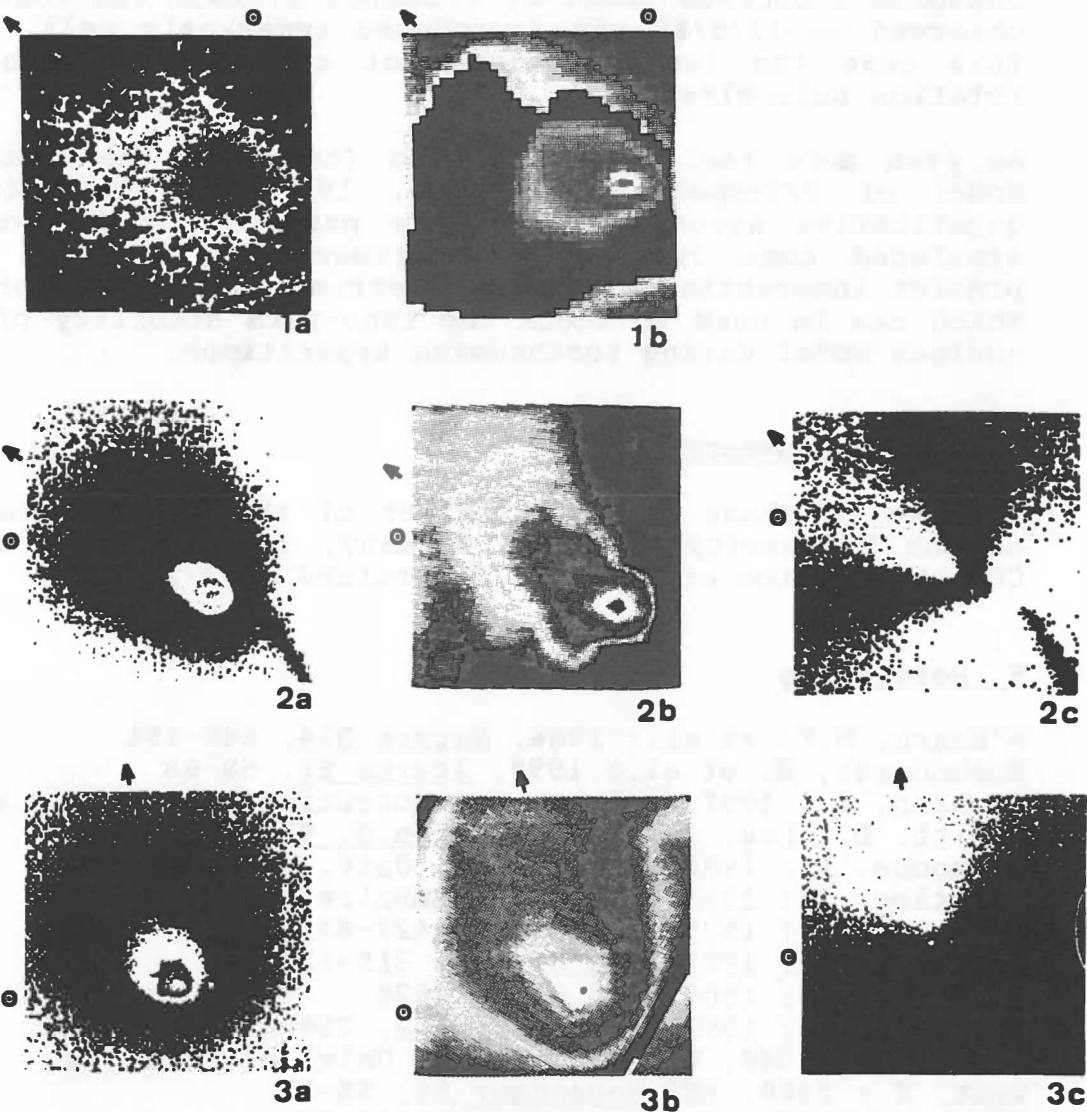
3. Coma morphology - observations and modelling

Figs. 1-3a show V-filter CCD exposures of comet P/Tempel 2 obtained on 17/5/88 (West, 1988), on 24/7/88 (Boehnhardt et al., 1990) and on 7/11/88 (Richtler, 1989, so far unpublished), respectively. All images exhibit a prominent fan-shaped coma, which can basically be interpreted as due to a jet of dust and gas emitted from a very active region located at high cometographic latitude. Since the V-filter transmission is dominated by reflected sunlight from the cometary dust, we assume that the coma images widely resemble the dust distribution as seen from Earth. The jet was smeared by the rotation of the nucleus which finally resulted in the fan-shaped coma of the comet. Sekanina (1979, 1987) has proposed a nucleus model for P/Tempel 2 which claims an activity centre at about 60 deg cometographic latitude as source for the coma fan. This centre rotates in about 9 hours (Jewitt and Luu, 1989) about the rotation axis at right ascension 147 deg and declination +55 deg (epoch 1950). The nucleus was found to be of size 16 x 8 x 8 km (see for instance Sekanina, 1988). According to Sekanina (1987) the fan axis observed should roughly indicate the direction of the projected rotation axis. In order to assess the fan axis more accurately the observations on 24/7/88 and 7/11/88 were computer-processed by the so called radial renormalisation method: this method reduces the general coma background and enhances faint inherent coma structures. It is comparable to the method successfully applied by A'Hearn et al. (1986) for the CN

Figure 1 to 3

P/Tempel 2 - a comparison of observed (a), calculated (b) and renormalized (c) coma images
 North is up and East to the right. the Sun is indicated by o, the direction of the projected rotation axis of the nucleus by an arrow.

- | | |
|---|---|
| 1 | P/Tempel 2 on 1988/05/17 (from West, 1988) |
| a | CCD image (42000 km x 42000 km) |
| b | computer simulation (25000 km x 25000 km) |
| | |
| 2 | P/Tempel 2 on 1988/07/24 |
| a | CCD image (30000 km x 30000 km) |
| b | computer simulation (190000 km x 190000 km) |
| c | renormalized coma image (17000 km x 17000 km) |
| | |
| 3 | P/Tempel 2 on 1988/11/07 |
| a | CCD image (60000 km x 60000 km) |
| b | computer simulation (200000 km x 200000 km) |
| c | renormalized coma image (58000 km x 58000 km) |



jets in comet P/Halley. For both observing dates the alignment of the fan axis with the predicted direction of the projected rotation axis is rather good (see figs. 2c, 3c). However, for the observation on 17/5/88 a significant discrepancy between fan axis and projected rotation axis can be found (see fig. 1a).

In order to check Sekanina's model for P/Tempel 2 more thoroughly computer simulations were performed using the ESOC dust coma modelling software. The physical principles and the computer programs of the software package are described in Massonne (1986). The results of this computer simulations for the dust coma of P/Tempel 2 are presented in figs 1-3b. The figures show the dust density distribution as seen from Earth for the three observation dates from above. Though in the present software version some simplified assumptions are made (spherical nucleus, fixed rotation axis, dust size distribution of P/Halley), the modelling verifies at least qualitatively Sekanina's nucleus model of P/Tempel 2. Even the coma morphology observed on 17/5/88 was reproduced remarkably well, although in this case the fan axis does not coincide with the projected rotation axis direction.

An even more realistic modelling (based on the updated nucleus model of P/Tempel 2; Sekanina, 1991) may lead to a better quantitative agreement (isophote pattern) of the observed and simulated coma images. The software may also be applied to predict interesting viewing geometries of the coma of P/Tempel 2 which can be used to check the long-term stability of Sekanina's nucleus model during forthcoming apparitions.

4. Acknowledgement

We like to thank Dr. T. Richtler of the Astronomical Institute of the University of Bonn, Germany, for providing us with the CCD observation of P/Tempel 2 obtained on 7/11/88.

5. References

- A'Hearn, M.F. et al.: 1986, *Nature* **324**, 649-651
- Boehnhardt, H. et al.: 1990, *Icarus* **86**, 58-68
- Cochran, A.: 1991, private communication during this conference
- Jewitt, D., Luu, J.: 1989, *Astron.J.* **97**, 1766-1790
- Massonne, L.: 1986, PhD thesis, Univ. of Heidelberg
- Richtler, T.: 1989, private communication
- Sekanina, Z.: 1979, *Icarus* **37**, 420-442
- Sekanina, Z.: 1987, *ESA SP-278*, 315-336
- Sekanina, Z.: 1988, *IAU Circ.* **4624**
- Sekanina, Z.: 1991, *Astron.J.* **102**, 350-388
- Weiss, M.: 1989, Diploma thesis, Univ. of Erlangen
- West, R.: 1988, *ESO Messenger* **54**, 55-56
- Wisniewski, W.: 1990, *Icarus* **86**, 52-57

COMA IMAGING OF COMET P/BRORSEN-METCALF AT CALAR ALTO IN LATE JULY TO MID AUGUST 1989

H. Boehnhardt (*mbp Software&Systems, Dortmund, and
Dr.-Remeis Sternwarte, Bamberg*)
V. Vanysek (*Charles University, Prague*)
K. Birkle (*Max-Planck-Institut für Astronomie,
Heidelberg*)

Abstract: Comet P/Brorsen-Metcalf was observed on 1989/07/28+30 and on 1989/08/04+12(+14) with the 3.5m telescope and the 0.8m Schmidt camera at Calar Alto/Spain. The images exhibit a narrow plasma tail pointing into anti-solar direction. On 1989/07/30 a triple tail was found which can be interpreted as tail ray event. The coma isophotes show prominent asymmetries with the nucleus located on the tailward side of the isophote foci and with a slightly higher brightness in the northern hemisphere of the coma. A strong curved jet feature was detected in the coma on 1989/07/30. The jet extended at least 30000 km into the sunward coma hemisphere. The rotation period of about 1.3 days, estimated from the curvature of the coma jet, needs verification by other observations.

1. Observations and Data Reduction

Comet P/Brorsen-Metcalf was observed on 1989/07/28+30 and on 1989/08/4+12(+14) from Calar Alto/Spain. The details of the 0.8m Schmidt camera and the 3.5m telescope CCD observations can be found in table 1. Standard reduction techniques were applied to the CCD frames. On the Schmidt photographic plates, the coma region and the calibration spots were digitized by means of a PDS machine. The relative calibration of the digitized exposures was performed using the intensity spots of the images. Since the isophote patterns of almost all images processed were not concentric with respect to the nucleus position, the radial renormalisation method was applied to six relative-calibrated frames. This method reduces the general coma background and enhances possible faint tail and coma structures in the images. The resulting frames are so called net images of the coma.

2. The Coma Structures

Almost all calibrated images of comet P/Brorsen-Metcalf clearly show a narrow cometary tail and an asymmetric isophote pattern in the coma. The latter phenomenon is characterized by the fact that, especially for the outer coma isophotes, the central brightness peak in the coma is not the focus point of the isophotes, and that it is often located "tailward" of the geometric coma midpoint.

2.1 The Tail

The cometary tail is clearly visible in R while in the B filter images the tail is much fainter or even undetectable at all. It is pointing approximately into anti-solar direction of the nucleus (table 1). While on 1989/07/28 and on 1989/08/04+12(+14) the tail exhibited only a single bright ray of about 5 deg opening angle, the triple tail on 1989/07/30 (figure 1a) may indicate a cometary tail ray event. The bright central parts of the tail rays seem to be embedded in a surrounding faint parabolic shell with vertex at the nucleus position. A fan-like bright region of about 7000 km extension is located at the vertex of this tail envelope on the anti-solar side of the nucleus.

Though the dust tail was viewed nearly edge-on from Earth during the observing interval (see table 1), it might not have contributed significantly to the R-filter brightness of the tail structures because of the very low dust-to-gas production ratio in comet P/Brorsen-Metcalf (DiSanti and Fink, 1989; Roettger et al., 1989). In particular, it cannot explain the tail rays observed on 1989/07/30. Therefore, the tail phenomena described above are assumed to have been caused by the cometary plasma (the transmission of the R filter peaks near strong emission bands of H₂O⁺).

2.2 The General Coma Structure

The net images of comet P/Brorsen-Metcalf, derived from the B and R filter CCD exposures on 1989/07/28+30 and from the B filter Schmidt plate on 1989/08/12, show enhanced relative brightness on the sunward side of the coma (figures 1a and b). This may indicate a higher activity on the sunlit part of the nucleus. Similar phenomena are known from other comets (for comet P/Halley see in Keller et al., 1987; for comet P/Tempel 2 see in Boehnhardt et al., 1989).

Furthermore, on the three observing dates mentioned above the general coma background was apparently brighter in the northern section of the sunward coma hemisphere than on the southern side. The highest deficits in the mean coma brightness were found in the southern part of the tailward coma hemisphere.

2.3 The Coma Jet

In both the B and the R filter net images of comet P/Brorsen-Metcalf on 1989/07/30 (figures 1a and b) a curved jet-like feature extended into the sunward inner coma. It originated from the nucleus at position angle of about 325 deg and turned towards the Sun during its expansion into the coma. In the B filter net image the jet can be detected above coma background to at least 30000 km projected nucleus distance. The jet and its curvature in the net images can clearly be related to the

Table 1 Overview on the observations of comet P/Brorsen-Metcalf at Calar Alto Observatory/Spain (observations used for this paper)

Date (UT)	89/07/28	89/07/28	89/07/30	89/07/30	89/08/04	89/08/12
Time (UT)	3:42-3:44	3:48-3:50	3:38-3:39	3:43-3:45	2:50-3:10	4:18-4:21
Telescope	3.5m	3.5m	3.5m	3.5m	Schmidt	Schmidt
Filter	R	B	R	B	RG610	RG385
Detector	CCD	CCD	CCD	CCD	IIIaF	IIIaJ
Field of view (")	256x156	256x156	256x156	256x156	344x344 ^t	688x688 ^t
Pixel resolution (")	0.25	0.25	0.25	0.25	0.89	0.89
Earth distance (AU)	0.68	0.68	0.66	0.66	0.63	0.63
Sun distance (AU)	1.11	1.11	1.08	1.08	0.99	0.85
Theta (deg)	79	79	77	77	70	70
Beta (deg)	64	64	67	67	74	84
Elong (deg)	-5.5	-5.5	-3.6	-3.6	0.8	8.1
Elat (deg)	1.9	1.9	1.3	1.3	-0.3	-2.8
Psi calculated (deg)	254	254	256	256	264	280
Psi measured (deg)	253	---	240/254/259	---	265	278
Tail opening angle (deg)	5	---	5/3/6	---	5	7

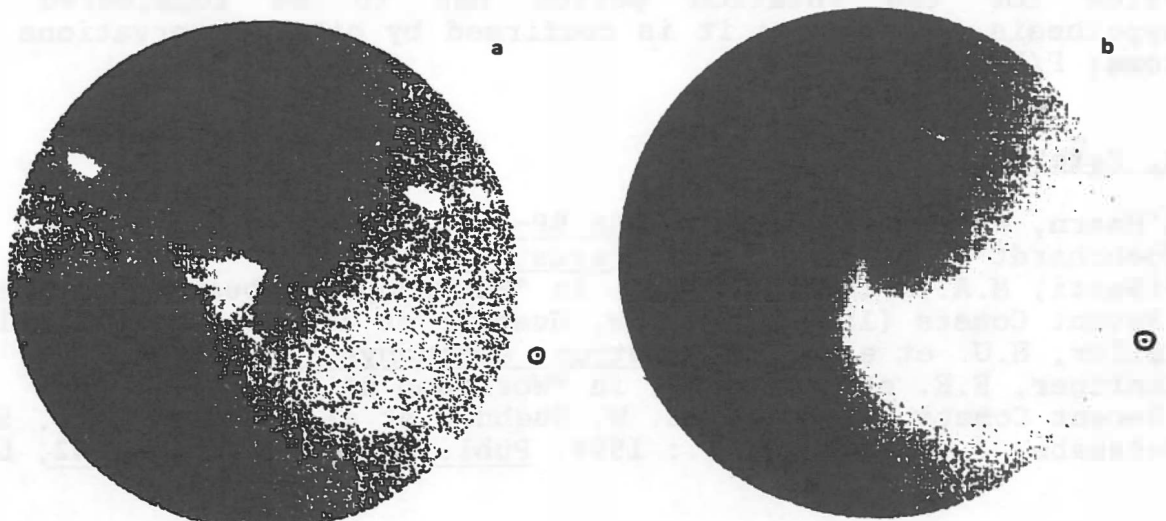
Explanations:

- Theta, Beta = Angles Sun-Earth-Comet, Sun-Comet-Earth
- Psi = Position angle of extended comet radius vector
(Zero point = North, 90 deg = East)
- Elong = longitude of Earth in the cometary orbit reference frame
(Zero point = Ascending node of cometary orbit)
- Elat = latitude of Earth in cometary orbit reference frame
(0 deg = orbital plane, 90 deg = orbit pole)
- ^t = valid for the PDS scan of the Schmidt plate only

Figure 1 CCD exposures of comet P/Brorsen-Metcalf on 1989/07/30

North is down and East is right. The direction of the Sun is marked by symbol 0. The coma brightness peak is in the centre of the field of view.

- a R filter net image (60 s exposure time). Field of view: radius = 31000 km
- b B filter net image (120 s exposure time). Field of view: radius = 31000 km



to at least 30000 km projected nucleus distance. The jet and its curvature in the net images can clearly be related to the asymmetric coma isophotes and their anti-clockwise change of orientation in the calibrated images.

The presence of the jet in the B and R filter exposures can be explained by reflection of solar light by the dust particles in the jet. However, the jet might have also contained a significant amount of gas which could have been produced by the dust grains in the jet (see the CN and C2 jets observed in comet P/Halley by A'Hearn et al., 1986). Similar jet features in the coma of comet P/Brorsen-Metcalf were not found in the B and R filter net images obtained on 1989/07/28 and on 1989/08/04+12.

The presence of the jet in the coma of comet P/Brorsen-Metcalf on 1989/07/30 can be interpreted as due to an isolated area of high dust and gas production on a rotating nucleus. Most likely the emission centre was active when exposed to sunlight (on 1989/07/30), since the jet emission concentrated in the sunward coma hemisphere. Apparently the jet was not or much less active during the other days when observations of the comet were obtained at Calar Alto Observatory. Because of the edge-on view of the orbital plane of the comet during the observing period one can conclude that the emission cone of the jet was intersected by the orbit plane since jet material was observed on both side of the projected extended radius vector of the comet (= tail direction). From the curvature of the jet we have estimated an approximate value of about 1.3 days for the rotation period of the nucleus (assuming the rotation axis close to the line of sight, an outflow velocity of 0.7 km/s for the jet material and neglecting possible projection effects). It compares well to the 30 to 40 hours rotation period derived by Watanabe and Nakamura (1990) from narrow band filter CCD observations of P/Brorsen-Metcalf in early August 1989. The alternative solution (13.5 to 15 hours) of these authors seems to be less likely because it implies a jet expansion velocity of more than 1.5 km/s and does not match all available jet observations. However, because of the simplifications made, our value for the rotation period has to be considered as hypothesis only unless it is confirmed by other observations of comet P/Brorsen-Metcalf.

3. References

- A'Hearn, M.F. et al.: 1986, ESA SP-250 II, 207
 Boehnhardt H. et al.: 1990, Icarus 86, 58
 DiSanti, M.A., Fink, U.: 1989, in "Workshop on Observations of Recent Comets (1990)", eds. W. Huebner et al., San Antonio, 18
 Keller, H.U. et al.: 1987, Astron. Astrophys. 187, 807
 Roettger, E.E. et al.: 1989, in "Workshop on Observations of Recent Comets (1990)", eds. W. Huebner et al., San Antonio, 59
 Watanabe, J., Nakamura, T.: 1990, Publ. Astro. Soc. Jap. 42, L7

A PRELIMINARY MODEL OF THE COMA OF 2060 CHIRON

D.C. BOICE, I. KONNO, S. ALAN STERN, and W.F. HUEBNER
Southwest Research Institute, San Antonio, TX 78228-0510 U.S.A.

Abstract. We have included gravity in our fluid dynamic model with chemical kinetics of dusty comet comae and applied it with two dust sizes to 2060 Chiron. A progress report on the model and preliminary results concerning gas/dust dynamics and chemistry is given.

1. INTRODUCTION

There has been much interest in 2060 Chiron since observations of comet-like activity and a resolved coma established it is a comet. Determinations of its radius range from 65 to 200 km, making Chiron unique among bodies with atmospheres in the Solar System. This unusually large size for a comet suggests that the atmosphere of Chiron is intermediate to the tightly bound, thin atmospheres typical of planets and satellites and the greatly extended atmospheres in free expansion typical of cometary comae. Under certain conditions (depending on molecular weight, temperature, heliocentric distance, and the size and mass of Chiron) it may gravitationally bind an atmosphere which is thick compared to its size while a significant amount of gas escapes to an extensive exosphere. These attributes coupled with reports of sporadic outbursts at large heliocentric distances ($\gtrsim 12$ AU) (1,2) and the identification of CN in the coma (3) make Chiron a challenging object to model. Simple models of gas production and a dusty coma have been recently presented by several investigators (see, e.g., 4-6) but a general consensus on many basic features has not emerged. We have begun development of a more complete coma model of Chiron (7). The objectives of this paper are to report progress on this model and give preliminary results for understanding Chiron.

2. GAS PRODUCTION

Throughout its orbit, Chiron remains too far from the Sun for direct sublimation of water to be important, but CO, N₂, and CH₄ ices could be the cause of activity throughout its complete orbit (4,7). CO₂ production "turns on" only about 10 years prior to perihelion. At perihelion, on the order of a Mg/s of CO can be released even if only a small amount (a few %) of Chiron's surface is active. At these activity levels, the mean free path of a CO molecule at the surface is on the order of 100 m, much smaller than the flow scale length, so the sublimating gas is collisionally coupled and the fluid dynamic approach is required. The extent of the collision region can be determined only by detailed modeling or observations but an upper limit can be estimated assuming free expansion (R⁻² density distribution) and isotropic emission. In this limit, its size is roughly $3 \cdot 10^3$ km, about the same as the collision zone of P/Halley at perihelion. Under the influence of Chiron's gravity (a few to 10 cm s⁻²), fluid dynamic conditions near the surface are even more favorable.

The sublimation of a volatile, like CO, leads to a gas temperature close to 30 K throughout Chiron's orbit (5), far below that of a blackbody in radiative equilibrium. This results in a thermal velocity that is comparable to the escape velocity (7), given uncertainties in the size and mass of Chiron. This situation may lead to a bound atmosphere with extensive exosphere as slower molecules in the Maxwellian distribution cannot escape while those traveling faster than the escape velocity leave. The loss of these more energetic molecules results in substantial cooling of the remaining gas, making it more tightly bound. However, slightly higher thermal velocities lead to hydrodynamic escape or "blow-off" of the atmosphere (8). This situation is complex and sensitive to the actual bulk parameters.

Other processes can heat and cool the gas (7), including photo-reactions (heating), radiative cooling, collisions with grains that are hotter than the gas (heating), sublimation from icy grains,

and expansion cooling of the gas. In the case of photo-destruction of CO, typical rates (9) at 10 AU yield a lifetime of 4.5 years, making this a minor source of energy and ions on smaller timescales. Charge exchange with the solar wind may be an important ion source at Chiron also. Each of these effects requires investigation with detailed modeling to assess its significance, as we are undertaking.

3. THE DUST COMA

The sublimating gas entrains dust particles as it leaves Chiron's surface. The dust dynamics is also influenced by the gravity and rotation of Chiron within a sphere of influence given by (10),

$$R_{GS} = r(M_{Chiron}/2M_{Sun})^{1/3}.$$

At $r = 10$ AU, adopting a radius of 120 km and a density of 1 g cm^{-3} for Chiron, $R_{GS} \approx 1500 R_{Chiron}$. Outside of this region, both solar gravity and radiation pressure must be taken into account. The maximum particle size that can be lifted by gas drag has been estimated to be on the order of $100 \mu\text{m}$ for CO sublimation (5). In a typical comet, the gas density decreases as R^{-2} , and for large particles (with velocities much smaller than the gas) the ratio of the gas drag to gravity is constant (11). Once lifted off the nucleus, these particles will leave the comet. However, considering gas production from restricted active areas and the effects of gravity on the gas, the gas density will decrease more rapidly than R^{-2} and these larger particles may decouple from the gas drag before escape, traveling in bound orbits and may eventually fall back to the surface. The extent of the gas-dust interaction region depends on particle size and bulk density. Based on our preliminary model, we estimate the size of the acceleration region to be on the order of ten Chiron radii for 1 to $10 \mu\text{m}$ particles.

Beyond the gas-dust interaction region, the dust trajectories are increasingly influenced by radiation pressure and can be approximated by the fountain model (12). Micrometer-sized particles follow parabolic orbits confined within an envelope which is a paraboloid with focus in the nucleus and apex in the sunward direction. The standoff distance can be roughly estimated for these particles, using typical parameters for Chiron, to be on the order of $100 R_{Chiron}$. At further distances, the solar gravity and the Poynting-Robertson effect influence the dust dynamics. Other effects that may need to be considered in a realistic model of the dust coma include grain-grain collisions and charging of particles by solar wind, secondary electron emission, or coma plasma.

4. PRELIMINARY MODEL OF 2060 CHIRON

One-dimensional, multi-fluid simulations of the coma of Chiron at perihelion have been performed. These simulations are based on our model that treats the physics and chemistry of the inner coma in great detail (9). Recent progress of the model includes incorporation of dust entrainment by the gas, dust size distributions, dust fragmentation, and distributed coma sources of gas-phase species related to the dust described in (13).

In this preliminary model of Chiron, CO is assumed to be the only volatile. Other model parameters include $r = 8.51$ AU, $R_{Chiron} = 120$ km, $A = 0.03$, $\rho_{Chiron} = 1$. The dust-to-gas mass production ratio (χ) is assumed to be 1. Two sizes of dust ($a = 1$ and $10 \mu\text{m}$) are considered and the dust mass distribution is approximated by a power law (exponent = 0.5). The model capabilities for dust fragmentation are not used in the present calculations. Being a diatomic molecule, CO is not an efficient emitter in the infrared so the radiative cooling term has been omitted in this first-order model. For comparison, a dust-free model ($\chi = 0$) and a model with a modest amount of dust ($\chi = 0.1$) were produced also.

In the simulations, gas and dust are rapidly accelerated upon leaving the nucleus as illustrated in Fig. 1. For standard dust densities, small particles are more efficiently entrained with the gas flow than large particles, resulting in higher terminal speeds. The acceleration zone for all particles is approximately within $10 R_{Chiron}$. The inclusion of dust has two important effects on

the gas flow. The first is an initial mass-loading of the gas, reducing the gas velocity to subsonic values close to the surface of the nucleus. The second effect is a strong coupling of the gas and dust temperatures near the nucleus as shown in Fig. 2. Upon release, the dust heats rapidly to its radiative equilibrium value of 95 K. Collisions of molecules with dust particles heat the gas (initially at 30 K) to 85 K within a Chiron radius. This results in a terminal gas velocity about 80% higher than that calculated from a pure gas model. Even with a modest amount of dust ($\chi = 0.1$), the gas is significantly heated in the near-nucleus region. A complete description of our model and more extensive results will be presented in a forthcoming publication.

Acknowledgements. This research was supported by grants from NASA (Nos. NAGW-2205 and NAGW-2370).

5. REFERENCES

- (1) Tholen D.J., Hartmann W.K., and Cruikshank D.P. (1988) *IAU Circ.* No. 4554.
- (2) Bus S.J., Bowell E., Harris, A.W., and Hewitt A.V. (1989) 2060 Chiron: CCD and Electronographic Photometry. *Icarus* **77**, 223-238.
- (3) Bus S.J., A'Hearn M.F., Schleicher, D.G., and Bowell, E. (1991) Detection of CN Emission from (2060) Chiron. *Science* **251**, 774-777.
- (4) Stern S.A. (1989) Implications of Volatile Release from Object 2060 Chiron. *PASP* **101**, 126-132.
- (5) Luu J.X. and Jewitt D.C. (1990) Cometary Activity in 2060 Chiron. *Astron. J.* **100**, 913-932.
- (6) Meech K.J. and Belton M.J.S. (1990) The Atmosphere of 2060 Chiron. *Astron. J.* **100**, 1323-1338.
- (7) Boice D.C., Stern S.A., and Huebner W.F. (1991) On the Atmosphere of 2060 Chiron. *LPSC* **XXII**, 121-122.
- (8) Hunten D.M. and Watson A.J. (1982) Stability of Pluto's Atmosphere. *Icarus* **51**, 665-667.
- (9) Schmidt H.U., Wegmann R., Huebner W.F., and Boice D.C. (1988) Cometary Gas and Plasma Flow with Detailed Chemistry. *Comp. Phys. Comm.* **49**, 17-59.
- (10) Öpik E. (1963) Survival of Cometary Nuclei and the Asteroids. *Adv. Astron. Astrophys.* **2**, 219-262.
- (11) Grün E. and Jessberger E.K. (1990) Dust. In *Physics and Chemistry of Comets* (W.F. Huebner, ed.), pp. 122-126. Springer-Verlag, Berlin.
- (12) Haser L. (1965) Calcul de Distribution d'Intensité Relative dans une Tête Comète. *Congrès Colloques l'Université de Liège*, **37**, 233-241.
- (13) Konno I., Huebner W.F., and D.C. Boice (1991) *Icarus*, submitted.

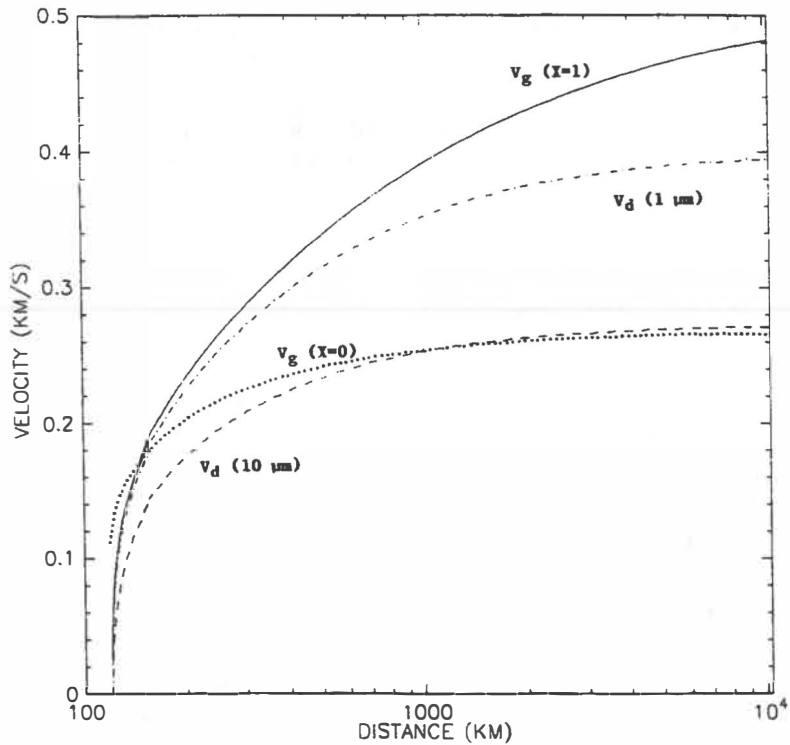


Figure 1. Gas and dust speeds for Chiron at perihelion. The dust acceleration region is within about $10 R_{Chiron}$. For comparison, the dotted line is the gas speed for a dust-free model ($\chi = 0$).

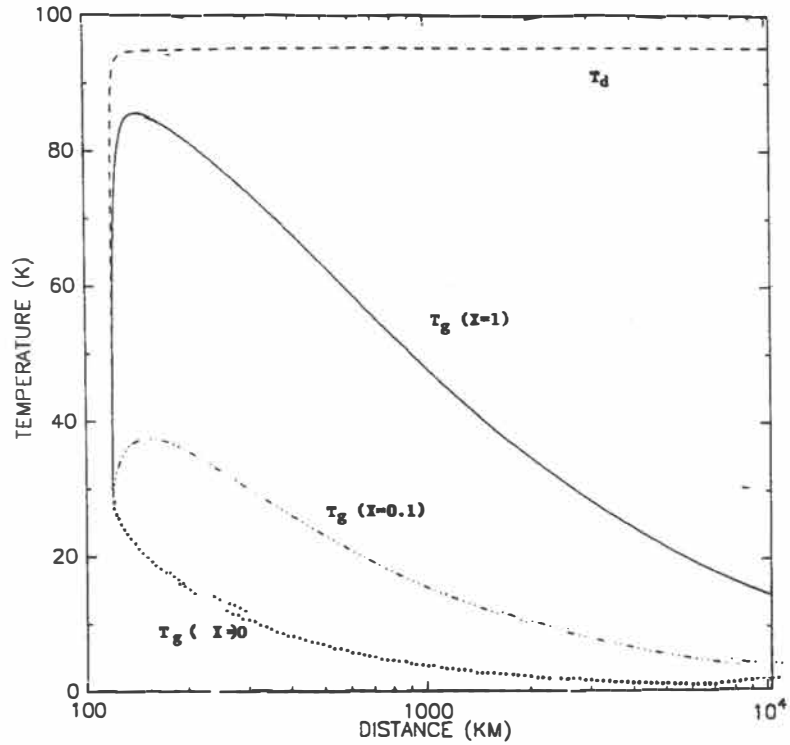


Figure 2. Temperature profiles of the gas and dust for Chiron at perihelion. Upon release from the nucleus, both sizes of dust quickly reach radiative equilibrium at 95 K. The gas is strongly heated by the dust in the near-nucleus region for the $\chi = 1$ case. Even with a modest dust-to-gas mass ratio ($\chi = 0.1$), the gas is heated significantly above the dust-free model ($\chi = 0$).

CCD Imaging of the Inner Coma Jets of Comet P/Halley

James Boswell & David W. Hughes. *Department of Physics, University of Sheffield, Sheffield, S3 7RH, UK.*

Abstract. In this paper we analyse the inner coma section of a CCD image of comet P/Halley taken at 1807 UT on 1986 March 13th using a C_2 filter (wavelength 5000 to 5200 Å, half maximum) with the 3.8 m Anglo Australian Telescope at Siding Springs, Australia. Atmospheric turbulence leads to a spreading of the image detail and this produces a blander image of the inner coma region with a slower radial decrease of brightness in comparison to the unaffected image. We remove this smearing by utilising the point spread function of a star on the same CCD image. Jets were then revealed by removing the average background. Analysis of the jet structure enabled us to estimate the lower limit of the parent molecule velocity. This is found to be 0.3 km s^{-1} .

Introduction

Within 2–3 AU of the Sun, sublimation of ice from active areas of cometary surfaces leads to the ejection of gas and dust in high velocity jets. These jets spread out to form a large, quasi-spherical cloud, known as the coma, which is, close to the Sun, typically 10^5 km across. The coma surrounds the small, solid nucleus and is responsible for scattering the majority of the incident sunlight.

This paper investigates the structure of these emissions using CCD images of comet P/Halley taken with a C_2 filter (wavelength 5000 to 5200 Å, half maximum) at the prime focus of the 3.8 m Anglo Australian Telescope at Siding Springs, New South Wales. The image coma region corresponds to a square of side 20,400 km in the plane of the sky passing through the cometary nucleus, encompassing pixels 145 to 203 on the horizontal axis and pixels 264 to 322 on the vertical axis. In displaying the data it is sometimes helpful to plot brightness as a ‘height’ above the two dimensional pixel array. Using this convention the CCD image of the comet takes the form of a ‘mountain’ and it becomes convenient to extend the analogy and refer to brightness as height and small local intensity peaks as ‘hillocks’.

Overcoming the problem of atmospheric blurring of the CCD image

One of the major problems with ground-based astronomical images is distortion caused by atmospheric turbulence. The effect of the atmospheric turbulence is to independently smear out each of the point elements, which would make up the undistorted image, into a two-dimensional brightness pattern. Background stars can be regarded essentially as point sources. Hence, in an ideal image, they should appear as a single bright pixel. However, in reality, atmospheric blurring causes their image to be spread out over many pixels. Hence, in an image of the comet they appear as small hillocks on the surface of the overall mountain that represents the cometary brightness distribution. The height of a hillock above the background indicates the brightness of the star that it represents, and in order to ensure energy conservation, the total integrated height of the hillock (i.e. the sum of all the hillock DN-values) must equal the height of the equivalent point in the undistorted image. However, the shape of all the hillocks are the same, regardless of the brightness of the star that they represent. Clearly, every point element in the undistorted image has been affected in exactly the same manner as the background stars. Thus the final image is simply the superposition of all these resultant smeared intensity distributions. In mathematical terms, the original intensity distribution is convolved with a point spread function (PSF) that corresponds to the shape of the hillocks. Hence, it is theoretically possible to reconstruct the undistorted image using Fourier Transform Theory to deconvolve the PSF from the CCD image. Unfortunately, a secondary effect of the Fourier Transform method is to reduce the signal-to-noise ratio of the image. In the case of the P/Halley images it was found that, the S/N ratio was reduced to such an extent that the signal (undistorted image) became completely swamped by the noise. Thus, an alternative approach must be sought in order to deconvolve the comet image successfully.

Image Deconvolution

The image of the comet can be more easily processed if the underlying Cartesian pixel array is replaced by an equivalent polar array which has the ‘summit’ of the mountain at the origin, and a radial pixel spacing that is the same as the original Cartesian spacing. The azimuthal spacing of the polar array should be chosen to ensure that there is no loss of resolution at the edges of the new image. Averaging the DN-values of all of the polar pixels for a complete azimuthal sweep then reduces the image to a one-dimensional brightness profile. Because of the inherent circular symmetry of the image, this average profile is a close approximation to any radial slice that is taken through the mountain. The same procedure may be applied to produce a brightness profile for a background star within the same field of view as

the comet. An approximate fit of the brightness profile of the comet may be obtained from the equation $DN(R) = R^{-n}$ (R is the radial pixel number, where the central pixel in the image is numbered 1, $DN(R)$ is its brightness and n may take any positive real number). However, n varies with R over a narrow range in the real profile, having values in the range 0 to 2. We can therefore generate a range of hypothetical brightness profiles for the cometary image by varying n between these limits. These hypothetical profiles are then convolved with the brightness profile generated for the background star, which acts as the PSF. The percentage change in brightness found on convolving the hypothetical profiles with the PSF may then be calculated.

It is found that this change is $< 1\%$ for pixels where $R > 10$ for all values of n , thus pixels with $R > 10$ may be ignored in the subsequent selection of the value of n that will ultimately be used. For all pixels the change in brightness is negligible for $0.25 < n < 0.40$. With this information it is possible to select a value of n which produces a brightness profile which best matches that of pixels with $r < 10$. The value of n which provides the best fit for the data is 0.37, so a hypothetical brightness profile was generated from the equation $DN(R) = R^{-0.37}$, and this profile is then convolved with the PSF. We may then derive a percentage change in brightness between the original hypothetical profile with $n = 0.37$ and the new profile after convolution. Each pixel of the original comet image can then be divided by the percentage change generated according to their equivalent R -value, in order to deconvolve the image.

Once the deconvolution has been performed, the integrated brightness of the deconvolved and the original images can be compared to assess the success of the operation. In this case, the integrated brightnesses were found to agree to within 1% over the complete image. The deconvolved image is shown in figure 1.

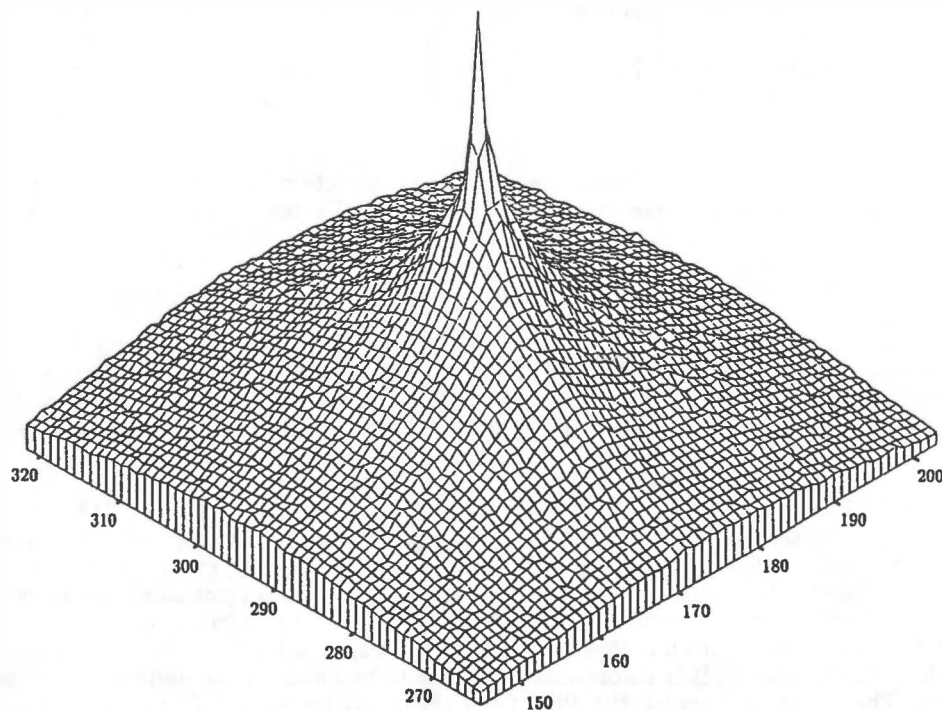


Figure 1. The deconvolved CCD image. The base grid represents the pixel array of the CCD image of comet P/Halley. The pixel numbers are shown. The vertical axis represents the deconvolved pixel DN value. Note the sharp peak at the central position i.e. at the nucleus. The base is at a DN 'height' of 2460 with the peak at 12220.

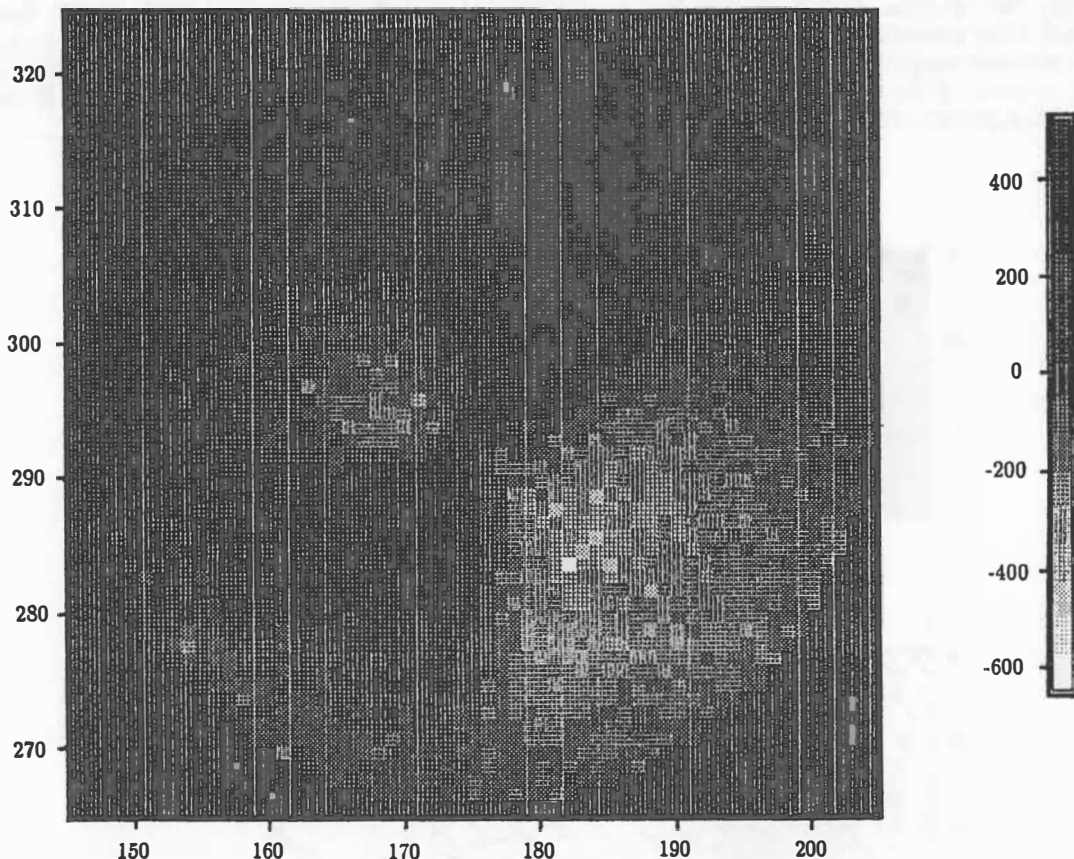


Figure 2. The deconvolved CCD pixel array with the average background removed. This is done by converting the pixel array from cartesian to polar coordinates, then finding the mean DN value over all θ for each value of R , and subtracting this from all pixels at distance R . Note the two raised regions (jets). The C_2 enhancement corresponds to, at maximum 9%.

Enhancing Image Detail

Once the image had been deconvolved, the average background brightness was removed. This was achieved by subtracting the average brightness profile, generated in the conversion from cartesian to polar coordinates, after deconvolution, from each pixel according to its R -value. Plotting the data as a greyscale map revealed two jets in the image (figure 2). This method of detail enhancement has been used previously by A'Hearn (1986).

Calculating Jet Velocity

By investigating the structure of the jets it is possible to make an estimate of the outflow velocity assuming that the effect of solar radiation pressure is negligible and that the outflow velocity is constant. If we adopt a 'lawn-sprinkler' model (Larson and Minton, 1972) to account for the curvature of the jets, the enhanced image may be reconstructed in 'quasi-polar' form such that radial displacement is displayed on the ordinate and azimuthal displacement is displayed on the abscissa (figure 3). Using this format the degree of curvature can be assessed from the angle of slope of the jets, which now form straight ridges across the image. Given the rotation period of P/Halley, a lower limit estimate of the outflow velocity can be made.

Unfortunately the rotation period of P/Halley is still the subject of investigation. Itoh (1985) first discovered a 2.2 day periodicity, but within a year Millis and Schleicher (1986) added a 7.4 day periodicity. Subsequent analysis supports both periods, leaving the issue unresolved. For the purpose of calculating the outflow velocity of the jets, v_G , the 7.4 day period provides a lower limit, $v_G \geq 0.1 \text{ km s}^{-1}$. If the 2.2 day period is proved correct, however, this limit may be raised to $v_G \geq 0.3 \text{ km s}^{-1}$.

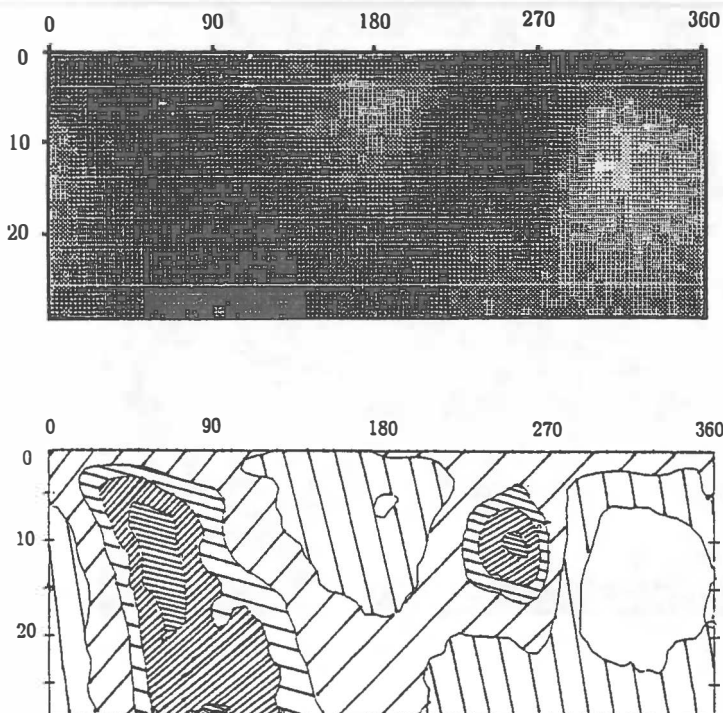


Figure 3. Both figures are essentially figure 2 redrawn with the abscissa representing the azimuthal distance θ , and the ordinate representing the radial pixel distance R . The grey scale used in the upper plot is the same as that used in figure 2. The lower plot has contours at -450, -250, -50, 150, 250 and 350. The degree of curvature of the jets can be assessed from their gradient on this plot.

References

- A'Hearn, M.F., Hoban, S., Birch, P.V., Bowers, C., Martin, R., Klingsmith III, D.A., 1986. *Nature*, **324**, 649–651.
- Larson, S.M., and Minton, R.B., 1972. *Comets: Scientific Data and Missions*, Kuiper, G.P., and Roemer, E., 183–208.
- Itoh, T., 1985. *IAU Circ*, **4155**
- Millis, R.L., and Schleicher, D.G., 1986. *Nature*, **324**, 646–649.

Initial Overview of Disconnection Events in Halley's Comet 1986

J.C. Brandt, C.E. Randall, Y. Yi, and M. Snow
University of Colorado/LASP

Abstract

We present an initial overview of the disconnection events (DEs) in Comet Halley in 1986. Although disconnection events are arguably the most spectacular of all dynamic comet phenomena, the mechanisms by which they occur are not fully understood. It is generally believed that the solar wind plays a major role in determining when disconnection events occur, but the details of the solar wind/cometary interactions responsible for initiating the tail disconnection are still under debate. The three most widely accepted models are (1) high speed streams in the solar wind cause the tail to disconnect due to pressure effects, (2) decreased production of cometary ions in a high speed stream allows magnetic field to slip away from the comet, and (3) the tail disconnects after frontside reconnection of the interplanetary magnetic field (IMF) as the comet crosses a magnetic field sector boundary. See the paper by Brandt (1990) for additional discussion and references.

We find that the front-side magnetic reconnection model is the best explanation for the DEs we have considered.

1 WHAT'S A DE?

The most spectacular of all plasma tail phenomena is the disconnection event or DE, in which the plasma tail is severed from the cometary head. Normally, the plasma tail is attached to the head region by the magnetic field lines embedded in the cometary ionosphere. Several individual DEs have been analyzed in comet Halley in order to understand the physical mechanisms involved when the tail and head are detached. An example of the analysis of an individual DE (16.0 March 1986) is given in the paper by Randall *et al.* (this volume). The number of analyzed DEs is now sufficient to begin considering them in groups.

2 POSSIBLE DE MECHANISMS

2.1 Pressure Effects

Higher than average values of solar wind speed or density (or both) could greatly compress the cometary ionosphere and allow the magnetic field

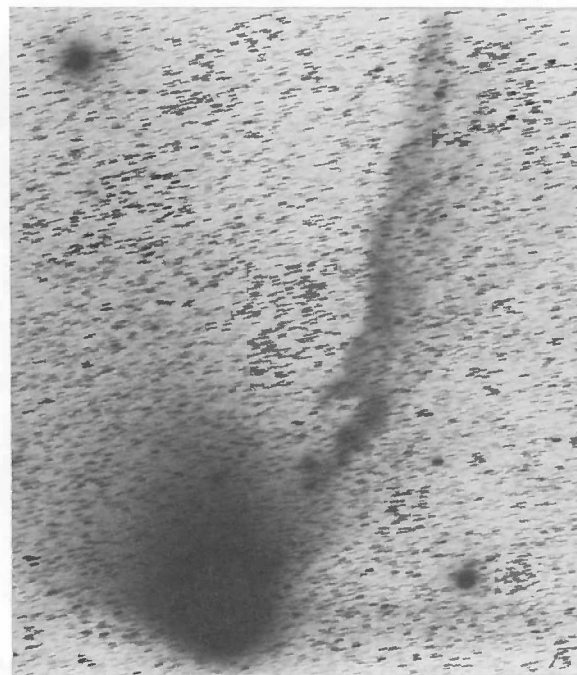


Figure 1: Comet Halley on 12 April 1986. DE began 10.9 April. (F. Miller, University of Michigan/CTIO)

lines (and hence the plasma tail) to slip around the head. In extreme cases, high pressure could simply blow the ionosphere and the tail away from the head region.

2.2 Ionization Effects

Suppression or cessation of ionization could alter the ionosphere and allow the field lines to slip away from the comet.

2.3 Magnetic Reconnection

Pressing magnetic field lines of opposite polarity into the cometary ionosphere (at sector boundaries or other instances of reversal of the Interplanetary Magnetic Field (IMF)) could sever the attachment by magnetic reconnection.

3 TESTING OF MECHANISMS

3.1 Solar Wind Density and Speed

These are determined from *in situ* measurements and are referenced to the comet by standard co-rotation methods. See the summary of solar wind conditions in table 1.



Figure 2: Comet Halley on 18 March 1986. DE began 16.0 March. (G. Pizarro, European Southern Observatory)

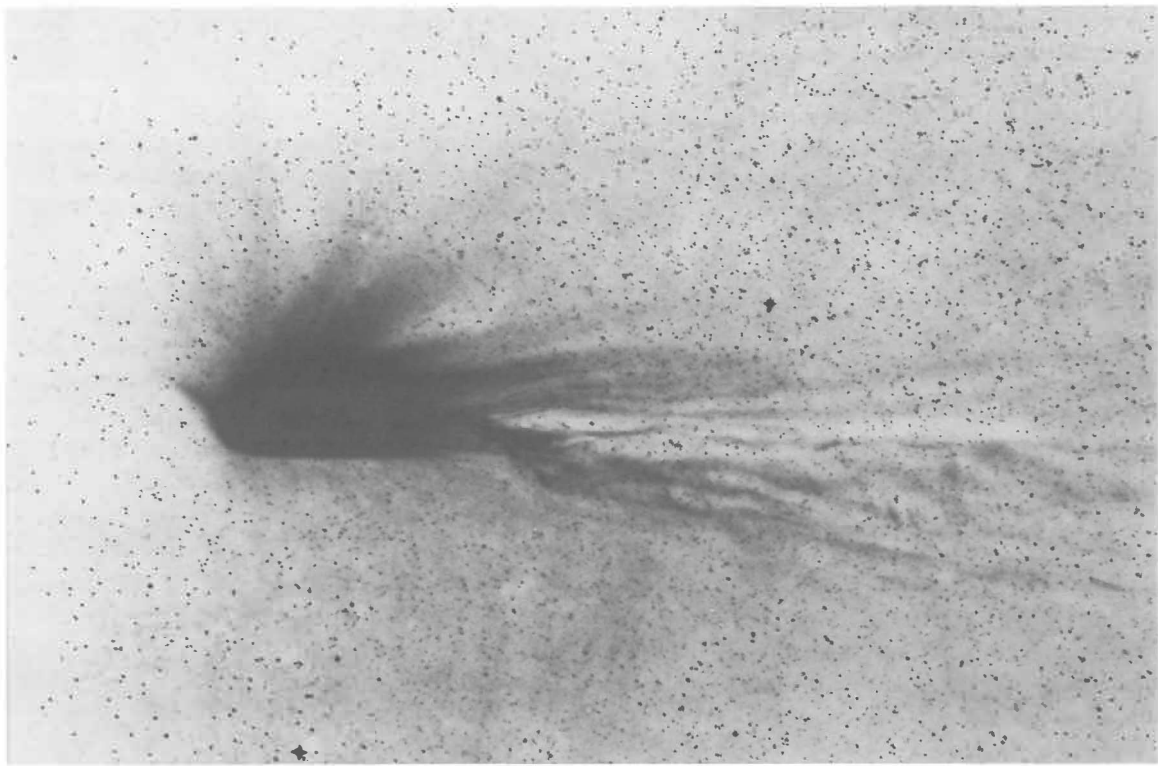


Figure 3: Comet Halley on 22 February 1986. DE began on 21 February. (UK Schmidt Telescope)



Figure 4: Comet Halley on 11 January 1986. DE began 9.7 January. (E. Moore/E. Marr, Joint Observatory for Cometary Research)

3.2 Sector Boundaries

These occur when the earth, comet, or spacecraft crosses the heliospheric current sheet. As a test of the front-side magnetic reconnection mechanism (Niedner and Brandt 1978), we can consider a specific area of the calculated heliospheric current sheet, which is projected into interplanetary space from potential models giving the magnetic field at approximately $2 R_{\odot}$. The projected positions of the heliospheric current sheet can be checked against the direct measurements from spacecraft such as IMP-8, ICE, and PVO. We find that while the heliospheric current sheet for January through April 1986 had a complex shape which changed with the solar rotation; the gross qualitative features remained relatively constant during this period. See figure 5 which shows the preliminary position of the current sheet. In particular, the highlighted area of figure 5 shows a portion of the heliospheric current sheet that is stable and highly inclined to the solar equator; these circumstances are favorable for comparisons with cometary data.

4 PRELIMINARY SECTOR BOUNDARY CROSSINGS OVERVIEW

The values given in Table 1 are derived from IMP-8 measurements at the earth which are correlated to the comet's location. The r^{-2} variation with heliocentric distance is also taken into ac-

Summary of Solar Wind Conditions

DE	Density N_e (cm^{-3})	Speed w (km/sec)	Magnetic Reversal
9 Jan 1986	$\sim 7 - 25$	~ 400	YES
21 Feb 1986	~ 25	~ 700	YES
16 Mar 1986	~ 8	~ 600	YES
10 Apr 1986	~ 10	~ 350	YES

Table 1: These conditions should be compared with the average conditions at earth of $N_e = 8 \text{ cm}^{-3}$ and $w = 400 \text{ km/sec}$.

count in our estimation of the density, N_e .

Figure 5 shows the calculated current sheet for Carrington rotations 1770 through 1773, spanning the time period from mid-December 1985 to mid-April 1986 (Hoeksema 1989). The solid circles denote the positions at which various spacecraft, (IMP-8, ICE, and PVO) measured magnetic field reversals. The generally good correspondence between these measurements and the calculated sector boundary supports the validity of the calculations for these latitudes. The asterisks denote the position of Comet Halley with respect to the current sheet at the beginning of the disconnection events on 10 April, 16 March, 21 February and 9 January (left to right). The salient point is that each of these events occurred immediately after the comet crossed the same part of the magnetic field sector boundary during each solar rota-

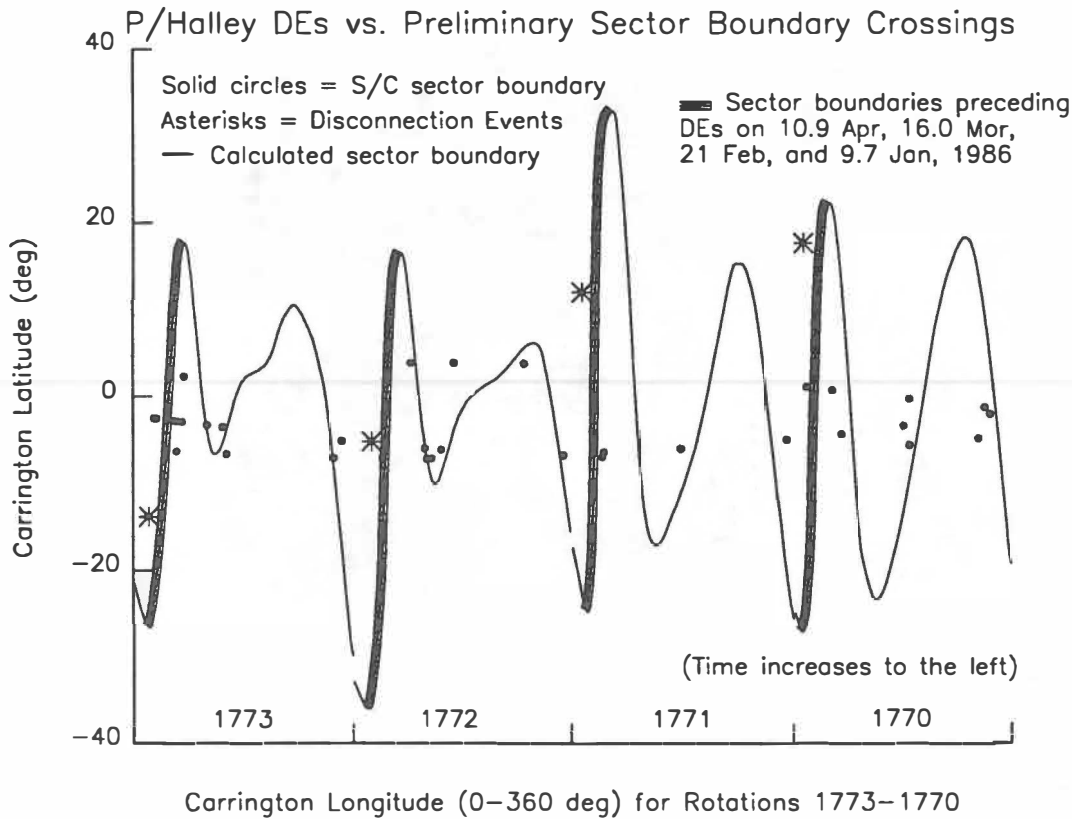


Figure 5: Carrington rotations 1770 through 1773 spanning the time period from mid-December 1985 to mid-April 1986.

tion (highlighted region of the calculated current sheet).

5 Conclusions

We find that the same area of the heliospheric current sheet, or sector boundary, encountered comet Halley on about 9 January, 21 February, 15 March and 10 April. On all four of these crossings, we find the corresponding DEs. At the times of these DEs, the solar wind speeds were average to somewhat elevated and the solar wind densities were normal with the exception of the 21 February DE and possibly the 9 January DE. Therefore, we conclude that the occurrence of DEs caused by front-side magnetic reconnection is the best possibility for the events studied here.

Further work is still necessary in order to refine the calculation of the sector boundary. This will include, for instance, consideration of various source surface radii in the potential field model, and the use of spacecraft measurements to determine fine structure. Work is also in progress to perform similar analyses of other DEs in Comet Halley. We note the recent paper by Delva *et al.* (1991) on this subject.

References

- Brandt, J. C. (1990) The Large-Scale Plasma Structure of Halley's Comet, 1985-1986. In *Comet Halley Investigations, Results, Interpretations Volume 1* (J.W. Mason ed.), pp 33-55, Ellis Horwood New York.
- Delva, M. *et al.* (1991), Comet Halley Remote Plasma Tail Observations and *in situ* Solar Wind Properties; Vega-1/2 IMF/Plasma Observations and Ground-Based Optical Observations from 1 December 1985 to 1 May 1986 *Planet, Space Sci.*, bf 39, 697-708.
- Hoeksema J. T. (1989) Extending the Sun's Magnetic Field Through the Three Dimensional Heliosphere *Adv. Space Res.*, 9, 141-152.
- Niedner, M. B., Jr. and J. C. Brandt, (1978) Interplanetary Gas XXIII. Plasma Tail Disconnection Events in Comets: Evidence for Magnetic Field Line Reconnection at Interplanetary Sector Boundaries? *Astrophys J.*, 223, 655-670.
- Randall, C. E. *et al.*, (1991) The Disconnection Event of 16.0 March 1986 in Comet Halley (this volume).

HIGH-RESOLUTION OBSERVATIONS OF THE SPATIAL AND VELOCITY DISTRIBUTION OF COMETARY HYDROGEN

Michael E. Brown and Hyron Spinrad
Dept. of Astronomy, University of California, Berkeley, CA

ABSTRACT

We have obtained high velocity and spatial resolution long-slit H α spectra of comets Austin (1989c₁) and Levy (1990c). Spectra of both comets clearly show the existence of a low velocity thermalized component of hydrogen gas. The amount of slow hydrogen is estimated for comet Austin. The Levy spectrum shows an unusual high-velocity spatially-confined blob of hydrogen emission of unknown origin.

INTRODUCTION

H α 6562Å emission has been observed in comets since Kohoutek (Huppler *et al.* 1975, Magee-Sauer 1988). Although the excitation mechanism is weak – H α emission is produced by fluorescence following solar Ly β excitation of cometary hydrogen – H α is observable because hydrogen is the most abundantly produced and longest-lived species in cometary comae.

Hydrogen is produced primarily by photodissociation of water through the following reactions (Crovisier 1989):



In reaction (1) the typical hydrogen ejection velocity is about 18 km/sec, while in reaction (2) the typical velocity is about 8 km/sec. Models of the hydrogen coma have also suggested the existence of a slow (~ 2 km/sec) thermalized component caused by hydrogen-water collision in the dense inner coma (Combi and Smyth 1987).

High resolution spectroscopy of H α should be able to disentangle the different velocity components of the hydrogen coma. Previous spectroscopy, using Fabry-Perot methods (Huppler *et al.* 1975, Magee-Sauer 1988) has not had sufficient resolution to separate the components. We present here the first spectra with sufficient resolution to clearly observe the difference between the slow thermal component and the faster ejection products.

OBSERVATIONS

We observed H α in comets Austin (1989c₁) and Levy (1990c) using the Lick Observatory Hamilton Echelle Spectrometer (Vogt 1988). An order sorting filter centered at 6562Å with a 15Å FWHM was placed in the light path to isolate the order containing H α , and the decker, which normally confines the spatial extent of the spectrum to about 3 arc seconds (about seven CCD pixels), was removed to allow use of the full one arc minute spatial height of the slit (about 200 pixels). The resulting long-slit spectrum covers 15Å at about ~ 0.05 Å resolution and has a projected spatial range of about 20000 km for comet Austin.

The raw spectrum is flat-fielded in the usual way, and the slit function and filter function are removed using a lunar spectrum. The spectrum now contain emissions from the sky, cometary dust (a reflected solar spectrum), coma gas, and geocoronal H α . The sky emission is removed by examining the dust continuum far from the nucleus: a lunar spectrum plus a constant sky is fit to the dust and sky spectrum. The proportion of lunar to constant is chosen such that the depths of the Fraunhofer lines agree. The constant

Table 1: Observational Parameters

comet	date (UT)	Δ (AU)	r	$\dot{\Delta}$ (km/sec)	\dot{r}
Austin (1989c ₁)	15 May 1990	0.32	0.96	-24	34
Levy (1990c)	12 Sept 1990	0.69	1.19	42	-17

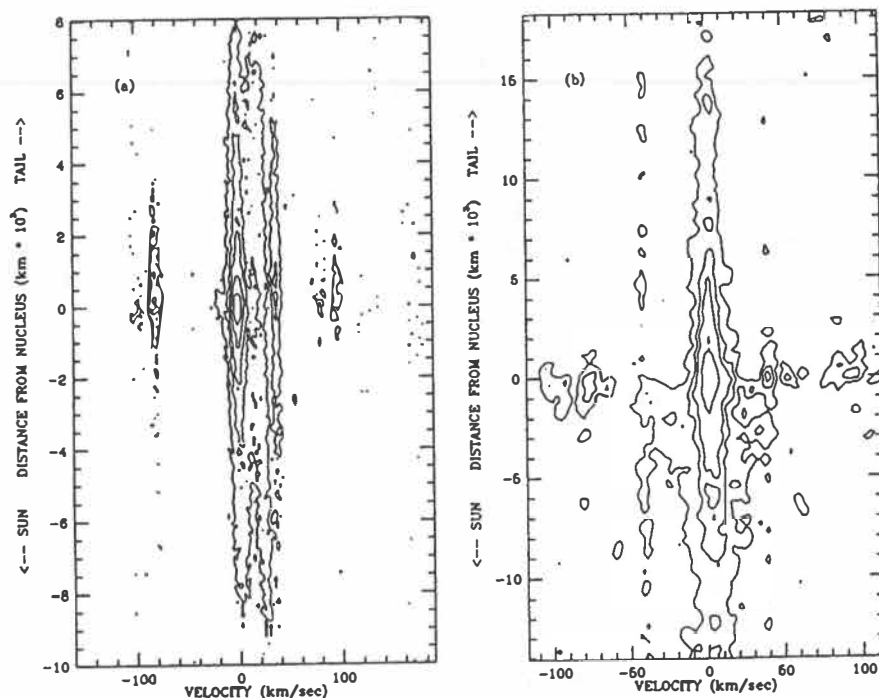


Figure 1: Long slit H α spectra. Distance is projected distance from nucleus; velocity is cometocentric velocity. (a) Austin: note that the line at +23 km/sec is geocoronal H α emission. Other lines are unidentified. (b) Levy: geocoronal H α is at -42 km/sec.

sky is then subtracted from the whole frame. The OH and geocoronal H α emission are easily separated from cometary emission as they are spatially constant along the slit. The earth-comet velocity separates geocoronal and cometary H α .

To analyze the H α emission, the reflected dust continuum must also be removed. This removal is accomplished by taking spatial profiles of the dust where it is uncontaminated by gas emission and then subtracting a lunar spectrum scaled by the dust spatial profile from the cometary spectrum. The resulting spectrum now contains only cometary gas emission (and sky and geocoronal line emission). Table 1 gives observational parameters of the Austin and Levy observations. Figure 1 shows the reduced two-dimensional spectra in contour form.

ANALYSIS OF THE OBSERVATIONS

Austin (1989c₁)

To analyze the velocity distribution of the high quality Austin data, we developed a simple radially symmetric collisionless Monte Carlo model based on the method of Combi

and Delsemme (1980). The model tracks the photodissociation of H₂O into H and OH and of OH into O and H. A long-slit spectrum of the model is constructed based on the real observational parameters.

Figure 2 (a) compares the velocity profile of the inner 1200 km of the Austin data (solid line) with the simulated data (dashed line). Clearly the Austin velocity distribution contains a surplus of low-velocity hydrogen not accounted for by the model. This is the first direct observation of slow thermalized hydrogen in a cometary coma.

Slow hydrogen can be artificially injected into the model. As an estimate for the amount of slow hydrogen expected we calculate the percentage of water dissociated within the collision radius,

$$r_c = \frac{Q_{H_2O}\sigma}{4\pi v}. \quad (3)$$

With a water production rate of $Q_{H_2O} = 10^{29}$ sec⁻¹, a collision cross section of $\sigma = 5 \times 10^{-15}$ cm² and a water outflow velocity of $v = 1$ km/sec, the collision radius is about 4000 km. For an exponential decay lifetime of τ , the fraction f of water dissociated within r_c is

$$f = 1 - \exp(-r_c/v\tau). \quad (4)$$

With $\tau = 8 \times 10^4$ sec, the fraction of water dissociated within the collision radius is about 5%.

Figure 2 (b) compares the Austin data with a model spectrum including 5% hydrogen at a velocity of 2 km/sec. This model begins to better reproduce the observed hydrogen velocity distribution, but still does not contain enough slow hydrogen. The best fit to the velocity distribution is a model with 20% of the hydrogen in the thermalized component, shown in Figure 2(c). The observed and modelled spatial distributions are shown in Figure 2 (d) - (f). The model spatial distributions have slow hydrogen components of zero, 5%, and 20%, respectively. Notice the different models are nearly indistinguishable; in all cases the modelled spectrum is more peaked than the true spectrum. We are currently attempting more sophisticated modelling to understand this behavior.

Levy (1990c)

Although the data for Levy are noisier, one feature stands out in figure 1 (b): a blob of fast gas is clearly visible from 0 to 5000 km sunward of the nucleus at velocities of 20 km/sec to 50 km/sec. This blob is puzzling because of both its high velocity and its spatial confinement. No known water dissociation ejects a large amount of hydrogen at such high velocities, yet the integrated intensity of emission within the blob is a significant fraction of the total H α emission. The hydrogen could have been ejected from a heavier-than-water parent, but its spatial distribution would still be difficult to understand: If the blob is travelling at a moderate, say 45° angle to the line-of-sight, it would take only six minutes to reach a projected distance of 5000 km. But the exposure time for this spectrum was 45 minutes, so the blob would have to have been fortuitously ejected in the six minutes just prior to the end of the exposure. If instead the blob were travelling directly towards the earth it could have been ejected anytime prior to the observation, but the range of angles that would force the blob to stay so sharply confined to the sunward side of the nucleus is so small as to make this scenario seem unreasonable also. We intend to continue monitoring H α in future comets in order to determine the frequency of such blobs and to understand the physical mechanism behind their formation.

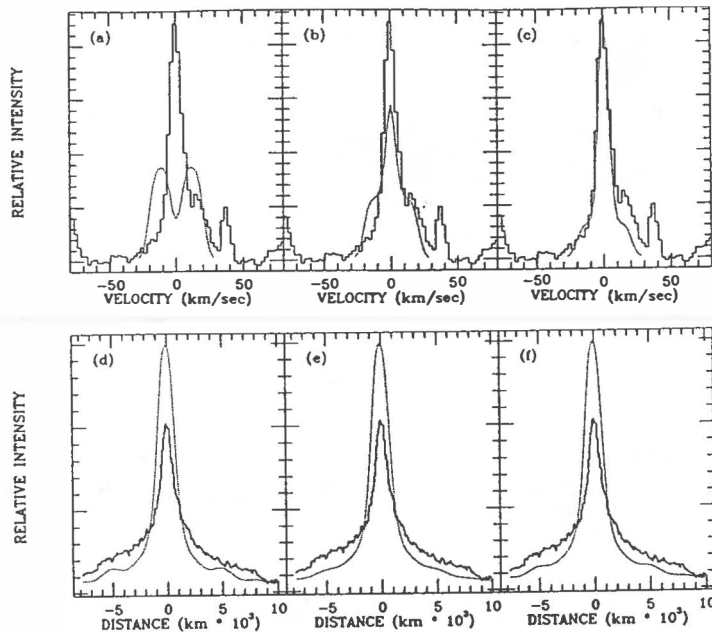


Figure 2: (a) Austin hydrogen velocity distribution (solid line) and model with no slow hydrogen (dotted line). Line at +23 km/sec is geocoronal H α emission. Other lines are unidentified. (b) Model with 5% slow hydrogen. (c) Model with 20% slow hydrogen. (d) Austin projected hydrogen spatial distribution (solid line) and model with no slow hydrogen (dotted line). (e) Model with 5% slow hydrogen. (f) Model with 20% slow hydrogen

ACKNOWLEDGEMENTS

We thank Tony Misch at Lick Observatory for obtaining the spectrum of comet Levy for us and Dr. Michael Combi for valuable discussions. M.E.B. is supported by a NSF Graduate Fellowship, and H.S. is supported by grants from the NSF and NASA.

REFERENCES

- Combi, M.R. and A.H. Delsemme (1980) Neutral cometary atmospheres. I. An average random walk model for photodissociation in comets, *Ap.J.*, **237**, 633-640.
- Combi, M.R. and W.H. Smyth (1988) Monte Carlo particle-trajectory models for neutral cometary gases. II. The spatial morphology of the Lyman-Alpha coma, *Ap.J.*, **327**, 1044-1059.
- Crovisier, J. (1989) On the photodissociation of water in cometary atmospheres, *A.Ap.*, **213**, 459-464.
- Huppler, D., R.J. Reynolds, F.C. Roesler, F. Scherb, and V. Trauger (1975) Observations of comet Kohoutek (1973f) with a ground-based Fabry-Perot spectrometer, *Ap.J.*, **202**, 276-282.
- Magee-Sauer, K. (1988) Ground-based Fabry-Perot observations of neutral and ionic atoms and molecules of comet Halley, Ph.D. thesis, University of Wisconsin-Madison.
- Vogt, S.S. (1987) The Lick Observatory Hamilton Echelle spectrometer, *PASP*, **99**, 1214-1228.

DEBRIS ABOUT ASTEROIDS: WHERE AND HOW MUCH?

Joseph A. Burns and Douglas P. Hamilton
Cornell University, Ithaca NY 14853 USA

We summarize several recent findings on the size and shape of the region within which material can stably orbit an asteroid. If the asteroid (with assumed density 2.38 g/cm^3) circles the Sun at 2.55 AU, co-planar prograde material will remain trapped whenever started on unperturbed circular orbits at less than about $220 R_A$ (asteroid radii); co-planar retrograde particles are stable out twice as far. Our 3-D stability surface, which encloses several hundred numerically calculated orbits that start with various inclinations, is shaped like a sphere with its top and bottom sliced off; its dimensions scale like the Hill radius $= (\mu/3)^{1/3} R$, where μ is the asteroid-to-solar mass ratio and R is the asteroid's orbital radius. If the asteroid moves along an *elliptical* orbit, a fairly reliable indicator of the dimensions of the hazard zone is the size of its Hill sphere at the orbit's pericenter. Grains with radii less than a few mm will be lost through the action of radiation forces which can induce escape or cause collisions with the asteroid on time scales of a few years; interplanetary micrometeoroids produce collisional break-up of these particles in $\sim 10^4$ yrs. The effects of *Jupiter* and of asteroids that pass close to the target asteroid allow particles to diffuse from the system, again shrinking the hazard zone.

None of the considered sources--primordial formation, debris spalled off the asteroid during micrometeoroid impact, captured interplanetary particles, feeder satellites, etc.--seem capable of densely populating distant orbits from the asteroid. No certain detections of debris clouds or of binary asteroids have been made. Thus it seems highly unlikely that a spacecraft fly-by targeted at $100 R_A$ from the asteroid over its orbital pole would encounter any material.

INTRODUCTION

Current NASA policy mandates that all outer solar system missions be devised so as to explore minor planets near any planned flight trajectory. In order to design observations properly, and more fundamentally in order to ensure a spacecraft's safety, mission planners need to know which regions of space surrounding the target asteroid might be dangerous and/or interesting. Thus critical questions are *Where might material orbit stably about minor planets?* and *What are the mechanisms whereby debris might be supplied and/or lost from this locale?* These two questions are very different: the first is a well-posed problem in celestial mechanics for which a simple response, including an estimate of its probable correctness, should be possible; in contrast and by necessity, the answer to the second query is much less clear since one always has the nagging worries that some supply mechanism may have been overlooked or that circumstances in the solar system today (upon which models are based) may not represent conditions at the time when the asteroid and any associated material originated.

The first spacecraft flyby of an asteroid occurred on October 29, 1991, when the Galileo spacecraft swung past the small S-class asteroid 951 Gaspra (nominal radius $R_A=10\text{km}$; orbital semimajor axis $a=2.2\text{AU}$, eccentricity $e=0.17$). The Cassini and CRAF missions are scheduled to visit other members of the diverse asteroid population about ten years from now. The latter mission's primary target, of course, is a comet for which mechanisms to supply its debris cloud are quite different than in the asteroid case; nevertheless, our ideas on the zone of stability remain equally valid for particles orbiting a cometary nucleus as for those circling an asteroid.

STABILITY SURFACE

The dynamics of an infinitesimal particle moving in the gravitational field of two masses which circle their mutual center of mass (the circular restricted three-body or CRTB problem) is one of the most

celebrated problems in mechanics (Szebehely 1967). While the particle's complete dynamics are generally not available analytically, a constant of the motion--the Jacobi constant, which is the total energy measured in the reference frame that rotates with the orbital rate of the two primaries--can be determined. By expressing this constant algebraically, in terms of the coordinates, restrictions can be placed on a particle's movement such that certain regions of space may be inaccessible to the particle once its initial conditions have been specified. These regions are bounded by zero-velocity curves (ZVCs) or Hill curves that the particle may not cross. Thus, whenever a particle near an asteroid has initial conditions such that the ZVCs do not enclose the asteroid, that particle can, but *is not required to*, leak away onto its own heliocentric path.

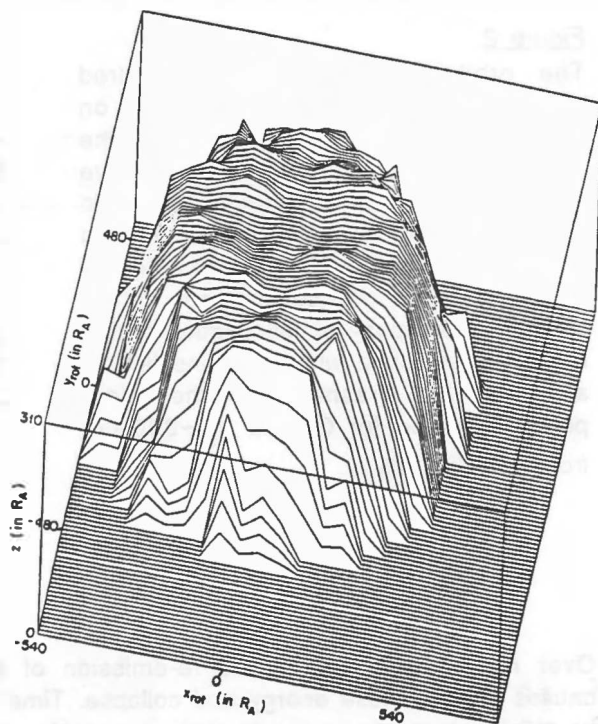
ZVCs are valuable indicators of regions of space actually visited by a particle, however, only for orbits that are prograde (i.e., moving in the direction of the orbital motion of the asteroid about the Sun) and co-planar (i.e., in the asteroid's orbital plane) (Chauvineau and Mignard 1990a, Hamilton and Burns 1991 [henceforth HB1]). The largest closed ZVC surrounding an asteroid is shaped like a football centered on the asteroid with the long axis pointing along the Sun-asteroid line (Szebehely, 1967). In the Sun's direction, this critical ZVC extends from the asteroid to the Hill radius, $r_H = (\mu/3)^{1/3} R$, while in the orthogonal directions it reaches about 2/3 as far. For an asteroid of density 2.38 g/cm³ located at 2.55 AU, $r_H \sim 450 R_A$. Particles that start within the critical ZVC with no initial velocity in the rotating frame will remain bound to the asteroid. Of course, if the particle begins with some velocity, the starting point at which escape can occur will generally be closer to the asteroid. For example, prograde particles that are started beyond the asteroid along the Sun-asteroid axis at distances greater than about $220 R_A$ on orbits which without the Sun's presence would be circular are seen numerically to be lost in fewer than 20 years (HB1); for the specified initial speed, this distance corresponds to a ZVC that is just barely open. Retrograde, co-planar particles, for which the ZVCs are poor indicators of escape, are found numerically to be stably bound even if they begin on circular orbits about twice this large (Zhang and Innanen 1988, HB1).

HB1 explore the nature of 3-D orbits near the stability boundary over relatively short times (about 20 years) for a range of initial conditions (particles start with various orbital sizes close to the escape distance and are given a circular speed that can be tilted at various inclinations i out of the asteroid's heliocentric orbital plane). Figure 1 depicts the upper half of the surface formed by the union of several hundred weakly bound orbits; that is, in all HB1's integrations no particles that remained in the asteroid's vicinity were found beyond the plotted surface along any particular latitude-longitude wedge. The stability surface is seen to be shaped like a sphere that has its top and bottom sliced off. This shape occurs since the dimension for orbits at low latitudes off the asteroid's orbital plane is set by primarily retrograde particles ($150^\circ < i < 180^\circ$), those that are far and away the most stable ones due to the Coriolis acceleration, which is inward-pointing for such paths. HB1 find that the Coriolis term is much less effective in retaining objects started with $90^\circ < i < 150^\circ$ and in fact drives away orbits at lower i .

Several complications have been added to this simple unperturbed CRTB problem in order to better represent reality. Chauvineau and Mignard (1990b) and Chauvineau et al. (1991) study the influence of perturbations due to Jupiter and to stray asteroids that pass close to the target asteroid. They find a gradual diffusion of the Jacobi constant over time and, for those particles whose "energy" is increased by such perturbations, this is equivalent to a slow opening of the ZVCs. Hence some material that started long ago at distances close to, but within, the stability boundary will be lost; other debris will be more firmly held in the asteroid's gravitational grasp.

Figure 1:

Plot of the upper half of the stability surface. This corresponds to the maximum distance achieved by particles orbiting an asteroid of density 2.38 g/cm^3 moving on a circular orbit of radius 2.55 AU. The flattened top surface is at an approximate altitude of $285 R_A$ off the asteroid's orbital plane, and the surface drops precipitously to the roughly circular base region ($r \sim 480 R_A$). Clearly stable orbits are more closely confined in the polar regions, at least for these initial conditions. From HB1.



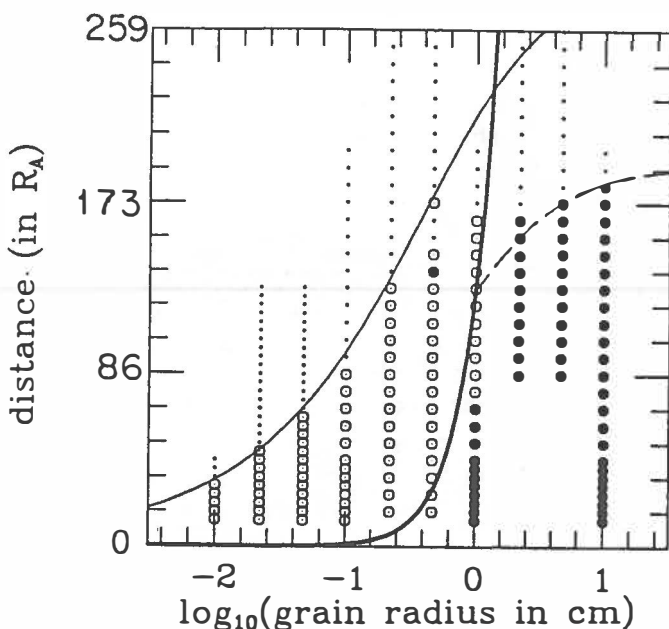
As soon as the asteroid's orbit has some eccentricity ($e \neq 0$), Jacobi constants and their associated ZVCs are no longer available to constrain motion. Nevertheless Hamilton and Burns (1992; henceforth HB2) have shown by analytic arguments and supporting numerical integrations that the opening of ZVCs evaluated at the asteroid's pericenter provide a good criterion for escape of co-planar prograde material, provided orbits are followed for only a few circuits of the asteroid around the Sun. For orbits that start at significant inclinations ($60^\circ < i < 120^\circ$), the size of the hazard zone can be characterized remarkably well by decreasing distance results for an asteroid on a circular orbit by the factor $1-e$, this amounts to scaling results as the Hill sphere calculated at the asteroid's pericenter. This same scaling appears to fail for purely retrograde orbits followed for 20 years; this at least partly reflects the fact that the integration times for retrograde particles were too short (HB2).

Solar radiation forces (Burns et al. 1979) are surprisingly effective in removing smallish particles from the circum-asteroidal environs. Accordingly, HB2 add radiation pressure to their numerical integrations; Fig. 2 shows the fate of several hundred initially circular prograde orbits around Gaspra after an elapsed time of 20 years. Moderate radiation pressure wreaks havoc on bound orbits, forcing particles to either strike the asteroid or flee the system. In fact, we find that bound orbits disappear altogether for particles less than 1 centimeter across! It's clear from Fig. 2 that bound, crash, and escape orbits are separated into three distinct regions; HB2 explain why different fates occur and derive theoretical curves that separate the regions. A similar plot results for retrograde orbits although, as expected, the Coriolis acceleration causes some enhanced stability when radiation pressure is weak. Orbits with substantial inclinations to the asteroid's orbital plane are somewhat more resistant to the mechanism causing particles to impact the asteroid and, accordingly, bound orbits are a bit more resilient. Nevertheless, all particles less than a few millimeters across either crash or escape; none remain bound. Although our results apply to specific initial conditions, we suggest that any millimeter and smaller grains existing in Gaspra's environment will be transitory. [In proof: Galileo's dust detector recorded no hits near Gaspra (Grün et al. 1991)] For scaling these results to other asteroids, we note that, if the dimensions of the minor planet are doubled while those of the orbiting particle are halved, identical equations of motion result.

Prograde Orbits

Figure 2:

The orbital fate of several hundred particles of different sizes started on prograde circular orbits around the asteroid 951 Gaspra, itself taken to have zero heliocentric eccentricity. A solid circle signifies an orbit that remained bound to the asteroid for at least twenty years, a small dot corresponds to an orbit that escapes to heliocentric space, and an open circle with a dot inside it is an orbit that crashes into the minor planet. Adapted for Gaspra ($r_H \sim 390 R_A$) from HB2 Fig. 15.



Over much longer times, the re-emission of absorbed solar radiation (Poynting-Robertson effect) causes orbits to lose energy and collapse. Time scales for the loss of heliocentric particles to the Sun or of planetocentric grains to their parent planet by this process are comparable (Burns et al. 1979). Thus particle lifetimes in the asteroid belt for totally absorbing grains are $10^8(r/\text{cm})$ yrs; and grains smaller than 50 cm are eliminated over the age of the solar system. As described below, collisions actually determine lifetimes for grains larger than about a mm.

The crucial point to make is that each of the added complications to the simple CRTB problem tends to remove material from asteroid orbit. In this sense previous results are conservative.

SUPPLY AND LOSS

The above discussion says nothing about whether particles are likely to originate in those orbits that have been tested for stability nor about how long small circum-asteroidal debris could survive before its destruction by other means. Several supply mechanisms for circum-asteroidal satellites or debris come to mind: (i.) primordial processes; (ii.) recent collisional formation in a nearly catastrophic event; (iii.) captured interplanetary debris; (iv.) impact ejecta from the asteroid itself; and (v.) ejecta from a feeder satellite.

By analogy with the processes that are believed to form regular planetary satellites, asteroidal satellites or primordial debris (categories i and ii) should develop only near the asteroid, if at all. These bodies will not evolve outward rapidly, unless they are large satellites, in which case they become tidally locked with the primary's spin at synchronous orbit. However, it must be admitted that no one is certain how the small distant Jovian satellites originated: nevertheless those theories that are available do not admit remote satellites of an asteroid. Hence we do not believe that particles of categories i or ii will be found at distances more than a few tens of radii, if at all. Virtually no interplanetary particles that might collide in the outer reaches of the asteroid's Hill sphere (category iii) will be captured; such collisions are ineffective suppliers because they are infrequent and, more importantly, because they provide debris almost exclusively with velocities well above local escape speed.

Even though the above processes (i to iii) cannot generate material much near an asteroid, some debris should always be present at relatively great distances from any celestial object. In particular, the ambient micrometeoroid density will be enhanced by the gravitational attraction of the body; this effect is negligible for our case because typical relative velocities are large compared to escape speeds. A more significant source of debris may be the ejecta leaving the asteroid following micrometeoroid impacts (category iv). There are three types of ejecta: material that leaves at speeds less than escape speed (since this recollides quickly, it can be ignored); second, a small fraction of particles that are launched at near the escape speed and may have their orbits perturbed enough (e.g., by the Sun) to extend their lifetimes and thereby to increase their circum-asteroidal number density (this is potentially the most threatening class of ejecta); and finally the most common particles, from energetic impacts like those expected in the asteroid belt (see Fig. 17 in Burns et al. 1984); these leave with speeds greater than Gaspra's escape speed of order 10 m/sec.

Since hypervelocity impacts at the typical speed in the asteroid belt generate ejecta with a total mass 10^3 to 10^4 times that of the impactor, and since--ignoring the tiny asteroid's gravity--the departing ejecta's density drops off like the inverse distance squared, the density of departing ejecta will match that of the ambient micrometeoroids at about $30\text{-}100 R_A$. Furthermore the path length through the debris cloud at a distance d from the asteroid is about d . Thus the hazard from the ejecta at any distance is at most a few times the hazard from the ambient micrometeoroids in the same vicinity. And, since the debris zone itself is so much smaller than the path across the full belt, the hazard from this cause can be ignored.

The most serious hazard could be posed by a different form of impact ejecta, collisional debris lost from another object--a so-called feeder satellite--which itself orbits the target asteroid at some distance. A larger fraction of debris from a feeder is trapped than from the primary because ejecta that barely escapes the feeder remains in orbit about the primary. Observations of the feeder would constitute a way to evaluate the danger of this source, but such are not feasible as no confirmed asteroid satellites have been discovered.

Particles in interplanetary space are destroyed by catastrophic fragmentation and by gradual erosion owing to micrometeoroid pitting and to sputtering by energetic particles. Although hunks of collisional detritus will be released in catastrophic impacts, the momentum transferred in the typical energetic event will generally be sufficient to permanently dislodge any circum-asteroidal particles since the latter are expected to be so weakly gravitationally tied to their primary. Davis et al. (1989; their Fig. 3) estimate that few, if any, objects smaller than 25 km can survive over the age of the solar system; they will be totally shattered and dispersed by the mutual hypervelocity collisions among members of the main asteroid belt. Surfaces in space are continually pelted by interplanetary micrometeoroids and by high-energy electrons and protons. Both of these processes cause a slow scouring of surfaces, which for our problem means that small grains have finite lifetimes; catastrophic fragmentation is even more effective. Grün et al. (1985; their Fig. 6) conclude that collisional lifetimes at 1 AU are shortest ($\sim 10^4$ yrs) for grains between 0.02 and 2 cm in radius; yet smaller particles have even shorter lifetimes due to Poynting-Robertson drag. While small grains are being destroyed, their orbits are inexorably collapsing due to the energy being drained by the Poynting-Robertson effect. Due to these ongoing destructive mechanisms, it is not enough to merely have once put material in distant orbit: if such objects are to be present today, they must either have been very large initially or there must be a continuing supply.

OBSERVATIONAL TESTS

Even though all observational evidence (direct searches, occultations, radar reflections, IRAS brightness levels across its several detectors, asteroid magnitudes in variable aperture photometers, etc.) to date can most simply be interpreted as indicating no debris, most planetary scientists feel that some fraction of the minor planets probably have companions; the remarkable radar discovery of the

"contact-binary" nature of 1989 PB (Ostro *et al.* 1990), a tiny Apollo asteroid, supports this viewpoint as do doublet craters on the Earth (Melosh and Stansberry 1991). Motivated by earlier claimed discoveries of binary asteroids (summarized by Weidenschilling *et al.* 1989) as much as by concerns for the Galileo spacecraft's safety, Gradie *et al.* (1985) and Terrile and Smith (1985) used coronagraphs to scan the neighborhoods of a few asteroids; these searches found neither debris clouds nor asteroidal satellites. CCD searches have been undertaken by Gradie *et al.* (1987) and Stern and Barker (1992), also with negative results.

In the case of comets, radar returns indicate that at least Halley (Campbell *et al.* 1989) and IRAS-Araki-Alcock (Harmon *et al.* 1989) are enshrouded by extensive clouds of cm-or-bigger objects. Infrared data obtained by the IRAS spacecraft have provided convincing evidence for debris trails along the orbital paths of a half-dozen comets (Sykes 1986, 1990); the material comprising these trails is thought to leave the comet at a relatively slow speed and hence to adopt orbits that are confined within a torus surrounding the comet's path. Similar physics should lead to analogous debris tori about the orbits of minor planets, albeit with much lower spatial densities because asteroids will be weak sources. The recently noted correlation between meteor streams and the orbits of some Apollo asteroids (Olsson-Steel 1988) endorses this viewpoint. Furthermore, some "asteroids"--notably 3200 Phaeton and perhaps Oljato--are likely defunct comets (Weissman *et al.* 1989). Thus one might wonder whether such trails might be hazardous to space missions that pass through the asteroid belt on their way to the outer solar system. The simple answer is that they pose very little risk as a straightforward consideration of optical depths indicates. The optical depth of the zodiacal cloud as a whole is $\sim 10^{-6}$, and the zodiacal bands are less than one-tenth that; the trails are even fainter, so that their optical depth is no more than $\sim 10^{-7}$ - 10^{-8} . Collisions are accordingly unlikely.

CONCLUSION

Beyond a fear of the unknown, there should be little to worry about as the Galileo spacecraft flies past 951 Gaspra at a planned distance of about 200 R_A in the asteroid's orbital plane. Had any similar consideration been made prior to the Pioneer and Voyager fly-throughs of the satellite systems of the giant planets, those regions would have almost surely appeared much more hostile than the environs of a small asteroid like Gaspra.

ACKNOWLEDGMENTS

This study originated and has been sustained through the interest of members of the Galileo Project, especially Clark Chapman, Torrence Johnson, Joseph Veverka and the late Clayne Yeates. The ideas on supply and loss mechanisms were developed at a 1984 JPL workshop chaired by JAB and attended by D. R. Davis, A. R. Dobrovolskis, A. W. Harris, K. R. Housen, K. Innanen, and P. Weissman among others. We thank D. R. Davis, A. W. Harris and S. J. Weidenschilling for commenting on an earlier version of this paper.

REFERENCES

- Burns, J. A., Lamy P. L., and Soter, S. L. (1979) Radiation forces on small particles in the solar system. *Icarus*, **40**, 1-48.
- Burns, J. A., Morfill G. E., and Showalter M. R. (1984) The ethereal rings of Jupiter and Saturn. In *Planetary Rings* (R. Greenberg and A. Brahic, eds.), pp. 200-272. Univ. Ariz. Press, Tucson.
- Campbell, D. B., Harmon J. K., and Shapiro I. I. (1989) Radar observations of comet Halley. *Astrophys. Jnl.*, **338**, 1094-1105.

- Chauvineau, B. and Mignard F. (1990a) Dynamics of binary asteroids I-Hill's case. *Icarus*, 83, 360-381.
- Chauvineau, B. and Mignard F. (1990b) Dynamics of binary asteroids II-Jovian perturbations. *Icarus*, 87, 377-390.
- Chauvineau, B., Farinella P., and Mignard F. (1991) The lifetime of binary asteroids vs. gravitational encounters and collisions. *Icarus*, 94, 299-310.
- Davis, D. R., Weidenschilling S. J., Farinella P., Paolicchi P., and Binzel R. P. (1989) Asteroid collisional history: Effects on sizes and spins. In *Asteroids II* (R. P. Binzel, T. Gehrels and M. S. Matthews, eds.), pp. 805-826. Univ. Ariz. Press, Tucson.
- Gehrels, T., Drummond J. D., and Levenson N. A. (1987) The absence of satellites of asteroids. *Icarus*, 70, 257-263.
- Gradie, J., Hammel H., and Pilcher C. (1985) A search for material around asteroid 29 Amphitrite. *Bull. Am. Astro. Soc.*, 17, 729.
- Grün, E. and 12 collaborators (1991) Interplanetary dust observed by Galileo and Ulysses. *Bull. Amer. Astron. Soc.*, 23, 1149.
- Grün, E., Zook H. A., Fechtig H., and Giese R. H. (1985) Collisional balance of the meteoritic complex. *Icarus*, 62, 244-272.
- Hamilton, D. P. and Burns J. A. (1991) Orbital stability zones about asteroids. *Icarus*, 92, 118-131.
- Hamilton, D. P. and Burns J. A. (1992) Stability zones about asteroids. II. The effects of eccentric orbits and of radiation. *Icarus*, 96.
- Harmon, J. K., Campbell D. B., Hine A. A., Shapiro I. I., and Marsden B. G. (1989) Radar observations of comet IRAS-Araki-Alcock 1983d. *Astrophys. Jnl.*, 338, 1071-1093.
- Melosh H. J. and Stansberry J. A. (1991) Doublet craters and the tidal disruption of binary asteroids. *Icarus*, 94, 171-179.
- Olsson-Steel, D. (1988) Identification of meteoroid streams from Apollo asteroids in the Adelaide radar orbit surveys. *Icarus*, 75, 64-96.
- Ostro, S. J., Chandler J. F., Hine A. A., Rosema K. D., Shapiro I. I., and Yeomans D. K. (1990) Radar images of asteroid 1989 PB. *Science*, 248, 1523-1528.
- Stern, A. S. and Barker E. S. (1992) A CCD search for distant satellites of asteroids 3 Juno and 146 Lucina, this meeting.
- Sykes, M. V., Lebofsky L. A., Hunten D. M., and Low F. J. (1986) The discovery of dust trails in the orbits of periodic comets *Science*, 232, 1115-1117.
- Sykes M. V., Lien D. J., and Walker R. G. (1990) The Temple 2 dust trail. *Icarus*, 86, 236-247.
- Szebehely, V. (1967) *Theory of Orbits: The Restricted Problem of Three Bodies*. Academic Press, New York.

Terrile, R. J. and Smith B. A. (1985) The coronagraphic search for material around Amphitrite. *Bull. Am. Astro. Soc.*, 17, 918.

Weidenschilling, S. J., Paollich P., and Zappala V. (1989) Do asteroids have satellites? In *Asteroids II* (R. P. Binzel, T. Gehrels and M. S. Matthews, eds.), pp. 643-658. Univ. Ariz. Press, Tucson.

Weissman, P. R., A'Hearn M. F., McFadden L. A. and Rickman H. (1989) Evolution of comets into asteroids. In *Asteroids II* (R. P. Binzel, T. Gehrels and M. S. Matthews, eds.), pp. 880-920. Univ. Ariz. Press, Tucson.

Zhang, S. P. and Innanen K. A. (1988) The stable region of satellites of large asteroids. *Icarus*, 75, 105-112.

GROSS-FRAGMENTATION OF METEOROIDS AND BULK DENSITY OF GEMINIDS FROM PHOTOGRAPHIC FIREBALL RECORDS; Z. Ceplecha, Astronomical Institute, Czechoslovak Academy of Sciences, 251 65 Ondrejov, Czechoslovakia; R. E. McCrosky, Smithsonian Astrophysical Observatory, 02138 Cambridge, USA.

The explicit solution of the drag and ablation equations of a single non-fragmenting meteoroid moving in any actual atmosphere was published several years ago (Pecina, Ceplecha 1983 and 1984). The solution yields theoretical relation of l , the distance flown by the meteoroid in its trajectory, as function of time, t , assuming that the height, h , is a known function of l . The photographic records of meteors and fireballs are coded by time marks, using a rotating shutter or a similar device to break the moving image. Time is thus the independent variable and for each time mark on a meteoroid trajectory, the observed distance along the trajectory, l_{obs} , as well as the observed height, h_{obs} , are values available from the geometry of double- or multiple-station photographs of the same meteoroid. Applying this solution to all available Prairie Network (PN) fireball-records (Ceplecha, McCrosky 1990), we recognized that majority of them gave good solutions with standard deviations somewhat bigger than the intrinsic geometrical precision of the data. We also noticed that, on an average, previous methods of evaluation of the meteoroid velocities (interpolation polynomials, numerical differentiation of the observed l_{obs}) used up to only several ten percent of the intrinsic precision of the PN observational data. When residuals of these solutions, i.e. $l_{\text{obs}} - l_{\text{com}}$, were represented as function of time, they proved to be random with time for about 75% of solutions. The remaining 25% of residuals showed systematic changes with time exceeding one standard deviation. We tried to explain these systematic time course of residuals by using different meteoroids first computed theoretically and then analysed by the same model as the natural PN fireballs were. The conclusion of these model computations: Systematic time changes of residuals in the non-fragmenting model exceeding one standard deviation are caused by sudden gross fragmentation at one or more trajectory points.

Thus we generalized the explicit solution of the drag and ablation equations of a single non-fragmentating meteoroid by allowing for one or more points, where sudden gross fragmentation can occur (Ceplecha 1992). Using this generalized solution, the distances along the meteoroid trajectory can be computed for any choice of input parameters and compared with the observed distances flown by the meteoroid. For the most precise and long fireball trajectories, the least-squares solution can thus yield the initial velocities, the ablation coefficients, the dynamical masses, the positions of gross-fragmentation points and the terminal mass. At a gross-fragmentation point, the ratio of the main mass to all the remaining fragments can be computed. The photometrically-determined meteoroid mass can be compared with the dynamic mass determined from our gross-fragmentation model and thus the meteoroid bulk density can be evaluated.

We applied the gross-fragmentation model to several PN

fireballs showing time changes of residuals and we recognized that, in all these cases, the new computed bulk densities of meteoroids resulted higher in comparison with the meteoroid densities determined with the no-gross-fragmentation model. Namely gross fragmentation early on the trajectory of a high velocity meteor makes quite a change in the computed meteoroid densities. As a part of the work we applied the gross-fragmentation model to Geminid meteoroids. From all the PN Geminids (McCrosky, Shao, 1990), only two (G15 and G54) have enough long and deep trajectories, enough observed change of velocity and enough precise heights and lengths measured for individual time-marks, that they allow the complete application of our gross-fragmentation model. If the previous non-gross-fragmentation model was used for G15 and G54, the time sequence of residuals of the solutions exhibited a prevailing systematic part and the bulk densities came out close to 1.0 g/cm^3 (Tab.1). If the new gross-fragmentation model was applied to the same observational data, the systematic part of the time sequence of residuals was completely gone and the bulk densities resulted in 3 to 4 g/cm^3 . Thus the value of the bulk density of Geminids, 1 g/cm^3 , advocated for a long time and depending on decelerations determined as rough values by indirect methods, may have been caused by neglect of the gross-fragmentation effects on the meteoroid motion.

We applied the same gross-fragmentation model to a small-camera record of Geminid 0 32611 from the Ondřejov Observatory (Spurný, 1991) and to the best record on a Super Schmidt Geminid (No. 9725: Jacchia et al., 1965). Both these records have better precision than $\pm 10 \text{ m}$ in the distances along the trajectory. The small camera Geminid was the only one, which exhibited a mild gross-fragmentation. Again the bulk densities resulted between 3 to 4 g/cm^3 . To check the credibility of this concept, we used the same model for the Lost City fireball (McCrosky et al. 1971) and compared the results with reality known from the recovered meteorites. But in this case we should keep some precaution, because the velocities are substantially lower than for Geminids and the effect of gross fragmentation is not so severe as for the high velocity Geminids.

The complete statistical analysis including the uncertainty of the fragmentation point position was possible only for the PN Geminid G54 (Tab. 2). The standard deviation of the bulk density inside the gross-fragmentation model for G54 is ± 0.4 (solution with 5 independent parameters). After adding the position of the fragmentation point as a sixth free parameter, the standard deviation is ± 1.2 , i.e. three times bigger. In all other cases the positions of the fragmentation points cannot be kept as free parameter and they were chosen so that the sum of residuals was minimum from all solutions of different choices of fragmentation points (i.e. solutions with 5 parameters). These minima in respect to the position of the fragmentation point were quite shallow in all cases except G54 and did not allow to add the position of the fragmentation point as the sixth independent parameter. This is caused by a limited geometric precision of the data, especially when the fragmentation point lies close to the

beginning of the luminous trajectory. In case of the small-camera Geminid O 32611, the precision is high, but the gross-fragmentation effect did not strip so much mass from the main body as in the other cases.

The reason why G54 gave the most reliable results is caused by combination of several circumstances: precision of the data (± 14 m in distances); big difference between the initial and terminal velocity; very low terminal height; and the most important effect: the gross-fragmentation point lies in the second half of the trajectory, where much lower precision of the distances along the trajectory still can give reliable data on the bulk density of the meteoroid (because of enough change in velocity).

After our partial experience with applying this model to the PN fireballs, we feel that gross fragmentation early on the luminous trajectory is a common phenomenon and may be responsible for the low bulk densities of meteoroids, when only simple models are used to compute the dynamic mass of the meteoroid. In the close future we intend to apply the gross-fragmentation model to all PN fireballs, which exhibit the time change of residua inside the no-gross-fragmentation solutions.

In case of the Lost City meteorite, the bulk density, the rough position of the fragmentation point, the shape coefficient and the terminal mass are known and since their values computed from our gross-fragmentation model came out quite close to this reality, it is highly probable that the bulk densities of Geminids in Table 1 are about 3 or 4 times greater than densities of the Geminid meteoroids postulated so far. This may also hold for at least a part of all the Geminids with gross fragmentation early on their trajectories.

References.

- Ceplecha Z. (1992) Gross-Fragmentation Impact on a Meteoroid Motion and Ablation. To be published in Publ. Astron. Inst. Czechosl. Ac. Sc., Ondřejov.
- Ceplecha Z., McCrosky, R.E. (1990) Single-Body No-Fragmentation Solutions for PN Fireballs. Smithsonian Astrophysical Observatory, USA, and Ondřejov Observatory, Czechoslovakia (available on floppy discs).
- Jacchia L.G., Verniani F., Briggs R.E. (1965) Smithsonian Contr. Astrophys., 10, 2. (Data on individual time-marks taken from the original archive at the SAO)
- McCrosky R.E., Shao C.- Y. (1990) Prairie Network Geminids. Smithsonian Astrophysical Observatory; available on floppy discs.
- McCrosky R.E., Posen A., Schwartz G., Shao C.- Y. (1971) J. Geophys. Res. 76, 4090. (Data on individual time-marks taken from the original archive at the SAO)
- Pecina P., Ceplecha Z. (1983) Bull. Astron. Inst. Czechosl. 34, 102
- Pecina P., Ceplecha Z. (1984) Bull. Astron. Inst. Czechosl. 35, 120
- Spurný P. (1991) Properties of Geminid Meteor Stream Derived from Photographic Records. Doctor Dissertation, Ondřejov Observatory.

Table 1
Bulk density δ , ablation coefficient σ , TA shape factor, h_F height of the fragmentation

meteor No.	TA	no gross fragmentation						gross fragmentation			
		1.0	1.1	1.2		1.0	1.1	1.2			
		δ g/cm ³	δ g/cm ³	δ g/cm ³	σ s ⁻² /km ²	δ g/cm ³	δ g/cm ³	δ g/cm ³	σ s ⁻² /km ²	h_F km	
SAO Geminid FN G15		0.5 $\pm .1$	0.6 $\pm .1$	0.7 $\pm .1$	0.0150 $\pm .0002$	3.1 ± 1.1	3.6 ± 1.3	4.1 ± 1.5	0.0127 $\pm .0002$	68.2	
SAO Geminid FN G54		0.9 $\pm .3$	1.1 $\pm .4$	1.2 $\pm .4$	0.0080 $\pm .0003$	3.0 $\pm .3$	3.4 $\pm .4$	3.9 $\pm .4$	0.0023 $\pm .0003$	56.4	
Small camera Ondřejov O 32611		2.4 $\pm .1$	2.7 $\pm .1$	3.1 $\pm .1$	0.0073 $\pm .0002$	2.5 $\pm .3$	2.9 $\pm .4$	3.3 $\pm .4$	0.001 $\pm .001$	62.2	
Super-Schmidt SAO Geminid 9725		0.9 $\pm .1$	1.1 $\pm .1$	1.2 $\pm .1$	0.0241 $\pm .0001$	2.7 ± 1.3	3.2 ± 1.5	3.6 ± 1.7	0.0237 $\pm .0001$	80.6	
SAO Lost City Fireball		1.9 $\pm .2$	2.2 $\pm .2$	2.5 $\pm .2$	0.0185 $\pm .0006$	2.8 $\pm .7$	3.2 $\pm .8$	3.7 $\pm .9$	0.038 $\pm .011$	26.1	
SAO Lost City Meteorite		-	-	-	-	-	-	3.73	-	≈ 27	

Standard deviations inside the models; errors in photometric mass not accounted for

Table 2
G54 : search for gross-fragmentation point (random part of residuals = 1.00)

	no fragmentation	fragmentation at				
		t=1.15 s	t=1.10 s	t=1.05 s	t=1.00 s	t=0.95 s
systematic part of residuals	1.85	no solution	0.35	0.00	0.26	0.54
bulk density δ g/cm ³	1.2 $\pm .4$		3.0 $\pm .3$	3.9 $\pm .4$	5.7 $\pm .9$	10. $\pm 3.$

resulting fragmentation point and density: t = (1.05 ± 0.06) s, $\delta = (3.9 \pm 1.2)$ g/cm³

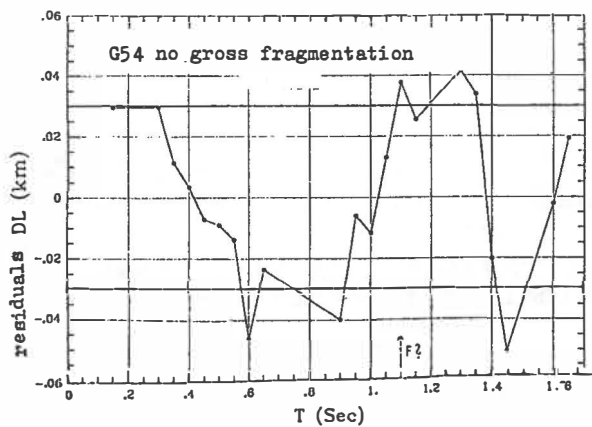


Fig. 1.

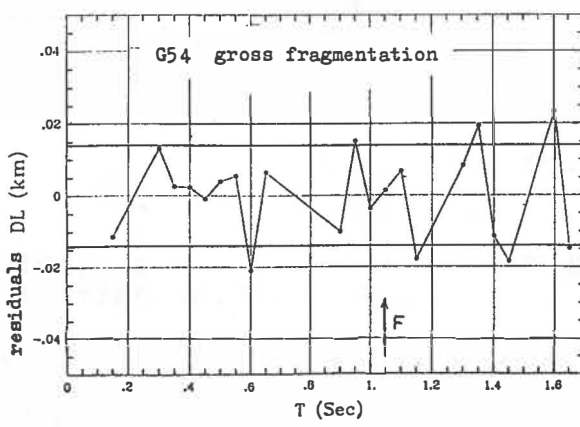


Fig. 2.

LIFETIME OF BINARY ASTEROIDS VS. GRAVITATIONAL ENCOUNTERS AND COLLISIONS

B. Chauvineau(1), P. Farinella(2), F. Mignard(1)

(1) : OCA/CERGA, Avenue Copernic, 06130 Grasse, FRANCE.

(2) : Dipartimento di Matematica, Università di Pisa, via Buonarotti 2, I-56127 Pisa, Italy.

Abstract : In this paper we investigate the effect on the dynamics of a binary asteroid in the case of a near encounter with a third body. The dynamics of the binary is modelled as a two-body problem perturbed by an approaching body in the following ways: near encounters and collisions with a component of the system. In each case, the typical value of the two-body energy variation is estimated, and a random walk for the cumulative effect is assumed. Results are applied to some binary asteroid candidates. The main conclusion is that the collisional disruption is the dominant effect, giving lifetimes comparable to or larger than the age of the solar system.

Introduction

The first indirect observations of binary asteroids have been made between 1977 and 1980. These observations are compiled in the article by Van Flandern et al in the 1979 *Asteroids* book. More recently, new observational evidence has been obtained. The secondary event observed during a stellar occultation by 146 Lucina (Arlot et al., 1985), peculiar light curves analysis by Leone et al. (1984), Cellino et al. (1985) and the spectacular observation by Ostro et al. in August 1989 (Ostro et al., 1990) increase the plausibility of the existence of binary asteroids.

This increasing number of observations has raised questions as to the stability and dynamical evolution of putative binary asteroids. Whipple and White (1985) and Zhang and Innanen (1988) have numerically investigated the effects of solar and Jovian perturbations on the relative motion of a binary asteroid over durations of the order of thousand years. More recently, Chauvineau and Mignard have obtained an estimation of the lifetime of a binary asteroid versus solar and Jovian tidal perturbations (1990a,b) and find that Jupiter causes a destabilizing effect over timescale comparable to the age of the solar system if the components are separated by a distance exceeding a few tens of radii of the primary.

In this paper, we present estimates of the typical lifetime of a binary asteroid versus close encounters and collisions.

I. Principle of the estimation

We do not present here the detailed study of close approaches and collisions, but only the main ideas of the developments together with the major results. See Chauvineau et al. (1992) for the detailed derivations. One must distinguish approaches, either close or distant, from the physical collisions.

1) Encounter cases

In case of encounters, the typical energy variation is estimated in three cases:

a) penetrating encounters: the impact parameter of the third body is comparable to the separation of the binary components. In this case, the effects of the encounter are different on each component of the binary asteroid;

b) close encounters: the impact parameter is larger than the orbital radius of the binary, but the encounter duration is short compared with its period. In this case, the effects on the two components of the binary system are comparable and the Hill's formalism is used (Chauvineau and Mignard, 1990c);

c) far encounters: here again, the impact parameter is much larger than the orbital radius, but the system completes several revolutions during the encounter time. For the same reasons, the Hill's formalism is used in this case too.

The cumulative effect in these three cases are estimated using the number of encounters per time interval dt :

$$d^3N = f(m)dm2\pi b db \frac{P_i}{\pi} dt$$

where $f(m)dm$ is the number of asteroids in the mass range $[m, m + dm]$ and b is the impact parameter. A power law ($f(m) \propto m^\gamma$) is assumed for f . P_i is a probability of encounter per unit surface and per unit time (Wetherill, 1967; Farinella and Davis, 1991) and d^3N is the number of asteroids of mass $[m, m + dm]$, passing at the distance $[b, b + db]$ of the binary system in the time interval $[t, t + dt]$. The energy diffusion is computed from a one-dimensional random walk. The binary asteroid is destroyed when its binding energy becomes positive. We find that the cumulative effect of far encounters is always negligible compared to the cumulative effects of close encounters.

2) Collision cases

In this case, the third body impacts with one of the two binary asteroid components. The effect of such an event can be sufficient to destroy the system. Two cases are considered:

a) Ejection: in this case, the anelastic assumption is made. The impacting and the impacted bodies are assumed to stick to each other after the collision. There is ejection if the energy of the new binary system is positive after the impact. Assuming here again a power law for f of exponent γ , it is found that the satellite ejection is more probable than the primary one because $\gamma \simeq 1.83 > 5/3$.

b) Collisional disruption: we consider in this case that the impacted asteroid (target)

is broken up by the impacting object. This phenomenon occurs if:

$$\frac{M_{proj}}{M_{target}} > \frac{4S}{\rho V^2}$$

where V is the impact velocity, ρ the typical asteroidal density and S the impact strength (Davis et al., 1989; Davis and Ryan, 1990; Housen and Holsapple, 1990).

II. Results

We give here typical lifetimes of some binary candidates versus the different phenomena listed previously. τ_1 , τ_2 , $\tau_{c.ej.}$ and τ_{dis} are respectively lifetimes for penetrating and close encounters, collisional ejection and disruption. Lifetimes are given in years.

146 Lucina

For this asteroid, one finds $\tau_1 = 1.7 \cdot 10^{12}$, $\tau_2 = 1.4 \cdot 10^{11}$, $\tau_{c.ej.} = 1.8 \cdot 10^{10}$ and $\tau_{dis} = 2 \cdot 10^9$.

216 Kleopatra

For this asteroid, one finds $\tau_2 = 9 \cdot 10^{11}$, $\tau_{c.ej.} = 1.2 \cdot 10^{11}$ and $\tau_{dis} = 3 \cdot 10^{10}$. In this case, τ_1 has no significance because collisions occur before cumulative effects of penetrating encounters are efficient.

532 Herculina

For this asteroid, one finds $\tau_1 = 1 \cdot 10^{13}$, $\tau_2 = 1.4 \cdot 10^{12}$, $\tau_{c.ej.} = 1.3 \cdot 10^{11}$ and $\tau_{dis} = 9 \cdot 10^9$.

1220 Crocus

For this asteroid, one finds $\tau_2 = 1 \cdot 10^{10}$, $\tau_{c.ej.} = 7 \cdot 10^9$ and $\tau_{dis} = 3 \cdot 10^9$. In this case again, τ_1 has no significance.

The conclusion is that these lifetimes are generally greater or of the order of the age of the solar system, and that binary stability in the present solar system is limited by collisional disruptions.

References

- Arlot J.E., Lecacheux J., Richardson C., Thuillot W. (1985); A possible satellite of 146 Lucina. *Icarus* 61, pp. 224-231.
- Cellino A., Pannunzio R., Zappalà V., Farinella P., Paolicchi P. (1985); Do we observe light curves of binary asteroids ? *Astron. Astrophys.* 144, pp. 355-362.
- Chauvineau B., Mignard F. (1990a); Dynamics of binary asteroids. I. Hill's case. *Icarus* 83, pp. 360-381.
- Chauvineau B., Mignard F. (1990b); Dynamics of binary asteroids. II. Jovian perturbations. *Icarus* 87, pp. 377-390.
- Chauvineau B., Mignard F. (1990c); Generalized Hill's problem. Lagrangian case. *Celest. Mech.* 47, pp. 123-144.

- Chauvineau B., Farinella P., Mignard F. (1992); The lifetime of binary asteroids vs. gravitational encounters and collisions. *Icarus*, in press.
- Davis D.R., Weidenschilling S.J., Farinella P., Paolicchi P., Binzel R.P. (1989); Asteroidal collisional history: effects on sizes and spins. In *Asteroids II* (R.P. Binzel, T. Gehrels and M.S. Matthews, Eds), pp. 805-826, Univ. of Arizona Press, Tucson.
- Davis D.R., Ryan E.V. (1990); On collisional disruption: Experimental results and scaling laws. *Icarus* 83, pp.156-182.
- Farinella P., Davis D.R. (1991); Collision rates and collision velocities in the main asteroidal belt. In preparation.
- Housen K.R., Holsapple K.A. (1990); On the fragmentation of asteroids and planetary satellites. *Icarus* 84, pp.226-253.
- Leone G., Farinella P., Paolicchi P., Zappalà V. (1984); Equilibrium models of binary asteroids. *Astron. Astrophys.* 140, pp. 265-272.
- Ostro S.J., Chandler J.F., Hine A.A., Rosema K.D., Shapiro I.I., Yeomans D.K. (1990); Radar images of asteroid 1989 PB. *Science* 248, pp. 1523-1528.
- Van Flandern T.C., Tedesco E.F., Binzel R.P. (1979); Satellites of asteroids. In *Asteroids* (T. Gehrels, ed.), pp. 443-465, Univ. of Arizona Press, Tucson.
- Wetherill G.W. (1967); Collisions in the asteroidal belt. *J. Geophys. Res.* 72, pp. 2429-2444.
- Whipple A.L., White L.K. (1985); Stability of binary asteroids. *Celest. Mech.* 35, pp. 95-104.
- Zhang S.P. Innanen K.A. (1988); The stable region of satellites of large asteroids. *Icarus* 75, pp. 105-112.

THE FIRST IDENTIFICATION OF C₂⁻ EMISSION BANDS IN COMET SCORICHENKO-GEORGE (1989e₁) SPECTRUM

Churyumov K.I., Chornyi G.F.

Astronomical Observatory of Kiev Shevchenko University,
Main Astronomical Observatory of Ukrainian Academy of Sciences

ABSTRACT

Wave lengths from 360 emissions within the spectral range $\lambda\lambda$ 3380-6290 Å in the spectrum of the comet Scorichenko-George, obtained with the help of the TV spectral scanner of a 6-meter reflector BTA (in Special AO) have been determined. The CN, C₂, C₃, NH, CH, CO, Na, NH₂, N₂⁺, CO⁺, CH⁺, CO₂⁺, H₂O⁺, and C₂⁻ emissions have been identified. For the first time it has been shown that emissions of C₂⁻ (the transitions 0-0, 0-1 et al.) in the cometary spectrum possibly exist. Molecular ions C₂⁻ column density with cross-section 1 cm² is $N = 1.44 \cdot 10^{-12}$ cm⁻² and their upper limit of gas C₂⁻ productivity is $Q(C_2^-) = 2 \cdot 10^{28}$ cm⁻²s⁻¹.

INTRODUCTION

The present paper was stimulated by the original spectral observations on the 6-m telescope BTA at Pastukhov's Mount (Northern Caucasus) and the calculations of radiative transition probabilities in C₂⁻ made by Rosmus and Werner (1984).

As early as 1963 it was noted that the low intensity of the Phillips emission bands from comets might be caused at least by one of two reasons. The first one: the C₂ molecules are formed initially in a triplet state and do not have any time to decay to the X^{1Σ_g+} state during the time when a comet is reasonably close to the Sun. The second one: the C₂ molecules are converted from the X^{1Σ_g+} state to the a^{3Π_u} state by an optical pumping mechanism that involves solar radiation, the conversion from singlet to triplet occurring via the perturbed levels (Ballik and Ramsay, 1963).

Later on an important work has been done to verify the mechanism of this type of optical pumping (Krishna Swamy, 1986). Noted by Krishna Swamy (1986) some overpopulation of the lower vibrational levels in the low triplet a^{3Π_u} state of the C₂ radical is connected with the optical pumping too.

There is, in principle, one more process which ideally promotes both the depopulation of the ground X^{1Σ_g+} state and the appearance of C₂⁻ mainly in the lower vibrational levels of the a^{3Π_u} state. The problem concerns the formation of the C₂⁻ anions

either by radiative attachment of electrons to the C_2 radicals or by dissociative attachment of electrons to the C_2H_2 molecules if C_2 is a granddaughter species of C_2H_2 . The C_2^- ions are formed in the ground $X^2\Sigma_g^+$ state. Afterwards under the influence of solar radiation they can be excited into the bound $B^2\Sigma_u$ electronic state and either perform a spontaneous transition to the ground state (with emission in the optical range) or autodecay. As soon as the excited C_2^- ions occur on the vibrational levels $v' \geq 6$ the autodecay rate can be comparable with the spontaneous transition rate. In its turn this autodetachment rate in $C_2a^3\Pi_u + e$ is about ten times more than it is in $C_2X^1\Sigma_g^+ + e$ (Jones et al., 1980). Because the level $C_2^-B^2\Sigma_u^+ v'=6$ interferes with the $C_2a^3\Pi_u v''=0$ and 1 levels, the autodetachment from the level $v'=6$ goes preferably to the levels $v''=0$ or 1 of the C_2 radical in the $a^3\Pi_u$ state.

Thus the process in question proceeds in the very direction the optical repumping process does. It may be true that both mechanisms of repumping coexist in cometary atmospheres. A quantitative study of the role of the C_2^- formation in the photochemical kinetics of cometary C_2 will be performed later. It is quite possible that the efficiency of this process (limited only by reagents abundances) is higher than the efficiency of the intercombination transitions $C_2a^3\Pi_u \rightarrow C_2X^1\Sigma_g^+$ and may be comparable with the efficiency of the $C_2a^3\Pi_u v \geq 4 \rightarrow C_2b^3\Sigma_g^- v' \rightarrow C_2a^3\Pi_u v < 4$ transitions surveyed in (Krishna Swami, 1986).

We have calculated g -factors of fluorescence efficiency in the $C_2^-B^2\Sigma_u^+ v' \rightarrow C_2X^1\Sigma_g^+ v''$ bands for a possible identification of emissions in the observed cometary spectra (Tab. I). We used the formula

$$g_{v,v''} r^2 / (\pi F_0) = 8.853 \cdot 10^{-6} \lambda_{v,v''}^2 f_{v,v''} \tilde{\omega}_{v,v''}$$

where r is the comet's heliocentric distance (AU), πF_0 - solar irradiance at $r=1$ AU (phot/(s nm cm²)). For the meaning of the rest of the variables see e.g. (Lutz, 1987). Missing oscillator strength in the absorption have been calculated by the formula

$$f_{v,v''} = 3.04 \cdot 10^{-6} \tilde{\nu}_{v,v''} q_{v,v''} |\langle X|z|B \rangle|^2$$

using the momenta $\langle X|z|B \rangle$ from (Rosmus and Werner, 1984).

Note also that some evidence on the presence of the radiative attachment of electrons to the cometary C_2 molecules can be seen in the observed cometary spectrum in the range 3642.3-3679.1 Å where the onset of $C_2X^1\Sigma_g^+ v=0 \rightarrow C_2X^1\Sigma_g^+ v=0$ emissions lies (in accordance with the electron affinity value 3.370-3.404 eV (Nichols and Simons, 1987)). The photoattachment cross-section for the $C_2 + e \rightarrow C_2^- + h\nu$ reaction is about 10^{-17} cm^2 (Feldman, 1970).

Table I. Oscillator strength $f_{v''v''}$ and g-factors of fluorescence efficiency for $B^2\Sigma_u^+ \rightarrow X^2\Sigma_g^+$ bands of C_2^- anion.

$v''v''$	band onset a)	b)	$ <X z B> ^2$	$\tilde{\omega}_{v''v''}$	$f_{v''v''} (10^{-1})$	$\frac{r^2 g_{v''v''}}{\pi F_\odot} (cm^2 nm)$
0 0	5415.87	0.7	1.1100	1/3	0.436 ^{c)}	$3.7739 \cdot 10^{-16}$
0 1	5984.82	0.2	1.1100	1/3	0.113	$1.1944 \cdot 10^{-16}$
1 0	4902.02	0.3	0.7742	1/5	0.144 ^{c)}	$0.6127 \cdot 10^{-16}$
1 1	5363.26	0.3	0.7742	1/5	0.132	$0.6723 \cdot 10^{-16}$
1 2	5912.69	0.3	0.7742	1/5	0.119	$0.7366 \cdot 10^{-16}$

^aHerzberg and Lagerqvist (1968), ^bJones et al.(1980), ^cRosmus and Werner (1984).

POSSIBLE IDENTIFICATION OF C_2^- EMISSIONS IN COMETARY SPECTRUM

The spectra of the comet Scorichenko-George (1989e₁) were observed by V.L.Afanasiev, A.I.Shapovalova and K.I.Churyumov on Feb.26.7 UT,1990 at the Special Astrophysical Observatory of the USSR Academy of Sciences (Nizhny Arkhyz) with the help of the TV scanner located on a spectrograph in the Nasmyth focus of a 6-meter reflector BTA. The spectrographic slit was observed with a mask that selects two regions of the comet that are separated from one another by the angular distance 20" (31000 km). This gave the opportunity during one exposition to accumulate in the computer memory two spectra, one of which is referred to the cometary nucleus, the other to the coma's region. The six spectra were recorded in three channels, which are characterized by the following spectral ranges: 1 - 3350-4450 Å, 2 - 4290 - 5390 Å, 3 - 5190 - 6290 Å. Spectral resolutions for each channel is 1.1 Å. The identification of the spectrum showed that it contains many typical cometary emissions (wave lengths of 360 emissions are measured with the precision up to ± 0.5 Å). Among them are: CN, C_2 , C_3 , CH, NH, NH_2 , Na, CO, CO^+ , N_2^+ , CH^+ , CO_2^+ , H_2O^+ and C_2^- . This spectrum for the first time has found out the emissions of the negative ions C_2^- (see λ_{obs} in the Table II):

Table II. Identification of C_2^- emissions in the comet's spectrum

$\lambda_{obs} \pm 0.5 \text{ Å}$	$\lambda_{v''v''} \text{ d}$	$v''v''$	$\lambda_{obs} \pm 0.5 \text{ Å}$	$\lambda_{v''v''} \text{ d}$	$v''v''$
5416.5	5415.9	0-0	4902.5	4902.0	1-0
5984.4	5984.8	0-1	5363.1	5363.3	1-1
			5913.1	5912.7	1-2

^d the theoretical $\lambda_{v''v''}$ from Table I

Comparison of the observable and theoretical data shows their

close coincidence within the measurement made. The sharp peaks in the spectrum are the transitions 0-0 and 0-1 (see Fig.a,b) that have the largest values of g-factors. The transitions 1-0, 1-1 and 1-2 have some emission peculiarities in the spectrum. The spectrum also contains the band in the wave length range 3642.3-3679.1 Å (the observed band is 3642.4-3678.7 Å), where lies the beginning of the transition $v' = OX^2\Sigma^+ C \rightarrow v'' = OX^2\Sigma^+_g C_2^-$ (Fig.c).

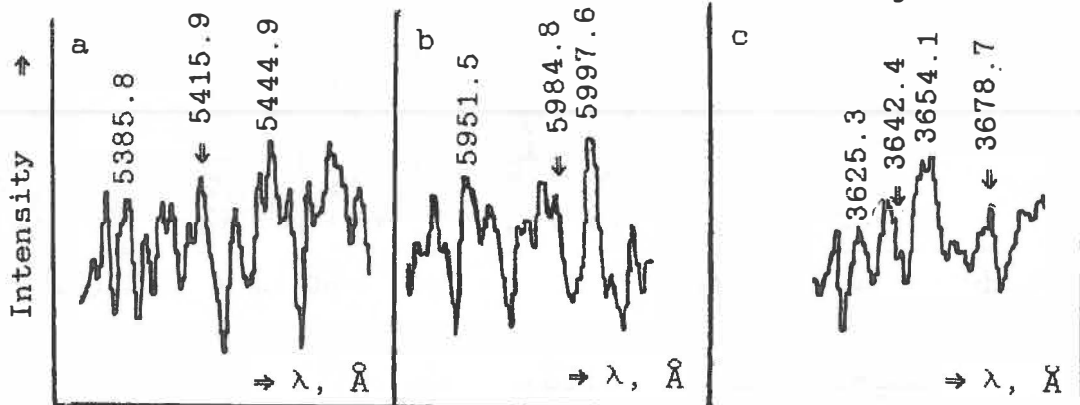


Fig. The fragments of the spectrum of comet 1989e with C_2^-
CONCLUSIONS

1. It has been shown that emissions of C_2^- in the cometary spectrum possibly exist. 2. The presence of ions C_2^- leads to the impoverishment of the singlet state of C_2 molecules and the enrichment of the triplet state of these molecules. This substantially enriches the chemical kinetics of C_2 and improves the model of the inner coma (the process of photochemical reactions). 3. Calculation of molecular ions C_2^- column density with cross section 1 cm^2 gives $N = 1.44 \cdot 10^{12} \text{ cm}^{-2}$.

REFERENCES

- Ballik E.A., Ramsay D.A. (1963) The $A^3\Sigma_g^- - X^3\Pi_u$ band system of C_2 molecule. *Astrophys.J.*, 137, 61-83.
 Feldman D. (1970) Photoablosung von Electronen bei einigen stabilen negativen Jonen. *Zeitschrift fur Naturforschung* 25, 621
 Herzberg G. and Lagerqvist A. (1968) A new spectrum associated with diatomic carbon. *Canad.J.Phys.*, 46, 2363-2373.
 Jones P.L., Mead R.D., Kohler B.E. and Lineberger W.C. (1980) Photo-detachment spectroscopy of C_2^- autodetaching resonances. *J.Chem.Phys.* 73, 4419-4432.
 Krishna Swami K.S. (1986) Physics of Comets. World Scientific, Singapore. 274 pp.
 Lutz B.L. (1987) Fluorescence efficiency factors for ionized water vapor. *Astrophys.J.* 315, L147-L150.
 Rosmus P. and Werner H.-J. (1984) Multireference-CI calculations of radiative transition probabilities in C_2^- . *J.Chem.Phys.*, 80, 5085

INFLUENCE OF SOLAR ACTIVITY UPON LIGHT CURVES OF COMETS P/HALLEY (1986 III) AND P/CHURYUMOV-GERASIMENKO (1982 VIII)

Churyumov K.I., Filonenko V.S.

Astronomical Observatory of Kiev Shevchenko University
Astronomical Observatory of Khar'kov University

ABSTRACT

It is shown that the comet P/Halley's (1986 III) total magnitudes correlate with changes in the solar activity indices and the solar wind velocity. A statistically reliable correlation between the outbursts of brightness and magnitude variations of the short-period comet Churyumov-Gerasimenko (1982 VIII) and the level of the solar activity has been found out.

INTRODUCTION

The dependence of cometary brightness from the level of solar activity was first obtained at the beginning of the 19th century. But despite a long, over a hundred-and-a-half-year history of such observations the mechanism of the Sun-comets relationship remains unknown. The situation is complicated by that that statistically cometary brightness is tied with a solar cycle phase, and for some comets variations of brightness do not well correlate with solar activity. Along with comets whose activity is closely connected with solar activity, there are comets that show such a link does not exist.

P/HALLEY (1986 III) AND SOLAR ACTIVITY

S.V.Orlov (1923) when analyzing observations of P/Halley (1910 II), obtained in 1909/1910, found out a distinctly observable connection between the comet's photometric nucleus magnitudes and the Wolf numbers. The comet's integral magnitudes appeared independent from the Wolf numbers. It was of interest to check this conclusion on new numerous observation data obtained in the framework of the IHW (more than 10000 estimates of P/Halley total magnitudes). In the present paper in order to compare variations of the comet's magnitudes with the solar activity the authors (1987) used a detailed light curve (over 5000 estimates of magnitudes) that covers the period July, 1985 - June, 1986. Taking into account that a correct comparison of the comet activity and solar activity may be obtained if the temporal shift, because of differences in the heliographical longitudes of the Earth and the comet does not exceed 4 days, there are two respective intervals on P/Halley's light curve: 1) October 15 - Dec. 29, 1985 (the comet's heliographical latitude was changing throughout this period from -3° to $+7^{\circ}$) and 2) (March 15 - 28, 1986 (the comet's heliographical latitude - from -3° to -13°).

The spots square during the first period of observations does not exceed 900 millionth of visible hemisphere and during some periods it was approaching zero. The comet's strong outburst with the maximum October 29-30, 1985 and its amplitude with more than 2^m coincides with the highest maximum of the solar spot-formation activity. Attention is drawn to the deep minimums on the light curve that correlate with the solar minimal activity (Filonenko, Churyumov, 1990). The comet's magnitudes minimums interval (25-27 days) is close to the Sun's rotation synodic period.

The character of the comet's flattened light curve corresponds to the character of changes of the solar indices. In order to obtain quantitative estimates of the degree of the correlation between the comet activity and the solar activity Dobrovolsky's method (1966) was applied. The 10-day average amplitude of the comet's brightness declination increases with the growing total spot area (S), with the linear correlation coefficient $R=0.62\pm 0.22$. The coupling coefficient $K_{SM}=1$ by $D=5.7$ shows that the total spot area maximum is always followed by the comet's brightness maximum. But the correlation coefficient calculated by Dobrovolsky's method is low - $R_{MS}=0.32\pm 0.14$. This is probably connected with that under low solar activity such indices as the spot area or those of calcium floccules cannot fully explain how the solar activity could influence the comet. The overlapping upon the flattened authors light curve quasiperiodic variations in the visual comet's brightness of a small amplitude (0.2^m-0.3^m) with a specific time scale between 7-8-day maximums and those blurring the correlation coefficient are, probably, the consequence of the comet's encounter with velocity waves in the solar wind (Ptitsyna et al., 1987). During the second interval the solar activity became even more low and that fact determined the character of the connection in question. For a month, March 15 - April 14, 1986, the solar activity was rather low and the rate of decrease in the comet's brightness became substantial. The increase in the solar spot-formation activity during the next four nights firstly slowed down the rate of decrease in the comet's brightness, though later it led to its growth. The comparison of the comet's light curve with the changing solar wind velocity in the former's periphery, measured by Vega-1 space probe, points to the existence of a reliable dependence with the correlation coefficient 0.71 ± 0.13 (see Fig.).

COMET P/CHURYUMOV-GERASIMENKO (1982 VIII) AND SOLAR ACTIVITY

The short-period comet Churyumov-Gerasimenko was discovered in 1969. But the conditions for observing it in 1969/1970 and in 1975/1976 apparitions were rather unfavourable. Because of this the comet's photometric behaviour remained practically unknown. Only during the comet's apparition in 1982/1981 great observation data (more 330 magnitude estimates) were obtained that made it possible to construct a detailed comet's light curve and to thoroughly study its peculiarities (Churyumov, Filonenko, 1989a; 1989b).

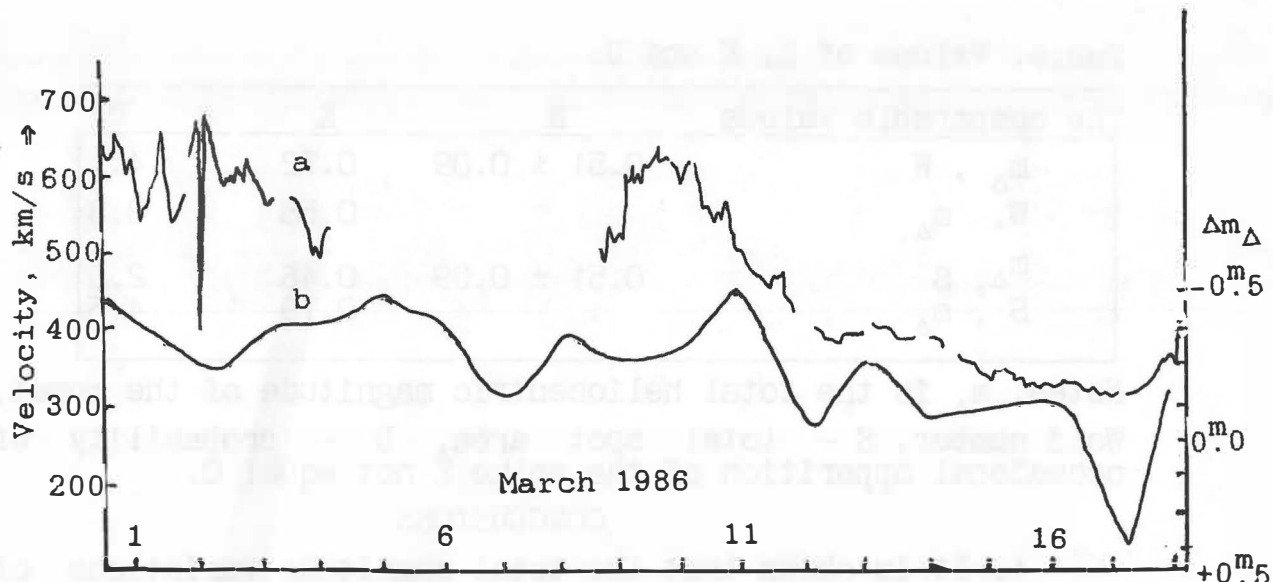


Fig. Changes of Δm_Δ (the declination of the total heliocentric magnitude from the minimal theoretical^{*} light curve (b)^{*}) and the velocity of the solar wind (a). Note: * - the photometric parameters H_y and n from the Orlov's formula $m_\Delta = H_y + 2.5n \log r$ were calculated by the Filonenko's method (1987).

The comet was active, and during six-months observations (late August, 1982 – early March, 1983) it had numerous outbursts (more than 16) and variations of its integral magnitudes. At that time the mutual space dislocation of the Earth, the Sun and the comet during the whole period of observations was exceptionally favourable from the point of view of the study of the solar activity influence upon the comet's light curve (Filonenko, Churyumov, 1990). A temporal shift preconditioned by the difference in the heliographical longitudes of the Earth and the comet did not exceed 2.3 of a day, and during October 25, 1982 – February 5, 1983 it was less than one day. The solar activity, visible from the Earth, when observed from the comet, changed insubstantially. The solar activity during the observation period was situated on the decrease branch of the 11-year solar activity cycle when most stable high-speed corpuscular streams were being formed. The comparison of P/Churyumov-Gerasimenko's light curve and the curve of the solar activity indices changes that are reduced to the comet's centre shows that the variations of the comet's brightness rather well correlate with the changes of the solar indices. Values of R, K and D are given in Table. It is evident that the correlation between the comet's brightness maximums and those of the solar activity indices is statistically meaningful and indicates that the growing spot total area increases the probability of the growth in the comet's brightness, but an increase in m_Δ may not be accompanied by an increase of S. The analogous connection with the Wolf numbers is less obvious and the maximum m_Δ with more probability is accompanied by the maximum W than by the maximum W by the brightness maximum.

Table. Values of R, K and D.

The comparable values	R	K	D
m_{Δ} , W	0.51 ± 0.09	0.72	4.1
W, m_{Δ}		0.58	3.3
m_{Δ} , S	0.51 ± 0.09	0.46	2.5
S, m_{Δ}		0.79	4.6

Notes. m_{Δ} is the total heliocentric magnitude of the comet, W is Wolf number, S - total spot area, D - probability of an occasional apparition of the value K not equal 0.

CONCLUSIONS

1. It is shown that the total magnitude variations of comet P/Halley (1986 III) correlate with changes of the solar activity indices and the solar wind velocity.
2. A statistically reliable correlation between the P/Churyumov-Gerasimenko (1982 VIII) outbursts and variations in its total magnitudes with such solar activity indices as the total spot areas and the Wolf numbers has been found out.

REFERENCES

- Churyumov K.I. and Filonenko V.S. (1987) The light curve of the comet Halley (1982). Data of the foreign observers. Kiev Comet Circular, 375, 2-3.
- Churyumov K.I. and Filonenko V.S. (1989a) The new peculiarity of the light curve of P/Churyumov-Gerasimenko (1982 VIII) and its photometric parameters. Kiev Comet Circular, 403, 5-7.
- Churyumov K.I. and Filonenko V.S. (1989b) The phase dependence of the total magnitude of P/Churyumov-Gerasimenko. Kiev Comet Circular, 404, 3-4.
- Dobrovolsky O.V. (1966) Comets. Nauka publ., Moskva.
- Filonenko V.S. (1987) On the one method of determination the photometric parameters of comets. Kiev Comet Circular, 368, 2-3.
- Filonenko V.S., Churyumov K.I. (1990a) Influence of solar activity upon light curve of comet P/Churyumov-Gerasimenko (1982 VIII). Kiev Comet Circular, 412, 10-12.
- Filonenko V.S., Churyumov K.I. (1990b) Brightness of comet Halley (1986 III) and solar activity. Kiev Comet Circular, 413, 4-6.
- Ptitsina N.G., Richter A.K., Breus T.K. (1985) Outbursts of the comet brightness and waves of velocity in the solar wind. Kosmicheskiye issledovaniya, XXIII, 6, 926-932.
- Orlov S.V. (1923) On connection between cometary brightness and activity on the Sun's surface. Proceedings of Astron. Obs. of Yuriev University, 21, 3.

PLASMA-BEAM INSTABILITIES IN COMETARY IONOSPHERES

K. I. Churyumov, N. Ya. Kotsarenko, G. V. Lizunov, and O. P. Verkhoglyadova

Department of Astronomy of Kiev Shevchenko University

ABSTRACT

It is shown that the interaction between the solar wind flux and the cometary ionosphere leads to the excitation of ion sound, whistler, electron-cyclotron, low hybrid and magnetohydrodynamic waves. We investigated the frequency spectrum and found linear-increasing increments and lengths of excited waves.

INTRODUCTION

A cometary ionosphere is separated from the circumfluent solar wind flux around it by a large interplanetary region (10^5 km thick) within which the solar wind plasma and that of a comet are mutually interpenetrating. This system develops plasma-beam instabilities exciting plasma waves of different types.

A wide spectrum of these waves was detected by the ICE-probe that encountered on September 11, 1985 the comet P/Giacobini-Zinner (1984e) plasma tail (Scarf *et al.*, 1986) and ICE, Vega-1,2, Sakigake, Suisei probes that passed through P/Halley's head in March 1986 (Tsurutani, 1991). The spectra obtained were of a specific type and they are shown by dashes in Fig. 1 (Tsurutani, 1991). The maximum on the right corresponds to the ion acoustic waves at the ion Langmuir frequency. Lower in frequencies are whistler mode waves with an intensity maximum at the Low Hybrid Frequency. Finally, ion-cyclotron and magnetohydrodynamic waves materialize as regular fluctuations of the magnetic field are registered in the lowest frequency range. The total energy density of the waves in question can be estimated from measurement data (Scarf *et al.*, 1986) as $1-2 \cdot 10^{-13}$ erg/cm³, which is 0.01% of the solar wind kinetic energy density.

The energy source and the exciting mechanism of the waves in question were investigated by many authors. The plasma-beam instability was studied by Chernikov (1974), Goldstein and Wong (1987), Gary and Madland (1988), Price and Lee (1988), and in a number of more recent papers presented by Tsurutani (1991). The authors investigated, rather thoroughly, applying analytical and numerical methods, the excitation of ion-cyclotron and magnetohydrodynamic waves that are important for cometary ions acceleration and that can affect shock structure and the cometary ionosphere as a whole. Instability of the remaining higher frequency plasma waves has not been investigated, except by Chernikov (1974). We investigated the ion acoustic instability, yet he did not study the strongest hydrodynamic mechanism of instability excitation. The above work focuses the purpose of the present paper, which deals with the whole plasma-beam instability frequency spectrum that occurs under the solar wind and cometary plasma interaction.

THE INITIAL MODEL

We examined an extended region of space where the solar wind plasma and the comet plasma mutually penetrating. *Scarf et al.* (1986), *Bame et al.* (1986), and *Ogilvie et al.* (1986) indicate that this region consists of the proper transition sheet and the comet sheet whose total thickness (for Giacobini-Zinner $\sim 10^5$ km) is much higher than the visual comet cross-section. The plasma parameters and the magnetic field configuration gradually change in the region in question, the cometary plasma density n_o greatly surpassing the solar wind density n_b , throughout the entire region except the outer edge of the transition sheet, with $\alpha = n_b/n_p \ll 1$. Since the characteristic scale of plasma heterogeneity is much greater than the pertinent wavelengths (from tens of meters for ion-acoustic waves up to hundreds of kilometers for magnetohydrodynamic waves), heterogeneity that can affect the development of instabilities can be neglected. Further, we investigated a simple model in which a small density homogeneous plasma beam (the solar wind) interacts with homogeneous cometary plasma.

It should be noted that the relative drift velocity of the two plasmas, V_o , agrees with the relation $V_{Ti} \ll V_o \ll V_{Te}$ where $V_{Ti,e}$ are the ion and electron heat velocities. Thus we deal with a hydrodynamic flux only of the ion plasma component, while the total velocity distribution function of electrons has a one-hump character. This condition enables us to elaborate a linear theory of the plasma-beam instability.

RESULTS OF CALCULATIONS

A general idea of the results obtained is shown in Fig. 1 (the dependence of instability growth rate γ on frequency ω). We shall consider the spectrum of excitation waves, moving from high frequency waves to low frequency ones.

a) *Langmuir Oscillations:* Plasma-beam instabilities do not excite the oscillations in question, under the given conditions, instabilities of all types (electron kinetic and hydrodynamic) are inhibited because of high temperature of the flux.

b) *Ion-Acoustic Oscillations:* Their instability is due to the interaction of the solar wind and comet plasma ion-acoustic waves. There are waves with the frequency $\omega \approx \omega_{pi}$ [where $\omega_{pi} = (4\pi e^2 n_p/M)^{1/2}$ is the cometary ion plasma Langmuir frequency] and the wave number $k \approx \omega_{pi}/V_o$. This brings about the maximum instability growth rate equal to $\gamma \approx \sqrt{3kV_o\alpha^{1/3}/2^{4/3}}$ (Mikhailovsky, 1975). For the characteristic values of plasma parameters $n_b = 50 \text{ cm}^{-3}$, $n_o = 5 \text{ cm}^{-3}$, $V_o = 100 \text{ km/s}$ we shall obtain $\omega \approx 4.2 \cdot 10^3 \text{ s}^{-1}$, $\gamma \approx 1.3 \cdot 10^3 \text{ s}^{-1}$. The ion sound wave length is $\lambda \approx 150 \text{ km}$.

c) *The Whistler Range Waves* ($\omega_{Hi} < \omega < \omega_{He}$, where $\omega_{Hi,e}$ are ion and electron gyration frequencies): In this range and in lower frequency ones the dispersion plasma properties are essentially affected by the presence of the outer magnetic field H_o , "frozen-in" the solar wind.

Electron cyclotron oscillations with the dispersion law $\omega \approx \omega_{He} \cos\theta$ [where $\theta = (\vec{k}, \vec{V}_o)$, with \vec{V}_o] can be excited due to kinetic instability of the electron flux, as was studied by Akhiezer (1962). After transforming the equations given for the maximum growth rate, one can get a simple equation $\gamma \approx \alpha \sqrt{\pi/2} \omega_{He}^5 \cos\theta \sin\theta / (3k^4 V_{Te}^3 V_o)$, valid for $\pi/2 - \theta > \sqrt{m_e/M_i}$. Simultaneously $k = (4/3)(\omega_{He}/V_o)^{1/2}$. With $\theta \approx \pi/2$ the electronic oscillation excitation is more effective on account of the ionic fluid hydrodynamic instability, with the growth rate maximum at the Low Hybrid Frequency $\omega \approx \omega_{LH}$ ($\omega_{He}\omega_{Hi}$)^{1/2} and equal to $\gamma \approx \alpha \omega_{LH}$ with $k = \omega_{He}/V_o$. Assuming $H_o = 20 \text{ nT}$, we obtain $\omega \approx 20 \text{ s}^{-1}$, $\gamma \approx 2 \text{ s}^{-1}$, $\lambda \approx 360 \text{ m}$. The dependency $\gamma(\omega)$ is given by curve 2.

In this frequency range, faster waves can be excited, whistlers with an electromagnetic character that interact with solar wind ionic acoustic waves. The dependency $\gamma(\omega)$ tabulated from the accurate formula taken from Akhieser (1974) $\gamma(\omega)$ is shown in Fig. 1 by curve 3.

d) **Magnetohydrodynamic (MHD) Waves:** Their excitation effectively occurs under cyclotron resonance of the ionic flux (with $\omega \approx kV_o \cos\theta - \omega_{Hi}$). A fast magnetosonic wave is unstable (*Akhieser*, 74) with the dispersion law $\omega = kV_A$ [where $V_A = H_0/(4\pi M_i n_p)^{1/2}$ is the Alfvén velocity], the wave number $k = \omega_{Hi}/(V_o \cos\theta - V_A)$ and the growth rate $\gamma \approx a^{1/2} \omega_{Hi}$ (see curve 4, Fig. 1). The order of values gives the following: $\omega \approx 0.4 \text{ s}^{-1}$, $\gamma \approx 0.7 \text{ s}^{-1}$, $\lambda \approx 520 \text{ km}$.

The results obtained give good account of the spectral composition of the radiation observed (see g. 1). Moreover, the absolute values of the instability increment of the whistler and MHD-waves e in good agreement with the results by *Price and Lee* (1988) and *Brinca and Tsurutani* (1988), who vestigated the excitation of waves by numerical methods.

CONCLUSIONS

The interaction of the solar wind plasma and the cometary ionosphere gets a wide spectrum of the waves that were excited (Fig. 1), namely: ion-acoustic ones with the ion Langmuir frequency, electron-cyclotron ones with the intensity maximum of low hybrid, whistlers and fast magnetic acoustic waves. With this wave energy of about 0.01% the solar wind kinetic energy is produced.

REFERENCES

- Akhieser* A. I., ed. (1974) *Electrodinamika Plazmy*. Nauka, Moscow. 720 pp.
Elme S. J. et al. (186) *Science*, 232, 356–361.
Brinca A. L. and *Tsurutani* B. T. (1988) *J. Geophys. Res.*, 93, 48–58.
Iernikov A. A. (1974) *Astronomicheskiy J.*, 51, 852–858.
Soldstein M. L. and *Wong* H. K. (1987) *J. Geophys Res.*, 92, 4695–4700.
Ikhailovsky A. B. (1975) *Teoriya Plazmennykh Neustojchibostey*, 1, Nauka, Moscow. 272 pp.
Gilvie K. W. et al. (1986) *Science*, 232, 374–377.
Price C. P. and *Lee* L. C. (1988) *Astrophys. J.*, 324, 606–620.
Neugebauer F. L. et al. (1986) *Science*, 232, 377–381.
Tsurutani B. T. (1991) Cometary plasma waves and instabilities. In *Comets in the Post-Halley Era*, Vol. 2 (R. L. Newburn, M. Neugebauer, and J. Rahe, eds.), pp. 1171–1210. Kluwer Academic Publishers.

g. 1. The dependence of instability growth rate γ on frequency ω . Curve 1 — an ion-acoustic wave, — electron-cyclotron wave, 3 — whistler, 4 — magnetosonic wave. The dashed line shows the spectral density $I(\omega)$ of radiation that was observed experimentally (*Tsurutani*, 1991).

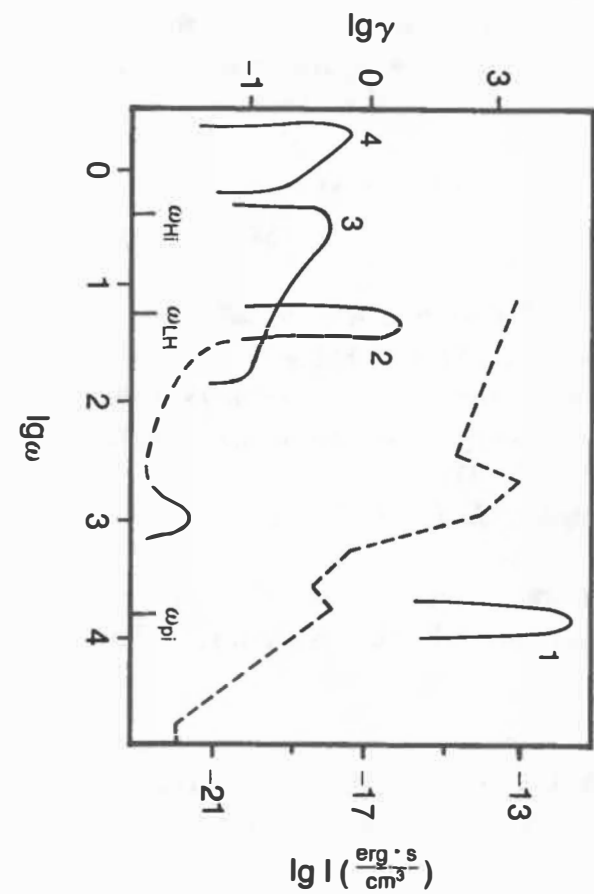


FIGURE 1.

DUST AND GAS JETS. EVIDENCE FOR A DIFFUSE SOURCE IN HALLEY'S COMA

J. Clairemidi, P. Rousselot, F. Vernotte, G. Moreels
Observatoire de Besançon B.P. 1615
25010 BESANCON CEDEX FRANCE

ABSTRACT

The distribution of dust-scattered intensity in Halley's inner coma is measured with the Vega three-channel spectrometer at three selected wavelengths : 377, 482 and 607 nm. The variation along a cometo-centric radius may be described by a p^{-s} law where p is the distance between nucleus and optical axis and s is an exponent which is equal to 1 except in an intermediate 3000 < p < 7000 km region where $s = 1.5$. The shape of the radial distribution may be explained with a model including solar radiation pressure effect and quantum scattering efficiencies calculated from Mie theory. Monochromatic images inside an angular sector having its apex at the nucleus show evidence of two dust jets which extend to 40000 Km. The pixel-to-pixel ratio of two images of dust intensity at 377 and 482 nm shows that the scattered intensity presents an excess of blue coloration in a zone located around the jets between 10000 and 25000 km. This coloration is interpreted as being due to a population of sub-micronic grains which results of the fragmentation of dust particles transported in the jets. It is suggested that the diffuse source where an additional quantity of CO was detected might be connected with the presence of a dust jet. In present scheme, grain particles with a size of several μm or 10 μm would be transported inside a dust jet to distances of several 10 000 km where they would suffer fragmentation and produce sub-micronic particles and a release of gas which would be at the origin of the diffuse source.

INTRODUCTION

The video cameras of Giotto (Keller *et al.*, 1986) and Vega (Sagdeev *et al.*, 1986) have clearly demonstrated the existence of jets originating from the nucleus. The field of view of these close-up images is of the order of 100 km. Images obtained at a greater scale, from the ground, show the presence of gas jets (A'Hearn *et al.*, 1986), but do not give evidence of dust jets (Cosmovici *et al.*, 1987). In order to know what is the source of the emissive molecules of the gas jets, it is of importance to evaluate at what distance the dust jets can extend.

A second type of measurement has introduced a new insight into the coma. It is the detection by the NMS instrument of Giotto (Eberhardt *et al.*, 1987) of a diffuse source of CO located as far as 10 000 to 15 000 km from the nucleus. The detection of H₂CO in comets Austin and Levy (Crovisier, 1991; Schloerb and Weigu 1991) has led to a confirmation of this concept of extended source.

RADIAL DISTRIBUTION

The data used here are the spectra transmitted by the Vega 2 three-channel spectrometer during the approach and encounter session on March 9, 1986. The scanning capability of the instrument allows to explore an angular sector of the inner coma having its apex at the nucleus and a radial extent of 40000 km. Monochromatic images in the major emissions, OH, NH, CN, C₃ and C₂ can be assembled and compared (Clairemidi *et al.*, 1990,a,b). In the case of dust-scattered intensity, three spectral windows are selected in the blue-near-UV at 377 nm, the visible at 482 nm and the red at 607 nm, where the contribution of molecular emissions are minimum.

The radial distribution of dust intensity is plotted in Fig. 1. For each wavelength, two radial profiles are plotted, along a radius where no jet is present (labelled "valley") and along a radius which follows a jet pattern (labelled "jet"). Both profiles show the degree of anisotropy of the coma at distances of several 10000 km. The overall shape of the curves may be described by a p^{-s} law where p is the distance from the nucleus to the optical axis and s an exponent. The exponent value measured in Fig. 1 is $s \cong 1$ for $p < 3000$ km and $p > 7000$ km and $s \cong 1.5$ in the intermediate 3000 - 7000 km region.

In order to analyse the main features of the measured radial profile, a dust fountain model was elaborated. It includes the effects of gravitation and radiation pressure of solar origin. The treatment of particle trajectory is conducted as explained by Massonne (1985). The mass distribu-

tions of particles at cometocentric distances > 8100 km are derived from Mazets et al., (1987). At distances < 8100 km, the mass distribution is not known for the time of observation. The data of Mazets were extrapolated and a parameter was introduced to adjust the particle population in the small mass decades 10^{-16} - 10^{-12} g. The Mie scattering quantum efficiency, Q_{sca} is calculated in using the method of Eaton (1984). The complex index is taken as $n = 1.387 - 0.031 i$ which is the value recommended by Mukai et al. (1987)

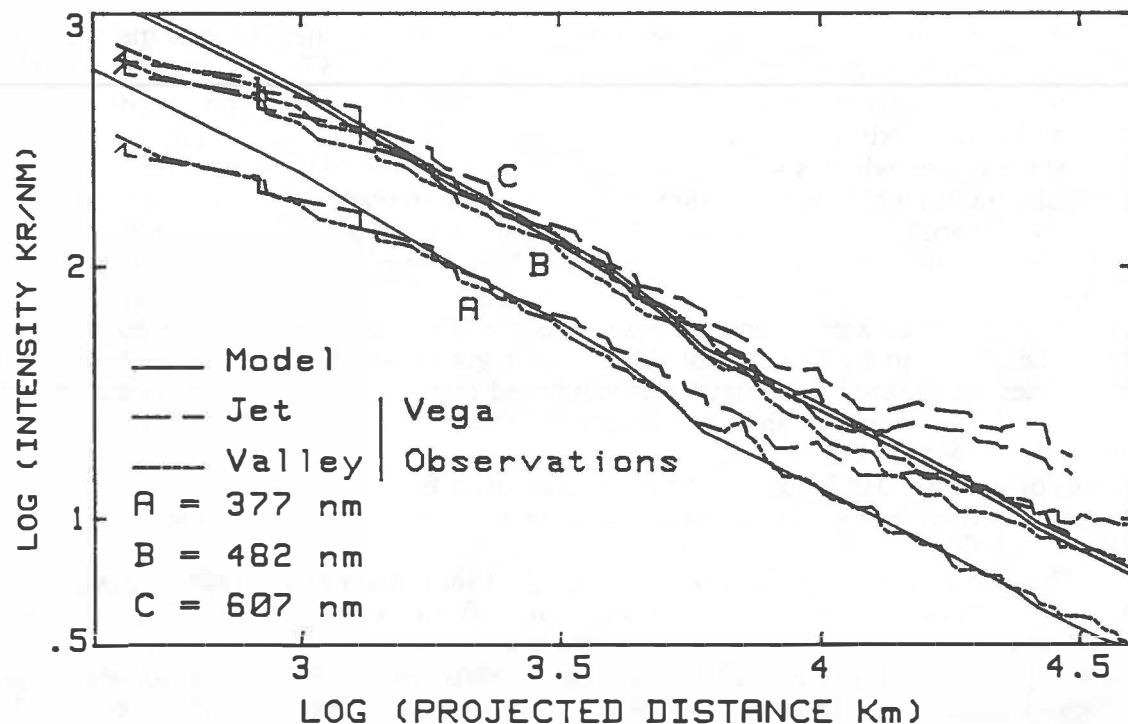


Fig. 1 Radial profiles of dust-scattered intensity measured during the Vega 2 encounter session and compared with the results of a simple model based on Mie theory for spheres and the mass distribution function of particles for $r > 8100$ km given by Mazets et al., (1987). The intensity profiles are compared at three selected wavelengths: 377 nm (A), 482 nm (B) and 607 nm (C). For each wavelength, three profiles are drawn: as calculated with the model (full line), as measured in the main jet (dashed line) and as measured in the valley (dotted-dashed line).

The results, given in Fig 1, show a good quantitative agreement with the measured intensities. The change in the slope value between 4000 and 6000 km is due to the reflexion of small particles in the 10^{-14} - 10^{-12} g range under the effect of radiation pressure. At distances $p < 1000$ km, the calculated intensity is higher than the measured value because the model, in its present version, does not take into account the actual relative rotation motion of the optical axis around the nucleus during the close encounter period.

The computed intensity, expressed in photon units, is :

$$I(p, \lambda) = \int_{z1}^{\infty} \int_{m1}^{m2} n'_m(z) \cdot \Pi a^2 \cdot Q_{\text{sca}}(a, \lambda) \cdot \Phi(\phi) \cdot F_0(\lambda) \cdot dm \cdot dz$$

where: z is a coordinate measured along the optical axis, m is the dust particle mass, $n'_m(z)$ is the dust particle density per mass unit, a is the particle radius, $\Phi(\phi)$ is the phase function; ϕ : phase angle for dust, $F_0(\lambda)$ is the solar flux of photons per surface unit and time unit.

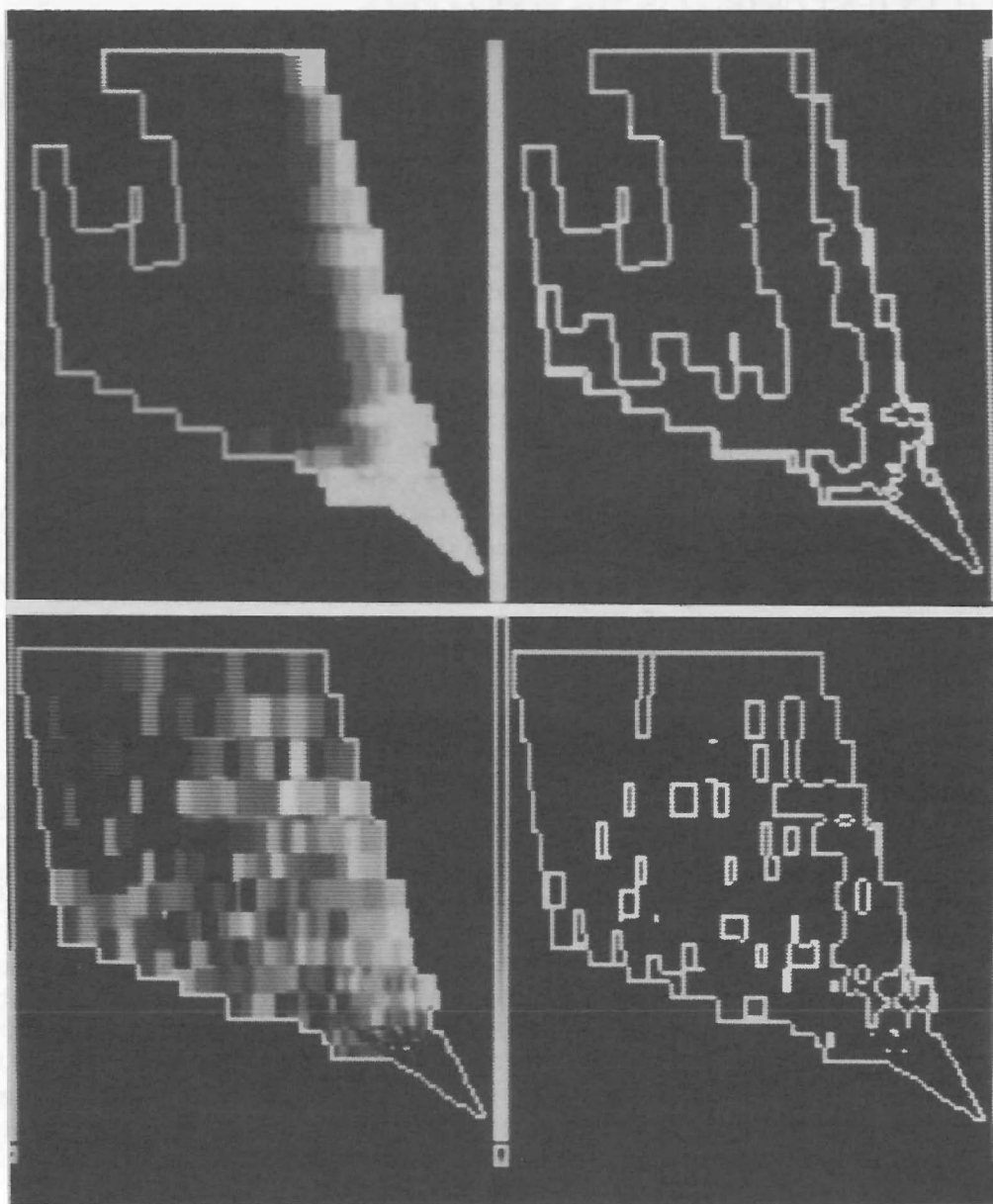


Fig 2a, upper left: intensity plot; **Fig 2b**, upper right: intensity contour plots
Composite monochromatic image of dust-scattered intensity at 482 nm. The nucleus is located at the apex, on the lower right. The radial extent of the field of view is 40000 km. The Sun is located on the left.

Fig 2c, lower left: radiation color plot; **Fig 2d**, lower right: color contour plots
Pixel-to-pixel ratio of two images of dust-scattered intensities at 377 nm and 482 nm. This composite image shows that the visible jets in Fig 2a,b present a slight blue coloration in the 10000-25000 km range.

The calculation is based upon the assumption that the cometary dust particles are spherical and homogeneous, which is far from reality when considering particles with a size of several μm or $10 \mu\text{m}$. However, it shows that the high value of the exponent s measured in the 4000-7000 km region implies that, on the basis of the fountain model, a population of small sub-micronic grains exists in the inner coma.

SPATIAL EXTENT OF DUST IN THE INNER COMA

The radial profiles presented in Fig. 1 may be completed with a bi-dimensional representation of the scattered intensity inside the field of view scanned by the spectrometer. A composite image of this type, which depicts the intensity at 482 nm is given in Fig. 2a,b. Two jets appear in this monochromatic image: a weaker one, on the left, in the direction of the Sun and a stronger one, in a perpendicular direction. As a result, the distribution of dust at distances of 10000 to 40000 km from the nucleus appears as strongly anisotropic. As shown in Fig. 1, the intensity inside the jets is two times more intense than inside the valley (between the jets).

PRODUCTION OF AN EXTENDED SOURCE BY DUST JETS

The spatial distribution of dust particles may be visualized at different wavelengths, in the near-UV at 377 nm and the red at 607 nm. A pixel-to-pixel ratio of the images at $\lambda_1 = 377$ and $\lambda_2 = 482$ nm is presented in Fig. 2c,d. A slight excess of blue coloration, of the order of 25% in intensity, is apparent in the 10000-25000 km region, closely correlated with the presence of jets. This coloration is interpreted as being due to the existence of a population of sub-micronic grains located in the vicinity of the jets. The calculation of the ratio of the quantum efficiencies at two wavelengths, $Q_{\text{sc}}(\lambda_1) / Q_{\text{sc}}(\lambda_2)$ based upon Mie theory shows that a small excess of tiny grains with $a < 0.8 \mu\text{m}$ can produce a slight coloration of the scattered radiation. In present case, we calculated that the observed coloration may be reproduced if one assumes that a fraction of 10^{-7} - 10^{-6} of the dust particles present at 20000 km undergoes fragmentation and produces small grains of mass 10^{-15} - 10^{-13} g. This results from the fact that the optical scattering efficiency of a given mass of dust particles is roughly inversely proportional to the average radius of the particles.

In an attempt to explain the dust-scattered radiation measurements in the inner coma, it is necessary to introduce a fragmentation mechanism which produces sub-micronic particles. The existence of dust jets and the slight coloration observed in the vicinity of the jets give serious arguments supporting the following process : dust jets originating from fissures at the nucleus surface and extending to several 10000 km. A small fraction of the dust particles would suffer fragmentation after having been heated for several hours starting from their ejection from the nucleus. During this process, they would release gas components such as the CO molecules which were found to form, during the Giotto encounter (Eberhardt *et al.*, 1987), an extended source around 10000 km.

CONCLUSION

The spatial distribution of dust-scattered intensity in the inner coma shows the existence of two well-contrasted dust jets inside the field of view of the spectrometer. A model based on Mie theory and the particle measurements of Mazets *et al.*, (1987) shows that the slight coloration observed in the jets between 10000 and 25000 km may be explained by a population of sub-micronic particles of mass 10^{-15} - 10^{-13} g. It is proposed that this population of very small grains results from the fragmentation of the dust particles inside the jet and that the gas released during this process constitutes the diffuse source measured in CO in comet Halley and in H₂CO in comet Levy.

REFERENCES

- A'Hearn M.F., Hoban S., Birch P.V. *et al.* (1986) Cyanogen jets in comet Halley *Nature*, **324**, 649-651.
- Clairemidi J.*et al.* (1990a) Spectro-imagery of P/Halley'sinner coma *Astron. Astrophys.*, **231**, 235-240.
- Clairemidi J.*et al.* (1990b) Gaseous CN, C₂ and C₃ jets in the inner coma of comet P/Halley *Icarus*, **86**, 115-128.
- Cosmovici C.B. *et al.* (1988) Gas and dust jets in the inner coma of comet Halley *Nature*, **332**, 705-709.
- Crovisier J. (1991) Radio spectroscopy of comets : recent results and future prospects *ACM 91*, Abstract p. 45.
- Eaton N. (1984) Comet dust - Applications of Mie scattering *Vistas in Astronomy*, **27**, 111-129.
- Eberhardt P.. *et al.* (1987) The CO and N₂ abundance in comet P/Halley *Astron. Astrophys.*, **187**, 481-484.
- Keller H.U. *et al.* (1986) First Halley Multicolour Camera imaging results from Giotto *Nature*, **321**, 320-326.
- Massone L. (1985) Coma morphology and dust emission pattern of comet Halley *Adv. Space Res.*, **5**, **12**, 187-196.
- Mazets E.P. *et al.* (1987) Dust in comet P/Halley from Vega observations *Astron. Astrophys.*, **187**, 699-706.
- Mukai T *et al.* (1987) Complex refractive index ...deduced of comet P/Halley *Astron. Astrophys.*, **187**, 650-652.
- Sagdeev R.Z. *et al.* (1986) Television observations of comet Halley from Vega spacecraft *Nature*, **321**, 262-266.
- Schloerb H.P.*et al.* (1991) Sub-millimeter molecular line observations of comet Levy *ACM 91*, Abstract p. 187
- Suzuki B.*et al.* (1991) C₂ jets in recent comets *ACM 91*, Abstract p. 212.

OBSERVATIONS OF COMETARY PARENT MOLECULES WITH THE IRAM RADIO TELESCOPE.

P. Colom¹⁾, D. Despois²⁾, G. Paubert³⁾, D. Bockelée-Morvan¹⁾, J. Crovisier¹⁾

- 1) Observatoire de Paris, Section de Meudon, F-92195 Meudon, France
2) Observatoire de Bordeaux, BP 89, Avenue Pierre Sémirot, F-33270 Bordeaux, France
3) IRAM, Avenida Divina Pastora, 7, N.C., E-18012 Granada, Spain

Abstract

Several rotational transitions of HCN, H₂S, H₂CO and CH₃OH were detected in comets P/Brorsen-Metcalf 1989 X, Austin (1989c1) and Levy (1990c) with the IRAM 30-m radio telescope. This allows us to determine the production rates of these molecules and to probe the physical conditions of the coma.

OBSERVATIONS

Comets P/Brorsen-Metcalf 1989 X, Austin (1989c1) and Levy (1990c) were observed on September 2-7 1989, May 21-25 and August 26-31 1990, respectively, with the IRAM (Institut de Radio Astronomie Millimétrique) 30-m radio telescope at Pico Veleta (Spain). Three SIS mixer receivers were used simultaneously (85-115, 130-170 and 209-270 GHz). The spectrometers consisted in two banks of 128x100 kHz channels, two banks of 512x1 MHz channels, and an AOS (Acousto Optical Spectrometer) of 864 channels with a 505 MHz bandwidth.

RESULTS

The results concerning the detected species are summarized in the table. More details were (or will be) published by Bockelée-Morvan *et al.* (1990, 1991), Colom *et al.* (1990, 1992) and Crovisier *et al.* (1990, 1991).

HCN, H₂CO and H₂S production rates were derived from the observed line intensities using models treating the evolution of the excitation conditions from the collision dominated region (inner coma, collisions with H₂O, $s = 10^{-14} \text{ cm}^2$, $T_{\text{kin}} = 50 \text{ K}$) to the radiation dominated region (outer coma, IR excitation of the vibrational bands by the Sun). For CH₃OH, we assume LTE and used a rotational temperature of 30 K, in agreement with the observed relative line intensities. For the density distribution we assumed isotropic outflow from the nucleus at constant velocity (0.8 km s⁻¹) and took into account the molecular lifetime against photodissociation.

Hydrogen cyanide

The J(1-0) 89 GHz and J(3-2) 266 GHz rotational transitions of HCN were marginally detected in comet P/Brorsen-Metcalf, whereas clear detections were obtained in comet Austin (1989c1) and Levy (1990c). HCN seems to be more abundant by at least a factor of two in periodic comets (P/Halley, P/Brorsen-Metcalf) than in non periodic comets (Wilson, Austin, Levy). This suggests a chemical difference between periodic and new comets. The very low upper limit obtained on the relative abundance of HC₃N (5×10^{-5}) shows that it is not the major lacking source of CN radicals.

Formaldehyde

The observations of the H₂CO 3₁₂-2₁₁ transition at 226 GHz in comet P/Brorsen-Metcalf gave only a marginal detection ($S/N = 4$). The 226 GHz line was easily detected in comet Austin ($S/N \approx 10$) and in comet Levy ($S/N = 8$). Observations of the 5₁₅-4₁₄, 2₁₂-1₁₁, 3₀₃-2₀₂, 3₂₂-2₂₁ and 3₂₁-2₂₀

lines were negative, in agreement with excitation models (Bockelée-Morvan and Crovisier 1992). Production rates inferred in the assumption of release from the nucleus show that formaldehyde is a minor component of the nucleus with an abundance relative to water which ranges from 4×10^{-4} in Levy to 3×10^{-3} in P/Brorsen-Metcalf (Colom *et al.* 1992). These abundances are at least an order of magnitude less than the Vega IKS value for P/Halley (4%; Combès *et al.* 1988).

Hydrogen sulfide

The observation of $\text{H}_2\text{S} 1_{10}-1_{01}$ at 169 GHz in comet Austin led to the first detection of hydrogen sulfide in a comet. In addition to the 169 GHz ortho line, the $2_{20}-2_{11}$ para line of H_2S at 217 GHz was detected in comet Levy. H_2S is a minor component, with a relative abundance of 2×10^{-3} . The other sulfur-bearing molecules observed (SO_2 , OCS, H_2CS) are less abundant than hydrogen sulfide. (Crovisier *et al.* 1991.)

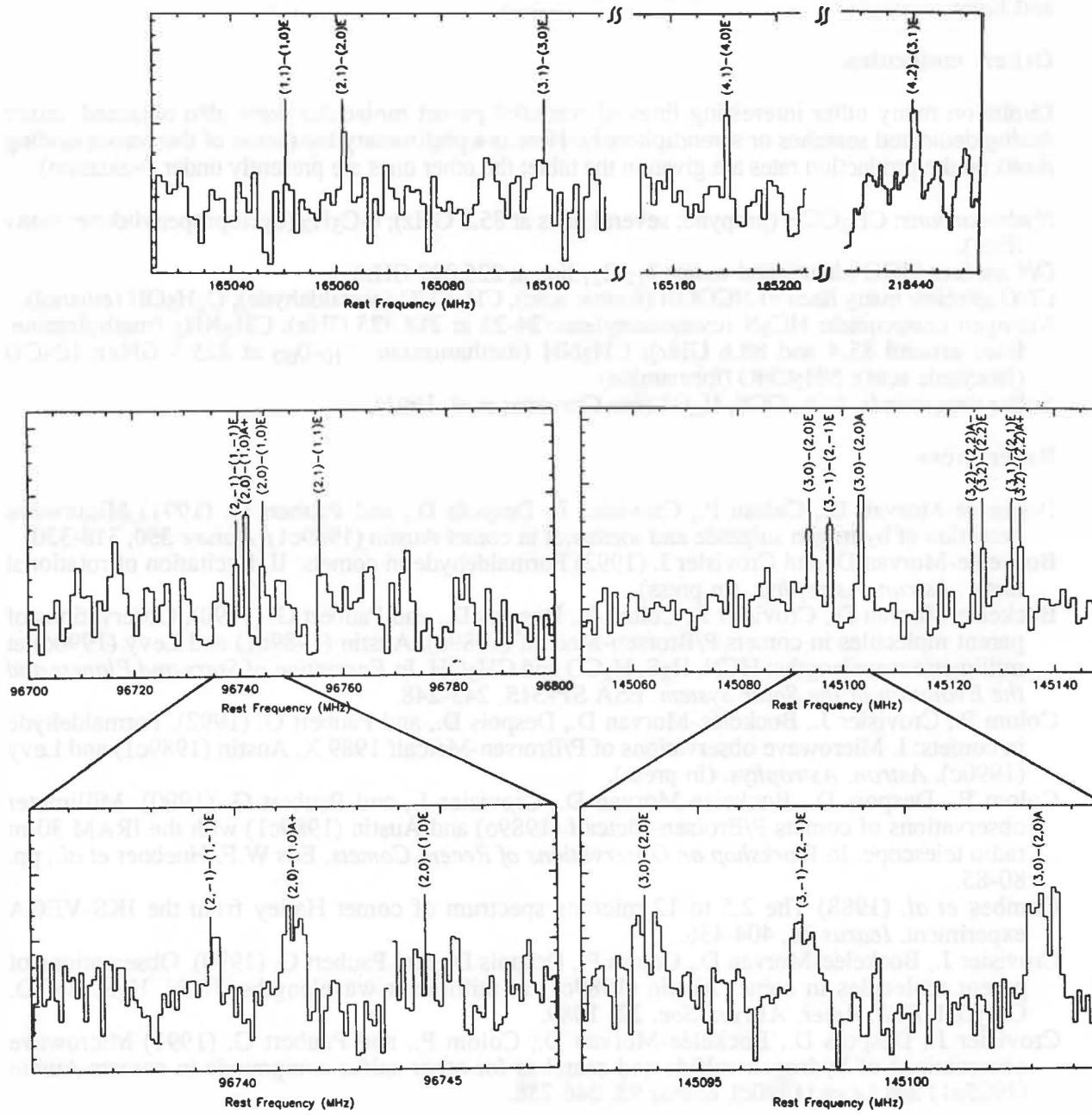
Production rates and abundances.

Comet and molecule	Date	Q a) [s^{-1}]	$Q/Q[\text{H}_2\text{O}]$ b)
<i>P/Brorsen-Metcalf (1989 X)</i>			
HCN J(1-0)	89/09/04-07	4.5×10^{26}	1.8×10^{-3}
$\text{H}_2\text{CO} 3_{12}-2_{11}$	89/09/04-07	7.6×10^{26}	3.0×10^{-3}
<i>Austin (1989cI)</i>			
HCN J(1-0)	90/05/23	2.0×10^{25}	5.0×10^{-4}
$\text{H}_2\text{CO} 3_{12}-2_{11}$	90/05/21-25	4.6×10^{25}	1.1×10^{-3}
$\text{H}_2\text{S} 1_{10}-1_{01}$	90/05/24-25	1.1×10^{26}	2.7×10^{-3}
$\text{CH}_3\text{OH} (3,0)-(2,0)\text{A}$	90/05/25	2.0×10^{26}	5.0×10^{-2}
<i>Levy (1990c)</i>			
HCN J(1-0)	90/08/29	6.6×10^{25}	2.6×10^{-4}
$\text{H}_2\text{CO} 3_{12}-2_{11}$	90/08/26-30	1.0×10^{26}	4.0×10^{-4}
$\text{H}_2\text{S} 1_{10}-1_{01}$	90/08/30-31	5.0×10^{26}	2.0×10^{-3}
$\text{CH}_3\text{OH} (3,0)-(2,0)\text{A}$	90/08/27	1.8×10^{27}	7.2×10^{-3}
$\text{HC}_3\text{N J}(24-23)$	90/08/27	$< 1.2 \times 10^{25}$	$< 5.0 \times 10^{-5}$
$\text{SO}_2 7_{17}-6_{06}$	90/08/29	$< 6.0 \times 10^{26}$	$< 2.5 \times 10^{-3}$
OCS J(18-17)	90/08/28	$< 5.0 \times 10^{26}$	$< 2.0 \times 10^{-3}$
$\text{H}_2\text{CS} 4_{14}-3_{13}$	90/08/28	$< 2.5 \times 10^{26}$	$< 1.0 \times 10^{-3}$

a Assuming a parent distribution.

b $Q[\text{H}_2\text{O}]$ from OH 18-cm observations: $2.5 \times 10^{29} \text{ s}^{-1}$ for P/Brorsen-Metcalf and Levy, $4.0 \times 10^{28} \text{ s}^{-1}$ for Austin.

observed with a 1-MHz resolution. It is 22.1 MHz at 10 GHz, which corresponds to the peak frequency of the 10-GHz emission. The peak frequency of the 10-GHz emission is 10.0 GHz, which corresponds to the peak frequency of the 10-GHz emission.



The spectra of methanol (CH_3OH) observed with the IRAM 30-m radio telescope in comet Levy (1990c). The upper panels show spectra observed with a 1-MHz spectral resolution. The lower panel shows parts of the spectra around 97 GHz and 145 GHz observed with a 100-kHz resolution.

Methanol

CH_3OH was detected in comet Austin through its $J(2-1) \Delta K = 0$ transitions at 97 GHz and its $J(3-2) \Delta K = 0$ transitions at 145 GHz. It was the first detection of methanol in a solar system body. A dozen of CH_3OH lines were detected in comet Levy, as is shown in the Figure. Methanol is a substantial component of the nucleus, with a relative abundance of the order of 1% in comets Austin and Levy.

Other molecules.

Limits on many other interesting lines of potential parent molecules were also obtained, either during dedicated searches or serendipitously. Here is a preliminary list (some of the corresponding limits on the production rates are given in the table; the other ones are presently under evaluation):

Hydrocarbons: CH_3CCH (propyne; several lines at 85.3 GHz); $c\text{-C}_3\text{H}_2$ (cyclopropenylidene: many lines).

OH species: HDO (deuterated water: $3_{12}-2_{21}$ line at 225.897 GHz).

CHO species: many lines of HCOOH (formic acid), CH_3CHO (acetaldehyde), $\text{C}_2\text{H}_5\text{OH}$ (ethanol).

Nitrogen compounds: HC_3N (cyanoacetylene: 24-23 at 218.325 GHz); CH_3NH_2 (methylamine: lines around 85.4 and 88.6 GHz); CH_2NH (methanimine: $1_{10}-0_{00}$ at 225.5 GHz); HNCO (isocyanic acid); NH_2CHO (formamide).

Sulfur compounds: SO_2 , OCS, H_2CS (see Crovisier et al. 1991).

References

- Bockelée-Morvan D., Colom P., Crovisier J., Despois D., and Paubert G. (1991) Microwave detection of hydrogen sulphide and methanol in comet Austin (1989c1). *Nature* **350**, 318-320.
- Bockelée-Morvan D., and Crovisier J. (1992) Formaldehyde in comets: II. Excitation of rotational lines. *Astron. Astrophys.* (in press).
- Bockelée-Morvan D., Crovisier J., Colom P., Despois D., and Paubert G. (1990). Observations of parent molecules in comets P/Brorsen-Metcalf (1989o), Austin (1989c1) and Levy (1990c) at millimetre wavelengths: HCN, H_2S , H_2CO and CH_3OH . In *Formation of Stars and Planets and the Evolution of the Solar System*. ESA SP-315, 243-248.
- Colom P., Crovisier J., Bockelée-Morvan D., Despois D., and Paubert G. (1992). Formaldehyde in comets: I. Microwave observations of P/Brorsen-Metcalf 1989 X, Austin (1989c1) and Levy (1990c). *Astron. Astrophys.* (in press).
- Colom P., Despois D., Bockelée-Morvan D., Crovisier J., and Paubert G. (1990). Millimeter observations of comets P/Brorsen-Metcalf (1989o) and Austin (1989c1) with the IRAM 30-m radio telescope. In *Workshop on Observations of Recent Comets*. Eds W.F. Huebner et al., pp. 80-85.
- Combes et al. (1988) The 2.5 to 12 microns spectrum of comet Halley from the IKS-VEGA experiment. *Icarus* **76**, 404-436.
- Crovisier J., Bockelée-Morvan D., Colom P., Despois D., and Paubert G. (1990). Observations of parent molecules in comet Austin (1989c1) at millimeter wavelengths: HCN, H_2S , H_2CO , CH_3OH . *Bull. Amer. Astron. Soc.* **22**, 1089.
- Crovisier J., Despois D., Bockelée-Morvan D., Colom P., and Paubert G. (1991) Microwave observations of hydrogen sulfide and searches for other sulfur compounds in comets Austin (1989c1) and Levy (1990c). *Icarus* **93**, 246-258.

RADIO SPECTROSCOPY OF COMETS: RECENT RESULTS AND FUTURE PROSPECTS.

J. Crovisier

Observatoire de Paris, Section de Meudon, F-92195 Meudon, France

Abstract

We review the recent results of cometary radio spectroscopy (since 1988). Successful observations with several instruments yielded the detection of new molecular species, the simultaneous investigations of several rotational transitions of the same molecule, and mapping of the coma.

INTRODUCTION

Since the observations of comet Kohoutek in 1973 and several pioneering attempts before, cometary radio spectroscopy has been a long series of hopes and frustrations. Just after the P/Halley campaign (recently reviewed by Crovisier and Schloerb 1991), the only firm successes were the observations of the OH lines at 18 cm in many comets and the confirmed detection of HCN at 3 mm in comet Halley. However, since that time, significant new results were obtained with the detection of new molecules and new molecular transitions. This announces a new start of cometary radio spectroscopy, not only due to the recent apparition of bright targets (P/Brorsen-Metcalf 1989 X, Austin 1989c1, Levy 1990c), but also to the opening of higher-frequency windows to large instruments.

Spectroscopic radio observations performed on recent comets are listed in Table 1. OH observations at 18 cm were conducted at several places and a daily monitoring was made at the Nançay radio telescope. Centimeter observations were made at the VLA (P/Brorsen-Metcalf) and at Effelsberg (comet Austin). Millimeter observations were made at IRAM, FCRAO, Nobeyama and SEST. Submillimeter observations were conducted at CSO. Interferometric observations at millimeter wavelengths (HCN 1-0 line) were also attempted on comet Austin at BIMA and IRAM.

The OH observations provided a follow-up of the gas production rates for all comets (Bockelée-Morvan *et al.* 1990, 1991). For comet Levy 1990c, the observing conditions were exceptionally good: high inversion of the OH ground state Λ -doublet of OH from July to September, and at the beginning of September, the cometary OH maser amplified an enhanced continuum background due to the crossing of the galactic plane by the comet. At that moment, the OH radio lines reached the record value of 1.5 K in antenna temperature. The high signal-to-noise ratio permitted (i) the detection of Zeeman effect and the measurement of the cometary magnetic field; (ii) the observation of the OH satellite lines at 1721 and 1612 MHz, revealing hyperfine anomalies due to second-order effects in the excitation mechanism; (iii) the mapping of the OH coma and the probing of the OH distribution (Bockelée-Morvan *et al.* 1991).

NEW MOLECULAR LINES

The highlights of the millimeter and submillimeter observations were the detections of the rotational lines of several molecular species: new transitions for the already known species HCN and H₂CO, and the detection of the new species H₂S and CH₃OH. Since these results are presented at this conference by Colom *et al.* (1991) for the IRAM observations and by Schloerb and Ge (1991) for the CSO observations, we will only comment some points of general interest.

Formaldehyde was unambiguously detected with high signal-to-noise ratio in comets Austin and

Table 1: Summary of spectroscopic radio observations of recent comets.

Comet Date	Telescope ^{a)}	Wave- length	Molecules ^{b)}	Investigators or reference ^{c)}
P/Brorsen-Metcalf 1989 X				
890804-891031	Nançay	18 cm	OH	Bockelée-Morvan <i>et al.</i> 1990
890901-890905	FCRAO	3 mm	HCN	Schloerb and Ge
890902-890907	IRAM 30-m	1-3 mm	HCN, H ₂ CO	Colom <i>et al.</i> 1991
890902-890911	VLA	6 cm	H ₂ CO, HC ₃ N	Snyder <i>et al.</i> 1990
890908-890909	Green Bank 140'	18 cm	OH	Schloerb
Okazaki-Levy-Rudenko 1989 XIX				
891003-891202	Nançay	18 cm	OH	Bockelée-Morvan <i>et al.</i> 1990
	Green Bank 140'	18 cm	OH	Schloerb
	FCRAO	3 mm	HCN	Schloerb and Ge
891105	IRAM 30-m	1 mm	H ₂ CO	Colom <i>et al.</i> 1991
Aarseth-Brewington 1989 XXII				
891208-891230	Nançay	18 cm	OH	Bockelée-Morvan <i>et al.</i> 1990
Austin 1989c1				
900215-900614	Nançay	18 cm	OH	Bockelée-Morvan <i>et al.</i> 1990
900401-900430	Nobeyama	3 mm	HCN, HC ₃ N, CH ₃ CN	Irvine, Kawaguchi
900402	IRAM 30-m	1-3 mm	HCN, H ₂ CO	Colom <i>et al.</i> 1991
900402-900403	FCRAO	3 mm	HCN	Schloerb and Ge
900404-900531	Dwingeloo 25-m	18 cm	OH	Tacconi-Garman 1990
900406-900520	Green Bank 140'	18 cm	OH	Schloerb
900411-900518	Effelsberg	1-6 cm	OH, H ₂ CO, NH ₃ , CH ₃ OH	Walmsley <i>et al.</i>
900412-900414	Onsala	3 mm	HCN	Ekelund and Winnberg
900424-900430	FCRAO, BIMA	3 mm	HCN	Palmer <i>et al.</i> 1990
900521-900525	IRAM 30-m	1-3 mm	HCN, H ₂ CO, H ₂ S, CH ₃ OH	Colom <i>et al.</i> 1991
900525-900528	IRAM interfero.	3 mm	HCN	Delannoy and Wink
900528-900601	CSO	1 mm	H ₂ CO ?	Schloerb and Ge
Levy 1990c				
900616-900930	Nançay	18 cm	OH	Bockelée-Morvan <i>et al.</i> 1991
900826-900831	IRAM 30-m	1-3 mm	HCN, H ₂ CO, H ₂ S, CH ₃ OH	Colom <i>et al.</i> 1991
900829-900901	CSO	1 mm	HCN, H ₂ CO, CH ₃ OH	Schloerb and Ge 1991
900927	SEST	1 mm	HCN	Winnberg 1990

a) BIMA: Berkeley-Illinois-Maryland Array; CSO: Caltech Submillimeter Observatory; FCRAO: Five College Radio Astronomical Observatory; IRAM: Institut de Radio Astronomie Millimétrique; SEST: Swedish-ESO Submillimetre Telescope; VLA: Very Large Array.

b) Detections are indicated in boldface.

c) Private communication from the investigators when no year is given for the reference.

Levy through its $2_{12}-1_{11}$ transition. This is a firm confirmation of the presence of this molecule in comets, which was already observed at $3.56\text{ }\mu\text{m}$ in P/Halley (Combes *et al.* 1988) but could not be retrieved in other cometary infrared spectra, and for which the 6 cm line was observed in P/Halley at the VLA, but with a poor signal-to-noise ratio (Snyder *et al.* 1989). In addition, the $5_{15}-4_{14}$ line was observed at the CSO in comet Levy. The space distribution of H_2CO , from both CSO and IRAM observations, might not be that of a parent molecule, but rather that of a distributed source. This renders difficult the evaluation of the H_2CO abundance. For the recent comets, this abundance is in any case lower than 1%, which is smaller than what was derived for comet P/Halley (4%). In a re-analysis of the VLA observation of H_2CO in P/Halley of Snyder *et al.* (1989), Bockelée-Morvan and Crovisier (1991) failed to reconcile the 6 cm line intensity with a believable formaldehyde production rate.

Hydrogen cyanide could be observed in several rotational transitions, some of the observations being simultaneous (or nearly simultaneous): $J=1-0$ at IRAM and Nobeyama, $3-2$ at IRAM, CSO and SEST, $4-3$ at CSO. As anticipated by excitation models, the $3-2$ line is very strong, so that reliable mapping of the line brightness distribution could be performed at the CSO. This line is apparently optically thick, and radiative transfer should be taken into account in the analysis. After the observations of this molecule in P/Halley, it was concluded that the HCN abundance could not totally explain the CN production rate, and that another source (dust grains or other parent molecules?) should be present. The recent observations, which constrain the excitation models, and will lead to improved estimations of the HCN abundances, may help resolving this problem.

The methanol observations are very promising, because several rotational transitions could be measured simultaneously with the same instrumental beam. This gives unique information on the rotational distribution of the molecule. We are thus provided with a way to probe the excitation conditions of the inner coma. From first analysis, the apparent temperature is rather cold (about 30 K), suggesting a relaxed rotational distribution. The only other parent molecule for which such information was obtained, up to now, was the water molecule for which the relative intensities of the rovibrational lines in the $2.7\text{ }\mu\text{m}$ band were observed from the KAO. The CH_3OH abundance retrieved by radio observations is relatively high: 1% relative to water. This suggests that methanol should have detectable vibrational bands in the infrared. Indeed, the $3.52\text{ }\mu\text{m}$ emission feature observed in several comets could be attributed to the v_3 band of CH_3OH (Hoban *et al.* 1991). The v_2 and v_9 bands should also contribute significantly to the $3.4\text{ }\mu\text{m}$ emission, as well as the v_1 band to the $2.9\text{ }\mu\text{m}$ cometary emission.

The detection of hydrogen sulfide gives insights upon the nature of sulfur depositories in comets. The inferred abundance of H_2S is 0.2% relative to water. That of HCN is about 0.1%. This shows how radio spectroscopy may be sensitive to minor components of cometary atmospheres.

PROSPECTS

Despite many efforts, centimetric observations were less successful than the observations at shorter wavelengths. CH_3OH , conspicuous everywhere in the millimeter range, was undetected at cm wavelengths at Effelsberg. This is also the case for H_2CO at 6 cm , H_2O and NH_3 at 1 cm , OH at 5 cm . This is in agreement with our present knowledge of molecular excitation and abundances in comets.

The millimeter-submillimeter instruments now in use typically probe the first few thousand km of the coma. In this region, molecules are not yet at fluorescence equilibrium, but evolve between rotational relaxation, radiative excitation, and collisions. Excitation models are still fairly primitive and rely on several uncertain parameters such as kinetic temperatures and collision rates. It may be expected that important constraints on these models will be obtained from the derivations of molecular rotational distributions.

With the large millimeter and submillimeter antenna now in use, the beams may be as small as 10''. In contrast with optical observations, there is no way to check the real position of the comet. Therefore, the radio observer must rely, more than ever, on accurate ephemeris and he is strongly dependent upon his astrometrist colleagues for the rapid diffusion of updated orbital elements.

The obvious advantage of radio spectroscopy is that it allows unambiguous identification of the detected features, in contrast with low-resolution infrared spectroscopy and *in situ* mass spectroscopy investigations. Recent observations proved its ability to detect minor species such as HCN or H₂S, and complex molecules such as the 6-atom methanol molecule. It is very likely that several other minor and/or complex constituents are still to be found in cometary atmospheres, and that radio spectroscopy will help us unravelling their nature.

References

- Bockelée-Morvan D., Colom P., Crovisier J., Gérard E., and Bourgois G. (1991) Observations of comet Levy (1990c) with the Nançay radio telescope. In *Asteroids, Comets, Meteors 1991* (this volume).
- Bockelée-Morvan D., and Crovisier J. (1991) Formaldehyde in comets: II. Excitation of rotational lines. *Astron. Astrophys.* (in press).
- Bockelée-Morvan D., Crovisier J., Gérard E., and Bourgois G. (1990) OH radio observations of comets P/Brorsen-Metcalf (1989o), Okazaki-Levy-Rudenko (1989r), Aarseth-Brewington (1989a1) and Austin (1989c1) at the Nançay radio telescope. In *Workshop on Observations of Recent Comets*. Eds W.F. Huebner *et al.*, pp. 75-79.
- Colom P., Despois D., Paubert G., Bockelée-Morvan D., and Crovisier J. (1991) Observations of cometary parent molecules with the IRAM radio telescope. In *Asteroids, Comets, Meteors 1991* (this volume).
- Combes *et al.* (1988) The 2.5 to 12 microns spectrum of comet Halley from the IKS-VEGA experiment. *Icarus* **76**, 404-436.
- Crovisier J., and Schloerb F.P. (1991) The study of comets at radio wavelengths. In *Comets in the Post-Halley Era*. Eds R.L. Newburn *et al.*, Kluwer, pp. 149-173.
- Hoban *et al.* (1991) A tentative identification of methanol as the progenitor of the 3.52 μm emission feature in several comets. *Icarus* **93**, 122-134.
- Palmer P. *et al.* (1990) Simultaneous imaging of optical CN lines and radio HCN lines in comet Austin. In *Workshop of Observations on Recent Comets*. Eds W.F. Huebner *et al.*, pp. 40-43.
- Schloerb F.P., and Ge W. (1991) Sub-millimeter molecular line observations of comet Levy. In *Asteroids, Comets, Meteors 1991* (this volume).
- Snyder L.E., Palmer P., and de Pater I. (1989) Radio detection of formaldehyde emission from comet Halley. *Astron. J.* **97**, 246-253.
- Snyder L.E., Palmer P., and de Pater I. (1990) VLA searches for formaldehyde and cyanoacetylene emission from comet P/Brorsen-Metcalf (1989o). In *Workshop on Observations of Recent Comets*. Eds W.F. Huebner *et al.*, pp. 86-91.
- Tacconi-Garman L.E. (1990) Observations of the 18-cm OH absorption from comet Austin (1990c1). *Astron/NFRA Newsletter* No 2.
- Winnberg A. (1990) Comet Levy detected by SEST. *The Messenger* **62**, 66-67.

THE GREAT ASTEROID NOMENCLATURE CONTROVERSY OF 1801

Clifford J. Cunningham

With the almost complete neglect of 19th century asteroid research by professional historians of science, it is scarcely surprising that great gaps exist in our knowledge of that important field. This paper will focus on one of the many issues that faced the astronomers involved with the study of the first asteroid- what should it be named? This seemingly innocuous issue assumed great importance because many believed the object discovered by Giuseppe Piazzi at Palermo Observatory to be the eighth primary planet of the solar system.

Within a few months of discovering the object on Jan. 1, 1801, Piazzi named the object Ceres Ferdinandea, to honor both the patron goddess of Sicily and his own patron, King Ferdinand of Naples and Sicily. The first hint of trouble came in a letter from his friend Barnaba Oriani, dated July 25, 1801.

"I must tell you that the name Hera or Juno has been given universally by all of Germany, for which it will be very difficult now to rename it Ceres." Piazzi testily replied on Aug. 25: "If the Germans think they have the right to name somebody else's discoveries they can keep calling the new star the way they want, for we will always call it Ceres. I will be glad if you and your colleagues will do the same."

It is a remarkable fact that the first asteroid was actually given a name 15 years before it was discovered. In the early 1780's a young baron, Franz von Zach, began searching for an object between Mars and Jupiter. Even though he was initially unsuccessful, his patron, the Duke of Gotha, was so impressed that he dubbed the unseen object Hera, the Greek form of Juno. Thus, when the object of von Zach's search was revealed, it automatically was given the name assigned to it by the Duke. The stage was thus set for a battle royal amongst the astronomers of Europe, a battle largely played out in the world's only astronomical journal, the *Monthly Correspondence*. Fittingly, it was edited by Baron von Zach.

As the Baron himself wrote in the MC: "The Greek name Hera is preferred to the Latin name Juno, because 1) the latter has already been ascribed to the planet Venus; 2) Hera is the name of a city in Sicily, through which the memory of the discoveries made on this island and the glorious name of the discoverer of this eighth primary

planet will be contained and immortalized."

But some people were not content with a choice between Hera and Ceres. An unnamed source suggested the name Vulkan, because it "would not be improper to give the god who forged the weapons of Achilles a place in the sky next to the god of war, the husband of Venus next to her lover." A certain Dr. Reimarus in Hamburg suggested the name Cupido, another lover of Venus. "Others believe that the name Cupido is also fitting because the name is associated with the idea of blindness. The new planet appears only as a magnitude eight star and cannot be seen with the naked eye."

Meanwhile, in France, the object was known as "La planete Piazzi". "I will never agree," Joseph La Lande wrote to von Zach in 1801, "to remove from this planet the name of my pupil Piazzi and replace it with Ceres because the name means nothing to me." Even so, the most important person in France agreed with the Germans. "Napoleon would have preferred the name Juno," Pierre Laplace wrote to von Zach, "instead of Ceres. Regarding this, I agree. It is natural to put Juno close to Jupiter."

Thus, a consensus was building for the adoption of the name Hera or Juno. Piazzi decided it was time to fight back, and he did so with an acerbic attack published in the MC. "I've noted in your journal the desire of a few to give this new planet the name Juno instead of Ceres. I trust that these astronomers, who are peaceful people, will never consent to having their deities called the name of a goddess as anxious, jealous and vindictive as Juno. Jupiter finally chased her from the sky; in her place he had Ceres appear, who has so much more right to the homage of mankind."

This turned the tables in his favor. Johann Bode, who been in the Juno camp, switched sides. "I accept with much pleasure the name Ceres Ferdinandea. You discovered it in Taurus, and it has been found again in Virgo, the Ceres of ancient times. These two constellations are the symbol of Agriculture. The chance is very singular."

In England, the Astronomer Royal Nevil Maskelyne joined the chorus applauding Piazzi's choice. "You had the right to name the planet, which you discovered, and you paid due homage to your King, patron of the Arts and Sciences and founder of your observatory. I will call, and it will be called in England, Ceres Ferdinandea."

Von Zach also gracefully agreed to accept Piazzi's choice. "Since Piazzi has baptized his own child and named it Ceres Ferdinandea, which is entirely within his right as the discoverer, we on our part also subscribe to this fitting designation with genuine pleasure."

Not surprisingly, Piazzi himself had the last word.
"Being the first in the discovery of this new planet, I thought to have the full right to name it in the most convenient way to me, like something I own. Thankful to my master, thankful to the Sicilian nation, willing to maintain a certain coherence with the other planetary names, it looked right to me to name it Ceres Ferdinandea. I will always use the name Ceres Ferdinandea, nor by giving it another name will I suffer to be reproached for ingratitude towards Sicily and its King, who with so much zeal, protects the sciences and arts, and without whose favor, perhaps we may never had arrived at this discovery. It is not adulation, but tribute, right and fair homage."

This and many other asteroid-related controversies will be examined in more depth in the forthcoming book *The Asteroid Pioneers: 19th Century Asteroid Research*.

Clifford J. Cunningham
250 Frederick St., Apt. 1707
Kitchener,
Ontario N2H 2N1
Canada

THE ORBITAL EVOLUTION OF REAL ASTEROIDS NEAR THE 4:1 MEAN-MOTION RESONANCE WITH JUPITER

M. Dahlgren¹, G. Hahn^{1,2}, C.-I. Lagerkvist¹ and M. Lundström¹

¹Astronomiska Observatoriet, Box 515, S-75120 Uppsala, Sweden.

²Department of Astronomy, The University, Manchester M13 9PL, England, U.K.

ABSTRACT

Numerical integrations of the orbits of ten asteroids with osculating elements near the 4:1 mean-motion resonance with Jupiter have been performed over 200,000 years into the future. A variety of orbital evolutions was found, depending on the start values of the semi-major axis. The orbit of asteroid 1983 RJ₄, which lies almost exactly at the resonance centre, experiences large variations in eccentricity, evolving into an Earth-crosser on a time-scale of a few 10⁴ years. This makes this region a potential source for Apollo objects and meteoritic material, although the width of the resonance region in semi-major axis seems to be very narrow.

INTRODUCTION

In this study we intend to investigate the 4:1 mean motion resonance with Jupiter as a possible source for Apollo asteroids and meteorites by following the orbital evolution of real asteroids. Yoshikawa (1989) investigated the 4:1 resonance using a semi-analytical model and numerical integrations in a simplified solar system model. Following a similar study on the 5:2 resonance (Hahn et al., 1991) we examine whether the asteroids presently near the 4:1 resonance – semi-major axis $a = 2.064$ AU – experience orbital evolutions which bring them into planet-crossing trajectories.

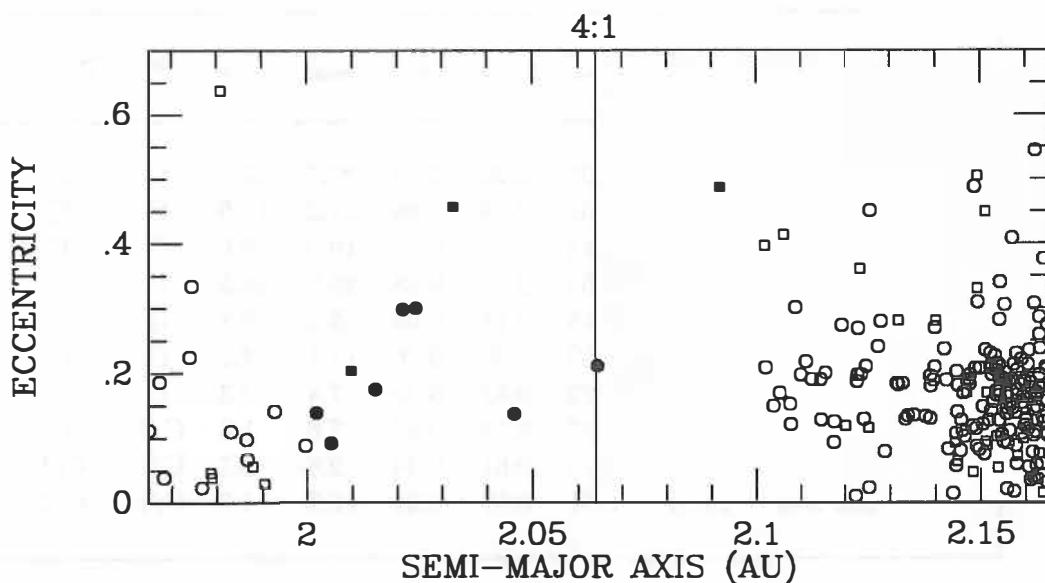


Figure 1: Distribution of asteroids near the 4:1 mean motion resonance. Circles designate unnumbered, numbered asteroids; the filled symbols represent the asteroids integrated in this paper.

The 4:1 resonance is located at the inner boundary of the asteroid belt, where also the secular resonances ν_6 and ν_{16} are situated, making it a complex region. These secular resonances influence the orbital evolution on timescales of the order of some 10^6 years (see e.g. Froeschlé and Scholl, 1989).

We selected orbits of both numbered and unnumbered asteroids, taken from the Minor Planet Centre orbital database, in the range $2.0 < a < 2.1$ AU. (See filled symbols in Figure 1.) No variations of the elements have been considered, implying larger uncertainties for the orbital elements of the unnumbered asteroids. Nonetheless, the results should be indicative for the orbital behaviour and it is planned to continue this study with further integrations of both varied and fictitious orbits for those asteroids which showed large orbital variations.

CALCULATIONS

In our calculations we numerically integrate the equations of motion of the planets and the asteroids simultaneously, using the 15th order RADAU integrator (RA15) by Everhart (1985). As described in detail in Hahn et al. (1991), a solar system model which takes into account the perturbations due to all planets except Mercury and Pluto was used, and the integrations have been performed over 200,000 years into the future.

RESULTS

The results are summarised in Table 1, where the minimum and maximum values for the semi-major axes, eccentricities and inclinations are shown. The behaviour of the critical argument $\sigma = (4\lambda_j - \lambda - 3\tilde{\omega})$, $\tilde{\omega} - \tilde{\omega}_j$, the approximate resonance arguments $(\tilde{\omega} - \tilde{\omega}_s)$ for the ν_6 and $(\Omega - \Omega_j)$ for the ν_{16} secular resonances are also shown. The subscript j and s refer to Jupiter and Saturn respectively, no subscript refer to the asteroid, λ is the mean longitude and $\tilde{\omega}$ is the longitude of perihelion. In Figure 2 the evolution of the eccentricity for all asteroids is graphically summarized.

	Asteroid	a_{max}	a_{min}	e_{max}	e_{min}	i_{max}	i_{min}	σ	$\tilde{\omega} - \tilde{\omega}_j$	$\tilde{\omega} - \tilde{\omega}_s$	$\Omega - \Omega_j$
4276	Clifford	2.011	2.009	0.26	0.14	27.7	17.2	C	C	C	C
	1986 RM ₂	2.003	2.001	0.19	0.09	27.3	19.9	C	C	C	C
	1989 UK ₂	2.047	2.044	0.18	0.08	19.0	9.6	C	C	C	C
	5481 T-2	2.006	2.005	0.16	0.08	25.0	18.5	C	C	C	C
	1987 UV ₁	2.016	2.015	0.18	0.06	5.4	0.8	C	C	L	C
	3551	1983 RD	2.094	2.069	0.50	0.20	11.1	4.7	C	C	L
		1987 DA ₇	2.038	2.022	0.42	0.29	7.4	2.3	C	C	L
		1981 EJ ₃₀	2.091	1.997	0.54	0.30	7.6	1.8	C/L	C	L
3288	Seleucus	2.102	1.973	0.61	0.44	9.8	2.7	C/L	C/L	C	C
	1983 RJ ₄	2.091	1.965	0.59	0.20	12.2	4.6	C/L	C/L	C/L?	C

Table 1: Summary of the orbital evolution of the asteroids during 200,000 years. L means librating resonance argument and C a circulating one.

Below we discuss in some detail those asteroids which exhibit orbital evolutions of particular interest.

(3551) 1983 RD is at present an Amor asteroid. As can be seen from Figure 2, there is a clear secular trend of decreasing e , meaning that the orbit is evolving outwards, away from the Earth. This confirms and extends the results found by Milani et al., (1989), where (3551) is classed as an "Alinda" evolving into an "Eros".

1983 RJ₄, which is the only asteroid in our sample presently almost exactly at the resonance, (see Figure 1), experiences a very rapid increase in eccentricity and becomes Earth crossing after 50,000 years. Close encounters with Earth remove the asteroids from the 4:1 resonance 5,000 years later. The eccentricity remains high and 1983 RJ₄ is an Apollo asteroid until 120,000 years. The critical argument σ is librating with a slowly moving libration centre and $\omega - \omega_0$ librates when 1983 RJ₄ is in the 4:1 resonance.

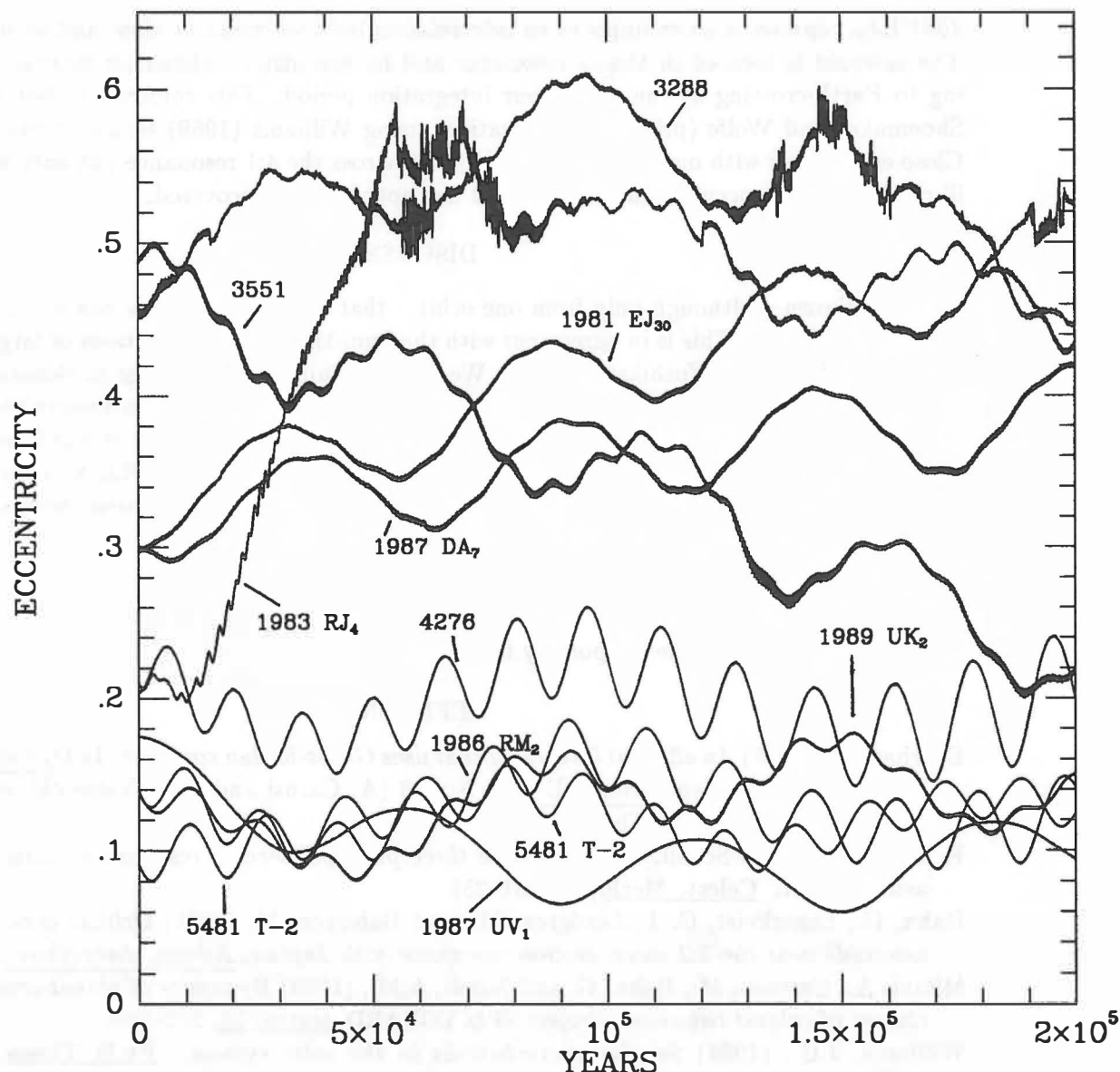


Figure 2: Evolution of the eccentricities over 200,000 years for all asteroids.

This rapid evolution into an Earth-crossing orbit may explain the lack of objects in this region. But we also conclude that the range in a , leading to such a dramatic orbital change, seems to be very narrow. In order to quantify this statement we need further studies of this orbit from an ensemble of slightly varied starting elements to determine the width of the resonant region. In the light of the results, attempts to improve the orbit of this asteroid should be made. The orbit is based on 6 observations only, from an arc of 27 days (MPC 10750) and the asteroid has not been recovered since its discovery apparition. The next favourable opposition would be in the end of 1992.

(3288) *Seleucus*, the second Amor asteroid in our sample, experiences two phases where σ is librating, but it also evolves into an Earth-crosser – Apollo type orbit, or as found by Milani et al. (1989) evolving from an "Alinda" into a "Geographos". Close encounters with the Earth are responsible for the removal from the resonance.

1981 *EJ₃₀* represents an example of an interrelation between mean motion- and secular resonances. The asteroid is located in the ν_6 resonance and its eccentricity shows an increasing trend, leading to Earth-crossing at the end of our integration period. This confirms earlier calculations by Shoemaker and Wolfe (priv. communication) using Williams (1969) secular perturbation theory. Close encounters with our planet move the orbit across the 4:1 resonance but only very short-lived librations of σ do occur. Also this asteroid has not yet been recovered.

DISCUSSION

We have shown – although only from one orbit – that large changes in e can occur on time-scales less than 10^5 years. This is in agreement with the semi-theoretical predictions of large variations on similar time-scales by Yoshikawa (1989). We also conclude that the range in element space, giving rise to large orbital variations, seems to be very narrow. The fact that we observe objects currently situated in this region of the asteroid belt could be an indication of their recent injection into such orbits. We also stress the necessity of improvement of the orbit of 1983 *RJ₄* and encourage further search for objects around the 4:1 resonance as potential candidates for parent bodies of Near-Earth asteroids and of meteorites.

ACKNOWLEDGMENT

G. Hahn acknowledges the support by the SERC.

REFERENCES

- Everhart, E. (1985) *An efficient integrator that uses Gauss-Radau spacings*. In Dynamics of Comets Their Origin and Evolution, IAU Coll. No. 83 (A. Carusi and G.B. Valsecchi, eds.), pp. 185–202. Reidel, Dordrecht, The Netherlands.
- Froeschlé, Ch. and Scholl, H. (1989) *The three principal secular resonances ν_5 , ν_6 and ν_{16} in the asteroid belt*, Celest. Mech., **46**, 231–251.
- Hahn, G., Lagerkvist, C.-I., Lindgren, M., and Dahlgren, M. (1991) *Orbital evolution studies of asteroids near the 5:2 mean motion resonance with Jupiter*, Astron. Astrophys., **246**, 603–618.
- Milani, A., Carpino, M., Hahn, G. and Nobili, A.M., (1989) *Dynamics of planet-crossing asteroids. classes of orbital behavior. Project SPACEGUARD*. Icarus, **78**, 212–269.
- Williams, J.G., (1969) *Secular perturbations in the solar system*, Ph.D. Thesis, University of California, Los Angeles.
- Yoshikawa, M., (1989) *A survey of the motions of asteroids in the commensurabilities with Jupiter*, Astron. Astrophys., **213**, 436–458.

INTERPLANETARY MAGNETIC FIELD CHANGES AND CONDENSATIONS IN COMET HALLEY'S PLASMA TAIL

Magda Delva, K. Schwingenschuh
Space Research Institute, Inffeldg. 12, 8010 Graz, Austria

ABSTRACT

In a time-dependent three dimensional MHD simulation for cometary plasmas, Schmidt-Voigt (1989) could observe the formation of condensations in the plasma tail after a 90 degree change in the interplanetary magnetic field (IMF) sweeping over the comet. We investigated the IMF measurements of the Vega SC in the vicinity of the comet Halley for 90 degree changes in the clock angle and studied the relation between them and optical observations of condensations in the plasma tail. For the time interval 24 Feb. 86 to 14 Mar. 86, we could not find a correlation between such changes and the release of condensations from the cometary head.

INTRODUCTION

In a paper by Schmidt-Voigt (1989), a time-dependent three dimensional MHD simulation of cometary plasmas was presented. It studied how features in the plasma tail of a comet change if conditions in the onstreaming solar wind are modified. Especially, 90 degree changes in the direction of the interplanetary magnetic field (IMF) were investigated. The author found the following effects on the modelled plasma tail: at the time where the magnetic discontinuity sweeps over the cometary head, the plasma density is locally enhanced due to the additional effect of the magnetic stresses $(\mathbf{B} \cdot \nabla) \mathbf{B}/(4\pi)$ from the original and modified magnetic field. Because of the draping of the original field in front of and the new IMF behind the discontinuity, the magnetic stresses of both fields act together and compress the plasma in front of the comet from two sides. A condensation is formed and subsequently transported down the tail (see Schmidt-Voigt (1989), fig. 11). Since the total pressure is cylindrically symmetric with respect to the tail axis and the total pressure gradient radially away from it is small, the condensation does not expand radially. Only the (also small) pressure gradient along the tail axis will allow a slow spreading of the plasma along it, while the condensation is moving down the tail. The condensation can be seen as enhancement of the column density, for several hours its brightness is even higher than that of the coma (see Schmidt-Voigt (1989), fig. 12) and therefore possible to be observed optically.

The Soviet SC Vega-1 and Vega-2 passed near Halley's comet on 6.3042 March 1986 in 8890 km, resp. 9.3042 March in 8030 km distance and almost continuously measurements of the interplanetary magnetic field have been recorded by the magnetometer experiment on board. The relative positions of the SC and the comet around closest approach are shown in Delva et al. (1991), fig. 1.

On the other hand, a big effort was made by the IHW to make different types of ground-based observations of the development of the comet. Especially many plates of the plasma tail were taken; they show several features like condensations moving down the tail, disruptions (so called disconnection events) of the whole tail, etc.

We therefore here investigated the available IMF data, measured directly in the neighbourhood of Halley's Comet, for 90 degree changes in the direction and looked if there is any correspondence between them and the plasma tail condensations observed.

ANALYSIS OF THE DATA

Magnetometer Data

Due to the compression of the onstreaming IMF in front of the comet, the angles of the B -vectors with the line Sun - Comet are aligned to 90 degree angles, so the cone angle plays no longer a role and the clock angle (clock angle = $\arctan(B_z/B_y)$ for B_x in direction to the Sun, B_z to ecliptic north) is the main parameter of the field when sweeping over the comet. In the time series of our IMF data, we searched for 90 degree changes in the clock angle for an interval of about 20 days around the closest approach of the Vega-1 SC (24 Feb. to 14 Mar. 1986). First, the data were averaged over intervals with only small changes, to accentuate the global behaviour of the clock angle. Changes between 75 and 105 degrees were picked out (to allow slight deviations from the sharp 90 degree limit). The time of occurrence of the change at the SC was corotated to the position of the comet by means of formula (1) of Delva et al. (1991), using the actual solar wind velocity as measured on the SC by the PLASMAG-instrument (M. Tatrallyay (1991)). For calculation of the corotation time, differences in ecliptic latitude were neglected: it was only looked when the same arc of Archimedean spiral that passed over the SC swept over the comet. For this time interval, the difference in ecliptic longitude between SC and comet is small and corotation times are short, up to about 36 hours at most.

The 90 degree changes in the clock angle are shown in Fig. 1, at the time they are expected to reach the comet, and in terms of numbers of events per day, with a total of 26 events. The changes on March 6 are shown only dashed, since the field there is influenced by the comet and due to the draping some events can be measured several times.

Observations of Comet Halley's Plasma Tail

A detailed list of plasma tail observations of Comet Halley was published by Celnik and Schmidt-Kaler (1987). These authors observed the plasma tail for a period of more than two months and identified series of condensations moving down the tail. From their time-distance data, they determined the time of release of the condensation from the cometary head (Celnik et al. (1988)). We took the data of emissions of condensations from their Table 4. They are here shown in Fig. 2 in terms of number of emissions per day, with a total of 31 events.

Representation of the Data

The IMF data show sometimes several subsequent changes as well as some more "quiet" times (Fig. 1). The same is the case for the release of condensations from the cometary head. Due to the slight inaccuracy introduced through the necessary corotation of the IMF features, a comparison of a single IMF clock angle change with a single condensation seems to be a risky task. For sake of correctness, we prefer to correlate only the general behaviour of both parameters: if more 90 degree changes occur over a short time (e.g. per day), we should expect more releases of condensations at that time. Therefore, we present the two datasets as histograms of events per day.

Fig. 1: Histogram of 90 degree changes in the clock angle of the IMF, measured by Vega-1 and corotated to comet Halley, in nr. of changes per day; total number of events: 26 (or 30 including the dashed ones).

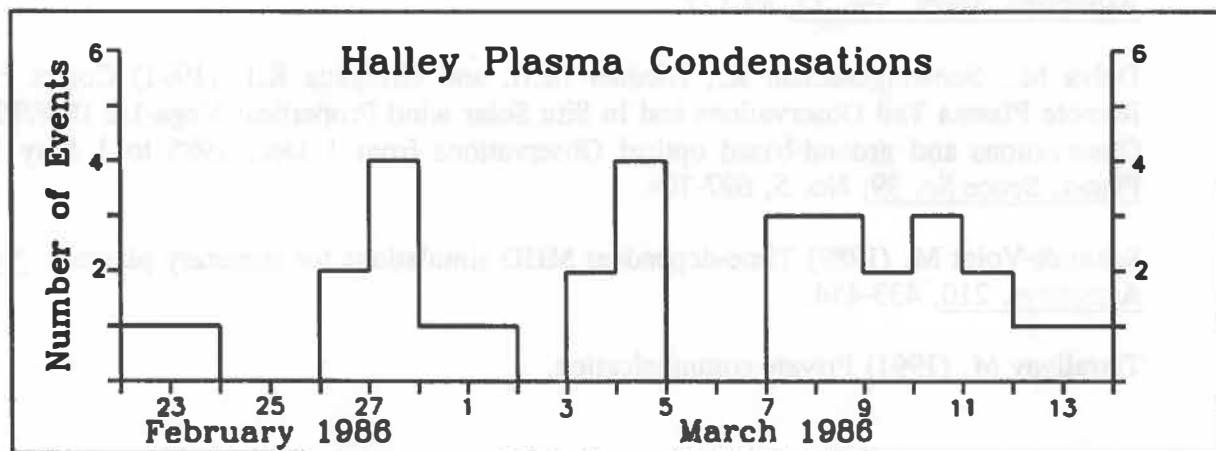
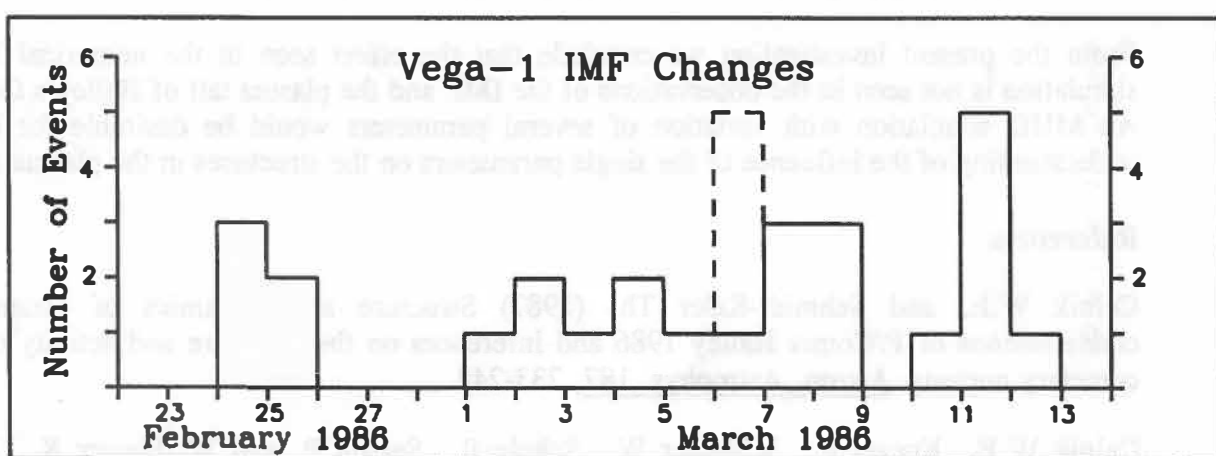


Fig. 2: Histogram of release of plasma clouds from the cometary head (after Celnik and Schmidt-Kaler (1987), Table 4) in nr. of releases per day; total number of events: 31.

RESULTS AND DISCUSSION

If a correlation as suggested by Schmidt-Voigt exists, then Fig. 1 and 2 should have similar shapes: a high number of 90 degree changes should coincide with a high number of releases of condensations. However, from Fig. 1 and 2 we can see no such correlation: sometimes many condensations are released without any 90 degree clock angle change (e.g. 27 Feb.). Sometimes the situation is vice versa (e.g. 11 Mar.) and on other days both types of events occur.

From the PLASMAG-experiment on the Vega SC of the same period, measurements of the solar wind velocity show a high spread stream with a sharp velocity enhancement up to 700 km s^{-1} to arrive at the Comet on 28 Feb., a slow decline to 400 km s^{-1} until 6 - 7 Mar. and again a steep enhancement to 600 km s^{-1} on 8 - 9 Mar. with decline until 12 Mar. (M. Tatrallyay (1991)). In Fig. 2, a higher number of releases can be seen on days of high solar wind velocity sweeping over the comet. This may indicate that the variation of the solar wind velocity plays a role in the development of plasma condensations.

From the present investigation we conclude that the effect seen in the numerical MHD simulation is not seen in the observations of the IMF and the plasma tail of Halley's Comet. An MHD simulation with variation of several parameters would be desirable for better understanding of the influence of the single parameters on the structures in the plasma tail.

References

- Celnik W.E. and Schmidt-Kaler Th. (1987) Structure and dynamics of plasma-tail condensations of P/Comet Halley 1986 and inferences on the structure and activity of the cometary nucleus. *Astron. Astrophys.* 187, 233-248.
- Celnik W.E., Koczet P., Schlosser W., Schulz R., Svejda P. and Weißbauer K. (1988) Structure and dynamics of plasma tail condensations of P/Comet Halley 1986. *Astron. Astrophys. Suppl. Ser.* 72, 89-127.
- Delva M., Schwingenschuh K., Niedner M.B. and Gringauz K.I. (1991) Comet Halley Remote Plasma Tail Observations and In Situ Solar wind Properties: Vega-1/2 IMF/Plasma Observations and ground-based optical Observations from 1 Dec. 1985 to 1 May 1986. *Planet. Space Sc.* 39, No. 5, 697-708.
- Schmidt-Voigt M. (1989) Time-dependent MHD simulations for cometary plasmas. *Astron. Astrophys.* 210, 433-454.
- Tatrallyay M. (1991) Private communication.

The Origin and Evolution of the Zodiacal Dust Cloud

S. F. Dermott, D. D. Durda, B. Å. S. Gustafson, S. Jayaraman, and Y. L. Xu

Department of Astronomy, University of Florida, Gainesville, FL 32611 USA

R. S. Gomes

Observatorio Nacional, Departamento de Astronomia, Rio de Janeiro, Brazil

P. D. Nicholson

Department of Astronomy, Cornell University, Ithaca, NY 14853 USA

ABSTRACT

We have now analysed a substantial fraction of the IRAS observations of the zodiacal cloud, particularly in the $25 \mu m$ waveband. We have developed a gravitational perturbation theory that incorporates the effects of Poynting-Robertson light drag (Gomes and Dermott, 1992). We have also developed a numerical model, the SIMUL model, that reproduces the exact viewing geometry of the IRAS telescope and calculates the distribution of thermal flux produced by any particular distribution of dust particle orbits (Dermott and Nicholson, 1989). With these tools, and using a distribution of orbits based on those of asteroidal particles with $3.4 \mu m$ radii whose orbits decay due to Poynting-Robertson light drag and are perturbed by the planets, we have been able to: (1) account for the inclination and node of the background zodiacal cloud observed by IRAS in the $25 \mu m$ waveband; (2) relate the distribution of orbits in the Hirayama asteroid families to the observed shapes of the IRAS solar system dustbands; and (3) show that there is observational evidence in the IRAS data for the transport of asteroidal particles from the main belt to the Earth by Poynting-Robertson light drag.

INTRODUCTION

We need to know the origin of the particles that constitute the zodiacal cloud: are these particles predominantly cometary or asteroidal? Interplanetary dust particles (IDPs) are collected in the Earth's upper atmosphere and returned to Earth for analysis. However, because these particles are collected only after atmospheric braking, all knowledge of their interplanetary orbits is lost. Fortunately, there are other sources of information.

The Infrared Astronomical Satellite (IRAS) has provided us with our most detailed view of the zodiacal cloud. It is now known that the cloud is not featureless: IRAS discovered circumsolar near-ecliptic bands of dust that appear to be related to the prominent Hirayama asteroid families (Dermott and Nicholson, 1989) suggesting that the asteroid belt as a whole is a significant source of IDPs. We consider that the high quality of the IRAS observations, particularly those in the $25 \mu m$ waveband, requires a new approach to the modeling of the

zodiacal cloud. The approach that was started at Cornell University by Dermott and Nicholson (1989), and is now being pursued at the University of Florida, is the subject of this short note.

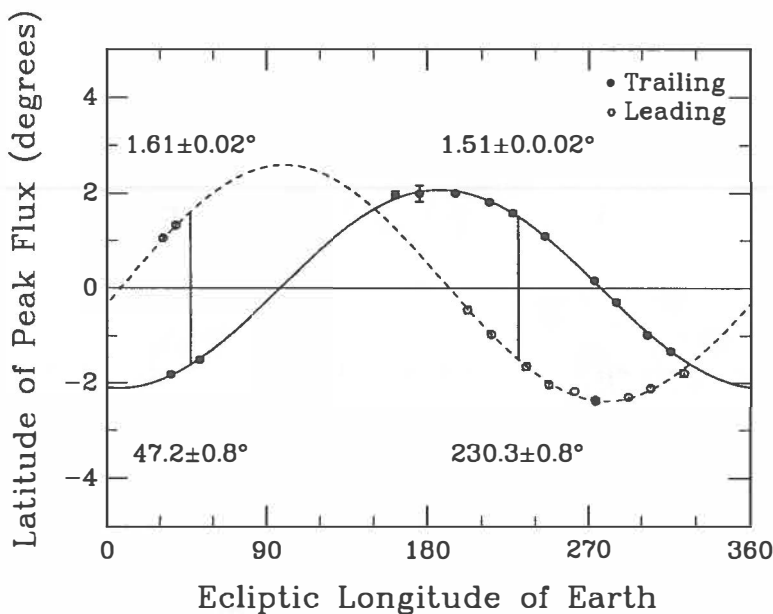


Figure 1. Variation of the ecliptic latitude of the peak background zodiacal emission with the position of the Earth observed by IRAS in the 25 micron waveband at an elongation angle of 90 degrees in either the leading or trailing directions. The numbers and vertical lines refer to the inclinations and the ascending and descending nodes of the cloud.

MODELING THE ZODIACAL CLOUD

Most previous attempts at modeling the zodiacal cloud have been based on finding a distribution of particle number density $n(r)$, where r is the heliocentric position vector, that satisfies the various observations. The number density function is not derived from first principles, rather it is usually assumed to have the form

$$n(r, \beta) = n_o(r/AU)^{-\nu} f(\beta)$$

where n_o is the particle number density at Earth orbit and β is the heliocentric latitude (Giese and Kneißel, 1989). The models are heliocentric and rotationally symmetric and do not distinguish between the plane of symmetry of the cloud and that of the ecliptic. We consider that the quality of the new spacecraft observations (see Fig. 1) demands an approach that is both more direct and more physically meaningful.

Our approach is to start with a postulated source of particles, either asteroidal or cometary, and then describe:

- the size-frequency distribution of the particles and its variation with distance from the Sun (Gustafson *et al.*, 1992; Durda *et al.*, 1992)
- the thermal and optical properties of the particles and their variation with particle size (Gustafson, 1992)

- the orbital evolution of the particles due to Poynting-Robertson drag, using equations of motion that include light pressure and gravitational perturbations (Gomes and Dermott, 1992).

Once the structure of the cloud has been specified in terms of the distribution of orbital elements and the distribution of particles on the orbits, we need a means of viewing the model cloud and comparing the predicted fluxes with the observations. We have constructed a three-dimensional numerical model (the SIMUL model) that calculates the distribution of flux produced by any particular distribution of dust particle orbits. This model reproduces the exact viewing geometry of the IRAS telescope and allows for the eccentricity of the Earth's orbit. The result is a model for the variation with ecliptic latitude of the brightness observed in a given waveband as the line of sight of the telescope sweeps through the model cloud at a constant elongation angle.

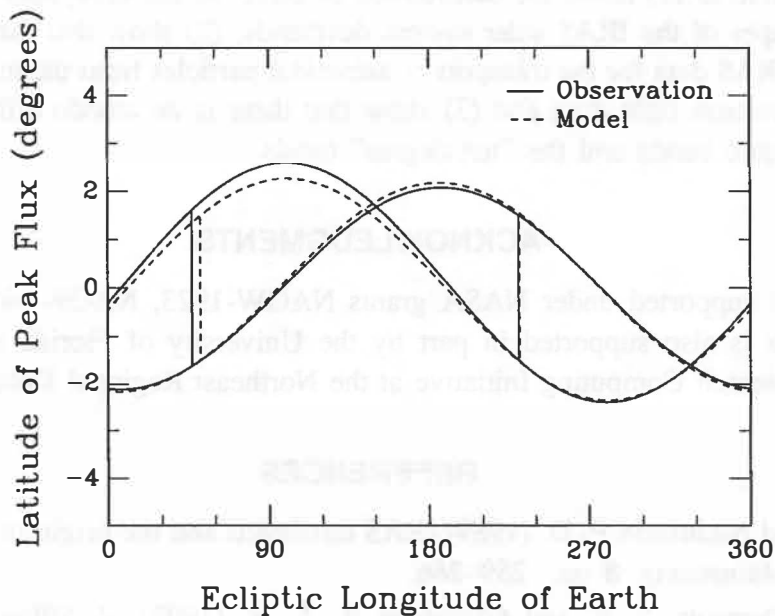


Figure 2. Comparison of the IRAS observations shown in Figure 1 with our model of the cloud based on asteroidal particles of 3.4 micron radii whose orbits decay due to PR drag.

Because the IRAS data set has given us precise information on the various asymmetries of the cloud, both those of the background (Fig. 1) and those associated with the dustbands, and because of the known association of the Hirayama asteroid families with the IRAS solar system dustbands (Dermott and Nicholson, 1989), our initial emphasis has been on the dynamical evolution of asteroidal particle orbits, but future work will include cometary orbits. Flynn (1992), at this meeting, reported on his analysis of the atmospheric heating of large micrometeorites and concluded that survival without melting demands a low relative velocity and that this favors an asteroidal source. Grün (1992), also at this meeting, reported that measurements by the Galileo and Ulysses spacecraft of the variations of the dust particle fluxes with the orientations of the detectors indicate that the dust particle orbits are more consistent with an asteroidal than a cometary source. Schramm *et al.* (1989) analysed 200 interplanetary dust particles and

concluded that 45% are probably cometary but 37% have characteristics (chemical alteration by liquid water) that suggest an asteroidal origin. Thus, it is clear that both sources do need to be considered.

If the size-frequency distribution of the dust is a simple power law, then the effective area of the dust seen in a given waveband λ increases as the particle radii decrease until the absorption coefficient falls off to zero at some radius $\lesssim \lambda/2\pi$. Detailed calculations indicate that the flux in the $25 \mu m$ waveband should be dominated by that from particles of radius $3.4 \mu m$ (Gustafson, 1992) and, for ease of calculation, we assume here that all the particles in the cloud have that radius: future work will include more realistic size-frequency distributions. Predictions for a zodiacal cloud of particles that originate in the main asteroid belt and whose orbits decay due to PR drag are shown in Fig. 2. The agreement with the IRAS observations is remarkable.

Using the same tools, and making the same assumption about the dominant particle size, we have also been able to (1) relate the distribution of orbits in the Hirayama asteroid families to the observed shapes of the IRAS solar system dustbands; (2) show that there is observational evidence in the IRAS data for the transport of asteroidal particles from the main belt to the Earth by Poynting-Robertson light drag and (3) show that there is an albedo difference between the central, near-ecliptic bands and the "ten-degree" bands..

ACKNOWLEDGMENTS

This work is supported under NASA grants NAGW-1923, NAG9-440, NAG5-1725 and NAGW-1257. It is also supported in part by the University of Florida and the IBM Corp. through their Research Computing Initiative at the Northeast Regional Data Center.

REFERENCES

- Dermott S. F. and Nicholson P. D. (1989) IRAS dustbands and the origin of the zodiacal cloud. *Highlights of Astronomy*, **8** pp. 259–266.
- Durda, D. D., Dermott, S. F. and Gustafson B. Å. S. (1992) Modeling and calibration of asteroidal dust production rates. These proceedings.
- Flynn G. J. (1992) Large micrometeorites: Atmospheric entry survival, relation to mainbelt asteroids, and implication for the cometary dust flux. These proceedings.
- Giese, R. H. and Kneißel, B. (1989) Three-dimensional models of the zodiacal dust cloud. II. Compatability of proposed infrared models. *Icarus*, **81**, pp. 369–378.
- Gomes, R. S. and Dermott, S. F. (1992). *Icarus* (to be submitted).
- Grün E., et al. (1992) Interplanetary dust near 1 AU. These proceedings.
- Gustafson B. Å. S. (1992). *Icarus* (submitted).
- Gustafson, B. Å.S., Grün, E., Dermott, S. F. and Durda, D. D. (1992) Collisional and dynamic evolution of dust from the asteroid belt. These proceedings.
- Schramm, L. S., Brownlee, D., and Wheelock, M. M. (1989) Major Element Composition of Stratospheric Micrometeorites. *Meteoritics*, (in press).

A PHOTOMETRIC SURVEY OF OUTER BELT ASTEROIDS¹

Di Martino M. [‡], Gonano-Beurer M. ^{*}, Mottola S. ^{*}, Neukum G. ^{*}

[‡]Osservatorio Astronomico di Torino, I-10025 Pino Torinese, Italy.

^{*}DLR German Aerospace Research Establishment, D-8031 Oberpfaffenhofen, F.R.G.

ABSTRACT

Since 1989 we have been conducting a research program devoted to the study of the Trojans and outer belt asteroids (Hilda and Cybele groups), in order to characterize their rotational properties and shapes. As an outcome of several observational campaigns we determined rotational periods and lightcurve amplitudes for 23 distant asteroids, using both CCD and photoelectric photometry. In this paper we compare the rotational properties of main belt asteroids and Trojans, based on the preliminary results of this survey.

INTRODUCTION

In the last decade the information on the spectral and photometric properties of the distant asteroids has strongly increased, leading to the formulation of specific questions, the answer to which will enable to draw a comprehensive picture of this class of bodies. Recently numerous observational campaigns, undertaken by American and European groups, have given some intriguing results. In particular, French (1987) and Hartmann et al. (1988) have noted that the Trojans, and possibly the Hildas, display larger lightcurve amplitudes compared to those of main belt asteroids in a similar size range. This empirical evidence has been taken as an indication that the outer belt asteroids have a more elongated shape. Zappalá et al. (1989) performed a study of the rotational properties of the distant asteroids and checked, by means of a formal statistical analysis, their compatibility with those of the main belt. These authors confirmed the occurrence of a deviation in the distribution of the lightcurve amplitudes of the outer belt asteroids, when compared with that of the main belt. However, until now no general consensus has been reached on the statistical significance of this deviation. Furthermore, no plausible mechanism explaining the observed elongated shapes has been proposed yet.

In order to characterize the rotational behaviour of the outer belt asteroids with a better statistical significance, we started in 1989 a systematic observational survey of the asteroids belonging to the Trojan, Hilda and Cybele groups (Mottola et al., 1990; Gonano et al., 1991). This survey has so far yielded high quality new photoelectric and CCD lightcurves of 23 outer belt asteroids (see Table 1), collected at different observatories in Italy, Germany, USA and Chile.

The high photometric accuracy of the collected data and their good time-sampling allowed us to compute reliable amplitudes, periods and Fourier coefficients for most of the lightcurves.

¹Based in part on observations collected at the European Southern Observatory, La Silla (Chile).

Table 1. List of the observed outer belt asteroids

Asteroid	Group	Asteroid	Group	Asteroid	Group
617 Patroclus	Tro	3564 Talthybius	Tro	1180 Rita	Hil
1143 Odysseus	Tro	3596 Meriones	Tro	1748 Mauderli	Hil
2207 Antenor	Tro	3708 1974 FV1	Tro	1902 Shaposhnikov	Hil
2759 Idomeneus	Tro	4035 1986 WD	Tro	4196 1982 SA 13	Hil
2893 Peiroos	Tro	4086 1985 VK2	Tro	87 Sylvia	Cyb
2895 Memnon	Tro	4348 1988 RU	Tro	909 Ulla	Cyb
3317 Paris	Tro	4709 1988 TU2	Tro	1280 Baillauda	Cyb
3540 Protesilaos	Tro	1989 CK1	Tro		

PRELIMINARY RESULTS OF THE SURVEY

In this paper we compare the distributions of the rotational periods and the lightcurve amplitudes of Trojan asteroids with the distributions of a selected sample of main belt asteroids. As a reference group we chose a sample of main belt asteroids in the diameter range 40 - 150 km from the Asteroid Photometric Catalogue (Lagerkvist et al., 1989). Particular care has been devoted to the selection of the reference sample, in order to limit the incidence of the observational bias present in the catalogue (see discussion in Binzel et al., 1989). The sample of Trojan asteroids we used for the analysis of the rotational period distribution is based on the present results of our observational survey and also includes several objects observed by French (1987), Hartmann et al. (1988), Zappalá et al. (1989), Hartmann and Tholen (1990) and by others.

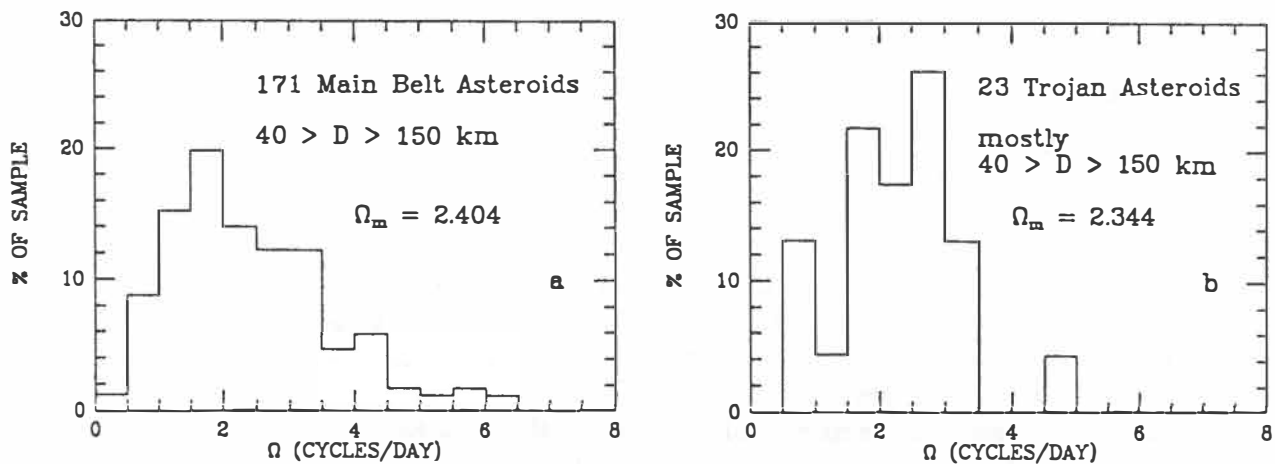


Fig. 1a) Histogram of the rotation rates for a sample of main belt asteroids, where the range of 0 to 8 revolutions/day has been divided into 16 equal bins. b) The same as a) but for the Trojan asteroids with known rotational period.

Figures 1a and 1b show the histogram of the rotational frequencies of a reference group of 171 main belt asteroids and that of 23 Trojans, respectively. By applying the Kolmogorov-Smirnov

test, we have checked the null hypothesis that the two observed distributions derive from the same population. The result of the test is that the two distributions cannot be distinguished at the 90% confidence level.

We similarly compared the distribution of the lightcurve amplitudes of 16 Trojans observed during this survey and of a reference group of 175 main belt asteroids (see Fig. 2a, b). To account for the fact that the main belt asteroids are normally observed at larger solar phase angles than the distant Trojans, we have reduced the observed amplitudes of the MBA group to zero phase angle by using the Amplitude-Phase relationship (APR) described by Zappalà et al. (1990). Also in this case the Kolmogorov-Smirnov test gives $Q \ll 90\%$, indicating that no systematic difference between the two distributions is detected with this data sample. It is interesting to note that the distribution of the amplitudes we measured for the Trojans in this survey has a mean value ($A=0.21$ mag), which is very close to that of the main belt asteroids ($A=0.22$ mag) in this diameter range.

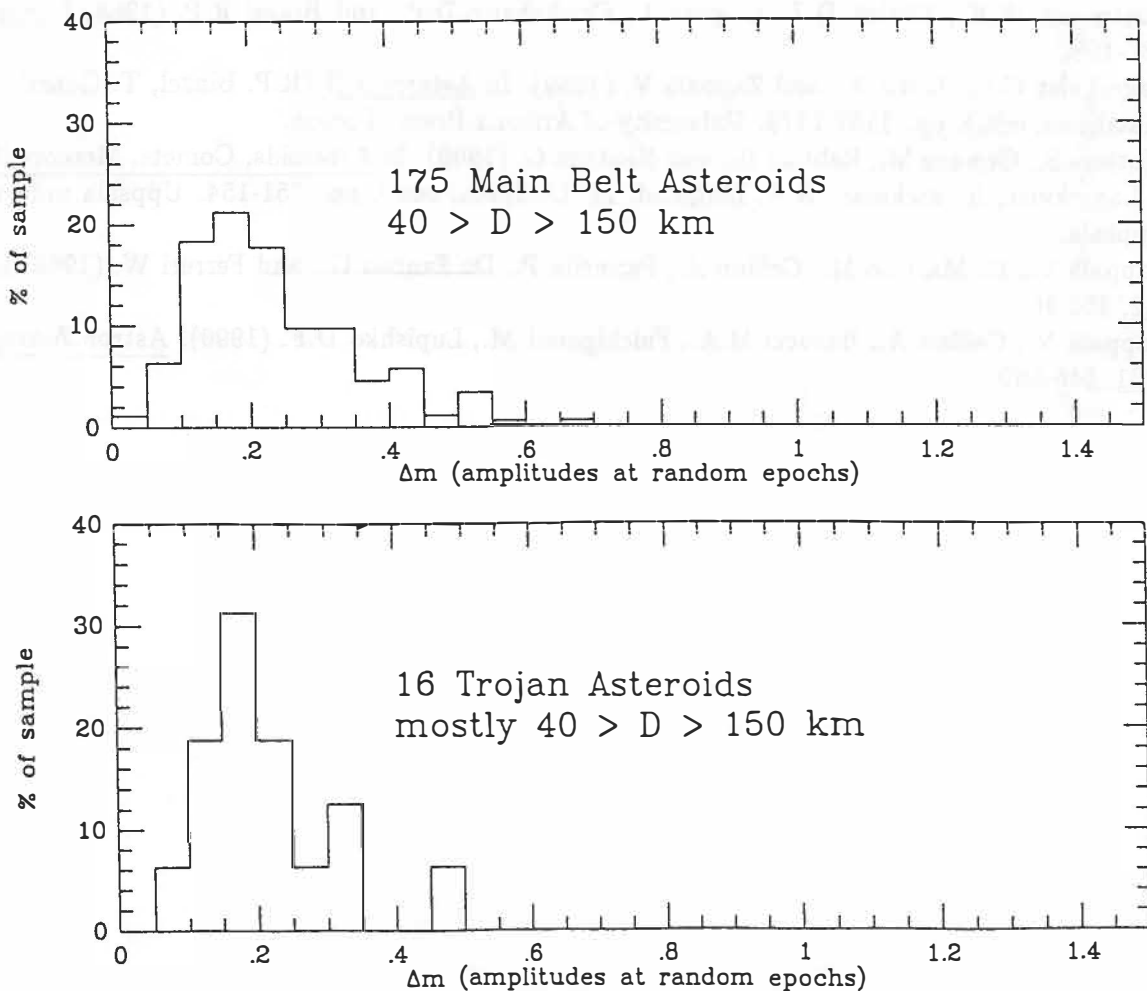


Fig. 2a) Histogram of the lightcurve amplitudes for a sample of main belt asteroids. **b)** The same as a) for the Trojan asteroids observed during the survey.

In this sense our sample taken by itself does not provide evidence for the presence of anomalously elongated shapes among the Trojans. The survey is still ongoing and its completion will allow to perform a statistically more significant comparison between the rotational periods and lightcurve amplitudes of main belt and Trojan asteroids, which is presently not achievable due to the low number of reliable observations available for the distant asteroids.

REFERENCES

- Binzel R.P., Farinella P., Zappalà V., and Cellino A. (1989). In Asteroids II (R.P. Binzel, T. Gehrels, M.S. Matthews, eds.), pp. 416-441. University of Arizona Press, Tucson.
- French L.M. (1987) Icarus, 72, 325-342.
- Gonano M., Di Martino M., Mottola S., and Neukum G. (1991) Adv. Space Res., Vol. 11, No. 12, 197-200.
- Hartmann W.K., and Tholen D.J. (1990) Icarus, 86, 448-454.
- Hartmann W.K., Tholen D.J., Goguen J., Cruikshank-D.P., and Binzel R.P. (1988) Icarus, 73, 487-498.
- Lagerkvist C-I., Harris A., and Zappalà V. (1989). In Asteroids II (R.P. Binzel, T. Gehrels, M.S. Matthews, eds.), pp. 1162-1179. University of Arizona Press, Tucson.
- Mottola S., Gonano M., Rebhan H., and Neukum G. (1990). In Asteroids, Comets, Meteors III (C-I. Lagerkvist, H. Rickman, B.A. Lindblad, M. Lindgren, eds.), pp. 151-154. Uppsala universitet, Uppsala.
- Zappalà V., Di Martino M., Cellino A., Farinella P., De Sanctis G., and Ferreri W. (1989) Icarus, 82, 354-368.
- Zappalà V., Cellino A., Barucci M.A., Fulchignoni M., Lupishko D.F. (1990). Astron. Astrophys., 231, 548-560.

Modeling of Asteroidal Dust Production Rates

D. D. Durda, S. F. Dermott, and B. A. S. Gustafson

Department of Astronomy, University of Florida, Gainesville, FL 32611 USA

ABSTRACT

The production rate of dust associated with the prominent Hirayama asteroid families and the background asteroidal population are modeled with the intent of using the families as a calibrator of mainbelt dust production. However, the dust production rates of asteroid families may be highly stochastic; there is probably more than an order of magnitude variation in the total area of dust associated with a family. Over 4.5×10^9 years of collisional evolution, the volume (mass) of a family is ground down by an order of magnitude, suggesting a similar loss from the entire mainbelt population. Our collisional models show that the number of meteoroids deliverable to Earth also varies stochastically, but only by a factor of 2 to 3.

INTRODUCTION

Since the discovery of the IRAS solar system dust bands, the contribution made by mutual asteroidal collisions to the background zodiacal cloud has received renewed attention. The interplanetary dust particle fluxes observed by the Galileo and Ulysses spacecraft indicate a population with low-eccentricity and low-inclination orbits (Grün *et al.*, 1992), consistent with an asteroidal origin of the particles. From computer simulations of the entry heating of large micrometeorites and comparison of the collisional destruction and transport lifetimes of asteroidal dust, Flynn (1992) has concluded that much of the dust collected at Earth from the interplanetary dust cloud is of asteroidal origin. Analysis of the IRAS dust bands using the SIMUL model of Dermott and Nicholson (1989) has established their connection with the prominent asteroid families and provides observational evidence of the delivery of asteroidal material to the Earth. Given that the Hirayama families contribute significantly to the interplanetary dust complex, we would expect that collisions among the background population of asteroids should contribute a substantial portion of the interplanetary dust in the zodiacal background. With their collisional origin well established, the prominent Hirayama families may provide us with a means of calibrating both the amount of dust to associate with the collisional destruction of a single asteroid and the amount of dust contributed to the zodiacal cloud by the mainbelt asteroids. Analysis using the SIMUL model gives the total effective areas associated with the IRAS dust bands, while ongoing analysis (Dermott *et al.*, 1992) will give the effective area of the entire zodiacal background. By comparing the observed ratio of family to background dust with the ratio determined from the models to be described in the following section, we will determine the extent of the contribution made to the background zodiacal cloud by mutual collisions within the mainbelt asteroid population.

MODELING DUST SOURCE PRODUCTION RATES

Description of the Model

The collisional model described here is a simplified form of the ACE model presented by Gustafson *et al.* (1992) with some modifications. Our model includes particles from 1 mm through the largest asteroidal sizes and in this early version ignores the effects of radiation forces on the small particles.

An asteroid of a given size is collisionally destroyed, its fragments following a power-law size distribution given by

$$dN = Br^{-p}dr,$$

where the constant B is determined by conservation of mass. The exponent p is taken to be somewhat larger than the equilibrium value of 2.511 (0.837 in mass units) in accord with laboratory experiments and the observed size-frequency distributions of the prominent Hirayama families, although it is recognized that in reality a single value may not well represent the size distribution at all sizes. The fragments are distributed among approximately 60 logarithmic size bins, the precise number depending upon the diameter of the parent asteroid. All particles are assumed to have the same density and impact strength. The characteristic size of each bin, determined from the total mass and number of particles in the bin, is used along with the assumed material properties of the particles and the assigned collision rate to associate a mean collisional lifetime with each size bin. The number of fragments distributed into smaller size bins in one timestep is calculated as in ACE, with the modification that only integer numbers of particles are allowed to be destroyed. For small size bins this procedure gives the same results as ACE as the number of particles involved is large. For the larger size bins considered in this model, however, the procedure more realistically treats the particles as discrete bodies and allows for the stochastic destruction of asteroid sized fragments.

To study the production rate and orbital evolution of dust sized particles (1 to 100 μm) we must account for the action of Poynting-Robertson drag and light pressure. The model described here, which does not include these effects and follows the collisional evolution of particles 1mm in diameter and larger, models the production rate of the immediate *sources* of asteroidal dust.

Model Results

Families. The preliminary results described here are indicative of more detailed and extensive calculations currently being run. The reader is referred to Durda *et al.*, (1992) for a more complete discussion of the collisional models, constraints upon the assumed collision parameters, and results. Figure 1a shows, as a function of time, the total geometrical cross-sectional area down to 1mm diameter particles associated with the collisional destruction of a 300 km diameter asteroid. As the dust production rate is proportional to the total area of the source particles, Fig. 1a is indicative of the production rate of dust sized particles and therefore the total area associated with the dust as a function of time. Following the initial, relatively smooth, decrease in area as the small particles created directly from the breakup of the parent body are destroyed, the production rate is seen to become more highly stochastic with

time: while the overall area continues to decrease, the contribution to the total area from the destruction of intermediate size fragments becomes more significant. Over the age of the solar

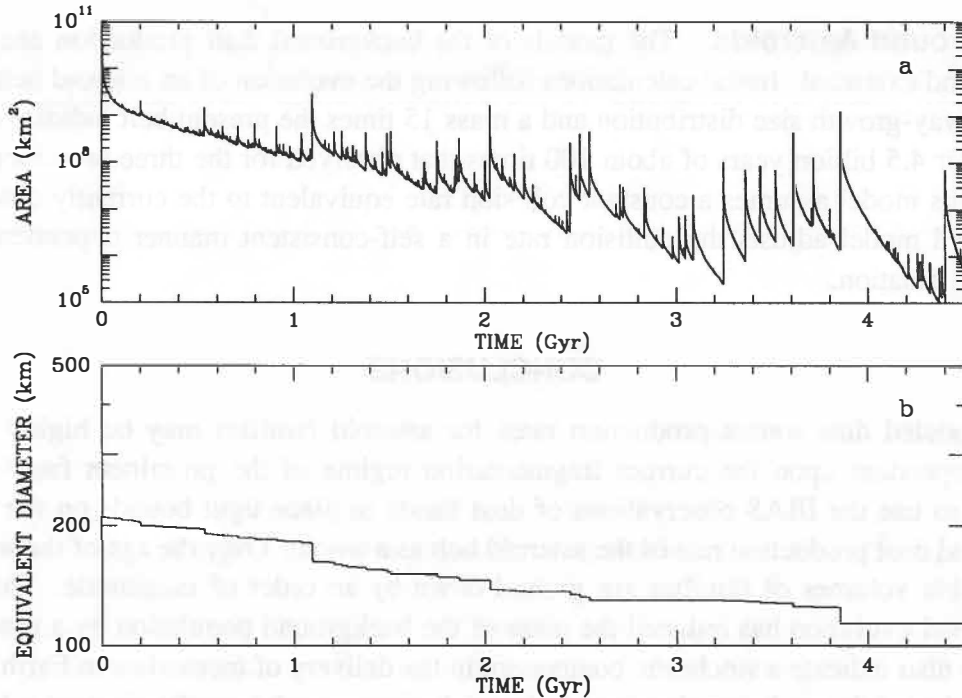


Figure 1. Modeled cross-sectional area to 1mm and equivalent diameter as a function of time for the fragments resulting from the collisional destruction of a 300 km parent asteroid.

system the observable volume of the family would be reduced by approximately a factor of ten, even assuming today's relatively placid collision rates. This is reflected in the decrease in an equivalent volume or diameter as illustrated in Fig. 1b. By extension, it is likely that the mass of the entire asteroid belt has been reduced by a similar factor by collisional grinding alone — a vast quantity of asteroidal dust was delivered to the inner solar system in the past.

The spikes in the dust source production evident in Fig. 1a are due to the breakup of small to intermediate size asteroids, some of which may be smaller than the diameter to which the actual families are complete with respect to discovery. Comparison of Fig. 1a and 1b illustrates that while the observable volume of the family may remain fairly constant and well-defined, the total dust area associated with the family during that time may vary by an order of magnitude or more. This effect becomes increasingly important with time as debris from the original breakup event decays away, to the extent that for very old families (or younger families made of weaker material) it may be difficult or impossible to predict the dust area to associate with the visible extent of large family members. It should be noted, however, that the magnitude of the variation exhibited in Fig. 1a is sensitive to the exponent p in the power-law size distribution of collision fragments. The spikes are subdued for values of p less than or equal to the equilibrium value.

We note that the production rate of small, meteoroid size particles is also stochastic. Preliminary models of the production of fragments larger than 1 meter in the region surrounding the 3:1 resonance indicate that the numbers of meteoroids potentially deliverable to Earth-crossing

orbits varies within a factor of 2 or 3, thus supporting Wetherill and Chapman's (1988) statement that "there is a significant, but probably not dominant stochastic component" in the delivery of meteorites from the 3:1 Kirkwood gap.

Background Asteroids. The models of the background dust production are still being developed and extended. Initial calculations following the evolution of an asteroid belt beginning with a runaway-growth size distribution and a mass 15 times the present belt indicate a total area to 1 mm after 4.5 billion years of about 100 times that observed for the three prominent families. However, this model assumes a constant collision rate equivalent to the currently observed rate. The extended model adjusts the collision rate in a self-consistent manner dependent upon the projectile population.

CONCLUSIONS

The modeled dust source production rates for asteroid families may be highly stochastic. As such, dependent upon the current fragmentation regime of the prominent families, it may be difficult to use the IRAS observations of dust bands to place tight bounds on the collisional evolution and dust production rate of the asteroid belt as a whole. Over the age of the solar system the observable volumes of families are ground down by an order of magnitude. This suggests that collisional evolution has reduced the mass of the background population by a similar factor. The models also indicate a stochastic component in the delivery of meteorites to Earth. Although more refined models are being developed, the preliminary model results suggest a background to family dust production ratio sufficient to allow an asteroidal source of the zodiacal cloud.

ACKNOWLEDGMENTS

This work is supported under NASA grant NAGW-1923.

REFERENCES

- Dermott S. F. and Nicholson P. D. (1989) IRAS dust bands and the origin of the zodiacal cloud. *Highlights of Astronomy*, **8** pp. 259–266.
- Dermott S. F., Durda D. D., Gustafson B. Å. S., Jayaraman S., Xu Y.-L., Gomes R. S., and Nicholson P. D. (1992) The origin and evolution of the zodiacal dust cloud. These proceedings.
- Durda D. D., Dermott S. F., and Gustafson B. Å. S. (1992) To be submitted to *Icarus*.
- Flynn G. J. (1992) Large micrometeorites: Atmospheric entry survival, relation to mainbelt asteroids, and implication for the cometary dust flux. These proceedings.
- Gustafson B. Å. S., Grün E., Dermott S. F., and Durda D. D. (1992) Collisional and dynamic evolution of dust from the asteroid belt. These proceedings.
- Grün E., *et al.* (1992) Interplanetary dust near 1 AU. These proceedings.
- Wetherill G. W. and Chapman C. R. (1988) Asteroids and meteorites. In *Meteorites and the Early Solar System* (J. F. Kerridge and M. S. Matthews, eds.), pp. 35–67. Univ. of Arizona Press, Tucson.

FROM ASTEROID CLUSTERS TO FAMILIES: A PROPOSAL FOR A NEW NOMENCLATURE

P. Farinella¹, D.R. Davis², A. Cellino³, V. Zappalà³

1. Dipartimento di Matematica, Università di Pisa, Pisa, Italy

2. Planetary Science Institute, Tucson, Arizona, USA

3. Osservatorio Astronomico di Torino, Pino Torinese, Italy

Abstract. Some confusion on the number, reliability and characteristics of asteroid families is the result of using the single word “family” for naming asteroid groupings identified in very different ways. Here we propose a new terminology which in our opinion would alleviate this problem.

The studies on asteroid families have been often frustrated by the large disagreements existing among family lists and family memberships identified by different investigators (see Carusi and Valsecchi, 1982). A part of the problem certainly arises from the differences in the asteroid population used for the family searches and the corresponding proper orbital elements (which have been derived through different secular perturbation theories). However, such differences are unavoidable, and sometimes may even provide useful insights about the properties of families found in various portions of the proper elements space and/or in various subsets of the asteroid population.

Definitely worse, in our opinion, are the problems caused by the use of different statistical methods for identifying groupings in the proper elements space and for assessing their statistical significance against the background of “field asteroids”. Here, confusion and ambiguities arise as a result of using the single word “family” for naming asteroid groupings identified in different ways and subjected to statistical significance tests having various degrees of rigor. This is true in particular when groupings identified “by eye”, i.e., found through visual inspection of the asteroid distribution in the proper elements space (such as those of Williams, 1979) are compared with groupings found by fully automated clustering algorithms (such as those of Zappalà et al., 1990, and Bendjoya et al., 1991).

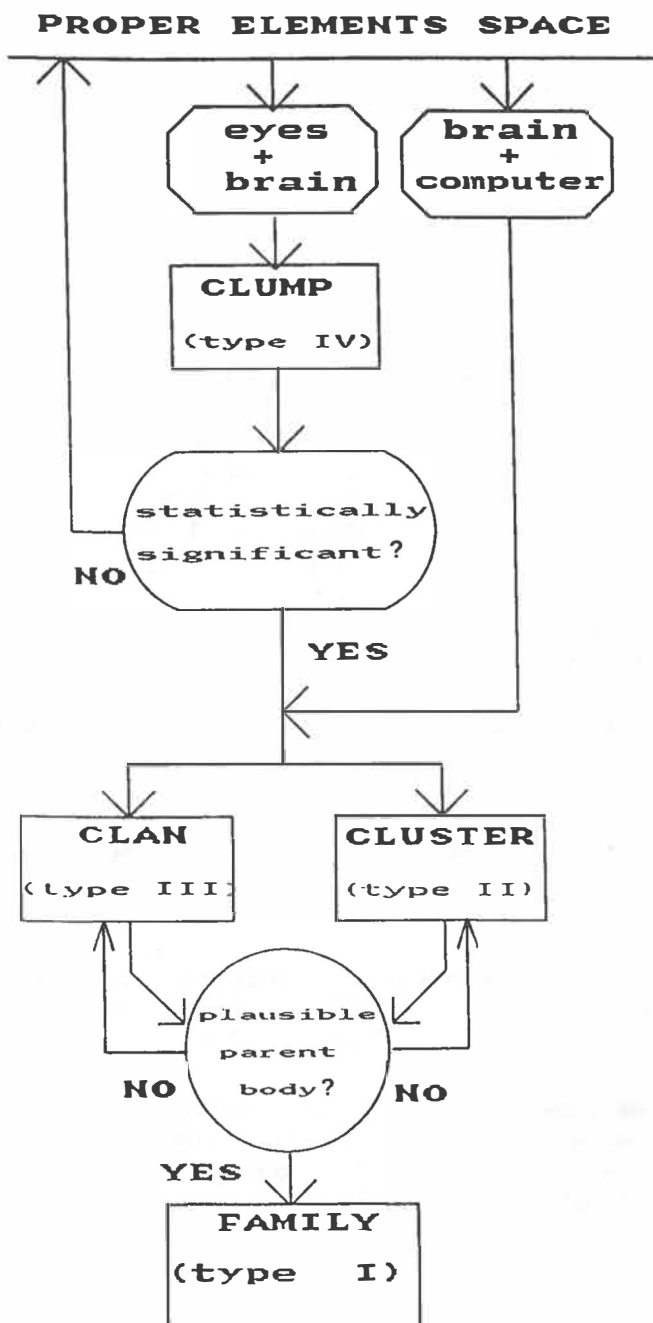
Our scheme (see Figure) recognizes four types of groupings in proper elements space, distinguished by the techniques used to identify them and the significance criteria or tests (possibly) applied. We call “clumps” (or “associations”, or *type IV* families) the groupings recognized by visual inspection but not subjected to rigorous tests for significance. On the other hand, groupings shown to be statistically significant (family identification techniques such as that of Zappalà et al. include such significance tests) may be divided into two categories: “clusters” (or *type II* families), for which an unequivocal membership definition is possible through a clearcut separation from the random background and from other groupings; and “clans” (or “tribes”, or *type III* families), for which unequivocal membership definition and/or separation from other “clans” is impossible. In other words, “clans” are statistically significant, but lie within a background so dense and/or are so close to each other that they cannot be separated in a clearcut manner, and their membership depends in a sensitive way on the adopted cut-off distance criterion.

Finally, “clusters” and “clans” would be called (*type I*) “families” only when some physical evidence indicates that their members have a genetic relationship, namely are the outcomes of the breakup of a common parent body. This evidence can be based on collisional physics — e.g., the relative velocities inferred from the proper elements differences should be physically reasonable; or it could be based on taxonomy, with the family shown to be a cosmochemically plausible assemblage of asteroid taxonomic types. When this type of physical evidence is missing, observational efforts should be encouraged to obtain the relevant data. Negative evidence about a genetic relationship can also be provided by dynamical arguments, e.g. for asteroid *groups* (such as Phocaeas, Hildas and Cybeles) isolated by mean motion or secular resonances.

We give a few examples of use of the nomenclature described above, applied to the results of Zappalà’s et al. search: the three populous Hirayama families (Eos, Themis and Koronis) are of course “type I families”; the Eunomia complex is a set of “clans”, or possibly a single large “tribe”; and the Flora region is dominated by a large “clump” or “association”.

References

- Bendjoya Ph., Slezak E., and Froeschlé C. (1991). The wavelet transform: A new tool for asteroid family determination. *Astron. Astrophys.*, **251**, 312–330.
- Carusi A., and Valsecchi G.B. (1982) On asteroid classifications in families. *Astron. Astrophys.* **115**, 327–335.
- Williams J.G. (1979) Proper elements and family memberships of the asteroids. In *Asteroids* (T. Gehrels, ed.), pp. 1040–1063. University of Arizona Press, Tucson.
- Zappalà V., Cellino A., Farinella P., and Knežević Z. (1990) Asteroid families. I. Identification by hierarchical clustering and reliability assessment. *Astron.J.*, **100**, 2030–2046.



INJECTING ASTEROID FRAGMENTS INTO RESONANCES

P. Farinella*, R. Gonczi#, Ch. Froeschlé#, Cl. Froeschlé#

* Dipartimento di Matematica, Università di Pisa, Pisa, Italy

O.C.A. — Observatoire de Nice, Nice, France

Abstract. We have quantitatively modeled the chance insertion of asteroid collisional fragments into the 3 : 1 and $g = g_6$ resonances, through which they can achieve Earth-approaching orbits. Although the results depend on some poorly known parameters, they indicate that most meteorites and NEAs probably come from a small and non-representative sample of asteroids, located in the neighbourhood of the two resonances.

Most meteorites and Near-Earth Asteroids (NEAs) are widely believed to be asteroidal fragments, coming from the asteroid belt through chaotic dynamical routes associated with mean motion and secular resonances (for recent reviews, see Wetherill and Chapman, 1988; Greenberg and Nolan, 1989). Numerical experiments carried out over the last decade have pointed out two specific source locations: the 3 : 1 mean motion resonance with Jupiter near 2.5 AU (Wisdom, 1983) and the inner edge of the main belt near 2.1 AU, where the dynamics is dominated by the $g = g_6$ (or ν_6) secular resonance (Scholl and Froeschlé, 1991). Continuing dynamical studies will hopefully provide accurate quantitative estimates of both the *width* of the resonances (i.e., of the strip in the phase space bordering the exact resonance surface where chaotic eccentricity jumps can occur) and their *effectiveness* (i.e., the probability and timescale with which the jumps actually occur at any given location in the phase space). On the other hand, we believe that some modeling effort is worthwhile today, by adopting some simplifying assumptions about the dynamical mechanisms and testing the sensitivity of the results to changes in these assumptions.

Therefore, we developed a numerical model for the first part of the meteorite/NEAs delivery process, namely the ejection of fragments from impact cratering or break-up of the existing asteroids, and the chance insertion of the escaping fragments into the "dangerous" regions of the phase space close to the 3 : 1 and $g = g_6$ resonances where chaotic behavior may arise. For every parent asteroid, the efficiency of this process depends on several factors: (i) the amount of ejected material per unit time; (ii) the mass vs. ejection velocity distribution of the fragments; (iii) the escape velocity of the parent body; (iv) the ΔV required to approach a resonance surface; (v) and the width of the "resonant strip". Finally, the overall yield depends on the size distribution of the asteroids. By varying some model parameters, we estimated the fraction of ejected fragments falling in the two resonances from a large number of main-belt asteroids.

Our model works in the following way. For all the 2355 numbered asteroids up to no. 4265, with semimajor axis $a < 2.8$ AU, eccentricity $e < 0.3$, inclination $i < 30^\circ$ and perihelion distance > 1.1 AU (to exclude outer-belt, high-eccentricity/inclination and Earth-approaching objects), we simulated the isotropic ejection of a large number ($\approx 10^3$) of fragments. The distribution of the ejection velocity V_{ej} was derived from laboratory data on the outcomes of hypervelocity impacts: $dN(V_{ej}) \propto V_{ej}^{-\alpha} dV_{ej}$ for $V_{ej} > V_{min}$, $dN(V_{ej}) = 0$ for $V_{ej} < V_{min}$; for the exponent α we adopted the value 3.25, while for the lower-cutoff V_{min} we tested the three values 50, 100 and 200 m/s, which are consistent with the properties of asteroid families (Zappalà et al., 1990). For every asteroid, we then computed an escape velocity $V_{esc} = (120 \text{ m/s})(R/100 \text{ km})$, with the mean radius R taken from the data base of Cellino et al. (1991); fragments for which $V_{ej} > V_{esc}$ were assumed to escape "to infinity" with a velocity $V = (V_{ej}^2 - V_{esc}^2)^{1/2}$. For each escaped fragment, we used the Gauss formulae (see, e.g., Zappalà et al., 1990, eq.(1)) for computing its proper elements from those of the parent asteroid. The proper elements, derived according to the theory of Milani and Knežević (1990), were then tested using a numerical grid in the 3-dimensional proper elements space whether the fragment's apsidal secular frequency g was such that $|g - g_6| < \delta$ (with $g_6 = 28.2455 \text{ arcsec/yr}$ and $\delta = 0.5$ or 1 arcsec/yr); if so, the fragment was assumed to lie in the $g = g_6$ secular resonance, where large eccentricity increases may occur (see Knežević et al., 1991, for further details about this procedure). A fragment was also assumed to lie within the $g = g_6$ chaotic region for $a < 2.10$ AU, as the whole zone bordering from inside the main belt is dominated by $g = g_6$ and other resonances (see Scholl and Froeschlé, 1991). On the other hand, a fragment was considered as injected in the chaotic zone associated with the 3 : 1 resonance whenever its osculating elements were such that $a > (2.497 - e/8.85)$ AU and $a < (2.510 + e/9.615)$ AU, in agreement with the results of numerical experiments on the dynamics of this resonance and the observed width of the corresponding Kirkwood gap (Wisdom, 1983; Yoshikawa, 1990). In this way, for each asteroid and for six

parameter choices (two for δ times three for V_{min}), we could compute the fraction of escaped fragments falling into either of the two resonances.

The next issue is: for any given parent asteroid, can we compute a fragment production rate from both cratering and fragmentation events, taking into account the different probabilities of these events? Or can we at least estimate the relative *fragment production efficiencies* of asteroids of different sizes? Let us consider separately (1) impact fragmentation and (2) cratering, and assume that the projectile population has a cumulative size distribution close to a power law with (negative) exponent $-b$ (this assumption is not necessarily a good approximation, see Cellino et al., 1991, and later in the text). (1) For fragmentations, if we assume a size-independent impact strength, we get that the critical projectile-to-target size ratio is also independent of size. Then the number of projectiles capable of shattering a target of size R is $\propto R^{-b}$, and taking into account the target's cross-section the probability of fragmentation per unit time is $\propto R^{(2-b)}$. Since the mass ejected per fragmentation event is $\propto R^3$, the mass delivered per asteroid of size R per unit time is $\propto R^{(5-b)}$. However, since only fragments with $V_{ej} > V_{esc}$ escape reaccumulation, for $R > R_{min}$ (R_{min} being the size for which $V_{esc} = V_{min}$, namely the minimum size for which part of the fragments are reaccumulated), the fraction of escaping fragments is $(R/R_{min})^{1-\alpha}$, hence the mass delivered per unit time becomes $\propto R^{(6-b-\alpha)}$. (2) During cratering events, we assume that projectiles eject an amount of mass proportional to their own mass, up to a maximum value proportional to the target mass. Therefore, the projectile forming the largest possible crater has a size $R_{cr} \propto R$. The mass ejected by cratering events per unit time is proportional to the total impacting mass per unit time, which is proportional to the cross-section times $R_{cr}^{(3-b)}$, namely to $R^{(5-b)}$. Again, this is correct only for $R < R_{min}$, otherwise the escaping mass is $\propto R^{(6-b-\alpha)}$. Thus, within the simplifying assumptions described above, the same scaling rule applies to both cratering and fragmentation. For each target asteroid, we have therefore derived a *relative fragment delivery efficiency* by multiplying the fraction of ejected fragments falling into either resonance times a scaling factor proportional to $R^{(5-b)}$ for $R < R_{min}$, and to $R^{(6-b-\alpha)}$ for $R > R_{min}$. We have used as "nominal" values $\alpha = 3.25$ and $b = 2.5$, but we have tested the way results are affected when different values are adopted. The value $b = 2.5$ corresponds to an equilibrium size distribution for a collisionally evolving population, provided the parameters determining collisional outcomes are size-independent (Dohnanyi, 1969); however, for different zones of the asteroid belt and different size ranges, Cellino et al. (1991) have actually found that b varies in the range from ≈ 1 to ≈ 3 . Notice that since for small bodies the scaling factor is $R^{(5-b)}$ and their cumulative number is also roughly proportional to R^{-b} , the choice of b may critically affect the overall fragment production efficiency of the different size ranges.

Some results of these computations are shown in Tables 1 and 2, referring to the "nominal" parameter values given above and to the case $\delta = 1 \text{ arcsec/yr}$, $V_{min} = 100 \text{ m/s}$ (for a more detailed discussion and a parameter sensitivity analysis, see Gonczi et al., 1992, in preparation). Table 1 lists all the asteroids with nos. < 1000 that deliver at least 20% of their escaping fragments to one of the two resonances; it can also be considered a list of the asteroids lying closest to the "dangerous" resonant strips. Notice that some asteroids (nos. 6, 304, 631, 759, 907, 930) are found to be *inside* the $g = g_6$ strip, yielding fragment percentages $> 50\%$. Although this may be due to an overestimate of the resonance width or to its location being inaccurately determined near these bodies, at least in one case (759 Vinifera) this result has been confirmed by numerical integrations (Froeschlé and Scholl, 1987); Vinifera did not show chaotic behavior, but this may be due to a "lucky" dynamical configuration (Morbidelli and Henrard, 1991). In any event, we believe that the asteroids listed above are so close to the resonant surface that they should be considered as promising potential sources of Earth-approaching fragments. Table 2 gives the total fragment delivery efficiencies (in arbitrary units) for some subsamples, sorted according to size and taxonomic type. As for size, we recall that according to Cellino et al. (1991) our overall asteroid sample is complete only for $D > 44 \text{ km}$, and is increasingly affected by discovery selection effects for smaller sizes; similar selection effects certainly apply to taxonomic types also. An interesting finding was that in the S-type and $150 \text{ km} < D < 200 \text{ km}$ subsamples, some 90% of the total fragment delivery efficiency to $g = g_6$ is contributed by the single large asteroid 6 Hebe.

Although the results depend on some parameters which are not well known (the width of the secular resonance, the mass vs. velocity distribution of the fragments, the mass distribution index of small asteroids), we summarize our results as follows: (1) both resonances are effective channels for fragment collection and delivery and their efficiencies are of the same order of magnitude, but they sample in a different way the orbital elements and the physical properties (size and taxonomic type) of the parent objects; (2) a large

fraction of NEAs and meteorites can be generated by a small fraction of the overall asteroid population (mostly located in the vicinity of resonances), whose average properties do not necessarily coincide with those of the overall population; (3) as suggested by Knežević et al. (1991), the $g = g_6$ resonance is probably an effective fragment delivery channel in the moderate-inclination (15° to 20°) regions near 2.4 and 2.8 AU, where several relatively large asteroids are located (e.g., nos. 6, 304, 631, 907), as well as near the inner edge of the belt, populated by a larger number of small asteroids.

Acknowledgments. We are grateful to D.R. Davis, Z. Knežević, A. Milani and G.W. Wetherill for helpful discussions and comments. This work was partially supported by the EEC research contract no. SC1-0011-C(GDF).

Ast. n°	a(AU)	e	i(deg)	$V_e(km/s)$	R(km)	% 3:1	% $g = g_6$
6	2.425	0.169	15.052	0.115	96.00	2.3	83.9
17	2.471	0.134	4.865	0.056	46.60	30.	1.6
46	2.526	0.124	2.493	0.079	65.50	39.8	0.3
198	2.459	0.183	10.673	0.035	29.35	21.4	2.6
304	2.404	0.091	15.480	0.041	34.25	0.8	94.4
330	2.470	0.226	6.281	0.008	6.30	44.8	1.5
335	2.475	0.161	4.681	0.056	46.80	40.9	1.3
355	2.539	0.121	4.870	0.015	12.85	26.1	0.3
421	2.539	0.255	7.550	0.011	8.80	42.8	0.3
475	2.594	0.240	19.767	0.019	15.50	1.1	76.9
495	2.487	0.126	2.550	0.025	20.85	48.7	1.4
518	2.535	0.189	7.418	0.011	8.80	43.1	0.4
556	2.465	0.120	6.090	0.024	19.75	28.3	1.2
603	2.542	0.209	8.158	0.009	7.60	34.1	0.2
619	2.520	0.025	13.851	0.023	19.00	23.9	3.6
623	2.460	0.125	14.797	0.028	23.00	18.0	48.0
631	2.793	0.060	19.487	0.036	30.25	0.0	64.9
649	2.549	0.240	11.947	0.009	7.20	33.2	0.4
660	2.535	0.105	15.035	0.027	22.10	30.2	1.6
695	2.539	0.097	15.035	0.031	25.60	20.7	0.5
714	2.535	0.086	15.135	0.025	20.50	25.0	1.2
724	2.455	0.248	11.660	0.005	4.10	29.4	4.8
759	2.618	0.196	19.597	0.032	26.35	0.6	72.5
765	2.547	0.245	6.690	0.009	7.25	32.4	0.4
787	2.540	0.085	15.058	0.018	15.15	20.6	1.1
797	2.536	0.090	5.394	0.020	16.95	27.2	0.5
877	2.487	0.148	3.382	0.024	19.80	53.5	1.4
879	2.531	0.095	14.851	0.009	7.85	31.9	2.0
900	2.472	0.120	11.759	0.014	11.35	30.5	8.6
907	2.801	0.168	19.548	0.039	32.90	0.0	69.9
908	2.475	0.197	12.240	0.017	14.00	49.6	8.9
930	2.431	0.112	15.391	0.023	19.55	1.8	87.4
969	2.463	0.176	3.405	0.012	10.25	28.1	1.1
974	2.534	0.077	4.485	0.015	12.40	24.5	0.5
994	2.530	0.068	15.129	0.016	13.60	29.3	1.6

Table 1

All the asteroids with nos. < 1000 yielding a fraction > 20% of escaped fragments to either the 3:1 or the $g = g_6$ resonance. Parameters choice : $V_{min} = 100 m/s$, $\delta = 1 \text{ arcsec/yr}$, $\alpha = 3.25$, $b = 2.5$.

$Eff1 (D < 50 \text{ km}) = 20.073$	$Eff2 (D < 50 \text{ km}) = 6.182$
$Eff1 (50 \leq D < 100 \text{ km}) = 24.528$	$Eff2 (50 \leq D < 100 \text{ km}) = 18.167$
$Eff1 (100 \leq D < 150 \text{ km}) = 29.358$	$Eff2 (100 \leq D < 150 \text{ km}) = 2.360$
$Eff1 (150 \leq D < 200 \text{ km}) = 12.513$	$Eff2 (150 \leq D < 200 \text{ km}) = 57.577$
$Eff1 (200 \leq D < 250 \text{ km}) = 12.069$	$Eff2 (200 \leq D < 250 \text{ km}) = 0.281$
$Eff1 (250 \leq D < 300 \text{ km}) = 0.591$	$Eff2 (250 \leq D < 300 \text{ km}) = 0.296$
$Eff1 (D \geq 300 \text{ km}) = 3.169$	$Eff2 (D \geq 300 \text{ km}) = 0.989$
$Eff1 (C) = 15.483$	$Eff2 (C) = 12.443$
$Eff1 (S) = 30.664$	$Eff2 (S) = 62.333$
$Eff1 (M) = 1.154$	$Eff2 (M) = 1.156$
$Eff1 (F) = 2.769$	$Eff2 (F) = 0.050$
$Eff1 (V) = 2.067$	$Eff2 (V) = 0.689$
$Eff1 (P) = 14.303$	$Eff2 (P) = 0.104$
$Eff1 (X) = 35.860$	$Eff2 (X) = 10.125$

Table 2

Fragment delivery efficiencies (arbitrary units) to the 3:1 ($Eff1$) and $g = g_6$ ($Eff2$) resonances for different size ranges and taxonomic types. Parameters choice : $V_{\min} = 100 \text{ m/s}$, $\delta = 1 \text{ arcsec/yr}$, $\alpha = 3.25$, $b = 2.5$.

References

- Cellino A., Zappalà V., and Farinella P. (1991). The asteroid size distribution from IRAS data. *Mon. Not. R. astr.Soc.*, in press.
- Dohnanyi J.W. (1969). Collisional model of asteroids and their debris. *J. Geophys. Res.* **74**, 2531–2554.
- Froeschlé Ch., and Scholl H. (1987). Orbital evolution of asteroids near the secular resonance ν_6 . *Astron. Astrophys.* **179**, 294–303.
- Greenberg R., and Nolan M.C. (1989). Delivery of asteroids and meteorites to the inner solar system. In *Asteroids II* (R.P. Binzel, T. Gehrels, and M.S. Matthews, eds.), pp. 778–804. University of Arizona Press, Tucson.
- Knežević Z., Milani A., Farinella P., Froeschlé Ch., and Froeschlé Cl. (1991). Secular resonances from 2 to 50 AU. *Icarus*, in press.
- Milani A., and Knežević Z. (1990). Secular perturbation theory and computation of asteroid proper elements. *Cel. Mech.* **49**, 247–411.
- Morbidelli A., and Henrard, J. (1991). The main secular resonances ν_5 , ν_6 and ν_{16} in the asteroid belt. *Celest. Mech.*, in press.
- Scholl H., and Froeschlé Ch. (1991). The ν_6 secular resonance region near 2 AU: A possible source of meteorites. *Astron. Astrophys.* **245**, 316–321.
- Wetherill G.W., and Chapman, C.R. (1988) Asteroids and meteorites. In *Meteorites and the Early Solar System* (J.F. Kerridge and M.S. Matthews, eds.), pp. 35–67. University of Arizona Press, Tucson.
- Wisdom J. (1983). Chaotic behavior and the origin of the 3/1 Kirkwood gap. *Icarus* **56**, 51–74.
- Yoshikawa M. (1990) Motions of asteroids at the Kirkwood gaps, I. On the 3:1 resonance with Jupiter. *Icarus* **87**, 78–102.
- Zappalà V., Cellino A., Farinella P., and Knežević Z. (1990) Asteroid families. I. Identification by hierarchical clustering and reliability assessment. *Astron. J.*, **100**, 2030–2046.

IUE Observations of Periodic Comets Tempel-2, Kopff and Tempel-1

P. D. Feldman

Department of Physics and Astronomy
The Johns Hopkins University
Baltimore, MD 21218, USA

M. C. Festou

Observatoire Midi-Pyrénées
31400 Toulouse, France

ABSTRACT

We summarize the results of observations made between 10 June and 18 December 1988 with the *International Ultraviolet Explorer* of comet P/Tempel-2 during its 1988 apparition. The derived water production rate and relative gas/dust ratio are compared with those of P/Halley, observed with *IUE* in 1985–86, and other potential CRAF target comets, P/Kopff and P/Tempel-1, both observed with *IUE* in 1983.

I. INTRODUCTION

Periodic comet Tempel-2 (1988 XIV) is the current primary target comet for the Comet Rendezvous/Asteroid Flyby (CRAF) mission. It was also the target comet in 1987 so that extensive observations were planned for its apparition to provide information about the gas and dust environment to be expected for the spacecraft and the scientific instruments. Although the CRAF project schedule led to a subsequent change in target to periodic comet Kopff (1983 XIII), observations of Tempel-2 by the *International Ultraviolet Explorer* (*IUE*) satellite were carried out as planned over the period 10 July to 18 December 1988 and produced ultraviolet spectra on ten separate dates during this period. The observation parameters are listed in Table 1, together with the measured brightness (in a nominal $10.^{\circ}3 \times 15.^{\circ}1$ aperture) of the OH(0,0) and CS(0,0) bands at 3085 \AA and 2575 \AA , respectively. Also given is the continuum flux in a 100 \AA wide band centered at 2950 \AA , reduced to the parameter $A f \rho$ defined by A'Hearn *et al.* (1984). Here, A is the mean grain albedo, f is the filling factor of the grains in the aperture and ρ is the radius of the aperture.

II. COMET P/TEMPEL-2

The derived water production rates have already been presented by Roettger *et al.* (1990). They are summarized in Table 1 and shown in Figure 1 as a function of heliocentric distance, r . To facilitate a comparison with previously published production rates derived from *IUE* data, the

Table 1: Observational data

Comet/Date	r(AU)	Δ (AU)	B_{OH} (R)	B_{CS} (R)	$Af\rho$ (cm)	$Q_{H_2O}(s^{-1})$	$Q_{CS}(s^{-1})$
P/Tempel-2							
1988 June 10	1.72	0.79	45	—	< 40	1.1×10^{27}	—
1988 July 28	1.48	0.80	640	20	60	1.2×10^{28}	5.6×10^{24}
1988 August 20	1.42	0.86	1500	60	110	2.4×10^{28}	1.7×10^{25}
1988 September 6	1.39	0.92	2130	—	120	3.5×10^{28}	—
1988 September 14	1.38	0.94	2100	65	100	3.6×10^{28}	1.8×10^{25}
1988 September 29	1.39	1.02	2510	70	130	3.8×10^{28}	2.2×10^{25}
1988 October 4	1.40	1.04	2570	75	110	3.6×10^{28}	2.4×10^{25}
1988 October 28	1.45	1.21	2620	60	120	3.2×10^{28}	2.4×10^{25}
1988 November 15	1.52	1.36	1700	—	150	2.4×10^{28}	—
1988 December 18	1.69	1.74	510	—	140	1.0×10^{28}	—
P/Kopff							
1983 July 18	1.59	0.81	1960	50	430	5.1×10^{28}	3.5×10^{25}
P/Tempel-1							
1983 July 18	1.50	1.00	450	20	160	1.0×10^{28}	5.4×10^{24}

model used in the derivation assumed a parent molecule velocity of 1.0 km s^{-1} independent of r . The CS production rates are also given in Table 1, assuming a short-lived parent (presumably CS_2), and the ratio Q_{CS}/Q_{H_2O} derived from the data is in the range of $5 - 8 \times 10^{-4}$, typical of all comets observed by IUE at this range of heliocentric distances. The H_2O production rate follows the same pre-/post-perihelion asymmetry as exhibited by the visual light curve, as has been demonstrated by Roettger *et al.* (1990).

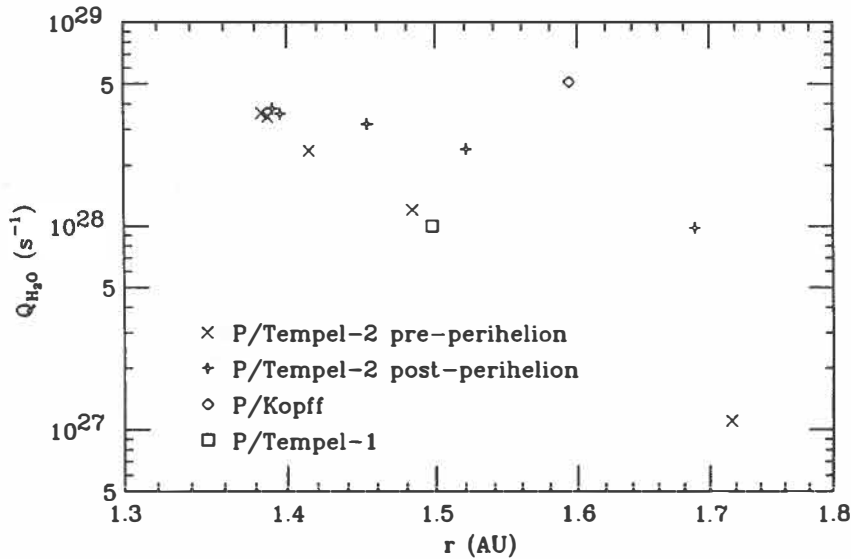


Figure 1: Water production rate as a function of heliocentric distance.

Figure 2 shows the values of $Q_{H_2O}/Af\rho$ as a function of heliocentric distance. This quantity is a measure of the gas-to-dust ratio in the coma, although it is model dependent in that the assumptions of a constant ratio of dust velocity to gas velocity and a constant dust size distribution

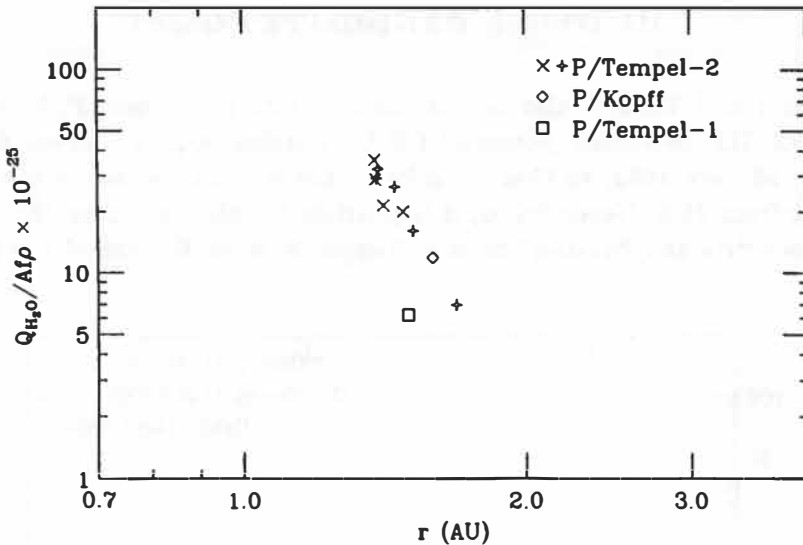


Figure 2: The ratio of water production rate to $Af\rho$ as a function of heliocentric distance.

as a function of heliocentric distance are required for this quantity to be proportional to Q_{gas}/Q_{dust} . A comparison with other comets is given in Figures 3 and 4. The first of these is an updated version of a similar figure from Feldman and A'Hearn (1985), and with the caveat noted above, indicates that at larger heliocentric distances, the ultraviolet continuum appears to dominate the gas emission. Even so, there is a clear indication of varying gas/dust ratios in this sample of comets. Figure 4 shows $Q_{H_2O}/Af\rho$ for comets P/Halley (1986 III), Wilson (1987 VII) and Bradfield (1987 XXIX), three "dusty" comets observed over a wide range of heliocentric distances by IUE. These data indicate a variation in gas/dust with heliocentric distance, as is also indicated for P/Tempel-2, although over a much more limited range of r , in Figure 2. For P/Tempel-2, all of the continuum measurements were made at phase angles between 40 and 46°, so a change in observational geometry cannot be responsible for the range of $Q_{H_2O}/Af\rho$ values.

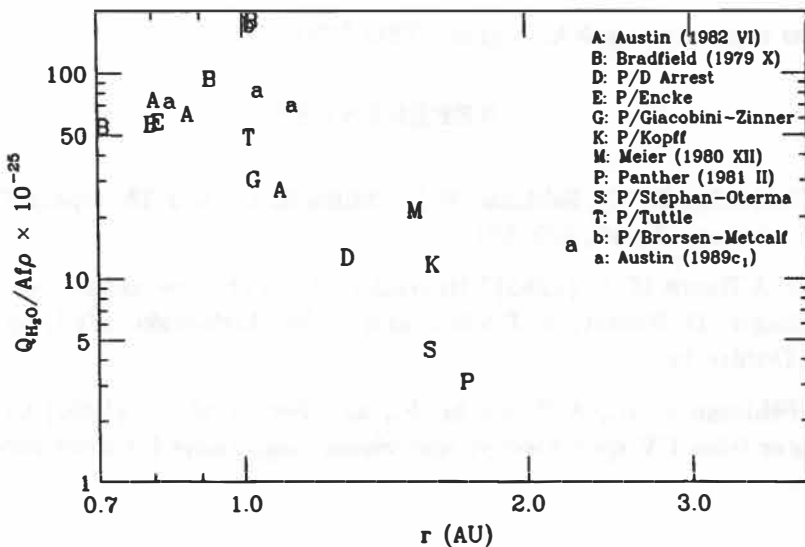


Figure 3: Same as Figure 2 for several comets observed by IUE.

III. OTHER CANDIDATE COMETS

Figures 1 and 2 and Table 1 also include similar data for comets P/Kopff (1983 XIII) and P/Tempel-1 (1983 XI), two other potential CRAF mission targets. These data were obtained on a single date, 18 July 1983, so that no information is available about the evolution of these comets with time from *IUE*. Nevertheless, it is possible to infer that near their perihelia P/Kopff is somewhat more active and "dustier" than P/Tempel-2, while P/Tempel-1 is less active and also fairly "dusty".

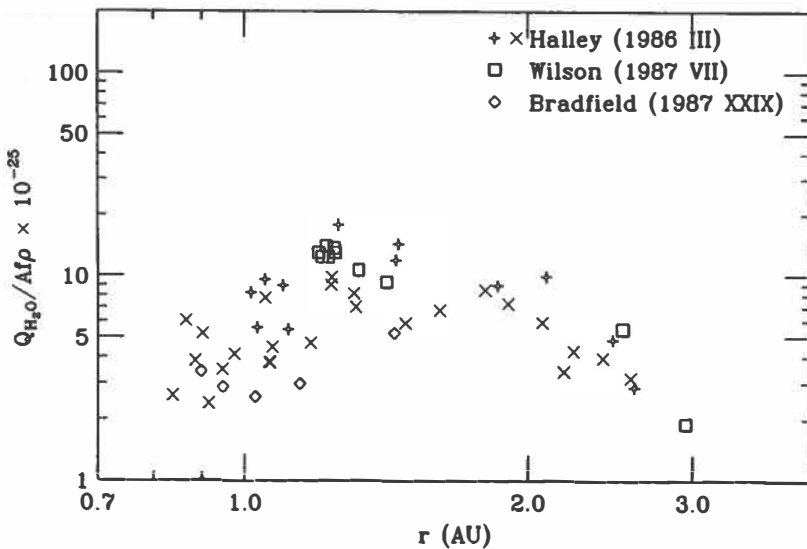


Figure 4: Same as Figure 2 for three "dusty" comets.

ACKNOWLEDGEMENTS

This work was supported by NASA grant NSG-5393.

REFERENCES

- A'Hearn M. F., Schleicher D. G., Feldman P. D., Millis R. L., and Thompson D. T. (1984) Comet Bowell 1980b. *Astron. J.*, **89**, 579–591.
- Feldman P. D. and A'Hearn M. F. (1985) Ultraviolet albedo of cometary grains. In *Ices in the Solar System* (J. Klinger, D. Benest, A. Dollfus, and R. Smoluchowski, eds.), pp. 453–461. Kluwer Acad. Publ., Dordrecht.
- Roettger E. E., Feldman P. D., A'Hearn M. F., and Festou M. C. (1990) Comparison of water production rates from UV spectroscopy and visual magnitudes for some recent comets. *Icarus*, **86**, 100–114.

WATER AND DUST PRODUCTION RATES IN COMET P/HALLEY DERIVED FROM ULTRAVIOLET AND OPTICAL OBSERVATIONS

M.C. Festou

Southwest Research Institute, San Antonio, TX, 78228, USA and Observatoire Midi-Pyrénées,
URA 285 du CNRS, F-31400 Toulouse, France

ABSTRACT

We evaluate whether the activity of comet P/Halley is due solely to the presence of discrete active areas. We preliminarily conclude that the dark areas of the nucleus contribute to the formation of the coma.

I. INTRODUCTION

Comet P/Halley (1986 III) was observed with the IUE instruments between April 1985 and July 1986 to simultaneously characterize its ultraviolet spectrum, record the evolution of its spectrum and monitor the activity of its nucleus over the widest possible range of heliocentric distances (Feldman *et al.* 1987). Superimposed on a marked pre-post perihelion asymmetry, very different activity levels were recorded on a few hour time scale. Variations far exceeded what could have been expected from the mere change of the heliocentric distance of the comet and this was interpreted as the apparition of active areas into sunlight. Since the FES camera records the light scattered by CN and C₂ radicals and dust particles, since the IUE records the emission of OH and that of the continuum, the modelization of both the spectroscopic and FES observations is possible and only requires the knowledge of the dust to gas production ratio. This will allow us to separate the short and long activity terms of the comet production of matter.

II. OBSERVATIONS AND DATA INTERPRETATION

387 raw FES count rates and 136 low resolution spectra of comet P/Halley (Festou, 1990), recorded while the slit was positioned at the center of the coma, were employed in this study. OH(0-0) fluxes and the Afp parameter (reduced to zero phase angle assuming the phase function of Divine *et al.*, 1985) were used to evaluate the water and dust productions, respectively. Due to the phase effect alone, the continuum signal decreased by about 30% from September 1985 until mid-January 1986 and it increased by $\approx 70\%$ from March until July 1986, an effect that partially explains the post-perihelion brightening of the comet.

We first simulated the FES observations. Recent works on abundance correlations in comets (e.g. Cochran 1987, 1989a,b) indicate that it is fair to assume that the ratio of the C₂ to the main coma gases productions is constant from comet to comet, and that this ratio is known. C₂ production rates were taken in Schleicher *et al.* (1990). Continuum fluxes in the FES bandpass were determined using our own IUE measurements obtained in the 2920-3020 Å window, taking into account the FES camera characteristics. Fig. 1. shows that our modelization mimics quite well the evolution of the FES count rates. Then we separated the short and long terms in the FES curve (this was obtained by assuming that when the FES count rates remained at a nearly constant level, the active areas did not contribute, see Fig. 2). We finally derived the dust and the water productions curves.

We have found that the comet was on average twice as 'gassy' before perihelion than after. There is also an indication that the comet had the same gas to dust ratio far from perihelion on both legs of its orbit, when the insulating conditions of the nucleus were rather similar, which suggests the existence of a marked seasonal effect. Closer to perihelion, one observes a net decrease of the gas production relative to that of the dust. This could be either a real decrease of the water evaporation rate, as this parameter did not increase as the energy available at the nucleus, or be an increase of the number of dust particle total cross section because of the larger lifting power of the gas, a change in the dust to gas content of the emissive areas or fractionation of the particles into smaller grains. These hypotheses cannot be tested in that short study.

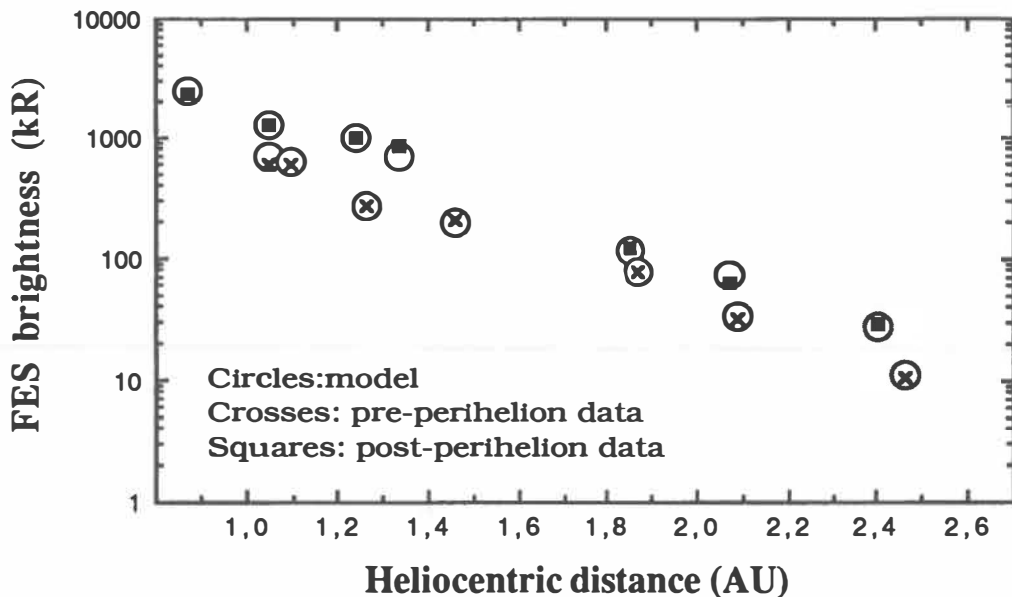


Fig. 1: simulation of the FES observations. Within some 10-15%, the relative contributions of the gas and dust emissions can be evaluated.

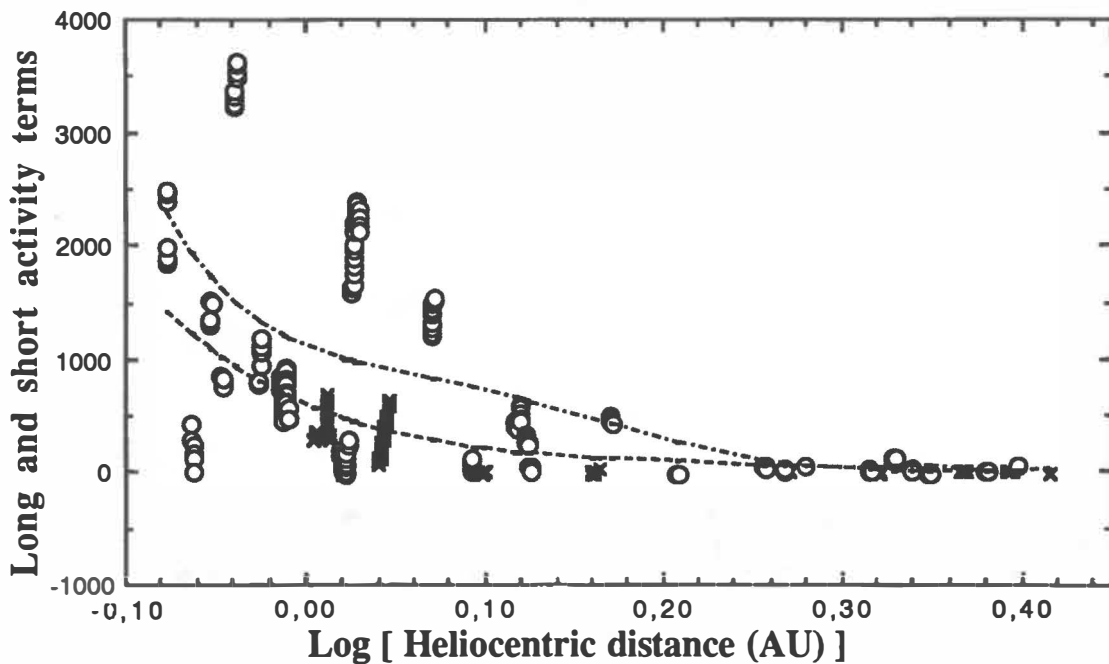


Fig. 2: long (dashed line) and short (dots and crosses) activity terms of the nucleus of comet P/Halley

REFERENCES

- Cochran A.L., 1987. *Astron. J.* **92**, 231-238.
 Cochran A.L. 1989a,b. In *Asteroids, Comets, Meteors III*, Lagerkvist C.-I., Rickman H., Lindblad B.A., Lindgren M., Eds, Uppsala Observatory, 281-284 and 285-288.
 Divine N. et al., 1986. *Space Sc. Rev.* **43**, 1-104.
 Feldman P.D. et al., *Nature*, **324**, 433-436.
 Feldman P.D. et al., 1987. *Astron. Astrophys.* **187**, 325-328.
 Festou M.C., 1990. ESA SP-1134. IUE - ULDA Access Guide n°2. Comets. W. Wamsteker Ed. ESTEC, Noordwijk, The Netherlands.
 Schleicher D.G. et al., 1990. *Astron. J.* **100**, 3, 896-912.

THE GAS PRODUCTION RATE OF PERIODIC COMET d'ARREST

M.C. Festou¹, P.D. Feldman² and M.F. A'Hearn³

1- Southwest Research Institute, San Antonio, TX, 78228, USA and Observatoire Midi-Pyrénées, F-31400 Toulouse, France

2- Department of Physics and Astronomy, The Johns Hopkins University, Baltimore, MD, 21218, USA

3- Astronomy Program, University of Maryland, College Park, MD 20742, USA.

ABSTRACT

Comet P/d'Arrest is a potential target for a rendez-vous mission to a short period comet. Its light curve is rather peculiar, the comet being active only after perihelion passage. One apparition out of two is easy to observe from the ground. The 1995 apparition of the comet will offer a unique opportunity to characterize the outgassing properties of its nucleus.

I. INTRODUCTION

Comet P/d'Arrest is a short period comet of period about 6.5 years. Its minimum magnitude is between 5 and 6 and one apparition out of two is a favorable sighting. The orbit is chaotic: in 1600, the comet perihelion distance was about 1 AU; in 2200, it will be close to 2 AU. Since it was discovered - in 1851 - the comet has circulated on one of three orbits having perihelion distances of ≈ 1.17 , ≈ 1.28 or ≈ 1.36 AU, respectively. Carusi et al.'s (1991) identification of comet P/d'Arrest with comet La Hire of 1678 ($q = 1.16$ AU) requires a strong non-gravitational effect that remained constant over a few centuries. Since the comet makes close and easy to observe approaches to the Earth, the light curve of that comet is well documented. The comet brightness increases very rapidly just before perihelion and then remains nearly constant, or even slightly increases, during a few weeks while the comet is receding from the sun. In this brief study, we will review the main available observations of that comet, including unpublished results obtained in 1982 with the International Ultraviolet Explorer (IUE), and discuss the implications of the rather unusual light curve (LC) shape of the comet.

II. THE VISUAL LIGHT CURVE FROM THE ICQ ARCHIVE

The visual observations listed in the International Comet Archive (ICQ) were used to derive the recent visual LC shown in Fig. 1. A detailed investigation by Kamél (1991) shows that there is a strong indication that the shape of the LC (hence the light curve asymmetry) has not much changed since the discovery of the comet. Note that the non gravitational parameter listed in Table 1, A_2 , remained constant since the comet discovery in 1851, and even probably since 1678 (Carusi et al. 1991). Festou et al. (1990) showed that this can be expected if the light curve shape does not change since the non gravitational effect is primarily induced by the light curve asymmetry. Brightness maxima occur 40 ± 20 days after perihelion, depending mostly on the geocentric distance and the elongation of the comet. There is some indication that the brightness decreases rapidly about 100 days after perihelion passage (apparitions in early spring and late fall are not good - $\Omega + \omega = 315^\circ$ - and, since the comet is then always far south, few observations are then available). With the exception of 1976, the minimum of the apparent magnitude occurred at the time of the minimum indicated in column 3 of Table 1. When the $10 \log R_h$ factor artificially applied to the original data by Kresák and Kresáková (1989) is reintroduced, the very very similar LCs of Fig. 1 become slightly different and, more important, the determination of the time of occurrence of the brightness maximum depends obviously on the exact observing geometry. The maxima of brightness given by Kresák and Kresáková (1989) sample the real LC in a manner that is not well characterized. Due to the fact the perihelion distance is changing, one would expect a slight deformation of the LC near perihelion time: comparison of the 1976 and 1982 apparitions shows no significant differences between the two LCs. However, one should note that the 1976 magnitudes may have been globally underestimated because of the proximity of the comet (about 0.3 to 0.4 AU against 0.8 to 1.4 at most of the other apparitions). It appears highly desirable to monitor well photometrically the favorable apparition of 1995 (the comet will be well placed for a six month period starting about two months prior to perihelion passage).

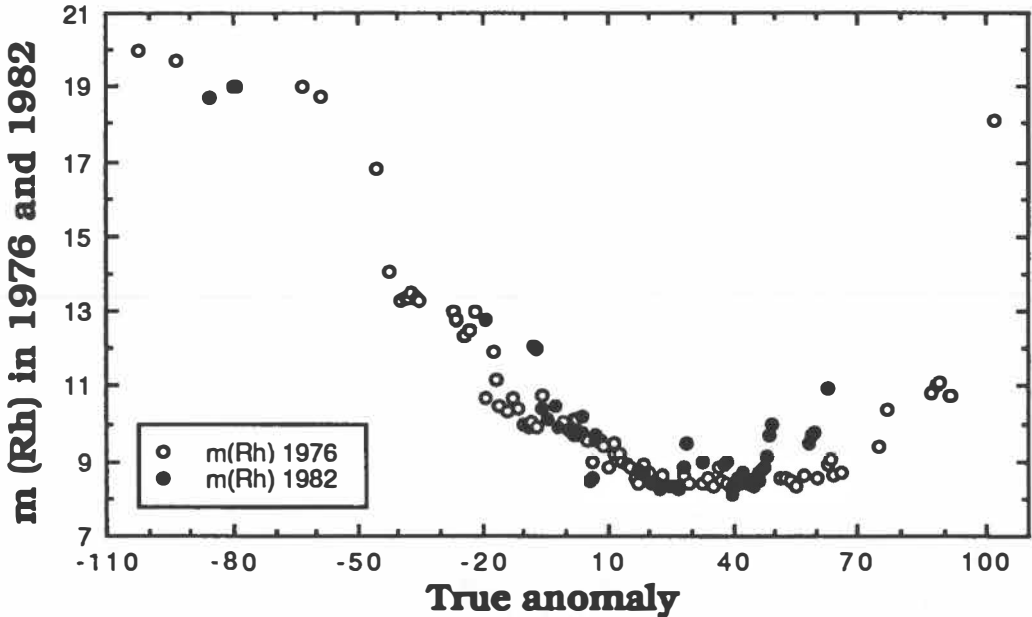


Fig. 1: The heliocentric magnitude of P/d'Arrest in 1976 and 1982. This parameter is a measure of the total outgassing rate of the comet. Only lower values of the magnitude (say inside a $[m_{\max}, m_{\max} + 0.4]$ bracket) have been considered: all other measurements reflect the difficulties experienced by the observers to capture a good sighting of the comet.

Table 1: Magnitude of comet P/d'Arrest at its 15 observed apparitions¹

Comet number	Perihelion distance	$t-t_p$ (days)	min [m(1,1)] 2	$m(R_h)$ 3	A_2 4,5	R_h (at time $t-t_p$)	Δ
1678	1.164	≈ 45	≈ 7.5	≈ 8.5	≈ 0.10	≈ 1.28	≈ 0.35
1851 II	1.173	56	8.7	10.1		1.375	0.820
1857 VII	1.170	8	7.4	8.5	0.104	1.296	1.315
1870 III	1.280	26	7.4	8.5		1.281	1.327
1877 IV	1.318	61	6.7	8.7		1.590	1.858
1890 V	1.321	30	8.0	9.4	0.096	1.367	0.913
1897 II	1.326	69	7.2	8.4		1.330	1.455
1910 III	1.270	38	8.8	10.4		1.442	1.027
1923 II	1.357	57	8.0	9.6	0.094	1.437	1.015
1943 III	1.385	12	9.8	10.6		1.194	0.964
1950 II	1.377	15	7.8	9.2	0.098	1.389	0.850
1963 VII	1.369	73	8.8	10.8		1.596	1.938
1970 VII	1.167	58	7.7	8.5	0.120	1.197	1.549
1976 XI	1.164	42	6.7	7.5		1.198	0.348
1982 VII	1.291	29	7.7	8.3	0.116	1.336	0.869

1- Minimum magnitudes are taken in Kresák and Kresáková (1989); orbital parameters are from Marsden (1983). 2- Observed brightness maxima after correction of the observations for the $5 \log(\Delta) + 10 \log(R_h)$ factor. In other words, that magnitude is m (observed) - $5 \log \Delta - 10 \log R_h$. The heliocentric magnitude is m (observed) - $5 \log \Delta$. 3- Heliocentric magnitude = 4th column corrected to remove the $10 \log(R_h)$ factor introduced by Kresák and Kresáková. 4- From Rickman *et al.* (1991). Except for the last value given, which results from linking the 1976 and 1982 orbits, A_2 s given here represent the linkages with three consecutive orbits.

III. IUE OBSERVATIONS IN 1982

Comet P/d'Arrest (1982 VII) was observed with the IUE during the first 30 days following the 1982 perihelion passage. During this long period, both the heliocentric and geocentric distance varied very little, allowing thus a quasi model independent comparison of the observations. Table 2 summarizes the observations and gives the water production rates, derived in the usual manner using vectorial model parameters valid for the stable activity level of the sun in September-October 1982:

$$v(\text{water}) = 0.85 \text{ km/s}; v(\text{OH}) = 1.05 \text{ km/s}$$

$$\tau_{\text{Total}}(\text{water}) = 65000 \text{ s}; \tau_{\text{Diss}}(\text{water}) = 72500 \text{ s}; \tau_{\text{Total}}(\text{OH}) = 160000 \text{ s}$$

OH(0-0) g-factors were taken in Schleicher and A'Hearn (1982). The water production shows the trend exhibited by the visual LC and increases with increasing distance to the sun. It is quite possible that the gas production increased by some 10-20% after our last observation. The CS emission was never detected. A conservative upper limit of the CS emission is 50 R (10 by 20 arc sec slit) which corresponds to an upper limit of the CS production of $1.5 \cdot 10^{25} / \text{s}$ (with $g_{\text{CS}} = 7 \text{ e-4/s}$). This limit is slightly larger than what one could have expected from past IUE observations (Weaver *et al.* 1981; Azoulay and Festou, 1985). Upper limits for the other species are too high to be of any usefulness.

Table 2: 1982 IUE observations of comet P/d'Arrest (LWP spectra only)

Exposure	expo time	R_h	Δ	phase	Cont. flux *,**	OH(0-0) flux **	g(0-0) ***	Q(w) ****	t- τ
LWR 14181	60	1.2912	0.7410	50.97	-	337	2.33	1.451	1.141
LWR 14232	70	1.2949	0.7651	50.70	27?	280	2.60	1.228	8.268
LWR 14317	90	1.3089	0.8083	49.83	45	480	3.36	1.967	18.040
LWR 14347	85	1.3200	0.8353	49.18	26	522	3.73	3.025	23.057
LWR 14397	90	1.3366	0.8720	48.27	-	560	4.03	2.035	29.056

* 2920-3020 Å; ** $10^{-14} \text{ erg/cm}^2/\text{s}$; *** 10^{-4} s ; **** 10^{28} s (spectra are shown in Festou, 1990)

The continuum was clearly detected only once, at the end of September 1982. Interestingly, although the apparent flux was still increasing, there is some indication that the continuum emission was decreasing some 3 weeks after perihelion, which corresponds to the time the comet is described as having a more diffuse or no central condensation. Afp was about 190 cm, a number to be compared to those observed in comet P/Halley near 1.4 AU pre- and post- perihelion, ≈ 1000 and ≈ 4500 cm, respectively (at similar phase angles of $\approx 50^\circ$). It is customary to state that short period comets are 'non-dusty': the present data rather suggest that the expression 'less dusty' is more appropriate, and that the lack of a conspicuous dust tail might actually indicate a deficiency in micron-sized particles or simply reflect an observational limitation due to the large R_h at which the comet is observed.

IV. PHOTOMETRIC OBSERVATIONS PRIOR TO 1982

Few observations of the comet are available. The largest set of published data is found in A'Hearn *et al.*, 1979 (see Table 3). The important conclusions from that study are i) the variation of the dust production rate is mostly due to a phase effect; ii) the maximum of the gas production occurs at least 30 days after perihelion passage; iii) the ratio $Q(\text{CN}) / Q(\text{C}_2)$ is nearly constant ($= 0.38$) which compares well with Cochran's 1987 value: comet P/d'Arrest is an 'average' comet. The data from A'Hearn *et al.* (1979) also

Table 3: summary of the results obtained by A'Hearn *et al.* (1979)

Date	R_h (AU)	Δ (AU)	Phase ($^\circ$)	$Q(\text{dust})^*$	Coeff.**	$\log Q(\text{CN})$	$\log Q(\text{C}_2)$
12.26/8/76	1.164	0.151	4.4	10.0	1.014	25.12	25.60
13.29	1.164	0.151	3.4	10.06	1.062	25.10	25.49
14.30	1.164	0.152	3.3	10.08	1.062	25.14	25.47
19.31	1.167	0.158	10.5	10.02	1.212	25.23	25.63
31.79	1.189	0.203	25.7	9.96	1.602	25.26	25.66
14.73/9	1.238	0.284	31.3	9.89	1.775	25.19	25.97
20.59	1.447	0.566	29.6	9.85	1.720	25.38	25.83

* logarithmic scale of arbitrary origin; ** correction to be brought to continuum measurements to compute the zero phase flux using Divine *et al.*'s, 1985, phase function.

show that the continuum light reflected by dust particles does not contribute much to the overall brightness of the coma, as shown in the Table 4 below and the coma brightness measures the gas content of the coma. This is confirmed by the direct comparison of visual and photometric (A'Hearn *et al.*, 1979) observations. It is found that the C₂ production rate and the heliocentric magnitude are proportional. This is to be expected

Table 4: relative brightness of the dust and gas comae, after A'Hearn *et al.* (1979)

R _h (AU)	Δ (AU)	Phase (°)	Diaph. size (")	Log Q(C ₂)	Log F(5236)
1.164	0.151	4.4	109	-9.4	-12.2
1.447	0.566	29.6	109	-9.66	-12.92

since, if the comet gas production is steady, the total brightness of the comet (propr. to 1/ 2.5^m) is proportional to Q(C₂) $\tau^{-1}(C_2) g(C_2)$, where τ is the lifetime of the C₂ radicals. A similar result was obtained on a statistical basis by Festou (1986) using a data set of IUE observations on about 15 comets. The correlation observed in 1976 in A'Hearn *et al.*'s data shows that despite the comet was receding from the sun, thus making the comet cloud more diffuse and more extended to visual observers, the visual magnitude remained proportional to the coma content in C₂ radicals and that such a correlation certainly holds in the range R_h = [perihelion - 1.5 AU].

Table 5: visual brightness and heliocentric magnitude, derived from A'Hearn *et al.* (1979)

t _{obs} -t _{perih.}	R _h	log [Q (C ₂)]	m (R _h)	[Q(C ₂) * 2.5 ^m] / 10 ²⁸
-0.6	1.164	25.60	9.4	2.2
0.4	1.164	25.49	9.4	1.7
1.4	1.164	25.47	9.4	1.6
6.4	1.167	25.63	9.0	1.6
19.0	1.189	25.66	8.4	1.0
32.9	1.238	25.97	8.4	2.0
49.7	1.447	25.83	8.3	1.4

The constancy of the ratio in the last column (known with an accuracy not better than about 50% because of the uncertainty attached to the evaluation of the heliocentric magnitude) shows that the visual magnitude and the C₂ production rate varied in parallel in the [perihelion - 1.45 AU] heliocentric distance range and that consequently, the visual magnitude is a good indicator of the C₂ production for the apparitions for which no photometric observations are available.

In 1976, comet P/d'Arrest was observed with COPERNICUS by Festou *et al.* (1983). The data show a large increase of the HI production at a time we described the comet as having a nearly constant gas production:

19 Sept. 1976, R_h = 1.27 AU, Δ = 0.313, Q (water) = 1/2 Q (H) = 2.6 10²⁸ s⁻¹

03 Oct. 1976, R_h = 1.33 AU, Δ = 0.425, Q (water) = 1/2 Q (H) = 9.0 10²⁸ s⁻¹

Although a short term variability of the gas production is not excluded by the visual LC (possibly masked by the rapid rotation period indicated by Fay and Wisniewski, 1978; high time resolution observations during the favorable 1995 apparition should certainly be secured to eventually reveal it), this large change of Q(H) could be erroneous due to the difficulty to separate the geocorona and comet contributions to the signal. However, the possibility that the C₂ to water production ratio varied should not be disregarded too rapidly. Using the A'Hearn *et al.* (1979) data, the Q (CN) / Q (water) [= Q(H) / 2] and the Q (C₂) / Q (water) ratios are found to be $\approx 1.2 \cdot 10^{-3}$ and $\approx 3 \cdot 10^{-3}$ around mid-September 1976, respectively, which are almost the mean values given by A'Hearn (1982) from a large set of data. Unpublished data collected in 1982 by A. Cochran and her collaborators indicate a few interesting facts that reinforce our conclusion that the comet should be thoroughly observed in 1995. First, one observes that the CN to C₂ production rate is close to unity and that consequently the water to C₂ production ratio was perhaps in 1982 close to the upper

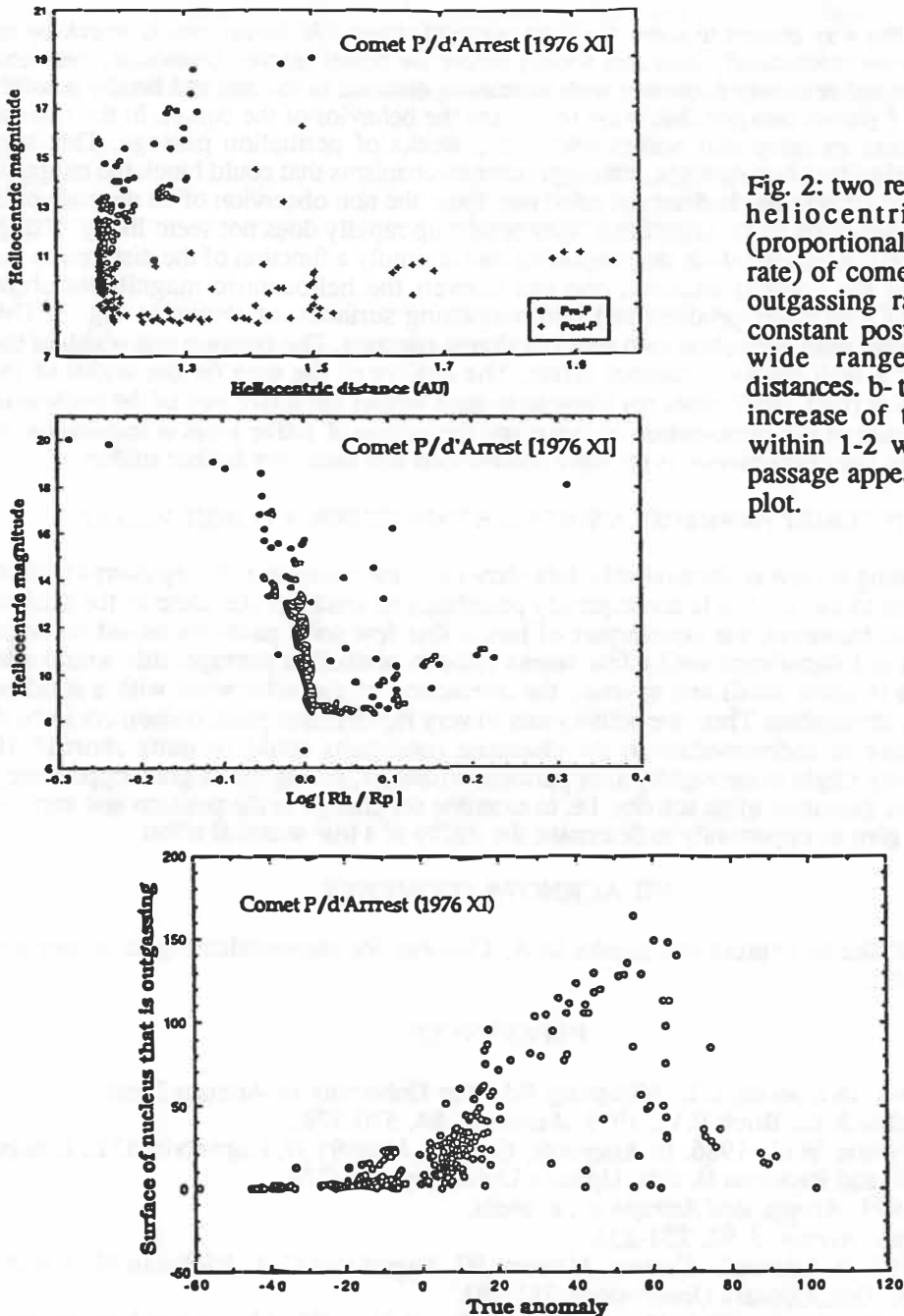


Fig. 2: two representations of the heliocentric magnitude (proportional to the outgassing rate) of comet P/d'Arrest. a- the outgassing rate remains nearly constant post-perihelion over a wide range of heliocentric distances. b- the extremely abrupt increase of the gas production within 1-2 weeks of perihelion passage appears very well in this plot.

Fig. 2: the surface (km^2) of the nucleus that is outgassing if the insulating conditions are those of a uniformly lit spherical non rotating nucleus. The large distance of the comet from the sun implies a large outgassing surface, actually as large as that obtained for comet P/Halley under the same assumptions at the same heliocentric distance.

value indicated above. Second, the observations span a very long period, from May until December 1982. The C_2 production remained almost constant from October until mid-December 1982, suggesting that the 'plateau' of the LC might be wider than the visual observations suggest it. That the activity be due to an active area situated at high cometocentric latitude or simply to the peculiar orientation of an elongated nucleus is unclear. One will observe however that the outgassing surface that is required to justify the observed outgassing rate of the nucleus is quite high, of order the surface of half a nucleus of a few kilometer radius.

V. CONVERTING OUTGASSING RATES INTO OUTGASSING SURFACES

Whatever the way chosen to show the light curve of comet P/d'Arrest, one is struck by the fact the heliocentric brightness dramatically increases shortly before the comet reaches perihelion, then remains level for 4-6 weeks, then rather slowly decreases with increasing distance to the sun and finally possibly falls off quite rapidly. Fig. 2 shows two possible ways to present the behavior of the comet. In the two cases, there is a sharp brightness increase that occurs within 1-2 weeks of perihelion passage. This suggests the apparition of an active area into sunlight, although other mechanisms that could block the outgassing until a specific point on the orbit is reached are not ruled out. From the non observation of an increase of the dust to gas content, the assumption that a superficial layer breaks up rapidly does not seem likely. Using a simple model of a spherical nucleus in which the outgassing rate is simply a function of the distance to the subsolar point and ignoring the nucleus rotation, one can convert the heliocentric magnitudes shown above (equivalent to the C₂ or water productions) into outgassing surfaces, as shown in Fig. 3. This surface increases very rapidly after perihelion then remains almost constant. The position and width of the 'plateau' in Fig. 3 suggests a well marked seasonal effect. The quality of the data (is the width of the plateau significantly different from 180°?) does not allow us to state whether the active part of the nucleus is at a high cometocentric latitude or if a combination of shape and repartition of active areas is responsible for what is observed. However, the phenomenon is strongly pronounced and deserves further studies.

VI. IS COMET P/d'ARREST A SUITABLE TARGET FOR A COMET MISSION?

The preceding review of the available data shows that the comet is not very dusty (1/10 of P/Halley at a similar distance to the sun): it is consequently possibility to send a probe close to the nucleus without much danger for it. However, the counterpart of this is that few solid particles would be detected. The nucleus activity is not significant until a few weeks prior to perihelion passage: this would allow one to image the nucleus in great detail and to study the interaction of the solar wind with a solid body or an extremely tenuous atmosphere. Then, the activity sets in very rapidly: that phenomenon could be difficult to study since the time to accommodate to the changing conditions could be quite short (6-10 weeks). However, the activity might cease rapidly after perihelion passage, giving thus a great opportunity to image the nucleus after the cessation of its activity, i.e. to examine the change in the position and surface of active areas as well as to give an opportunity to determine the reality of a true seasonal effect.

VII. ACKNOWLEDGMENTS

We would like to express our thanks to A. Cochran for communicating to us her unpublished observations of 1982.

REFERENCES

- A'Hearn M.F., 1982. In *Comets*, L.L. Wilkening Ed., The University of Arizona Press.
- A'Hearn M.F., Millis R.L., Birch P.V., 1979. *Astron. J.* **84**, 570-578.
- Azoulay G. and Festou M.C., 1986. In *Asteroids, Comets, Meteors II*, Lagerkvist C.I., Lindblad B.A., Lundstedt H. and Rickman H. Eds, Uppsala University, 273-278.
- Carusi A. et al., 1991. *Astron. and Astrophys.*, in press.
- Cochran A.L., 1987. *Astron. J.* **92**, 231-238.
- Cochran A.L., 1989. in *Asteroids, Comets, Meteors III*, Lagerkvist C.-I., Rickman H., Lindblad B.A., Lindgren M., Eds, Uppsala Observatory, 281-284.
- Divine N., Fechtig H., Gombosi T.I., Hanner M.S., Keller H.U., 1985. The comet dust environment.
- Fay T.D. and Wisniewski W., 1978. *Icarus* **34**, 1-9.
- Festou M.C., 1990. ESA SP-1134. IUE - ULDA Access Guide n°2. Comets. W. Wamsteker Ed. ESTEC, Noordwijk, The Netherlands.
- Festou M.C., Rickman H., Kamél L., 1990. *Nature* **345**, 235-238, 1990.
- Festou M.C., Keller H.U., Bertaux J.L. and Barker E.S., 1983. *Astrophys. J.* **265**, 925-932.
- Kamél L., 1991. Doctoral Dissertation, Uppsala University, Sweden.
- Kresák L. and Kresáková M., 1989. *Bull. Astron. Inst. Czechosl.* **40**, 269-284.
- Marsden B.G., 1983. Catalog of cometary orbits, Enslow Publisher, Hillside, NJ, USA.
- Rickman H., Froeschlé C., Kamél L., Festou M.C., 1991. *Astron. J.*, in press.
- Schleicher D.G. and A'Hearn M.F., 1982. *Astrophys. J.* **258**, 864-877.
- Weaver H.A., Feldman P.D., Festou M.C., A'Hearn M.F. and Keller H.U., 1981. *Icarus* **47**, 449-463.

Production rates for comet P/Temple 2 from long slit CCD spectroscopy

Uwe Fink and Michael Hicks

Lunar and Planetary Laboratory, University of Arizona, Tucson, AZ 85721

Since comet P/Temple 2 is one of the potential targets for the CRAF (Comet Rendezvous Asteroid Flyby) mission we obtained long slit spectroscopic data with our CCD spectrograph during its 1988 apparition. As the same spectrograph had been extensively used for observations of P/Halley this allowed a direct spectroscopic comparison between the two objects. Furthermore we could choose a P/Halley spectrum which was taken at a heliocentric distance very close to that of P/Temple 2. Finally, we could adjust the integration windows along the slit to compensate for the different geocentric distances, so that roughly the same projected distance of the comets' comae was observed. The parameters for our observations are given in Table 1.

The spectra of the two comets using the integration windows in Table 1 were both divided by a solar type comparison star. These resulted in a flat ratio spectrum and required that the absolute flux scale at the left be given as fractional solar flux. Both comets show emission by the $C_2 \Delta v = -1$ band sequence, a number of NH_2 bands, the red CN system and the forbidden O I D lines at 6300Å and 6364Å. All of these emission bands are labelled in the figure. To facilitate visual comparison between the two spectra they were scaled to make the emission intensities by C_2 , NH_2 and CN roughly equal. This immediately points out a major difference in chemical composition between the two comets. Comet P/Temple 2 exhibits a considerably stronger OI emission relative to the other species than comet P/Halley. In addition P/Temple 2 has a lower continuum level.

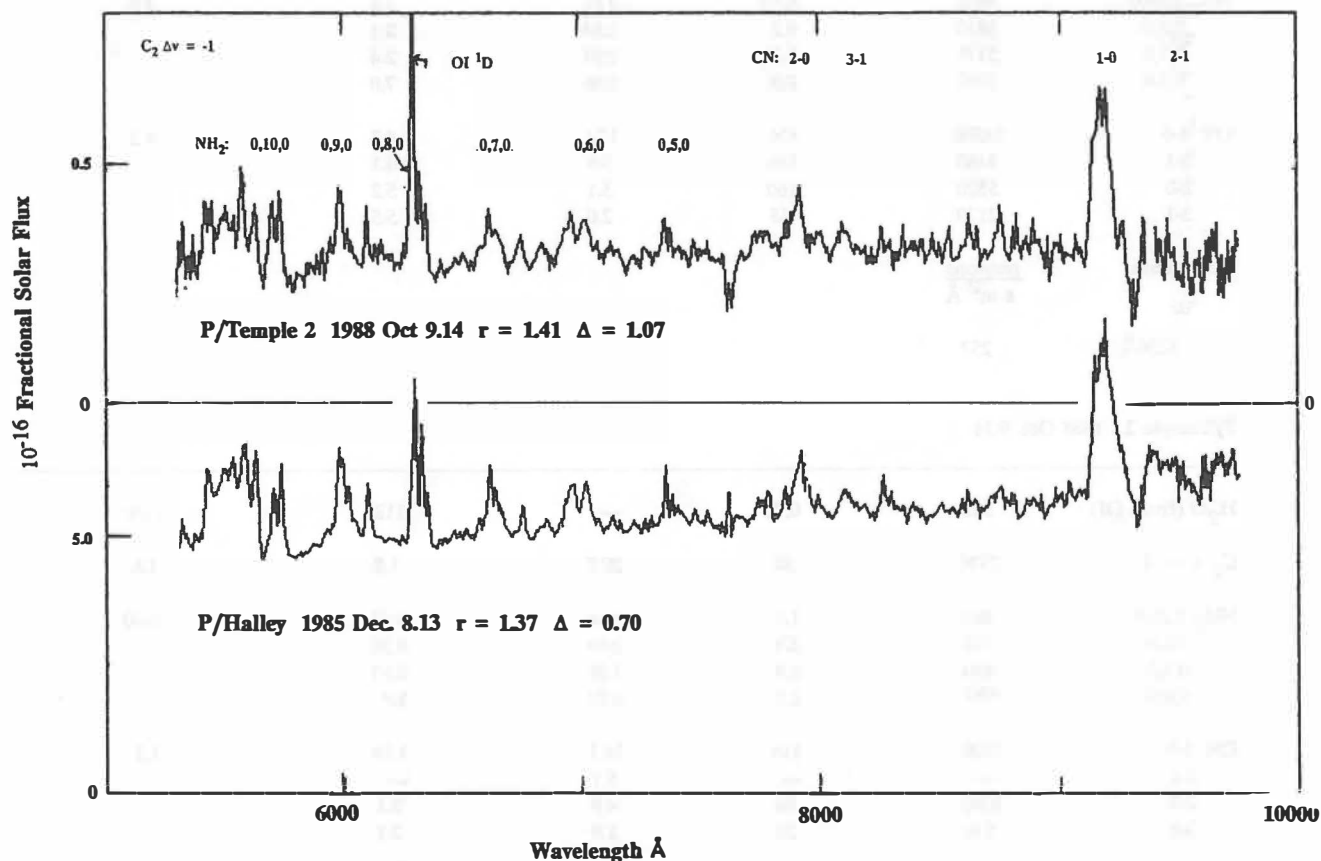


Fig. 1. Ratio spectra of comet P/Temple 2 (top) and P/Halley (bottom) with solar type comparison stars BS 8148 and BS 8931 respectively. The two comets were observed at very similar heliocentric distances. Lack of a comparison star with close air-mass match leaves some residual telluric bands such as O₂A and H₂O in the P/Temple 2 spectrum.

Table 1. Circumstances of Observations

	P/Temple 2	P/Halley	
Perihelion passage:	1988 Sept. 16.73	1986 Feb. 9.45	
Observation date:	1988 Oct. 9.14	(1) 20 min exposure	1985 Dec. 8.13
Sun/Earth distances:	r = 1.41 AU	Δ = 1.07 AU	r = 1.37 AU
Integration window:	106° x 2.5°	(72,650km x 1,984km)	151° x 2.5°
			(77,220km x 1,270km)

Table 2. Fluxes and production rates: P/Halley 1985 Dec. 8.13

Species	Flux in slit photons s ⁻¹ m ⁻²	Band Luminosity 10 ²⁸ photons s ⁻¹	g-factor 10 ⁻³ s ⁻¹	Production rate 10 ²⁶ molecules s ⁻¹	Q Adopted 10 ²⁶ molecules s ⁻¹
H ₂ O (from OI)	1702	1.17	—	1870	1870
C ₂ Δv=-1	20810	232	30.4	7.0	7.0
NH ₂ 0,10,0	4080	6.50	2.82	2.4	2.6
0,8,0	5810	9.2	2.64	3.1	
0,7,0	5170	8.2	2.94	2.4	
0,6,0	5030	8.0	0.98	7.0	
CN 1-0	14500	436	17.1	4.3	4.3
2-1	4480	135	5.4	4.1	
2-0	5320	160	5.1	5.2	
3-1	2170	65	2.0	5.5	
Continuum	photons s m ² Å				
6250Å	257				

P/Temple 2 1988 Oct. 9.14

Species	Flux in slit photons s ⁻¹ m ⁻²	Band Luminosity 10 ²⁸ photons s ⁻¹	g-factor 10 ⁻³ s ⁻¹	Production rate 10 ²⁶ molecules s ⁻¹	Q Adopted 10 ²⁶ molecules s ⁻¹
H ₂ O (from OI)	562	0.70	—	1120	1120
C ₂ Δv=-1	2530	58	28.7	1.8	1.8
NH ₂ 0,10,0	480	1.5	2.66	0.47	0.60
0,8,0	700	2.3	2.49	0.76	
0,7,0	490	1.9	2.78	0.57	
0,6,0	680	2.2	0.92	1.9	
CN 1-0	2030	116	16.1	1.14	1.2
2-1	—	—	5.1	—	
2-0	1060	66	4.9	2.1	
3-1	530	26	1.9	2.2	
Continuum	photons s m ² Å				
6250Å	15.0				

In order to determine the production rates for the observed species we integrated each band over its spectral extend and along the slit over the integration window given in Table 1. The raw counts were converted to photons/s m² by observing an absolutely calibrated flux standard, BS 718 and BS 3314 in the case of P/Halley and BS 718 for P/Temple 2 (Johnson 1980). For these standard stars the slit was opened to 10" yielding photometric calibrations. After correction to unit airmass the observed fluxes collected by our slit aperture are listed in column 2. Next the band luminosities were calculated by using a Haser model correction factor and the appropriate dilution factor ($4\pi\Delta^2$) for each comet. These band luminosities are given in column 3. For the Haser model corrections we employed our recently determined scale lengths (Fink, Combi, and DiSanti 1991 a,b). Since the two comets were observed at nearly identical heliocentric distances, this makes any model dependent errors in a composition comparison between the two comets quite small. Not considering the different projected slit widths, the Haser corrections for the slightly larger distance of P/Temple 2 were about 1.16 times higher for all species.

For transitions excited by solar resonance fluorescence such as those of C₂, NH₂ and CN the proper fluorescence efficiencies, or g-factors must be applied to obtain production rates. For the C₂ $\Delta v = -1$ sequence we used the standard value of Schleicher et al. (1987) for the $\Delta v = 0$ band sequence, multiplied by 0.50. The latter number came from measurements of a number of spectra showing both the $\Delta v = 0$ and $\Delta v = -1$ C₂ emissions (e.g. A'Hearn 1975). For NH₂ we used the values recently calculated by Tegler and Wyckoff (1989). For the CN red system we used the same numbers as in our analysis of 4 comets some years ago (Johnson, Fink and Larson 1984). We calculated these values using the average "f" values given in Sneden and Lambert (1982), Cartwright and Hay (1982), Duric et al. (1978) and Lambert (1968). The g factors listed in Table 2 have been converted to the appropriate heliocentric distances.

The OI emission is not produced by fluorescence but results from the direct photo-dissociation of H₂O to the ¹D state. The procedure to obtain H₂O production rates follows that given in our recent paper on the production rate of H₂O for comet P/Halley (Fink and DiSanti 1990). The variation in branching ratio for this process with change in solar activity is discussed in DiSanti and Fink (1991) and concludes that for equal OI 6300 luminosity the rate of production of water is a factor of 1.23 smaller during periods of active sun. Since this is not a significant change we did not consider variations in solar activity in this analysis. The production rates for H₂O and the parents of C₂, NH₂, and CN for the bands used in our analysis are given in column 5 of Table 2. Of the four NH₂ bands used the most reliable one is 0,8,0 while 0,6,0 gives a rather deviant production rate either due to a contamination in that band or to an erroneous g-factor. The production rate adopted (in column 6) is a weighted average of the other three bands. For CN the most reliable number is that for the 1-0 band which was therefore given most weight for our adopted value.

The comparison of the production rates between P/Halley and P/Temple 2 is illustrated in Table 3. Since we have recently carried out such a comparison for P/Brorsen-Metcalf (DiSanti and Fink 1991), production rates for this comet are also included as are nominal values for a number of comets from photometry given by Schleicher et al. (1987).

Table 3. Production rate comparison

	P/Halley 1986 Dec. 08 $r=1.37 \Delta=0.70$	P/Temple 2 1988 Oct.09 $r=1.41 \Delta=1.07$	P/Brorsen-Metcalf 1989 July 13 $r=1.36 \Delta=0.89$	"Nominal comets"
H ₂ O:	1870 ^a ~ 100%	1120 ~ 100%	257 ~ 100	100
C ₂ :	7.0 ~ 0.37%	1.8 ~ 0.16%	0.94 ~ 0.36%	0.20%
NH ₂ :	2.6 ~ 0.14%	0.60 ~ 0.054%	0.15 ~ 0.06%	—
CN:	4.3 ~ 0.23%	1.2 ~ 0.11%	0.47 ~ 0.18%	0.30%
<u>Cont. Å⁻¹</u> H ₂ O	0.15	0.027	0.0085	

^a All production rates are in 10^{26} molecules/sec.

We note that the water production rate of P/Temple 2 is actually quite close to that of P/Halley at a comparable distance. At first sight this result may appear incongruous since the continuum flux for P/Temple 2 was down by a factor of ~ 17 . However, inspection of Fig. 1 shows that the OI lines are much stronger relative to other emissions and the continuum in P/Temple 2. The OI flux gathered by our slit aperture is thus only a factor of 3.0 lower for P/Temple 2 and after the dilution factor is taken into account the water production rate is only a factor of 1.7 lower. Our P/Temple 2 water production rate is considerably higher than the IUE values of $\sim 350 \times 10^{26}$ reported by Roettger et al. (1990). We offer the following comments on this discrepancy. The lightcurve of P/Temple 2 (Sekanina, 1991) can allow a factor of ~ 1.75 variation. Changing solar activity yields a factor of 1.23. The IUE H₂O production rates are a factor of 2.6 lower than ground based measurements by A'Hearn et al. (1989) and are also lower than values of Spinrad (reported in Roettger et al., 1990).

If we compare the production rates of the observed species with that of water (=100), we find that the abundance of C₂ and NH₂ is roughly one third that of P/Halley while CN is about one half. For P/Brorsen-Metcalf on the other hand, C₂ and CN are in similar proportion (w.r.t. water) as P/Halley but NH₂ is down by a factor of 3 close to the P/Temple value. The values for nominal comets are reasonably close for C₂ but are somewhat higher for CN which could come from differences in g values between the CN blue and red system. The continuum flux compared to water is largest for comet P/Halley, a factor of 5 lower for P/Temple 2 and another factor of 3 lower for P/Brorsen-Metcalf.

We conclude that P/Temple 2 is either enhanced in H₂O over P/Halley if the abundances of C₂, CN and NH₂ are comparable; or if the water abundance in the two comets is equivalent, P/Temple 2 is depleted in C₂, CN and NH₂. The absolute H₂O production rate does not give a clue as to which of the above two scenarios is correct since it depends on the size of the area active in each comet.

This research was supported by NASA grant NAGW 1549.

References

- A'Hearn, M.F. (1975). *Astron. J.* **80**, 861.
- A'Hearn, M.F., Campins, H., Schleicher, D.G., Millis, R.L. (1989). *Ap. J.* **347**, 1155.
- Cartwright, D.C. and Hay, P.J. (1982). *Ap. J.* **257**, 383.
- Duric, N., Erman, P. and Larson, M. (1978). *Physica Scripta* **18**, 39.
- DiSanti, M.A. and Fink, U. (1991). *Icarus* **91**, 105.
- Fink, U., Combi, M.R. and DiSanti, M.A. (1991 a). *Ap. J.* **383**, in press.
- Fink, U., Combi, M.R. and DiSanti, M.A. (1991 b). *AMC Conference extended abstracts*.
- Fink, U. and DiSanti, M.A. (1990). *Ap. J.* **364**, 687.
- Johnson, H.L. (1980). *Rev. Mex. Astron. Astrofis.* **5**, 25.
- Johnson, H.L., Fink, U. and Larson, S.M. (1984). *Icarus* **60**, 351.
- Lambert, D.L. (1968). *JQSRT* **8**, 1265.
- Roettger, E.E., Feldman, P.D., A'Hearn, M.F. and Festou, M.C. (1990). *Icarus* **86**, 100.
- Schleicher, D.G., Millis, R.L. and Birch, P.V. (1987). *Astron. and Astrophys.* **187**, 531.
- Sekanina, Z. (1991). *Astron. J.* **102**, 350.
- Sneden, C. and Lambert, D.L. (1982). *Ap. J.* **259**, 381.
- Tegler, S. and Wyckoff, S. (1989). *Ap. J.* **343**, 445.

P/Halley: Spatial distribution and scale lengths for C_2 , CN, NH_2 , and H_2O

Uwe Fink, Michael Combi¹ and Michael A. DiSanti²
Lunar and Planetary Laboratory, University of Arizona

From P/Halley long slit spectroscopic exposures on 12 dates, extending from 1985 Oct. to 1986 May, spatial profiles were obtained for emissions by C_2 , CN, NH_2 , and OI (1D). Examples of our derived spatial profiles are given in Fig. 1. The qualitative trend of the scale lengths for the different species is nicely exemplified in this figure. C_2 has the longest parent scale length followed by CN and NH_2 . OI which tracks the parent H_2O distribution is quite narrow but slightly wider than the continuum profile which has a center essentially indistinguishable from the stellar seeing disk. Comparison of C_2 and CN also shows that C_2 is falling off faster in the wings so that daughter scale length of CN must be larger than that of C_2 .

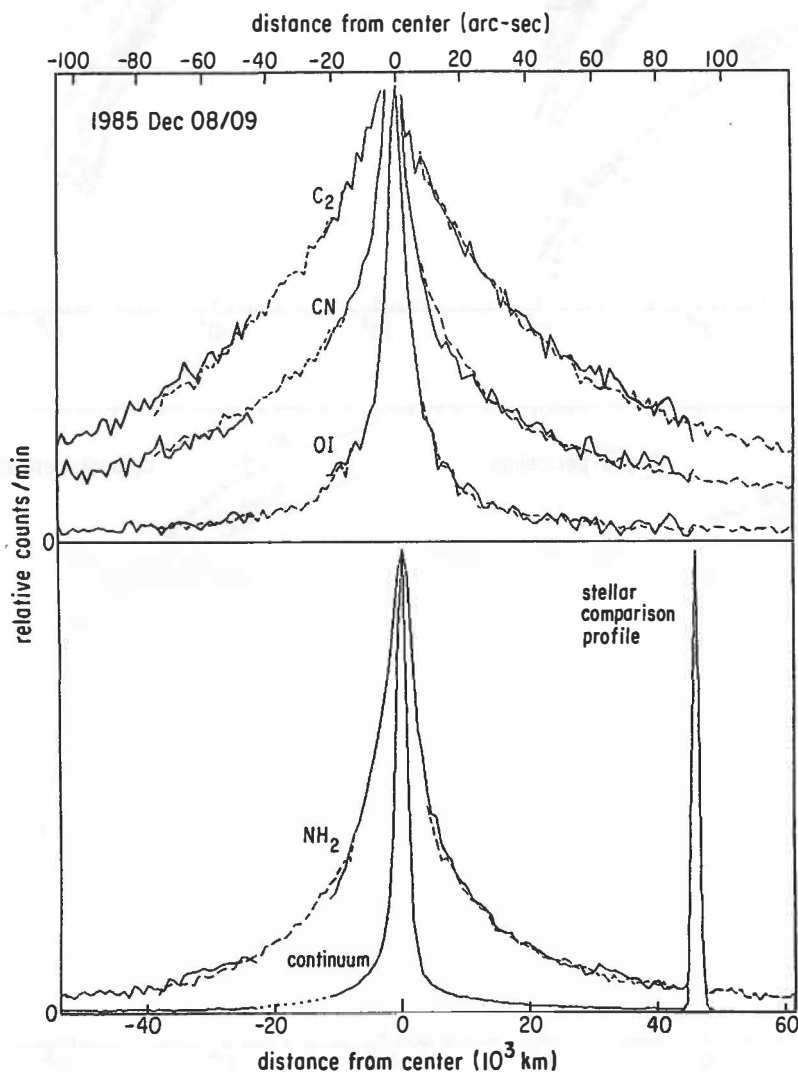


Fig.1. Spatial profiles for 1985 December 8 and 9. Solid curves are the sums of four 5 minute exposures from December 8 and 9. Dashed curve is from a 20 minute exposure on December 9 in which the nucleus was placed behind an occulting mask. All profiles are shown with their correct signal levels at the ends of the slit. The core of the continuum distributions is essentially equal to the stellar seeing profile as illustrated by the solar-type comparison star BS 8931 taken within a few minutes of the P/Halley data. The two data sets of masked and unmasked profiles show excellent agreement.

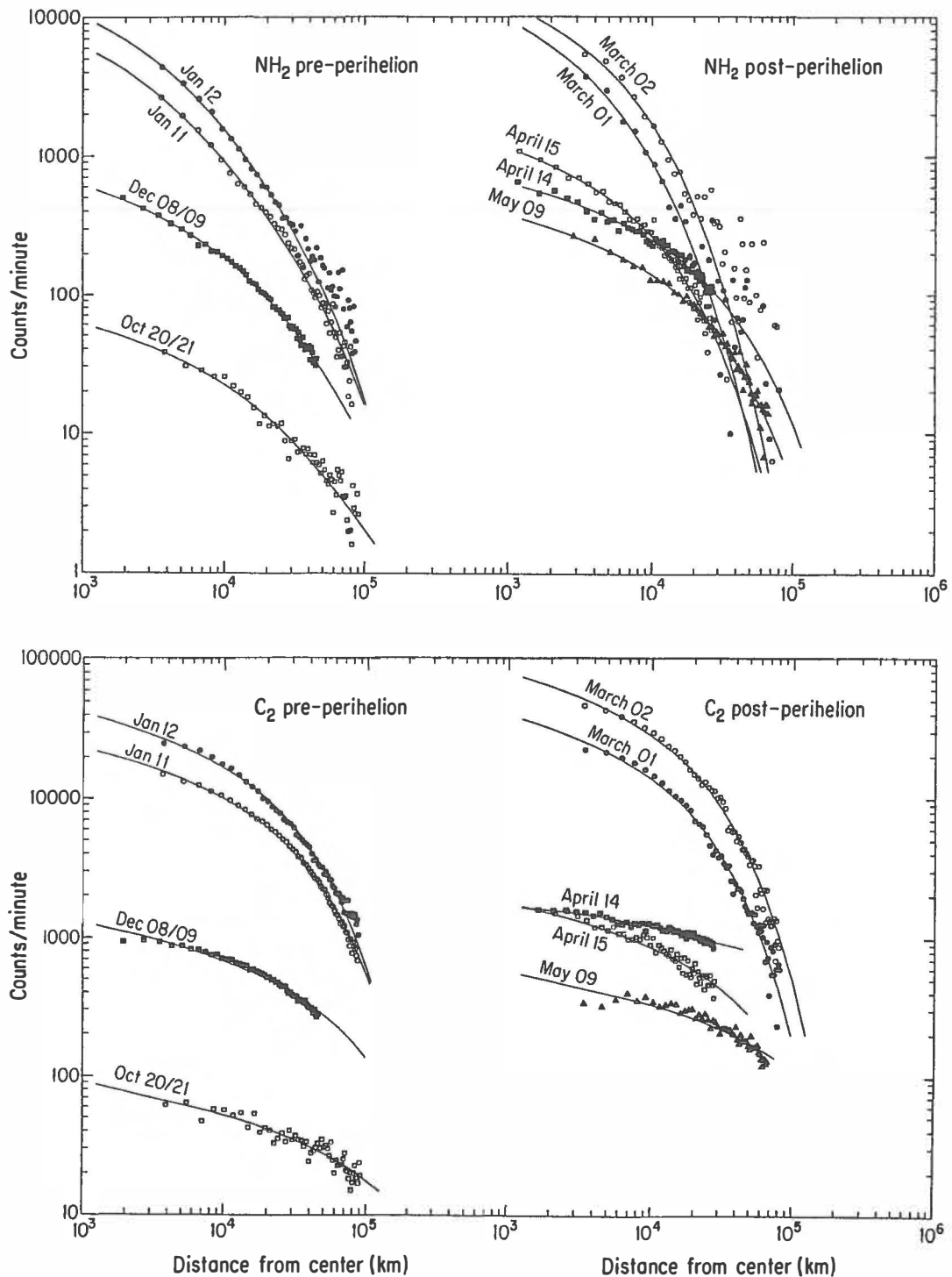


Fig. 2. Summary plot of pre- and post-perihelion NH_2 and C_2 profiles and Hauer model fits. April 14 is shown by solid squares, and April 15 is shown by open squares; symbols for other profiles are unambiguous. The change in scale length (curvature of profiles) for various heliocentric distances is well demonstrated. The profiles for April 14 and April 15 which are strongly perturbed by P/Halley's varying production rate stand out clearly.

Our data and Haser model fits are plotted on a log/log scale in Fig. 2 for NH₂ with its relatively narrow profile and for C₂ with its longer parent scale length. The fitting to the observed radial profiles was accomplished using a differential correction least-squares fitting routine (Combi 1979). The figure illustrates that the comparatively simple Haser model can provide an excellent fit to the observed radial intensity distributions. The resulting pre-perihelion scale lengths demonstrate good consistency and can be used for production rate determinations whenever it is necessary to extrapolate from observed column densities within finite observing apertures.

However, the data also show that the time-varying production rate of P/Halley, especially severe after perihelion, can strongly affect the profiles. The worst case is exemplified by April 14.3/15.3. The former was taken during a period of rapidly decreasing activity, while the April 15.3 data were observed on a rising slope of the lightcurve (Millis and Schleicher 1986). Thus for the latter date we are seeing a substantial enhancement in the center of the profile which has not yet had time to spread outward. The effect is stronger for NH₂ since its short parent lifetime allows it to respond quickly. On the other hand for April 14.3, the wings of the profiles are enhanced since the increased species production rate some time before has now had time to propagate outward. In order to interpret these profiles correctly, a time-dependent production rate model was developed and presented as a separate paper at this conference (Combi and Fink 1991).

Excluding the data set of April 14.3/15.3, which was clearly affected by P/Halley's time dependent production rate we obtained the following results for our scale lengths.

	parent (10^3 km)	daughter (10^3 km)
C ₂	58±20	58±20
CN	28±15	320+200/-100
NH ₂	4.9±1.5	62±20
H ₂ O	74±60	--

For C₂ a slight flattening of the profile close to the nucleus could not be fitted with a two step Haser model but can be accommodated with a CHON halo model (Combi and Fink 1991). If the inner region is excluded from the fit, the daughter/parent scale length ratio changes from near one to about 6. However, when production rates are sought using a two step Haser algorithm, only an equal scale length model comes close to providing an acceptable fit. Only three observations yielded CN daughter scale lengths because our profiles did not extend sufficiently far. The long daughter of CN also makes this emission very sensitive to production rate variations causing greater scatter in the parent values. A curious asymmetry of the scale lengths for NH₂ was found with the post-perihelion parent being about twice the pre-perihelion value, but the daughter being about half the pre-perihelion number. Since a line spectrum from pre-dissociation dominates the UV photo-absorption cross section for both NH₃ and NH₂ the Swings effect is the most likely explanation for this pre-/post-perihelion difference. Most of the OI ¹D profiles, which effectively map out the comet's H₂O distribution, deviated very little from a $1/r$ fall off so that it was not possible to obtain a reliable H₂O parent scale length, although consistency with the nominal lifetime of 80×10^3 seconds is demonstrated. A considerably more detailed description of our data analysis, reduction procedure and scale length determination has been accepted for publication (Fink, Combi and DiSanti 1991).

This research was supported by NASA grant NAGW 1549 and NAGW 1907.

References

- Combi, M.R. (1979). *Ph.D. thesis*, University of Toledo.
- Combi, M.R. and Fink, U. (1991). *AMC Conference*, extended abstracts.
- Millis, R.L. and Schleicher, D.G. (1986). *Nature*, 324, 646.

¹ Michael R. Combi: Space Research Building, University of Michigan, Ann Arbor, MI 48109-2143

² Michael A. DiSanti: Infrared & Radio Astronomy Branch, NASA-Goddard, Code 693, Greenbelt, MD 20771

SPECTROSCOPY OF D-TYPE ASTEROIDS

A. Fitzsimmons, Dept. of Physics, The Queen's University of Belfast, Belfast BT7 1NN, Northern Ireland.

M. Dahlgren and C. -I. Lagerkvist, Astronomiska Observatoriet, Box 515, S-751 20 Uppsala, Sweden.

P. Magnusson and I. P. Williams, School of Mathematical Sciences, Queen Mary and Westfield College, London E1 4NS, England.

ABSTRACT

We have performed a spectroscopic survey of 19 D-type asteroids. Comparison with previous photometry shows excellent agreement. Although the majority have similar colours to cometary nuclei, no cometary emission bands were present in any of the spectra. Absorption bands sporadically appearing were apparently due to stellar objects, and no features inherent to the asteroids were observed.

INTRODUCTION

The D-type asteroids are one of the most interesting groups of objects in the solar system. It was suggested over a decade ago by Gradie and Veverka (1980) that their reddish colouration stems from complex hydrocarbons covering their surfaces. Thus such objects are expected to be among the most primitive of asteroids available for study. Their general low albedos give them an uncanny resemblance to cometary nuclei, whose optical properties they share (*e.g.* Weissman *et al.*, 1989). Thus we have embarked on a spectroscopic survey of asteroids classified as D-type in the taxonomy of Barucci *et al.* (1987), who used both IRAS measured albedos and the ECAS data of Zellner *et al.* (1985) to identify such objects.

OBSERVATIONS AND REDUCTION

All spectra were obtained using the Faint Object Spectrograph on the 4.2m William Herschel Telescope at the Observatory de Roque de los Muchachos, La Palma. The spectrograph is a fixed-format instrument with a 150 lines mm⁻¹ plane transmission grating, recording data in two spectral orders covering wavelengths 3400–4900Å and 4800–9600Å. The detector is a cooled coated 400×590 pixel GEC CCD, giving resolutions of 4.3Å pixel⁻¹ and 8.6Å pixel⁻¹ respectively. Both detector and spectrograph are permanently mounted at the cassegrain focus of the telescope, giving great stability to the system. All targets were observed with

a slit of dimensions 2 arcsec by 20 arcsec, and placed with the long axis at the parallactic angle to minimise the effects of atmospheric dispersion. The asteroids were observed on two consecutive observing runs, on the nights of 8th December 1990 and 7th-8th March 1991. Observations of the solar analogues 16 Cyg B and Hyades 64 were also performed to allow production of reflectance spectra. Details of data reduction will be given in a forthcoming paper (Fitzsimmons *et al.*, 1991, in preparation).

RESULTS

Reflectance spectra were produced in an analogous manner to Luu and Jewitt (1990). However, our resulting spectra were normalised at 5500Å to facilitate comparison with previous photometry published in the ECAS and TRIAD databases (Zellner *et al.*, 1985; Chapman and Gaffey, 1979). The agreement is generally excellent as can be seen from figure 1. In none of the asteroids did we detect any sign of the cometary emission that would be expected from a weakly active cometary nucleus. This should not be surprising though, as the majority of our targets lie in stable main-belt orbits.

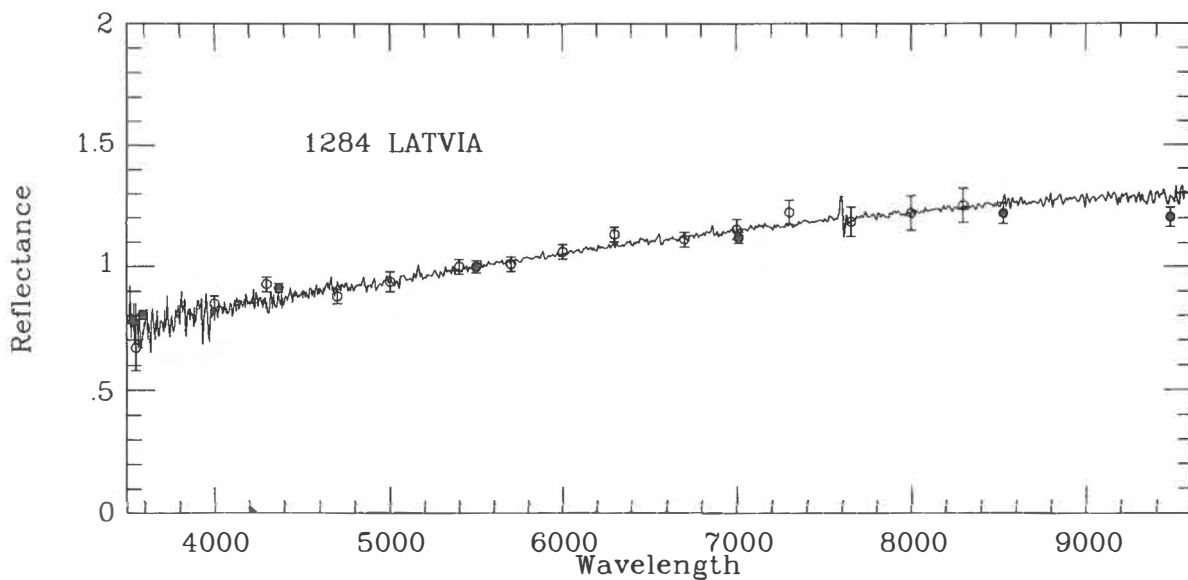


Figure 1. Reflectance spectrum of 1284 Latvia, showing good agreement with both ECAS data (solid points) and TRIAD data (open points).

Spectra of 1583 Antilochus and 2260 Neoptolemus did show transient absorption features in their reflectance spectra, similar to those suspected on other asteroids (Fitzsimmons *et al.*, 1990). Two spectra of Neoptolemus taken 90 minutes apart on 8th March 1991 are shown in figure 2. A very similar pair of discrepant spectra were also obtained for Antilochus. Recent photometry by Binzel (R.B.Binzel, private communication) indicates that both of these

objects have a rotation period of at least 12 hours. A variation due to surface properties would not thus be expected with a timescale of 90 minutes. Comparison of the abnormal spectra with the spectra of K0-K4 stars as presented by Margon (1991) shows a very similar set of absorption features and a possibility is therefore contamination by such a star being present in

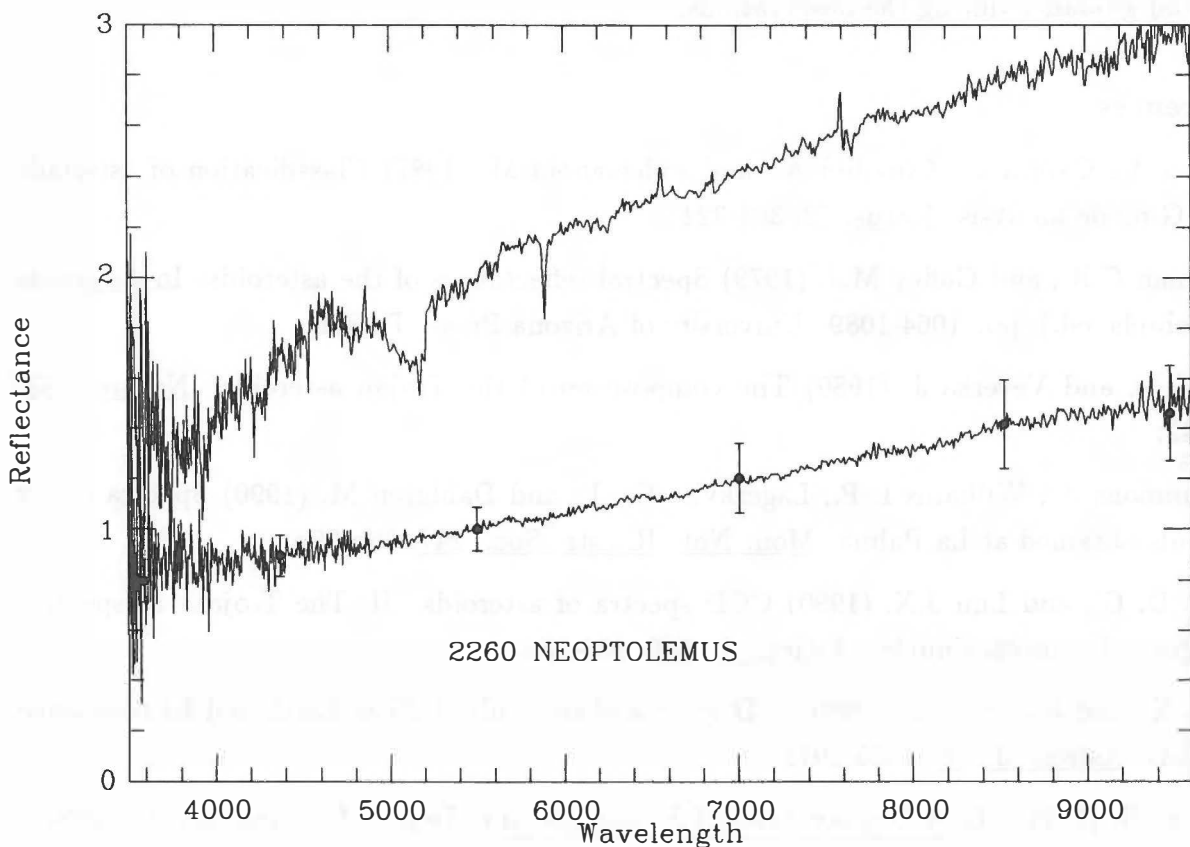


Figure 2. Spectra of 2260 Neoptolemus obtained on 8th March 1991. The upper spectrum has been shifted upwards by unity to ease comparison. Photometric points are taken from the ECAS database.

the slit of the spectrograph. However there was no evidence for such a star being present in the TV finder screen on any of the exposures and neither was there evidence for a secondary source in the original two-dimensional image. We also note that Jewitt and Luu (1990) possibly observed a similar feature at about 5100Å in the Trojan asteroid 1988by1. If contamination turns out to be the correct interpretation, it shows that more care than has hitherto been taken by observers is necessary to eliminate overlapping stars. Inspection of the field and of the CCD chip before reduction may not be adequate.

ACKNOWLEDGEMENTS

AF and PM acknowledge support from the Science and Engineering Research Council. CIL and MD acknowledge support from the Swedish Research Council. The authors would like to thank the staff of the Observatorio de Roque de los Muchachos on La Palma for their help and guidance during the observations.

References

- Barucci A., Capria T., Coradini A., and Fulchignoni M. (1987) Classification of asteroids using G-mode analysis. *Icarus*, **72**, 304-324.
- Chapman C.R., and Gaffey M.J. (1979) Spectral reflectances of the asteroids. In *Asteroids* (T. Gehrels, ed.), pp. 1064-1089. University of Arizona Press, Tucson.
- Gradie J., and Veverka J. (1980) The composition of the Trojan asteroids. *Nature*, **283**, 840-842.
- Fitzsimmons A., Williams I. P., Lagerkvist C. -I., and Dahlgren M. (1990) Spectra of six asteroids obtained at La Palma. *Mon. Not. R. astr. Soc.*, **247**, 26p-29p.
- Jewitt D. C., and Luu J.X. (1990) CCD spectra of asteroids. II. The Trojans as spectral analogues of cometary nuclei. *Astron. J.*, **100**, 933-950.
- Luu J. X., and Jewitt D. C. (1990) CCD spectra of asteroids. I. Near-Earth and 3:1 resonance asteroids. *Astron. J.*, **99**, 1985-2011.
- Margon, B. (1991). In *A Display Atlas of Stellar Spectra*. Dept. of Astronomy, University Of Washington, Seattle.
- Weissman P. R., A'Hearn M. F., McFadden L. A., and Rickman H. (1989) Evolution of comets into asteroids. In *Asteroids II* (R. P. Binzel, T. Gehrels, and M. S. Matthews, eds.), pp. 880-920. University of Arizona Press, Tucson.
- Zellner B., Tholen D. J., and Tedesco E. F. (1985) The eight-color asteroid survey: results for 589 minor planets. *Icarus*, **61**, 355-416.

**ATMOSPHERIC ENTRY SURVIVAL OF LARGE MICROMETEORITES:
IMPLICATIONS FOR THEIR SOURCES
AND FOR THE COMETARY CONTRIBUTION TO THE ZODIACAL CLOUD**

George J. Flynn
Dept. of Physics
SUNY - Plattsburgh
Plattsburgh, NY 12901 USA

ABSTRACT

Atmospheric entry heating simulations indicate that a large fraction of the micrometeorites larger than 100 μm in diameter which survive atmospheric entry must have entered the Earth's atmosphere with velocities very near the Earth escape velocity. Thus, these particles must have been captured by Earth from heliocentric orbits with small eccentricities and low inclinations, indicating a main-belt asteroidal source. Space exposure ages measured on these large micrometeorites are also consistent with a main-belt asteroidal source. However, dynamical calculations have previously indicated that particles larger than 100 μm in diameter were likely to be destroyed by catastrophic collisions in the time required for orbital evolution from the main-belt to Earth capture by Poynting-Robertson drag. The absence of a large amount of collisional debris in the <50 μm size range indicates these large micrometeorites are not the few, rare survivors of a mostly collisionally disrupted population. The measured space exposure ages, which are about an order of magnitude larger than their calculated catastrophic collision lifetimes, confirm the survival of these large micrometeorites for times much longer than the calculated catastrophic collision lifetimes. Since collisions with cometary dust <20 μm in size were expected to be the major contributor to the collisional destruction of these larger particles the contribution of cometary material to the zodiacal cloud is likely to be much smaller than previously believed.

INTRODUCTION

The atmospheric entry survival of micrometeorites smaller than about 50 μm in diameter ($\sim 10^{-7}$ grams) was suggested by Opik (1937), and confirmed experimentally by the recovery of unmelted micrometeorites from the Earth's stratosphere by balloons and aircraft during the 1970's (Brownlee, 1985). Most micrometeorites larger than $\sim 100 \mu\text{m}$ in diameter were expected to be vaporized on atmospheric entry (Whipple, 1950; Fraundorf, 1980), and the radar detection of meteor trails from objects as small as 10^{-6} grams (Hughes, 1978) provides experimental confirmation of this predication. The recovery of large quantities of micrometeoritic material from 100 μm to larger than 1000 μm in diameter, both melted and apparently unmelted, from the ocean floor (Brownlee, 1985), lakes in Greenland (Maurette et al., 1988), and the Antarctic ice (Maurette et al., 1991) has resulted in a reexamination of the atmospheric entry heating of large micrometeorites.

PROPERTIES OF LARGE MICROMETEORITES

The extraterrestrial origin of the large (>100 μm in diameter) micrometeorites is established by the presence of spallogenic Ne (Olinger et al., 1990), and the cosmogenic radionuclei ^{10}Be and ^{26}Al (Raisbeck and Yiou, 1987; Raisbeck and Yiou, 1989; Nishiizumi et al., 1991) in both large spherules, assumed to have been melted on atmospheric entry, and large, irregularly shaped particles which appear to be unmelted.

The irregularly shaped, apparently unmelted, particles should best preserve information on the original composition of the large micrometeorites. These particles have major element abundances generally consistent with the CI and/or CM chondritic meteorites, though Ni and S are both significantly depleted from their chondritic values (Maurette et al., 1991). Three of four irregularly shaped micrometeorites from Greenland also have minor/trace element abundances, including the volatile elements Cu, Zn, Ga, and Ge, consistent

with the range of chondritic meteorites (Flynn et al., 1991). Sutton et al. (1988) suggest that the compositions of 3 of 9 melted spheres they analyzed were more consistent with ordinary chondrite rather than carbonaceous chondrite material. The major minerals are generally olivine and pyroxene, consistent with the chondritic meteorites (Maurette et al., 1991).

ATMOSPHERIC ENTRY HEATING

The heating experienced by micrometeorites on atmospheric entry can be calculated using the model developed by Whipple (1950). Computer simulations of the Whipple entry heating model, which calculate the temperature profile during atmospheric deceleration for micrometeorites with a range of initial velocities, densities, diameters, and impact parameters, have been developed (Flynn, 1989b; Love and Brownlee, 1991). Entry heating simulations for large micrometeorites indicate that particles larger than 100 μm in diameter must have geocentric velocities $< 5 \text{ km/sec}$ for any significant fraction of them to survive entry (Flynn 1990; Love and Brownlee, 1991). The results for particles 60 μm and 200 μm in diameter are shown in Figure 1 for particles having geocentric velocities, prior to Earth gravitational infall acceleration, of 1, 5, 10, and 20 km/sec. Taking 1600K as the melting temperature, Figure 1 shows that a large fraction of incident 60 μm diameter particles with velocities up to 10 km/sec survive entry unmelted. However, for 200 μm diameter particles only those with large impact parameters survive entry even with a 5 km/sec geocentric velocity.

IMPLICATIONS FOR SOURCES

Geocentric velocities less than 5 km/sec are characteristic of particles arriving at Earth in heliocentric orbits of low eccentricity and inclination. Flynn (1989a) has shown that for small particles evolving under the influence of solar gravity and Poynting-Robertson drag, such low geocentric velocities are possible for particles derived from main-belt asteroidal parent bodies, but are inconsistent with the geocentric velocities calculated for even the most favorable presently active comet (Comet Kopff). Comet Schwassmann-Wachmann 1, which is in a nearly circular orbit of low eccentricity, would contribute dust with orbital parameters similar to the main-belt asteroids,

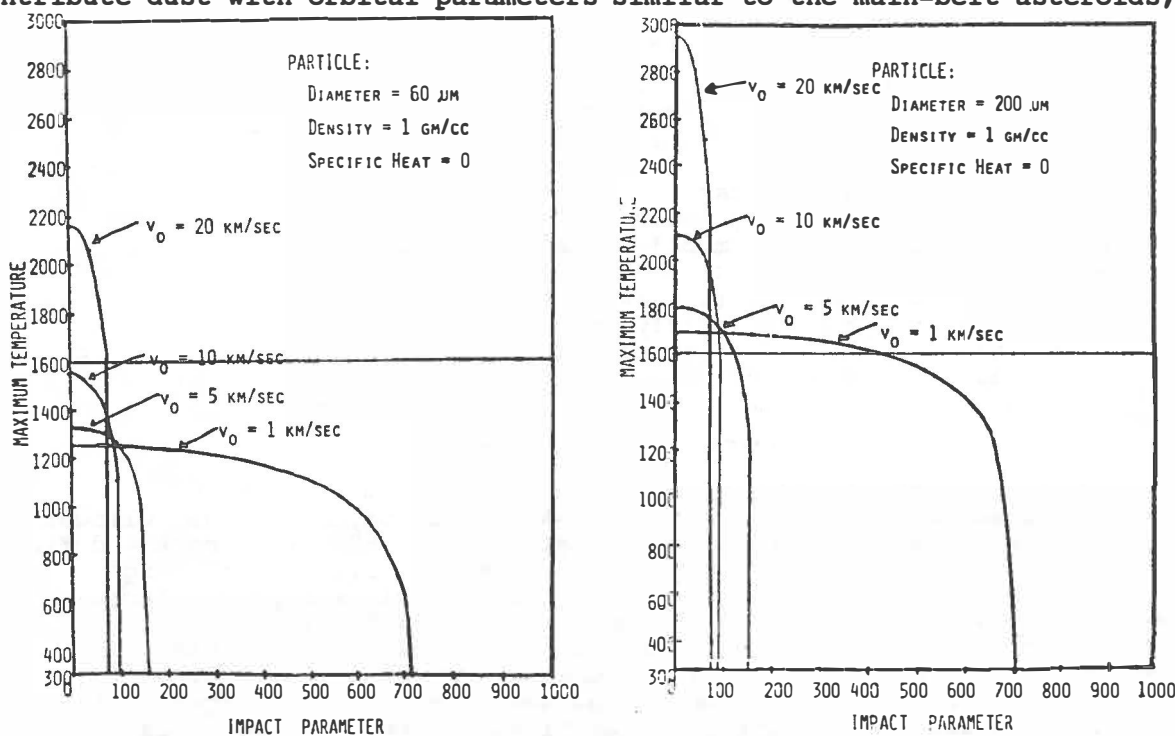


Figure 1: Maximum temperature (K) reached on atmospheric entry versus impact parameter ($\times 10^5$ meters) for particles of 60 μm diameter (left) and 200 μm diameter (right).

but Schwassmann-Wachmann 1 has a low dust emission rate (Jewitt, 1990). Orbital evolution simulations including the effect of planetary gravitational perturbations confirm that very few cometary particles arrive at Earth with geocentric velocities lower than 5 km/sec (Gustafson et al., 1987), while a large fraction of the main-belt asteroidal particles do arrive at Earth with such low velocities. Thus, most large ($\geq 200 \mu\text{m}$) micrometeorites which survive Earth atmospheric entry unmelted are likely to be derived from main belt asteroidal parent bodies (Flynn 1990; Love and Brownlee, 1991).

The exposure ages inferred from radiogenic nuclei (Raisbeck and Yiou, 1989; Nishiizumi et al., 1991) and spallogenic ^{21}Ne (Olinger et al., 1990) are in the 10^5 to 2×10^7 year range, consistent with the Poynting-Robertson orbital evolution times from the main-belt to Earth for particles in this size range. In addition, the radiogenic nuclei confirm that the large micrometeorites were irradiated in space in roughly the sizes we see them now, indicating they are not debris from much larger meteors which fragmented either just before or during Earth atmospheric entry (Raisbeck and Yiou, 1989; Nishiizumi et al., 1991). Nishiizumi et al. (1991) have further inferred that the exposure must have been in the inner solar system, eliminating particles in the highly elliptical orbits characteristic of cometary material.

The chemical compositions of the large micrometeorites are consistent with an asteroidal source for this material (Maurette et al., 1988). The isotopic composition of carbon in melted micrometeorites from Greenland and Antarctica is also consistent with the macromolecular material in CI and CM carbonaceous meteorites, suggesting these are asteroidal particles (Yates et al., 1991). The evidence indicates most large micrometeorites, which survive atmospheric entry melted or unmelted, are from main-belt asteroidal parent bodies.

COLLISIONAL LIFETIMES OF MAIN-BELT ASTEROIDAL DUST

The contribution of main-belt asteroids to the flux of large ($\geq 200 \mu\text{m}$) particles at Earth has previously been assumed to be very small (Flynn 1989a; Zook and McKay, 1986) because the calculated catastrophic collision lifetimes ($\sim 10^4$ to 10^5 years for a $100 \mu\text{m}$ diameter particle) were substantially shorter than the times required for Poynting-Robertson orbital evolution from the main-belt to an Earth intersecting orbit ($> 10^6$ years for a $100 \mu\text{m}$ diameter particle) as shown in Figure 2.

The longest catastrophic collision lifetime estimates for $100 \mu\text{m}$ to 10,000 μm diameter particles are an order-of-magnitude less than the Poynting-Robertson lifetimes (see Figure 2), indicating that most of the main-belt dust in this size range should be destroyed by collisions long before reaching Earth. Since more than ten collisional lifetimes would have elapsed during the orbital evolution, the particle flux would be reduced by at least a factor of $2^{10} = \sim 1000$. The debris resulting from these collisions would then be collectable at Earth, since, for particles smaller than $100 \mu\text{m}$ in diameter the Poynting-Robertson lifetimes are smaller than the collisional lifetimes (Dohnanyi, 1978). This assumes the debris orbits do not differ dramatically from the orbit of the original particle, so the near-Earth gravitational

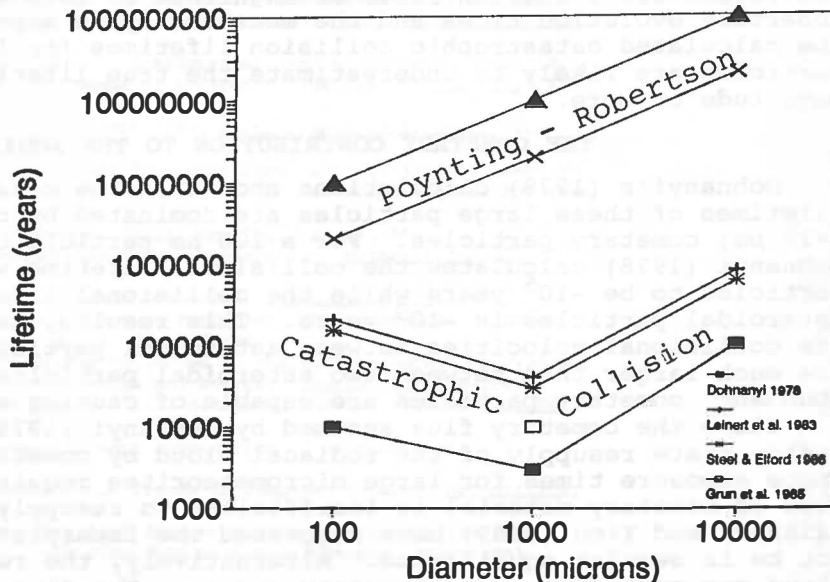


Figure 2: Poynting-Robertson and catastrophic collision lifetimes for particles from $100 \mu\text{m}$ to $10,000 \mu\text{m}$ in diameter.

enhancement factor is similar for both debris and survivors. The large momentum of the micrometeorite, which has about 1000 times the mass of the disrupting particle, should assure this condition is met. The required debris is not seen.

Particles in the 100 to 1000 μm size range are at the peak of the mass-frequency distribution (Hughes, 1978) as shown in Figure 3. Yiou et al.

(1989) estimate the global input of cosmic spherules in polar ice cores to be ~1500 tons/year, while Maurette et al. (1991) infer an even higher accretion rate. This indicates that a minimum of 10% of the mass influx of 100 μm to 1000 μm particles survives entry while the remainder forms meteors. Since less than 1/1000 of the starting mass in the 100 to 10,000 μm diameter range would be expected to survive collisional processes and reach Earth, we would expect to find $1000 \times 1,500 \text{ tons/year} = 1.5 \times 10^6 \text{ tons/year}$ of debris in the form of particles $<50 \mu\text{m}$ in size. The total mass accretion rate at Earth for particles $<50 \mu\text{m}$ in diameter is only $\sim 10^3 \text{ tons/year}$ based on satellite flux measurements (Hughes, 1978), a factor of 1000 less than required by the calculated collision lifetimes.

The absence of large quantities of debris smaller than 50 μm in diameter confirms that the large micrometeorites are not the few, rare survivors of a starting population which was mostly disrupted by collisions.

The space exposure ages measured by radiogenic nuclei and spallogenic ^{21}Ne confirm that particles 100 μm and larger have space residence times longer than 10^6 years. Raisbeck and Yiou (1989) have noted the measured space exposure ages substantially exceed the catastrophic collision lifetimes calculated by Dohnanyi (1978). Although more recent modeling has increased the calculated catastrophic collision lifetimes, as shown in Figure 3, these new values still fall an order-of-magnitude or more short of the Poynting-Robertson evolution times and the measured space exposure durations. Thus, the calculated catastrophic collision lifetimes for 100 μm to 1000 μm particles are likely to underestimate the true lifetimes by an order-of magnitude or more.

THE COMETARY CONTRIBUTION TO THE ZODIACAL CLOUD

Dohnanyi's (1978) calculations show that the catastrophic collision lifetimes of these large particles are dominated by collisions with smaller ($<20 \mu\text{m}$) cometary particles. For a 100 μm particle orbiting in the main-belt Dohnanyi (1978) calculates the collisional lifetime with small cometary particles to be $\sim 10^5$ years while the collisional lifetime with other main-belt asteroidal particles is $\sim 10^9$ years. This results, in part, from the fact that the collisional velocities between asteroidal particles and cometary particles are much larger than between two asteroidal particles, so smaller, more abundant, cometary particles are capable of causing a catastrophic collision.

Since the cometary flux assumed by Dohnanyi (1978) was that needed for steady state resupply of the zodiacal cloud by cometary material, the observed space exposure times for large micrometeorites require the recent ($\sim 10^6$ years) flux of cometary material is insufficient to resupply the zodiacal cloud. Raisbeck and Yiou (1989) have suggested the interplanetary dust complex may not be in secular equilibrium. Alternatively, the resupply of the zodiacal cloud may come from a non-cometary source. The discovery of dust bands in the main-belt (Low et al., 1984), presumably from asteroid-asteroid collisions, suggests an asteroidal source for at least some of the zodiacal cloud material. Direct examination of the 5 to 30 μm size dust collected from the

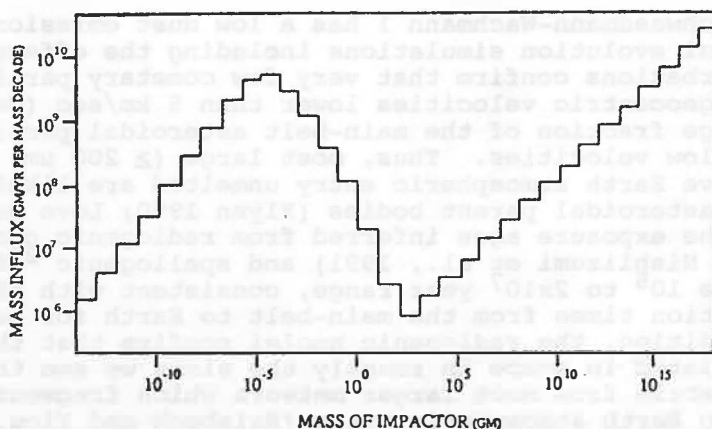


Figure 3: Meteoritic mass influx per mass decade at Earth (adapted from Kyte and Wasson, 1986).

Earth's stratosphere suggests a substantial fraction of this dust is derived from main-belt asteroidal parent bodies. Space exposure ages inferred from solar flare track densities (Sandford, 1986) and the distribution of peak temperatures reached on atmospheric entry, inferred from the presence of volatile elements, low-temperature minerals, and unannealed solar flare tracks (Flynn, 1989a; Sandford and Bradley, 1990) all suggest a large fraction of the cosmic dust recovered from the Earth's stratosphere is from main-belt asteroidal sources. Mineralogical evidence, in particular aqueous alteration, also suggests that the flux of asteroidal particles exceeds that of cometary particles for the cosmic dust recovered from the Earth's stratosphere (Schramm et al., 1989).

The survival of large micrometeorites in the inner solar system for 10^6 to 10^7 years indicates that the recent ($\sim 10^6$ to 10^7 year) cometary contribution to the smaller interplanetary dust particles is insufficient for steady-state resupply of the zodiacal cloud. If the zodiacal cloud is presently in equilibrium then main-belt asteroidal material is likely to be the major contributor to the zodiacal dust.

ACKNOWLEDGEMENT: This work was supported by NASA Grant NAG-9-469.

REFERENCES

- Brownlee D. E. (1985) Cosmic Dust Collection and Research, *Ann. Rev. Earth Planet. Sci.*, **13**, 147-173.
 Dohnanyi J. S. (1978) Particle Dynamics, in *Cosmic Dust* (ed J. A. M. McDonnell), John Wiley, New York, 527-605.
 Flynn G. J. (1989a) Atmospheric Entry Heating: A Criterion to Distinguish between Asteroidal and Cometary Sources of Interplanetary Dust, *Icarus*, **77**, 287-310.
 Flynn G. J. (1989b) Atmospheric Entry Heating of Micrometeorites, *Proc. Lunar Planet. Sci. Conf. 19th*, 673-682.
 Flynn G. J. (1990) Atmospheric Entry Survival of Large Micrometeorites: Clues to their Sources and to the Flux of Cometary Dust, *Meteoritics*, **25**, 365.
 Flynn G. J., S. R. Sutton, and W. Klock (1991) Volatile Trace Elements in Large Micrometeorites from Greenland, (abstract) *Meteoritics*, in press.
 Fraundorf P. (1980) The Distribution of Temperature Maxima for Micrometeorites in the Earth's Atmosphere Without Melting, *Geophys. Res. Lett.*, **10**, 765-768.
 Grun E., H. A. Zook, H. Fechtig, and R. H. Giese (1985) Collisional Balance Of the Meteoritic Complex, *Icarus*, **52**, 244-272.
 Gustafson B. A. S., N. Y. Misconi, and E. T. Rusk (1987) Interplanetary Dust Dynamics. II. Poynting-Robertson Drag and Planetary Perturbations on Interplanetary Dust, *Icarus*, **72**, 568-581.
 Hughes D. M. (1978) Meteors, in *Cosmic Dust* (ed. J. A. M. McDonnell), John Wiley, New York, 123-185.
 Jewitt D. (1990) Continuous Activity in Comet P/Schwassmann-Wachmann 1, *Asteroids, Comets, Meteors III* (eds. C.-I. Lagerkvist, H. Rickman, B. A. Lindblad, M. Lindgren), Uppsala University, 347-352.
 Kyte F. T., and J. T. Wasson (1986) Accretion Rate of Extraterrestrial Matter: Iridium Deposited 33 to 67 Million Years Ago, *Science*, **232**, 1225-1229.
 Leinert C., S. Roser, and J. Buitrago (1983) *Astron. Astrophys.*, **118**, 345.
 Love S. G. and D. E. Brownlee (1991) Heating and Thermal Transformation of Micrometeoroids Entering the Earth's Atmosphere, *Icarus*, **89**, 26-43.
 Low, F. J. et al. (1984) Infrared Cirrus: New Components of the Extended Infrared Emission, *Astrophys. J.*, **278**, L19.
 Maurette M., C. Hammer, M. Pourchet, and D. E. Brownlee (1988) The "Blue Lake II" Expedition of July-August 1987 in Greenland, and the Search for mm-size Unmelted Extraterrestrial Particles, *Lunar Planet. Sci. XIX*, 744-745.
 Maurette M., C. Olinger, M. C. Michel-Levy, G. Kurat, M. Pourchet, F. Brandstatter, and M. Bourot-Denise (1991) A Collection of Diverse Micrometeorites Recovered from 100 Tonnes of Antarctic Blue Ice, *Nature*, **351**, 44-47.
 Nishiizumi K. et al. (1991) Exposure History of Individual Cosmic Particles, *Earth Planet. Sci. Lett.*, in press.
 Olinger C. T., M. Maurette, R. M. Walker, and C. M. Hohenberg (1990) Neon Measurements of Individual Greenland Sediment Particles: Proof of an Extraterrestrial Origin and Comparison with EDX and Morphological Analyses, *Earth Planet. Sci. Lett.*, **100**, 77-93.
 Opik E. J. (1937) Basis of the Physical Theory of Meteor Phenomena, *Tartu Obs. Pub.*, **29**, 51-66.
 Reisbeck G. M., and Yiou F. (1987) 10 Be and 26 Al in Micrometeorites from Greenland Ice, *Meteoritics*, **22**, 485-486.
 Reisbeck G. M., and Yiou F. (1989) Cosmic Ray Exposure Ages of Cosmic Spherules, *Meteoritics*, **24**, 318.
 Sandford S. A. (1986) Solar Flare Track Densities in Interplanetary Dust Particles: The Determination of an Asteroidal Versus Cometary Source of the Zodiacal Cloud, *Icarus*, **68**, 377-394.
 Sandford S. A. and J. Bradley (1990) Interplanetary Dust Particles Collected in the Stratosphere: Observations of Atmospheric Entry Heating and Constraints on Interrelationships and Sources, *Icarus*, **82**, 146-166.
 Steel D. I. and W. G. Elford (1986) Collisions in the Solar System - III. Meteoroid Survival Times, *Mon. Not. R. Astr. Soc.*, **218**, 185-199.
 Schramm L. S., Brownlee D. E., and Wheelock M. M. (1989) Major Element Composition of Stratospheric Micrometeorites, *Meteoritics*, **24**, 99-112.
 Sutton S. R., G. Herzog, and R. Hewins (1988) Chemical Fractionation Trends in Deep-Sea Spheres, *Meteoritics*, **23**, 304.
 Yates P. D., I. P. Wright, and C. T. Pillinger (1991) A Possible Link Between Melted Micrometeorites from Greenland and Antarctica with an Asteroidal Origin: Evidence from Carbon Stable Isotopes, (abstract) *Meteoritics*, in press.
 Yiou F., G. M. Raisbeck, and C. Jehanno (1989) Influx of Cosmic Spherules to Earth during the Last $\sim 10^5$ years as Deduced from Concentrations in Antarctic Ice Cores, *Meteoritics*, **24**, 344.
 Whipple F. L. (1950) The theory of micro-meteorites. Part I: In an Isothermal Atmosphere, *Proc. Natl. Acad. Sci. USA*, **36**(12), 687-695.
 Zook H. A. and D. S. McKay (1986) On the Asteroidal Component of Cosmic Dust, *Lunar Planet. Sci. XVII*, 977-978.

POLYNOMIAL APPROXIMATIONS OF POINCARÉ MAPS FOR HAMILTONIAN SYSTEMS

Claude Froeschlé and Jean-Marc Petit

Observatoire de Nice, O.C.A., B.P. 139, 06003 Nice Cedex, France

Abstract Different methods are proposed and tested for transforming a non-linear differential system, and more particularly a Hamiltonian one, into a map without integrating the whole orbit as in the well-known Poincaré return map technique. We construct piecewise polynomial maps by coarse-graining the phase-space surface of section into parallelograms and using either only values of the Poincaré maps at the vertices or also the gradient information at the nearest neighbours to define a polynomial approximation within each cell. The numerical experiments are in good agreement with both the real symplectic and Poincaré maps.

A synthetic approach

Poincaré maps are now of common use for studying the qualitative behaviour of differential equations (see Hénon, 1981). Moreover, in order to study stability problems, many authors have sought explicit algebraic mappings which approximate, at least qualitatively, the Poincaré maps obtained from the original Newton equations. Froeschlé and Petit (1990, paper I) have reviewed some of these mappings and showed that they are reliable only as long as one remains within the domain of validity of the approximations made in order to isolate either — in the case of deterministic mappings — an integrable part and some instantaneous perturbations, or — for stochastic mappings — a source of endogenous/exogenous stochasticity (see Froeschlé and Rickman, 1988). All these mappings are *ad hoc* and reliable only in some region of the phase space and for some specific purpose. In paper I we built a mapping valid everywhere in the phase space, following an idea already used by Varosi et al. (1987) but in the framework of non-Hamiltonian systems (i.e., systems where attractors do exist). The method consists of coarse-graining the phase-space surface of section and then interpolating the value of the image of a point. Linear interpolation requires a rather fine graining of the phase space, hence it is necessary to compute a lot of points on the grid. However, Taylor expansions of order 3 and 5 can provide very good results as long as symmetrical interpolation formulae are applied, for which it is necessary to use an extended grid. Since there are cases where one cannot cross a given limit, asymmetrical interpolation formulae have been tested, but their accuracy was found to be inferior. Therefore Petit and Froeschlé (1991, paper II) have developed another type of interpolation, where the information, including that on the gradients, is stored to the same level of accuracy only for the nearest-neighbouring vertices. Thus, not only images of vertices are computed, but also tangential mappings at each vertex.

There are in any case two key parameters: the number of bins in each direction $N = (\text{total number of cells})^{1/D}$, where D ($= 2$ and 3 in papers I and II) is the dimension of the surface of section, and M the order of the Taylor expansion. In order to explore the validity of the synthetic approach, we have applied our method in two cases:

- 1) An algebraic area-preserving mapping for which the computation of orbits is very fast. This allows one to follow a large number of orbits and to carry out enough iterations for a meaningful comparison.
- 2) A special case of the restricted three-body problem, already studied by Duncan et al. (1989).

In the former case the well-known standard mapping has been used (Froeschlé, 1970; Lichtenberg and Lieberman, 1983):

$$\begin{aligned}x^{(n+1)} &= x^{(n)} + a \sin(x^{(n)} + y^{(n)}), \\y^{(n+1)} &= x^{(n)} + y^{(n)}.\end{aligned}\quad (\text{mod } 2\pi)$$

Fig. 1 shows orbits of the standard mapping for $a = -1.3$. Indeed such a mapping exhibits all the well-known typical features of problems with two degrees of freedom, such as invariant curves, “islands”, and stochastic zones where the points wander in a chaotic way. Figs. 1b and 1c are magnifications of the

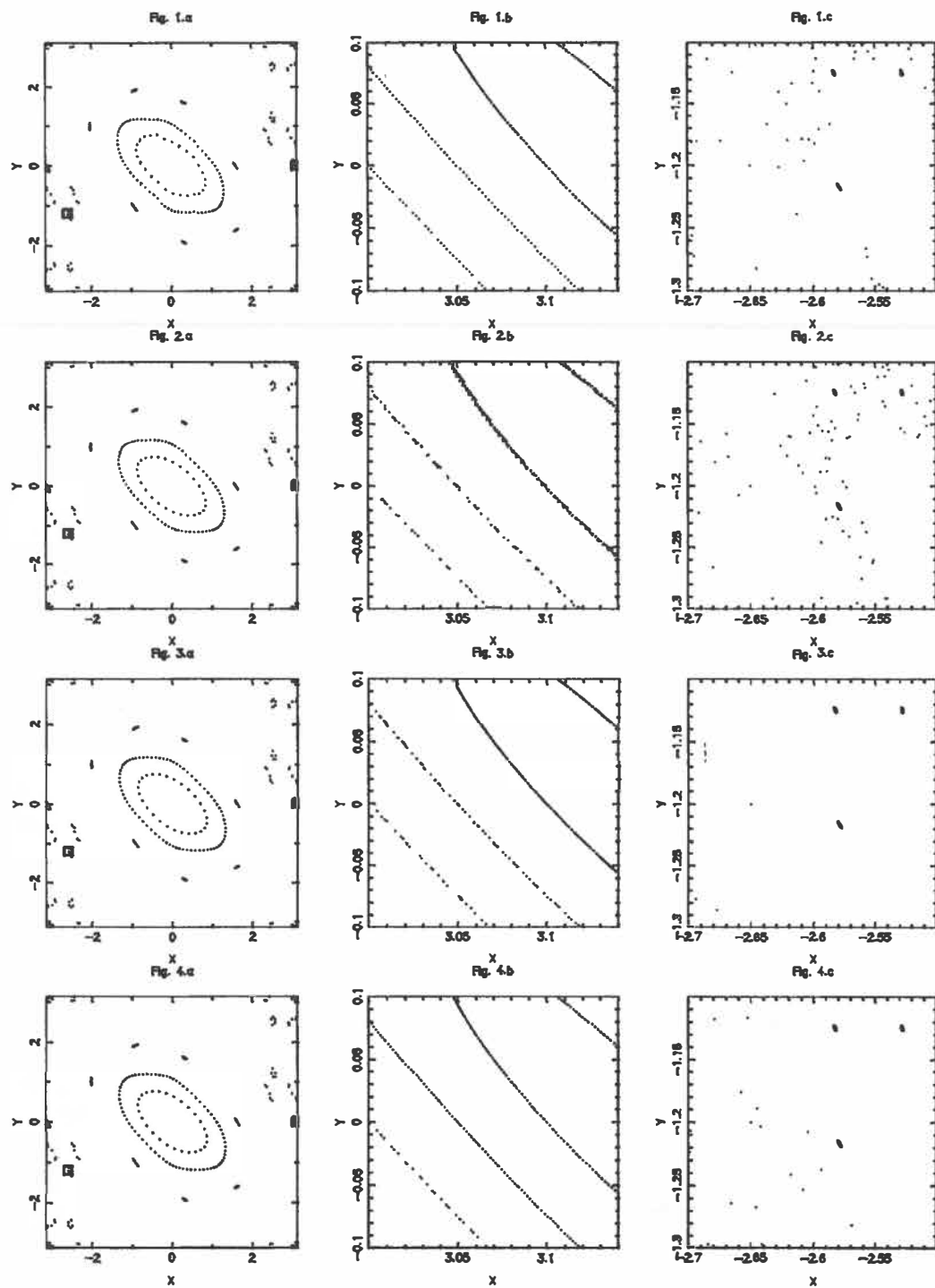


Fig. 1: (a) Plots of the standard mapping for $a = -1.3$. (b) and (c) are enlargements of the small boxes shown in (a), respectively at the right border and near the left border.

Figs. 2a-c: Same as in Figs. 1a-c but using a Taylor approximation of order 3 with a regular grid and decentered formulae.

Figs. 3a-c: The same as in Figs. 1a-c but using a Taylor approximation of order 3 with a non-regular grid and decentered formulae.

Figs. 4a-c: The same as in Figs. 1a-c but using a Taylor approximation of order 3 with a regular grid and the gradient method.

small boxes indicated in Fig. 1a. At this magnification level, details like second-order islands become evident and the approximation levels of the synthetic maps are easily visualized. Figs. 2a, 2b and 2c correspond to the same orbits and the same magnifications as Figs. 1a-c, but using the Taylor interpolation mapping of order $M = 3$ with decentered formulae on the edges of the mapping; here the grid was regular and characterized by $N = 40$. The results are very similar to those of the original map, except for the box close to the frontier. Figs. 3a-c correspond to the same formulae, but with cells having half the size of the previous ones close to the edges. Apparently, this does not improve drastically the quality of the mapping in the frontier box. On the other hand, a definite improvement is obtained using the gradient formulae (for more details about these formulae, see papers I and II).

Fig. 5.a

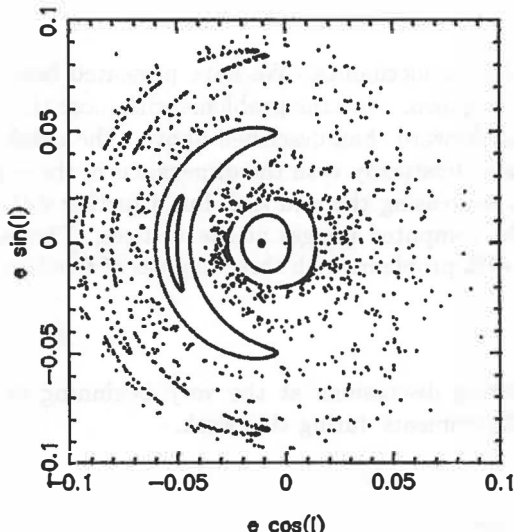


Fig. 5.c

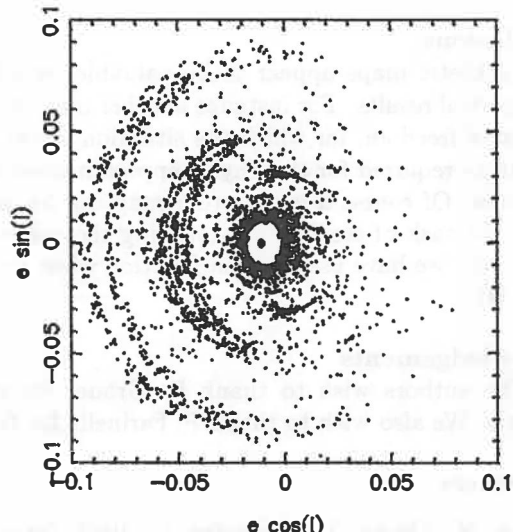


Fig. 5.d

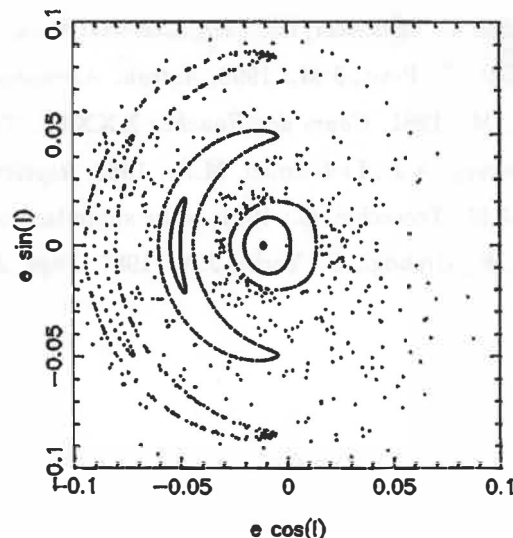
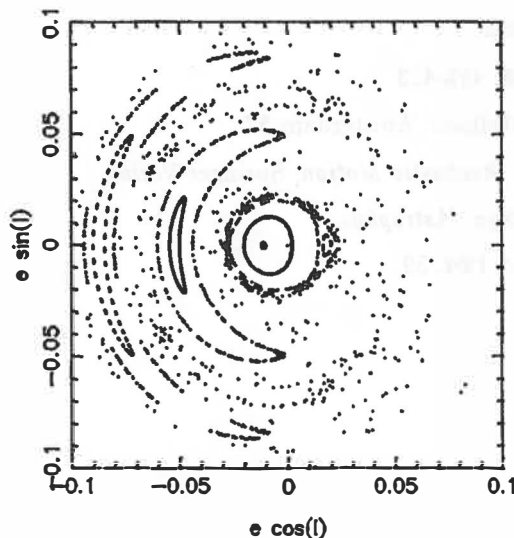


Fig. 5a: Trajectories of the Poincaré map of the restricted three-body problem, in the plane giving (as polar coordinates) eccentricity and mean longitude at conjunction with the planet, for the Neptune-to-Sun mass ratio $m/M_0 = 5.178 \cdot 10^{-5}$ and a Jacobi constant of 3.0080694.

Figs. 5b-d: The same as Fig. 5a but for the synthetic maps T1, T3 and T5, respectively.

Let us switch to the tests of the method on a special case of the restricted three-body problem, for which Duncan *et al.* have developed a special mapping. Fig. 5a shows orbits of the Poincaré map taking as surface of section the plane defined by the eccentricity and the mean longitude as polar coordinates, at the times when the particle is in conjunction with the planet (i.e., in the rotating frame, when $y = 0$ and $\dot{y} > 0$). Figs. 5b-d show plots of the corresponding orbits for the Taylor synthetic mappings of order 1, 3 and 5, using a grid with $N = 100$. While the linear mapping T1 displays only poor qualitative similarities with the Poincaré map, the map T3 correctly reproduces the locations, shapes and sizes of the zones containing regular orbits. Of course, the T5 map is even better. It should be noted that in order to obtain the same accuracy, we had to use a smaller grid size (i.e., more points) than for the standard map, since the functions which have to be interpolated are less regular.

Conclusions

Synthetic maps appear to be valuable tools for celestial mechanics. We have presented here only some partial results. For instance another important development concerns problems with more than two degrees of freedom, for which the situation is less straightforward than described above. The number of operations required for the Taylor approximation increases drastically with the dimensions of the surface of section. Of course a lower-order map can be used by decreasing the grid size, but a further difficulty lies in the task of storing and recalling the values of the computed images at the vertices. This is the reason why we have used a hash function when dealing with problems with three degrees of freedom (see paper II).

Acknowledgements

The authors wish to thank R. Grauer for stimulating discussions at the very beginning of this research. We also wish to thank P. Farinella for fruitfull comments during this work.

References

- Duncan, M., Quinn, T., Tremaine, S.: 1989, *Icarus* **82**, 402
- Froeschlé, C.: 1970, *Astron. Astrophys.* **9**, 15
- Froeschlé, C., Rickman, H.: 1988, *Celestial Mech.* **43**, 265
- Froeschlé, C., Petit, J.M.: 1990, *Astron. Astrophys.* **238**, 413-423
- Hénon, M.: 1981, *Cours des Houches XXXVI*, North Holland, Amsterdam 57
- Lichtenberg, A.J., Lieberman, M.A.: 1983, *Regular and Stochastic Motion*, Springer-Verlag.
- Petit, J.M., Froeschlé, C.: 1991, to be submitted to *Astron. Astrophys.*
- Varosi, F., Grebogi, C., Yorke, J.A.: 1987, *Phys. Lett. A* **124**, 59

The effect of secular resonances in the asteroid region between 2.1 and 2.4 AU

Ch. Froeschlé, H. Scholl

Observatoire de la Côte d'Azur, Laboratoire G.D. Cassini
B.P. 139, F-06003 Nice Cedex, France
E-mail scholl@haendel.obs-nice.fr

Abstract.

The asteroid region between 2.1 and 2.4 AU appears to be depopulated at inclinations $i > 12^\circ$. This region is surrounded by the three main secular resonances ν_5 , ν_6 and ν_{16} and is crossed by higher order secular resonances. Secular resonances appear to overlap in this region. Numerical integrations of the orbits of seventeen fictitious asteroids with initial inclinations $12^\circ \leq i \leq 20^\circ$ show that: (1) this particular asteroid region is not depopulated in our computer experiment on timescales of 2.7 Myrs; (2) inclinations are pumped up by successive crossings through higher order secular resonances while eccentricities are not increased sufficiently to produce planet-crossers; (3) bodies located in the bordering ν_6 resonance with semi-major axes $a \leq 2.4$ AU become Earth-crossers on a time scale of 1 Myr; (4) we confirm Milani and Knežević's result (1990 Cel. Mech. 49, 247) that modes due to higher order secular resonances must be eliminated when proper elements are computed.

1 Introduction.

Morbidelli and Henrard (1991) developed a semi-numerical secular perturbation theory which allows to map locations of the principal and also of higher order secular resonances (fig.1). Morbidelli and Henrard's approach avoids any expansion of the main term of the Hamiltonian with respect to the eccentricity or the inclination of the perturbed body. Suitable action-angle variables are introduced which take into account properly the dynamics of the perihelion argument of the perturbed body. Thus, the theory is valid for large inclinations and eccentricities.

According to fig.1, the region between 2.1 and 2.4 AU is depopulated for inclinations $i \geq 12^\circ$. This region is surrounded by the three main secular resonances ν_5 , ν_6 and ν_{16} . The respective secular arguments are:

$$\varpi - \varpi_J, \quad \varpi - \varpi_S, \quad \text{and } \Omega - \Omega_J.$$

This depopulated region is crossed by the three higher order resonances R4, R9, R11 (the enumeration was originally introduced by Milani and Knežević (1990)):

$$R4: (\varpi - \varpi_J) + (\Omega - \Omega_J)$$

$$R9: (\varpi - \varpi_J) + (\varpi - \varpi_S)$$

$$R11: (\varpi - \varpi_S) - (\Omega - \Omega_J)$$

In order to investigate the influence of the secular resonances in this region, we integrated over 2.7 Myrs, the orbits of four sets of fictitious bodies with the respective starting semi-major axes: $a = 2.1, 2.2, 2.3$, and 2.4 AU. The integrations were carried out

in the frame of the four body model: Sun – Saturn – Jupiter – small body. The DVdq integrator of Krogh (1970) was used.

The two first sets contain 5 bodies with starting inclinations varying from $i = 12^\circ$ to $i = 20^\circ$ with an increment of $\Delta i = 2^\circ$. The initial inclinations for the third set ($a = 2.3$ AU) containing 4 bodies range from 14° to 20° , while for the fourth set ($a = 2.4$ AU) the starting inclinations vary from 16° to 20° with the same increment $\Delta i = 2^\circ$.

This gives a total of 17 bodies. All the bodies have the same starting eccentricity $e = 0.14$.

2 Results.

We now discuss the orbital evolutions of the bodies considering the different sets.

Set 1:

The two first bodies with respective starting inclinations of 12° and 14° cross the secular resonances R11, ν_{16} , and finally R9. The inclinations are gradually pumped up to 30° and 28° , respectively.

The three remaining bodies are located from the beginning in the ν_{16} secular resonance. Their resonance argument $\Omega - \Omega_J$ librates around 180° . The inclinations suffer large oscillations up to 28° .

The eccentricities of these five bodies remain comparatively small with a maximum value of $e = 0.19$.

Set 2:

The body with the starting inclination of $i = 12^\circ$ librates temporarily in the ν_6 secular resonance. Its resonance argument $\varpi - \varpi_S$ librates, as predicted by Morbidelli and Henrard, around 0° . During this period, the eccentricity varies between 0. and 0.30, while the inclination oscillates between $12^\circ \leq i \leq 15^\circ$.

The bodies with respective starting inclinations $i = 16^\circ, 18^\circ$ and 20° have qualitatively similar orbital evolutions. All three are located at the beginning in the higher order resonance R11, R9, and R4 respectively, and later enter the main secular resonance ν_{16} . The inclinations are pumped up. The body with starting inclination $i = 18^\circ$ repeatedly enters and leaves the higher order resonance R9 during the time interval $0 \leq t \leq 1.5 * 10^6$ years. At $1.5 * 10^6$ years, this body leaves R9 and enters the ν_{16} resonance region. During the time interval $1.9 * 10^6 \leq t \leq 2.7 * 10^6$ the body is located in three resonances, namely in ν_{16} , R4 and ν_5 . Entering this overlapping region, the inclination increases and oscillates between 29° and 34° (Fig.2).

The body with $i = 20^\circ$ leaves the resonance ν_{16} and enters the overlapping region of the resonances ν_5 and R4. Like in the former cases, the inclination becomes large; i varies between 30° and 35° .

During the integration time of 2.7 Myrs, the eccentricities remain bounded, not exceeding $e = 0.22$. Hence, no planetary crossing occurs.

Set 3:

The body with $i = 14^\circ$ is a ν_6 secular resonance case. The resonant argument $\varpi - \varpi_S$ librates around 0° . The eccentricity suffers large oscillations, i.e. $0.0 \leq e \leq 0.7$, while the maximum of inclination is 25° . The body becomes an Earth-crosser over a timescale of $t \simeq 1$ Myr.

During 2.7 Myrs, the body with $i = 18^\circ$ is located in the R11 resonance. The secular argument $(\varpi - \varpi_S) - (\Omega - \Omega_J)$ librates around 0° . There are neither large variations in

eccentricity ($0.03 \leq e \leq 0.2$) nor in inclination ($17^\circ \leq i \leq 22^\circ$). A long periodic oscillation with a period $T \simeq 15 * 10^5$ years appears in eccentricity and in inclination. This result shows that the higher order secular resonances affect the orbital elements, and have, as pointed out by Milani and Knežević (1990), to be taken into account in calculating the proper elements.

Set 4:

Only one body presents a peculiar behaviour. Until $9 * 10^5$ years, the body with $i = 16^\circ$ is located in the ν_6 secular resonance. The argument $\varpi - \varpi_S$ librates around 0° , then it stays in the neighbourhood of 180° for a period of more than 1.5 Myr, then the body becomes an outer circulator. The eccentricity is maximum $e \simeq 0.87$ when the transitions occur, namely at $t \simeq 0.9 * 10^6$ years and again when the body becomes an outer circulator ($t \simeq 2.5 * 10^6$ years). The inclination varies also very strongly around the transition states. During the periods $0.5 * 10^6$ yrs $\leq t \leq 1 * 10^6$ yrs and $1.9 * 10^6$ yrs $\leq t \leq 2.7 * 10^6$ yrs, i oscillates between 10° and 40° . Outside these time intervals, i varies in the range $16^\circ \leq i \leq 18^\circ$. We would like to point out that even at semi-major axes of 2.4 AU, bodies located in/or close to the secular resonance ν_6 may become Earth-crossers in less than 1 Myr.

3 Conclusions

These numerical computations have confirmed the locations of secular resonances determined by Morbidelli and Henrard (1991) and, in particular, the overlapping of the resonances ν_5 , ν_{16} and R4 at high inclinations $i \geq 30^\circ$. The passage of bodies through different secular resonances seems to pump up their inclinations. This phenomenon may be a possible mechanism to produce highly inclined Apollo-Amor objects. It also may explain the very low density of asteroids for semi-major axes $a \leq 2.3$ AU and inclinations $12^\circ \leq i \leq 30^\circ$.

Taking into account our previous results (Scholl and Froeschlé 1991), we conjecture that the secular resonance ν_6 is a good candidate to produce Earth-crossers for semi-major axes $2.0 \leq a \leq 2.4$ AU on time scales of at least 1 Myr.

The higher order secular resonances affect, as found previously by Milani and Knežević (1990), the determination of proper elements.

It is well known that overlapping resonances are in general associated with chaotic regions. It is an open problem whether or not the overlapping of main and higher order resonances produces planet-crossers. The bodies in our experiment do not become planet-crossers except those which are located in the ν_6 resonance. Of course, it is hard to guess what could happen over a much longer time scale than $2.7 * 10^6$ years. Much longer extended experiments are needed to explain completely the depletion of the considered region.

References

- [1] Krogh F. T. (1970) JPL Technical Utilization Document, No.CP-238
- [2] Milani A., Knežević Z. (1990) Secular perturbation theory and computation of asteroid proper elements. Celest. Mech. **49**, 247–411.
- [3] Morbidelli A., Henrard J. (1991) Secular resonances in the asteroidal belt: theoretical perturbed approach and the problem of their location. Celest. Mech., in press.

- [4] Scholl H., Froeschlé Ch. (1991) The ν_6 secular resonance region near 2 AU: a possible source of meteorites. Astron. Astrophys. **245**, 316–321.

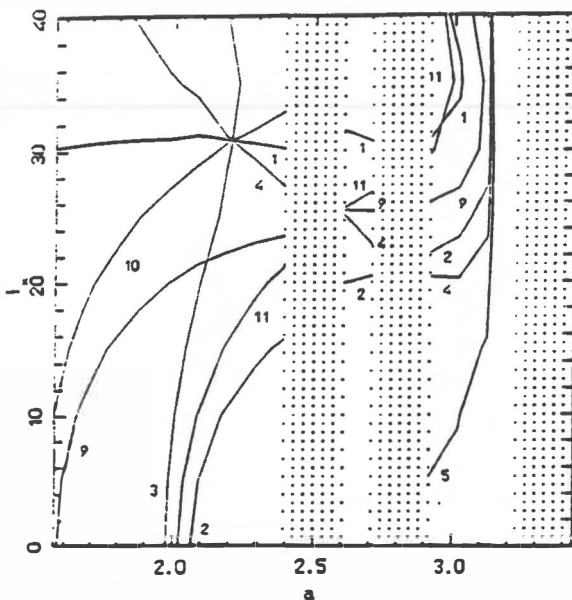


Fig.1. The locations of the secular resonances (taken from Morbidelli and Henrard 1991) ν_5 , ν_6 , ν_{16} , R4, R9 and R11 are labeled respectively by the numbers 1, 2, 3, 4, 9 and 11. The shaded areas are regions of overlapping with the mean motion resonances 3:1, 5:2 and 2:1.

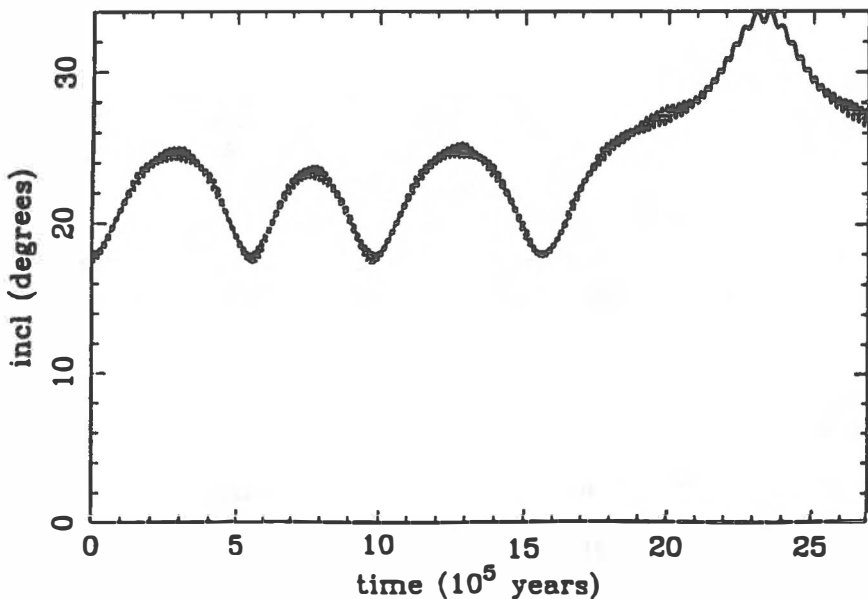


Fig.2. Time evolution of a body with starting osculating elements: $a=2.2$ AU, $e=0.14$, $i=18^\circ$. The body crosses the secular resonances ν_{16} , R4, and ν_5 .

Figure Captions

Fig.1. The locations of the secular resonances (taken from Morbidelli and Henrard 1991) ν_5 , ν_6 , ν_{16} , R4, R9 and R11 are labeled respectively by the numbers 1, 2, 3, 4, 9 and 11. The shaded areas are regions of overlapping with the mean motion resonances 3:1, 5:2 and 2:1.

Fig.2. Time evolution of a body with starting osculating elements: $a=2.2$ AU, $e=0.14$, $i=18^\circ$. The body crosses the secular resonances ν_{16} , R4, and ν_5 .

A STRONG 3.4 μ m EMISSION FEATURE IN COMET AUSTIN 1989c1

S.F. Green¹, J.K. Davies², T.R. Geballe³, T. Brooke⁴ & A.T. Tokunaga⁴.

¹Unit for Space Sciences, Physics Laboratory, University of Kent at Canterbury, Kent, CT2 7NR

²Royal Observatory, Blackford Hill, Edinburgh EH9 3HJ

³Joint Astronomy Centre, 665 Komohana St., Hilo, Hawaii.

⁴Institute for Astronomy, University of Hawaii, 2680 Woodlawn Drive, Honolulu, 46822 Hawaii.

ABSTRACT

High resolution 2.8-4.0 μ m spectra of the "new" comet Austin 1989c1, taken on May 15 & 16 1990 confirm the presence of the broad emission features around 3.4 and 3.52 μ m seen in a number of bright comets and ascribed to organic material. Both the 3.4 μ m band strength and the 3.52/3.36 μ m flux ratios are among the largest so far observed. The data are consistent with the relationship between band strength and water production rate derived by Brooke et al (Astron. J., 101, 268 1991). Excess emission at 3.28 and 3.6 μ m cannot be unambiguously identified as features due to the poor signal-to-noise ratio.

3.4 μ m EMISSION IN COMETS

Our knowledge of the composition of comets, believed to be the most primitive material in the solar system, and perhaps retaining relatively unprocessed interstellar grains, has advanced in recent years through direct sampling by spacecraft and the consequent intensive observing campaigns. A 3.4 μ m infrared emission band first detected in Comet P/Halley (Wickramasinghe & Allen, 1986; Knacke et al 1986; Danks et al, 1987; Baas et al, 1986; and Tokunaga et al, 1987) together with infrared spectral features observed by the Vega I IKS experiment (Combes et al, 1986; Moroz et al, 1987) have been interpreted as superpositions of C-H band stretching vibrations in gaseous or solid hydrocarbons. The presence of a substantial organic component in small (10^{-19} - 10^{-15} kg) cometary grains was confirmed by the Giotto and Vega mass spectrometers, PIA and PUMA (Kissel et al, 1986a; 1986b). The 3.4 μ m emission feature has been observed in several, but not all, bright comets over the last few years with detections for Comet Wilson 1986I (Allen & Wickramasinghe 1987; Brooke et al, 1989), Bradfield 1987s (Brooke et al, 1990), Austin 1989c1 (this paper) and Levy 1990c (Davies et al, 1991) but not for Encke (Gehrz et al, 1989), West 1975n (Oishi et al, 1978), Ira-Araki-Alcock 1983d (Hanner et al, 1985) or pre-perihelion in Halley (Gehrz et al, 1989).

The observed emission bands exhibit considerable structure presumably due to differences in the C-H band strength and frequencies in different molecules. For example, 3.4 μ m emission is characteristic of the C-H stretching frequency of saturated hydrocarbons (Bellamy, 1975) which shortens to 3.3 μ m for unsaturated hydrocarbons. The specific molecules responsible for the range of observed features are not known, and it is not certain if they are in the gaseous or solid (or both) phases. The features have been observed above both the scattered solar continuum and the grain thermal emission continuum, dependent on heliocentric distance, for comet Halley. Since the observed feature near 3.4 μ m can be produced by almost any molecule containing CH₃ and CH₂ clusters, the identification of parent molecules will depend not only on detailed structure within the spectral region but the presence or absence of features in other spectral regions, and the provision of a plausible emission mechanism. The major features at 3.28 and 3.36 μ m are interpreted by Encrenaz et al (1987) as due to resonance (fluorescence) scattering of solar infrared radiation by unsaturated and saturated hydrocarbon gas molecules respectively. However, this requires hydrocarbon abundances of ~ 30% of that of H₂O, and high resolution spectra of comet Halley (Drapatz et al, 1987) showed no prominent line structure typical of gas-phase emission (Chyba et al, 1989) while Brooke et al (1991b) found that the methane abundance is less than 0.0034 of that of water in comet Levy 1990c. Much lower abundances are required by Chyba et al for thermal emission from sub-micron organic grains. Predicted features at longer wavelengths which are not observed are masked by thermal emission from the larger, non-carbonaceous grain population in their two-component model. A third mechanism, requiring molecular production of only 0.15% of water, involves UV excited infrared fluorescence from very small grains (large molecules) (Baas et al, 1986).

Emission features around 3.52 μ m and near 3.6 μ m have been attributed to formaldehyde (Knacke et al, 1986; Danks et al, 1986; Moroz et al, 1987) although Brooke et al (1989) found a very poor fit between the observations of comets Halley and Wilson and their predicted model spectrum for formaldehyde. They suggest that polyoxymethylene (POM, paraformaldehyde) could contribute to the observed emission but saturated and unsaturated hydrocarbons are also required. Although the 3.52 μ m feature is observed in all comets exhibiting infrared emission in this region, the 3.6 μ m band is not always seen. Tokunaga et al (1987) observed an unidentified emission band at 2.8-2.9 μ m in comet Halley, later seen in comets Wilson (Brooke et al, 1989) and Bradfield (Brooke et al, 1990). This has been tentatively assigned to the long wavelength component of H₂O gas emission bands (Bockelée-Morvan & Crovisier, 1989). Other, less pronounced, features may be present in some data.

Brooke et al, (1991a; hereafter BTK) conclude, from ratios of the 3.4 μm feature and continuum with water production rate, that organics are present in all comets at comparable abundances with respect to water, although there are potentially significant differences in details of their spectra. They deduced that the 3.4 μm band strengths were correlated with water production rate rather than dust production.

After its discovery in December 1989 at a heliocentric distance of 2.4AU, comet Austin 1989c1 did not brighten as expected but still reached a total visual magnitude ~ 4 in April 1990 after perihelion passage at 0.35AU., providing an ideal opportunity for detailed spectroscopic study of a "new" comet. IUE spectra taken during the period 7-13 May were characteristic of a non-dusty comet (Festou et al, 1990).

OBSERVATIONS AND DATA REDUCTION

Observations of comet Austin were made with the cooled grating spectrometer CGS2 on the UK Infrared Telescope (UKIRT) on Mauna Kea, Hawaii during service observations on 15 and 16 May 1990 when the comet was at a heliocentric distance of 0.97AU. Service observations attempted on 3, 4 and 14 May were prevented by cloud which was also present to a lesser extent on the two nights when spectra were obtained. Multiple scans were made in the wavelength ranges 2.8-3.65 μm and 3.15-3.9 μm on the 15th and in the longer range only on the 16th. Sampling was at 1/4 resolution element steps (0.0022 μm at a wavelength of 3.4 μm) to allow for complete sampling despite the loss of 2 of the 7 elements in the detector array. Sample time was 1.5s per point with an aperture of 5 arcseconds centred on the peak signal. Details are in Table 1. The stars BS8130 and BS8430 (F2IV, mag 2.60 at 3.45 μm with blackbody temperature 6800K and F5V, mag 2.59 at 3.8 μm with blackbody temperature 6400K respectively) were used for flux calibration. Corrections for the thin cloud attenuation were made by normalising scans to those with the maximum average signal. Uncertainties in the flux calibration are estimated at $\sim 25\%$. Despite the generally poor quality of the raw data, the presence of emission in the 3.4 μm region is confirmed and some structure is evident. In order to improve the signal-to-noise ratio, each spectrum has been gaussian filtered with a profile having FWHM-1/2 a resolution element (0.004 μm). These are shown in figure 1. The "combined" spectrum has been produced from a weighted mean of the three datasets, normalised to the flux for the 16th May over the region of overlap. The "features" apparent around 3.2 and at 3.31 μm are due to incorrect atmospheric correction for strong telluric absorption lines.

TABLE 1. Observations.

Date	15 May	15 May	16 May
Wavelength range (μm)	2.8-3.65	3.15-3.9	3.15-3.9
Mid-observation time (UT)	14:01	14:57	13:39
Number of scans	7	6	10
Mean airmass	1.37	1.16	1.43
Heliocentric distance (AU)	0.96	0.96	0.98
Geocentric distance (AU)	0.32	0.32	0.30
Calibration star	BS8130	BS8430	BS8130

DISCUSSION

The broad 3.4 μm emission band seen in other bright comets is confirmed in comet Austin, together with the band centred on 3.52 μm . The slowly rising continuum is consistent with grain thermal emission which will be dominant at these wavelengths for a heliocentric distance of less than 1AU. Possible emission at $\sim 3.62\mu\text{m}$ is present in all three spectra but data longward of 3.52 μm are too noisy to positively confirm any structure present. Although atmospheric water absorption is high below 2.85 μm the data indicate the edge of a bright emission feature peaking shortward of this cut-off. No 3.28 μm feature is apparent above the noise in these spectra although there is emission at that wavelength in excess of the continuum

Using an interpolation of the continuum (between 2.9-3.2 and 3.6-3.9 μm) the 3.36 μm flux to continuum ratio is 3.5 ± 0.4 . This value is higher than for most comets observed at the same heliocentric distance but consistent with the results of BTK who find high feature-to-continuum ratios for comets with low dust-to-gas ratios. Following their procedure, the continuum flux at 3.36 μm and the continuum-subtracted integrated flux (between 3.31 and 3.56 μm) have been corrected to an effective instrument aperture projected radius of 980km and geocentric distance of 1AU., for comparison with results from other comets. The corrected continuum flux $F^*_{\text{cont}} = (0.18 \pm 0.05) \times 10^{-14} \text{ W m}^{-2} \mu\text{m}^{-1}$ and integrated 3.4 μm flux $I^*_{3.4} = (0.8 \pm 0.2) \times 10^{-15} \text{ W m}^{-2}$. The water production rate deduced from IUE spectra (Festou et al, 1990) was $1.1 \times 10^{29} \text{ s}^{-1}$ on 9 May and similar on 13 May. Allowing for uncertainties of 50% in this value for 15/16 May,

$$F^*_{\text{cont}} / Q_{\text{H}_2\text{O}} = 0.16 \pm 0.09 \quad (10^{-14} \text{ W m}^{-2} \mu\text{m}^{-1} / 10^{29} \text{ s}^{-1})$$

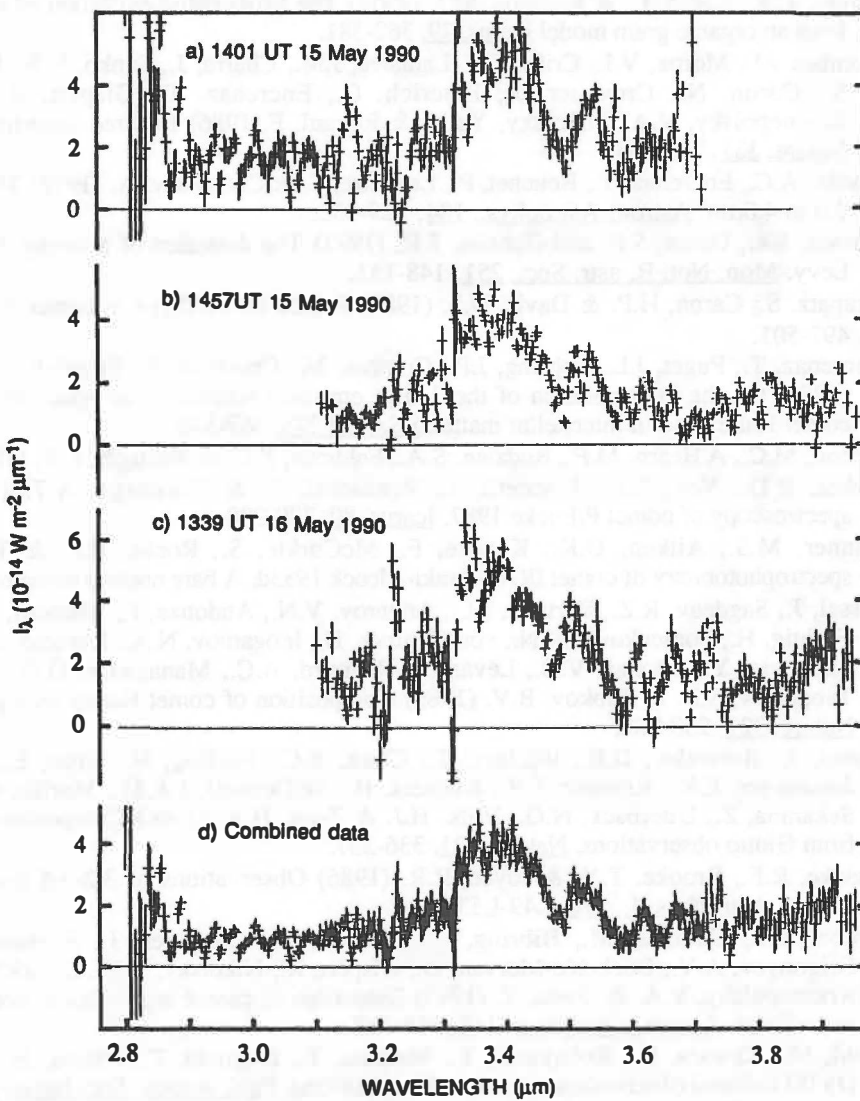
$$I^*_{3.4}/Q_{H_2O} = 0.7 \pm 0.4 (10^{-15} \text{ W m}^{-2}/10^{29} \text{ s}^{-1})$$

These values are consistent with the results of BTK who found that the $3.4\mu\text{m}$ band strength is better correlated with water production rates rather than with dust production rate. The relative strength of the $3.52\mu\text{m}$ feature to the broad emission $\sim 3.4\mu\text{m}$ appears higher for comet Austin than any other comet. The ratio of continuum subtracted fluxes, $F_{3.52}/F_{3.36} = 0.5 \pm 0.2$, is twice the typical value for other comets. Interpretation of such observations is difficult because of the uncertainty in continuum determination and relative strengths of scattered and thermal continua at different heliocentric distances. It is clear, however, that real differences are present in the structure of these features since BTK find the $3.52\mu\text{m}$ peak strongest for the dust-poor comets Okazaki-Levy-Rudenko 1989r and P/Brorsen-Metcalf, despite the fact that they were observed at small heliocentric distances where the thermal emission continuum dominates and might be expected to mask the longer wavelength feature to a greater extent. The FWHM of the broad feature in comet Austin is $\sim 0.15\mu\text{m}$, comparable with the range 0.12-0.18 found for other comets. No detailed interpretation of the shape is possible due to the poor signal-to-noise.

Comet Austin displayed the characteristics of a "new" comet both dynamically and physically (high activity at large heliocentric distance pre-perihelion but with a subsequent low heliocentric brightness power law exponent, $n < 3$).

There appears to be no obvious correlation between age of the comet and the presence (or absence) of particular features in the 3 to $4\mu\text{m}$ region. Although the $3.4\mu\text{m}$ emission may be ubiquitous (previous non-detections in comets West, Encke and Iras-Araki-Alcock being explainable by low signal to noise) real compositional differences in the organic content of comets may be present. In order to understand fully the structure and composition of the emitting material, high resolution observations of a number of comets, both 'old' and 'new', at different heliocentric distances, are required. These will permit a combination of detailed modelling to fit the range of observed features, and an understanding of the evolution of cometary material as it 'ages'.

Figure 1. CGS2 spectra of comet Austin 1989c1. Data have been filtered with a gaussian profile with $\sigma = 0.002\mu\text{m}$ (i.e. FWHM $\sim 1/2$ resolution element). Spectrum d is a normalised weighted mean of all the data. Error bars are standard deviation of counts from co-added scans.



Acknowledgements

UKIRT is operated by the Royal Observatory Edinburgh on behalf of the Science and Engineering Research Council. We thank all UKIRT staff involved in the service observing programme. Data reduction was performed partly on the Starlink computer network.

References

- Allen, D.A. & Wickramasinghe, D.T. (1987) Discovery of organic grains in comet Wilson. *Nature*, **329**, 615-616.
- Baas, F., Geballe, T.R. & Walther, D.M. (1986) Spectroscopy of the 3.4 μm emission feature in comet Halley. *Astrophys. J.*, **311**, L97-L101.
- Bellamy, L.J. (1975) *The infrared spectra of complex molecules Vol. 1*. Chapman & Hall, London.
- Bockelée-Morvan, D. & Crovisier, J. (1989) The nature of the 2.8 μm emission feature in cometary spectra. *Astron. Astrophys.*, **216**, 278-283.
- Brooke, T.Y., Knacke, R.F., Owen, T.C. & Tokunaga, A.T. (1989) Spectroscopy of emission features near 3 microns in comet Wilson (1986). *Astrophys J.*, **336**, 971-978.
- Brooke, T.Y., Tokunaga, A.T., Knacke, R.F., Owen, T.C., Mumma, M.J., Reuter, D. & Storrs, A.D. (1990) Detection of the 3.4- and 2.8 μm emission features in comet Bradfield. *Icarus*, **83**, 434-440.
- Brooke, T.Y., Tokunaga, A.T. & Knacke, R.F. (1991a) Detection of the 3.4 μm emission feature in comets P/Borsen-Metcalf and Okazaki-Levy-Rudenko (1989R) and an observational summary. *Astron. J.*, **101**, 268-278.
- Brooke, T.Y., Tokunaga, A.T., Weaver, H.A., Chin, G. & Geballe, T.R. (1991b) A sensitive upper limit on the methane abundance in comet Levy (1990c). *Astrophys. J. Lett.*, **379**, L113-116.
- Chyba, C.F., Sagan, C. & Mumma, M.J. (1989) The heliocentric evolution of cometary infrared spectra: Results from an organic grain model. *Icarus*, **79**, 362-381.
- Combes, M., Moroz, V.I., Crifo, J.F., Lamarre, J.M., Charra, J., Sanko, N.F., Soufflot, A., Bibring, J.P., Cazes, S., Coron, N., Crovisier, J., Emerich, C., Encrenaz, T., Gispert, R., Grigoryev, A.V., Guyot, G., Krasnopolsky, V.A., Nikolsky, Yu.V. & Rocard, F. (1986) Infrared sounding of comet Halley from Vega I. *Nature*, **321**, 266-268.
- Danks, A.C., Encrenaz, T., Bouchet, P., LeBertre, T. & Chalabaev, A. (1987) The spectrum of comet Halley from 3.0 to 4.0 μm . *Astron. Astrophys.*, **184**, 329-332.
- Davies, J.K., Green, S.F. and Geballe, T.R. (1991) The detection of a strong 3.28 μm emission feature in comet Levy. *Mon. Not. R. astr. Soc.*, **251**, 148-151.
- Drapatz, S., Caron, H.P. & Davis, D.S. (1987) Search for methane in comet P/Halley. *Astron. Astrophys.*, **187**, 497-501.
- Encrenaz, T., Puget, J.L., Bibring, J.P., Combes, M., Crovisier, S., Emerich, C., d'Hendecourt, L. & Rocard, F. (1987) On the interpretation of the 3.4 μm emission feature in the spectrum of comet Halley: Abundances in comet Halley and in interstellar matter. *ESA-SP-278*, 369-376.
- Festou, M.C., A'Hearn, M.F., Budzien, S.A., Feldman, P.D. & Roettger, E.E. (1990) *IAUC 5012*.
- Gehrz, R.D., Ney, E.P., Piscitelli, J., Rosenthal, E. & Tokunaga, A.T. (1989) Infrared photometry and spectroscopy of comet P/Encke 1987. *Icarus*, **80**, 280-288.
- Hanner, M.S., Aitken, D.K., Knacke, F., McCorkle, S., Roche, P.F. & Tokunaga, A.T. (1985) Infrared spectrophotometry of comet IRAS-Araki-Alcock 1983d: A bare nucleus revealed? *Icarus*, **62**, 97-109.
- Kissel, J., Sagdeev, R.Z., Bertaux, J.L., Angarov, V.N., Audouze, J., Blamont, J.E., Büchler, K., Evlanov, E.N., Fechtig, H., Fomenkova, M.N., von Hoerner, H., Inogamov, N.A., Khromov, V.N., Knabe, W., Krueger, F.R., Langevin, Y., Leonas, V.B., Levasseur-Regourd, A.C., Managadze, G.G., Podkolzin, S.N., Shapiro, V.D., Tabaldyev, S.R. & Zubkov, B.V. (1986) Composition of comet Halley dust particles from Vega observations. *Nature*, **321**, 280-282.
- Kissel, J., Brownlee, D.E., Büchler, K., Clark, B.C., Fechtig, H., Grün, E., Hornung, K., Igenbergs, E.B., Jessburger, E.K., Krueger, F.R., Kuczera, H., McDonnell, J.A.M., Morfill, G.M., Rahe, J., Schwehm, G.H., Sekanina, Z., Utterback, N.G., Völk, H.J. & Zook, H.A. (1986) Composition of comet Halley dust particles from Giotto observations. *Nature*, **321**, 336-337.
- Knacke, R.F., Brooke, T.Y. & Joyce, R.R. (1986) Observations of 3.2-3.6 micron emission features in comet Halley. *Astrophys. J.*, **310**, L49-L53.
- Moroz, V.I., Combes, M., Bibring, J.P., Coron, N., Crovisier, J., Encrenaz, T., Crifo, J.F., Sanko, N., Grigoryev, A.V., Bockelée-Morvan, D., Gispert, R., Nikolsky, Y.V., Emerich, C., Lamarre, J.M., Rocard, F., Krasnopolsky, V.A. & Owen, T. (1987) Detection of parent molecules in comet P/Halley from the IKS-Vega experiment. *Astron. Astrophys.*, **187**, 513-518.
- Oishi, M., Kawara, K., Kobayashi, Y., Maihara, T., Noguchi, T., Okuda, H., Sato, S., Iijima, T. & Ono, T. (1978) Infrared observations of comet West (1975n). *Publ. Astron. Soc. Japan*, **30**, 149.
- Tokunaga, A.T., Nagata, T. & Smith, R.G. (1987) Detection of a new emission band at 2.8 μm in comet P/Halley. *Astron. Astrophys.*, **187**, 519-522.
- Wickramasinghe, D.T. & Allen, D.A. (1986) Discovery of organic grains in comet Halley. *Nature*, **323**, 44-46.

DEIMOS: A REDDISH, D-TYPE ASTEROID SPECTRUM

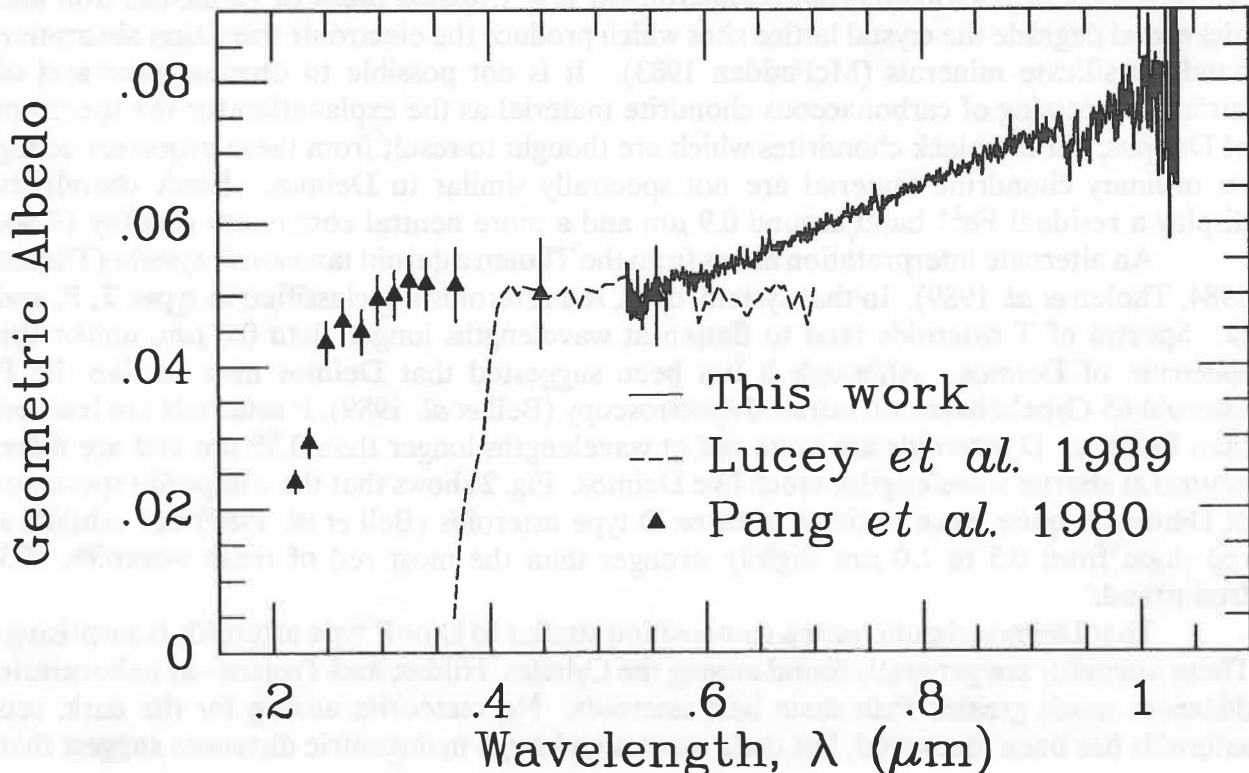
William M. Grundy and Uwe Fink
Lunar and Planetary Laboratory, University of Arizona, Tucson, AZ 85721.

We have obtained high quality CCD spectra of Deimos from 0.5 to 1.0 μm at a spectral resolution of 15 Å. The spectra are remarkably red, similar to the spectra of D type asteroids rather than those of carbonaceous chondrites or C type asteroids.

During the 1988 opposition of Mars, we obtained new CCD spectra of its outer satellite, Deimos. The data were obtained over a 2½ hour period on the night of October 9, using the 1.54 meter Catalina telescope and the LPL long-slit CCD spectrometer. From 0.5 to 1.1 μm , the spectrum is dispersed across an 800×800 Texas Instruments CCD chip at a scale of 7.21 Å per pixel for an effective $\lambda/\Delta\lambda \approx 500$.

The primary observational difficulty in ground based spectroscopy of Deimos was its proximity to Mars. To minimize scattered light from Mars, Deimos was observed near greatest elongation. The spectrograph slit was narrowed to 2.5 arcseconds, slightly larger than the seeing disk. An apodizing mask at the re-imaged telescope primary, to remove the diffraction cross of Mars light caused by the telescope's secondary mirror mount. Residual scattered light was modeled and removed in data reduction. Solar analog stars BS560, BS2007, and BS8931 were observed to allow removal of telluric absorptions. The resulting spectrum is plotted with other data in Fig. 1.

Fig. 1 Composite of Deimos Spectra



Our spectrum has not been smoothed; the signal-to-noise ratio and the resolution are significantly higher than previously available spectra of Deimos. Also plotted in Fig. 1 are the spectra of Pang *et al.* (1980) and Lucey *et al.* (1989). The geometric albedo normalization is from Pang *et al.* and may be an underestimate (Zellner *et al.* 1974, Klaasen *et al.* 1979, Veverka *et al.* 1980). At wavelengths longer than 0.6 μm , the spectrum has a markedly red slope, increasing in albedo by a factor of $\sim 50\%$ over one octave in wavelength. Between 0.4 and 0.6 μm , the albedo shows little wavelength dependence (Veverka *et al.* 1977). Other than this change in slope (perhaps caused by a broad, shallow absorption feature around 0.5 μm), the spectrum is remarkably featureless at visible and longer wavelengths. At shorter wavelengths, the albedo falls off sharply. The ground based spectrum of Lucey *et al.* is not consistent with the Mariner 9 spectrometry of Pang *et al.* in the ultra-violet and does not show the red slope we observe at longer wavelengths.

The absence of VNIR (visible and near infrared) absorption bands in the spectrum of Deimos is in marked contrast with Martian surface spectra, observed contemporaneously. No trace of the Fe^{2+} electronic transition absorption band around 1 μm is observed. Its absence would rule out the presence of significant quantities of minerals such as pyroxenes and olivines on the surface of Deimos, were it not for the fact that fine grained dark materials are remarkably effective at masking mineral absorption bands. At present it is not possible to derive much compositional information from such a dark, featureless spectrum.

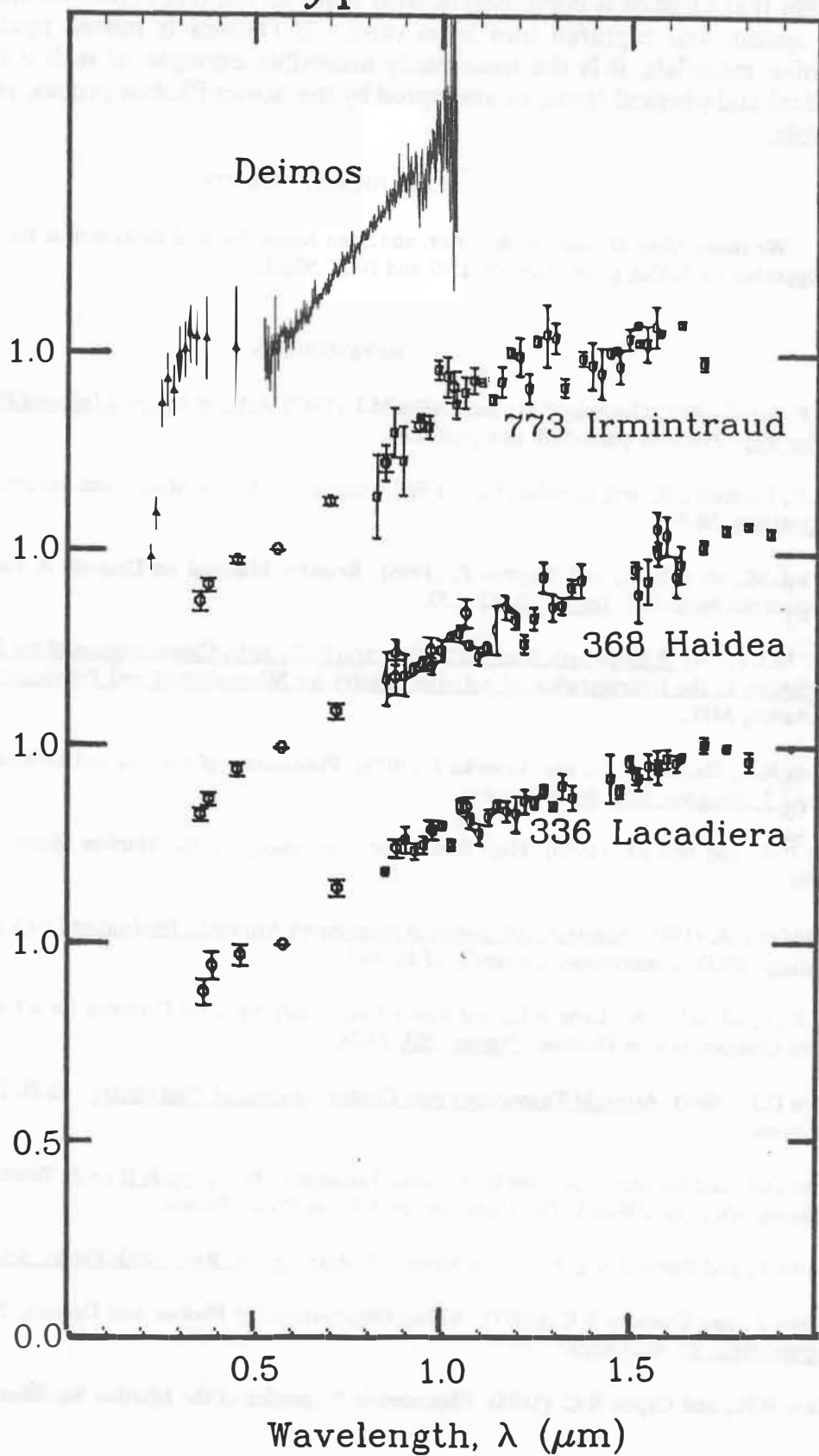
Based on the short wavelength spectra, the surface of Deimos has been interpreted as being similar to powdered carbonaceous chondrites and thus to C type asteroids (Pang *et al.* 1980, Veverka *et al.* 1980, French *et al.* 1988, Lucey *et al.* 1989). We are not aware of carbonaceous meteorites with VNIR spectra as red as that of Deimos. The same is true of C type asteroids. There may be some surface process which renders ordinary or carbonaceous chondritic material dark and red under the conditions experienced in Mars orbit. Shock effects of micrometeoroid bombardment may disperse blebs of elemental iron and nickel and degrade the crystal lattice sites which produce the electronic transition absorption bands in silicate minerals (McFadden 1983). It is not possible to dismiss some sort of surface processing of carbonaceous chondrite material as the explanation for the spectrum of Deimos, but the black chondrites which are thought to result from these processes acting on ordinary chondritic material are not spectrally similar to Deimos. Black chondrites display a residual Fe^{2+} band around 0.9 μm and a more neutral continuum (Gaffey 1974).

An alternate interpretation arises from the Tholen asteroid taxonomic system (Tholen 1984, Tholen *et al.* 1989). In that system, dark, red asteroids are classified as types T, P, and D. Spectra of T asteroids tend to flatten at wavelengths longer than 0.8 μm , unlike the spectrum of Deimos. Although it has been suggested that Deimos may be like the P asteroid 65 Cybele based on infrared spectroscopy (Bell *et al.* 1989), P asteroids are less red than Deimos. D asteroids are quite red at wavelengths longer than 0.55 μm and are more neutral at shorter wavelengths, much like Deimos. Fig. 2 shows that the composite spectrum of Deimos is quite close to those of three D type asteroids (Bell *et al.* 1987) but exhibits a red slope from 0.5 to 1.0 μm slightly stronger than the most red of these asteroids, 773 Irmtraud.

That Deimos should have a composition similar to D or P type asteroids is surprising. These asteroids are generally found among the Cybeles, Hildas, and Trojans - at heliocentric distances much greater than main belt asteroids. No meteorite analog for the dark, red asteroids has been recovered, but their spectra and large heliocentric distances suggest that

Fig. 2

D Type Asteroids



their surfaces are rich in dark organic materials and partially hydrated clay minerals. It is possible that Deimos is composed of such material scattered from further out in the early solar system and captured into Mars orbit. If Deimos is indeed made of such exotic, primitive materials, it is the most easily accessible example of such a body. A detailed chemical and physical study, as attempted by the Soviet Phobos probes, could be extremely valuable.

ACKNOWLEDGEMENTS

We thank Mike DiSanti, Rick Porter, and Sean Keane for vital assistance at the telescope. This work was supported by NASA grants NAGW 1549 and NGT 50661.

REFERENCES

- Bell J.F., Hawke B.R., Owensby P.D., and Gaffey M.J. (1987) Atlas of Asteroid Infrared Reflection Spectra (0.8-2.5 Microns). Privately published, non-paginated.
- Bell J.F., Piscitelli J.R., and Lebofsky L.A. (1989) Deimos: Hydration State From Infrared Spectroscopy. LPSC XX Abstracts, 58-59.
- French L.M., Veverka J., and Thomas P. (1988) Brighter Material on Deimos: A Particle Size Effect in a Carbonaceous Material? Icarus, 75, 127-132.
- Gaffey M.J. (1974) A Systematic Study of the Spectral Reflectivity Characteristics of the Meteorite Classes with Applications to the Interpretation of Asteroid Spectra for Mineralogical and Petrological Information. Ph.D. Dissertation, MIT.
- Klaasen K.P., Duxbury T.C., and Veverka J. (1979) Photometry of Phobos and Deimos from Viking Orbiter Images. J. Geophys. Res., 84, 8478-8486.
- Lucey P.G., and Bell J.F. (1989) High Resolution Spectroscopy of the Martian Moons. LPSC XX Abstracts, 598-599.
- McFadden L.A. (1983) Spectral Reflectance of Near-Earth Asteroids: Implications for Composition, Origin and Evolution. Ph.D. Dissertation, University of Hawaii.
- Pang K.D., Rhoads J.W., Lane A.L., and Ajello J.M. (1980) Spectral Evidence for a Carbonaceous Chondrite Surface Composition on Deimos. Nature, 283, 27-28.
- Tholen D.J. (1984) Asteroid Taxonomy From Cluster Analysis of Photometry. Ph.D. Dissertation, University of Arizona.
- Tholen D.J., and Barucci M.A. (1989) Asteroid Taxonomy. In Asteroids II (R.P. Binzel, T. Gehrels, and M.S. Matthews, eds.), pp. 298-315. The University of Arizona Press, Tucson.
- Veverka J., and Burns J.A. (1980) The Moons of Mars. Annu. Rev. Earth Planet. Sci., 8, 527-558.
- Veverka J., and Duxbury T.C. (1977) Viking Observations of Phobos and Deimos: Preliminary Results. J. Geophys. Res., 82, 4213-4223.
- Zellner B.H., and Capen R.C. (1974) Photometric Properties of the Martian Satellites. Icarus, 23, 437-444.

DID EARTH-APPROACHING ASTEROIDS 3551, 3908, OR 4055 PRODUCE METEORITES?

B.Å.S. Gustafson¹ and I.P. Williams²

1) Department of Astronomy, University of Florida, Gainesville, FL 32611 USA

2) Astronomy Unit, Queen Mary and Westfield College,
University of London, Mile End Road, London E1 4NS, UK

ABSTRACT

Orbital integrations show that Amor asteroid 3908 could have ejected one out of four plausible groups of meteorite producing fireballs during a collision in the asteroid belt. It has been suggested by others that such a collision may also have split asteroids 3551 and 3908. A member of this group of fireballs is listed as one of the better possibilities for recovery.

INTRODUCTION

Amor asteroids 3551 and 3908 approach the Earth on adjoining orbits and have nearly identical spectra (Cruikshank *et al.*, 1991). Their spectra also resemble those of nearby asteroid 4055 and main belt asteroid Vesta, even more intriguing is their similarity to laboratory spectra obtained from basaltic meteorites, i.e., Eucrites, Howardites, and Diogenites or HED meteorites. Drummond and Wisniewski (1990) suggest that 3551 and 3908 may be fragments of a common parent asteroid who's disruption created a stream of meteorite dropping basaltic meteoroids. Cruikshank *et al.* (1991) went one step further, suggesting that a Vesta-like asteroid is the parent or grandparent of all three Amor asteroids and the basaltic meteorites. Do meteorite dropping meteoroids move in orbits close to asteroids 3551 and 3908? Cruikshank *et al.* (1991) found no clear correlation between the present orientation of the asteroid orbits and occurrence of 41 HED meteorite falls. Drummond and Wisniewski (1990) claimed to find two meteor orbits in the Super-Schmidt photographic data by McCrosky and Posen (1961) and one Prairie Network fireball orbit by McCrosky *et al.* (1978) that satisfy both the D_{SH} and D' criteria commonly assumed to indicate stream membership (Drummond, 1981). A closer examination, using Southworth and Hawkins' (1963) exact formula for D_{SH} rather than the approximation that was also given by them, shows that no meteor orbits in these surveys satisfy both criteria. We examine meteorite producing fireball data from the Canadian Meteorite Observation and Recovery Project (MORP) listed by Halliday *et al.* (1989) and show, using orbital integrations, that a collision suffered by 3908 in the asteroid belt could have ejected one of the four tight groups proposed by Halliday *et al.* (1990) and that 3908 may have split from 3551 at that time.

METEORITE DROPPING FIREBALL ORBITS

Figure 1 shows orbital eccentricity versus reciprocal semimajor axis of meteorite dropping MORP fireball orbits listed by Halliday *et al.* (1989). Also shown are asteroids 3551, 3908, 4055, and Vesta with the region corresponding to the main asteroid belt. Earth-crossing orbits fall above the dashed line delineating perihelia at 1 AU ($1/a < 1$) and aphelia at 1 AU ($1/a > 1$). Meteorite dropping fireballs preferentially enter Earth's atmosphere near their perihelion with aphelia in the asteroid belt or beyond. Semimajor axes cluster near and inside the inner part of the asteroid belt. Meteoroids from the outer half of the belt are also abundant in the MORP data but are not listed as meteorite producing. This may be a

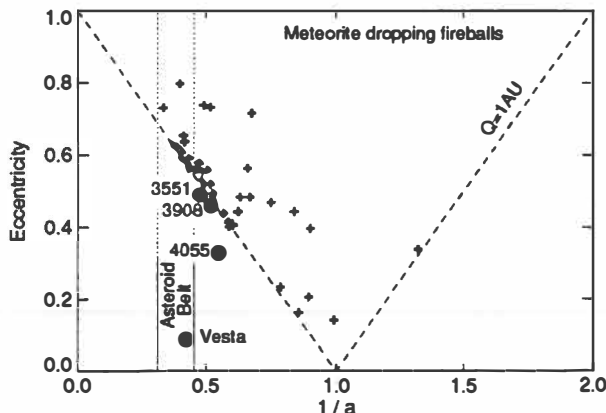


Figure 1. The shape and size of meteorite producing fireball orbits from the MORP survey, crosses, indicate that a large fraction could have been perturbed from the asteroid belt (solid lines) into Earth-crossing orbits (bracketed by the dashed lines). But there is an excess of less eccentric orbits with smaller major axes that may be related to the Amor asteroids 3551, 3908, and 4055.

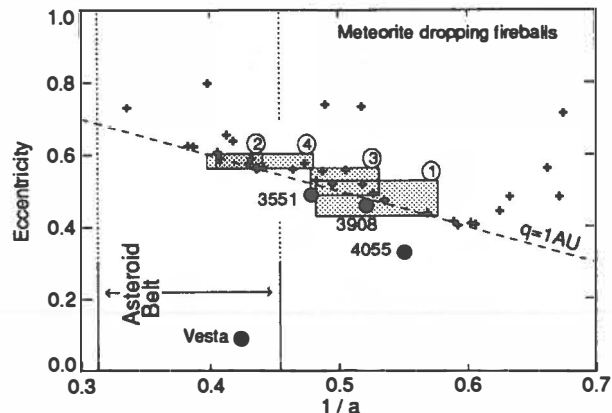


Figure 2. This detail of Figure 1 shows the extent of four groups of meteorite producing fireball orbits. Group 2 and 4 orbits may be perturbed directly from the inner edge of the asteroid belt while the orbits of group 1 and 3 are similar in size and shape to those of asteroids 3551 and 3908.

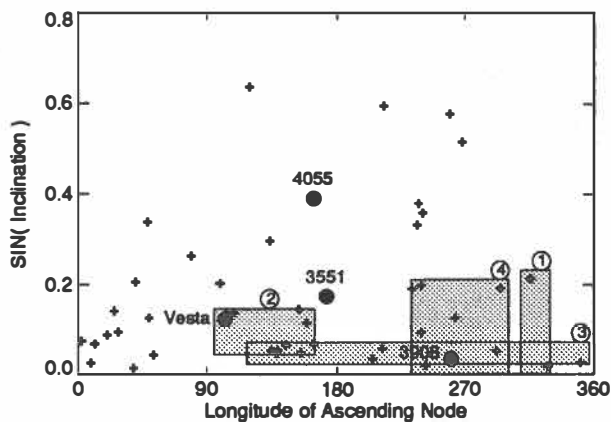


Figure 3. The orientation of group 3 orbital planes are consistent with low relative ejection velocities and differential precession. The other groups may have started out with higher relative velocities but are less affected by precession. Notice that the orientation of 3908's orbital plane is typical of group 3.

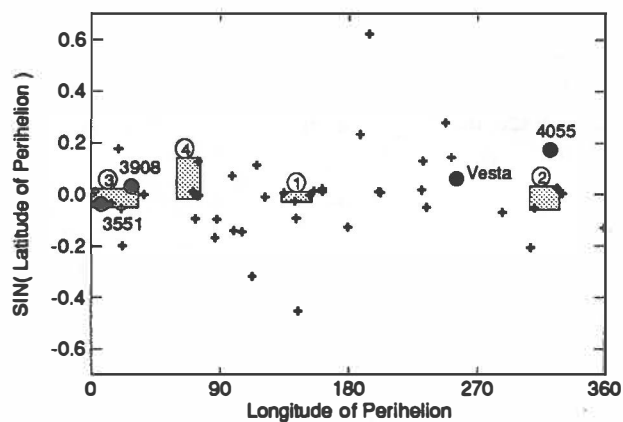


Figure 4. The major axis orientation of group 3 orbits is like those of asteroids 3551 and 3908. This orientation is relatively stable to planetary perturbations unlike the orientation of the orbital plane.

consequence of higher entry velocities or of morphology. Wetherill (1988) summarized the process by which main-belt asteroids and asteroidal meteoroids may be perturbed into Earth-crossing orbits. This article concentrates on the possible relation between the excess of orbits with semimajor axes just inside the asteroid belt and the set of Earth approaching asteroids proposed to be their parents. Figure 2 shows this region in more detail with the numbered zones corresponding to Halliday *et al.*'s (1990) groups of apparently related meteoritic orbits with the same numbers. The meteoroids in zones 2 and 4 may arrive more or less directly from the asteroid belt while zones 1 and 3 are close to or overlap asteroids 3551 and 3908 in this orbital parameter projection. The perihelion of 4055's orbit may be too distant for a tightly associated stream to intersect the Earth. Figure 3, shows that the primary difference between group 3 orbits is in the longitude of the ascending node, as is expected for an aging group of debris ejected at low relative velocity. The nodes of the low inclination orbits could spread about that of 3908 by differential precession. The orientation of the major axes is a relatively stable property of eccentric orbits and the tight association between 3908, 3551, and group 3 in Figure 4 is further evidence of their kinship to each other, at least between the meteoroids and 3908. A relation between 3551 or 3908 and group 4 could also be suspected.

ORBITAL EVOLUTION AND METEOROID EJECTION

Did orbits in zone 3 intersect the orbit of 3908 or 3551 in the past? If so, did this occur in the asteroid belt where chances for collisions is largest and could the relative velocities at the point of intersection be obtained by impact ejecta? Orbital integrations accounting for perturbations by the planets Mercury through Neptune show that the mean orbit of zone 3 meteoroids, as given by Halliday *et al.* (1990), intersected that of 3908 repeatedly over the last 10^4 years. Intersections last occurred approximately 4000 years ago, in the middle of the asteroid belt (2.75 AU) at relative velocities of approximately 100 m/s. Ejection velocities of that order are easily obtained in a collision.

Group 3 orbits also intersect the orbit of 3551 approximately 6000 years ago and then again 2500 years ago at relative velocities of the order of 500 m/s respectively more than 1 km/s. These are suspiciously high ejection velocities, especially that the low velocity dispersion required to form a stream as tight as the group 3 meteoroids would also have to be explained. The 6000 year old event would have taken place near 1.3 AU, a region between Earth and Mars where collisions are unlikely, but the more recent higher relative velocity intersection is in the asteroid belt near 2.8 AU. Both are unlikely ejection events.

Intersections with both asteroid orbits are primarily due to differential precession and repeat with approximately 2×10^4 and 1×10^4 year periods respectively, so that intersections occur again at the mentioned epoch and an integer times the period. Differential precession also makes the orbits of 3551 and 3908 intersect three times per 10^4 year period, approximately 9000, 3000, and 1000 years ago. The intersection 3000 years ago took place in the asteroid belt (near 2.8 AU). The other intersections occur near perihelion where chances for collisions are small.

In conclusion, it is possible that meteorite dropping fireballs were ejected from Amor asteroid 3908. If the narrow group of meteor orbits labeled No. 3 by Halliday *et al.* (1990) are related, they are likely ejecta from 3908. They would result from a collision in the asteroid belt, approximately $N(2 \times 10^4) + 4000$ years ago where N is an integer. One might speculate that this event coincided with a split between 3551 and 3908, approximately 3000 and an integer times 10^4 years ago considering that the periodicity is approximate. Drummond and Wisniewski (1990) and Cruikshank *et al.* (1991) suggested that asteroids 3551, 3908, and possibly 4055, may be related to each other and to meteorite dropping meteoroids based on spectral similarity and their present orbits. We have investigated the orbits and show that it

is dynamically possible for one group of meteoroids to be ejecta from 3908. There is no evidence for recent ejecta from 3551 or 4055 but such ejecta may exist without being in Earth intersecting orbits.

That the group of meteorite producing fireballs may be ejecta from a collision in the asteroid belt is in contrast to the origin of another group of meteoroids thought to be related to an asteroid, the Geminids. Orbital integrations of 20 high precision meteoroid orbits showed that they were ejected from Phaethon near perihelion, probably during a cometary phase in the Parent's evolution (Gustafson, 1989).

According to *Halliday et al.* (1989) meteorites from group 3 members are probably ordinary chondrites but one, the Allan Sask event, also could be a carbonaceous chondrite. It fell on farmland of western Canada in October of 1979. Recovery and spectral classification of this meteorite would help test the link to the Amor asteroids. According to *Halliday et al.* (1989), another member fireball, the Middle Lake event of September 1975 remains one of the best possibilities for recovery.

ACKNOWLEDGMENTS

This work was supported by NASA grant No. NAGW-1257. B.Å.S.G. also gratefully acknowledges support from the visitors program of the School of Mathematical Sciences, Queen Mary and Westfield College, University of London, UK, where this work was initiated.

REFERENCES

- Cruikshank, D.P., D.J. Tholen, W.K. Hartmann, J.F. Bell, and R.H. Brown, 1991. Three basaltic Earth-approaching asteroids and the source of the basaltic meteorites. *Icarus*, **89**, p. 1-13.
- Drummond, J.D., 1981. A test of comet and meteor shower associations. *Icarus*, **47**, p. 545-553.
- Drummond, J.D., and W.Z. Wisniewski, 1990. The rotational poles and shapes of 1580 Betulia and 3908 (1980PA) from one apparition. *Icarus*, **83**, p. 349-359.
- Gustafson, B.Å.S., 1989. Geminid Meteoroids Traced to Cometary Activity on Phaethon. *Astron. Astrophys.*, **225**, p. 533-540.
- Halliday I., A.T. Blackwell, and A.A. Griffin, 1989. Detailed records of many unrecovered meteorites in western Canada for which further searches are recommended. *J. Roy. Astron. Soc. Can.*, **83**, No. 2, p. 49-80.
- Halliday I., A.T. Blackwell, and A.A. Griffin, 1990. Evidence for the existence of groups of meteorite-producing asteroidal fragments. *Meteoritics*, **25**, p. 104-130.
- McCrosky R.E., and A. Posen, 1961. Orbital elements of photographic meteors. *Smithson. Contr. Astrophys.*, **4**, No. 2, p. 15-84.
- McCrosky, R.E., C.-Y. Shao, and A. Posen, 1978. *Meteoritica*, **37**, p. 44-59.
- Southworth R.B., and G.S. Hawkins, 1963. Statistics of meteor streams. *Smithson. Contr. Astrophys.*, **7**, p. 261-285.
- Wetherill G.W., 1988. Where do the Apollo objects come from? *Icarus*, **76**, p. 1-18.

COLLISIONAL AND DYNAMIC EVOLUTION OF DUST FROM THE ASTEROID BELT

B.Å.S. Gustafson¹, E. Grün², S.F. Dermott¹, and D.D. Durda¹

- 1) Astronomy Department, University of Florida 211 SSRB, 32611 Florida, USA.
- 2) Max-Planck Institut für Kemphysik, Postfach 10 39 80, D-6900 Heidelberg 1, FRG.

ABSTRACT

The size and spatial distribution of collisional debris from main belt asteroids is modeled over a 10 million year period. The model dust and meteoroid particles spiral toward the Sun under the action of Poynting-Robertson drag and grind down as they collide with a static background of field particles.

INTRODUCTION

Analysis of the solar system dust bands in the IRAS data using the SIMUL model (Dermott and Nicholson, 1989) has established both the bands' origin in the prominent Hirayama families and the transport of asteroidal dust to 1 AU (Dermott *et al.*, 1992). Durda *et al.* (1992) show how the production rate of 1 mm and larger debris from any one family varies stochastically over time. The comminution or collisional break-up of smaller particles and their transport to 1 AU is addressed in this article.

THE ASTEROID COMMINEUTE EVOLUTION (ACE) MODEL

The present form of our Asteroid Commminate Evolution (ACE) model accounts for the collision of asteroid fragments with a static background of field particles while the fragments spiral toward the Sun under the action of Poynting-Robertson drag and radiation pressure. The combined effects of gravitational forces due to the planets and radiation forces may be accounted for in future models using a new secular perturbation theory by Gomes and Dermott (1992).

A body of given size and density is in a circular heliocentric orbit of given radius. A collision breaks the body into fragments following a size distribution of the form

$$\frac{dN}{dm} = C m^{-(1+\eta)},$$

where dN is the number of fragments in the mass range m to $m + dm$. The exponent η usually equals 0.83 with the largest fragment retaining 30% of the total mass (Fujiwara *et al.*, 1977). Conservation of mass defines the constant C . Fragments in the mass range from 10^{-12} to 10^{18} g (from β-meteoroids to 4 or 5 km radius asteroids) are divided into 60 logarithmic size bins. For computational convenience, every fragment is assumed to be homogeneous, of equal density, and

spherical in shape. To further reduce computational overhead while conserving mass, particles are reassigned a mass equal to the arithmetic mean associated with its bin. Radiation pressure instantly distorts the pre-break-up circular orbit to an ellipse with perihelion at the breakup point. This distortion is important for small bodies and the smallest particles leave the solar system as β -meteoroids. After break-up, particles within a given mass bin are placed in identical circular orbits at the time averaged heliocentric distance of their orbits. Every particle bin is characterized by the average particle mass and heliocentric distance in a two dimensional matrix. Fragments smaller than the lower cut-off limit and any fragments on orbits beyond 5.425 AU are assumed to escape the solar system, the accumulated mass of such β -meteoroids is recorded. Fragments collide with a population of interplanetary grains represented by the empirical interplanetary flux model of Grün *et al.* (1985). This distribution closely fits fluxes derived from Pioneer 8, 9, and HEOS-2 measurements. The mass distribution is observationally supported up to approximately 100 g corresponding to meteoroids a few cm in radius. As the number of larger field objects is small, their detailed distribution is not decisive to modeling over a few million years. The number of fragments produced by particles in a given size bin in one time step is calculated from the probability for catastrophic collisions per unit time multiplied by the time interval and the number of particles. Average collision probabilities were used in these simulations. In contrast, in the simulations by Durda *et al.* (1992) a random number generator was used to investigate the extent of statistical fluctuations. Fragments instantly move to higher orbits while the surviving particles lose height due to PR-drag at each time step.

RESULTS

The distribution of fragments is immediately distorted as radiation pressure expels the smallest particles as β -meteoroids. Dust sized particles (1 to 100 μm in radius) are initially dispersed on elliptic orbits and reside most of the time outside the orbit of the parent asteroid. PR-drag soon reduces the size and eccentricity of their trajectories and the smallest particles are first to arrive at 1 AU even though radiation pressure originally pushed them furthest out. A supply of fresh debris is constantly produced as larger particles collide with the meteoric complex, break-up, and produce miniature dust clouds analogous to the break-up of the asteroid. The size and spatial distribution changes rapidly at first, but dust below 10^{-8} g (10 μm) reach a nearly steady distribution at 1 AU over the first 10^5 years. Figure 1 shows the size distribution at 1 AU resulting from the break-up of a 100 km radius asteroid, of 2.5 g cm^{-3} density, near the outer edge of the asteroid belt (3 AU). Particles ranging up to approximately 10^{-5} g (100 μm) arrive at 1 AU after 10^6 years (dashed line) and also appear to reach a nearly steady size distribution with larger particles still arriving over the 10^7 year period (solid curve). The distribution of dust from an asteroid on the inner edge of the main belt (2 AU) shown in Figure 2 confirm the overall features shown in Figure 1 and meteoroids in the 10^{-4} to 10^{-5} g range appear to have reached an equilibrium distribution. Meteoroids of 10^{-2} g or about a millimeter arrive from 2 AU after 10^6 years (Figure 2) and their numbers did not change from 10^6 to 10^7 years. Intermediate size meteoroids are destroyed and feed the dust population. While the computations indicate that some millimeter sized meteoroids arrive from a break-up at 3 AU their numbers are so small that they are not seen in Figure 1. The dust size distribution (below 10^{-5} g or 100 μm) established over the first 10^6 years remains remarkably stable in both figures.

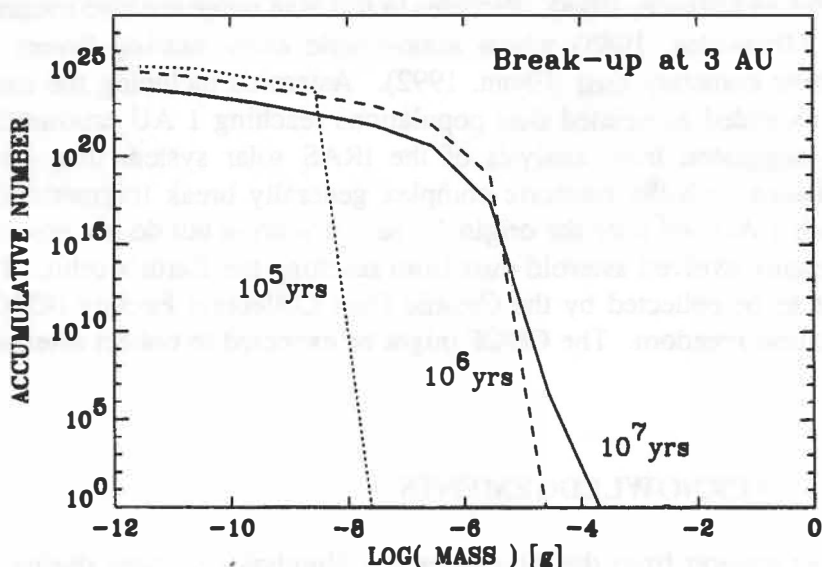


Figure 1. Size distribution of collisionally evolved asteroidal debris at 1 AU, 10^5 , 10^6 , and 10^7 years after the break-up of an asteroid near the outer edge of the main belt. The original power law size distribution is altered as debris collide, grind down, and spiral in to Earth's orbit under the action of PR-drag. Fragments in the size range 10^{-5} to 10^{-11} g (or 100 to 1 μm) reach 1 AU within the first 10^6 years and their size distribution then remains remarkably stable.

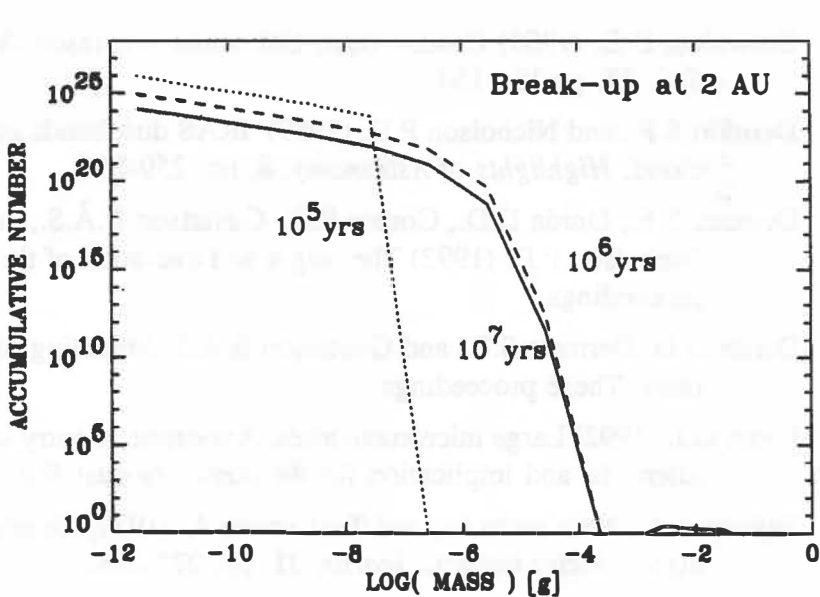


Figure 2. Size distribution at 1 AU of collisionally evolved debris from an asteroid that broke up near the inner edge of the asteroid belt. A nearly steady size distribution is attained within the first million years after the break-up. Meteoroids in the 10^{-2} g or 1 mm size range reach the Earth's orbit after 10^6 years but intermediate size particles are ground down before they reach the Earth.

These are significant results as particles in the 10 to 100 μm size range are thought to produce most of the zodiacal light (Röser and Staude, 1978). Particles in this size range are also routinely collected in the stratosphere (Brownlee, 1985) where atmospheric entry heating favors the survival of asteroidal debris over cometary dust (Flynn, 1992). Asteroids including the major Hirayama families may have extended associated dust populations reaching 1 AU produced as member asteroids collide, as suggested from analysis of the IRAS solar system dust bands (Dermott *et al.*, 1992). Collisions with the meteoric complex generally break fragments into smaller pieces before they reach 1 AU and alter the original size distribution but do not preclude significant amounts of collisionally evolved asteroid dust from reaching the Earth's orbit. This is also the size range particles to be collected by the Cosmic Dust Collection Facility (CDCF) planned to fly on the Space Station Freedom. The CDCF might be expected to collect asteroidal dust particles for analysis.

ACKNOWLEDGEMENTS

B.Å.S. Gustafson acknowledges support from the Alexander von Humboldt Stiftung during his stay at the Max-Planck Institut für Kernphysik where this work was initiated. Partial support from NASA Grant No. NAGW-1257 is also acknowledged.

References

- Brownlee, D.E. (1985) Cosmic dust: Collection and research. *Ann. Rev. Earth. Planet. Sci.*, **13**, pp.134-150.
- Dermott S.F., and Nicholson P.D. (1989) IRAS dust bands and the origin of the zodiacal cloud. *Highlights of Astronomy*, **8**, pp. 259-266.
- Dermott S.F., Durda D.D., Gomes R.S., Gustafson B.Å.S., Jayaraman S., Xu Y.-L., and Nicholson P.D. (1992) The origin and evolution of the zodiacal dust cloud. These proceedings.
- Durda D.D, Dermott S.F., and Gustafson B.Å.S. Modeling of asteroidal dust production rates. These proceedings.
- Flynn G.J. (1992) Large micrometeorites: Atmospheric entry survival, relation to mainbelt asteroids, and implication for the cometary dust flux. These proceedings.
- Fujiwara, A., Kamimoto G., and Tsukamoto A. (1977) Destruction of basaltic bodies by high-velocity impact. *Icarus*, **31**, pp. 277-288.
- Gomes R.S., and Dermott S.F. (1992). To be submitted to *Icarus*
- Grün E., Zook H.A., Fechtig H., and Giese R.H. (1985) Collisional balance of the meteoritic complex. *Icarus*, **62**, pp. 244-272.
- Röser S., and Staude H.J. (1978) The zodiacal light from 1500 Å to 60 micron. *Astron. Astrophys.*, **67**, pp. 381-394.

LONG-TERM EVOLUTION OF 1991 DA: A DYNAMICALLY EVOLVED EXTINCT HALLEY-TYPE COMET

G. Hahn¹ and M.E. Bailey

Department of Astronomy, The University, Manchester M13 9PL, England, U.K.

ABSTRACT

The long-term dynamical evolution of 21 variational orbits for the intermediate-period asteroid 1991 DA has been followed for up to $\pm 10^5$ years from the present. 1991 DA is close to the 2:7 resonance with Jupiter; it avoids close encounters, within 1 AU, with this planet for at least the past 30,000 years even at the node crossing. The future evolution typically shows no close encounters with Jupiter within at least 50,000 years. This corresponds to the mean time between node crossings with either Jupiter or Saturn. Close encounters with Saturn and Jupiter lead to a chaotic evolution for the whole ensemble, while secular perturbations cause large-amplitude swings in eccentricity and inclination (the latter covering the range $15^\circ \lesssim i \lesssim 85^\circ$) which correlate with deep excursions of the perihelion distance to values much less than 1 AU. These variations are similar to those found in P/Machholz and a variety of other high-inclination orbits, e.g. P/Hartley-IRAS. We emphasize the connexion between the orbital evolution of 1991 DA and that of Halley-type comets. If 1991 DA was once a comet, it is not surprising that it is now extinct.

INTRODUCTION

1991 DA is the only known asteroid which moves in an intermediate-period comet-like orbit of high inclination; its perihelion distance ($q \simeq 1.58$ AU) and inclination ($i \simeq 61^\circ.9$) suggest that it should be classified as a Halley-type comet; but, despite deep imaging with CCD detectors (IAUC 5208), no outgassing has yet been reported. The evolution of 1991 DA is of exceptional interest, and in order to clarify the possible dynamical history we have carried out a long-term integration of an ensemble of 21 orbits with initial elements similar to those of the present object (cf. Hahn & Bailey 1990).

We consider initial orbits centred on the elements of 1991 DA as reported in March 1991. The variational elements were chosen so as to cover the expected uncertainty in this preliminary orbit, and a comparison with more recently published elements (MPC 18127 and MPC 18299) shows that this procedure was justified. The integrations covered $\pm 90,000$ years and $\pm 100,000$ years, the former using the orbit reported in IAUC 5208 and a 6-planet solar system (Earth+Moon through Neptune), the latter using the orbit reported in MPC 17971 and a 4-planet solar system (Jupiter through Neptune). The elements for 1991 DA and some representative test particles are shown in Table 1.

The integrations were carried out using the variable-step-size integrator RADAU to 15th order (RA 15) described by Everhart (1985). The 4-planet solar system model was calculated with an initial step size of 40 days and an internal accuracy parameter of 10^{-12} , and the 6-planet model with a smaller initial step size (1 day) and higher accuracy (10^{-13}). Details of all close encounters within 1 AU of the Jovian planets and 0.1 AU of the terrestrial planets were recorded, whilst away from close encounters the positions and velocities of each body were sampled every 2,500 days.

LONG-TERM EVOLUTION

Although 1991 DA crosses the orbit of Mars, Jupiter, Saturn and Uranus, suggesting that its orbital evolution (like that of many planet-crossing asteroids; Milani *et al.* 1989) should be strongly chaotic, a striking feature of our results is the orbit's extreme stability. This is illustrated in Figure 1 which shows the evolution of DA 06(6) for $\pm 90,000$ yr. Although 1991 DA is now close to the 2/7 mean-motion resonance with Jupiter, most of the orbits in our ensemble are in associated higher-order resonances, sometimes jumping from one to another due to weak planetary perturbations. This situation persists for approximately the first $\pm 30,000$ years from the present; Jupiter is the controlling planet, but perturbations by Saturn, and to a lesser extent Uranus and Mars, also play a rôle.

A detailed description of our results is given by Bailey & Hahn (1992), but it is clear from Figure 1 that the orbit's remarkable stability is due to the lack of close encounters with Jupiter and Saturn. The first

¹Present address: Astronomiska Observatoriet, Uppsala Universitet, Box 515, S-75120, Uppsala, Sweden.

Object	a (AU)	e	i (deg)	M (deg)	Epoch (JD)
1991 DA (6)	11.863912	0.866923	61.8932	0.000	2448228.4579
DA 01 (6)	11.863	0.8668	61.89	0.000	2448228.5000
DA 02 (6)	11.863	0.8669	61.89	0.000	2448228.5000
DA 03 (6)	11.863	0.8670	61.89	0.000	2448228.5000
DA 05 (6)	11.864	0.8669	61.89	0.000	2448228.5000
DA 09 (6)	11.865	0.8670	61.89	0.000	2448228.5000
1991 DA (4)	11.8639121	0.8669226	61.89324	1.72553	2448300.0000
DA 00 (4)	11.863912	0.866923	61.8932	0.000	2448228.4579
DA 01 (4)	11.75	0.866	61.89	1.73	2448300.0000
DA 02 (4)	11.75	0.867	61.89	1.73	2448300.0000
DA 03 (4)	11.75	0.868	61.89	1.73	2448300.0000
DA 05 (4)	11.85	0.867	61.89	1.73	2448300.0000
DA 09 (4)	11.95	0.868	61.89	1.73	2448300.0000

Table 1: Orbital elements for 1991 DA and test particles $DAnn$. Those marked (6) were integrated in a 6-planet model solar system with angular elements $\Omega = 313^\circ.4108$ (1991 DA), rounded to $313^\circ.41$ ($DAnn$), and $\omega = 191^\circ.2467$ (1991 DA), rounded to $191^\circ.25$ ($DAnn$). Those marked (4) were integrated in a 4-planet model solar system with angular elements $\Omega = 313^\circ.41077$ (1991 DA) and $313^\circ.4108$ (DA 00), rounded to $313^\circ.41$ ($DAnn$), and $\omega = 191^\circ.24673$ (1991 DA) and $191^\circ.2467$ (DA 00), rounded to $191^\circ.25$ ($DAnn$).

Saturn encounters (at $t \lesssim -20,000$ yr and $t \gtrsim 40,000$ yr) cause small orbital changes which may or may not break the mean-motion resonance with Jupiter, while some particles remain protected from close encounters with Jupiter at the first node crossing.

Figure 1 also shows libration of the critical argument σ for DA 06 (6), in which the semi-major axis is close to one or another mean-motion resonance with Jupiter for almost the whole time considered. The critical argument σ is defined, for an asteroid in the $(p+q)/p$ resonance, by $\sigma = (p+q)\lambda_J - p\lambda - q\varpi$

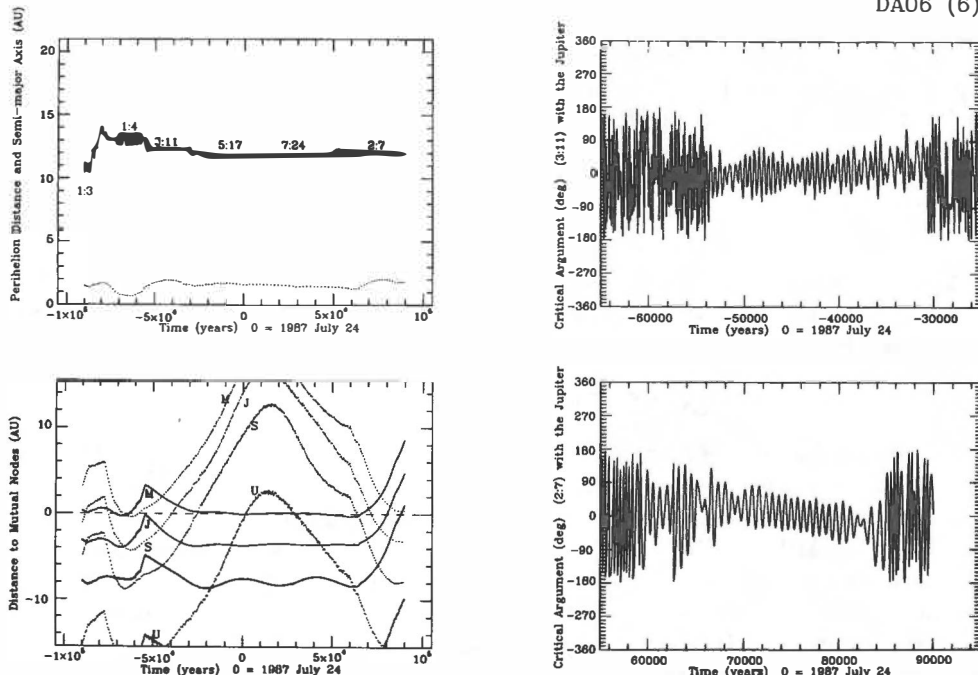


Figure 1: Evolution of DA 06 (6) for $\pm 90,000$ yr in a 6-planet model solar system, showing extreme stability of the present orbit and mean-motion resonances. The distances to the mutual nodes with respect to Mars, Jupiter, Saturn and Uranus are also shown, as too are the librations of the critical argument σ .

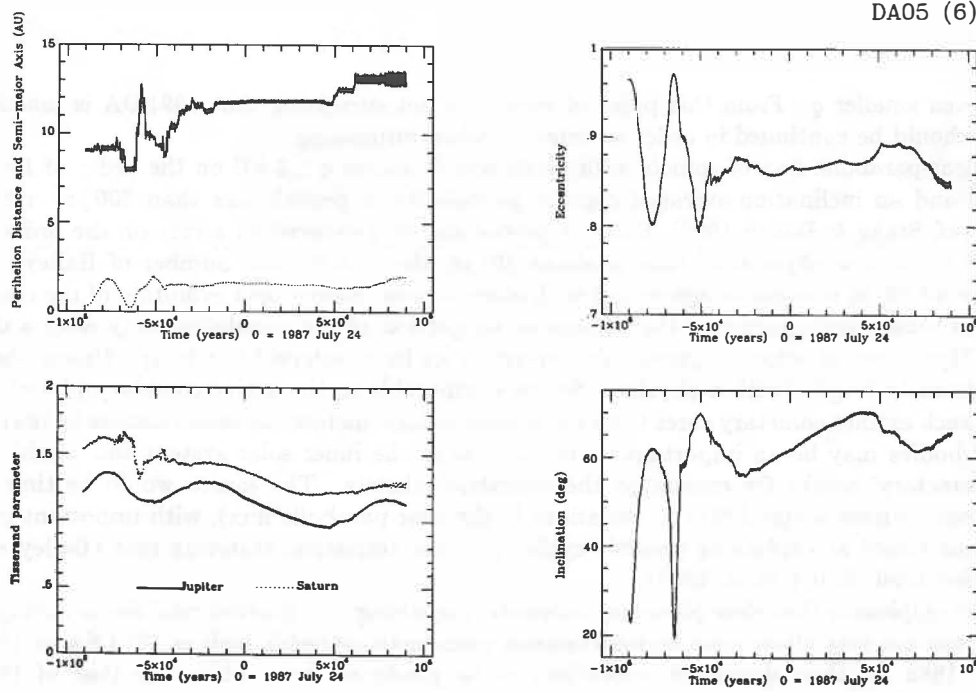


Figure 2: Evolution of DA 05 (6) for $\pm 90,000$ yr from the present, showing the semi-major axis and perihelion distance, the Tisserand parameters with respect to Jupiter and Saturn, and the deep surges in eccentricity and perihelion distance correlating with large swings in inclination.

(Yoshikawa 1989), where λ and λ_J are the mean longitudes of the asteroid and Jupiter respectively, and ϖ denotes the longitude of perihelion of the asteroid. p and q are integers; e.g. $p = 7$ and $q = -5$ for the 2/7 resonance. A qualitatively similar behaviour was observed for other orbits in the ensemble, though following close encounters with Saturn most did not remain protected against close encounters with Jupiter.

An important feature of the evolution is the length of time in which only slight changes in semi-major axis occur. The semi-major axis stays close to a mean-motion resonance with Jupiter for a time comparable with the period between node crossings with Jupiter or Saturn, and during these relatively stable periods large excursions in the perihelion distance, eccentricity and inclination occur (Figure 2). This behaviour is characteristic of the evolution of high-inclination, intermediate-period orbits with small perihelion distance, and is seen in P/Machholz (Green et al. 1990, McIntosh 1990), and also in long-term integrations of P/Hartley-IRAS and the sungrazers (Bailey et al. 1991a).

Although several bodies were briefly captured to or from longer periods, there was only one case of ejection to a parabolic orbit. This indicates a dynamical half-life for 1991 DA on the order of 1–3 Myr. Since this is probably much shorter than the time necessary for evolution of a mainbelt asteroid into an orbit with the inclination and eccentricity observed in 1991 DA we conclude that a cometary source for 1991 DA is the more likely. During a dynamical lifetime on the order of 2 Myr, it presents itself to Jupiter and Saturn many times (i.e. at intervals on the order of the node-crossing period, $\approx 5 \times 10^4$ yr), suffering close encounters at each node crossing, and eventually undergoes a chaotic orbital evolution.

DISCUSSION

These arguments suggest that 1991 DA is indeed an extinct comet, probably captured by Jupiter within the past 1 Myr from a nearly parabolic orbit of originally small perihelion distance ($\lesssim 2$ AU) and inclination on the order of 45° or more. There is an important link between 1991 DA and active comets of the Halley family, and with orbits such as those of P/Machholz and P/Hartley-IRAS, and our calculations provide firm evidence that 1991 DA has been circulating in more or less its present orbit for at least the past 25,000 yr — and will probably continue to do so for another 50,000 yr. With a period close to 40 yr, it has already made at least 600 revolutions with a perihelion distance on the order of 1 AU, some of which may have included

episodes of even smaller q . From this point of view it is not surprising that 1991 DA is inactive, though observations should be continued in order to detect residual outgassing.

With a near-parabolic flux of comets with perihelion distances $q \lesssim 2$ AU on the order of 1 yr^{-1} (Bailey et al. 1991b) and an inclination-averaged capture probability to periods less than 200 yr on the order of $(1-3) \times 10^{-3}$ (cf. Stagg & Bailey 1989), Halley-type comets are produced at a rate on the order of 1–3 per 10^3 years. If the active physical lifetime is about 10^4 yr, the steady-state number of Halley-type comets should be around 20, in reasonable agreement with observations. Subsequent evolution of the cometary core leads either to total disintegration of the nucleus or to ejection of the remaining body after a time on the order of 1–3 Myr, most of which is presumably spent as an inert asteroid-like body. Unless the cometary nucleus is extremely fragile (with a physical lifetime comparable to the active cometary phase), one would expect many such extinct cometary cores to be circulating in high-inclination orbits similar to 1991 DA. These undiscovered bodies may be an important source of dust in the inner solar system and would represent a significant ‘cometary’ source for craters on the terrestrial planets. The source would be time-dependent (since it responds within about 1 Myr to variations in the near-parabolic flux), with important implications for mechanisms aimed at explaining possible cyclicity in the terrestrial cratering rate (Bailey et al. 1987, Clube & Napier 1990, Bailey et al. 1990).

Finally, we emphasize that close planetary encounters or strong non-gravitational forces during the small- q phases of evolution may allow some high-inclination near-earth asteroids such as 1973 NA or 1982 YA (see Milani et al. 1989 for their dynamical evolution) to be produced from orbits like that of 1991 DA (cf. Nakamura 1983). Further observations of 1991 DA should be encouraged, as too should searches to discover other ‘unexpected asteroids’ far from the ecliptic plane.

ACKNOWLEDGMENTS

We thank D. Steel for suggesting that we should begin this investigation. The calculations were performed at low priority on the Manchester STARLINK VAX-cluster and the work was supported by the SERC.

REFERENCES

- Bailey, M.E. & Hahn, G., 1992. *Orbital evolution of 1991 DA and implications for near-earth asteroids*, Proceedings of International Workshop on Periodic Comets, eds. J.A. Fernández & H. Rickman, University of Montevideo, Uruguay.
- Bailey, M.E., Wilkinson, D.A. & Wolfendale, A.W., 1987. *Can episodic comet showers explain the 30-Myr cyclicity in the terrestrial record?* Mon. Not. R. Astron. Soc., **227**, 863–885.
- Bailey, M.E., Clube, S.V.M. & Napier, W.M., 1990. *The Origin of Comets*, Pergamon Press, Oxford.
- Bailey, M.E., Chambers, J.E. & Hahn, G., 1991a. *Origin of sungrazing comets: a widespread cometary end-state*, in preparation.
- Bailey, M.E., Hahn, G., Rickman, H., Tancredi, G. & Valtonen, M.J., 1991b. *The origin of short-period comets*, in preparation.
- Clube, S.V.M. & Napier, W.M., 1990. *The geomagnetic reversal frequency as a probe of Galactic structure*, Preprint.
- Everhart, E., 1985. *An efficient integrator that uses Gauss-Radau spacings*. In: *Dynamics of Comets: Their Origin and Evolution*, IAU Coll. No. 83, 185–202, eds. Carusi, A. & Valsecchi, G.B. Reidel, Dordrecht, The Netherlands.
- Green, D.W.E., Rickman, H., Porter, A.C. & Meech, K.J., 1990. *The strange periodic comet Machholz*, Science, **247**, 1063–1067.
- Hahn, G. & Bailey, M.E., 1990. *Rapid dynamical evolution of giant comet Chiron*, Nature, **348**, 132–136.
- McIntosh, B.A., 1990. *Comet P/Machholz and the Quadrantid meteor stream*, Icarus, **86**, 299–304.
- Milani, A., Carpino, M., Hahn, G. & Nobili, A.M., 1989. *Dynamics of planet-crossing asteroids: classes of orbital behavior. Project SPACEGUARD*. Icarus, **78**, 212–269.
- Nakamura, T., 1983. *Steady state number of extinct comets in high-inclination orbits*. In: *Dynamical Trapping and Evolution in the Solar System*, IAU Coll. No. 74, 97–104, eds. Markellos, V.V. & Kozai, Y. Reidel, Dordrecht, The Netherlands.
- Stagg, C.R. & Bailey, M.E., 1989. *Stochastic capture of short-period comets*, Mon. Not. R. Astron. Soc., **241**, 507–541, and Microfiche MN 241/1.
- Yoshikawa, M., 1989. *A survey of the motions of asteroids in the commensurabilities with Jupiter*, Astron. Astrophys., **213**, 436–458.

LIGHTCURVE OF COMET AUSTIN(1989C1) AND ITS DUST MANTLE DEVELOPMENT

Hitoshi Hasegawa

ASTEC, Inc., BR Ichigaya, 6 Minamicho Shinjuku Tokyo 162 Japan

and

Jun-ichi Watanabe

National Astronomical Observatory, Osawa Mitaka Tokyo 181 Japan

Abstract

Brightness variations of comet Austin(1989c1) were investigated in terms of the variations of water production rate. We translated the visual brightness data into water production rates using Newburn's semi-empirical law. The curve of the water production rates as a function of heliocentric distance was compared with the model calculations that assumed energy balance between the solar incident and vaporization of water. Thermal flow in a dust mantle at a surface of the nucleus is also included in the model. The model calculations including the dust mantle are more favorable for the observed rate than non-dust mantle cases. The extinction after the perihelion passage suggests that the dust mantle developed gradually.

1 Introduction

Visual magnitude observations of comets are one of the useful indices to understand cometary activities. We have a great deal of visual estimations of the brightness of comets. These cometary magnitudes, however, do not compare directly with other physical quantities such as gas production rates. To perform these comparisons, Newburn(1983) developed a semi-empirical method which translates a cometary brightness into a water production rate. Roettger *et al.*(1990) verified the method by comparing translated water production rates from visual observations for some recent comets with those observed by the IUE(*International Ultraviolet Explorer*) and found them to be in good agreement for the some comets studied. We have applied this technique to the lightcurve analysis of comet Austin(1989c1). The comet showed an asymmetric lightcurve, in which it became fainter after its perihelion passage. This type of brightness variation is often recorded in the case of new comets that are first coming into the inner solar system from the Oort cloud (see Whipple, 1977 for example). Comet Austin was probably a "new" comet(*IAU Circular*, No.4919). We will illustrate such an asymmetric lightcurve using a dust mantle model that was described by Mendis and Brin(1977). In the model, released dust particles, which could not exceed their escape velocity, accumulate on the surface. As a result the mantle acts as a insulating layer from the solar incident because of its low thermal conductivity. We will consider that the mantle developing would be responsible for the asymmetric lightcurve that is extinct after the perihelion.

2 Data Reduction

The visual observations of comet Austin that we used were the values that were reported in the IAU circular and the HAL(Hoshi-no-hiroba Astro Letter, the circular of a Japanese amateur observers group) and were also contributed by the comet section of the Astronomical Union of Universities(also an amateur group in Japan). Totally, the number of usable observations we used were 535, eliminating some extremely inaccurate data, which deviated more than 3 magnitudes from others. Fig. 1 shows the visual magnitudes of the comet reduced to 1-AU geocentric distance as a function of heliocentric distance. We can see in the figure that the comet became fainter after the perihelion.

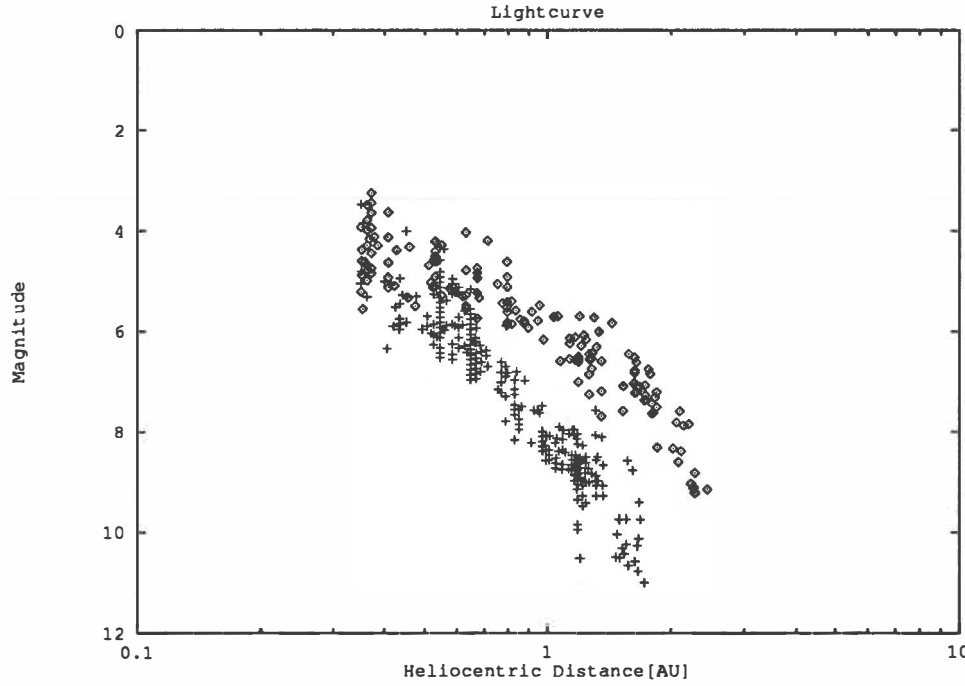


Figure 1: Visual magnitudes of comet Austin(1989c1). The plotted data are reported in IAU Circular, HAL(Hoshi-no-hiroba Astro Letter) and contributed by AUU(Astronomical Union of Universities). Diamond symbols and plus symbols indicate pre and post perihelion data respectively.

To compare the visual magnitude data with water production rates, we applied Newburn's semi-empirical method (Newburn, 1983) that aimed to reduce visual magnitude observation m_v into a water production rate $Q_{\text{H}_2\text{O}}$. We can obtain the rate by,

$$Q_{\text{H}_2\text{O}}(m_v) = \frac{1}{2} \left[\frac{10^{0.4(m_\odot - m_v)}}{\tau_{C_2}(1 + ar^n)R} \right]^{1/2} \times 1.4968 \times 10^8, \quad (1)$$

where τ_{C_2} is the lifetime of C_2 at 1 AU, m_\odot is the magnitude of the sun, r is the heliocentric distance in AU. ar^n is the relative contribution of dust and gas to the visual magnitude, and R is the fluorescence efficiency of C_2 . The values that we used for these parameters are the same as Roettger *et al.*(1990). The reduced water production rates using this method are plotted in Fig.2. To check the validity of the translated data, we compared them with IUE post perihelion data (Budzin *et al.*,1990), and found that they were in agreement, although the IUE data were somewhat larger than the reduced rate.

3 Model Calculations

We can then compare directly the water production rates obtained from visual brightness data with those from model calculations. The dust mantle model that we used here is a subset of Mendis and Brin's model(1977). The model is based on an energy balance between the solar incident and used by sublimation of water ice when a dust mantle, that has a low thermal conductivity, covers the surface to the depth Δ . The mantle surface temperature T_s is mainly governed by radiative equilibrium, while the ice core temperature T_e is controlled by the sublimation of ice. The energy balance through the dust mantle is written in the following equations,

$$\frac{1 - As}{r^2} J \cos \theta = \epsilon_s \sigma T_s^4 - K(T) \Delta T|_s \quad (2)$$

$$-K(T) \Delta T|_{s=c} = \frac{L}{N_0} \dot{Z}(T_e), \quad (3)$$

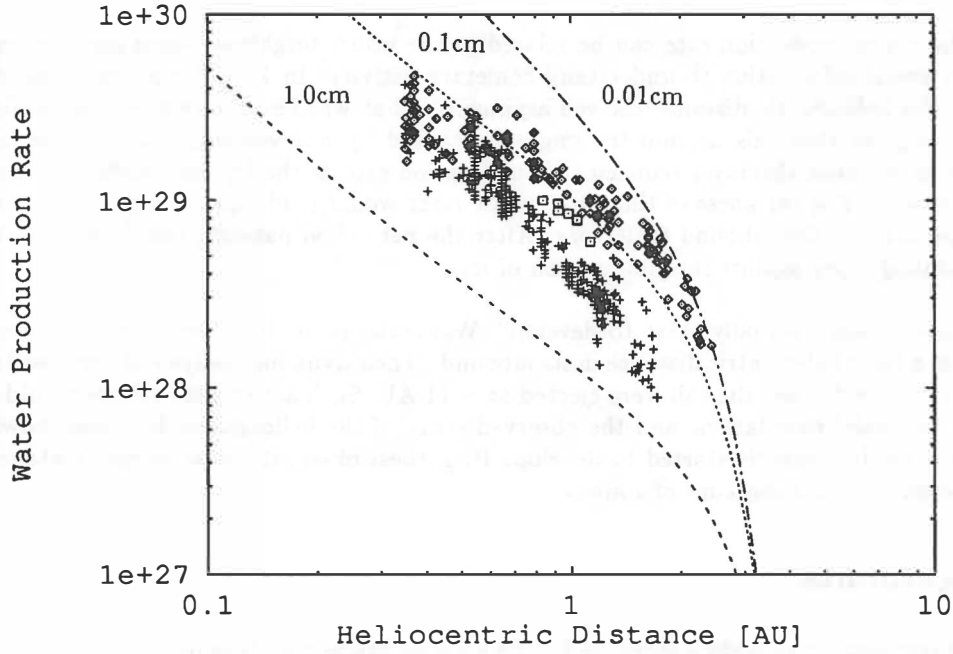


Figure 2: Reduced and calculated water production rates. The plotted curves are computed production rates for the dust mantle case. The values in the graph are depths of the dust mantle. The symbols are as the same as the Fig.1. The IUE data that were observed after the perihelion are also plotted as square symbols.

where A_s and ϵ_s are the albedo at visible and infrared emissivity respectively. We assumed $A_s = 0.05$ and $\epsilon_s = 0.9$. σ is the Stefan-Boltzmann constant. J is the solar constant and L is the latent heat of water vapor. N_0 is the Avogadro number, $Z(T_e)$ is the sublimation rate at the icy core surface of the nucleus. We calculated L and Z according to Cowan and A'Hearn(1979). θ is the solar incident angle. If we consider a rapidly rotating nucleus, the averaged value for $\cos \theta$ is 0.25. The heat conducted through the non-volatile mantle is represented as the term $(-K(T)\Delta T|_s)$. The thermal conductivity K is given by,

$$K(T) = K_c + 4\sigma\epsilon_s l T^3, \quad (4)$$

where the K_c is the bulk conductivity of the mantle material and l is the intergrain distance. We assumed $60.0 \text{ ergcm}^{-2}\text{s}^{-1}\text{K}^{-4}$ and $100\mu\text{m}$ for the the conductivity and the distance respectively.

Solving the above set of equations, we can evaluate the water production rate per unit area at a given heliocentric distance. If the nucleus is spherical, we can simply translate it into a total production rate by assuming its radius. To adjust the calculated rates with the observed rates using the above value at the early part of its inbound, where the mantle would not have been well developed, we took 3km radius for the the nucleus.

As our model does not include the accretion process of dust particles on the surface of the nucleus, the depth of the mantle is assumed to be constant. Instead, we calculated the rate at several depth cases. Fig. 2 shows the computed production rates for several mantle thickness and the reduced production rates from the visual observations. From the case of our calculation, it suggest that the surface of the nucleus was initially mantle free, and the mantle developed gradually as the comet was approaching the sun. Near the perihelion, the thickness of the mantle grew several millimeters, but the rate of the mantle developing became to decrease after the perihelion. This change would be caused by the insulating effect of the well developed mantle layer.

4 Concluding Remarks

We showed that the water production rate can be related to the visual brightness variation of Comet Austin. These data give us useful information to understand cometary activity. In Fig. 2, the variation of the water production rate versus heliocentric distance showed asymmetry that was less active after the perihelion. Our model calculations suggest that this asymmetry might be caused by a developing dust mantle layer on the surface of the nucleus, because this layer reduced the sublimation rate at the icy core surface as a result of its low thermal conductivity. The thickness of the dust mantle layer would gradually be increased by accretion of the emitted dust particles in the inbound trajectory. After the perihelion passage, the developed dust mantle might act as an insulating layer against the sublimation of ice.

When did the dust mantle initially start to develop? Watanabe *et al.*(1990) reported that comet Austin showed a dust tail at a large heliocentric distance in its inbound. Their dynamic analysis of the dust tail revealed that the dust particles that formed the tail were ejected at ~ 11 AU. Such active dust release would also create the dust mantle. Our model calculations and the observed range of the heliocentric distances, however, could not determine when the dust mantle started to develop. Brightness observations at farther distance from the sun are needed to improve our knowledge of comets.

Acknowledgements

We thank Mr. A.Nakamura for providing Hoshino-Hiroba's visual brightness data in a machine readable form, and Mr. J.Kinoshita of ASTEC for providing facilities for computing. We thank also Mr. D.R.StClair for helpfull comments for us.

References

- [1] Budzin,S.A.,Feldman,P.D.,Roettger,E.E.,A'Hearn,M.F., and Festou,M.C.(1990) IUE Observations of Comet Austin(1989c1). Workshop on observations of recent comets(1990).
- [2] Cowan,J.J. and A'Hearn,M.F.(1979) Vaporization of Comets Nuclei: Light curves and Life Times. The Moon and the Planets, 21, 155-171.
- [3] Mendis,D.A. and Brin,G.D.(1977) Monochromatic Brightness Variations of Comets. The Moon, 17, 359-372.
- [4] Newburn,R.L.Jr. (1983) Modeling the Newtral Gas Environment of Comets with Special Application to P/Halley. Adv.Space.Res, 2, 111-120.
- [5] Roettger,E.E.,Feldman,P.D.,A'Hearn,M.F.,and Festou,M.C.(1990) Comparison of Water Production Rates from UV Spectroscopy and Visual Magnitudes for Some Recent Comets. Icarus, 86, 100-114.
- [6] Watanabe,J.,Tsumura,M., and Sugawara,K.(1990) On the Dust Tail of Comet Austin 1989c1. Publ. Astron. Soc. Japan, 42, L69-L73.
- [7] Whipple,F.L. (1977) The constitution of cometary nuclei. in Comets, Asteroids, Meteors(Delsemme,A.H. ed.), pp. 25.

Palomar Planet-Crossing Asteroid Survey (PCAS): Recent Discovery Rate

Eleanor F.Helin, Jet Propulsion Laboratory

ABSTRACT

The discovery rate of Near-Earth Asteroids (NEAs) has increased significantly in the last decade. As greater numbers of NEAs are discovered, worldwide interest has grown leading to new programs. With the introduction of CCD telescopes throughout the world, an increase of 1-2 orders of magnitude in the discovery rate can be anticipated. Nevertheless, it will take several decades of dedicated searching to accomplish a 95% completeness, even for large objects.

The discovery rate of Near-Earth Asteroids (NEAs, including Apollo, Amor, and Aten class asteroids) has increased significantly in the past decade, particularly in the last few years. As greater numbers of near-space objects have been found, some making relatively close approaches to Earth, there has been an attendant increase in the awareness of the potential they have for impacting Earth (e.g., Morrison, 1992). Tens of NEAs which have made, or will in the future make, very close approaches to the Earth have been recorded. It is the larger number of still undetected objects that has become a serious concern. Our immediate goal is to increase the number of known objects to improve estimates of the total population as a function of size of these objects. The ultimate goal, as outlined by Morrison (1992) is to inventory essentially all (>95%) NEAs larger than about 1 km in diameter. The latter goal is beyond the capability of present facilities, so new larger telescopes will be required to achieve completeness in a meaningfully short time, of the order of a decade.

Fifteen to twenty years ago the discovery of 1-2 Near-Earth Asteroids (NEAs) per year was typical from one systematic search program, Palomar Planet-Crossing Asteroid Survey (PCAS), and the incidental discovery from a variety of other astronomical programs. Sky coverage and magnitude were both limited by slower emulsions, requiring long exposures. The 1970s' sky coverage of 20 to 30 thousand sq. deg. per year led to about one NEA discovery every 13,000 sq. deg. (e.g., Helin and Shoemaker, 1979; Helin and Dunbar, 1984, 1990).

Looking at the years from 1987 through 1990, we find that by comparing 1987/1988 and 1989/1990 the worldwide discovery rate of NEAs went from 20 to 43, a little more than a twofold increase. More specifically, PCAS' results when grouped into the two year periods, show an increase from 5 discoveries in 1987/1988 to 20 in the 1989/1990 time period, a fourfold increase. Also, PCAS discoveries went from representing about 25 percent of the worldwide total to contributing roughly 50 percent of the discoveries worldwide in the 1989/1990 period. This trend continues into 1991, whereby PCAS is discovering about one NEA per month. As the discovery rate continues to increase, with significant contributions coming from McNaught/Steel in Australia, Gehrels, Scotti and Rabinowitz in Arizona, and the Shoemakers at Palomar, I anticipate a doubling again in discoveries in the 1991/1992 period. Of course, an important aspect of these more recent discoveries is the inclusion of objects fainter than sky magnitude 20-21, extending to objects as small as H magnitude

28 (1991 BA). At the same time, several very bright asteroids have been discovered which indicates that in the NEA population we have not achieved completeness even to an absolute magnitude H of 13-14. The PCAS discovery of (4954) Eric = 1990 SQ at H magnitude 12.5 surpasses (1627) Ivar as the brightest known asteroid in the NEA population. It is rather remarkable that our most recent NEA discoveries in 1990/1991 include the brightest, (4954) Eric, and the faintest, 1991BA, on record, certainly suggesting that a wide range of undetected objects still roam in earth-approaching and -crossing orbits. The surge of discoveries enjoyed by PCAS in particular is attributed to new fine grain sensitive emulsions, film hypering, more uniformity in the quality of the photograph, more equitable scheduling, better weather, excellent team members and coordination of efforts.

Greater worldwide interest in NEOs is leading to the establishment of new programs using existing telescopes; or by scanning photographic plates taken for other programs as well as reviewing archived plates for asteroid trails (Steel and McNaught, 1991). These efforts are producing excellent results. Spacewatch Telescope has recently created great excitement with the discovery of 1991 DA and 1991 VG as well as a growing list of NEAs (Gehrels, 1991; Rabinowitz, 1991).

We are currently considering upgrading the 18" Palomar Schmidt with an array of CCDs at the focal plane, and to be able to scan at faster-than-sidereal rate. With these modifications, we will be able to maintain our wide field sky coverage and also be able to extend our detection threshold to about sky magnitude 19.5-20.0. This upgrade should result in about a 5-fold increase in discovery rate. Nevertheless, in order to achieve completeness to 1 km or less diameter objects on a timescale of 1 decade, we will need to increase the discovery rate by about 2 orders of magnitude above today's rate, so new, larger telescopes will be required (Morrison, 1992).

REFERENCES

- Gehrels, T. (1991) Scanning with Charged-Coupled Devices. *Space Science Reviews* 58, 347-375.
- Helin, E. F., and Dunbar, R.S. (1990) Search Technique For Near-Earth Asteroids. *Vistas in Astronomy* 33, 21-37.
- Helin, E. F., and Dunbar, R. S. (1984) International Near-Earth Asteroid Search. *Lunar and Planetary Science XV*, 358.
- Helin E. F., and Shoemaker, E. M. (1979) Palomar Planet-Crossing Asteroid Survey, 1973-1979. *Icarus* 40, 321-328.
- Morrison, D., ed. (1992) The Spaceguard Survey: Report of the NASA International Near-Earth-Object Detection Workshop. Washington: NASA report.
- Rabinowitz, D. L. (1991) Detection of Earth-approaching asteroids in near real time. *Astron. J.* 101, 1518.
- Steel, D. and McNaught, R. (1991) The Anglo-Australian near-Earth asteroid survey. *Australian Journal Astr.* 4, 42-48.

SPECTROSCOPIC OBSERVATIONS OF COMET AUSTIN (1989c)

Rodney Heyd, Susan Wyckoff, Peter Wehinger (Arizona State University),
and Peter Mack (Michigan-Dartmouth-MIT Observatory)

ABSTRACT

Longslit CCD spectra ($\lambda = 5100 - 6400 \text{ \AA}$, $\Delta\lambda \sim 3 \text{ \AA}$) were obtained with the Michigan-Dartmouth-MIT 1.3 meter telescope in May 1990 ($r = 0.74 \text{ AU}$, $\Delta = 0.50 \text{ AU}$). The spectra have been reduced with IRAF. Spectral extractions offset sunward and tailward from the nucleus were analyzed. Species identified in the spectra include: C_2 , $\text{NH}_2(10-0)$, $\text{NH}_2(9-0)$, H_2O^+ , and CO^+ . Spatial extractions of rotational line intensities in the $\text{NH}_2(10-0)$ band extend $\sim 10^{4.5} \text{ km}$ from the nucleus. A fit of the vectorial model to the $\text{NH}_2(10-0)$ spatial profile is consistent with an NH_3 parent molecule. The NH_2 production rate and an ammonia to water abundance ratio, $\text{NH}_3/\text{H}_2\text{O} \sim 0.3\%$ have been derived. The ammonia abundance obtained for comet Austin is consistent with that found for several other comets, and is indicative of comet formation under very homogeneous conditions.

1. INTRODUCTION

The ammonia abundances of comets provide a sensitive diagnostic for models of comet formation. If comet volatiles originated from condensation of solar nebula gases, the ammonia/water abundance ratios of comet comae provide unique probes of the degree of homogeneity in the solar nebula 4.5 billion years ago. If, on the other hand, comets represent conglomerates of icy interstellar grains which survived processing in the proto-solar nebula collapse phase, then the ammonia/water ratios in comets represent the conditions prevailing in the precursor dense molecular cloud. Ammonia has not yet been directly detected in a comet, and was not uniquely identified in the *in situ* mass spectrometer measurements of the Giotto spacecraft in comet Halley (Krankowsky *et al.* 1986). The amine radical (NH_2) is observed in fluorescence in comet spectra, and has been used to derive ammonia abundances in several comets. For six comets, the ammonia abundances indicate production rate ratios in the range, $Q(\text{NH}_3)/\text{H}_2\text{O} \sim 0.1-0.5\%$ have been found for the group of long and short period comets. (Tegler and Wyckoff 1989, Magee-Sauer *et al.* 1989, Wyckoff, Tegler and Engel 1991, Schleicher *et al.* 1990). The EUV solar flux photodissociates NH_3 into NH_2 with a branching ratio of 97%, and there are no other known significant sources of NH_2 observed in comets, so that the abundance of NH_2 essentially gives a direct measurement of the ammonia content of comets (Tegler 1989, Tegler and Wyckoff 1989, Wyckoff, Tegler and Engel 1991, Tegler *et al.* 1991).

In December 1989 a new comet was discovered by R. Austin (Bortle 1990), which was later shown to be a long-period comet with a parabolic orbit. Its perihelion distance was one of the closest to the sun in recent years ($q \sim 0.37 \text{ AU}$), and the comet attained an apparent visual magnitude ~ 0.1 shortly after perihelion which occurred 1990 April 9.97 UT. Here we present spectroscopic observations of comet Austin (1989c) from which we derive an ammonia/water abundance ratio. We also present spectra of the plasma tail of

comet Austin from which the neutral species' coma spectrum has been subtracted. The tail spectrum shows clear evidence for the unidentified bands first discovered in the ion tail spectrum of comet Halley. Here the unidentified molecular ion bands show resolved structure for the first time.

2. OBSERVATIONS

The long-slit spectra were obtained 4-8 May 1990 with the Michigan-Dartmouth-M.I.T. 1.3-m telescope and CCD spectrograph when the comet had a geocentric distance ~ 0.5 AU and a heliocentric distance ~ 0.8 AU. The slit size projected on the sky was $1.5 \text{ arcsec} \times 540 \text{ arcsec}$, which scales to $540 \text{ km} \times 190,000 \text{ km}$ at the comet on May 4. The spectra cover the wavelength range, $5100\text{-}6400 \text{ \AA}$, with a spectral resolution $\sim 3.1 \text{ \AA(FWHM)}$, and a sampling of 3 pixels/FWHM. The scale perpendicular to the direction of dispersion corresponded to $1.35 \text{ arcsec/pixel}$. The spectrograph slit was oriented along the projected tail axis of the comet and typical integration times ranged from 600 to 3600 s. The spectra were reduced with the software reduction package, Image Reduction and Analysis Facility(IRAF) developed and distributed by the National Optical Astronomical Observatories(NOAO). A spectrum at a projected distance $\sim 16,000$ km from the comet nucleus extracted from the two-dimensional long-slit CCD image is shown in Figure 1.

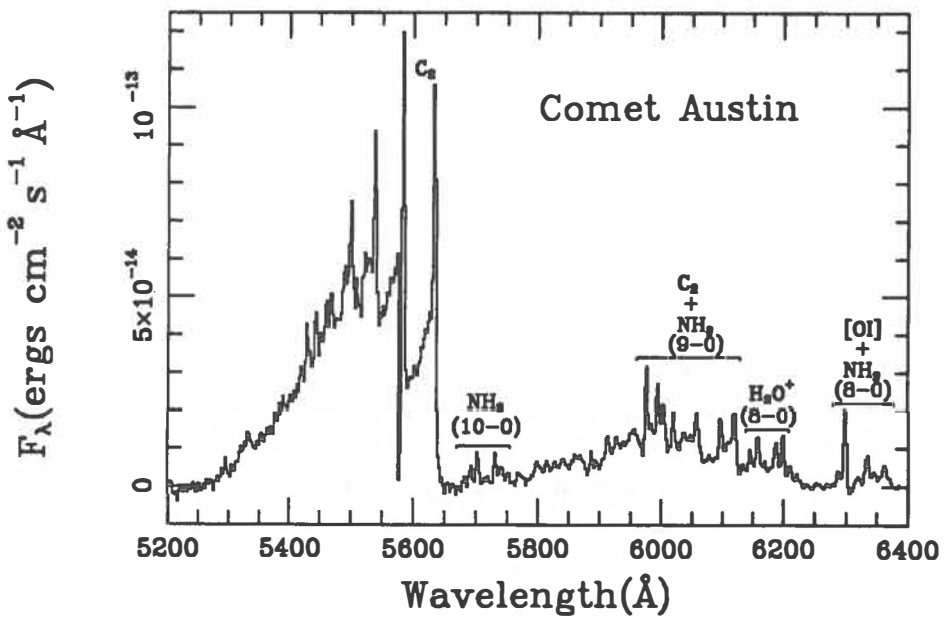


Figure 1 - Observed spectrum of Comet Austin(1989c) extracted from a CCD spectral image(resolution $\sim 3 \text{ \AA}$) obtained with the 1.3-m Michigan-Dartmouth-MIT telescope 4 May 1990. The spectrum shows the neutral radicals NH_2 , C_2 , and the H_2O^+ ion features offset ~ 16000 km from the comet nucleus. The [OI] lines have been corrected for night sky contamination.

Integrated fluxes were obtained from a spectrum extracted \sim 8300 km from the nucleus for the observations on the night of May 4. In Figure 2 we show the spectrum of the plasma tail \sim 34,600 km from the comet nucleus.

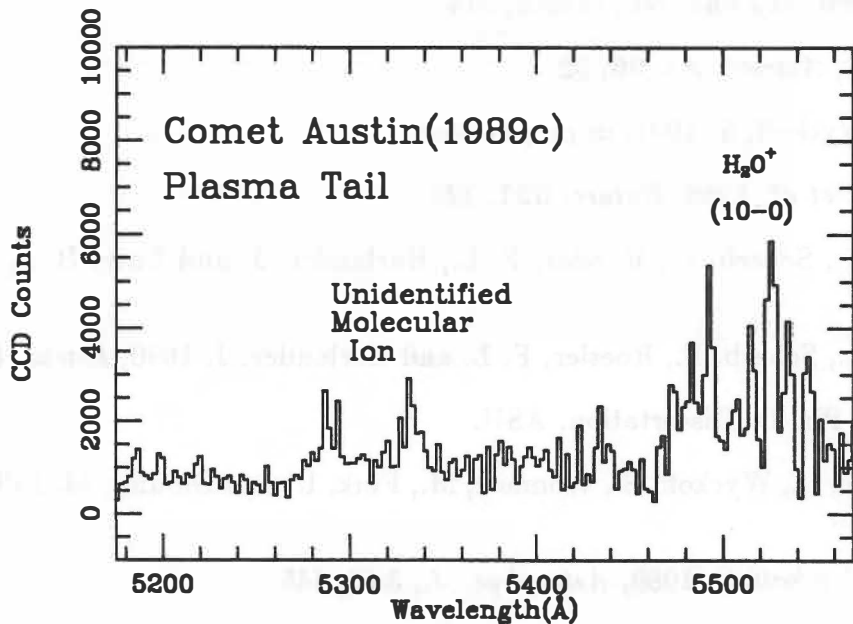


Figure 2 - Observed tail spectrum of Comet Austin(1989c) extracted 33,000 km (1.6 arcmin) tailward from the nucleus. The extraction includes 10,000-57,000 km, and shows the strongest unidentified ion features near 5300 Å as well as the (10-0) band of H_2O^+ at 5500 Å .

III. RESULTS

The spatial profile of NH_2 extracted from the spectrum exhibited a size scale from the NH_2 distribution consistent with photolysis of NH_3 (Heyd and Wyckoff 1991). Therefore we assume that the observed NH_2 derives predominately from ammonia released from the comet nucleus. The flux of the (10-0) NH_2 band at 5700 Å is a spectral extraction 1.5 X 8.1 arcsec, measured at a projected distance 8,300 km tailward from the nucleus was, $F = 2.3 \times 10^{-13}$ erg cm^{-2} s^{-1} . for a fluorescence efficiency, $g = 0.0053 \text{ s}^{-1}$, a column density, $N(\text{NH}_2) = 3 \times 10^{11} \text{ cm}^{-2}$ was derived. The production rate derived using the vectorial model (Festou 1981), was $Q(\text{NH}_2) = 2 \times 10^{26} \text{ s}^{-1}$, which for a branching ratio of 97% for $\text{NH}_3 \rightarrow \text{NH}_2$ corresponds to an ammonia production rate, $Q(\text{NH}_3) = 2 \times 10^{26} \text{ s}^{-1}$. Scott Budzien (private communication) determined the OH production rate from IUE spectra of comet Austin on the approximate same date as our observations, and found $Q(\text{H}_2\text{O}) = 8 \times 10^{28} \text{ molecules s}^{-1}$. Thus we derive $Q(\text{NH}_3)/Q(\text{H}_2\text{O}) = 0.003$ in good agreement with previous results which are in the range 0.1-0.5 %.

The unidentified ions indicated in Figure 2 were observed in comet Halley, and do not correspond in wavelength to any known molecular ion so far observed in laboratory

spectra (Herzberg 1990, private communication).

VI. References

Bortle, J. E. 1990, *Sky and Tel.*, March, 274.

Festou, M. 1981, *Astron. Ap.*, **96**, 52.

Heyd, R. and Wyckoff, S. 1991, in preparation.

Krankowsky, D. et al. 1986, *Nature*, **321**, 326.

Magee-Sauer, K., Scherb, F., Roesler, F. L., Harlander, J. and Lutz, B. L. 1989, *Icarus*, **82**, 50.

Magee-Sauer, K., Scherb, F., Roesler, F. L. and Harlander, J. 1990, *Icarus*, **84**, 154.

Tegler, S. 1989, Ph. D. Dissertation, ASU.

Tegler, S., Burke, L., Wyckoff, S., Womack, M., Fink, U. and DiSanti, M. 1991, *Astrophys. J.*, in press.

Tegler, S. and Wyckoff, S. 1989, *Astrophys. J.*, **343**, 445.

Wyckoff, S., Tegler, S. and Engel, L. 1991, *Astrophys. J.*, **368**, 427.

METALLIC ATOMS AND IONS IN COMETS: COMET HALLEY 1986 III

S. Ibadov

Institute of Astrophysics, Dushanbe 734670, USSR

Abstract

The origin of metallic atoms and ions in the cometary comae is investigated theoretically. Two effects are revealed in the comas of bright comets, namely Na anomalous type effect is possible within the gas-dust jets of comet P/Halley 1986 III due to cooling cometary dust by cryogenic gas flow from the nucleus, and the production of ions of refractory elements (Fe^+ , Si^+ , etc.) at large heliocentric distances is possible in the comas of the Halley type dusty comets due to high-velocity impacts between cometary and zodiacal dust particles. Spectral observations of comets with high sensitivity and spatial resolution are important for studying both comets and interplanetary dust.

Introduction

The investigation of a metallic component in comets is important in different aspects. The emissions of the refractory metallic atoms (Fe, Ni, Si, etc.) have usually been detected in Sun-grazing comets at heliocentric distances $R = 0.01$ AU (see, e.g., Preston, 1967; Oppenheimer, 1980, and references therein). Meanwhile, in situ measurements carried out within the coma of comet P/Halley 1986 III by VEGA and GIOTTO spacecraft near $R = 1$ AU led to the discovery of metal ions of the Fe^+ type (Gringauz et al., 1986; Krankowsky et al., 1986; Balsiger et al., 1986).

Anomalous distribution (i.e. intensity maximum displaced from the cometary nucleus towards the Sun) of the Na D-line emissions in the head of the bright comet Mrkos was detected by 200-inch Palomar telescope in 1957, the origin of which is the puzzle in the physics of comets (cf. Greenstein and Arpigny, 1962; Wurm, 1963; Dobrovolsky, 1966; Ibadov, 1985).

Metallic atoms have the low ionization potentials and in this connection the short photoionization time scale - of the order of 10^{-4} sec at $R = 1$ AU (Shklovsky, 1960; Wurm, 1963), so that generation mechanisms of metal atoms may also be important in the problem of the ionization of the cometary matter, particularly, of the inner coma, giving the onset of the ray structure of the ion tails of comets (see Marochnik, 1964; Jackson and Donn, 1968; Wurm, 1968).

In the present report the problem of the origin of metal atoms and ions in cometary comae related to the data from VEGA and GIOTTO spacecraft is considered taking into account both modern view on the physical conditions in the near-nuclear region of bright comets and high-velocity interaction between cometary coma and ZodiacaI dust cloud.

Possible anomalous distribution of sodium atom emission in the coma of comet Halley

Sodium atom emissions are observed at heliocentric distances $R \leq 1$ AU not only in the cometary heads but also in the type II cometary tails (see Levin, 1964), i.e. at cometocentric distances which are essentially more

than the photoionization scale length for sodium atoms. This indicates that the source of metallic atoms are dust particles emitted from the cometary nucleus and irradiated by solar radiation.

The rate of evaporation of dust particles depends on their temperature exponentially, so that for the appearance of the anomalous distribution of free sodium atoms in the cometary head it is essentially not only the character of a distribution of dust particles concentration (for example, the presence of a dust envelope) in the coma, but also of dust particles temperature $T = T(r)$. This question is actual and requires the special consideration in connection with the essential progress, achieved during the last years in the understanding of the physical conditions in the cometary comas.

The temperature of gas in the inner comae of both telescopic and bright comets is extremely low: $T_g \lesssim 200$ K at cometocentric distances $r \lesssim 10^3$ km (see, e.g., Shimizu, 1976; Bisikalo and Strelnitskij, 1985; Marov and Shematovich, 1987). Along with that the density of molecules near the nuclei of bright comets is sufficiently great ($n_g \gtrsim 10^{13}$ molecules/cm³ see Dobrovolsky, 1966 p.204; Shulman, 1987 p.18), so that the application of a vacuum approximation to the thermal regime of dust particles of the cometary atmospheres become invalid: the depression of the temperature of cometary dust due to cooling by intense gaseous flow from the subsolar zone of a nucleus is possible (Ibadov, 1987a). The displacement of the zone of the onset of dust particles evaporation and, respectively, of the zone of maximal concentration (and emission) of sodium atoms towards the Sun is determined as

$$r_{\max} = 2.5 [\alpha V_g M_g R^{3/2} / (\varepsilon^{1/4} \sigma^{3/4} \mu_g k_s)]^{1/2} = \{ \begin{array}{l} 7 \times 10^5 / k_s^{1/2}, \\ 2 \times 10^6 / k_s^{1/2}. \end{array}$$

Here the numerical estimate is made for comet Halley 1986 III, when the formula parameters (in CGS) have the following values: accommodation coefficient of the gas molecules (of the H₂O type) on the surface of dust grain α ($T_g \lesssim 200$ K) = 1; the local mean thermal velocity of molecules of gas V_g ($T_g = 200$ K) = 5×10^4 cm/s; the gas production rate of the nucleus M_g ($R = 0.8$ AU) = 4×10^7 g/s, the molecular weight of sublimating molecules $\mu_g = 18$ (Gringauz et al., 1986); the integral coefficients of an absorption of the solar radiation and a heat emission from dust grain $\varepsilon = \sigma = 1$ for the upper line (corresponds to strongly absorbing particles with the albedo $A \approx 0$) and $\varepsilon = \sigma = 0.1$ for the lower line (corresponds to metallic particles); $k_s = S_a / S_t$ is the anisotropy coefficient of matter ejection from the cometary nucleus, S_a is the area of the effectively emitting subsolar zone (i.e. the area occupied by gas-dust jets) of the nucleus, S_t is the total surface of the nucleus, so that at $k_s = 0.1$ (Keller et al., 1986) we have $r_{\max} = 20$ km and 70 km for the two types of dust particles, correspondingly. During the periods of cometary brightness outbursts when M_g increases by several times $r_{\max} = 100$ km.

Thus, the displacement of the brightness maximum of the sodium D-lines (and emissions of other atoms and molecules ejected from grains) towards the Sun to the cometocentric distance $r_{\max} = 20-70$ km is possible within gas-dust jets of comet Halley due to depression of dust temperature

(and its evaporation rate) caused by expanding cryogenic relatively dense gas in the nearnuclear region. As shows above formula, the gas production rate of a comet may be determined, if the value of a displacement of emission maximum of the sodium type volatile metal atoms is determined from observations. So, it is important spectral observations of comets with high spatial resolution.

Origin of refractory metal ions in the coma of comet Halley 1986 III

The presence of the Fe^+ type ions in the comet Halley's coma was discovered by the VEGA and GIOTTO in situ measurements on march 1986 (see Gringauz et al., 1987). At the same time calculations show that at heliocentric distances under consideration ($R \geq 0.8$ AU) the sublimation of refractory dust particles of the cometary coma in the field of electromagnetic and corpuscular radiations of the Sun is negligibly small for appearing the detectedions of the Fe type (Ibadov, 1980; Dobrovolsky and Ibadov, 1981; Ip and Axford, 1986; Geiss et al., 1986).

In the head of comet Halley the dust to gas production rate ratio $\mu = \dot{M}_d / M_g \geq 0.1$ (Sagdeev et al., 1986). The passage of such dusty comets through the Zodiacial dust cloud is accompanied, mainly, not by the meteor-like, but by the explosion-type process, namely by production of expanding plasma clots from high-velocity collisions of cometary and zodiacal dust particles (Ibadov, 1987b).

Using the continuity equation for the mass flow of the ionization products of colliding dust particles we can find the relation for the quasistationary concentration of metallic ions in the region of collision, $n_i(r_e, R)$; r_e represents the action radius of the explosion-type mechanism, i.e. the cometocentric distance where the intense transformation of dust particles onto plasma clots takes place.

According to GIOTTO measurements the concentration of ions in the cometary coma varies as $1/r$ in the region of $r \leq 10^4$ km (Balsiger et al., 1986). Taking it into account, the radial distribution of the concentration of ions, produced from collision of cometary and interplanetary dust, may be presented in the form

$$n_i(r, R) = [(k_m A_i \rho_s V) / (m_i V_i)] (r_e / r), \quad r_e = \dot{M}_d \sigma_{dd} / (4m_d V_d k_s).$$

Here k_m is the coefficient for producing plasma clots from cometary and interplanetary dust; A_i is the mean abundance of the kind i element in the colliding dust grains (in stony meteoroids $A_i = 0.15, 0.2, 0.15$ for Fe, Si, Mg, respectively); $\rho_s \equiv \rho_s(R)$ is the spatial mass density of the Zodiacial dust cloud; $V \equiv V(R)$ is the relative velocity of the colliding dust particles; m_i is the ion mass; V_i is the expansion velocity of the coma ion component; $\sigma_{dd} = 2\pi a^2$ is the effective cross section for the collisions of cometary and zodiacal dust particles, m_d is the probable mass of the coma dust particles, V_d is the mean velocity of their outflowing from the nucleus.

Using the value of the concentration of Fe^+ ions measured by Vega-2 spacecraft $n_i(r = 2 \times 10^9 \text{ cm}, R = 0.8 \text{ AU}) \approx 1 \text{ ion cm}^{-3}$ (Gringauz et al., 1987) and accepting $k_m = 2$, $A_i(\text{Fe}) = 0.2$, $V = 8 \times 10^6 \text{ cm/s}$, $m_i = 10^{-22} \text{ g}$

$v_t = 10^5 \text{ cm/s}$, $\dot{M}_d (R = 0.8 \text{ AU}) = 10^7 \text{ g/s}$, $\sigma_{dd} = 6 \times 10^{-8} \text{ cm}^2$, $m_d = 10^{-12} \text{ g}$, $v_d = 5 \times 10^4 \text{ cm/s}$, $k_s = 0.3$ (Sagdeev et al., 1986; Keller et al., 1986) we find by above formula $\rho_s (R = 0.8 \text{ AU}) = 6 \times 10^{-22} \text{ g cm}^{-3}$. This value corresponds to the expected mean mass density of the interplanetary dust (see, e.g., Grun et al., 1985).

Conclusion

Distribution of the emissions of atoms of volatile metals, such as Na, may serve as indicators of physical conditions in the inner coma of comets, particularly, in the gas-dust jets.

Ions of refractory elements, such as Fe^+ , detected in the coma of comet Halley 1986 III by VEGA and GIOOTTO spacecraft, may be generated due to high-velocity impacts between cometary and zodiacal dust particles, and may serve as indicators of interplanetary dust clouds.

Spectral observations of comets with high sensitivity and spatial resolution are important for studying both comets and interplanetary dust.

References

- Balsiger, H., Altwegg, K., Buhler, F. et al. 1986. Nature 321, 330.
 Bisikalo, D.V., and Strelnitskij, V.S. 1985. Pisma v Astron. J. USSR
 11, 475.
 Dobrovolsky, O.V. 1966. Comets. Nauka, Moscow.
 Dobrovolsky, O.V., and Ibadov, S. 1981. JPL Publ. 81-68, p. 39-41.
 Geiss, J., Bochsler, P., Ogilvie, K.W., Coplan, M.A. 1986. As. Ap. 166, L1.
 Greenstein, F.L., and Arpigny, C. 1962. Astrophys. J. 135, 892.
 Gringauz, K.I., Gombosi, T.I., Remizov, A.P. et al. 1986. Nature 321, 282.
 Gringauz, K.I., Verigin, M.I., Richter, A.K. et al. 1987. As. Ap. 187, 191.
 Grun, E., Zook, H.A., Fechtig, H., and Giese, R.H. 1985. Icarus 62, 244.
 Ibadov, S. 1980. Dokl. Acad. Nauk Tajik SSR 23, 76.
 Ibadov, S. 1985. Komety i Meteor. USSR 37, 8.
 Ibadov, S. 1987a. Astr. Inst. Czechoslovak Acad. Sci. Publ. No. 67, 51.
 Ibadov, S. 1987b. ESA SP-278, 655.
 Ip, W.H., and Axford, W.I. 1986. Nature 321, 682.
 Jackson, W.M., and Donn, B. 1968. Icarus 8, 270.
 Keller, H.U., Arpigny, C., Barbieri, C. et al. 1986, Nature 321, 320.
 Krankowsky D., Lammerzahl P., Herrwerth I. et al. 1986, Nature 321, 326.
 Levin, B.J. 1964. Icarus 3, 497.
 Marochnik, L.S. 1964. Uspekhi Phys. Nauk USSR 82, 221.
 Marov, M.Ya., and Shematovich, V.I. 1987. Keldysh Inst. Appl. Mathem.
 USSR Acad. Sc. Preprint No. 90. Moscow.
 Oppenheimer, M. 1980. Astrophys. J. 240, 923.
 Preston, G.W. 1967. Astrophys. J. 147, 718.
 Sagdeev, R.Z., Blamont, J., Galeev, A.A. et al. 1986. Nature 321, 259.
 Shimizu, M. 1976. Astrophys. Space Sci. 40, 149.
 Shklovsky, I.S. 1960. Iskusstvennie Sputniki Zemli USSR 4, 195.
 Shulman, L.M. 1987. Nuclei of Comets. Nauka, Moscow.
 Wurm, K. 1963. Icarus 2, 29.
 Wurm, K. 1968. Icarus 8, 287.

ASTEROID-TYPE ORBIT EVOLUTION NEAR THE 5:2 RESONANCE.

S.I. Ipatov,

M.V. Keldysh Institute of Applied Mathematics, Moscow, USSR

In the case of the 5:2 commensurability with the motion of Jupiter an asteroid can reach the orbits of Mars, Earth and Venus when eccentricity e is greater than 0.41, 0.65 and 0.74, respectively. For individual fictitious asteroids Ipatov [1] and Yoshikawa [6] obtained a growth in e from 0.15 to 0.74-0.76. Rates of changes in orbital orientations are different for Mars, Earth, Venus and the asteroid. Therefore, for corresponding values of e the asteroid could encounter these planets and leave the gap at those encounters. In order to investigate this hypothesis of the 5:2 Kirkwood gap formation Ipatov [2] studied the regions of initial data for which the eccentricities of asteroids located near the 5:2 commensurability exceeded 0.41 during evolution. The orbit evolution for 500 fictitious asteroids was investigated by numerical integration of the complete (unaveraged) equations of motion for the three-body problem (Sun-Jupiter-asteroid). The equations of motion were integrated in the time intervals $T \geq 5 \cdot 10^3 t_J$ (t_J is the heliocentric orbital period of Jupiter) in the planar model, $T \geq 10^4 t_J$ at initial inclination $5^\circ \leq i_0 \leq 20^\circ$ and $T = 10^5 t_J$ at $i_0 = 40^\circ$. The larger interval T was taken at $i_0 = 40^\circ$ because in this case for the majority of runs maximum values of e and i were reached in the time $\Delta t > 2 \cdot 10^4 t_J$.

Various initial orientations of orbit of the asteroid and its location in orbit were considered when initial value of asteroidal semimajor axis a_0 was equal to the resonance value $a_{5/2}$. It was obtained that maximum value e_{\max} of asteroidal eccentricity during evolution exceeded 0.41 and 0.65, respectively, for 2/3 and 1/3 of all investigated asteroids with the initial asteroidal eccentricity $e_0 = 0.15$, $i_0 \leq 20^\circ$, $a_0 = a_{5/2}$ and the present-day value of Jupiter's eccentricity e_J . If at $a_0 = a_{5/2}$ and some starting values of e , i , the argument of perihelion ω , the longitude of the ascending node Ω and the true anomaly v it was obtained that $e_{\max} \geq 0.41$, then with the same starting values of e , i , ω , Ω and v we have $e_{\max} \geq 0.41$ also for the values a_0 located in some vicinity of $a_{5/2}$. For all the fictitious asteroids examined with $i_0 = 40^\circ$ we obtained $e_{\max} \geq 0.6$. Since earlier e_J exceeded 0.06, we took $e_J = 0.06$ when determining the maximum region of a_0 and e_0 for which fictitious asteroids with some initial orbital orientations were Mars crossers. It was shown that the outer boundaries of this region coincided with the boundaries of the 5:2 Kirkwood gap. For $e_0 \leq 0.2$ and $i_0 \leq 20^\circ$ the regions of initial data for which fictitious asteroids were Earth crossers and Mars crossers are close to each other. Since the radius of Earth is approximately twice that of Mars, it is likely that meteorites, after having migrated from the 5:2 gap, impacted Earth more often than Mars. Both the range free of real asteroids for which $i > 5^\circ$ and the range of a_0 and e_0 with $5^\circ \leq i_0 \leq 20^\circ$ for which $e_{\max} \geq 0.41$ are larger to the right of the resonance (for $a > a_{5/2}$)

than to the left (particularly for $e \geq 0.2$).

Analytical studies of the circular three-body (Sun-Jupiter-asteroid) problem, carried out by Williams [5], showed that e reached a maximum when $\Delta\tilde{\omega} = \tilde{\omega} - \tilde{\omega}_J = 0$ or $\Delta\tilde{\omega} = 180^\circ$ where $\tilde{\omega}$ is the longitude of asteroidal perihelion and its value for Jupiter is designated by subscript "J". This relation between e and $\Delta\tilde{\omega}$ was obtained for most of the fictitious asteroids. Different cases of the interrelation of the time variations in e and $\Delta\tilde{\omega}$ have been examined repeatedly [1-3, 6-7]. Our calculations showed that asteroids are Mars crossers and Earth crossers as a rule for certain types of interrelations of variations in e and $\Delta\tilde{\omega}$. For the most of considered fictitious asteroids the osculating elements changed in time almost periodically. We can distinguish several periodical components in the plotted time dependence of e and $\Delta\tilde{\omega}$ with different amplitudes which may vary during evolution. Let us denote by T_e the period of variation in e with the largest amplitude, and by $T_{\tilde{\omega}}$ the period of long-term variations in $\Delta\tilde{\omega}$ if $\Delta\tilde{\omega}$ librate around some constant usually equal to 0 or 180° , or the time during which $\Delta\tilde{\omega}$ change by 360° if $\Delta\tilde{\omega}$ circulate. It was obtained for most runs that $T_{\tilde{\omega}}=T_e \approx \text{const}$. In this case we can distinguish several types of interrelations $N_{\tilde{\omega}}$ for variations in $\Delta\tilde{\omega}$ and e . They are characterized by the formula $\Delta\tilde{\omega} = 360^\circ(t-t_+)S_{\tilde{\omega}}/T_e + \xi + \Delta\tilde{\omega}_e^+$ and by the values of $S_{\tilde{\omega}}$, $\Delta\tilde{\omega}_e^+$, $S_{\tilde{\omega}}^+$, $\Delta\tilde{\omega}_e^-$, $S_{\tilde{\omega}}^-$ and N_a presented in Table I. We have $N_a=R$ if a value of asteroidal semimajor axis reaches $a_{5/2}$ during evolution and $N_a=N$ if it doesn't reach $a_{5/2}$. The first term in the right-hand side of this formula is the monotonic component in variation of $\Delta\tilde{\omega}$, with $S_{\tilde{\omega}}$ denoting the sign of this component. There is no monotonic component when $S_{\tilde{\omega}}=0$. The term $\Delta\tilde{\omega}_e^+$ denotes the value of $\Delta\tilde{\omega}$ at time $t=t_+$ when $e(t_+) \approx e_{\max}$, and $\Delta\tilde{\omega}_e^-$ is the value of $\Delta\tilde{\omega}$ at time $t=t_-$ when $e(t_-) \approx e_{\min}$. The ξ is the oscillatory component in the variation of $\Delta\tilde{\omega}$. It was calculated that during evolution $|\xi| < 180^\circ$ and $\xi \approx 0$ for $t=t_+ \pm k \cdot T_e / 2$, where $k=0, 1, 2, 3, \dots$. We introduce the plot of $\tilde{\omega}(t)$ with $\tilde{\omega}(t)$ averaged over the shot-periodic oscillations. It was considered that $S_{\tilde{\omega}}^+=1$ if $\partial\tilde{\omega}/\partial t > 0$ at $t=t_+$ and $S_{\tilde{\omega}}^-=1$ if $\partial\tilde{\omega}/\partial t < 0$. The values of $S_{\tilde{\omega}}^-$ for $t=t_-$ are denoted in the same way. For $N_{\tilde{\omega}}=T$ the value of $\Delta\tilde{\omega}$ almost didn't changed with time and it was considered that $S_{\tilde{\omega}}^-=S_{\tilde{\omega}}^+=0$. When $\Delta\tilde{\omega}=0$ for $N_{\tilde{\omega}}=B$ or $N_{\tilde{\omega}}=H$ the eccentricity has, as a rule, a local maximum which is several times lower than the main maximum obtained at $\Delta\tilde{\omega}=180^\circ$. This local maximum is higher than the minimum by 0.05-0.1 for $N_{\tilde{\omega}}=B$ and by 0.02-0.05 for $N_{\tilde{\omega}}=H$.

In some cases at $i_0=40^\circ$ the eccentricity doesn't reach maximum at $\Delta\tilde{\omega}=0$ or $\Delta\tilde{\omega}=180^\circ$. In these cases some types $N_{\tilde{\omega}}$ shown in Table II strongly depend on N_a , S_Ω and S_ω . If $\Delta\omega=\omega-\omega_J$ librated during evolution about 0 or 180° with the amplitude $\delta\omega \leq 20^\circ$, then it was

assumed that $S_\omega=0$. For all other investigated cases the $\Delta\omega$ increases during evolution (neglecting short-periodical variations) and $S_\omega=1$. The variable Ω decreased during evolution if $i < 90^\circ$ and increased if $i > 90^\circ$. The values of S_Ω show the sign of changes in Ω . For all types $N_{\tilde{\omega}}$ presented in Table I it was obtained that $S_\omega=1$ and $S_\Omega=-1$. The type $N_{\tilde{\omega}}=Y_1$ is a particular case of the type $N_{\tilde{\omega}}=Y$. Subtypes $N_{\tilde{\omega}}=U^-$ and $N_{\tilde{\omega}}=U^+$, $N_{\tilde{\omega}}=W^-$ and $N_{\tilde{\omega}}=W^+$ are the parts of types $N_{\tilde{\omega}}=U$ and $N_{\tilde{\omega}}=W$, respectively. Each of these subtypes is replaced by other subtype when i reaches 90° . It was obtained for types $N_{\tilde{\omega}}=U$ and $N_{\tilde{\omega}}=W$ that $e_{\max} > 0.99$ and the maximum value of i during evolution $i_{\max} \approx 160^\circ$. We obtained for one asteroid that $e_{\max}=0.9999$. Types J , T , E , Y_1 as well as all the types presented in Table II were not obtained by Yoshikawa [7].

TABLE I

Types of interrelations $N_{\tilde{\omega}}$ for the long-term variations in e and $\Delta\tilde{\omega}$

$N_{\tilde{\omega}}$	B	C	D	H	J	Q	T	Z	O	I	E	Y_1
N_a	R	R	R	R	R	R	R	R	N	N	N	N
$S_{\tilde{\omega}}$	1	0	-1	0	0	1	0	-1	1	0	0	-1
$\Delta\tilde{\omega}_e^+$	180°	180°	0	0	0	0	180°	180°	0	0	90° or 180°	180°
$S_{\tilde{\omega}}^+$	1	1	-1	-1	1	1	0	-1	1	1	1	-1
$\Delta\tilde{\omega}_e^-$	0	180°	180°	0	0	180°	180°	0	180°	0	90° or 180°	0
$S_{\tilde{\omega}}^-$	1	-1	-1	1	-1	1	0	-1	1	-1	-1	-1

TABLE II

Types $N_{\tilde{\omega}}$ when e does not reach a maximum at $\Delta\tilde{\omega}=0$ or $\Delta\tilde{\omega}=180^\circ$.

$N_{\tilde{\omega}}$	X	W^-	W^+	Y	U^-	U^+
N_a	R	R	R	N	N	N
S_Ω	-1	-1	1	-1	-1	1
S_ω	0	1	1	0	1	1

Let us consider interrelations of variations in orbital elements with periods less than T_e for the three-dimensional model. The times during which $\Delta\omega$ and Ω change by 360° are denoted by T_ω and T_Ω . For the types $N_{\tilde{\omega}}=X$ and $N_{\tilde{\omega}}=Y$ the value of T_ω is the period of libration of $\Delta\omega$. Periods of long-term variations in i are denoted by T_i and T_i^* ($T_i \leq T_i^*$). For most of the considered asteroids $T_i^*=T_e$. Computer simulation results showed that for variations in i with the period T_i the local maximum of e always corresponds to the minimum of i and the local minimum of e – to the maximum of i . It was obtained that $2T_i=T_\omega$ for most computer runs with $i_0 \neq 0$. For this

equality the minimum of i was reached at $\Delta\omega=0$ or at $\Delta\omega=180^\circ$. The greater are the values of e_0 and i_0 , the greater are the variations in i and e with period $T_i=T_\omega/2$. Two other equalities between T_i and T_ω : $T_i=T_\omega$ and $T_i=2T_\omega$ were obtained more rarely. For both cases i reached minimum at $\Delta\omega=180^\circ$.

The relation $T_i^*=T_\Omega$ was fulfilled as a rule; besides for the considered runs i reached minimum at $\Omega=180^\circ$ and maximum at $\Omega=0$ for those cases when we observed no variations in e and i with the period $T_i=T_\omega/2$. Interrelations of periods of variations for four orbital elements (i , e , Ω and ω) were obtained mainly for $5^\circ \leq i_0 \leq 10^\circ$ and $e_0 \leq 0.15$. For some asteroids with $N_{\tilde{\omega}}=J$ the relation $T_i^*=T_i=T_\omega=T_e=T_\Omega=T_{\tilde{\omega}}$ was fulfilled and in this case the minimum i and the maximum e were reached at $\Omega=180^\circ$ and $\Delta\omega=180^\circ$, while the maximum i and the minimum e – at $\Omega=0$ and $\Delta\omega=0$. If $N_{\tilde{\omega}}=O$, it was obtained for most of the considered asteroids that $T_i^*=T_i=2T_\omega=T_e=T_\Omega$ when $i_0=10^\circ$ and $e_0 \leq 0.05$.

For some fictitious asteroids the limits Δa of variation in a exceeded the width of the gap and the asteroids could migrate from one side of the gap to the other side. Maximum values of $\Delta a/a_J$ for types $N_{\tilde{\omega}}$ denoted by C , T , W and U reached 0.01 and for $N_{\tilde{\omega}}=B$ and $N_{\tilde{\omega}}=Q$ – 0.013 and 0.016 respectively.

In the three-dimensional space (e_{\max}, a_0, e_0) , the surface of values of e_{\max} has a number of "plateaus" separated by steep "cliffs". Each plateau corresponds to a certain type $N_{\tilde{\omega}}$. The cliffs were obtained at the boundaries of initial data corresponding to different types $N_{\tilde{\omega}}$ (excluding the transitions between types $N_{\tilde{\omega}}=Q$ and $N_{\tilde{\omega}}=O$ as well as $N_{\tilde{\omega}}=J$ and $N_{\tilde{\omega}}=I$) and were almost absent in a number of cases with $e_0=0.3$. With initial data near these boundaries the transitions between the types were obtained for six asteroids in the planar model and for twenty asteroids in the three-dimensional model. Šidlichovsky [4] obtained that an orbit was chaotic if initially small starting eccentricity exceeded 0.3 during evolution. At types $N_{\tilde{\omega}}$ denoted by B , C , D , H , W , Z , E and U for all considered asteroids it was obtained that $e_{\max} \geq 0.41$ and $\Delta e = e_{\max} - e_{\min} \geq 0.24$. Therefore, the number of chaotic orbits may be considerably larger than the number of asteroids for which such transitions were obtained.

References:

- [1] Ipatov, S.I. (1988) *Kinematics Phys. Celest. Bodies.* 4, N 4, 49.
- [2] Ipatov, S.I. (1989) *Sov. Astron. Lett.* 15, 324.
- [3] Scholl, H., and C.F. Froeschlé (1975) *Astron. Astrophys.* 42, 457.
- [4] Šidlichovsky, M. (1987) In "Figure and dyn. Earth, Moon, and planets" *Proc. Int. Symp.* Pt. 2, 571, Prague.
- [5] Williams, J.G. (1969) Ph.D. dissertation, University of California, Los Angeles.
- [6] Yoshikawa, M. (1989) *Astron. Astrophys.* 213, 436.
- [7] Yoshikawa, M. (1990) *Icarus* 87, 78.

Formation of Ions and Radicals From Icy Grains in Comets

William M. Jackson
Department of Chemistry
University of California
Davis, California 95616

ABSTRACT

Two theoretical models for the formation of radicals from ice grains are examined to determine if this can explain the jets in comets. It is shown that the production rates for these radicals by the photolysis of molecules in the icy grains are not high enough to explain the jets. A new mechanism is proposed involving the release of cations and anions in the gas phase as the icy mantle surrounding the grains is evaporated. Solar visible radiation can then form radicals by photodetachment of the electrons from these anions. The production rate of radicals formed in this manner is in accord with the production rates of the observed radicals.

Introduction

Recent observations of jet-type CN and C₂ structures with diameters of 24,000 km in Halley's comet by A'Hearn et. al. [1986] have prompted their group as well as others [Clairemidi et al., 1990a, 1990b] to suggest that radicals might be produced directly from the photodissociation of molecules in the grains. In this paper, this idea will be investigated along with the possibility of producing radicals via photodetachment of electrons from negative ions that might already be present in the grains.

Photochemical Production of Radicals from Grains

Combi [1987] attempted to model the photochemical production of radicals from grains by assuming they were produced by photosputtering of radicals and atoms from the grains. In this model, the photodissociation rate was assumed to be the same as it was in the gas phase. The photodissociation rate in the grains will depend, however, on the photodissociation mechanisms of the individual molecules. Those molecules which dissociate in one molecular vibration, i. e., direct dissociation, after they are electronically excited will be less affected by the presence of the solid than those molecules that only dissociate after many molecular vibrations, i.e., predissociate. The former process will occur in times of the order of 0.01 to 0.1 ps while the latter process will take place in times of the order of 1 to 100 ps. Photodissociation in the grains will compete with quenching of the excited state energy into the phonon modes of the solid, which will occur on a time scale of 0.1 to a few ps. A further complication is the "cage effect", which is the enhanced recombination of the fragments because of the surrounding solid matrix [Schriever, et al., 1991]. Thus, bulky or slow fragments are not able to escape the surrounding cage before they collide with each other and recombine to form the original molecule. Hydrogen atoms and other first row atoms escape more effectively from the cage than heavier atoms or fragments because they are smaller and recoil with a higher velocity. These ideas are incorporated in the following equations describing the total yield, Y, for free radical production from one icy grain in a Halley type comet at 1 AU;

$$Y(r_g) = \{\sum_{\lambda} \Phi(\lambda) I_{\lambda} 2\pi r_g^2 [1 - \exp(-\sigma_{\lambda} \rho 2r_g)]\} \tau \quad (1)$$

In Eq. 1, the radius of the grain is r_g , the intensity at a given wavelength (λ) of the solar radiation at 1 AU is I_{λ} , the number density of the molecules in the grain is ρ , the absorption cross-section of the molecule, σ_{λ} , and τ is the lifetime of the grain, which is taken to be 10⁵ s. The quantum yield, $\Phi(\lambda)$, for dissociation is equal to $[k_d/(k_d + k_q)]$, where k_d and k_q are the rate constants for

dissociation and quenching, respectively. Both of these rate constants can vary with wavelength, and they are unknown quantities that can drastically reduce the yield of the free radicals. For simplicity, the quantum yield is assumed to be one. Equation 1 was used in Eq. 2 to compute the production rate of the radical R, Q(R), by multiplying it by the flux at a particular r_g , F(r_g), and then summing over all r_g :

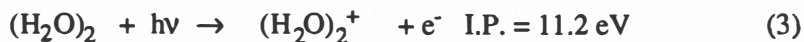
$$Q(R) = S_{r_g} Y(r_g) F(r_g) \quad (2)$$

The grain fluxes were taken from the in-situ measurements of Giotto [McDonnell, et al., 1987]. The Q(R) for OH is $1.8 \times 10^{25} \text{ s}^{-1}$, which is four orders of magnitude less than the observed rate [Feldman, 1991]. Clearly, this mechanism does not explain any OH jets in the comets because the contrast between the OH produced by gas phase photolysis will be too small. The calculated Q(R)'s for CN from HCN and C₂N₂ are 8.4×10^{24} and $3.2 \times 10^{25} \text{ s}^{-1}$, respectively. This is closer calculated rates are based upon very optimistic assumptions. The calculated rates assume that the quantum yield is one and independent of wavelength. Both HCN and C₂N₂ are known to predissociate, so the true rates will be much smaller than those that were calculated. The calculated rates also assume the radicals formed on the interior of the grain eventually arrive in the gas phase. This can only be true if the grains completely evaporate and if the radicals do not recombine before evaporation. Thus it can be concluded that the photochemical production of gas phase radicals from grains can not be used to explain the jets in comets.

Free Radicals from the Photodetachment of Negative Ions

Blakely et al. [1980] have shown that ions can be generated in the gas phase without the use of an external ionizer, if ice particles containing anions and cations are evaporated. When this happens, the positive and negative ions that were trapped inside of the ice particle are released. This mechanism does not require charged ice particles because overall neutrality is maintained, since the charges on the anions and cations balance. If the icy grains in comets contain both cations and anions, then the radicals in the coma might be formed by photodetachment of electrons from the gas phase anions in the coma.

All of the models of comets suggest they were originally formed 10^9 to 10^{10} years ago in the primordial solar nebula or in the nearby interstellar medium [Swamy, 1986]. It is thought that this occurred by agglomeration of ice particles and mineral grains. Ions in the grains could be formed by cosmic radiation, radioactive decay and photoionization before the ice particles agglomerate to form the comet nucleus. Photoionization is the most efficient mechanism for forming ions in a small ice particle. The photoionization threshold for a single H₂O molecule is at 12.6 eV [Lide, 1990], however, when the molecule dimerizes and forms clusters the following type of reactions will lower this threshold [Nishi et al., 1984]:



This will decrease the photoionization lifetime by a factor of five due to the increase in the photon flux [Huebner and Carpenter, 1979]. In Eqn. 2, a free radical and an ion are both produced by a single photon. This is a result of the added stability of the protonated ion, which not only lowers the ionization potential of the cluster relative to water, but also leads to a lower dissociation energy for the radical and the ion. Similar mechanisms should be possible for other hydrated molecules [Nishi et al., 1986, and Castleman et al. 1986].

The wavelength distribution of the UV radiation present during comet formation should be similar to the UV distribution in H II regions around young stars. Greenberg and Hage [1990] have shown that it only takes 10^4 years to completely process the mantle of a grain. This is a very short time compared to the 10^8 to 10^9 years available for this purpose, so it is likely that the

outer mantel has been processed many times before the grains agglomerate to form the cometary nucleus. The shortest wavelength of VUV radiation in the H II region is at 13.6 eV, which is low enough to ionize most of the possible cometary molecules except CO and CO₂ [Duley and Williams, 1984]. The electrons that are formed during the photoionization process can attach themselves to atoms and radicals with a high electron affinity, E.A. The E. A. of the most common cometary ions such as CH, OH, CN, C₂, and C₃ are 1.24, 1.82, 3.82, 3.39, and 1.98 eV, respectively [Lide, 1990]. Thus, some of the most stable negative ions can be formed from cometary radicals. The charge on the negative ions formed from these radicals can be counterbalanced by the positive charges on stable species such as H₃O⁺, and H₂CO⁺. Both CO and CO₂ could be bound up in CO₃⁻, which could be formed by the reaction of O₂⁻ and O⁻ with them in the icy grains. If these grains are shielded from visible radiation inside the nucleus and are kept cold, then these cations and anions will be stable for long periods of time. When these negative ions are later released from the grain into the gas phase they will quickly form free radicals, since the photodetachment lifetimes are only of the order of a few seconds. These arguments suggest that it is not unreasonable to believe that the VUV radiation in a HII region could have formed cations and anions in the mantles of icy grains that later form the nucleus of a comet.

An estimate of the production rate of radicals that can be produced via the release of anions that are trapped in the icy grains can be made by calculating the number of molecules in the mantle, N(r_g), as a function of the grain radius. The thickness of the mantle is independent of the grain size, and can be approximated from the optical depth of water ice in the VUV spectral region. This is 0.03 mm for ice grains with a density of 1 gm/cc and a mean absorption cross section of 1×10^{-17} cm². The production rate, Q⁻(R), is then calculated using Eqn. 5 by multiplying N(r_g) by the flux of grains with a given radius, the fraction, ξ , of the mantle that contains the radical anion precursor, and then summing over all grain radii:

$$Q^-(R) = \sum_{r_g} N(r_g) F(r_g) \xi \quad (5)$$

The result of this calculation is that the Q⁻(R) for all of the mantle molecules is 2.4×10^{29} s⁻¹. The ratios of the production rate of OH to the production rates of C₂, C₃, and CN are 250, 6700, and 770, respectively [Fink, et al., 1991]. The production of OH in Halley at 1 AU was 4×10^{29} s⁻¹ [Feldman, 1991], thus only tenths to hundredths of a percent of the escaping molecules must be anions to explain the observation of jet structures in comets. There is no physical reason why this cannot be the case, since stable solids such as ionic crystals can be made with 100 % ions.

Conclusions

Theoretical calculations have shown that even with the most optimistic assumptions, the yield of free radicals from the photochemical destruction of grains is much too low to explain the observed jets in comets. An alternate mechanism for the production of free radicals and ions in the gas phase from cometary ice grains has been proposed. This mechanism involves the direct evaporation of trapped anions and cations in the icy grain. Radicals are then produced by photodetachment of the electrons on the anions by solar radiation.

Acknowledgements: William M. Jackson gratefully acknowledges the support of NASA under grant NAGW-1144.

References

- A'Hearn M. F., Hoban S., Birch P. V., Bowers C., Martin R., and Klingsmith III D. A., (1986) Cyanogen jets in comet Halley, *Nature*, **324**, 649-651.
- Blakely C. R., Carmondy J. J., and Vestal M. L., (1980) A new soft ionization technique for mass spectrometry of complex molecules, *J. Am. Chem. Soc.*, **102**, 5931-5933.
- Castleman Jr. A. W., Albertoni C. R., Marti Kurt, Hunton D. E., and Keese R. G., (1986) Photodissociation of negative ions and their clusters, *Faraday Discuss. Chem. Soc.*, **82**, 261-273.
- Clairemidi J., Moreels G., and Krasnopolksy V. A. , (1990a) Spectro-imagery of P/Halley's inner coma in the OH and NH ultraviolet bands, *Astron. Astrophys.*, **231**, 235-240.
- Clairemidi J., Moreels G., and Krasnopolksy V. A. , (1990b) Gaseous CN, C₂, and C₃ Jets in the Inner Coma of Comet P/Halley Observed from the Vega 2 Spacecraft, *Icarus*, **86**, 115-128.
- Combi M. R. (1987) Sources of Cometary Radicals and Their Jets: Gasses or Grains, *Icarus*, **71**, 178-191.
- Duley W. W., and Williams D. A. (1984) *Interstellar Chemistry*, Academic Press, London, p.72.
- Feldman P. D., (1991) Ultraviolet spectroscopy of Cometary Comae. In comets in the Post-Halley Era, Vol. 1, (R. L. Newburn, Jr., M. Neugebauer, and J. Rahe, eds.), pp139-148, Kluwer Academic Publishers, Dordrecht..
- Fink Uwe, Combi Michael R., and DiSanti Michael A.,(1991) P/Halley: Spatial distributions and scale lengths for C₂, CN, NH₂, and H₂O, Submitted *Ap. J.*
- Greenberg Mayo J., and Hage J. I., (1990) From Interstellar Dust to Comets: A Unification of Observational Constraints, *Ap. J.*, **361**, 260-274.
- Heubner W. F., and Carpenter C. W. (1979) *Solar Photo Rate Coefficients*, LA-8085-MS, Los Alamos Scientific Laboratory, pp 10.
- Lide David R. ed.(1990) *CRC Handbook of Chemistry and Physics*, 71st ed., CRC Press, Boca Raton FL.
- McDonnell J. A. M., Alexander W. M., Burton W. M., Bussoletti E., Evans G. C., Evans S. T., Firth J. G., Grard R. J. L., Green S. F., Grun E., Hanner M. S., Hughes D. W., Igenbergs E., Kissel J., Kuczera H., Lindblad B. A., Langevin Y., Mandeville J. C., Nappo S., Pankiewicz G. S. A., Perry C. H., Schwehm G. H., Sekanina Z., Stevenson T. J., Turner R. F., Weishaupt U., Wallis M. K., and Zarnecki J. C. (1987) The dust distributions within the inner coma of comet P/Halley 1982i: encounter by Giotto's impact detectors, *Astron. Astrophys.*, **187**, 719-741.
- Nishi N., Shinohara H., and Okuyama T. (1984) Photodetachment, photodissociation and photochemistry of surface molecules of icy solids containing NH₃ and pure H₂O ices, *J. Chem. Phys.*, **80**, 3898-3910.
- Nishi N., Shinohara H., Yamoto K., Nagashima U., and Washida N., (1986) Fragmentation of Hydrogen-bonded Molecular Clusters on Photoionization, *Faraday Discuss. Chem. Soc.*, **82**, 359-370.
- Schriever R., Chergui M., and Schwenter N., (1991) Cage Effect on the Photodissociation of H₂O in Xe Matrices, *J. Phys. Chem.*, **95**, 6124-6128.
- Swamy K. S. Krishna, (1986) *Physics of Comets*, World Scientific Pub. Co., Philadelphia PA.

Cometary Implications of Recent Laboratory Experiments on the Photochemistry of the C₂H and C₃H₂ Radicals

William M. Jackson, Yihan Bao, Randall S. Urdahl, Xueyu Song, Jai Gosine and Chi Lu

Department of Chemistry

University of California

Davis, California 95616

Abstract

Recent laboratory results on the photodissociation of the C₂H and C₃H₂ radicals are described. These studies show that the C₂ and C₃ radicals are produced by the 193 nm photolysis of the C₂H and C₃H₂ radicals, respectively. The quantum state distributions that were determined for the C₂ radicals put certain constraints on the initial conditions for any models of the observed C₂ cometary spectra. Experimental observations of C₂ formed by the 212.8 nm photolysis of C₂H are used to calculate a range of photochemical lifetimes for the C₂H radical.

Introduction

The formation of C₂ and C₃ in comets has been an intriguing problem in cometary astrophysics [Jackson, 1976]. Numerous laboratory studies suggest that these radicals cannot be produced as a daughter product by photolyzing a parent molecule. Rather, it has been postulated that they are formed as granddaughters via the following reaction scheme [Jackson, 1976]:



Cometary observations of the spatial profiles of C₂ and C₃ radicals have generally supported the idea that these are granddaughter species [Cochran, 1985 and O'Dell, 1988]. Alternate explanations are that these radicals result from ion-molecule reactions in the coma or some type of direct volatilization from grains and the cometary nuclei. These explanations are certainly more complicated than the photochemical formation of granddaughter species. It is important to test this proposed mechanism to determine what limitations must be placed on using it to explain cometary observations. In this paper, we will describe some recent laboratory experiments that do put restrictions on the use of this postulate to explain cometary observations.

C₂

The laser-induced fluorescence (LIF), visible emission, time-resolved Fourier transform infrared emission spectroscopy, and photofragment time-of-flight techniques have all been used to establish that the mechanism for the primary and secondary photolysis of acetylene at 193 nm can be summarized by the following two reactions:



Fletcher and Leone have observed that the C₂H radical formed in reaction (2) is vibrationally excited with several quanta of energy in the bending mode [Fletcher and Leone, 1989]. Earlier it

had been argued that this must be the case, since the C₂H radical has enough internal energy such that a 193 nm photon can be used to excite it to the second excited state in the linear configuration, i.e., the B^{2Σ⁺ state [Urdahl, et al., 1988]. Ab-initio theoretical calculations have shown the energies of this and the third excited state decrease when the C₂H radical bends away from the linear configuration of the ground state [Shih et al., 1979]. The energies of these excited states are still not accurately known, but recent experiments in our laboratory suggest that the B^{2Σ⁺, which becomes the 3²A' in the bent configuration, must be at about 47,200 ± 700 cm⁻¹ above the ground state. This number was derived from the observation of C₂(a³Π_u) radicals with the LIF technique when C₂H₂ was photolyzed at 212.8 nm. The error bars arise because the C₂H radical intermediate could have as many as 2 quanta of vibrational energy in the v₂ bending mode. In comets, all of the C₂H radicals will be in the lowest vibrational and rotational levels of the ground electronic state. Thus one needs to add 700 cm⁻¹ to the above figure to compensate for the vibrational energy that was present in the laboratory experiments. A correction also needs to be made for the fact that the energy of the C₂H excited state is higher when it is linear than when it is bent. The ab-initio theoretical calculations suggest that this correction could be as high as 8100 cm⁻¹ [Shih et al., 1979]. The experimental observations and the theoretical calculations imply that photons with energies between 47,200 and 55,300 cm⁻¹ will be able to dissociate cold C₂H radicals in comets.}}

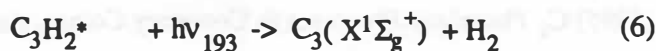
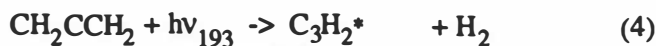
Maximum photochemical lifetimes can be calculated, with a few assumptions, using the above information and the data on the solar flux reported by Heubner and Carpenter, [1979]. First, it is assumed that the absorption cross section for solar radiation can be replaced by an averaged absorption cross section, <σ>. This averaged absorption cross section is then combined with the solar radiation for a variety of different absorption bandwidths. The largest absorption bandwidth corresponds to a long wavelength absorption limit of 210.5 nm, while the smallest absorption bandwidth corresponds to an upper wavelength limit of 180.2 nm. Table 1 shows that the estimated photochemical lifetime can vary from 329 s to 3.8 × 10⁵ s depending on the absorption coefficient and bandwidth. The absorption bandwidth could be limited further if errors could be put on the ab-initio calculations, however the range of lifetimes are certainly within the range of lifetimes required by cometary observations [Fink et al., 1991].

The C₂ products formed in reaction (3) have been observed to contain electronic, vibrational, and rotational energy. In comets, these radicals will also be excited since they will arise from the same excited electronic state of the C₂H radical. Once the C₂ radicals are formed in comets, they will emit radiation in the singlet and the triplet manifolds and populate the various vibrational and rotational levels of the X^{1Σ_g⁺ and the a³Π_u states, respectively [Jackson, et al., 1991]. In the singlet manifold, the laboratory studies have shown that the A^{1Π_u, B^{1Δ_g, and the B'^{1Σ_g⁺ states are produced. Radiation from these excited singlet states could produce at least three different rotational and vibrational distributions in the X^{1Σ_g⁺ state. Similarly, the laboratory}}}}}

studies have also shown that C_2 is formed in the $a^3\Pi_u$ and $b^3\Sigma_g^+$ states, so two distributions of vibrational and rotational levels could be present in the C_2 ($a^3\Pi_u$) in comets. Once the radicals reach their lowest electronic states in the singlet and triplet manifolds, they cannot relax further via infrared emission because the C_2 radical has no permanent electric dipole moment. This argument suggests that the C_2 radical in comets will be formed with two initial vibrational and rotational distributions in the $a^3\Pi_u$ state, and at least three initial vibrational and rotational distributions in the $X^1\Sigma_g^+$ state. Modeling of the Swan and the Phillips systems in comets should take into account these initial distributions [Gredel et al., 1989].

C_3

Laboratory studies on allene (CH_2CCH_2), and propyne (CH_3C_2H), using the photofragment time-of-flight and laser-induced fluorescence techniques have shown that the C_3 radical is produced by the following sequence of photochemical reactions at 193 nm:



LIF spectra taken during the photolysis of allene and propyne at 193 nm show that the rotational distributions of the C_3 ($X^1\Sigma_g^+$) radicals are identical, even though the spectrum obtained using propyne is considerably weaker than it is with allene [Gosine et al., 1991]. Theoretical calculations using RRKM theory suggest that the excited propyne molecules must first isomerize to excited allene before undergoing dissociation. For comets, the importance of this result is that it suggests that the C_3H_2 radical, which is known to be one of the most abundant interstellar molecules, can be photolyzed to form C_3 . It also suggests that the C_3H_2 radical can be produced from a number of different parent molecules.

Conclusions

Laboratory studies on photochemical sources for the daughter radicals that can dissociate to produce the C_2 and C_3 radicals have revealed certain constraints on their formation in comets. The acetylene studies suggest that an initial bimodal distribution of vibrational and rotational levels should be used in any modeling of the Swan system in comets. Limits have been placed on the energy of the upper electronic state of C_2H that may be involved in the production of C_2 radicals in comets. A range of photochemical lifetimes have been calculated for the C_2H radical, and the results are consistent with cometary observations. Any molecule that can dissociate to produce the intermediate daughter radicals C_2H and C_3H_2 will probably lead to the formation of the C_2 and C_3 cometary radicals.

Acknowledgements

The authors gratefully acknowledge the support of this work by NASA under grant number NAGW-903.

Table 1**Calculated C₂H Photochemical Lifetime at 1 AU**

Long Wavelength Absorption Edge (nm)	Averaged Absorption Cross Section $\langle\sigma\rangle(\text{cm}^2)$			LIFETIME, τ , (s)
	1×10^{-16}	1×10^{-17}	1×10^{-18}	
210.5	329	3290	32900	
200.0	844	8440	84400	
190.5	1683	16830	168300	
180.2	3786	37860	378600	

References

- Cochran C.R. (1985) C₂ Photolytic Processes in Cometary Comae, *Astrophys. J.*, **289**, 388-391.
- Fink Uwe, Combi Michael R., and DiSanti Michael A. (1991) P/Halley: Spatial distributions and scale lengths for C₂, CN, NH₂, and H₂O, Submitted *Ap. J.*
- Fletcher T.R. and Leone S.R. (1989) Photodissociation dynamics of C₂H₂ at 193 nm: Vibrational distributions of the CCH radical and the rotational state distribution of the A(010) state by time-resolved Fourier transform infrared emission. *J. Chem. Phys.*, **90**, 871-879.
- Gosine Jaimini N., Song Xueyu, Bao Yihan, Urdahl Randall S., and Jackson William M. (1991) The 193 nm multiphoton dissociation of allene and propyne; Evidence for photoisomerization, in preparation.
- Gredel R., van Dishoeck E.F., and Black J.H. (1989) Fluorescent vibration-rotation excitation of cometary C₂, *Astrophys. J.*, **338**, 1047-1070.
- Heubner W. F., and Carpenter C. W. (1979) Solar Photo Rate Coefficients, LA-8085- MS, Los Alamos Scientific Laboratory, pp 10.
- Jackson W.M. (1976) The photochemical formation of cometary radicals, *J. Photochem.*, **5**, 107-118.
- Jackson William M., Bao Yihan, and Urdahl Randall S. (1991) Implications of C₂H photochemistry on the modeling of C₂ distributions in comets., *J. Geophys. Research.*, **96(E2)**, 17,569-17,572.
- O'Dell C.R., Robinson R.R., Swamy K.S.K., McCarthy P.J., and Spinrad H. (1988) C₂ in comet Halley: Evidence for its being third generation and resolution of the vibrational population discrepancy, *Ap. J.*, **334**, 476-488.
- Shih, Shing-Kuo, Peyerimhoff Sigrid D., and Buenker Robert J. (1979) Calculated Potential Surfaces for the description of the emission spectrum of the C₂H radical, *J. Mol. Spectrosc.*, **74**, 124-135.
- Urdahl R.S., Bao Y., and Jackson W. M. (1988) Observation of the LIF spectra of C₂(a ³P₁) and C₂(A ¹P₁) from the photolysis of C₂H₂ at 193 nm, *Chem. Phys. Lett.*, **152**, 485-490.

H₂O⁺ STRUCTURES IN THE INNER PLASMA TAIL OF COMET AUSTIN

K. Jockers*, T. Bonev*†, E. H. Geyer‡

*Max-Planck-Institut für Aeronomie, D-W-3411 Katlenburg-Lindau, F.R.G.

†Department of Astronomy of Bulgarian Academy of Sciences, Sofia 1784, Bulgaria

‡Observatorium Hoher List, D-W-5568 Daun, F.R.G.

Abstract

We present images of comet Austin 1989c₁ in the light of H₂O⁺ from which the contribution of dust continuum and gas coma has completely been removed. We describe the behaviour of the H₂O⁺ plasma in the inner coma where it is reliably observed for the first time.

OBSERVATIONS AND DATA REDUCTION

To study the spatial distribution and temporal behaviour of water ions in the inner coma, comet Austin 1989c₁ was observed with our focal reducer/CCD camera and tunable Fabry-Perot interferometer (FPI) at the 1m Cassegrain telescope of Hoher List Observatory in the period Apr 30 - May 7 1990. On May 7 the comet's heliocentric distance was 0.789 AU and the geocentric distance 0.453 AU. The phase angle was 105.5°. The piezoelectrically controlled FPI has a spectral resolution of 3.7 Å. Images were taken at wavelengths of 6203 (one image per night) and at 6199 Å (all other images) to register continuum and the line doublet at 6198.747 and 6200.030 Å of the 0-8-0 transition of the $\tilde{\Lambda}^2A_1 - \tilde{X}^2B_1$ electronic system of H₂O⁺. At the 1m telescope the angular size of one image element is 1.6 arcsec which corresponds to approximately 600 km at the comet. The exposure time was 20 min and the time difference between individual images was 22 - 23 min. In total 25 frames of the plasma tail were obtained.

A special formalism was applied to correct the spatial modulation of the monochromatic signal introduced by the FPI and to completely remove the continuum (Bonev and Jockers 1991). The doublet structure of the emission was explicitly taken into account. The images were absolutely calibrated and converted to column densities. After the full processing cycle a portion of approximately 2×10^5 km of the cometary images contains useful information. The images show the spatial and temporal behaviour of the H₂O⁺ plasma in the inner coma where it is usually hidden by the neutral and dust coma emissions. Some examples are presented below.

DESCRIPTION OF THE IMAGES

The following description refers to the whole data set of 25 plasma frames. Figure 1 shows isocontours of the images obtained May 6 (left side) and May 7 (right side). The lowest contour corresponds to 1.6×10^{10} particles cm⁻² and each subsequent contour increases by a factor of $\sqrt[3]{2}$. The level of 10^{11} particles cm⁻² is enhanced. The coordinate system is centered at the photocenter of the raw ion frames (i.e. before removal of the continuum)

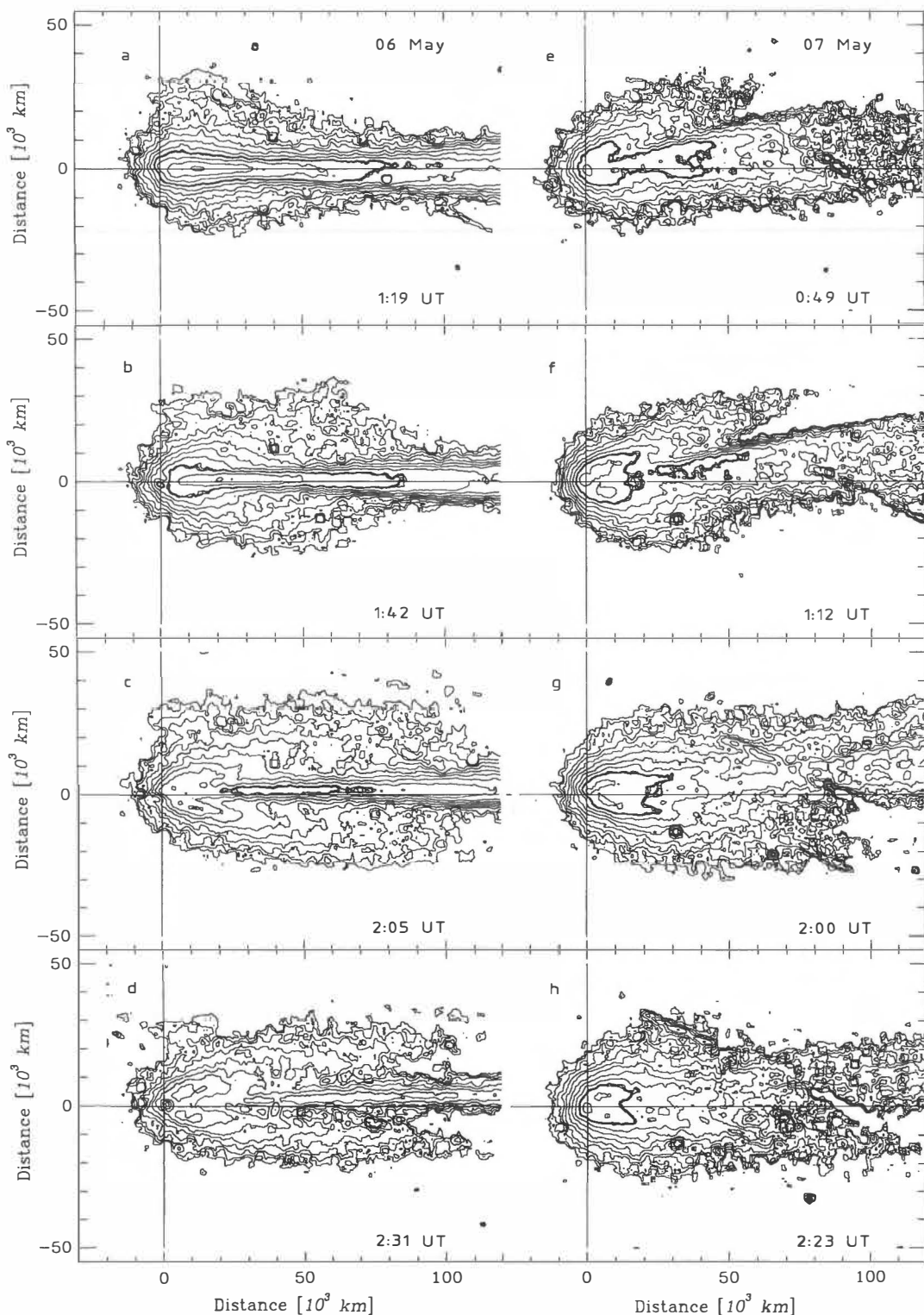


Fig. 1: Isophotes of the H_2O^+ coma and inner tail of comet Austin 1989c₁. Left: May 6, 1990. Right: May 7, 1990. Isocontours increase with factors $\sqrt[3]{2}$. The enhanced contour is at $10^{11} \text{ H}_2\text{O}^+ \text{ particles cm}^{-2}$.

and oriented along the solar-antisolar direction. From the big changes between subsequent images it is clear that the temporal plasma behaviour is only insufficiently resolved.

Around the nucleus there is an "ion coma", i.e. the plasma distribution is extended in a coma-like fashion and not as narrow as the ion tail itself. Before generation of new rays the ion coma is particularly extended. The region represented approximately by the enhanced contour of 10^{11} particles cm^{-2} , is very flat in contrast with the sharply peaked dust and gas coma and changes its shape in a characteristic fashion. A two-lobed "boomerang-shaped" structure resembles the "root" of the youngest tail rays present (see Figure 1d and g). When the rays move towards the tail axis new lobes will form out of the diffuse ion coma at the outer sides of the old ones. When this happens it seems that the old rays are not anymore supplied with plasma and their column densities decrease (see Hoffmeister, 1943). Often, but not always, the old rays will merge. If their density is still sufficient, together with the new rays they will give the inner contours a three-lobed "mushroom" type appearance (Figure 1e). In two cases (both shown, Figure 1c and f) the stem of the mushroom disconnects from the mushroom's hat. A separate ion column density maximum forms and moves down the tail. The observation of separate maxima demonstrates the close connection between the tail ray phenomenon and the disconnection events. In the two observed cases the disconnection occurs tailwards of the nucleus and represents a local column density minimum.

Superimposed on the birth and decay of tail rays are turns of the tail axis. On May 5 we see tail ray activity only at the lower side of the main tail. It is followed by a downward turn of the main tail in accordance with a rule derived by Jockers (1985). On May 4 and 7 the behaviour is mixed i.e. tail rays form on both sides of the main tail alternatingly. On May 6 the tail looks particularly narrow and symmetric. It is possible that the observer happens to be in the plane of the tail current sheet (see below).

COMPARISON WITH PUBLISHED MODEL CALCULATIONS

Numerical models of several authors show that under stationary conditions the ion tail becomes increasingly flatter with distance from the nucleus extending more in the plane perpendicular to the magnetic field, i.e. in the plane of the current sheet. We call this plane in the following the plasma plane. Already in the plasma coma the plasma density is enhanced in the plasma plane, perpendicular to the magnetic plane. On May 6 the plasma tail is narrow and has a large column density. Therefore it is suggestive to assume that at the time of the exposures, for the outer part of the tail, the observer was located close to the plasma plane and that the magnetic plane was closely coinciding with the sky plane.

Schmidt and Wegmann (1982) have proposed that ion clouds and associated tail rays may originate if a solar wind tangential discontinuity with a magnetic field rotation of about 90° is swept through the comet. Let us apply this idea to the images of May 6. On the tailward (right) side, the magnetic field would be in the plane of the sky squeezing the tail and making it narrow perpendicular to the line of sight and extended along the line of sight, thereby increasing its column density. On the upwind (left) side the magnetic field is along the line of sight. As it enters the plasma coma, it is increasingly wrapped around the comet, sweeping up the plasma and creating an ion cloud. The newly created plasma behind the discontinuity is separated from the old plasma on the right side by the turned magnetic

field and is ejected sideways, forming the plasma lobes which later become tail rays. The described process will also work if the turn of the field is not exactly at right angle.

This idea has been followed up by Schmidt-Voigt (1989), who numerically simulated the passage of such a tangential discontinuity through a comet. The model successfully produces a cloud but, because of a limited number of grid points in the three-dimensional numerical grid, the resolution is insufficient to produce the tail rays. One model is available with a production rate of water of 10^{29} particles s⁻¹, very close to the one observed for comet Austin (Festou et al., 1990). Schmidt-Voigt provides a plot of the temporal development of the maximum column density in the cloud which is most useful for the comparison. The plot refers to our case with the original magnetic field in the sky plane. At the time of the separation of the cloud from the near-nucleus maximum the peak column density is 2.05×10^{11} cm⁻². This agrees with the observed value of 2×10^{11} cm⁻² (Figure 1a). We would, however, expect the model value to be higher, because the model has only one ion channel and in reality H₂O produces several kinds of ions from which we observe only H₂O⁺. After 72 minutes (Figure 1d) the maximum in the observed cloud is already by a factor of $\sqrt[3]{2} = 1.26$ less than the two maximum lobes close to the nucleus. In the model the cloud remains brighter than the near nucleus plasma for more than 210 minutes. It seems that the model underestimates the leakage of plasma into the rays, but there is at least some qualitative agreement.

So far we have discussed the case when the plasma plane turns from along the line of sight to the sky plane. In the framework of the Schmidt-Voigt model the opposite case should be about as frequent. Schmidt-Voigt points out that the cloud represents a real ion concentration and appears as column density enhancement no matter if the observer is in the plasma plane or not. If the original magnetic plane is in the line of sight, the associated tail rays extend along the line of sight and therefore would not be observable. In our data set there are only two cases when plasma clouds are ejected (Figure 1c and f). Both are associated with tail rays. We have no case of a cloud without rays.

References

- Bonev, T., Jockers, K. (1991) Spatial demodulation of 2-D Fabry-Perot images, In ESO data analysis workshop, in press, European Southern Observatory, München.
- Festou, M. C., A'Hearn, M. F., Budzien, S. A., Feldman, P. D., Roettger, E. E. (1990) Comet Austin 1989c₁, IAU Circular 5012.
- Hoffmeister, C. (1943) Physikalische Untersuchungen an Kometen. I. Die Beziehungen des primären Schweifstrahls zum Radiusvektor, Z. Astrophys., 22, 265-285.
- Jockers, K., (1985) The ion tail of comet Kohoutek 1973 XII during 17 days of solar wind gusts, Astron. Astrophys. Suppl. Ser., 62, 791-838.
- Schmidt, H. U., Wegmann, R. (1982) Plasma flow and magnetic fields in comets, in Comets (L.L. Wilkening ed.) pp. 538-560, University of Arizona Press, Tucson.
- Schmidt-Voigt, M. (1989) Time-dependent MHD simulations for cometary plasma, Astron. Astrophys., 210, 433-454, 1989.

FIRST IMAGES OF A POSSIBLE CO⁺-TAIL OF COMET P/SCHWASSMANN-WACHMANN 1 OBSERVED AGAINST THE DUST COMA BACKGROUND

K. Jockers*, T. Bonev*†, V. Ivanova†, H. Rauer*

*Max-Planck-Institut für Aeronomie, D-W-3411 Katlenburg-Lindau, F.R.G,

†Department of Astronomy of Bulgarian Academy of Sciences, Sofia 1784, Bulgaria

Abstract

Comet P/Schwassmann-Wachmann 1 was observed with the 2m-Ritchey-Crétien Telescope of the Bulgarian National Observatory, Rozhen, Bulgaria, using the CCD-camera and focal reducer of the Max-Planck-Institute for Aeronomy. Images were taken in a red continuum window and in the 2-0 $A^2\Pi - X^2\Sigma^+$ band of CO⁺ located in the blue part of the spectrum. The red images reveal an extended dust coma. From a comparison of the red and blue images a dust reddening of 13.2 % per 1000 Å is derived. At 642 nm the magnitude of the comet within a square diaphragm of 4.5 arcsec is 16.6. The blue images, taken in the CO⁺ band, show a significantly different brightness distribution which is interpreted as presence of a CO⁺ coma and tail superimposed on the continuum. A column density of several 10^{10} CO⁺ molecules cm⁻² is derived. The tail thickness of 10^5 km is unexpectedly small. We estimate the CO⁺ production rate to about 6×10^{26} CO⁺ particles s⁻¹. This value does not support the idea that the outbursts of this comet are caused by crystallization of amorphous water ice. An extended version of this paper has been submitted to *Astronomy and Astrophysics*.

INTRODUCTION

Cochran et al. (1980) and Larson (1980) have observed the presence of CO⁺-emission in otherwise featureless spectra of comet Schwassmann-Wachmann 1 (SW1 in the following). More recently, Cochran and Cochran 1991 have been able to determine column densities of CO⁺ and CN (derived from the 0-0 vibrational band). Like the brightness outbursts, also the CO⁺-emission seems to occur only sporadically but unrelated to the outbursts (Larson 1980). In order to supplement the spectrographic observations an attempt was made to image comet SW1 in the 2-0 band of the CO⁺ comet tail system ($A^2\Pi - X^2\Sigma^+$) and in a continuum window to study the spatial extent of the dust coma and possibly detect the CO⁺-tail.

OBSERVATIONS

Comet SW1 was observed with the 2m-RCC-Telescope of the Bulgarian National Observatory, Rozhen, Bulgaria in the night 2/3 Sep 1989. Attached to the telescope was the focal reducer with CCD camera of the Max-Planck-Institute for Aeronomy. This instrument transforms the F/8 telescope beam via collimator and camera lens to F/1.5 and is therefore well suited to detect extended weak emissions. At the 2m-telescope, 1 CCD pixel corresponds to 1.5 arcseconds and the full field is 14.4 × 9.6 arcmin. The images analyzed in this study

were obtained in the night 2/3 Sep 1989 from 22:09 to 01:25. They consist of a sequence of five 30 min exposures taken in the (2-0) band of CO⁺ through a filter centered at 426 nm with halfwidth of 6 nm and of a pair of 15 min exposures taken in a red continuum window through an interference filter of 3 nm halfwidth centered at 642 nm. The spectrophotometric standard stars 70 Psc and ϕ Gem were observed for absolute calibration of the comet images (Voloshina et al. 1982).

IMAGE ANALYSIS

Data reduction of the images was standard but had to be done extremely carefully because of the low signal to noise ratio. Images taken with the same filters were combined and put to absolute scale to yield a single red and blue image. To derive an image of the CO⁺ tail the continuum contribution must be removed from the blue image. We cannot simply use the red image because the dust of comet SW1 is known to be reddened. Therefore we determine a maximum value of the number c such that the equation

$$(\text{blue image}) - c \times (\text{red continuum}) \geq 0 \quad (1)$$

is satisfied everywhere in the image. This procedure assumes that the dust colour is uniform in the observed dust coma. A value of $c = 0.75$ is derived which corresponds to a reddening of 13.2 % per 1000 Å. The resulting difference image was transformed to CO⁺ column densities using the known transmission function of the interference filter and the g-factor given by Magnani and A'Hearn (1986). Figure 1 shows traces through the nucleus of CO⁺ column densities at position angle 109° (horizontal in Figure 2) derived for c -values of 0.5 (30.9% reddening), 0.75 and 1.0 (no reddening) and indicates the satisfactory continuum subtraction achieved with $c = 0.75$.

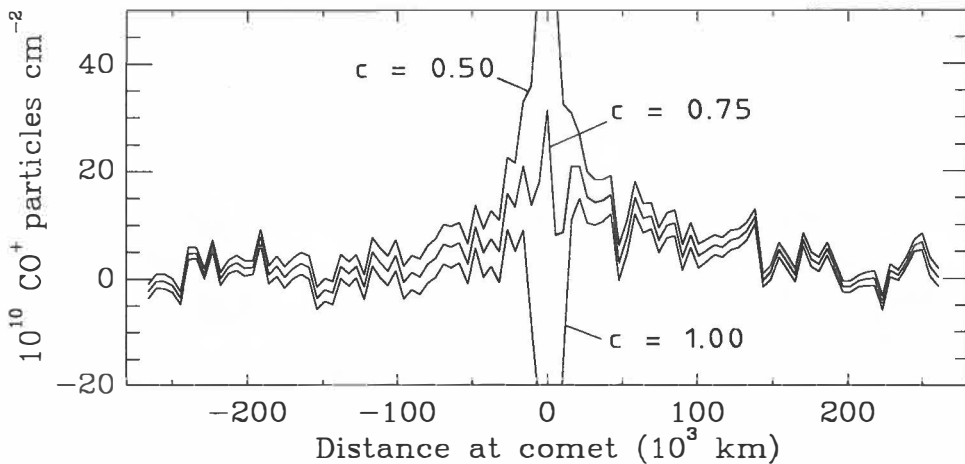


Fig. 1: Traces through "CO⁺" images with different constants c .

RESULTS AND DISCUSSION

The red continuum image

Isocontours of the red continuum image are presented in Figure 2a. We provide the absolute continuum in units of mean solar disk intensities (Schwarzschild and Kron 1911). The

outermost contour of 12.5×10^{-15} mean solar disk intensities corresponds to 22.7 stellar mag arcsec $^{-2}$. In all panels of Figure 2 subsequent contour levels are related by a factor of $\sqrt{2}$. The dust coma is elongated in the direction of η (the vector perpendicular to the antisolar direction pointing in the direction opposite to the cometary motion). In our red passband at 642 nm we find for comet SW1 within a square diaphragm of 4.5 arcsec $m = 16.6$ and within 10.5 arcsec $m = 15.9$. These values agree with those published by Jewitt (1990) for quiescent periods of the comet.

The CO $^+$ image

The isophotes of the blue image are shown in Figure 2b and isophotes of the resulting CO $^+$ image in Figure 2c. The comet is very close to opposition. The phase angle earth-comet-sun was 4°. Therefore we look nearly along the plasma tail. Because the solar wind direction frequently deviates from the radial direction any position angle is possible with angles close to η slightly more probable. The plasma tail appears as a cloud, similar to images of the CO $^+$ -rich comet Humason 1962 VIII when it was observed close to opposition (Guigay 1966)

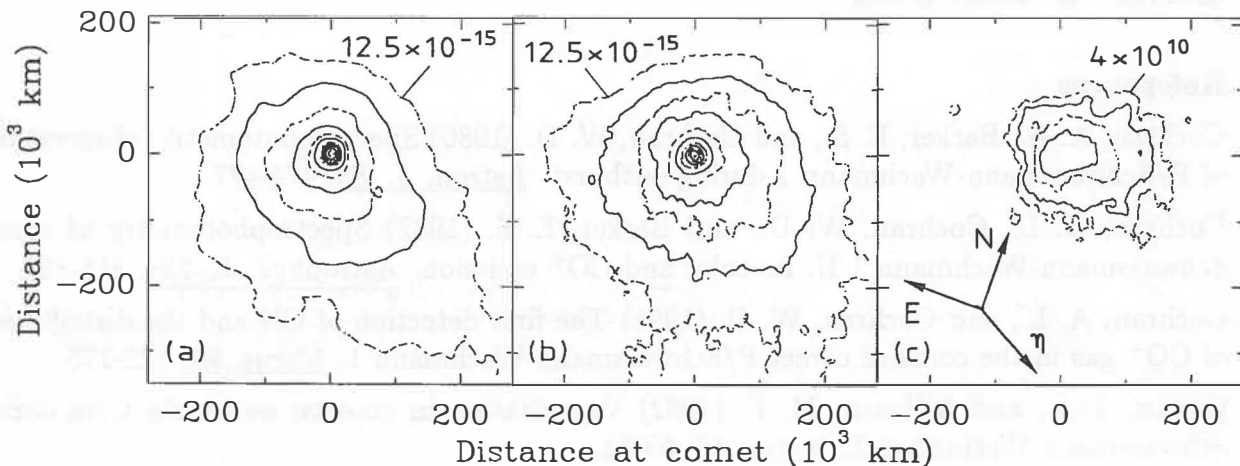


Fig. 2: a: red (continuum) image, b: blue image, both in mean solar disk intensity units, c: CO $^+$ image (particles cm $^{-2}$). Contours increase with factors $\sqrt{2}$.

around August 21, 1962. The CO $^+$ column densities are similar to those found by Cochran and Cochran (1991). The thickness of the tail of 10^5 km is similar to the thickness of ion tails observed around 1 AU and therefore seems not to scale with the square of the heliocentric distance. The spectra of Cochran and Cochran (1991) are consistent with such a short CO $^+$ scale length. It is, however, likely that a huge, less dense, CO $^+$ cloud surrounds the observed tail which is below the detection limit. A crude estimate of the CO $^+$ production of SW1 can be obtained from the product

$$\text{column density} \times \text{tail width} \times \text{ion velocity, projected on sky (this value most uncertain)} \\ \approx 6 \times 10^{10} \text{ cm}^{-2} \times 10^{10} \text{ cm} \times 10^6 \text{ cm s}^{-1} = 6 \times 10^{26} \text{ CO}^+ \text{ particles s}^{-1}. \quad (2)$$

Assuming for SW1 a nucleus of 40 km diameter (Cruikshank and Brown 1983), which is CO $_2$ dominated, we find a production rate in excess of 10^{28} CO $_2$ molecules s $^{-1}$ (Cowan and A'Hearn 1982). Our estimated production rate of 6×10^{26} , which is likely to be a lower limit, can be provided by such a nucleus (and even more by a CO dominated nucleus), if

only part of the surface is active, but not by a water dominated nucleus. If SW1's outbursts were caused by crystallization of amorphous water ice (Jewitt 1990) most of the CO⁺ would be released during the outbursts. During quiet times evaporation would be controlled by crystalline water ice and only very little CO⁺ is expected in contrast to our observations.

Is the CO⁺ image spurious?

We have very carefully checked many possibilities which may produce a spurious CO⁺ image. Remaining image defects caused by cosmic rays, stars, bad columns and hot lines introduced by a bright star which was accidentally exposed during acquisition of the comet can be ruled out as well as inaccurate flatfielding and background subtraction. The time difference between blue and red exposures is to by far too small to explain the difference between blue and red image by temporal evolution of the dust tail. The red interference filter is centered on a very good continuum window. The blue filter also transmits the CN 0-1 band but so far this band has not been detected spectroscopically. Reflections in the focal reducer optics of bright stars close to the comet may produce such spurious images but we tend to think that the CO⁺ image is real.

References

- Cochran, A. L., Barker, E. S., and Cochran, W. D. (1980) Spectrophotometric observations of P/Schwassmann-Wachmann 1 during outburst. *Astron. J.*, **85**, 474-477.
- Cochran, A. L., Cochran, W. D., and Barker, E. S. (1982) Spectrophotometry of comet Schwassmann-Wachmann 1 II. Its color and CO⁺ emission. *Astrophys. J.*, **254**, 816-822.
- Cochran, A. L., and Cochran, W. D. (1991) The first detection of CN and the distribution of CO⁺ gas in the coma of comet P/Schwassmann-Wachmann 1. *Icarus*, **90**, 172-175.
- Cowan, J. J., and A'Hearn, M. F. (1982) Vaporization in comets; outbursts from comet Schwassmann-Wachmann 1. *Icarus*, **50**, 53-62.
- Cruikshank, D. P., and Brown, R. H. (1983) The nucleus of comet P/Schwassmann-Wachmann 1. *Icarus*, **56**, 377-380.
- Guigay, G. (1966) Étude de la forme réelle de la queue de la comète Humason 1961e. In *Nature et origine des comètes*, Mém. Soc. Roy. Sci. Liège Coll. 8°, Série V, **12**, 369-378.
- Jewitt, D. (1990) The persistent coma of comet P/Schwassmann-Wachmann 1. *Astrophys. J.*, **351**, 277-286.
- Larson, S. M. (1980) CO⁺ in comet P/Schwassmann-Wachmann 1 near minimum brightness. *Astrophys. J.*, **238**, L47-L48.
- Magnani, L., and A'Hearn, M. F. (1986) CO⁺ fluorescence in comets. *Astrophys. J.* **302**, 477-487.
- Schwarzschild, K., and Kron, E. (1911) On the distribution of brightness in the tail of Halley's Comet. *Astrophys. J.* **34**, 342-352.
- Voloshina, I. B., Glushneva, I. N., Doroshenko, V. T., Kolotilov, E. A., Mossakovskaya, L. V., Ovchinnikov, S. L., and Fetisova, T. S. (1982) *Spektrophotometriya yarkykh zvezd*, Nauka, Moskva.

DOPPLER VELOCITIES IN THE ION TAIL OF COMET LEVY 1990c

K. Jockers*, H. Rauer*, C. Debi-Prasad*, and E. H. Geyer†

*Max-Planck-Institut für Aeronomie, D-W-3411 Katlenburg-Lindau, F.R.G.,

†Observatorium Hoher List, D-W-5568 Daun, F.R.G.

Abstract

We have obtained time alternating sequences of column density maps and Doppler velocity fields in the plasma tail of comet Levy 1990c. We describe the observing technique and data analysis and present first results.

OBSERVATIONS

The study of mass balance in cometary plasma tails requires the knowledge of column densities and velocities of the ions. From August 17 to 25, 1990, at the Observatory Hoher List comet Levy 1990c was observed to obtain these quantities and their temporal variation. On August 24 the geocentric distance was 0.43 AU and the heliocentric distance 1.41 AU. The phase angle was 20.3°. At the 1m-reflector our focal reducer/CCD system was used with its short focus camera. This gives a scale of 3 arcsec per pixel (corresponding to 938 km at the comet) and a field of about 20 arcmin diameter which in the corners is already limited by the hole in the main mirror of the telescope. The camera was rotated to put the antisolar direction along the long side of the chip to provide optimum coverage of the plasma tail. Our interference filter for H_2O^+ of 3 nm FWHM has its peak transmission at 620 nm. Following a suggestion of Scherb et al. (1990) it was decided to observe the short wave side of the

Table 1: Lines contributing to the interferogram

H_2O^+	Intensity	Int. $\times T(\lambda)$	Order	CO^+	Intensity	Order
6135.54 Å	2.3	0.01	2951.49	6194.28 Å	2	2923.50
→6158.64 Å	16.0	10.30	2940.42			
6158.86 Å	10.7	6.89	2940.32	6189.71 Å	6	2925.66
6166.92 Å	1.0	0.56	2936.47			
6166.96 Å	0.8	0.45	2936.45			
6187.86 Å	2.3	0.19	2926.54			
6198.75 Å	26.0	0.18	2921.40			
6140.53 Å	3.0	0.10	2949.09	6190.62 Å	5	2925.23
→6146.80 Å	16.0	3.41	2946.09	6192.80 Å	3	2924.20
6186.59 Å	3.0	0.37	2927.14			
6134.76 Å	3.0	0.02	2951.87	→6189.27 Å	8	2925.87
6140.92 Å	2.0	0.07	2948.91	6189.47 Å	7	2925.78
6147.38 Å	8.0	1.98	2945.81	6191.59 Å	4	2924.77

0–8–0 band of H_2O^+ . Therefore the filter was tilted by 11.25° . To minimize changes of the filter transmission along the plasma tail the axis of tilt was aligned with the long side of the CCD. Standard stars were observed for absolute calibration. In this way it was possible to obtain column density distributions of H_2O^+ . To derive Doppler velocities we used a Fabry-Perot etalon with a fixed air gap of 0.90545 mm which was put into the parallel beam of the focal reducer. Interferograms were taken alternating with filter images. The etalon has a free spectral range of 2.1 Å and a finesse exceeding 20, which in the present setup was, however, reduced because of the undersampling caused by the combination of the short focus lens and the CCD. The tilted filter used for the images also was employed for the interferograms. Each night one image of the cometary continuum was recorded through a filter of 3 nm FWHM centered at 642 nm. Before and after each interferogram fringes of one rubidium and two neon lines at 6159.63 Å and at 6143.062 and 6163.593 Å were recorded via a diffusing screen placed at the Cassegrain focus. The exposure time was 15 min for the filter image and 30 min for the interferogram. One full cycle consisting of one image and one interferogram including instrument changes and calibrations took about 90 min. Interferograms were obtained on Aug 16, 17, 21/22, 23/24 and 24/25. In the last two nights three full cycles and one additional image were taken.

DATA REDUCTION

In addition to the usual steps of CCD data reduction from each plasma image and interferogram the dust image of the same night was subtracted to remove the continuum contribution in the plasma frames. A slight C_2 coma (0–2 head of the Swan band) remains in the plasma images. The tail ion lines contributing to the fringes are listed in Table 1. For H_2O^+ intensity estimates are taken from Wehinger et al (1974) and are given also with the prefilter transmission taken into account (third column). For the lines of the 0–3 band of CO^+ the line strengths were assumed to decrease with distance from the (red degraded) band head as no better information is available. As can be seen from the fractional Fabry-Perot order the lines form three groups of which the strongest lines are marked with an arrow. The

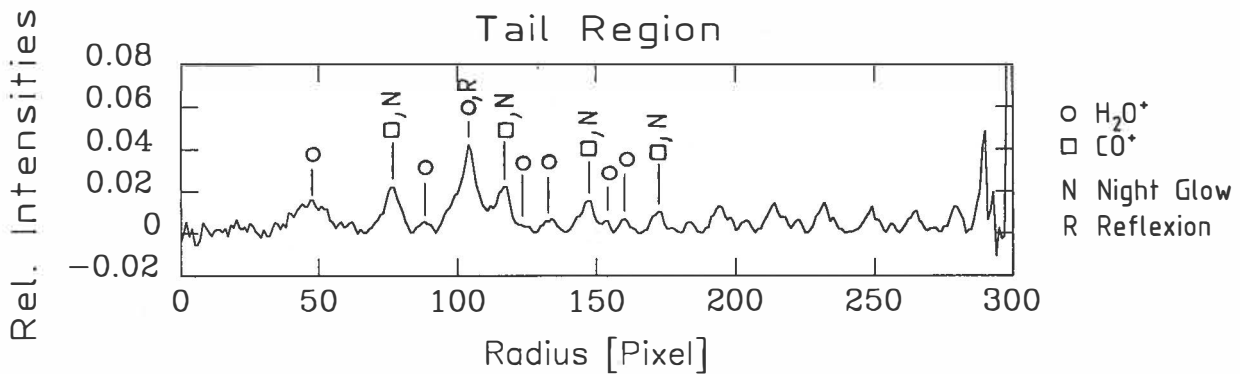


Fig. 1: Trace through interferogram from Aug 23/24 along the far tail.

third peak is caused by CO^+ . An auroral oxygen line at 6155.98 Å (the observations were conducted during solar maximum at a geographic latitude of 53°) forms airglow fringes which

partially blend the ion lines. Figure 1 gives a trace through the interference fringes along the tail as they were obtained in the night Aug 23/24. The width of the unblended H_2O^+ lines is about 0.5 Å. Figure 2 presents an example of H_2O^+ column density contours with

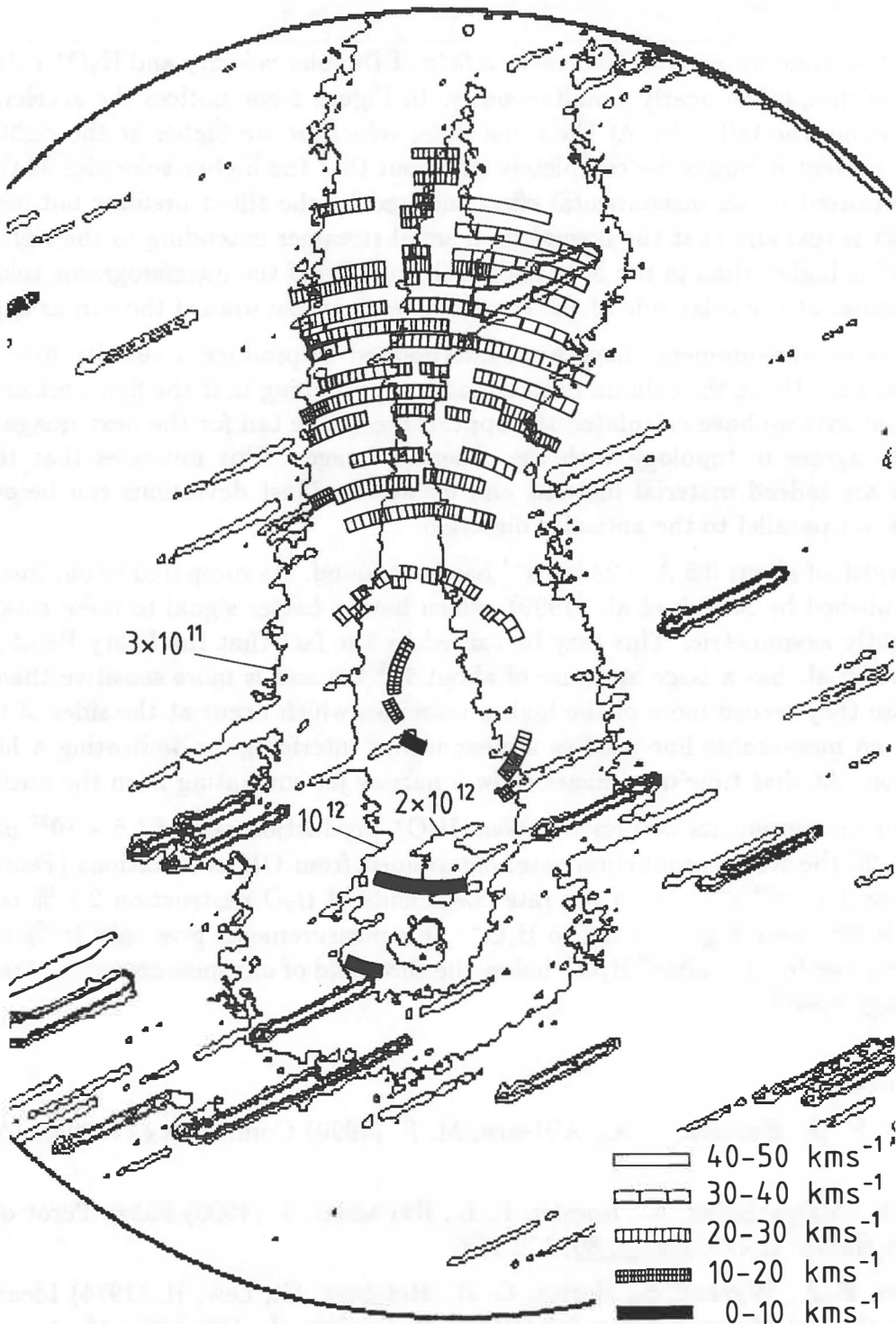


Fig. 2: Column density contours (cm^{-2}) of a plasma tail image obtained on Aug 23/24. Superimposed are the velocities along the tail derived from an interferogram.

superimposed velocities, derived from the Doppler shift under the assumption that the velocity vector is along the line of sight.

RESULTS AND DISCUSSION

For the first time we are able to present a field of Doppler velocity and H_2O^+ column density measurements, taken nearly simultaneously. In Figure 2 one notices the acceleration of the plasma along the tail axis. At the same time, velocities are higher at the right side of the tail. At present it cannot be completely ruled out that the higher velocities at the right side may be caused by an instrumental effect induced by the tilted prefilter but we think that the effect is real and that the flow along a small streamer extending to the right side of the main tail is higher than in the bent main tail. In some of the interferograms velocities could be measured at the solar side of the comet. They increase toward the sun as expected.

The velocity measurements have been interpolated to produce a velocity field everywhere along the tail. Using the column density data and assuming that the flow vectors are parallel to the tail axis we have calculated the appearance of the tail for the next image. The result generally agrees in topology with the observed image. This indicates that the observed motions are indeed material motions and no waves. Most deviations can be explained by motions not parallel to the antisolar direction.

A line width of about $0.5 \text{ \AA} = 24 \text{ km s}^{-1}$ has been found. As compared to our line profiles the ones published by Scherb et al. (1990), which have a better signal to noise ratio, are wider and slightly asymmetric. This may be caused by the fact that the Fabry-Perot photometer of Scherb et al. has a large aperture of about 10^5 km and is more sensitive than our setup. Therefore they record more of the higher velocities which occur at the sides of the tail. On Aug 17 no measurable line profiles appear in our interferogram indicating a high velocity dispersion. At that time our images show a narrow jet emanating from the nucleus.

From our measurements we derive a mean H_2O^+ production rate of $1.5 \times 10^{27} \text{ particles s}^{-1}$. On Aug 26 the water production rate, determined from OH observations (Feldmann et al. 1990) was $3 \times 10^{29} \text{ s}^{-1}$. From the rate coefficients of H_2O destruction 2.8 % of the water, i.e. 8.4×10^{27} should get ionized to H_2O^+ . Our measurements give only 18 % of this value indicating loss by "invisible" H_2O^+ below the threshold of our measurements streaming with rather high speed.

References

- Feldman, P. D., Budzien, S. A., A'Hearn, M. F. (1990) Comet Levy (1990c), *IAU Circular* 5081.
- Scherb, F., Magee-Sauer, K., Roesler, F. L., Harlander, J. (1990) Fabry-Perot observations of comet Halley, H_2O^+ , *Icarus*, 86, 172-188.
- Wehinger, P. A., Wyckoff, S., Herbig, G. H., Herzberg, G., Lew, H. (1974) Identification of H_2O^+ in the tail of comet Kohoutek (1973f), *Astrophys. J.*, 190, L43-L46.

EVOLUTION OF THE QUADRANTID METEOR STREAM

J. Jones, Physics Department, University of Western Ontario,
London, Ontario, Canada, N6A 3K7,
W. Jones, Physics Department, University of Sheffield, S3 7RH, U.K.

Abstract

According to the orbital calculations of Babadzhanov and Obrubov (1987), the last close approach of the Quadrantid stream with Jupiter occurred 3200 years ago at which time the parent comet of the stream may have been captured into its present short-period orbit. If this is the case the stream may be only a few thousand years old. We have modelled the evolution of the stream to determine if such a short time scale is consistent with the observed features of the Quadrantid/ δ-Aquarid/Arietid/Ursid complex. A detailed modelling of a stream consisting of 500 test particles released 4000 yr ago and which included the effects of the gravitational perturbations of 6 planets as well as the likely spread in the initial orbital elements resulting from the ejection of the grains from the comet was carried out. Our calculations indicate that an intense shower should be seen a few days before the Quadrantid shower and that 4000 yr is too short a period for the branch corresponding to the D-Arietid branch to appear. We have considered the quasi constants of motion $1/a$ and J , the Tisserand quantity, and find that the Ursids and the D-Arietids are unlikely to be members of the complex and that the complex is probably less than 4000 yr old.

Introduction

The strength and short duration of the Quadrantid meteor shower indicate a relatively young stream since shower activity decreases with age and stream width increases as the result of gravitational and other perturbations. It is generally held that since meteor streams are produced by disintegration of comets, the birth of a stream corresponds to the capture of the comet into a short-period orbit by one of the major planets. For the Quadrantid stream the most likely perturbing planet is Jupiter. According to the calculations of Babadzhanov and Obrubov (1987), the inclination of the Quadrantid orbit has varied with a period close to 3500 yr. Using their orbital elements we find the last close encounter of the stream with Jupiter took place about 3200 yr ago as shown in Figure 1 below which shows how the minimum distance between the orbit of the stream and that of Jupiter has varied over the past few thousand years. The question arises whether the parent comet was captured at the last close approach or at some previous, more distant encounter.

In one of the most important papers in recent years dealing with the evolution of meteor streams, Babadzhanov and Obrubov (1987) showed that the Quadrantid stream is likely to be part of a complex of eight meteor streams which includes the D-Arietids, the N and S δ-Aquarids and the Ursids.

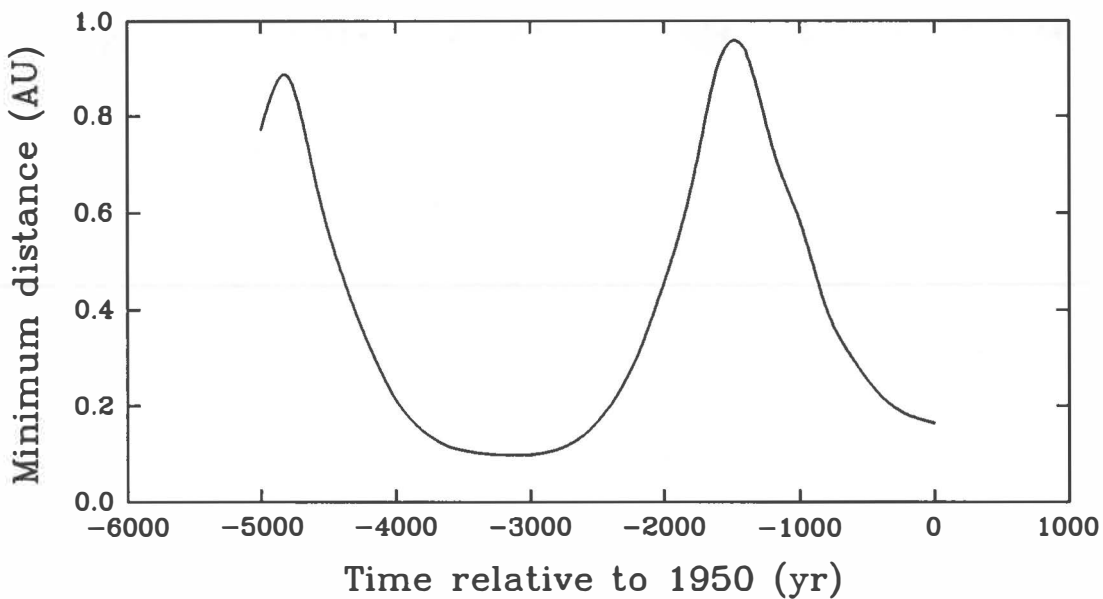


Figure 1. Closest distance between the Quadrantid stream and Jupiter's orbit in recent times based on the orbital calculations of Babadzhanov and Obrubov (1987).

The model

It is very difficult to estimate the orbit of a comet several thousand years ago if the present orbital elements are not known very precisely. We can be much more confident about the mean orbit of a meteor stream since, by definition, the small random-like perturbations resulting from the differing positions of the stream members have been averaged out and the "ring of mass" approximation for the perturbing planets should yield a good initial orbit for the stream. In the subsequent modelling of the stream the planets are treated as point masses traversing their present orbits. The motions of 500 test particles in the stream were calculated by integrating their equations of motion numerically taking into account the gravitational forces of the Sun, Venus, Earth, Jupiter, Saturn, Neptune, and Uranus. A simple fourth order Runge-Kutta integrator was used with the step length depending on the nearest perturbing body as described by Jones (1985). The starting orbital elements of the parent comet were taken as those given by Babadzhanov and Obrubov for 2050 BC. Test particles of mass 1g and density 0.8g/cm³ were assumed to be ejected uniformly from the sunward side of the comet with velocities according to Whipple's (1951) formula. The present distributions of the nodes of these orbits are shown in Figure 2.

Discussion

The S and N δ-Aquarids are evident in the ascending and descending node plots as is the tight descending node loop close to New Year which Babadzhanov and Obrubov associate with the Quadrantid and the Ursid showers. There is no trace of the D-Arietids which should appear on the descending node plot early in June.

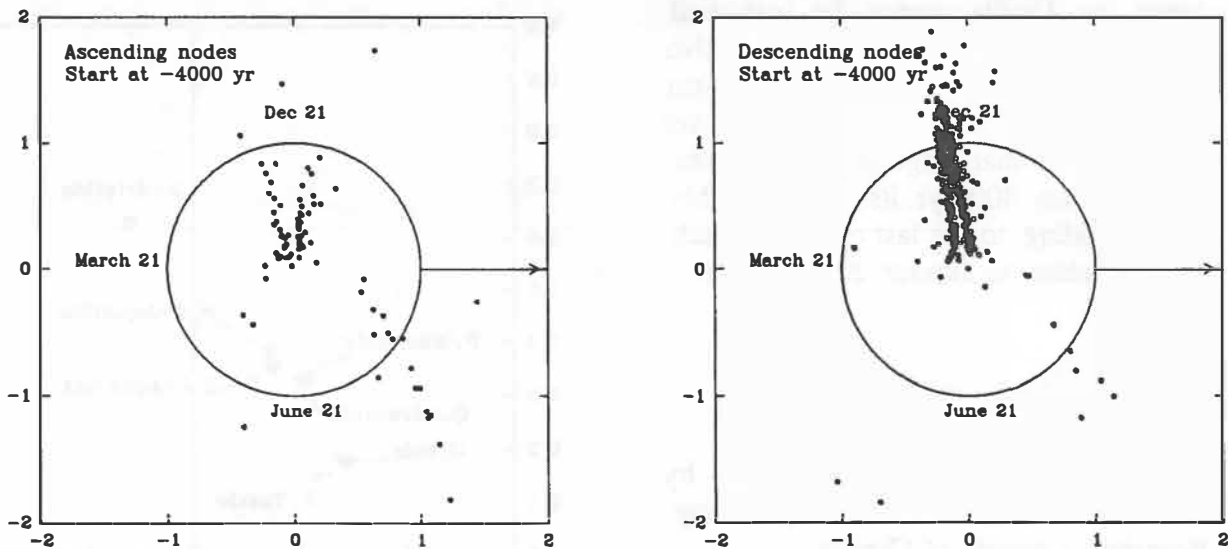


Figure 2. The present nodes for the model complex.

If the D-Arietids belong to this family of streams then the complex must be considerably older than 4000 yr. We therefore need some indicator of membership in the complex. We have chosen two well-known quasi-constants of motion: $1/a$ and J , the Tisserand quantity given by

$$J = \frac{a_J}{a} + 2\cos(i) \sqrt{\frac{a}{a_J}(1-e^2)}$$

In Figure 3 below we have plotted the points corresponding to the various meteor showers concerned as well as the points corresponding to comets Tuttle and Machholz. Clearly the points for the δ -Aquarid and Quadrantid showers form a tight cluster as would be expected for members of the complex while the points for the Ursids and D-Arietids are well-separated from the cluster. We also note that our plot strongly supports the long-supposed association of the Ursid stream with comet Tuttle. Not only is the point for the D-Arietids far from the main cluster but its J value is > 3 which implies that particles in this stream never make a close approach to Jupiter. We therefore conclude that neither the Ursids nor the D-Arietids belong to the Quadrantid complex.

McIntosh (1990) suggested both Comet 1491-I and Comet P/Machholz (1986 VIII) as possible parent comets for the Quadrantid stream. The orbital elements of comet 1491-I are uncertain and it is usually assumed to be in a parabolic orbit which would place it on the abscissa of Figure 3 and therefore far from the central cluster. However, the $1/a$ and J values for Comet P/Machholz are in excellent agreement with those of the cluster and therefore from this point of view it is a likely candidate for the parent comet.

Since the Ursids cannot be identified with the shower that would be active shortly before the Quadrantids, we must conclude that the complex has not yet developed to that stage and is therefore younger than 4000 yr, its birth probably corresponding to the last close approach of the stream to Jupiter 3200 yr ago.

Acknowledgments

This work has been supported by the Natural Sciences and Engineering Research Council of Canada.

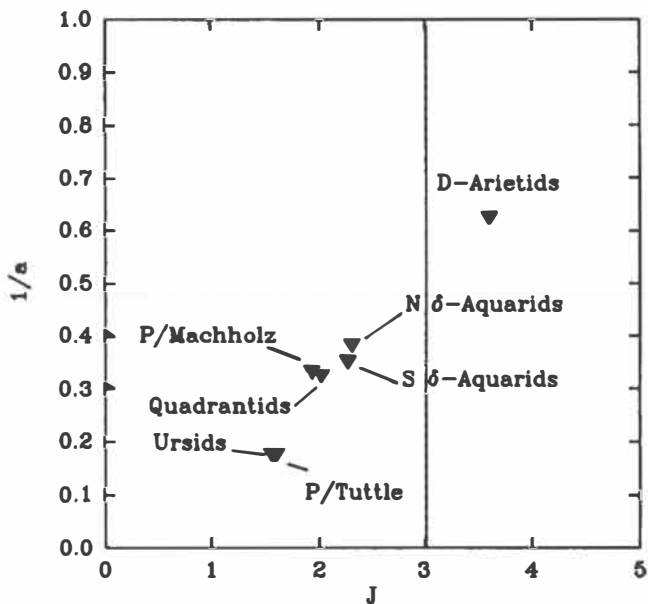


Figure 3.

References

- Babadzhanov, P.B. and Obrubov, Yu.V. (1987) Evolution of meteoroid stream. Proc. X'th Europ. Region. Astron. Meeting of the IAU., 2. 141-150.
- Jones, J. (1985) The structure of the Geminid meteor stream. Mon. Not. R. astr. Soc., 217, 523-531.
- McIntosh, B.A. (1990) Comet P/Machholz and the Quadrantid Meteor Stream. Icarus, 86, 299-304.
- Whipple, F.L., (1951) A Comet model -II. Astrophys. J. 113, 464-474.

FORWARD-SCATTER RADIANT MAPPING

J. Jones, Physics Department, University of Western Ontario,
London, Ontario, Canada. N6A 3K7.

and

A.R. Webster, Department of Electrical Engineering,
University of Western Ontario, London, Ontario, Canada. N6A 5B9.

Abstract

Forward-scatter systems have been much neglected for the study of meteors and meteor streams. A great deal of this neglect stems from the complicated geometry which has made the interpretation of results difficult in the past. This no longer presents a problem because of the computer power now available. There are practical advantages in using forward-scatter in that low-power transmitters are much easier to handle than the high-power ones used in pulsed back-scatter radars. The data reduction of the CW signals is also significantly simpler. Because the forward-scatter reflection geometry increases the duration of the echoes relative to the back-scatter case the problem of the underdense ceiling is partially alleviated. We have built a "short hop" forward-scatter system between Ottawa and London (Ont) for which the transmitter and receiver are separated by about 500 km. With it we are able to measure unambiguously the directions of arrival of the echoes using a 5-antenna interferometer. Morton and Jones (1982, MN, 198, 737) have shown how the echo direction distribution can be deconvolved to yield the meteor radiant distribution for back-scatter data. We have extended the technique to the forward-scatter case and present some preliminary meteor radiant distribution maps.

Introduction

Pulsed back-scatter meteor radars are expensive, dangerous and temperamental because of the high power and voltages required. If range information is not needed, a continuous-wave (CW) forward-scatter offers a much simpler approach since a high-power transmitter is not required to accommodate the large bandwidth associated with pulsed radars. The forward-scatter geometry is such that the echo durations are in general longer than for back-scatter because of the reduced destructive interference of the waves scattered from the electrons in the train. The duration enhancement increases with the forward-scatter angle so partially alleviating the attenuation due to the "underdense ceiling" which has plagued traditional VHF back-scatter studies.

In spite of advantages listed above, forward-scatter systems have not enjoyed much popularity for the study of meteors and meteor streams because data from forward-scatter systems has been difficult to interpret primarily because of the complicated geometry. This is no longer the case since small computers which are easily able to cope with the relatively low data rate are readily available.

The equipment.

Our system consists of a 100W-transmitter operating at 48.7 MHz located in Ottawa and a complex of receivers located in Elginfield close to London(Ont). Identical horizontal two-element antennas directed towards each other are used at both the transmitter and the receivers. The echo directions are determined from the differences in phases of the signals measured from five spaced antennas as shown in Figure 1 below.

All spacings in wavelengths

To Ottawa

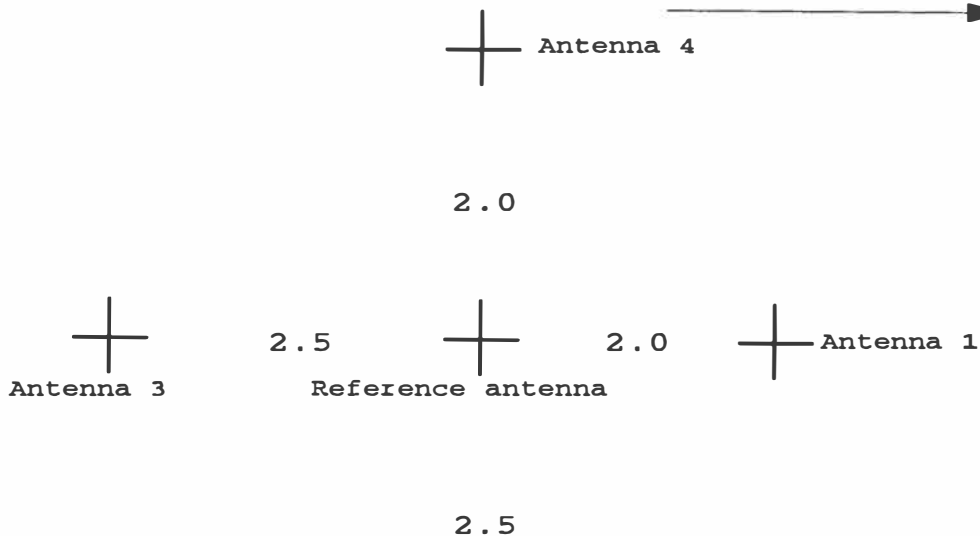


Figure 1.



Figure 1. Receiver antenna arrangement at Elginfield (close to London, Ont).

This particular arrangement was chosen because it enabled us to eliminate the ambiguities usually associated with interferometers. Noise in the system introduces errors into determinations of the echo directions and simulations have shown that with a signal ratio of 20 dB, the measured direction will probably be accurate to better than 1° for elevation angles above 20° ; below this the measurement errors increase rapidly.

The distribution of normals to the meteor trains is required to determine the radiant distribution. Whereas for the back-scatter case the echo direction is perpendicular to the

meteor train, for forward-scatter geometry the normal, n , must be calculated from

$$n = r_1 + r_2$$

where r_1 and r_2 are unit vectors from the transmitter and receiver to the reflection point and we have calculated r_2 assuming the reflection point to be at 100 km. The production of the maps such as Figures 2 and 3 above then proceeds exactly as described by Morton & Jones (1982) for back-scatter.

Discussion.

We have demonstrated the feasibility of radiant mapping using a forward-scatter system. The present system could be greatly improved by reducing the receiver bandwidth and we estimate it would not be difficult to increase the sensitivity such that the echo rate could be increased from its present 500/day to 2000/day. We have also become aware of some important problems in a system such as ours. The first is the difficulty of measuring accurate echo directions for angles of elevation much below 20° which makes it very difficult to apply this technique to a long baseline forward-scatter and effectively precludes the exploitation of the reduced attenuation resulting from the geometry. The second is the uncertainty in the geometry caused by the ignorance of the height of the reflection point. We have found that a 10 km change in the assumed height produces about a 5° error in the declination. If the position of the radiant is well known it would be possible to use this to determine the average heights of the reflection points of shower meteors.

Acknowledgment.

This work was supported by the Government of Canada through Supply and Services Canada.

References

- Morton, J.D. and Jones, J. (1982) A method for imaging radio-meteor radiant distributions. *Mon. Not. R. astr. Soc.* **198**, 737-746.

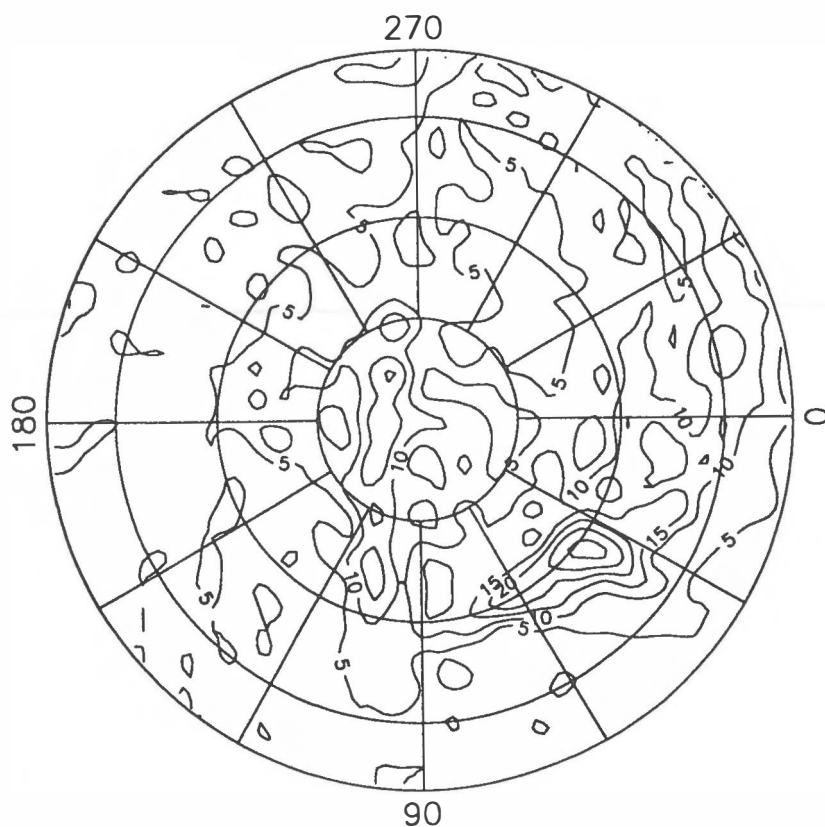


Figure 2. Radiant distribution for June 6, 1991. The circles correspond to declinations of 60° , 30° , 0° and -20° . Note the strong region of activity due to the Arietids close to $\alpha=40^\circ$, $\delta=25^\circ$.

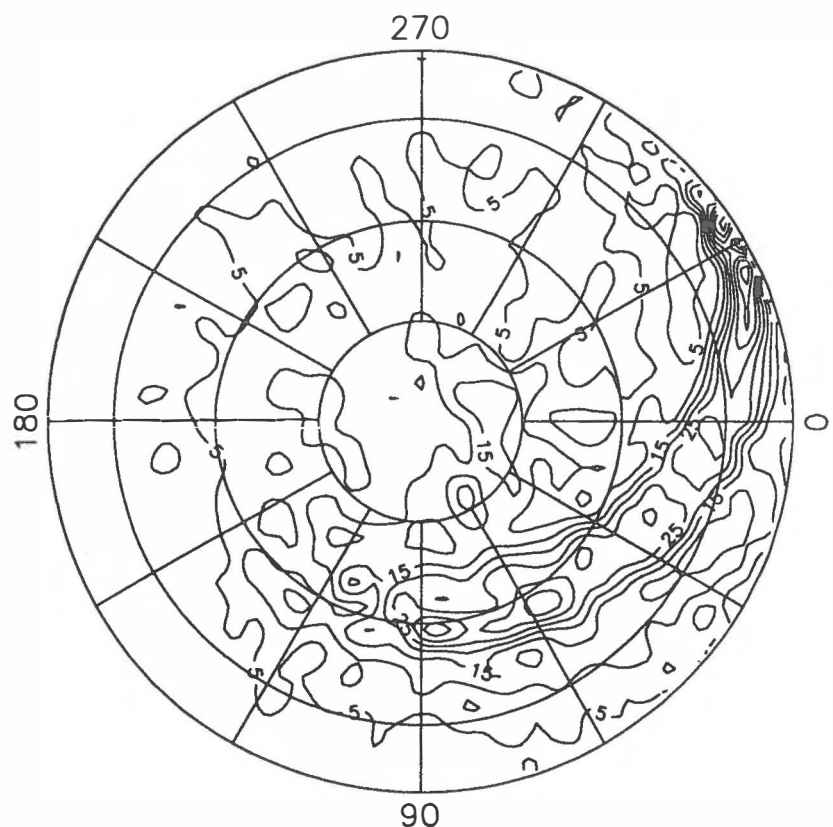


Figure 3. Radiant distribution for July 26, 1991. The circles correspond to declinations of 60° , 30° , 0° and -20° . Note the strong region of activity due to the δ -Aquarids close to $\alpha=330^\circ$, $\delta=-17^\circ$.

Effect of the geomagnetic field on the diffusion of meteor trains

W Jones Physics Dept The University Sheffield S3 7RH and J Jones Physics
Dept University of Western Ontario London Ontario N6A 3K7 Canada

ABSTRACT

A solution to the problem of the diffusion of a meteor train in the geomagnetic field from an initial line density may be written in closed form in terms of effective diffusion coefficients depending on direction, enabling detailed calculations across the entire range of angle of train to field and relevant heights.

While the effective diffusion coefficient in the plane of train and field then remains close to the zero field ambipolar value right up to 90° the effective coefficient in the direction of the normal to plane of train and field drops steadily to its $\theta = 0$ value at $\theta = 90^\circ$. At 95 km this corresponds to a change of almost 5km, in "diffusion height", that is, the height of an underdense meteor calculated on the basis of the exponential decay of its radar echo. We have estimated the consequent changes in the expected distribution of diffusion heights for various orientations of radar antenna and find the dependence on azimuth is very marked. The effect of the field is relatively minor for a south pointing beam but very strong if the beam is pointing north.

INTRODUCTION

The theoretical description of the diffusion of meteor trains in the Earth's magnetic field is a long standing problem of considerable interest. At first sight it would appear that the field could have an effect on all meteors ablating above 95km, or so but it was suggested by Kaiser (1968) that the effect is appreciable only if the meteor is very closely aligned with the field. Detailed numerical work was carried out by Kaiser, Pickering and Watkins (1969), and Pickering and Windle (1970), in which the meteor was modelled as an irregularity in a uniform ionised background and the distribution of ions and the electric field or potential were calculated at the points of a grid within a rectangle perpendicular to the meteor axis, so that the partial differential equations could be reduced to a finite system of linear equations. These calculations appeared to support Kaiser's contention, though later work by Pickering (1973) and Lyatskaya and Klimov (1988) suggests that the magnetic field may well have considerable influence when the train and field are not closely aligned. This is also the conclusion of Rozhansky and Tzendin (1977) in their qualitative assessment of the main features of the diffusion of irregularities. However, their work is concerned with changes in the ionisation much less than that of the ambient plasma, so that any application to meteors must be treated with caution. Furthermore, all the detailed numerical calculations mentioned above were limited in scope. The complexity of the numerical procedure and the requisite computing time limited the computations to an unrealistically small ratio of meteor ionisation to background (of the order of three or so). Moreover, the boundary conditions imposed at the perimeter, that the electric potential and the normal component of the ionic number density be zero, are artificial. In the interpretation of observations of meteors, it has been almost always assumed that one can ignore the effect of the magnetic field in practice.

In a recent examination of the problem a direct analytical generalisation of the standard solution for the zero-field case, describing the time development from an initial line density of ionisation, has been sought (Jones 1991). It was found that such a generalisation is indeed possible, enabling detailed calculations across the entire range of angles and relevant heights, these calculations being essentially exact within the framework of the model. Our results show that for heights of 95km, and above the diffusion is severely inhibited by the field if θ , the angle between train axis and the field lines, is close to zero, and that this effect diminishes very rapidly as θ is increased. This is in accordance with the original suggestion by Kaiser (1968) but the important new feature of the present results is that, for θ greater than about 2° , the effective diffusion coefficient in the direction of the normal to plane of train and field, drops steadily to its $\theta = 0^\circ$ value at $\theta = 90^\circ$. The effect is very marked - even for a height as low as 95km, the magnetic field can reduce the diffusion by a factor of two below the zero field value. In contrast the diffusion coefficient in the plane of train and field remains close to the zero field ambipolar value right up to 90° . These results are in general agreement with existing experimental results (see Baggaley and Webb 1980), which, however, have primarily been concerned up to now with the exploration of the small θ dependence.

The question now arises as to how this will affect the detailed nature of the results and interpretation of meteor observations and we shall illustrate this here by discussing the radio echoes from underdense meteors. The heights of underdense meteors are commonly estimated on the basis of diffusion theory. Assuming that one can neglect the influence of the magnetic field, the theory predicts that the exponential decay time of the radar echo will be inversely proportional to the diffusion coefficient D and thus directly proportional to the air density. As we shall see, this assumption must be profoundly modified, the "diffusion heights" obtained in this way being strongly dependent on the orientation of the meteor relative to the field.

AVERAGING OF DIFFUSION HEIGHTS OF SPORADIC METEORS

To obtain the average diffusion height of meteors of a given true altitude it is necessary to estimate weightings for given θ and μ , the angle between the incoming wavevector and the normal to the plane of the train and the magnetic field. It is reasonable to assume that the incident directions of sporadic meteors are uniformly distributed over the celestial sphere (see Kaiser 1953), but the degree of ionisation will depend on the zenith angle x . In the conventional theory of meteoric ionisation (Herlofson 1951, Jones and Kaiser 1966) the ionisation at a given height is a function of the maximum line density α_m only, and this in turn may be expressed as $\alpha_m = \alpha_z \cos x$, where α_z characterises the meteor independent of x (in fact as one can see, α_z is the maximum line density the meteor would have if it were incident vertically). The proportion of meteors within the range $(\alpha_z, \alpha_z + d\alpha_z)$ may be approximated by $C \alpha_z^{-s} d\alpha_z$ where C and s are constants; from this one can see that for a given angle x the proportion of meteors with maximum line density in the range $(\alpha_m, \alpha_m + d\alpha_m)$ is

$$C \alpha_m^{-2} (\cos x)^{-s-1} d\alpha_m \quad (6.1)$$

It appears that we may set $s = 2$ to a good approximation (Kaiser 1954), in which case the dependence on zenith angle is simply $\cos x$, and we have taken this to be the case.

We have performed detailed calculations for a pencil beam at an elevation angle of 30° , this corresponding to the maximum of a half-wave dipole above perfect ground. Figure 6 shows the average diffusion height, for various true heights, as a function of beam azimuth, while in figure 5 we show the proportion of echoes, as a function of diffusion heights; in this example the azimuth of the beam is 90° and the true heights 102 and 108km. The results for 95 and 97.5km are roughly similar, though much more compressed, the respective ranges of diffusion height being 1.7 and 3.5km.

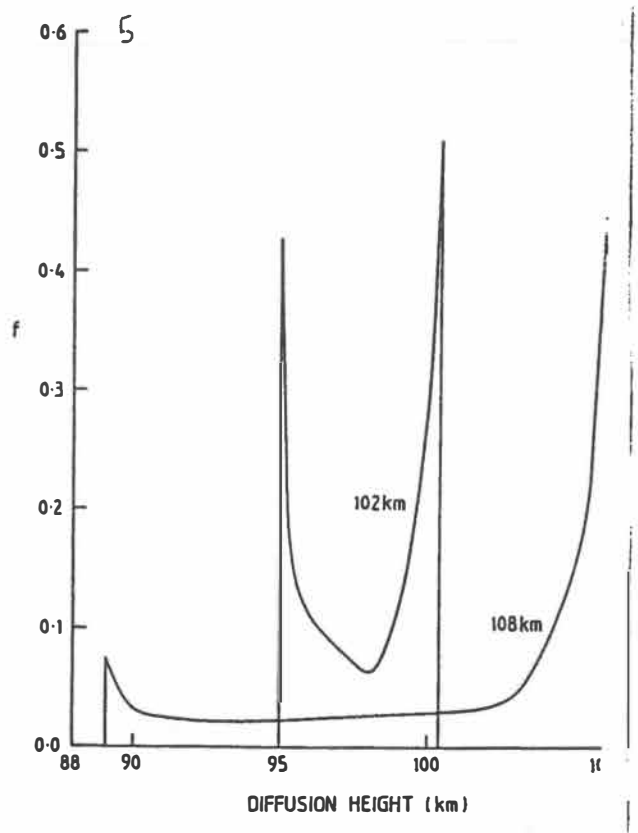
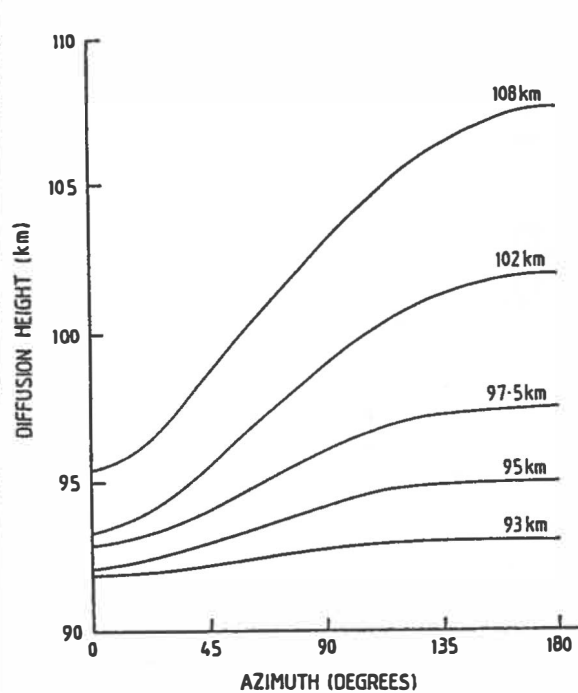
DISCUSSION

We have presented calculations of the diffusion heights of meteors taking into account the effect of the geomagnetic field by a direct generalisation of the analytic solution for the zero-field case within the quasineutrality approximation, the meteor train being treated as a cold cylindrical plasma.

As we have already remarked, in the interpretation of observations of meteors it has almost always been assumed that one can ignore the effect of the magnetic field in practice. Recent results (Jones 1991) indicate that for heights of 95km, and above the diffusion is severely inhibited by the field if θ , the angle between train axis and the field lines, is close to zero, and that this effect diminishes very rapidly as θ is increased up to about 2° . However, an important new aspect of the results is that as θ is increased further D_v , the effective diffusion coefficient in the direction of the normal to plane of train and field, drops steadily to its $\theta = 0^\circ$ value at $\theta = 90^\circ$. In contrast D_u , the diffusion coefficient in the plane of train and field, remains close to the zero field ambipolar value right up to 90° . Even for a height as low as 95km, the magnetic field can reduce D_v by a factor of two below the zero field value. This corresponds to a change of almost 5km in "diffusion height", that is, the height of an underdense meteor estimated on the basis of the exponential decay of its radar echo.

To illustrate how this will affect the detailed nature of the results and interpretation of meteor observations we present here calculations of "diffusion heights", i.e., heights obtained from the decay of underdense echoes by the application of the standard diffusion theory, under reasonable assumptions as to meteor ablation and distribution.

In Figure 1 we show calculations of the proportion f of echoes, as a function of diffusion heights for a pencil beam at 30° elevation and a magnetic azimuth (azimuth relative to magnetic north) of 90° . Figure 2 shows calculations of the mean diffusion height, again for a pencil beam at 30° elevation, against magnetic azimuth. The azimuthal dependence is very marked. For a south pointing beam the mean diffusion height and true height are in good agreement but for a north pointing beam the effect of the magnetic field is to pull down the diffusion heights considerably, especially for the true heights of more than 100km. That is, the effect of the magnetic field is to elevate the "echo ceiling". This arises from two effects, (i) the finite radius of formation increases with height and (ii) the ionised trail diffuses faster than it is formed if the height is great enough. We expect the initial radius to be largely unaffected by the field but once the train is formed the field will greatly diminish the rate of decay of the radar echo from diffusion provided the orientation is favourable.

Figure 1.Figure 2.**REFERENCES**

- Baggaley W J and Webb T H (1980) *Planet Space Sci* 28 997
 Herlofson N (1952) *Rep Prog Phys* 11 444
 Jones W and Jones J (1990) *J Atmos Terr Phys* 52 185
 Jones W (1991) *Planet Space Sci* (in press)
 Kaiser T R (1968) in *Physics and Dynamics of Meteors* (edited by Kresak R and Millman P M) p27, Reidel Dordrecht
 Kaiser T R Pickering W M and Watkins C D (1969) *Planet Space Sci* 17 519
 Lyaskaya A M and Klimov M P (1988) *J Atmos Terr Phys* 50 1007
 Pickering W M (1973) *Planet Space Sci* 21 1671
 Pickering W M and Windle D W (1970) *Planet Space Sci* 18 1153
 Poulter E M and Baggaley W J (1978) *J Atmos Terr Phys* 39 757
 Rozhansky W A and Tzendin L D (1977) *Geomagn Aeron* 17 1001

OBSERVATION OF METEORS BY MST RADAR
W. Jones and S.P. Kingsley, University of Sheffield, UK

ABSTRACT

The observation of meteor trails by a vertical MST radar beam has the advantage of good height resolution and an approximate knowledge of the zenith angle since the trails are horizontal or near-horizontal. An extension of the ablation theory of meteors has been developed for near horizontal trails which takes into account the curvature of the earth.

Observations of the Geminid meteor shower by MST radar reveal the "diffusion heights" to be in fair agreement with the true height, but with some discrepancies that can amount to 4km. The true heights are almost entirely confined to the range 87-91km, although the upper limit is attributed to the coherent integration time of the existing MST radar processing.

INTRODUCTION

The vast majority of meteors give appreciable back scatter radar echoes only from a region near the "reflection point" on the perpendicular from the train to the receiver (see McKinley 1961). This implies trains observed with the vertical beam of an MST radar to be horizontal; thus relatively few meteors will be observed, the majority having burned up before reaching the reflection point. On the other hand, the height resolution is very good and the zenith angle is fairly accurately known, so that the circumstances of observation are worth further investigation. We should mention that the use of an MST radar as a meteor radar has been discussed before (see Avery *et al.*, 1983) but we shall be concerned here with the physics of the meteors themselves rather than as tracers for the measurement of atmospheric winds.

The first point that needs to be emphasised is that when considering the ablation of a meteor observed with a vertical or near vertical beam, it is essential to take account of the curvature of the Earth. From fairly general assumptions, principally that the rate of ablation is directly proportional to the energy of impact with the molecules of the atmosphere, one obtains an expression in which the rate of change with time is converted into a rate of change with height under the assumption that the Earth may be taken to be flat so that the height changes as $v \cos \chi$, where χ is the zenith angle (Herlofson 1948). This leads to an expression in which the rate of ablation is proportional to $\cos \chi$, so that it is predicted to be zero for horizontal meteors. In the following we shall examine the requisite modifications to the usual theory when the effect of the Earth's curvature is included.

We have used the MST radar at Aberystwyth, Dyfed, Wales to observe the Geminid meteor shower of December 1990, recording heights and the rate of decay of the echo, and in the following we shall present these preliminary results. We shall interpret the results as far as we can by means of the modified ablation theory. With regard to echo decay we should also note that the heights of underdense meteors are commonly estimated on the basis of diffusion theory. This theory predicts that the exponential decay time of the radar echo will be inversely proportional to the diffusion coefficient D and thus directly proportional to the air density. However, because of the difficulty of estimating the meteor height by other means, confirmation of this procedure has been largely statistical and not completely satisfactory. The MST radar provides us with accurate heights for individual meteors, and since the zenith angle is known, we can use the true heights to compare with the estimates of the diffusion theory.

ATMOSPHERIC HEATING OF NEAR-HORIZONTAL METEORS

It appears that most meteoroids are fragile in structure (so that one speaks of the object as " friable" or as a "dustball") although the Geminids do appear to be more solid than the constituents of most streams (see Bronshten 1983). It is reasonable to suppose that the "grains", the basic or ultimate particles, can be treated as solid bodies to which the "classical" ablation theory applies.

Because at the point of observation with the MST radar the meteor is moving horizontally, or near horizontally, we must modify the usual ablation theory (Herlofson 1948, Jones and Kaiser 1966) to take account of the curvature of the Earth. Because of limitations of space we omit the detailed derivation and merely quote the relevant final results, valid for particles of sufficient size that radiation and retardation effects may be neglected.

We introduce T_a the temperature at which the material ablates, ρ the atmospheric density, ρ_m the density of the meteoric material, v the velocity of the meteoroid, L the latent heat of the meteoric material, r the particle radius, r_∞ the original radius at infinity, R the radius of the Earth and χ the zenith angle of the meteor trail. Coefficients η and γ are also introduced, for mathematical convenience, with $\eta=v^2/(8\rho_m L)$ and $\gamma=CT_a/L$, C being the specific heat. A locally isothermal atmosphere is assumed, so that we may write $\rho \propto \exp(-h/H)$ where h is the height and H the scale height.

Provided ablation begins, the radius of the particle at the point of observation is found to be

$$r = r_\infty [1 + \gamma/3 - \eta \rho I(0, \chi)/r_\infty] \quad (1)$$

where

$$I(\chi) = \sqrt{(\pi RH/2)} \exp[R \cos^2 \chi / (2H)] \operatorname{erfc} [(R \cos \chi) / \sqrt{2RH}] \quad (2)$$

We might note that using the asymptotic expansion for $\operatorname{erfc}(x)$ we may show that

$$I(\chi) \rightarrow H/(\cos \chi) \quad (\cos^2 \chi \gg 2H/R) \quad (3)$$

in which case eqn (3.6) reduces to the result of previous theory (Jones and Kaiser 1966),

However,

$$I(\chi) \rightarrow \sqrt{(\pi RH/2)} \quad (\cos^2 \chi \ll 2H/R) \quad (4)$$

and this is the appropriate result when using the vertical beam of the MST radar.

Universal form of the ablation curve

The line density of ionisation can be expected to be given by an expression of the form

$$\alpha = C r^2 dr/dt \quad (5)$$

where C is a constant. From (1) we now obtain an expression for the ionisation in the "universal" form

$$\alpha = 9\alpha_m [1 - \rho/(3\rho_m)] \rho/(4\rho_m) \quad (6)$$

in terms of the density ρ_m at the height of observation for which the line density is a maximum α_m , these quantities being given by

$$\rho_m = (1 + \gamma/3)r_\infty \quad (7)$$

and

$$\alpha_m = 4(1 + \gamma/3)^3 r_\infty^3 / (27\eta) \quad (8)$$

When the limit (3) applies (6) and (7) give the usual result for the variation of ionisation with height.

Meteors are often characterised by α_z , the maximum line density the meteoroid would produce if incident vertically (see Kaiser 1954). From the above it will be seen that

$$\alpha_z = \alpha_m \times I(\chi)/H \quad (9)$$

For horizontal meteors ($\chi = 0$) we find $\alpha_m \approx \alpha_z/40$

Limits to observational size

It is evident that equation (1) can be valid only provided

$$r_\infty < 3\eta\rho_0/\gamma \times I(0) \quad (10)$$

(otherwise the equation predicts that r will increase) and the detailed theory in fact shows that if this inequality is not satisfied the particle will not ablate at all, thus giving an upper limit to observable size. On the other hand, the particle will have burnt out before the observation point if the right-hand side is negative, which yields a lower limit to size for a particle to be observable, viz,

$$r_\infty > \eta\rho/(1 + \gamma/3) \times I(0) \quad (11)$$

We take as typical values $\rho_m = 4 \times 10^3 \text{ kg m}^{-3}$, $L = 6 \times 10^6 \text{ J kg}^{-1}$ (stone). For horizontal meteors observed at 90 km, these conditions then give $5 < r_\infty < 50$, where the radius is measured in millimetres.

EXPERIMENTAL RESULTS

We observed the Geminids on the night of 13 December 1990 using the newly commissioned MST radar at Aberystwyth. Since the meteor trains must be perpendicular to the beam to be observed, they must be horizontal to be detected by the vertical beam - that is, the radiant must be rising or setting. We identified the meteors as members of the Geminid meteor shower by virtue of the fact that in the time that observations were made echoes were in fact detected only within ten minutes of the rising or setting of the radiant.

As already remarked, the heights of underdense meteors are commonly estimated on the basis of diffusion theory. This theory predicts that the exponential decay time of the radar echo will be inversely proportional

to the diffusion coefficient D and thus directly proportional to the air density. In the figure we show the results we obtained for underdense meteors, plotting the actual height as registered by the radar with the diffusion height obtained from Verniani's empirical formula

$$0.086h_D = \log_{10}D + 7.23 \quad (12)$$

where D is the diffusion coefficient given by $D = \lambda^2(16\pi^2\tau)$, λ being the wavelength and τ the time taken for the echo amplitude to decay to 1/e of its original value. It will be seen that our results are restricted in height range, a fact to be commented on shortly, but where they exist they are in good agreement with Verniani's, though there is considerable scatter about the mean. The new element here is that the radar height estimates are accurate to $\pm 0.1\text{km}$ so that we can identify the scatter as principally due to variation in diffusion height.

A striking aspect of the figure is the restricted height, as already remarked. The absence of echoes above 93km, can be attributed to the fact that at present the radar presents data only at intervals of 1/12th second so that the echo from any underdense meteor at greater altitude would decay before being recognised as such. However, the almost complete absence of echoes below 87km indicated a sharp cutoff in the size distribution.

CONCLUSIONS

The principal aim of the present investigation has been to evaluate the potential of MST radars in the investigation of meteors and this has involved the extension of the usual ablation theory to meteors with horizontal or near-horizontal trails.

Ablation theory

We have found that the usual analytic expression of the "classical" ablation theory may be generalised to take into account the curvature of the Earth, this being essential in considering near-horizontal meteor trains. The theory allows us to estimate upper and lower limits as to the initial size of the meteoroid particles: if a particle is too small it will have burnt out before reaching the zenith at Aberystwyth, whereas if it is too large it will have not become hot enough to ablate. Taking the values suggested by Jones and Kaiser (stony meteoroids) this gives the sizes of observable particles to be between 0.5 and 5cm, at 90km.

Preliminary experimental results

We observed the Geminid meteor shower on the evening of 13 December 1990 using the newly commissioned radar at Aberystwyth, with results for underdense meteors as displayed in fig.1.

Diffusion heights

Because the MST radar has a very accurate height resolution we wished to investigate the expression, based on diffusion theory, commonly used to estimate the heights of underdense meteors, and the "diffusion heights", using the formula of Verniani (1973), are shown in the figure. It will be seen that while there is reasonable statistical agreement between the true and diffusion heights there is considerable scatter. We hesitate to ascribe this to variations in the diffusion process at the moment as comparatively few data points were obtained per meteor, the radar returning information only every 1/12th of a second.

Height and size distribution

It will be seen that the meteors are clustered between 87 and 92km. We attribute the upper limit as due to the fact that the radar returns data every twelfth of a second so that an underdense meteor will decay too quickly to record more than one data point. The almost entire absence of echoes below 87km, would however appear to be the result of a fairly sharp cutoff in the size distribution. Eqn(2.14) above, with the values for stony meteoroids as quoted, gives the minimum size for observation at 87km, to be about a centimetre. An interesting possibility is that the cutoff results from the fracture of larger particles by thermal shock and we intend to investigate the generalisation of the work of McCrosky and Ceplecha (1970) to horizontal trails.

Further experimental work

It is clear that the further use of MST radars in the observation of meteor trains will be very fruitful. It will be important, however, to modify the data collection so that it is essentially on a pulse to pulse basis, rather than at the 1/12th second used for atmospheric work. A straightforward way of doing this would be to install a separate receiver and data processing unit of the same design as currently used in meteor radars and it is the intention to do this at Aberystwyth.

References

- Avery, S.K., Riddle, A.C. and Balsley, B.B., 1983, The Poker Flat, Alaska, MST radar as a meteor radar, *Radio Science*, **18**, 1021.
- Bronshten, V.A., 1983, *Physics of Meteoric Phenomena* (D. Reidel).
- Herlofson, N., 1948, Theory of meteoric ionisation, *Rep. Prog. Phys.*, **11**, 444.
- Jones, J. and Kaiser, T.R., 1966, The effects of thermal radiation, heat capacity and conduction on meteoric ablation, *Mon. Not. R. Soc.*, **133**, 411.
- Kaiser, T.R., 1954, Theory of the meteor height distribution, *Mon. Not. R. Soc.*, **114**, 39.
- McCrossky, R.E. and Ceplecha, Z., 1970, Fireballs and the physical theory of meteors, *Bull. Astr. Inst. Czech.*, **21**, 217.
- McKinley, D.W.R., 1961, *Meteor Science and Engineering* (McGraw-Hill).
- Verniani, F., 1973, The height distribution of radio meteors, *J. Geophys. Res.*, **83**, 6225.

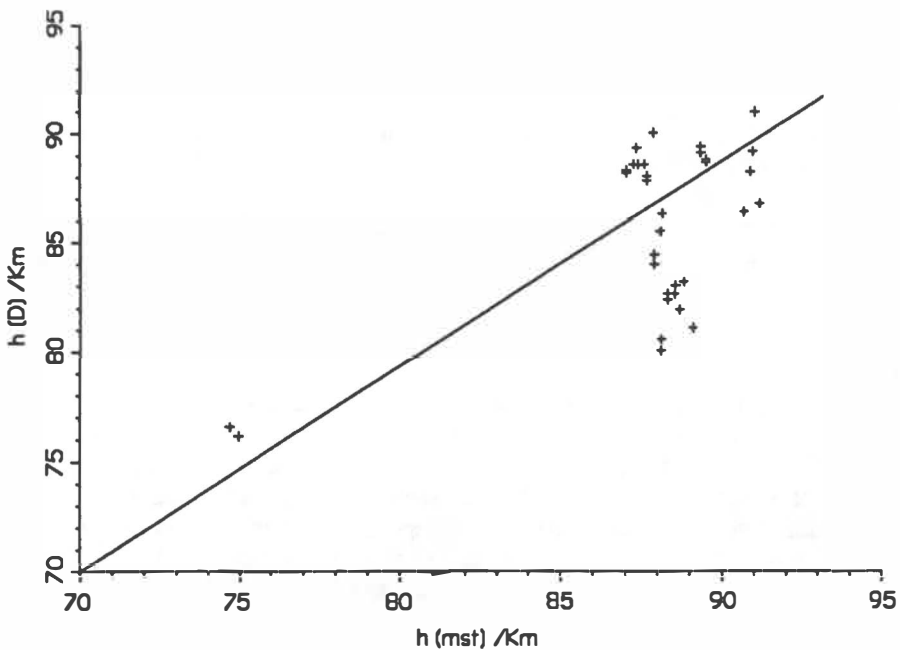


Fig. 1. Diffusion height, $h(\text{D})$, against true height, $h(\text{MST})$ for Geminids

THE CORRELATION BETWEEN WATER PRODUCTION RATES AND VISUAL MAGNITUDES IN COMETS

L. Jorda^{1, 2)}, J. Crovisier¹⁾ and D.W.E. Green³⁾

1) Observatoire de Paris, Section de Meudon, F-92195 Meudon, France

2) European Southern Observatory, La Silla, Chile

3) Smithsonian Astrophysical Observatory, Cambridge, MA 02138, USA

Abstract

From the visual magnitudes of the *International Comet Quarterly* data base and the OH radio lines measured at the Nançay radio telescope, the law $\log Q[\text{H}_2\text{O}] = 30.74 (\pm 0.02) - 0.240 (\pm 0.003) m_h$ is derived from a sample of 13 comets.

INTRODUCTION

A fundamental problem in comet studies is to relate gas production rates and visual magnitudes. If such a problem can be solved, it will be possible to use the large historical data set of visual magnitude measurements to investigate the evolution of gas production along the orbit. It will also be possible to assess the feasibility of spectroscopic observations (from radio to UV) of new comets from their brightness behaviour.

DATA SET AND METHOD

We have now two homogeneous data sets in computer-readable form:

- 1) The compilation of visual magnitudes of the *International Comet Quarterly*. The base consists of more than 35 000 entries in the 1990 version (Green, 1990), most of them coming from amateur astronomers.
- 2) The data base of 18-cm OH cometary spectra measured with the Nançay telescope. 35 comets were observed since 1973, and most of the data are now incorporated in a computer base (Gérard *et al.*, 1990).

Water production rates can be derived from the OH radio lines following the model of Bockelée-Morvan *et al.* (1990). The model includes pumping by UV fluorescence, collisional quenching, and a coma expansion velocity deduced from the radio line shapes. The production rates from radio and UV observations of OH are now in agreement when consistent sets of model parameters are used. We assume $Q[\text{H}_2\text{O}] = 1.1 Q[\text{OH}]$.

We have studied the correlation between the water production rate and the visual magnitude in 13 comets. The water production rates were evaluated for a selection of 81 time-averaged OH spectra which have sufficient signal-to-noise ratios to get reliable results (the corresponding OH data are published in more detail by Bockelée-Morvan *et al.* 1990a, 1990b and 1991). The visual magnitudes m_v were reduced to heliocentric magnitudes m_h according to $m_h = m_v - 5 \log \Delta$ and averaged (or interpolated) over the same time intervals as the OH spectra. This averaging process smoothes the large dispersion of the total visual magnitude measurements. The heliocentric distances of the resulting sample range from 0.32 to 2.8 AU.

RESULTS AND DISCUSSION

$Q[\text{H}_2\text{O}]$ is plotted as a function of m_v for the whole sample and for different groups of comets in the figures. The error bar on $Q[\text{H}_2\text{O}]$ is that resulting from the noise in the OH spectrum (it does

not include model uncertainties). The error bar on m_h is that resulting from the dispersion on the measurements. The empirical law deduced from a regression analysis applied to the whole sample is:

$$\log Q[\text{H}_2\text{O}] = 30.74 (\pm 0.02) - 0.240 (\pm 0.003) m_h$$

with a regression coefficient of -0.92. We note that:

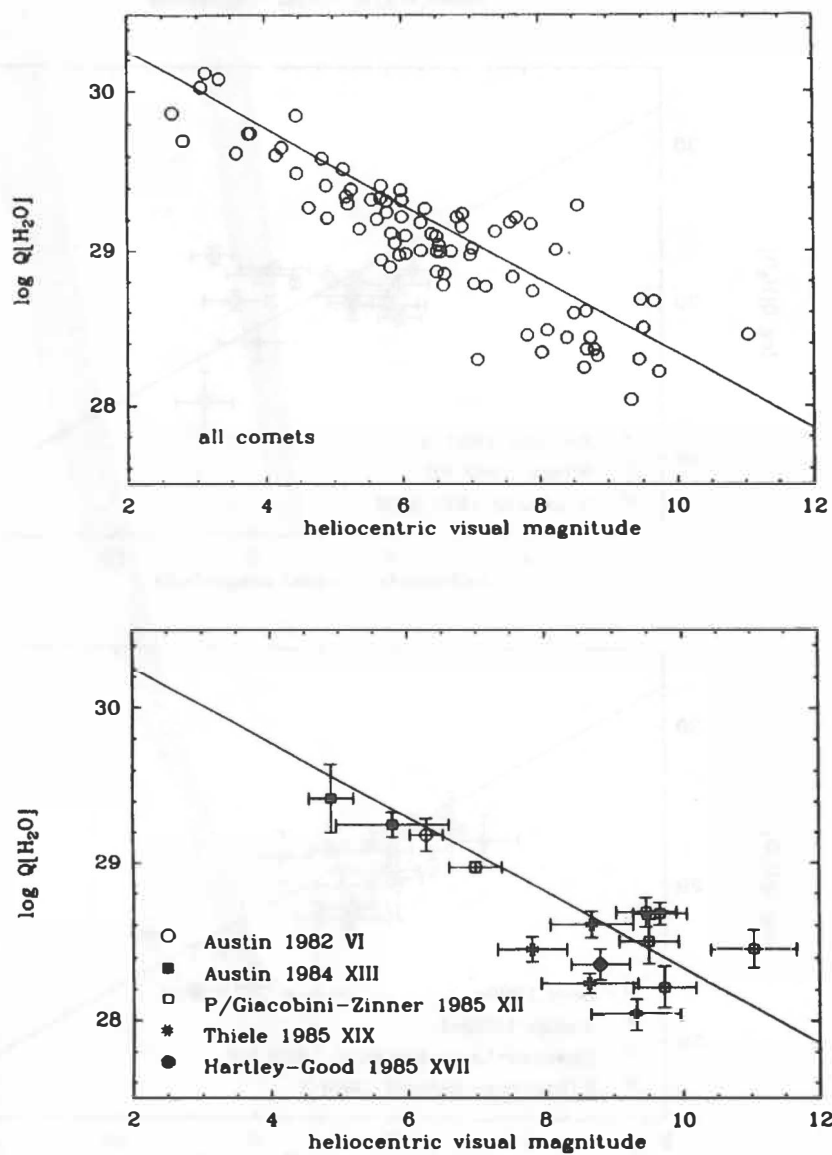
- there is no strong deviation to this law for individual comets. From first inspection, the law does not depend upon gas-to-dust ratio. Although the sample includes short-period, long-period and new comets, there is no obvious difference between these different classes.
- the slope of the law is steeper for P/Halley (-0.303) than for the set of the 12 other comets (-0.213).

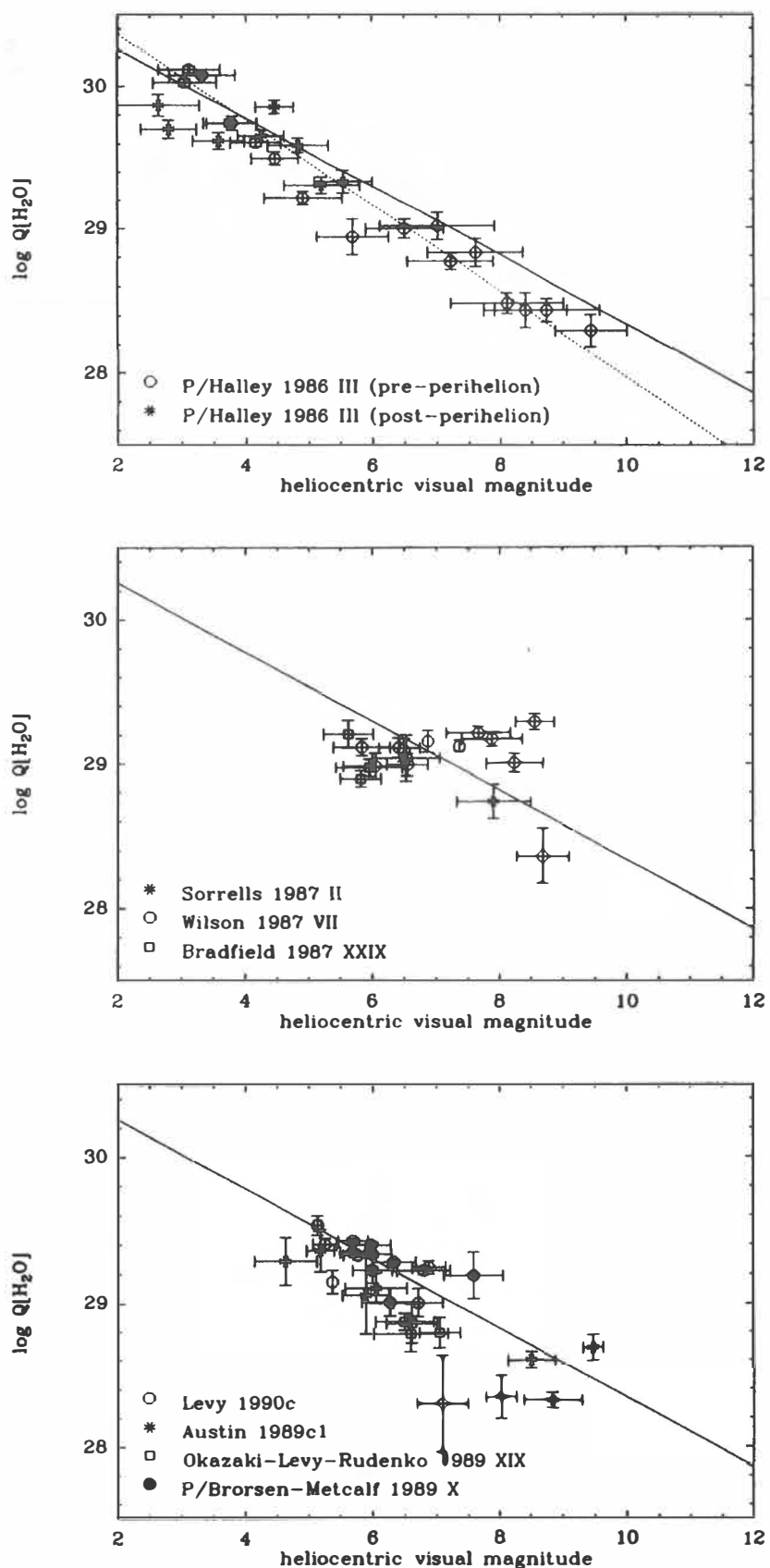
Similar studies were performed in the past: from OH radio measurements by Bockelée-Morvan *et al.* (1981), from UV OH measurements by Festou (1986) and Roettger *et al.* (1990), for comet P/Halley alone by Sekanina (1989) and many others. Our regression law is intermediary between those of Bockelée-Morvan *et al.* and of Festou; it is in agreement with the one Sekanina proposed for P/Halley (which may be fortuitous). When comparing these studies, one must have in mind that they use gas production rates estimated with different models. We believe that our work is an improvement over the preceding ones, owing to the larger size of our sample.

References:

- Bockelée-Morvan D., Colom P., Crovisier J., Gérard E., and Bourgois G. (1991) Observations of comet Levy (1990c) with the Nançay radio telescope. In *Asteroids, Comets, Meteors 1991* (this volume).
- Bockelée-Morvan D., Crovisier J., and Gérard E. (1990a). Retrieving the coma gas expansion velocity in P/Halley, Wilson (1987 VII) and several other comets from the 18-cm OH line shapes. *Astron. Astrophys.* **238**, 382-400.
- Bockelée-Morvan D., Crovisier J., Gérard E., and Bourgois G. (1990b) OH radio observations of comets P/Borsen-Metcalf (1989o), Okazaki-Levy-Rudenko (1989r), Aarseth-Brewington (1989a1) and Austin (1989c1) at the Nançay radio telescope. In *Workshop on Observations of Recent Comets*. Eds W.F. Huebner *et al.*, pp. 75-79.
- Bockelée-Morvan D., Crovisier J., Gérard E. and Kazès I. (1981). Observations of the OH radical in comets at 18 cm wavelength. *Icarus* **47**, 464-469.
- Festou M.C. (1986). The derivation of OH gas production rates from visual magnitudes of comets. In *Asteroids Comets Meteors II* (C.-I. Lagerkvist *et al.* eds.), pp. 299-303. Uppsala Univ. Press, Uppsala.
- Gérard E., Bockelée-Morvan D., Bourgois G., Colom P., and Crovisier, J. (1990). 15 years of observations of the OH radical in comets with the Nançay radio telescope. In *Asteroids Comets Meteors III* (C.-I. Lagerkvist *et al.* eds.), pp. 317-320. Uppsala Univ. Press, Uppsala.
- Green D.W.E., edt. (1990). *Int. Comet Q.* Archive of Cometary Photometric Data, magnetic tape, fourth edition, June 1990.
- Roettger E.E., Feldman P.D., A'Hearn M.F., and Festou M.C. (1990). Comparison of water production rates from UV spectroscopy and visual magnitudes for some recent comets. *Icarus* **86**, 100-114.
- Sekanina Z. (1989). Nuclei of two earth-grazing comets of fan-shaped appearance. *Astron. J.* **98**, 2322-2345.

Figures: Water production rates derived from the OH 18-cm lines observed at Nançay, as a function of heliocentric visual magnitudes derived from the ICQ archives. The error bars are $\pm 1 \sigma$. The full line shows the least-square linear fit to the whole sample and is repeated on each figure. The dashed line is the fit to P/Halley data alone.





INVERSION METHODS FOR INTERPRETATION OF ASTEROID LIGHTCURVES

M. Kaasalainen^{1,2}, L. Lamberg³, and K. Lumme¹

¹ University of Helsinki, Observatory and Astrophysics Laboratory, Tahtitorninmaki, 00130 Helsinki, Finland

² (From Oct 91) University of Oxford, Department of Theoretical Physics, 1 Keble Road, Oxford OX1 3NP, England

³ University of Helsinki, Department of Mathematics

Abstract

We have developed methods of inversion that can be used in the determination of the three-dimensional shape or the albedo distribution of the surface of a body from disk-integrated photometry, assuming the shape to be strictly convex (Kaasalainen et al. 1990a, 1990b, 1991a). In addition to the theory of inversion methods, we have studied the practical aspects of the inversion problem, and applied our methods to lightcurve data of 39 Laetitia and 16 Psyche (Kaasalainen et al. 1991b).

Practical Aspects of Inversion

The result obtained in inversion is a finite spherical harmonics series as a function of the direction of the surface normal. In practice, one must decide in each case whether this result is taken to describe shape rather than albedo features, or if the surface is not convex on a global scale. Fortunately, there are some indicators for this: certain nonzero coefficients in the series indicate albedo variegation, and substantially negative values of the sum of the series imply a nonconvex shape. A solution ascribed to shape is less sensitive to errors in lightcurve data than one ascribed to albedo variegation.

There are many observational factors having an influence on the outcome of inversion. Also, one must make some a priori assumptions that are used in the inversion process. The most important points are:

- The assumed spin vector of the asteroid. The inversion procedures are not too sensitive to the pole position, as long as it is known to an accuracy of about 15°. The sidereal rotation period of the asteroid should be very precisely known if it is to be used in computing the absolute rotational phases, which should be known to the same accuracy as the pole position. Another possibility is to determine the phases using prominent features or other properties of lightcurves. Although this may not always be a properly justified approach, the phases can usually be determined within a reasonable limit of uncertainty. One can also use a series of small deviations from the a priori spin vector and choose the result that gives the best fit in this series.
- The number and the range of the observing geometries. These should, of course, be as large as possible. Especially the aspect angle (the angle between the line of sight and the rotation axis) should extend well outside the equatorial zone; if this is not possible, the solution obtained tends to be numerically not well determined. Nonzero solar phase angles can in principle provide information unobtainable at opposition if the scattering of light is geometric there. In practice, obtaining this information is difficult because of the small phase angles. Accurate observations as far away from opposition as possible are required; also, the light-scattering law should be well known. Aspect angles far from equator, or equatorial aspects when the illumination direction is not near the equatorial plane, are best for this purpose.
- The accuracy of lightcurves. The magnitude of noise in the lightcurve data primarily determines the truncation point of the spherical harmonics series obtained in inversion. This stems from the fact that high-degree components of the shape contribute less to the total

brightness than low-degree ones. A typical truncation point is at degree 4, which is enough to provide a coarse description of the shape.

- The convexity of the surface. If the surface is globally nonconvex, the inversion procedure cannot obtain a description of its shape. However, an indication of nonconvexity can be obtained. Local nonconvex features, such as craters, often make no significant contributions to lightcurves and are thus no real obstacles for inversion under the convexity assumption. For globally nonconvex objects there probably is no analytical or 'numerically algorithmic' inversion scheme.

Applications to Real Lightcurve Data

In testing the inversion methods, we have used synthetic lightcurve data. A strictly convex body without albedo variegation, shown in Figure 1, was used as a test object. A shape solution obtained from 16 lightcurves at well distributed observing geometries is shown in Fig. 2. The lightcurves contained an artificial noise level of about two percent, corresponding to about 0.02 mag.

We have applied the methods to lightcurve data of 39 Laetitia and 16 Psyche (Lumme et al. 1992), which cover observation geometries well. For the former, 16 lightcurves were used (solar phase angle α ranging from 6° to 23° , and aspect θ from 41° to 151°); for the latter, 18 lightcurves ($2^\circ \leq \alpha \leq 21^\circ$ and $17^\circ \leq \theta \leq 150^\circ$), ten of which were concentrated within an aspect interval of a few degrees. The pole positions for the asteroids were computed using the spherical harmonics method (Lumme et al. 1990, 1992). Both spherical harmonics series describing the outcomes of inversion were truncated at degree 4. The scattering law used was a combination of the Lommel-Seeliger law and Lambert's law (relative contributions of 1 and 0.3, respectively, provided the best fits) with the Lumme-Bowell phase functions (Lumme et al. 1990).

The result for 39 Laetitia indicated no substantial albedo features. In the case of 16 Psyche, albedo variegations are more probable but still minor compared to the shape effects. The obtained solutions fitted the original data to an average accuracy of about two percent (0.02 mag). The shape results are shown in Figs. 3 and 4. It should be noted that the solutions are the *convex* shapes best reproducing the original data with the assumptions for the scattering law and spin vectors. In both cases nonconvexities are possible, but convex surfaces can probably describe the global shapes adequately.

References

- Kaasalainen, M., Lamberg, L., and Lumme, K. (1990a) Photomorphography of atmosphereless bodies: asteroid shapes from lightcurves. In *Asteroids, Comets, Meteors III* (C.-I. Lagerkvist, H. Rickman, B. A. Lindblad, M. Lindgren, eds.), pp. 115–118. University of Uppsala, Uppsala, Sweden.
- Kaasalainen, M., Lamberg, L., Lumme, K., and Bowell, E. (1990b) Photomorphography of atmosphereless bodies: new methods in asteroid lightcurve inversion. *Bull. Amer. Astron. Soc.*, **22**, 1113.
- Kaasalainen, M., Lamberg, L., Lumme, K., and Bowell, E. (1991a) Interpretation of lightcurves of atmosphereless bodies. I. General theory and new inversion schemes. Submitted to *Astron. Astrophys.*
- Kaasalainen, M., Lamberg, L., and Lumme, K. (1991b) Interpretation of lightcurves of atmosphereless bodies. II. Practical aspects of inversion. Submitted to *Astron. Astrophys.*
- Lumme, K., Karttunen, H., and Bowell, E. (1990) A spherical harmonics method for asteroid pole determination. *Astron. Astrophys.*, **229**, 228–239.
- Lumme, K., Karttunen, H., and Bowell, E. (1992) In preparation.

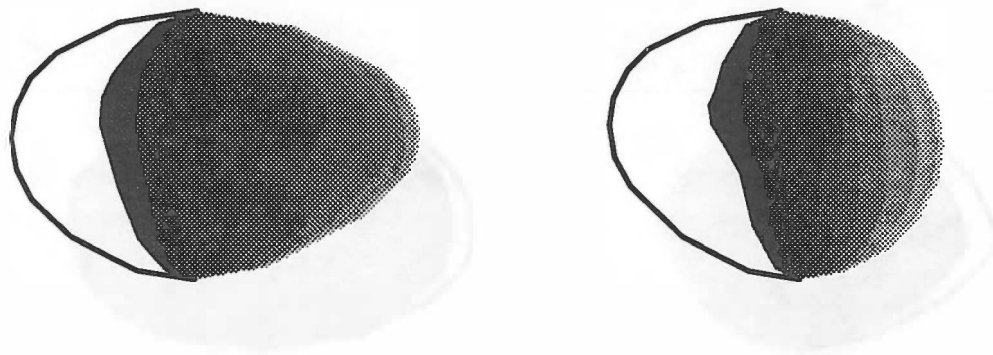


Fig. 1. An object used in testing the inversion methods, shown as viewed from two mutually perpendicular directions; the direction of the rotation axis is vertical. Synthetic lightcurves can be produced using this object. In both images the solar phase angle is 60 degrees, the illumination direction being perpendicular to the rotation axis. The shadowed part of the limb is also shown. The 'contours' on the surfaces appear because of the image producing technique. The scattering law used in the images is the Lommel-Seeliger law.

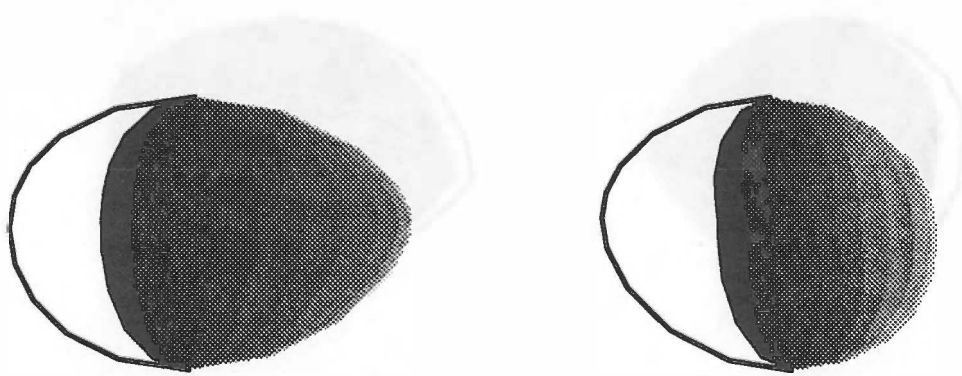


Fig. 2. A solution obtained in inversion from 16 synthetic lightcurves at well distributed observing geometries. An artificial noise level of about two percent was added to the lightcurves. The viewing/illumination directions are the same as in Fig. 1.

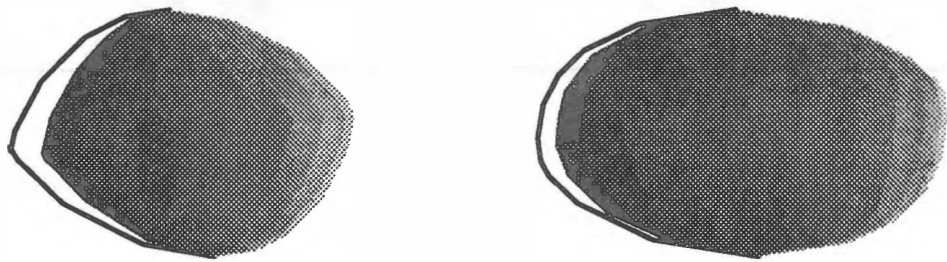


Fig.3. The shape result for 39 Laetitia. The viewing directions are as in Fig. 1; the solar phase angle is 30 degrees.

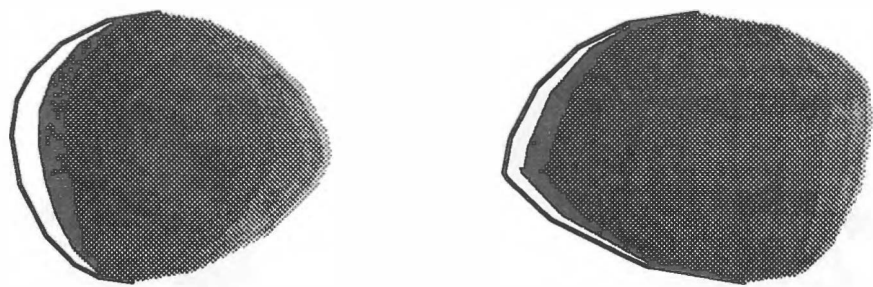


Fig. 4. The shape result for 16 Psyche, represented in the same manner as 39 Laetitia in Fig. 3.

MODIFICATION OF PRIMORDIAL ICES BY COSMIC RAYS AS SIMULATED BY CYCLOTRON IRRADIATION

R.I. Kaiser and K. Roessler

Institut für Nuklearchemie, Forschungszentrum Jülich, Postfach 1913, D-5170 Jülich, Germany

ABSTRACT

Frozen CH₄ and CH₄/Ar mixtures closed into metal cuvettes and open to the vacuum were irradiated at 15 and 77 K with 10 to 20 MeV p and ³He²⁺ ions in order to simulate the effect of cosmic rays on solid organic matter in space. Ices exposed to vacuum represent surfaces of icy systems whereas closed systems stand for bulk ices. The products were analysed by MS, SEM, RBS, ERDA, ¹H-NMR, HPLC, GC-MS, NEXAFS and FT-IR. Volatile products consisted of a mixture of low molecular species, e.g. C₂H₂, C₂H₄, C₂H₆, and long linear aliphatic and olefinic compounds. The formation of polycyclic aromatic hydrocarbons (PAHs) and related species in solid CH₄ is due to a multi center reaction within one collision cascade and is governed by energy density effects with critical linear energy transfer values L_T between 2 and 10 keV μm⁻¹. Open ices exhibit preferential hydrogen release resulting in an increased carbonisation as compared to more hydrogen rich molecules protected inside large icy bodies.

INTRODUCTION

High energetic particles may modify primordial matter in space to complex compounds and even to precursor molecules for biological evolution. Solid CH₄ has frequently been chosen as a deliberately simple model substance to study the modification of hydrocarbons (Strazzulla and Johnson 1991; Roessler 1991). However, a detailed comparison of closed and open CH₄ targets and systematic studies of dose and energy density effects has not yet been executed. Thin ice condensates in the vacuum may represent surfaces of ices whereas CH₄ targets, closed into metall cuvettes, stand for the bulk.

EXPERIMENTAL

In the actual experiments, 11.1 μm layers of CH₄ and 9.7 μm of CH₄/Ar (1:12) (CH₄: 99.999 %, Ar: 99.999 %) were condensed at 10 - 15 K on an (111) Si wafer attached to an aluminium cold finger of a bath cryostat. A second set of experiments was performed with closed targets consisting of 1 mm frozen CH₄ layers between a stainless steel backing and a Ti foil at 77 K. Both irradiation arrangements are described in detail in (Patnaik et al. 1990; Kaiser 1991). The ices were irradiated at 2*10⁻⁷ mbar with 250 nA cm⁻² beams (fluence some 10¹⁵ cm⁻²) of 17.6 MeV protons and 16.9 MeV ³He²⁺ ions of the CV 28 compact cyclotron of Forschungszentrum Jülich. Irradiation times varied from 5 to 90 min giving rise to doses between 0.07 and 16.8 eV per carbon atom. The linear energy transfer with respect to CH₄, L_T(CH₄), was increased from 161 (p//Ar/CH₄) via 1800 (p//CH₄) to 10810 eV μm⁻¹ (³He²⁺//CH₄).

RESULTS

The volatile species released from the open samples during irradiation and in the warm-up phase to 293 K were detected by a quadrupole mass spectrometer (MS). Immediately after onset of irradiation, species containing one carbon atom such as CH₂ and CH₄ appear and dominate all mass spectra. CH and CH₃ show lesser intensity. In all experiments, C₂H₄ and C₂H₂ were liberated some minutes after onset of beam. The yields of both products increased with time but were observed in lower yields than CH₂. C₂H₆ emerged later at the expense of the unsaturated species. Higher molecular-weight hydrocarbons were detected only in later stages of irradiation and in the warm-up phase in yields of approx. 1 - 2 % each. In closed cuvettes, up to 94 % of CH₄ were converted into volatiles, i.e. C₂H₂, C₂H₄, C₂H₆ and C₃H₈ (each up to 20 %) and lower yields of molecules containing up to 9 C atoms (~ 0.5 % each). Furtheron, He-irradiation of closed targets induced a formation of cycloalkanes and cycloalkenes such as cyclopropane, cyclopentane, cyclohexane and cyclohexene besides small amounts of benzene (Patnaik et al. 1990) whereas CH₄ ices

exposed to vacuum yielded mostly unsaturated species, i.e. mono- and disubstituted benzenes, 1,2-dihydro-naphthaline, 1,2,3,4-tetrahydronaphthaline and anthracene and/or phenanthrene (Kaiser et al. 1992a). The solid residues were analysed by visual inspection, optical microscopy (OM), Fourier transform infrared spectroscopy (FT-IR) in transmission at 293 K, scanning electron microscopy (SEM), Rutherford backscattering and elastic recoil detection analysis (RBS-ERDA), and near edge X-ray absorption fine structure spectroscopy (NEXAFS). In the targets exposed to vacuum CH_4 was finally converted into inhomogeneous solid residues, stable at room temperature and with a thickness of approx. 0.5 μm (Kaiser et al. 1992b). Aliphatic features dominate the IR spectra, whereas no unsaturated modes could be detected. With a method of higher sensitivity, H-C \equiv bonds were analysed by NEXAFS, manifestating their concentration between 1 μmole and 1 nmole. FT-IR half widths increasing with irradiation time (factor 3 to 4) can be interpreted as an increase in oligomerization with dose. The segregation of different phases observed by SEM and OM substantiate these results as shown in Fig. 1a-b. It coincides with an overall H:C ratio decrease from originally 4 (CH_4) to 1.4, whereas samples in closed metal cuvettes exhibit a H:C ratio of 2. This indicates an preferential hydrogen release from open targets. The soluble fraction of the residues was dissolved in CDCl_3 (99.95 %) and $^1\text{H-NMR}$, HPLC and GC-MS spectra were recorded. Concerning the open targets, up to approx. 90 % of the soluble phase consist of linear alkanes and 5 to 6 % of alkadienes, both containing up to 28 C atoms. $^1\text{H-NMR}$ spectra show 4-5 % of hydrogen located at olefinic carbon atoms. Eventually, about 0.1 % aromatic species were detected. Substituted benzenes were synthesized in all irradiated samples, but higher annulated rings and complex polycyclic aromatic hydrocarbons (approx. 0.1 %) such as naphthaline and pyrene were limited to $^3\text{He}^{2+}$ -irradiations with highest $L_r(\text{CH}_4)$. They could not be detected in proton irradiated open and closed samples, although proton irradiation doses (1.4 - 2.8 eV per C atom) were similar to those of $^3\text{He}^{2+}$ -irradiations (0.1 - 15 eV per C atom), Fig. 2.

DISCUSSION

The dualism of radiation dose and energy density and the definite differences in open and closed ice targets constitute ideal tools to discuss the experimental results. The correlation of the C_2 species in the mass spectra shows unequivocally that C_2H_2 , C_2H_4 , and C_2H_6 descend from the same precursor, i.e. excited methylcarbene [$\text{CH}-\text{CH}_3$] $^{\bullet}$ formed by insertion of hot carbon into a C-H bond of CH_4 (Stöcklin 1969). Hydrogen elimination of methylcarbene leads to ethyne. H-rearrangement yields ethene. Conspicuously, C_2H_6 is only formed at higher doses with a critical H concentration necessary to stimulate hydrogen pick-up of methylcarbene followed by deexcitation. The higher molecular species like propane were synthesized by additional radical attack and combination. The formation of a few % polycyclic aromatic hydrocarbons and partially hydrogenated analogs is governed by a critical linear energy transfer $L_r(\text{CH}_4)$ of about 2 to 10 keV μm^{-1} which induces a multi center reaction (Roessler et al. 1990), i.e. aggregation of individual insertion products of hot carbon secondaries in CH_4 and radicals such as CH , CH_2 and CH_3 in a single collision cascade. If $L_r(\text{CH}_4)$ is below this critical value, the concentration of aggregating species is too low in the activated zone to lead to the formation of complex two- or three-dimensional molecules in the relaxation phase. Thus, the accumulated radiation dose seems to be of minor importance in the synthesis of PAHs as compared to the $L_r(\text{CH}_4)$ value. Classical hot atom reactions such as insertion, abstraction and addition (Stöcklin 1969, Roessler 1991) cannot explain the synthesis of PAHs at lowest doses of 0.1 eV per C atom. Step-by-step production in overlapping cascades should contribute to a radiolytical formation only at doses exceeding some 100 eV per C atom. Thus, He-ions and heavier components of cosmic energetic particles are very effective in processing organic material. The synthesized species point to different chemical conversion of the original CH_4 in the bulk and near surfaces. Ices exposed to vacuum exhibit H_2 formation in aligned cascades and elimination from excited intermediates which can be considered as a kind of oxidation. H-outdiffusion as well as the loss of reactive intermediates is restricted in closed targets. Consequently, molecules are protected from being oxidized: saturated cyclic compounds were solely formed in closed samples. The hydrogen loss of icy surfaces results in an increasing carbonization, such as shown by the low H:C ratio of 1.4 and the formation of amorphous carbon and amorphous hydrogenated carbon in specific areas.

The linear energy transfer is the limiting factor in formation of complex molecules in space (Fig. 3). At the relatively long irradiation times at low fluxes in space, the annealing of defects and reactive species may decrease the necessary concentration for build-up of larger units.

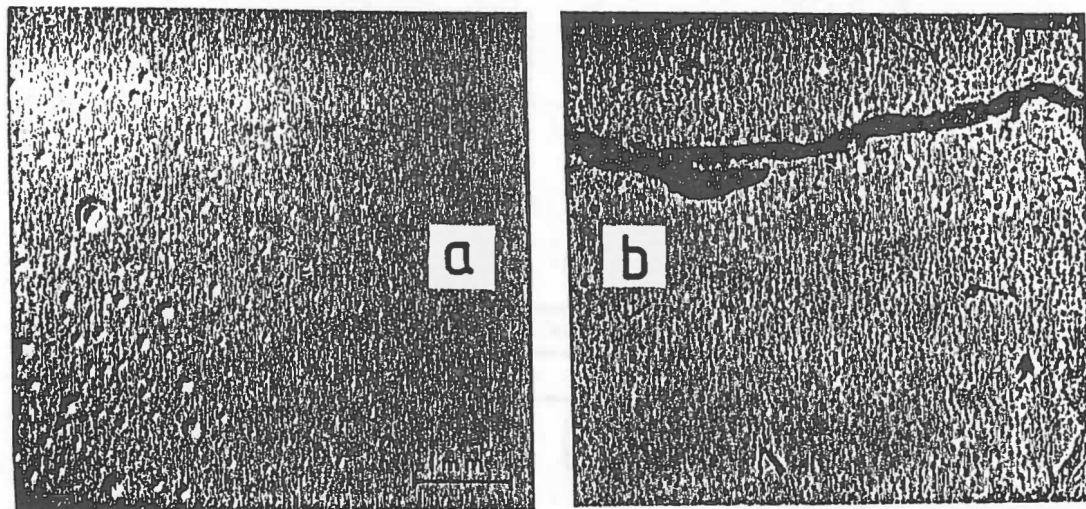
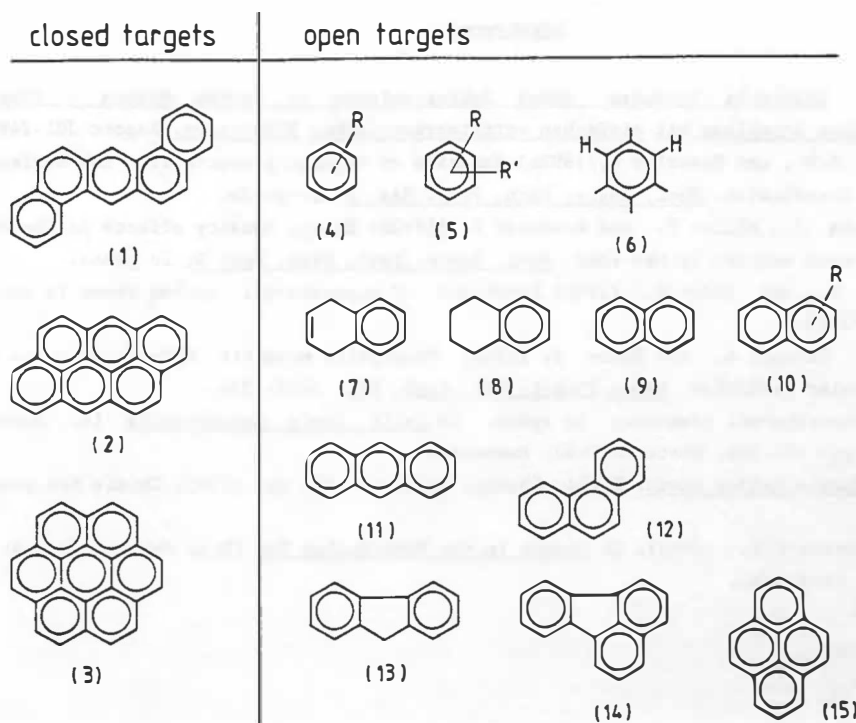


Fig.1a-b : Microscopy of residues on Si wafer. a) p//Ar/CH₄, D* = 0.07 eV/C, L_T(CH₄) = 161 eV μm⁻¹; b) ³He²⁺//CH₄, D* = 16.87 eV/C, L_T(CH₄) = 10810 eV μm⁻¹.

Fig.2 : Polycyclic aromatic hydrocarbons formed in open targets and in metall cuvettes (1:dibenzo[a,b]anthracene, 2:dibenzo[def,mno]chrysene, 3:coronene, 4-6:mono-, di and tetrasubstituted benzenes, 7:1,2-dihydronaphthaline, 8:1,2,3,4-tetrahydronaphthaline, 9:naphthaline, 10:alkylnaphthaline, 11:anthracene, 12:phenanthrene, 13:fluorene, 14:fluoranthene, 15:pyrene).



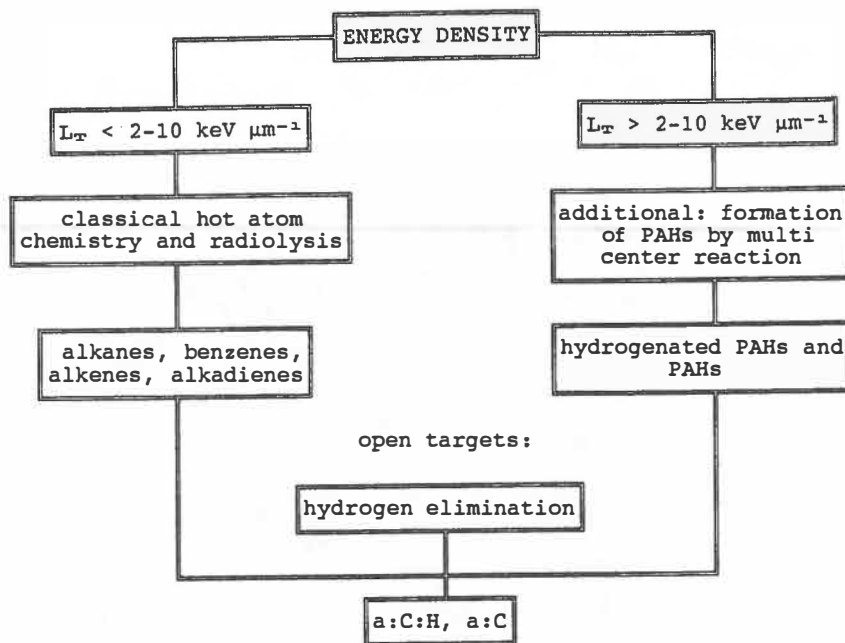


Fig.3 : Mechanisms of modification of pure CH_4 and synthesized species under MeV particle irradiation.

ACKNOWLEDGEMENTS

The authors thank Prof. G. Götz and Mr. P. Müller, Jena for recording and helpful discussions of RBS-ERDA spectra. They are indebted to the CV 28 cyclotron crew of Forschungszentrum Jülich for irradiations, Prof. J. Lauterwein and Mrs. K. Busse, Münster for recording the NMR spectra, Dr. E. Wallura, Jülich for SEM measurements, and Prof. G. Grunze, Heidelberg for NEXAFS spectra.

REFERENCES

- Kaiser R.I. (1991) Chemische Prozesse durch Zyklotronionen in festem Methan - Simulation der Wechselwirkung kosmischer Strahlung mit einfachen extraterrestrischen Eiskörpern. Report JüI-2492, 130 pp.
- Kaiser R.I., Mahfouz R.M., and Roessler K.(1992a) Emission of organic products from the surface of frozen methane under MeV ion irradiation. Nucl. Instr. Meth. Phys. Res. B, in press.
- Kaiser R.I., Lauterwein J., Müller P., and Roessler K. (1992b) Energy density effects in the formation of organic residues in frozen methane by MeV ions. Nucl. Instr. Meth. Phys. Res. B, in press.
- Patnaik A., Roessler K., and Zádor E. (1990) Reactions of suprathermal carbon atoms in solid methane. Radiochim. Acta, **50**, 75-85.
- Roessler K., Eich G., Patnaik A., and Zádor E. (1990) Polycyclic aromatic hydrocarbons via multicenter reactions induced by solar radiation. Lunar Planet. Sci. Conf. XXI, 1035-1036.
- Roessler K. (1991) Suprathermal chemistry in space. In Solid State Astrophysics (E. Bussoletti and G. Strazzulla, eds.), pp. 197-266, North Holland, Amsterdam.
- Stöcklin G. (1969) Chemie heißer Atome. Verlag Chemie, Weinheim. 283 pp. (1972) Chimie des atomes chauds, Masson et Cie, Paris.
- Strazzulla G. and Johnson R.E. (1991). In Comets in the Post-Halley Era (R.L. Newburn Jr., et al., eds), 1, pp. 243-275 Kluwer, Dordrecht.

METEOR FIREBALL SOUNDS IDENTIFIED

Colin Keay

Physics Department, University of Newcastle, NSW.

Abstract:

Sounds heard simultaneously with the flight of large meteor fireballs are electrical in origin. Confirmation that Extra/Very Low Frequency (ELF/VLF) electromagnetic radiation is produced by the fireball has been obtained by Japanese researchers. Although the generation mechanism is not fully understood, studies of MOPR and other fireball data indicate that interaction with the atmosphere is definitely responsible and the cut-off magnitude of -9 found by Astapovich for sustained electrophonic sounds is supported by theory. Brief bursts of ELF/VLF radiation may accompany flares or explosions of smaller fireballs, producing transient sounds near favourably placed observers. Laboratory studies show that mundane physical objects can respond to electrical excitation and produce audible sounds. Reports of electrophonic sounds should no longer be discarded. A catalog of over 300 reports relating to electrophonic phenomena associated with meteor fireballs, aurorae and lightning has been assembled. Many other reports have been catalogued in Russian by Bronshten. These may assist the full solution of the similar long-standing and contentious mystery of audible auroral displays.

Instantaneously audible sounds associated with the flight of large meteor fireballs were first described by the Chinese in 817 AD (Astapovich 1951, LaPaz 1958). Edmund Halley (1719), in his description of a very large meteor fireball seen over England on the evening of 1719 March 19, was one of the first to distinguish the sounds produced instantaneously by a distant meteor fireball from the delayed sounds propagated acoustically. He wrote: "Of several Accidents that were reported to have attended its Passage, many were the effect of pure Fantasy; such as the hearing it hiss as it went along, as if it had been very near at hand:....But what is certain, and in no way to be disputed, is the wonderful Noise that follow'd its Explosion".

More than half a century later, in 1783, another very large fireball passed over England and the Secretary of the Royal Society, Charles Blagdon (1784), attributed the instantaneous sounds to "an affrighted imagination, or an illusion produced by the fancied analogy of fireworks." But because of the considerable testimony in support of such sounds, he decided that he "would leave it as a point to be cleared up by future observers".

In the year 1784 a physical solution was impossible: Auguste Coulomb had not yet developed his famous electrostatics law, and it was a further century before Heinrich Hertz demonstrated the existence of radio waves. Even when electrical discharges and radio waves became well understood, the solution remained elusive. The only evidence was anecdotal and the incidence of the sounds was highly capricious, sometimes being heard by only one or two members of a group of observers standing close to each other.

Leading meteor investigators in the first half of the present century, such as W.F. Denning (1907, and several other references) and C.C. Wylie (1932), were convinced that the anomalous sounds from meteor fireballs were purely psychological in origin, despite some well attested cases where the sounds clearly preceded the optical sighting of the fireball.

A Texas engineering professor, J.A. Udden (1917a), came rather close to the answer when he discussed the detailed observations which he collected of a large fireball. After analysing nine reports of instantaneous sounds, he concluded "If these observations are not subjective, the cause of the sound

may perhaps be sought in ether waves that, on meeting the earth, or objects attached to the earth, such as plants or artificial structures, are in part dissipated by being transformed into waves of sound in the air." This conclusion was evidently prompted by one observer who "seems to refer this sound to objects attached to the ground." (Udden 1917b).

As recently as 1979, leading meteor specialists still invoked a psychological explanation for the sounds, with the result that many potentially illuminating observations of the phenomenon were ignored and rejected from the literature (except in the Soviet Union). One revealing report of instant fireball sounds by a Cornell University radiophysicist eventually surfaced seven years after the event, in the New York State Journal of Medicine! (Ingalls 1967). The observer, Dr Bruce Hapke, who was with his wife, reported "The hissing and crackling noises were definitely associated with the meteor, although we cannot be sure whether or not they appeared to be coming from the meteor or from all around us. However, it can be stated with certainty that they did not appear to come from behind the meteor as they would have, had the object been a high-flying jet plane."

On 1978 April 7, at 4.44 a.m., a magnitude -16 fireball passed over eastern New South Wales (Keay 1980a), and hundreds of observers swamped the news media with reports. Of 36 reports investigated, no fewer than eight included sounds heard simultaneously with the fireball's flight, and a further two people heard sounds prior to sighting the fireball, or its glare.

A careful investigation of these reports (Keay 1980b) led to the following conclusions:

- (i) Large fireballs produce electrical and/or electromagnetic energy in the Extra and Very Low Frequency (ELF/VLF) region of the spectrum. Previous spectrum searches had proved negative (Hawkins 1958a), leading to the comment "Meteors therefore show a surprisingly low efficiency in converting kinetic to radio energy" (Hawkins 1958b). However the ELF/VLF region of the spectrum was not examined by Hawkins during his search.
- (ii) The generation of ELF/VLF energy by the fireball is at least partially explainable as the release of energy stored as "magnetic spaghetti" when the geomagnetic field is trapped and scrambled in the turbulent plasma wake of the fireball. Bronshten (1983) has confirmed that through this mechanism bright fireballs may produce radiated power levels of the order of kilowatts. For such a fireball the kinetic energy dissipation rate exceeds ten gigawatts.
- (iii) The ELF/VLF energy is directly transduced into acoustic form by mundane objects which happen to be on or in the close vicinity of fireball observers. Early laboratory trials showed that rapidly varying electric fields produced rustling sounds audible by test subjects with appropriate hair styles or wearing glasses (Keay 1980c). Later laboratory tests showed that transduction by mundane artifacts, such as household items, and plant foliage could generate acoustic sound levels of up to 60 DbA from intense electric fields varying at audible frequencies (Keay and Ostwald 1991).

At any given location, the rare occurrence of large meteor fireballs makes it rather impractical to set up suitable instrumentation to record their ELF/VLF emissions. In the mid-1980s, after reports emerged of hissing sounds being heard during space shuttle re-entries over the American Midwest, attempts were made to tape them (Keay 1985) but this effort came to an abrupt end when the Challenger was lost. It will be interesting to try again, since overland shuttle re-entries have recently resumed for some missions. The incentive for doing so has now diminished, because crucial records of instantaneous fireball sounds have emerged from Japan.

Three cooperating groups in Japan have placed the emission of ELF/VLF energy from meteor fireballs beyond doubt (Watanabe, Okada and Suzuki 1988). For an exceptionally bright Perseid fireball they managed to obtain simultaneous photographic and radio records, together with an electrophonic sound report from a member of the photographic team. The radio emission lasted less than a fifth of a second, coincident with maximum light, when the fireball flared to a maximum brightness of -7 magnitude (Figure 1).

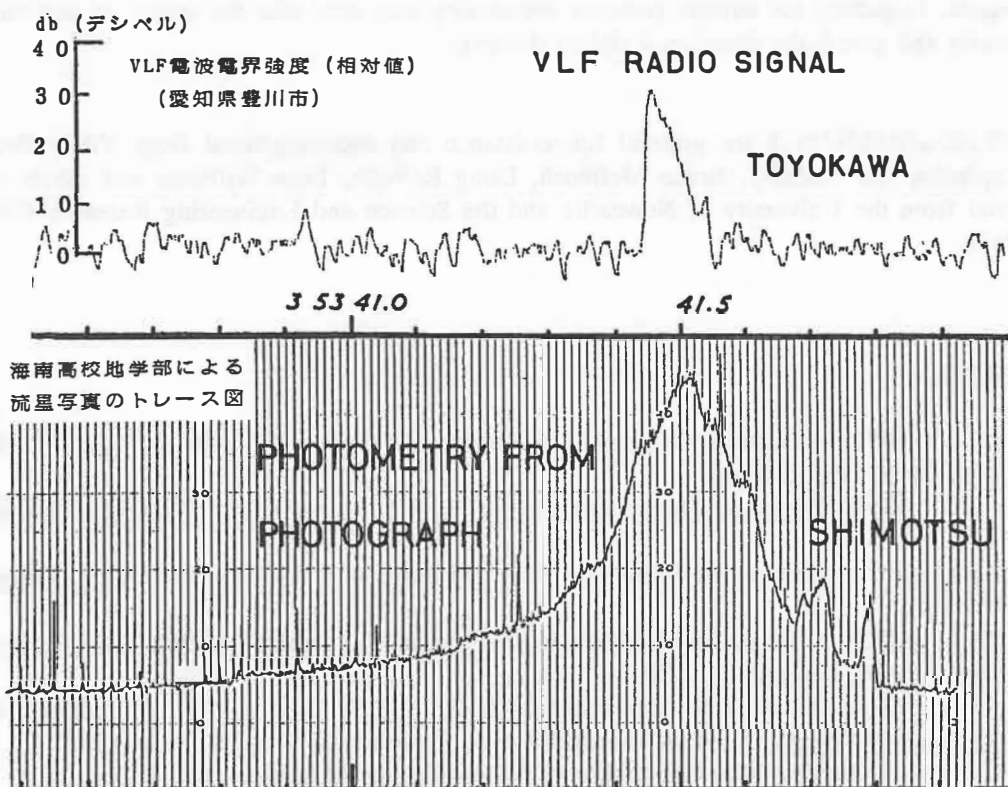


FIGURE 1 The Very Low Frequency radio signal recorded at Toyokawa, Japan, over 100 kilometres from a bright Perseid fireball photographed simultaneously from Shimotsu (courtesy of T. Watanabe and K. Suzuki).

Longer duration electrophonic sounds arise only from meteor fireballs brighter than -9 magnitude, according to leading Soviet meteor researcher, I.S. Astapovich (1958), who reached this empirical conclusion on the basis of an extensive body of observational evidence. A study of fireball light curves, obtained principally from the Canadian Meteorite Observation and Recovery Program (MORP) (Halliday, et al 1989, and personal communication), has verified Astapovich's result (Keay 1991b). The study indicates that the production of radio emission is dependent on the fireball penetrating the atmosphere to the point where continuum flow conditions prevail, at which stage a shock front is formed and turbulence arises in the plasma wake of the fireball.

The realisation and demonstration that intense radio emissions at audio frequencies are directly transducible into sound has provided an explanation for the immediate audibility of lightning strikes under favorable conditions. This may also hold for audible clicks derived from the electromagnetic pulse produced by a nuclear explosion. There is also the strong likelihood that the audibility of intense aurorae has a similar basis, but in this case the evidence for sufficient ELF/VLF electromagnetic or purely electrical emissions from aurorae remains very tenuous and is a challenge to researchers in that field (Keay 1990).

To ameliorate the scarcity of observational data on these phenomena, a catalog of over 300 reports of instantaneous audible sounds associated with meteor fireballs, lightning and aurorae has been assembled and is being expanded as data comes to hand. In a parallel endeavour, many reports have recently been catalogued in Russian by Bronshcen, et al (1988).

A last comment. The advent of a viable physical explanation for the so-called "anomalous sounds" from meteor fireballs, and its acceptance, has led to a dramatic upsurge in the transmission of reports of these sounds (Keay 1991a). Hitherto such reports had been shunned and, since the scathing verdicts

of Denning and Wiley, only rarely mentioned in the literature. The same is still true for reports of auroral sounds. Hopefully the auroral research community may now take the matter of auroral sounds more seriously and give it the attention it rightly deserves.

ACKNOWLEDGEMENTS: I am grateful for assistance and encouragement from Vitaly Bronshten, Zdenek Ceplecha, Ian Halliday, Bruce McIntosh, Doug ReVelle, Iwan Williams and others. Support was received from the University of Newcastle and the Science and Engineering Research Council of Great Britain.

REFERENCES:

- Astapovich I.S. (1951) Acoustical phenomena occurring simultaneously with the flight of Bolides. *Meteoritika*, **9**, 71-101 (in Russian).
- Astapovich I.S. (1958) *Meteoric Phenomena in the Earth's Atmosphere*, Fizmatgiz, Moscow (in Russian).
- Blagdon C. (1784) An Account of Some late fiery Meteors; with Observations. *Phil. Trans. Roy. Soc.*, **74**, 201-232.
- Bronshten V.A. (1983) A Magnetohydrodynamic Mechanism for Generating Radio Waves by Bright Fireballs. *Solar System Research*, **17**, 70-74.
- Bronshten V.A., Grebennikov V.S. and Rabinski D.D. (1988) Catalog of Electrophonic Bolides. *Collection of Scientific Works*, Siberian Division, USSR Academy of Sciences (in Russian).
- Denning W.F. (1907) Audible Meteors. *Symons's Meteorological Magazine*, **42**, 10-11.
- Halley E. (1719) An Account of the Extraordinary Meteor seen all over England, on the 19th of March 1719. *Phil. Trans. Roy. Soc.*, **30**, 978-990.
- Halliday I., Blackwell A.T. and Griffen A.A. (1989) Detailed records of many Unrecovered Meteorites in Western Canada for which further searches are recommended. *J. Roy. Astron. Soc. Canada*, **83**, 49-80.
- Hawkins G.S. (1958a) A Search for Radio Emission from Meteors. *Ap. J.*, **128**, 724-726.
- Hawkins G.S. (1958b) Radio Noise from Meteors. *Nature*, **181**, 1610.
- Ingalls C.E. (1967) Sensation of Hearing in Electromagnetic Fields. *New York State Jour. Medicine*, **67**, 2992-2997.
- Keay C.S.L. (1980a) The 1978 New South Wales Fireball. *Nature*, **285**, 464-466.
- Keay C.S.L. (1980b) Anomalous Sounds from the Entry of Meteor Fireballs. *Science*, **210**, 11-15.
- Keay C.S.L. (1980c) Audible Sounds Excited by Aurorae and Meteor Fireballs. *J. Roy. Astron. Soc. Canada*, **74**, 253-260.
- Keay C.S.L. (1985) In Quest of Meteor Sounds. *Sky and Telescope*, **70**, 623-625.
- Keay C.S.L. (1990) C.A. Chant and the Mystery of Auroral Sounds. *J. Roy. Astron. Soc. Canada*, **84**, 373-382.
- Keay C.S.L. and Ostwald P.M. (1991) A Laboratory Test of the Production of Electrophonic Sounds. *J. Acous. Soc. Am.*, **89**, 1823-1824.
- Keay C.S.L. (1991a) Physics, Psychology and Respectability. *Scientometrics*, **22**, 341-345.
- Keay C.S.L. (1991b) Electrophonic Sounds from Large Meteor Fireballs. *Meteoritics*, Submitted for publication.
- LaPaz L. (1958) The Effects of Meteorites upon the Earth. *Adv. Geophys.*, **4**, 217-350.
- Udden J.A. (1917a) The Texas Meteor of October 1, 1917. *Univ. Texas Bulletin*, No. 1772, 45-47.
- Udden J.A. (1917b) A Texas Meteor. *Science*, **46**, 616-617.
- Watanabe T., Okada T. and Suzuki K. (1988) Meteors and Radio Waves, *HAM Journal* (Japan), No. **54**, 109-115 (in Japanese).
- Wylie C.C. (1932) Sounds from Meteors. *Popular Astronomy*, **40**, 289-294.

ON THE ASTEROIDAL JET-STREAM FLORA A

Jozef Klačka

Department of Astronomy and Astrophysics MFF
Comenius University, Mlynská dolina F1
CS-842 15 Bratislava
Czecho-Slovakia

Abstract

The problem of the virtual existence of the (1) Flora I separated from the rest of the Flora family and (2) jet-stream Flora A (Alfvén 1969) is discussed in connection with the observational selection effects. It is shown that observational selection effects operate as a whole and can be important in incomplete observational data set.

1 Introduction

The virtual existence of the most significant asteroidal jet-stream Flora A is fully explained as a consequence of observational selection effects (Klačka 1991). The aim of this paper is to point out the continuous presence of observational selection effects in incomplete set of observational data (e. g., many faint asteroids are members of these data). We discuss the problem of the existence of the jet-stream Flora A and structure of the Flora family in E - I (i. e. proper eccentricity - the sine of proper inclination, Brouwer and van Woerkom 1950) diagram, for this purpose.

2 Flora I and asteroidal jet-stream Flora A

The situation for the Flora family in E - I diagram for two data sets is depicted in Fig. 1. Fig. 1a represents Flora family selected from the first 1563 numbered asteroids (Alfvén 1969), Fig. 1b represents the current status (Klačka 1987). We see that the gap separating Flora I from the rest of Flora family occurring in Alfvén's data does not exist in reality. The explanation of the situation in 1969 is natural: the virtual separation of Flora I from Floras II - IV is simply due to the observational selection effects.

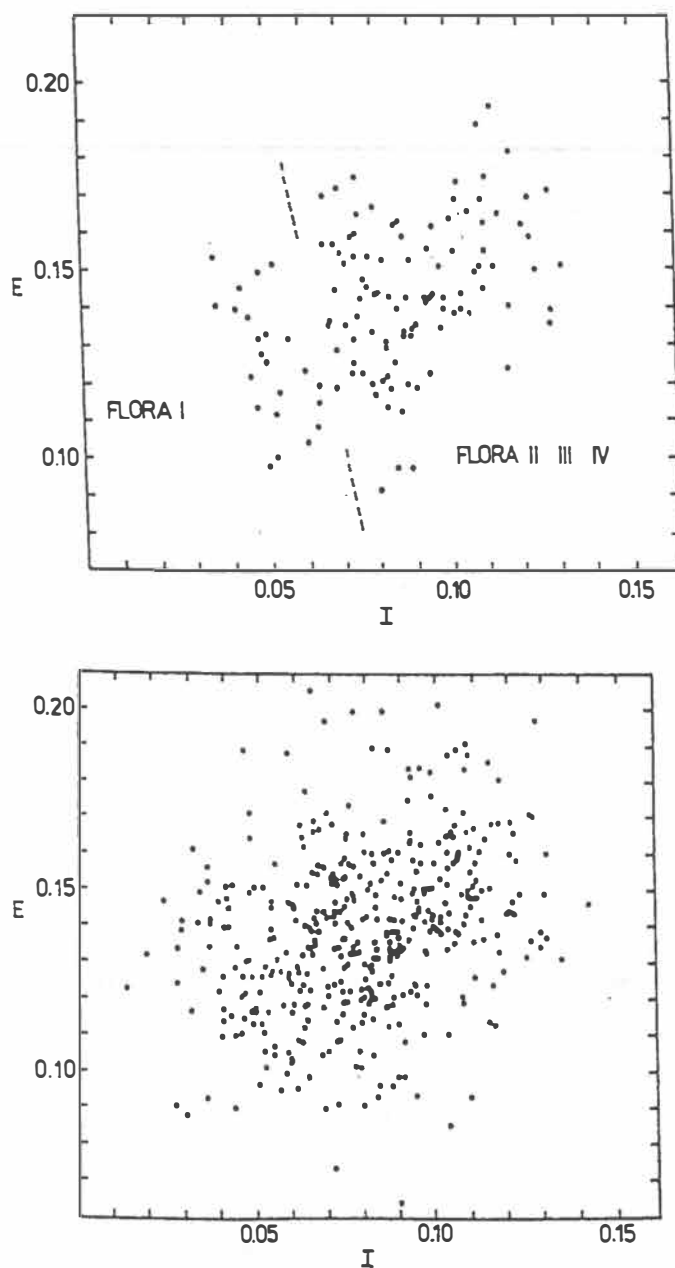


Fig. 1 Flora family in E - I diagram.

- a) According to Alfvén (1969), upper.
- b) According to Klačka (1987), lower.

We can summarize: Observational selection effects were important in observational data used by Alfvén (1969). They caused the virtual existence of (1) the gap separating the Flora I from the rest of the Flora family, (2) the asteroidal jet-stream Flora A.

At present there exists no gap in E - I diagram for Flora family. It, however, does not mean that no observational selection effect can be found in observational data. We perform the following "Gedankenexperiment" for a proof. Let us introduce the virtual gap (line) in Fig. 1b corresponding to the line presented in Fig. 1a. We can look for asteroidal jet-streams in virtual Flora I obtained by this procedure. What is the result? We find asteroidal jet-stream as Alfvén in 1969 (but less significant). How can we understand it? (If you want, you can solve this problem as an exercise. Hint: see Klačka 1991.) Virtual Flora I is formed mainly by asteroids with small inclinations, if observational selection effects are important. This explains the concentration of asteroids in proper element Θ_1 (Klačka 1991). If we take into account observational selection effects important for discoveries of faint asteroids and manifested in Π_1 (Klačka 1991), one should expect the existence of virtual jet-stream. Of course, the significance of such virtual jet-stream decreases with increasing number of numbered asteroids used (incompleteness of the set which manifests itself in the distribution of asteroids according to the Π_1 - and Θ_1 -elements clearly becomes less relevant as we enlarge the considered set).

In conclusion we can say that the virtual existence of Flora I is generated by the observational selection effects manifested in the incomplete data set mainly due to preference of asteroids with small inclinations. The same observational selection effects and some others (closely related to the formers), which manifest themselves in the distribution of asteroids according to the Π_1 -element, cause the virtual existence of the jet-stream, then. All this can be put down in a logical scheme:

$$A \Rightarrow B \Leftrightarrow \text{non}B \Rightarrow \text{non}A ,$$

where:

A = The gap, separating Flora I from the rest of Flora family, exists (or, is artificially created in E - I diagram),

B = Jet-stream (Flora A) exists,
if observational selection effects are important.

Acknowledgement

The author would like to thank Dr. M. Saniga for a kind help during the final stage of the manuscript's preparation.

References

Alfvén H. (1969) Asteroidal jet-streams. *Astrophys. Space Sci.*, **4**, 84-102.

- Brouwer D. and van Woerkom A. J. J. (1950) The secular variations of the orbital elements of the principal planets. Astron. Papers Amer. Ephemeris, 13, 83-107.
- Klačka J. (1987) Flora Family. Graduate Thesis, Comenius University, Bratislava. (in Slovak)
- Klačka J. (1991) Asteroidal jet-stream Flora A. Earth, Moon and Planets, in press.

*Current address: Astronomical Institute, Slovak Academy of Sciences, CS-059
60 Tatranská Lomnica, Czechoslovakia.*

ASTEROID PROPER ELEMENTS AND SECULAR RESONANCES: PROGRESS REPORT

Z. Knežević ‡§ and A. Milani §†

‡ Astronombska opservatorija, Volgina 7, 11050 Beograd, Yugoslavia

§ Dipartimento di Matematica, Università di Pisa, Via Buonarroti 2, I-56127 Pisa, Italy

† Observatoire de Paris, 5, Place J. Janssen, 92195 Meudon Cedex, France

In a series of papers (e.g. Knežević, 1991; Milani and Knežević, 1990; 1991) we reported on the progress we were making in computing asteroid proper elements, both as regards their accuracy and long-term stability, and the efficiency and “intelligence” of our software. At the same time, we studied the associated problems of resonance effects, and introduced the new class of “nonlinear” secular resonances; we determined the locations of these secular resonances in proper-element phase space and analysed their impact on the asteroid family classification. Here we would like to summarize the current status of our work and possible further developments.

Improved proper elements

The basis for our studies is an analytical theory of asteroid secular perturbations developed by Yuasa (1973), corrected and completed by Knežević (1988, 1989), and further improved by ourselves (Milani and Knežević, 1990; 1991). This theory is incorporated in a fully automated and reasonably efficient software system that performs a complex sequence of operations, including an iterative procedure, and allows the production of large catalogues of proper elements. The proper elements are tested for accuracy by means of a conceptually simple, but technically delicate procedure based on their operational definition: we numerically integrate orbits of a number of representative asteroids (family heads, dynamically peculiar objects), compute the corresponding time series of proper elements, and measure the deviation of these elements from constancy. The validity of the tests for the entire asteroid population and for time spans much longer than those covered by numerical integrations cannot be rigorously proved, but the very existence of some accuracy estimates is already an essential improvement (see Zappalà et al., 1990 for the use of our accuracy estimates in assessing the reliability of family classification) and the results are already almost always good enough (see below) for family identification.

The current version (release 5.7) of our software differs from the previous one ((4.2), discussed in Milani and Knežević, 1990) in several respects. The basic theory is the same (for a discussion of the iterative procedure see Milani, 1990), but the dynamical model of the solar system used in the current version is significantly more complete: we have included all the terms we could compute by a straightforward generalisation of the procedure and which could be significant for at least some asteroids; the procedure is now flexible enough to accommodate different choices of the model for different applications. Laplace, Leverrier and Yuasa coefficients are computed by means of a more consistent and

reliable algorithm, an additional quality code based on the convergence of proper elements is defined, a secular resonance monitoring has been introduced, and the data set increased by $\simeq 500$ asteroids (up to No. 4722). The most important differences between the previous and current versions are summarized in Table 1. (note that version 5.6 pertains to the model used for the accuracy tests without the inner planets).

Table 1

Version	5.6	5.7	4.2
Planets affecting linear secular frequencies	5-8	2-8	5-6
Planets affecting forced terms	5-8	5-8	5-6
Planets included to second order	5-6	5-6	5
Planets included to degree 4	5-6	5-6	5
Secular frequencies in degree 4 (perihelia)	5,6	5,6	5,6
Secular frequencies in degree 4 (nodes)	6,7	6,7	6

Tests of the stability of the proper elements

A total of 22 asteroids representative of the most populated regions of the main belt have been chosen for tests of the accuracy of the theory, and their orbits, as a massless body attracted by the Sun and the four outer planets (solved a full 5-body gravitational problem), have been numerically integrated for a time span of 400,000 yr. For 10 test bodies results were found to be fully satisfactory, with rms changes in the proper elements less than 5×10^{-5} AU for a , less than 2.4×10^{-3} for e and less than 0.9×10^{-3} for $\sin I$. Although there is an obvious decrease of the accuracy with increasing inclination, the stability of proper elements was always satisfactory and in particular good enough for the identification of asteroid families. The most important unremoved oscillation of the proper elements in these cases was one with frequency $g + g_5 - 2g_6$ (in five cases it is responsible for more than 80% of the spectral power of the proper eccentricity changes), due to the fact that the forced term with this frequency was not accounted for by the theory (future versions of the theory will have to take account of this term and possibly for other similar ones).

For five test asteroids the results were inferior because of the nearby low-order mean motion resonances. Most of these objects have proper semimajor axes significantly less stable than the objects in the previous group, and poorly determined secular frequencies; nevertheless, their proper eccentricities and inclinations were of satisfactory, or even high, accuracy. From the point of view of family identification the most significant effect of the resonance pertains to the difficulty in identifying all the family members in the Themis family.

Four test asteroids, located in the inner part of the main belt ("Flora region"), are affected by the strongest secular resonance $g - g_6$. Therefore, the formal errors of the proper eccentricities and inclinations are substantial, although, for example, the error in the proper eccentricity of 8 Flora itself is much smaller than in the previous version of the theory

(due to the fact that the fundamental frequencies are determined with comparatively high precision). Typically, variations of all three proper elements are quite irregular, comprising several oscillations, some with periods in excess of 400,000 yr. We estimate that to be safe from the violent resonant perturbations and with proper elements reliable enough for the purpose of the asteroid family classification, the orbits must depart from the resonance (in terms of the frequency) by at least $\sim 4 \text{ arcsec/yr}$.

The last group of test asteroids (three of them) consists of bodies for which a nonlinear resonance warning was issued by our secular resonance monitoring routine. Small divisors representing combinations of four frequencies affect computation of proper elements in a significant way, although the slices in phase space in which these resonances are effective are very narrow. Removal of the resonant terms and the use of an "adapted" theory results in a remarkable improvement of the accuracy of proper elements.

On the basis of the above results we can conclude that over the time span covered by our integration and probably even somewhat longer (say, a few million years), the proper elements are in general stable to an accuracy which is better than required for family identification purpose. There are, in contrast, quite a few "exceptions" for which, unfortunately, this is not completely true or even not at all true: objects in the high inclination zones, slices near the main mean motion resonances, near the $g - g_6$ secular resonance, near the $g + g_5 - 2g_6$ resonance because of the missing forced term, and even near other nonlinear secular resonances. Furthermore, no rigorous conclusion can be proven on the stability of the proper elements over time spans much longer than that covered here, since the number of resonances concerned becomes much larger. The above list of problem cases determines the future directions of our work; all of them are understood and most of them can be solved, but at great effort.

Nonlinear secular resonances

To understand the nonlinear secular resonances and their impact to the family classification, we used our proper-element generation software to study the dynamical behaviour of orbits in a resonance of this new class: we modified the software so as not to remove the critical term, and manufactured "adapted" proper elements for all the asteroids within a box defining the family. For two families—one large (Eos) and one small (Lydia)—affected by the $g + s - g_6 - s_6$ secular resonance, the position of the libration region (as inferred from a time series of proper elements freed from the other important secular variations) has been compared with the position of the family.

In the case of the Eos family we have tested seven family members for 5.4 Myr, and found libration of the critical argument for some of them; for asteroid 339 Dorothea we found a maximum libration amplitude of about 108° , and proper eccentricity and proper sine of inclination oscillations of amplitudes 5.9×10^{-3} , and 2.6×10^{-3} , respectively. The family head—221 Eos—was found also to be in deep resonance, although amplitudes of libration and proper elements are significantly smaller than in the previous case. The critical argument of the $g + s - g_6 - s_6$ resonance slowly circulates for the other tested family members, for two of which, however (1075 Helina and 320 Katharina), the critical argument of the nearby $g + s - g_5 - s_7$ resonance librates. This libration of one critical argument is synchronized with the circulation of the other in a super resonance, or secondary resonance

between two resonances; the libration centre moves very little for 1075 Helina, slowly wanders for 320 Katharina. Note that, apart from these asteroids, this kind of resonance is known to occur for only one other body in the solar system: the planet Pluto (Milani et al., 1989). The overall effect of the secular resonances on the Eos family appears not to be very important since the widths of both resonances are significantly smaller than the spread of proper elements within the family; therefore, the classification of an asteroid as a family member is not vitiated by the resonance, unless the singularity occurring exactly at the resonance surface results in completely wrong proper elements (in the case of the Eos family, however, we found that only one of more than 200 family members is missing from the Zappalà et al., 1990 list for this reason).

The 110 Lydia family has been studied for the effect of the nonlinear resonance on a small family. According to Zappalà et al. (1990) this is a minor family, consisting of six members, which does not survive the reliability test against the error in proper elements. Because of the lower accuracy of the proper elements near the resonance, some family members are removed by the statistical reliability tests and too few were left for the family to be significant. However, the use of an adapted theory (with resonant term not removed from the osculating elements), quality codes and resonance warnings allowed us to correctly identify this family and to reliably reconstruct its membership. Thus, we found that at least two additional asteroids probably belong to the Lydia family, and that the family is statistically robust provided special care is taken because of the peculiar dynamical behaviour of its members.

References

- Knežević, Z. (1988) Asteroid mean orbital elements. *Bull. Astr. Obs. Belgrade* **139**, 1–6.
- Knežević, Z. (1989) Asteroid long-periodic perturbations: the second order Hamiltonian. *Celestial Mechanics* **46**, 147–158.
- Knežević, Z. (1991) Asteroid long-periodic perturbations: derivation of proper elements and assessment of their accuracy. *Astron. Astrophys.* **241**, 267–288.
- Milani, A. (1990) Perturbation methods in celestial mechanics. In *Les méthodes modernes de la mécanique céleste* (D. Benest and C. Froeschlé, eds.) pp. 109–150, Editions Frontière, Gif-sur-Yvette.
- Milani, A., A. M. Nobili, and M. Carpino (1989) Dynamics of Pluto. *Icarus* **82**, 200–217.
- Milani, A., and Z. Knežević (1990) Secular perturbation theory and computation of asteroid proper elements. *Celestial Mechanics* **49**, 247–411.
- Milani, A., and Z. Knežević (1991) Asteroid proper elements and secular resonances. *Icarus*. submitted.
- Yuasa, M. (1973) Theory of secular perturbations of asteroids including terms of higher order and higher degree. *Publ. Astron. Soc. Japan* **25**, 399–445.
- Zappalà, V., A. Cellino, P. Farinella, and Z. Knežević (1990) Asteroid families I: identification by hierarchical clustering and reliability assessment. *Astron. J.* **100**, 2030–2046.

INTEGRATED SOFTWARE PACKAGE "STAMP" FOR MINOR PLANETS

Kochetova O.M., Shor V.A., Institute of Theoretical Astronomy of the USSR Academy of Sciences, Naberezhnaya Kutuzova 10, St. Petersburg, 191187 USSR.

Abstract. The integrated software package STAMP elaborated for rapid and exact reproducing the tables of the year-book "Ephemerides of Minor Planets" and solving the typical problems connected with the use of the year-book is described.

The year-book "Ephemerides of Minor Planets" (EMP) is a publication widely used in many astronomical institutions of the world. It contains all necessary information on the orbits of all numbered minor planets and the astronomical coordinates of each planet during certain period suitable for its observations.

In accordance with the resolution of IAU the year-book is prepared and published by the Institute of Theoretical Astronomy of the USSR Academy of Sciences (ITA). The research workers of a number of astronomical institutions of different countries contribute to preparation of the data for some tables of EMP.

The use of data from EMP in astronomical practice is rather varied, but it is possible to indicate the main points of it :
a) planning the astronomical and astrophysical observations of minor planets and making preparation for them.
b) comparing results of observations with predicted values of coordinates, brightness and other data.
c) investigation of structure of the asteroid belt.

The problems connected with above points are solved with the aid of ten following tables of the year-book :

1. Information on new elements
2. Elements
3. Lost minor planets
4. Osculating elements of perturbing planets
5. Minor planet lightcurve parameters
6. Opposition dates
7. Ephemerides
8. Ephemerides of some unusual planets
9. Status of minor planet observations
10. Antisun and Moon

The principal tables are those of 'Elements', 'Opposition dates' and 'Ephemerides'. The table of elements contains the osculating elements of 4646 numbered planets (EMP for 1992, see Batrakov, 1991) and their photometric parameters. The data of the table are used as the initial ones for calculation of ephemerides and for statistical study of minor planets, their distribution in space and/or the frequency distributions of their orbital elements and some functions of them.

The table "Opposition dates" determines the time most suitable for observations of each planet.

The table "Ephemerides" contains ephemeris data with ten day step for several thousand minor planets having the opposition within current year. Every ephemeris embraces 70 days interval

in the vicinity of opposition and gives calculated positions and other data taking into account the perturbations from all perturbing planets.

The usual practice of using EMP data is based on solving the elementary logical problems and carrying out such actions as interpolating, selecting, sorting and other more or less time-taking operations.

Personal computers make it possible to facilitate the use of EMP for solving majority of the problems widely met in practice (Shor, 1990). The software package "STAMP" seems to be decided step in this direction.

STAMP incorporates the elements of data base as well as program and graphics packages.

When elaborating STAMP, the principle of the "electronic book" was applied.

All the data from ten tables of EMP are inputted in the internal data base of the system as they are published in the year-book. In this way speedy and exact reproduction of the tables is ensured.

Apart from straightforward reproduction of the tables, the following potentialities are inherent in STAMP.

1. Movement along table forward and backward; outputting the table at printer or its recording in file (it is equally valid for any selection from table).
2. Selecting from table in conformity with some condition or combination of conditions imposed on elements of the Table or on certain functions of the elements.
3. Calculating some additional widely used functions of the orbital elements such as the perihelion and aphelion distances, the period of revolution, the mean daily motion in arcsec, the mean opposition magnitude and so on.
4. Sorting tabular data or results of calculations.
5. Drawing frequency distribution graphs (histograms) and computations of some statistical characteristics of the distributions.

The above possibilities are realized for the table of elements.

6. Interpolating the data using the tabular differences of various orders that retain the formal precision of EMP data. In case of close approach with the Earth, ten day step of ephemeris is too large for accurate interpolation of coordinates. The precise coordinates can be found in such case through the use of ephemerides of unusual planets. It must be also noted that interpolation does not provide desired precision for the phase angle in the vicinity of opposition, especially for very small values.

7. Computation of O - C (observed minus computed) for the numbered minor planets. Observed positions can be inputted directly by typing the data according to conventional format or the input file can be formed in some way in advance.

8. Comparison of observed position of unnumbered object(s) with ephemeris of certain minor planet.

9. Identification of the planets, that is to say, ascribing the

observed positions of some object(s) to the numbered minor planet(s). User has a possibility to change the limits of allowable deviations from computed positions.

10. Preparation of the list of minor planets which can be seen at the moment within certain sky region and visualization of their mutual positions.

The most time-consuming operation is the identification. It takes about three minutes when using 286 processor. In the next version of STAMP which is under development the more economical algorithm will be used.

STAMP is written in programming language 'Clipper'. The system can work on an arbitrary IBM PC XT/AT or a compatible computer under the MS DOS. The system needs not less than 2.5 Mbytes free space on the hard disk for placing the STAMP itself and not less than 640 Kbytes of main memory.

This version of the STAMP system is supplied on a single 1.2 Mbytes distribution diskette.

Dealing with the system is organized in the form of dialogue. Description of job is specified through choice of corresponding points of menu. In some cases, that is followed by specifying dialogue to input the values of job parameters. In a number of cases the user has to edit the file typed at screen or create new file.

If required, user can appeal to 'helper' for advice. Besides, the package incorporates "Introduction" and description of each table. All that enables us to hope that the package is a useful tool not only for professional astronomers, but for amateurs as well.

At present the package is ready for use for 1991 and 1992. STAMP-92 is prepared taking into account the two last resolutions of the IAU Commission 20 concerning the usage of the new fundamental epoch 2000.0 and the new list of photometric parameters of minor planets.

The present version of STAMP (v.1.1) has prospects for future development. As it was noted, more effective algorithms of some processes can be introduced. A possibility exists for incorporating unnumbered planets with sufficiently reliable orbits into the package.

Constructive suggestions on improvement of the package are welcome.

References

- Batrakov Yu.V., ed. (1991) Ephemerides of Minor Planets for 1992, 'Nauka', Leningrad. 492 pp.
Shor V.A. (1990) Ephemerides of minor planets today and tomorrow. In Asteroids, Comets, Meteors III, (C.-I. Lagerkvist, H. Rickman, B.A. Lindblad, M. Lindgren, eds), pp.179-182, Uppsala univ., Uppsala.

PARTICLE EMISSION FROM ARTIFICIAL COMETARY MATERIALS

Gabriele Kölzer*, Hermann Kochan**, Klaus Thiel*

* Abtlg. Nuklearchemie, Universität zu Köln, Zülpicher Str. 47, W-5000 Köln 1, FRG

**WB-RS, DLR, Postfach 906058, W-5000 Köln 90, FRG

ABSTRACT

During KOSI (comet simulation) experiments mineral-ice mixtures are observed in simulated space conditions. Emission of ice-/dust particles from the sample surface is observed by means of different devices. The particle trajectories are recorded with a video system. In the following analysis we extracted the parameters: particle count rate, spatial distribution of starting points on the sample surface and elevation angle and particle velocity at distances up to 5 cm from the sample surface. Different kinds of detectors are mounted on a frame in front of the sample to register the emitted particles and to collect their dust residues. By means of these instruments the particle count rates, the particle sizes and the composition of the particles can be correlated. The results are related to the gas flux density and the temperature on the sample surface during the insolation period. The particle emission is interpreted in terms of phenomena on the sample surface, e. g. formation of a dust mantle.

INTRODUCTION

In the comet simulation (KOSI) project the behaviour of mineral-ice mixtures under simulated space conditions is studied. The experiments take place in the space simulation chamber at DLR in Köln (Kochan et al. (1988)).

This paper refers to the KOSI 5 experiment performed in November 1989. The sample composition was 70 % H₂O, 9 % minerals (olivine : montmorillonite = 9:1), 4 % CH₃OH, and 17 % CO₂ by weight. The mixture of minerals and volatiles was produced by spraying a suspension of water, minerals and methanol into liquid nitrogen. The resulting ice is then mixed with carbondioxide ice. During the experiment the sample container was tilted by an angle of 40° with respect to the horizontal plane. It was irradiated for about 12 hours with an intensity of 1.16 solar constants on the sample surface. During the irradiation phase the particle emission which is described in this paper, the thermal behaviour of the sample (Benkhoff and Spohn (1991) and Grün et al. (1991)) and the gas release (Hesselbarth et al. (1991)) is monitored.

PARTICLE DIAGNOSTICS

In front of the sample about 77 cm below and approximately 20 cm away from the surface center a frame is placed on which different kinds of particle collectors and detectors are mounted (Thiel et al. (1991)). Special ice particle detectors have been developed (Mauersberger et al. (1991)) to measure the volatile component of the emitted particles by ion gauges and to collect the dust residues in ten different cups. The size range of particles which can be registered is 7 - 220 μm equivalent radius. It has been found that there occur two kinds of signals which strongly differ in the rise time and the decay time of the ice sublimation rate. They are interpreted as two different types of particles. The particles with low ice sublimation rate presumably contain the volatiles inside a porous mineral cover while the high ice sublimation rate of the other type of particle indicates a pure ice composition (Mauersberger et al. (1991)).

In a distance of approximately 105 cm from the sample 10 piezoceramic acoustic detectors are attached to the frame. These detectors register particles greater than 250 μm with a time resolution of 100 sec (Kohl (1989)).

The time development of the particle emission during the insolation period shows the following characteristics (Mauersberger et al. (1991), Michel (1990) and Kölzer et al. (1990)): Pure ice particles are only

emitted in the beginning of irradiation. The emission of mineral-ice particles starts about 15 minutes after beginning of insolation. The count rate has its maximum after about 0.5 hours of irradiation. The count rate shows a steep increase and a slow decrease. The signals of the impact detectors indicate an superposition of pure ice and mineral-ice particles (Kölzer et al (1990)). The largest amount of dust residues in the collectors coincide with the highest activity of mineral-ice particle emission. While the count rate of ice and mineral-ice particles is negligible after two hours of insolation there is still emission of pure dust particles.

The dust residues which are collected on the frame in front of the sample are investigated by an optical microscope in transmitted light and the particle sizes measured by means of an image processing system. The lower threshold of the size measurements is $5000 \mu\text{m}^2$ ($\cong 40 \mu\text{m}$ equivalent radius). It turns out that the size distribution of the dust residues which are collected in the ice particle detectors does not change over hours (Kölzer (1991)). The exponents which are found for the best fit power laws have values between 1.8 and 1.9. These results are in fair agreement with the theoretical models developed by Brin and Mendis (1979), Fanale and Salvail (1984), Podolak and Herman (1985), and others. As long as there are no in situ measurements of the sizes of the dust particles on the sample surface during the experiment it is assumed that this exponent also characterizes the size distribution in the dust mantle, which is considered as a constant parameter during the evolution of the mantle.

DYNAMICAL PARAMETERS OF THE EMITTED PARTICLES

The emission of ice-/dust particles from the sample surface is observed by different devices. The particle trajectories are recorded with a video system (Kochan et al. (1991)). The video tapes are evaluated with an image processing system.

To establish the time dependence of the emission process nine definite time intervals covering the total insolation period were evaluated. Each time interval was defined by the total number of at least 400 emission events. The single event is characterized by the recorded particle trajectory. The average count rate is established by the recorded particles per time interval. In Figure 1 the particle count rate is plotted versus the time of irradiation. The highest count rate is observed at about half an hour after irradiation has started. Then the emission activity decreases exponentially with a time constant of about 143 min.

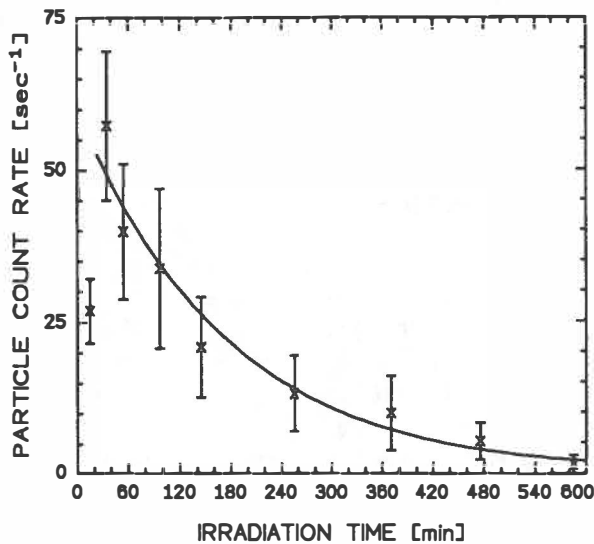


Figure 1 Count rate of emitted particles versus irradiation time. The decay of the emission activity is fitted by the function $y(t) = N \cdot \exp(-\frac{t}{t_0})$ with the parameters: $N = 800000 \frac{1}{\text{sec}}$ and $t_0 \approx 143 \text{ min}$.

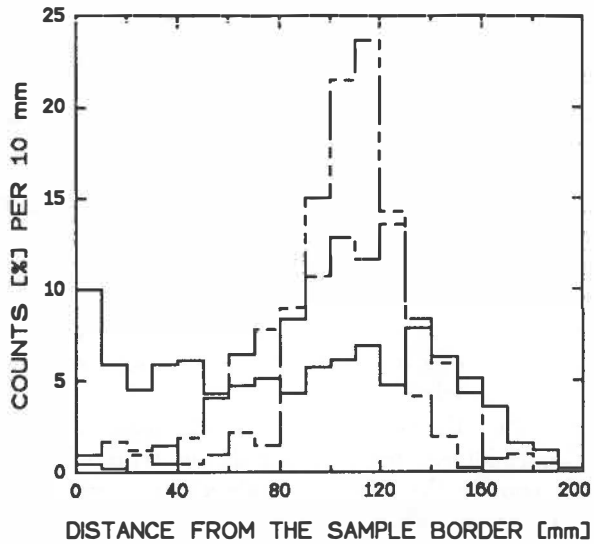


Figure 2 Distribution of starting points of the emitted particles on the sample surface 35 min (—), 370 min (---) and 585 min (— · —) after beginning of irradiation.

The particle velocity is calculated from the first two recorded points of the trajectory. The elevation angle is given by the connecting line of the first two points of the particle trajectory and the sample surface.

Both parameters are then attributed to the intermediate trajectory point. By the foot of the surface normal intersecting this intermediate point a reference point on the sample surface is defined. The distance of this foot point from the lower rim of the sample container is called 'starting point' in the following text.

In Figure 2 the distribution of the starting points on the sample surface is shown for three different times. The abscissa presents the distance to the lower rim of the sample. The number of particles starting in a 10 mm interval is counted and normalized to the number of starting particles in the respective time interval. During the first 2.5 hours of insolation the distribution of starting points is rather flat. In the next seven hours the lower part of the sample surface becomes inactive with increasing time.

The particle velocity ranges from 0.4 to 2.4 m/sec with a mean of 1.1 m/sec. This mean is constant in time. The elevation angle ranges from 0° to 80° . The mean elevation angle decreases with time from 36° to 22° during 450 minutes.

DISCUSSION

The results of the observation of particle emission and the measurements of the gas flux density (Hesselbarth et al. (1991) and Lämmerzahl (1991)) and the temperature (Heidrich (1990)) on the sample surface which are summarized in Figure 3 lead to the following scenario on the sample surface during the insolation period in the KOSI 5 experiment: At the beginning of irradiation the sample surface is covered by a thin layer of frozen H₂O vapour. Only emission of pure ice particles is observed at this time. After the ice cover is removed the emission of mineral-ice particles starts (Michel (1990)). The highest activity of this type of particle appears after about half an hour of insolation. After about two hours of irradiation the emission of ice containing particles has leveled off. The sample surface is covered by dry dust residues which are still emitted. It also happens that these dust particles roll downward on the tilted sample surface. After a while the particle emission and probably the gas flux are suppressed in the lower parts of the sample surface. The inactive region extends upward to about 8 cm measured from the lower rim. Investigations of the sample in a glove box after the experiment (Roessler (1991)) show that a dust mantle of 2 - 4 mm thickness has formed on a 2 - 4 cm thick mineral-ice crust. This modification of the sample may also influence the gas flux. The angle of the sample surface with respect to the horizontal plane is 35° while it was 40° at the beginning of the experiment. From the experimental results one may deduce that: (1) Successive emission of three different particle species (ice, ice-dust, dust) from mineral-ice mixtures, (2) quenching of particle emission by dust layers exceeding 5 mm in thickness, and (3) nearly constant emission velocity for a given particle size range at constant insolation intensity should also be relevant surface phenomena on a comet nucleus.

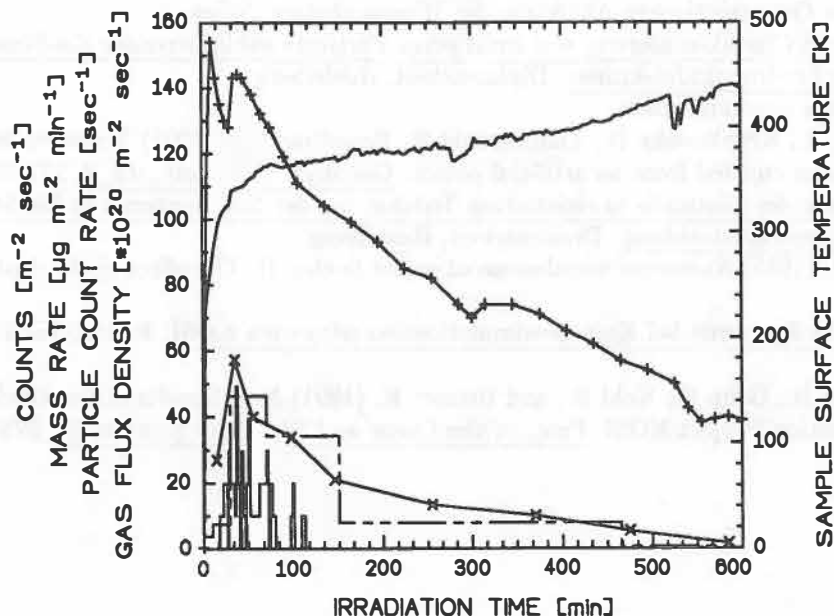


Figure 3 Temperature (—, curve, right y-axis) and gas flux density (-+---+, left y-axis) on the sample surface and count rate of particles recorded by the video system (-x-x-, left y-axis), total masses of dust residues per collector in the ice particle detector in a distance of about 500 mm from the center of the sample surface (---, left y-axis) and counts of mineral-/ice particles (—, step function, left y-axis) (see Michel (1990)) of the same detector during the insolation period in the KOSI 5 experiment.

ACKNOWLEDGEMENT

This work is financially supported by Deutsche Forschungsgemeinschaft in the Schwerpunktprogramm "Kleine Körper im Sonnensystem" under contract numbers Ko 973/1-3 and Th 320/5-1.

The authors would like to thank the KOSI team for cooperation, the space simulator crew of DLR in Köln for technical support.

REFERENCES

- Benkhoff J. and Spohn T. (1991) Thermal histories of the KOSI samples. Geophys. Res. Lett., 18, 2, 261-264.
- Brin G. D. and Mendis D. A. (1979) Dust release and mantle development in comets, Astrophys. J., 229, 402-408.
- Devine N. (1981) Numerical models for Halley dust environments. In The Comet Halley Dust and Gas Environment. ESA SP-174, 25-30.
- Fanale F. P. and Salvail J. R. (1984) An idealized short-period comet model: Surface insolation, H₂O flux, dust flux, and mantle evolution. Icarus, 60, 476-511.
- Grün E., Benkhoff J., Heidrich R., Hesselbarth P., Kohl H., and Kürth E. (1991) Energy balance of the KOSI 4 experiment. Geophys. Res. Lett., 18, 2, 257-260.
- Heidrich R. (1990) Eichung von Messanordnungen zur Bestimmung von Beiträgen zur Energiebilanz bei Kometensimulationsexperimenten. Diplomarbeit, Heidelberg.
- Hesselbarth P., Krankowsky D., Lämmerzahl P., Mauersberger K., Winkler A., Hsiung P., and Roessler K. (1991) Gas release from an artificial comet. Geophys. Res. Lett., 18, 2, 269-272.
- Kochan H., Benkhoff J., Bischoff A., Fechtig H., Feuerbacher B., Grün E., Joo F., Klinger J., Kohl H., Krankowsky D., Roessler K., Seboldt W., Thiel K., Schwehm G., and Weishaupt U. (1988) Laboratory Simulation of a cometary nucleus: Experimental setup and first results, Proc. 19th Lunar and Planetary Science Conf., 487-492.
- Kochan H., Markiewicz W. J., and Keller H.U. (1991) KOSI: Gas drag derived from ice/dust-particle trajectories, Geophys. Res. Lett., 18, 2, 273-276.
- Kölzer G., Kohl H., Thiel K., and Grün E. (1990) Laboratory studies on time dependent particle emission from cometary analogues. Proc. of the 24th ESLAB Symposium on the Formation of Stars and Planets and the Evolution of the Solar System. ESA SP-315, 197-201.
- Kölzer G. (1991) Size distributions of dust particles emitted from mineral-ice-mixtures under space conditions. In Theoretical modelling of comet simulation experiments (N. I. Kömle, S. J. Bauer, and T. Spohn, eds.), pp. 67-76, Verlag der Österreichischen Akademie der Wissenschaften, Wien.
- Kohl H. (1989) Messung und Charakterisierung von emittierten Partikeln sublimierender Eis-Staub-Gemische mit Hilfe piezokeramischer Impaktdetektoren. Diplomarbeit, Heidelberg.
- Lämmerzahl P. (1991) private communication.
- Mauersberger K., Michel H. J., Krankowsky D., Lämmerzahl P., Hesselbarth P. (1991) Measurement of the volatile component in particles emitted from an artificial comet. Geophys. Res. Lett., 18, 2, 277-280.
- Michel H. J. (1990) Messungen des Eisanteils in emittierten Teilchen bei der Sublimation von Eis-Staub-Gemischen unter künstlicher Sonnenbestrahlung. Diplomarbeit, Heidelberg.
- Podolak M., and Herman G. (1985) Numerical simulations of comet nuclei: II. The effect of the dust mantle. Icarus, 61, 267-277.
- Roessler K. (1991) Chemische Probleme bei Kometensimulationsexperimenten KOSI. Report-JüL-2446, KfA Jülich.
- Thiel K., Kölzer G., Kochan H., Grün E., Kohl H., and Bremer K. (1991) New Results of the Dust Investigations in the Comet Simulation Project KOSI. Proc. of the Lunar and Planetary Science, 21, 579-589.

The Effect of a Non-Volatile Dust Mantle on the Energy Balance of Cometary Surface Layers

Norbert I. Kömle and Gerhard Steiner

Space Research Institute, Austrian Academy of Sciences,
Lustbühel Observatory, A-8042 Graz, Austria

Abstract

It is likely that large parts of a cometary surface layer consist of porous ices, which are covered by a thin layer of non-volatile debris, whose structure is also fluffy and porous. In this paper the results of model calculations are presented, which show the effect of ice and dust pore sizes, and of the dust mantle thickness upon the thermal behavior of such a dust-ice system, when it is irradiated by the sun. In particular, it is found that the average pore size of the ice and the dust material has a large influence both on the dust surface temperature and on the temperature at the dust-ice interface.

INTRODUCTION

Several lines of evidence make the existence of dust mantles on the surface of cometary nuclei (at least temporarily) probable. One argument comes from the fact that during the close-up observations of comet Halley by the spacecraft Giotto and VEGA only a small part of the nucleus showed 'activity' in the form of dust particle emission (Keller, 1990). The rest of the surface appeared inactive, which might be caused by a dust mantle overlying the cometary ice. The build-up and removal of dust mantles in response to varying solar irradiation conditions may be responsible for many features of cometary light curves (Jewitt, 1991). Recently, the build-up of dust mantles during irradiation of ice-dust mixtures could even be directly observed in the laboratory, although under terrestrial gravity conditions (Grün et al., 1991). In the following we present some results of model calculations, which demonstrate the influence of a dust mantle on the thermal behavior of a dust-ice system. Hereby it is assumed that both the dust mantle and the underlying ice have a porous, grainy structure, which can be characterized by an average pore size and a volume porosity. It is investigated in detail how the variation of these pore sizes and the variation of the dust mantle thickness affect dust and ice temperature and the heat flow to the interior.

GOVERNING EQUATIONS

Before presenting the results, we give a short survey of the basic equations used in our model and the geometry assumed. As we are only interested in surface layers, a one-dimensional geometry is chosen, where all variables depend only on the depth coordinate x and on time t . The total thickness of the dust-ice layer is chosen as 8 cm. It is assumed that the system is heated up at the upper end by absorption of solar radiation and kept at a constant low temperature at the lower

end. The thermal equation for the dust mantle is given by

$$(1 - \psi_d)\rho_d c_d \frac{\partial T}{\partial t} = \frac{\partial}{\partial x} \left[\lambda_d(T) \frac{\partial T}{\partial x} \right] - f_g c_g \frac{\partial T}{\partial x} \quad (1)$$

where the thermal conductivity of the mantle

$$\lambda_d = \lambda'_d + 4r_d \varepsilon \sigma T^3 \quad (2)$$

consists of a contribution λ'_d caused by conduction via contact points and a radiative term proportional to the average pore radius r_d of the mantle material. The gas mass flux through the mantle (f_g) is calculated from a simple Knudsen law, where the gas pressure is computed from the Clausius Clapeyron equation with two experimental parameters (a and b). It is proportional to the ratio r_d/D , where D is the thickness of the dust mantle. Thus the factor r_d/D determines largely the permeability of the mantle for a gas flowing through. For that part of the system which consists of porous ice, a somewhat different heat conduction equation has to be utilized. It is given by

$$(1 - \psi_i)\rho_i c_i \frac{\partial T}{\partial t} = \frac{\partial}{\partial x} \left[\lambda_{\text{eff}}(T) \frac{\partial T}{\partial x} \right] - \phi_g c_g \frac{\partial T}{\partial x} \quad (3)$$

where ϕ_g is the gas flux into the interior, and λ_{eff} is the sum of the ice matrix conductivity and the conductivity caused by sublimation-condensation processes inside the pores:

$$\lambda_{\text{eff}}(T) = h \frac{567}{T} + \frac{8}{3} \psi_i \left(\frac{m}{2\pi kT} \right)^{1/2} \frac{b}{T^2} a e^{-b/T} H r_i \quad (4)$$

where h is the so-called Hertz factor describing the reduction of the solid state conductivity of compact ice caused by the grainy structure, r_i is the average radius of the pores in the ice, and H is the latent heat of sublimation. The remaining symbols in equations (1)–(4) are the porosity ψ , the density ρ , and the heat capacity c . The indices i , d , and g stand for ice, dust mantle, and gas, respectively. For all other symbols standard notation is used. Both estimates and detailed calculations (Steiner et al., 1991) have shown that the convective term in equations (1) and (3) has only a very minor influence on the result and can be neglected. For completeness, it was included in the following calculations. In the volume element containing the sublimation front (dust-ice interface) the difference of in- and outgoing heat fluxes is set equal to the energy flux carried by the gas escaping through the mantle. At the dust surface the absorbed energy is partially re-radiated as thermal radiation and partially conducted downward through the mantle.

RESULTS

Inspection of equations (1)–(4) reveals that the thermal evolution of a dust-ice system depends on a number of parameters. Among the most sensitive ones (because they may vary over a wide range in cometary ices and are largely unknown) are the solid state conductivity of the ice matrix (determined by the Hertz factor h), the solid state conductivity of the dust mantle (λ'_d) and the average pore sizes in the ice and dust material (r_i, r_d). In the following we show some representative examples illustrating the dependence of the dust mantle surface temperature T_d and the dust-ice interface temperature on the pore sizes and on the thickness of the non-volatile mantle. Hereby the solid state conductivity of the mantle is taken as $\lambda'_d = 0.12 \text{ WK}^{-1}\text{m}^{-1}$, which corresponds to the conductivity of coal dust (Grigull and Sandner, 1986). The Hertz factor for the ice is taken as 5×10^{-3} , a value found to be representative for porous water ice used in recent laboratory experiments (Kömle et al., 1991). In all cases the calculations of the thermal evolution of the

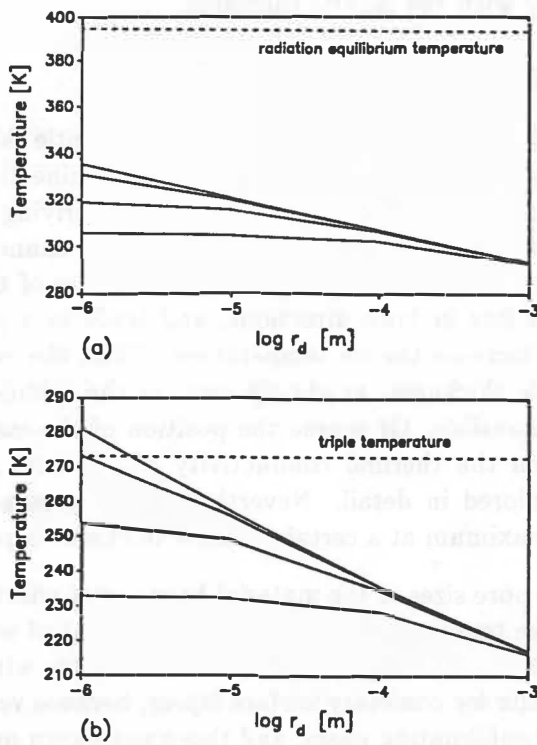


Figure 1 (a) Dust surface temperature and (b) dust-ice interface temperature for a coal dust layer of 1 cm thickness overlying porous ice. The temperatures are plotted as a function of dust mantle pore radius r_d . The different curves correspond to ice pore radii of (top to bottom) 1 μm , 10 μm , 100 μm , and 1 mm.

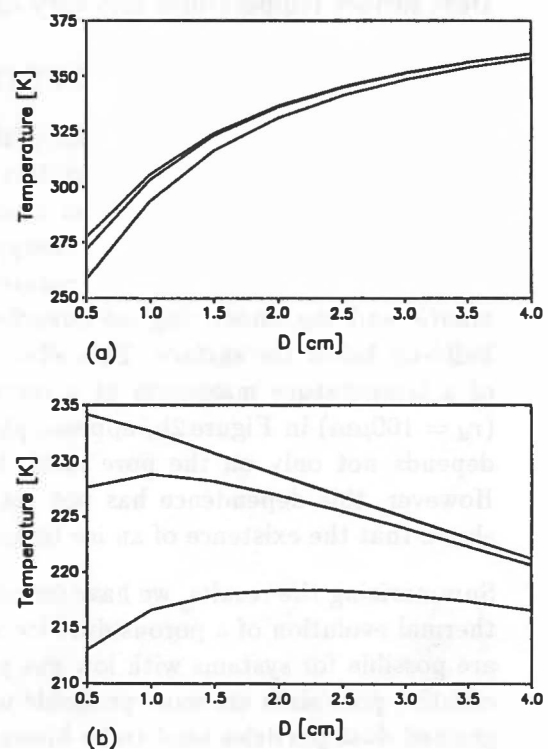


Figure 2 (a) Dust surface temperature and (b) dust-ice interface temperature as a function of dust mantle thickness. It is assumed that the ice is coarse grained ($r_i = 1 \text{ mm}$). The different curves correspond to dust mantle pore radii of (top to bottom) 10 μm , 100 μm , and 1 mm.

system have been pursued to the point, where a quasi-stationary value was reached for T_i and T_d . This was the case after 4 hours of irradiation with 1 solar constant, assuming an albedo of zero and an infrared emissivity of one.

Figures 1a and 1b show the dependence of T_d and T_i on the pore radii r_d and r_i for a 1 cm thick coal dust mantle irradiated with 1 solar constant. Note that for ice containing only very fine capillaries which is covered by a similarly unpermeable dust mantle the ice temperature may increase up to the triple point of water ice (273 K). For coarse-grained mantle material with pore sizes in the millimeter range typical ice temperatures lie around 215 K. This is still higher than the corresponding free sublimation temperature of 205 K, which a black water ice in absence of a dust mantle would reach. Looking at Figure 1a one sees that the dust surface temperature also is quite sensitive to the pore sizes and varies between 295 K and 335 K in our example. It always remains clearly below the radiation equilibrium temperature of 394 K, which indicates the importance of inward directed heat flow in the case of such a moderately insulating mantle. Finally, Figures 2a and 2b illustrate the variation of T_d and T_i as a function of dust mantle thickness, for an ice of high permeability ($r_i = 1 \text{ mm}$) and different values of r_d . Note that in the case of a dust mantle with low permeability the ice temperature decreases with increasing mantle thickness, while for a mantle with high permeability a temperature maximum at a certain mantle thickness is seen.

Dust surface temperatures also vary significantly with the mantle thickness.

DISCUSSION AND CONCLUSIONS

What is the reason for the behavior of the ice surface temperature as a function of mantle thickness, displayed in Figure 2? There are two counteracting physical processes that determine the value of T_i . On the one hand the dust mantle acts as a thermal insulator for the underlying ice. A significant part of the incoming energy is re-radiated already from the surface and cannot reach the ice any more. This tends to reduce T_i . On the other hand, the gas flow resistance of the dust mantle and the underlying ice quenches the gas flux in both directions, and leads to a pressure build-up below the surface. This effect tends to increase the ice temperature. Thus, the existence of a temperature maximum at a certain mantle thickness, as clearly seen in the middle curve ($r_d = 100\mu\text{m}$) in Figure 2b, appears physically plausible. Of course the position of the maximum depends not only on the pore radii, but also on the thermal conductivity of the dust mantle. However, this dependence has not yet been explored in detail. Nevertheless, the present study shows that the existence of an ice temperature maximum at a certain mantle thickness is possible.

Summarizing the results, we have found that the pore sizes of the material have a vast effect on the thermal evolution of a porous dust-ice system. Ice temperatures up to the triple point of water ice are possible for systems with low gas permeability. However, we believe that the cases with large effective pore sizes are more probable to be realistic for cometary surface layers, because very fine-grained dust particles tend to be blown away by sublimating gases, and those not blown away are likely to form aggregates with larger pore sizes. Only if a reasonable amount of organic (tar-like) material is present, which might 'seal' the pores and give the mantle a certain amount of coherence, higher ice temperatures may—at least temporarily—occur below cometary dust mantles.

Acknowledgement. This work was supported in part by the Austrian 'Fonds zur Förderung der wissenschaftlichen Forschung' under grant P7246-GEO.

References

- Grigull U. and Sandner H. (1986) Wärmeleitung. Springer, Berlin. 158 pp.
- Grün E. et al. (1991) Laboratory Simulation of Cometary Processes. In Comets in the Post-Halley Era (R. L. Newburn, M. Neugebauer, and J. Rahe, eds.), Volume 1, pp. 277–297. Kluwer, Dordrecht.
- Jewitt D. (1991) Cometary Photometry. In Comets in the Post-Halley Era (R. L. Newburn, M. Neugebauer, and J. Rahe, eds.), Volume 1, pp. 19–65. Kluwer, Dordrecht.
- Keller H. U. (1990) The Nucleus. In Physics and Chemistry of Comets (W. F. Huebner, ed.), pp. 13–68. Springer, Berlin.
- Kömle N. I. et al. (1991) Ice Sublimation Below Artificial Crusts: Results from Comet Simulation Experiments. Planet. Space Sci., 39, 515–524.
- Steiner G., Kömle N. I., and Kührt E. (1991) Thermal modelling of comet simulation experiments. In Theoretical Modelling of Comet Simulation Experiments (N. I. Kömle, S. J. Bauer, and T. Spohn, eds.), pp. 11–29, Austrian Academy of Sciences, Vienna.

DISTURBANCES OF BOTH COMETARY AND EARTH'S MAGNETOSPHERES EXCITED BY SINGLE SOLAR FLARES

I. Konno¹, T. Saito², Y. Kozuka², K. Nishioka³, M. Saito⁴, and T. Takahashi²

1. Southwest Research Institute, USA 2. Geophysical Institute, Tohoku University, Japan 3. Olympus Optical Co. Ltd., Japan 4. Saito Astronomical Observatory, Japan

INTRODUCTION

In the solar wind a comet plays the role of a windvane that moves three-dimensionally in the heliomagnetosphere. Among the solar system bodies, only comets have a wide range of inclination angles of their orbital planes to the ecliptic plane ranging from 0° to 90°. Therefore, observations of cometary plasma tails are useful in probing the heliomagnetospheric conditions in the high heliolatitudinal region. A comet can be compared to a polar-orbiting probe encircling the Sun. We will introduce two rare cases in which the magnetospheres of both the comet and the Earth are disturbed by a single solar flare.

DISTURBANCES OF COMET P/BORSEN-METCALF AND THE EARTH

An outstanding disturbance of Comet P/Brorsen-Metcalf was observed on August 13, 1989. Figure 1 shows the comet in eight panels of the identical portion of the sky from 17h17m to 18h51m UT. An outstanding disconnection event (DE) took place and a plasmoid was swept away at very high speed. About half a day later, the Earth's magnetosphere suffered a disturbance as inferred in Figure 2 that shows the geomagnetic variation of the horizontal component observed at the Onagawa Magnetic Observatory in Japan. Two storm sudden commencements (SCs) occurred successively at 01h51m and 06h13m.

We surveyed many solar flares to find the sources of the two SCs of the magnetic storm at the Earth. Assuming that a solar flare gave rise to a shock front which propagated at a constant speed from the Sun to the Earth causing the SCs, the propagating speed for each of the flares was calculated. If we assume that the possible flares are larger than 2B of importance in the central disk with the propagating speed of 1000 ± 100 km s^{-1} , the two flares at 07h56m and 13h57m on August 12 are regarded to be the sources of the SCs.

Figure 3a and 3b show the relation of the positions between the Sun, the Earth, and P/Brorsen-Metcalf on August 13, 1989, on the meridian plane and the ecliptic plane, respectively. It is quite possible judging from the figure that the identical flare disturbed both the Earth's magnetosphere and the cometary magnetosphere. The probable propagating speed of the shock wave from the flare to the comet is either 1017 km s^{-1} or 1190 km s^{-1} (There are two possible source flares that occurred about the same time.)

It has been suggested by Niedner and Brandt (1978) that a DE is caused by a magnetic field line reconnection at the dayside associated with a sector boundary crossing. However, it is suggested, from observations, that a night-side reconnection associated with a rapid increase of a dynamic pressure caused by a high-speed stream is one of the causes of DEs (Russell et al., 1986; Saito et al., 1986). We assume that the DE in question was like an SC-triggered substorm (Saito et al., 1987) that starts usually within five minutes after a sudden increase of the dynamic pressure of the solar wind.

DISTURBANCES OF COMET OKAZAKI-LEVY-RUDENKO AND THE EARTH

Disturbances in Comet Okazaki-Levy-Rudenko were observed in Hokkaido, Japan, during about 19h~20h UT on November 16, 1989. The plasma tail suffered complex disturbances including a disconnection event as seen in Figure 4. Figure 5 shows a magnetogram obtained at the Onagawa Magnetic Observatory indicating the magnetic storm that commenced with an SC at 09h20m UT on November 17, 1989. The solar flare that occurred at 06h38m UT on November 15 is found to be the possible source for the magnetic storm considering the propagating speed of 825 km s^{-1} and the position of the flare. Figures 6a and 6b show the geometrical relation between the Sun, Earth, and Comet Okazaki-Levy-Rudenko on November 16, 1989, on the meridian plane and ecliptic plane, respectively. We conclude that a single solar flare again gave rise to the disturbances of the magnetospheres of both Comet O-L-R and the Earth. The propagating speed of the shock wave from the flare to the comet is about 740 km s^{-1} .

References

- Niedner Jr., M.B. and Brandt J.C. (1978) Interplanetary gas XXIII. Plasma tail disconnection events in comets: Evidence for magnetic field line reconnection at interplanetary sector boundaries?, *Astrophys. J.*, **223**, 655.
- Russell C.T., Saunder M.A., and Phillips J.L. (1986) Near-tail reconnection as the cause of cometary tail disconnections, *J. Geophys. Res.*, **91**, 1417.
- Saito T., Yumoto K., Hirao K., Saito K., Nakagawa T., and Smith E.J. (1986) A disturbance of the ion tail of comet Halley and the heliospheric structure as observed by Sakigake, *Geophys. Res. Lett.*, **13**, 821.
- Saito T., Yumoto K., Hirao K., Minami S., Saito K., and Smith E. (1987) Structure and dynamics of the plasma tail of comet P/Halley I. Knot event on December 31, 1985, *Astron. Astrophys.*, **187**, 209.

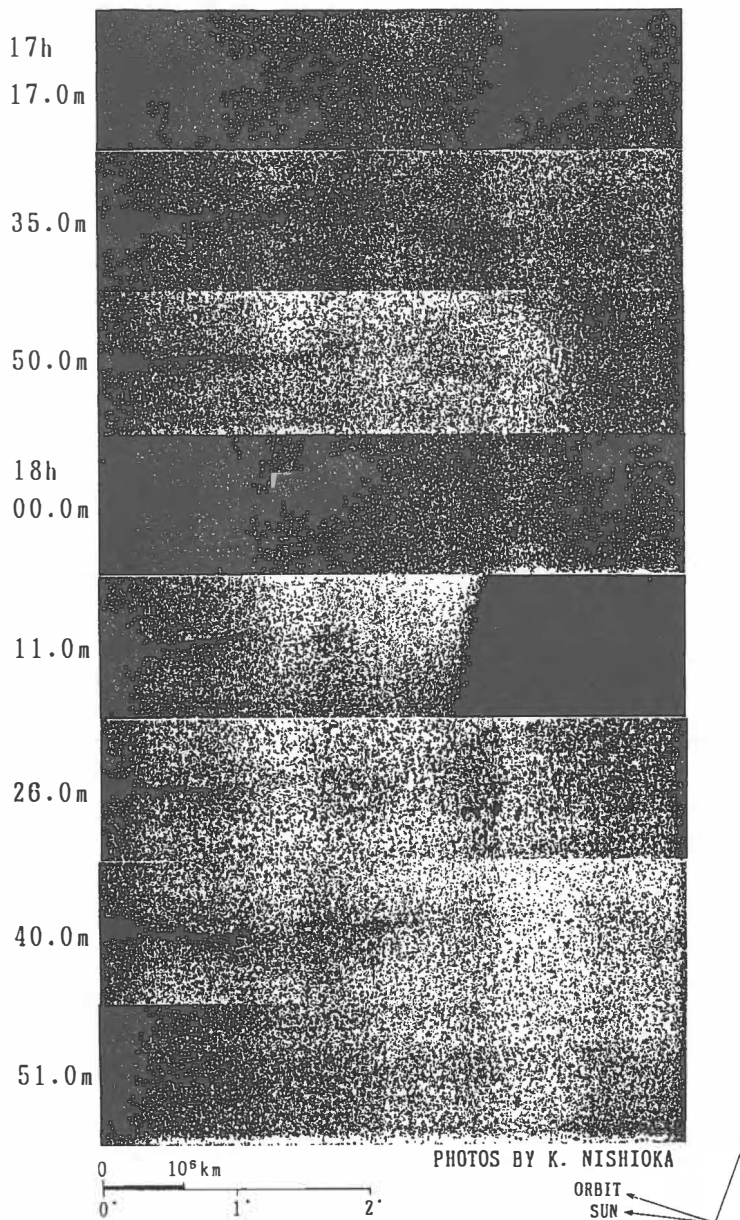


Fig. 1. – DE in Comet P/Brorsen-Metcalf on August 13, 1989 (UT).

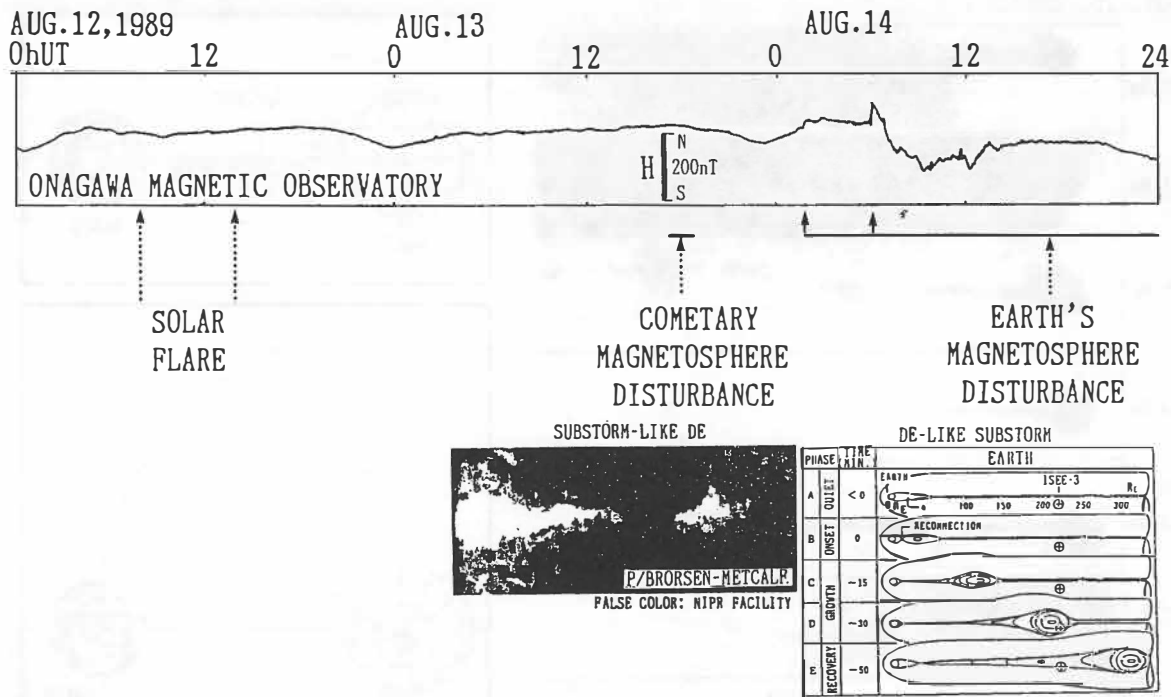


Fig. 2. – Geomagnetic variation of the horizontal component observed in Japan. Two storm sudden commencements occurred on August 14, 1989.

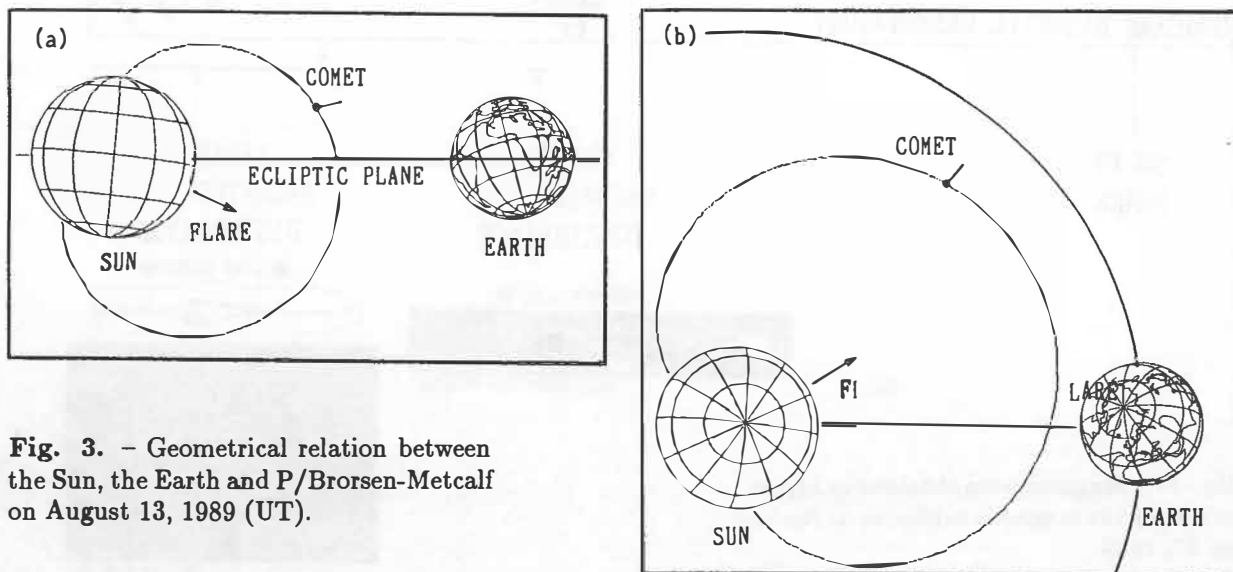


Fig. 3. – Geometrical relation between the Sun, the Earth and P/Borsten-Metcalf on August 13, 1989 (UT).

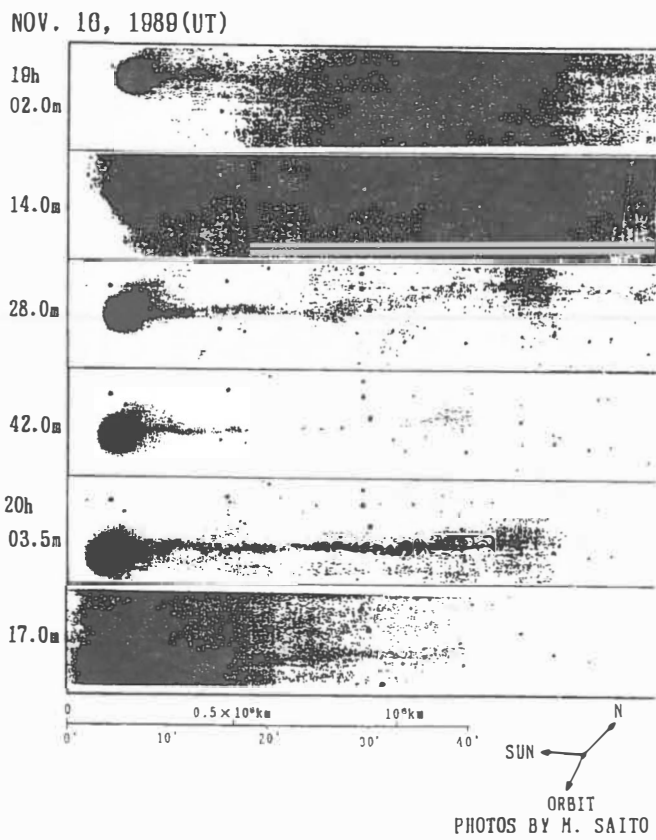


Fig. 4. – Disturbances of the plasma tail of Comet Okazaki-Levy-Rudenko on November 16, 1989 (UT).

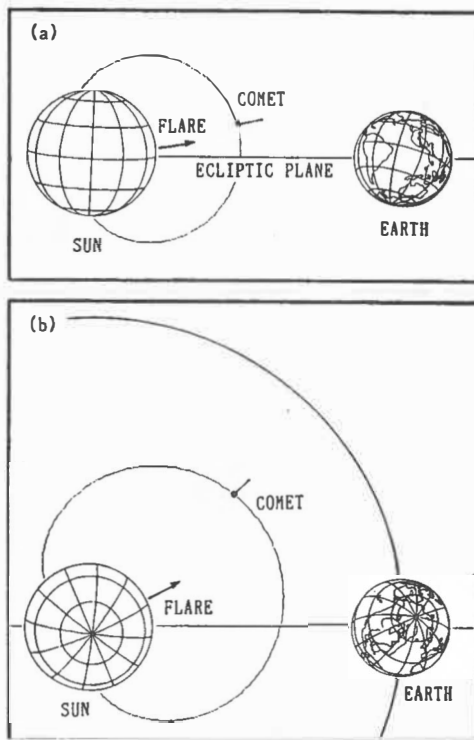


Fig. 6. – Geometrical relation between the Sun, the Earth and C/Okazaki-Levy-Rudenko on November 16, 1989 (UT).

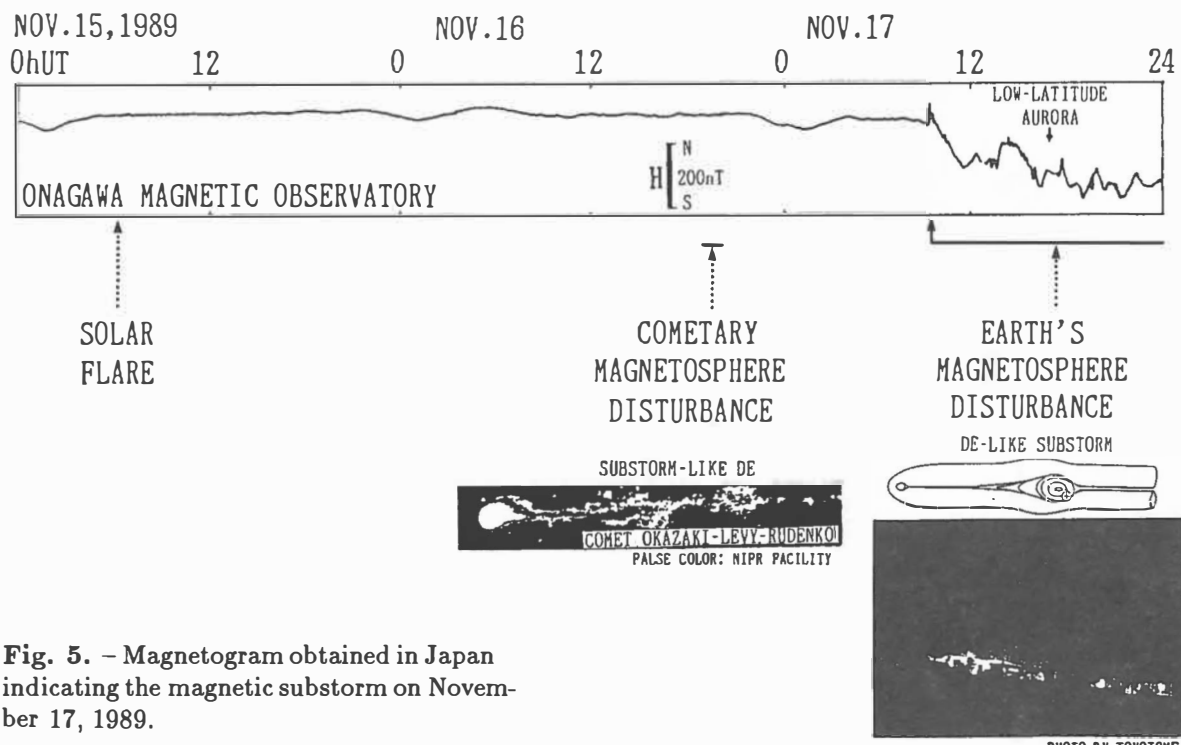


Fig. 5. – Magnetogram obtained in Japan indicating the magnetic substorm on November 17, 1989.

A NEW MEASUREMENT OF THERMAL CONDUCTIVITY OF AMORPHOUS ICE AND ITS IMPLICATIONS FOR THE THERMAL EVOLUTION OF COMETS

A. Kouchi(1), J. M. Greenberg(1), T. Yamamoto(2), T. Mukai(3),
and Z. F. Xing(1)

- (1) Laboratory Astrophysics, University of Leiden, 2300RA
Leiden, The Netherlands
- (2) Institute of Space and Astronautical Science, Yoshinodai,
Sagamihara, Kanagawa 229, Japan
- (3) Department of Earth Sciences, Kobe University, Nada, Kobe
657, Japan

ABSTRACT

Very slowly deposited amorphous ice has a thermal conductivity about four orders of magnitude or more smaller than hitherto estimated. Using the exceedingly low value of the thermal conductivity of comets deduced from the properties of amorphous ice leads to the expectation that internal heating of comets is negligible below the outer several tens of centimeters.

INTRODUCTION

Although the importance of knowing the thermal conductivity, κ , of vapor-deposited amorphous ice ($a\text{-H}_2\text{O}$) for predicting the thermal evolution of comets has been widely recognized (e.g., Klinger, 1980; Espinasse et al., 1991 and references therein), there has been no direct measurement available. Therefore, most of the discussions on comet evolution have been based on a theoretical estimation of κ by Klinger(1980). On the basis of our new experimental results and a reanalysis of data found in literature, we have arrived at a new estimate of the κ for $a\text{-H}_2\text{O}$ (Kouchi et al., 1991). We discuss the thermal evolution of comet using the new value of κ .

MEASUREMENT OF THERMAL CONDUCTIVITY

Kouchi et al.(1991) investigated the thermal diffusion in ice thin film during deposition, and gave the following relation:

$$h = (T_h - T_s) \bar{\kappa} / [(1 - \bar{A}) \sigma T_R^4 - \bar{\epsilon} \sigma T_h^4 + VL] \quad (1)$$

where h is the thickness of ice film, T_h , T_s and T_R the temperature of the surface of ice film, that of a substrate and that of the ambient radiation field, respectively, \bar{A} the Planck averaged albedo of the sample at temperature T_R , $\bar{\epsilon}$ the Planck averaged emissivity at temperature T_h , σ the Stefan-Boltzmann constant, V the deposition rate, L the heat of deposition per unit volume, and

$$\bar{\kappa} = (T_h - T_s)^{-1} \int_{T_s}^{T_h} \kappa(T) dT,$$

the mean thermal conductivity between T_s and T_h . If we obtain the whole set of data: T_s , T_h , T_R , h and V , we can calculate the $\bar{\kappa}$ of a-H₂O using eq. (1). However, it is very difficult or almost impossible to measure the surface temperature T_h because the thickness of a-H₂O is very small compared to the size of the thermometer (e.g., thermocouples), and because the thermal conductivity of a-H₂O is smaller than that of any known thermometer.

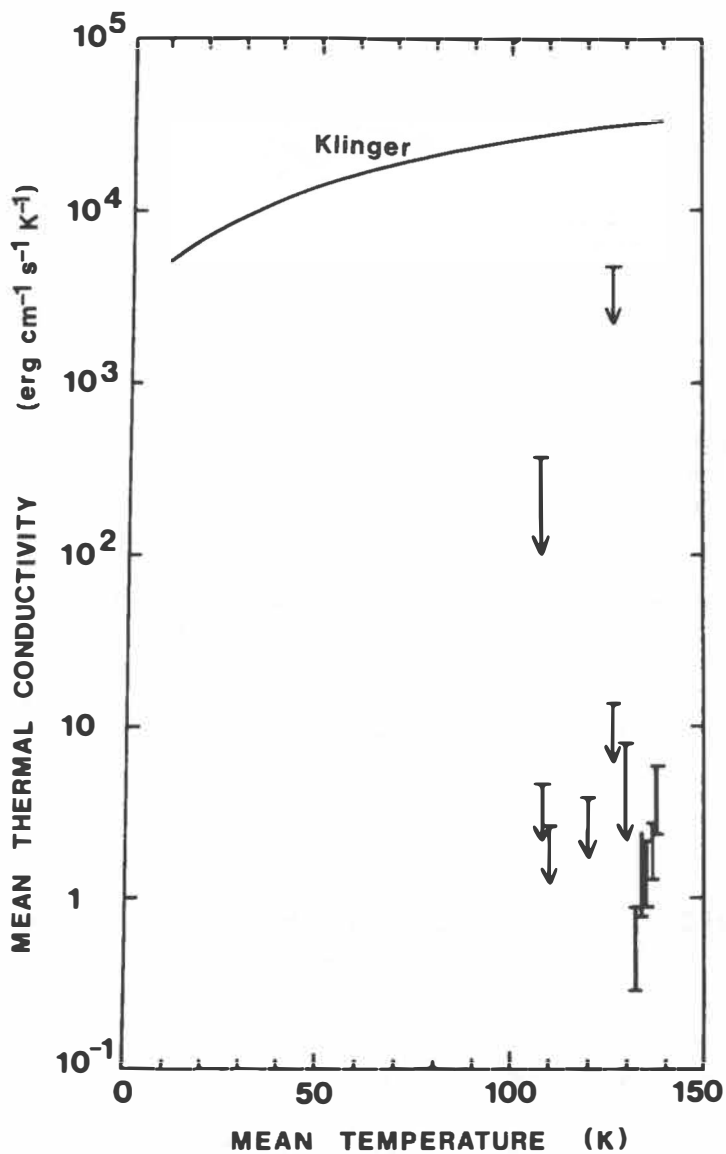


Fig.1 Mean thermal conductivities of amorphous ice obtained by Kouchi et al. (1991) and that estimated by Klinger (1980).

Kouchi et al. (1991) observed the structural change of ice films during deposition at $T_s = 125-130$ K using reflection electron diffraction. At thicknesses smaller than h_c , deposition of a-H₂O occurred, while at a thickness larger than h_c , cubic ice (ice I_c) was deposited. This clearly shows that the surface temperature of the ice film at the thickness of h_c corresponds to the temperature of phase transition from a-H₂O to ice I_c, which occurs at around 140 K. Furthermore, this enables us to measure the T_h and, by assuming $\bar{A} \sim 0$, $\bar{\epsilon} \sim 1$ in eq. (1), to determine upper bound of $\bar{\kappa}$ of a-H₂O. Figure 1 shows the $\bar{\kappa}$ of a-H₂O obtained by Kouchi et al. (1991). It is clear that the $\bar{\kappa}$ is at least one to four orders of magnitude smaller than that estimated by Klinger (1980).

HEAT TRANSFER IN A COMET NUCLEUS

Since the cometary nucleus is very porous, the thermal conductivity of the nucleus may be one to two orders of magnitude smaller than that of constituent icy grains. This suggests that the thermal conductivity of the comet nucleus is certainly smaller than 1 erg cm⁻¹ s⁻¹ K⁻¹ and possibly as low as 10⁻², a quite shocking result. With such a small value of κ , the major mechanism of heat transfer in the comet nucleus on short time scales may not be only by conduction. However, radiation transport both by visual and infrared and diffusive heat transport by evaporated water molecules are also negligible (Kouchi et al., 1991). The more volatile molecules like CO, CO₂ may be expected to play a more important role in diffusive heat transport than H₂O (Espinasse et al., 1991).

THERMAL EVOLUTION OF COMETS

Greenberg et al. (1991) investigated the pre-history of a new comet: from the protosolar nebula to the Oort cloud, then in the Oort cloud, and from the Oort cloud to the inner solar system. They found that all new comets return to the inner solar system at a temperature lower than their formation temperature in the protosolar nebula and a rough estimate is that it is reduced by about 1/2.

Greenberg et al. (1991) also investigated how little the solar heating affects the interior of a periodic comet. Table 1 shows some typical results for a comet of any size with the initial temperature of 16 K. It appears unlikely that below 25 cm, or even less, the temperature in a periodic comet will rise enough to evaporate CO and will certainly not be enough to evaporate or crystallize water ice.

The conclusion that even periodic comets preserve pristine interstellar matter in cold storage at relatively shallow depth mandates that a greater effort be made to provide the lowest possible return temperature—preferably less than 20 K—than to require probe depth to some meters.

Table 1. Illustrative examples of limited heat penetration (ΔT) below the surface of a periodic comet nucleus. $\Delta T = T - 16$ K, T_0 is the surface temperature, and $\kappa = 10^{-2}$ erg cm⁻¹ s⁻¹ K⁻¹.

a) $T_0 = 300$ K (~1AU)

Δr (cm)	time (yr)					
	1	3	10	30	100	1000
5	0	7	61	135	197	256
10	0	0	4	43	123	228
20	0	0	0	1	33	176
50	0	0	0	0	0	61
75	0	0	0	0	0	18

b) $T_0 = 130$ K (~5AU)

Δr (cm)	time (yr)			
	1	10	100	1000
5	0	25	79	103
10	0	2	49	92
20	0	0	13	71
50	0	0	0	25
75	0	0	0	7

ACKNOWLEDGEMENTS

The authors would like to thank the Netherlands Organization for Scientific Research and the Japan Society for the Promotion of Science for their support. Part of this research was supported by NASA grant (# NGR 33-018-148). One of the authors (T.Y.) acknowledges the support from the University of Tsukuba, Japan. One of the authors (A.K.) was supported by the Yamada Science Foundation, Japan.

REFERENCES

- Espinasse S., Klinger J., Ritz C., and Schmitt B. (1991) Modeling of the Thermal Behavior and of the Chemical Differentiation of Cometary Nuclei. *Icarus*, 92, 350-365.
- Greenberg J. M., Yamamoto T., and Xing Z. F. (1991) The Peter Pan of the Solar System:Preservation of Protosolar Nebula Matter in Comets by their Exceedingly Low Thermal Conductivity. submitted to Nature.
- Klinger J. (1980) Influence of a Phase Transition of Ice on the Heat and Mass Balance of Comets. *Science*, 209, 271-272.
- Kouchi A., Greenberg J. M., Yamamoto T., and Mukai T. (1991) Extremely Low Thermal Conductivity of Amorphous Ice:Relevance to Comet Evolution. submitted to Ap. J. Lett..

THE SOLAR WIND STRUCTURE THAT CAUSED A LARGE-SCALE DISTURBANCE OF THE PLASMA TAIL OF COMET AUSTIN

Yukio Kozuka¹, Ichishiro Konno², Takao Saito¹, and Shigemi Numazawa³

1. Geophysical Institute, Tohoku University, Japan 2. Southwest Research Institute, USA 3. Japan Planetarium Laboratory

OBSERVATION

The plasma tail of Comet Austin (1989c₁) showed remarkable disturbances because of the solar maximum period and its orbit. Figure 1 shows photographs of Comet Austin taken in Shibata, Japan, on April 29, 1990 UT, during about 20 minutes with the exposure times of 90 to 120 s. There are two main features in the disturbance; one is many bowed structures, which seem to move tailwards, and the other is a large-scale wavy structure. The bowed structures can be interpreted as arcade structures brushing the surface of both sides of the cometary plasma surrounding the nucleus. We identified thirteen structures of the arcades from each of the five photographs and calculated the relation between the distance of each structure from the cometary nucleus, x , and the velocity, v . The result is shown in Figure 2, which indicates that the velocity of the structures increases with distance. This is consistent with the result obtained from the observation at the Kiso Observatory which is shown by the open circles in Figure 2 (Saito et al., 1990).

SOLAR WIND STRUCTURE RESPONSIBLE FOR THE DISTURBANCE

According to the windsock theory (Brandt and Rothe, 1976), the direction of the cometary plasma tail is determined by the velocities of the solar wind and the orbital motion of the comet. Therefore, if the direction of the solar wind flow is radial from the sun, the plasma tail axis changes in the orbital plane of the comet with changes of the speed of the solar wind. From the large-scale configuration of the tail, the solar wind speed, v , as expected from the windsock theory is obtained with the nucleus-structure distance, x , as shown in Figure 3. Comparing this result with the observation, we find that the expected speeds are far smaller than the observed speeds, especially for $x > 2 \times 10^6$ km. Therefore the large-scale disturbance must be explained by a non-radial flow of the solar wind.

As proposed by Colburn and Sonett (1966) and Dessler (1967), a non-radial flow can be caused by a stream interaction between a high-speed flow and a low-speed flow. The non-radial flow has also been postulated observationally by Brandt et al. (1980) showing that the event of Comet Bradfield (1979I) on February 6, 1980 was caused by a change of the polar component of the solar wind flow by 50 km/s. Pizzo (1989) has reported a model of the variation of the solar wind parameters in the interaction region using a 2-D MHD simulation. When the speed and the direction of the solar wind change as shown in Figure 4a (Pizzo, 1989), the simulation shows a deformation of the plasma tail as in Figure 4b (Kozuka et al., 1990). For the Comet Austin event, we deduced the solar wind structure from the deformation of the wavy structure of the plasma tail observed for 21 min 42 s. The result is shown in Figure 5. It suggests that a velocity discontinuity in the solar wind crossed the comet.

The non-radial flow in the solar wind discussed above must have originated in some solar phenomenon. We found no solar flares responsible for the large-scale cometary disturbance on that date. Another possible cause is that the comet crossed the heliospheric neutral sheet. The source point of the solar wind flow which was to pass by the comet that day was located on the solar source surface. Since the distance from the source point to the nearest neutral line is as far as 56°

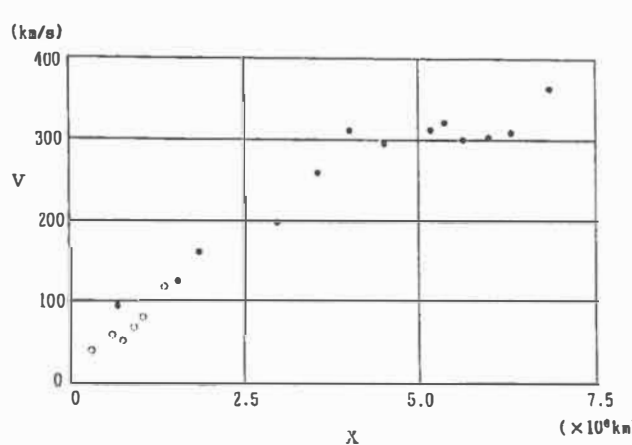
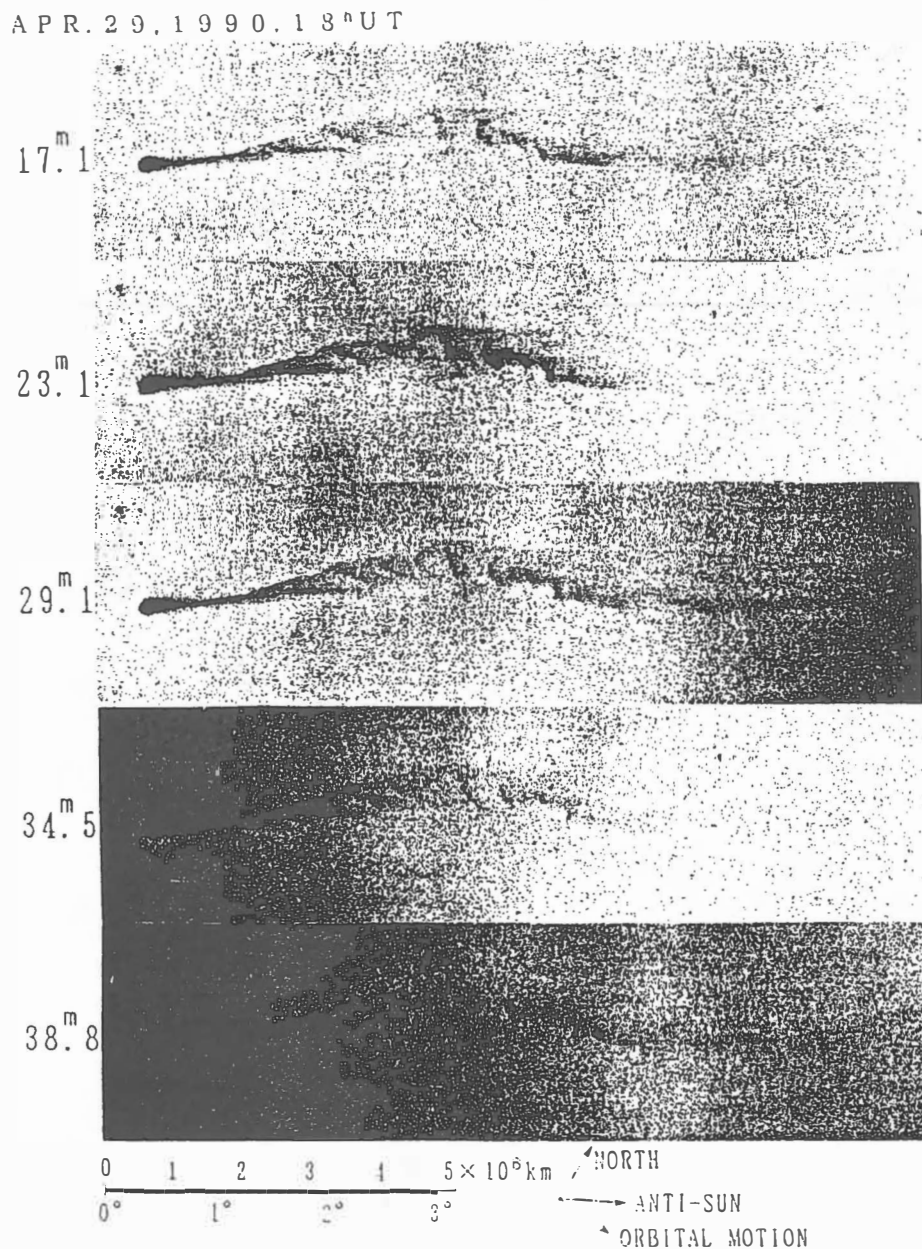


Fig. 1. – The plasma tail of Comet Austin taken in Shibata, Japan, on April 29, 1990 UT, with exposure times of 90 to 120 s. There are many bowed structures and a large-scale wavy structure.

Fig. 2. – Relation between the velocity of the structures and the distance from the nucleus.

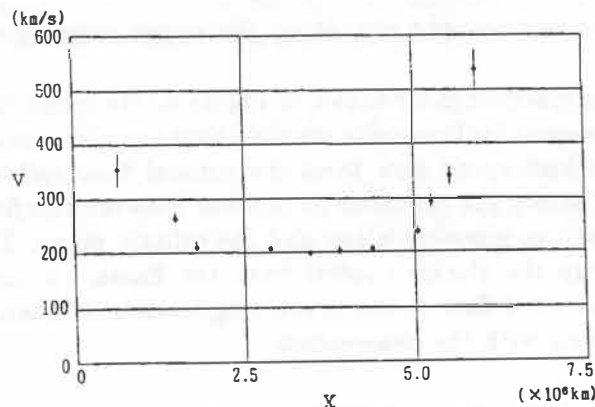


Fig. 3. – Solar wind speed expected from the windsock theory.

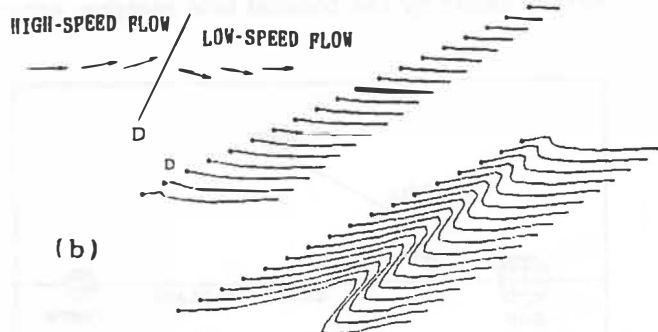
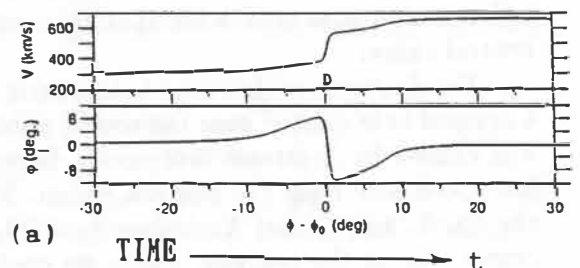


Fig. 4. – (a) Two-dimensional MHD simulation showing the variation of the solar wind parameters by a corotating stream (Pizzo 1989). (b) Tail-bending simulation.

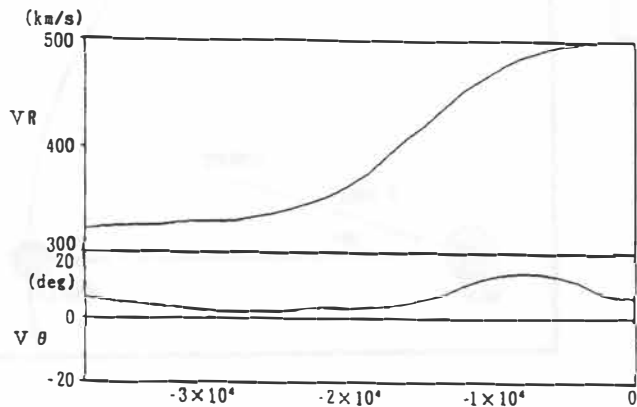
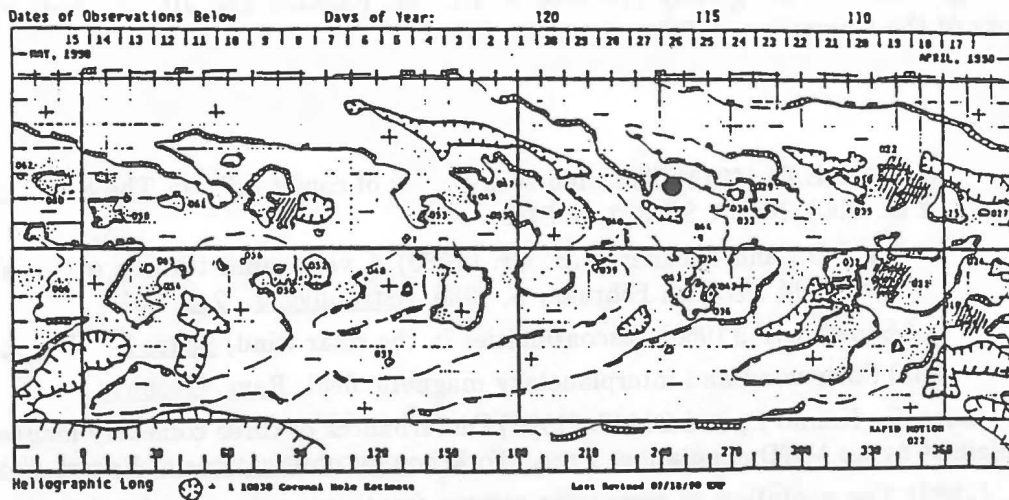


Fig. 5. – Solar wind velocity obtained from the deformation of the tail.



in longitude, it is concluded that this cometary event was not caused by the comet crossing the neutral sheet.

Finally, we surveyed the photospheric H-alpha synoptic chart shown in Figure 6. We found that a coronal hole existed near the source point. Consequently, it is quite possible that the disturbance was caused by a stream interaction between the high-speed flow from the coronal hole and the low-speed flow from the western region. Figure 7 shows the geometrical relation between the Sun, the Earth, and Comet Austin on April 29, 1990 on the meridian plane and the ecliptic plane. The comet was at the position where we could look up the Parker's spiral from the Earth. It must be concluded then, that the deflection of the solar wind flow in the corotating stream interaction region caused by the coronal hole matches quite well with the observation.

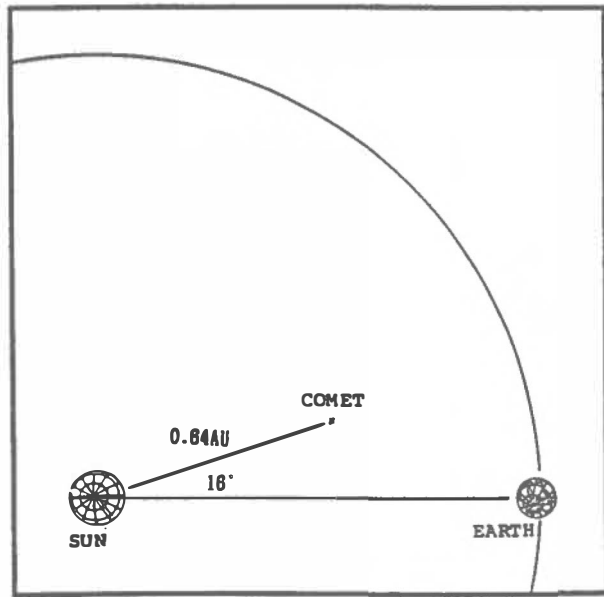
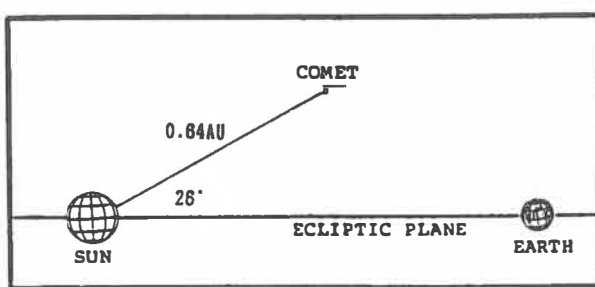


Fig. 7. – Geometrical relation between the comet, the Earth, and the Sun on April 29, 1990.

Acknowledgment: We are greatly indebted to Dr. M. Hamabe and Dr. T. Aoki at the Kiso Observatory of the University of Tokyo for their assistance with the observation.

References

- Brandt J.C. and Rothe E.D. (1976) The wind-sock theory of comet tails, in The Study of Comets, (B. Donn *et al.* eds.), NASA SP-393, p. 878.
- Brandt J.C., Hawley J.D., and Niedner M.B., Jr. (1980) A very rapid turning of the plasma-tail axis of comet Bradfield 1979l on February 6, 1980, Astrophys. J., **241**, L51.
- Colburn D.S. and Sonett C.P.,(1966) Discontinuities in the solar wind, Space Sci. Revs., **5**, 439.
- Dessler A.J. (1967) Solar wind and interplanetary magnetic field, Rev. Geophys., **5**, 1.
- Kozuka Y., Saito T., Konno I., and Oki T. (1990) Disturbances of three cometary magnetospheres as explained by an MHD simulation, Proc. Workshop on observations of Recent Comets, 137.
- Pizzo V.J. (1989) The evolution of corotating stream fronts near the ecliptic plane in the inner solar system 1. Two-dimensional fronts, Geophys. Res., **94**, 8673.
- Saito T., Takeuchi H., Kozuka Y., Okamura S., Hamabe M., Aoki T., Minami S., and Isobe S. (1990) A new observation on dynamics of the cometary magnetosphere with a mosaic CCD method, Proc. 23rd ISAS Lunar Planet. Symp.

SPIN VECTOR AND SHAPE OF 532 HERCULINA

T. Kwiatkowski and T. Michałowski

Astronomical Observatory, Adam Mickiewicz University,
ul. Słoneczna 36, 60–286 Poznań, Poland
E-mail : TKASTR@PLPUAM11 (EARN / BITNET)

LIGHTCURVES AVAILABLE

Herculina has been observed during 7 oppositions: 1954 (*Groeneveld and Kuiper, 1954*), 1963 (*Chang and Chang, 1963*), 1978 (*Harris and Young, 1979*), 1982 (*Drummond et al., 1985; Weidenschilling et al., 1990*), 1984 (*Taylor et al., 1987*), 1985 (*Erikson et al., 1991*), and 1987 (*Lebofsky et al., 1988; Weidenschilling et al., 1990*). This asteroid has very unusual lightcurves. They exhibit two maxima and minima in 1978, 1984 and 1987, and only one maximum and minimum in 1954, 1963 and 1982 per rotation cycle of about 9.4 hours. The 1985 lightcurve which is very close in aspect to those from 1963, shows two maxima and minima. The primary minimum is very similar to a single minimum in 1963, while the secondary one is only 0.06 mag deep. In 1963 no secondary minimum was visible.

PREVIOUS RESULTS

Drummond et al. (1985) observed Herculina by speckle interferometry techniques on 17 and 18 January 1982. These observations yielded triaxial ellipsoid dimensions of $263 \times 218 \times 215 \text{ km}^3$ and a north pole with ecliptic coordinates $\lambda_p = 132^\circ, \beta_p = -59^\circ$. In addition a spot some 75% brighter than the rest of the asteroid was inferred from both speckle interferometry and Herculina's lightcurves. This bright spot, centered at astero-centric latitude -35° , longitude $145^\circ - 165^\circ$ has a diameter of 55° (115 km). With this model *Drummond et al. (1985)* were able to reproduce the observed lightcurves from the oppositions 1954–1982, but their amplitudes were greater than the observed ones.

Using the Photometric astrometry method and the minima of Herculina's lightcurves from the 1954–1984 period, *Taylor et al. (1987)* obtained the retrograde rotation, $\lambda_p = 276^\circ, \beta_p = 1^\circ$ and $P_{\text{sid}} = 0^d 3918711$. In order to explain the lightcurves of Herculina, they proposed a new model of this asteroid. The model was a sphere with two dark regions that were each about 0.13 times the brightness of the surrounding surface. The regions were at 0° astero-centric longitude, $+15^\circ$ latitude, with radius of 30° , and 170° longitude, -38° latitude, with a radius of 26° . This model, sidereal period and north pole generated lightcurves consistent with both the observed amplitudes and the timings of extrema during the 1954–1984 the period.

Applying the Standard Thermal Model for asteroids, *Lebofsky et al. (1988)* could produce lightcurves at both reflected and emitted wavelengths, for the model proposed by *Taylor et al. (1987)*. In the reflected wavelength, maxima occur when high-albedo areas are visible, while minima occur when dark areas are in view. In the thermal infrared, more solar insolation is absorbed by the darker areas and reemitted, so that maxima occur

when warmer dark areas are visible. Thus, for Herculina's model, the two lightcurves should be about 90° (in rotation) out of phase with one another. Also, the amplitudes should be very different. Thermal lightcurve amplitudes tend to be smaller than those of reflected lightcurves. *Lebofsky et al.* (1988) observed Herculina by infrared technique. Their reflected and thermal lightcurves were in phase. The amplitudes of both lightcurves were close to each other. This was contrary to the predictions based on the albedo-variation model proposed by *Taylor et al.* (1987). These results argued that the lightcurves were dominated by shape or topography rather than by albedo. *Lebofsky et al.* (1988) concluded that Herculina was nonspherical and probably irregular in shape, but they had not yet been able to explain the lightcurves with single maxima and minima.

NON-ELLIPSOIDAL SHAPE OF HERCULINA

Recently, *Cellino et al.* (1989) and *Kwiatkowski* (1991) obtained numerically modelled lightcurves of non-ellipsoidal bodies. In their method the shape was formed by merging together eight octants of ellipsoids having different semiaxes with the constraint that adjacent octants must have two equal semiaxes in common. Moreover, the homogeneous internal density distribution was assumed. Such shapes can produce lightcurves which are very similar to those observed in the case of Herculina (see Fig.1).

Having in mind conclusions derived from infrared observations by *Lebofsky et al.* (1988), we decided to check a possibility of fitting the non-ellipsoidal model to observed light variations of Herculina. Using the pole obtained by *Taylor et al.* (1987) we calculated a wide set of synthetic lightcurves for systematically changed parameters describing the shape of the asteroid. Unfortunately we have not obtained a shape which could reproduce both the observed amplitudes and number of extrema. An example of good approximation to Herculina's amplitudes but big discrepancy in overall shape of lightcurves is presented in Fig.2.

Table 1. Results for Herculina

λ_p	Pole β_p	Axial ratios $\frac{a}{b}$	$\frac{b}{c}$	Sidereal period (days)	Sense of rotation	Ref.
284 ± 9	$+34 \pm 8$	1.13 ± 0.04	1.05 ± 0.04	0.3918764 ± 8	P	PW
276	+1			0.3918711	R	T
312	+59	1.21	1.01		R	D

Sense of rotation: P—prograde, R—retrograde

References: PW—present work, T—*Taylor et al.* 1987, D—*Drummond et al.* 1985

NEW POLE

Because of our inability to obtain the non-ellipsoidal model of Herculina we tried to

verify pole coordinations obtain by the others. We have decided to use only the lightcurves with two maxima and minima. In our method (*Michałowski 1988, 1991; Michałowski and Velichko, 1990*) we used the epochs, magnitudes of maxima of brightness, and the amplitudes, all taken from 17 lightcurves from the 1978, 1984, 1985, and 1987 apparitions. We have obtained the sidereal period, sense of rotation, pole, and triaxial ellipsoid which should be a rough estimation of the shape of Herculina (see Table 1). The results by *Drummond et al. (1985)* and *Taylor et al. (1987)* are given for comparison.

CONCLUSIONS

A visible discrepancy in the coordinates of Herculina's pole obtained by different methods, indicate a necessity to use a qualitatively new method. It should make it possible to obtain simultaneously the pole, sidereal period, sense of rotation and non-ellipsoidal shape of the asteroid. Of course, other possibilities (regular ellipsoid with albedo variegation, and/or internal density gradient) should not be neglected. According to the estimated poles, nearly in all observations Herculina was seen from its northern hemisphere. Therefore, new observations showing the southern parts of its surface are required.

Acknowledgements.

We wish to express our appreciation to Mr. R.Jokiel for the help in preparation of the manuscript. One of us (T.M.) gratefully acknowledges the receipt of financial support from the Organizing Committee and Stefan Batory Foundation to allow attendance of the conference.

REFERENCES

- Cellino A., Zappala V., Farinella P. (1989) Asteroids shapes and lightcurve morphology. *Icarus*, **78**, 298–310.
 Chang Y. G., Chang C.- S. (1963) Photometric observations of variable asteroids, II. *Acta Astron. Sin.*, **11**, 139–149.
 Drummond J. D., Hege E. K., Cocke W. J., Freeman J. D., Christou J. C., Binzel R. P. (1985) Speckle interferometry of asteroids. II 532 Herculina. *Icarus*, **61**, 232–240.
 Erikson A., Cutispoto G., Debehogne H., Hahn H., Lagerkvist C.- I., Lindgren M., Magnusson P. (1991) Physical studies of asteroids XXIII : Photometric observations of the asteroids 6, 32, 196, 243, 416, 532 and 1580. *Astron. Astrophys. Suppl.*, submitted.
 Groeneveld I., Kuiper G. R. (1954) Photometric studies of asteroids. I. *Astrophys. J.*, **120**, 200–220.
 Harris A. W., Young J. (1979) Photoelectric lightcurves of asteroids 42 Isis, 45 Eugenia, 56 Melete, 103 Hera, 532 Herculina and 558 Carmen. *Icarus*, **38**, 100–105.
 Kwiatkowski T. (1991) in preparation.
 Lebofsky L. A., Greenberg R., Tedesco E. F., Veeder G. J. (1988) Infrared lightcurves of asteroids 532 Herculina and 45 Eugenia : proof of the absence of significant albedo markings. *Icarus*, **75**, 518–526.
 Michałowski T. (1988) Photometric astrometry applied to asteroids : 6, 15, 43, and 624. *Acta Astron.*, **38**, 455–468.
 Michałowski T. (1991) in preparation.
 Michałowski T., Velichko F. P. (1990) Photoelectric photometry, parameters of rotation and shapes of asteroids 22 Kalliope and 79 Eurydome. *Acta Astron.*, **40**, 321.
 Taylor R. C., Birch P. V., Drummond J. D., Pospieszalska-Surdej A., Surdej J. (1987) Asteroid 532 Herculina : lightcurves, pole orientation and a model. *Icarus*, **69**, 354–369.
 Weidenschilling S. J., Chapman C. R., Davis D. R., Greenberg R., Levy D. H., Binzel R. P., Vail S. M., Magee M., Spaute D. (1990) Photometric geodesy of main-belt asteroids. III. Additional lightcurves. *Icarus*, **86**, 402–447.

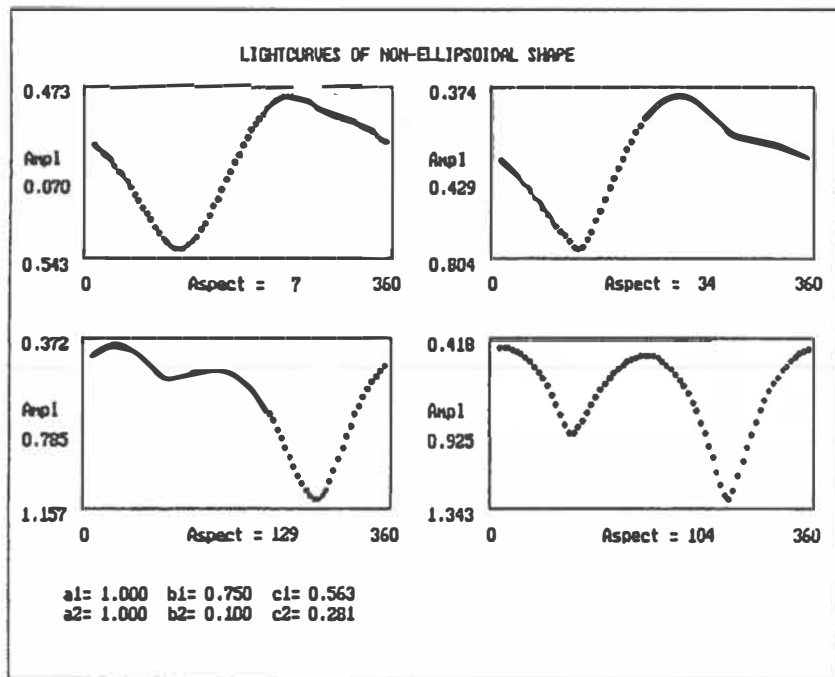


Fig. 1. Examples of lightcurves obtained from a non-ellipsoidal model
(Lommel-Seeliger scattering law, pole coord. $\lambda = 276$, $\beta = 1$)

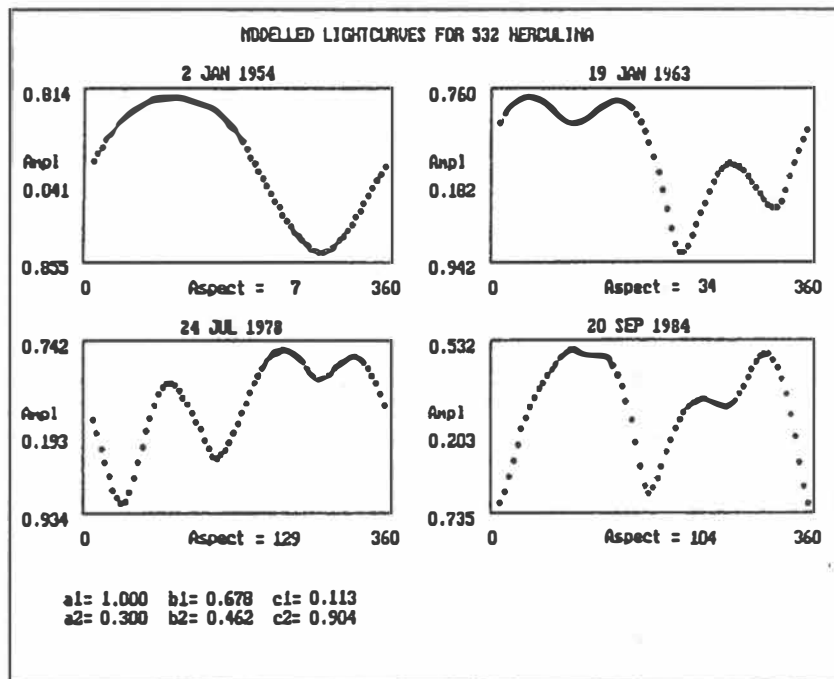


Fig. 2. Lightcurves obtained from the non-ellipsoidal model of
Herculina, reflecting observed amplitudes
(Lommel-Seeliger scattering law, pole coord. $\lambda = 276$, $\beta = 1$).

EVALUATING SOME COMPUTER ENHANCEMENT ALGORITHMS THAT IMPROVE THE VISIBILITY OF COMETARY MORPHOLOGY

Stephen M. Larson

Lunar and Planetary Laboratory
University of Arizona
Tucson, AZ. 85721

Charles D. Slaughter

Photometrics Ltd.
3440 Britannia Dr.
Tucson, AZ. 85706

ABSTRACT

Digital enhancement of cometary images is a necessary tool in studying cometary morphology. Many image processing algorithms, some developed specifically for comets, have been used to enhance the subtle, low contrast coma and tail features. We compare some of the most commonly used algorithms on two different images to evaluate their strong and weak points, and conclude that there currently exists no single "ideal" algorithm, although the radial gradient spatial filter gives the best overall result. This comparison should aid users in selecting the best algorithm to enhance particular features of interest.

INTRODUCTION

The observed morphology of cometary comae and tails is determined by ejection circumstances and the interaction of the ejected material with the cometary environment. Temporal data on the anisotropic emission of dust and gas over time can provide useful information on such things as location of active areas on the nucleus, the nucleus spin vector, and gas/dust interaction. Time sequences may also be particularly useful in following the formation and evolution of fast moving ion structures near the nucleus. However, discrete coma features are usually diffuse, of low amplitude, and they are superimposed on a steep intensity gradient radial to the nucleus. The usual 8-bit display does not usually show much detail because for large intensity ranges the contrast of coma structure is too small, or if the contrast is increased, only a small intensity range is visible.

To improve the visibility of these features, a variety of digital enhancement algorithms have been employed with varying degrees of success. They usually produced some spatial filtering, and were chosen to optimize visibility of certain detail. Since information in the image is altered, it is important to understand the effects that parameter selection and processing artifacts can have on subsequent interpretation. Our definition of the ideal algorithm is that it must enhance low contrast features while not introducing misleading artifacts. We require that features seen in the enhanced image also be seen in the unenhanced version with appropriate contrast and intensity windowing. We have not found the ideal algorithm; all of those that we have tried or developed have strong and weak elements depending upon the type of features of interest. To help assess the suitability of various algorithms, we have processed two images in a variety of ways so they can be directly compared. We attempt to identify the strong and weak points of each in the context of optimizing visibility while maintaining positional integrity of features at the expense of photometric information.

Figures 1 and 2 show the effects of various image processing on two sample images containing a variety of coma and tail features. An attempt has been made to generate hard copy that shows as

much detail as possible for each image. We do not assert that these results will be the most appropriate for other data. Experience with many data sets taken with a variety of telescopes and plate scales indicate that the sample frequency (pixel size) to resolution ratio can be important in selecting the algorithm or processing parameters. In general, there is more parameter leeway with over-sampled data (pixel size/"resolution" < 1) than for under-sampled data because of reduced centroid (or registration) uncertainty and pixelization artifacts are smaller relative to the features of interest. The two sample images and their processed versions are shown in Figures 1 A-H and 2 A-H. The figure letters correspond to the subheading letters below.

A. THE UNPROCESSED IMAGES

The sample image in Figure 1 is a composite which includes a mostly H₂O⁺ CCD image of P/Brorsen-Metcalf taken with a narrow-band filter transmitting the H₂O⁺ (0,8,0) band near 619 nm, and some of the C₂ (0,2) band. This comet was extremely dust-poor, so the ion streamers were relatively high contrast, and the C₂ is easily seen to be restricted near the nucleus. However, since this is not usually the case for a "typical" dusty comet, we have added a 1/r intensity gradient to the central condensation that might be expected from isotropic emission of dust from a rapidly rotating nucleus. The resulting test image has a "dust"/ion intensity ratio of 50:1. A second combination using an image of P/Brorsen-Metcalf taken 15 minutes later was used for the temporal derivative. The scale of the image is 0.7 arcsec per pixel, or 400 km per pixel at the comet.

The sample image in Figure 2 is a broad red-band CCD image of P/Halley that contains several dust jets, an antisunward dust jet, and ion streamers. A second image taken 45 minutes later was used for the temporal derivative. Both are three co-added 120 second exposures, and are also 0.7 arcsec per pixel, or 640 km per pixel at the comet.

B. LOG 10 INTENSITIES

The simplest operation is to alter the intensity scale by some non-linear contrast stretch (such as the base 10 logarithm) to suppresses the steep intensity peak near the photocenter. In this case, the resulting pixel value (I) becomes;

$$I_{(x,y)} = \log I_{o(x,y)}$$

where I_o = original pixel count value. This helps bring the brightness of the faint outer regions of the coma closer to those in the inner coma. No artifacts are introduced, but there is only a modest improvement in visibility of low contrast features. In general, such non-linear stretches do not allow appreciable increase in local feature contrast relative to the background. The subjective result is to convert linear-response electronic images to a photographic-like response. The strong point is that the image is easily understandable and interpretation is straight forward. Because the operation involves no special parameter selection (or "interpretation"), this is the form Near Nucleus Studies Network images appear in the International Halley Watch printed archive.

SPATIAL DERIVATIVES

C. Linear Shift-difference

Spatial derivative, or "shift-difference" algorithms enhance intensity discontinuities, but only in the direction of the shift (Klingsmith, 1982);

$$I_{(x,y)} = I_{o(x,y)} - I_{o(x+n,y+m)}$$

where, n, m are the amount of the shift in x and y. The simple linear shift-difference is very effective for bringing out ion tail structure when the shift is perpendicular to the tail axis. The magnitude of shift is a compromise between showing the smallest detail and enhancing the noise. The most serious problems with this method is that the results are directionally dependent, and are

not easily interpretable. The resulting features, showing the rate of change of intensity, enhance the edges of jets and shells. In both of these examples, the shift is perpendicular to the tail axis to best show the ion features. The residual radial gradient is directly related to the magnitude of shift. However, a smaller shift would leave only the highest spatial frequencies (mostly system noise). Coma detail is particularly difficult to interpret.

D. Rotational Shift-difference

Radial and rotational shift-difference algorithms were developed in response to the fact that particles generally move radially away from the nucleus, and that nucleus rotation produces spiral features (Larson and Sekanina, 1984). In polar coordinates, the combination radial and rotational shift gives;

$$I_{(r,\theta)} = I_{o(r,\theta)} - I_{((r+\Delta r), (\theta+\Delta\theta))}$$

where Δr = the radial shift, and $\Delta\theta$ = the rotational shift. The rotational derivative used in this comparison emphasizes rotational intensity discontinuities, such as radial jets and ion streamers. A radial derivative emphasizes discontinuities concentric to the nucleus, such as hoods and evolved jets. In one variation, such shifts are done in combination with rotational shifts of different directions but different amounts to reduce the directional dependency of the enhancement. The reproduced images show features in a 10^0 rotational derivative, however, ion streamer overlap may cause confusing aliasing. The angular shift produces a radial dependency on the linear scale of edges that become enhanced. For some types of gas jets that become more diffuse farther from the nucleus, rotational shift-differencing is useful, but for ion features, it is usually confusing. With the rotational derivative, it is possible to see features down to the central condensation.

Since the synthetic test image contains no radial discontinuities, nothing appears in a radial shift-difference, but the Comet Halley image shows the outer envelope well. By combining the radial plus rotational shift difference the directional dependency of feature visibility is reduced but not eliminated. Interpretation requires great care since it is the edges of features that are enhanced. Finding the best combination of rotational and radial shifts can be difficult and enhances only a limited spatial frequency range. Radial and combination derivatives are not shown in the figures.

E. TEMPORAL DERIVATIVE

Differencing carefully registered images taken at different times yield features that have moved. Such temporal derivative images are projected velocity maps that (among other things) make it easy to distinguish rapidly varying ion features from the slower moving dust structures (e.g. Larson and Minton, 1971; Larson, 1986).

$$I_{(x, y)} = I_{o(xt_1, yt_1)} - I_{o(xt_2, yt_2)}$$

where t_1 and t_2 are different times. Successful short-term difference images bring out ion features which are normally a minor component of a broad-band image. This method places great demands upon sets of images with nearly identical quality and very precise registration. Registration on the centroid of a several pixel area around the central condensation is usually necessary to reduce the effects of noise. Variations in seeing and guiding can complicate the result. Interpretation must be made with care, since the result is an image of moving feature edges.

The synthetic test image processed this way shows the ion features best of all of the algorithms used, as all of the radial intensity gradient is eliminated. The rapid ion motions require images taken only a few minutes apart to show detail at this resolution. The Comet Halley image also shows the ion streamer motions, but also a lot of garbage resulting from imperfect flat fields, scattered twilight, and possible differential extinction at the large airmass. These problems cause the coma to have dark and light components that have nothing to do with the comet. The best temporal derivatives resulting from consistent, regularly spaced sequences of images are relatively easy to interpret.

F. AZIMUTHAL RENORMALIZATION

Azimuthal function algorithms reduce the radial gradient by either subtracting the average value in the annulus of constant distance from the photocenter, or by subtracting a best-fit, low-order function to the annulus (A'Hearn, et al., 1986).

$$I(r, \theta) = I_0(r, \theta) - ((\sum I(r))/n)$$

where n = number of pixels falling within the annulus of radius r , and are summed over all theta. Averaging and function fitting is more easily done after a polar to rectangular coordinate transformation (with the photocenter at the origin). This method is very efficient in eliminating the radial gradient, does not have any directional dependencies, and interpretation is straightforward. The photocenter must be determined very carefully, especially for undersampled data, or spurious features close to the nucleus may be produced. Options in the A'Hearn and Klavetter (Univ. Maryland) program includes normalization to mean or median values at constant radius, or normalizing to a functional profile. Our own implementation of this algorithm normalizes to the mean of the annulus without a polar to rectangular coordinate conversion step (fig. 2F).

The synthetic image responds very well by eliminating all of the radial gradient and leaving the ion features intact. The noise becomes rather apparent, but there are options for averaging over various ranges of r and theta that the authors did not have time to try. We are not confident that the optimum parameters for this algorithm were used, however, the result is the most easily interpretable version for this image. The Comet Halley image, primarily because of the large amplitude of the sunward asymmetry, does not respond as well to an azimuthal normalization to a mean value. Similarly, normalization to an azimuthally symmetric function produces over-compensation in the tail direction, and under-compensation in the sunward direction. Although this algorithm does not work very well for primarily continuum images it works very well on images of the more symmetrical gas comets.

Another approach is to subtract a synthetic image based on a generalized model of particle outflow. This assumes some *a priori* knowledge of the ejection function. If there is enough data, subtraction of a mask produced by the median of many images over time may also work (Jewitt, 1991). In a sense, this is similar to a temporal derivative.

G. SPATIAL FILTERING

Traditional spatial filtering algorithms reduce the radial gradient by eliminating the low spatial frequency domain in the image. A "high-pass" gaussian deconvolution retains features in the image smaller than the gaussian, and by eliminating the broad radial gradient, the contrast of the smaller features can be increased. There is no directional dependency, but "ringing" artifacts can be seen around bright stars and the central condensation of the comet. Selecting the optimum size gaussian usually depends upon the characteristic size of the features of interest. Although large, complete filter kernels are more rigorous, our spatial filtering algorithm uses an abbreviated kernel convolution to reduce the computation time. A 3×3 pixel kernel is used, but the kernel size is adjusted by varying the spacing between kernel pixels. This allows filtering over a wide range of spatial domains, while operating on a small number of pixels. The kernel shape is dictated by weights given the "corner" and "medial" pixels in the kernel.

$$I(r, \theta) = I_0(r, \theta) - \sum I_0(r', \theta') w_1 - \sum I_0(r'', \theta'') w_2$$

where; w_1 = "corner" weights; w_2 = "medial" weights, nominally $(w_1 + w_2) = 1.0$; $\Delta x = \Delta y$ = kernel pixel separation, and $r = (x^2 + y^2)^{1/2}$, $r' = ((x \pm \Delta x)^2 + (y \mp \Delta y)^2)^{1/2}$, $r'' = (x^2 + (y \mp \Delta y)^2)^{1/2}$; $((x \pm \Delta x)^2 + y^2)^{1/2}$, $\theta = \arctan(y/x)$; $\theta' = \arctan((y \mp \Delta y)/(x \pm \Delta x))$, $\theta'' = \arctan(y/(x \pm \Delta x))$, $((y \mp \Delta y)/x)$

Processing the synthetic image brings out the ion tail fairly well up to the point that the spatial component of the radial gradient becomes smaller than the effective kernel FWHM near the

central condensation. Use of a smaller kernel to reduce this residual gradient emphasizes the noise and is better suited to high S/N ratio images. The P/Halley image shows nearly all of the jet, envelope and ion features quite well. The kernel size was chosen to optimize over-all visibility of features, but there is a residual small gradient close to the central condensation. Interpretation of this image is not difficult.

H. RADIAL GRADIENT SPATIAL FILTERING

Since cometary features typically become larger farther from the nucleus, spatially selective spatial filtering might be desirable. We have recently developed a variable kernel deconvolution routine that passes increasingly higher frequencies closer to the photocenter. This enhances a larger spatial range of coma features which often exist in an image. The previous algorithm is used, but the spacing ($\Delta x, \Delta y$) is variable from the photocenter,

$$\Delta x = \Delta y = (a + (r/b)), a = \text{kernel pixel separation}, b = \text{radial scale factor}.$$

The processed synthetic image shows the ion tail well, but does not show the folding rays as well as the temporal derivative. Note the strong pixelization pattern radiating from the nucleus. The processed P/Halley image shows detail of the central condensation as well as the ion streamers. The parameters w_1, w_2, a and b must be chosen empirically to ensure that features in the various spatial regimes are visible. Field stars may present problems with "ringing" (dot patterns in this abbreviated kernel).

CONCLUSIONS

We find that for coma jets, spatial filtering provides the best overall enhancement with minimal artifacts, and the results are readily interpretable. The radially variable convolution kernel provides a range of spatial filtering appropriate for different regions of the comet (high-pass at the center, lower near the edges). For ion structure, we find that temporal derivatives are the most useful in not only bringing out low contrast detail, but providing a "velocity map" of ion motions.

Acknowledgments

This work is supported by NASA Planetary Atmospheres grant NAGW 1974. The authors are indebted to M. A'Hearn and especially J. Klavetter (Univ. Maryland) for sharing their azimuthal renormalization code.

References

- A'Hearn, M. F., Hoban, S., Birch, P.V., Bowers, C., Martin, R., and Klinglesmith, D.A. (1986) Cyanogen jets in Comet Halley, Nature, 324, 649-651.
- Jewitt, D. (1991) Cometary photometry. In Comets in the Post-Halley Era (R. L. Newburn, M. Neugebauer and J. Rahe eds.), pp 19-65. Kluwer, Dordrecht.
- Klinglesmith, D. A. (1981) The interactive astronomical data analysis facility - - Image enhancement techniques applied to Comet Halley. In Modern Observational Techniques for Comets (J. C. Brandt, J. M. Greenberg, B. Donn and J. Rahe eds.) pp. 223-231. JPL publication 81-68, Pasadena.
- Larson, S. M. (1986) A review of some digital image processing in cometary research. In Asteroids Comets Meteors II (C. -I. Lagerkvist, B. A. Lindblad, H. Lundstedt, and H. Rickman, eds.), pp. 449-459. Uppsala universitet, Uppsala.
- Larson, S. M. and Minton, R. B. (1972) Photographic observations of Comet Bennett, 1970II. In Comets - Scientific Data and Missions (G. P. Kuiper and E. Roemer, eds.), pp. 183-208. Lunar and Planetary Laboratory, Tucson.
- Larson, S. M. and Sekanina, Z. (1984) Coma morphology and dust emission pattern of periodic Comet Halley.I. High resolution images taken at Mount Wilson in 1910. Astron. J., 89, No.4, 571-578 and 600-606.

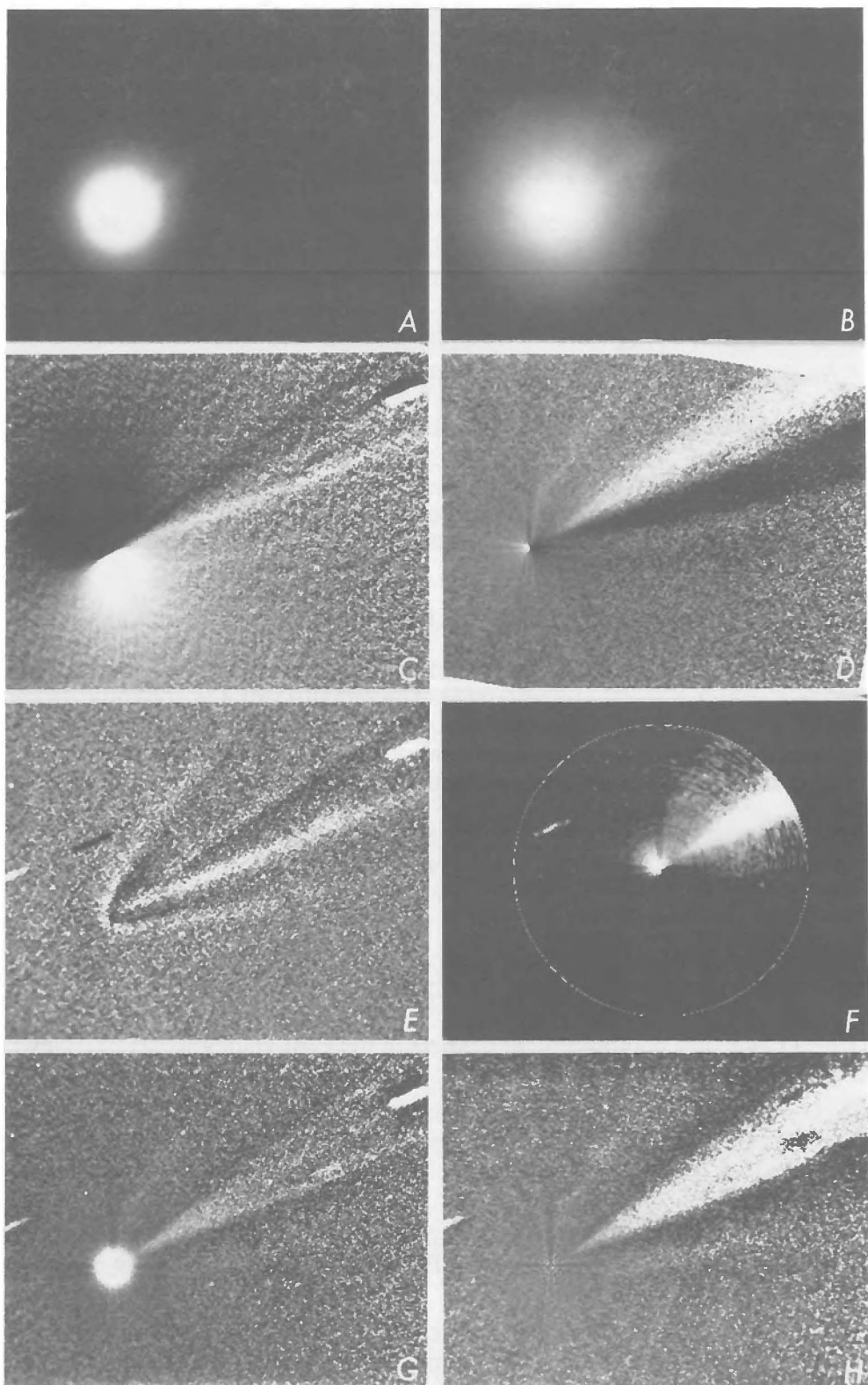


Fig. 1. A. Test image with ion features and a symmetric $1/r$ intensity gradient (see text), B. displayed as the base 10 logarithm of the counts, C. linear derivative (perpendicular to the tail axis), D. rotational derivative, E. temporal derivative, F. azimuthal renormalization, G. constant spatial filter, and H. radially varying spatial filter.

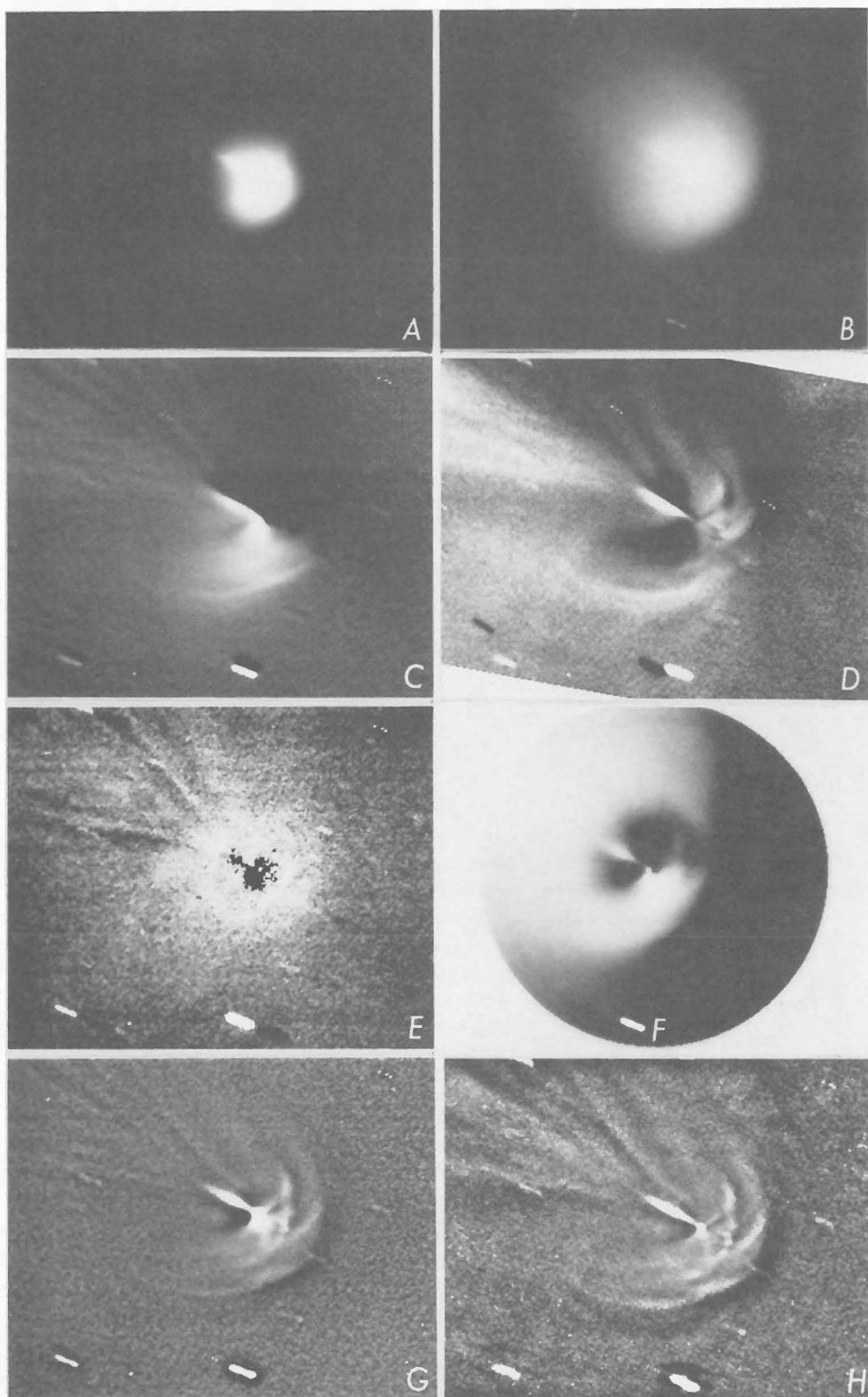


Fig. 2 A. Image of P/Halley (see text), B. displayed as the base 10 logarithm of the counts, C. linear derivative (perpendicular to the tail axis), D. rotational derivative, E. temporal derivative, F. azimuthal renormalization, G. constant spatial filter, and H. radially varying spatial filter.

HELIOCENTRIC DISTANCE DEPENDENCIES OF THE C₂ LIFETIME AND C₂ PARENT PRODUCTION RATE IN COMET P/BRORSEN-METCALF (1989o)

Lazzarin M.¹, Tozzi G.P.², Barbieri C.^{1,3} and Festou M.C.⁴

¹ Dipartimento di Astronomia dell'Università - Vicolo dell'Osservatorio - I 35122 Padova

² Osservatorio Astrofisico di Arcetri - Largo E. Fermi 5 - I 50125 Firenze

³ Osservatorio Astronomico di Padova - Vicolo dell'Osservatorio - I 35122 Padova

⁴ Observatoire Midi-Pyrénées - 14, Av. Edouard-Belin - F 31400 Toulouse

1 Summary

Comet P/Brorsen-Metcalf (1989o) has been extensively observed in the visible and in the ultraviolet during its latest apparition of summer 1989. In this paper we report a preliminary determination of the C₂ production rates and lifetimes and we compare those rates to the H₂O production rates obtained from UV data.

2 Observations.

Visible spectra of P/Brorsen-Metcalf (1989o) were recorded from 26 July until 25 August 1989 while the heliocentric and the geocentric distances changed from 1.1 to 0.6 AU and 0.6 to 0.7 AU, respectively. This set of 14 spectrophotometric optical observations (7 of them analyzed; see table I) overlaps a set of 6 ultraviolet observations obtained with the International Ultraviolet Explorer (IUE) collected around 1 August 1989.

The long slit visible spectra were collected with the 1.5 m f/8 Cassegrain telescope of the Loiano Observatory (I) equipped with a Boller & Chivens spectrograph and a CCD as detector. As shown on table I, the spectra cover usually the range 4500-5800 Å or 4000-7000 Å, with an instrumental FWHM of 5 or 10 Å, depending on the diffraction grating used. The projected slit length was 4.8 arc min on the sky ($\Rightarrow 120\text{-}150 \times 10^3$ km at the comet distance) with a pixel size of 1.6 arc sec ($\Rightarrow 700\text{-}800$ km). The effective spatial resolution was dominated by the seeing conditions and by the guiding errors of the telescope. In a typical night of observation two cometary spectra were recorded, with different slit position angles: one in the sun-comet direction and the other perpendicular to that line. Bias, flat field, calibration lamp, sky and standard star spectra were recorded each night in order to calibrate the cometary spectra. These data allow the study of the spatial profiles of the C₂, $\Delta\nu = +1, 0, -1$ Swan band emissions and the determination of C₂ production rates as a function of heliocentric distance.

Low resolution IUE spectra recorded between 27 July and 5 August 1989 are used to determine the water production rate.

Table I - Observing log of the analyzed visible spectra

Date	R_h AU	Δ AU	β deg.	Spectral Range (Å)	Dispersion Å/pixel
29 Jul.	1.09	0.67	65.2	3800-6800	5.9
31 Jul.	1.06	0.65	66.5	3800-6800	5.9
7 Aug.	0.94	0.62	77.9	3800-6800	5.9
10 Aug.	0.89	0.63	82.0	5800-7100	2.6
13 Aug.	0.84	0.64	85.6	4500-5800	2.6
18 Aug.	0.75	0.68	89.9	4500-5800	2.6
21 Aug.	0.70	0.71	91.1	4500-5800	2.6

3 Data reduction and analysis.

Since the comet and sky spectra were not recorded at the same time and in similar conditions, sky spectra were only used to determine the position of the strongest undesirable lines in the comet spectra. Those latter were used to perform the sky subtraction in the manner described by Festou et al. (1990), i. e. by using information contained near the edge of each frame, away from the emission lines of the comet.

The dust component in this comet was generally weak, so that no particular care was necessary to subtract it from the cometary spectra. When it was stronger, at the end of August, a synthetic dust spectrum has been created and subtracted.

The radial intensity profiles for each observed species were constructed using the largest possible bandpass. The actual extension of these profiles were almost the same, of the order of 10^5 km during the entire observing period, which allowed us to perform an investigation of the creation and destruction processes of the observed species.

After discarding the non photometric data (standard stars were observed before and after the comet observations), it was found that the absolute calibration errors were always below the $\pm 15\%$ level.

Absolute calibration, reduction procedure, seeing, tracking quality and S/N affect the relative uncertainty of the individual data points in a complex manner. The sky subtraction procedure can *a priori* introduce a significant systematic error: our technique, that use the comet frames themselves in regions where no comet lines are present, allows to reduce this source of uncertainty to a very low level. Far from the center of the coma, where the signal is weak, the scattering of the data points gives an idea of the internal consistency of the data. Near the center of the coma, where relative photometric inaccuracies are small, the shape of the profile is mostly determined by the tracking quality. The quality of this parameter can be determined by examining the shape of the continuum near the center of

the coma: in the worse case, the combined effects of tracking and seeing are equivalent to a drift of 5 arc seconds along the sun-comet line. That effect was taken into account in the data analysis by appropriately enlarging the simulated instrumental slit.

4 Interpretation.

The entire data set was interpreted with the vectorial model (Festou, 1981a,b). Parent molecule velocities were assumed to vary with the heliocentric distance according to the law $0.85R_h^{-0.5}$ km/s (Cochran and Barker, 1986). Water and OH lifetimes were computed for the solar flux conditions of mid 1989.

The water production rate has been computed from the mean intensity, averaged over the 10 by 20 arc sec IUE slit, of the OH(0-0) and OH(1-0) bands.

The nucleus activity was assumed to be steady, an assumption found *a posteriori* to be valid over periods of time of the order of one day. In our model-data fitting attempts, once the production channel for the coma species is selected (one or two photodissociation steps), only the parent lifetime, the daughter species velocity and lifetime are adjustable parameters. In what follows, we will restrict ourselves to the results concerning the C₂ radicals.

Guided by preceding analysis of similar nature, we first tested a single photodissociation as the production channel of the radicals. When the comet is far from the sun, only the parent lifetime significantly affects the computed profile and this parameter can be evaluated (the lifetime of the radicals is then taken as 10⁵ s at 1 AU and the velocity is set to 1 km/s). A value close to 20 10³ s was found using our complete set of profiles. This value is not compatible with the C₂ radicals being produced by the dissociation of C₂H₂ parents. When the comet is closer to the sun, since our profiles still extend out to about 10⁵ km, the radical lifetime and velocity become measurable quantities. The two parameters have non independent values: as an example, if the C₂ velocities are assumed to be 1 and 1.4 km/s, C₂ lifetimes of 0.9 to 1.5 10⁵ and 1.2 to 2. 10⁵ seconds are found, respectively.

It is important to note here that none of the inner coma theoretical profiles fits the observations: the observed profiles are too flat (see Fig.1), a strong indication that either the C₂ radicals are produced via a two step process or that two parents at least contributed to their production. An extended source of the nature of that found in comet P/Halley (1986 III) does not seem likely (or it would not contribute much) since the comet was not very dusty.

We evaluated the C₂ production rates assuming the canonical value of 1 km/s for the radial velocity (other parameters are thus derived quantities). Fig. 2 shows our results: i) short term variations of no more than 15-30% are possibly present (each point in this figure represents generally an average of about 6 individual measurements), ii) the long term variation of the water and the C₂ production rates vary according to R_h^{-3.5±0.3} law, iii) the water to C₂ production rate ratio is of the order of 500, which indicates that comet

1989o was "normal", iv) the variation of the C₂ lifetime is compatible with a R_h² variation and photodissociation of parent molecules appears as the most likely production process.

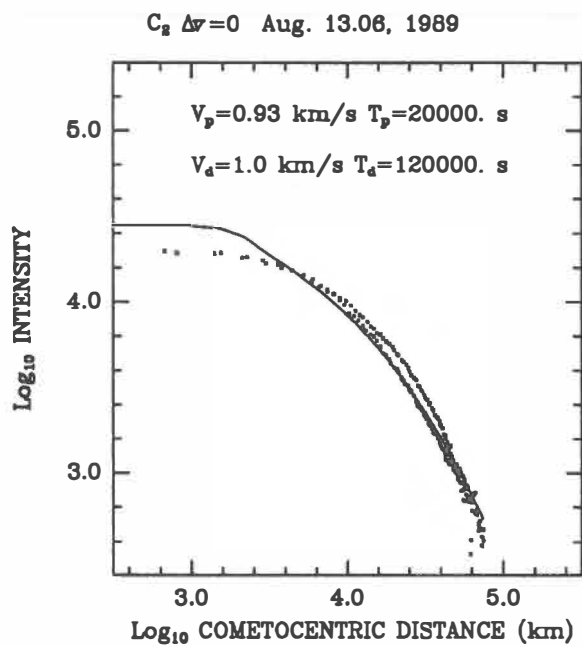


Fig. 1 – Intensity profile of C₂ $\Delta v=0$ band.

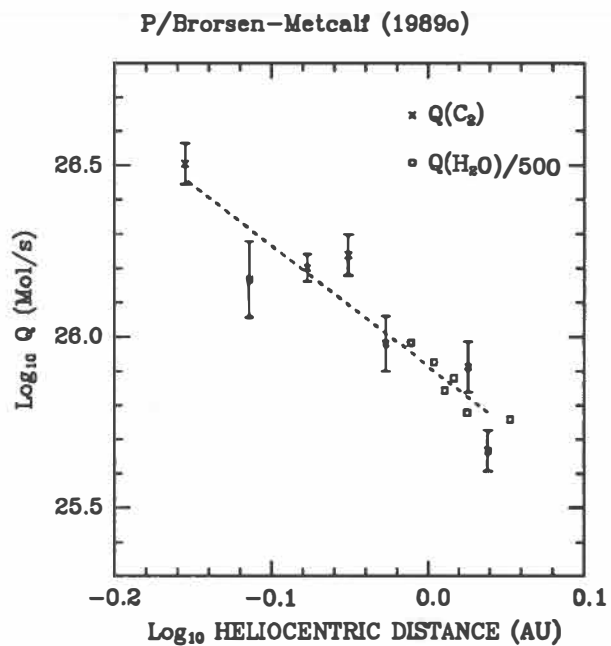


Fig. 2 – Gas production rate vs R_h

5 References

- Cochran, A. L. and Barker E. S. (1986) Spectrophotometric observations of comet Halley in Exploration of Halley's Comet pp 439-444 - ESA SP 250
- Festou, M. C. (1981a) The density of neutral compounds in cometary atmosphere I. Astronom. Astrophys., 95, 69-79
- Festou, M. C. (1981b) The density of neutral compounds in cometary atmosphere II. Astronom. Astrophys., 96, 52-57
- Festou, M. C., Tozzi, G. P., Smaldone, L. A., Felembok, P., Falciani R. and Zucconi, J.-M. (1990) Did an outburst occur on 4 December 1985 in Halley's comet? Astronom Astrophys., 227, 609-618

POLARIMETRIC OBSERVATIONS OF COMET LEVY 1990c AND OF OTHER COMETS : SOME CLUES TO THE EVOLUTION OF COMETARY DUST

A.Ch. Levasseur-Regourd, J.B. Renard and E. Hadamcik
Université Paris 6 / Service d'Aéronomie, BP 3, 91371 Verrières, France

ABSTRACT. The evolution with the phase angle α of the polarization degree P of light scattered by comet Halley's dust is well documented. No significant discrepancy is found between Halley and Levy polarization curves near the inversion point. From all available cometary observations, we have derived polarimetric synthetic curves. Typically, a set of about 200 data points in the red wavelengths range exhibits a minimum for ($\alpha \approx 10.3^\circ$, $P \approx -1.8\%$) and an inversion point for ($\alpha \approx 22.4^\circ$, $P = 0\%$), with a slope of about 0.27% per degree.

A significant spreading of some data (comets Austin 1982VI, Austin 1989c₁, West 1976VI) is found at large phase angles. The analysis of our polarimetric maps of Levy reveals that the inner coma is heterogeneous. The increase of the inversion angle value with increasing distance from the photometric center is suspected to be due to the evolution with time of the grains ejected from the nucleus. A fan like structure could be produced by a jet of grains freshly ejected.

POLARIMETRIC OBSERVATIONS OF HALLEY 1986III

Numerous measurements of the linear polarization degree of solar light scattered by comet Halley's dust have been performed in 1985-1986. Polarization compilations have been published (e.g. Dollfus et al., 1988) or are available from IHW (International Halley Watch) archives. There is a fair agreement among all the observers, at least as far as the solar distance is smaller than 2 AU and the polarization is estimated over the whole coma.

The evolution of polarization degree P with phase angle α shows a negative branch (direction of polarization in the scattering plane) for α smaller than α_0 , with a minimum (α_{\min} , P_{\min}) and an almost linear increase at a rate h near the inversion point (α_0 , 0). Synthetic curves (Levasseur-Regourd, 1990) derived from all available data in the blue and red wavelengths ranges lead respectively to $\alpha_{\min} = (9.6 \pm 2.0)^\circ$, $P_{\min} = (-1.3 \pm 0.8)\%$, $\alpha_0 = (21.2 \pm 1.0)^\circ$, $h = (0.21 \pm 0.03)\%$ per degree and to $\alpha_{\min} = (10.4 \pm 2.0)^\circ$, $P_{\min} = (-1.5 \pm 0.8)\%$, $\alpha_0 = (22.3 \pm 1.0)^\circ$, $h = (0.25 \pm 0.03)\%$ per degree. New polarimetric observations performed since the return of comet Halley allow comparisons to be made.

POLARIMETRIC OBSERVATIONS OF LEVY 1990c

We have obtained CCD polarimetric images of the inner coma of comet Levy 1990c from the Pic du Midi 2 meters telescope on five consecutive nights, August 15 to 19, 1990. The phase angle was decreasing from 21.6° to 17.6° , and the effective width of the images was equal to 6800 km. Four polaroid filters mounted at 45° from one another were used ; measurements with the 0° (component I_1) and 90° (component I_2) oriented filters were made consecutively, while measurements made with the 45° and 135° filters allowed the orientation to be checked. Two red continuum filters, centered at 650 nm and 684 nm, were used to provide gas emission free signals. Details on the observational techniques and on the data reduction can be found in Renard et al. (1991).

Two results appear immediately from the analysis of the intensity ($I_1 + I_2$) and polarization ($(I_1 - I_2) / (I_1 + I_2)$) maps derived from the images. First, the intensity maps are quite smooth, with an anisotropy with respect to the solar/antisolar direction (ratio of about 1.4) ; secondly, the polarization maps are found to be heterogeneous. Fig. 1 shows typical scans ; the resolution is of about 200 km.

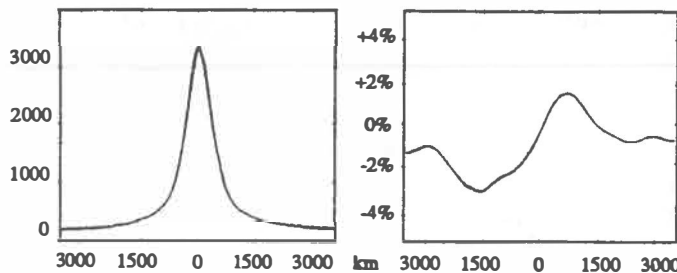


Figure 1 - Scans of intensity map (left, arbitrary units) and polarization map (right, %) obtained on the 19 August 1990 around 01h16m. Each (east-west) scan is 6800 km long and is made through the photometric center (linear scale).

Besides, from data obtained relatively far away from the nucleus (typically in a 1800 km wide frame located at 2500 km from the photometric center), the evolution of polarization with phase angle is found to fit perfectly with that obtained for Halley ; α_0 is computed to be equal to $(22.0 \pm 0.8)^\circ$ and h to be equal to $(0.29 \pm 0.03)\%$ per degree.

PHASE ANGLE EFFECT

From the good agreement between the results from comets Levy (outer coma observations) and Halley (large aperture observations mainly corresponding to the outer coma, due to a dilution of the polarization variations), it makes sense to compare all the available polarimetric observations. The data are restricted to : i) the same wavelengths range, ii) solar distances smaller than 2 AU.

Figure 2 (left) presents, in the blue range, the data from Bastien et al. (1986), Dollfus and Suchail (1987), Kikuchi et al. (1987, 1989), Kiselev and Chernova (1978), Le Borgne et al. (1987), Michalsky (1981), Myers (1985), Sen et al. (1991) and Visvanathan et al. (1991). The derived synthetic curve leads to $\alpha_{\min} = (9.8 \pm 2.0)^\circ$, $P_{\min} = (-1.4 \pm 1.0)\%$, $\alpha_0 = (21.7 \pm 1.0)^\circ$ and $h = (0.22 \pm 0.03)\%$ per degree.

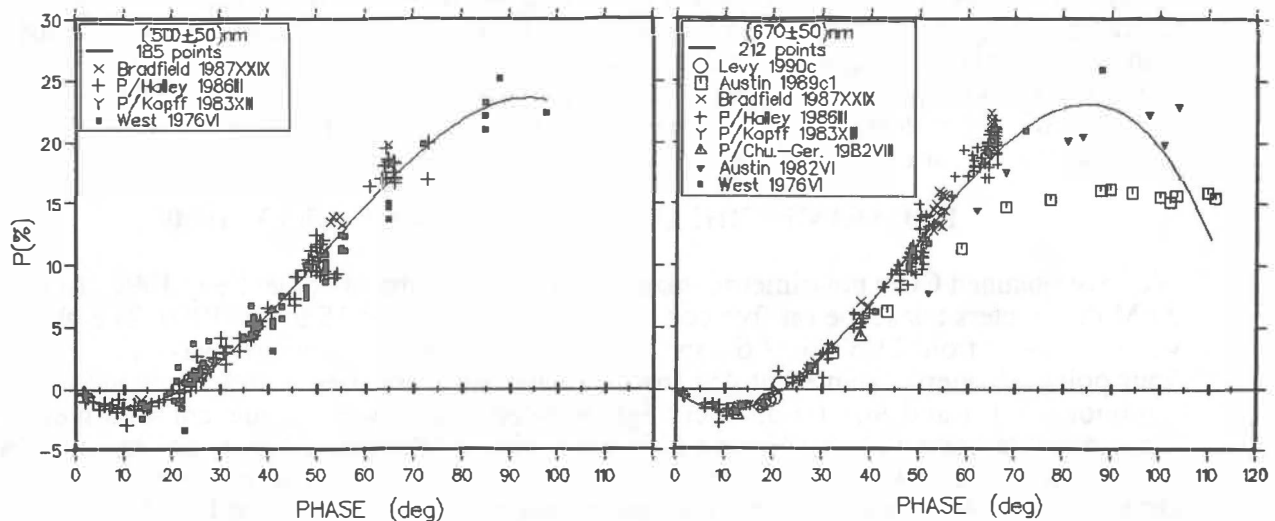


Figure 2 - Evolution of the linear polarization degree with phase angle for $\lambda \approx 500$ nm (left) and $\lambda \approx 650$ nm (right). Synthetic curves are superimposed on the data points from 8 different comets.

Figure 2 (right) presents, in the red range, data from Bastien et al. (1986), Kikuchi et al. (1987, 1989), Myers (1985), Myers and Nordsieck (1984), Renard et al. (1991) and Sen et al. (1991). The derived synthetic curve leads to $\alpha_{\min} = (10.3 \pm 2.0)^\circ$, $P_{\min} = (-1.8 \pm 1.0)\%$, $\alpha_0 = (22.4 \pm 1.0)^\circ$ and $h = (0.27 \pm 0.03)\%$ per degree.

There are no significant discrepancies between Halley's and other comets data at phase angles smaller than about 45° . However, as already mentioned by Mukai et al. (1991), significant discrepancies seem to occur at large phase angles, and specially in the 80° to 110° maximum region. More cometary observations are certainly needed at large phase angles.

DISTANCE TO THE NUCLEUS EFFECT

It had been noticed (Bastien et al., 1986 ; Dollfus and Suchail, 1987) that the polarization of Halley was changing with the size of the diaphragm. We have derived from our observations of Levy (Renard et al., 1991, fig. 4) that, on the average, α_0 slightly increases while h drastically decreases when the distance from the (near nucleus) photometric center increases. Such an effect is likely to be due to the heterogeneity of the polarization distribution in the inner coma.

Fig. 3 presents three polarization maps obtained from observations performed on 18/19 August 1990. The black regions correspond to a negative polarization of the order of $(-3.3 \pm 0.3)\%$. The white regions correspond to a positive polarization progressively increasing from 0.1% to 1.6% . The relative contribution of the white fan like structure increases with decreasing distance to the nucleus ; it could induce an effect similar to the effect previously mentioned for comet Halley.

It is likely that such a structure is due to a jet of grains freshly ejected from the nucleus. The velocity is estimated to be of the order of $(120 \pm 20) \text{ m s}^{-1}$, as measured on the observational plane. Since the Sun's direction is at about 70° from this plane, the outflow velocity in the jet can be roughly estimated to be in a 120 to 400 m s^{-1} range.

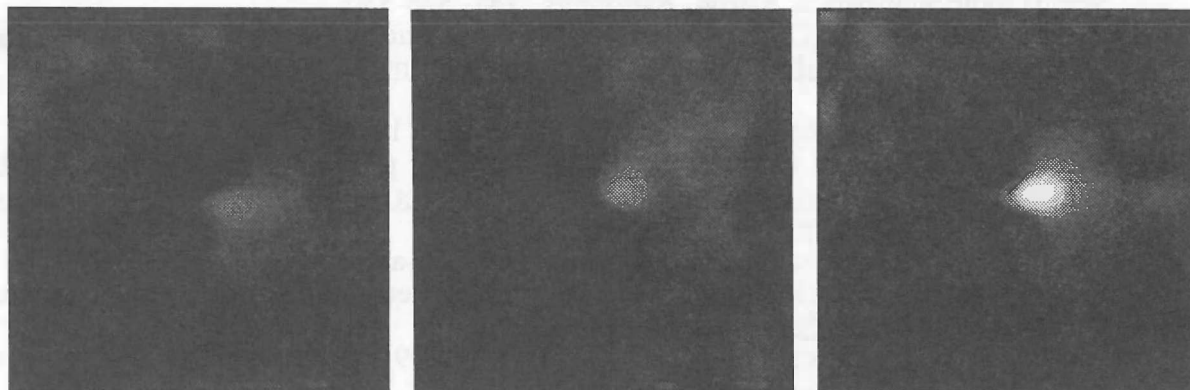


Figure 3 - Polarization maps (field of view 6800 km) of the inner coma of comet Levy, for the 18/19 August 1990, near 23h20m (left), 00h11m (center) and 01h16m (right). Black regions corresponds to $P \approx -3\%$ and white regions to $P \approx +1\%$.

CONCLUSION

The evolution with phase angle of the polarization degree is remarkably similar for all comets below 45° phase angle, at least as long as they are observed over the whole coma. Some discrepancies in the results obtained for various comets in the 80° - 110° maximum region could be indicative of physical differences in the aging dust grains. Some heterogeneities are observed on the polarization maps (obtained near the inversion angle) of the inner coma of comet Levy ; they are likely to be due to the evolution with time after ejection of the partly sublimating grains ejected with different velocities.

ACKNOWLEDGEMENTS. We thank specially A. Dollfus and R. Olombel. This work was partly supported by Programme National de Planétologie, France.

REFERENCES

- Bastien P., Ménard F. and Nadeau R. (1986) Linear polarization observations of P/Halley, Mon. Not. R. Astron. Soc., **223**, 827-834.
- Dollfus A. and Suchail J.L. (1987) Polarimetry of grains in the coma of P/Halley : I. Observations, Astron. Astrophys., **187**, 669-688.
- Dollfus A., Bastien P., Le Borgne J.F., Levasseur-Regourd A.C. and Mukai T. (1988) Optical polarimetry of P/Halley : synthesis of the measurements on the continuum, Astron. Astrophys., **206**, 348-356.
- Kikuchi S., Mikami Y., Mukai T., Mukai S. and Hough J.H. (1987) Polarimetry of comet P/Halley, Astron. Astrophys., **187**, 689-692.
- Kikuchi S., Mikami Y., Mukai T. and Mukai S. (1989) Polarimetry of comet Bradfield, Astron. Astrophys., **214**, 386-388.
- Kiselev N.N. and Chernova G.P. (1978) Polarization of the radiation of comet West 1975n, Astron. Zh., **55**, 1064-1071.
- Le Borgne J.F., Leroy J.L. and Arnaud J. (1987) Polarimetry of comet P/Halley : continuum versus molecular bands, Astron. Astrophys., **187**, 526-530.
- Levasseur-Regourd A.C. (1987) Comets and their evolution in the solar system. In Formation of stars and planets, and the evolution of the solar system, (B. Battrick, ed.), pp. 105-111, ESA SP-315, Noordwijk.
- Michalsky J.J. (1981) Optical polarimetry of comet West 1976VI, Icarus, **47**, 388-396.
- Mukai S., Mukai T. and Kikuchi S. (1991) Scattering properties of cometary dust based on polarimetric data. In Origin and evolution of interplanetary dust, (A.C. Levasseur-Regourd and H. Hasegawa, eds.), pp. 249-252, Kluwer, Tokyo.
- Myers R.V. (1985) Polarization of comets at small phase angles, Icarus, **63**, 206-216.
- Myers R.V. and Nordsieck K.H. (1984) Spectropolarimetry of comets Austin and Churyumov-Gerasimenko, Icarus, **58**, 431-439.
- Renard J.B., Levasseur-Regourd A.C. and Dollfus A. (1991) Polarimetric CCD imaging of comet Levy 1990c, Annales Geophysicae, accepted.
- Sen A.K., Deshpande M.R. and Joshi U.C. (1991) Polarimetric properties of Halley's dust. In Origin and evolution of interplanetary dust, (A.C. Levasseur-Regourd and H. Hasegawa, eds.), pp. 285-288, Kluwer, Tokyo.
- Visvanathan N., Meglick Z. and Wickramasinghe D.T. (1991) Spectropolarimetry of comet Halley. In Origin and evolution of interplanetary dust, (A.C. Levasseur-Regourd and H. Hasegawa, eds.), pp. 245-248, Kluwer, Tokyo.

The State of Knowledge Concerning the Kuiper Belt

Harold F. Levison

Orbital Mechanics Dept., U.S. Naval Observatory, Washington DC 20392

ABSTRACT

The arguments for and against the idea that most short-period comets originate in the Kuiper belt are discussed. Observational constraints on the distribution of mass in the Kuiper belt are reviewed as well as a model of the physical conditions that now exist. Finally, predictions from this model about the detectability of the Kuiper belt are compared to optical surveys.

INTRODUCTION

There has been a lot of interest recently in the idea the most of the short-period comets (SPC, $P \lesssim 200$ years) originate in disk of material that lies just beyond the orbit of Neptune. The idea was first put forward by Fernández (1980), but the current interest was prompted by a paper by Duncan, Quinn, & Tremaine (1988). This disk of material has come to be known as the Kuiper belt. A significant amount of research, both observational and theoretical, has been done since the publication of Duncan, Quinn, & Tremaine. Thus, it was decided to have a special session on the Kuiper belt at this meeting. I was asked to present a review talk on this topic. This paper summarizes that presentation.

For the purpose of this paper, I divide SPC into two groups. Halley-family comets (HFC) are those comets with periods between 20 and 200 years, Jupiter-family comets (JFC) are those objects with periods less than 20 years. These classifications are not arbitrary because these two groups appear to have very different dynamics. JFC are always found in low inclination prograde orbits. The mean inclination of JFC is 10° . The distribution of HFC is somewhat more isotropic, having a mean inclination of 41° . Several Halley-family comets are on retrograde orbits, including Halley itself. Recall that the long-period comets are isotropic. Any theory that attempts to explain short-period comets must explain the observed inclination distribution.

It was usually believed that SPC originated in the Oort cloud and evolved into SPC through gravitational interactions with the planets (Newton 1893, see also Everhart 1972). In recent years several lines of argument have been put forward that put doubt on this idea, see Levison (1992) for a complete review. In my opinion, the strongest of these is that it is not possible to reproduce the inclination distribution of JFC from the spherical distribution of long-period comets. Since space in this paper is somewhat limited, I only discuss this point. I also only consider the two most recent papers on this subject; Quinn, Tremaine, & Duncan (1991), hereafter QTD, and Stagg & Bailey (1989), hereafter SB.

These two papers use very different methods to integrate the orbits of a large number of test particles. These particles are initially on Neptune-crossing orbits and they are followed until they become 'visible' comets ($q < 1.5$ AU for QTD and $q < 2.5$ AU for SB). This is a very difficult problem because the evolution time scale is very long. Both sets of authors needed to adopt some simplifications in order to perform the integrations. SB treated the problem as a stochastic process, giving the particles energy kicks in a well defined, but random fashion. The inclination of the particles is assumed to be constant and the change in perihelion distance is calculated from the Tisserand parameter. QTD directly integrate the orbits of the particles, but in order to decrease the time scales they increased the mass of the planets by a factor of 10. In my opinion, neither of these methods are very satisfactory and both will produce inaccurate results. However, I think that QTD's method is more physical and hence more likely to produce the more accurate orbit integrations. Another problem with both papers is that orbits are only followed until they become visible comets. Neither set of authors allow one type of short-period comet to evolve into another. Lingren (1991) has shown that the orbits of visible comets can significantly change over a comet's lifetime. Indeed, a comet can become visible, evolve to large perihelion distances, can become visible again, and so on over its lifetime. Therefore, it is not strictly appropriate to compare the orbital element distribution of SPC derived by SB and QDT to the observed distribution.

The results of the two papers agree on several important points. They both conclude that HFC are most likely captured long-period comets. They both agree that in order to *dynamically* produce a very flat distribution of comets, the comets must have started in a very flat distribution. Note that SB assumes that the inclination of a comet remains constant. Thus, the inclination distribution of JFC

cannot be reproduced from captured long-period comets unless some non-dynamical effects are included. For example, SB suggests that it may take longer for high inclination comets to become captured. These older comets may be fainter and thus less likely to be discovered. The flat distribution of JFC may be a selection effect. QDT attempt to model this and find that this selection effect is not strong enough to explain the observations.

The papers disagree as to whether the Kuiper belt can be the source of the JFC. SB finds that only about a third of the objects that start on low inclination, prograde, Neptune-crossing orbits become Jupiter-family comets. The rest become Halley-family comets. Thus they argue that it is not possible to reproduce the flat distribution of JFC and the more isotropic distribution of the HFC from the Kuiper belt. Indeed, they cannot explain the JFC with strictly dynamical effects, and as stated above they suggest a few non-dynamical processes that may produce them. Contrary to this, QTD find that all objects that start on low inclination, prograde, Neptune-crossing orbits become Jupiter-family comets, and thus, the Kuiper belt can be the source for the JFC. I think that it is clear from my previous comments that both these papers have some problems. To resolve this dispute, better calculations must be performed. This may be possible within the next few years as computers become faster and numerical methods become more powerful. As I stated above, I believe that the approximations made by QTD are more accurate than those used by SB.

It is now possible to construct a 'complete theory' of the origin of Jupiter-family comets. As Kuiper (1951) pointed out, it seems likely that the disk of planetesimals that formed the planets would not have abruptly ended at the orbit of Neptune, but would have extended far outside the planetary region. The composition of the objects that formed in this region is most likely similar to the satellites of Neptune and Uranus and thus presumably resembles present day comets.

Torbett (1989) and Torbett & Smoluchowski (1990) have shown that all particles with initial values of perihelion distance less than $\sim 45AU$ and eccentricity greater than ~ 0.01 are chaotic on timescales of 10 million years and therefore can in principle leave the Kuiper belt. However, they could not predict the time scale on which objects leave this region. In two previous papers (Levison 1991a and Levison 1991b, hereafter L1 and L2 respectively) I have shown that the timescale for objects leaving the Kuiper belt is on the order of the age of the solar system. I predict that approximately 50% of the objects formed in the Kuiper belt are still there and yet they are leaving in large enough numbers to explain the Jupiter-family comets. However, I must point out that there are some possible problems with the technique that I employ in these papers, which essentially treats the long-term behavior of objects as a diffusion problem in orbital element space. The diffusion coefficients are calculated from relatively short direct orbit integrations. It is possible that the diffusion coefficients I calculate are too large if very long-period oscillations exist because they will be included in the drift rates. See L1 for a complete discussion of the draw backs of this technique. Finally, QTD have shown that these objects evolve into a population with orbital parameters consistent with those of Jupiter-family comets.

PHYSICAL CHARACTERISTICS OF THE KUIPER BELT

I now address our limited understanding of the physical characteristics that currently exists in the Kuiper belt. Unfortunately, very few observational constraints can be applied to the Kuiper belt. I start by discussing the size distribution of comets.

Shoemaker & Wolfe (1982) show that the number of comets with radii between a and $a + da$, $n(a)da$, follows a power law, a^{-3} . They derive this number from studying the magnitude distribution of comets as well as the distribution of crater sizes on Ganymede. Unfortunately, their work does not extend to very big comets. The large objects are interesting because they present our only opportunity to observationally detect objects in the Kuiper belt. If all comets were less than or approximately the same size as Halley, it would be impossible to detect them outside the orbit of Neptune with current technology.

There are two arguments that suggest that very large objects may reside in the Kuiper belt. Chiron, which is a roughly $100km$ sized object, is on a Saturn-crossing orbit that is unstable on a timescale of $10^5 - 10^6$ years (Oikawa & Everhart 1979). It has recently been discovered to exhibit cometary behavior (Luu & Jewett 1990) such as the formation of a resolved coma (Meech & Belton 1990). Because of the short lifetime of its current orbit, it seems likely that Chiron originated farther out in the solar system and that it is representative of a much larger population of similar objects which currently reside in the Kuiper belt.

Somewhat more speculatively, Stern (1991) argues that there may be a few Pluto sized objects in the Kuiper belt. His argument is based on the fact that the three 'pluto-like' objects in the solar system; Pluto, Charon, and Triton; are found on very rare but long-lived orbits. The most reasonable way to explain how these orbits got populated is to envision a large number of pluto-like objects in the outer solar system at early epochs. The number of such objects was large enough so that we expect that a few rare long-lived orbits will be populated. The objects not on long-lived orbits have since been removed from the solar system. A few of these objects may still be in the Kuiper belt.

Thus, it seems reasonable to speculate that there are objects as large as Chiron, and perhaps as large as Pluto, in the Kuiper belt. But it is clearly not appropriate to assume that Shoemaker & Wolfe's power law extends to large objects. Following Levison & Duncan (1990), let the number of comets, n , with radii between a and $a + da$, be

$$n(a) \propto \begin{cases} 0 & \text{if } a < a_{cut} \\ a^{-(b_1+1)} & \text{if } a_{cut} \leq a < a_0, \\ a^{-(b_2+1)} & \text{if } a \geq a_0 \end{cases} \quad (1)$$

where a_0 is the radius where the power law breaks and a_{cut} is the smallest object that can become a visible short period comet. The parameters b_1 and b_2 are constants. This follows Tremaine (1990) except that he sets $a_{cut} = 0$. He argues that $3 \leq b_2 \leq 7$ and sets $a_0 = 10\text{km}$. As stated above, Shoemaker & Wolfe (1982) show that $b_1 = 2$. Levison & Duncan use $a_{cut} = 0.75\text{km}$.

It is possible to calculate the total mass of the Kuiper belt using the available numerical models. The rate at which Jupiter-family comets are being produced, R_{JFC} , is simply

$$R_{JFC} = N_{KB} r_{Nz} f_{JFC}, \quad (2)$$

where N_{KB} is the current number of comets in the Kuiper belt, r_{Nz} is the fraction of particles that leave the Kuiper belt per year, and f_{JFC} is the fraction of particles that become Jupiter-family comets once they leave the Kuiper belt. Fernández (1985) assigned a value of 10^{-2}yr^{-1} to R_{JFC} . However, this value is very uncertain because of the uncertainty in the mean lifetime of Jupiter-family comets. The true value of R_{JFC} may differ from Fernández by as much as a factor of 10. From their numerical integrations DQT found that $f_{JFC} = 0.17$. In L2 I found that $r_{Nz} = 4 \times 10^{-11}\text{yr}^{-1}$. Using these values, there are approximately 1.5×10^9 comets in the Kuiper belt. Weissman (1990) states that the mean mass of a comet is $6.4 \times 10^{-12}M_\oplus$. Thus the total mass in the Kuiper belt is $0.01M_\oplus$. This is quite small and it would not be possible to detect the gravitational effects of this amount of mass on other objects in the solar system (Tremaine 1990 and Hogg, Quinlan, & Tremaine 1991). Recall that these numbers may vary by as much as a factor of 10 because of the uncertainty in R_{JFC} .

I presented a model for the current density distribution in the Kuiper belt in L2. This model predicts that the density of objects is quite small at 45AU . The density quickly increases with distance from the sun until it peaks at about 70AU . Unfortunately, this result implies that the Kuiper belt will be much harder to observationally detect than previously thought, because, most observers have assumed that most of the mass in the Kuiper belt is at about 45 or 50AU .

DETECTABILITY OF THE KUIPER BELT

There have been several optical surveys to search for slow moving objects in the outer regions of the solar system. Typically, the searches cover a particular area of the sky down to some limiting magnitude. No objects beyond Neptune were found. From this it is possible to calculate an upper limit for the number of objects per square degree brighter than the limiting magnitude of the survey, Σ_{obs} . The limit of each survey is plotted in Figure 1 as a function of limiting magnitude. The symbol marked with a 'T' refers to a survey by Tombaugh (1961) that covered $1530(\text{deg})^2$ to a limiting magnitude of 17.5 in V. Luu & Jewett (1988) performed a survey that covered $200(\text{deg})^2$ to a limiting magnitude of 20 in V using a Schmidt telescope, labeled LJ(S). They also searched an area of $0.34(\text{deg})^2$ using a CCD system. They state that this survey reached a limiting magnitude of 24 in R, or approximately 24.5 in V, labeled LJ(C). The symbol labeled 'K' refers to Kowal (1989) which covered $6400(\text{deg})^2$ to a limiting magnitude of approximately V = 20. The symbol labeled 'LD' refers to Levison & Duncan (1990) which covered $4.9(\text{deg})^2$ to a limiting magnitude of approximately V = 23.5. Notice that all of the surveys outlined here would be unable to detect Chiron at distances from the Sun greater than 55AU .

From the model presented in the last section, would we have expected to find objects with these surveys? In L2, I projected the model into the sky and calculated Σ as a function of magnitude. I assumed that the albedo of the objects is 0.1 and that all the objects lie within 10° of the ecliptic. This value is plotted in Figure 1 as a function of magnitude for 3 values of b_2 . Note that none of the searches are near my predictions and, therefore, it is not surprising the no objects were found. If my predictions are correct then future searches need to either survey about an order of magnitude more area of the sky or go approximately 2 magnitudes fainter!

CONCLUDING REMARKS

The only possible *dynamical* explanation for the inclination distribution of Jupiter-family comets is that they originate in a disk of material that lies just beyond the orbit of Neptune. However, there is some disagreement as to whether this model indeed works. More accurate numerical models must be constructed. I tend, however, to trust the results of Quinn, Tremaine, & Duncan (1991) who claim that the model does indeed work.

If the numerical models are accurate, then it is possible to put constraints on the current physical conditions of the Kuiper belt. The combination of the results from QDT and L2 predicts that there are approximately 10^9 comets in the Kuiper belt with a total mass of approximately $0.01M_\oplus$. Most of this mass will be beyond $60AU$ from the Sun. Again, this makes it very difficult to detect. The only optical search that I believe can succeed is one that goes very faint and covers a large area of the sky (tens of square degrees).

I would like to thank Martin Duncan for useful discussions. I am also grateful to Alan Stern for suggesting that I present the review talk at this meeting.

REFERENCES

- Duncan, M., Quinn, T., & Tremaine, S. (1988) *Astrophys. J. Lett.* **328**, L69.
 Everhart, E. (1972) *Ap. Letters.* **10**, 131.
 Fernández, J. (1980) *Mon.Not.Roy.Astron.Soc.* **192**, 481.
 Fernández, J. (1985) *Icarus.* **64**, 308.
 Hogg, D., Quinlan, G., & Tremaine, S. (1991) *Astron.J.* **101**, 2274.
 Kowal, C. (1989) *Icarus,* **77**, 118.
 Kuiper, G. (1951) in *Astrophysics: A Topical Symposium* (ed. Hynek, J.A.), 357.
 Levison, H. (1992) to be submitted to *Pub. Astron. Soc. Pac.*
 ———. (1991a) *Astron.J.* **102**, 787. (L1)
 ———. (1991b) Submitted to *Nature.* (L2)
 Levison, H., & Duncan, M. (1990) *Astron.J.* **100**, 1669.
 Lingren, M. (1991) to appear in *Asteroids, Meteriods, and Comets II*.
 Luu, J., & Jewitt, D. (1988) *Astron.J.* **95**, 1256.
 ———. (1991) *Astron.J.* **100**, 913.
 Marsden, B. (1983) *Catalog of Cometary Orbits* (Hillside:Enslaw).
 Meech, K., & Belton, M. (1990) *Astron.J.* **100**, 1323.
 Newton, H. (1893) *Mem. Natl. Acad. Sci.* **6**, 7.
 Oikawa, S., Everhart, E. (1979) *Astron.J.* **84**, 134.
 Quinn, T., Tremaine, S., & Duncan, M. (1990) *Astrophys.J.* **355**, 667. (QTD)
 Shoemaker, E., & Wolfe, R. (1982) in *Satellites of Jupiter* (ed. Marrison, D.), 277.
 Stagg, C., & Bailey, M. (1989) *Mon.Not.Roy. Astron.Soc.* **241**, 507. (SB)
 Stern, A. (1991) *Icarus*, **90**, 271.
 Tombaugh, C. (1961) in *Planets and Satellites*, (eds. Kuiper, G. and Middlehurst, B.) p12-30 (University of Chicago Press, Chicago).
 Torbett, M. (1989). *Astron.J.* **98**, 1477.
 Torbett, M., & Smoluchowski, S. (1990). *Nature*, **345**, 49.
 Tremaine, S. (1990) in *Baryonic Dark Matter*, (eds. D. Lynden-Bell, D. and G. Gilmore, G.) 37.
 Weissman, P. (1990) in *In Global Catastrophes in Earth History*, (eds. Sharpton, V. and Ward, P.), Geological Society of America Special Paper 247, 263.

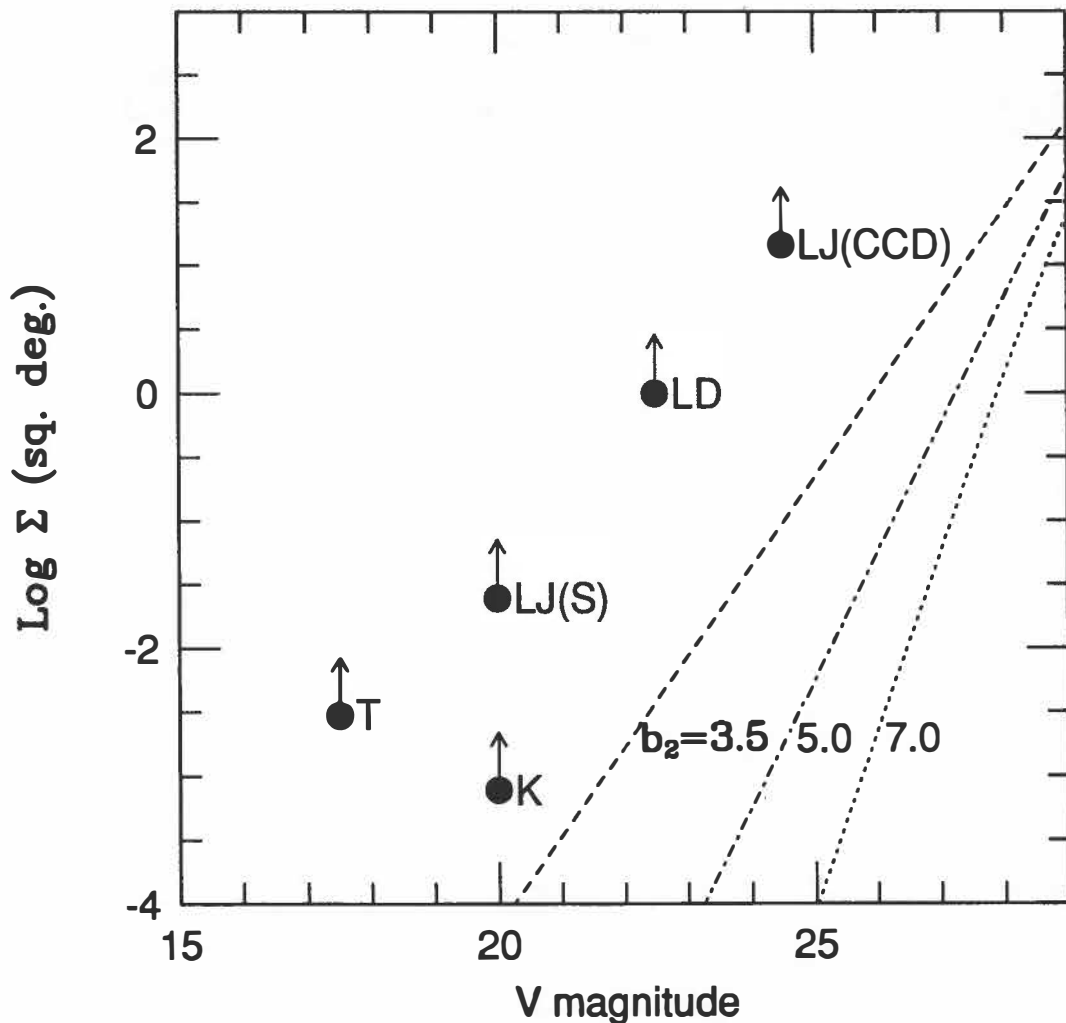


FIGURE 1 — The number of observable Kuiper belt objects per square degree, Σ , as a function of a survey's limiting magnitude in V. The curves represent our model with different values of b_2 . The marked symbols refer to lower limits of real surveys: $T \rightarrow$ Tombaugh (1961), $K \rightarrow$ Kowal (1989), $LJ \rightarrow$ Luu & Jewitt (1988), $LD \rightarrow$ Levison & Duncan (1990). Luu & Jewitt performed two searches. The results of their search with a Schmidt telescope is marked with a (S), and the results of their CCD search is marked with a (CCD). See Levison & Duncan for complete discussion.

Numerical Simulations of Cometary Dust

David J. Lien

Bucknell University

Most observations of comets are done photometrically or spectrophotometrically. The interpretation of the aperture-averaged flux is relatively simple for an isotropic, radially expanding coma of infinite extent – the canonical model. However, the interpretation of the observations is not so clear when the motion of the dust is affected by radiation pressure, or when the emission is time-varying and anisotropic. For example, in a sample of CCD images of 10 comets, Jewitt and Meech (1987, *Ap.J.* 317, 992) found that the photometric profiles of only three comets were consistent, within the observational errors, with the profiles predicted from the canonical model. Photometric observations with large apertures, however, seem to suggest that the canonical model may be quite adequate (c.f. Osip, Schleicher, and Millis, 1992, *Icarus* 98, 115).

The dust itself is characterized by a size distribution, with size dependencies on the expansion velocity, the scattered and thermal radiation, the response to radiation pressure, and probably the density. How good then are the approximations normally used in determining the production rates of the dust when these effects are present?

Given an isotropically expanding dust envelope (from a non-moving nucleus), the radial profile can be shown to decrease as the inverse of the projected cometcentric distance:

$$\sigma(\rho) = \int_{-\infty}^{\infty} \frac{Q}{4\pi(\rho^2 + l^2)v} dl = \frac{Q}{4\rho v} \quad (1)$$

where $\sigma(\rho)$ is the column density at the radial distance ρ , Q is the production rate [s^{-1}], and v is the expansion velocity. If the limits are not $\pm\infty$, then

$$\sigma(\rho) = \int_{-R}^{R} \frac{Q}{4\pi(\rho^2 + l^2)v} dl = \frac{Q\pi}{2\rho v} \tan^{-1}\left(\frac{\sqrt{R^2 - \rho^2}}{\rho}\right) \quad (2)$$

where R is the edge of the envelope.

The total number of particles inside an aperture of projected radius s is

$$N(s) = \int_0^s 2\pi\rho\sigma(\rho)d\rho = \frac{Q}{v} \left[s \tan^{-1}\left(\frac{\sqrt{R^2 - s^2}}{s}\right) - \sqrt{R^2 - s^2} + R \right] = \frac{\pi Q s}{2v} \quad (3)$$

where the last equality is for $R = \infty$. Since the time over which the dust is emitted is finite, the total number of dust particles in the coma is just the product of the production rate and the interval of time over which the dust was emitted. Evaluating equation 3 for an aperture equal to the outer edge of the coma yields $N(R) = \frac{QR}{v} = Qt$, as expected.

As part of a program to better understand the dynamics of cometary dust and gas, a computer program has been developed which numerically simulates the emission of both

dust and gas from the nucleus of a tilted rotating nucleus. Only the dust coma will be discussed here. The dust coma simulation includes the effects of the size dependencies on the expansion velocity, and scattering or thermal emissivity (based on either approximations or Mie theory calculations) and on the response to radiation pressure. Anisotropic emission is approximated by a gaussian jet centered at any latitude and longitude on a rotating nucleus of arbitrary rotation rate and obliquity.

The "image" of the gas or dust coma can be generated, as well as aperture- or annulus-averaged fluxes. An example of the annulus-averaged flux is presented below for P/Halley on 15 March 1986. Figure 1a shows $\sigma(\rho)$ from the numerical simulation of dust emission for 14 days at $v = 0.025 \text{ km/s}$ with $\beta = 0$. This gives a maximum size of the coma of about $44''$. A least squares fit of equation (2) to the data is displayed as the solid line in Figure 1a. The solid line in this and subsequent figures corresponds to the theoretical fit, and the dotted line is derived from the numerical simulations. The aperture averaged flux is shown in Figure 1b, along with a least squares fit of equation (3) to the data.

Since the production rate is constant and known from the parameters input into the numerical simulation, the $R = \infty$ solution can be solved for Q based on the results in Figure 1b. This is shown graphically in Figure 1c, where the production rate, Q , derived by assuming the $R = \infty$ solution to equation (3) is plotted as a function of the aperture size, s . The thin horizontal line indicates the true production rate. For this simple model, the $R = \infty$ approximation overestimates the production rate for small apertures, and underestimates Q for large apertures. As expected, the agreement between the $R = \infty$ approximation and the simulations improves as R increases.

The dynamics of a large dust particle once well away from the nucleus depend primarily on the initial velocity vector of the particle and the ratio of the radiative pressure force to the force of gravity, β . Small charged dust grains are not considered here. As β increases, the coma becomes increasingly non-spherical, and one expects that the application of spherical approximations to the coma will become increasingly inaccurate. To test this statement, a series of models were run with $v = 0.025 \text{ km/s}$ and a single β from the range $0.0001 < \beta < .5$. These parameters were chosen such that a spherically expanding, $\beta = 0$ envelope would occupy approximately $\frac{1}{2}$ the length of the image array. Figure 2 ($\beta = 0.0001$) and Figure 3 ($\beta = 0.1$) show both a projection against the sky of a subset of the total number of particles used in each simulation (typically 50,000), and the value of Q as a function of the aperture diameter. Again, the thin horizontal line indicates the input value of Q . In these models, even a small β causes a significant change, with the predicted Q more than a factor of 2 too low for most aperture sizes. It is interesting to note that these simulations suggest that spectrophotometric observations, with relatively small apertures, will yield higher dust production rates than the larger aperture photometric observations.

The question of a size distribution on the predicted Q is illustrated in Figure 4. To illustrate the effects of a size distribution, a β distribution which is rectangular in $\log(\beta)$ (equal numbers of particles in equal size bins in $\log(\beta)$ with β within the range $0.0001 < \beta < 0.1$ was used. Each particle contributes an equal amount to the flux, and the velocity scales as $\sqrt{\beta}$. The scale factor is chosen so that the velocity of the center of the β distribution is 0.025 km/s . Figure 4 shows the results of this simulation.

To more realistically simulate the scattering or thermal emission properties of real grains, the same input parameters used in Figure 4 were modified by having each particle contribute a flux proportional to β^{-2} . This relationship is derived from the inverse relationship between the diameter of the particle and the value for β , which is valid for particles large compared with the wavelength of light. The results are shown in Figure 5. To determine the production rate, an "average" flux and velocity must be chosen. The values for the center of the β distribution was used to determine Q from the simulations. The production rate is overestimated by as much as 2 orders of magnitude ($Q = 0.041 \text{ s}^{-1}$), even with a large aperture. This result suggests that the derived production rate is very sensitive to the choice of the optical properties of the "average" particle.

Although the results of most of the simulations run with a single β are consistent with the statement that the production rate derived by assuming $R = \infty$ is correct to better than a factor of 5, this conclusion is misleading. As illustrated in Figure 5, when a broad size distribution with the intensity proportional to β^{-2} is used, the derived production rate is off by orders of magnitude. The main difficulty lies in determining the "average" velocity and β . Future work will concentrate on more realistic models: longer emission time, incorporation of the optical properties of spheres composed of potential cometary-dust materials, and a more realistic size or β distribution. Additionally, efforts will be focused on using the results of these simulations to aid in the interpretation of photometric and spectrophotometric observations. The results from the simulations presented here suggest that the canonical model, which assumes a radial outflow of dust, is inadequate in measuring the dust production rate. However, further simulations with more realistic input parameters are needed before any final conclusions can be drawn.

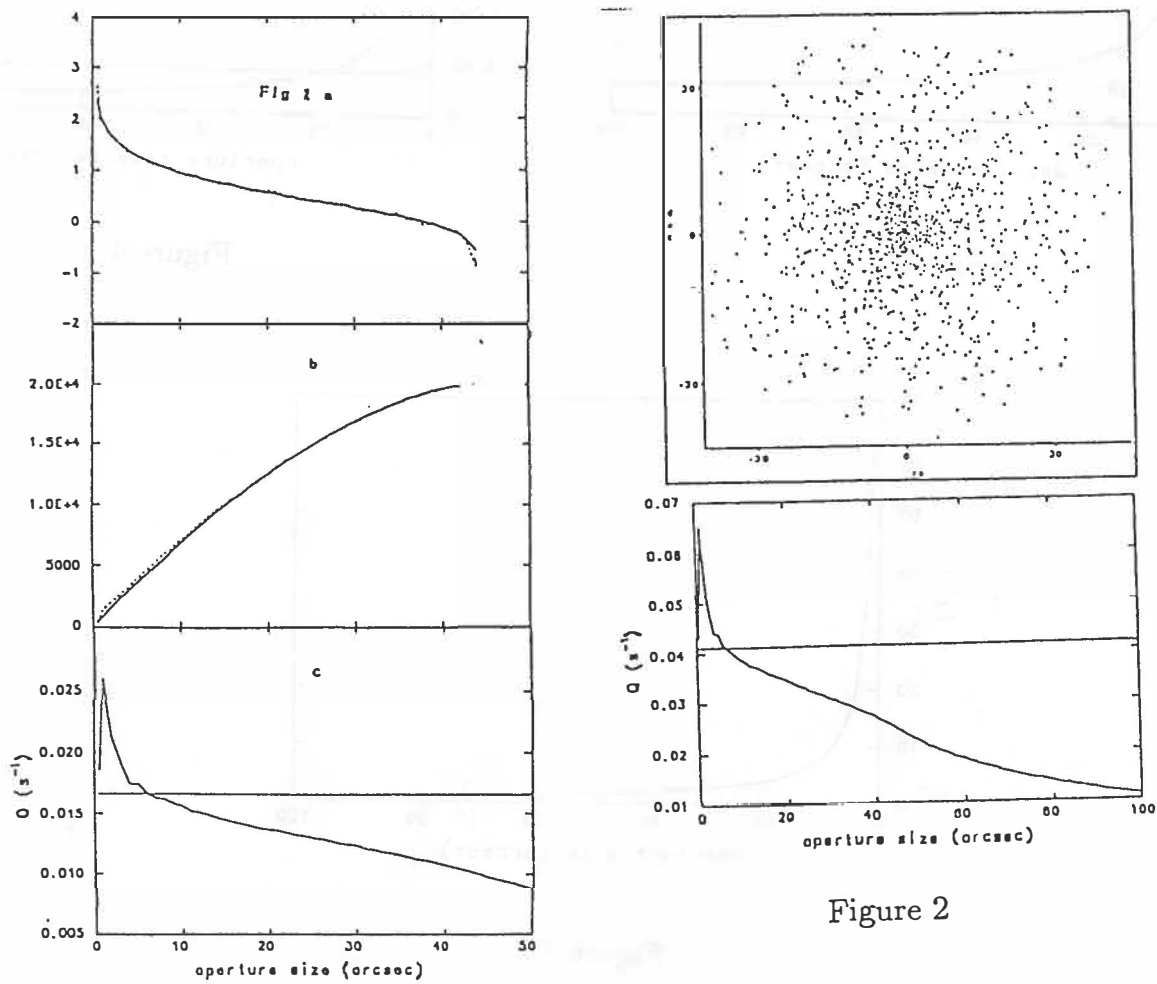


Figure 2

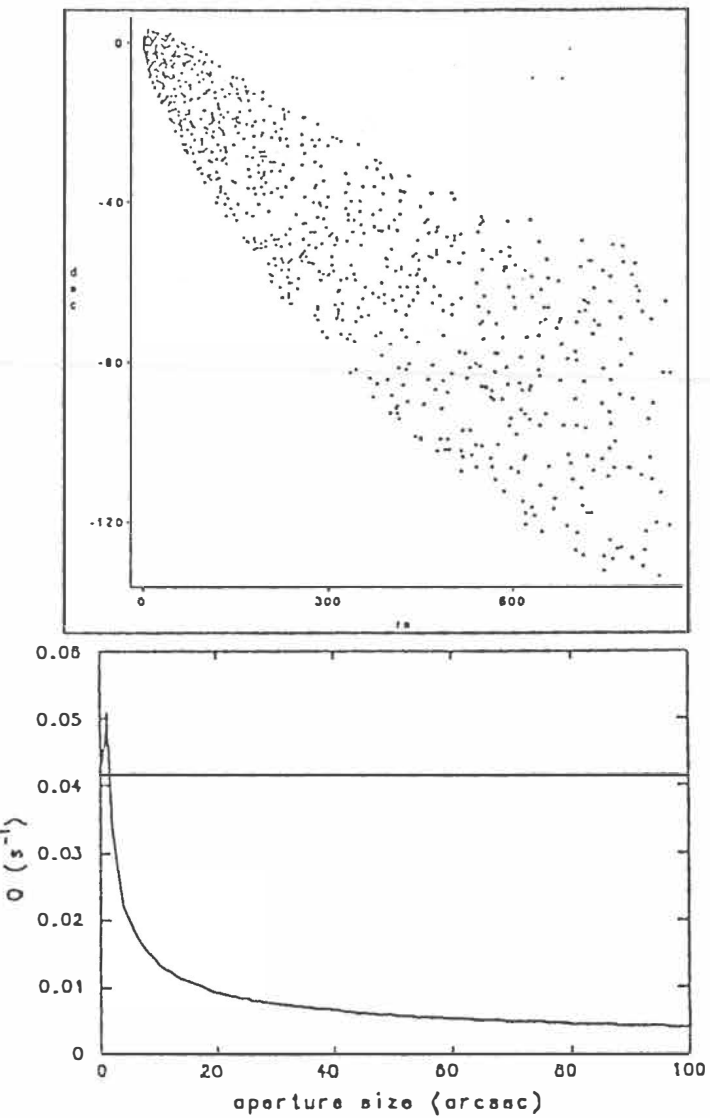


Figure 3

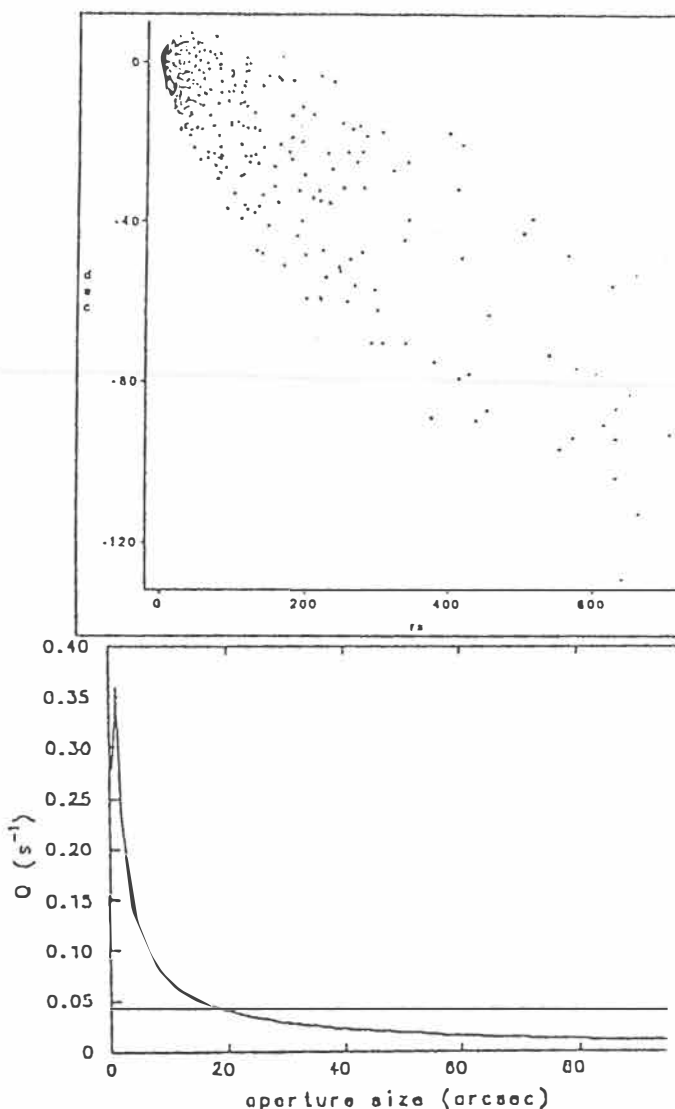


Figure 4

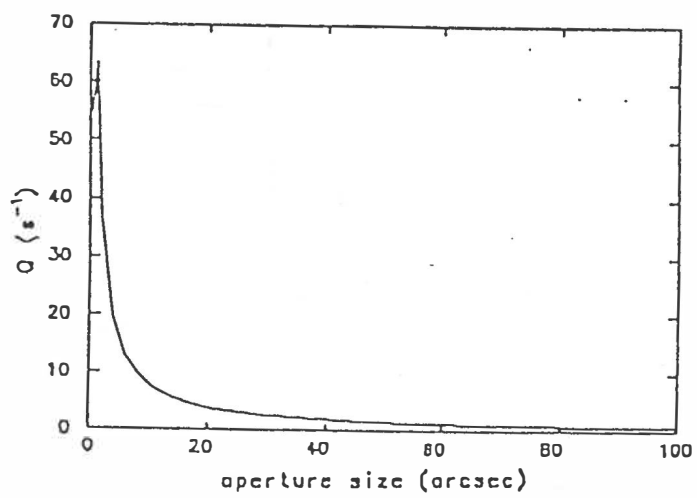


Figure 5

A COMPUTER SEARCH FOR ASTEROID FAMILIES

B.A. Lindblad, Lund Observatory, Box 43, S-221 00 Lund, Sweden

Abstract - The improved proper elements of 4100 numbered asteroids have been searched for clusterings in a , e , i space using a computer technique based on the D-criterion. A list of 14 dynamical families each with more than 15 members is presented. Quantitative measurements of the density and dimensions in phase space of each family are presented.

Introduction - Large scale clustering in the proper elements of the minor planets was first noticed by Hirayama (1918), who coined the term "families" to indicate such clusterings. Hirayama (1928, 1933) added additional members to the previous families. Extensive lists of asteroid families have subsequently been compiled by Brouwer (1951), Arnold (1969), van Houten et al. (1970), Lindblad and Southworth (1971), Williams (1979), Kozai (1979a, 1983) and others. Unfortunately the criterion for family membership is not always stated, and it appears that the limits of a family in proper element space are largely a matter of personal judgement. A strict criterion of family membership based on the D-criterion of Southworth and Hawkins (1963) was introduced by Lindblad and Southworth (1971). The D-criterion has been used in numerous meteor stream studies and subsequently also for studying clustering amongst asteroid and comet orbits (Lindblad and Southworth 1971, Kresák 1982, Lindblad 1985). The D-criterion for orbital similarity in proper a , e , i space may be written

$$D(m, n)^2 = (e_n - e_m)^2 + (q_n - q_m)^2 + (2 \cdot \sin \frac{i_n - i_m}{2})^2 \quad (1)$$

where m and n represent two orbits to be compared. The search program computes $D(m, n)$ for all possible pairs in the sample. If $D(m, n)$ is less than a stipulated value D_s the program accepts these two orbits as belonging to a cluster. During the continued comparison process more and more pairs are linked together to form a cluster. The program numbers the various groups and lists their members, computes the mean orbit M of the group and also the deviation $D(M, n)$ of each individual member from the mean orbit. Finally it computes the mean $D(M, n)$ for all members in a group.

In a search in three dimensional space the discriminant D_s should vary inversely as the cubic root of the sample size, if the samples are otherwise similar. Lindblad and Southworth (1971) noted that the best agreement with the classifications of Hirayama and Brouwer was obtained using $D_s = 0.020$ in a sample of 1697 numbered asteroids and $D_s = 0.013$ in a mixed sample of 2652 numbered asteroid and PLS orbits. Based on these results we may write

$$D_s = 0.24 \cdot N^{-1/3} \quad (2a)$$

$$D_s = 0.18 \cdot N^{-1/3} \quad (2b)$$

where equation (2a) is appropriate for asteroids with registration numbers less than about 2000 and equation (2b) for samples exhibiting a higher degree of concentration to the ecliptic plane.

Improved proper elements - Early computations of proper elements involved only low-order expansions in the eccentricities and inclinations. Subsequently Williams (1979), Yuaza (1973), Kozai (1979b), Knězević (1986) and Knězević and Milani (1989) have improved the theory of computing proper elements by developing methods to accurately handle high inclinations and/or large excentricities. A set of proper elements for 4100 minor planets computed by Knězević and Milani, forms the data base for the present study.

Results of computer search - In the Knězević-Milani sample of 4100 orbits the asteroid population with serial numbers above 2000 showed a much stronger concentration to the ecliptic plane than the first 2000 numbered asteroids. It follows that a family search in this sample must be made at a rather strict rejection level. Eq. (2b) suggests a D_s value in the range 0.011 - 0.012. In order to take a conservative approach the search was made at $D_s = 0.011$. The search produced a list of 316 "families" totaling 2163 members, i.e. slightly more than 50 % of the asteroid population was grouped into families. However, 211 families had only 2 members, 54 had 3, 18 had 4, 6 had 5 members each, etc. Pending a detailed study of the possible significance of small families the present report focuses on the fourteen largest families only. A more detailed study will be published elsewhere.

Table 1 lists all asteroid families with 15 or more members together with their mean proper elements and mean $D(M, n)$ value. Families are named after the asteroid of lowest serial number. In a few cases a double name has been introduced so as to facilitate a comparison with the results of other workers. All the Hirayama families, except Phocaea, are detected. In addition nine "new" families with from 15 to 100 members appear. The three families: Eunomia, Nysa and Vesta have been previously mentioned by other investigators. The six new families in Table 1 represent small, but very compact groups.

Dimension and density of asteroid families in phase space - As a check on the consistency of the data we have for each family in Table 1 computed the product of the three standard deviations $\sigma(a)$, $\sigma(e)$ and $\sigma(i)$. This product is a measure of the extent of each family in phase space. In order to obtain suitable numerical values we define

$$\sigma = \sigma(a) \cdot \sigma(e) \cdot \sigma(i) \cdot 10^5 \quad (3)$$

The product σ is listed in column seven of Table 1. In Fig. 1 we have plotted $\log \sigma$ versus the equivalent radius $\overline{D}(M, n)$. A high correlation between $\overline{D}(M, n)$ and σ is evident, (correlation coefficient $r = 0.89$), i.e. both parameters are measures of the extent of an asteroid family in phase space. In column eight of Table 1 we list the number of family members per unit volume of phase space. Table 1 shows that Koronis, Dora and Adeona are extremely dense groups, whereas the other eleven families all have about the same density.

Statistical significance of asteroid families - The statistical significance of the families listed in asteroid studies is a matter of some concern. In most studies dynamical families are identified as groupings in proper a , e , i space and the boundaries are drawn rather subjectively. Since the agreement between the various lists of families is only partial, one is inclined to doubt the correctness of the used statistical significant tests. A different approach to the statistical significance problem was used by Lindblad and Southworth (1971). These authors constructed random samples of asteroid orbits and searched them at the same rejection level d_s as was used in the real sample. The random samples were created by scrambling the proper elements a and e of the asteroids under study. This procedure preserves the frequency distribution of each orbital element, but does not preserve any correlations which may exist between the proper elements a and e . Fortunately, this correlation is very low. In the present study a number of random samples are being searched at the rejection level $D_s = 0.011$. When these searches are completed one can directly derive the probability that a family of N members is due to a chance grouping in proper a , e , i space. In the previous study (Lindblad and Southworth 1971) it was found that in a sample of about 1700 orbits about 50% of the two-and three-member families and 30% of the four-member families were random groupings in the data.

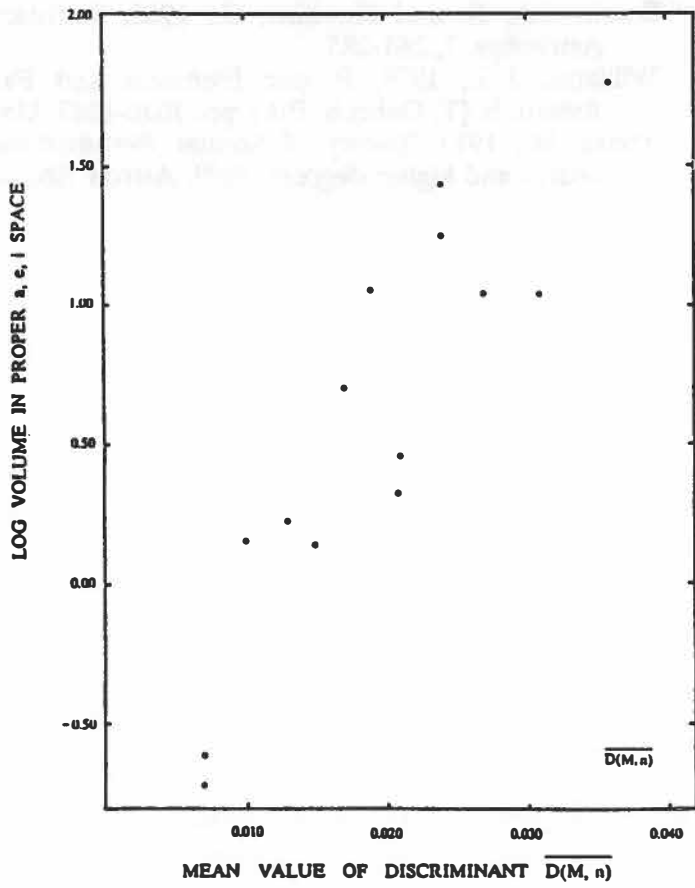
Acknowledgements - This investigation was supported by grant no. 204-301 from the Swedish Natural Science Research Council. Travel grants were received from Kgl. Fysiografiska Sällskapet in Lund and from the Swedish Board for Space Activities. The sample of 4100 proper elements was made available through the courtesy of Drs. Z. Knězević and A. Milani.

Family name	N	a	e	i	$\overline{D(M, n)}$	σ	N/σ	Comments
Themis	212	3.144	0.156	1.4	0.027	10.9	19.5	
Eos	215	3.014	0.077	10.1	0.024	27.0	8.0	
Koronis	141	2.874	0.049	2.1	0.021	2.08	67.8	Compact
Maria	36	2.555	0.091	15.0	0.021	2.85	12.6	Compact
Flora	440	2.231	0.137	4.5	0.036	62.5	7.0	Loose assoc.
Eunomia	100	2.626	0.149	13.2	0.031	10.8	9.3	Brouwer 19-20
Nysa-Hertha	56	2.392	0.163	3.0	0.024	17.7	3.2	
Vesta	41	2.354	0.103	6.5	0.019	11.5	3.6	
Amalasuntha	39	2.446	0.153	2.9	0.017	5.04	7.7	Rel. to Flora
Mildred-Beer	17	2.385	0.190	2.2	0.015	1.37	12.4	Rel. to Flora
Oppavia-Gefion	17	2.789	0.136	9.1	0.013	1.68	10.1	
Dora	16	2.787	0.196	7.8	0.007	0.19	83.3	Compact
Adeona	16	2.674	0.167	11.6	0.007	0.24	66.7	Compact
Goberta	15	3.174	0.135	1.1	0.010	1.45	10.3	

Table 1. Mean proper elements, mean discriminant $\overline{D(M,n)}$, volume σ and spatial density N/σ of large families detected in search amongst 4100 asteroids at rejection level $D_s = 0.011$.

Fig. 1. Log σ versus equivalent radius

$\overline{D(M, n)}$.



References

- Arnold, J., 1969, Asteroid Families and Jet Streams. *Astron. J.* 74, 1235-1242.
- Brouwer, D., 1951, Secular Variations of the Orbital Elements of Minor Planets. *Astron. J.* 56, 9-32.
- Hirayama, K., 1918, Groups of Asteroids Probably of Common Origin. *Astron. J.* 31, 185-188.
- Hirayama, K., 1928, Families of Asteroids, *Jap. J. Astron. Geophys.* 5, 137-162.
- Hirayama, K., 1933, Present State of the Families of Asteroids, *Proc. Imp. Acad. Japan*, 9, 482-485.
- van Houten, C., van Houten-Groeneveld, I., Herget, P. and Gehrels, T., 1970, *Astron. Astrophys. Suppl.* 2, 339-448.
- Knězević, Z., 1986, Comparison of the Asteroid Proper Elements Obtained from Various Theories. In *Asteroids Comets Meteors II* (C.-I. Lagerkvist, B.A. Lindblad, H. Lundstedt and H. Rickman, Eds.), 129-134. Uppsala Universitet, Uppsala.
- Knězević, Z. and Milani, A., 1989, Asteroid Proper Elements from an Analytical Second Order Theory, in *Asteroids II* (Binzel, R., T. Gehrels and Mathews, M., Eds.), 1073-1089, Univ of Arizona Press, Tucson.
- Kozai, Y., 1979a, Families of Asteroids by a New Criterion. *Ann. Tokyo Astron. Obs. Second Ser.* 17, 194-220.
- Kozai, Y., 1979b, The Dynamical Evolution of the Hirayama Family, in *Asteroids* (T. Gehrels, Ed., 334-358, Univ. of Arizona Press, Tucson.
- Kozai, Y., 1983, Families of Asteroids. In *Dynamical Trapping and Evolution in the Solar System* (V.V. Markellos and Y. Kozai, Eds.), 117-122, Reidel, Dordrecht (IAU Coll. 74).
- Kresák, L., 1982, *Bull. Astron. Inst. Czechosl.*, 33, 150.
- Lindblad, B.A., 1985, Do Comet Groups exist? In A. Carusi and G. Valsecchi (eds), *Dynamics of Comets. Their Origin and Evolution*, D. Reidel, Dordrecht.
- Lindblad, B.A. and Southworth, R., 1971, A Study of Asteroid Families and Streams by Computer Techniques, in *Physical Studies of Minor Planets* (T. Gehrels, ed.), NASA SP-267.
- Southworth, R. and Hawkins, G., 1963, Statistics of Meteor Streams. *Smithson. Contrib. Astrophys.* 7, 261-285.
- Williams, J.G., 1979, Proper Elements and Family Memberships of the Asteroids. In *Asteroids* (T. Gehrels, Ed.), pp. 1040-1063. University of Arizona Press, Tucson.
- Yuasa, M., 1973, Theory of Secular Perturbations of Asteroids, including terms of higher orders and higher degrees, *Publ. Astron. Soc. Japan*, 25, 399-445.

ACTIVITY OF THE LYRID METEOR STREAM

B.A. Lindblad, Lund Observatory, Box 43, S-221 00 Lund, Sweden
V. Porubčan, Astron. Inst., Slovak Acad. of Sciences, 842 28 Bratislava, Czechoslovakia

Abstract - The activity of the Lyrid meteor stream is in most years fairly low with a visual rate at maximum (21-22 April) of 5-10 meteors per hour. Short bursts of very high Lyrid activity, with visual hourly rates of 100 or more, have sometimes been reported. These observations generally refer to faint visual meteors. The reported bursts of high activity have occurred in a very narrow interval of solar longitudes (31°.24 to 31°.38 equinox 1950.0), while the recurrent or "normal" maximum for bright meteors occurs at solar longitude 31°.6, or slightly later. A mass separation of the meteors in the shower is thus indicated.

Introduction - The Lyrid meteor stream is associated with Comet Thatcher (1861 I). The shower appears in the period 15-24 April with a maximum on April 21-22. An early discussion in the scientific literature of a possible, annual meteor shower in mid-April is due to Herrick (1838). For further references see Lindblad and Porubčan (1991). The present visual h.r. at maximum is low, about 5-10 meteors per hour. It is, however, known that the Lyrid meteor stream in the past has given rise to intense meteoric displays. Less well known is that short, intense outbursts of Lyrid activity have been observed on several occasions during the 19th and 20th century. The present paper summarizes the historical records and attempts to determine the precise solar longitude at which the Lyrid outbursts have occurred. Unfortunately several records before 1900 could not be used since they do not give the precise time - in some cases there is also an uncertainty as to the date of the display.

Observations - Table 1 summarizes those reports after 1800 for which precise date and time information has been found. Table 1 shows that the Lyrid outbursts have occurred in a narrow range of solar longitudes (31°.24 to 31°.38). In some cases the activity maximum can be specified to within 1 minute corresponding to approximately 0°.001 in solar longitude. Owing to the rapid change in Lyrid rates near the peak, there is in some cases an uncertainty as to the exact meaning of the published hourly rates. Most observers give an hourly rate corresponding to the rate at peak activity. Rates listed in Table 1 are zenithal hourly rates for a single observer, i.e. if group watches were made they were corrected to zenith and to rates for one observer. A few comments on the data of Table 1 are given below.

Contemporary newspaper accounts of the 1803 Lyrid display were collected by Olmsted (1834), Herrick (1839) - and a century later by Fisher (1931). Olmsted's report led Herrick (1838) to suspect the existence of an annual meteoric display in April. Herrick's conclusions were discussed by Benzenberg (1838) and other European astronomers. Subsequently Herrick (1839) confirmed the existence of an April Lyrid shower by direct visual observations, and determined a radiant at $\alpha = 273^\circ$, $\delta = 45^\circ$. The 1803 Lyrid display was evidently a meteoric storm of length several hours and with an hourly rate of 670 or more.

For the 1922 and 1946 apparitions time information is available from two independent sources. There is an apparent discrepancy between the time of the 1922 maximum as reported by Russel and Gadomski. We note that Russel's observations were accidental. On April 21, 1922 he happened to observe an intense shower with a radiant near α Lyrae. Russel counted meteors during three time intervals, with a break between 21:40 and 21:55 hrs local time. Since Gadomski lists 21:40 as the time of shower maximum, it is evident that Russel's observations were incomplete. There is thus no contradiction between the two reports.

For the 1946 Skalnate Pleso observations Porubčan and Stohl (1983) list a zenithal hourly rate corrected to a single observer of ≈ 40 . Inspection of the original records reveals that this rate refers to 6 observers averaged over a 60 minute time interval. If the most experienced observer (Mrkos) is selected and his h.r. is based on the 20 minute peak interval we deduce an h.r. of 110 in good agreement with results reported from Prague.

The 1982 Lyrid apparition was observed both visually and by radar. It is therefore the best studied display on record. Detailed information on the magnitude and/or mass distribution is available. A predominance of faint meteors in the shower is evident from McLeod's visual observations (Adams 1982). A peak zenithal rate of about 250 meteors per hour, persisting for 15 minutes between half-maximum values, was reported by McLeod. He also reported for the same period an observed mean Lyrid magnitude of 3.62 - to be compared with his "normal" Lyrid mean magnitude of 2.84. A detailed study of the 1982 radar observations has been published by Porubčan and McIntosh (1987). They report a shower duration of 22 minutes between half-maximum points. In a subsequent paper Porubčan and Hajdukova (1988) studied the most active part of the outburst and determined a mass index $s = 2.2$. This value may be compared with the "normal" Lyrid value of $s = 1.6$. Again an excess of small meteoroids in the 1982 Lyrid stream is indicated.

In conclusion we note that most observers state that the 1922-82 Lyrid outbursts were of short duration (total duration 2 hours or less and period of peak activity about 15 minutes) and that they mainly consisted of faint meteors.

Normal Lyrid activity profile - For comparison purposes we derive the visual activity profile of the recurrent or "normal" Lyrid meteor shower. This is difficult to determine because of the very low number of Lyrids observed in most years. For our study we have used three data sets: 1) Visual rates obtained by British and American observers in 1969 (Hindley 1969). 2) Rates obtained by Dutch observers in 1984-88 (Jenniskens and Veltman 1988). 3) Rates obtained in 1982-90 by the Arbeitskreis Meteore, Potsdam (Rendtel 1990). Hourly rate curves for all three groups are plotted in Fig. 1A. All rates have been reduced by the original authors to the zenithal hourly rate of a single observer. We note that the rates are very consistent with peak rates of 14.0, 13.5 and 10.4 observed at solar longitudes $31^\circ.5$, $31^\circ.6$ and $31^\circ.75$ by Hindley, Jenniskens and Veltman, and Rendtel, respectively. Fig. 1B shows an activity profile based on two series of long-term radar observations (Porubčan, Simek and McIntosh 1989). It is evident that radar and visual data are in good agreement and that both types of data place the recurrent or "normal" Lyrid maximum at solar longitude $31^\circ.6$ (equinox 1950.0).

Discussion. -It is evident that there exists a filamentary structure in the Lyrid stream consisting mainly of small particles. The Earth transits this filament in about one hour, indicating a flux tube of transverse extension of about 100 000 km. Since the Lyrid outbursts do not occur every year, there exists a longitudinal structure in the filament. The persistence of such structures over long time periods is difficult to explain. Since the Earth encounters this filament about 0.25 days earlier than it encounters the main maximum of the stream a mass separation in the stream is indicated. The filament could be due to small particles which were ejected from the parent comet at a different time than the main Lyrid release. An alternative explanation is to postulate the operation of some unknown mass dependent dispersive mechanism (the Poynting-Robertson effect operates in the orbital plane of the stream and is therefore not applicable).

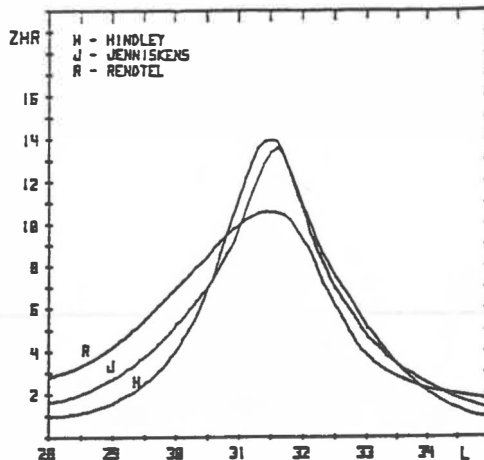
Acknowledgements - The authors are indebted to J. Rendtel, Arbeitskreis Meteore, Potsdam, for data on their Lyrid obsevations and to Dr. L. Kresak for valuable comments. We wish to thank the Swedish and Czechoslovak Academies of Sciences for exchange visits.

<u>Y M D</u>	<u>UT</u> (h m)	<u>Solar L</u> (1950.0)	<u>ZHR</u>	<u>Location</u>	<u>Reference</u>	<u>Comments</u>
1803 04 19	--	31°35	670	Eastern USA	Herrick, E.C., 1838, Am. Journ. Sci., 34, 398 Benzenberg, J.F., 1838, Astron. Nachr. 355, 325-327	Newspaper reports. 01-03 hrs in the morning (local time). Duration > 2 hrs
1922 04 21	19 40	31°294	360-600	Southern Poland	Gadomski, J., 1929, Publ. Astron. Obs. Warzawa Univ. 5, 69-70	Gadomski and two co-observers. Max. at JD = 2423166.32
1922 04 21	19 58	31°306	180	Greece	Olivier, C., 1929, Publ. Leander McCormick Obs., 5, 24-25	Observations by H.N. Russell. Maximum at 21.58 (local time)
1934 04 21	23 15	31°370	56-80	Sonneberg	Teichgraeber, A., 1934, Die Sterne 14, 137	Observers C. Hoffmeister and A. Teichgraeber
1945 04 21	15 50	31°243	100	Japan	Olivier, 1946, Meteor Notes, Pop. Astron. 54, 305-307	Observations by K. Komaki 00.00-01.17 (local time), 22 April
1946 04 21	22 40	31°266	110	Skalnate Pleso	Porubcan,V. and Stohl, J., 1983, Contr. Astron.Obs. Skalnate Pleso, 11, 169-184	Observations by A. Mrkos 23.40 (local time)
1946 04 21	22 46	31°270	≈80	Prague	Guth, V. 1947, Bull. Astron. Inst. Czechosl. 1, p. 1-4 Lhotsky,O. and Gaertner,L., 1946, Rize Hvezd, 27, 137-138	Observations by a large group ZHR refers to a single observer
1982 04 22	06 48	31°376	253	North America	Adams, M.T., 1982, Meteor News 581	Observations by N.W. McLeod
1982 04 22	06 49	31°377	--	Ottawa	Porubçan,V. and McIntosh,B.A., 1987 Bull. Astron. Inst. Czech., 38, 313-7	Springhill high power radar
1982 04 22	06 38	31°369	--	Budrio	Porubçan, V. and Cevolani, G., 1985, Contr. Astron. Obs. Skalnate Pleso 13, 247-253	Budrio radar

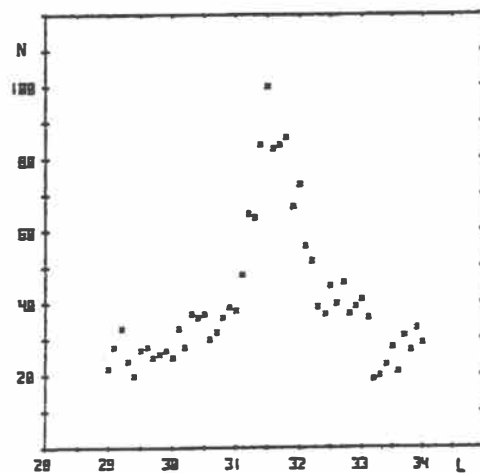
Table 1. Visual and radar observations of exceptional Lyrid activity

Fig. 1A

Visual zenithal hourly rates of "normal" Lyrid shower versus solar longitude 1950. Observations by three experienced groups.

**Fig. 1B**

Radar activity profile based on 18 years of observations at Ottawa and Ondrejov. Hourly rate of radar echoes normalized to 100.



References

- Adams, M.T., 1982, Meteor News, No. 58, 1.
 Benzenberg, J.F., 1838, Astron. Nachr. 355, 325-327.
 Fisher, W.J., 1931, Pop. Astron., 39, 256-263.
 Gadomski, J., 1929, Publ. Astron. Obs. Warzawa Univ., 5, 69.
 Guth, V., 1947, Bull. Astron. Inst. Czechosl., 1, 1.
 Herrick, E.C., 1838, Am. Journ. Sci., 34, 398.
 Herrick, E.C., 1839, Am. Journ. Sci., 36, 358-363.
 Hindley, K., 1969, Rep. Meteor Section, Journ. BAA, 79, 475.
 Jenniskens, P. and Veltman, R., 1988, de Radiant, Journ. Dutch Meteor Soc., No. 7, 74-75.
 Lhotsky, O. and Gaertner, L., 1946, Rise Hvezd, 27, 137-138.
 Lindblad, B.A. and Porubčan, V., 1991, Bull. Astron. Inst. Czechosl. (in press).
 Olivier, C.P., 1929, Publ. Leander McCormick Obs., 5, I, 1-40.
 Olivier, C.P., 1946, Pop. Astron. 54, 305-307.
 Olmstedt, D., 1834, Am. Journ. Sci. (1), 26, 132-137.
 Porubčan, V. and Stohl, J., 1983, Contr. Astron. Obs. Skalnaté Pleso, 11, 169.
 Porubčan, V. and Cevolani, G., 1985, Contr. Astron. Obs. Skalnaté Pleso, 13, 249.
 Porubčan, V. and McIntosh, B.A., 1987, Bull. Astron. Inst., Czechoslov., 38, 313.
 Porubčan, V. and Hajduková, M., 1988, Acta Astron. et Geophys. Univ. Comen., 13-14, 77.
 Porubčan, V., Simek, M. and McIntosh, B.A., 1989, Bull. Astron. Inst. Czechosl., 40, 298.
 Rendtel, J., 1990, private communication.
 Teichgraeber, A., 1934, Die Sterne, 14, 137.

DYNAMICAL TIMESCALES IN THE JUPITER FAMILY

MATS LINDGREN

Astronomical observatory, Box 515, 751 20 Uppsala, Sweden

ABSTRACT

Numerically integrated fictitious comets starting in orbits perihelion tangent to Jupiter have been used to estimate the duration of a typical visit to the observable Jupiter family of comets. The results show values of 3 to 6 thousand years, narrowing the previously estimated interval of 10³ to 10⁴ years.

INTRODUCTION

The time a short-period comet typically spends in the observable Jupiter family has not yet been investigated in detail. This paper presents preliminary first results from a project where dynamical simulations using a large number of fictitious orbits integrated for several tens of thousands of years, are used.

Why is the typical duration of a Jupiter family visit important to know? First, looking at the large scale dynamical evolution of the cometary population as a whole, one of the problems is how to explain the apparent steady state of the Jupiter family. Models for this must consist of balancing the dynamical infeed of comets from some source population with a combination of dynamical and physical loss (see e.g. Ip and Fernández, 1991, and Levison, 1991).

Secondly, a detailed study of the duration of Jupiter family visits appears to be of considerable interest when making models of the physical evolution of the comets over longer timescales than just a few revolutions, especially regarding the question of how the process of dust mantling of the nuclei works (e.g. Rickman et al., 1990).

METHOD

These calculations are based on the orbital evolutions derived from numerical integrations of 1000 fictitious comets for 50000 years, in a dynamical model of the Solar system consisting of the Sun, Jupiter in its present orbit and the (massless) objects. To be able to handle the close encounters with Jupiter without sacrificing accuracy, an integrator with variable stepsize (RADAU), as described by Everhart (1985), has been used.

In Quinn et al. (1990) it is concluded that the origin of the Jupiter family comets is a low-inclination distribution of Neptune crossers random-walking due to Neptune perturbations until the orbital period becomes comparable with Jupiter's, when they will evolve according to the Tisserand criterion

$$T = \frac{2a_J}{(Q + q)} + 2\sqrt{\frac{2Qq}{(Q + q)a_J}} \cos i = \text{constant}$$

where Q and q is the aphelion distance and perihelion distance respectively for the comet, i the inclination, and a_J is the semi-major axis of Jupiter's orbit.

The initial orbits in this study were thus chosen such that the comets already are on low-inclination orbits in the Jupiter—Saturn region. As is shown in figure 1 the initial perihelion distances are between 4 and 6 AU, aphelion distances between 4 and 10 AU (leading to an eccentricity interval of 0 to 0.43), and an inclination distribution between 0° and 30°. The remaining angular elements were evenly distributed between 0° and 360°.

The orbits were integrated for 50000 years, and the osculating elements were stored every 50 years. A plotted example of a perihelion distance evolution can be seen in figure

2. This example clearly shows the principal problem with how to define the time during which the comet is in the observable Jupiter family: it is not enough just to define a visit to the observable Jupiter family as when the perihelion distance is below a certain level. The "noise" around any one level gives misleading results. Rather, the definition of the duration of a visit is the time a comet spends in a "deep" capture, i. e., the time spent with perihelion distance less than 4 AU if at any time during this period the perihelion distance is less than 2 AU, while having an orbital period less than 20 years (figure 2).

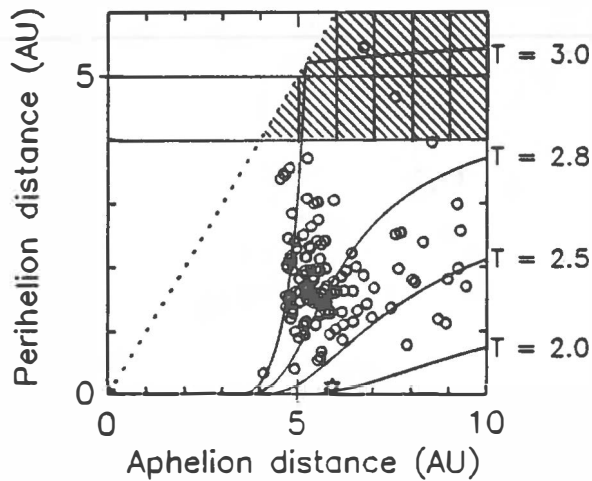


Figure 1. Shown in the figure are the initial values for perihelion- and aphelion distance (hatched area), together with the distribution of the known Jupiter family comets (rings). The labeled curves indicate the dynamical evolution according to the Tisserand criterion using inclination 0° .

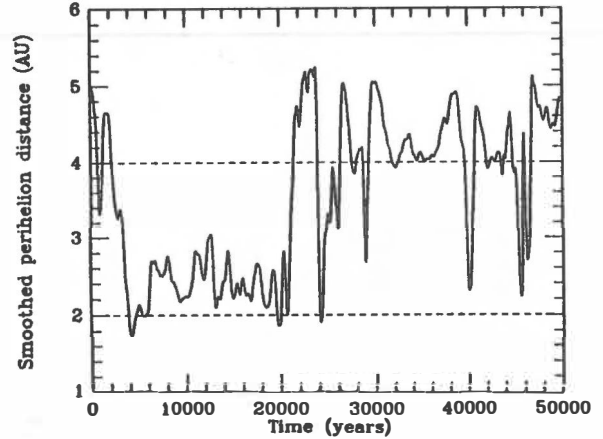


Figure 2. An example of orbital evolution for one comet. Plotted is the perihelion distance during 50000 years. The dashed lines show the chosen limits for the definition of a Jupiter family visit (see text).

Another problem with the raw data is the effect of the constant sampling interval. This means that the osculating elements sometimes are recorded at times when the comet is at a close encounter with Jupiter, which leads to a non-representative osculating orbit. To compensate for this the data has been smoothed slightly using a smoothing function covering 7 timesteps, and with the 3 central weights at 0.2, and the weights on each side at 0.1. Tests showed that without smoothing there was an overrepresentation of fictitious 50 year visits.

RESULTS AND DISCUSSION

The smoothed orbital evolutions for the 1000 comets was used to generate statistical values for the duration of the visits to the observable Jupiter family. Seven runs were made, using different subsets of initial orbits. A histogram showing the distribution of the duration of visits for all 1000 initial orbits can be seen in figure 3 and table 1. In the figure the median value is shown, as well as the quartiles and the arithmetic mean value. Results for the 6 remaining runs, with subsets of the initial orbits, can also be seen in table 1.

Initial orbits	Duration of visit (years)				
	$T_{0.25}$	$T_{0.50}$	$T_{0.75}$	$\langle T \rangle$	n
All	2100	4375	8800	6876	348
$4 < q < 5$ AU	2300	4950	9450	7261	228
$5 < q < 6$ AU	1850	3650	7650	6153	120
$0^\circ < i < 15^\circ$	1600	3525	6850	5149	158
$15^\circ < i < 30^\circ$	2900	5850	11550	8422	190
$0 < e < 0.21$	2050	3950	7975	6616	182
$0.21 < e < 0.43$	2100	5000	9850	7134	166

Table 1. Results from 7 runs using different initial orbits. $T_{0.25}$, $T_{0.50}$ and $T_{0.75}$ stands for the 25% quartile, median and 75% quartile, respectively. $\langle T \rangle$ the arithmetic mean value, and n is the number of visits the T-values are based on.

Table 1 shows that the typical visit to the observed Jupiter family, as defined above, is between 3 and 6 thousand years. This number corresponds well with previously quoted values of 10^3 to 10^4 years (e.g. Fernández, 1984).

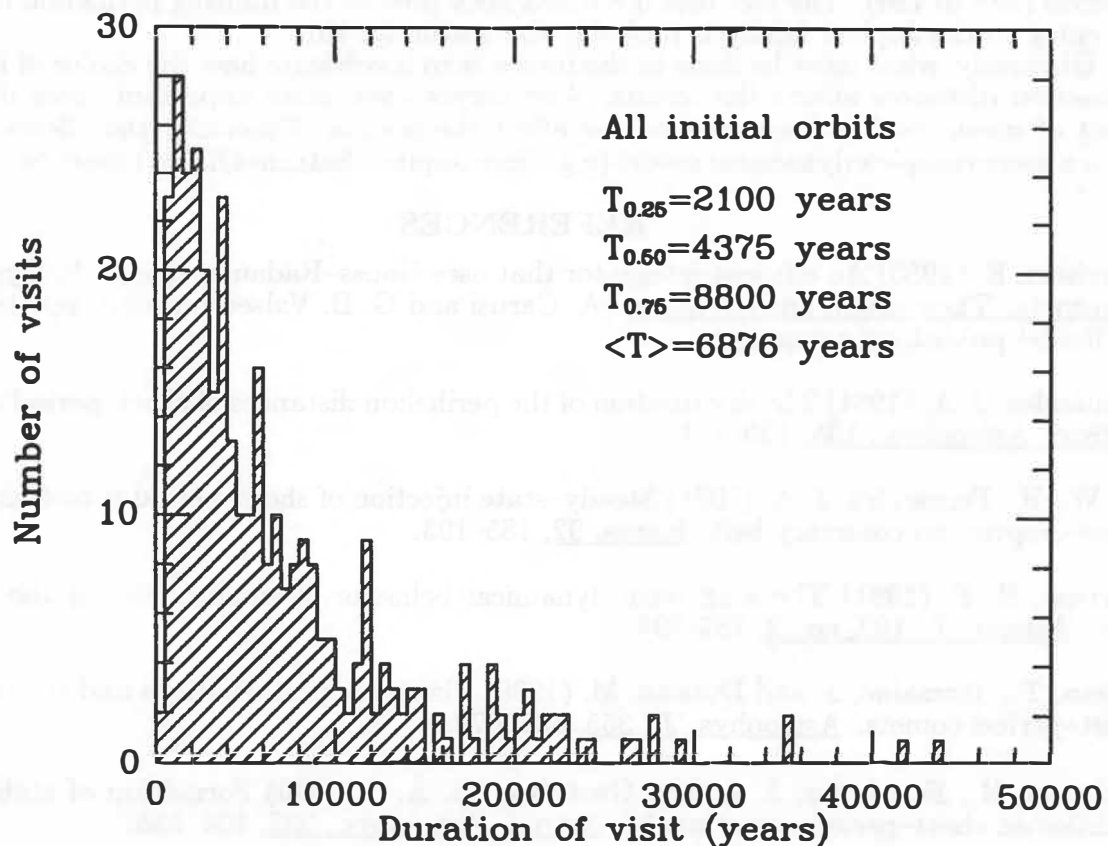


Figure 3. The distribution of duration of visits to the observable Jupiter family using all initial orbits. The width of each bin is 500 years.

No far-reaching conclusions will be made here based on this small amount of data. But looking at the results for the different subsets of initial orbits a few observations can be made. All three subset pairs (q , i and e) show a difference of more than a thousand years. This must be of significance. Perhaps surprising is the fact that both initially lower inclination and lower eccentricity orbits suffer shorter visits than higher inclination and higher eccentricity orbits. Maybe the shorter visits for the lower eccentricity orbits can be explained by the fact that comets in these orbits undergo encounters with Jupiter at relatively lower velocities, with correspondingly larger perturbations. Thus there would be a situation where the probability of a low-velocity/large-perturbation encounter with Jupiter within a short time is not too small. On the other hand comets in higher eccentricity orbits have on the average higher velocity encounters with corresponding smaller perturbations. But when a large perturbation does occur, the lower probability of another large perturbation within a short time is smaller than in the low-eccentricity case. In short: once a higher eccentricity comet has been captured into the Jupiter family it takes longer to leave. This should show up in the number of visits column in table 1, but only a hint of this can be seen (166 high e visits compared to 188 low e visits).

In principle, the same kind of argument could be used to explain the difference in the inclination subset pair. A comet in a high inclination orbit has a lower probability of encountering Jupiter, but when it does the equally low probability of an encounter soon after leads to a longer visit to the Jupiter family. Unfortunately this is not reflected in a smaller number of visits for higher inclination orbits, rather the opposite: 190 high i visits compared to 158 low i visits.

Regarding the perihelion distance subset pair the most striking fact is that there seems to be nearly a factor of two in difference for the number of visits in favour of the 4 to 5 AU interval (228 to 120). The fact that 4 AU has been used as the limiting perihelion distance for entry to the Jupiter family is probably the reason for this.

Obviously, what must be done in the future is to investigate how the choice of limiting perihelion distances affects the results. And maybe even more important: how does the effect of mean motion resonance locking affect the results. Especially the effects arising from a more complex dynamical model (e.g. Sun-Jupiter-Saturn-Object) must be studied.

REFERENCES

- Everhart, E. (1985) An efficient integrator that uses Gauss-Radau spacings. In Dynamics of comets: Their origin and evolution (A. Carusi and G. B. Valsecchi, eds.), pp. 185–202. D. Reidel publishing company.
- Fernández, J. A. (1984) The distribution of the perihelion distances of short-period comets. Astron. Astrophys., **135**, 129–134.
- Ip, W.-H., Fernández, J. A. (1991) Steady-state injection of short-period comets from the trans-Neptunian cometary belt. Icarus, **92**, 185–193.
- Levison, H. F. (1991) The long-term dynamical behavior of small bodies in the Kuiper belt. Astron. J., **102**, no. 2, 787–794.
- Quinn, T., Tremaine, S. and Duncan, M. (1990) Planetary perturbations and the origin of short-period comets. Astrophys. J., **355**, 667–679.
- Rickman, H., Fernández, J. A. and Gustafson, B. Å. S (1990) Formation of stable dust mantles on short-period comet nuclei. Astron. Astrophys., **237**, 524–535.

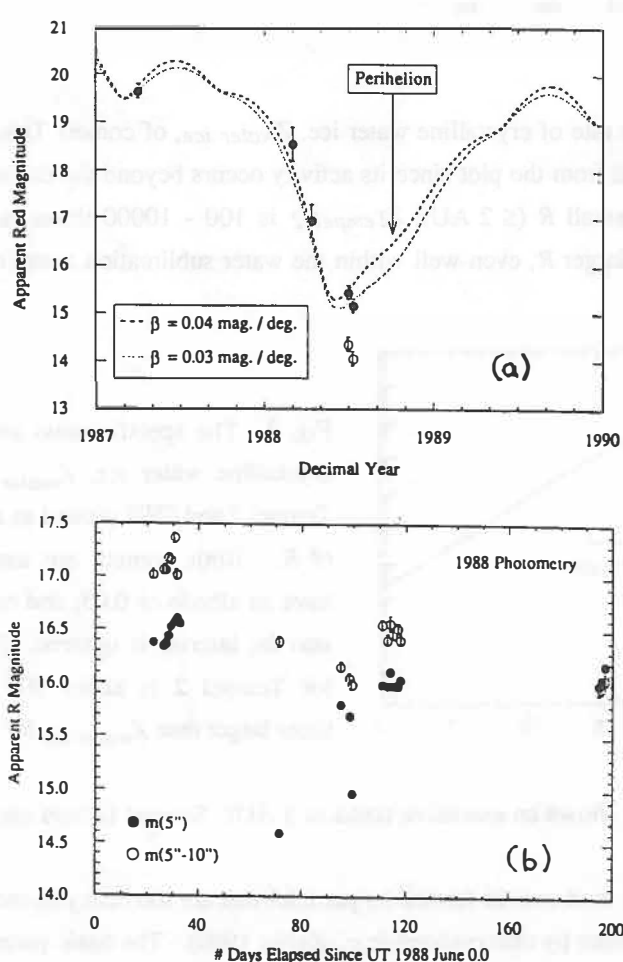
Activity in Distant Comets

Jane X. Luu (Harvard-Smithsonian Center for Astrophysics)

Abstract. Activity in distant comets remains a mystery in the sense that we still have no complete theory to explain the various types of activity exhibited by different comets at large distances. This paper will explore the factors that should play a role in determining activity in a distant comet, especially in the cases of comet P/Tempel 2, comet Schwassmann-Wachmann 1 (hereafter SW1), and 2060 Chiron.

1. Introduction

From the 1988 observing campaign on Tempel 2, we know that this comet is essentially asteroidal (photometrically and visually) at heliocentric distance $R \geq 2.3$ AU (Jewitt and Luu 1989). The long term photometric behavior of Tempel 2 is illustrated in Fig. 1a, where a plot of the cometary magnitude vs. the date of observation is presented. The two lines represent the inverse-square ("asteroidal") law for a phase-darkened nucleus for two different phase coefficients. Except for the data points represented by the hollow dots (which were measured after a resolved coma had been observed around the comet), the asteroidal models provide a very good fit to the photometry, proving that Tempel 2 was indeed a bare nucleus at these distances.



SW1, on the other hand, has never been observed in a bare nucleus state in spite of its large semimajor axis (~ 6 AU). In his extensive two-year study of the comet, Jewitt (1990) reported that SW1 displayed an extended coma on all dates of observation. The persistent coma is different from the impulsive outbursts for which SW1 is famous (Whipple 1980). Fig. 1b shows the nightly mean magnitudes of SW1 measured in two different apertures and monitored over 7 months in 1988. The Figure shows outbursts (e.g., day numbers 71 and 99) superimposed on the steady coma.

Fig. 1. a) Mean R magnitudes of Tempel 2 vs. the epoch of observation. Solid dots denote nucleus magnitudes; hollow dots denote magnitudes within a 20"-radius aperture. The 2 lines show the "asteroidal model" with 2 different phase coefficients (from Jewitt and Luu 1988). b) Mean R magnitudes of SW1 vs. the date of observation in 1988. $m(5'')$ is the magnitude measured within a 5"-radius aperture, while $m(5''-10'')$ is the annular magnitude within the inner and outer radius 5" and 10", respectively (from Jewitt 1990).

Chiron differs from both Tempel 2 and SW1 in that it exhibits a resolved coma at the unusually large distance $R \sim 12$ AU (Hartmann *et al.* 1990), although non-asteroidal photometric behavior has been observed since 1988 (Tholen *et al.* 1988). A graphical summary of the photometric behavior of Chiron is shown in Fig. 2, where I have plotted all the photometry known to me up to 1990. The years 1980 - 87 represent a faint state, whereas in 1988 - present, Chiron is up to a magnitude brighter.

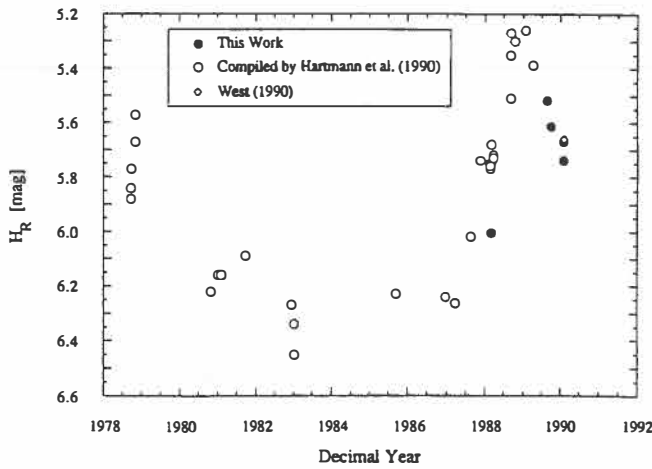


Fig. 2. Integrated photometry of Chiron reduced to red absolute magnitudes and plotted as a function of the date of observation. The data compiled from Hartmann *et al.* (1990) were transformed from H_V to H_R by $H_R = H_V - 0.37$. Errors are generally too small to be seen at the scale of the plot (from Luu and Jewitt 1990).

2. Tempel 2 vs. SW1

In Fig. 3, we plot the specific mass loss rate of crystalline water ice, $Z_{\text{water ice}}$, of comets Tempel 2 and SW1 as a function of R . (Chiron is excluded from the plot since its activity occurs beyond the distance range where water sublimation is feasible). At small R (≤ 2 AU), $Z_{\text{Tempel 2}}$ is 100 - 10000 times larger than Z_{SW1} , but drops to an insignificant level at larger R , even well within the water sublimation zone (nominally ≤ 5 AU for most comets).

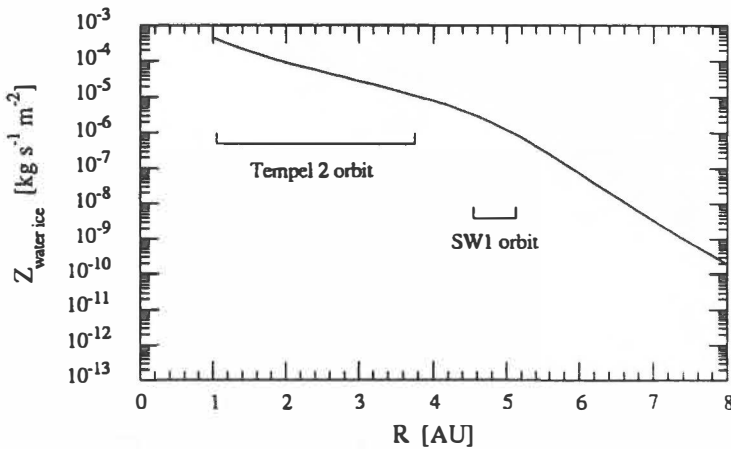


Fig. 3. The specific mass loss rate of crystalline water ice, $Z_{\text{water ice}}$, for Tempel 2 and SW1 plotted as a function of R . Both comets are assumed to have an albedo of 0.05, and conduction into the interior is ignored. $Z_{\text{water ice}}$ for Tempel 2 is about 100 - 10000 times larger than $Z_{\text{water ice}}$ for SW1.

Why is Tempel 2 a bare nucleus while SW1 shows an extensive coma at 5 AU? Several factors are likely to play a role:

- 1) The size of the active area. The idea of an inert mantle formed by particles that are too heavy to escape from the nucleus is now established and firmly proven by observations (e.g., Keller 1990). The basic parameters of cometary activity in Tempel 2, SW1 and Chiron are listed in Table 1. The fractional active areas F_{active} on SW1 and Tempel 2 are comparable ($\sim 1\%$), but since SW1 is much larger than Tempel 2, the absolute active area

A_{active} of SW1 is 100 times larger than that of Tempel 2.

Table 1. Activity Parameters

Comet	Radius [km]	F_{active}	A_{active} [m^2]
P/Tempel 2	5	0.1 - 1%	$(0.6 - 6) \times 10^6$
P/SW1	~ 20	2%	10^8
2060 Chiron	60 - 150	$10^{-3} - 10^{-5}\%$	$10^4 - 10^6$

2) Spin axis and rotation period. If a comet rotates very slowly or is insolated pole-on (the spin axis pointing at the Sun), the surface temperature can stay sufficiently high for sublimation to take place even at large distances like 5 AU. The rotational properties of SW1 are unknown but both Whipple (1980) and Jewitt (1990) showed some evidence that SW1 is a very slow rotator (rotation period \geq 5 days).

3) Interior volatiles. By the nature of its orbit, Tempel 2 has been thoroughly heated by the Sun and thus may have an interior consisting largely of crystalline ice instead of amorphous ice (the metastable form of ice that exists before turning into crystalline ice at \sim 150 K). SW1 is large, on a nearly circular orbit (eccentricity \sim 0.04), thus its interior should still retain a large fraction of amorphous ice. It is likely that the interior ice inventory would affect sublimation at the surface.

4) Mantle structure. At least two mantle-forming processes are known: a) due to left-over grains that were too heavy to escape from the nucleus, and b) due to cosmic ray bombardment, whether in the Oort cloud or Kuiper belt. Again, since SW1 has not been subjected to intense solar heating like Tempel 2, it might retain more of its cosmic ray-induced crust than Tempel 2. It is not known how such a mantle affects sublimation as compared to a mantle formed by left-over large grains.

3. Chiron

Chiron is distinguished from other short-period comets by its large size (radius \leq 150 km) and large semimajor (\sim 12 AU). As mentioned above, factors such as the large size and mantle structure are likely to influence the amount of cometary activity on Chiron. With such a large nucleus, not much area is needed before a detectable coma is generated. Chiron's activity also cannot be caused by water ice, and is reminiscent of activity in other distant comets such as comet Halley (\sim 15 AU, Hainaut *et al.* 1991) and Bowell (\sim 14 AU, Meech and Jewitt 1987). At such large distances, materials more volatile than water ice have to be responsible for cometary activity, such as CO and CO₂ (Luu and Jewitt 1990).

In particular, the mantle of Chiron may differ from that of other short-period comets by the size distribution of its mantle grains, and by the fact that it is likely to be entering the inner Solar System for the first time (Hahn and Bailey 1990). The size distribution of mantle grains is determined by the volatiles that sublimate and eject dust grains through gas drag. The more volatile materials responsible for activity on Chiron should leave behind on the surface a size distribution of grains that is different from those left behind by water ice, the driving volatile in common short-period comets. Furthermore, if Chiron is making its first voyage inward to the Sun, its mantle is likely to be mainly caused by cosmic ray bombardment, which might produce a non-volatile crust capable of surviving a few passages in the inner Solar System (Strazzula *et al.* 1983). The cosmic-ray induced mantle (as

opposed to the mantle formed by large heavy grains) may explain why the dynamically new comets seem to be more active than the short-period comets at comparably large distances.

The last possible cause of activity at large distances that I will mention is electrostatic charging of the nucleus. Mendis *et al.* (1981) have shown that electric currents, generated by solar wind ions and UV radiation, can electrostatically charge the nucleus surface, causing levitation and subsequent expulsion of loose, submicron-sized dust from the surface. This process may apply to small comets where the escape velocity is relatively small.

4. Conclusion

As Tempel 2, SW1 and Chiron have exemplified, activity in distant comets can take on quite distinct flavors whether in the form of a bare nucleus or continuous activity. However, the ubiquitous mantle has emerged as an increasingly important factor in controlling the activity on cometary surfaces, and our understanding of its physical properties is still woefully lacking. Until the surface and interior of the nucleus are better understood, a simplistic conclusion that can be reached thus far is the following: if we assume that all comets formed basically in the same manner, 3 major factors are likely to influence the types of cometary activity at large distances: a) the size of the nucleus, b) the rotation period and pole direction of the comet, and c) the details of its thermal history, as caused by its dynamical history.

Acknowledgments

I am grateful for critical comments from D. Jewitt and for financial support from a Smithsonian Postdoctoral Fellowship.

References

- Hahn, G., and Bailey, M. (1990). Rapid dynamical evolution of giant comet Chiron. *Nature*, **348**, 132 - 136.
- Hartmann, W. K., Tholen, D. J., Meech, K., and Cruikshank, D. P. (1990). 2060 Chiron: colorimetry and cometary behavior. *Icarus*, **83**, 1 - 15.
- Jewitt, D. C. (1990). The Persistent Coma of Comet P/Schwassmann-Wachmann 1. *Ap. J.*, **351**, 277 - 286.
- Jewitt, D. C., and Luu, J. X. (1989). A CCD Portrait of Comet P/Tempel 2. *A. J.*, **97**, 1766 - 1790.
- Keller, U. H. (1990). The Nucleus. In *Physics and Chemistry of Comets* (W. F. Huebner, ed.), pp. 13 - 68. Springer-Verlag, Berlin.
- Luu, J. X. and Jewitt, D. C. (1990). Cometary activity in 2060 Chiron. *A. J.*, **100**, 913 - 932.
- Meech, K. and Jewitt, D. (1987). Comet Bowell at record heliocentric distance. *Nature*, **328**, 506 - 509.
- Mendis, D. A., Hill, J. R., Houpis, H. L. F., and Whipple, E. C., Jr. (1981). On the electrostatic charging of the cometary nucleus. *Ap. J.*, **249**, 787 - 797.
- Strazzula, G., Pirronello, V., and Foti, G. (1983). Physical and chemical effects induced by energetic ions on comets. *Astron. Astrophys.*, **123**, 93 - 97.
- Tholen, D. J., Hartmann, W. K., and Cruikshank, D. P. (1988). IAU Circular 4554.
- Hainaut, O., Smette, A., and West, R. (1991). IAU Circular 5189.
- Whipple, F. L. (1980). Rotation and outbursts of Comet P/Schwassmann-Wachmann 1. *A. J.*, **85**, 305 - 313.

PHILOSOPHY AND UPDATING OF THE ASTEROID PHOTOMETRIC CATALOGUE

P. Magnusson¹, M.A. Barucci², M.T. Capria³,
M. Dahlgren⁴, M. Fulchignoni⁵, C.-I. Lagerkvist⁴

¹Queen Mary and Westfield College, London E1 4NS, U.K.

²Observatoire de Paris-Meudon, Place Jules Janssen, F-92195 Meudon, France

³Istituto di Astrofisica Spaziale, CNR, Viale dell'Università, 11, I-00185 Roma, Italy

⁴Astronomiska Observatoriet, Box 515, S-751 20 Uppsala, Sweden

⁵Istituto Astronomico, Università "La Sapienza", Via Lancisi, 29, I-00161 Rome, Italy

The Asteroid Photometric Catalogue (Lagerkvist et al. 1987, 1989, 1992) now contains photometric lightcurves for 584 asteroids. We discuss some of the guiding principles behind it. This concerns both observers who offer input to it and users of the product.

Any systematic work on asteroid lightcurve properties and lightcurve inversion for pole, shape and albedo variegation will involve analysis of data from a very large number of publications. For example, the lightcurves of a single interesting object like 4 Vesta are spread out in more than 20 papers.

A biennial printed catalogue (Lagerkvist et al. 1987, 1989, 1992) tabulates all observations with uniform aspect data and complete references. In addition, the new observations not included before are displayed in lightcurve diagrams (Fig. 1). These have been transformed to a standard format to make comparisons easier. In particular, the axis scales are kept constant for all observations of the same object.

A database containing both new and old observations in digital form is also maintained. It is available free of charge except for media costs. In contrast to the printed version, we try to keep the contents of the digital one as close to the original publications as possible, thus making checking of the data against the original feasible. This means that the data are given in a multitude of units, some as composite lightcurves, and with various reductions applied to them. All this information is stored with the data, and we have software to extract a uniform data set for a particular application. We are happy to assist users with software and/or uniform data for specific projects. An IBM-PC database presentation system is also available on request.

The second update of the catalogue, containing observations published before the end of 1990, is now in press. Contact Claes-Ingvar Lagerkvist for further information. An increasing proportion of observers have kindly submitted their published data to us in

digital form. This has greatly increased the reliability of the catalogue and made our job easier. Observers are encouraged to continue this trend. Such data need not at all be close to the form of presentation in the observers own publication.

It is important to identify which steps in the data reduction observers are best equipped to do, and what is best left undone in a database for future use. Clearly, weather and equipment-dependent reductions such as extinction correction and transformation to a standard magnitude system must be done by the observing group. Harris and Lupishko (1989) have summarized and stressed good principles to follow. The resulting table of magnitudes as a function of observing time (UT) is ideal for the digital database. Frequently it will include data points which "stand out" from the rest and which can be rejected with varying degree of confidence. It is natural for observers to remove the ugliest ones from their published diagrams, but we believe these points, suitably marked as rejected, have a mission in the database. Knowledge that the pruning has been done with prudence increases confidence in the data, and there is a possibility that future re-analysis will promote a rejected point. Further reduction of the data, especially model-dependent ones like composite construction or transformation to a particular solar phase angle, are best left out of the database.

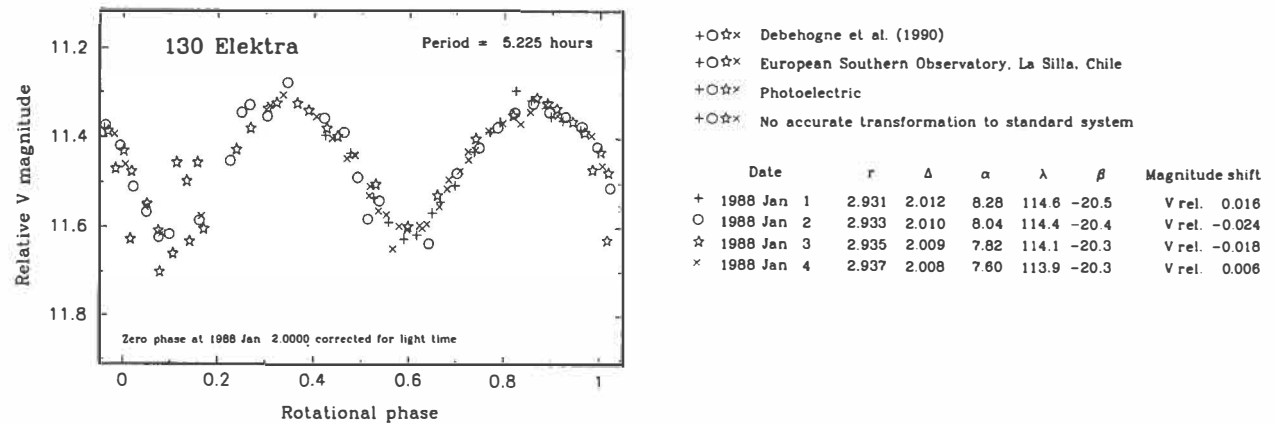


Fig. 1. Example of lightcurve presentation in the Asteroid Photometric Catalogue

References

- Harris, A.W., Lupishko, D.F. (1989). Photometric lightcurve observations and reduction techniques. In *Asteroids II* (R.P. Binzel, T. Gehrels, M.S. Matthews, eds.), University of Arizona Press, 39-53.
- Lagerkvist, C.-I., Barucci, M.A., Capria, M.T., Fulchignoni, M., Guerriero, L., Perozzi, E., Zappalà, V. (1987). *Asteroid Photometric Catalogue*. Consiglio Nazionale Delle Ricerche, Rome.
- Lagerkvist, C.-I., Barucci, M.A., Capria, M.T., Fulchignoni, M., Magnusson, P., Zappalà, V. (1989). *Asteroid Photometric Catalogue, First Update*. Consiglio Nazionale Delle Ricerche, Rome.
- Lagerkvist, C.-I., Barucci, M.A., Capria, M.T., Dahlgren, M., Fulchignoni, M., Magnusson, P. (1992). *Asteroid Photometric Catalogue, Second Update*. Uppsala Astronomical Observatory. In press.

Cometary orbital evolution in the outer planetary region

A. Manara¹ and G.B. Valsecchi²

¹Osservatorio Astronomico di Brera, via Brera 28, 20121 Milano, Italy

²IAS — Planetologia, viale dell'Università 11, 00185 Roma, Italy

Abstract

Numerical integrations of fictitious objects are carried out in order to elucidate the dynamical behaviour of potential short-period comets when they move in orbits at distances from the Sun comparable to those of Uranus and Neptune. As in the case of observed short-period comets, close encounters with the planets play a major role for the orbital evolution, and this is especially true for encounters with initial orbits nearly tangent to that of the planet. A comparison with integrations in which the planetary masses are larger by a factor 10 shows that, in the latter case, the orbital evolution is greatly accelerated, but the dynamical paths in phase space followed by the comets are altered.

Introduction

A key question about the origin of Jupiter-family comets (those of orbital period $P < 20$ yr) is whether they come from a flattened trans-neptunian disk or from an isotropic inner core of the Oort cloud (Quinn et al., 1990). To model the orbital evolution of potential short-period comets from the situation in which they are under the dynamical control of Neptune to the orbits in which they can be observed requires a formidable amount of computer time, and in fact the only attempt done so far has used a model of the solar system in which the masses of the four outer planets are enhanced by a factor $\mu = 10$ to shorten the process in terms of number of orbits (and thus of CPU time) required (Quinn et al., 1990).

Researches done in the past on the dynamical evolution of short-period comets have led to a rather clear overall picture of the dynamics in the region of Jupiter and Saturn, and an equally good overall picture of the dynamics of comets also in the Uranus and Neptune region would be desirable. We try to accomplish this by examining in some detail the orbital evolutions of fictitious comets started from low-eccentricity, low-inclination orbits not far from those of the planets.

The numerical integrations

The model of the solar system used in this work consists of the Sun and the four outer planets Jupiter, Saturn, Uranus and Neptune, with the inner planets added to the Sun; the four outer planets are on elliptical unperturbed orbits (further details are given in Manara and Valsecchi, 1991).

We have integrated the motion of 100 fictitious comets with Everhart's routine RADAU (Everhart, 1985); the objects are divided in four groups of 25 each, whose initial conditions are set up choosing at random:

- the reciprocal semimajor axis $1/a$, such that: $0.9 \times 1/a_p < 1/a < 1.1 \times 1/a_p$, where a_p is, in turn, the semimajor axis of each of the four outer planets; thus, for each group of 25 objects we have $0.173 \text{ AU}^{-1} < 1/a < 0.211 \text{ AU}^{-1}$, $0.094 \text{ AU}^{-1} < 1/a < 0.115 \text{ AU}^{-1}$, $0.047 \text{ AU}^{-1} < 1/a < 0.057 \text{ AU}^{-1}$, and $0.030 \text{ AU}^{-1} < 1/a < 0.037 \text{ AU}^{-1}$ respectively;
- the eccentricity e and the inclination i , such that: $0 < e < 0.1$, $0 < \sin i < 0.1$;
- the argument of perihelion ω , the longitude of node Ω , and the mean anomaly M , such that: $0^\circ < \omega < 360^\circ$, $0^\circ < \Omega < 360^\circ$, $0^\circ < M < 360^\circ$;
- the mean anomalies of the outer planets M_J , M_S , M_U , and M_N , such that: $0^\circ < M_J < 360^\circ$, $0^\circ < M_S < 360^\circ$, $0^\circ < M_U < 360^\circ$, $0^\circ < M_N < 360^\circ$,

for each comet to be started.

Each object is followed for 1000 revolutions about the Sun, keeping track of its close planetary encounters.

The role of close encounters

Close planetary encounters, i.e. encounters within the planetary Hill radius

$$r_H = a_p \sqrt[3]{\frac{m_p}{3m_{Sun}}}$$

where m_p and m_{Sun} are respectively the masses of the planet and the Sun, are found to govern the evolution of the majority of the comets that show substantial orbital changes at the end of the simulation (Manara and Valsecchi, 1991). This is true mostly for objects interacting with Jupiter and Saturn; comets started close to Uranus and Neptune have a more limited orbital evolution, and in fact none of them encounters closely either Saturn or Jupiter before the end of our integrations. In their case, close encounters with Uranus and Neptune do influence the evolution, but are not able to spread the orbital elements all over the available phase space, as it happens with Jupiter and Saturn.

The distribution of perturbations at close encounters shows distinct tail asymmetries that are related to the positions of the pre-encounter orbits in the phase space of orbital elements $a-e-i$. Moreover, the majority of the strongest perturbations, i.e. of those contained in the asymmetric tails of the distribution, are experienced by comets in orbits nearly tangent to that of the planet encountered (Manara and Valsecchi, 1991). This suggests that the regions of phase space corresponding to orbits nearly tangent to those of the planets constitute a preferential path followed by comets on their way towards short-period orbits. In fact, those objects started from the vicinity (in $a-e-i$ space) of Neptune, that tend to pass from the dynamical control of the latter planet to that of Uranus, do so moving along the "nearly-tangent-orbits" path; they first have the perihelion distance q lowered at constant aphelion distance $Q \simeq 30$ AU, and then, when $q \simeq 20$ AU, have Q lowered due to encounters with Uranus, while q remains nearly constant.

What happens for larger planetary masses

As seen in the previous section, the orbital evolution in the Uranus-Neptune region appears to be less dominated by planetary close encounters than it is in the Jupiter-Saturn region. This may seem to support the plausibility of a treatment of the multi-stage process of capture of comets into short-period orbits as a diffusion process, as done by Quinn et al. (1990), thus justifying the enhancement of planetary masses used in their integrations.

However, Valsecchi (1991) finds, using Öpik's theory of close encounters (Öpik, 1976; Carusi et al., 1990) — which is valid in the case of encounters in crossing orbits (Greenberg et al., 1988) — that changing the planetary masses by a factor μ as large as 10 changes also significantly the distributions of energy perturbations at close encounters.

We have recomputed the first 25 objects, those started close to the orbit of Neptune, from the same initial conditions, with $\mu = 10$, as done by Quinn et al. (1990). The aim of this computation is a comparison with that done with the realistic masses, in order to check if the effect of the increased masses is only that of shortening the multi-stage capture process, in terms of number of revolutions of the comets integrated, or if the alteration of the energy perturbation distribution also affects the paths followed in phase space by the comets.

A preliminary analysis of the output of this additional integration shows that the orbital evolutions are not only (and simply) accelerated, but that they take place along different routes in phase space, at larger eccentricities and inclinations than in the case of the actual masses. This happens essentially because planetary encounters displace the orbits in $a-e-i$ space in such a way as to approximately preserve the value of the Tisserand invariant T_p relative to the planet encountered

$$T_p = \frac{a_p}{a} + 2\sqrt{\frac{a(1-e^2)}{a_p}} \cos i$$

(T_p would be more precisely conserved in a restricted circular 3-body problem), so that to larger $1/a$ perturbations generally correspond larger perturbations in e and i . As a consequence of this, the objects started in Neptune's zone, that for $\mu = 1$ had shown a smaller sensitivity to the effects of planetary close encounters, for $\mu = 10$ are scattered all over the available phase space, and the nearly-tangent-orbits path for passing under the control of Uranus is practically not recognizable any more in our data. The overall behaviour is similar to that of the fictitious comets started close to Jupiter and Saturn in the $\mu = 1$ integration, for which close encounters are evidently governing the evolution. The detailed analysis of the outcomes of this integration will appear in Valsecchi and Manara (1991).

Summarizing, it appears that, for low-eccentricity and low-inclination initial conditions, the orbital evolution for $\mu = 1$ is dominated by close planetary encounters in the region of Jupiter and Saturn, but not so much so in that of Uranus and Neptune; for $\mu = 10$, however, also the evolution in the Uranus-Neptune region appears to be dominated by close encounters. This finding casts doubts on the plausibility of treating the multi-stage capture of comets into short-period orbits as a diffusion process, given the stochastic nature of a scattering process essentially dominated by close planetary encounters. The question of the necessity of postulating the Kuiper belt to explain the observed population of Jupiter-family comets, as done by Quinn et al. (1990), basing on computations performed with $\mu = 10$, should therefore be considered as still open.

References

- Carusi A., Valsecchi G.B., and Greenberg R. (1990) Planetary close encounters: geometry of approach and post-encounter orbital parameters. *Celest. Mech.*, **49**, 111-131.
- Everhart E. (1985) An efficient integrator that uses Gauss-Radau spacing. In *Dynamics of Comets: their Origin and Evolution* (A. Carusi and G.B. Valsecchi, eds.) pp. 185-202. D. Reidel, Dordrecht.
- Greenberg R., Carusi A., and Valsecchi G.B. (1988) Outcomes of planetary close encounters: a systematic comparison of methodologies. *Icarus*, **75**, 1-29.
- Manara A. and Valsecchi G.B. (1991) Dynamics of comets in the outer planetary region. I A numerical experiment. *Astron. Astrophys.*, **249**, 269-276.
- Öpik E.J. (1976) *Interplanetary Encounters*. Elsevier, New York. 155 pp.
- Quinn T., Tremaine S., and Duncan M. (1990) Planetary perturbations and the origin of short-period comets. *Astrophys. J.*, **355**, 667-679.
- Valsecchi G.B. (1991) Presented at the International Workshop on Periodic Comets, Montevideo, Uruguay, 5-7 August 1991.
- Valsecchi G.B. and Manara A. (1991) Dynamics of comets in the outer planetary region. II Evolutionary paths in phase space. In preparation.

THE ELEVEN OBSERVATIONS OF COMETS BETWEEN 678AD AND 1114AD RECORDED
IN THE ANGLO SAXON CHRONICLE. E. G. Mardon, A. A. Mardon, J. Williams; Red Deer
College, Red Deer, Canada; Texas A & M University, College Station, Texas, USA;
Edmonton, Alberta, Canada, T4P-A5S.

This research paper is an examination of the eleven cometary references [679AD, 729AD, 892AD, 905AD, 975AD, 995AD, 1066AD, 1097AD, 1106AD, 1110AD & 1114AD] found in the various manuscripts of The Anglo Saxon Chronicle between 678 AD and 1114 AD on the Old English text and scientific observations. The manuscripts contain more than 35 celestial observations. This is an examination of astronomical phenomena and other climatic or natural events, that are described in The Anglo Saxon Chronicle, which is also referred to as The Old English Annals. The Anglo Saxon Chronicle is an Old English history of events begun under the direction of King Alfred the Great in the 9th Century and containing earlier material in adapted form. It was written from records kept at various English Monasteries. After the account of King Alfred's wars which started with the invading Danes, the Anglo Saxon Chronicle was officially kept up year by year until the last entry dated for 1154 AD. It survives in seven manuscripts. The Anglo Saxon Chronicle contains factual material with references often verifiable through other contemporary or near contemporary sources, like the Bayeux Tapestry containing a panel of the 'long-haired comet' [Refer to Illustration One], that appeared in 1066 AD, a few months prior to the invasion of England by William the Conqueror.

Background. The annalists who compiled the Anglo Saxon Chronicle were keen astronomical observers. A total of 35 eclipses of either the Sun, or the Moon; comets; falling stars; and brilliant Aurora Borealis, are noted as occurring on such and such a date in a certain year. The Anglo Saxon Chronicle uses the Roman method of calculating the date, i.e. the day of the month. At the time of the Venerable Bede (c.725 AD) the English custom was to begin the year on Christmas Day; eventually this was to fall into disuse in favour of September, due to the fact that the Byzantine Greeks at that time commenced their year on September 1st.

The question of provenance of the Anglo-Saxon Chronicle. Seven manuscripts of the 'Chronicle' are extant. Others were destroyed during civil strife in the late Medieval period or at the time of the English Reformation in the 16th. Century. For this research, the following four manuscripts were consulted:

- i) 'The Parker Chronicle'[A], which is part of the Cambridge, Corpus Christi Manuscript collection. It is believed to have been written by a Winchester monk.
- ii) 'The Abington Chronicles'[B] and [C]. The former concerns the period from 2 AD to 977 AD, while the latter is from 60 BC, corresponding nearly to Julius Caesar's attempted invasion of Britain (55 BC), to 1066 AD, the year of the Norman Conquest of England. Both of these manuscripts are in the Cotton Manuscript collection in the British Museum [London].
- iii) 'The Worcester Chronicle'[D]. The entries cover the period from 2 AD to 1079 AD with the addition of an annal that brings the entries up to 1130 AD. It is also in the Cotton Manuscript collection of the British Museum.
- iv) 'The Land Chronicle'[E]. It was written at the Peterborough monastery, and its entries cover the period from 2 AD 1153 AD. It is now in the Bodleian Library at Oxford. This manuscript was found to be the most readable for a non Anglo Saxon scholar. The Old

COMET OBSERVATIONS IN THE ANGLO SAXON CHRONICLES: E. G. Mardon, and A. A. Mardon

English text can be understood if read very slowly with a completely open mind regards to the spelling of words and the use of gender endings.

The Anglo Saxon Chronicle is the name applied to a group of surviving manuscripts that serve as the chief source for English history during the Anglo Saxon age that came to an end with the Norman conquest in 1066 AD. The Anglo Saxon Chronicle is actually clearly divisible into several distinct units, which are never the less ordinarily treated by scholars as parts of the same overall series of annuals. Large Monasteries were in the habit of keeping calendars for the purpose of determining the date of Easter. In time, the important events of a centre year were noted by a scribe with personal comments. Generation after generation of monks or scribes wrote entries. Many of them are either a religious or political nature, such as the date of a bishop or king, the invasion of a Viking host; or a natural disaster, such as a famine or a crop failure. However, in the entries selected in this research project, astronomical events, such as eclipses of the sun, or of the moon, the appearance of comets or shooting stars, or the occurrence of a meteor shower are noted. Often the time of day and duration of the eclipse are added to the entries. Sometimes, the day of the week is mentioned or some other details such as the lighting of the candles so a meal could be eaten during an eclipse of the sun. Work on the earliest portion is derived from other Latin sources. The Anglo Saxon scribes translated them into old English by 892 AD. Monks at Winchester, possibly on the behest of King Alfred were adding entries. Legend states that King Alfred aided in the editing of the Anglo Saxon Chronicle. His well known personal interest in astronomy may have been one of the reasons that 40 entries deal with astronomical phenomena. It is worth noting that a total of twenty-five entries included in this study commence with the celestial reference. The scribe who appears to be doing this places emphasis on the unusual astronomical occurrence. The year numbers (always Roman numerals) are usually in the left-hand margin as disposed in the printed text.

The Dating of Events: The scribes who wrote the entries recorded the events dependent upon the annalistic year. In Medieval times the year could begin on different dates.

- 1) The Anglo Saxon Chronicle commenced on September 24th according to the Caesarean Indictions
- 2) The Christian Church year commenced on Lady Day, March 25th.

Several astronomical entries(5), which do not have assigned dates have not been examined in this paper.

COMET REFERENCES:

First Cometary reference in The Anglo Saxon Chronicle 678 AD

"678 AD. HERATEWEDE COMETA AND SCAN III MON AS AELCE MORGAN SWILCE SUNNE BEAM."

"In this year appeared the star called comet, in August, and shone for three months each morning like a sunbeam."

COMET OBSERVATIONS IN THE ANGLO SAXON CHRONICLES: E. G. Mardon, and A. A. Mardon

[Note: The scribe writes in a matter of fact way. States the fact and the length of time the comet was in vision. He did not appear to be concerned at this unusual astronomical phenomena.]

[Not mentioned by Marsden in Catalogue of Cometary Orbits.]

Second Cometary reference in The Anglo Saxon Chronicle 729 AD

þr cometa refærra hine oþre ƿær ægbricht forfænde

"HERATEWODEN TWEGAN COMETAN."

"In this year appeared two comets."

[Not mentioned by Marsden in Catalogue of Cometary Orbits.]

Third Cometary reference in The Anglo Saxon Chronicle 892 AD

*þr ilcan geare ofer eastron ymbe gang das o aer aet eowde se sunz
steorra e mon on boc laeden haet cometa same men cwe a o englisc aetce
healfe steorra ford aem baer stent lang leoma of hwilum on aelce healfe : 7*

"892 AD. I Y ILCAN GEARE OFER EASTRON YMBE GANG DAGAS O AER AET EOWDE SE STEORRO E MON ON BOC LAEDEN HAET COMETA, SAME MEN CWE A O ENGLISC AETCE HEALFE STEORRA. FORD AEM BAER STENT LANG LEOMA OF HWILUM ON AELCE HEALFE."

"And the same year after Easter during Rogation-tide or earlier appeared the star which in Latin is called 'comet', likewise men say in English that a comet is a (flax) long-haired star, because long beams of light shine there forth, sometimes on one side, sometimes on every side."

[Not mentioned by Marsden in Catalogue of Cometary Orbits.]

Fourth Cometary reference in The Anglo Saxon Chronicle 905 AD

"HER COMETA AET EOWD XIII KL NOUEBRIS."

"In this year the comet appeared thirteen days before the Kalends of November 1."

[This was the Roman way of dating, it is possible that this method of dating was used in a public record for the last time in The Anglo Saxon Chronicle]

[Also mentioned in Marsden's Catalogue of Cometary Orbits, taken from Hasegawa 1979 Publication of the Astronomical Society Japan, 31, 257.]

Fifth Cometary reference in The Anglo Saxon Chronicle 975 AD

*na on þam ilcan geare on heipferde æterde cometa
re ƿœrija .*

COMET OBSERVATIONS IN THE ANGLO SAXON CHRONICLES: E. G. Mardon, and A. A. Mardon

"975 AD. AND HER EANWARD EADGARES SUNU FEN TO RICE AND A SONA ONILCAN GEARE ON HERFESTE AETEOWDE COMETA SE STEORRA AND COM EAFTTRAN GEARE SWI E MYCEL HUNGOR."

"And in this year Edward, Edgar's son, succeeded to the Kingdom, and soon at harvest time of the same year appeared that star known as Comet. And the next year came great hunger (Famine)."

[Note: Our Saxon ancestors attempted to see cause and effect and believed that astronomical phenomena was a kind of fore shadowing of coming events. In my father's lifetime (1909) when Halley's Comet appeared, many predicted awful consequences. The Great War started 5 years later. E.G. M.]

[Not mentioned by Marsden in Catalogue of Cometary Orbits.]

Sixth Cometary reference in The Anglo Saxon Chronicle 995 AD

þær on hirrum geare ætropde
cometu ye heoripa. ȝrige aƿicð foniðfende.

"995 AD. HER ON ISSUM GEARE AETEWDE COMETA SE STEORRA."

"In this year appeared the comet or star."

[Not mentioned by Marsden in Catalogue of Cometary Orbits.]

Seventh Cometary reference in The Anglo Saxon Chronicle 1066 AD

x ant. v i l o w . x v i .
On hirru geare man halgode þer
mynsteri æt pestmynstrie on cilda mæsse dæg. ȝ se cyng
eadwulf foniðfende on tƿelfta mæsse æfen. ȝ hine man
be býngede on tƿelftan mæsse dæg. innan þærne riwa.
halgodie cƿitean on pestmynstrie. ȝ hanold eorl ƿeng
to engla lander cyne rice. spa spa se cyng hit him ge ude.
ȝ eac men hine þærni to ȝecuron. ȝ þær ge bletsod to cyn

"1066 AD. AND A EASTRAN ON DAELEG XVI KALEND MAI. THA WEARTH GEOND ENGLA LAND SWYLC TACEN ON HEFOAENUM GE SEWEN SWYLCE NAN MANN AER NE GESEH. SUME MENN CWAEDON THA HYT COMETA SE STEORRA WAERE, THONE SUME MENN HATATH THONE FEXEDON STEORRAN HE AET EOWDE AERESTON THONE AEFEN LETANIA MAIRA THA YS VIII KALEND SWA SCEAN EALLE THA VII NIHT."

"And Easter was on the fourteenth day before the Kalends of May. Then it happened that all through England such a sight in the heavens was seen as no man had seen before. Some men said that it was the star comet, that some men called the long haired star; it appeared on the eve of Letania Maior that is the eighth day before the Kalend of Mai, and so shone for all seven nights"

COMET OBSERVATIONS IN THE ANGLO SAXON CHRONICLES: E. G. Mardon, and A. A. Mardon

[Note: Many of the Chronicles, both native and foreign, regard the appearance of the comet as ominous of great events which took place in England this year.

Artifactual Record: "The Bayeux Tapestry", made within decades of the events of 1066, has a panel of its embroidery showing the comet crossing the sky.



Illustration One: Panel from "The Bayeux Tapestry" depicting King Harold consulting an Astrologer who explained the evil omen of Halley's Comet. [Pictured on the Bayeux Tapestry taken from MacLagan, Plate Number 34.]

Halley's Comet: The appearance of Halley's Comet would correspond to the following references in the Anglo Saxon Chronicles to cometary appearances 1066AD. Within the period that is covered by the Anglo Saxon Chronicle the calculated appearances of Halley's Comet would be in the years with perihelion dates of October 2, 684AD; May 20, 760AD, February 28, 837AD, July 18, 912AD, September 5, 989AD, March 20, 1066AD, April 18, 1145AD; and September 28, 1222AD.]

[Also mentioned in Marsden's Catalogue of Cometary Orbits. The calculated perihelion date of Halley's Comet is March 20th, 1066.]

Eighth Cometary reference in The Anglo Saxon Chronicle 1097 AD

ða
upon sce mīchāl'mæssan. iiiii. nōctōbrī. æt ydē an selcud
ſteoripa on æpen scynende ſona to ſetle gannde.

"DA UPON SCE MICHAEL'S MASSAN IIIII N OCTOBR AETYWDE AN SELCUTH STEORRA ON AEFEN SCYNENDE SONA TO SETLE GANNGAENDE. HE WAES GE SEWEN SUTH WEAST SE LEOMA DE HIM OFSTOD WAES SWITHE LANG GE DUHT SUTH EAST SCINENDE FOR NEAH EALLE DA WUCAN ON DAS WISAN AETYWDE. MANIGE MEN LETO DA HIT COMETA WEARE."

"Then after Michaelmas fourth day before the Nomen of October there appeared a rare star shining in the evening, and soon sinking into its setting. It was seen in the southwest, and the beam of light which stood out from it seemed very long, shining in the south east, nearly all week it appeared in this way. Many men supposed it was a comet."

[Not mentioned by Marsden in Catalogue of Cometary Orbits.]

Ninth Cometary reference in The Anglo Saxon Chronicle 1106 AD

... on þe ne rymian længten pucan
on hōn fyrige dæg on æpen æt ydē an ungesunelic ſteoripa.
y lange fandē hōn æft þes celœ æpen ge ſepen hpile ſanende.

COMET OBSERVATIONS IN THE ANGLO SAXON CHRONICLES: E. G. Mardon, and A. A. Mardon

"ON THAERE FORMAN LAENGTEM WUCAN ON THON FRIGE DAEG XIII K' MR' ON AEFEN AETYWDE AN UN GEWUNELIC STEORRA. AND LANGE STUNDE THAER AEFT' WAES AELCE AEFENGESSEWEN HWILE SCINENDE. SE STEORRA AETYWDE INNON THE SUTH WEST. HE WAES LITEL GETHUHT. AND DEORC. AC SE LEOMA THE HI FRA STOD WAES SWITHE BEORHT. AND SWILCE ORMAETE BEAM GETHUHT NOTH EAST SCINENDE. AND SUNE AEFEN GESAEWEN SWILCE SE BEAM ONGEAN WEARDES WITH THES STEORRAN WARD FYRCLIENDE WAERE."

"In the first week of Lent, on Friday, the fourteenth day before the Kalends of March a strange star appeared in the evening and for a long time afterwards was seen shining for a while each evening. The star made its appearance in the south west, and seemed to be small and dark, but the light that shone from it was very bright and appeared like an enormous beam of light shining in opposite direction to the star. Some said that they had seen other unknown stars about this time, but we cannot speak about these without reservation, because we did not ourselves see them. On the eve of Cena Domini, Thursday before Easter two moons were seen in the sky before day, one in the east and one in the west and both at the full, and that day the moon was 14 days old. The light from the tail of a comet seemed to be streaming towards instead of from the nucleus."

[Not mentioned by Marsden in Catalogue of Cometary Orbits.]

Tenth Cometary reference in The Anglo Saxon Chronicle 1110 AD

*'þa færijan ofer eall þa heofon fridē beorhtcē scinende. ȝ
tīoƿ pēstnāl pūrīdon hēre nihtcē hūph forfīte fridē for mū-
mene. Æft' æft' on iunie monðe acrypde an færija nōrðan
eastan. ȝhī leoma stod to foran hī on het sudwest.'*

"1110 AD TRE OW WAESTMAS WURDON THAERE NIHTE THURH FORSTE SWIDE FOR NUMENE. THAER AETER ON JUNIES MONTHE AETYWDE AN STEORRA NORTHAN EASTAN HIS LEOMA STOD TO FORAN HIM ON THET SUTHWEST THUS MANEGA NIHT WAES GE SAEWAN FURTHOR NIHTES SYTH THAN HE UFOR ASTAH HE WAS GE SEWAN ON BAEC ON THE NORTH WEST GANENDE."

"Tree-fruits were that night largely taken by frost. Thereafter in the month of June appeared a star in the northeast. Thus it was seen for many nights. Further on in the night, when it rose higher, it was seen going back in the northwest."

[Not mentioned by Marsden in Catalogue of Cometary Orbits.]

Eleventh Cometary reference in The Anglo Saxon Chronicle 1114 AD

*'þeƿi æft' iunian septemb' he for mō-
sē in to norimandys. Ðisey gearey on æfter apid mai pēfse feyen
an selcud færija mid langan leoman manegē niht scinende.'*

"1114 AD. THISES GEARES ON AEFTEWARD MAI WAES GESEWEN AN SELCUTH STEORRA MID LANGAN LEOMAN MANEGE NIHT SCINENDE."

"This year towards the end of May was seen a star with a long beam of light shining for

COMET OBSERVATIONS IN THE ANGLO SAXON CHRONICLES: E. G. Mardon, and A. A. Mardon

many nights."

[Not mentioned by Marsden in Catologue of Cometary Orbits.]

**List of references to Comets in two cited edition's of the
Anglo Saxon Chronicle:**

<u>Year</u>	<u>Page from 1865 ASC</u>	<u>Page from 1889 ASC</u>	<u>ASC Manuscript</u>
1) 678 AD	Page 53	Page 38	The Parker Ms.(A)
2) 729 AD	Page 60	Page 44	The Parker Ms.(A)
3) 892 AD		Page 82-83	The Parker Ms.(A)
4) 905 AD	Page 112	Page 93	The Worcester Ms.(D)
5) 975 AD		Page 121	The Laud Ms.(E)
6) 995 AD	Page 145	Page 129	The Laud Ms.(E)
7) 1066 AD	Page 194	Page 195	The Laud Ms.(E)
8) 1097 AD	Page 236	Page 233	The Laud Ms.(E)
9) 1106 AD		Page 240	The Laud Ms.(E)
10) 1110 AD	Page 246	Page 242	The Laud Ms.(E)
11) 1114 AD	Page 247	Page 244	The Laud Ms.(E)

List of references to Astronomical Events in the Anglo Saxon Chronicle:

538	Sun Eclipse	540	Sun Eclipse	664	Sun Eclipse	678	Comet
729	Two Comets	734	Moon-Red	744	Meteor	793	Dragon (Meteor?)
795	Moon Eclipsed	802	Moon Eclipsed	806	Moon Eclipsed	809	Eclipse
827	Moon Eclipsed	879	Sun Eclipsed	885	Sun Eclipsed	892	Comet
904	Moon Eclipsed	905	Comet	926	Aurora Borealis	975	Comet
995	Comet	1066	Comet	1095	Falling Stars	1097	Comet
1104	Sun Halo	1106	Comet	1107	Moon Waxing	1110	Comet
1114	Comet	1117	Moon red	1121	Moon Eclipse	1122	Aurora Borealis
1131	Aurora Borealis	1135	Sun Eclipse	1140	Sun Eclipse		
					Total Comets-	11	
					Total Solar Eclipses-	7	
					Total Lunar Eclipses-	6	
					Total Meteor Showers-	2(3?)	
					Total Aurora Borealis-	3	

With the aid of modern technology, we have made startling advances in the field of astronomy. But let us not forget the written reports of the ancients who recorded astronomical phenomena a thousand years ago. For example, the Anglo Saxon Chronicle, probably initiated c.891AD at the command of King Alfred the Great, is an annual commentary of significance events. Seven manuscripts survive. The monk authors recorded recommended episcopal appointments; deaths of kings, and bishops; natural disasters such as flood, crop failures, and wind storms; civil wars; and Viking invasions. The Anglo Saxon Chronicle is unique and is the most important prose work in Old English. No Western European people during these centuries possessed such a relatively complete and revealing record of their history. The unknown scribes were interested in recording astronomical occurrences including solar eclipses, lunar eclipses, aurora borealis, meteor showers and sighting of comets.

COMET OBSERVATIONS IN THE ANGLO SAXON CHRONICLES: E. G. Mardon, and A. A. Mardon**Bibliography**Editions of The Anglo Saxon Chronicle:

- The Parker Chronicle. Edited A. H. Smith. New York: Appleton-Century-Croft, 1966.
- The Parker Chronicle and Laws. [Corpus Christi College, Cambridge, Ms. 173]: A Facsimile. Edited by R. Flower and H. Smith. Oxford: Early English Text Society- Oxford University Press, 1941.
- The Peterborough Chronicle. [The Bodleian Manuscript Laud Misc. 636]. Edited D. Whitelock. Copenhagen: Rosenkilde, 1954.
- Two of the 'Saxon Chronicles'. Edited by John Earle. Oxford: Clarendon Press, 1865.
- Two of the 'Saxon Chronicles'. Edited by Charles Plummer. Oxford: Clarendon Press, (1889).
- The Parker Chronicle. Edited A. H. Smith. New York: Appleton-Century-Croft, 1966.

Other Works:

- MacLagan, E. The Bayeux Tapestry. London: Penguin Books, 1953.
- Marsden, Brian G. Catalogue of Cometary Orbits. Enslow Publishers, Hillside, New Jersey, 1983.

Comment by editor:

The authors of the above paper were unable to make revisions to their manuscript before publication. We feel the reader should be informed of a significant point raised by the referee:

"All of the cometary apparitions mentioned in this paper have been recorded by the Chinese, Japanese, Korean, or European observers. For example, Pingre's work in 1783-1784, Ho Peng Yok's 1962 work and Yeomans' 1991 book detail these observations."

Readers wishing to gain a broader insight into these historical observations may wish to consult those references.

Ho Peng Yoke. *Vistas in Astronomy*, 1962, vol.5, p. 127-225.

Pingre, A. G. *Cometographia*. Paris, 1783-1784.

Yeomans, D. K. *Comets: A Chronological History...* Wiley and Sons, 1991.

THE RECOVERY OF ASTEROIDS AFTER TWO OBSERVATIONS

BRIAN G. MARSDEN

Harvard-Smithsonian Center for Astrophysics, Cambridge, MA 02138, U.S.A.

ABSTRACT

It is shown that a generalization of the use of "Väisälä orbits", briefly mentioned at the *Asteroids II* conference, can be very conveniently accomplished by means of an inversion of the "GEM" form of the Gauss method. The procedure can also be applied to Apollo objects and to indeterminate cases of normal three-observation orbit computation, and there is also a simple extension to situations involving four or more observations.

A popular procedure for planning and then identifying the third night's observations of an asteroid is to utilize sets of orbits fitted to positions on the first and second nights on the assumption that the object is then at perihelion—or aphelion, a circular solution being the transition between the two sets. In the proceedings of the *Asteroids II* conference Bowell *et al.* (1989) briefly considered that this procedure (Väisälä 1939) might be generalized to delineate the precise region of the sky in which a main-belt asteroid must lie. In a typical application the third night will be in the dark of the moon following that of the first and second nights, which—to avoid incorrect linkage—should themselves be separated by no more than about five days; and the two lunations will tend to surround or adjoin the asteroid's being at opposition. Here I shall discuss in more detail how the "generalized Väisälä procedure" can conveniently be carried out in practice.

If the asteroid had actually been identified on the third night, it would be reasonable to attempt a three-observation orbit computation from one position on each night. This could be accomplished by the Gauss (1809) method, preferably in the rigorous "GEM" (Gauss-Encke-Merton) form I described (Marsden 1985) in response to Taff's (1984) misguided claim that the Gauss method is not mathematically valid.

In the GEM form the orbit computation is made in Cunningham's (1946) coordinate system, where the xy plane passes through the observations at times t_1 and t_3 , the x axis being directed toward that at t_3 . For reasons that will shortly become apparent, I shall consider t_1 to refer to the first observation and t_3 to the second observation. The time t_0 will then refer to the hypothetical third observation. The Cunningham coordinate system has the great advantage that the usual vector equation of the Gauss method separates into

$$\begin{aligned}\rho_0 &= (Z_0 - c_1 Z_1 - c_3 Z_3)/n_0 \\ \rho_1 &= (\rho_0 m_0 - Y_0 + c_1 Y_1 + c_3 Y_3)/c_1 m_1 \\ \rho_3 &= (\rho_0 l_0 - c_1 \rho_1 l_1 - X_0 + c_1 X_1 + c_3 X_3)/c_3,\end{aligned}\tag{1}$$

where the (l_i, m_i, n_i) and (X_i, Y_i, Z_i) represent the components of the unit vectors from the observer to the asteroid and of the vectors from the observer to the sun at the times t_i . The scalar distances ρ_i from the observer to the asteroid at the t_i are initially unknown, as are the scalars c_1 and c_3 , the usual ratios of the areas of the triangles that are associated with the Gauss method. Eqs. (1) can simply be evaluated in turn as successive approximations to these scalars become available.

The first of Eqs. (1) is fundamental to the Gauss method, and standard to any evaluation of it is consideration of the analogous equation

$$\rho_0^o = (Z_0 - c_1^o Z_1 - c_3^o Z_3)/n_0,\tag{2}$$

where c_1 and c_3 are approximated by the ratios of the areas of the corresponding sectors,

$$\begin{aligned}c_1^o &= (t_3 - t_0)/(t_3 - t_1) \\ c_3^o &= (t_0 - t_1)/(t_3 - t_1),\end{aligned}\tag{3}$$

and can be immediately computed. Migration from Eq. (2) to the first of Eqs. (1) requires use of the "sector-triangle ratios", and in view of the well-known power-series expansions for these it has been usual to establish this in the form

$$\rho_0 = \rho_0^o(1 - \gamma_0/r_0^3), \quad (4)$$

where r_0 , the asteroid's heliocentric distance at time t_0 , is also related to ρ_0 geometrically, and γ_0 is another quantity that is modified during the iterative process.

Although not essential to the normal orbit-determination process, it is useful for the present purpose also to define a quantity

$$\alpha^o = m_0/(m_1 c_1^o), \quad (5)$$

and since m_0 and m_1 are the sines of the angles between, respectively, the observations at t_0 and t_3 and at t_1 and t_3 , in a short-arc orbit the ratio m_0/m_1 goes roughly as the time ratio c_1^o , in which case $\alpha^o \sim 1$.

Although Gauss used Eq. (4) and its geometric counterpart quite rigorously and computed the sector-triangle ratios in terms of the hypergeometric function, others have instead relied heavily on power-series expansions, and since these expansions can certainly diverge, Taff's criticism has been understandable. In the case of a main-belt asteroid observed for up to a month or so near opposition, $\gamma_0 \sim R_0^3$, where $R_0 = (X_0^2 + Y_0^2 + Z_0^2)^{\frac{1}{2}}$, and convergence is to be expected. Nevertheless, acknowledging Taff's comments, and also because Eq. (4) is in reality a pure contrivance, I recommended (Marsden 1985) that the orbit solution be carried out by incorporating successive iterates for the c_1 and c_3 directly into Eqs. (1).

In the particular situation being considered here, however, the unit vector (l_0, m_0, n_0) at the isolated third observation is unknown. This suggests that Eqs. (2) and (5) should be inverted and written

$$\begin{aligned} \bar{n}_0 &= (Z_0 - c_1^o Z_1 - c_3^o Z_3)/\bar{\rho}_0 \\ \bar{m}_0 &= \bar{\alpha} m_1 c_1^o. \end{aligned} \quad (6)$$

One can therefore assume suitable values of $\bar{\rho}_0$ and $\bar{\alpha}$ and compute the corresponding \bar{n}_0 , \bar{m}_0 and $\bar{l}_0 = (1 - \bar{m}_0^2 - \bar{n}_0^2)^{\frac{1}{2}}$. The sets of $(\bar{l}_0, \bar{m}_0, \bar{n}_0)$ can then, on the one hand, be transformed from the Cunningham system back to the equatorial system and unique sets of values of the right ascension and declination, and on the other hand, be substituted for the (l_0, m_0, n_0) in Eqs. (1) and each time subjected to the full GEM orbit-determination process. The region of the sky to be searched can then be restricted on the basis of those orbital solutions that give acceptable values of semimajor axes a and eccentricities e (and perhaps also the inclinations i , although this requires conversion back from the Cunningham coordinate system).

It is useful to attempt the computation of a circular orbit from the observations at t_1 and t_3 . The resulting position at t_0 can be substituted in Eqs. (2) and (5) to give ρ_0^c and α^c , say, and the trial values needed in Eqs. (6) are then taken in the vicinity of $\bar{\rho}_0 = \rho_0^c$ and $\bar{\alpha} = \alpha^c$. It is not clear *a priori* how extended that vicinity should be, although I note that, for a main-belt object, Eq. (4) implies that $\bar{\rho}_0$ is ~ 0.1 AU larger than ρ_0 , and since, near opposition, $\rho_0 \sim r_0 - 1$ AU, to meet the extremes of perihelion and aphelion distance considered by Bowell *et al.* (1989) requires $0.7 \lesssim \bar{\rho}_0 \lesssim 3.1$ AU.

For an example, I use that of 1985 FZ considered by Bowell *et al.* (1989), and Fig. 1 is an adaptation of their Figure. The times of the connected observations are $t_1 = \text{Mar. } 21.301 \text{ UT}$, $t_3 = \text{Mar. } 24.323$, and the isolated plate was taken on $t_0 = \text{Apr. } 14.287$. The circular orbit from the March observations yields $a = 2.79$ AU, $\rho_0^c = 1.924$ AU, $\alpha^c = 0.952$, and Fig. 1 shows that all the acceptable solutions are contained within $0.8 < \bar{\rho}_0 < 2.8$ AU, $0.82 < \bar{\alpha} < 1.02$. The original Apr. 14 candidate, denoted by "A", has an orbit with $a = 2.66$ AU, $e = 0.206$, $i = 5^\circ.5$. However, Williams (1991) has shown that this observation, but not the March observations, refers to a different object. There is another candidate to the north, "B", and this has an orbit with $a = 2.36$ AU, $e = 0.253$, $i = 4^\circ.2$.

If the motion in ecliptic latitude is too high, it may not be possible to calculate a circular orbit. Near opposition, and if i is ignored, the radius of the orbit (in AU) can be approximated by

$$a = 1 + k(t_3 - t_1)(1 - as)/m_1, \quad (7)$$

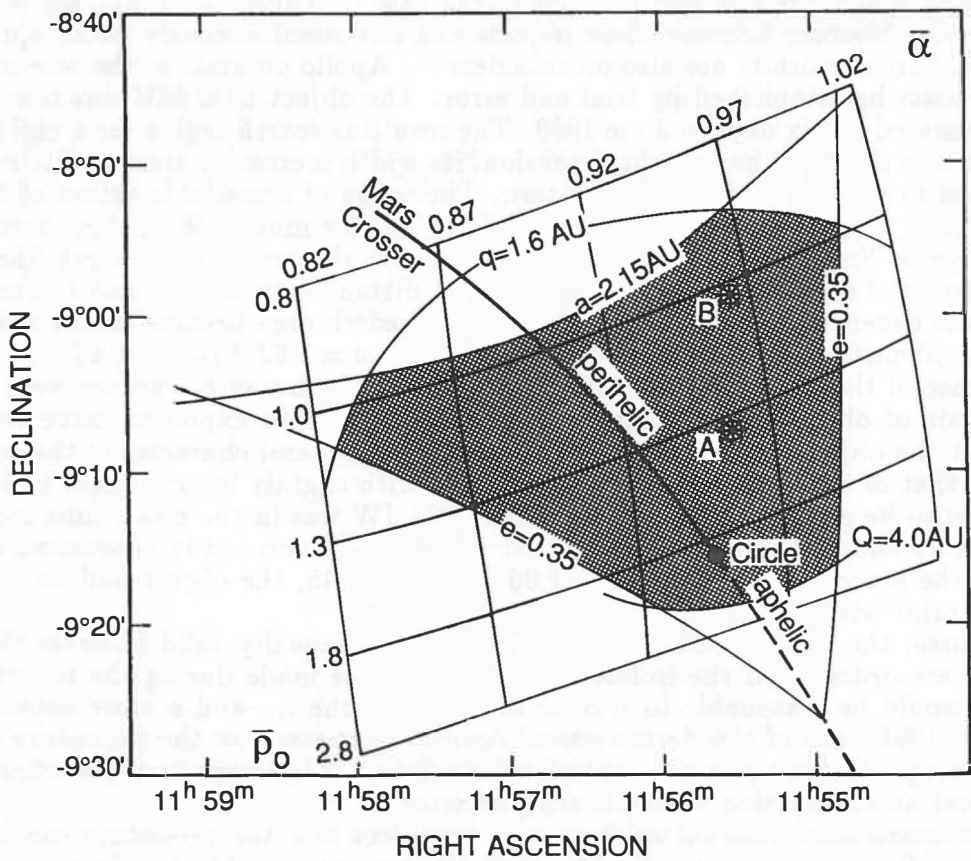


Fig. 1. The region of the sky (equinox 1950.0) in which 1985 FZ was located on 1985 Apr. 14, showing the positions in terms of the quantities \bar{p}_0 and $\bar{\alpha}$. The shaded region refers to acceptable orbits. The Väisälä locus of perihelic and aphelic orbits (including a circle) is shown. "A" is the original candidate, "B" an alternate candidate.

where the times are measured in days and the object's mean daily motion $s = a^{-\frac{1}{2}}$ is in units of the earth's mean daily motion k , i.e., the Gaussian constant 0.017202. For the 1985 FZ example, $m_1 = +0.01185$, and Eq. (7) can be solved iteratively to give $a = 2.73$ AU.

The quantity $\bar{\alpha}$ describes the foreshortening of the apparent motion, and for a circular orbit in the plane of the ecliptic with observations placed symmetrically about opposition it follows that $\bar{\alpha} = 1$. The foreshortening is greater than or less than unity according as to whether the observations are mainly before or mainly after opposition, the approximate time of which is given by

$$t_{\text{opp}} = t_3 + Y_3(t_3 - t_1)/(Y_1 - Y_3). \quad (8)$$

For 1985 FZ, $Y_1 = +0.09084$, $Y_3 = +0.03992$, so that $t_{\text{opp}} = \text{Mar. } 26.692$. The foreshortening can then be approximated by

$$\bar{\alpha} = (1 + \frac{1}{2}k^2 P)^T, \quad (9)$$

where, with the time intervals in days,

$$T = (t_0 - t_1)(t_{\text{opp}} - t_{\text{mean}}), \quad (10)$$

i.e., -86.64 day 2 in the example, t_{mean} being the mean observation time Mar. 30.304, and

$$P = (1 - as^3)/(1 - as) + 3a[(1 - s)/(a - 1)]^2, \quad (11)$$

i.e., 4.12 for $a = 2.73$ AU, so that $1 + \frac{1}{2}k^2 P = 1.00061$ and $\bar{\alpha} = 0.949$. The factor P increases between limits of 1 and $\frac{55}{4}$ as a decreases from ∞ to 1 AU, or between 3.5 and 5.2 over the main belt. Unless $|T|$ is very large, the expression 1.0006^T is therefore quite sufficient for establishing the initial trial value of $\bar{\alpha}$ for a main-belt object.

The new procedure can also be used in the case of Apollo asteroids, for which Väisälä orbits are troublesome because these objects can not simultaneously be at opposition and perihelion. Circular orbits are also meaningless for Apollo objects, so the relevant ranges of $\bar{\rho}_0$ and $\bar{\alpha}$ must be established by trial and error. The object 1990 MU was observed on two nights separated by six days in June 1990. The resulting search region for a night one month later extended some 1.5 hr in right ascension, its width increasing from as little as 1° at the eastern end to more than 5° at the western. The range of acceptable values of $\bar{\alpha}$ was ~ 0.3 - 1.3 , with $\bar{\rho}_0 \sim 0.9$ AU for small $\bar{\alpha}$, up to 0.8-1.5 AU for moderate $\bar{\alpha}$, then down to 0.6-0.9 AU for large $\bar{\alpha}$. Small values of $\bar{\rho}_0$ put the object near the earth and in earth-like orbits, and large $\bar{\rho}_0$ involved solutions that made the object distant with large e and i . For the largest $\bar{\alpha}$ the orbits degenerated into Aten type, and the search area became rather nebulous. The object was identified at $\bar{\rho}_0 = 1.28$ AU, $\bar{\alpha} = 0.89$ with $a = 1.62$ AU, $e = 0.66$, $i = 24^\circ$.

The case of the Apollo object 1991 JW is interesting because searches were to be made on the basis of observations spanning only a single 46-min exposure three weeks earlier. Given that the object was retrograding, however, the general character of the solutions was similar to that of the 1990 MU solutions, though with slightly larger ranges in $\bar{\rho}_0$ and $\bar{\alpha}$ not anticipated to be greater than 1.1. Although 1991 JW was in the mean time independently discovered by another astronomer, the first observer did succeed in recovering it right in a corner of the search area. With $\bar{\rho}_0 = 1.06$ AU, $\bar{\alpha} = 0.45$, the object had an exceptionally earth-like orbit with $a = 1.04$ AU, $e = 0.11$, $i = 8^\circ$.

Of course, the procedure outlined in this paper is equally valid however the three observations are ordered—if the isolated observation were made during the month *before* the others, it would be reasonable to reverse the order of the t_i —and a more detailed write-up in the Oct. 1991 issue of the *Astronomical Journal* discusses how the procedure can be used with advantage when a three-observation orbit solution is indeterminate, or where one might suspect that an observation is significantly in error.

The *Astronomical Journal* write-up also considers how the procedure can be extended to handle additional observations. The 1985 FZ example would have fared much better if there had been a second night of observations to verify the correct linkage of the object in April. Given such a “verification” observation, made at time t_{ver} , preferably only a few days from t_0 , it is not difficult to compute, *still for the time t_0* , a $\bar{\rho}_0 = \rho_0^v$ and an $\bar{\alpha} = \alpha^v$ that exactly satisfy the verification observation. If the linkage is correct, these should be very similar to ρ_0^o and α^o , and the residuals at t_0 and t_{ver} can then be better distributed by adopting the means $\rho_0^m = \frac{1}{2}(\rho_0^o + \rho_0^v)$, $\alpha^m = \frac{1}{2}(\alpha^o + \alpha^v)$. Obviously, further observations could also be included in these means, and the outcome resembles that of Herget’s (1965) method and “poor man’s” least-squares fit, the residuals of the observations at t_1 and t_3 remaining precisely zero. Herget’s example of 1935 QA, with the observations in the order $t_1 = \text{Aug. 30}$, $t_0 = \text{Sept. 6}$, $t_{\text{ver}} = \text{Sept. 23}$, $t_3 = \text{Oct. 21}$, results in $\rho_0^o = 1.78999$ AU, $\alpha^o = 0.95298$, $\rho_0^v = 1.78883$ AU, $\alpha^v = 0.95296$. The means ρ_0^m and α^m yield residuals (in arcsec in the equatorial system) of +0.4, +0.1 at t_0 and -1.1, -0.6 at t_{ver} . These are a little larger than Herget’s values because of the wide separation of t_0 and t_{ver} . Residuals more comparable to Herget’s follow if ρ_0^m and α^m are weighted closer to ρ_0^v and α^v .

REFERENCES

- Bowell E., Chernykh N. S., and Marsden B. G. (1989) Discovery and follow-up of asteroids. In *Asteroids II* (R. P. Binzel, T. Gehrels, and M. S. Matthews, eds.), pp. 21-38. University of Arizona, Tucson.
- Cunningham L. E. (1946) *The determination of preliminary orbits*. Ph.D. thesis, Harvard University, Cambridge. 95 + 61 pp.
- Gauss C. F. (1809) *Theoria Motus Corporum Coelestium*. Perthes und Besser, Hamburg. xi + 227 + 20 pp.
- Herget P. (1965) Computation of preliminary orbits. *Astron. J.*, **70**, 1-3.
- Marsden B. G. (1985) Initial orbit determination: the pragmatist’s point of view. *Astron. J.*, **90**, 1541-1547.
- Taff L. G. (1984) On initial orbit determination. *Astron. J.*, **89**, 1426-1428.
- Väisälä Y. (1939) Eine einfache Methode der Bahnbestimmung. *Astron.-Optika Inst. Univ. Turku Informo*, No. 1. 32 pp.
- Williams G. V. (1991) 1983 RC₅. *Minor Planet Circ.*, No. 18283. 1 p.

COMET NONGRAVITATIONAL FORCES AND METEORITIC IMPACTS

John J. Matese Patrick G. Whitman Daniel P. Whitmire
*Department of Physics, The University of Southwestern Louisiana,
Lafayette, LA 70504-4210*

Abstract

We have considered those comets whose original orbits have been determined to be hyperbolic when only planetary perturbations are accounted for. It is found that formally unbound incident trajectories correlate most confidently with orbits that have small perihelion distances and move in a retrograde sense relative to planetary motion. Arguments are presented that these results are not due to measurement error or to selection effects. We conclude that the phenomenon is attributable to enhanced volatility leading to abnormally large nongravitational forces. Since the effect is absent in the prograde small-perihelia population, increased insolation is not the sole explanation. It is suggested that the significance of the retrograde correlation is connected with a larger energy of relative motion between retrograde comets and a population of prograde ecliptic meteoroids which impact the comet mantle exposing the underlying volatiles. The subsequent enhanced outgassing is the cause of the larger nongravitational forces.

INTRODUCTION

The Oort effect [Oort 1950] is the tendency for near-parabolic comet energies to cluster in a narrow, bound, range of values. When corrected for planetary perturbations, long-period (> 200 yr) comets have $\approx 25\%$ of their energies occurring in the upper 0.2% of the bound range. An additional 10% are found to be unbound. The energy distribution of comets whose orbit determinations have been designated as highest quality (class I) [Marsden 1989] is shown in Fig. 1. These results are in reasonable agreement with the idea that the detected Oort cloud is the external region of a contiguous comet distribution made observable by the actions of the Galactic tidal torque [Heisler and Tremaine 1986; Duncan, Quinn and Tremaine 1987; Matese and Whitman 1989]. The tidal torque is capable of explaining that part of the observed distribution in the range $5 \leq 1/a \leq 50$ (in units of 10^{-6} AU $^{-1}$). In contrast, energies $1/a \leq 0$ (and $1/a \geq 50$) require an alternative explanation. Matese *et al.* [1991] have discussed those comets which have been determined to be hyperbolic originally. The question of interest is “Are these comets truly hyperbolic in origin or, if not, what is the explanation for the erroneous hyperbolic designation?”

POSSIBLE INTERPRETATIONS

- *Hyperbolic designations are due to measurement error.*

In Table 1 we list those comets for which the osculating value of $1/a$ is hyperbolic at a level $\geq 5 \times$ the formal measured error, δ . Marsden *et al.* [1978] have noted that the true measured error may be as much as $3 \times$ the formal value. Therefore multiples ≤ 5 may not be significant indicators of hyperbolic orbits. Matese *et al.* [1991] demonstrated that attributing unbound

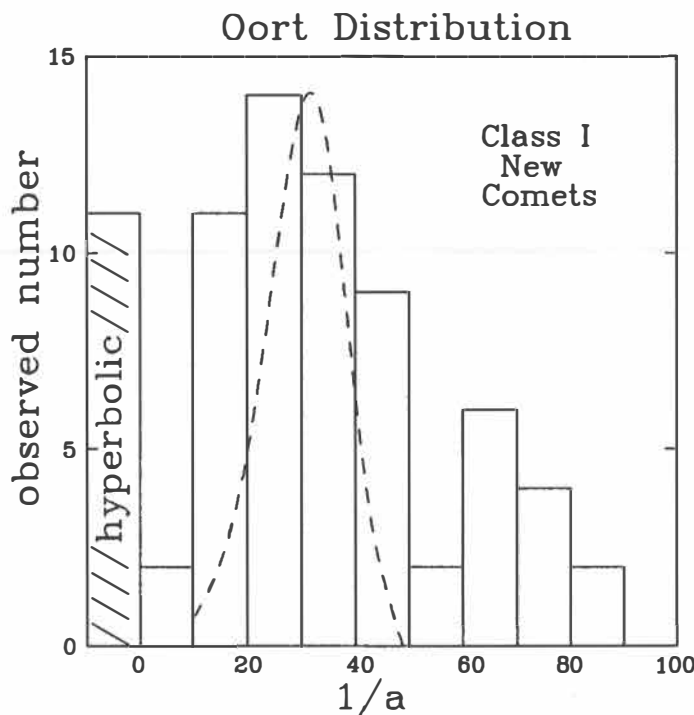


FIG. 1. The observed distribution in reciprocal semimajor axis (units= 10^{-6} AU $^{-1}$) of new class I comets. Also shown as a dashed curve is the Galactic tidal theory prediction in arbitrary units.

designations to measurement error can be rejected at a confidence level $\geq 95\%$ when "t" and "F" statistics are considered. This conclusion holds for both class I and class II comets.

- *Measurement errors for hyperbolic comets are badly underestimated.*

Although true measurement errors $\leq 3\times$ formal values cannot provide an explanation, the results shown in Table 1 could be attributed to errors if formal values were underestimated by factors ≥ 10 for small- q retrograde comets. However, there is no reason to expect that this is the case [Marsden, personal communication].

- *The injection mechanism for these comets is distinct from the tidal torque.*

One observes that the clearly hyperbolic comets have two distinguishing correlations; they all have small perihelia and they all move in a retrograde sense relative to the Solar system planets. Injection from the outer Oort cloud by passing stars or other distant impulses cannot explain the small- q preponderance. Nor can the correlations be explained if the comets were interstellar in origin.

- *These comets are not truly hyperbolic originally but only appear to be because of the neglect of nongravitational forces due to outgassing, flaring or splitting.*

This has previously been suggested [Marsden and Sekanina 1978] and is supported by the fact that six of the seven comets listed in Table 1 have been noted to have physically split or to have their orbit residuals significantly reduced by the inclusion of modeled nongravitational forces. The suggestion is consistent with the small- q correlation but requires an explanation for the correlation with retrograde orbits. Matese *et al.* [1991] have demonstrated that small- q prograde comets exhibit no comparable hyperbolic tendency.

Table 1. Comets That are Most Confidently Hyperbolic

Class	Name	1/a	\pm	δ	$\cos i$	q	Comment
I	1895 IV	-172	\pm	8	-0.784	0.192	a
I	1953 II	-125	\pm	9	-0.125	0.778	c
I	1899 I	-109	\pm	9	-0.832	0.327	a
I	1957 III	-98	\pm	6	-0.498	0.316	b
II	1955 V	-727	\pm	121	-0.301	0.885	a
II	1989 XIX	-218	\pm	34	-0.003	0.642	b
II	1960 II	-135	\pm	23	-0.937	0.504	b

a. known to have split

b. residuals improved by modeling nongravitational forces

c. inconclusive improvement in residuals from modeling

COLLISIONAL SURFACE PROCESSING

We now argue that the distinction between small- q prograde and retrograde Oort cloud comet energies occurs because in the latter case comet mantle processing will be increased due to more energetic collisions with ecliptic plane material. In essence, impacts on small- q comets are most important for their catalytic role in the creation of large nongravitational forces. It has been noted that neglecting nongravitational forces will induce a systematic error in the estimate of the original energy causing it to appear more hyperbolic [Marsden *et al.* 1978].

Marsden and Sekanina (1971) have suggested that physical splitting and erratic behavior of coreless short-period comets could be attributed to the single impacts of an ecliptic plane population of objects of mass $\sim 10^8$ g if their spatial density was $\sim 2 \times 10^{-18}$ g cm $^{-3}$. Such densities are $\sim 10^4 \times$ larger than is known to exist in the vicinity of the earth. We suggest instead that at sufficiently high relative velocities the known meteoroidal population can indirectly expose a significant fraction of the volatiles underlying a cometary mantle.

The relative velocity between a near-parabolic comet and material in a circular ecliptic-plane orbit of radius r is

$$U(r) = \frac{V_{\oplus}}{\sqrt{r(\text{AU})}} \sqrt{3 - \sqrt{\frac{8q}{r} \cos i}} .$$

One observes that at $r \approx q$ relative velocities in the range 50–150 km s $^{-1}$ occur for the comets listed in Table 1. Following Marsden and Sekanina [1971], the meteoroidal mass required to create a crater of diameter d_o in loose mantle material is

$$m = 4 \times 10^{-7} d_o^3 (\text{cm}) \left(\frac{U}{100 \text{ km s}^{-1}} \right)^{-2} \text{ g.}$$

The local meteoroidal distribution peaks at a mass $\sim 10^{-5}$ g [Grün *et al.* 1985]. Therefore the bulk of the meteoroidal mass distribution is capable of exposing the underlying volatiles in mantles of thickness $h \sim d_o \leq 3$ cm if the impact velocity is comparable to that obtained for the retrograde small- q hyperbolic comets that are listed in Table 1.

The impact flux (energy/area/time) on a comet surface due to meteoroids is $\frac{1}{8} \rho_m U^3$ where ρ_m is the spatial mass density of all objects $\geq m$. Leinert *et al.* [1983] adopted a spatial distribution $\propto r^{-1.3} \exp(-2.1|z/r|)$, $0.1 \text{ AU} \leq r \leq 3 \text{ AU}$. We have integrated the orbits to estimate

the impact energy per unit area inside 1 AU. For the four class I comets that are listed in Table 1 the estimated values are $(1.6, 0.04, 0.9, 0.5) \times 10^5$ erg cm $^{-2}$. At values $\sim 10^5$ erg cm $^{-2}$ we see that a typical meteoroid of 10^{-5} g at a speed ~ 100 km s $^{-1}$ will yield \sim one 3 cm diameter crater per m 2 of comet surface. Thus \leq one part in 10^3 of the underlying volatile surface can be expected to be directly exposed (if the mantle thickness $h \leq 3$ cm). Activity from such a small fraction of the surface cannot, in itself, cause a large nongravitational force.

The nature of comet mantles is insufficiently understood to allow a definitive analysis of the growth (or healing) of impact-produced volatile crater areas. However a dimensional argument suggests that if a crater of initial diameter $d_o \approx h$ does grow to diameter $d \gg h$, the linear growth time scale will be $\tau \sim \rho_{mantle} d / \bar{\phi}$ where $\bar{\phi}$ is the time averaged mass flux from the outgassing crater. For small- q , crater growth to $d \approx 100$ cm is suggested over time scales on the order of days since ϕ is an extremely sensitive function of r . We emphasize that a number of small craters would have their net area grow faster than a single crater with the same initial area. Marsden [1989] has listed 17 class I new comets whose perihelia are inside 1 AU. Of this number 8 are retrograde and half of these are clearly hyperbolic. We infer that the probability that a retrograde small- q Oort cloud comet will have its surface processed sufficiently to induce detectable nongravitational effects is $\approx \frac{1}{2}$ while that of a prograde small- q comet is $< \frac{1}{9}$.

The authors would like to acknowledge the support of a NASA/Ames University Consortium Grant and a grant from the Louisiana Education Quality Support Fund.

References

- [1] Duncan M., Quinn T. and Tremaine S. (1987) The formation and extent of the Solar System comet cloud. Astron. J., **94**, 1330-1338.
- [2] Heisler J. and Tremaine S. (1986) Influence of the Galactic tidal field on the Oort cloud. Icarus, **65**, 13-26.
- [3] Marsden B.G. (1989) Catalogue of Cometary Orbits 6th edn. Smithsonian Astrophysical Observatory, Cambridge.
- [4] Marsden B.G. and Sekanina Z. (1971) Comets and nongravitational forces. IV. Astron. J., **76**, 1135-1151.
- [5] Marsden B.G., Sekanina Z. and Everhart E. (1978) New osculating orbits for 110 comets and analysis of original orbits for 200 comets. Astron. J., **83**, 64-71.
- [6] Matese J.J. and Whitman P.G. (1989) The Galactic disk tidal field and the nonrandom distribution of observed Oort cloud comets. Icarus, **82**, 389-401.
- [7] Matese J.J., Whitman P.G. and Whitmire D.P. (1991) Gravitationally unbound comets move in predominantly retrograde orbits. Nature, **352**, 506-508.
- [8] Oort J.H. (1950) The structure of the cloud of comets surrounding the solar system, and a hypothesis concerning its structure. Bull. Astron. Inst. Neth., **11**, 91-110.
- [9] Grün E., Zook H.A., Fechtig H. and Giese R.H. (1985) Collisional balance of the meteoritic complex. Icarus, **62**, 244-272.
- [10] Leinert C., Röser S. and Buitriago J. (1983) How to maintain the spatial distribution of interplanetary dust. Astron. Astrophys., **118**, 345-357.

The spatial distribution of large cometary meteoroids in the inner solar system

Neil McBride & David W. Hughes. Department of Physics, University of Sheffield, Sheffield, S3 7RH, UK.

Abstract. A model for the spatial density distribution of large ($m > 10^{-3}$ g) cometary meteoroids in the inner solar system is obtained assuming that they have orbits closely associated with that of their parent comet. Distributions of the orbital parameters of the Taurid, Quadrantid and Perseid meteoroid streams are used in developing the model.

Introduction

Hughes & McBride (1990) used the group of 135 known short-period comets as listed by Marsden (1986), and placed meteoroids on each orbit. This effectively turned each orbit into a thin meteoroid stream. The relative spatial density distribution of the cometary meteoroids was then obtained. The semi-major axis distribution of the Quadrantid meteoroid stream was incorporated to improve the model.

In this paper, each short-period comet orbit is replaced by a suite of 175 new orbits, the orbital characteristics of which reflect a 'typical' meteoroid stream. 1000 equal mass particles are then put on each of the 23,625 orbits such that the mass flow (g s^{-1}) is constant. The particles are assumed to be large ($m > 10^{-3}$ g) such that they can be taken to be in stream closely associated with their parent comet. The relative spatial density distribution of all the particles is then obtained.

Modelling a meteoroid stream

Fig. 1 shows histograms of the semi-major axis distributions of Taurid, Quadrantid and Perseid meteoroids. The 57 Quadrantid meteor orbits were measured by the Radio Meteor Project (see Sekanina, 1970), the 178 Taurid (67 Northern and 111 Southern) and the 12 Perseid meteor

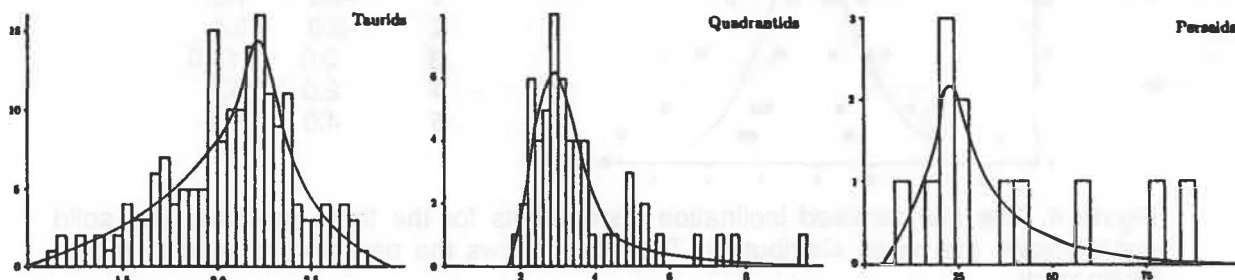


Figure 1. The semi-major axis distributions. The abscissae are in AU.

orbits were obtained from the meteor data base held at the International Meteor Data Centre, University of Lund, Sweden. For this simple model, cosmic weightings have not been applied as the variation in velocity within each given stream is relatively small. Smooth curves were

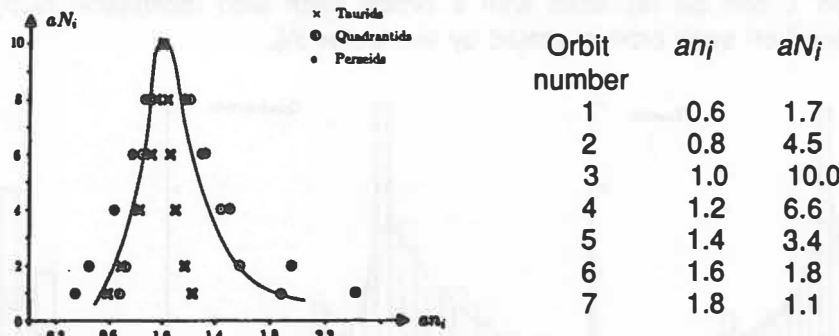


Figure 2. The standardised semi-major axis distributions for the three streams. The solid curve shows the mean distribution. The table shows the parameters used to model semi-major axis.

fitted to the histograms such that the areas under each histogram and its fitted curve is equal. The peak of each curve has an ordinate of N_p and an abscissa of x_p . Points were recorded from each curve, each point having an ordinate N and an abscissa x . These points were then replotted on the graph shown in Fig. 2. Here the ordinate is ten times the ratio N/N_p and is labelled aN_i . The abscissa gives the ratio x/x_p and is labelled an_i .

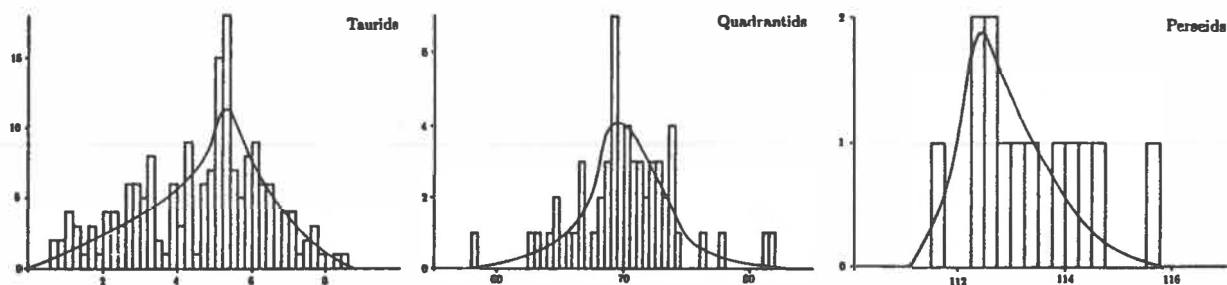


Figure 3. The inclination distributions. The abscissae are in degrees.

By doing this, the three distributions shown in Fig. 1 have been 'standardised', and are easily inter-compared. To obtain a 'typical' semi-major axis distribution, a curve was fitted such that any point on the curve represents the mean of the three stream distributions. Seven points were then read off this curve, having ordinates aN_i and abscissae an_i ($i=1$ to 7). These are given in the table in Fig. 2. Any comet orbit with semi-major axis a can then be replaced with 7 orbits each with semi-major axis $an_i \times a$. The modelling is completed by scaling the number of particles on each orbit by the factor aN_i .

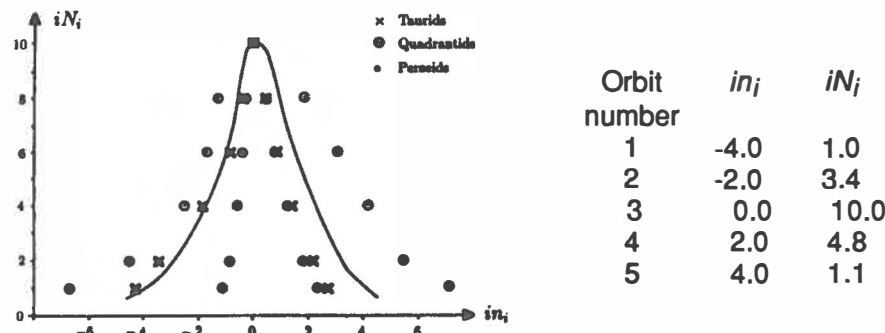


Figure 4. The standardised inclination distributions for the three streams. The solid curve shows the mean distribution. The table shows the parameters used to model inclination.

The orbital inclination i is modelled in a similar fashion. Fig. 3 shows histograms of the inclination distribution for 3 streams, and Fig. 4 shows the standardised distributions. The ordinate in Fig. 4 is now labelled iN_i and the abscissa in_i . Note that the abscissae are now given by $x-x_p$. Points from the mean distribution give the values shown in the table. Any comet orbit with inclination i , can be replaced with 5 orbits each with inclination $i+in_i$. The number of meteoroids placed on each orbit is scaled by the factor iN_i .

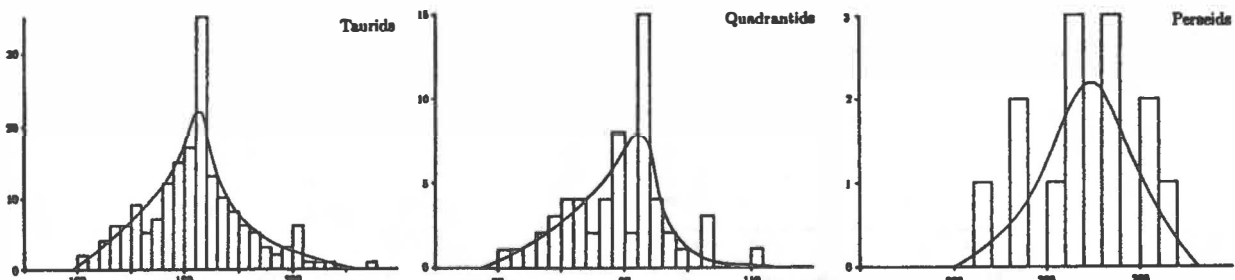


Figure 5. The longitude of perihelion distributions. The abscissae are in degrees.

Finally, the longitude of perihelion L (defined here as $\omega + \Omega$) is modelled in the same way as the inclination. Fig. 5 shows histograms of L for the 3 streams. The standardised distribution is shown by the graph in Fig. 6, where the ordinate is labelled LN_i , and the abscissa is labelled Ln_i . The table gives the scaling factors such that a comet orbit with longitude of perihelion L can be replaced with 5 orbits each with longitude of perihelion $L + Ln_i$. The number of particles on each orbit are scaled by the factor LN_i . It is seen then that by taking a comet orbit and generating new orbital parameters as described above (in a 'nested loop' fashion), 175 orbits are produced.

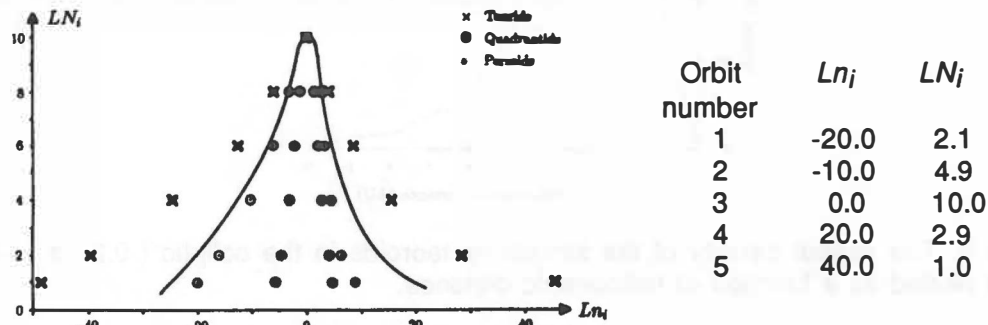


Figure 6. The standardised longitude of perihelion distributions for the three streams. The solid curve shows mean distribution. The table shows the parameters used to model longitude of perihelion.

Modelling the spatial density distribution of cometary meteoroids

Each of the 135 short-period comet orbits were replaced by 175 generated orbits, the orbital parameters of which depending on the orbital parameters of the parent comet, as described above. 1000 particles were put on each orbit, this number being scaled by the factors a_{ni} , i_{ni} and Ln_i . A z and R co-ordinate system was used where

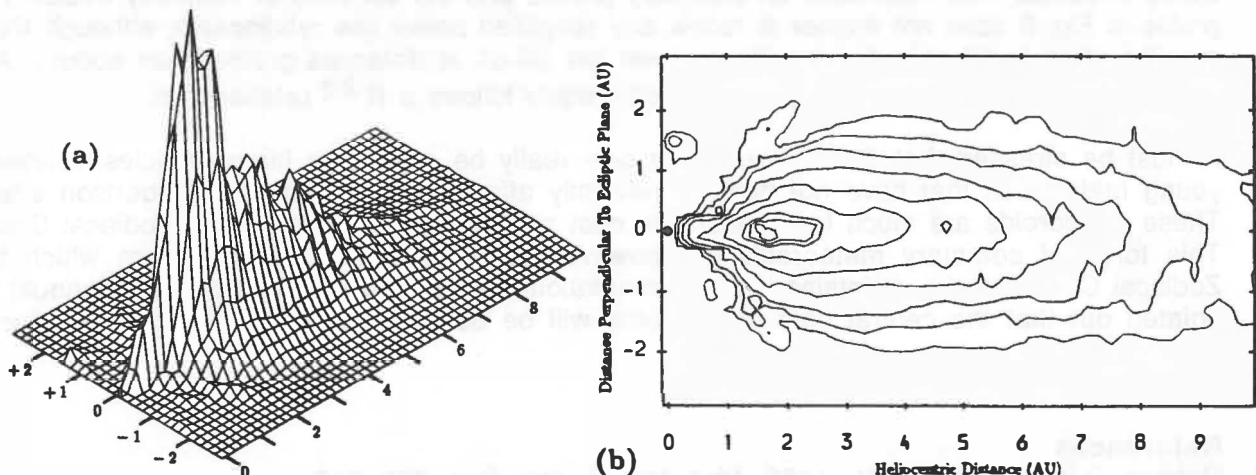


Figure 7. (a) The height represents the spatial density. The ground level corresponds to the z - R plane with $0 < R < 10$ AU and $-3 < z < +3$ AU. The black dot represents the Sun. (b) A contour plot of Fig. (a). The abscissa is the distance R and the ordinate is the distance z . The spatial density is in arbitrary units, the contours representing 10, 25, 50, 100, 200, 400, 760, 890 and 1020 these units.

R is defined as the meteoroid heliocentric distance projected into the ecliptic, and z is the distance perpendicular to the ecliptic. The particles can then be binned into grid squares in this z - R plane. A grid square in this plane represents the volume of space swept out by revolving the square around an axis which is perpendicular to the ecliptic and passes through the Sun. The spatial density was found by dividing the number of particles binned in the square by this volume. This spatial density distribution in the z - R plane is shown in Fig. 7. The ecliptic spatial density is shown in Fig. 8, this being the spatial density of the particles with $-2.0 < z < +2.0$ AU.

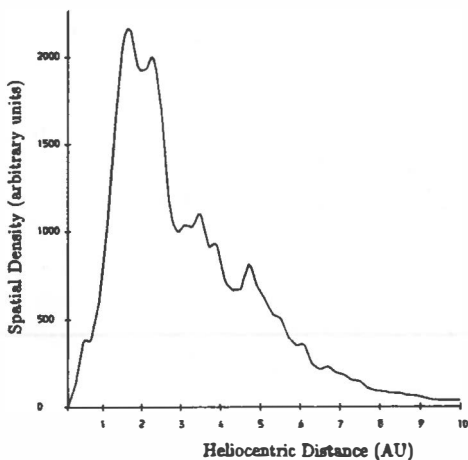


Figure 8. The spatial density of the stream meteoroids in the ecliptic ($-0.2 < z < +0.2$ AU) is plotted as a function of heliocentric distance.

It can be seen from Figs. 7 and 8 that the distribution of large cometary meteoroids has a torus-like shape, centred on the Sun. The central hole extends to about 0.5 AU, and the outer edge is around 6 AU. It can be seen that the spatial density varies in a rather complicated way as a function of the ecliptic heliocentric distance. Note that the density at 1 AU is not typical. In the meteoroid particle size range under consideration there is a considerable increase in the spatial density as one moves out from the Sun to an ecliptic heliocentric distance of about 1.7 AU. The density near the 1.7 AU peak is around four times the 1.0 AU value. The relative spatial densities at the orbits of the Earth, Mars, Jupiter and Saturn are in the ratios 1.0 : 2.5 : 0.7 : 0.1. It is only beyond about 2.5 AU that the density starts to decrease dramatically and space becomes less hazardous for planetary probes and the surfaces of cometary nuclei. The profile in Fig. 8 does not appear to follow any simplified power law relationship, although there may be some justification for arguing a power law fall-off at distances greater than about 2 AU. At this distance ($2 < R < 10$ AU) the drop-off crudely follows a $R^{-2.2}$ relationship.

It must be stressed that these results can only really be applied to large particles; relatively young meteoroids that have not been significantly affected by the Poynting-Robertson effect. These meteoroids are much larger than the dust particles responsible for the Zodiacal Cloud. This torus of cometary meteoroids will however act as a mass reservoir from which the Zodiacal Cloud can be maintained (by fragmentation due to impacts and erosion). It should be pointed out that the central hole of the torus will be occupied by these smaller dust decay products.

References

- Hughes, D.W. & McBride, N., 1990. *Mon. Not. R. astr. Soc.*, **243**, 312.
- Marsden, B.G., 1986. *Catalogue of Cometary orbits*, 5th edn, International Astronomical Union.
- Sekanina, Z., 1970. *Icarus*, **13**, 459.

THE GEOCENTRIC PARTICULATE DISTRIBUTION: COMETARY, ASTEROIDAL OR SPACE DEBRIS?

J.A.M. McDonnell & P.R. Ratcliff

Unit for Space Sciences
University of Kent at Canterbury
Canterbury, Kent CT2 7NR
UK

ABSTRACT

Definition of the Low Earth Orbit (LEO) particulate environment has been refined considerably with the analysis of data from NASA's Long Duration Exposure Facility (LDEF). Measurements of the impact rates from particulates ranging from sub-micron to millimetres in dimension and, especially, information on their directionality has permitted new scrutiny of the sources of the particulates. Modelling of the dynamics of both *bound* (Earth orbital) and *unbound* (hyperbolic interplanetary) particulates intercepting LDEF's faces leads to the conclusion that the source is dominantly interplanetary for particle dimensions of greater than some 5 microns diameter; however the anisotropy below this dimension demands lower velocities and is compatible with an orbital component. Characteristics of the LDEF *interplanetary* component are compatible with familiar meteoroid sources and deep space measurements. Understanding of the orbital component which exceeds the interplanetary flux by a factor of 4 is less clear; although the very small particulates in orbit have been associated with space debris (Lawrence and Brownlee, 1986) this data conflicts with other measurements (McDonnell, Carey and Dixon, 1984) at the same epoch. By analysis of trajectories approaching the Earth and its atmosphere, we have shown that a significant contribution could be captured by *aerocapture*, i.e. atmospheric drag, from either asteroidal or cometary sources; such enhancement is unlikely however to provide the temporal and spatial fluctuations observed by the LDEF Interplanetary Dust Experiment (Mullholland et al. 1992). A further new mechanism is also examined, that of *aerofragmentation capture*, where an atmospheric grazing trajectory, which would not normally lead to capture, leads to fragmentation by thermal or mechanical shock; the microparticulates thus created can be injected in large numbers, but only into short-lifetime orbits. The concentration in one particular orbit plane, could explain the temporal fluctuations seen on LDEF; space debris could also explain the phenomenon.

THE LEO ENVIRONMENT FROM LDEF'S IMPACT DATA

The successful retrieval of LDEF in January 1990 after 5.75 years in orbit has provided a vast and unique amount of data on the LEO particle population. Extensive analysis of craters and perforations seen on the various experiments, and on the vehicle, has been performed. Impacts reveal the crater size distribution and directional characteristics from sub-micron dimensions to millimetres, representing more than nine magnitudes in mass.

Computer modelling of various particulate distributions intercepting LDEF in orbit shows that the majority of the intermediate and large particles ($>5\mu\text{m}$) are compatible with a distribution of interplanetary origin, with a geocentric approach velocity of 17.4 ± 3 km/s (Sullivan and McDonnell, 1992). However, using modelling of Zook (1991 and 1992) a value of 20 km/s results. The anisotropy of the smaller particulates reveals the presence of a significant orbital component; further, the IDE experiment also revealed time-dependence in the flux of these smaller particles.

PERSPECTIVE OF LDEF DATA IN THE INTERPLANETARY SCENE.

Interplanetary flux data at 1 AU (Grün et al, 1985) are compatible with the LDEF penetration data observed on the West (trailing) and Space faces. With their similar velocities orbital components cannot access these faces. On the forward faces, however, the orbital component clearly exceeds the interplanetary flux. We will examine how, with aerodrag the interplanetary component could effect this, but must note that space debris could readily provide a source (ESA SP Space Debris, 1988). Impact comminution from rockets and satellites, flecks from the erosion of satellite paint and also Al_2O_3 spheres from rocket motor burns are prime candidates for this micro-debris population.

We note early fears of the existence of the "Earth's dust belt" (Whipple, 1961). Prompted by unreliable satellite and rocket measurements, its 'lifetime' was short lived and dismissed by Nilsson (1966) and other workers. The studies now reported refer to very much smaller masses, where higher drag altitudes and hence greater scale heights pertain; LDEF data also calls for much smaller enhancements than the 3 or 4 magnitudes previously investigated.

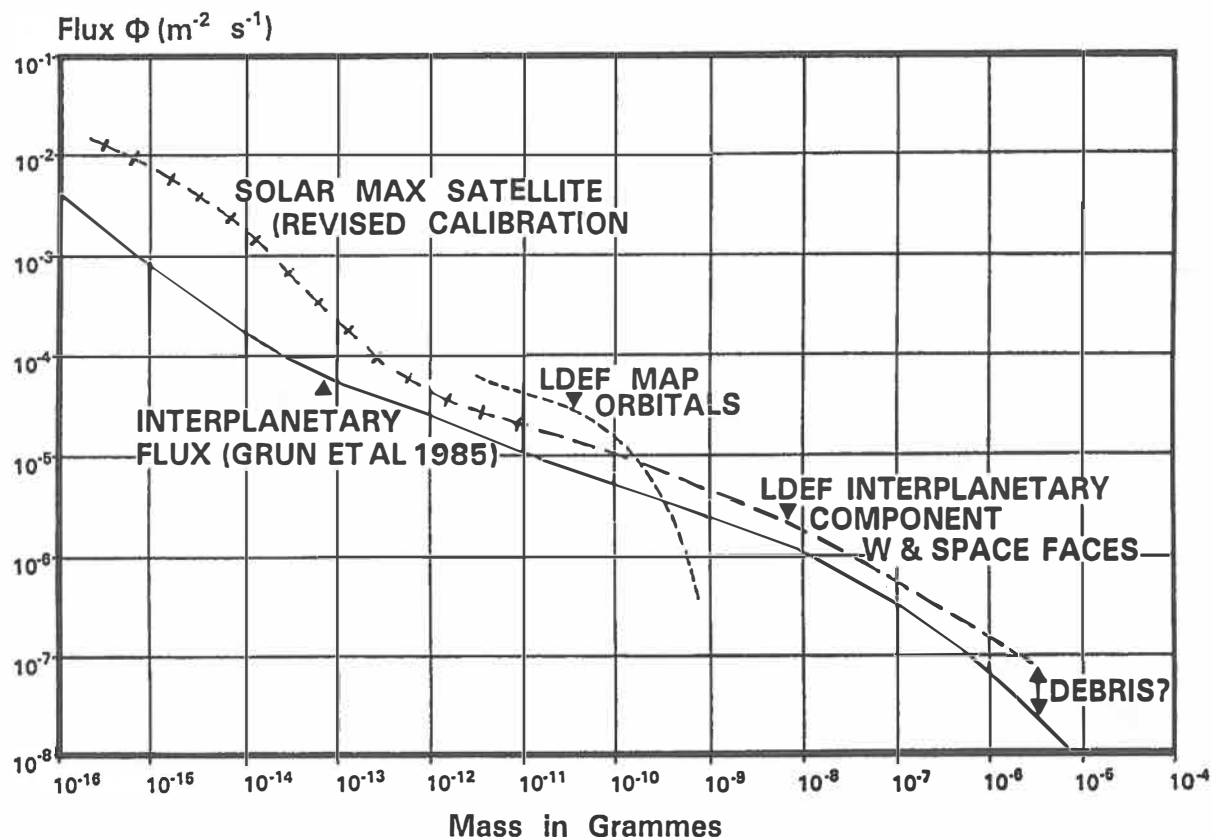


Figure 1 LDEF flux data from the West (trailing) and space-pointing faces, corrected for Earth shielding and gravitational focussing, yielding the expected flux at 1 A.U. heliocentric distance (McDonnell et al., 1991). They compare favourably with (though a factor of 2 higher than) deep space measurements. In contrast the excess orbital component on LDEF's leading face (orbitals) dominates the interplanetary unbound component at LDEF's altitude for particles $< 10^{-10}$ g mass.

Aerocapture of Interplanetary Particulates.

Interplanetary particles that penetrate below a certain height in the Earth's atmosphere, known as the critical atmospheric height, will lose too much kinetic energy to remain on a hyperbolic orbit, and will eventually be absorbed by the atmosphere. Figure 2 shows schematically the trajectories studied by computer using the standard atmosphere and a 7th order "gear" method for numerical trajectory integration. Those that penetrate just below this height will be captured into orbit, and may complete several orbits before capture, while those that penetrate deeper on the first pass will be directly absorbed. For spherical particles of a given density, the critical atmospheric height is a function of the particle mass and geocentric velocity; the relationship established by these is shown in Fig. 3.

The relative probability of capture (i.e. normalised to the probability of absorption) for particulates of $1\mu\text{m}$, $10\mu\text{m}$ and $100\mu\text{m}$ diameter is also shown (Fig. 4) as a function of geocentric velocity. The probabilities are generally low, indicating that the orbital particles will not dominate the directly intercepted IP flux in LEO, unless the particles are able to complete a large number (>100) of orbits, which is not the case. The majority of all captured particles are absorbed after <10 orbits, as is shown e.g. by the circular orbit lifetimes stated in Fig. 5. Longer lifetimes are only possible for particles with high initial perigees, which is limited to the particles with very low geocentric velocities since the critical atmospheric height defines the maximum possible initial perigee - unless the possibility of orbital perturbations thereafter can be invoked.

The orbital residence time of aerocaptured particles can be long due to the high initial apogee and hence will enhance, but not dominate the natural material in LEO. We note that capture is effective only for small particles with very low values of V_∞ , low (solar) eccentricity and low inclination orbits. Thus, the capture of asteroidal material is favoured above that of short period comets, and even more strongly favoured over that of long period comets. These strong selection effects must caution us regarding a likely bias towards asteroidal sources in the results expected from the study of intact residue studies on LDEF.

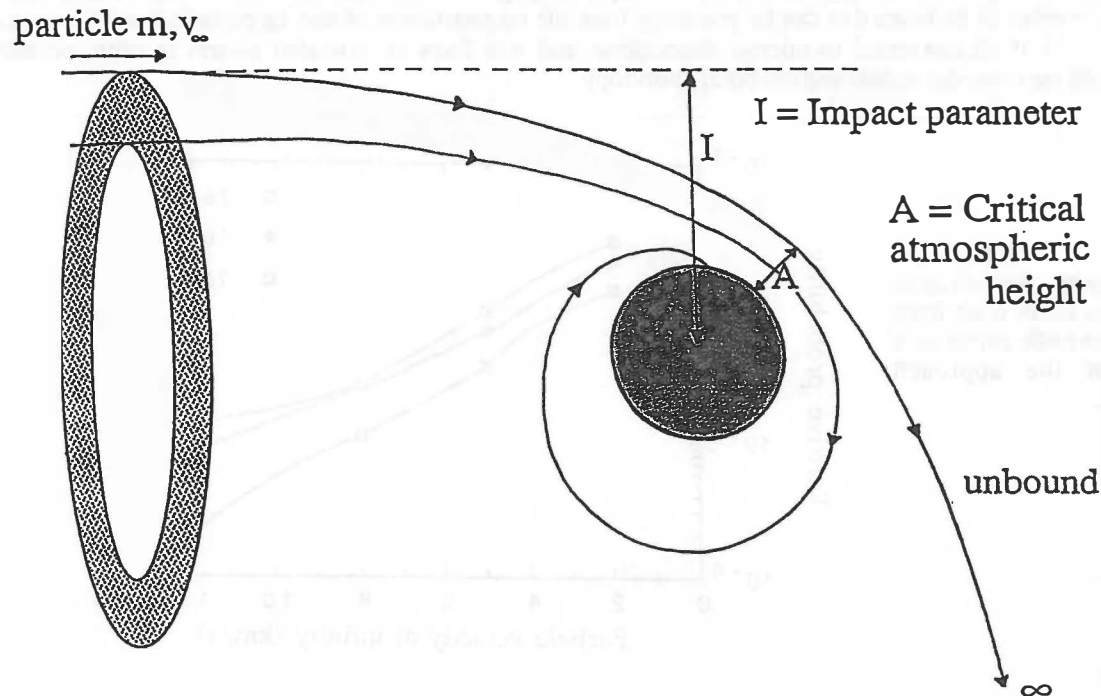
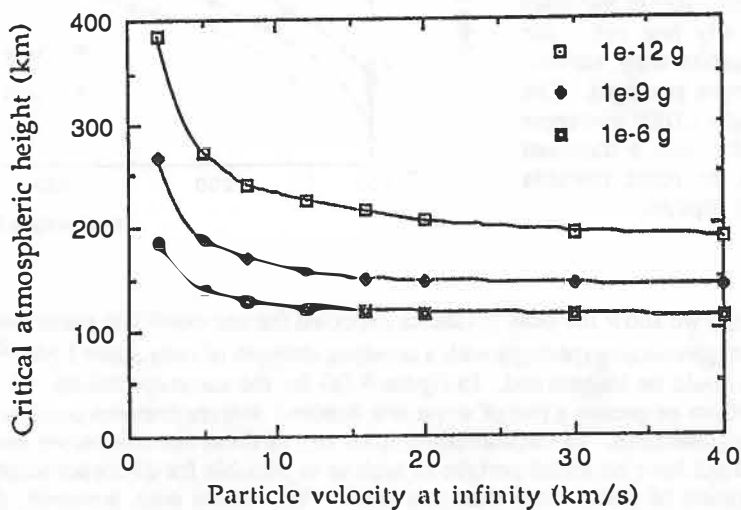


Figure 2. Schematic for computer trajectory analysis performed to identify the fraction of interplanetary particulates captured into Earth-bound orbits relative to the total number approaching from within the critical impact parameter I . The fraction captured is shown in Figure 4. The lifetime in Earth orbit results from a folding of the number of subsequent perigee passages before reentry, and the (decreasing) orbital period. The capture mechanism strongly favours low values of V_∞ .

Figure 3. Critical atmospheric height at perigee for the first passage of unbound particulates as a function of V_∞ for particulate diameters $1\mu\text{m}$ (10^{-12}g), $10\mu\text{m}$ (10^{-9}g) and $100\mu\text{m}$ (10^{-6}g). LDEF's mean orbital altitude of 458 km is comparable to that of slow micron dimension particles.



Aerofragmentation Capture. In order for either larger or faster particles to be captured, they must lose a larger amount of kinetic energy on the first pass than is required for the smaller, slower particles. This can result in the particles experiencing very large temperatures and pressures which may result in fragmentation of the particle, particularly if the particle is a large fluffy agglomerate. This is frequently seen in meteor streams. Particles on an initially marginally hyperbolic orbit may also be fragmented, whereupon the fragments, by virtue of their smaller critical atmospheric height, will be captured into orbit. This process is unlikely to be efficient in terms of the

fractional number of particles so fragmented, and the captured fragments are unlikely to be in long-lifetime orbits, but the total number of particles that can be generated from the fragmentation of one 1g particle is very large e.g. potentially 10^{11} if all converted to micron dimensions, and will form an extended swarm in orbit, possibly consistent with the observed spatial and temporal anisotropy.

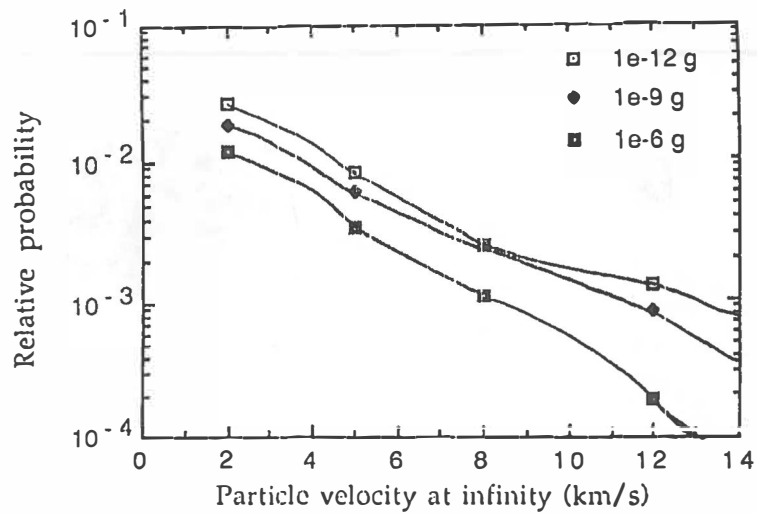


Figure 4. Fraction of interplanetary particulates captured into Earth orbit from initially hyperbolic orbits as a function of the approach velocity V_∞ .

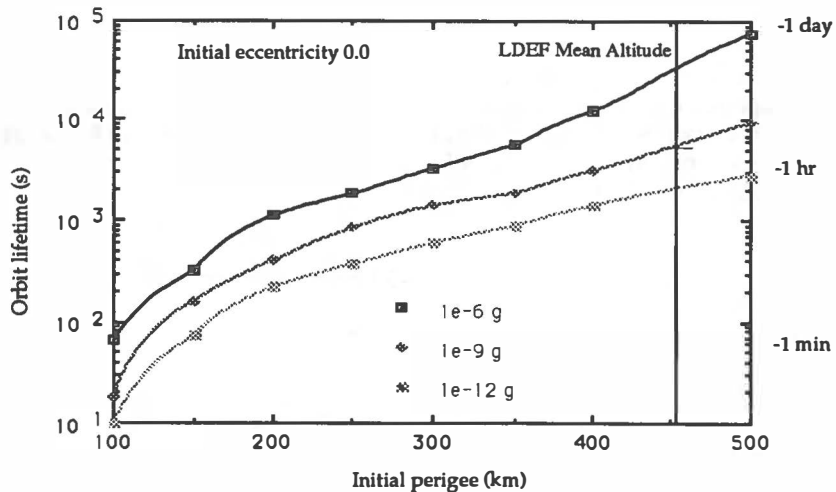


Figure 5. Circular orbit lifetimes of particles as a function of initial perigee for the 3 candidate particulate sizes. LDEF's mean altitude of 458 km is shown, along with the circular orbital period at this altitude. We see that 10 μm diameter (10^{-9} g) particles complete only one orbit; for eccentric orbits they survive several perigee passages. The orbitals which LDEF intercepts are generally only a transient population, en route towards atmospheric capture.

In figure 6 (a) we show the peak pressures expected for our candidate particulates on marginally hyperbolic orbits. For fragile agglomerates (perhaps with a crushing strength of only some 1 Nm^{-2}) we see that particulates of greater than $10 \mu\text{m}$ could be fragmented. In figure 6 (b) for the same conditions, we plot the temperatures experienced. Again for $10 \mu\text{m}$ or greater a rise of some few hundred degrees imposes conditions which could release the bonding forces of agglomerates. In fragmentation from any of these conditions, we see that particles released from larger masses will not have an initial perigee as high as is possible for direct aerocapture, and it is difficult to envisage a shower duration of much more than one orbit. We should note, however, the high availability of mass in the meteoroid range 10^{-7} to 10^{-5} g.

Intact capture on LDEF. Unbound orbits have a minimum value of the Earth's escape velocity at LDEF's altitude, viz. 10.8 km/s . For targets which are not 'under-dense' e.g. multi layer insulation or foams, the impact pressure will exceed the strength of all known projectile materials. This has the interesting consequence that if intact residues of cosmic origin are discovered on LDEF, they must arise from an aerocaptured interplanetary particle; the search to identify these fragments could therefore yield evidence on these mechanisms.

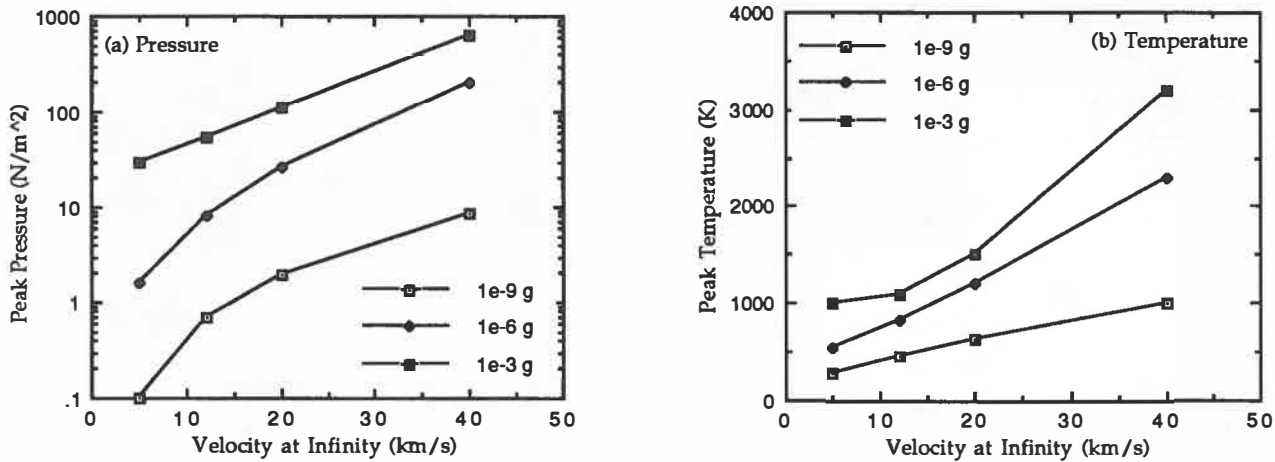


Figure 6. For the particulate sizes at their respective but different critical heights (see fig. 4) peak aerodynamic drag pressures are shown (a). For the same conditions the peak temperatures under radiative (black body) equilibrium are established, 6 (b).

Acknowledgements

We acknowledge the help of Sunil Deshpande, Steven Mullen and Simon Green in the preparation of this paper. We also acknowledge the SERC funding through rolling grant GR/F/80463.

References

- Grün E., Zook, H.A., Fechtig, H. and Giese, R.H., (1985) Collisional Balance of the Meteoritic Complex, *Icarus*, **62**, pp. 244-272.
- Lawrance, M.R. and Brownlee, D.E., (1986) The Flux of Meteoroids and Orbital Space Debris Striking Satellites in Low Earth Orbit, *Nature*, Vol. 323, pp. 136-138.
- McDonnell J.A.M., Carey, W.C. and Dixon, D.G., (1984) Cosmic Dust Collection by the Capture Cell Techniques on the Space Shuttle, *Nature*, Vol. 309, No. 5965, pp. 237-240.
- McDonnell, J.A.M., Deshpande, S.P., Green, S.F., Newman, P.J., Paley, M.T., Ratcliff, P.R., Stevenson, T.J. and Sullivan, K., (1991) First Results of Particulates Impacts and Foil Perforations on LDEF, *Adv. Space Res.*, Vol. 11, No12, pp. 109-114.
- Mulholland, J.D., Oliver, J.P., Singer, S.F., Weinberg, J.L., Cooke, W.J., Montague, N.L., Kassel, P.C., Wortman, J.J., Kinard, W.H. and Simon, C.G., (1992) LDEF Interplanetary Dust Experiment: A high Time-Resolution Snapshot of the Near-Earth Particulate Environment, *Proc. Workshop on Hypervelocity Impacts in Space*, University of Kent at Canterbury. In submission.
- Nilsson, C. S., (1966) Some doubts about the earth's dust clouds, *Science*, **153**, 1242-1246.
- Ratcliff P. R. and McDonnell J. A. M. (1992) 2-D Numerical Computation of the Contribution of Natural Material to the Orbital Component of the Near-Earth Particle Population. *Proc. Workshop on Hypervelocity Impacts in Space*, University of Kent at Canterbury. In submission.
- Space Debris (1988). ESA SP-1109 (Report of the Space Debris Working Group).
- Sullivan, K., and McDonnell, J.A.M., (1992) LDEF Flux Anisotropy: Dynamic Modelling and Flux Transformations to Define the Interplanetary Micrometeoroid Environment, *Proc. Workshop on Hypervelocity Impacts in Space*, University of Kent at Canterbury. In submission.
- Whipple, F.L. (1961) The Earth's Dust Belt. *Astronautical Sciences Review*, Vol III, pp17-20.
- Zook, H.A., (1991) Meteoroid Directionality on LDEF and Asteroidal versus Cometary Sources, Abstract, *Proc. 22nd Lunar Planet Sci Conf*, pp 1577-1578.
- Zook, H.A., (1992) Meteoroid directionality on LDEF: Asteroidal versus cometary sources and how to obtain an effective velocity for beta meteoroids, *Workshop on Hypervelocity Impacts in Space*, University of Kent, Canterbury. In submission.

Near Infrared Reflectance Spectra: Applications to Problems in Asteroid - Meteorite Relationships

Lucy A. McFadden & Alan B. Chamberlin

California Space Institute, University of California, San Diego, La Jolla, CA 92093

INTRODUCTION

An observing program designed to search for evidence of ordinary chondrite parent bodies near the 3:1 Kirkwood Gap was carried out in 1985 and 1986. Studies by Wisdom (1985), Wetherill (1985), and subsequent work by Milani et al. (1989) indicate that the 3:1 Kirkwood gap is the most probable source region for the majority of ordinary chondrite meteorites. Figure 1 shows the location (in eccentricity vs semimajor-axis space) of the observed asteroids as well as the chaotic zone of the 3:1 (Wisdom, 1983) and the 5:2 Kirkwood Gaps.

The diversity of the reflectance spectra among this small data set is surprising. Early work by Gaffey and McCord (1978) showed that the inner region of the main asteroid belt is dominated by high albedo objects with mafic silicate surfaces. One would expect to see mostly spectra with 1- and 2- μm absorption bands based on this earlier work. Only 5 (of 12) spectra have these expected features. The distribution of taxonomic types presented by Gradie and Tedesco (1982) is in most cases a useful simplification of the compositional structure of the asteroid belt. The range of spectral characteristics seen with higher resolution in the near-IR has not been previously reported and is not represented in the standard asteroid taxonomy. Near-IR spectra contain valuable mineralogical information which enhances knowledge of the composition and structure of asteroids.

OBSERVATIONS AND INSTRUMENTATION

Two observing runs were carried out at the Infrared Telescope Facility (IRTF), Mauna Kea, Hawaii, on 10-12 August 1985 UT and 2-4 December 1986 UT. A single, liquid-Helium cooled, InSb detector and two circular variable filters (CVFs) cooled to liquid-Nitrogen temperature were used. The filters cover the region from 0.8- μm to 2.6- μm . A 10" entrance aperture was used. The signal from the detector passed through a preamplifier and then a "lockin" amplifier. A voltage-to-frequency converter was used to convert the output of the lockin amplifier to a digital signal.

DATA REDUCTION

The background sky flux was subtracted from the asteroid flux. Extinction coefficients were calculated using a least squares fit to both the rising and setting fluxes of standard stars versus airmass. The fits were calculated separately for rising and setting measurements. With these coefficients, the flux of the standard star is scaled to that at the airmass of

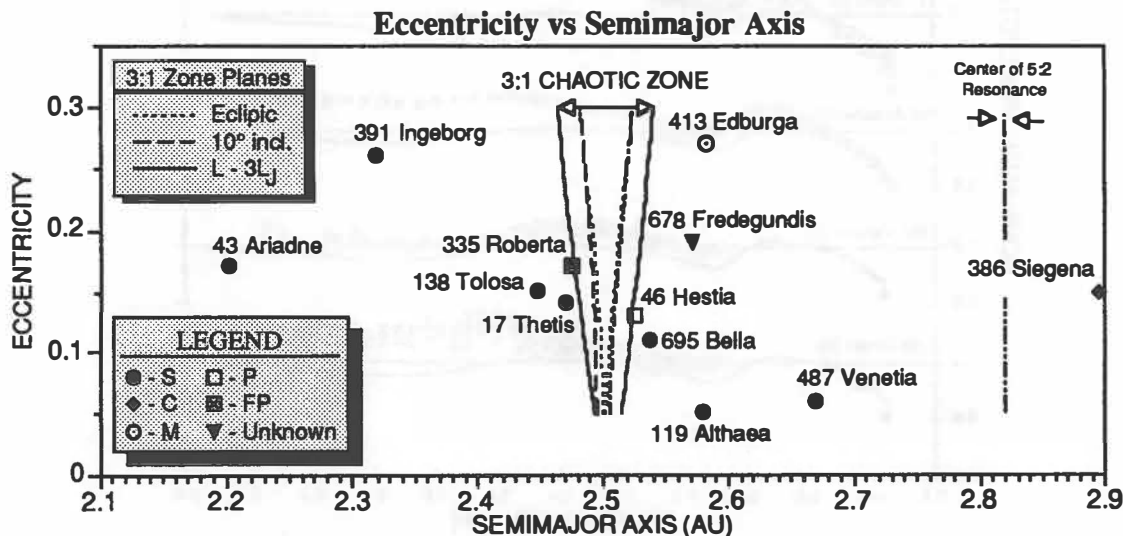


Figure 1. Eccentricity vs Semimajor Axis of the 12 Asteroids Observed.

the asteroid. The asteroid flux is divided by the extinction corrected standard star flux to eliminate instrumental noise. Each asteroid/standard star pair is averaged and converted to a relative flux by multiplying by the standard star/Sun ratio. This latter ratio is calibrated from many previously acquired data sets assuming the flux of the solar-type stars 16 Cygnus B and 13 Orionis is equivalent to that of the Sun.

Non-linear Error Correction

The IRTF lockin amplifiers experienced an abnormal non-linearity during the observations in December 1986. The effect of the lockin non-linearity was seen in the raw data (counts per second). A correction curve (20 discrete datapoints) was provided by the IRTF staff. The non-linear correction program used linear interpolation between the two closest correction curve data points to convert raw data to corrected raw data. In the case of a raw data point lying outside the range of discrete correction points, the two closest correction points (the closest end points) were used for the linear interpolation.

THE DATA

The calibrated spectra are placed into four groups with similar spectral features. Each group is discussed instead of each spectrum. In figures 2-5, an H4 ordinary chondrite spectrum is plotted as a solid line while the asteroid spectra are plotted as discrete points with error bars.

Group 1 - These asteroids have bands at 1- and 2- μm , and a UV absorption band (Figure 2). The spectral differences between these asteroids and the H4 ordinary chondrite imply chemical and mineralogical differences in pyroxene composition and olivine/pyroxene abundance shown by different positions and strengths of the 1- and 2- μm absorption bands. All 5 asteroids of this group are classified type S by Zellner et al. (1985). The absorption features are due to the presence of olivine and pyroxene on the asteroid surface.

Group 2 - We placed three asteroids, 413 Edburga, 678 Fredegundis, and 46 Hestia, in a group (Figure 3) because they lack 1- and 2- μm absorption bands and their reflectance increases with increasing wavelength. The different taxonomic types represented, M, S, and P are a reminder that the taxonomy is based on colors in a different spectral region. The

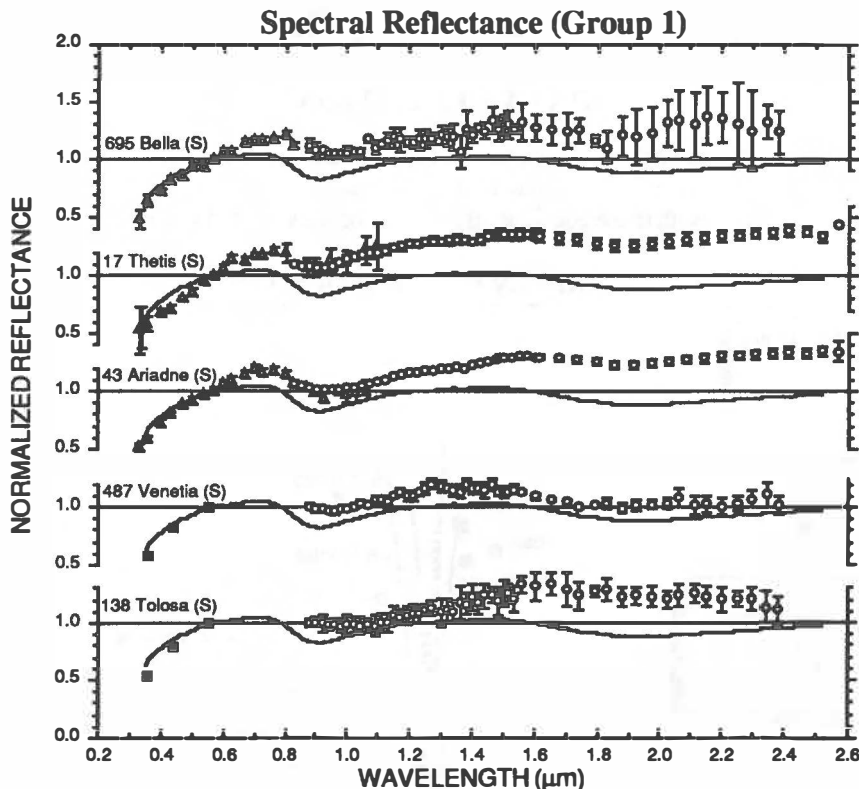


Figure 2. Spectral Reflectance of Group 1 Asteroids Compared to an H4 Ordinary Chondrite.

method of grouping used is for convenience and has no significance in relation to taxonomy, though it is interesting to consider whether inclusion of near-IR data would contribute to a classification scheme. The low signal to noise and the incomplete removal of telluric water bands in spectra of 413 and 678 increase the uncertainty of these data, though the absence of crystal field absorptions at 1- and 2- μm is established to within 10-20%.

Group 3 - The two spectra in this group (Figure 4), 386 Siegena and 335 Roberta, have UV absorption band edges and

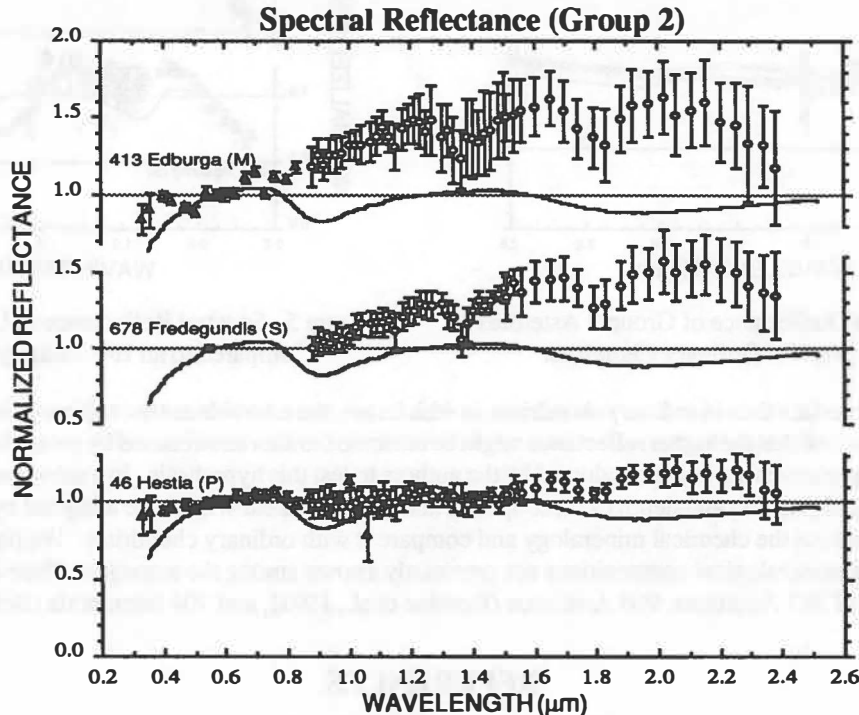


Figure 3. Spectral Reflectance of Group 2 Asteroids Compared to an H4 Ordinary Chondrite.

weak absorption bands in the 1- μm region. In the spectrum of 386 Siegena the UV absorption edge is strong and extends into the visible to 0.56- μm indicating a significant iron abundance. The presence of a weak 1- μm band is also consistent with an iron-rich surface. The flat reflectance in the near-IR combined with the assumed low albedo of a C-type asteroid indicates the presence of an opaque material which masks the 2- μm pyroxene band. The broad and weak feature seen in the spectrum of 335 Roberta is similar to that in 704 Interamnia observed by Bell et al. (1987). Terrestrial plagioclase minerals have broad, weak bands in this spectral region (Adams, 1975), though plagioclase-rich assemblages have not been previously reported.

Group 4 - The group 4 asteroids (Figure 5) have unusually strong 2- μm bands and include asteroids 119 Althaea and 391 Ingeborg. There are two explanations for these spectra. Either the tracking of these objects was off (though there is no mention of this in the data logbooks), or the mineralogy of these asteroids is unusual. The mineralogical interpretation of 119 Althaea implies a very iron and calcium-rich pyroxene. A terrestrial rock with this spectrum would be called a hedenbergite, it is a highly differentiated assemblage. The strong, broad band in the spectrum of 391 Ingeborg is similar to features seen in laboratory spectra of spinels (Adams, 1975). Because these features have not been seen in asteroids before, the spectra of these asteroids should be confirmed by repeated measurements. Recent, almost concurrent reports of additional asteroids with strong 2- μm features have been reported (Burbine et al. 1991).

DISCUSSION

Of the 12 spectra in our sample, only those in group 1 have the combination of features that are also found in spectra of ordinary chondrite meteorites yet there are differences among these spectra and the ordinary chondrites. The near-infrared reflectance of the asteroids is higher than the ordinary chondrites. What is the mineralogical and cosmochemical significance of these spectral differences? An explanation for the higher IR reflectance may be that there is more metallic

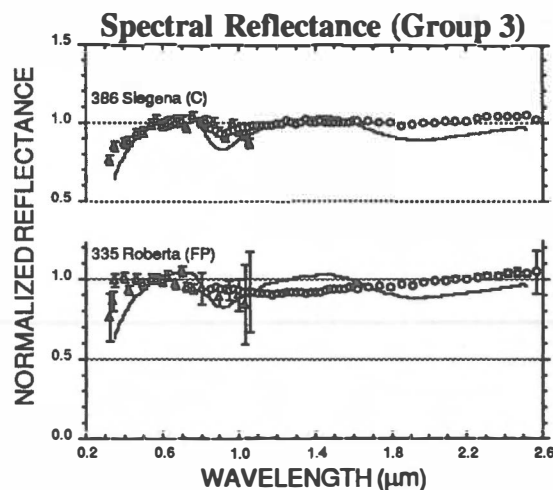


Figure 4. Spectral Reflectance of Group 3 Asteroids Compared to an H4 Ordinary Chondrite.

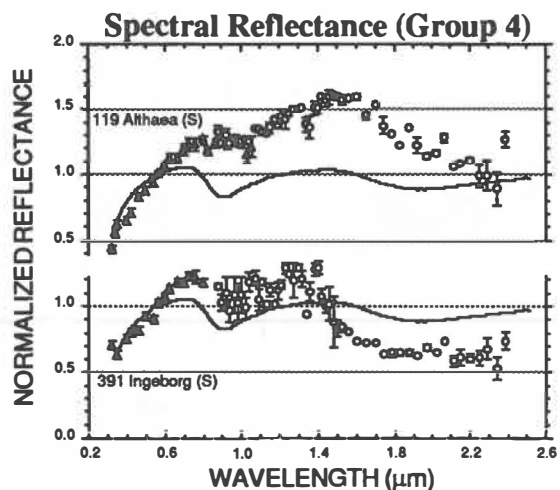


Figure 5. Spectral Reflectance of Group 4 Asteroids Compared to an H4 Ordinary Chondrite.

iron on the asteroid surface than in ordinary chondrites, in which case, the asteroids are not ordinary chondrite analogues. It has been hypothesized that the higher reflectance might be attributed to alteration caused by proton bombardment from the solar wind. Experiments are being conducted by the authors to test this hypothesis. In a subsequent publication we will measure the band position and depth of these spectra and compare them with those analyzed by Gaffey (1991) to quantitatively determine the chemical mineralogy and compare it with ordinary chondrites. We have found possibly three asteroids with mineralogical compositions not previously known among the asteroids. Their compositions may be similar to those of 387 Aquitania, 980 Anacostia (Burbine et al., 1991), and 704 Interamnia (Bell et al., 1987).

REFERENCES

- Adams J. B. (1975) Interpretation of visible and near-infrared diffuse reflectance spectra of pyroxenes and other rock forming minerals. In Infrared and Raman Spectroscopy of Lunar and Terrestrial Minerals (J. C. Karr, ed.), pp. 91-116. Academic Press, New York.
- Bell J. F., Hawke B. R., Owensby P. D. and Gaffey M. J. (1987) Atlas of asteroid infrared reflectance spectra (0.8-2.5 microns). unpublished.
- Burbine T. H., Gaffey M. J. and Bell J. F. (1991) S Asteroids 387 Aquitania and 980 Anacostia: Possible Fragments of the Breakup of a Spinel-Rich Parent Body. B.A.A.S., **23**, 1142.
- Gaffey M. J. (1991) Variations in magmatic processes among igneous asteroids. Abstracts for The International Conference On Asteroids, Comets, Meteors 1991, Flagstaff, AZ, p. 71.
- Gaffey M. J. and McCord T. B. (1978) Asteroid surface materials: Mineralogical characterizations from reflectance spectra. Space Sci. Rev., **21**, 555-628.
- Gradie J. and Tedesco E. (1982) Compositional structure of the asteroid belt. Science, **216**, 1405-1407.
- Milani A., Carpino M., Hahn G. and Nobili A. M. (1989) Dynamics of planet-crossing asteroids: Cases of orbital behavior Project SPACEGUARD. Icarus, **78**, 212-269.
- Wetherill G. W. (1985) Asteroidal source of ordinary chondrites. Meteoritics, **20**, 1-22.
- Wisdom J. (1983) Chaotic Behavior and the Origin of the 3/1 Kirkwood Gap. Icarus, **56**, 51-74.
- Wisdom J. (1985) Meteorites may follow a chaotic route to Earth. Nature, **315**, 731-733.
- Zellner B., Tholen D. J. and Tedesco E. F. (1985) The eight-color asteroid survey: Results for 589 minor planets. Icarus, **61**, 355-416.

SPIN VECTORS OF ASTEROIDS 21 LUTETIA, 196 PHILOMELA, 250 BETTINA, 337 DEVOSA AND 804 HISPANIA

T. Michałowski

Astronomical Observatory, Adam Mickiewicz University,
ul. Słoneczna 36, 60–286 Poznań, Poland
E-mail: MICHASTR@PLPUAM11 (EARN/BITNET)

INTRODUCTION

Such parameters as shape, orientation of spin axis, prograde or retrograde rotation are important for understanding the collisional evolution of asteroids since the primordial epochs of solar system history. These parameters remain unknown for most asteroids and poorly constrained for all but a few. In this work I present results for five asteroids: 21, 196, 250, 337, and 804.

I have used epochs of lightcurve maxima, amplitudes and absolute magnitudes of the maxima. The method of calculation is described in *Michałowski 1988, 1991* and *Michałowski and Velichko 1990*. This method allows me to obtain senses of rotation, sidereal periods, poles, and axial ratios of the ellipsoids which describe the shapes of asteroids.

RESULTS

Most of the lightcurves I have used were taken from the *Asteroid Photometric Catalogue* (hereafter *APC*) – *Lagerkvist et al. 1987, 1988*. Results of the calculations are presented in Table 1. When results by other authors exist, they are given in Table 1 for comparison.

21 Lutetia

Six lightcurves from the 1962, 1981, 1983 and 1985 oppositions are used in the analysis. All of them are taken from *APC*. My sidereal period is shorter than the one by *Lupishko and Velichko 1987*. From a comparison between their results and results of independent determinations for a few additional asteroids (cf *Magnusson 1989*) I conclude that their method of determining the sidereal periods does not work very well.

196 Philomela

I can use only three lightcurves from the 1964, 1981 and 1989 oppositions (*APC* and *Erikson et al. 1991*). This maybe the cause of my inability to determine the sidereal period and sense of rotation. There are a few sets of synodic cycles which give different P_{sid} for both prograde and retrograde rotation. I think the next observation will allow me to calculate these values. There are no previous results for this asteroid.

Table 1. Results

λ_p	Pole β_p	Axial ratios		$\frac{b}{c}$	Sidereal period(days)	Sense of rot.	Ref.
21 Lutetia							
55±8	+44±5	1.32±0.04	2.01±0.28	0.3400261±3	P	PW	
241±9	+40±8	1.28±0.05	1.36±0.30	0.3400260±5	P	PW	
42	+40	1.25	1.09	0.3402774	P	LV	
223	+48				L		
196 Philomela							
78±15	26±12	1.57±0.04	1.05±0.05	see text		PW	
266±15	24±12	1.59±0.04	1.06±0.05	see text		PW	
250 Bettina							
85±9	-9±7	1.33±0.05	1.70±0.09	0.2106219±5	R	PW	
260±12	-35±10	1.33±0.07	1.61±0.10	0.2106218±7	R	PW	
104	-16	1.318	1.375	0.210622248	R	D	
337 Devosa							
199±7	-51±8	1.24±0.04	1.34±0.07	0.1938078±5	R	PW	
804 Hispania							
90±12	28±10	1.17±0.05	1.92±0.15	see text		PW	

Sense of rotation: P—prograde, R—retrograde

References: PW—present work, LV—Lupishko and Velichko 1987, D—Drummond et al. 1991,
L—Lupishko et al. 1989

250 Bettina

There are nine lightcurves from the 1980, 1983, 1984 and 1989 apparitions (*APC* and *Weidenschilling et al. 1990*). My results are in good agreement with those by *Drummond et al. 1991*.

337 Devosa

I have used ten lightcurves from the 1977, 1983, 1984–85, 1986, 1987 and 1988 oppositions (*APC* and *Weidenschilling et al. 1990*), obtaining one solution only. There are no previous results for this asteroid.

804 Hispania

There are six lightcurves from the 1979, 1982 and 1987 oppositions. I have been able to use only three epochs of the primary maxima and probably this is the reason of my inability to obtain the sidereal period and sense of rotation. New observations are required.

Acknowledgements.

I wish to express my appreciation to Mr. R.Jokiel for the help in preparation of the manuscript. I am also grateful to the Organizing Committee and Stefan Batory Foundation for financial support without which my attendance to the conference would not have been possible.

REFERENCES

- Drummond J. D., Weidenschilling S. J., Chapman C. R., Davis D. R. (1991) Photometric geodesy of main-belt asteroids. IV. An updated analysis of lightcurves for poles, periods and shapes. *Icarus*, 89, 44–64.
- Erikson, A., Cutispoto, G., Debehogne, H., Hahn, G., Lagerkvist, C.–I., Lindgren, M., Magnusson P. (1991) Physical studies of asteroids XXIII : Photometric observations of the asteroids 6, 32, 196, 243, 416, 532 and 1580. *Astron.Astrophys.Suppl.*, submitted.
- Lagerkvist C.–I., Barucci M. A., Capria M. T., Fulchignoni M., Guerriero L., Perozzi E., Zappalà V. (1987) *Asteroid Photometric Catalogue*, Consiglio Nazionale Delle Ricerche, Roma.
- Lagerkvist C.–I., Barucci M. A., Capria M. T., Fulchignoni M., Magnusson P. (1988) *Asteroid Photometric Catalogue, first update*, Consiglio Nazionale Delle Ricerche, Roma.
- Lupishko D. F., Velichko F. P. (1987) Sense of rotation of asteroids 21, 63, 216 and 349. *Kinematics and Physics of Celestial Bodies*, 3, 57–65.
- Lupishko D. F., Velichko F. P., Belskaja I. N., Schevchenko V. G. (1989) *Kinematics and Physics of Celestial Bodies*, 5, 36.
- Magnusson P. (1989) Pole determinations of asteroids. In *Asteroids II* (R.P.Binzel, T.Gehrels, M.Matthews, Eds.), pp. 1180–1190. Univ. of Arizona Press, Tucson.
- Michałowski T. (1988) Photometric astrometry applied to asteroids : 6, 15, 43 and 624. *Acta Astron.*, 38, 455–468.
- Michałowski T. (1991) in preparation.
- Michałowski T., Velichko F. P. (1990) Photoelectric photometry, parameters of rotation and shapes of asteroids 22 Kalliope and 79 Eurynome. *Acta Astron.*, 40, 321–332.
- Weidenschilling S. J., Chapman C. R., Davis D. R., Greenberg R., Levy D. H., Binzel R. P., Vail S. M., Magee M., Spaute D. (1990) Photometric geodesy of main-belt asteroids. III. Additional lightcurves. *Icarus*, 86, 402–447.

GROUND-BASED OBSERVATIONS OF 951 GASPRA: CCD LIGHTCURVES AND SPECTROPHOTOMETRY WITH THE GALILEO FILTERS ¹

Mottola S. *, Di Martino M. ‡, Gonano-Beurer M. *, Hoffmann H. *, Neukum G. *

*DLR German Aerospace Research Establishment, D-8031 Oberpfaffenhofen, F.R.G.

‡Osservatorio Astronomico di Torino, I-10025 Pino Torinese, Italy.

ABSTRACT

This paper reports the observations of 951 Gaspra carried out at the European Southern Observatory (La Silla, Chile) during the 1991 apparition, using the DLR CCD Camera equipped with a spare set of the Galileo SSI filters. Time-resolved spectrophotometric measurements are presented. The occurrence of spectral variations with rotation suggests the presence of surface variegation.

INTRODUCTION

CCD photometry and spectrophotometry of 951 Gaspra have been undertaken by our group since the apparition of 1988 to characterize the physical and dynamical properties of this asteroid. The aim of this work is to provide a ground-based reference to be integrated and compared with the data which will be obtained during the Galileo encounter of October 1991.

At the time of the 1991 apparition, we performed observations of 951 Gaspra with the ESO 1-m telescope, using the DLR CCD Camera equipped with a subset of filters of the Galileo Solid-State Imaging (SSI) subsystem (Fig. 1). This campaign has been mainly devoted to the study of the spectrophotometric properties of this small-sized and atypical S-type asteroid. The acquisition of high time-resolution, high signal-to-noise lightcurves in different spectral channels made it possible to search for the occurrence of surface heterogeneity on a hemispherical scale.

INSTRUMENTATION AND DATA REDUCTION

The DLR CCD camera houses a Thomson 384x576 pixel TH-7882 Charge Coupled Device with a read-out noise of 7 electrons RMS. The front side of the detector is coated with a down-converting phosphor dye in order to extend the sensitivity of the device to the blue and ultraviolet regions of the spectrum. As a result the spectral coverage is $250 \leq \lambda \leq 950$ nm with a quantum efficiency $\geq 10\%$. A computer-driven filter-wheel houses the spare set of the Galileo (GLL) interference filters. The integration times were chosen accordingly to the sensitivity of each spectral channel, typically ranging between 2 and 10 minutes.

Several comparison stars were present each night in the same CCD field of the asteroid, and a careful placement of the asteroid's image in the frame allowed the stars to advance across the image still remaining in the same field of the asteroid for the whole duration of the observations. For the purpose of spectral calibration we used the stars Tau Sco and 42 Lib, selected from the catalogs of Aller et al. (1966) and Cochran (1980), respectively. Due to the small angular distance between the asteroid and the calibration stars (≤ 10 deg), it was possible to observe the stars each night at airmasses very close to that of the asteroid, thus minimizing the contribution of the extinction uncertainty on the overall error budget.

Flat fields were obtained each night in every filter from exposures of regions of the sky taken at dawn and dusk; they were successively bias-subtracted and averaged to improve the signal-to-noise ratio.

The data reduction was performed using the software package for CCD image processing in use at DLR. A version of this code available on a portable computer allowed us to perform the complete reduction of the data during daytime after each observing night. The first step of the processing consisted in the bias subtraction and flat-fielding of the scientific frames. After the images were decalibrated, the instrumental fluxes of each source in the field were evaluated by applying a synthetic aperture photometry procedure.

¹Based on observations collected at the European Southern Observatory, La Silla (Chile).

Typical apertures had a diameter of 8 - 10 arcsec. Differential photometry between the asteroid and the field stars resulted in lightcurves with an internal consistency better than 0.008 mag in the GLL filters 3 and 7, and better than 0.003 in the other three channels.

OBSERVATIONS AND DISCUSSION

We obtained high-quality lightcurves of 951 Gaspra during three nights in May 1991 in five spectral channels. The log of the observations is reported in Table 1. Conditions were photometric with good seeing on all three nights. On May 16 and 17, full cycle lightcurves were obtained with the GLL filters 1, 2 and 3, 7 respectively, and a partial coverage on May, 13 (three hours of time interval) with the GLL filter 4.

The folding of the lightcurves in all channels with a Fourier analysis fitting procedure (Harris et al., 1989) yields a synodic rotational period $P = 7.0394 \pm 0.0002$ hr.

The mean magnitude values of the lightcurves in these five spectral channels have been corrected for the changing phase angle and sun- and earth-asteroid distance variations. Phase reddening has been neglected, since in the phase angle range of interest this effect is in the millimag range. The resulting reflectance spectrum is shown in Fig. 2. The reflectivities are scaled to unity at $\lambda = 560$ nm, corresponding to GLL filter 1. For the purpose of comparison, the data of the ECA survey (Zellner et al., 1985) are also shown. The two spectra are in good agreement and exhibit a strong drop-off towards the UV, a maximum in reflectance near 760 nm and the presence of the 1- μm absorption band.

Table 1. Aspect data of 951 Gaspra.

	Date (UT)	Long.1950 (deg)	Lat.1950 (deg)	r (AU)	Δ (AU)	Phase (deg)	Filter
1991 05 13.3		243.3	-1.7	2.490	1.492	-4.8	GLL 4
05 16.2		242.6	-1.6	2.486	1.482	-3.4	GLL 1,2
05 17.2		242.3	-1.6	2.485	1.478	-2.9	GLL 3,7

For further evaluation, we have combined the lightcurves obtained with the GLL filters 1, 2, 3 and 7 (Fig. 3) into a composite. This has been successively fitted with a low order Fourier expansion, in order to derive the "mean" lightcurve. To detect possible spectral variations with rotation, we have then plotted the difference between the single lightcurves and the Fourier expansion (Fig. 4).

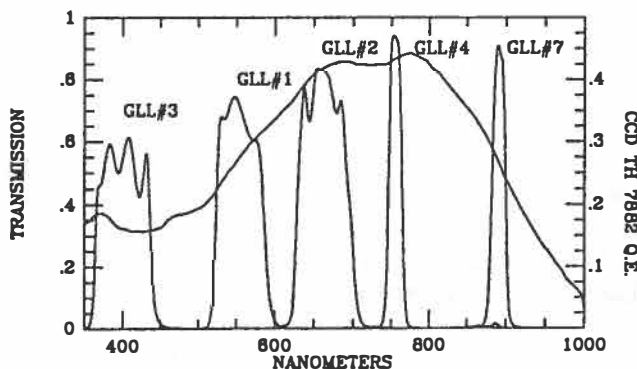


Fig. 1. Quantum efficiency of the TH 7882 CCD and spectral transmission of the GLL filters used in this work.

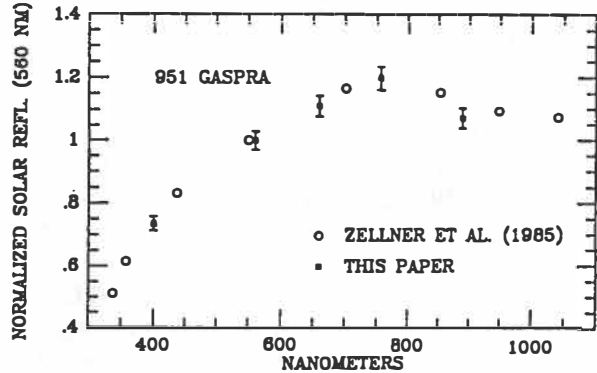


Fig. 2. Spectral reflectance of 951 Gaspra obtained with the GLL filters. The ECAS spectrum is also shown.

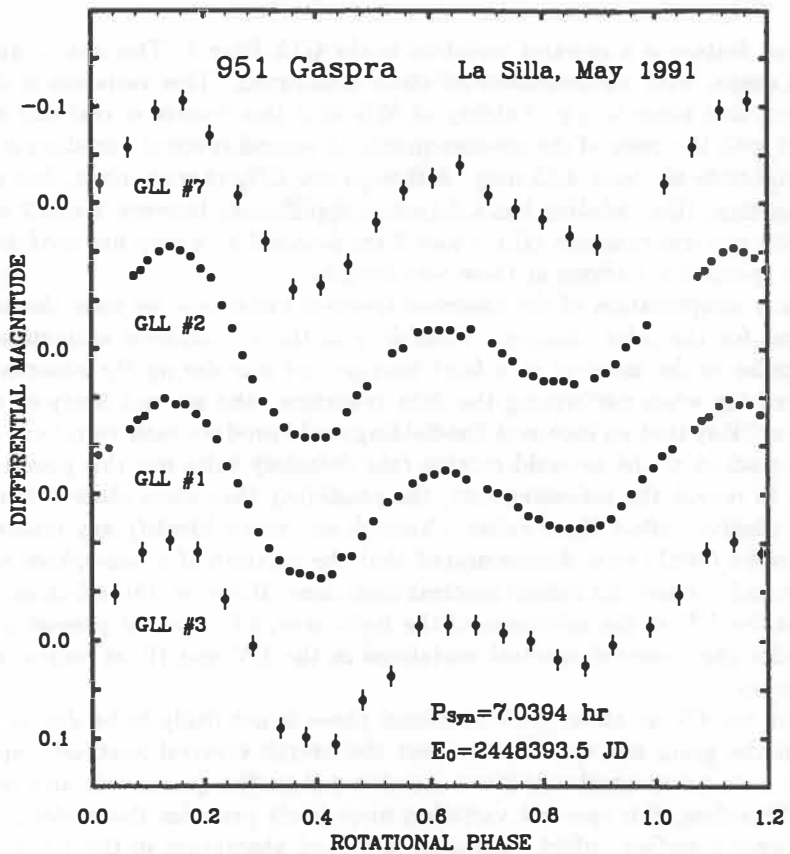


Fig. 3. Lightcurves of 951 Gaspra obtained with the GLL filters. The data points beyond the rotational phase 1.0 are repeated.

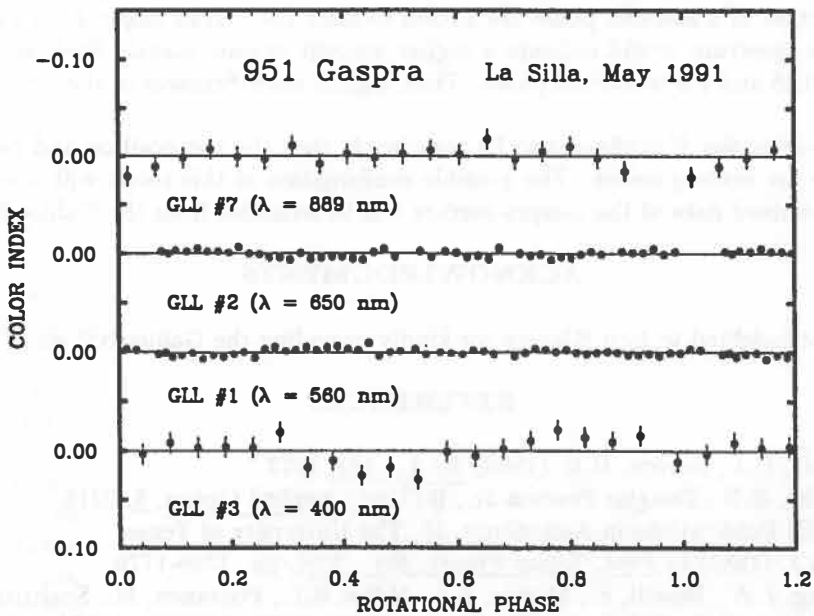


Fig. 4. Differences between the lightcurves in each filter and the mean lightcurve (see text).

The most evident feature is a spectral variation in the GLL filter 3. This has an approximately double-periodic sinusoidal shape, with an amplitude of about 0.035 mag. This variation is detected at a level of about 2σ , signifying that there is a probability of 95% that this feature is real and not due to a random variation associated with the noise of the measurements. A second spectral variation is detected in the GLL filter 7, with an amplitude of about 0.03 mag. Although not fully characterized, due to a short gap in the data acquisition sequence, this variation has a detection significance between 1 and 2σ (probability $\geq 65\%$). Subtle changes in the spectral channels GLL 1 and 2 are detected at a very low confidence level, thus being compatible with no spectral variations at these wavelengths.

Before giving any interpretation of the observed spectral variations, we have checked whether spurious effects could account for the color changes. Variability in the atmospheric extinction, in the comparison stars, the close appulse of the asteroid to a faint background star during the observations, have been detected and accounted for when performing the data reduction, and are not likely to explain the observed behavior. It is also unlikely that an incorrect flat-fielding could produce such variations and the fact that the telescope has been tracked at the asteroid motion rate definitely rules out this possibility. However, since it was not possible to repeat the measurements, the possibility that some observational or data reduction error produced the observed effect there exists, although we cannot identify any reasonable cause.

Gradie and Veverka (1981) have demonstrated that the rotation of a non-spherical body with uniform surface composition and texture can induce spectral variations. However, this effect accounts for an increase of the reflectance in the UV at the minimum of the lightcurve, which is not present in our measurements. Therefore we consider the observed spectral variations in the UV and IR as indicators of surface heterogeneities of 951 Gaspra.

The minimum in the UV at about 0.45 rotational phase is not likely to be due to a textural variation, since any change in the grain size would also affect the overall spectral contrast, especially the depth of the 1 μm -band. In fact, no spectral variations are detected in the green, red, and infrared filters at this rotational phase. Therefore, this spectral variation most likely provides the evidence for a compositional heterogeneity of Gaspra's surface, which causes an increased absorption in the UV due to charge transfer processes.

The IR minimum close to 1.0 rotational phase represents an increase of the 1 μm absorption and could be due either to a lower olivine to pyroxene ratio or to an augmented content of mafic minerals. There appears to be a possible correlation between the variation in the IR and a minor darkening in the UV at this rotational phase. If this is true, the presence of additional textural surface variegations cannot be excluded. Changes in the content of a metallic phase are known to alter the overall slope of the spectral reflectance. A reddening of the spectrum would indicate a higher amount of pure metal. Such an effect, however, is not observed near 0.45 and 1.0 rotational phase. Thus, significant differences in the metallic content can be excluded.

The observed variations, if confirmed to be real, imply that the composition and possibly the texture of Gaspra's surface are heterogeneous. The possible confirmation of this result will come when the multi-spectral spatially resolved data of the Gaspra surface will be available from the Galileo flyby.

ACKNOWLEDGMENTS

The authors are indebted to Ken Klaasen for kindly providing the Galileo SSI set of filters.

REFERENCES

- Aller, L.H., Faulkner, D.J., Norton, R.H. (1966) *Ap.J.*, **144**, 1073.
- Arvesen, J.C., Griffin, R.N., Douglas Pearson Jr., B. (1969) *Applied Optics*, **8**, 2215.
- Cochran, A.L. (1980) *Publications in Astronomy*, **16**, The University of Texas.
- Gradie, J., Veverka J. (1981) In *Proc. Lunar Planet. Sci.*, **12B**, pp. 1769-1779.
- Harris, A.W., Young, J.W., Bowell, E., Martin, L.J., Millis, R.L., Poutanen, M., Scaltriti, F., Zappalà, V., Schober, H.J., Debehogne, H., Zeigler, K.W. (1989) *Icarus*, **77**, 171.
- Zellner, B., Tholen, D.J., Tedesco, E.F. (1985) *Icarus*, **61**, 355.

CCD-photometry of comets at large heliocentric distances

B.E.A. Mueller, Kitt Peak National Observatory, 950 N. Cherry Avenue, Tucson AZ 85719

INTRODUCTION

CCD imaging and time series photometry are used to determine the state of activity, nuclear properties and eventually the rotational motion of cometary nuclei. Two extreme examples of quite different behavior of activity are P/Halley and P/Tempel 2. On one hand P/Halley had a rather surprising outburst at 14.3 AU (Hainaut et al. 1991, Meech 1991), on the other hand P/Tempel 2 had an activity onset during its last apparition at only 1.9 AU (Boehnhardt et al. 1990). Cometary activity at large heliocentric distances and mantle evolution are not yet fully understood. What is the difference between the nuclei of different comets? How does this influence the activity? It is thus very important to understand the temporal evolution of comets and therefor the differences between new and old comets and a possible relation to asteroids.

OBSERVATIONS

The observations were carried out at the 2.1 m telescope on Kitt Peak April 10-12 and May 15-16, 1991. The TI2 chip (binned 2×2) with a resolution of $0.^{\circ}38/\text{pixel}$ and the Tek2 with $0.^{\circ}34/\text{pixel}$ were used as detectors, respectively. The standard Kitt Peak Harris filter set for V, R and I (Cousins system) was used. The observational circumstances for the objects are given in table 1.

Table 1: Observations of Comets and Asteroids in 1991

Object	$^1\Delta$ [AU]		2r [AU]		$^3\alpha$ [degree]	
	April	May	April	May	April	May
P/Churyumov-Gerasimenko	3.91	4.01	4.87	4.97	4.1-3.6	15.5-15.6
P/Giacobini-Zinner	2.92	2.60	3.75	3.53	9.9-9.5	6.4-6.6
P/Tempel 2	-	5.07	-	4.74	-	9.3-9.2
(2060) Chiron	10.38	-	10.44	-	5.5	-
(951) Gaspra	1.74	1.48	2.53	2.49	17.2	3.2-4.0
1991 JR	-	0.06	-	1.07	-	17.7

1 geocentric distance, 2 heliocentric distance, 3 phase angle

PHOTOMETRIC RESULTS

Landolt stars (Landolt 1983) and the Clusters NGC 4147 and M 92 (Davis, private communication 1991) were used as magnitude standards. (2060) Chiron in April and P/Giacobini-Zinner in May both showed clearly a coma. Digital apertures of 10 pixels ($\pm 3.^{\circ}8$) and of 6 pixels ($\pm 2.^{\circ}0$) were used for their photometry, respectively, minimizing (but not nullifying) the coma contribution. Magnitude variations of the objects are mostly smaller than the errors except for P/Giacobini-Zinner in May which is definitely variable. Because variability can neither be confirmed nor excluded, mean values and the maximal differences for the R-filter are given in tables 2 and 3.

In table 4 mean colors of the objects are given. Single measurements for P/Giacobini-Zinner in May are $V-R = 0.57 \pm 0.12$, 0.47 ± 0.12 , 0.52 ± 0.11 , $R-I = 0.58 \pm 0.14$, 0.60 ± 0.12 , 0.33 ± 0.14 , $V-I = 1.15 \pm 0.15$, 1.06 ± 0.12 , 0.84 ± 0.13 . Their variability can be attributed to different coma contribution.

The colors corrected for solar values (Scheffler & Elsässer 1974) are plotted in a (V-I)/(R-I) diagram (figure 1). The near earth approacher 1991 JR is the bluest object followed by (951) Gaspra, an S-type (Tholen 1989). 1991 JR was classified as a C-type asteroid by E. Howell (1991, private communication), the first one ever photometrically measured in this size range (≈ 170 m, cf. Rabinowitz 1991). The colors of P/Giacobini-Zinner differ considerably in April and May, but this is most probably due to the coma present in May. P/Giacobini-Zinner in April is the reddest "nucleus" in this sample. An existing coma affects the measured colors because of the emitting gas and dust and molecule emission lines. Hartmann &

Table 2: Mean R-magnitudes of Comets and Asteroids in April 1991

Object	10		11		12	
	R	ΔR_{max}	R	ΔR_{max}	R	ΔR_{max}
¹ P/CG	21.55 ± 0.12	0.29	21.99 ± 0.15	0.55	21.38 ± 0.12	0.10
P/Giacobini-Zinner	21.30 ± 0.09	0.33	21.13 ± 0.09	0.28	20.90 ± 0.17	0.41
(2060) Chiron	16.16 ± 0.01	0.00				
(951) Gaspra	15.22 ± 0.01	0.03	15.21 ± 0.01	0.02	15.05 ± 0.02	0.02

1 P/Churyumov-Gerasimenko

Table 3: Mean R-magnitudes of Comets and Asteroids in May 1991

Object	15		16	
	R	ΔR_{max}	R	ΔR_{max}
P/Churyumov-Gerasimenko	22.04 ± 0.09	0.29	21.79 ± 0.08	0.19
P/Giacobini-Zinner	20.57 ± 0.12	0.43	20.39 ± 0.05	0.14
P/Tempel 2	20.98 ± 0.13	–	21.02 ± 0.09	0.10
(951) Gaspra	14.40 ± 0.03	0.07	14.40 ± 0.02	–
1991 JR			17.42 ± 0.03	0.01

Table 4: Colors of Comets and Asteroids in 1991

Object	April 10			May 16		
	V-R	R-I	V-I	V-R	R-I	V-I
¹ P/CG	0.16 ± 0.32	0.72 ± 0.42	0.88 ± 0.50	0.54 ± 0.26	0.52 ± 0.33	1.06 ± 0.41
² P/GZ	0.51 ± 0.20	0.91 ± 0.19	1.42 ± 0.25	0.52 ± 0.09	0.51 ± 0.12	1.01 ± 0.13
P/Tempel 2				0.53 ± 0.17	0.81 ± 0.17	1.34 ± 0.21
(2060) Chiron	0.44 ± 0.04	0.53 ± 0.02	0.97 ± 0.04			
(951) Gaspra	0.46 ± 0.04	0.41 ± 0.02	0.87 ± 0.04	0.48 ± 0.04	0.43 ± 0.10	0.91 ± 0.05
1991 JR				0.39 ± 0.04	0.36 ± 0.04	0.75 ± 0.04

1 P/Churyumov-Gerasimenko, 2 P/Giacobini-Zinner

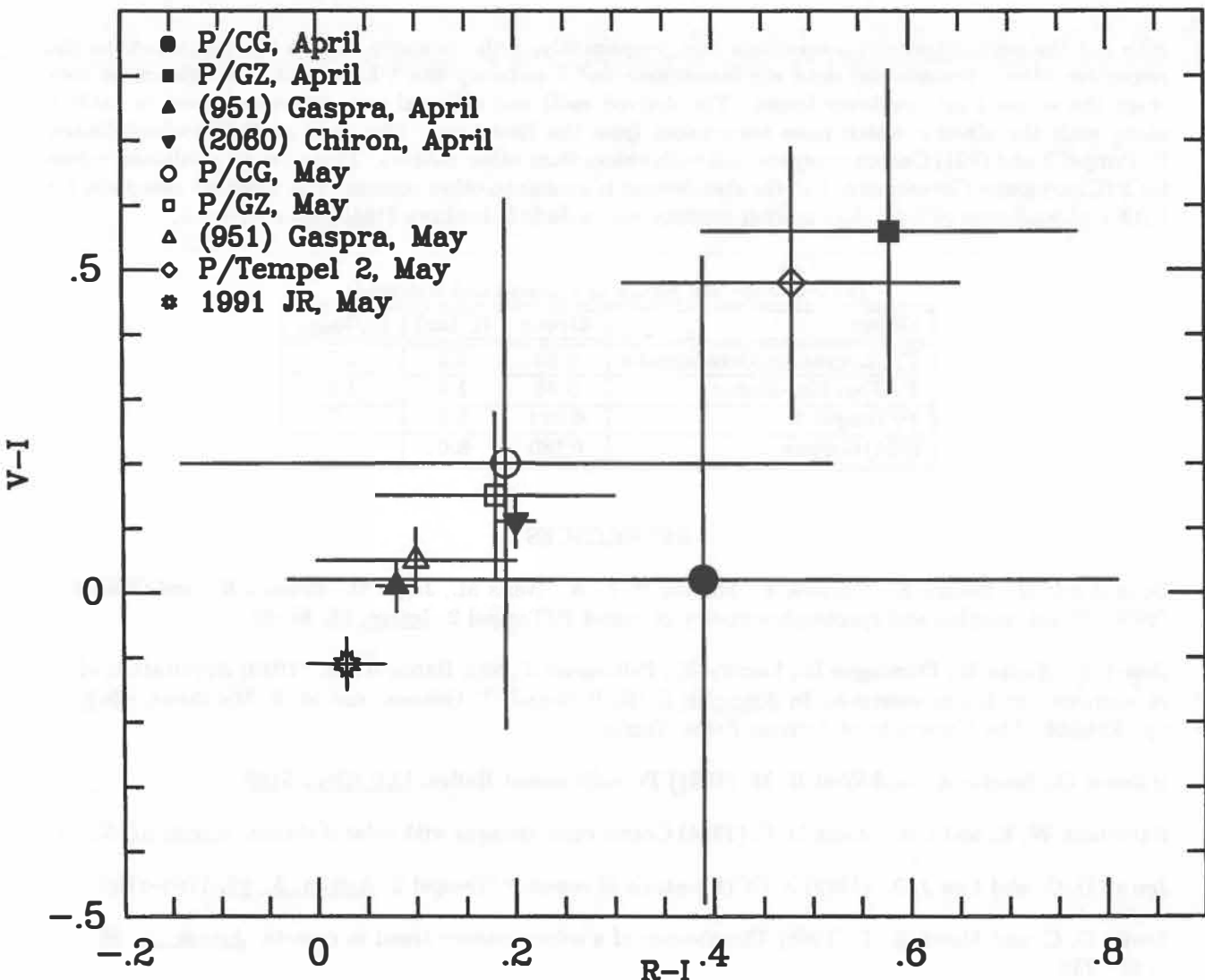


Figure 1: $(V-I)/(R-I)$ color-color diagram. The colors are corrected for the Sun.

Cruikshank (1984) found a color-distance trend in comets in the infrared, but this was disputed by Jewitt & Meech (1988). But these measurements were all taken of comets exhibiting a coma. It is not clear if a color-distance relation for nuclei exists and how it is connected to composition, shape, rotation and phase. The data are much too sparse to infer a color dependence of the orbit location of a comet of physical differences among different comets. Further observations of the same and new objects are planned in order to test a color-distance relation and to determine nuclear properties.

NUCLEAR RADII AND SHAPES

The size of the nucleus (R) can be estimated by the formula (Spinrad et al. 1979)

$$R^2 A = r^2 10^{0.4(M_\odot - m(\alpha) + 5 \log \Delta)}$$

with $m(\alpha) = m_{obs} - c \alpha$ and $c \approx 0.03^m/\deg$ (Jewitt & Luu 1989), α being the phase angle, r the heliocentric distance in km, Δ the geocentric distance in AU, M_\odot the absolute solar magnitude and m_{obs} the observed magnitude in the respective filter, and A the albedo. For (951) Gaspra the formulae by Bowell et al. (1989) were used to derive a radius. The axes ratio of a nucleus can be simply calculated by (provided the amplitude of the magnitude difference is due to rotation)

$$I_{min}/I_{max} = 10^{-0.4(m_{min} - m_{max})} = b/a$$

with a, b the semi-major and semi-minor axis, respectively, I the intensity and m the magnitude in the respective filter. Because my data are incomplete and I certainly don't have complete light-curve coverage the values I get are lower limits. The derived radii and minimal axes ratios are given in table 5 along with the albedos which have been taken from the literature. The radii of P/Giacobini-Zinner, P/Tempel 2 and (951) Gaspra compare well with values from other authors. There are no published values for P/Churyumov-Gerasimenko but the size derived is similar to other comets. The minimal axes ratio for P/Giacobini-Zinner of 1:1.5 does neither confirm nor exclude Sekanina's (1985) value of 1:8.3.

Table 5: Size and Shape of Comets and Asteroids

Object	Albedo	R [km]	$(a/b)_{min}$
P/Churyumov-Gerasimenko	0.03	3.2	1.7
P/Giacobini-Zinner	0.05	1.9	1.5
P/Tempel 2	0.024	5.9	1.7
(951) Gaspra	0.186	8.0	—

REFERENCES

- Boehnhardt H., Beisser K., Vanysek V., Mueller B. E. A., Weiss M., Jäger M., Reinsch K., and Grün E. (1990) Direct imaging and spectrophotometry of comet P/Tempel 2. *Icarus*, **86**, 58–68.
- Bowell E., Hapke B., Domingue D., Lumme K., Peltoniemi J., and Harris A. W. (1989) Application of photometric models to asteroids. In *Asteroids II* (R. P. Binzel, T. Gehrels, and M. S. Matthews, eds.), pp. 524–556. The University of Arizona Press, Tucson.
- Hainaut O., Smette A., and West R. M. (1991) Periodic comet Halley. *IAU Circ.*, **5189**.
- Hartmann W. K. and Cruikshank D. P. (1984) Comet color changes with solar distance. *Icarus*, **57**, 52–62.
- Jewitt D. C. and Luu J. X. (1989) A CCD portrait of comet P/Tempel 2. *Astron. J.*, **97**, 1766–1790.
- Jewitt D. C. and Meech K. J. (1988) The absence of a color-distance trend in comets. *Astron. J.*, **96**, 1723–1730.
- Landolt A. U. (1983) UBVRI photometric standard stars around the celestial equator. *Astron. J.*, **88**, 439–460.
- Meech K. J. (1991) Periodic comet Halley. *IAU Circ.*, **5196**.
- Rabinowitz D. L. (1991) The flux of small asteroids near the earth. In *Asteroids, Comets, Meteors III* (A. Harris and E. Bowell, eds.), submitted. Lunar and Planetary Institute, Houston.
- Scheffler H. and Elsässer H., eds. (1974) *Physik der Sterne und der Sonne*. Bibliographisches Institut, Mannheim. 78 pp.
- Sekanina Z. (1985) Precession model for the nucleus of periodic comet Giacobini-Zinner. *Astron. J.*, **90**, 827–845.
- Spinrad H., Stauffer J., and Newburn R. L., Jr. (1979) Optical spectrophotometry of comet Tempel 2 far from the sun. *Publ. Astron. Soc. Pacific*, **91**, 707–711.
- Tholen D. J. (1989) Asteroid taxonomic classifications. In *Asteroids II* (R. P. Binzel, T. Gehrels, and M. S. Matthews, eds.), pp. 1139–1150. The University of Arizona Press, Tucson.

ASTEROID ORBITAL ERROR ANALYSIS: THEORY AND APPLICATION

K. Muinonen and E. Bowell

Lowell Observatory, 1400 West Mars Hill Road, Flagstaff, AZ 86001, U.S.A.

We present a rigorous Bayesian theory for asteroid orbital error estimation in which the probability density of the orbital elements is derived from the noise statistics of the observations. For Gaussian noise in a linearized approximation the probability density is also Gaussian, and the errors of the orbital elements at a given epoch are fully described by the covariance matrix. The law of error propagation can then be applied to calculate past and future positional uncertainty ellipsoids (Cappellari *et al.* 1976, Yeomans *et al.* 1987, Whipple *et al.* 1991).

To our knowledge, this is the first time a Bayesian approach has been formulated for orbital element estimation. In contrast to the classical Fisherian school of statistics, the Bayesian school allows a priori information to be formally present in the final estimation. However, Bayesian estimation does give the same results as Fisherian estimation when no a priori information is assumed (Lehtinen 1988, and references therein).

BAYESIAN THEORY OF ORBIT ESTIMATION

Assume that N pairs of right ascensions and declinations $\ell = (\alpha_1, \delta_1; \dots; \alpha_N, \delta_N)^T$ have been observed for a certain asteroid at times $t = (t_1, \dots, t_N)^T$. Let the corresponding computed sky-plane positions be described by the vector $L(P)$ for the orbital elements $P = (\tau, \omega, \Omega, i, e, a)^T$. The orbital elements are, respectively, the time of perihelion, argument of perihelion, longitude of ascending node, inclination, eccentricity, and semimajor axis. The astrometric observations and computed positions are related to each other through the so-called observation equation

$$\begin{aligned}\ell &= L(P) + \epsilon \\ \epsilon &= (\epsilon_{\alpha_1}, \epsilon_{\delta_1}; \dots; \epsilon_{\alpha_N}, \epsilon_{\delta_N})^T,\end{aligned}\quad (1)$$

where ϵ describes the noise.

Following Bayesian estimation, or statistical inversion theory, the a posteriori probability density of the orbital elements is related, via Eq. (1), to the a priori and noise probability densities through

$$p_{post}(P) \propto p_{pre}(P) p_{2N}(\epsilon) = p_{pre}(P) p_{2N}(\ell - L(P)). \quad (2)$$

The a priori probability density can be assumed constant, so no constraining assumptions are made about the orbital elements. Eq. (2) describes the entire solution of the orbit inversion problem in terms of probability densities.

Next, assume that the noise probability density is Gaussian with a diagonal covariance matrix; i.e., the noise is not correlated. In spite of this simplifying assumption, it is evident from Eq. (2) that the a posteriori density for orbital elements is rather complicated. In the present context, we do not study the general probability density but proceed by linearizing the sky-plane positions in the neighborhood of the ephemeris from a least-squares orbit solution P_0 . The resulting a posteriori probability density for the orbital element deviations is Gaussian and has inverse covariance matrix

$$\Sigma_{P_i P_j}^{-1} = \sum_{k=1}^N \frac{\cos^2 \delta_k}{\sigma_k^2} \frac{\partial \alpha}{\partial P_i}(P_0, t_k) \frac{\partial \alpha}{\partial P_j}(P_0, t_k) + \frac{1}{\rho_k^2} \frac{\partial \delta}{\partial P_i}(P_0, t_k) \frac{\partial \delta}{\partial P_j}(P_0, t_k), \quad (3)$$

in which σ_k and ρ_k are the standard deviations in right ascension and declination, respectively. Numerical inversion of this matrix yields the covariance matrix of the orbital elements.

Instead of using a priori error estimates of the observations to obtain σ_k and ρ_k for Eq. (3), the following self-consistent method of determining the standard deviations can be used: Determine the orbit by the usual means of differential correction, in which equal weight is given to each observation; compute the rms errors σ (allowing for $\cos \delta$) and ρ , and then set $\sigma_k = \sigma$, $\rho_k = \rho$, $k = 1, \dots, N$ in the error analysis.

A number of analytical results can be derived from the covariance matrix in a two-body orbit approximation (with minor changes, the results are valid for perturbed orbits). For example, as an observational arc (T) is lengthened, the accuracy of the semimajor axis is improved faster ($\Sigma_{aa} \propto T^{-3}$) than that of the other orbital elements ($\Sigma_{P_i P_i} \propto T^{-2}$). This is analogous to lightcurve error analysis, in which the period improves faster than the Fourier coefficients (Karttunen and Muinonen 1991). Moreover, the variances of the mean, eccentric, and true anomalies have a quadratic time dependence. It is also worth noting that the correlations among the orbital elements are relatively insensitive to the arc length. This arises from geometric restrictions of the optical groundbased observations, and could be alleviated by radar or spacecraft observations.

In the general formalism, the probability density for the range \tilde{R} , declination $\tilde{\delta}$, and right ascension $\tilde{\alpha}$ at time t can be obtained from the a posteriori probability density of the orbital elements from

$$p(\tilde{R}, \tilde{\delta}, \tilde{\alpha}; t) = \frac{1}{\tilde{R}^2 \cos \tilde{\delta}} \int dP p_{post}(P) \delta_D(\tilde{R} - R(P, t)) \delta_D(\tilde{\delta} - \delta(P, t)) \delta_D(\tilde{\alpha} - \alpha(P, t)), \quad (4)$$

where δ_D is Dirac's function. The factor preceding the integral derives from the spherical coordinate system. The numerical computation of this integral is straightforward, though time-consuming. Note that to compute the real uncertainties for a future observation, the probability density in Eq. (4) should still be convolved with the noise of that observation.

Using the linearized approximation for the orbital elements and linearizing the Dirac function arguments, a Gaussian probability density results for the equatorial spherical coordinates (from the integral part of Eq. (4)) with covariance matrix

$$\Lambda = \Psi^T \Sigma \Psi, \quad \Psi = \begin{pmatrix} \frac{\partial R}{\partial \tau} & \frac{\partial \delta}{\partial \tau} & \frac{\partial \alpha}{\partial \tau} \\ \vdots & \vdots & \vdots \\ \frac{\partial R}{\partial a} & \frac{\partial \delta}{\partial a} & \frac{\partial \alpha}{\partial a} \end{pmatrix}. \quad (5)$$

Here, for a prediction at time t , the partial derivatives must be evaluated at (P_0, t) . It should be noted that the linearized approach is an approximation that fails, for example, when a long time has elapsed from the observations and the uncertainties have become very large. The covariance matrix Λ gives an error ellipsoid in three-dimensional space. As is well known, the sky-plane error ellipse is usually very elongated and aligned with the line of variation. Using Eq. (5), it can be shown that, asymptotically, the range, declination, and right ascension uncertainties increase linearly with time in the two-body approximation.

MARS TROJAN 1990 MB

As an example, we study the orbit of the Mars Trojan asteroid 1990 MB using 43 observations spanning 1979 Nov. 21 through 1990 Oct. 14. A two-body orbital error analysis gives the following error estimates for the orbital elements at epoch 1991 Dec. 10.0 (B1950.0 for ω , Ω , and i):

$$\begin{aligned} \tau &= 1992 \text{ Sep. } 15.26887 \pm 0.00184 & i &= 20^\circ 28098 \pm 0^\circ 00007 \\ \omega &= 95^\circ 39992 \pm 0^\circ 00137 & e &= 0.0647663 \pm 0.00000028 \\ \Omega &= 244^\circ 44755 \pm 0^\circ 00007 & a &= 1.5235591 \text{ AU} \pm 0.0000003 \text{ AU} \end{aligned} \quad (6)$$

Note that the semimajor axis is very accurately known, as predicted by the error analysis. Because of the rather small eccentricity, the argument of perihelion has a larger error than the longitude of the ascending node. The error in the time of perihelion also reflects the small eccentricity. The covariance matrix reveals high correlations between semimajor axis and eccentricity, as well as between time of perihelion and argument of perihelion.

Figure 1a shows the sky-plane $1-\sigma$ uncertainty $\sqrt{\Lambda_{\alpha\alpha} \cos^2 \delta + \Lambda_{\delta\delta}}$ in position prediction for a 10-yr interval. The maxima correlate well with the minimum geocentric distance, which suggests that, for optimum ephemeris improvement, future observations should be made near the minimum distance of the object. As a demonstration, we simulated a pair of observations on 1992 Jul. 26, close to opposition. There is a three-fold improvement in the orbit. For a simulated pair of observations far from opposition on 1992 Mar. 26, there is virtually no ephemeris improvement. Figure 1b shows the present and simulated $1-\sigma$ uncertainties $\sqrt{\Lambda_{RR}}$ in range prediction. Since the true orbit is not the least-squares solution, orbital and ephemeris errors are somewhat underestimated.

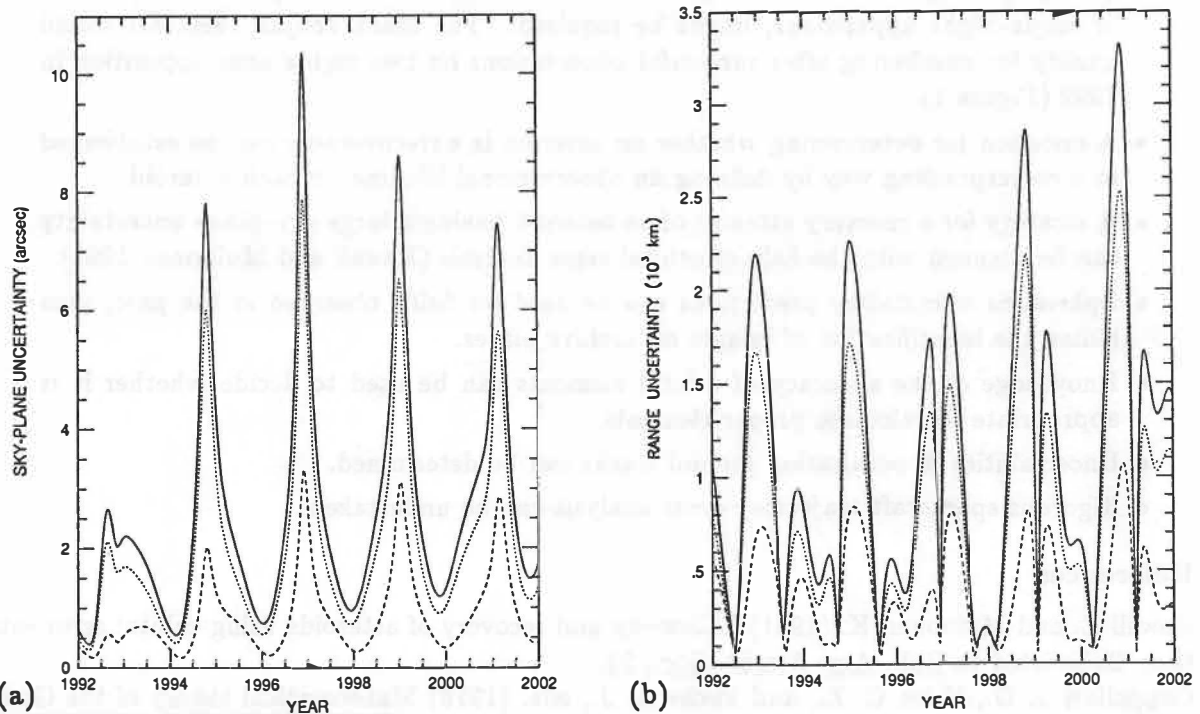


Fig. 1. Sky-plane (a) and range (b) uncertainty predictions for the Mars Trojan 1990 MB over an interval of 10 years (solid lines). The uncertainties after adding a simulated pair of observations on 1992 Jul. 26 (dashed line, close to opposition) and on 1992 Mar. 26 (dotted line, far from opposition) underscore the importance of observation date and geometry.

FUTURE WORK AND APPLICATIONS

In future work, the two-body partial derivatives should be checked against integrated derivatives. It will be important to compare the uncertainty predictions with approximate and accurate derivatives. The linearized approximation should be checked against the general Bayesian approach. Finally, we suggest that a public-domain file of covariance matrices of orbital elements, together with computer programs for error analysis and position prediction, be established. Information about the orbital uncertainties and covariance matrices could also be published in the *Minor Planet Circulars*.

We summarize selected applications of the orbital error analysis as follows:

- In orbit computation, the behavior of the covariance matrix serves as a guide for eliminating poor observations and suggests a way to automate the process.
- In the case of newly discovered asteroids, a strategy for follow-up or recovery can be devised. For example, one may decide whether an asteroid having a one-apparition orbit is recoverable using a narrow- or wide-field instrument and what the extent of the search should reasonably be (Bowell and Muinonen 1991).
- A figure of merit is associated with each possible future observation, thereby suggesting an observational strategy to optimize orbit improvement and to avoid making observations that would not contribute significantly.
- A criterion for numbering an asteroid can be established on the basis of the predicted ephemeris uncertainty over a suitable interval (Muinonen and Bowell 1991). For example, an ephemeris accuracy of 10 arcsec or better over 20 years, independent of single-night apparitions, might be required. The Mars Trojan 1990 MB would qualify for numbering after successful observations on two nights near opposition in 1992 (Figure 1).
- A criterion for determining whether an asteroid is unrecoverable can be established in a corresponding way by defining an observational lifetime for each asteroid.
- A strategy for a recovery attempt of an asteroid having a large sky-plane uncertainty can be planned with the help of orbital error analysis (Bowell and Muinonen 1991).
- Ephemeris uncertainty predictions can be used for fields observed in the past, thus aiding the identification of images on archive plates.
- Knowledge of the accuracy of orbital elements can be used to decide whether it is appropriate to calculate proper elements.
- Uncertainties in occultation ground tracks can be determined.
- Rigorous spacecraft trajectory error analysis can be undertaken.

References

- Bowell E. and Muinonen K. (1991) Follow-up and recovery of asteroids using orbital error estimation. Submitted to Bull. Am. Astron. Soc., 23.
- Cappellari J. O., Velez C. E., and Fuchs A. J., eds. (1976) Mathematical theory of the Goddard trajectory determination system. Goddard Space Flight Center Report X-582-76-77.
- Karttunen H. and Muinonen K. (1991) Error analysis of lightcurve periods. Astron. Astrophys., 242, 513–520.
- Lehtinen M. (1988) On statistical inversion theory. In Theory and Applications of Inverse Problems (Haario, H., ed.), 9pp. Pitman Research Notes in Mathematics, Series 167, Longman Scientific and Technical, Harlow.
- Muinonen K. and Bowell E. (1991) A criterion for numbering asteroids based on orbital error analysis. Presentation at the 21st General Assembly of International Astronomical Union, Commission 20 (Buenos Aires, Argentina).
- Whipple A. L., Hemenway P. D., and Ingram D. (1991) Initial refinement of minor planet orbits for pointing and observation with the Hubble Space Telescope. Astron. J., 102, 816–822.
- Yeomans D. K., Ostro S. J., and Chodas P. W. (1987) Radar astrometry of near-Earth asteroids. Astron. J., 94, 189–200.

LONG-TERM ORBITAL EVOLUTION OF SHORT-PERIOD COMETS FOUND IN PROJECT "COSMO-DICE"

Tsuko NAKAMURA (National Astronomical Observatory, Mitaka, 181 Tokyo) and
Makoto YOSHIKAWA (Communications Research Laboratory, Kashima, Ibaraki, 314 Japan)

ABSTRACT. Orbital evolutions of about 160 short-period (SP) comets are numerically integrated for 4400 years in the framework of a realistic dynamical model. By the round-trip error in closure test, a reliable time span of the integrated orbits is estimated for each comet. Majority of the SP comets with their Tisserand's constant (J) between 2.8 and 3.1 are found to evolve within the past 1000-2000 years from the orbits whose perihelia are near the Jovian orbit to the orbits with perihelia of 1-2 AU. This evolution is much more rapid than that expected from Monte Carlo simulations based on symmetric distribution of planetary perturbations, thus suggesting that asymmetry of perturbation distribution play an important role in cometary evolution. Several comets are shown to evolve from the near-Saturn orbits and then to be handed over under the control of Jupiter. We also find that a few comets were captured from long-period orbits ($a = 75\text{-}125$ AU) via only a few close encounters with Jupiter. It is confirmed that the captured SP comets of low-inclination with $2.8 < J < 3.1$ show more or less strong chaotic behavior. On the other hand, comets with longer orbital period and/or of high inclination reveal slow or quasi-periodic orbital evolution.

1. Introduction

"Cosmo-DICE" is a project, named after Dynamical Investigation of Cometary Evolution and after the erratic nature of SP comet motions just like casting dice. By this project we intend to provide reliable results of long-term orbital evolution of SP comets in the framework of a dynamical model as realistic as possible both for comets and planets. Although this work may look like only a successor of Carusi et al. (1985a), there are some important differences between theirs and ours. First, the time span covered by our calculations is 8.5 times toward the past and 2.5 times toward the future longer than those by Carusi et al. (1985a), which are both 400 years. For this achievement, some specific devices described below were necessary in terms of choice of integrators and calculation accuracy. As a result of this, we could find substantial orbital evolution of many SP comets, whereas, in Carusi et al. (1985a), only very limited cases of orbital evolution can be seen. Second, our calculations are characterized by an elaborate error check of integration for each orbit. This enables us to have a reliable time interval of integration for each comet.

Of course, considering the errors of the adopted orbital elements and possible non-gravitational effects which are not taken into account here, we cannot claim that every orbit in our calculations represents the true evolution for the 4400-year full time span. The main purpose of this project is, rather, to provide a standard database for statistical studies of long-term orbital evolution of SP comets, such as chaotic nature of their orbits, capture into and ejection out of resonant motions, interrelation between asteroids and comets, and so on.

In section 2 we describe briefly the dynamical model and method of integration. Section 3 discusses the reliable time span of our integration in relation to the error

growth rate. In section 4 are given the general characteristics of the orbital evolution of SP comets found in this project. The details of orbital evolution for each comet have been published in Nakamura and Yoshikawa (1991). A FITS-formatted magnetic tape including all the results is also available on request from the authors.

2. Dynamical Model and Method of Integration

Orbital elements as the initial conditions for numerical integration are taken for the most part from the Catalogue of Cometary Orbits, 6th edition (Marsden 1989) and the Minor Planet Circular. Planetary positions from Mercury through Pluto are not integrated simultaneously with comets, but are taken from the JPL numerical ephemerides DE102 (Newhall et al. 1983), which covers from BC 1411 through AD 3002.

In order to overcome the orbital instability inherent in SP comets, we adopted a quadruple-precision version of a variable-step extrapolation-type integrator (Bulirsch and Stoer 1966). The truncation parameter is set to 10^{-22} at $r = 1$ AU, which is a best compromise between CPU time and the accuracy requirement from orbital instability. Because of the variable-step control, regularization techniques are not used.

3. Error Estimate

After several trials we found that the round-trip error in closure test (Carusi et al. 1985b) is best as an error checker of integration for our purposes. Namely, integration is started from the present epoch toward the past up to BC 1411, and then this final state is integrated back to the present. The difference of these two orbital paths at each time step is expected to be a good measure of the error in the numerical integration. This is because the integration toward the present should reproduce exactly the original initial state if there is no error in the integration.

Fig. 1 shows some examples in the time history of the absolute value of the round-trip error in true longitude. General trend of these curves is always of linearly growing nature on the semi-log scale, though the error growth rate can be different by several order of magnitude from comet to comet. The error growth rate is found to have intimate relations with the orbital instability. This is reasonable because the Lyapunov characteristic exponent for a chaotic orbit should be positive (Lichtenberg and Lieberman 1983) and thus the linear error growth like Fig. 1 is expected.

We adopt here as a practical measure of orbital instability the elapsed time since BC 1411 in the backward integration within which the absolute error in true longitude attains one deg arc. This limit of time (T_{lim}) is calculated for each comet and the correlation of T_{lim} with J value is plotted in Fig. 2. We see that the mean T_{lim} for low-inclination SP comets is about 2000 years, and the low-inclination comets with their J near 3.0 show chaotic motions whereas the high-inclination ones behave more regularly. The T_{lim} is also useful to estimate the reliable time interval of the orbit calculation for a given error of adopted orbital elements. The error growth rate for the mean T_{lim} of 2000 years is about 10 per century. The relative error of best orbital elements determined from observations, on the other hand, is currently 10^{-7} or so. This implies that for an orbital longitude error of one deg arc the reliable time span of integration is about 700 years.

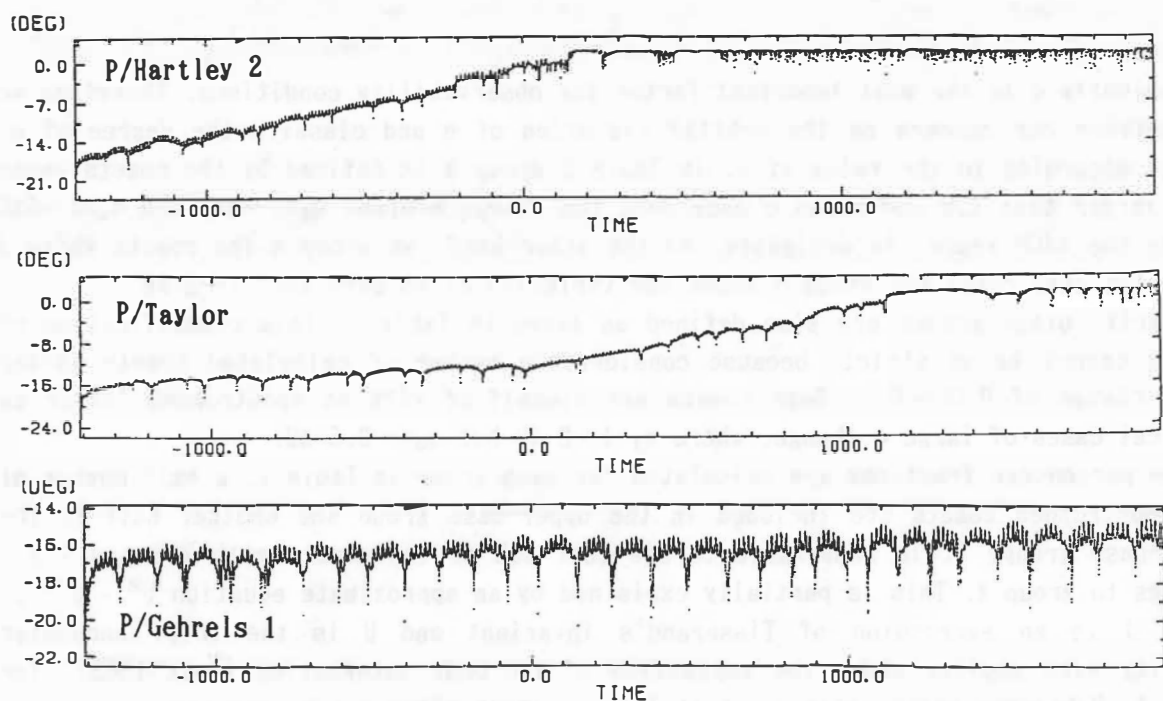


Fig.1: Some examples of the time history of the absolute value of the round-trip error in true longitude. The ordinate is in the scale of log(deg).

Table 1: q-change for 159 SP comets

<u>Group</u>	<u>J</u>	<u>Number</u>	<u>Fraction</u>
A	$2.9 \leq J$	41	85%
A'		3	
a		6	15
B	$2.8 \leq J < 2.9$	11	57%
B'		2	
b		8	43
C	$2.7 \leq J < 2.8$	13	52%
C'		8	
c		12	48
D	$2.5 \leq J < 2.7$	6	33%
D'		1	
d		13	67
E	$2.5 > J$	1	3%
e		34	97

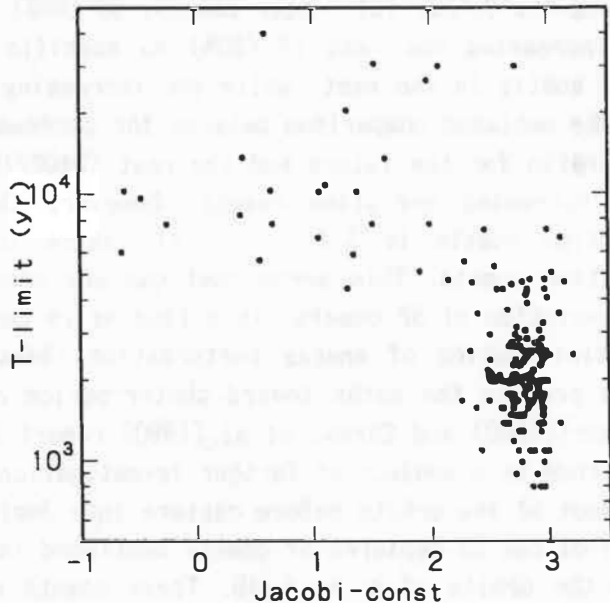


Fig.2: Tisserand(Jacobi) const. vs. T-limit

4. General Trends of Orbital Evolution

The following is some overall characteristics of orbital evolution of the SP comets found in this project. We have to keep in mind that these conclusions are more or less inevitably statistical and the orbital evolution of individual comets should not always be taken at their face value.

(1) Majority of the SP comets that show drastic change of perihelion distance (q) have the Tisserand's constant (J) of $2.7 \sim 3.1$:

Since the solar radiation makes comets luminous, the heliocentric distance or

equivalently q is the most important factor for observability conditions. Therefore we concentrate our concern on the orbital evolution of q and classify the degree of q -change according to the value of J . In Table 1 group A is defined by the comets whose J is larger than 2.9 and whose q undergoes the change between $q_1=1\sim 2$ AU and $q_u=4\sim 5$ AU during the 4400 years. We designate, on the other hand, as group a the comets whose J is in the same range but whose q shows the variation of no more than $1\sim 2$ AU.

Similarly, other groups are also defined as given in Table 1. This classification of course cannot be so strict, because considerable number of calculated comets showed the J -change of $0.05\sim 0.1$. Some comets are classified with an apostrophed letter as critical cases of large q change, where $q_1=1\sim 2$ AU but $q_u=\sim 3.5$ AU.

When percentage fractions are calculated for each group in Table 1, a half number of the apostrophed comets are included in the upper-case group and another half in the lower-case group. It is remarkable to see that 85% of the comets with $2.9 \leq J < 3.1$ belongs to group A. This is partially explained by an approximate equation $U^2 = 3 - J$, where J is an expression of Tisserand's invariant and U is the total encounter velocity with Jupiter under the assumption of two-body interaction (Öpik 1963); for group A, U becomes nearly zero, so that large perturbations can be induced.

(2) The number of the large q -change comets whose q , semi-major axis, and aphelion distance decrease globally in their orbital evolution is much more than that of the comets that evolve in the opposite sense:

Among the 85 capital-letter comets, 59 (69%) showed the decreasing evolution, 9(11%) the increasing one, and 17 (20%) no specific trend. The decreasing evolution takes place mostly in the past, while the increasing one in the future. Therefore, in order to make unbiased comparison between the decreasing and increasing evolutions, the time span ratio for the future and the past (3400/1000) must be corrected to the number of the increasing evolution comets. However, the corrected number of the increasing evolution comets is $3.4 \times 9 = 31$, which is still only a half of the decreasing evolution comets. This means that capture process is more favoured than ejection in the evolution of SP comets. This finding is consistent with the reported asymmetry in the distribution of energy perturbation (Nakamura 1981; Manara and Valsecchi 1991) which prefers the paths toward shorter-period orbits. Interestingly, on the contrary, Everhart(1969) and Carusi et al.(1990) report the opposite tendency. This discrepancy will thus be a subject of further investigations.

(3) Most of the orbits before capture into Jupiter family have $q \sim 5$ AU:

All of the 59 captured SP comets mentioned in the previous paragraph were originated from the orbits of $q \sim 5$ AU. These comets correspond to the ones in the "capture region" by Jupiter, first confirmed numerically by Everhart (1972). The orbits before capture are also characterized by the very flat nature of q . Eight out of the 59 captured comets are shown to evolve from the orbits near Saturn and then to be relayed under the control of Jupiter; this is the first manifestation of the multiple-stage capture mechanism proposed by Everhart (1977). Some of the examples are given in Fig. 3. P/Hein-Roman-Alu 2, P/Honda-Mrkos-Pajdusakova, and P/Barnard 3 are found to be captured from the long-period orbits of $a = 75\sim 125$ AU into SP orbits through a few close encounters with Jupiter (Fig. 4).

(4) The evolutionary time scale for capture is much shorter than that predicted by

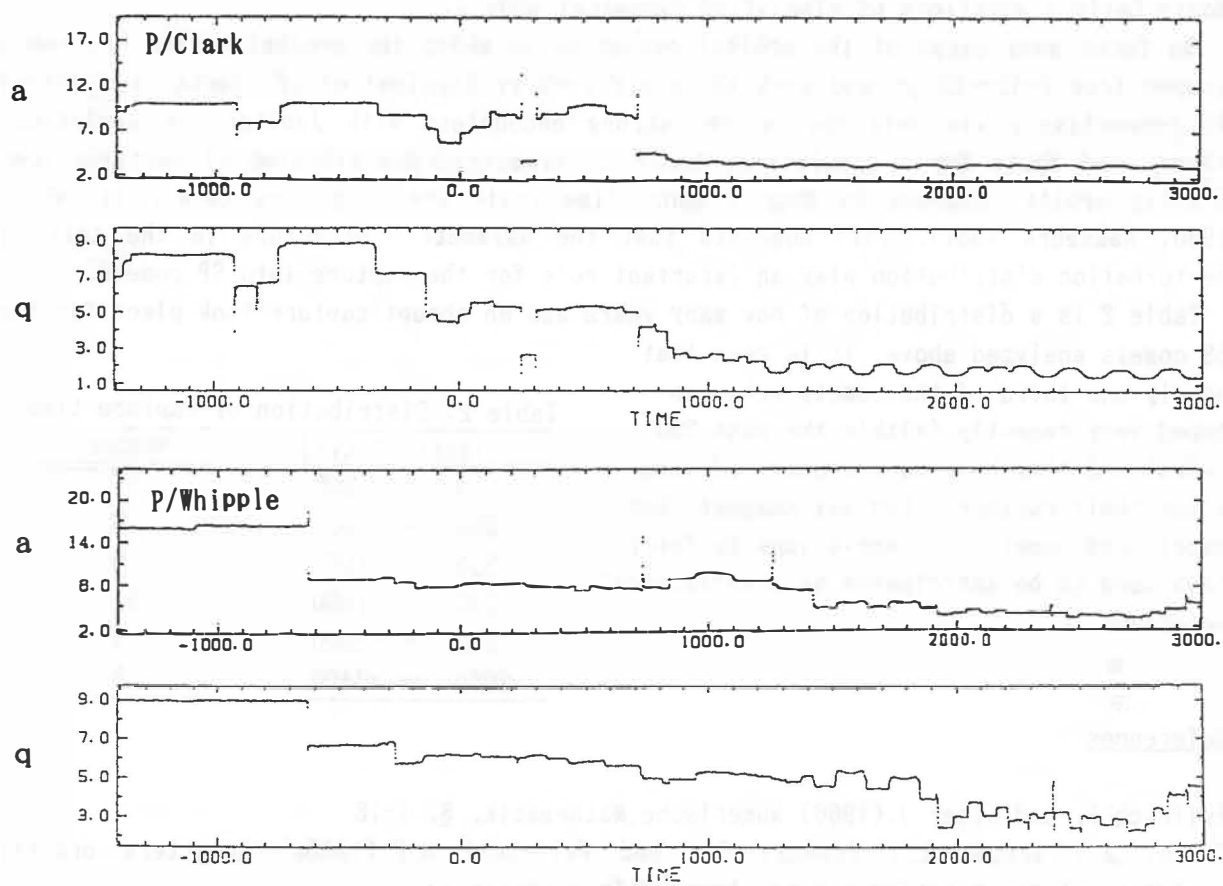


Fig. 3: Examples of relayed capture. The ordinate is in AU.

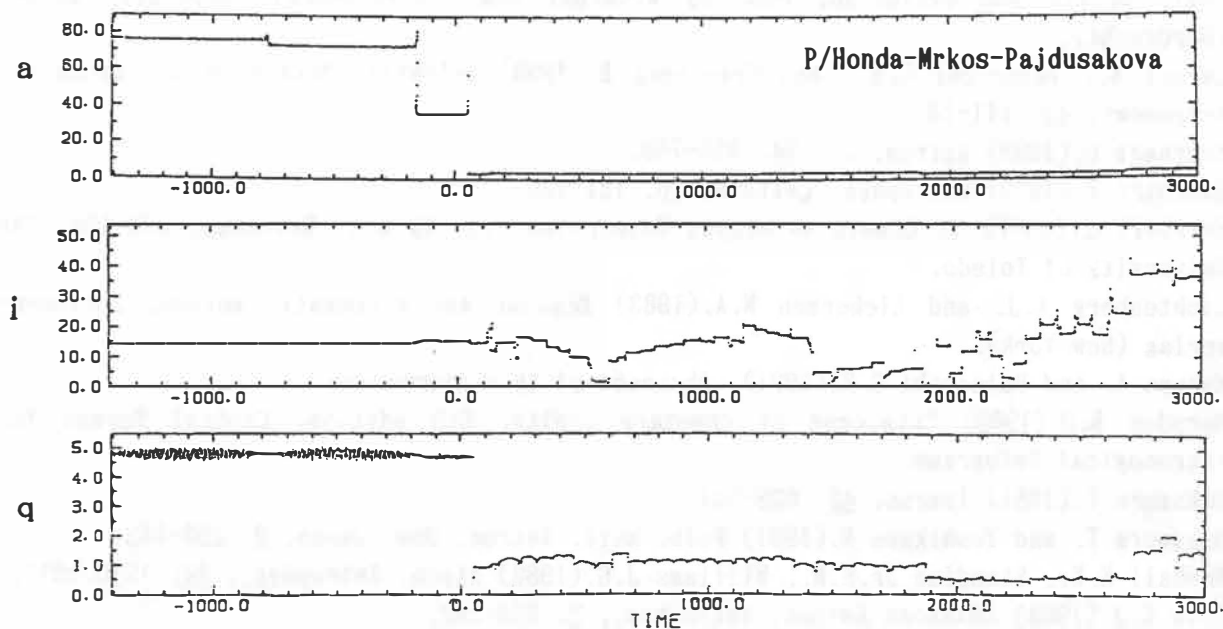


Fig. 4: An example of violent capture from a long-period orbit. a and q are in AU and inclination (i) is in degrees.

Monte Carlo simulations of simplified dynamical models:

We found many cases of the orbital evolution in which the orbital period (P) and q jumped from $P=12\sim20$ yr and $q\sim5$ AU into $P=6\sim7$ yr (typical of SP comets) and $q=1\sim2$ AU respectively via only one or two strong encounters with Jupiter. In analytical theory and Monte Carlo simulations based on symmetric distribution of perturbation, drastic orbital changes in such a short-time scale are very rare (e.g., Yabushita 1980; Nakamura 1981). This suggests that the asymmetric structure in the tail of perturbation distribution play an important role for the capture into SP comets.

Table 2 is a distribution of how many years ago an abrupt capture took place for the 59 comets analyzed above. It is seen that nearly one third of the comets were captured very recently (within the past 200 years) and they have been discovered soon after their capture. This may suggest that overlooked comets in observations be fewer than used to be anticipated as observational selection.

Table 2: Distribution of capture time

Interval (yr)	Number
0 ~ -200	17
-200 ~ -500	9
-500 ~ -1000	5
-1000 ~ -1500	11
-1500 ~ -2000	9
-2000 ~ -3400	8

References

- Bulirsch R. and Stoer J.(1966) *Numerische Mathematik*, 8, 1-13.
 Carusi A., Kresak L., Perozzi E., and Valsecchi G.B.(1985a) Long-term orbital evolution of short-period comets, Adams Hilger (Bristol).
 Carusi A., Kresak L., Perozzi E., and Valsecchi G.B.(1985b) in *Dynamics of Comets: Their origin and evolution*, eds. by A.Carusi and G.B.Valsecchi, p203-214, Reidel (Dordrecht).
 Carusi A., Valsecchi G.B., and Greenberg R.(1990) *Celestial Mechanics and Dynamical Astronomy*, 49, 111-131.
 Everhart E.(1969) *Astron. J.*, 74, 735-750.
 Everhart E.(1972) *Astrophys. Letters*, 10, 131-135.
 Everhart E.(1977) in *Comets Asteroids Meteorites*, ed. by A.H. Delsemme, p99-104, The University of Toledo.
 Lichtenberg A.J. and Lieberman M.A.(1983) *Regular and stochastic motion*, Springer-Verlag (New York).
 Manara A. and Valsecchi G.B.(1991) Abstract of this symposium.
 Marsden B.G.(1989) Catalogue of cometary orbits, 6th edition, Central Bureau for Astronomical Telegrams.
 Nakamura T.(1981) *Icarus*, 45, 529-544.
 Nakamura T. and Yoshikawa M.(1991) *Publ. Natl. Astron. Obs. Japan*, 2, 293-383.
 Newhall X.X., Standish Jr.E.M., Williams J.G.(1983) *Atron. Astrophys.*, 84, 1910-1917.
 Öpik E.J.(1963) *Advances Astron. Astrophys.*, 2, 219-262.
 Yabushita S.(1980) *Mon. Not. Roy. astr. Soc.*, 190, 71-73.

ROTATIONAL BEHAVIOR OF COMET NUCLEI UNDER GRAVITATIONAL PERTURBATIONS

P. Oberti¹, E. Bois², C. Frœschlé¹

Observatoire de la Côte d'Azur

¹Le Mont Gros, B.P. 139, F-06003 Nice Cedex, France

²Av. Nicolas Copernic, F-06130 Grasse, France

Abstract. A dynamical qualitative study of the rotational motion for cometary-type bodies submitted to gravitational perturbations has been performed by numerical simulations, including the Sun and Jupiter's disturbing torques in the model. Results show small gravitational disturbing effects from the Sun on Halley-type orbits, as well as from Jupiter on most close-approach configurations. Only a very close-approach induces notable effects, presenting then some interesting sensitivity to initial conditions.

INTRODUCTION

Nucleus rotation is assumed to greatly influence solar exposure and thus gas ejection, or more generally non-gravitational forces. Some preliminary works investigating gravitational effects on the rotational motion of cometary-type bodies are required to figure out the basic mechanisms. They are developed in Bois *et al.* (1991), including solar and jovian gravitational disturbing torques in the numerical simulations.

Two different angular sequences are used to locate a body-fixed rotating frame (O, x, y, z) relative to a fixed reference frame (O, X, Y, Z), both with the origin at the center of mass: 3-1-3, and 1-2-3. Numbers 1, 2, and 3 refer respectively to the axes x or X , y or Y , z or Z . Shifting rules can be found in Bois (1986). The two sequences are of different types, and the singularities occur for different configurations. However, after the integration has been carried out, the motion is only described in the classical 3-1-3 sequence (precession ψ , nutation θ , proper rotation φ), making it easier to interpret the results. Throughout the paper, the comet nucleus is modeled by an ellipsoid, its three axes of inertia being chosen with the following order: $a > b > c$. The rotation of greatest energy is applied around c . For every figure, the angle φ is plotted without its mean rotation.

SOLAR GRAVITATIONAL PERTURBATION

In the following, the solar gravitational torque acts on an assymmetric comet nucleus. Tests are performed for the following initial orientation: $\psi = 0$, $\theta = 60$, $\varphi = 0$ deg, with only one initial period: $P_\varphi = 2.2$ days. The shape is given by: $a = 10$, $b = 5$, and $c = 1$ km, and the orbit is Halley's one. The curves present the differences between non-perturbed and perturbed cases, plotted at perihelion, with identical initial conditions. Figure 1 shows the variations of the angular momentum. Librations shown on figure 2 are then due to the solar disturbing action. They are of order several hundreds of arc seconds on this 20-day simulation. The solar gravitational perturbation changes a little bit the rotational pattern at each perihelion passage. Its action remains to be compared with non-gravitational effects (Peale and Lissauer, 1989).

JOVIAN CLOSE-APPROACH

The comet is moving on an inner orbit in Jupiter's mean plane. Comet parameters are chosen in such a way that the close encounter occur near the aphelion of both the comet and Jupiter, for different minimum distances between the two bodies. The eccentricity is Halley's one.

For an encounter distance of 1 AU, Jupiter's influence is almost negligible. When the encounter occurs for 0.1 AU, only small effects can be detected on the rotational motion, in contrast to the great changes on the orbital motion.

When the encounter distance is planned to occur at 0.01 AU, the comet is ejected from an almost

keplerian orbit two days before the anticipated aphelion. The osculating semi-major axis and eccentricity undergo a brief but strong impulse before decreasing. Their initial values were 2.77 AU and 0.965. For the last three figures, angular initial values are: $\psi = 0, \theta = 60, \varphi = 0$ deg, and initial periods are: $P_\psi = 7.4, P_\varphi = 2.2$ days. Because the close-approach happens far from the Sun, the angular momentum is almost constant until 2 or 3 days before the encounter (fig. 3). After the encounter, an almost constant pattern returns, and libration amplitudes for the angles have strongly increased (fig. 4). Figure 5 shows the pulse shape of Jupiter's torque. The motion is greatly sensitive to particular sets of initial conditions, then depending on the particular comet orientation at the encounter moment. With almost identical initial conditions, the global behavior can be opposite to the previous one, with largely decreased libration amplitudes.

CONCLUSION

Physical librations due to gravitational solar perturbations have small amplitudes relative to simple oscillations obtained without perturbations. A close-approach with Jupiter leads to a limited change on the rotational motion compared to the orbital one. However, the motion is greatly sensitive to particular sets of initial conditions. This could be a hint for a possible zone of non-predictible motions in the phase space. This preliminary but necessary study of gravitational effects on a rotational pattern has to be extended by modeling non-gravitational forces, investigating that way other possible motions in the Sun's vicinity.

References

- Bois, E. (1986) First-order theory of satellite attitude motion - Application to Hipparcos. *Celestial Mech.*, **39**, 309-327.
- Bois, E., Oberti, P., Frœschlé, C. (1991) Gravitational Model of Comet Nucleus Rotation. *Celestial Mech.*, submitted.
- Peale, S.J., Lissauer, J.J. (1989) Rotation of Halley's comet. *Icarus*, **79**, 396-430.

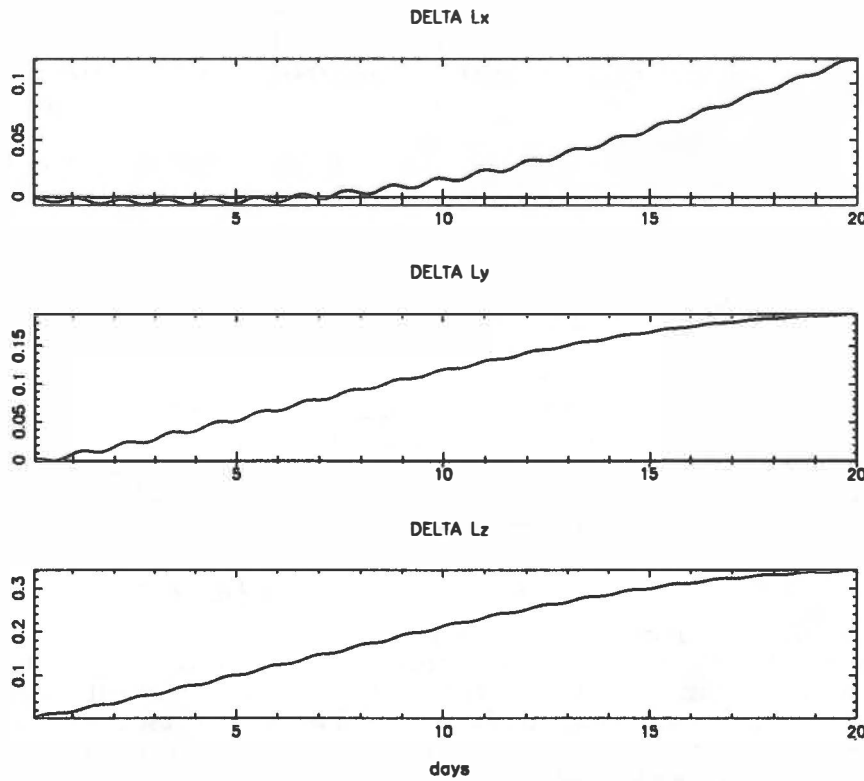


Fig. 1. Solar perturbation on the angular momentum

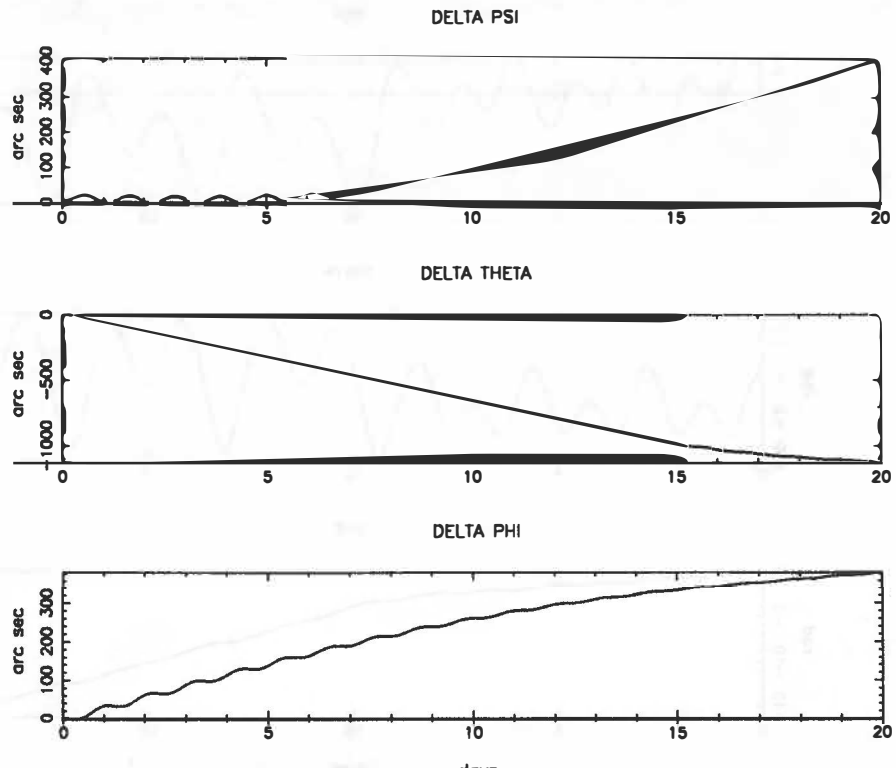


Fig. 2. Physical librations due to solar torque

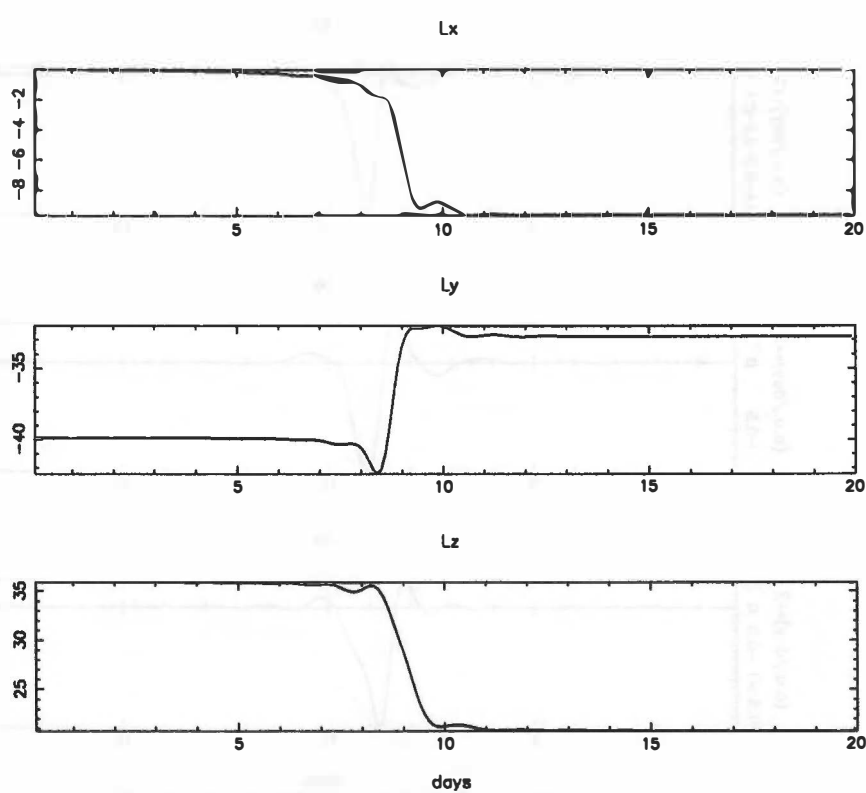


Fig. 3. Jovian perturbation on the angular momentum

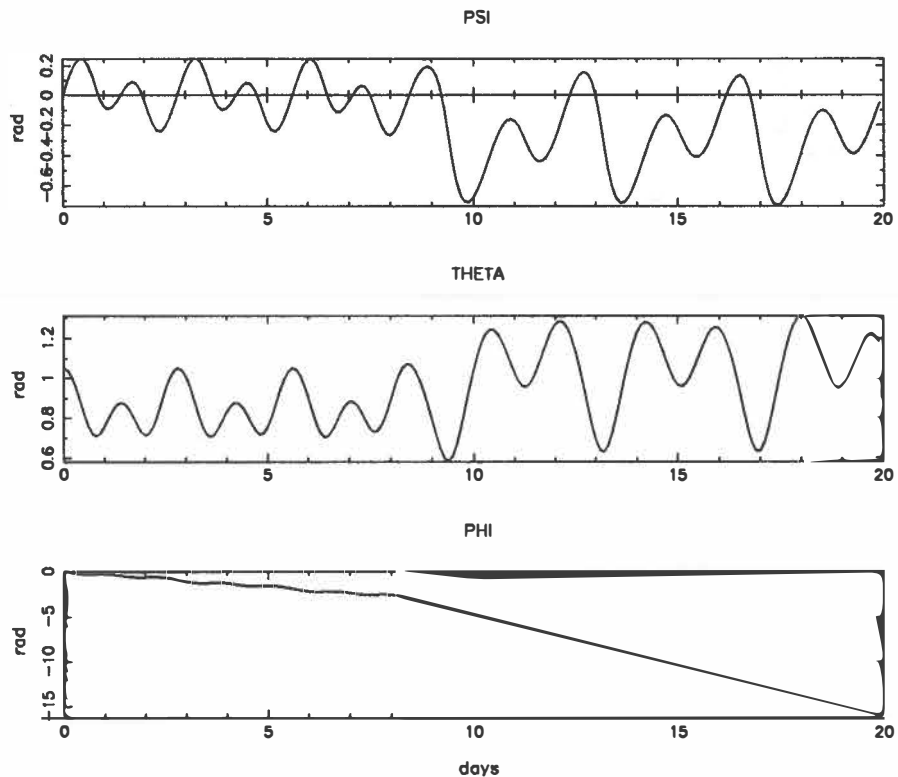


Fig. 4. Jovian close-approach effect

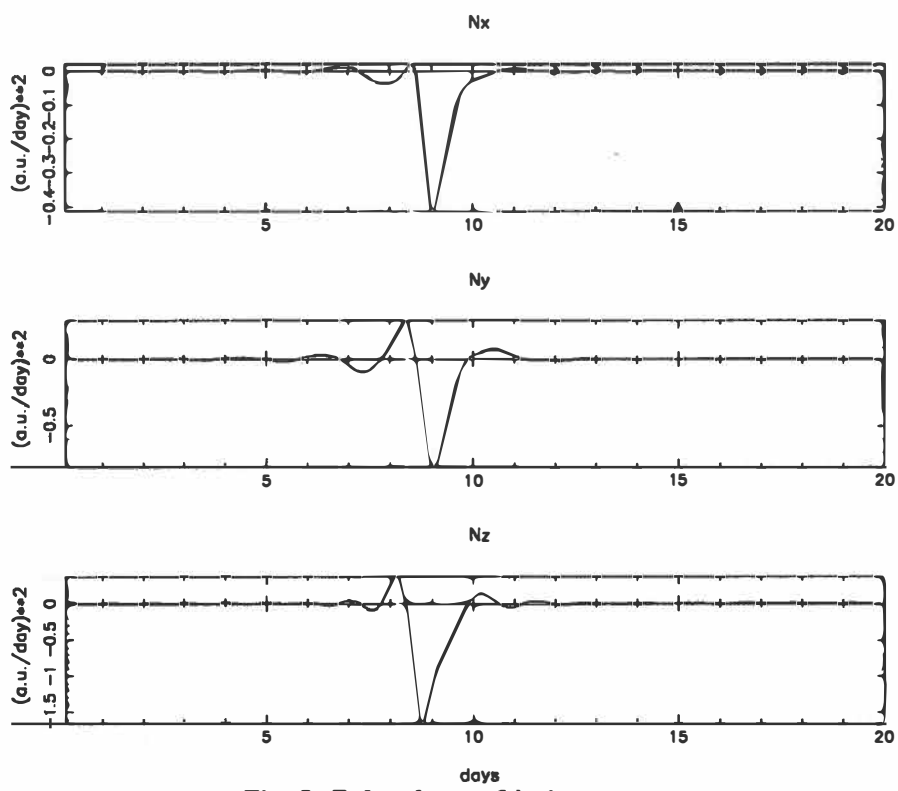


Fig. 5. Pulse shape of jovian torque

15 Years of Comet Photometry: A Comparative Analysis of 80 Comets.

D.J. Osip^{4,1}, D.G. Schleicher¹, R.L. Millis¹, M.F. A'Hearn², P.V. Birch³

1. Lowell Observatory 2. University of Maryland

3. Perth Observatory 4. University of Florida

ABSTRACT

In 1976 we began a program of narrowband photometry of comets that has encompassed well over 400 nights of observations. To date, the program has provided detailed information on 80 comets, 11 of which have been observed on multiple apparitions. In this paper we present the observed range of compositions (molecular production rate ratios) and dustiness (gas production compared with $Af\rho$) for a well sampled group of comets. Based on these results we present preliminary analysis of taxonomic groupings as well as the abundance ratios we associate with a 'typical' comet.

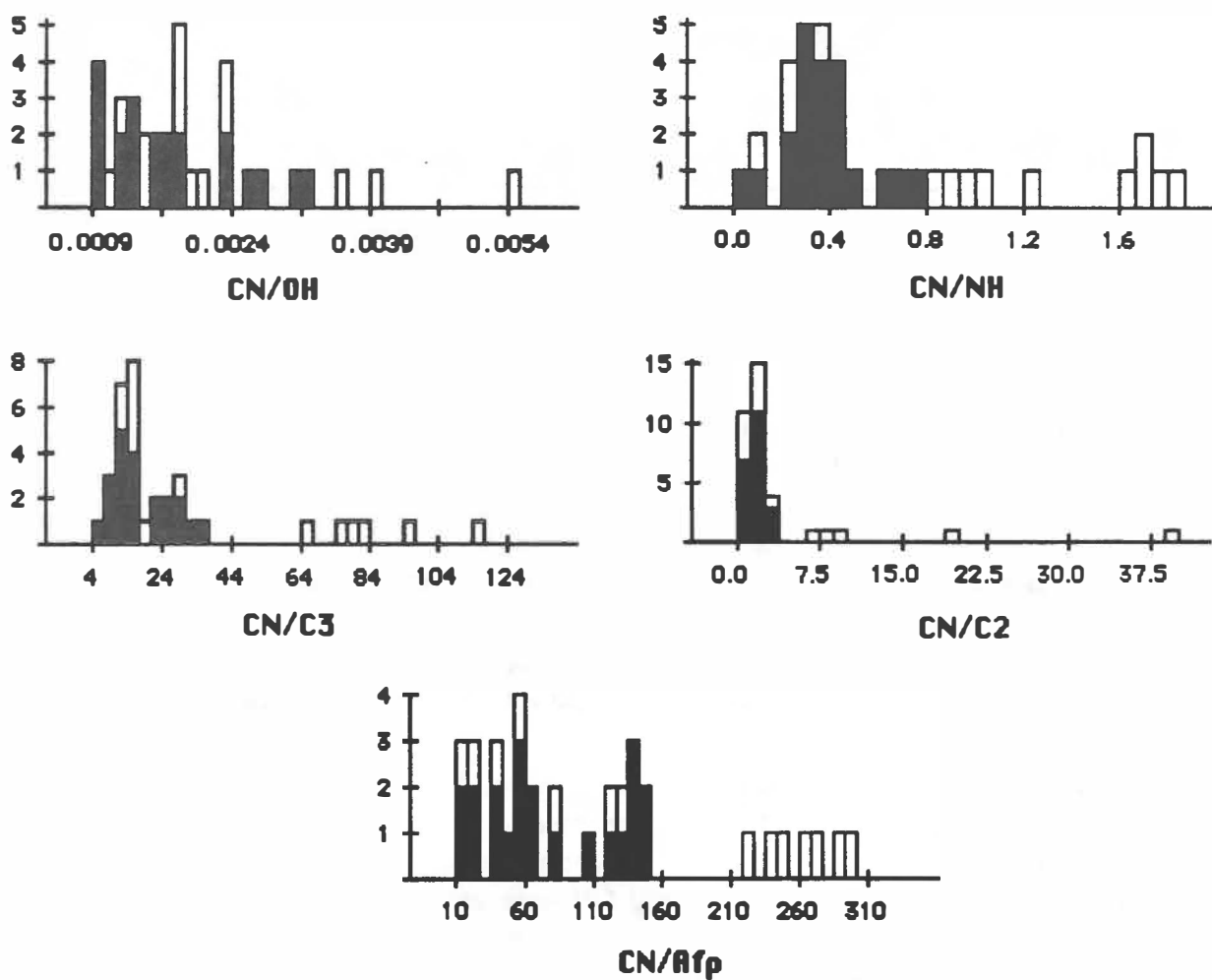
INTRODUCTION

Given the ever increasing number of comets that have been studied extensively, it is becoming possible to consider a statistically meaningful database of cometary observations and to determine what is typical for the production rate ratios (or molecular abundances) of comets. It is just such a database of observations that will be considered here, with 80 comets observed on 428 nights over the past 15 years. By applying some reasonably stringent criteria to initially limit the discussion to only the comets with well determined and verified abundances, one is able to define which comets are typical and which have deviations that may indicate actual taxonomic groupings. One wishes also to determine the correlations in the behavior of different molecular abundances, i.e., to determine which molecular species are most closely related in their apparent activity in comets as a whole.

The narrowband filter photometry observations discussed here are part of a 15 year program begun in 1976 by A'Hearn and Millis (A'Hearn *et al.* 1977). The project began with filters isolating emission of CN and C₂ as well as continuum band filters and later additional filters isolating the emission bands of C₃, NH, and OH were included. Observational techniques and reduction methods used have been detailed recently by Schleicher *et al.* (1991) and references therein. Parameters involved in the reduction and modelling of the data have evolved over time and accordingly, we have recently re-reduced the entire database. The Haser model was applied to convert molecular measurements to production rates, Q, as an aperture independent quantity. Similarly, in order to quantify the production of dust grains from our continuum data, we have used the now familiar quantity $Af\rho$, the product of the albedo of the grains, the fraction of the aperture filled by the grains, and the projected aperture radius (A'Hearn *et al.* 1984).

ANALYSIS and DISCUSSION

To minimize any errors introduced by modelling, prior to the actual analysis of the general characteristics of comets, the data for each individual comet was normalized to a common heliocentric distance of 1.5 AU using an r_H -dependence of -3 for the emission species and -2 for the dust. In the normalization and calculation of a mean production rate for each species, only the observational data obtained between 0.8 AU and 2.8 AU were included due to the adverse effects that a change in scalelengths used can have outside of this region. To insure that the observations were indeed representative of the comet, a given comet had to be observed on two or more nights and have three or more observations. Finally, only comets with observations in all filters (OH, NH, CN, C₃, C₂, and continuum) were included in this early analysis. Histograms showing the ratios of CN to each of the emission species as well as dust are given in the following figure for the 30 comets that satisfy all the above criteria.



The most important thing to note in the histograms is that the comets that stand out as anomalous in one molecular abundance ratio are not necessarily the same as those that stand out in another ratio. In fact, we have observed two strong correlations; one between those that stand out as depleted in C₂ and C₃ and another between those that are anomalously low in OH and NH with respect to CN. Although not presented here, separate two dimensional plots of the species

in question versus CN show the correlations very clearly. Further analysis also indicates the groupings that are suggested by the histograms are real and when one applies a rigorous cluster analysis, the groupings are clearly identifiable. It is not yet possible, however, to distinguish in all cases between distinct groups or the tail of a continuous distribution.

While the comets that are anomalous in some of the abundance ratios can appear quite ordinary in others, only those that show no anomalous behavior in any ratios are used to determine the range for a 'typical' comet. Note that four of the comets that exhibit normal molecular abundance ratios but have distinctly high gas-to-dust ratios are also excluded from the determination. The results for a 'typical' comet as determined by this reduced set of 17 of the 30 comets are the dark shaded regions of the histograms. The majority of the remaining 50 comets that did not meet the original selection criteria can also be classified within the bounds set here for a 'typical' comet. This supports our preliminary analysis defining what kind of molecular abundance ratios can be considered ordinary for a 'typical' comet.

CONCLUSIONS

Preliminary analysis of our data indicates a division of taxonomic groupings among comets based on differing molecular abundances. As indicated in the histograms, groupings include: a) comets depleted in C₂, C₃, and to a lesser degree, NH; b) comets with anomalously low OH, NH, and dust with respect to CN, but with normal ratios amongst the carbon bearing species; and c) a number of comets with distinctly high gas-to-dust ratios but indicating normal abundances for the emission species. Also apparent in the data are strong correlations between OH and NH, and between C₂ and C₃.

Finally, our preliminary analysis suggests the following molecular abundance ratios as normal for a 'typical' comet based on the restricted database.

	CN/OH	CN/NH	CN/C3	CN/C2	CN/dust
Mean	1.75e-3	0.65	20.69	1.64	91.72
Sigma	0.6e-3	0.34	9.43	0.76	57.21

ACKNOWLEDGMENTS

This work is supported by NASA grant NAGW-2366 and by NSF grant AST-87180871.

REFERENCES

- A'Hearn, M.F., Thurber, C.H., Millis, R.L. (1977) Evaporation of Ices from Comet West. *Astron J.* **82**, 518-524.
 A'Hearn, M.F., Schleicher, D.G., Feldman, P.D., Millis, R.L., Thompson, D.T. (1984) Comet Bowell 1980b. *Astron J.* **89**, 579-591.
 Schleicher, D.G., Millis, R.L., Osip, D.J., and Birch, P.V. (1991) Comet Levy (1990c): Groundbased Photometric Results. *Icarus*, in press.

THE SHAPE OF ASTEROID 1917 CUYO

S. J. Ostro

Jet Propulsion Laboratory, California Institute of Technology

and

W. Z. Wisniewski

Lunar and Planetary Laboratory, University of Arizona

ABSTRACT

Lightcurves obtained for 1917 Cuyo at solar phase angles near 54° have an amplitude $\Delta m = 0.44$ mag. However, convex-profile inversion of the lightcurves yields an estimate of the asteroid's mean cross section (\mathcal{Q} , a 2-D average of the 3-D shape) that is only slightly noncircular, with an elongation ~ 1.15 . The estimate of \mathcal{Q} undoubtedly contains systematic errors, the most severe of which could arise from non-equatorial viewing/illumination geometry. However, Cuyo's radar echo shows very little variation in bandwidth vs. rotation phase, supporting the hypothesis that this asteroid's elongation is rather modest.

INTRODUCTION

The Amor asteroid 1917 Cuyo (1968 AA) passed within 0.15 AU from Earth in October 1989, during the most favorable apparition for groundbased astronomy until 2030 (Harvey, 1989). The object was observed by one of us (WZW) with a CCD camera on the 2.3-meter Steward Observatory telescope on Kitt Peak and with radar by Ostro et al. (1991) from Arecibo and Goldstone during a two-week period near closest approach (Table 1). Figure 1 shows the lightcurves and results of inverting those data, and Fig. 2 shows radar echo spectra. All analyses discussed here use the apparent rotation period, $P = 2.693$ h, determined from the lightcurves.

Table 1. Observations of Cuyo

Observation	UTC dates spanned	RA	Dec.	Distance (AU)	
		(h)		Earth	Sun
radar (Arecibo)	1989 Sep 26 to 30	20.3	9°	0.17	
CCD photometry	1989 Oct 7	21.0	-13°	0.14	1.08
	to 8	21.1	-16°	0.14	1.08
radar (Goldstone)	1989 Oct 9 to 11	21.3	-22°	0.14	

SHAPE CONSTRAINTS FROM LIGHTCURVES

Under certain ideal conditions, one can use "convex-profile inversion" of a lightcurve to estimate a profile that is a 2-D average of the asteroid's shape (Ostro et al. 1988). That profile is called the mean cross section, \mathcal{Q} , and is defined as the average of the envelopes on all the surface contours parallel to the equator. The ideal conditions for estimating \mathcal{Q} include Condition GEO, that the scattering is uniform and geometric; Condition EVIG, that the viewing-illumination geometry is equatorial; and Condition PHASE, that the solar phase angle ϕ is known and nonzero. The logic behind these conditions is that they collapse the 3-D lightcurve inversion problem, which cannot be solved uniquely, into a 2-D problem that can.

Condition EVIG, that the sub-Earth and sub-Sun points lie on the equator, and Condition PHASE imply that ϕ equals its equatorial component ϕ_{eq} ; this component creates the mapping between odd harmonics in ζ and those in the lightcurve. If $\phi_{eq} = 0$, then an equatorial lightcurve of a uniform, geometrically scattering asteroid will contain no odd harmonics. For this reason, inversion of an opposition lightcurve furnishes an even-harmonic-only version of ζ called the symmetrized mean cross section, ζ_s .

Convex-profile inversion of the Cuyo lightcurves yields the estimates of ζ and ζ_s shown in Fig. 1. These averages of Cuyo's shape rotate clockwise. The Earth is at the top of the page and the Sun is ϕ degrees clockwise from that direction. For each date, the rotation phase origin is defined by the first data point on that date. A subtlety of Condition PHASE is that the sign of ϕ used in "convex-profile inversion" corresponds to the asteroid's rotation sense. The sign is positive if the asteroid rotates through ϕ from the Earth direction to the Sun direction, a configuration that pertains to Cuyo in October 1989 if the asteroid's rotation is direct. The inversions in Fig. 1 that use a positive sign for ϕ are labeled "+DS" because here our view of the mean cross section is from the south, i.e., parallel to the spin vector. The sign of ϕ is negative if the asteroid rotates through ϕ from the Sun direction to the Earth direction, a configuration that pertains to Cuyo in October 1989 if the asteroid's rotation is retrograde. The inversions in Fig. 1 that use a negative sign for ϕ are labeled "-RN" because here our view of the mean cross section is from the north, i.e., antiparallel to the spin vector. For our data, the two signs are equally acceptable and give nearly identical results.

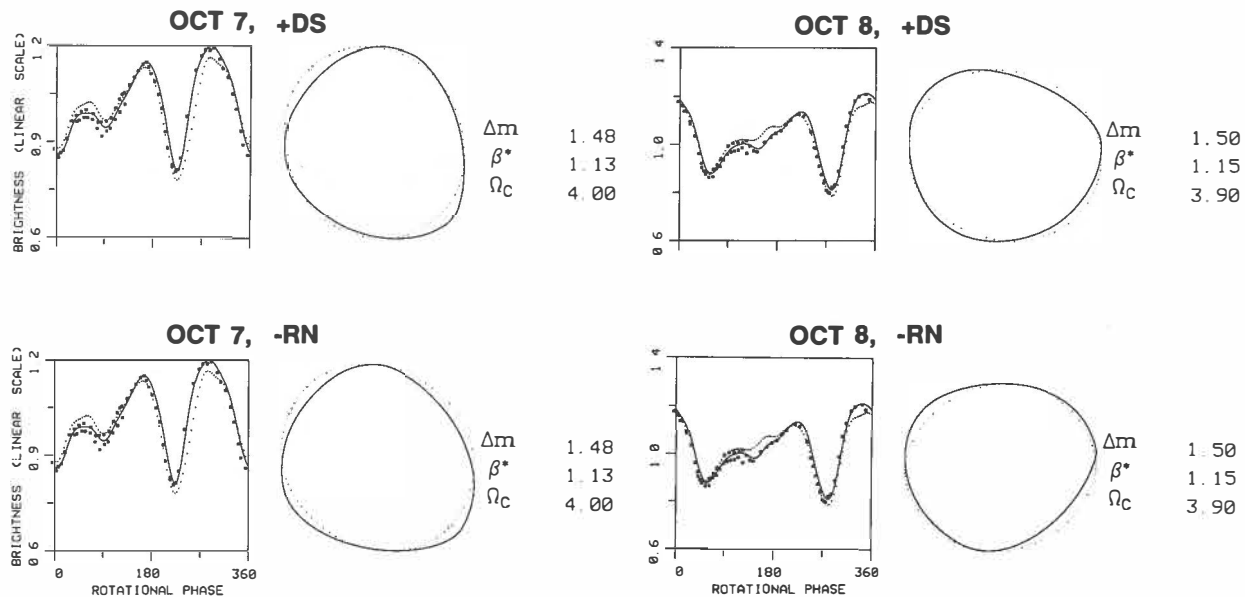


Figure 1. Cuyo lightcurves obtained on Oct. 7 and 8, and convex-profile inversion results obtained for each date using +/- signs for the solar phase angle (top/bottom plots). Estimates of ζ and ζ_s are shown as solid profiles and dotted profiles. Lightcurves are plotted on linear scales, with unit average brightness; the large symbols are the data, the solid curve was derived from a Fourier series fit to the data, and the dotted curve was derived from a constrained Fourier series corresponding to the estimate of ζ . On the right, Δm is the ratio of the lightcurve's maximum to its minimum; β^* is ζ 's breadth ratio; and Ω_c is ζ 's non-circularity, defined as the "distance" of the mean cross section from a circle (Ostro et al. 1988).

Cuyo's elongation

The mean cross section \mathcal{L} can be represented by a radius-of-curvature function or by that function's Fourier series \mathbf{x} . Under the ideal conditions, there is a one-to-one mapping from the coefficients in \mathbf{x} to the coefficients in the Fourier series for the lightcurve. At phase angles as large as those during the Cuyo photometry, \mathcal{L} 's third harmonic (and to a lesser extent each of its higher odd harmonics) propagates very efficiently into the lightcurve's corresponding harmonic; see Fig. 3 of Ostro et al. 1988. That is why convex-profile inversion of Cuyo's lightcurves, which contain a very strong third harmonic, yields a "quasi-triangular" estimate of mean cross section.

The breadth ratio, β^* , of Cuyo's mean cross section is estimated to be about 1.14. That is, the elongation of the asteroid's mean latitudinal contour is apparently very small. Here we have a good example of how the amplitude of a large- ϕ lightcurve severely overestimates elongation. This bias, which is commonly referred to as the phase-amplitude relation, is a consequence of basic aspects of lightcurve-acquisition geometry that are codified in convex-profile inversion theory (Ostro et al. 1988).

The estimates of \mathcal{L} and hence β^* can contain systematic error if Conditions GEO or EVIG are violated, as they must be to some extent). Ostro et al. (1988) studied such error under simplified circumstances. At large ϕ , nongeometric scattering can distort estimates of \mathcal{L} , but the distortions are not very severe. On the other hand, if the viewing/illumination geometry is far from equatorial, then an elongated asteroid's β^* can be severely underestimated unless the Earth and Sun are opposite sides of the object's equatorial plane; see section IV.A of the referenced paper.

INFORMATION FROM RADAR

The Cuyo datasets from Arecibo and Goldstone (Ostro et al. 1991) consist of echo spectra that provide fine rotation-phase coverage but are not quite strong enough to yield a reliable estimate of the object's pole-on silhouette, as has been done for a few other objects. However, visual inspection of the spectra leads to two useful conclusions, as follows.

First, the echo bandwidth varies imperceptibly with rotation, supporting the inference from the lightcurve inversion that this asteroid is not very elongated. Second, the Goldstone and Arecibo weighted-sum spectra have bandwidths (~ 160 Hz, ~ 40 Hz) only slightly larger than the ratio of the telescopes' transmitter frequencies (8495 MHz, 2380 MHz), implying that $\cos \delta$, the cosine of the asteroid-centered declination of the radar, did not change very much during Sep 26 - Oct 11 despite a 34° change in geocentric direction. This result suggests that the view during the photometry was closer to equatorial than to pole-on, and that the view may have been slightly closer to equatorial during the October observations than in September. Hence, we find no evidence in the radar spectra for severe violation of Condition EVIG.

CONCLUSION

Our photoelectric and radar observations support the hypothesis that 1917 Cuyo is a relatively unelongated asteroid.

ACKNOWLEDGMENTS

WZW gratefully acknowledges support by NASA Grant NAGW-716. Part of this research was conducted at the Jet Propulsion Laboratory, California Institute of Technology, under contract with the National Aeronautics and Space Administration (NASA).

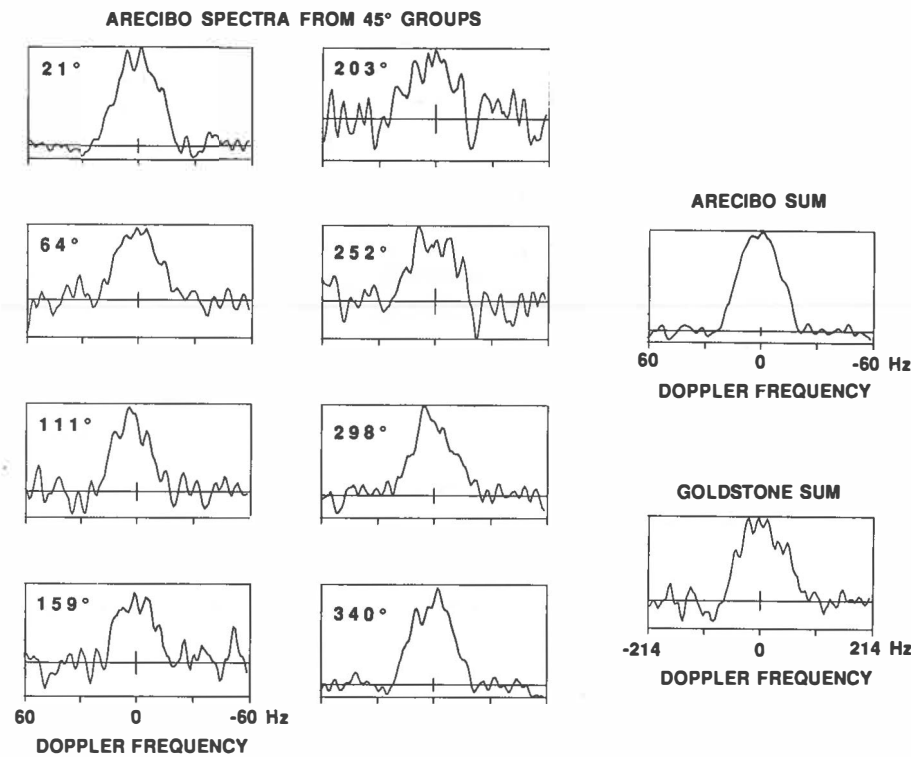


Figure 2. Radar echo spectra for 1917 Cuyo from observations reported by Ostro et al. (1991). In each plot, echo power in the OC polarization is plotted on an arbitrary linear scale vs. frequency, relative to the central frequency estimated by those authors. A horizontal line is drawn at the zero power level and a vertical bar at the origin indicates ± 1 standard deviation. At the left are weighted sums of Arecibo spectra from eight, 45° intervals of rotation phase; the weighted-mean phase is given. On the right are Arecibo and Goldstone weighted-sum spectra, smoothed to frequency resolutions (4.0, 14.3 Hz) and vignetted to windows (120, 428 Hz) in the same ratio as the instruments' transmitter frequencies (2380, 8495 MHz). These spectra can be thought of as one-dimensional images, or brightness scans across Cuyo's disc through a slit parallel to the projected spin vector. The length equivalent, in units of $\text{km}/\cos \delta$, of frequency is the same for all the spectra in this figure. δ , the asteroid-centered declination of the radar, may have changed during the dates spanned by the radar observations; see text. The ~40-Hz bandwidth of the Arecibo sum, when combined with the rotation period from the lightcurve, implies that the maximum breadth of Cuyo's pole-on silhouette is ~3.9 $\text{km}/\cos \delta_A$, with δ_A the value of δ during the Arecibo runs.

REFERENCES

- Harvey G. R. (1989) Close approach ephemerides of 1865 Cerberus and 1917 Cuyo. *Minor Planet Bull.*, **16**, 36-37.
- Ostro S. J., Connelly R., and Dorogi M. (1988) Convex-profile inversion of asteroid lightcurves: Theory and applications. *Icarus*, **75**, 30-63.
- Ostro S. J., Campbell D. B., Chandler J. F., Shapiro I. I., Hine A. A., Velez R., Jurgens R. F., Rosema K. D., Winkler R., and Yeomans D. K. (1991) Asteroid radar astrometry. *Astron. J.*, **102**, 1490-1502.

THE IMPORTANCE OF GUIDING ON THE MOTION OF A COMET IN ASTROMETRIC OBSERVATIONS

Thierry PAUWELS

Koninklijke Sterrenwacht van België, Ringlaan 3, B-1180 Brussel, Belgium

Abstract. In this paper we discuss the influence of guiding on the motion of a comet on the derived astrometric position.

Key words: comets - astrometry

1. THEORY

When doing astrometric observations of a comet, one is not interested in a beautiful picture, nor in showing the tail of the comet. Often it may seem unnecessary to guide on the motion of the comet. A plate guided on the motion of the stars and with a trailed image of the comet can look very acceptable to be measured for an astrometric position. However, positions obtained in this way show a systematic error.

When observing for an astrometric position, one is interested in the nucleus of the comet. The nucleus itself can never be observed directly, but the central condensation will give a very good approximation of the position of the nucleus. One tries to find the maximum of the light distribution of the cometary image and to take that as the position of the comet. In reality the eye will not point the maximum itself, but the centre of some isophote surrounding this maximum closely.

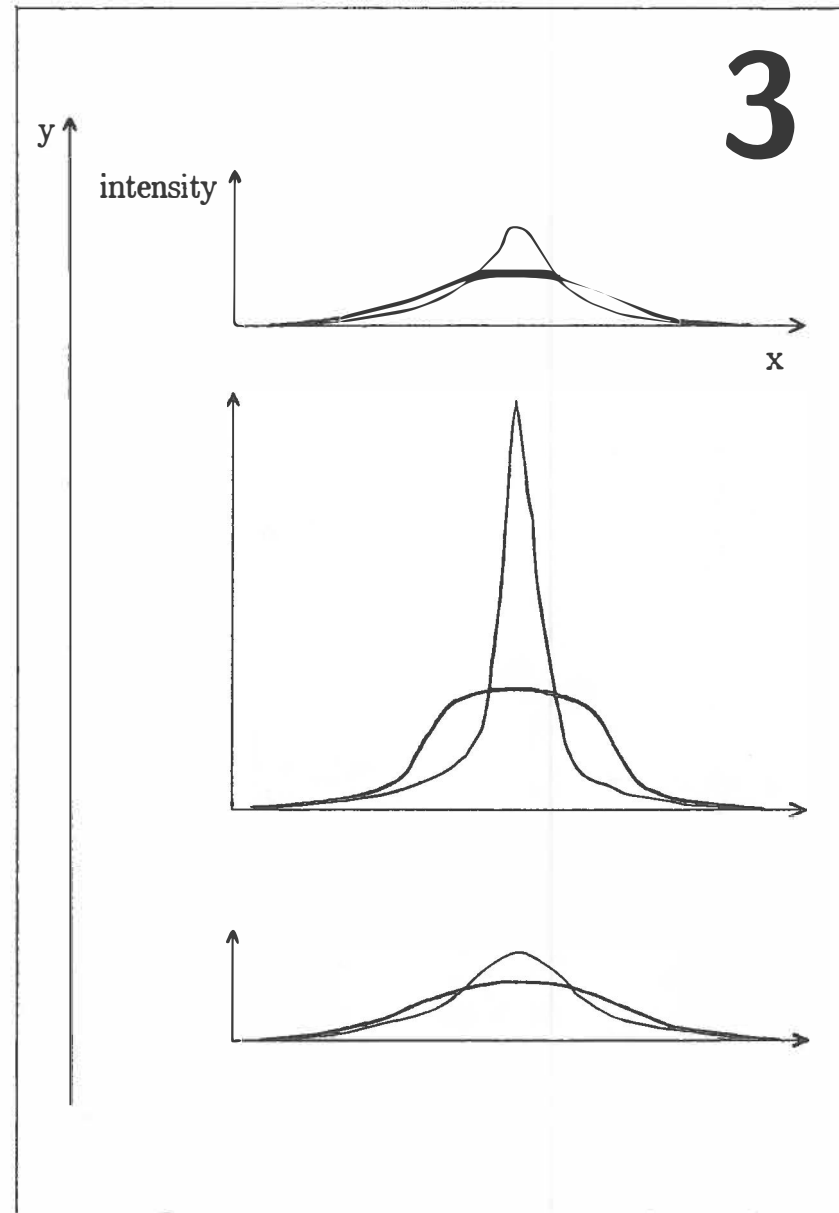
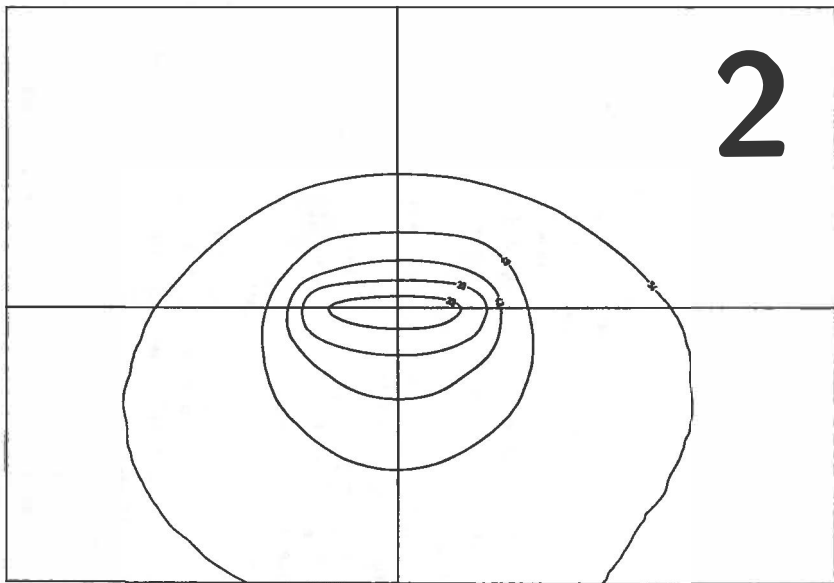
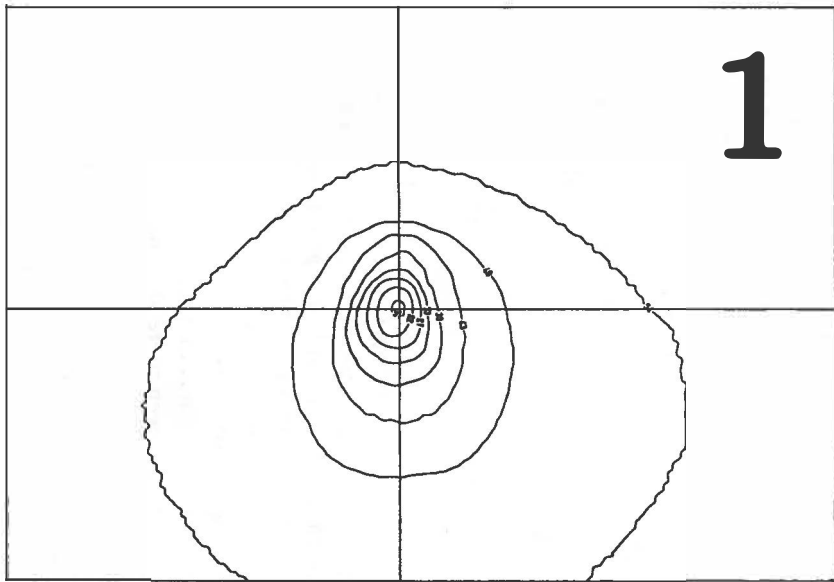
If the comet has moved (say, perpendicularly to the direction of the tail) during the exposure, then it may look as if there is a trailed central condensation, which can be measured quite well. However, this line of maximum intensity on the plate is not just the trail of the point of maximum intensity of the comet. At each point on the plate, the intensity is the integral of the intensity of the comet, integrated along the path of the comet on the plate. If we simplify by considering an infinitely long motion (say, parallel to the x-axis), then the intensity on the plate for the moving comet will be a function of one coordinate only (the y-coordinate). The intensity distribution on the plate will be the marginal distribution of the original light distribution of the comet. The maximum of this marginal distribution does not correspond to the y-coordinate of the maximum light intensity of the comet itself.

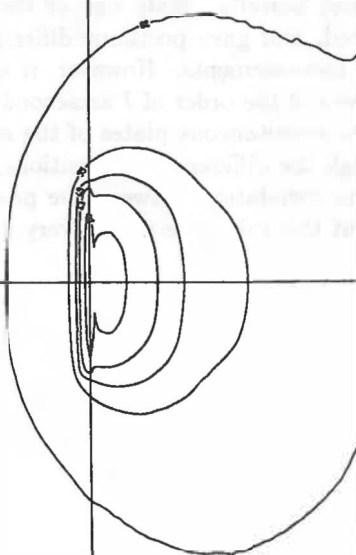
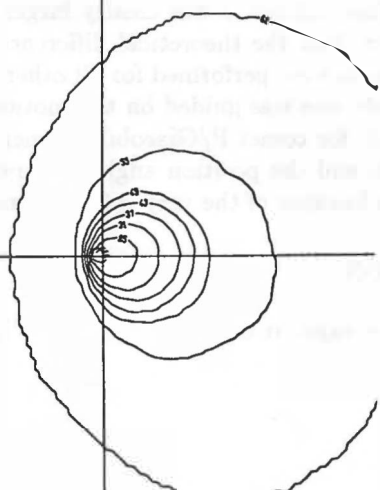
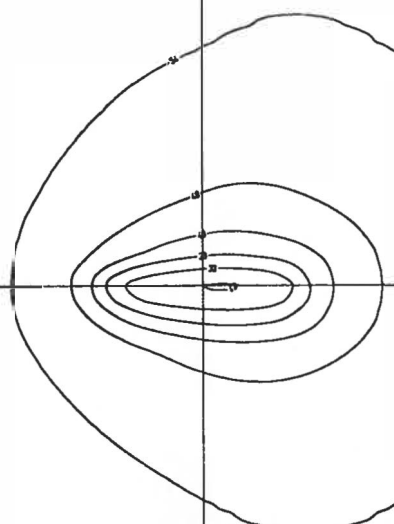
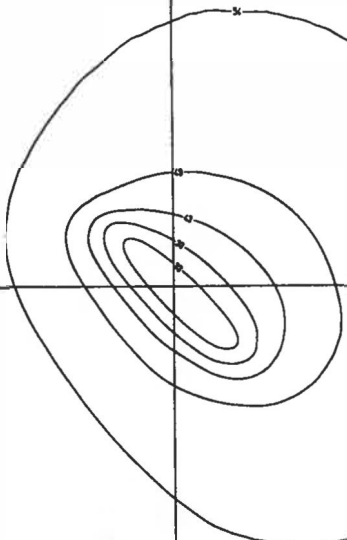
Figure 1 shows the light distribution of Comet Sorrells (1987 II) as measured on a plate taken with the Double Astrograph at Uccle. The comet is oriented with the tail down (parallel to the y-axis). The cross shows the position of maximum intensity (the derived position of the comet). Figure 2 shows the intensity distribution that would be obtained on a plate by letting the cometary image move horizontally at a constant speed, and with the same total exposure time. The minimum is slightly shifted down.

Figure 3 shows the two intensity distributions along the x-axis along cuts in different y-positions. The intensity for the moving comet is the convolution of the intensity for the non-moving comet with a block function. In the limit of infinitely long motion, it is just the area under the intensity distribution of the non-moving comet. For a cut through the maximum, the non-moving comet gives a sharp and high maximum; for a cut under (towards the tail) the maximum, due to the asymmetric light distribution of the original comet along the y-axis, the distribution along the x-axis will have a lower, but also less sharp maximum, i.e. with more prominent wings. The total area under the function can be larger, and thus give more intensity on a plate with a moving comet. For a cut above the maximum, the maximum will be sharp and low, and consequently give a much smaller area. Thus the maximum of the light distribution along the y-axis will be shifted towards the tail if the comet has moved on the plate during the exposure.

Figure 4 shows the intensity distribution for the same comet, but now moving parallel to the direction of the tail, and Figure 5 the same for a diagonal motion. The results are even more striking.

Figure 6 shows the same as figures 1 and 2, but now for a fictitious cometary image showing more asymmetry in the light distribution in the coma and with a more pronounced and sharper central condensation, in order to visualize better what is happening. The moving comet now gives two intensity maxima on the plate. The lower one is obtained in the same way as the maxima in the previous cases, and is the result of the asymmetry in the light distribution in the coma; the upper one comes from the trail of the central condensation. Measuring the latter one would give good positions, but in real cases the central condensation is too faint to show this trail.



6**4****5**

2. COMPARISON WITH OBSERVATIONS

This effect was found by taking two simultaneous plates at the Double Astrograph (Ukkel, Belgium) of Comet Sorrells. Only one of them could be guided on the motion of the comet. Both plates were measured, and gave positions differing by 4 arcseconds. This difference was clearly larger than the error on the measurements. However, it seemed to be also larger than the theoretical difference, which should have been of the order of 1 arcsecond. The same measurements were performed for all other cases where we had two simultaneous plates of the same comet of which only one was guided on the motion of the comet. Although the differences in positions could be very large ($40''$ for comet P/Giacobini-Zinner), there seemed to be no correlation between the position angle of the shift, and the position angle of the direction to the sun. But this might be due to very imprecise measurements because of the very diffuse cometary images.

3. CONCLUSION

Although it was theoretically proved that the effect does exist, it could not be shown irrefutably from observations.

A NEW METHOD FOR ASTROMETRIC OBSERVATIONS OF ASTEROIDS

Thierry PAUWELS

Koninklijke Sterrenwacht van België, Ringlaan 3, B-1180 Brussel, Belgium

Abstract. In this paper we propose a new method for photographic astrometric observations of asteroids. We discuss its advantages and disadvantages and compare them to the advantages and disadvantages of the classical photographic methods. The new method is best suited for observations on a spot where no CCD cameras, blink or stereo comparators are available and when a fast detection of unknown objects is required.

Key words: asteroids – astrometry

1. INTRODUCTION

When no accurate positions are known, on astrographic plates asteroids reveal themselves among the stars by their motion only. Therefore astrographic observations of asteroids are always done in such a way that moving objects can easily be detected on plates. Nowadays, plate scanners or CCD cameras have made this detection easier. However, CCD's still have a small field and are not available everywhere. Plate scanners are often not available close to the observing site. So, in many cases observers still have to use the old photographic methods, and afterwards scan the plates with their eyes. Here, we propose a new photographic method and compare its advantages and disadvantages with those of the well-known classical photographic methods. Since the proposed method is of no use in CCD observations, we shall not compare it to CCD observations.

2. SIX METHODS

First method. One long exposure: moving objects show trails.

DISADVANTAGES

- Much sky background on plate.
- Very difficult and uncertain detection of objects, especially when the exposure time is not too long: double stars can look exactly like moving objects.
- No indication of the sense of the motion of moving objects.
- Large reference stars, difficult to measure.
- Elongated moving objects, difficult to measure.

ADVANTAGES

- Detection of moving objects is reasonably fast.
- Very good plates for archival purposes (historical record for possible later use in other astronomical applications).

Second method. Trépied-Metcalf exposure: guided on the expected (mean) motion of the target object(s). Objects with this motion show circular images. Objects with slightly different motions show slightly elongated images.

DISADVANTAGES

- Detection of moving objects is very difficult, and almost impossible when no position is known in advance. Therefore this method should be used in combination with another method.
- Elongated reference stars, difficult to measure.
- Bad for archival purposes.
- Not possible when different target objects have very different motions.
- Target objects can be wiped out by star trails.

ADVANTAGES

- Moving objects will give very good measurements.
- Ideal for very faint objects.

Third method. Gated exposure: several exposures on the same plate without any shift between the exposures. The interruptions must be long enough to give detached images for objects moving at the expected speed. Usually the gating is asymmetric in order to give the sense of the motion.

DISADVANTAGES

- Much sky background on plate.
- Large reference stars, difficult to measure.
- Loss of time during the interruption(s).
- Images of object can be elongated, difficult to measure.
- Several images of the objects to be measured for only one position.
- Problem with epoch determination of position, especially if the shortest exposure(s) give images too faint to be measured.

ADVANTAGES

- Very fast and secure detection of moving objects.
- The sense of the motion of moving objects can be derived, provided that the gating is asymmetric.
- Good plates for archival purposes.

Fourth method. Two plates. These are taken with a certain time interval, so that moving objects have different positions. Moving objects are detected by blinking the plates or by stereo comparison. This method can be combined with the Trépied-Metcalf technique.

DISADVANTAGES

- Detection of moving objects impossible without a stereo or (expensive) blink comparator.
- Very slow detection of moving objects.

ADVANTAGES

- Very secure detection of moving objects.
- The sense of the motion of moving objects can be derived.
- No loss of time between the two plates (except when target objects are very slow).
- Good plates for archival purposes.
- Two independent positions can be derived.
- Possible even for extremely slow objects.

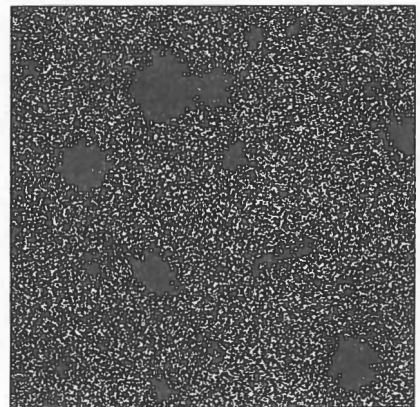
Fifth method. Several exposures on the same plate. Between the exposures there is a shift, so that all objects show several images. Moving objects, however, will show a different pattern. This method can be combined with the Trépied-Metcalf technique.

DISADVANTAGES

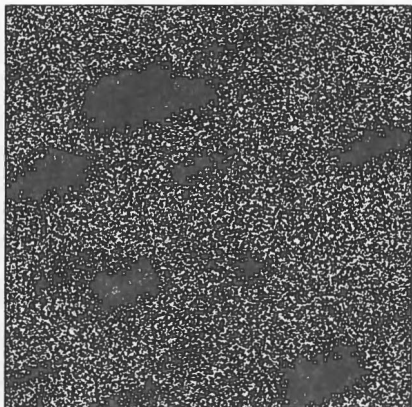
- Much sky background on plate.
- Very bad plates for archival purposes.
- Difficult detection of moving objects in crowded fields.

ADVANTAGES

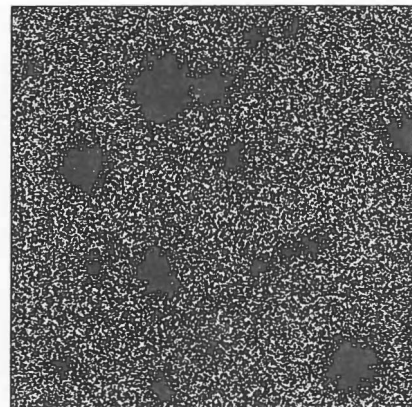
- Reasonably easy detection of moving objects in low-density fields.
- The sense of the motion can be derived.
- No loss of time between the exposures (except when target objects are very slow).
- Several independent positions can be derived.



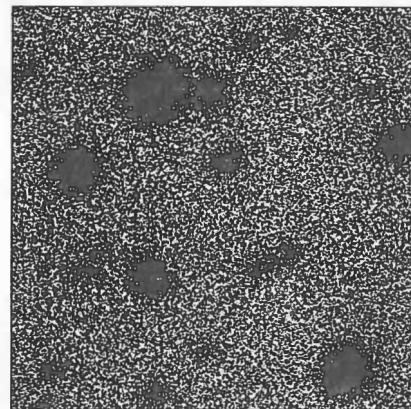
First method.



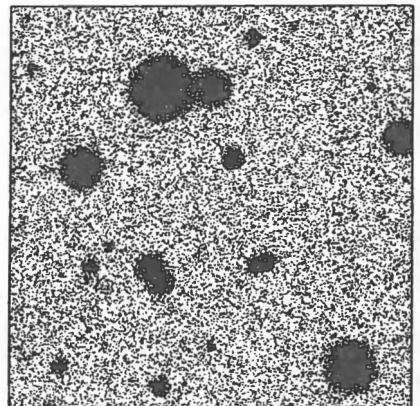
Second method.



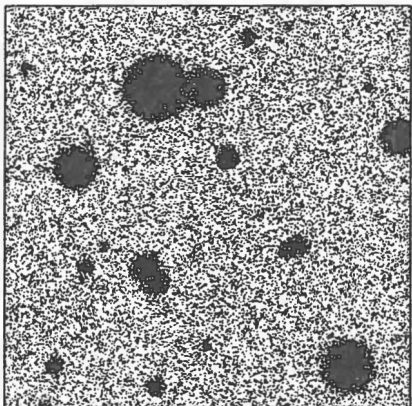
Third method.



Proposed method.



Fourth method.



Fifth method.

Figure. How a fictitious star field with an asteroid looks like in the classical methods and the proposed method. For a good view, hold about one metre from you.

Proposed method. Several superimposed Trépied-Metcalf exposures. A first exposure is started with the telescope guiding at the average motion of the target objects. After some time, the telescope is brought back to the starting position, and a new exposure is started. This is done as many times as the number of exposures (and asteroid images) wanted, with all exposures of the same length. The duration of these exposures should correspond to a motion that is at least the diameter of the images of the target objects on the plate, in order to get detached images for the target objects. Stars will show only one (elongated) image, while moving objects will show several images. For objects with exactly the introduced motion, the images are circular; for objects with slightly different motions, the images will be slightly elongated.

DISADVANTAGES

- Much sky background on plate.
- Reference stars are somewhat elongated, and difficult to measure.
- Only moderately good plates for archival purposes.
- Several images of the moving objects to be measured for only one position.
- The minimal exposure times must be long enough to detach the different images of the moving objects.
- Not possible when different target objects have very different motions.
- Not possible when target objects are too slow.

ADVANTAGES

- Very fast and secure detection of moving objects.
- No loss of time between the exposures.
- High accuracy measurements thanks to several almost circular images of moving objects.
- Good for faint objects.
- The sense of the motion can be derived.

3. CONCLUSION

All methods described here have their own advantages and disadvantages. The specific conditions in which observations are done will determine which of the advantages and disadvantages are dominant, less important or irrelevant. On a very good location with a very dark sky or with an instrument with long focal length the quantity of sky background is less important. When observing well-known objects the detection speed is irrelevant. Large stars are difficult to measure in the classical way, but this is no longer the case when using a Schmidt telescope (giving sharp spikes around bright stars), or when digitizing the plates. Combining two methods can also remove some of their disadvantages.

The proposed method seems to be best suited for observing on a site where no CCD cameras are available, where no blink or stereo comparator is at hand and where a fast detection of unknown moving objects is required. The observer can also use the proposed method for the discovery of objects, and use one of the classical methods (or small field CCD observations) for the follow-up.

Acknowledgements. The author would like to thank Dr. E. Bowell for his useful comments and for bringing the last disadvantage of the second method to his attention.

On LAMs and SAMs for Halley's Rotation

S. J. Peale

Dept. of Physics
University of California
Santa Barbara, CA

Abstract

Non principal axis rotation for comet Halley is inferred from dual periodicities evident in the observations. The modes where the spin axis precesses around the axis of minimum moment of inertia (long axis mode or LAM) and where it precesses around the axis of maximum moment of inertia (short axis mode or SAM) are described from an inertial point of view. The currently favored LAM model for Halley's rotation state satisfies observational and dynamical constraints that apparently no SAM can satisfy. But it cannot reproduce the observed post perihelion brightening through seasonal illumination of localized sources on the nucleus, whereas a SAM can easily produce post or pre perihelion brightening by this mechanism. However, the likelihood of a LAM rotation for elongated nuclei of periodic comets such as Halley together with Halley's extreme post perihelion behavior far from the Sun suggest that Halley's post perihelion brightening may be due to effects other than seasonal illumination of localized sources, and therefore such brightening may not constrain its rotation state.

INTRODUCTION

The properties of cometary comas which vary with time include the overall brightness, the intensities of emission lines from constituent molecules and the corresponding abundances of these molecules, the overall abundance of dust particles, and both molecular and dust jets that spray like garden hoses from the rotating nucleus. Superposed on the long term variation in comet activity due to the changing heliocentric distance are quasiperiodic variations of relatively short time scale. Both the long term and short period changes will concern us here. The extreme localization of the gas and dust emitting regions on the cometary nucleus was revealed in the images of comet Halley's nucleus obtained at the time of the encounter by the spacecraft Giotto (Keller *et al.* 1987). It is then natural to adopt a model of a cometary nucleus like the Halley prototype, where the surface is an insulating crust pierced in only a few places to allow volatiles to escape from the localized spots when warmed by the Sun. Much of the short term variability in the coma properties and the garden hose jets are then understood in terms of the distribution of localized sources being periodically warmed with resulting periodic gas and dust emission as the comet rotates under the Sun. As other physical processes also contribute to comet variability, it is important to understand the rotation state and its evolution in order to isolate for study the many processes affecting comet activity.

Toward that end, an enormous effort has been made to constrain the rotation state of Comet Halley. References to the many observational constraints are contained in papers in which models of Halley's rotation are constructed (*e.g.*, Julian, 1987, Peale and Lissauer, 1989, Belton, 1990, Belton *et al.* 1991, Samarasinha and A'Hearn, 1991). Although there is some range in the precise values of the periods of variation deduced by the observers (Belton, 1990), the case for the existence of two dominant periods, one near 2.5 days and the other near 7.4 days, is compelling. The dual periodicity seems to require that Halley's nucleus be in a state of non principal axis rotation, where precession of the instantaneous spin axis in a frame of reference fixed in the body leads to a periodic variation in the geometry of the solar illumination of the several localized sources that is superposed on a higher frequency variation caused by the rotation itself.

Non principal axis rotation is a common theme for all recently published models for Halley's rotation. In this state, the changing position of the spin axis relative to a frame of reference fixed in the nucleus leads to a corresponding change in the instantaneous equator. The centrifugal distortion of the nucleus due to the rotation thereby also periodically changes, and this flexing leads to dissipation of rotational kinetic energy. A completely isolated body would then eventually assume a minimum energy state of rotation about the axis of maximum moment of inertia consistent with the conserved angular momentum. For Halley, the time constant for an exponential decay to this state is about $10^6 Q$ years (Peale and Lissauer, 1989), where $1/Q$ is the specific dissipation function with Q having values near 100 for rock and probably smaller values for ice. Even with $Q = 1$, it is clear that non principal axis rotation, excited by either a piece breaking off the nucleus and suddenly changing the inertia tensor or by torques from the reaction to the localized jet emissions, would persist for many apparitions, and we may neglect the effects of damping.

The spin axis can precess stably about either the axis of maximum moment of inertia (Short Axis Mode or SAM) or that of minimum moment of inertia (Long Axis Mode or LAM). If E is the rotational kinetic energy and M is the spin angular momentum, the two modes can be distinguished conveniently with

$$\begin{aligned} A &\leq \frac{M^2}{2E} < B, \quad \text{for a LAM,} \\ B &< \frac{M^2}{2E} \leq C, \quad \text{for a SAM,} \end{aligned} \tag{1}$$

where $A < B < C$ are the principal moments of inertia. Although both SAMs and LAMs have been proposed for Halley's nucleus, Belton *et al.* (1991) and Samarasinha and A'Hearn (1991) independently find the same LAM model for Halley as the only one satisfying a long list of compelling observational constraints, where no SAM will do. However, one constraint not satisfied by this LAM model is the extreme post perihelion brightening and increased amplitude of short term variation in the light curve observed in both the 1910 and 1986 apparitions of comet Halley (Newburn, 1981; Schleicher, *et al.* 1990).

In the following we shall describe LAM's and SAM's as viewed from inertial space, construct light curves for particular published Halley models of source distribution and strength and rotation state, demonstrate why LAM's cannot yield the post perihelion brightening shown by Halley's light curve without unlikely high energy states or additional degrees of freedom beyond the simplest assumptions, show that such asymmetry is easy to produce with a SAM model by demonstrating a light curve that is asymmetric about perihelion, state the effects of torques on two published models where LAMs gain support for Halley's rotation state, describe a conjecture about the expectation of LAMs, and end with a discussion softening the remaining objection to a Halley LAM.

LAM

Halley's nucleus is about twice as long as it is thick, so we shall always approximate the nucleus with smooth ellipsoids of roughly this shape in describing the two rotational modes. If the equivalent ellipsoid is axially symmetric about the long axis ($B=C$), the only possible rotational mode is a LAM. Halley's long axis is easy to define, so we follow its motion as viewed from inertial space. Figure 1 shows a LAM which is characterized by the long axis and the angular velocity $\bar{\omega}$ rotating around the fixed angular momentum with average period P_ϕ while the nucleus rotates around the long axis with period P_ψ . The angular velocities ω_ϕ and ω_ψ corresponding to P_ϕ and P_ψ are shown as projections of $\bar{\omega}$ onto \mathbf{M} and the long axis respectively. If $B = C$, the rates are constant, P_ϕ is constant, the path of $\bar{\omega}$ on the

surface of the ellipsoid is a circle (indicated by the dashed curve in Figure 1) and the long axis traces out a small circle on the sky. If $B < C$, the time P_ϕ between successive passes of the long axis through the same longitude is no longer constant, and the long axis now nods about a small circle on the sky with a nodding period $P_\psi/2$. The amplitude of the nodding depends on $C - B$. P_ψ is just the period of precession of the spin axis in the frame of reference fixed in the body. The important characteristics of a LAM are that the nucleus rotates through 360° about the long axis as the long axis nods about a complete small circle on the sky whose center is pierced by an extension of the angular momentum.

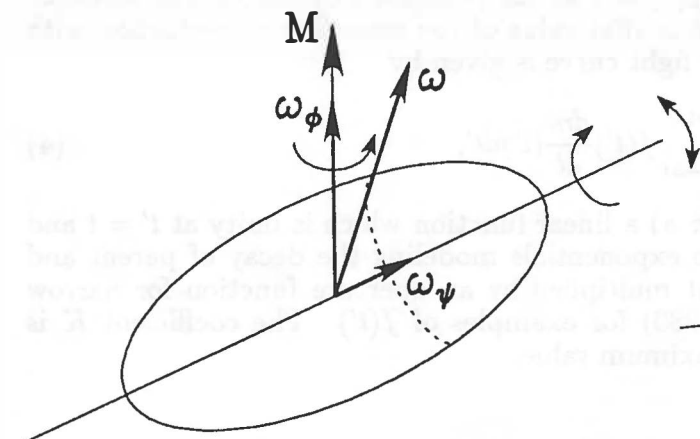


Figure 1. LAM

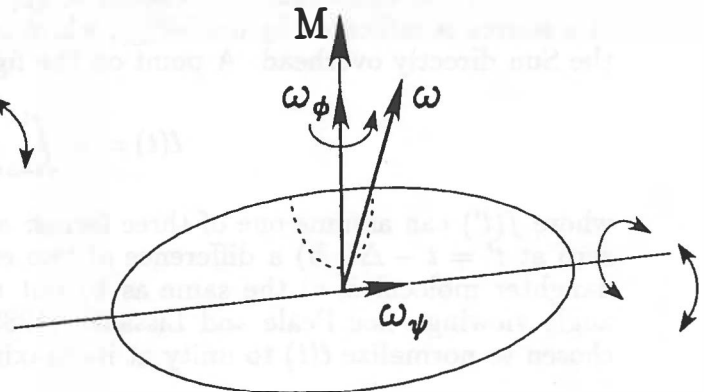


Figure 2. SAM

SAM

In Figure 2 we have shown a representation of a SAM for a shape similar to Halley's, where the long axis rotates about the angular momentum M as before, but now it nods about a great circle in the plane perpendicular to M with period P_ψ instead of about a small circle. The nucleus no longer rotates completely around the long axis but oscillates with an angular amplitude less than 90° with period P_ψ . This latter period is just the period of precession of the angular velocity in the body frame of reference. Again P_ϕ , the time between successive passes of the long axis through the same longitude, is not constant. The trace of spin vector $\bar{\omega}$ on the ellipsoid surface is the curve shown dashed in Figure 2. The important characteristics of the SAM which distinguish it from a LAM are that the nucleus now oscillates about the long axis through a limited range of angles while the long axis spins about the angular momentum while nodding about a great circle on the sky. In both LAMs and SAMs the ratio of the periods is determined within limited ranges by the initial conditions. (See Samarasinha and A'Hearn (1991) for a complete exposition of rigid body motion for a Halley-like shape from the inertial point of view.)

LIGHT CURVES

What are the consequences for light curves for LAMs and SAMs? To construct a light curve from a given rotational model, we distribute a finite number of localized sources of gas and dust over the nucleus and assume that the amount of light emitted by the coma is proportional to the currently visible mass. The rate of mass ejection is represented by

$$\frac{dm}{dt} = \sum_i \frac{dm^{(i)}}{dt_{\max}} g_p(r) \cos \theta_{\odot}^{(i)}; \quad \theta_{\odot}^{(i)} < 90^\circ. \quad (2)$$

The superscript i indicates the i 'th source, $\theta_{\odot}^{(i)}$ is the angle between the normal to the surface at the source position and the direction to the Sun. The contribution to dm/dt from the i 'th source is zero if $\theta_{\odot}^{(i)} > 90^\circ$, i.e., if the source is in shadow. The function

$$g_p(r) = \alpha \left(\frac{r}{r_0} \right)^{-\beta} \left[1 + \left(\frac{r}{r_0} \right)^{\gamma} \right]^{-\delta} \quad (3)$$

is a measure of the dependence of the evaporation of water ice on heliocentric distance r (Marsden *et al.* 1973), where $\beta, \gamma, \delta = 2.15, 5.093, 4.6142$, $r_0 = 2.808$ AU, and where the subscript p indicates that α is chosen so $g_p(r) = 1$ at the perihelion distance. The strength of a source is indicated by $dm/dt_{max}^{(i)}$, which is that value of the mass flux at perihelion with the Sun directly overhead. A point on the light curve is given by

$$\ell(t) = K \int_{t-\Delta t}^t f(t') \frac{dm}{dt}(t') dt', \quad (4)$$

where $f(t')$ can assume one of three forms: a) a linear function which is unity at $t' = t$ and zero at $t' = t - \Delta t$, b) a difference of two exponentials modeling the decay of parent and daughter molecules, c) the same as b) but multiplied by an aperture function for narrow angle viewing. See Peale and Lissauer (1989) for examples of $f(t')$. The coefficient K is chosen to normalize $\ell(t)$ to unity at its maximum value.

Perihelion passage	T	=	Feb. 9.45894, 1986
Perihelion distance	r_p	=	0.5871029 AU
Eccentricity	e	=	0.9672755
Period	P	=	75.99094 years
Semimajor axis	a	=	17.94077 AU

Table 1: Parameters for Halley's orbit

Figure 3 shows the light curve generated by the LAM model of Belton *et al.* (1991), where the distribution of the sources on the nucleus can be found in their paper and the remaining parameters are given in the figure. The linear weighting function is used to generate the curves in both Figures 3 and 4 with $\Delta t = 2$ days. The parameters used for Halley's orbit are given in Table 1 (Yeomans, Private communication, 1989). The curve was generated by integrating in both directions from an initial orientation of the nucleus at the Giotto encounter. This model is an axially symmetric LAM with the ratios of the lengths of the axes of the equivalent ellipsoid being indicated by $a : b : c$. Note that this model produces a light curve that is more or less symmetric about perihelion with similar amplitudes of short period variation pre and post perihelion. The favored axially symmetric LAM model of Samarasinha and A'Hearn (1991) with the source distribution of Belton *et al.* yields a similar light curve, except there is greater similarity in the shape of the short period variations from period to period on one side of perihelion. This increased similarity results from the adjustment of the parameters to make P_ϕ and P_ψ exactly commensurate. Schleicher *et al.* (1990) advocate this commensurability to generate nearly the same orientation of the nucleus with respect to the Sun about every 7.4 days after perihelion. This in turn leads to the observed repeatability of the shape of the short period variation in the light from the molecules C_2 and C_3 . For comparison the light curve for the least objectionable SAM model of Samarasinha and A'Hearn is shown in Figure 4. The distribution and relative strengths of the sources from Belton *et al.* and the nucleus orientation at encounter are used again, but the integration proceeds in one direction starting from 172 days before perihelion. The axis

ratios are somewhat arbitrarily chosen to make it easy to get the desired ratio of the periods with reasonable initial conditions. This light curve is also symmetric about perihelion passage with similar amplitudes of variation pre and post perihelion. The commensurate periods lead to the striking similarity in the shape of the light curve from period to period with, however, a phase shift as the comet passes perihelion.

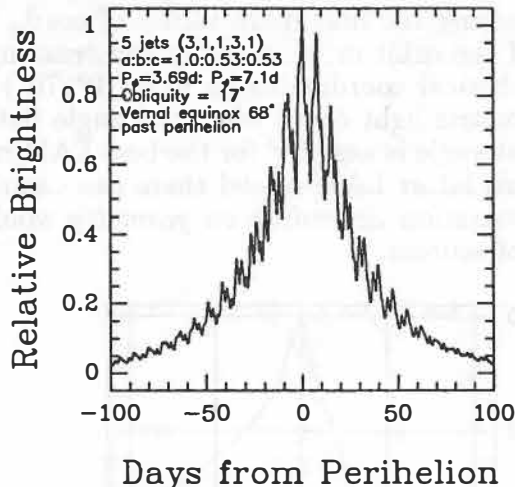


Figure 3. Light curve for LAM model of Belton *et al.* (1991).

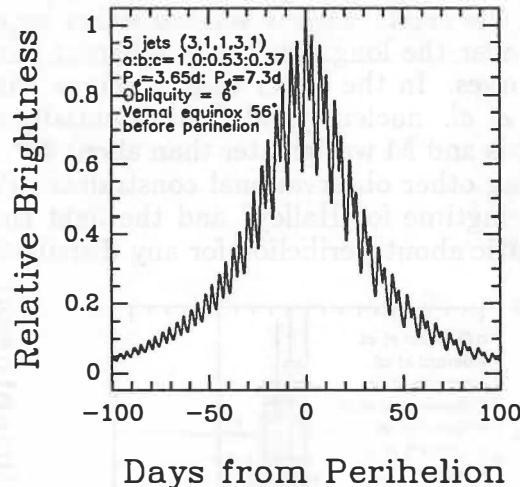


Figure 4. Light curve for SAM model of Samarasinha and A'Hearn (1991).

But Halley is considerably more active after perihelion than before. This is indicated in Figure 5, where estimates of the H_2O production rate from several sets of observations ranging from the ultraviolet to the radio regions of the spectrum are shown. Although there is a large scatter among the various estimates, all except those from the radio observations of OH by Gérard *et al.* show a marked increase in production after perihelion. From the localized nature of the sources of coma material on Halley's nucleus, Weissman (1987) has proposed that this asymmetry results from a seasonal effect where some major localized sources remain in shadow pre perihelion but become illuminated post perihelion in the springtime of the appropriate hemisphere. For Halley's shape and likely value of $M^2/2E$ relatively far from its minimum value of A , this requires a SAM model for the rotation state. Recall that rotation about the long axis in the SAM state was limited to an oscillation, which restricted, say, the positive axis of maximum moment of inertia to always make an acute angle with the angular momentum vector M . If M has a non negligible inclination to the orbit normal (obliquity) and the equinox is near the perihelion, a localized source near the axis of maximum moment would receive little illumination either pre or post perihelion depending on which hemisphere the source was located. The ease with which asymmetric light curves are generated with a SAM model is illustrated by the solid curve in Figure 5, where the axis ratios and initial energy state of Figure 4 are used. But the obliquity of M is 30° , the equinox is 30° before perihelion, and two sources having ordinary spherical coordinates in the body frame (z and x axes along axes of maximum and minimum moments respectively) of $\phi, \theta = -90^\circ, 20^\circ$ and $144^\circ, 109^\circ$ are assumed with the source near the pole having 6 times the strength of that near the equator. Pre perihelion dominance of the light curve can be generated by leaving M where it is and reflecting the sources through the origin of the body frame, or by leaving the sources as they were and interchanging the positions of the vernal and autumnal equinoxes.

An asymmetric light curve can also be generated with a LAM provided $M^2/2E$ is sufficiently close to A . In the latter case the angle between the axis of minimum moment (x axis) and M is relatively small and the cone swept out by x axis as it rotates around M

with period P_ϕ has a small angle. In this case, one could hide a source from the Sun for part of the orbit if it is placed close to the tip of the long axis of the nucleus and M is given a significant obliquity. However, as the cone angle (angle between the x axis and M) increases for lower energy states, the fact that the nucleus rotates completely around the x axis for a LAM as the x axis rotates completely around M makes it more and more difficult to keep a source, even near the tip, from receiving full illumination sometime during the cycle at any part of the orbit. This is verified either by comparing the maximum values of $\cos\theta_\odot$ for a source near the long axis tip in different parts of the orbit or by actually constructing the light curves. In the latter case, a source with spherical coordinates $(\phi, \theta) = (0^\circ, 70^\circ)$ on a Belton *et al.* nucleus yielded an essentially symmetric light curve when the angle between the x axis and M was greater than about 45° . That angle is near 65° for the best LAM model satisfying other observational constraints. For this latter LAM model there can clearly be no "Springtime for Halley" and the light curve variation *depending on geometry* would be symmetric about perihelion for any distribution of sources.

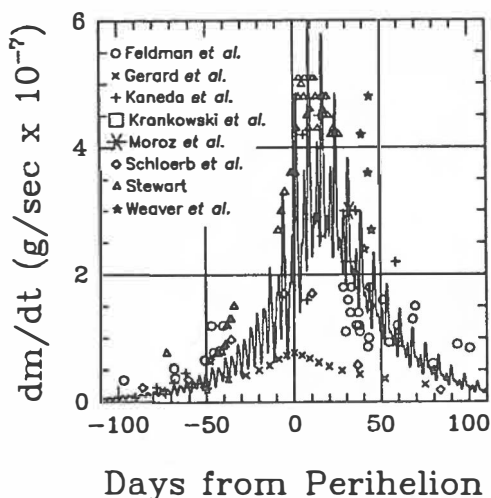


Figure 5. Estimates of H_2O production rates from observations and a sample asymmetric light curve for a SAM model.

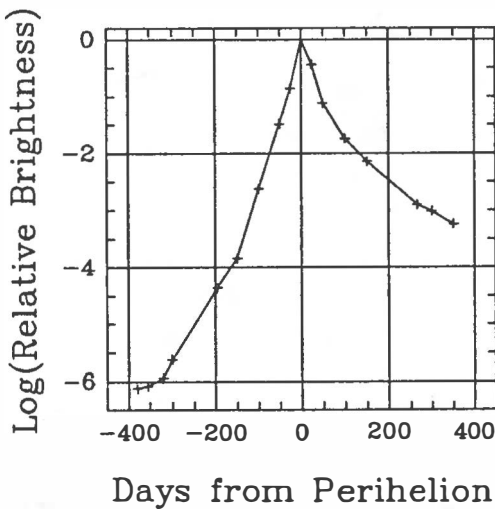


Figure 6. Mean light curve of Comet Halley from Green and Morris (1987).

OTHER CONSIDERATIONS

Non gravitational forces lead to an increasing orbital period for Comet Halley of 4 days per apparition, which has apparently remained unchanged for 2000 years (Yeomans and Kiang, 1981). These non gravitational forces are interpreted as a reaction to the jet emission of material from the nucleus coupled with a phase lag in the response of a source to the periodic illumination and/or the asymmetry in dm/dt about perihelion. Since the jets are extremely localized, torques on the nucleus must accompany the secular acceleration. But the rotational state of Halley's comet seems to be stable over the past 20 centuries, in spite of the fact that torques from the jets are capable of significant changes over a single apparition (Peale and Lissauer, 1989; Julian, 1990). This stability favors the LAM model for Halley's rotation state (Julian, 1990). If we distribute 2×10^7 g/sec (*e.g.* Krankowski, *et al.*, 1986) over the 5 Belton *et al.* sources at the time of encounter, extrapolate back to the perihelion with Eq. (3) to obtain $dm/dt_{max}^{(i)}$, assume all the jets are perpendicular to the surface of the equivalent ellipsoid, and give the ejected mass a velocity of 0.3 km/sec (*e.g.*, Peale, 1989), the LAM rotation state of Belton *et al.* is essentially unchanged from before to after an apparition, whereas the (least objectionable) SAM of Samarasinha and A'Hearn had P_ϕ decreased from 3.65 to 3.24 days and P_ψ decreased from 7.3 to 6.44 days.

The reason for this contrasting behavior is clear from the description of the two modes of rotation above. Recall that for the LAM, the nucleus rotates repeatedly through 360° about the long axis as the long axis rotates around M. A source displaced from the central part of the nucleus could at some point be illuminated as that part of the nucleus was receding from the Sun in the ϕ motion. As such the reaction would contribute a torque in the direction of the angular momentum and P_ϕ would be decreasing. However, after the nucleus has rotated 180° about the long axis, that same source will be illuminated as that part of the nucleus is approaching the Sun. The reaction then gives a torque opposite M and P_ϕ is increased by the reaction. As the rotation periods are relatively short compared to the time Halley is close to the Sun, the gains in angular momentum are almost balanced by the losses. The imbalance that occurs because Halley is closer to the Sun (stronger jets) during last half of the period P_ϕ on the inbound leg does change the rotation state, but this change is essentially erased on the outbound leg where Halley is further from the Sun during the last half of the period P_ϕ . The result is little net change in the rotation state after the apparition. This behavior is consistent with the apparently stable rotation state for Halley's nucleus. For a SAM the nucleus only oscillates about the long axis as that axis spins around M. This means that most sources that are illuminated as their part of the nucleus is receding from the Sun will always be illuminated in such a receding geometry and the change in the angular momentum and hence the rotation state will be secular. The only way a SAM state could remain unchanged against the reaction torques would be if the sources were distributed in an unlikely special way to balance each other's effects.

But the contrasting response of LAMs and SAMs to the torques only results if we restrict the jets to be perpendicular to the equivalent ellipsoidal surface of the nucleus. For example, if we give the *direction* of the Belton *et al.* jet #4 a 10° rotation about the long axis in the LAM model, there is a secular torque about that axis and initial periods $P_\phi, P_\psi = 3.69, 7.38$ days change to $3.85, 8.38$ days in a single apparition. This effect led Julian (1990) to reject significant inclination of the jets, because of Halley's apparent stability. But the images of Halley reveal a rugged topography, and inclination of the jets to the equivalent ellipsoidal surface should be the rule rather than the exception. The stability of Halley's rotation may mean that we are overestimating the torques from the observed mass flux.

Given that a LAM is the currently a favored rotation state for Halley, are LAMs to be expected on other grounds? For a nucleus shaped like Halley's, the answer is a qualified yes. First of all, only a LAM is possible for a symmetric rotator ($A < B = C$). Halley is probably not dynamically symmetric but may be nearly so, such that $B < M^2/2E < C$ for a SAM is a small range for $B \lesssim C$. A reasonable conjecture is that random jets eventually drive rotation away from either extreme energy state in the absence of significant dissipation. For $B \lesssim C$ a relative small change in energy will change a SAM into a LAM such that LAMs may be the preferred state for *long, thin nuclei* of short period comets that have made many perihelion passes.

If LAMs are not unlikely, can the favored LAM for Halley be embellished by another degree of freedom such as activating additional sources after perihelion? Weissman (1987) finds that thermal inertia effects are totally inadequate to explain the post perihelion brightening for Halley, but comets are a varied lot showing all sorts of erratic behaviors (e.g., Jacchia, 1974), so almost anything else proposed may not be totally unreasonable. Samarasinha and A'Hearn (1991) offer the nuclear model of Brin and Mendis (1974) where more and more insulating crust is blown off the nucleus as it approaches the Sun. The nucleus departs with more exposed area than it had on approach and is therefore brighter post perihelion. The dust layer rebuilds itself as the comet wanes such that it can repeat the performance at the next apparition. Some periodic comets are brighter pre perihelion at each apparition (e.g. Encke, Yeomans, private communication, 1991), which could be the effect of geometry with stable sources, but it appears that effects other than geometry may be good candidates as

contributors to the asymmetry of Halley's light curve.

This is especially true when one considers the complete light curve for Halley determined by Green and Morris (1987). Points from this light curve are shown in Figure 6. Like the estimates for the H₂O production rates in Figure 5, the light curve within ± 100 days of perihelion shows an asymmetry of a factor of a few. However, on day 350 the estimated brightness is about 620 times that on day -350—a difference of about 7 magnitudes! At 350 days, Halley is about 4.8 AU from the Sun. The function $g_p(r)$ defined in Eq. (3) plummets drastically beyond 2 or 3 AU and our synthetic light curves generated using this function obviously cannot even be close to reality for Halley with any rotation state with fixed sources that we could choose. As g_p is based on the evaporative properties of water ice, it appears that some other volatile must be dominating the activity during the distant post perihelion phase. There was even an outburst of dust from Halley when it was 14.3 AU from the Sun post perihelion (West, *et al.* 1991). Yeomans (private communication, 1991) notes that the CO outgassed from Halley is about 17% that of H₂O), and it is the likely volatile causing the distant activity. He also points out that if the nucleus is very inhomogeneous, a pocket of CO could emerge from shadow or have a protective covering removed as Halley retreats from the Sun. But this would require a relative low energy SAM! Weissman (1988) points out evidence that sizable pieces break off from and stay close to the nuclei of some comets as they pass perihelion. The increase in surface area would yield a post perihelion brightening. However, in Halley's case the same behavior would have to occur at each apparition, and the increased surface area would not be expected to be so much more effective at 5 or 14 AU than it was at, say, 1 AU. Asymmetries due to seasonal effects on fixed sources whose output remains simply proportional to the instantaneous illumination tend to dominate close to perihelion, where the most rapid changes in solar aspect occur. The large distant asymmetries seem to be due to something else, and that something else may have also influenced the asymmetry near the perihelion. These considerations leave open the possibility that the asymmetry in Halley's light curve may be found within the nuclear properties rather than in a rotational geometry change from a LAM to a SAM.

ACKNOWLEDGEMENTS

Thanks are due Don Yeomans and Paul Weissman for reading the manuscript and suggesting improvements. This work is supported in part by the NASA Planetary Geology and Geophysics Program under Grant NAGW 2061.

REFERENCES

- Belton M.J.S. (1990) Rationalization of Comet Halley's Periods, *Icarus*, **86**, 30–51.
- Belton M.J.S., Julian W.H., Anderson A.J., and Mueller B.E.A. (1991) *Icarus*, In Press.
- Feldman P.D., Festou M.C., A'Hearn M.F., Arpigny C., Butterworth P.S., Cosmovici C.B., Danks A.C., Gilmozzi R., Jackson W.M., McFadden L.A., Parriarchi P., Schleicher D.J., Tozzi G.P., Wallis M.K., Weaver H.A., and Woods T.N. (1987) IUE observations of comet P/Halley: Evolution of the ultraviolet spectrum between September 1985 and July 1986, *Astron. Astrophys.*, **187**, 325–328.
- Gérard, E., Bockelée-Morvan D., Bourgois G., Colom P., and Crovisier J. (1987) 18-cm wavelength radio monitoring of the OH radical in comet P/Halley 1982i *Astron. Astrophys.*, **187**, 653–660.
- Green D.W.E., and Morris C.S. (1987) The visual brightness behavior of P/Halley during 1981–1987, *Astron. Astrophys.*, **187**, 560–568.
- Jacchia L.J. (1974) The brightness of comets, *Sky and Telescope*, **47**, 216–220.

- Julian W.H. (1987) Free precession of the Comet Halley nucleus, Nature, 326, 57–58.
- Kaneda E., Hirao K., Shimizu M., and Ashihara O. (1986) Activity of Comet Halley observed in the ultraviolet. Geophys. Res. Lett., 13, 833–836.
- Keller H.U., Delamere W.A., Huebner W.F., Reitsema H.J., Schmidt H.U., Whipple F.L., Wilhelm K., Curdt W., Kramm R., Thomas N., Arpigny C., Barbieri C., Bonnet R.M., Cazes S., Coradini M., Cosmovici C.B., Hughes D. W., Jamar C., Malaise D., Schmidt K., Schmidt W.K.H., and Seige P. (1987) Comet P/Halley's nucleus and its activity, Astron. Astrophys., 187, 807–823.
- Krankowski, D., Lämmerzahl P., Herrwerth I., Woweries J., Eberhardt P., Dolder U., Herrmann U., Schulte W., Berthelier J.J., Illiano J.M., Hodges R.R., and Hoffman J.H. (1986) *In situ* gas and ion measurements at Comet Halley. Nature, 321, 326–329.
- Moroz V.I., Combès M., Bibring J.P., Coron N., Crovisier J., Encrenaz T., Crifo J.F., Sanko N., Grigoryev A.V., Bockelée-Morvan D., Gispert R., Nikolsky Y.V., Emerich C., Lamarre J.M., Rocard F., Krasnopolsky V.A., and Owen T. (1987) Detection of parent molecules in comet P/Halley from the IKS-Vega experiment, Astron. Astrophys., 187, 513–518.
- Newburn R.L., in The Comet Halley Gas and Dust Environment, ESA SP-174, p 3.
- Peale S.J. (1989) On the density of Halley's Comet, Icarus, 82, 36–49.
- Peale S.J. and Lissauer J. J. (1989) Rotation of Halley's Comet, Icarus, 79, 396–430.
- Samarasinha N.H. and A'Hearn M.F. (1991) Observational and dynamical constraints on the rotation of comet P/Halley Icarus, In press.
- Schleicher D.G., Millis R.L., Thompson D.T., Birch P.V., Martin R., Tholen D.J., Piscitelli J.R., Lark N.L., and Hammel H.B. (1990) Periodic variations in the activity of comet P/Halley during the 1985/1986 apparition, Astron. J., 101, 896–912.
- Schloerb F.P., Claussen J.J., and Tacconi-Garman L. (1987) OH radio observations of Comet P/Halley, Astron. Astrophys., 187, 469–474.
- Stewart A.I.F. (1987) Pioneer Venus measurements of H, O, and C production in Comet P/Halley near perihelion, Astron. Astrophys., 187, 369–374.
- Weaver H.A., Mumma M.J., and Larson H.P. (1987) Infrared investigation of water in Comet P/Halley, Astron. Astrophys., 187, 411–418.
- Weissman P.R. (1987) Post-perihelion brightening of comet P/Halley: Springtime for Halley, Astron. Astrophys., 187, 873–878.
- Weissman P.R. (1988) Why was Halley's Comet so bright? Bull. Amer. Astron. Soc., 20, 825.
- West R.M., Hainaut O. Smette A. (1991) Post-perihelion observations of P/Halley .3. An outburst at R=14.3 AU. Astron. Astrophys., 245, L77–L80.
- Yeomans D.K. and Kiang T. (1981) The long term motion of Comet Halley, Mon. Not. Roy. Ast. Soc., 197, 633–646.

BURST OF THE 1969 LEONIDS AND 1982 LYRIDES

V. Porubčan and J. Štohl

Astronomical Institute of the Slovak Academy of Sciences,
Czech and Slovak Federal Republik

Abstract

Radar observations of the last bursts of the Leonids in 1969 and Lyrids in 1982, carried out at the Springhill Meteor Observatory, Canada, both of very short duration, with the rates exceeding a quarter-maximum rate within 50-55 minutes, are used for a study of the mass distribution of meteoroids. In both cases the mass distribution exponents of the meteoroids in the dense clouds largely differ from the values obtained for the older populations of the streams. The highest mass exponent $s \sim 2.2-2.4$ is found around the peak of the activity, confirming high contribution of smaller meteoroids, and thus also a recent origin of the dense clouds. Consequences of this findings are discussed.

Activity and mass distribution

The showers were observed at the Springhill Meteor Observatory, the 1969 Leonids by the high power radar and the 1982 Lyrids by the patrol radar. (For details about the equipments cf. Millman and McIntosh, 1964, and Neale, 1966a,b).

The 1969 Leonid shower observations cover a five-hour interval of November 17, 07:37-12:40 UT. The peak occurred on November 17, at 09:02 UT (solar longitude 234.577, epoch 1950.0), with 460 echoes in one minute. The duration of the storm was 15 minutes between half-maximum points, and 55 minutes between quarter-maximum points. The 1982 Lyrid peak occurred on April 22, at 06:49 UT (solar longitude 31.380, epoch 1950.0), with 33 echoes in one minute. The duration of the storm was 22 and 50 minutes between half-maximum and quarter-maximum points, respectively.

In Fig. 1 we present two activity curves of the 1969 Leonids storm. The dotted one was derived by Millman (1970) from visual observations carried out at the Springhill Meteor Observatory. The corresponding radar activity curve (the full line) was derived from our data using the same smoothing procedure as was applied to the visual data by Millman. A striking feature of the activity curves is their similarity not only in the positions and width of their main maxima, but also in the secondary maxima, in both cases occurring at about 08:00 UT. The activity curve of the 1982 Lyrids burst can be found in Porubčan and Hajduková (1988).

The mass distribution of meteoroids of the form $dN \sim m^{-s} dm$ and the differential mass exponent s can be derived from the echo

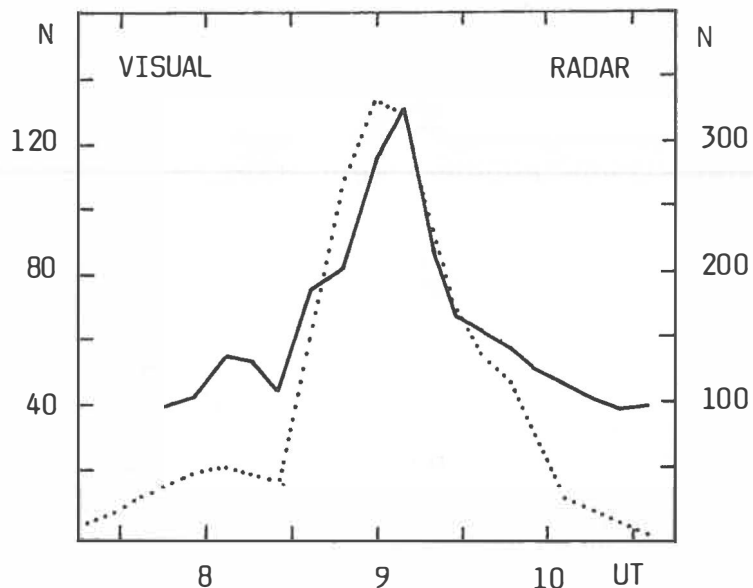


Fig. 1. Activity of the Leonids 1969 observed visually (dotted line) and by radar (full line). The values represent 10-minute counts of meteors by 6 visual observers and of echoes with duration ≥ 0.4 sec.

durations. The minimum echo duration considered in our analysis was 0.4 sec. Mass exponent s obtained for the 1969 Leonids is listed in Table 1, together with the results for the Lyrids 1982 derived earlier by Porubčan and Hajduková (1988). From Table 1 we can see that for the mass exponent s the radar observations give relatively high values. Let us remind that for the 1969 visual Leonids the value $s = 2.2$ was derived by Millman (1970).

Statistical reliability of this value, however, is low owing to the relatively small number of meteors available for the analysis. The same value $s = 2.2$ was also derived from the patrol radar observations of the Springhill Meteor Observatory for the 1966 Leonid storm by McIntosh and Millman (1970) and for the peak of the 1982 Lyrids bursts by Porubčan and Hajduková (1988). More reliable high power radar values presented in Table 1 are still higher, especially for the peak period of the 1969 Leonids ($s = 2.43$).

Table 1. Mass exponent s of the 1969 Leonids and 1982 Lyrids

1969 Leonids:			1982 Lyrids:		
UT	n	s	UT	n	s
8:30-9:30	840	2.31	6:00-6:35	63	1.75
8:55-9:10	353	2.36	6:35-7:00	201	2.21
9:00-9:05	152	2.43	7:00-8:00	126	1.55

Discussion of the origin

High values of the mass exponent $s \sim 2.2-2.4$ for meteoroids of the 1966 and 1969 Leonids and 1982 Lyrids bursts confirm a very high incidence of small particles in the corresponding dense clouds of the two streams. It follows that the small particles have not yet been removed from these places by cumulative dispersive effects

which begin to influence structure of a stream immediately after the ejection of meteor particles from the parent bodies. Thus dense clouds consisting of small particles in the streams must be of recent origin.

In the case of the Leonid storms there seems to be no serious problem in accepting this consequence. As was concluded by Yeomans (1981) from his analysis of the Leonid showers over the 902-1969 interval, most of the stream particles are fresh ejecta from its parent comet P/Tempel-Tuttle (1966 I, period 33 years). For the 1969 storm of the Leonids McIntosh (1973) has found that the corresponding cloud of small particles, lagging the comet 1600 days, was ejected from the comet before 5-6 orbital evolutions, i.e. less than 200 years ago. There still remains a problem of the dispersion of the particles orbits which would demand appearance of the bursts in several years about the encounter time (Williams, 1990), but the conclusion about recent origin of the particles by ejection from their parent comet seems to be firmly established.

Origin of the 1982 Lyrids burst, however, must be different and demands another scenario. The corresponding cloud of small particles is lagging the parent comet P/Thatcher (1861 I, period 415 years) over 120 years and does not therefore allow an explanation of its origin in recent ejection directly from the comet. On the other hand, the dense cloud predominantly consisting of small particles does demand a recent origin. Moreover, the cloud of small particles is imbedded into an older Lyrid population containing larger particles, which follows from the low mass exponent $s = 1.6$ of the standard Lyrid population (Porubčan and Šimek, 1988), as compared with $s = 2.2$ observed at the peak of the 1982 burst.

One possibility how to explain the 1982 Lyrids burst is that the small particles had their origin in a secondary, relatively large body loosed from the parent comet Thatcher at an earlier time, perhaps together with smaller particles that dispersed more quickly along the orbit due to their higher ejection velocities. The chunk could disintegrate later on, producing a dense cloud of non-ejected particles of various sizes, moving in similar orbits for relatively longer period, since not influenced by the dispersion of velocities occurring at an ejection process. Evidence for such an origin on a larger scale can be seen in disintegrations of cometary nuclei followed by strong meteor storms, as was the case with the comet P/Biel and the Andromedids. On much smaller scale, an evidence can be seen in non-random groupings of meteoroids observed in young, dense meteor streams (Porubčan, 1979), resulting in a continuing process of disintegration of large meteoroids into smaller ones. As for the time-scale of loosing the chunk from the comet Thatcher we can make a simplified estimation. Neglecting other effects and considering ejection velocity of e.g. 1 m.s^{-1} at the perihelion in the direction of comet motion we obtain that the chunk left the comet 36 revolutions ago, which is about 1.5×10^4 years.

Acknowledgements

The authors are indebted to the Herzberg Institute of Astrophysics in Ottawa and to S. A. McIntosh for the kind permission to use the original Canadian radar records from the Springhill Meteor Observatory. The research was supported by the Slovak Academy of Sciences Grant 493/1991.

References

- McIntosh S.A. (1973) Origin and evolution of recent Leonid meteor showers. In Evolutionary and Physical Properties of Meteoroids (C.L. Hemenway, P.M. Millman, and A.F. Cook, eds.), pp. 193-198. NASA SP-319. NASA Washington, O.C.
- McIntosh S.A. and Millman P.M. (1970) The Leonids by radar - 1957 to 1968. Meteoritics, 5, 1-18.
- Millman P.M. (1970) Meteor news. Roy. Astron. Soc. Canada, 64, 55-57.
- Millman P.M. and McIntosh S.A. (1964) Meteor radar statistics I. Canad. J. Phys., 42, 1730-1742.
- Neale M.J. (1966a) Radar equipment for continuous meteor observations. Canad. J. Phys., 44, 1021-1028.
- Neale M.J. (1966b) A megawatt pulse transmitter for meteor research. Canad. J. Phys., 44, 1573-1582.
- Porubčan V. (1979) Clustering of particles in meteor streams. Contr. Astron. Obs. Skalnaté Pleso, 8, 89-96.
- Porubčan V. and Hajduková M. (1988) Mass distribution exponent of the Lyrid meteor shower enhanced activity in 1982. Acta Astron. Geophys. Univ. Comenianae, 13-14, 77-82.
- Porubčan V. and Šimek M. (1988) Distribution of Lyrid meteoroids in a large range of echo duration. Bull. Astron. Inst. Czechosl. 39, 165-168.
- Williams I.P. (1990) The formation of meteor streams. In Asteroids, Comets, Meteors III (C.-I. Lagerkvist, H. Rickman, B.A. Lindblad, and M. Lindgren, eds.) pp. 585-594 Uppsala Universitet, Uppsala.
- Yeomans D.K. (1981) Comet Tempel-Tuttle and the Leonid meteors. Icarus, 47, 492-499.

ON ASSOCIATIONS OF APOLLO ASTEROIDS WITH METEOR STREAMS

V. Porubčan¹, J. Štohl¹ and R. Vaňa²

- 1) Astronomical Institute, Slovak Academy of Sciences,
84228 Bratislava, Czech and Slovak Federal Republik
- 2) Department of Astronomy and Astrophysics, Comenius University
84215 Bratislava, Czech and Slovak Federal Republik

Abstract

Potential associations of Apollo asteroids with meteor streams are searched on the basis of the orbital parameters comparison. From all Apollo asteroids discovered through 1991 June those are only selected for further analysis whose orbits approach to less than 0.1 AU to the Earth's orbit. Their orbits are compared with precise photographic orbits of individual meteors from the Meteor Data Center in Lund. Results on the associations of asteroids with meteor streams are presented and discussed.

Introduction

Since the time of the discovery of the asteroid 3200 Phaethon in 1983 and of its strong association with the Geminid meteor shower, earlier suggestions of the association of meteoroid streams with asteroids (cf. Sekanina, 1973, 1976; Drummond, 1982) have become more substantiated. Recently an attempt was made to find out asteroids-meteor streams associations on the basis of comparison of individual radar orbits of meteors determined by the Adelaide meteor orbit surveys with orbits of the Apollo asteroids (Olsson-Steel, 1988, 1990). Several asteroids have been proposed as very probable candidates for association with meteors. Similar search with the mean orbits of the Cook's working list of meteor streams lead Olsson-Steel to the same conclusions.

In the present paper a search for associations of asteroids with meteors is carried out on the basis of comparison between the orbits of asteroids and precise photographic meteor orbits available from the IAU Meteor Data Center in Lund.

Data and the association search

Through 1991 June there have been 174 orbits of Apollo, Amor and Aten asteroids available. Only those of them were included into our analysis, which approach the orbit of the Earth to less than 0.1 AU, their number being 90. For each of them the date of the closest approach to the Earth was calculated, together with the limiting ecliptical longitudes within which orbit of a particular asteroid is closer to the Earth orbit than 0.1 AU. These

longitudes were than accepted as limits for search of association of the particular asteroid with meteor orbits.

As a counterpart to the orbits of asteroids 3500 orbits of individual meteors from the IAU Meteor Data Center in Lund were searched. Orbit of each asteroid was compared with all meteor orbits falling within the longitudinal limits of 0.1 AU. For finding the asteroid-meteors associations the Southworth-Hawkins' D-criterion was applied (Southworth and Hawkins, 1963). As a limit for the orbital match the value $D = 0.25$ was taken into account, though for the association a stronger limit $D = 0.20$ was only accepted.

Among the 147 Apollo, Amor and Aten asteroids there were 84 cases for which no meteor orbit has been found matching their orbits within the limit of $D = 0.25$; for another 31 asteroids there were no meteor orbits found fulfilling the association criterion $D = 0.20$. We have thus 59 asteroids, for which the association with meteor streams can be accepted with various degree of probability.

Asteroids-meteors associations and their discussion

In Table 1 general results of the search are presented in a concise form. Asteroids are somewhat arbitrarily divided into 4 groups according to the number of meteor orbits $N.20$ and $N.25$ matched to the orbits of particular asteroids within the limits, $D = 0.20$ and $D = 0.25$, respectively. The groups are chosen as follows: I - $N.20 \geq 8$ or $N.25 > 13$; II - $N.20 \geq 6$ or $N.25 > 9$; III - $N.20 \geq 4$ or $N.25 > 6$; IV - $N.20 \leq 3$. Total numbers of asteroids

Table 1. Associations of asteroids with meteors

Group	Number of asteroids	Asteroids
I. High	14 13P, 1M	(Cf. Table 2)
II. Medium	13 8P, 5M	1950 DA, 1983 LC, <u>1991 JX</u> , 1 <u>1991 FB</u> , <u>1987 SF3</u> , 4197 (1982 TA), <u>2061 Anza</u> , 1990 UQ, 1990 MF, <u>3361 Orpheus</u> , <u>3908 (1980 PA)</u> , <u>3757 (1982 XB)</u> , 1984 KB
III. Low	13 12P, 1M	<u>1989 UP</u> , 4486 Mithra, 1917 Cuyo, 1988 EG, <u>1989 DA</u> , 4450 Pan, 1990 TG1, <u>4515 (1979 VA)</u> , 1990 UN, 1989 JA, 1988 VP4, Hermes
IV. Very low	19 15P, 2M 2T	1566 Icarus, 1862 Apollo, 2101 Adonis, 2340 Hathor, 2608 Seneca, 4034 (1986 PA), 4183 (1959 LM), 4581 (1989 FC), 4769 (1989 PB), 1983 TF2, 1987 OA, 1988 XB, 1989 QF, <u>1989 UQ</u> , 1989 UR, 1990 SP, 1990 SS, 1991 GO, <u>1991 JR</u>

falling into each group is given in Table 1, Col. 2, together with following specification of the asteroids: P-Apollo, M-Amor, T-Aten. The asteroids underlined have $V_G < 10 \text{ km s}^{-1}$.

Group I with the largest number of meteor orbits associated with the asteroids is presented in Table 2 in more details. For each asteroid following data are given: Δr_{\min} - minimum distance of the asteroidal orbit from the Earth orbit in AU, Date - the date at which Δr_{\min} occurs, Δt - number of days when $\Delta r < 0.1 \text{ AU}$, V_G - the geocentric velocity of the asteroid corresponding to Δr_{\min} , δ - declination of the expected radiant, N - total number of meteor orbits within Δt , N_{sh} - number of meteor orbits belonging to various showers as was determined by original authors of the orbits, N.25 and N.20 - number of meteor orbits associated with the asteroid within the limits $D = 0.25$ and 0.20 , respectively.

As was expected, the association of 3200 Phaethon with meteors, in this case belonging to the Geminid shower, is the most prominent. On the other hand, there are several other asteroids, for which the number of matched meteors is much higher than might be expected from random coincidences. They include asteroids which had been proposed by several authors as being associated with the Taurid meteor complex (5025 P-L, 2201 Oljato, 4197-1982 TA, 1984 KB) or with some minor showers (3671 Dionysius-1984 KD -- τ Herculids, 1983 LC - Scorpiids, 1917 Cuyo - α Cygnids, 2061 Anza - Northern ϵ Aquarids, 1950 DA - May Ursids, 3757-1982 XB -- δ Leonids, 1986 JK - Lybrids etc.). Closer inspection of individual meteor orbits found to be matched with the orbits of asteroids reveals other close associations of asteroids with known meteor showers. Such is the case with the Delta Arietids (Kronk, 1988) which we suppose to be associated with 1990 HA showing moreover that the activity of this minor shower extends from November 26 till December 15 at least. Some of the asteroids

Table 2. Most probable associations of asteroids with meteors

Asteroid	Δr_{\min}	Date	Δt	V_G	δ	N	N_{sh}	N.25	N.20
3200 Phaethon	0.025	14 Dec	6	33.6	+32	312	212	210	203
4179 Toutatis	0.007	24 Sep	58	11.9	-14	639	133	32	18
5025 P-L	0.082	8 Nov	6	28.5	+24	81	28	26	15
1990 HA	0.062	4 Dec	20	15.9	+11	437	242	23	14
3671 Dionysius	0.029	17 Jun	40	11.2	+33	186	2	15	11
1989 VB	0.016	10 Oct	86	6.4	-34	905	194	14	10
1986 JK	0.007	4 Jan	49	13.4	-9	211	3	13	10
1990 OS	0.009	15 Aug	67	9.6	-25	1349	684	14	9
1991 BA	0.001	17 Jan	21	18.0	+19	83	3	10	9
1990 UA	0.012	18 May	28	14.8	-14	111	1	12	8
4660 1982 DB	0.021	11 Dec	59	6.3	+23	696	329	19	7
1980 AA	0.054	10 Jan	56	5.2	+32	527	247	15	7
2201 Oljato	0.009	21 Dec	17	20.2	+20	305	180	13	7
1988 TA	0.026	13 May	31	12.8	-20	137	14	14	6

from Groups I-III are included in the Drummond's associations I-IV (Drummond, 1991).

It should be emphasized that the number of meteor orbits matched to the orbit of an asteroid by itself is not a sufficient measure of the reality of an association. There are several factors by which this number can be overestimated (random coincidences) or underestimated (especially low geocentric velocity which can reduce the observed number of meteors to 1-2 orders). Confirmation or refusal of the reality of the proposed associations demands therefore a careful elimination of all these effects.

The research was supported by the Slovak Academy of Sciences Grant 493/1991.

References

- Drummond J.D. (1982) Theoretical meteor radiants of Apollo, Amor and Aten asteroids. Icarus, 49, 143-153.
- Drummond J.D. (1991) Earth-approaching asteroid streams. Icarus, 89, 14-25.
- Kronk G.V. (1988) Meteor showers: A Descriptive Catalog, Enslow Publ., 296 pp.
- Olsson-Steel D. (1988) Identification of meteoroid streams from Apollo asteroids in the Adelaide radar orbit surveys. Icarus, 75, 64-96.
- Olsson-Steel D. (1990) Apollo asteroid-related meteoroid streams, In Asteroids, Comets, Meteors III (C.-I. Lagerkvist, M. Rickman, B.A. Lindblad, and M. Lindgren, eds.), pp. 159-162. Uppsala Universitet, Uppsala.
- Sekanina Z. (1973) Statistical model of meteor streams. III. Stream search among 19 303 radio meteors. Icarus, 18, 253-284.
- Sekanina Z. (1976) Statistical model of meteor streams. IV. A study of radio streams from the synoptic year. Icarus, 27, 265-321.
- Southworth R.B., and Hawkins G.S. (1963) Statistics of meteor streams. Smithson. Contr. Astrophys., 7, 261-285.

OBSERVATIONS OF COMET LEVY 1990c IN THE [OI] 6300-Å LINE WITH AN IMAGING FABRY-PEROT

C. Debi Prasad, K. Jockers, H. Rauer, Max-Planck-Institut für Aeronomie,
D-W-3411 Katlenburg-Lindau, Germany
E.H. Geyer, Observatorium Hoher List, D-W-5568 Daun, Germany

ABSTRACT

We have observed the comet Levy 1990c during 16-25 August 1990 using the MPAE focal reducer system based Fabry-Perot etalon coupled with the 1 meter telescope of Observatory of Hoher List. The free spectral range and resolution limit of the interferometer was $\sim 2.18 \text{ Å}$ and $\sim 0.171 \text{ Å}$ respectively. Classical Fabry-Perot fringes were recorded on a CCD in the cometary [OI] 6300 Å line. They are well resolved from telluric air glow and cometary NH_2 emission. Our observations indicate that the [OI] is distributed asymmetrically with respect to the center of the comet. In this paper we report the spatial distribution of [OI] emission and its line width in the coma of comet Levy.

INTRODUCTION

The mapping of [OI] 6300 Å emission in the cometary coma provides information about the distribution of its source O¹D, which is a major dissociation product of H₂O. The earlier studies of the cometary spectrum in 6300 Å region mostly used high resolution grating spectrometers and central aperture scanning Fabry-Perot (FP) spectrometers (Arpigny et al., 1987, Combi and McCrosky 1991, Magee-Sauer et al., 1989, Debi Prasad et al., 1988). Whereas the high resolution grating spectrometers provide the one-dimensional distribution along the slit, the central aperture scanning FP averages across the field of view. The FP in imaging mode has been used by Magee-Sauer et al. (1988) to map the O¹D distribution in the inner coma region and, with limited signal to noise ratio, Debi Prasad and Desai (1989) have derived the velocity information. We have used the Fabry-Perot interferometer in classical mode and recorded the fringe system in wide field of view with a focal reducer and CCD. This paper reports the 6300 Å line width and intensity distribution in the coma of comet Levy.

OBSERVATIONS AND DATA ANALYSIS

Comet Levy was observed with MPAE focal reducer based FP interferometer and CCD camera (Jockers et al, 1987) which can be rapidly switched between the imaging and interferometric mode. The free spectral range, resolution limit and optical gap of the FP interferometer derived from the spectral lamp calibration frames at the time of observation are 2.2 Å, 0.12 Å and 905.45 micron respectively. The field of view and spatial resolution of the focal reducer are 29×20 arcmin and 3.0 arcsec pixel⁻¹ respectively. The observations of August 1990, 17.95 UT are reported here. During the observations the cometary heliocentric (r_h) and geocentric distances are 1.48 and 0.51 AU respectively. The geocentric velocity was -30.7 km/s, which corresponds to 0.64 Å Doppler shift of cometary line with respect to the terrestrial line at 6300 Å. The focal reducer images of comet Levy in 6300 Å filter (I_{L+C}) were obtained with the FP etalon in the collimated part of the optical path. The FP etalon was removed while exposing for the continuum images (I_C) with 6420 Å pre-filter. The images of a diffuser screen illuminated by a continuum source were taken with and without FP etalon. The ratio of these two bias subtracted images normalized to unity with the average counts in the central region of the frame, (I_R) serves for correcting distortion in intensity distribution that might be caused by introducing the FP etalon. The position of the comet in CCD pixel coordinate was the same during interferogram and imaging exposures.

The images are bias subtracted and flat-field corrected. In I_{L+C} the airglow, cometary lines and continuum light is convolved with the periodic Airy function with the instrumental finesse 19

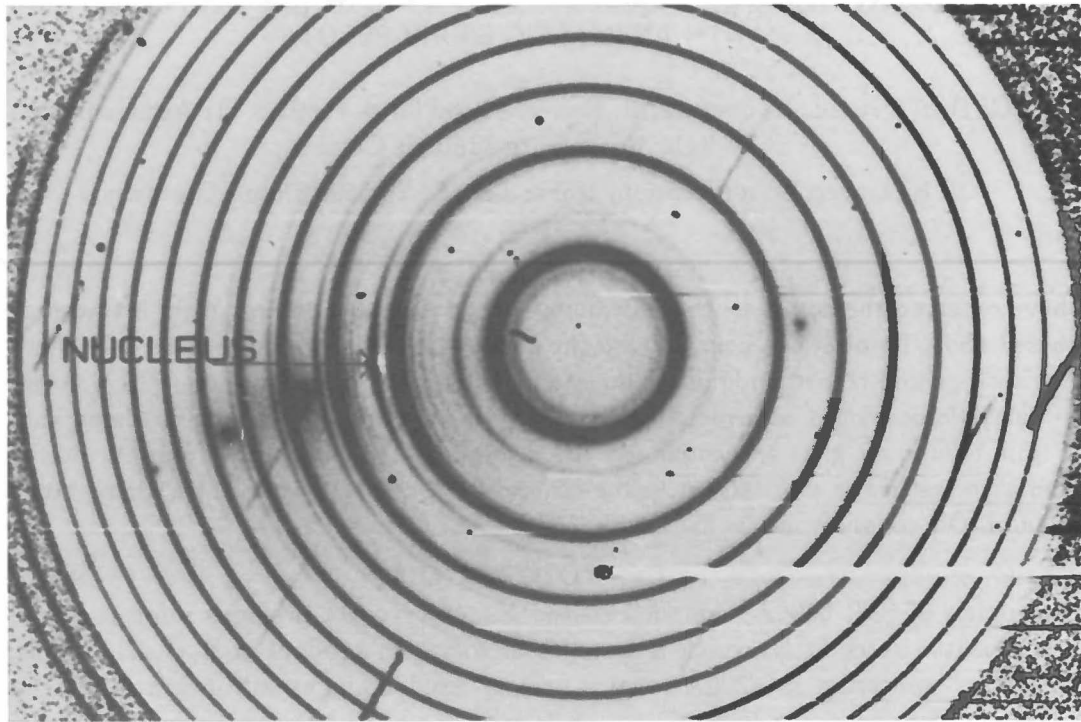


Figure 1: Fabry-Perot Interferogram of Comet Levy in 6300Å. The bright points not marked by arrow are due to instrumental reflections. Sun is to the left.

which is determined from the spectral lamp calibrations during the observations. The airglow and cometary profiles are broader than the instrumental profile. We have computed the Airy function with degraded finesse in order to fit the telluric and cometary O¹D emission. The best fit of Airy function with the observations was obtained for the effective finesse of 16 and 13 in the case of airglow and cometary emission. This indicates that the cometary lines are broader than the airglow. The FP interferogram due to the emission lines I_L obtained by using the relation,

$$I_L = (I_{L+C}) - (I_R \times I_C) \quad (1)$$

is shown in Figure 1. The full circles are due to the airglow and partial circles are due to the cometary emission. The cometary [OI] 6300Å is readily identified as the fringes are Doppler shifted from the airglow corresponding to its geocentric velocity. With respect to the cometary [OI] line the other cometary lines listed by Combi and McCrosky (1991) are identified by taking into account of the filter transmission and free spectral range of the FP. Further the inter-order overlap of the cometary lines transmitted by the pre-filter was also taken into account for the identification of NH₂ lines. Figure 2 shows an example of the radial scan from a part of the interferogram within one free spectral range corresponding to the two inner circles of the interferogram. The observed FP profile was divided by the computed instrumental transmission function for airglow and cometary [OI] emission in order to take into account the FP modulation. The absolute calibration is made by observing the the spectrophotometric standard star (29 Vul) with the pre-filter and FP etalon. The effect of FP etalon on the observation of the standard star have been taken into account. The calibrated cometary [OI] flux is extracted from four sectors A, B, C and D with respect to the center of the comet as shown in Figure 3. The sector A is in the tailward hemisphere and sector B is in the sunward hemisphere of the comet. The error in estimating the absolute values in [OI] intensity is $\sim 30\%$. The relative error in intensities is much smaller and does not exceed $\sim 10\%$.

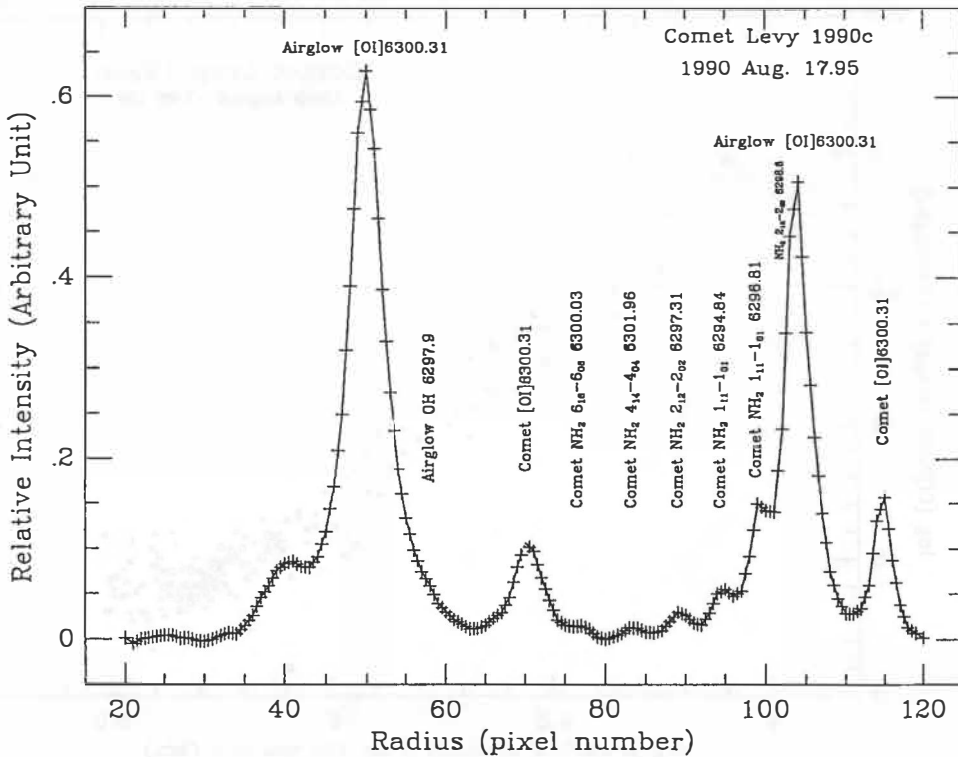


Figure 2: Radial scan within two inner circles of the interferogram

RESULTS AND DISCUSSION

The line profile analysis show that, in general the cometary [OI] emission line is wider than the airglow profile. In a selected area of $3 \times 24''$ ($3 \times 29 \times 10^3$ km) with the long side perpendicular to the fringe, at cometocentric distance of 2.2×10^5 km in the sunward side, we find the half width at half maximum to be 2.25 km/s. This refers to the outflow speed of oxygen atom within the field of view of the cometary atmosphere, since the natural width of O¹D line is small. Our values are slightly higher than similar measurements in the case of comet Kohoutek and Halley (Huppler et al, 1975, Magee-Sauer et al, 1988, Debi Prasad et al, 1988). However, the earlier measurements have used a large field of view, as a result, the contribution from the low velocity component at the near nucleus region is dominant in these signal. On the other hand, our data corresponds to a narrow field of view, isolating the signal from the near nucleus region. The dusty-gas-dynamic Monte-Carlo model by Combi (1989) in case of comet Halley predicts an outflow speed of 0.91 km/s at a heliocentric distance of 1.5 AU in the post-perihelion epoch within the collision zone. According to this model the expected velocity at the distance of our measurements is ~ 1.5 km/s.

We have traced the cometary [OI] emission up 3×10^5 km from the nucleus of comet Levy as shown in Figure 3. Our data show an approximate r_h^{-1} distribution of O¹D within a radial distance of 1.2×10^5 km from the nucleus which is close to the photo-dissociation scale length of water at the heliocentric distance of our observation, beyond which the distribution is flat. Earlier the [OI] distribution have been reported up to $\sim 10^5$ km from the nucleus (Magee-Sauer et al, 1988), with which our results are in agreement. The flat distribution beyond the photo-dissociation scale length of water could be due to the parent molecules with longer life time such as CO and CO₂. A sunward to antisunward asymmetry in the distribution of [OI] emission is noticeable up to a cometocentric distance of 10^5 km beyond which the signal is not strong enough. As in case of comet Halley (Combi and McCrosky, 1991) the observed asymmetry can be understood as the

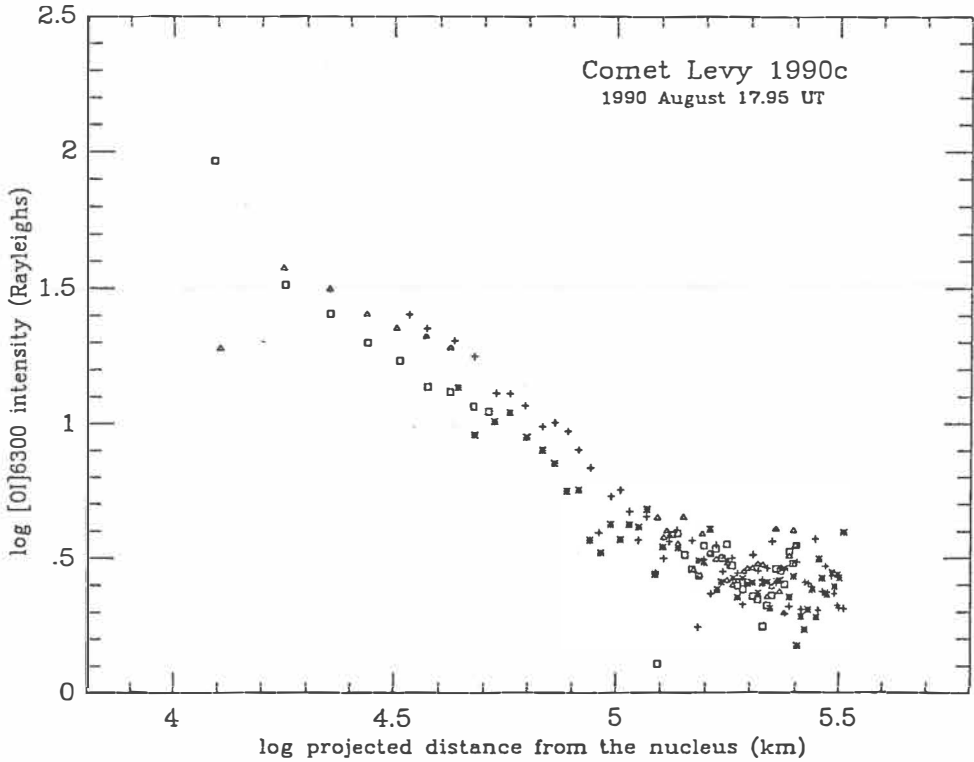


Figure 3: Distribution of cometary [OI] 6300 Å emission from four sectors of the interferogram (Δ :A; $+$:B; \square :C, $*$:D). See text for the explanation of different sectors.

result of preferential sunward ejection of material from the cometary nucleus. The inner coma imaging of comet Levy with the Hubble Space Telescope, indeed reveal a fan-shaped inner coma in which the sunward facing hemisphere is significantly brighter (by a factor of ~ 2.5) than the tailward hemisphere (Weaver et al, 1991), consistent with our observations.

REFERENCES

- Arpigny, C., Manfroid, J., Magain, P., and Haefner, R., 1987, On the forbidden red lines of oxygen in comets. In *Proceedings of the symposium on the diversity and similarity of comets*, ESA SP **278**, 571-576.
- C. Debi Prasad, T. Chandrasekhar, J. N. Desai and N. M. Ashok, 1988, High-resolution studies of [OI] and NH_2 line emission at 6300 Å in Halley's Comet, *Pub. Astron. Soc. Paci* **100**, 702.
- C. Debi Prasad and Desai, J. N., 1989, Imaging Fabry-Perot Observations of [OI] 6300 Å emission in the coma of Halley's comet 1982i, *Earth, Moon and Planets* **44**, 191-195.
- Combi, M. R. and McCrosky, R. E., 1991, High-Resolution Spectra of the 6300-Å region of comet P/Halley, *Icarus* **91**, 270-279.
- Huppler, H., Reynold, R. J., Roesler, F. L., Scherb, F. and Trauger, J., 1975, Observation of comet Kohoutek (1973f) with a ground-based Fabry-Perot spectrometer, *Astrophys. J.* **202**, 276-282.
- Jockers, K., Geyer, E. H., Rosenbauer, R. and Hänel, A., Observations of ions in comet P/Halley with a focal reducer, *Astron. Astrophys.* **187**, 256- 260.
- Magee-Sauer, K., Roesler, F. L., Scherb, F. and Harlander, J., 1988, Spatial distribution of O¹D from Comet Halley, *Icarus* **76**, 88-99.
- Weaver, H. A. et al, 1991, This conference.

THE FLUX OF SMALL ASTEROIDS NEAR THE EARTH

D. L. Rabinowitz, Lunar and Planetary Laboratory
The University of Arizona, Tucson AZ 85721

Tom Gehrels, Jim Scotti, and I have been scanning for Earth approachers since September of 1990. By Earth approacher (EA), I mean any object that approaches the sun to within 1.3 astronomical units (AU). Information about our scanning technique has been presented elsewhere in these proceedings (Scotti et al. 1991a) and in other publications (Rabinowitz 1991, Gehrels et al 1990). We have discovered fifteen new EAs since September, among them the smallest asteroids on record: 1990 UN, 1991 BA, and 1991 JR, which are in the 10 to 100m size range (Scotti et al. 1991b). For the first time, we can make estimates of the fluxes near the Earth of these small objects, thought to be the immediate parents of meteorites, from direct observation. In this paper, I show that for EAs larger than a few 100m, the magnitude-frequency dependence we observe is consistent with the cumulative magnitude-frequency relation, $m(H)$, established for the main belt asteroids. Assuming this relation extends to smaller sizes, however, the probability for discovering both 1990 UN and 1991 JR was 15%, and for discovering 1991 BA only 1%. Objects smaller than ~100m are therefore increasingly overabundant compared to an extrapolation from larger objects, with this excess increasing with decreasing size. Near 10m, the most probable flux near the Earth is two orders of magnitude higher. This is in agreement with the flux extrapolated from observations of bright meteors and fireballs. It is thus likely that processes other than collisional breakup of asteroidal material begin to supply the population of small objects near the Earth at sizes near 100m. Tantalizing clues from spectral measurements and orbital associations suggest that these objects may be the debris from extinct, short-period comets.

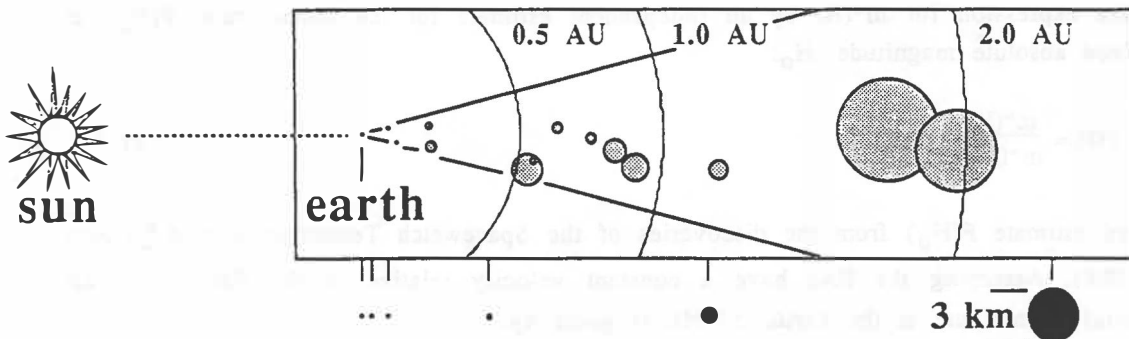


Fig. 1. Opposition geometry at discovery for Earth approachers discovered with the Spacewatch Telescope.

Discovery Geometry

A quick inspection of Fig.1 reveals that the larger EAs observed with the Spacewatch telescope have an incremental size distribution that is nearly proportional d^{-3} , where d is diameter. The figure is to scale, and shows the position in the ecliptic plane relative to the sun-earth line at the time of discovery for nearly all the EAs we have detected since September of 1990. The circles representing each object scale linearly with the estimated sizes. Notice that the number of objects we find does not depend strongly on object size. We have found EAs larger than 3 km as far as 2 AU from the earth, km-sized objects ~1 AU away, objects of ~200m diameter ~0.5 AU away, and smaller objects at nearer distances. Since the maximum geocentric distance, Δ_L , at which we can detect one of these objects is nearly proportional to d , and the number we detect of a given size goes as Δ_L^{-3}

(the search volume), the flatness of the spectrum we observe implies that the true incremental size distribution is proportional to d^{-3} . This same size distribution has been determined for the main-belt population (van Houten et al. 1970).

Detailed Analysis

The size distribution revealed by Fig.1 can be tested by a more rigorous analysis of the EAs discovered with the Spacewatch Telescope. I use a computer to simulate an arbitrarily large population of EAs with the same distribution of orbital elements, a , e , and i , as the population of known EAs, but random arguments of perihelion and ascending nodes. For each simulated EA, the computer assigns a random mean anomaly, solves for position and velocity, and evaluates the offset from apparent to absolute magnitude, $V-H$. Given an assumed form for $m(H)$, it can then predict the incremental number of simulated EAs, $\Delta n(H)$, that would be observed with the Spacewatch Telescope as a function of H . I then use the ratio of the actual number detected, $\Delta N(H)$, to the predicted number to correct $m(H)$ and arrive at the true magnitude-frequency for the Earth approachers, $m^*(H)$:

$$m^*(H) = \frac{\Delta N(H)}{\Delta n(H)} m(H) \quad (1)$$

This method of determining $m^*(H)$ is reliable to the extent that the orbits for the known EAs faithfully represent the true population. For example, an over-representation of orbits which are near to the orbit of the Earth, such as Aten-type orbits with low inclinations, would cause $\Delta n(H)$ to be over-estimated for large H values; hence, an underestimate for $m^*(H)$. This is because the smallest objects are only observable near the Earth.

In order to determine the cumulative impact rate at the Earth, $F(H)$, I must normalize the above expression for $m^*(H)$ by an independent estimate for the impact rate, $F(H_0)$, at some fixed absolute magnitude, H_0 :

$$F(H) = \frac{m^*(H)}{m^*(H_0)} F(H_0) \quad (2)$$

I can estimate $F(H_0)$ from the discoveries of the Spacewatch Telescope with $d \geq 1.0\text{ km}$ ($H_0 \leq 20.0$). Assuming the EAs have a constant velocity relative to the Earth, v , their incremental impact rate at the Earth, $\Delta F(H)$, is given by:

$$\Delta F(H) = \frac{\Delta N(H)}{\Omega(H)} 4\pi r^2 K v \quad (3)$$

where $\Omega(H)$ is the volume of space searched in order to find the asteroids of magnitude H , r is the radius of the Earth, and K is the flux enhancement due to gravitational attraction. As discussed above, $\Omega(H) \propto \Delta L^3$, and ΔL is the volume of a sphere with radius ΔL scaled by the fraction of the sky scanned by the Spacewatch Telescope. For the larger EAs observed near opposition and far from the Earth, it is straight forward to calculate ΔL for the Spacewatch Telescope as a function of H and the limiting magnitude, V_L . Evaluating $\Delta F(H)$ for magnitude intervals $H-\Delta H/2$ to $H+\Delta H/2$ and summing over the range spanned by the observations represented in Fig. 1 with $H < H_0$ yields $F(H_0)$.

Results

Fig. 2 shows F , as determined by equations (1) - (3) with $\rho=6400\text{ km}$, $K=1.8$ (Kresak 1978), $v=20\text{ km/s}$ (Shoemaker 1983), $V_L=20.5$, and $\Delta H=2.5$, plotted as a function of the impacting mass, m (black squares). The vertical error bars show the uncertainty owing to counting statistics. There is an additional systematic uncertainty of a factor of 2 owing to the uncertainty in the calculated normalization, $F(H_0)=4.6 \times 10^{-6} \text{ yr}^{-1}$ at $H_0=18.8$. I have converted from $F(H)$ to $F(m)$ assuming uniform spheres with density 3500 kg/m^3 and geometric albedo 0.12 ± 0.07 . The horizontal error bars show the uncertainty in this transformation. Also shown in Fig. 2 are the impact rates determined by other authors from observations of bright meteors (Ceplecha 1988), photographic surveys for asteroids (Shoemaker et al. 1990), and the size distribution of craters in lunar maria (Shoemaker 1983).

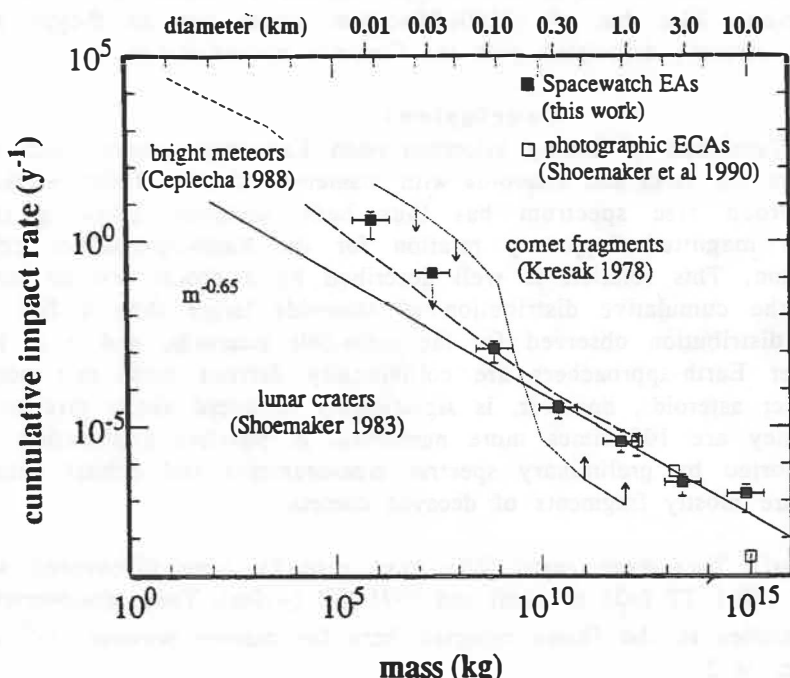


Fig. 2. The cumulative impact rate at the Earth as a function of impacting mass.

Examination of Fig. 2 shows that the values for F derived in this paper are within a factor of 2 of the results of photographic surveys (Shoemaker 1990) near $m=1.0 \times 10^{12}$ and $3.2 \times 10^{13} \text{ kg}$ ($d \sim 1\text{ km}$ and $d \sim 2\text{ km}$, respectively). These estimates, and the estimates from this paper for F at $m=3.2 \times 10^{10}$ and $1.0 \times 10^{15} \text{ kg}$ are fit well by a line with slope -0.65 (the solid line labeled " $m^{-0.65}$ " in the figure). This is the same m dependence seen in the population distribution of the main-belt asteroids, and revealed by Fig. 1. For $m < 3.2 \times 10^{10} \text{ kg}$ ($d < 150\text{ m}$), however, it is clear that the fluxes derived in this paper deviate significantly from the main-belt relation, with values 3 and 100 times larger than an $m^{-0.65}$ extrapolation would predict at $m=1.0 \times 10^9$ and $1.0 \times 10^6 \text{ kg}$, respectively. A similar deviation is seen in the fluxes derived from the size distribution of lunar craters, beginning at $m=3.2 \times 10^{10} \text{ kg}$ ($d \sim 200\text{ m}$) and continuing towards lower masses, but the deviation is smaller. The greatest deviation from the $m^{-0.65}$ extrapolation is shown by the fluxes of bright meteors, which are more than two orders of magnitude higher for $m < 10^4 \text{ kg}$. An extrapolation of the meteor curve to larger masses matches the flux reported in this paper at $m=1.0 \times 10^6 \text{ kg}$.

In addition to the measured flux curves plotted in Fig. 2, there is a curve showing the flux of cometary fragments predicted by Kresák (1978). As indicated by the vertical arrows, this curve is an upper limit below 10^9 kg, and a lower limit above 10^9 kg. The fluxes of Spacewatch EAs with masses $< 10^{10}$ kg approach this upper limit, suggesting that they are the cometary fragments envisioned by Kresák. This suggestion is supported by the orbital characteristics of 1991 BA ($Q=3.77$, $q=0.71$ $i=2.0^\circ$) and 1991 JR ($Q=1.77$, $q=1.04$, $i=10.1^\circ$). Though not decisively cometary, the orbit of 1991 BA explores the outer reaches of the asteroid-belt. In this respect, it is similar to the orbit comet P/Encke. The orbit of 1991 JR has been found to be clearly associated with the Φ Boötis meteor stream (J. Drummond, personal communication), which is a good indication that its source is cometary. 1991 JR also has a featureless C-type spectra (Mueller, 1991; E. Howell, personal communication), like that of (3200) Phaethon, which has an F-type spectrum (Tholen 1989) and is strongly associated with the Geminid meteor stream.

Conclusions

The Spacewatch Telescope is finding kilometer-sized Earth-approachers when they are farther than 1AU from the earth and asteroids with diameters of 10 to 100m within 0.1AU of the Earth. A broad size spectrum has thus been sampled, allowing the first determination of the magnitude-frequency relation for the Earth-approacher population from direct observation. This relation is well described by a power law in mass with exponent -0.65 for the cumulative distribution of asteroids larger than a few hundred meters. This is the distribution observed for the main-belt asteroids, and it is therefore likely that the larger Earth-approachers are collisionally derived from this population. The number of smaller asteroids, however, is significantly enhanced above this power law spectrum. At 10m they are 100 times more numerous. A possible explanation for this over-abundance, supported by preliminary spectral measurements and orbital analysis, is that small asteroids are mostly fragments of decayed comets.

note added in proof: Two more small EAs have recently been discovered with the Spacewatch Telescope: 1991 TT (~25 to 50m) and 1991 TU (~10m). These discoveries reduce the statistical uncertainties in the fluxes reported here for masses between 10^6 and 10^8 kg to less than a factor of 2.

Credit for the success of the Spacewatch Telescope goes to T. Gehrels, J. Scotti, R. McMillan and M. Perry at the Lunar and Planetary Laboratory (LPL). I also thank B. Marsden at the Minor Planet Center, B. Mueller at Kitt Peak National Observatory, E. Howell at LPL, and J. Drummond, formerly of LPL, whose efforts strengthened this work considerably.

References

- Cephecha, Z. (1988) Earth's influx of different populations of sporadic meteroids from photographic and television data. *Bull. Astron. Inst. Czechosl.* **39**, 221-236.
- Gehrels, T., McMillan, R. S., Scotti, J. V., and Perry, M. L (1990) Drift scanning with a TK 2048 CCD. In *CCD's in Astronomy* **8**, Astron. Soc. Pac. Conf. Series, (G. H. Jacoby, ed.), pp. 51-52. Brigham Young University, Utah.
- Kresák, L. (1978) The mass distribution and sources of interplanetary boulders. *Bull. Astron. Inst. Czechosl.* **29**, 135-149.
- Mueller, B.E.A. (1991) CCD-photometry of comets at large heliocentric distances. These proceedings.
- Rabinowitz, D.L. (1991) Detection of Earth-approaching asteroids in near real time. *Astron. Journ.* **101**, 1518-1529.

- Scotti, J.V., Rabinowitz, D.L., and Gehrels, T. (1991a) Automated detection of asteroids in real-time with the Spacewatch Telescope. These proceedings.
- Scotti, J.V., Rabinowitz, D.L., and Marsden, B.G. (1991b) Near miss of the Earth by a small asteroid. Nature, in press.
- Shoemaker, E.M. (1983) Asteroid and comet bombardment of the Earth. Ann. Rev. Earth Planet. Sci. 11, 461-494.
- Shoemaker, E.M., Wolfe, R.F., and Shoemaker, C.S. (1990) Asteroid and comet flux in the neighborhood of Earth. In Global catastrophes in Earth history. Geological Society of America Special Paper 247 (V.L. Sharpton and P.D. Ward, eds.), pp. 155-170.
- Tholen, D. J. (1989) Asteroid taxonomic classifications. In Asteroids II (R. P. Binzel, T. Gehrels, and M. S. Matthews, eds.), pp. 1139-1150. University of Arizona, Tucson.
- van Houten, C. J., van Houten - Groeneveld, I., Herget, P., and Gehrels, T. (1970) The Palomar-Leiden survey of faint minor planets. Astr. Astrophys. Suppl. 2, 339-448.

NARROW BAND PHOTOMETRY OF SELECTED ASTEROIDS

R.Rajamohan and S.G.Bhargavi

Indian Institute of Astrophysics, Bangalore-560034

Abstract

The CCD Photometry of selected asteroids was carried out to check for possible cometary activity in them. To distinguish the asteroids with possible cometary activity from those of the main belt ones, each object of interest was observed in two filters; one centered on the C₂ emission band at 5140A (90A bandpass) and the other centered on the nearby continuum at 4845A (65A bandpass). None of the observed asteroids appear to have any C₂ emission.

Summary

The possibility that some asteroids could be cometary in origin has been extensively reviewed recently by Weissman et al (1989). What fraction of the known asteroids have their origin in the distant cold regions of the solar system cannot easily be estimated. It appears that this fraction may be larger among the population of near earth asteroids (NEA) than among the main belt ones. Luu and Jewett (1990) have discussed this possibility among the NEA's and the Trojans as special analogs of cometary nuclei from their CCD reflectance spectra.

A detailed scrutiny to find the possible extinct comets among asteroids is difficult since the number of objects of interest is large and they are in general faint. Our endeavour is to short list such candidates for detailed future analysis from narrow band CCD photometry of all possible asteroids that are likely to show cometary activity. Our observational program also included a few faint comets for CCD photometry. Each object of interest was observed in two filters one centered on C₂ emission band at 5140A (90A bandpass) and the other one centered on nearby continuum at 4845A (65A bandpass) in order to easily distinguish the objects with cometary like activity from their intensity ratio in the two filters. During the four observing nights, (21st, 22nd February 1991 and 10th, 11th March 1991) at f/13 cassegrain focus of the one meter telescope of the Vainu Bappu Observatory (VBO), Kavalur, we could observe twelve asteroids, one comet and a few G type standard stars. Asteroids were chosen such that they were near stationary during the observing run. The EPHEM program by Dr.Dave Tholen was used to generate the ephemerides. The ex-

posure time through the two interference filters ranged from 5 to 30 minutes. Each object was observed in two filters. The motion of each object from one frame to the other was checked for consistency with the expected change in pixel position. Basic CCD calibration viz. corrections for bias, dark and flat field were done using the Starlink EDRS package available at the VAX-VMS, at the VBO. The mean bias value is subtracted from all the image frames. To correct for the pixel-to-pixel sensitivity a master flat is obtained (in each filter) which is the average of a few normalized flat fields taken from the morning/evening sky. The magnitudes were determined for each object by aperture photometry programs adapted from the Starlink software package and modified to suit the Comtal environment. The sky contribution was subtracted from measurements of a region nearby. The corrections for atmospheric extinction was done using the average extinction coefficient 0.25 in V valid for Kavalur. The observed magnitude difference through the two filters (m_c, m_l) was found to be peaking at a value of 0.5 for most of the asteroids while it is 1.18 for Comet Aarseth Brewingt. These results are given in Table 1. In Table 1, the column 3 gives the V magnitude at the time of observation and column 5 gives the magnitude difference through the two filters. All the results reported here are from a single act of measurements for each object. Results for the G-type stars observed are also included in Table 1 and Figure 1. As the exposure times for the stars are short, the results for them would be least affected by variation in the sky condition and hence would represent the lower limit to the expected ratio of intensities through the two filters. The slightly larger value found for 63 Ausonia, 665 Sabine and 754Malabar could be due to small variations in sky conditions between the two exposures and therefore needs to be confirmed.

As the CCD field at the f/13 focus of the one meter telescope is only 2'x 2'.5 we do not sometimes get a field star in each frame to monitor the variation in the sky between the two exposures. We hope to get over this problem by using prime focus of the 2.34-m Vainu Bappu Telescope where the CCD field is 4'x6'. This would also considerably reduce the exposure times and allow us to observe fainter objects. The histogram (Fig.1) shows that probably none of the asteroids observed have faint C₂ emission.

References

1. Jewitt, D.C. and Luu, J.X., (1990), CCD Spectra of Asteroids II. The Trojans as special analogs of cometary nuclei, Astron.J.100, 933..
2. Luu, J.X. and Jewitt, D.C., (1990), Charge Coupled Device Spectra of Asteroids I. Near Earth and 3:1 Resonance Asteroids. Astron.J.99, 1985.
3. Weisman, P.R., A' Hearn, M.F., McFadden, L.A. and Rickman, H., (1989) Evolution of Comets into Asteroids, in Asteroids II eds. Binzel, R.P., Gehrels, T., and Mildred Shapley Mathews, University of Arizona Press, p.880.

Sl.No.	Object	V	EXP(SEC)	(mc-m1)
1.	667 DENISE	12.84	300	0.60
2.	665 SABINE	13.30	900	0.72
3.	63 AUSONIA	11.20	300	0.70
4.	31 EUPHROSYNE	11.74	300	0.55
5.	109 HERA	12.42	600	0.54
6.	754 MALABAR	14.0	1800	0.68
7.	925 ALPHONSINA	12.56	1200	0.52
8.	449 HUMBURGA	13.5	1800	0.47
9.	68 LETO	12.16	1500	0.57
10.	11 PARTHENOPE	11.15	1200	0.55
11.	784 PICKERINGIA	13.41	1800	0.55
12.	912 MARITIMA	14.42	1800	0.51
13.	COMET AARSETH BREWINGT	7.69	300	1.18
14.	M67 REGION 3 STAR(12)	12.27	1200	0.48
15.	M67 REGION 3 STAR(17)	12.67	1200	0.49
16.	HR5235 (GO IV)	2.68	1	0.49
17.	HR5384 (G 1 V)	6.27	30	0.47
18.	HR140931 (GO V)	8.21	60	0.47
19.	HR5868 (GO V)	4.43	60	0.49

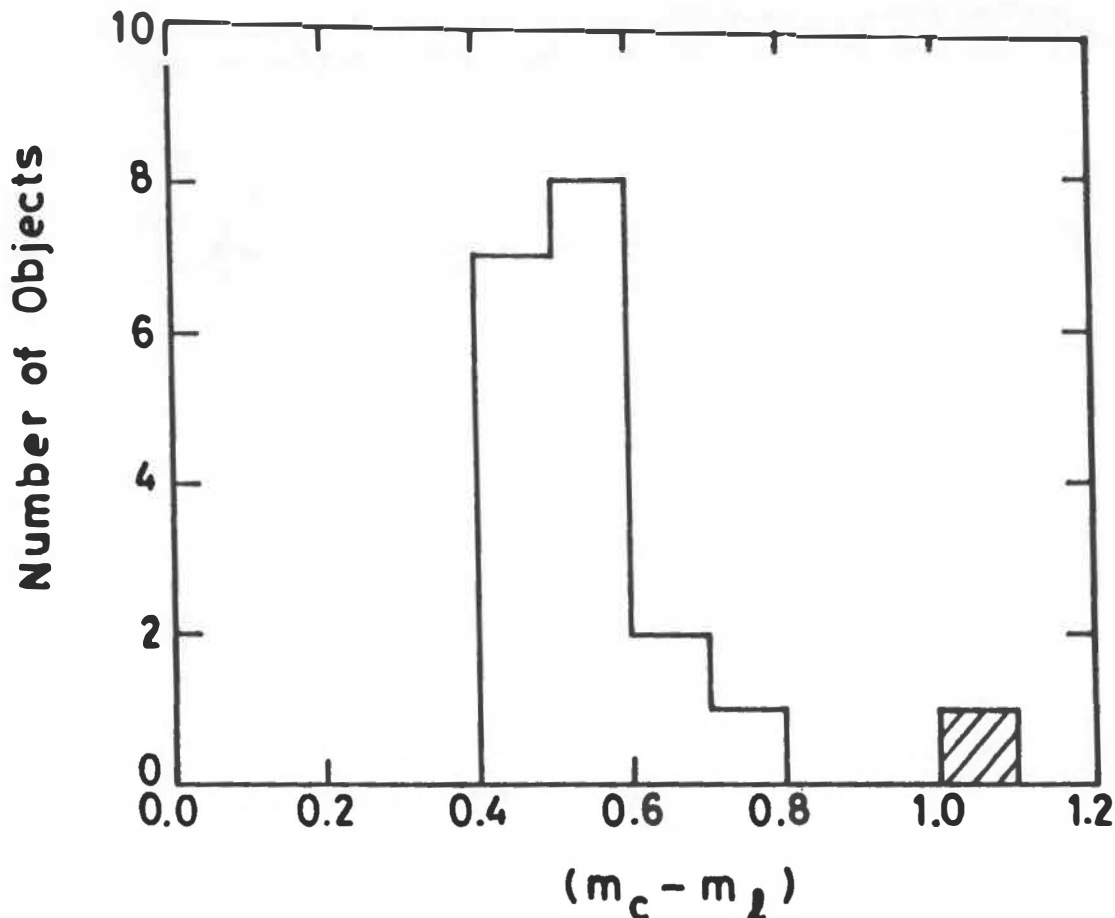


Fig. 1 Histogram of the observed magnitude difference in the continuum filter (4845 - 65Å band pass) and the C₂ emission band (5140 - 90Å band pass) in 12 asteroids, 6 G-type stars and the Comet Aaarseth Brewingt. The Comet value is shown shaded.

The Disconnection Event of 16.0 March 1986 in Comet Halley

C.E. Randall, J.C. Brandt, Y. Yi, and M. Snow
University of Colorado/LASP

Abstract

From kinematic extrapolation of tail/nucleus distance measurements on photographic images in the International Halley Watch (IHW) archive, we calculated the disconnection time of the 16-19 March 1986 event to be 16.0 (± 0.1) March. The solar wind conditions around Comet Halley at the time of the DE, inferred by corotation of IMP-8 satellite data to the comet, were such that (1) Comet Halley had just crossed the interplanetary magnetic field (IMF) sector boundary; (2) the solar wind density was $\sim 8 \text{ cm}^{-3}$; (3) the solar wind speed was $\sim 600 \text{ km/sec}$, (4) the IMF magnitude was $\sim 8 \text{ nT}$. Given these conditions, we conclude that the most likely cause of the 16.0 March DE was front-side magnetic reconnection, as described in the model of Niedner and Brandt (1978).

PHOTOGRAPHIC EVIDENCE

We have analyzed photographs from the International Halley Watch (IHW) archive throughout the 1985-1986 Comet Halley appearance. Figure 1 is a sequence of photos taken between 16 March 1986 and 19 March 1986.

They clearly show the occurrence of the disconnection event, and the evolution of the large scale structure of the comet tail on a daily basis after the DE. From the images we have determined the precise time of the DE, and have examined the solar wind conditions and interplanetary magnetic field at this time in order to ascertain whether any correlations were evident which would support one of the proposed mechanisms for DE occurrence.

RESULTS

From kinematic extrapolation of tail-nucleus distance measurements on the photographs, (see figure 2) we calculated the disconnection time of the 16-19 March 1986 event to be 16.0 (± 0.1) March. In calculating these distances, we assumed that the tail receded along the prolonged radius vector — a reasonable assumption during the first few days after the DE. The solid line through the data points is the best-fit second order polynomial assuming a constant acceleration of the disconnected tail from the nucleus. Because of this

assumption, we fit the polynomial to only the earliest data points (up to a distance of 5 million kilometers), during which time the acceleration appears constant. The extrapolated disconnection time of the DE is approximately 16.0 March with an uncertainty of about 0.1 days. The downstream acceleration of the disconnected plasma tail is about 15.6 cm/sec^2 , and the velocity at the time of disconnection is about 8.2 km/sec .

SPACECRAFT DATA

We inferred solar wind conditions around Comet Halley by corotating data from the IMP-8 satellite to the comet. Using this dataset, we determined that at the time of the DE the solar wind speed at the comet was $\sim 600 \text{ km/sec}$; the solar wind density was $\sim 8 \text{ cm}^{-3}$; and the IMF magnitude was $\sim 8 \text{ nT}$. These conditions are not particularly unusual, and thus would *not* be expected to have caused the observed DE via mechanisms such as ion production or pressure effects.

The relative trajectories of the Pioneer Venus Orbiter (PVO), IMP-8, the International Cometary Explorer (ICE), Vega-1, and comet Halley were calculated assuming an Archimedean spiral for the solar wind propagation, and are plotted in fig. 3 along with the calculated neutral line. The dots on the spacecraft (and comet) trajectories denote positions of the spacecraft (comet) on the dates designated in the figure. The open diamond-shaped marks on the trajectories of the spacecraft represent sector boundary detections by the corresponding spacecraft. The open triangles on the comet Halley trajectory represent times of observations of comet plasma tail DEs.

The two spacecraft observations (IMP-8 and Vega-1) available near the appropriate portion of the neutral line constrain the sector boundary very well. We have no PVO data for the end of February 1986 to further define the shape of the current sheet for this Carrington Rotation. From analysis of other DE's, we have found that a delay of ≈ 0.7 days between the comet crossing the sector boundary and the DE is typical (due to the merging and reconnection of the field lines on the front side of the comet which produces the disconnection of the tail).

DISCUSSION

We estimated the position of the IMF neutral sheet using two different methods: 1) the times and positions of 180-degree phase shifts in the IMF

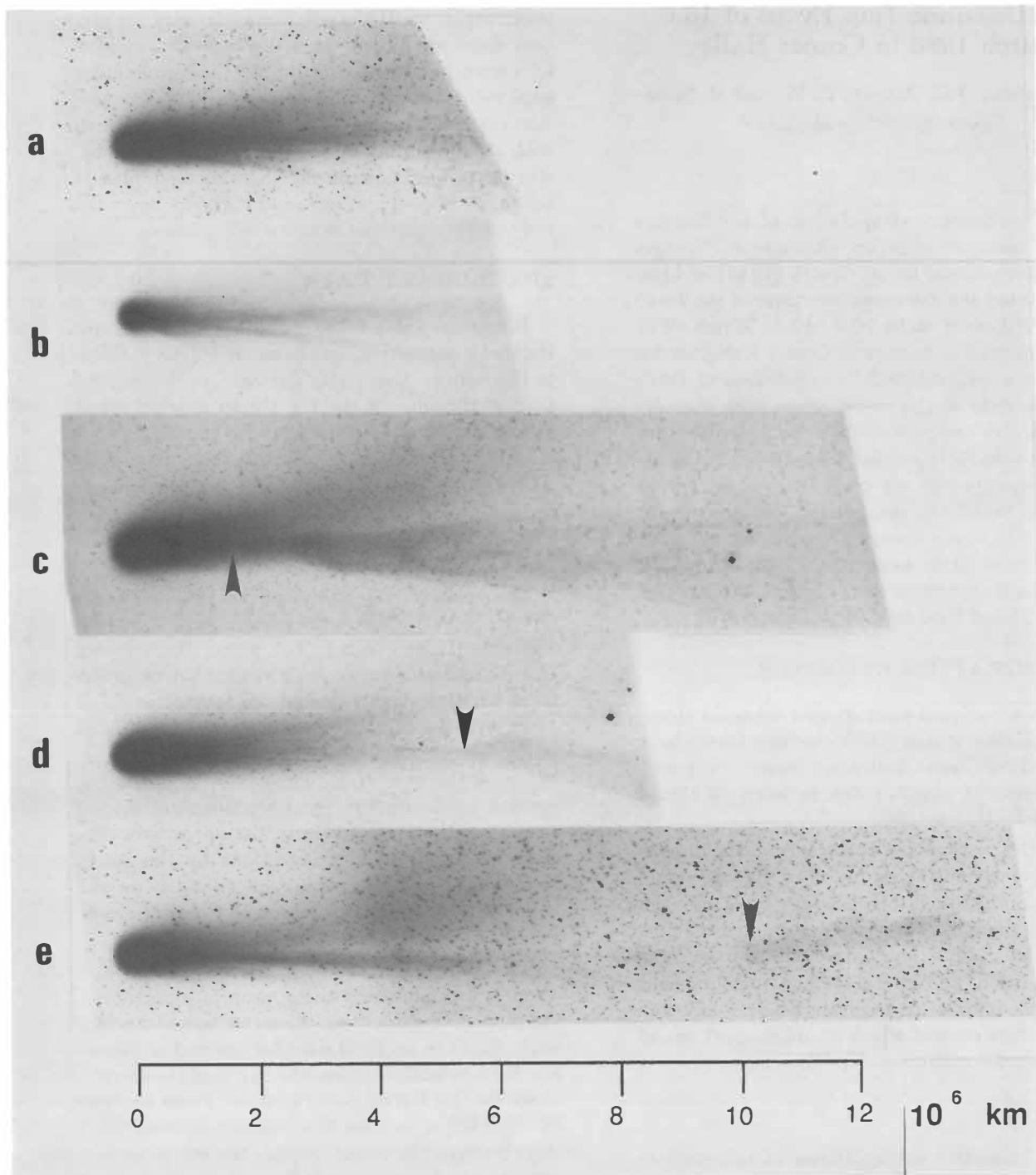


Figure 1: Time sequence of photographs of comet Halley depicting the-disconnection event of 16.0 March 1986. The dates of these images are (a) 15.97 March (K. Sivaraman, Indian Inst. for Astrophysics, Kavalur Sta.), (b) 16.36 March (F. Miller, University of Michigan/CTIO), (c) 17.37 March (G. Pizarro, European Southern Observatory), (d) 18.34 March (C. Torres/H. Wroblweski, Cerro el Roble Obs.), and (e) 19.47 March (W. Liller, LSPN Island Network).

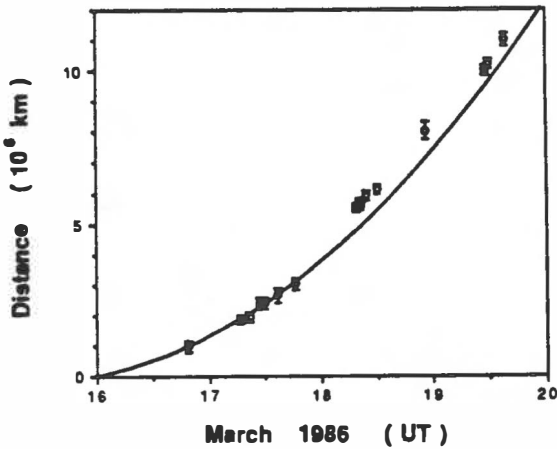


Figure 2: Distance of disconnected tail from nucleus.

direction were measured by the IMP-8, ICE, and PVO satellites, and then corotated to comet Halley's orbit, and 2) the neutral sheet calculated at the solar source surface was corotated out to the comet. Both methods are consistent with one another, and show that comet Halley crossed a magnetic field sector boundary shortly before the 16 March DE. The observations from IMP-8 of the particle density N_e and solar wind velocity w indicate that neither was particularly high at the time of this DE. We therefore conclude that the most likely cause of this disconnection event was front-side reconnection of the magnetic field.

References

Hoeksema J. T. (1989) Extending the Sun's Magnetic Field Through the Three Dimensional Heliosphere *Adv. Space Res.*, **9**, 141-152.

Niedner, M. B., Jr. and J. C. Brandt, (1978) Interplanetary Gas XXIII. Plasma Tail Disconnection Events in Comets: Evidence for Magnetic Field Line Reconnection at Interplanetary Sector Boundaries? *Astrophys J.*, **223**, 655-670.

Niedner, M.B., Jr. and K. Schwingenschuh, (1987) Plasma-tail Activity at the Time of the Vega Encounters *Astron. Astrophys.*, **187**, 103.

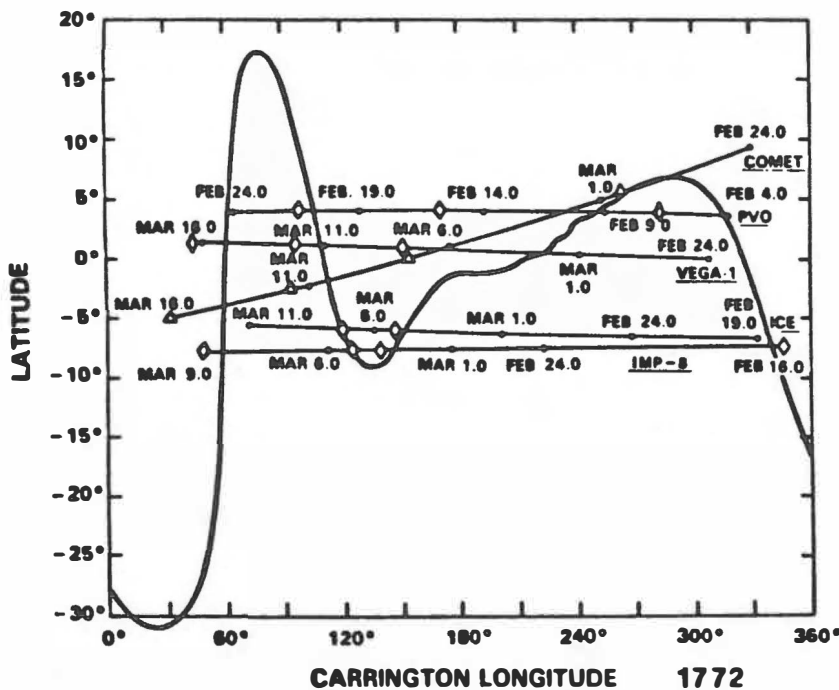


Figure 3: Carrington map of the computed coronal magnetic neutral line for Carrington rotation 1772. (Figure adapted from Niedner and Schwingenschuh (1987)).

Laboratory Studies on Cometary Crust Formation: The Importance of Sintering

L. Ratke, H. Kochan and H. Thomas
Institut für Raumsimulation, DLR Köln, FRG

ABSTRACT

It is demonstrated by experiments and theoretical considerations that sintering processes, so far used to describe the densification of metal and ceramic powders, are relevant for icy materials and therefore probably also for comets. A theoretical model is presented which describes the evolution of so called sinter necks, the contact zone between ice particles. With this model the strength increase of a porous, loosely packed icy body is calculated in which the sinter necks grow by evaporation and condensation of water vapour at a constant temperature. Experiments with ice powders validate the model qualitatively. An increase in strength up to a factor of four is observed during isothermal sintering. In order to check the relevance of the experimental results and the basic theoretical ideas with respect to real comets, more exact theories and improved experiments taking into account additional mass transport mechanisms are needed.

INTRODUCTION

During the experiments within the context of the KOSI (=Kometensimulation)-project two phenomena were observed which are of major importance for the dust emission of comets. First: The near surface observations of ice-/dust-particle emission from the surface of isolated ice/mineral mixtures revealed that the individual particles are bonded together. Before the particles can leave the surface their bonds to neighbours have to be eroded by the gas-jet which is caused from the sublimation of the volatile components, Kochan (1991). Second: The inspection of the material after isolation has shown a remarkable increase in hardness of more than one order of magnitude. Up to now this hardening was attributed solely to the recondensation of the volatiles in colder regions of the sample, Kochan et.al. (1989), leading to a decrease in porosity and an increase in bond area between the particles.

The formation of bonded areas between the ice/mineral particles or agglomerates may, however, not only be caused by recondensation of water vapour at the contact areas but can also occur without isolation by so called sintering processes. Sintering processes of particle agglomerates are a well known and investigated phenomena in the field of powder metallurgy, Ashby(1980). Generally any process leading to a rearrangement of particle agglomerates which is solely driven by curvature dependent gradients of the chemical potential is called sintering. In this paper we report on experimental and theoretical studies on sintering and show its importance for the comet simulation experiments.

THE PROCESS OF SINTERING

Sintering is driven by the minimization of the free surface energy of an ice particle agglomerate:

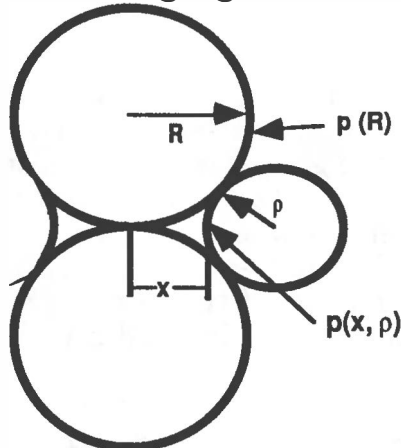
$$(1) \quad G = G(T, p) + \sum \sigma_i A_i \quad \text{with} \quad \delta G = \text{minimum}$$

with $G(T, p)$ the Gibbs free energy of massive ice, T the temperature and p partial pressure. σ_i is the surface tension of the i -th particle and A_i its surface area. The chemical potential of a single particle with radius R which is in thermodynamic equilibrium with its vapour depends linearly according to equation (1) on the particle curvature. Therefore the partial pressure of water above an icy particle depends exponentially on its curvature K :

$$(2) \quad p(R) = p_\infty \exp\left(\frac{\sigma \Omega K}{R_{\text{gas}} T}\right)$$

where p_∞ is the partial pressure above a flat surface, Ω the molar volume, K is equal to the sum of the two principal radii of curvature $1/R_1$ and $1/R_2$. R_{gas} is the universal gas constant. Gradients of the partial pressure lead to a transport of vapour within an agglomerate even at isothermal conditions!

If particles touch each other they will develop small neck areas by spontaneous adhesion, Swinkels and Ashby(1980). These necks form zones of concave curvature in contrast to the convex curvature of the spheres. Therefore the partial pressure at the neck areas is smaller than at the remaining areas of the particles (see Fig. 1). The difference in partial pressure leads to a mass transport from the convex to concave surfaces, thereby increasing the neck area. These bridges make the particles sticking together at the surface as well as in the interior.



$$\frac{dV_{\text{neck}}}{dt} = z(R, t) \cdot \Omega \cdot A_{\text{neck}}$$

$$z(R, t) = \frac{p(\rho, x) - p(R)}{\sqrt{2\pi \cdot \mu_{\text{mol}} \cdot R_{\text{gas}} T}}$$

z = sublimation rate

A_{neck} = neck surface area

V_{neck} = neck volume

μ_{mol} = molar mass of water vapour

Fig.1: Sinter neck between two particles. $p(R)$ is the partial pressure above the spheres, $p(x, \rho)$ the partial pressure above the concave neck surface.

There are different processes of sintering (see Swinkels and Ashby (1980)). In this paper we confine ourselves to the discussion of the vapour transport mechanism. A calculation of the neck surface area and volume according to the equations shown in Fig.1 reveals, that the neck radius x increases as:

$$(3) \quad x^3 = \frac{3\pi \cdot z_\infty \Omega^2 \sigma \cdot R}{2 \cdot R_{\text{gas}} \cdot T} \cdot t$$

if $x \ll R$. Therefore sintering will increase the bonded areas between ice particles in proportion to $t^{2/3}$. The strength of an agglomerate increases proportionally to the

neck area. A calculation of the strength increase of an ice agglomerate due to sintering according to eq.(3) and using the relationship $\sigma = \sigma_{\text{massive}} (x/R)^2$ for various particle sizes is shown in figure 2 a. Fig.2b shows $x(t,R)/R$ at 240 K without any approximation. The dashed straight lines are the approximation of eq.(3).

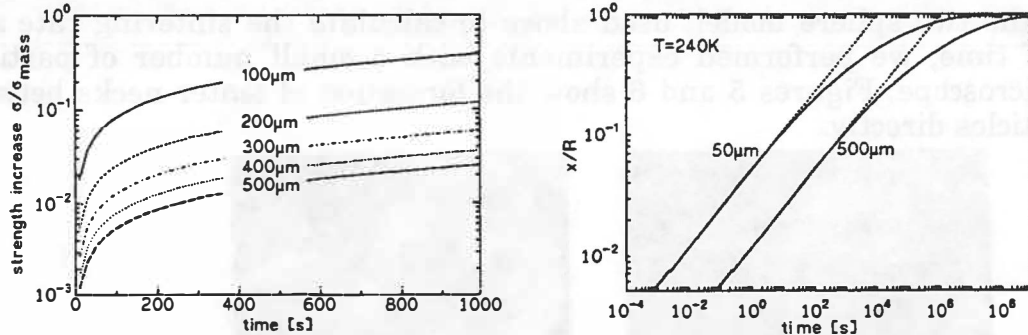


Fig.2a(left): Theoretical relative strength increase of a porous ice body due to sintering.
Fig.2b (right): Sinter neck radius as calculated from an exact theory for different particle sizes.

EXPERIMENTAL RESULTS

In order to validate the considerations made above about sintering of ice particles we performed experiments with porous ice. Spherical ice particles were made by spraying water into liquid nitrogen. The liquid nitrogen then at -20 °C evaporates while the ice powder is continuously stirred to avoid the formation of sinter necks prior to the experiment. The ice powder is filled into copper cans which were thermalized for a period of days to -20°C in a cold lab. The sintering of this isothermal powder as a function of time is examined by the measurement of the strength increase compared to the initially loosely packed powder bed. Care was taken to ensure the isothermality of the samples and a special procedure to fill the cans was developed making the measurements reproducible. The strength was measured with a spherical indentor which moved into the sample with a speed of 40 mm/min, Kochan et.al. (1989). Fig.3 shows a typical curve of stress versus penetration depth of the indentor. After an initially nearly linear increase in stress a maximum is reached after which the stress oscillates around

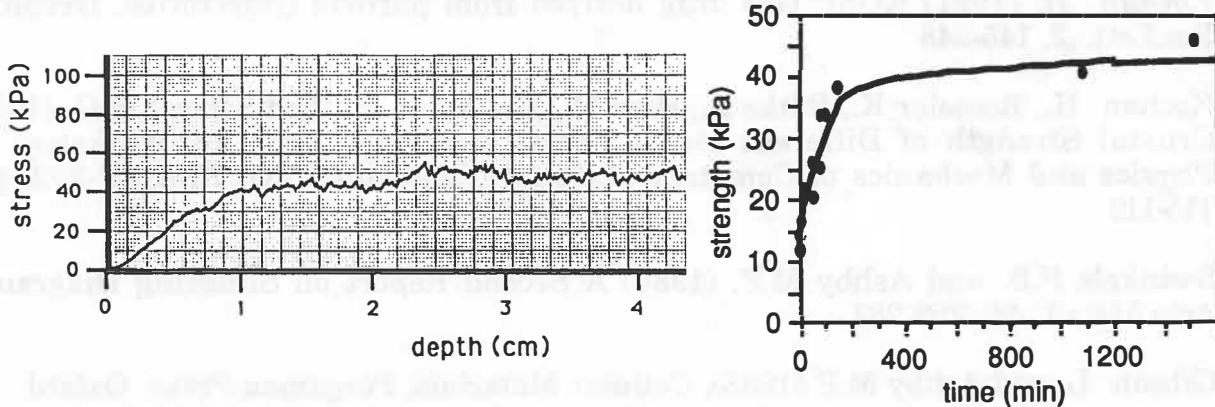


Fig.3(left): Measured stress of a porous ice body as a function of sample depth.

Fig.4(right): Strength of porous ice bodies at -20°C as dependent on sintering time.

a mean value in a random manner. This behaviour is typical for brittle porous bodies (Gibson and Ashby, 1988). The increase of strength as a function of sintering time is shown in fig.4. A comparison of this experimental result with the theoretical prediction of fig.2 qualitatively shows the same behaviour.

Following the two sphere model, used above to calculate the sintering rate as a function of time, we performed experiments with a small number of particles under a microscope. Figures 5 and 6 show the formation of sinter necks between the ice particles directly.

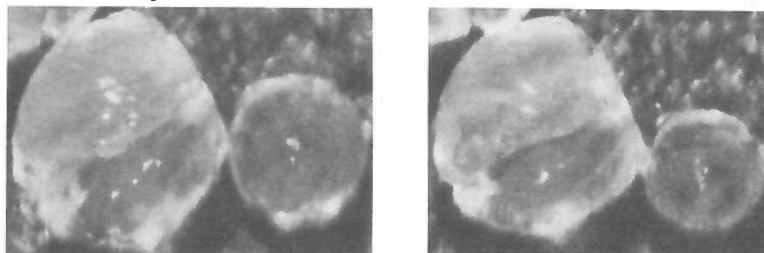


Fig.5 (left): Ice spheres just deposited under a microscope at -20°C. Fig.6 (right): Same arrangement of ice particles after 26h sintering.

CONCLUSIONS

It was demonstrated that sintering processes are even relevant in icy material and therefore most probably also within real comets. The theoretical description given is limited to sinter neck radii which are small compared with the particle radii. Better models are under development, especially taking into account the variation of particle sizes within a sample, which would induce an additional change in the morphology and texture of an ice agglomerate (Ostwald ripening, Voorhees (1985)). In order to check the relevance of these experimental results and the basic theoretical ideas for real comets more exact theories and improved experiments taking into account additional mass transport processes are needed. Further experiments using different porosities and ice-/mineral-mixtures are under preparation.

References

- Kochan H. (1991) KOSI: Gas drag derived from particle trajectories, *Geophys. Res.Lett.*, 2, 145-248
- Kochan H., Roessler K., Ratke L., Heyl M., Hellmann H., and Schwehm G. (1989) Crustal Strength of Different Model Comet Materials, Proc. Int.Workshop on Physics and Mechanics of Cometray Materials, Münster FRG, ESA SP-302, pp. 115-119
- Swinkels F.B. and Ashby M.F. (1980) A Second Report on Sintering Diagrams, *Acta Metall.*, 29, 259-281
- Gibson L. and Ashby M.F (1988), Cellular Materials, Pergamon Press, Oxford
- Voorhees P.W. (1985) The theory of Ostwald Ripening, *J.Stat.Phys.*, 38, 231-252

VISUAL DATA OF MINOR METEOR SHOWERS LIMITS OF THE METHOD

J. Rendtel and R. Koschack, Arbeitskreis Meteore, PSF 37, 1561 Potsdam, Germany
International Meteor Organization

Abstract Visual meteor observations are carried out on a regular basis by many experienced observers worldwide, thus supplying information about activity of meteor showers. The limits of the method are determined by the accuracy of the detection of the meteor trail. This study shows that visual meteor observations provide reliable data for an observable hourly rate of ≥ 3 .

Introduction

Most analyses and model calculations of meteor showers deal with so-called major showers which deliver a reasonable sample within rather short time intervals. In the case of low number density or/and low geocentric velocity the number of observable meteors is quite low ("minor showers").

Many data at hand were obtained by visual single-station observations. Their main disadvantage is the limited accuracy of the shower association of any meteor. In order to improve the material, the Visual Commission of the *International Meteor Organization, IMO*, formulated rules which visual observers should follow. Three essential quantities which can be obtained by well trained visual observers are considered for the shower association of meteors:

- (i) direction of the trail (tracing back the line must meet the radiant of a certain size)
- (ii) apparent trail length must not be longer than half the distance from its (possible) radiant; exception: fireballs penetrating to low end heights
- (iii) the angular velocity in dependence on the meteor's elevation and its distance from the radiant

In order to distinguish shower meteors from different showers as well as from the sporadic background, the observer is forced to look not more than 40° away from the radiant(s) under study. Furthermore, a radiant should be situated at least 30° above horizon. Otherwise the commonly used correction of the activity to zenith position becomes too large and the result is then uncertain.

Sporadic Pollution of Shower Activity

Gyssens (1989) analysed the probability that a sporadic meteor will be classified as belonging to a shower radiant assuming uniform distribution of sporadic meteors. For a radiant of 10° in diameter situated at the zenith this probability amounts to 5.6 percent.

Recent analyses confirm this quite well. We considered two "radians" at 30° and 60° elevation and of 10° diameter each. The assumed radians were distant enough from known ecliptical showers, and activity periods of Quadrantids as well as Lyrids were excluded. For each radiant we did three searches: Firstly we looked for an alignment of the meteor trails only (no velocity information and thus identically to the model of Gyssens (1989)). Secondly we assumed a geocentric velocity of $v_\infty = 60$ km/s for both radians, and finally we considered $v_\infty = 30$ km/s. The results are given in table 1.

Table 1: Portion of all observed meteors which may be associated with the assumed radiant of 10° diameter including the criteria described above. 1757 meteors observed by experienced observers in the period Jan – Jun 1990 and Jan – Apr 1991 were included in the sample.

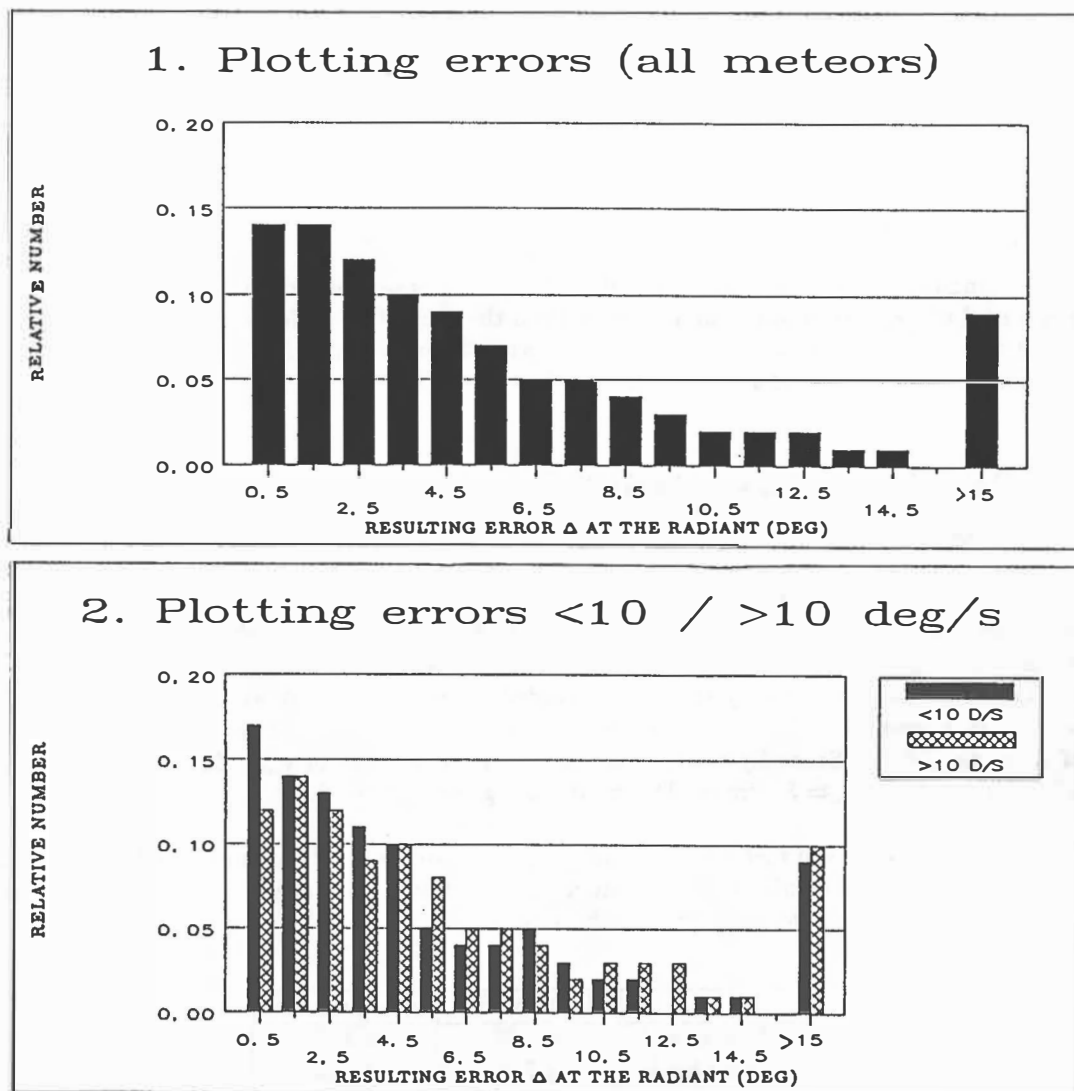
	elevation 60°	elevation 30°
v_∞ "unknown"	8.1 %	8.4 %
$v_\infty = 60$ km/s	4.7 %	4.6 %
$v_\infty = 30$ km/s	2.6 %	3.1 %

The pollution of the rate for a shower with known geocentric velocity by sporadic meteors may be expected to be less than 5 percent of the total rate. The total rate varies between about 5 in spring and 20 in autumn. Consequently, the pollution by sporadic background can be neglected for most periods.

Plotting Errors

On the other hand, there occurs a "loss" caused by the limited accuracy of visual observations. The main source of this is the uncertainty of the recorded direction. Most visual observers use gnomonic star charts to plot meteor trails. Different effects, which are hard to separate, cause tilts ε of the plotted trails. As a consequence, backwards traced shower meteors do not longer cross the radiant area and the rate should be lowered. Earlier analysis of plotting accuracy (e.g. Štohl and Lindblad, 1982) do not consider angular errors. But errors in length are not that much critical for the shower association. In order to obtain information about scatter in the directions of plots we analysed double or multiple plots on gnomonic star charts of the Atlas Brno by a team of experienced observers in October 1990. A detailed description will be given by Koschack (1991).

Fig. 1 shows the resulting errors at the radiant Δ (that is the minimal distance of the backwards prolongation of a meteor to its radiant) depending on the distance between meteor and radiant D for the whole sample.

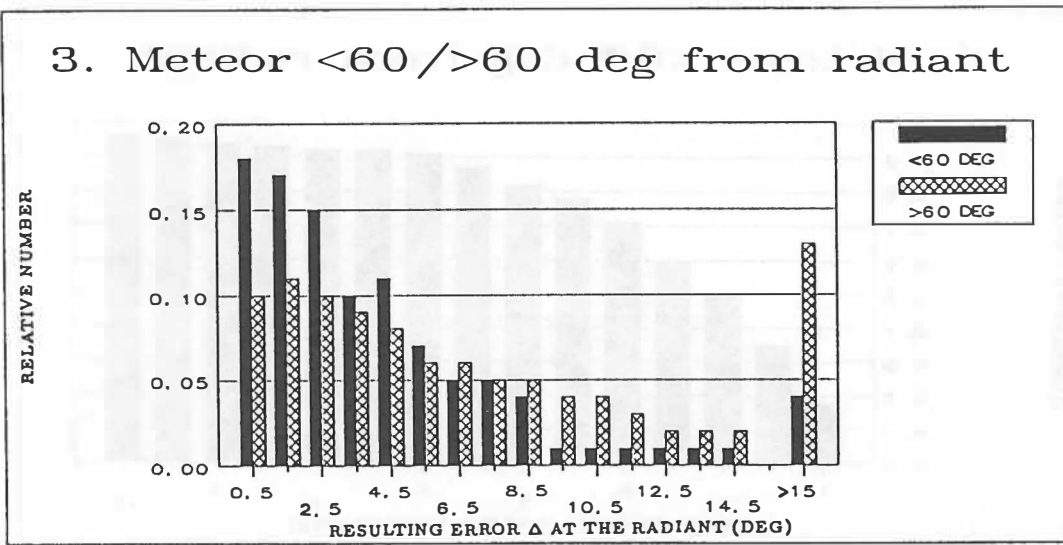


The result of Štohl and Lindblad that meteors of lower angular velocity are recorded with better accuracy can be confirmed (fig. 2), although the effect is not very significant.

The obvious difference for meteors observed in a distance $< 60^\circ$ or $> 60^\circ$ from the radiant shown in fig. 3 is of greater importance. A certain tilt ε of the trail causes an error Δ at the radiant depending on its distance to the radiant D :

$$\Delta = \varepsilon \times \sin D$$

Thus the rule fixed by the Visual Commission of IMO to center the field of view near the radiants under study is reasonable.



What are the conclusions from this study? The "loss" of true shower meteors due to plotting errors does not allow the assumption of small radiant sizes for visual work. Of course radiant positions and sizes are known from observations based on other techniques. To compensate the loss, a radiant diameter of at least 10° is required and the observer is forced to include the other criteria (see introduction) for shower association. Consequently, activity analyses of showers with neighbouring radiants from visual data do not make sense (e.g. several Aquarid radiants). Furthermore a radiant diameter of 15° causes a sporadic pollution of about 8 percent of the total rate. Both, the "loss" and the pollution set a limit to the observability of minor showers to a rate in the order of 3 per hour, as for this rate the ratio *true shower meteors : pollution by sporadics* is about 3 : 1 which should be considered as a limit for serious analyses.

Conclusions

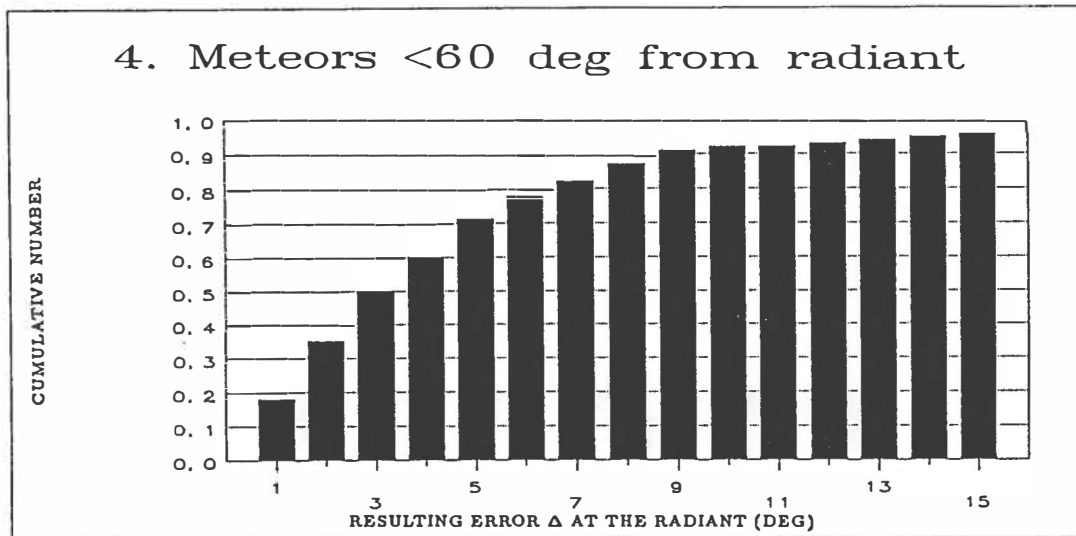
Visual meteor observations may be used to analyse minor showers as soon as their activity reaches an hourly (observable) rate of about 3 and the field of view of the observer is near the radiant position ($< 40^\circ$ distance). The radiant diameter should be assumed to be in the order of 10° . Fig. 4 shows the cumulative number of meteors having resulting errors $\leq \Delta$ at the radiant. This sample was obtained from plots of meteors seen $\leq 60^\circ$ from their radiant by experienced observers. Consequently, the radiant diameter which has to be assumed for shower association should urgently be included if visual meteor data are requested (as, for example, by Drummond (1991) or Hughes (1990)). Otherwise the material does not allow any valuable conclusion.

Minor showers producing hourly rates below 3 certainly exist. But visual observations are not appropriate for studies of their activity. We propose the use of video technique for studies of such showers. Even single station data may be useful since the method provides direction as well as precise angular velocity.

In the IMO working list of showers for visual work are included only showers that

- (i) reach a certain level of activity ($ZHR \approx 3$), and
- (ii) have known orbital elements (thus known geocentric velocity).

All other meteors are regarded to be sporadic. Since the meteor trails are plotted on gnomonic charts (except the periods of high activity near major shower maxima), searches for radiants being of interest only later, can be done from the stored trails. Furthermore, IMO prepared a positional database (PosDat). It contains positional data of visual and telescopic meteors and is connected with a radiant search program. This allows an effective search for instance for a possible activity of asteroid related radiants.



REFERENCES

- Drummond J., Reed K.L., and Gaffey M.J. (1991) Two meteor projects for amateurs. *Sky&Tel.*, 81, 478–479.
 Gyssens M. (1989) On the pollution of visual meteor stream counts by the sporadic background. *WGN*, 17, 217–222.
 Hughes D.W. (1990) The mass of comets and meteoroid streams and the shower / sporadic ratio in the incident visual meteoroid flux. *Mon.N.Roy.Astron.Soc.*, 245, 198–293
 Koschack R. (1991) Accuracy of meteor plots. *WGN*, 19, in preparation.
 Štohl J., Lindblad B.A. (1982) Plotting errors in visual meteor observations. *Bull.Astron.Inst.Czechosl.* 33, 129–141.

LONG SLIT SPECTROSCOPY OF NH₂ IN COMETS HALLEY, WILSON AND NISHIKAWA-TAKAMIZAWA-TAGO

Terrence W. Rettig and Stephen C. Tegler (University of Notre Dame), Susan Wyckoff and Rodney Heyd (Arizona State University), Raylee Stathakis (Anglo-Australian Observatory) and D. A. Ramsay (Herzberg Institute of Astrophysics, NRCC)

ABSTRACT

Long-slit spectra of comets Halley, Wilson and Nishikawa-Takamizawa-Tago were obtained with the 3.9 meter Anglo-Australian Telescope. Spectra of comets Halley and Wilson were obtained with the IPCS at a spectral resolution of 0.5 Å and a spatial resolution of 10³ km. Spectra of comets Wilson and Nishikawa-Takamizawa-Tago were obtained with a CCD at a spectral resolution of 1.5 Å and a spatial resolution of approximately 3x10³ km. Surface brightness profiles for NH₂ were extracted from the long-slit spectra of each comet. The observed surface brightness profiles extend along the slit to approximately 6x10⁴ km from the nucleus in both sunward and tailward directions. By comparing surface distribution calculated from an appropriate coma model with observed surface brightness distributions, the photodissociation timescale of the parent molecule of NH₂ can be inferred. The observed NH₂ surface brightness profiles in all three comets compares well with a surface brightness profile calculated using the vectorial model, an NH₃ photodissociation timescale of 7x10³ seconds, and an NH₂ photodissociation timescale of 34,000 seconds.

1. INTRODUCTION

Comets that pass sufficiently close (≤ 5 AU) to the sun develop a transient atmosphere due to sublimation of nucleus ices. These ices probably condensed from solar nebular gases 4.5 billion years ago at the earliest solar system epochs, and have remained relatively unprocessed. Therefore, analysis of the molecular composition of comet comae can reveal important information on the physical state and chemical abundances in the early solar nebula. Neutral molecules observed in the visible spectra of comets (C₂, C₃, CH, CN, NH₂, [OI]) are photodissociation fragments of parent molecules which sublimated from the nucleus. The identities of the parent molecules are largely unknown.

A technique used to determine the identities of parent molecules is to analyze the spatial distributions of the radicals using a suitable model. The parent molecule photodissociation timescales can be inferred from a comparison between calculated and observed surface brightness distributions. The parent photodissociation timescale identifies, hopefully uniquely, the parent molecule. Long slit spectroscopy has been used to determine the spatial distributions of individual molecules in comet coma (Cochran and Barker 1986, Wyckoff *et al.* 1988). In the past, low to moderate spectral resolution (~5-10 Å) long slit spectra have been used to trace the spatial distribution of a given molecular species in comet comae. Moderate resolution spectra, however, may not provide unique tracers of individual molecules because of confusion with other molecular emission lines and background dust continuum. The ideal technique to map the spatial distribution of a given molecular species in a comet coma is high resolution imaging spectroscopy using a long slit (>3 arcmin). Here we report observations of NH₂ spatial distributions in three comets at approximately the same heliocentric distance ($r \approx 1.3$ AU). The unambiguous NH₂ spatial profile has been analyzed to determine information about the source of NH₂.

2. OBSERVATIONS

Long-slit spectral observations of comets Halley, Wilson and Nishikawa-Takamizawa-Tago were obtained with the 3.9 meter Anglo-Australian Telescope. Observations of P/Halley were obtained on 1986 April 14 and observations of C/Wilson and C/Nishikawa-Takamizawa-Tago were

obtained on 1987 May 10. Spectra of comets Halley and Wilson were obtained with the Image Photon Counting System (IPCS) over the 3800 to 6800Å wavelength interval at a spectral resolution of 0.5 Å. In addition, long slit spectra of comets Wilson and Nishikawa-Takamizawa-Tago (NTT) were obtained with the CCD spectrograph over the 3800 to 6800Å spectral interval at a resolution of 1.5 Å. The size of the CCD images and IPCS images were 576x386 pixels and 2020x220 pixels. The IPCS and CCD sampling rates were 0.05Å/pixel and 0.7Å/pixel. The slit was centered on the peak brightness of each comet and oriented along the extended solar radius vector and had dimensions 3.6 arc min by 1 arc sec. The IPCS and CCD had spatial samplings of 1 arcsec/pixel and 0.56 arcsec/pixel respectively. The measured surface brightness profiles extend to approximately 6×10^4 km from the nucleus in both sunward and tailward directions. The three comets were observed at nearly the same heliocentric distance (1.240, 1.296 and 1.38AU for comets Wilson, NTT and Halley), the geocentric distances were 0.710, 0.771 and 0.430AU respectively.

Data reduction was performed with the Image Reduction and Analysis Facility (IRAF) at Arizona State University and Figaro at the Anglo-Australian Observatory. The CCD images were wavelength calibrated using standard Cu-Ar arc lamps and flux calibrated using a standard A1 IV star (BS 4819) and mean extinction coefficients. The IPCS images were wavelength calibrated using standard He-Ne-Ar arcs.

An extraction parallel to the dispersion axis resulted in a spectrum of the NH₂ (9-0) band for comet Wilson (Figure 1). This spectrum includes the underlying dust continuum. The three molecular lines used in this analysis are the 1₀₁-1₁₁, 0₀₀-1₁₀ and 1₀₁-2₁₁ lines.

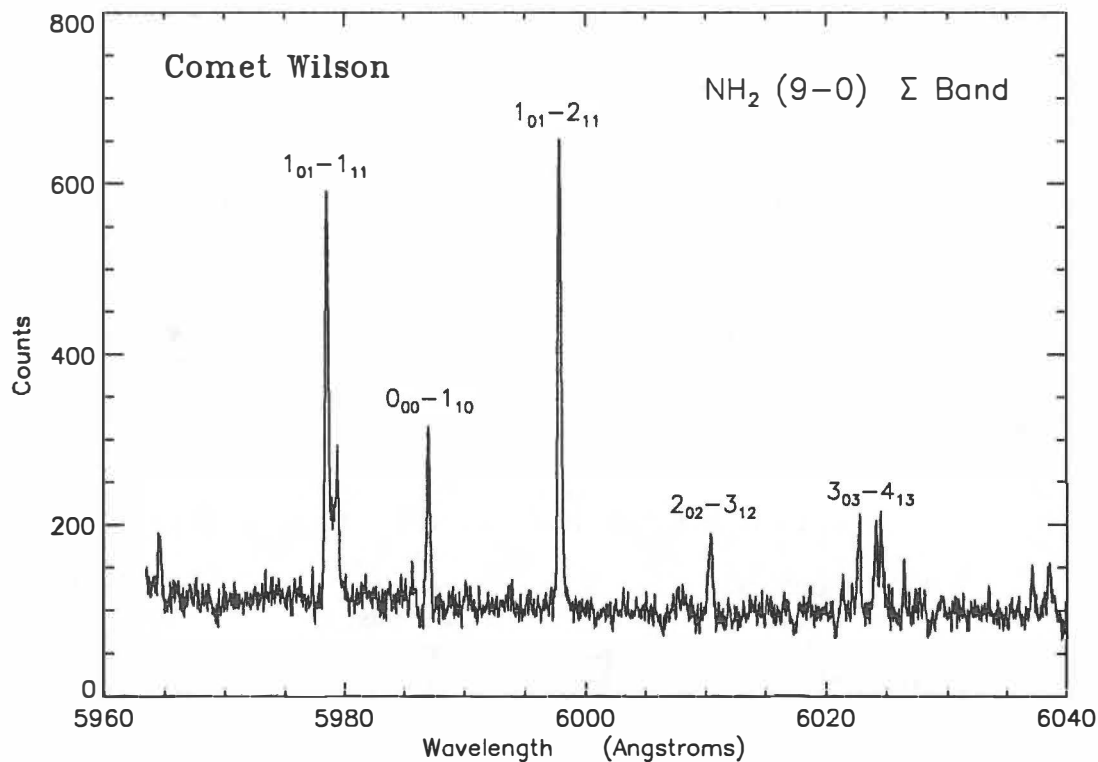


Figure 1. Spectra of the NH₂(9-0) band for comet Wilson.

Extractions perpendicular to the dispersion axis resulted in surface brightness profiles for NH₂. A surface brightness profile for each molecular line in Figure 1 was obtained as follows. First an

extraction centered on a molecular line was obtained. This extraction included not only the surface brightness of the molecular line, but also the surface brightness of the underlying continuum. The continuum contamination was removed by obtaining another extraction offset to a nearby continuum bandpass. The continuum surface brightness profile was subtracted from the molecular line plus continuum profile resulting in an isolated molecular line surface brightness distribution.

An examination of the 101-111, 000-110 and 101-211 rotation lines of the NH₂ (9-0) band showed that each line had the same surface brightness distributions within the observational uncertainties, hence, the individual profiles for the NH₂ lines were averaged for each comet. Figure 2 shows the average NH₂ (9-0) surface brightness profile for each comet. Also, the individual profiles showed no obvious systematic sunward - tailward asymmetry. The error bars in Figure 2 result from photon counting statistics. The NH₂ surface brightness profiles for the comets appear the same within the uncertainties.

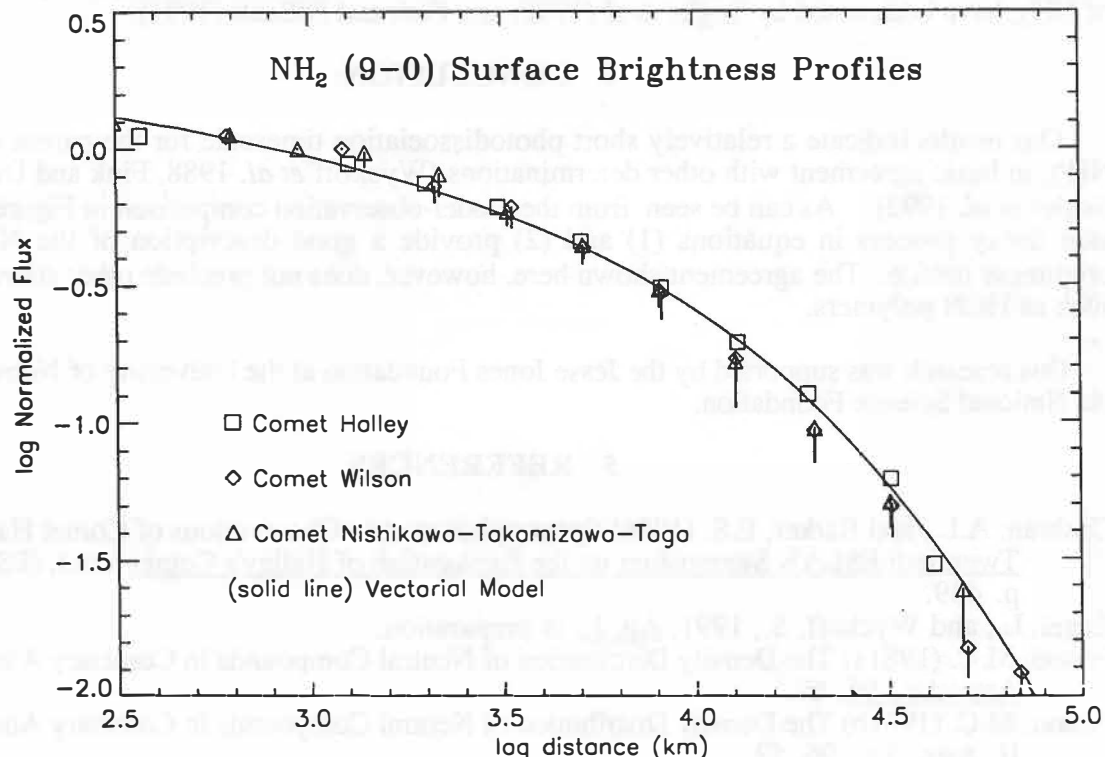


Figure 2. Surface brightness profiles for the NH₂(9-0) band for three comets.

3. DISCUSSION

It is important to identify the parent molecules of photodissociation fragments in the comae of comets because molecular abundances in comets provide significant constraints on the extent of chemical and physical processing in the early solar system. Using the observed surface brightness profiles of photodissociation fragments and a coma model, we can in principle determine the lifetimes of parent molecules and hence constrain the identity of parent molecules.

A surface brightness profile was calculated for NH₂ using the vectorial model (Festou 1981a,b). The calculation assumed NH₂ is created and destroyed by the reactions



and



The photodissociation timescales for the reactions in equations (1) and (2) were calculated from photodissociation cross-sections and satellite observed solar fluxes (Engel and Wyckoff 1991). In particular, NH₃ and NH₂ photodissociation time scales of 7700 and 34,000 seconds (1AU) were used in the calculation (Engel and Wyckoff 1991). A parent outflow velocity of 1km/sec was assumed in the calculation (Eberhardt *et al.* 1986, Lammerszahl *et al.* 1986, Larson *et al.* 1986, Scholerb *et al.* 1986) and the velocity imparted to daughter molecules resulting from the excess energy of photodissociation was assumed to be 1km/sec (Tegler *et al.* 1992).

In Figure 2, the calculated NH₂ surface brightness profile is shown (solid line). From Figure 2 the calculated and observed surface brightness profiles agree to within 10% out to a projected distance of $\log r = 4.8$ (6×10^4 km). The agreement between observed and calculated profiles is consistent with NH₃ being the parent molecule. Similar conclusions, that NH₃ is a parent molecule of NH₂, have been noted by Tegler *et al* (1992) and Fink and DiSanti (1991).

4. CONCLUSION

Our results indicate a relatively short photodissociation timescale for the parent molecule of NH₂, in basic agreement with other determinations (Wyckoff *et al.* 1988, Fink and DiSanti 1991, Tegler *et al.* 1992). As can be seen from the model-observation comparison in Figure 2, the two-step decay process in equations (1) and (2) provide a good description of the NH₂ surface brightness profile. The agreement shown here, however, does not preclude other sources for NH₂ such as HCN polymers.

This research was supported by the Jesse Jones Foundation at the University of Notre Dame and the National Science Foundation.

5. REFERENCES

- Cochran, A.L., and Barker, E.S. (1986) Spectrophotometric Observations of Comet Halley, In Twentieth ESLAB Symposium on the Exploration of Halley's Comet Vol.1, (ESA SP-230), p. 439.
- Engel, L., and Wyckoff, S., 1991, Ap. J., in preparation.
- Festou, M.C. (1981a) The Density Distribution of Neutral Compounds in Cometary Atmospheres, Astr. Ap., 95, 69.
- Festou, M.C. (1981b) The Density Distribution of Neutral Compounds in Cometary Atmospheres II, Astr. Ap., 96, 52.
- Fink, U., and DiSanti, M.A. (1991) P/Halley: Spatial Distributions and Scale Lengths for C₂, CN, NH₂ and H₂O, Ap. J., in press.
- Lammerzahl, P. *et al.* (1987) Expansion Velocity and Temperatures of Gas and Ions Measured in the Coma of Comet Halley, Exploration of Halley's Comet, 169-173.
- Larson, H.P., Davis, D.S., Mumma, M.J., and Weaver, H.A. (1986) Kinematic Properties of the Neutral Gas Outflow from Comet P/Halley, Exploration of Halley's Comet, 391-397.
- Schloerb, P., Claussen, M. and Tacconi-Garman, L. (1986) OH Radio Observations of Comet P/Halley, Exploration of Halley's Comet, 469-474.
- Tegler, S. C. *et al.* (1992) NH₃ and NH₂ in the Coma of Comet Borson-Metcalf Ap.J. 384 (in press)
- Wyckoff, S., Tegler, S., Wehinger, P., Spinrad, H., and Belton, M.J.S. (1988) Abundances in Comet Halley at the Time of the Spacecraft Encounters. Ap. J., 325, 927.

TWENTIETH CENTURY LIGHT CURVES AND THE NUCLEUS OF COMET P/TEMPEL 2

H. Rickman¹, M.C. Festou², G. Tancredi¹ and L. Kamél¹

¹ Astronomiska Observatoriet, Box 515, S-75120 Uppsala, Sweden

² Observatoire Midi-Pyrénées, URA 285 du CNRS, 14 Avenue E. Belin, F-31400 Toulouse, France

Abstract

Observations of P/Temepel 2 from 1899 to 1988 corresponding to 13 apparitions are analysed in order to estimate the perihelion asymmetry of the gas production curve for different periods of its evolution. Using the correlation found by Festou *et al.* (1990) between the perihelion asymmetries and the delay in perihelion passage due to the action of nongravitational forces, we estimate the mass of the comet to be $M \approx 1.6 \pm 0.5 \cdot 10^{14}$ kg. Assuming a volume of 500 km³, based on nuclear observations, a density of 0.3 ± 0.1 g/cm³ is obtained.

Introduction

In a recent paper (Festou *et al.* 1990) we studied the correlation between the perihelion asymmetries of the gas production curves of periodic comets and the nongravitational perturbations of their orbital periods. The result was that, in general, the perihelion asymmetries give the dominant contribution to these nongravitational effects and that for comets with strongly asymmetric production curves, a reasonable approximation is to neglect any remaining contribution whatsoever. This means in particular that if the asymmetry parameter E can be estimated in such a case, the reduced nongravitational effect $\Delta P'$ for the interval in question can be used to estimate the ratio Q_m/M of the maximum gas production rate to the mass of the nucleus. Since in general it is possible to estimate Q_m with fair accuracy, cometary mass estimates are thus sometimes feasible. For a discussion of uncertainties associated with this procedure, see Tancredi *et al.* (1991).

A case of considerable interest is comet P/Tempel 2, being a candidate spacecraft target. Indeed, its light curve data as compiled by Kamél (1991) indicates a strongly asymmetric gas production curve. Only a small amount of data is as yet available on the OH production rate, but the direct measurements are in good agreement with the expectation based on visual magnitude (Roettger *et al.* 1990) so the light curves can tentatively be used to indicate both the shape and the level of the gas production curve. Here we present an analysis of light curves of P/Tempel 2 during the 20th century. The gas production curve of the comet will thus be studied as a secularly evolving feature and correlated with the evolution of the non-gravitational effect. The aim is to deduce an estimate of the mass and density of the nucleus.

Light Curves

Table 1 summarizes the magnitude data that we had available for 13 apparitions of P/Tempel 2 from 1899 to 1988. This is the data contained in the Comet Light Curve Catalogue/Atlas (Kamél 1991). In order to estimate reliably the value of E , it is important to have a good coverage of the light curve both before and after perihelion. While in general terms the 1899, 1925, 1967, 1983 and 1988 apparitions were well observed, the material is sometimes heavily weighted to either side of perihelion. Thus we have to restrict our analysis to only a few composite light curves spanning several apparitions each. The 1957, 1972 and 1978 apparitions were even too badly observed to be included at all (e.g., in 1978 all magnitudes are explicitly nuclear). Some care has to be applied when joining the apparitions into composites since, as will be evident from Figs. 1-3, the shape and level of the curve has not remained constant during this century.

Fig. 1 shows a composite of the 1899-1930 apparitions, denoted by different symbols as indicated. The plot shows only magnitudes reported as total, but in some cases they are nonetheless so conspicuously faint that they must be regarded as quasi-nuclear. The curve denoted "nuclear mag." is the magnitude of the real nucleus, assumed to vary as $m_{\text{nuc}} = M_{\text{nuc}} + 5 \lg r$ with M_{nuc} determined from the observations by Jewitt and Luu (1989). We take the same approach as in earlier investigations (Rickman *et al.* 1987; Festou *et al.* 1990), in general trusting the brightest magnitudes as the best approximations to the true heliocentric magnitude. The abscissa of the diagram is $u = \pm \lg(r/q)$, where the sign is that of the true anomaly and q is the osculating perihelion distance for the apparition in question. Thus the chain of straight-line segments

fitting the upper envelope of the set of points means that we are modelling the heliocentric magnitude $m_H(r)$ by means of stepwise constant photometric indices. Using the formula $\lg Q_{OH} = 32.0 - 0.4m_H$ (Festou 1986), we get a locally exponential gas production curve which can easily be integrated to yield the value of E . The fit must be regarded as very uncertain concerning the leftmost segment owing to the lack of observations with $u \lesssim -0.08$, but our choice of a steep increase is supported by the fact that Jewitt and Luu (1989) purportedly observed the bare nucleus at $u \approx -0.2$. After perihelion we have two alternatives marked by (a) and (b). The (a) curve gives credence to a critical observation in Nov. 1920 by Barnard (1931), for which the aperture correction is important. The (b) curve assumes that this particular magnitude is too bright. The rapid fall-off of curve (a) just after the critical point is based on assumed similarity to a post-perihelion fit to later apparitions [curve (a) in Fig. 2]. The values of E obtained from fits (a) and (b) in Fig. 1 are $E = 0.19$ AU and $E = 0.16$ AU, respectively, indicating a pronounced post-perihelion excess. Nonetheless, the post-perihelion magnitudes appear undersampled, and thus it is likely that these fits underestimate the real value of E .

In Fig. 2 the 1946-1967 apparitions are combined. Comparing with Fig. 1, we note a marked change of the light curve. The bright magnitude at $u = -0.01$, observed by Van Biesbroeck (1946), is of low accuracy and possibly half a magnitude too bright. Therefore we have disregarded it. It seems that a change in the comet's physical behaviour must have occurred, such that it settled on a lower level of activity than at previous apparitions with a broader maximum for several apparitions to come. This change might, for instance, be the mantling of a previously active region on the nucleus. In view of the results by Rickman *et al.* (1991) on rapid mantling and purging in response to changes in the perihelion distance, one is tempted to look for a correlation with orbital changes. Although not conclusive, an encouraging feature is that the 1946 apparition is unique among those hitherto observed in that q had a sudden increase by 0.075 AU with respect to the preceding ones. Thus a dust mantle might persist on a previously protected part of the nuclear surface.

In this case the coverage is reasonably uniform all over the curve although the spread in magnitude is considerable. Our pre-perihelion fit disregards a few observations in 1967 that are deemed too bright, in part due to the observed lack of activity at $u \approx -0.2$ in 1988. Analogously to Fig. 1, we have plotted two alternative post-perihelion fits, and the critical observation was made in Nov. 1946 by Giclas (1947). The (a) curve, giving credence to this observation, yields a steep fall-off reminiscent of curve (a) in Fig. 1. The (b) curve, disregarding Giclas' observation, indicates a much slower fall-off reminiscent of curve (b) in Fig. 1. The E values differ considerably, being $E = 0.42$ AU for curve (a) and $E = 0.28$ AU for curve (b).

Fig. 3 shows a composite of the 1983 and 1988 apparitions. The shape of the light curve seems to have changed again, but there is still serious uncertainty over its post-perihelion behaviour. In addition, there is a problem with the pre-perihelion observations made in 1988 (u -values from -0.15 to -0.1). Negative results obtained at the same time, in part by the same observers, indicate a lower brightness. Nevertheless, we

Table I. Statistics of available magnitude data for P/Tempel 2. N_{tot} is the total number of magnitude estimates available, with N_{pre} and N_{post} as the number of pre- and post-perihelion estimates, respectively.

Apparition	N_{tot}	N_{pre}	N_{post}
1899 IV	83	61	22
1920 II	22	1	21
1925 IV	94	83	11
1930 VII	11	5	6
1946 III	25	6	19
1951 VIII	19	14	5
1957 II	3	0	3
1962 VI	24	9	15
1967 X	112	80	32
1972 X	8	7	1
1978 V	4	1	3
1983 X	206	18	188
1988 XIV	308	241	67

Table II. Results. Symbols are explained in the text

Linkage	$Q_m (10^{28} \text{ s}^{-1})$	$E (\text{AU})$	$M (10^{14} \text{ kg})$
1899-1930	9.3	0.18	1.1
1946-1967	3.8	0.35	1.7
1983-1988	9.7	0.27	1.6

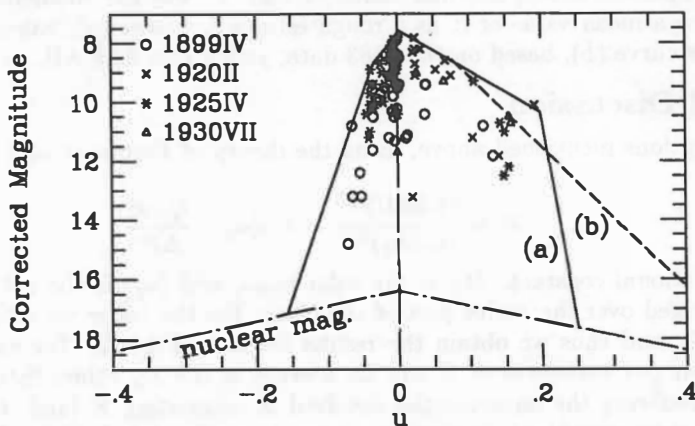


Fig. 1. Light curve data for comet P/Tempel 2, 1899–1930. Magnitudes obtained at different apparitions are marked by different symbols, as indicated. The observed magnitudes have been corrected for geocentric distance and observational effects. The u coordinate used as abscissa is explained in the text. Two possible fits to the post-perihelion data ($u > 0$) are shown as (a) –solid lines – and (b) – dashed line.

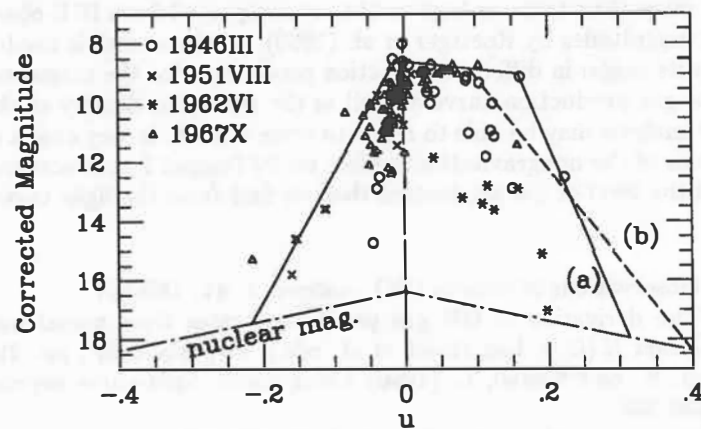


Fig. 2. Light curve data for comet P/Tempel 2, 1946–1967. Explanations are given in the caption to Fig. 1.

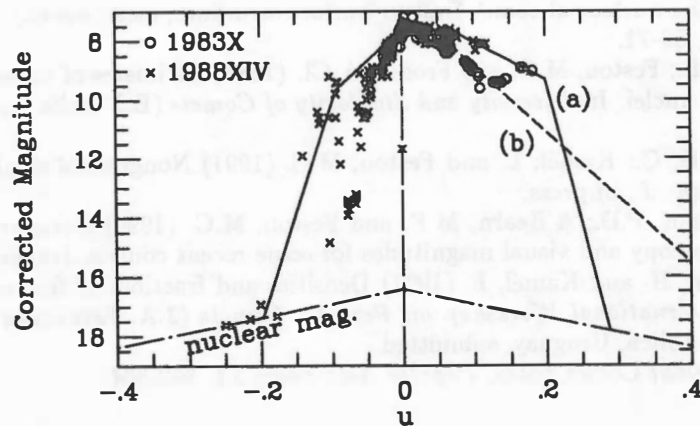


Fig. 3. Light curve data for comet P/Tempel 2, 1983–1988. Explanations are given in the caption to Fig. 1.

have some faith in the plotted magnitudes on the basis of their shear number and internal consistency, as shown by the fitted curve. After perihelion the two apparitions give quite different curves, and further work is needed in order to elucidate the internal relationship between these two curves as well as their possible similarity to earlier apparitions, in particular those in Fig. 1. For the moment we have only drawn the two fits in order to use a mean value of E as a rough estimate. Curve (a), based on the 1988 data, yields $E = 0.35$ AU, whereas curve (b), based on the 1983 data, yields $E = 0.18$ AU.

Analysis and Discussion

Under the assumptions mentioned above, using the theory of Festou *et al.* (1990), we get the mass of the nucleus from:

$$M \approx \frac{(3.5\text{AU})^{5/2}}{(GM_{\odot})^{3/2}} \cdot 6\pi m(u_g) \cdot \frac{Q_m E}{\Delta P'} \quad (1)$$

where G is the gravitational constant, M_{\odot} is the solar mass, and $\langle u_g \rangle$ is the net outflow speed of the gas from the nucleus averaged over the active part of the orbit. For the latter we estimate a value of 0.3 km/s (Rickman *et al.* 1987), and thus we obtain the results listed in Table 2. For each time interval we have taken an average of our two estimates of E and an average of the A_2 values listed by Marsden (1989) for computing $\Delta P'$. Considering the uncertainties involved in estimating E (and, to some extent, Q_m), the three mass values are quite consistent, indicating a true mass near $1.6 \cdot 10^{14}$ kg. The nucleus of P/Tempel 2 would thus be a near twin of that of P/Halley, not only regarding size and shape (Jewitt and Luu 1989) with a volume of around 500 km³, but also regarding mass and density. The latter can be estimated at 0.3 g/cm³, in good agreement with the result for P/Halley by Rickman (1989). The probable error of this estimate should amount to the order of $\pm 30\%$ in the mass, adding to an uncertainty of at least this order for the volume.

We note that the maximum water production rate inferred for the 1988 apparition from our composite light curve (Fig. 3) is more than twice as high as the rates reported from IUE observations and found to be consistent with visual magnitudes by Roettger *et al.* (1990). Further work is needed in order to resolve this discrepancy which has its origin in different correction procedures for the magnitudes. It should be evident that our results for the gas production curve as well as the mass and density of the nucleus are only rough estimates that further analysis may be able to refine to some extent. In any case a correlation seems to exist between the lower values of the nongravitational effect on P/Tempel 2 that occurred a few decades ago and the temporary drop in the level of gas production that we find from the light curves.

References

- Barnard, E.E. (1931) Observations of comets (IV), *Astron. J.* **41**, 180-184.
- Festou, M.C. (1986) The derivation of OH gas production rates from visual magnitudes of comets. In *Asteroids, Comets, Meteors II* (C.-I. Lagerkvist *et al.*, eds.), Uppsala Univ., pp. 299-303.
- Festou, M.C.; Rickman, H. and Kamél, L. (1990) Using comet light-curve asymmetries to predict comet returns, *Nature* **345**, 235-238.
- Giclas, H.L. (1947) Observations of comets, *Astron. J.* **52**, 206-208.
- Jewitt, D. and Luu, J. (1989) A CCD portrait of comet P/Tempel 2, *Astron. J.* **97**, 1766-1790
- Kamél, L. (1991) The Comet Light Curve Atlas, *Astron. Astrophys.*, in press.
- Marsden, B.G. (1989) *Catalogue of Cometary Orbits*, 6th edition, IAU Central Bureau for Astronomical Telegrams, Cambridge MA.
- Rickman, H. (1989) The nucleus of comet Halley: Surface structure, mean density, gas and dust production, *Adv. Space Res.* **9**(3), 59-71.
- Rickman, H.; Kamél, L.; Festou, M.C. and Froeschlé, Cl. (1987) Estimates of masses, volumes and densities of short-period comet nuclei. In *Diversity and Similarity of Comets* (E.J. Rolfe and B. Battrick, eds.), ESA SP-278, pp. 471-481.
- Rickman, H.; Froeschlé, C.; Kamél, L. and Festou, M.C. (1991) Nongravitational effects and the aging of periodic comets, *Astron. J.*, in press.
- Roettger, E.E.; Feldman, P.D.; A'Hearn, M.F. and Festou, M.C. (1990) Comparison of water production rates from UV spectroscopy and visual magnitudes for some recent comets, *Icarus* **86**, 100-114.
- Tancredi, G.; Rickman, H. and Kamél, L. (1991) Densities and fractions of free-sublimating area of short-period comets. In *International Workshop on Periodic Comets* (J.A. Fernández and H. Rickman, eds.), Universidad de la República, Uruguay, submitted.
- Van Biesbroeck, G. (1946) Comet notes, *Popular Astronomy* **54**, 362-364.

CARBON PETROLOGY IN COMETARY DUST

Frans J.M. Rietmeijer

Department of Geology, University of New Mexico, Albuquerque, NM 87131, U.S.A.

INTRODUCTION

Chondritic porous [CP] interplanetary dust particles [IDPs] are collected in the Earth's stratosphere. There exists an extensive database on major and minor element chemistry, stable isotopes, noble gas abundances and mineralogy of many CP IDPs, as well as infrared and Raman spectroscopic properties. For details on the mineralogy, chemistry and physical properties of IDPs, I refer to the reviews by *Mackinnon and Rietmeijer* [1987], *Bradley et al.* [1988] and *Sandford* [1987]. Texture, mineralogy [*Mackinnon and Rietmeijer, 1987*] and chemistry [*Schramm et al.*, 1989; *Flynn and Sutton, 1991*] support the notion that CP IDPs are a unique group of ultrafine-grained extraterrestrial materials that are distinct from any known meteorite class. Their fluffy, or porous, morphology suggests that CP IDPs probably endured minimal alteration by protoplanetary processes since their formation. It is generally accepted that CP IDPs are solid debris from short-period comets. The evidence is mostly circumstantial but this notion gained significant support based on the comet Halley dust data [*Brownlee, 1990*]. In this paper, I will accept that CP IDPs are indeed cometary dust.

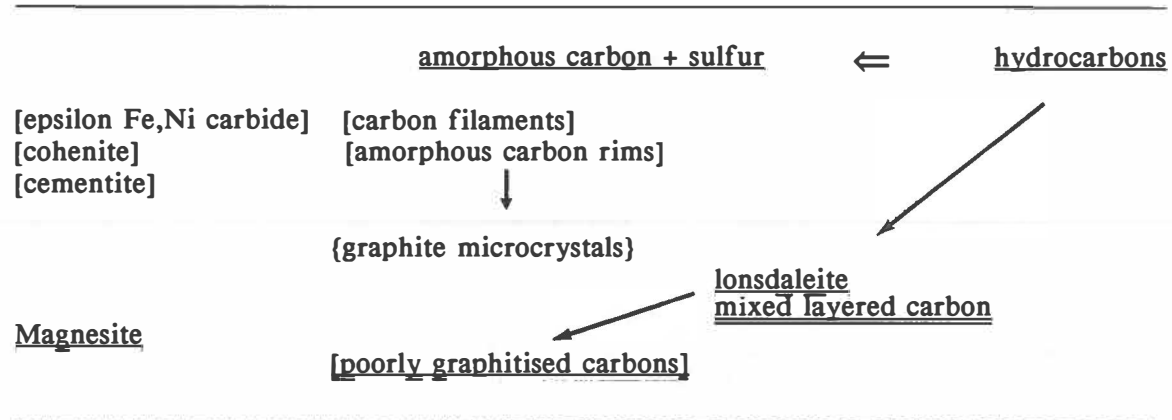
The C/Si ratio in CP IDPs is 3.3 times higher than in CI carbonaceous chondrites [*Schramm et al.*, 1989]. The intraparticle carbon distribution is heterogeneous [*Rietmeijer and McKay, 1986*]. Carbon occurs both in oxidised and reduced forms. Analytical electron microscope [AEM] and Raman spectroscopic analyses have shown the presence of several carbon forms in CP IDPs but the data are scattered in the literature. Carbons in cometary CP IDPs are among the most pristine Solar System carbons available for laboratory study. Similar to a recently developed petrological model for the diversity of layer silicates in CP IDPs [*Zolensky, 1991*] that is useful to constrain *in situ* aqueous alteration in comets [*Rietmeijer and Mackinnon, 1987a*], I here present the first effort to develop a petrological concept of carbons in CP IDPs. This concept is useful to constrain comet evolution. I also present the philosophical constraint facing Earth Scientists in studies of protoplanets that require a new approach to cometary dust studies.

CLASSIFICATION

This paper uses published data on carbons in CP IDPs that are presented in TABLE 1. This table should be perused with some caution as only a few CP IDPs reported contain more than two or three carbons listed in the table. It is presently not clear whether this situation is an experimental artifact (AEM analyses of CP IDPs are quite time-consuming) or whether it carries genetic information. In the table, carbon types are listed according to various stages in the lifetime of cometary dust from its formation in the early solar system to collection in the Earth's stratosphere. This approach is chosen because it might assist to "see through" the various processes that affected CP IDPs and the resulting carbons. For this purpose, I define three types of carbon in cometary dust:

- (1) *indigenous carbons* are pre-accretion solar nebula materials,
- (2) *metamorphic carbons* form during protoplanet alteration, and
- (3) *neoformed carbons* form during a transient (heating) event.

TABLE 1: CARBONS IN COMETARY DUST



Carbons are indigenous (underlined) or metamorphic (double underlined). Neoformed carbons form during transient events such as heterogeneous catalysis in the solar nebula and dynamic pyrometamorphism on atmospheric entry (brackets) or via solid-state grain boundary nucleation (braces).

The neoformed carbons form a diffuse group wherein individual carbons cannot yet be linked to a particular transient event. Two orthorhombic forms of Fe_3C , cementite and cohenite [Fraundorf, 1981; Bradley et al., 1984], and ϵ -(Fe,Ni)₃C crystals [Christoffersen and Buseck, 1983] could form during dynamic pyrometamorphism of IDPs due to atmospheric entry flash-heating, or could be products of Fischer-Tropsch synthesis in the solar nebula. The same uncertainty surrounds rare carbon filaments in these particles. Whatever environment is conducive to carbide and filamentous carbon formation, these carbons indicate that carburization reactions are important during CP IDP evolution which again shows the uniqueness of CP IDPs [Bradley et al., 1984].

Amorphous carbon forms thin coatings (up to 30 nm) on many submicron metal, carbide and metal-oxide grains in CP IDPs [Mackinnon and Rietmeijer, 1987; Bradley et al., 1988]. The amorphous coatings often have graphite microcrystals (up to 30 nm thick) at the interface with the enclosed grain. If these graphite microcrystals form via grain boundary nucleation to relieve grain boundary energy, they could form during dynamic pyrometamorphism. It is hard to understand that both amorphous carbon coatings and graphite microcrystals could form during this 10-15 second transient heating event. Thus, these microcrystals indirectly support a notion that the amorphous coatings are a 'pre-terrestrial' carbon. Unquestionably, neoformed carbons contain important information about the evolution of cometary dust. But unless it is possible to constrain their formation, this information cannot be placed in a proper context. Still, it seems possible to study the remainder of CP IDP carbons without concerns that they are seriously affected by the processes that produced neoformed carbons.

INDIGENOUS and METAMORPHIC CARBONS

The CP IDPs are loosely-bound aggregates of 'granular units' (or tar balls) with embedded micrometer-sized silicate crystals, e.g. pyroxene whiskers. A 'granular unit' consists of carbon material with embedded, heterogeneously-distributed, nanometer-sized olivines, pyroxenes and sulfides. Within a single 'granular unit' it is possible to find areas of almost pure carbon material and areas that have abundant silicates and sulfides. It is still an open question whether 'granular units' represent an accretion [Bradley, 1988]

or an annealing [Rietmeijer, 1989] event. In each scenario the carbon material, which includes hydrocarbons and amorphous carbon, is the solar nebula dust that accreted into CP IDPs. Evidence to support (as yet unidentified) hydrocarbons is slim [*cf. Mackinnon and Rietmeijer, 1987*]. The best evidence is from Raman spectroscopy [Wopenka, 1988] and ion microprobe analyses [*cf. Bradley et al., 1988*]. The hydrocarbons are the loci of D/H enrichments including a "hot spot" with $\delta D > 9000$ pro mille that possibly indicates an interstellar grain [McKeegan et al., 1987]. Some sulfur is associated with amorphous carbon in 'granular units' [Rietmeijer, 1989]. The modes of hydrocarbon and amorphous carbon occurrence in the units suggest that they could be the carbonaceous dust in the solar nebula prior to accretion. Whether both carbons in cometary dust are related is not yet known but volatile (H₂O,N) loss from hydrocarbons conceivably produces amorphous carbon, either during protoplanet accretion or alteration.

The formation of metamorphic carbons during protoplanet alteration is a challenging field of CP IDP research. If lonsdaleite, mixed layered carbon and poorly graphitised carbons (PGCs) are metamorphic carbons, they indicate considerable mineralogical activity in comet nuclei. These platey and fluffy carbons co-occur in individual CP IDPs, both separately and as individual grains. Crystalline lonsdaleite (or carbon-2H) forms thin (< 10 nm) lobate submicron sheets that probably contain a small amount of volatiles [Rietmeijer and Mackinnon, 1987b]. Another platey CP IDP carbon occurs as thin, sub-micron (up to 4.5 μm x 1.3 μm) sheets that have turbostratic layer stacking. This mixed layered carbon has considerable three-dimensional order of its pre-graphitic carbon layers that contain alicyclic and aromatic structures with variable C/[C+H+O+N] ratio between 0.35-0.75 [Rietmeijer, 1991]. A third metamorphic carbon has a distinct fluffy morphology. This PGC occurs as domains associated with both platey carbons and as discrete particles up to ~1.5 μm [Rietmeijer and Mackinnon, 1985] and it has a distinct microstructure of tangled loops and concentric subcircular to polygonal rings of graphite.

All three metamorphic carbons have natural terrestrial or synthetic analogs and we can understand the conditions and processes that lead to their formation. Layer silicates and magnesite ($MgCO_3$) [TABLE 1] that co-occur with metamorphic carbons support aqueous alteration in comets. Lonsdaleite formed via hydrocarbon hydrous pyrolysis at $T < 350^\circ C$ supported on catalytically-activated layer silicates [Rietmeijer and Mackinnon, 1987b]. Mixed layer carbon formation does not require the presence of water. This carbon supports kinetically controlled, early stages of hydrocarbon carbonisation. If the platey carbons are so-called graphitisable carbon, thermal annealing will (partially) transform these carbons into PGCs. If temperature is the only active parameter for PGC formation in CP IDPs, the thermal regime was at ~315°C [Rietmeijer and Mackinnon, 1985]. A thermal regime of this magnitude in active short-period comet nuclei (or protoplanets) is unlikely. Temporal and spatial variations in the water/rock ratio during aqueous alteration gives some degree of freedom but it probably requires temperatures at least similar to those for CI carbonaceous chondrite alteration (~125°C) and efficient catalysis supported by co-occurring layer silicates.

The principle of uniformitarianism states that the same processes and natural laws prevailed in the past as processes that we can presently observe, infer from direct observation, or derive from laboratory experiment. The only known natural terrestrial environment to serve as a comet nucleus analog is the Antarctic Dry Valley permafrost but its thermal regime and time scales differ significantly and its carbon content is very low [Rietmeijer, 1985]. Martian permafrost soils might be a better natural analog but an opportunity to study these soils is remote. The alternative is to develop an experimental program to constrain the hydrocryogenic ($T < 0^\circ C$) thermal regime that produces the metamorphic CP IDP carbons, the carbon reaction rates and paths and layer silicate - carbon catalytic interactions.

CONCLUSIONS

A listing of carbons in CP IDPs, that are solid debris of short-period comets, proves useful to discuss interrelations among these carbons and to define areas for IDP research. Carbons are listed as indigenous, metamorphic or neoformed. Natural analogs for studies of cometary carbons and carbon - silicate petrology are not readily available. I suggest the development of experiments based on our knowledge of the physical environment of evolving short-period comets.

I thank Rhian Jones for critical reading of this paper. This work is supported by NASA Grant NAG 9-160.

REFERENCES

- Brownlee D. E. (1990) Carbon in comet dust. In Carbon in the Galaxy: Studies from Earth and Space (Tartar J. C., Chang S. and DeFrees D. J., eds.), NASA Conf. Publ. 3061, 21-26.
- Bradley J. P. (1988) Analysis of chondritic interplanetary dust thin-sections. Geochim. Cosmochim. Acta, **52**, 889-900.
- Bradley J. P., Brownlee D. E. and Fraundorf P. (1984) Carbon compounds in interplanetary dust: Evidence for formation by heterogeneous catalysis. Science, **223**, 56-58.
- Bradley J. P., Sandford S. A. and Walker R. M. (1988) Interplanetary dust particles. In Meteorites and the Early Solar System (J. F. Kerridge and M. S. Matthews, eds.), pp. 861-895. University Arizona Press, Tucson.
- Christoffersen R. and Buseck P. R. (1983) Epsilon carbide: A low-temperature component of interplanetary dust. Science, **222**, 1327-1329.
- Flynn G. J. and Sutton S. R. (1991) Average minor and trace element contents in seventeen "chondritic" IDPs suggest a volatile enrichment. Meteoritics, **26**, in press.
- Fraundorf P. (1981) Interplanetary dust in the transmission electron microscope: Diverse materials from the early solar system. Geochim. Cosmochim. Acta, **45**, 915-943.
- Mackinnon I. D. R. and Rietmeijer F. J. M. (1987) Mineralogy of chondritic interplanetary dust particles. Reviews Geophys., **25**, 1527-1553.
- McKeegan K. D., Swan P., Walker R. M., Wopenka B. and Zinner E. (1987) Hydrogen isotopic variations in interplanetary dust particles (abstract). Lunar. Planet. Sci., **18**, 627-628.
- Rietmeijer F. J. M. (1985) A model for diagenesis in proto-planetary bodies. Nature, **313**, 293-294.
- Rietmeijer F. J. M. (1987) Ultrafine-grained mineralogy and matrix chemistry of olivine-rich chondritic interplanetary dust particles. Proc. 19th Lunar Planet. Sci. Conf., 513-521.
- Rietmeijer F. J. M. (1991) Microbeam analyses of carbon-rich materials in chondritic porous micrometeorites. In Microbeam Analysis - 1991 (D. G. Howitt, ed.), pp. 289-292. San Francisco Press, San Francisco.
- Rietmeijer F. J. M. and Mackinnon I. D. R. (1985) Poorly graphitized carbon as a new cosmothermometer for primitive extraterrestrial materials. Nature, **316**, 733-736.
- Rietmeijer F. J. M. and Mackinnon I. D. R. (1987a) Cometary evolution: Clues from chondritic interplanetary dust particles. European Space Agency Spec. Public., **278**, 363-367.
- Rietmeijer F. J. M. and Mackinnon I. D. R. (1987b) Metastable carbon in two chondritic porous interplanetary dust particles. Nature, **326**, 162-165.
- Rietmeijer F. J. M. and McKay D. S. (1986) Fine-grained silicates in a chondritic interplanetary dust particle are evidence for annealing in the early history of the solar system (abstract). Lunar. Planet. Sci., **17**, 710-711.
- Sandford S. A. (1987) The collection and analysis of extraterrestrial dust particles. Fund. Cosmic Phys., **12**, 1-73.
- Schramm L. S., Brownlee D. S. and Wheelock M. M. (1989) Major element composition of stratospheric micrometeorites. Meteoritics, **24**, 99-112.
- Wopenka B. (1988) Raman observations on individual interplanetary dust particles. Earth Planet. Sci. Lett., **88**, 221-231.
- Zolensky M. E. (1991) The relationship between hydrous and anhydrous interplanetary dust particles. In Microbeam Analysis - 1991 (D. G. Howitt, ed.), pp. 287-288. San Francisco Press, San Francisco.

WAKE IN FAINT TELEVISION METEORS

M.C. Robertson[†] and R.L. Hawkes

Physics Department, Mount Allison University,
Sackville, New Brunswick, Canada E0A 3C0

The two component dustball model was used in numerical lag computation. Detached grain lag is typically less than 2 km, with expected wakes of a few hundred meters. True wake in television meteors is masked by apparent wake due to the combined effects of image persistence and blooming. To partially circumvent this problem, we modified a dual MCP intensified CID video system by addition of a rotating shutter to reduce the effective exposure time to about 2.0 ms. Preliminary observations showed that only 2 of 27 analyzed meteors displayed statistically significant wake.

INTRODUCTION

Wake is the degree to which an instantaneous meteor image is spatially distributed. The classic wake paper (McCrosky, 1958) pointed out that a large proportion (28%) of Super-Schmidt meteors showed significant luminosity in "off" portions of rotating shutter photographs. Since wake was more prevalent in low velocity meteors, he argued that wake was due to differential grain deceleration (lag), and not the result of atomic excitation and decay processes. The lag of grains from a fragmenting dustball was consistent with the emerging view of meteoroids as low density, structurally weak bodies which fragmented during flight (Jacchia, 1955), which in turn was in agreement with Whipple's "dirty snowball" cometary model (Whipple, 1950, 1951). Studies of meteor wake provide one method of determining the size distribution of meteoroid constituent grains. McCrosky (1958) suggested that grains of the order of 10^{-8} kg matched observational wake evidence, a value in agreement with flare analysis results (Smith, 1954; Simonenko, 1968a). Although image intensified video detectors are common in meteor observation (Hawkes & Jones, 1986), to our knowledge this is the first study of television meteor wake.

NUMERICAL STUDY OF GRAIN LAG

We have previously performed numerical solutions of the coupled differential equations of meteoroid grain flight (Nicol et al., 1985; Fyfe & Hawkes, 1986). For this work we have added an equation specifying the lag of the grain, and have computed the luminous intensity. The rate of change of height, h , can be expressed as

$$\frac{dh}{dt} = -v \cos(z) \quad (1)$$

where v is the instantaneous meteor speed and z the zenith angle. The meteoroid grain deceleration is

$$\frac{dv}{dt} = -\frac{\Gamma A v^2 \rho_a}{m^{1/3} \rho_m^{2/3}} + g \quad (2)$$

with Γ the drag coefficient, A the grain shape factor, ρ_a the atmospheric density, m the instantaneous meteor mass, ρ_m the grain bulk density and g the acceleration due to gravity. The rate of mass loss is given by

$$\frac{dm}{dt} = \frac{Am^{2/3}}{L\rho_m^{2/3}} \left[4\sigma\varepsilon(T_b^4 - T_a^4) - \frac{\Lambda\rho_a v^3}{2} \right] \quad (3)$$

where L is the sum of the latent heats of vaporization and fusion, σ the Stefan-Boltzman constant, T_b the boiling point of the meteoroid material, T_a the effective atmospheric temperature, ε the emissivity and Λ the heat transfer coefficient. We have considered thermal radiation, but, assuming very small grains, have ignored thermal heat capacity. If lag, l , is defined as the separation between a grain and an undecelerated parent meteoroid

$$\frac{dl}{dt} = v_\infty - v \quad (4)$$

where v_∞ is the initial speed. This definition of lag is reasonable for grains ejected from much larger parent bodies. If the luminous visual power is proportional to the rate of change of kinetic energy of ablated meteoric atoms, and the luminous efficiency factor varies linearly with speed, the grain luminosity will be

[†] current address Physics Department, Queen's University, Kingston, Ontario, Canada K7L 3N6

$$M = -2.5 \log \left(-\frac{\tau_0}{2} \frac{v \sqrt{3dm}}{dt} \right) \quad (5)$$

We performed numerical integration of eqns. (1) through (4), and then applied equation (5), using a fourth-order Runge-Kutta procedure with adaptive step size control (a slightly modified form of procedure RKQC in Press et al., 1986). A cubic polynomial fit between height and the logarithm of the atmospheric density (according to the U.S. Standard Atmosphere) was used. Constant values used were $A = 1.21$, $g = 9.60$, $\Gamma = 1.0$, $L = 6.0 \times 10^6$, $\Lambda = 1.0$, $\epsilon = 1.0$, $T_a = 280$, $T_b = 2100$ and $\tau_0 = 1.0 \times 10^{-10}$ (in all cases SI units). We performed 2304 numerical runs, corresponding to all combinations of the following values: $\cos z$ (0.4, 0.7, 1.0); preatmospheric velocity (15, 41, 60, 66 km s^{-1}); initial grain mass ($10^{-8}, 10^{-9}, 10^{-10}, 10^{-11}, 10^{-12}, 10^{-13}, 10^{-14}, 10^{-15} \text{ kg}$); grain bulk density ($700, 3500 \text{ kg m}^{-3}$); and ejection height (75, 80, 85, 90, 95, 100, 110, 120, 130, 140, 150, 160 km). Space does not permit presentation of the complete numerical results (see Robertson, 1990). Fig. 1 illustrates typical results for 41 km s^{-1} velocity and $\cos(z) = 0.7$. For the smallest grains, even the higher speeds will not produce significant ablation, and no lag is plotted. As expected, the lag increases as the grain mass or grain density decreases, since the smaller mass to surface area ratio results in more rapid deceleration. The lag increases with increasing height of ejection. The principal reason to carry out lag computations is not to confirm these predictable trends, but rather to determine the order of magnitude of the lag. According to the dustball model of Hawkes &

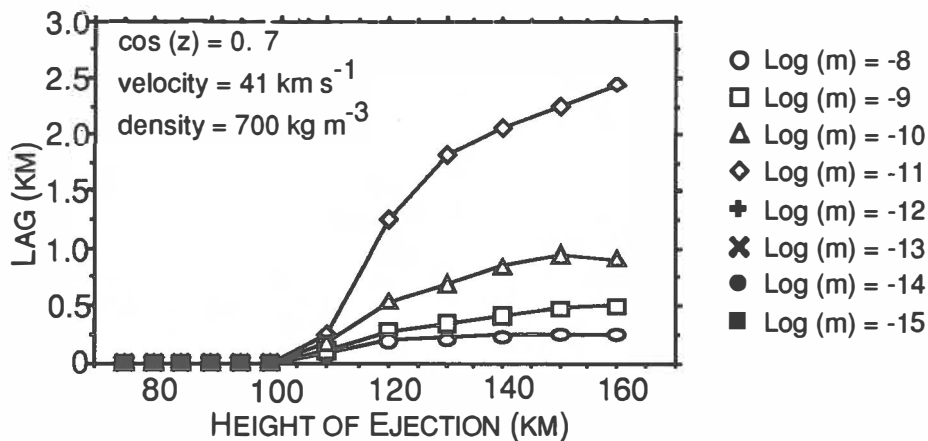
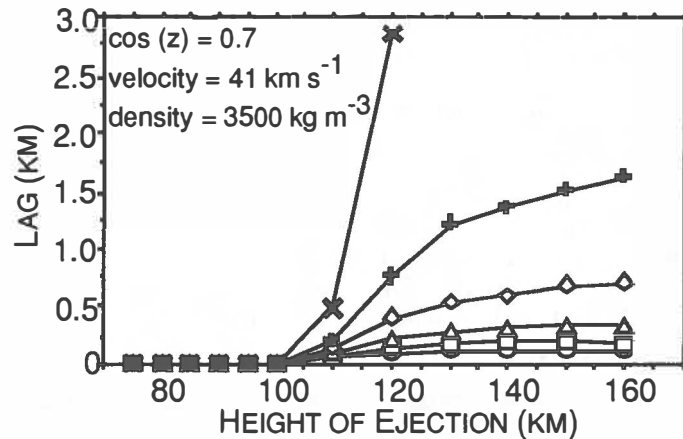


Figure 1

Plot of lag at maximum luminosity versus mass of detached grains and height of grain ejection. The above plot is for a meteoroid density of 700 kg m^{-3} , while the plot on the right is for 3500 kg m^{-3} .



Jones (1975) the composite meteoroid has two constituents, grains and a binding material of somewhat lower boiling point. For bright meteors grain release and grain ablation occur almost simultaneously. For faint meteors the grains will be released prior to grain ablation, and an essentially independent cluster of grains encounters the atmosphere. Wake could result from grains of uniform size released at different heights, or from grains of different

sizes ejected at the same height. For example, Fig. 1 suggests that a mixture of grains of size 10^{-9} to 10^{-10} kg would lead to wake of approximately 250 m. If grain release occurs high in the atmosphere, and at a variety of heights, rather spectacular lags and associated wakes result. Grains of size 10^{-11} kg released over a range from 110 to 150 km would result in about a 2 km wake.

OBSERVATIONAL EQUIPMENT

Interpretation will be most straightforward in the case of meteors small enough to have fragmented into a cluster of grains prior to the onset of intensive grain evaporation. Beech (1984, 1986) has applied techniques developed by Hapgood et al. (1982) to estimate the critical size, which he suggests may be -2 for Perseid meteors, -1 for Geminid meteors and +0.5 for Southern-Taurid meteors. However, there is considerable scatter in the data, and image intensified television systems should be used to achieve the required sensitivity with confidence. The problem with such systems is that the combined effects of persistence and meteor motion during the frame integration time results in extensive apparent wake which totally masks real wake. Blooming of bright images provides a further complication. The persistence problem can be reduced by making the effective image intensifier exposure short. The optimum way to accomplish this would be to employ an electronically gated image intensifier, but cost precluded our adoption of this approach. We chose instead to use a mechanical rotating shutter driven by a 30 Hz synchronous motor (to keep the shutter in phase with the line locked video camera). The shutter had two circular

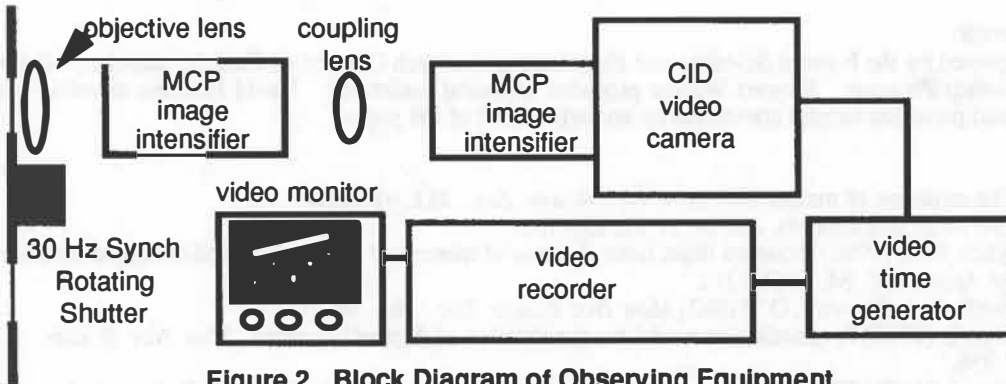


Figure 2 Block Diagram of Observing Equipment

holes of radii 3.0 cm in an overall shutter of radius 15.0 cm, resulting in one exposure per video field (1/60 s), with an effective exposure time of about 2.0 ms. A block diagram of our observational equipment is shown in Fig. 2. The first microchannel plate (MCP) image intensifier was a Varo model 3603-1 (luminous gain 30,000). It was lens coupled to an ITT 4562 camera (a MCP fibre-optically coupled to a GE TN2505 CID video camera). The sensitivity was about +7.5^M with a 135 mm/f3.5 objective lens (field of view 8.1° by 6.1°). The rotating shutter was clearly effective in reducing apparent wake due to image motion and persistence, with most frames indicating roughly circular meteor images.

ANALYSIS AND RESULTS

Data were collected during 5 nights in Aug. and Sep. 1989 from Sackville, N.B., Canada (long. 64° 22' 24" W; lat. 45° 53' 35" N). A total of 27 meteors were analyzed from a 24^h 48^m observing period. Each video frame was digitized using an Oculus-200 video digitizer in an IBM XT (resolution 512x512 pixels, 7 bit (128 gray levels) depth). If a meteor exhibits wake then the pixels contributing to the meteor's image should be noncircular with the best fit line through those pixels aligned with the meteor trajectory. After each video frame had been background corrected a linear regressional analysis was performed with every pixel weighted according to that pixel's luminous intensity. A meteor was only deemed to have wake if more than one of its images produced a slope in agreement (within the standard error) with the meteor trajectory. Of the 27 meteors studied, only 2 demonstrated statistically significant wake. To determine the size of the wake we started at the image centroid and moved backward in the direction of the trajectory until the pixel intensity was less than two standard deviations above the background noise. This apparent wake was then corrected for blooming and image motion during the

2.0 ms effective exposure. The maximum corrected wake was 30 pixels for one meteor, and 7 pixels for the other. In both cases the maximum wake point was near the end of the trajectory. A radiant-apparent speed check indicated that the two meteors were sporadic, and we can only estimate the statistically probable spatial dimension of the wake. At the elevation angle of 54°, assuming an ablation height of 95 km and 0.7 as a correction for the statistically probable trail orientation, the probable spatial dimensions of the wake at maximum are 780 m and 160 m.

DISCUSSION

The failure to find significant lag in most of the meteors is surprising. One explanation would be that grains were all of approximately the same size, and were ejected at about the same height, so that each grain would lag by the same amount. Simonenko (1968b) found that the range of fundamental meteoroid grain sizes was quite limited. Another possibility would be that the grains were very large, in which case they would have small lags which might not be evident with the spatial resolution of our observing system. The origin of fainter meteors is generally assumed to be cometary, but some authors (Olsson-Steel, 1988) have recently suggested that the asteroid belt may be an important source for smaller meteoroids. This might mean that the structure of small meteoroids is more compact, and not a loose collection of grains. The boiling point of the glue might be very similar to that of the grains in which case there would be little time for lag. One should keep in mind that these results are based on a small number of meteors, and with an observing system limited in spatial and intensity resolution.

Acknowledgements:

This work was supported by the Natural Sciences and Engineering Research Council of Canada and the Bell Junior Research Fellowship Program. Stewart Walker provided technical assistance. David Fleming assisted with image digitization and provided helpful comments on an earlier draft of the paper.

References:

- Beech, M. (1984) The structure of meteoroids. *Mon. Not. R. astr. Soc.* **211**, 617-620.
- Beech, M. (1986) The Draconid meteors. *Astron. J.* **91**, 159-162.
- Fyfe, J.D.D. & Hawkes, R.L. (1986) Residual mass from ablation of meteoroid grains detached during atmospheric flight. *Planet. Space Sci.* **34**, 1201-1212.
- Hapgood, M., Rothwell, P. & Royvrik, O. (1982) *Mon. Not. R. astr. Soc.* **201**, 569-577.
- Hawkes, R.L. & Jones, J. (1975) A quantitative model for the ablation of dustball meteors. *Mon. Not. R. astr. Soc.* **173**, 339-356.
- Hawkes, R.L. & Jones, J. (1986) Electro-optical meteor observation techniques and results. *Q.Jl. R. astr. Soc.* **27**, 569-589.
- Jacchia, L.G. (1955) The physical theory of meteors. VIII: Fragmentation as cause of the faint meteor anomaly. *Astrophys J.* **121**, 521-527.
- McCrosky, R.E. (1958) The meteor wake. *Astron. J.* **63**, 97-106.
- Nicol, E.J., Macfarlane, J. & Hawkes, R.L. (1985) Residual mass from atmospheric ablation of small meteoroids. *Planet. Space Sci.* **33**, 315-320.
- Olsson-Steel, D. (1988) Theoretical meteor radiants of recently discovered asteroids and comets, and twin showers of known meteoroid streams. *Aust. J. Astr.* **2**, 93-101.
- Press, W.H., Flannery, B.P., Teukolsky, S.A. & Vetterling, W.T. (1986) *Numerical Recipes: The art of scientific computing*. Cambridge Univ. Press, New York. 735 pp.
- Robertson, M.C. (1990) *A theoretical and observational study of meteor wake*. B.Sc. Honours Thesis, Mount Allison University, Sackville, N.B. Canada. 124 pp.
- Simonenko, A.N. (1968a) The behaviour of small particles detached from a meteoroid. *Soviet Astron. - AJ* **12**, 341-348.
- Simonenko, A.N. (1968b) The separation of small particles from meteor bodies, and its influence on some parameters of meteors. In *Physics and Dynamics of Meteors* (L. Kresak and P.M. Millman, eds.), 207-216. D. Riedel, Dordrecht.
- Smith, H.J. (1954) The physical theory of meteors. V. The masses of meteor-flare fragments. *Astrophys. J.* **119**, 438-442.
- Whipple, F.L. (1950) A comet model: I. The acceleration of Comet Encke. *Astrophys. J.* **111**, 375-394.
- Whipple, F.L. (1951) A comet model: II. Physical relations for comets and meteors. *Astrophys. J.* **113**, 464-474.

CHEMICAL AND PHYSICAL EFFECTS IN THE BULK OF COMETARY ANALOGS

K. Roessler, J. Bénit and M. Sauer

Institut Für Nuklearchemie, Forschungszeantrum Jülich, Postfach 1913, D-5170 Jülich, Germany

ABSTRACT

KOSI comet simulation experiments have been designed as a macroscopic tester for the studies of physico-chemical problems inherent to comet bodies. The analog samples consist of H₂O and CO₂ ice, organic admixtures, mineral dust and carbon. It is reported on two of the fundamental changes the analogs undergo when submitted to "insolation" by artificial sunlight, i.e. the diffusion of frozen gases and subsequent crust formation and the natural isotopic fractionation.

INTRODUCTION

KOSI experiments which involve many scientific groups cover a large array of both physical and chemical studies of the evolution of a "comet-like" body exposed to photon irradiation (Grün et al. 1991). The diversity of the output foreseen by the different teams implies various choices for the material used as well as for the exposure to the "sun". This is summarized in Table 1. This paper reports on sample stratigraphy and crust formation in KOSI-5 to 7 and isotopic studies in KOSI-7. KOSI is characterized by different phases which are, a) the conditionning of the sample into the space simulator, b) the irradiation, c) the further analysing of the irradiated analog. The latter requires sampling and storage under LN₂ conditions (Roessler et al. 1990, Roessler 1991). The study of the strength of the target material takes place immediately after the sample has been removed from the space simulator and has been placed into a large glove box cooled with LN₂. The sample profile is also visually inspected for the stratigraphy and material is taken layerwise (1 or 2 cm). This material is then analysed by different techniques (Hsiung and Roessler 1989, Roessler et al. 1992a).

RESULTS

GAS DIFFUSION AND CRUST FORMATION : The evidence for gas diffusion, both inward and outward, has been outlined by the basic visual inspection and by the more sophisticated technique of gas chromatography GC (Hsiung and Roessler 1989, 1990). The visual inspection exhibits some brilliant crystallites in the depth, which quality and number varies upon material composition. They are a proof for CO₂ recrystallization (Fig.1). The GC technique was used to follow the amount of CO₂ remaining at various depths of the analog after insolation. Figs. 2 to 4, show the stratigraphy of KOSI-5 to 7. Because of the different conditions of each of the experiments, only a few general conclusions can be drawn, a) ejection of grains (Thiel et al. 1991), b) large change in the frozen gas repartition c) formation of a crust near the surface, d) sometimes an internal crust is present. KOSI-5 and 7 are reported as high activity samples, implying important recession of the surface. This is attributed to the presence of CH₃OH in KOSI 5 and the high ratio volatiles/mineral grains in KOSI 7. The insolation conditions and the target composition largely determined the thickness and strength of the crust (for more details cf. Roessler 1991, Roessler et al. 1992a). A dry dust mantle covers the external crust. Underneath this crust are some ilots of hardened material. Then a more "virgin" material appears, anyhow depleted in "gases" (CO₂, CH₃OH). Finally a zone of higher concentration of gases is encountered below the above mentioned one due to the inward diffusion. It is found in this zone an internal crust. In Fig.5 of KOSI-5, the temperature profile at the end of the irradiation period (Benkhoff and Spohn 1991) and the CO₂ concentration profile are plotted versus the depth of the sample. The strong correlation between the temperature drop and the CO₂ excess proves the inward diffusion of gases and their recrystallization in a kind of thermochromatography. The fact of upper and internal crust formation is also witnessed by the test on material strength by drilling boreholes (Roessler 1991, Roessler et al. 1992a)

HEAVY ISOTOPE ENRICHMENT IN H₂O PHASE : KOSI-7 reported here was conducted with material of natural isotopic composition. The analysis was done by mass spectrometry for the heavy isotopes of water, D and ¹⁸O, for details cf. (Roessler 1992b). Studies on ¹³C in CO₂ are on their way. Figs.6 and 7 report on the isotopic abundance before and after insolation. It becomes obvious from Fig.6 that the procedure of filling the sample compartment (standard or analog) had no big effect on the isotopic ratio. It should be noted, however, a slight increase with the preparation i.e. the spraying procedure of the mineral-H₂O

suspension into LN₂, (Stöffler et al. 1991, Roessler et al. 1990). Therefore, the comparison of the status before and after insolation is significant. Fig.7 exhibits a substantial change with respect to the original abundance, but only in the region of the upper crust (Fig.8) where the effect of insolation on the isotopic ratio is fairly large. The changes for D and ¹⁸O are basically equivalent. The cut in the curve is observed in the same region, roughly 20 cm from the bottom, i.e. 10 cm from the original surface. Nevertheless, it should be mentionned that the curve increase coefficient is slightly smoother for D than for ¹⁸O.

DISCUSSION

It has been shown that a cometary type material undergoes drastic structural changes due to physico-chemical reactions when submitted to a visible solar equivalent radiation. In view of future cometary explorations (e.g. ROSETTA) these structural changes have to be taken into account for the scientific payload. Also the technical part of the mission will be affected by this new facts. It is obvious that the anchoring of a vessel on a body with almost no attraction requires a good knowledge of the surface characteristics and the possible internal structure, both to be able to choose remotely where to drill and to realize the sampling. One of the main interests in KOSI is to use it as a remote witness of the solar system past. From the present results it can be concluded that the presence of a strong isotopic effect from the insolation impedes somehow isotopic studies as a good tool for the determination of the nature of the pristine material in a comet. The processing of the sample is subject to, e.g. gas and grain ejection, solidification, gas diffusion, recondensation, etc. These many effects screen the possible knowledge of what can have been the material which formed the comets. Therefore, a strong deconvolution work has to be undertaken in order to propose possible scenarios of comet evolution under such condition as photon and ion irradiation, warming by tidal effects when passing by a large object, etc.

ACKNOWLEDGEMENTS

The authors want to thank the KOSI team, in particular Dr. H. Kochan (DLR-Köln), Prof. J. Klinger (Grenoble) and Messrs P. Trimborn (Neuherberg) and G. Eich (Jülich) for experimental assistance and for scientific discussion. Part of the work was sponsored by the Schwerpunktprogram "Kleine Körper im Sonnensystem" of Deutsche Forschungsgemeinschaft DFG.

REFERENCES

- Benkhoff J., and Spohn T. (1991) Thermal histories of the KOSI samples. *Geophys. Res. Letters*, **18**, pp. 261-264.
- Grün E., Bar-Nun A., Benkhoff J., et al. (1991) Laboratory simulation of cometary processes. In Comets in the Post-Halley Era, (R.L. Newburn Jr., M. Neugebauer and J. Rahe, eds.) **1**, pp. 227-297, Kluwer, Dordrecht.
- Hsiung P. and Roessler K. (1989) CO₂ depth profiles in cometary model substances of KOSI. In Physics and Mechanics of Cometary Materials, pp. 191-196, ESA-SP-302.
- Hsiung P. and Roessler K. (1990) Diffusion of volatiles in cometary analogs. In Lunar Planet. Sci. Conf. XXI, pp. 538-539.
- Roessler K., Hsiung P., Kochan H., Hellmann H., Düren H., Thiel K., and Kölzer G. (1990) A model comet made from mineral dust and H₂O-CO₂ ice : sample preparation development. In Proc. XXth Lunar Planetary Sci. Conf., pp. 379-383, Lunar and Planetary Institute, Houston.
- Roessler K. (1991) Chemische Probleme bei Kometensimulationsexperimenten KOSI, Report-JüL-2446.
- Roessler K., Bénit J. and Heyl M. (1992a) Crust formation in cometary analogs. In Proc. of ESA-workshop "Modelling, Simulation and Sounding of Cometary Nuclei", May 1991, Cagliari, to be published in *Annales Geophysicae*.
- Roessler K., Eich G., Klinger J., and Trimborn P. (1992b) Changes of natural isotopic abundances in comet simulation experiments KOSI. In Proc. of ESA-workshop "Modelling, Simulation and Souding of Cometary Nuclei", May 1991, Cagliari, to be published in *Annales Geophysicae*.
- Stöffler D., Düren H., Knölker J., Hische R., and Bischoff A. (1991) Cometary analogue material : preparation, composition, and thin section petrography. *Geophys. Res. Letters*, **18**, 285-288.
- Thiel K., Kölzer G., and Kohl H. (1991) Dust emission of mineral/ice mixtures: residue structure and dynamical parameters. *Geophys. Res. Letters*, **18**, 281-284.

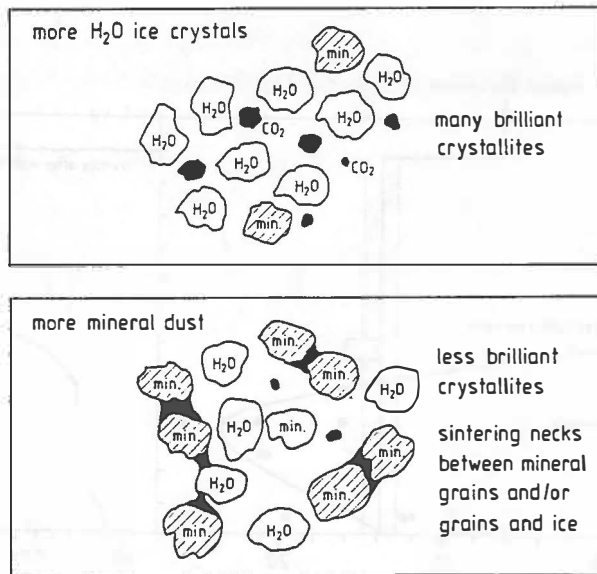


Fig.1 : Comparison of CO₂ recrystallization as a function of material composition (KOSI-6 and 7).

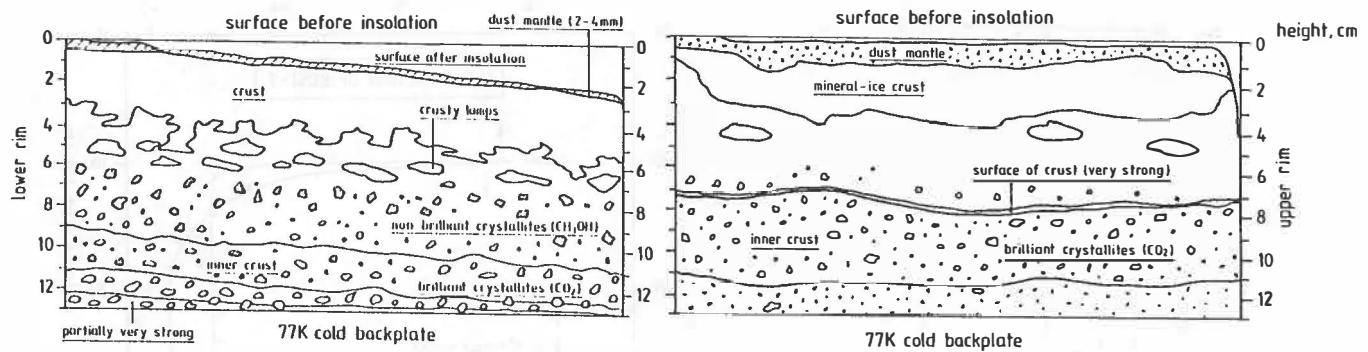


Fig.2 : Stratigraphy KOSI-5 after insolation.

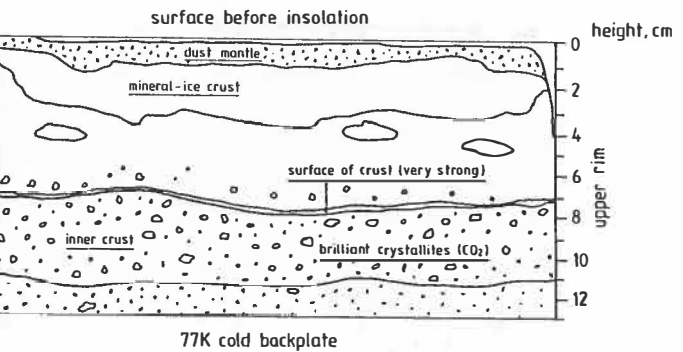


Fig.3 : Stratigraphy KOSI-6 after insolation.

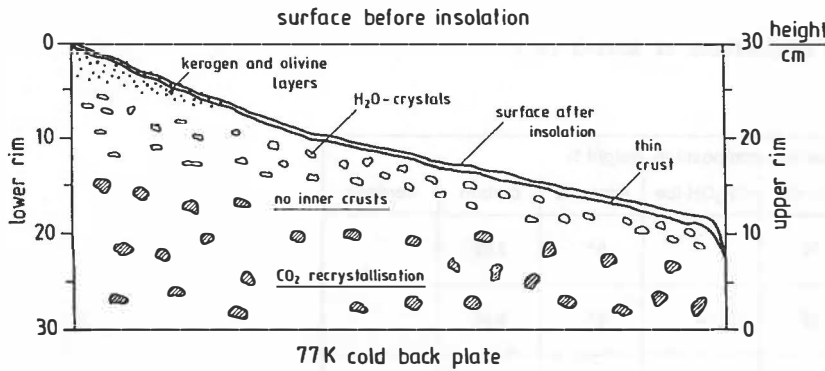


Fig.4 : Stratigraphy KOSI-7 after insolation.

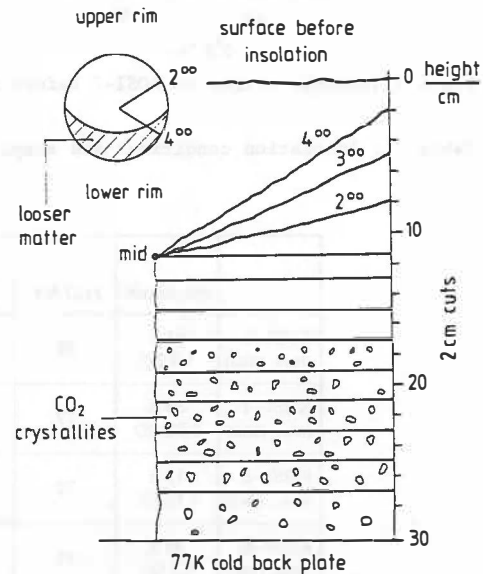


Fig. 8 : Detailed stratigraphy and sample taking geometry in KOSI-7.

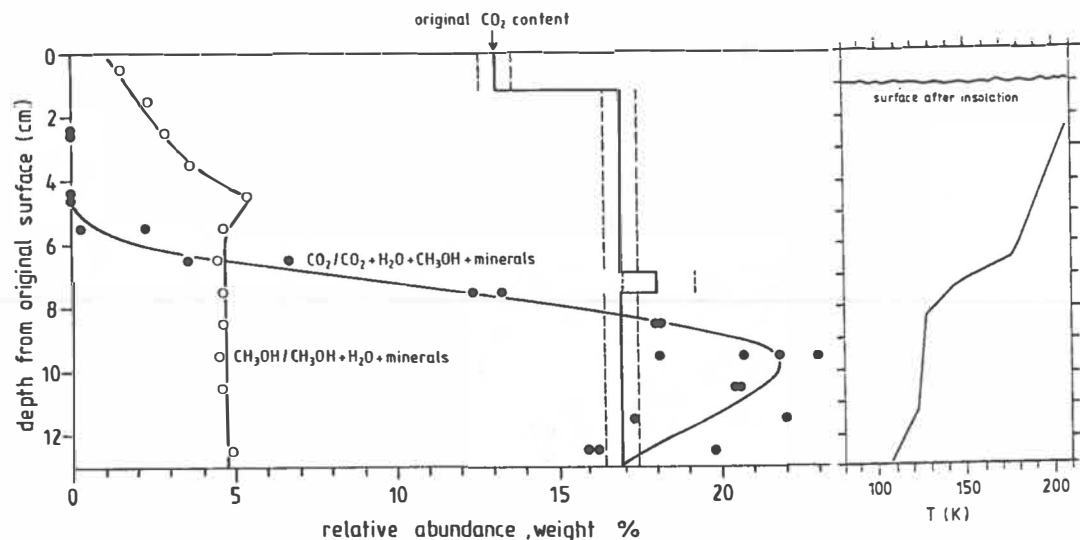


Fig. 5 : Temperature and CO_2 profile vs depth in KOSI-5, cf. Benkhoff and Spohn 1991.

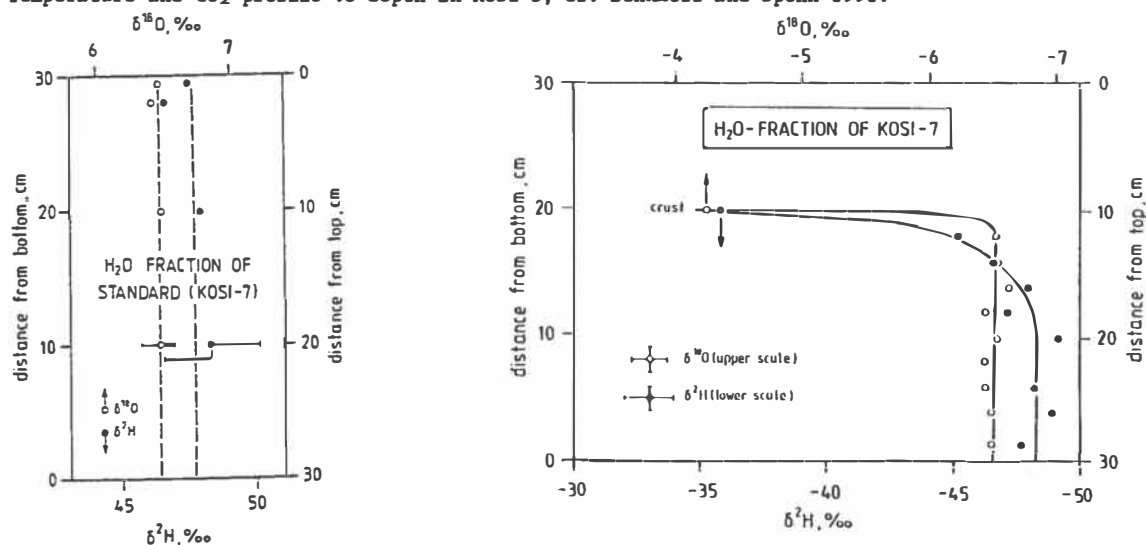


Fig. 6 : Isotopic ratios in KOSI-7 before insolation. Fig. 7 : Isotopic ratios in KOSI-7 after insolation.

Table 1 : Insolation conditions and samples composition of KOSI-3 to 7

	insolation	average composition, weight %					
		H_2O -Ice	CO_2 -Ice	CH_3OH -Ice	minerals	carbon	kerogen
KOSI-3 (Nov. 1988)	41 h 1.3 SC	78	14	—	8*	0.08	—
KOSI-4 (May 1989)	36 h 0.65 SC	77	15	—	8*	0.07	—
KOSI-5 (Nov. 1989)	12 h 1.16 SC	70	17	4	9*	0.07	—
KOSI-6 (May 1990)	24 h 1.2 SC	42	15	—	38**	5	—
KOSI-7 (Jan. 1991)	34 h 1.3 SC	83	15	—	2***	0.07	2.7 % in 2 cm surface layer

* olivine, montmorillonite 9:1; ** 4.2:1; *** olivine only

EVOLUTION OF NEAR UV HALLEY'S SPECTRUM IN THE INNER COMA

P. Rousselot, J. Clairemidi, F. Vernotte, G. Moreels
Observatoire de Besançon, BP 1615
25010 Besançon Cedex, France

Abstract

A direct way to observe the photodissociation of water vapor in a cometary coma consists to detect the OH prompt emission. This emission is shifted of $\delta\lambda=4$ nm with respect to the OH 309 nm fluorescence band. The extended data set obtained with the three-channel spectrometer on-board Vega 2 reveals at short distance of the nucleus (i.e. less than 600 km) an excess of emission on the right wing of the OH band which may be interpreted as being mainly due to prompt emission.

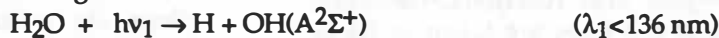
Introduction

The three-channel spectrometer embarked on Vega 2 transmitted approximately 3600 spectra during the encounter day on March 9, 1986.

The spectra cover the range 275 to 710 nm. They were obtained in a spectro-imagery mode, since the instrument scanned a rectangular field of view of $2 \times 1.5^\circ$. During the last half-hour before encounter, this field was restricted to a 2° line scanned in a see-saw motion. Taking advantage of the zoom effect which results of the approach motion, monochromatic images of the inner coma were constructed at selected wavelengths (Clairemidi *et al.*; 1990 a,b). They show the progressive increase of the emissions when the projected distance nucleus-optical axis decreases from 38 000 to 420 km. The distance between the spacecraft and the nucleus decreases then from 516 000 to 8 030 km.

The measured spectrum consists of molecular fluorescence bands superposed on a solar dust-scattered continuum. This solar component is carefully subtracted from the measurement signal in adjusting an absolute solar spectrum, taken from Labs *et al.* (1987) convoluted with the instrument response function, which has a FWHM of 7 nm.

A careful study of the OH emission in the inner coma is of special interest to obtain a direct record of H₂O photolysis. When a water molecule escapes from the nucleus, it is rapidly photodissociated under the following mechanism:



($\lambda_1 < 136$ nm)

Then the electronically excited OH releases a photon:



($\lambda_2 = 309$ nm)

The emission of the photon called $h\nu_2$, at the scale of the inner coma, occurs at the same place as where the H₂O molecule is photolysed. The lifetime of OH($\text{A}^2\Sigma^+$) is estimated to 0.83×10^{-6} s and the ejection velocity of H₂O to 1 km.s^{-1} (probably higher than the ejection velocity of OH with respect to H₂O). As a consequence, the $h\nu_2$ photon is emitted within a distance of about 1 mm from the place where H₂O photodissociation occurs.

This means that the observation of $h\nu_2$ photons is a straightforward way to show evidence of H₂O photodissociation. Since the distance of the nucleus to the optical axis is as small as 400 km, the detection of the OH prompt emission in the three-channel spectra can reasonably be expected.

Theoretical spectrum calculation

A difficulty arises when trying to detect the OH prompt emission because the OH molecules emit fluorescence radiation between the same $\text{X}^2\Pi_{\text{j}}$ and $\text{A}^2\Sigma^+$ states (Budzien and Feldman, 1991). This emission is dominant in the near UV, especially at 309 nm, which corresponds to the (0,0) transition. The fluorescence emission is superposed on the prompt emission which makes its detection difficult. However, a small difference exists, which is due to a temperature difference of the rotational levels.

Let us consider both processes:

- i) H₂O photolysis and prompt emission (fig. 1): in the present calculation, we have taken into account the effect of the solar Ly α only, because this line is responsible for 86 to 93% of the water

vapor photodissociation, depending upon solar activity (Festou, 1981). The rotational quantum number of OH($A^2\Sigma^+$) can reach $J'=23$ in the $v'=0$ and $J'=19$ in the $v'=1$ states.

ii) *Resonance fluorescence excitation* (fig. 2): here we have used the rotational population calculated in full detail in Schleicher's thesis (1983) for the case when the heliocentric component of the velocity is equal to $+24 \text{ km.s}^{-1}$. It may be noted that the only first four rotational levels of the $A^2\Sigma^+, v'=0$ and $v'=1$ states are significantly populated.

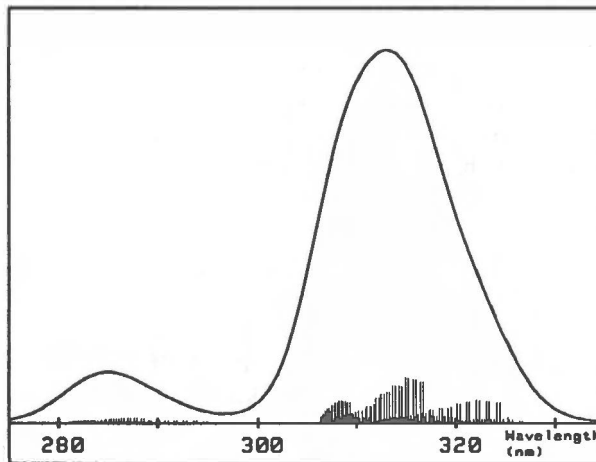


Fig. 1. Emission spectrum of OH ($A^2\Sigma^+ \rightarrow X^2\Pi_j$) due to H_2O photolysis. This spectrum is calculated with the relative population distribution of the rotational levels given by Carrington (1964) for $v'=1$ and by Simons and Smith (1984) for $v'=0$. The branching ratio $P(v'=1)/P(v'=0)$ is taken in Okabe (1980), and the wavelengths and rotational-transition probabilities of the lines are taken in Dieke and Crosswhite (1962). The convolution is calculated with a FWHM of 7 nm.

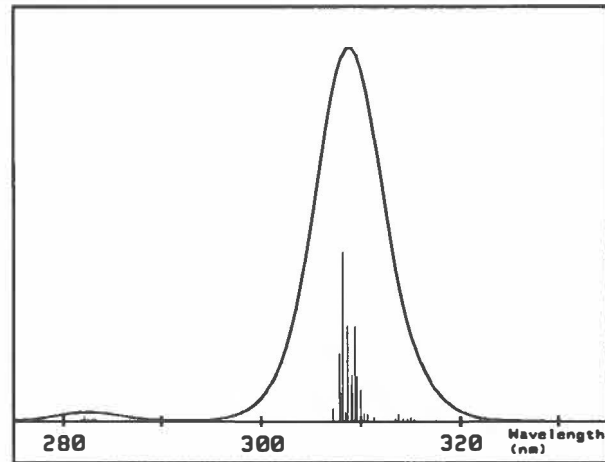


Fig. 2. Emission spectrum of OH ($A^2\Sigma^+ \rightarrow X^2\Pi_j$) excited by resonance fluorescence. The relative population distribution of the rotational levels are taken in Schleicher (1983) for a radial velocity $v=+24 \text{ km.s}^{-1}$. The wavelengths and rotational-transition probabilities of the lines are taken in Dieke and Crosswhite (1962). The convolution is calculated with a FWHM of 7 nm.

A close examination of both figures shows a difference in the wavelengths of maximum intensity, even after convolution: about 313 nm for prompt emission, and 309 nm for fluorescence. In order to know whether OH prompt emission is detectable or not it is necessary to compute the intensity ratio ρ of the two types of emission. We use here the formulae given by Bertaux (1986):

$$\rho = \epsilon(H_2O)/\epsilon(OH) = (g(H_2O)/g(OH)) (n(H_2O)/n(OH))$$

(under optically thin conditions)

where: $g(H_2O)$ and $g(OH)$ are the excitation rates, in $\text{photon.s}^{-1}.\text{molecule}^{-1}$
 $n(H_2O)$ and $n(OH)$ are the number of molecules along the line of sight

$$g(H_2O) = q\tau^{-1}$$

q and τ are, respectively, the fraction of OH radicals which are produced in the $A^2\Sigma^+$ state, and the lifetime of the water molecules against photodissociation by solar photons, both at the wavelength of Ly α .

The following values are obtained:

i) $\tau \approx 1.49 \times 10^5 \text{ s}$ at 0.83 AU (sun-comet distance on March 9, 1986), according to Lewis *et al.* (1983). Consequently, if we take q equal to 7.5%, the quantum efficiency is: $g(H_2O) \approx 5.5 \times 10^{-7} \text{ photon.s}^{-1}.\text{molecule}^{-1}$ at 0.83 AU (if Ly α is responsible for 90% of the process).

ii) $g(OH) \approx 1.67 \times 10^{-3}$ photon.s⁻¹.molecule⁻¹ according to Schleicher (1983). In this calculation we suppose that $g(OH)$ is proportional to r^2 , where r is the distance nucleus-sun in AU.

Consequently we obtain: $\rho \approx 3.3 \times 10^{-4} (n(H_2O)/n(OH))$

It is more difficult to estimate the ratio $n(H_2O)/n(OH)$ with accuracy. However, since H_2O is the major source of OH molecules, we shall examine spectra taken as close as possible of the nucleus.

TKS Observations

Figure 3 shows two spectra obtained around 309 nm which show the (0,0) transition of OH ($A^2\Sigma^+ - X^2\Pi_g$) and the much weaker (1,1) transition. The intensities of these two emission bands are normalized, in order to compare their features. They correspond to impact parameters of, respectively, 538 and 3631 km.

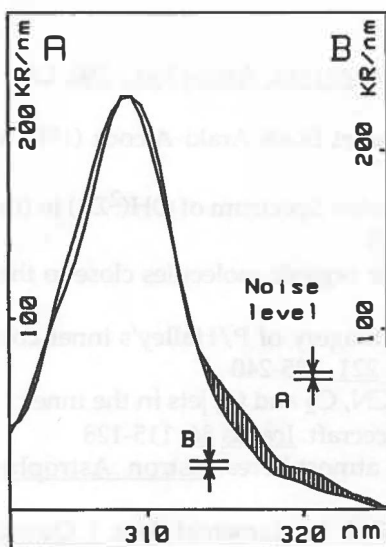


Fig. 3. Spectra obtained with TKS. The intensities are normalized in order to compare the features. The impact parameter ρ of the spectrum (A) is 538 km and of the spectrum (B) is 3631 km. Intensity units are KiloRayleighs/nm. The noise level, which is equal to about 4 KR/nm, is shown for A and B.

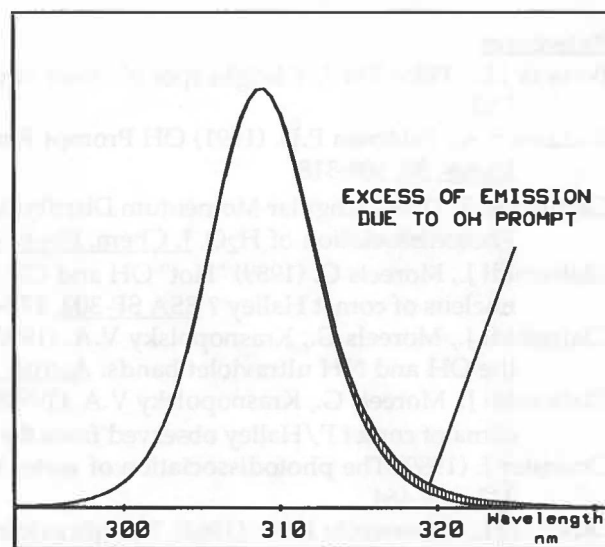


Fig. 4. Theoretical visualisation of OH prompt emission. The weaker spectrum is due only to a resonance fluorescence mechanism and the other is increased by 7.5 % of OH prompt emission. The intensities of the two spectra are normalized in order to compare their features. The convolutions are made with an instrument response function having a FWHM of 7 nm.

An excess of emission may clearly be seen on the right wing, which can be modelized (Fig. 4) with a spectrum of pure fluorescence and a spectrum mixed with 7.5% of prompt emission. This spectrum includes the (0,0) and (1,1) bands.

This modelization implies a ratio $n(H_2O)/n(OH)$ of nearly 230. Effectively, we have:

$$\rho = 0.075 = 3.3 \times 10^{-4} (n(H_2O)/n(OH)) \Rightarrow n(H_2O)/n(OH) \approx 230 \text{ at } 538 \text{ km of the nucleus}$$

This ratio is appreciably higher than the value obtained with Haser's classical model (1950) which gives $n(H_2O)/n(OH) \approx 40-45$. It may also be compared with the value of about 180 for comet IRAS-Araki-Alcock, that can be inferred from the calculation of Budzien and Feldman (1991, table II, exposure LWR 15914).

Therefore, the study of the radial distribution of OH radicals shows a slight decrease of the integrated intensity of this radical near the nucleus, which is not predicted by Haser's model (which overestimates appreciably the integrated OH quantity in this region). This decrease is may be due to an absorption of the solar photons by the inner coma (mainly the H_2O molecules).

The true ratio $n(\text{H}_2\text{O})/n(\text{OH})$ is consequently probably as high as 100-150, which gives the best agreement with the spectra obtained by TKS.

Conclusion

The spectra obtained with TKS in the inner coma of Halley's comet, on March 9, 1986, show that:

i) The intensity of the OH ($\text{A}^2\Sigma^+ \rightarrow \text{X}^2\Pi_g$) emission bands stops to increase when the distance to the nucleus decreases, below 2000 km.

ii) The emission shows an excess of intensity on the right wing of the (0,0) band, only in the vicinity of the nucleus (i.e. within a few hundred km of the nucleus).

The emission excess on the right wing can be partially explained in introducing an OH prompt emission due to the photolysis of water.

References

- Bertaux J.-L. (1986) The UV bright spot of water vapor in comets. *Astron. Astrophys.*, **160**, L7-L10
- Budzien S.A., Feldman P.D. (1991) OH Prompt Emission in Comet IRAS-Araki-Alcock (1983 VII). *Icarus*, **90**, 308-318
- Carrington T. (1964) Angular Momentum Distribution and Emission Spectrum of OH($^2\Sigma^+$) in the Photodissociation of H₂O. *J. Chem. Phys.*, **41**, 2012-2018
- Clairemidi J., Moreels G. (1989) "Hot" OH and CN. Evidence for organic molecules close to the nucleus of comet Halley ? *ESA SP-302*, 177-184
- Clairemidi J., Moreels G., Krasnopolsky V.A. (1990a) Spectro-imagery of P/Halley's inner coma in the OH and NH ultraviolet bands. *Astron. Astrophys.*, **221**, 235-240
- Clairemidi J., Moreels G., Krasnopolsky V.A. (1990b) Gaseous CN, C₂ and C₃ jets in the inner coma of comet P/Halley observed from the Vega 2 spacecraft. *Icarus*, **86**, 115-128
- Crovisier J. (1989) The photodissociation of water in cometary atmospheres. *Astron. Astrophys.*, **213**, 459-464
- Dieke G.H., Crosswhite H.M. (1962) The ultraviolet bands of OH: fundamental data. *J. Quant. Spectrosc. Radiat. Transfer*, **2**, 97-199
- Festou M.C. (1981) The density distribution of neutral compounds in cometary atmospheres. II. Production rate and lifetime of OH radicals in comet Kobayashi-Berger-Milon (1975 LX). *Astron. Astrophys.*, **96**, 52-57
- Haser L. (1957) Distribution d'intensité dans la tête d'une coma. *Académie royale de Belgique, Bull. cl. sciences*, **43**, 740-750
- Labs D., Neckel H., Simon P.C., Thuiller G. (1987) Ultraviolet solar irradiance measurement from 200 to 358 nm during Spacelab 1 mission. *Solar Physics*, **107**, 203-219
- Lewis B.R., Vardavas I.M., Carver J.H. (1983) The Aeronomic Dissociation of Water Vapor by Solar H Lyman α Radiation. *J. Geophys. Res.*, **88**, 4935-4940
- Moreels G. *et al.* (1987) Spectrophotometry of comet P/Halley at wavelengths 275-710 nm from Vega 2. *Astron. Astrophys.*, **187**, 551-559
- Okabe H. (1980) Photodissociation of nitric acid and water in the vacuum ultraviolet; vibrational and rotational distributions of OH($^2\Sigma^+$). *J. Chem. Phys.*, **72**, 6642-6650
- Schleicher D.G., A'Hearn M.F. (1982) OH fluorescence in comets: fluorescence efficiency of the ultraviolet bands. *Astrophys. J.*, **258**, 864-877
- Schleicher D.G. (1983) The fluorescence of cometary OH and CN. Ph.D. Thesis, University of Maryland, Department of Physics and Astronomy
- Schleicher D.G., A'Hearn M.F. (1988) The fluorescence of cometary OH. *Astrophys. J.*, **331**, 1058-1077
- Simons J.P., Smith A.J. (1984) Rotationally Resolved Photofragment Alignment and Dissociation Dynamics in H₂O and D₂O. *J. Chem. Soc., Faraday Trans. 2*, **80**, 1489-1501

MOSAIC CCD METHOD: A NEW TECHNIQUE FOR OBSERVING DYNAMICS OF COMETARY MAGNETOSPHERES

T. Saito¹, H. Takeuchi¹, Y. Kozuka¹, S. Okamura², I. Konno³, M. Hamabe², T. Aoki², S. Minami⁴, and S. Isobe⁵

1. Geophysical Institute, Tohoku University, Japan 2. Kiso Observatory, Japan 3. Southwest Research Institute, USA 4. Osaka City University, Japan 5. National Astronomical Observatory, Japan

OBSERVATION

On April 29, 1990, we observed the plasma tail of Comet Austin with a CCD camera on the 105-cm Schmidt telescope at the Kiso Observatory of the University of Tokyo. The area of the CCD used in this observation is only about 1 cm². When this CCD is used on the 105-cm Schmidt telescope at the Kiso Observatory, the area corresponds to a narrow square view of 12' × 12'. By comparing with the photograph of Comet Austin taken by Numazawa (personal communication) on the same night (see Figure 1), we see that only a small part of the plasma tail can be photographed at one time with the CCD. However, by shifting the view on the CCD after each exposure, we succeeded in imaging the entire length of the cometary magnetosphere of 1.6 × 10⁶ km. We call this new technique "the mosaic CCD method". In order to study the dynamics of cometary plasma tails, we imaged seven frames of the comet from the head to the tail region twice with the mosaic CCD method and obtained two sets of images as shown in Figure 2.

ANALYSIS

In Figure 2, six microstructures, including arcade structures, were identified in both the images. Figure 3 shows sketches of the plasma tail including microstructures.

The relation between the travel speed of the structure v and the distance of the structure from the nucleus projected onto the tail axis x is shown in Figure 4. The flow speed of the plasma very close to the coma was obtained for the first time from this observation. The $x - v$ relation obtained by Minami and White (1986),

$$v(x) = \{v_0[\cosh(x/x_0) - 1] + v_n\}/\cosh(x/x_0), \quad (1)$$

holds here and we have found that at $x = 0$, the flow velocity has a non-zero value, $v(0) = v_n = 35 \pm 5$ km s⁻¹. This velocity is much larger than the thermal velocity $v_{th} \sim 1 - 2$ km s⁻¹, which had been expected near the nucleus. A new interpretation is now needed to explain this observational result.

MODEL

We can explain the non-zero value of the flow velocity at the nucleus by a 3-D model of the cometary magnetosphere as shown in Figure 4. The figure on top is the view of the cometary magnetosphere seen from the equatorial plane and the figure on bottom is the view from the pole. The solar magnetic field stagnates in front of the cometary plasmapause and after winding around the plasmasphere, it passes through its side as shown in the figure by $a - b - c - d$. Therefore, the plasma has non-zero velocity when it crosses the Earth-comet line or at the apparent nucleus position ($x = 0$). The plasma winding around the magnetic lines is probably seen as arcade structures from the Earth as seen in Figures 2 and 3.

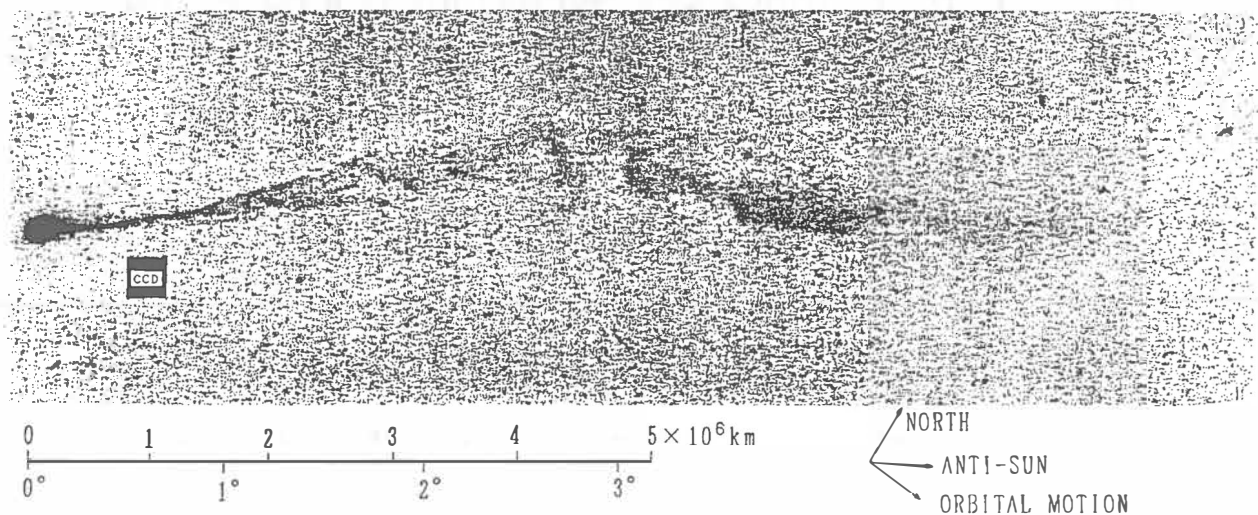


Fig. 1. – Comparison of the scale of the plasma tail of Comet Austin on April 29, 1990, taken by S. Numazawa and the size of the CCD used for the observation in this work.

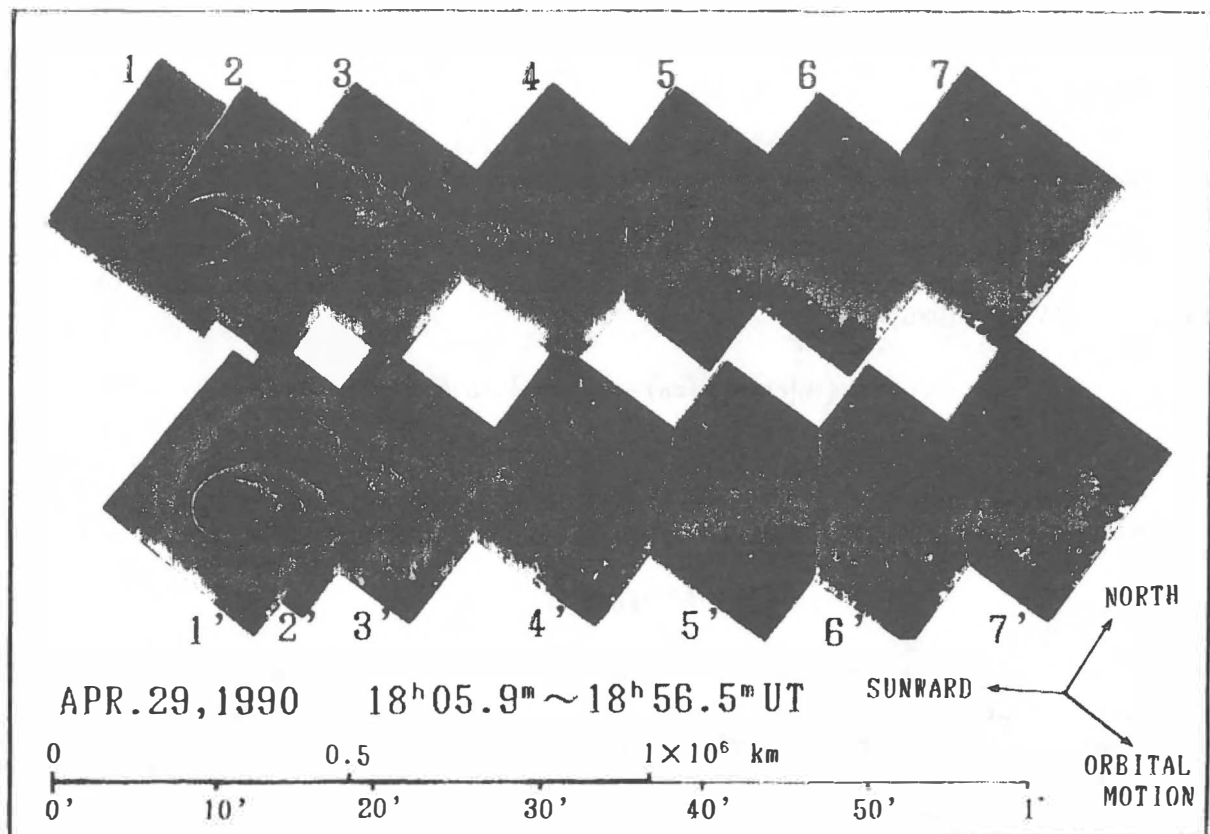


Fig. 2. – The plasma tail of Comet Austin on April 29, 1990, obtained with "the mosaic CCD method". Seven frames of the comet from the head to the tail region were imaged twice.

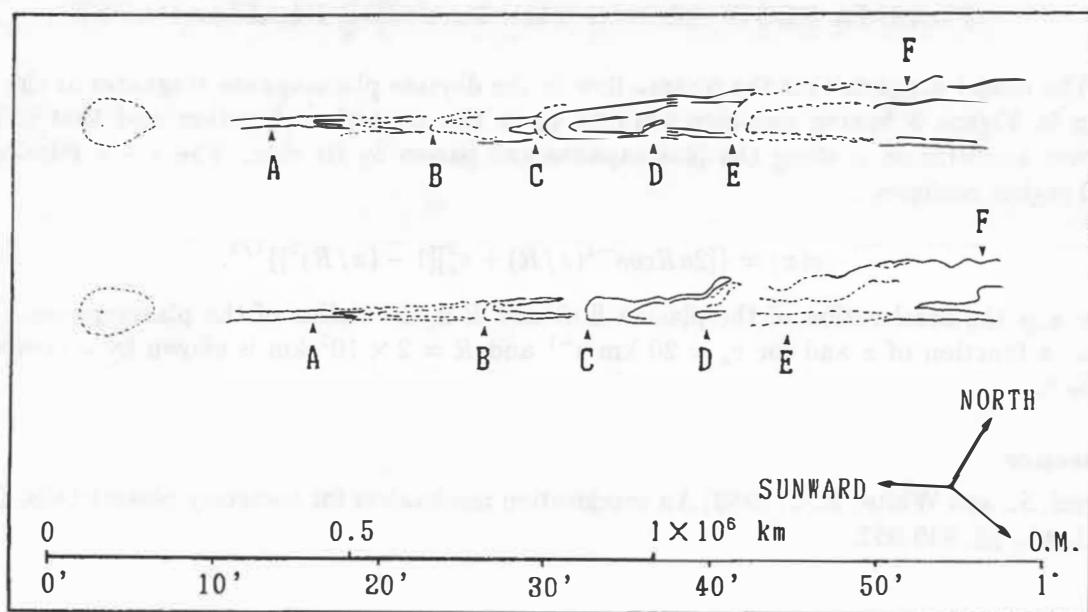


Fig. 3. – Sketches of the plasma tail of Comet Austin made from Fig. 2. Six microstructures, including arcade structures, were identified in both the images.

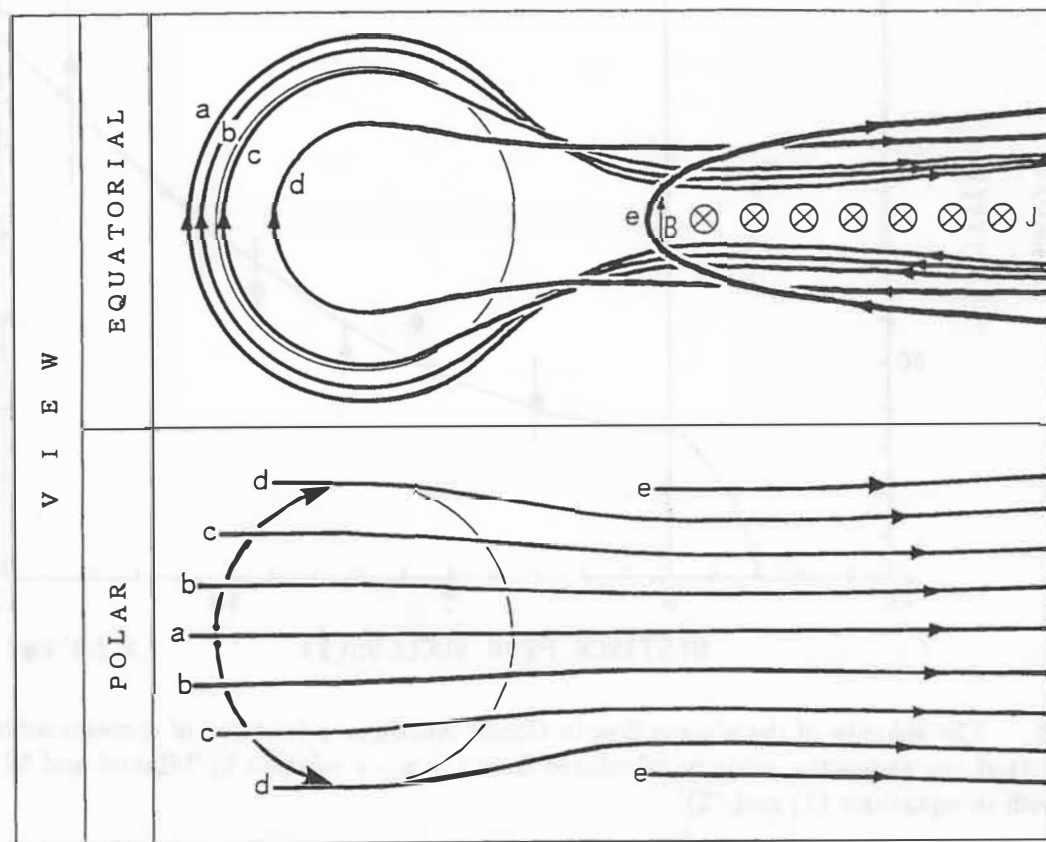


Fig. 4. – Equatorial and polar views of the 3-D model of the cometary magnetosphere. The solid lines are solar magnetic field lines. They stagnate in front of the cometary plasmapause and after widening around the plasmapause, they pass through the side as a – b – c – d – e.

PLASMA FLOW ALONG THE DAYSIDE PLASMAPAUSE

The model suggests that the plasma flow in the dayside plasmapause stagnates at the position shown in Figure 5 having non-zero velocity v_s in the azimuthal direction and that it is under constant acceleration a along the plasmapause and passes by its side. The $x - v$ relation in the $x < 0$ region becomes

$$v(x) = \{[2aR\cos^{-1}(x/R) + v_s^2][1 - (x/R)^2]\}^{1/2}, \quad (2)$$

where a is the acceleration of the plasma flow and R is the radius of the plasmapause. The plot of v as a function of x and for $v_s = 20 \text{ km s}^{-1}$ and $R = 2 \times 10^5 \text{ km}$ is shown by a dotted line in Figure 5.

Reference

Minami, S., and White, R.S. (1986) An acceleration mechanism for cometary plasma tails. *Geophys. Res. Lett.*, 13, 849-852.

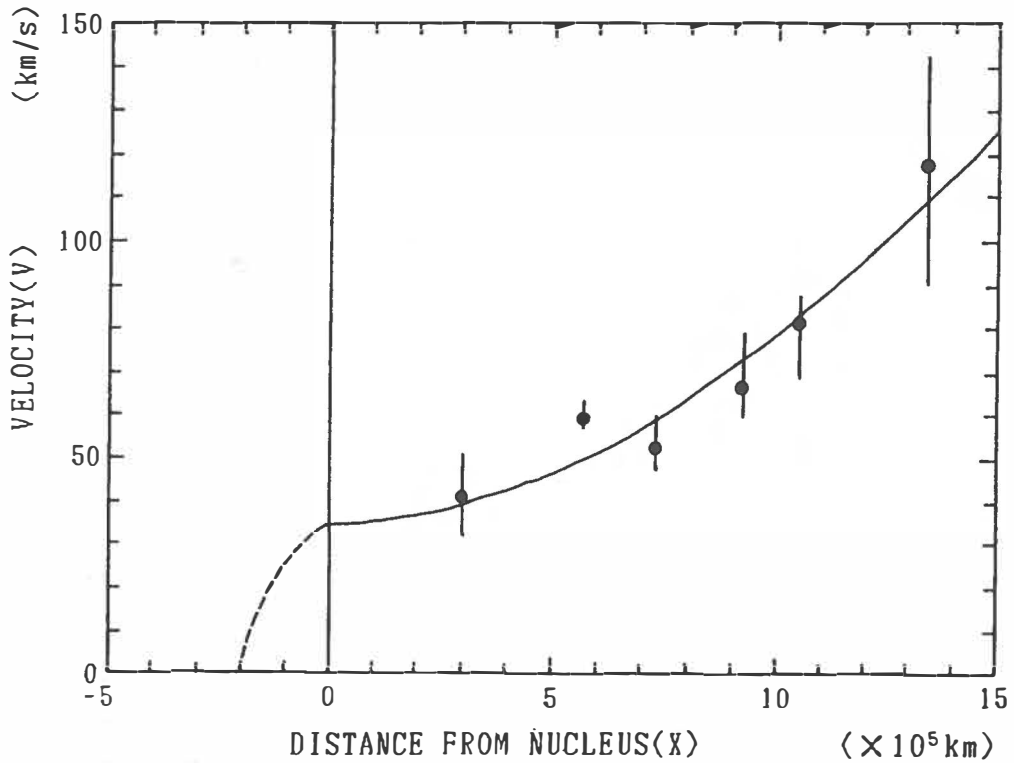


Fig. 5. – The velocity of the plasma flow in Comet Austin as a function of cometocentric distance. The dotted line shows the velocity calculated from the $x - v$ relation by Minami and White (1986) as shown in equations (1) and (2).

SUBMILLIMETER MOLECULAR LINE OBSERVATIONS OF COMET LEVY (1990c)

F. Peter Schloerb and Weigu Ge
Five College Radio Astronomy Observatory
Department of Physics and Astronomy
University of Massachusetts
Amherst MA 01003 U.S.A

ABSTRACT

We present observations of HCN and H₂CO in Comet Levy (1990c) obtained at the Caltech Submillimeter Observatory during August 1990. The HCN J=3-2 rotational line was measured at high spectral resolution (0.1 km s⁻¹) and mapped at 13 points over a region of approximately 1.5 arcmin. Analysis of the line profile and the map suggest only slight deviations from the distribution expected for isotropic outgassing of HCN from the nucleus at a velocity of 0.7 ± 0.1 km s⁻¹. Observations of the HCN J=4-3 and H₂CO 5₁₅-4₁₄ transitions were obtained simultaneously on two days following the HCN J=3-2 measurements. These transitions are the first submillimeter spectral lines to be detected in a comet. Five point maps of the emission show good consistency between the J=3-2 and J=4-3 HCN observations for an HCN production rate of 2 X 10²⁶ and a rotational temperature of approximately 30K. The map of H₂CO emission indicates that it is more extended than the prediction of models in which H₂CO originates entirely from the nucleus. We suggest that H₂CO may also originate from an extended source in the coma.

INTRODUCTION

Radio spectral line studies of comets offer an important means to study the physical state of the cometary coma and the chemical nature of the nucleus (Crovisier and Schloerb 1991). During the past year, important new molecular discoveries have been made in the millimeter wavelength band at the IRAM 30m telescope (*c.f.* Crovisier, this volume), and as the technology improves at these wavelengths, we anticipate a corresponding increase in our understanding of the nature of comets. A particularly important new area for this research will be the study of comets at submillimeter wavelengths, since many cometary transitions are intrinsically stronger in this part of the spectrum and the capabilities of submillimeter instrumentation are rapidly improving. In this paper, we report the first detection of submillimeter-wave spectral line emission from a comet and discuss some of the preliminary results derived from the observations.

OBSERVATIONS

Observations of Comet Levy (1990c) were obtained at the Caltech Submillimeter Observatory using the 10m antenna during 29 August - 1 September 1990. An SIS receiver was used for the HCN J=3-2 observations at 266 GHz; the single sideband system temperature measured on the sky by the chopper wheel method was approximately 700 K during the observations. For the HCN J=4-3 (354 GHz) and H₂CO (352 GHz) observations, the two lines were observed simultaneously by placing them in opposite receiver sidebands of the SIS receiver. The SSB system temperature of this receiver was approximately 1400K, as measured on the sky during the observations. Two Acousto-Optic Spectrometers (AOS) were used to detect the spectral lines. The AOS bandwidths were 500 MHz and 50 MHz, which yielded 0.5 MHz and 50 kHz resolution, respectively. Antenna pointing was verified on Saturn, which was relatively close to Comet Levy in the sky; the pointing uncertainties are estimated to be 3 arcsec rms. The antenna beam width is 28 arcsec at 266 GHz and 22 arcsec at 353 GHz. The beam efficiency at both frequencies is approximately 0.55.

Cometary observations pose a special problem for radio observers since typically the comet must be tracked blind. For these observations, we used orbital elements kindly supplied by D. Yeomans, JPL, at the beginning of our run to predict the position of the comet. However, subsequent improvements in the orbit, published in MPC 16841, indicated that we tracked a position about 13 arcsec NE of the actual position of the nucleus. This illustrates the need for good orbital solutions to support radio observations, and we appreciate the continuing efforts of those who provide astrometric data and ephemerides.

The HCN J=3-2 observations are illustrated in Figures 1 and 2. Figure 1 shows a high resolution (0.1 km s^{-1}) spectrum of the line and indicates the positions and relative strengths of the 6 hyperfine components of this transition. This interesting line shape is due to both the hyperfine structure and the line of sight velocity distribution of HCN in the coma, which is due primarily to the outflow morphology and speed of the coma gas. Figure 2 displays a set of low resolution spectra obtained at 13 positions on a 30 arcsec grid around the "nucleus" position that was tracked by the telescope during our observations. The map shows a significant asymmetry towards the south and west of this position in the direction of the offset between the ephemeris used for these observations and that of MPC 16841.

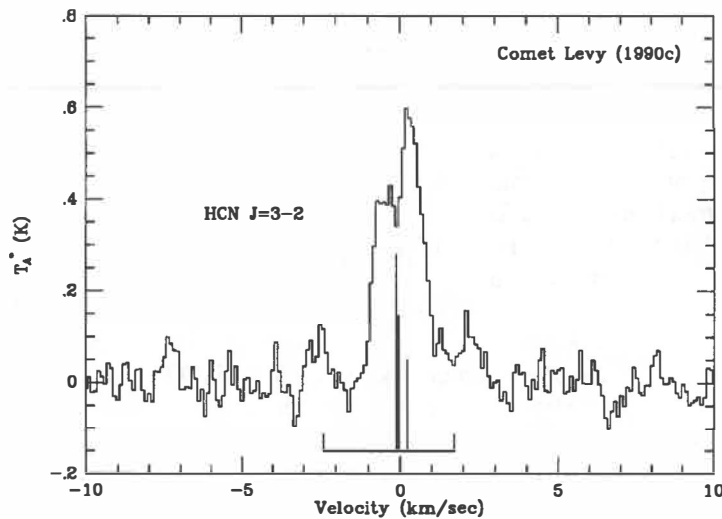


Figure 1 - HCN J=3-2 Spectrum of Comet Levy (1990c) obtained at 0.1 km s^{-1} resolution.

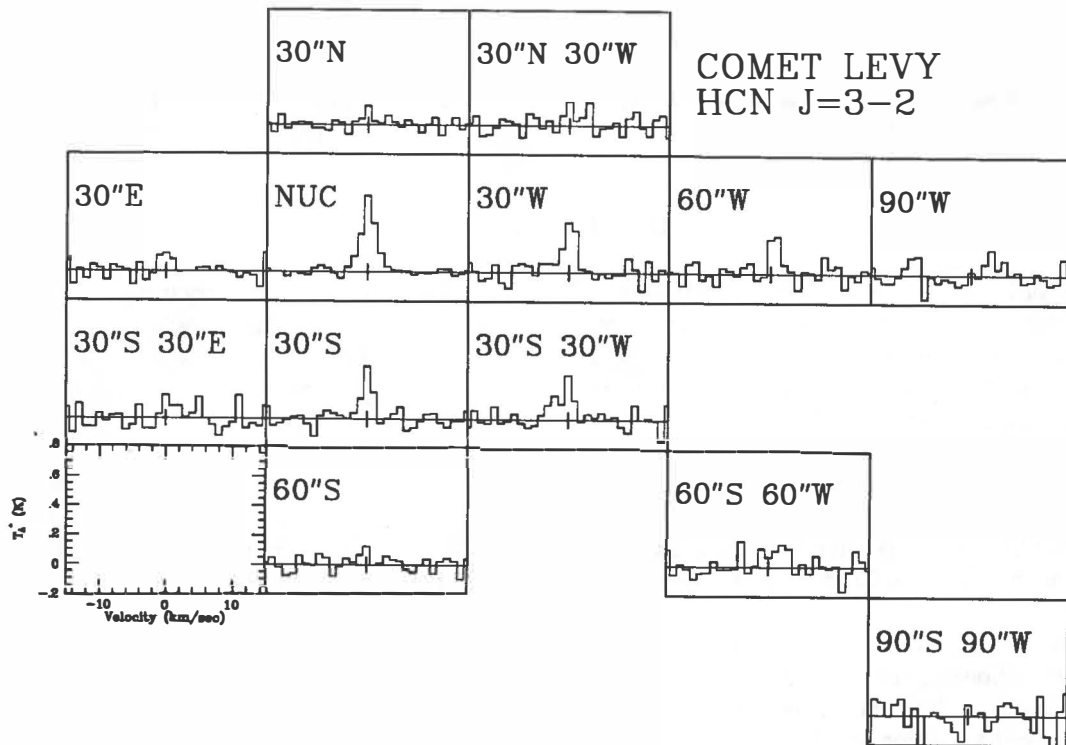


Figure 2 - HCN J=3-2 Map of Comet Levy (1990c). The spectra are sampled on a 30 arcsec grid about the "nucleus" position tracked by the telescope.

The HCN J=4-3 and H₂CO 5₁₅-4₁₄ transitions at the "nucleus" position tracked during our observations are shown in Figure 3. This is the first detection of submillimeter-wave spectral line emission from a comet. In addition to observations at the nominal nucleus position, spectra were also obtained at four positions offset by 30 arcsec in the cardinal directions from the nucleus. The distribution of brightness in the HCN J=4-3 transition is consistent with that observed in the J=3-2 maps, which provides verification of the pointing of the telescope with respect to the comet during these observations and confidence in the derived results.

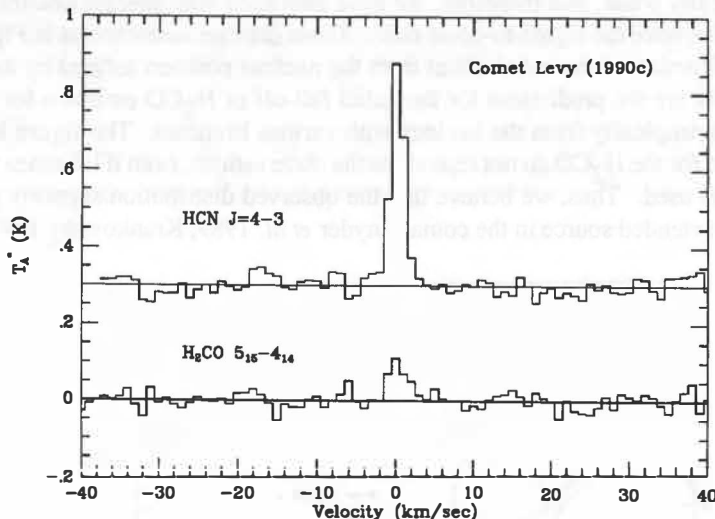


Figure 3 - HCN J=4-3 and H₂CO 5₁₅-4₁₄ spectra of Comet Levy (1990c).

RESULTS

Gas Outflow Velocity

The HCN J=3-2 line profile shown in Figure 1 is reproduced reasonably well by a model of isotropic outgassing of HCN from the nucleus of the comet with a velocity of $0.7 \pm 0.1 \text{ km s}^{-1}$. However, we also observe a slight redshift in the line position which could be due to a small deviation from isotropic gas emission from the nucleus. If the nucleus is modeled as having different production rates from its day and night sides, then the observed redshift would require that the night side emission rate is enhanced over the day side rate by approximately 20%.

HCN Distribution in the Coma

We have fit models of the radial distribution of HCN to the data displayed in Figure 2. One important parameter of the model is a possible offset between the "nucleus" position tracked during the observations and the true position of the nucleus. Assuming a nominal value for the HCN lifetime and isotropic emission of HCN from the nucleus, we find that the HCN map is fit reasonably well if the true position of the nucleus is offset $11 \pm 1 \text{ arcsec}$ West and $8 \pm 1 \text{ arcsec}$ South of the position tracked during the observations. These values compare favorably with the offsets of 10.1 arcsec West and 8.6 arcsec South that are predicted by the difference between the ephemeris we used and that of MPC 16841. Thus, we believe that the data are basically consistent with HCN emitted isotropically from the nucleus with a nominal lifetime of $8 \times 10^4 \text{ s}$, normalized to a heliocentric distance of 1 AU. However, small residuals do remain in the maps, and further investigation is underway.

HCN Production Rate and Rotational Temperature

The HCN J=3-2 and J=4-3 intensities are consistent with thermal excitation of the HCN molecule with a rotational temperature of approximately 30 K. Both this simple model and a more complex excitation model which accounts for both collisional and radiative excitation of HCN in the coma yield an HCN production rate of approximately $2 \times 10^{-26} \text{ s}^{-1}$, which is consistent with previous estimates of the HCN abundance in comets (c.f. Schloerb *et al.* 1987).

H₂CO Distribution

HCN and H₂CO were mapped simultaneously at five points in the coma on two separate nights during the run. This technique makes it possible to derive accurate information on their relative intensities, and since the HCN map permits us to deduce the position of the nucleus at the time of the observations, the H₂CO map may be interpreted without many of the limitations typically imposed by antenna pointing errors and ephemeris uncertainties. The H₂CO lines in the map are intrinsically weak, and therefore, we have averaged map spectra obtained at the same radial distance from the nucleus to improve the signal-to-noise ratio. These data are summarized in Figure 4 as a plot of the integrated line intensity as a function of the radial offset from the nucleus position defined by the ephemeris in MPC 16841. Also shown in the plot are the predictions for the radial fall-off of H₂CO emission for models in which the H₂CO molecule originates isotropically from the nucleus with various lifetimes. The figure indicates that models which assume a nuclear origin for the H₂CO do not reproduce the observations, even if lifetimes much longer than the nominal value of one hour are used. Thus, we believe that the observed distribution supports previous suggestions that H₂CO is produced in an extended source in the coma (Snyder *et al.* 1989, Krankowsky 1991).

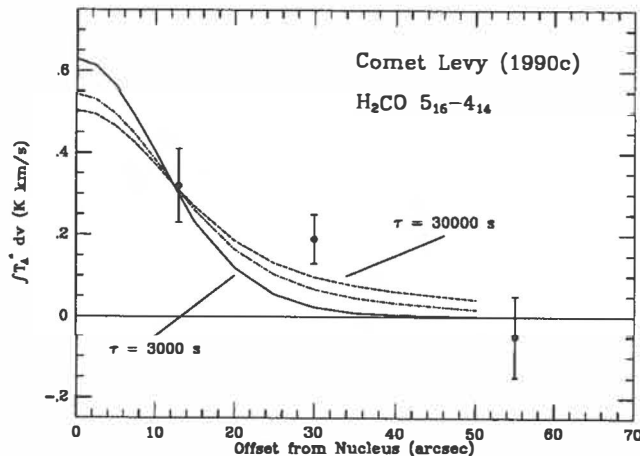


Figure 4 - Observed distribution of H₂CO emission compared to models in which H₂CO originates totally from the nucleus. The data indicate that H₂CO is more extended than the model predictions, suggesting that some H₂CO may originate from an extended source in the coma.

ACKNOWLEDGEMENTS

The authors gratefully acknowledge the assistance of the staff of the Caltech Submillimeter Observatory, and the timely production of orbital elements by Don Yeomans. Planetary Astronomy at the University of Massachusetts is supported by NASA Grant NAGW-1483.

References

- Crovisier J., and Schloerb, F.P. (1991) The Study of Comets at Radio Wavelengths. In Comets in the Post-Halley Era (R.L. Newburn Jr., M. Neugebauer, and J. Rahe, eds.), pp. 149-173. Kluwer Academic Publishers, Dordrecht, The Netherlands.
- Krankowsky, D. (1991) The Composition of Comets. In Comets in the Post-Halley Era (R.L. Newburn Jr., M. Neugebauer, and J. Rahe, eds.), pp. 855-877. Kluwer Academic Publishers, Dordrecht, The Netherlands.
- Schloerb, F.P., Kinzel, W.M., Swade, D.A., and Irvine, W.M. (1987) Observations of HCN in Comet P/Halley. Astron. Astrophys., 187, 475-480.
- Snyder, L.E., Palmer, P. and de Pater, I. (1989) Radio Detection of Formaldehyde Emission from Comet Halley. Astron. J., 97, 246-253.

SPATIAL AND TEMPORAL VARIATIONS IN THE COLUMN DENSITY DISTRIBUTION OF COMET HALLEY'S CN COMA

R. Schulz¹, W. Schlosser¹, W. Meisser¹, P. Koczet¹ and W.E. Celnik²

¹ Astr. Inst., Ruhr-Universität Bochum, Postfach 10 21 48, 4630 Bochum, F.R.G.

² Wilhelm-Foerster-Sternwarte, 1000 Berlin, F.R.G.

ABSTRACT

Mean radial column density profiles of comet P/Halley's CN coma were derived by combining photographic and photoelectric observations. The shape of the profiles as well as their temporal variations were analysed in detail and compared with the results of other CN observations of the comet.

INTRODUCTION

Several surprising characteristics were discovered in the CN coma of comet P/Halley during its apparition in 1986. Firstly, the structural analysis of CN photographs and CCD images led to the detection of shells (Schlosser et al., 1986) and jets (A'Hearn et al., 1986) in the CN coma and secondly, short term variabilities in the photometric lightcurve of comet Halley were also found by photoelectric measurements of the CN emission (Millis and Schleicher, 1986). To clarify, whether there is a connection between the variations in the CN production rate and the occurrence of structures in the CN coma, it is necessary to analyse the temporal variations of the CN distribution in the whole coma in detail. For this purpose a series of CN column density profiles covering several consecutive days was determined by combining photographic and photoelectric observations. Here, a sequence of mean radial column density profiles derived from April 1 to April 10, 1986 is presented.

OBSERVATIONS AND DATA REDUCTION

The CN observations were carried out as a part of the Bochum Halley Monitoring Program at ESO/La Silla from February 17 to April 17, 1986. The observation techniques were photographic as well as photoelectric photometry. A synopsis of the whole observation program is given by Celnik et al. (1988). The photographic CN observations are described in detail by Schulz and Schlosser (1989). The presented column density profiles were derived from CN photographs taken with a Lichtenknecker Flat-Field-Camera (focal length 760 mm, field of view $1^{\circ}8 \times 2^{\circ}7$) between 1 April and 10 April, 1986, respectively. The photographs were digitized and relative intensity calibrated with the use of sensitometric spots. Simultaneously to the photographic observations photoelectric measurements of the comet were obtained in nine different diaphragm sizes at the Bochum 61 cm Cassegrain telescope at La Silla with the standard IHW filter set. The photoelectric measurements were standard star calibrated and then converted into absolute CN fluxes using the calibration procedure described by A'Hearn and Vanysek (1986, 1989). With these data the relative intensities of the corresponding images were transformed into absolute fluxes. Figure 1 shows a typical calibration curve for the transformation of the relative intensities of the images into absolute CN fluxes. The integrated flux F in each aperture evaluated from the photoelectric measurements is plotted against the corresponding background corrected integrated intensity I_{rel} of each

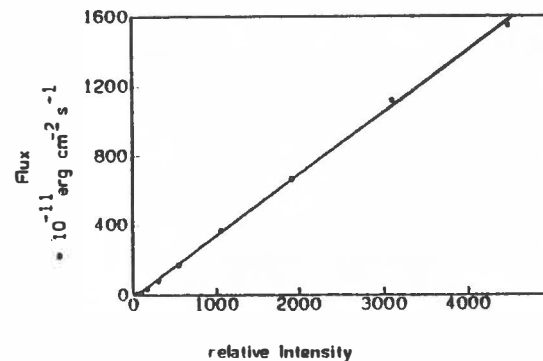
image. The slope m of the resulting straight line gives the calibration factor and the CN fluxes can then be converted into column densities by using the following equation:

$$N = 4 \pi \Delta^2 \cdot \frac{r^2}{g} \frac{F(CN)}{A} = 4 \pi \Delta^2 \cdot \frac{\Delta t}{E_{O2}} \frac{F(CN)}{A}$$

with Δ : geocentric distance r : heliocentric distance / AU
 E_{O2} : excitation energy g : g-factor (normalized to 1 AU)
 A : comet area corresponding to area of one pixel
 Δt : time difference between two excitations

The time difference between two excitations was set to $\Delta t = 18s$ as derived from the accelerated movement of the CN shells in tail direction (Schulz and Schlosser, 1989). The resulting images represent two-dimensional column density profiles of the CN coma.

Fig. 1 Calibration curve for the transformation of the relative intensities in the CN images into absolute fluxes
Photograph of April 8th, 1986, 7.35 - 8.25 UT



COLUMN DENSITY PROFILES

For the analysis of the column density distribution of the CN radical as a function of the nucleus distance, a one-dimensional mean radial column density profile was constructed from each image by azimuthal averaging around the nucleus. This presumes the column density distribution to be circular symmetric around the nucleus in first approximation, which means that the elliptical distortions caused by solar radiation pressure must be neglectable. To prove whether this is the case, one-dimensional cuttings through the coma were prepared and compared to the mean radial profile. This is demonstrated in Fig. 2.

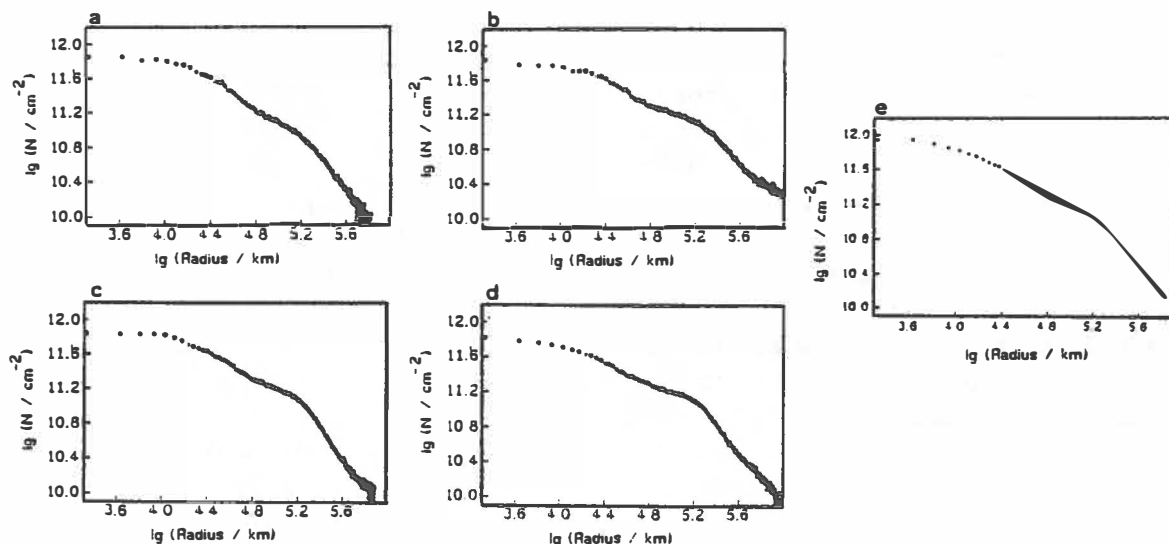


Fig. 2 One dimensional column density profiles of the CN coma in projected sun direction (a), projected tail direction (b) and the perpendicular profiles (c: upper part, d: lower part of the coma) compared to the mean radial column density profile (e). Photograph of April 8, 1986, 2.16 - 3.36 UT

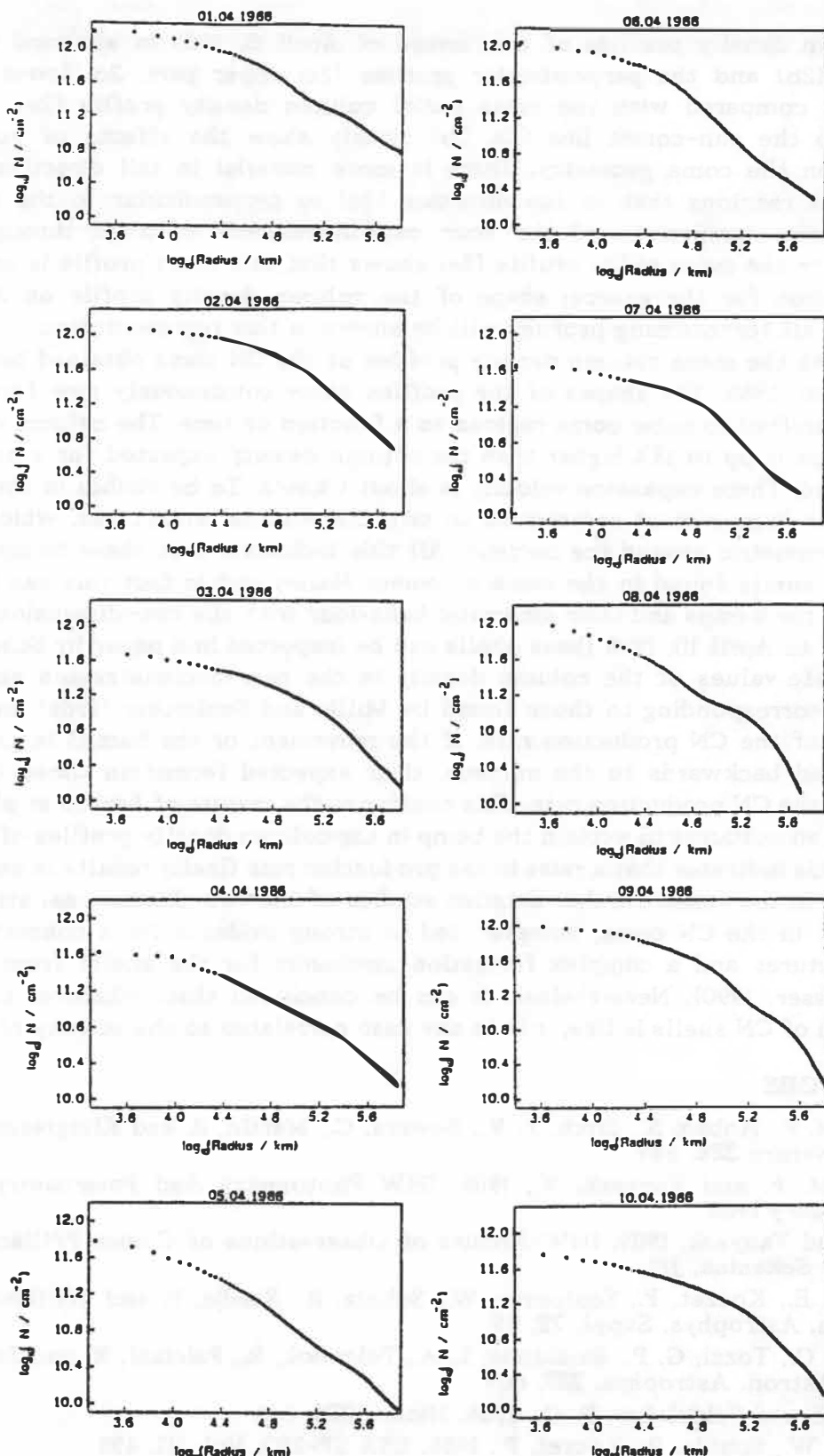


Fig. 3 The mean radial column density profiles of the CN coma between April 1st and April 10th, 1986

The column density profiles of one image of April 8, 1986 in sunward (2a) and tail direction (2b) and the perpendicular profiles (2c: upper part, 2d: lower part of the coma) are compared with the mean radial column density profile (2e). The profiles parallel to the sun-comet line (2a, 2b) clearly show the effects of solar radiation pressure on the coma geometry. There is more material in tail direction (2b) in the outer coma regions than in sun direction (2a) or perpendicular to the tail (2c, 2d). However, the comparison of the four one-dimensional cuttings through the coma (2a - d) with the mean radial profile (2e) shows that this mean profile is an appropriate approximation for the general shape of the column density profile on April 8, 1986. Therefore, all forthcoming profiles will be shown in this representation.

Fig. 3 shows the mean column density profiles of the CN coma obtained between April 1 and April 10, 1986. The shapes of the profiles show continuously new formed 'bumps', which are shifted to outer coma regions as a function of time. The column density inside these bumps is up to 15% higher than the column density expected for a smooth course of the curve. The expansion velocity is about 1 km/s. To be visible in the mean radial profiles the bumps must correspond to two-dimensional structures, which are almost circular symmetric around the nucleus. All this indicates, that these bumps correspond to the CN shells found in the coma of comet Halley and in fact this can be proved by comparing the bumps and their kinematic behaviour with the two-dimensional CN shells. For April 1 to April 10, 1986 these shells can be inspected in a paper by Schulz (1991). The absolute values of the column density in the near-nucleus region show temporal variations corresponding to those found by Millis and Schleicher (1986) and reflect the variations of the CN production rate. If the movement of the bumps in the profiles is extrapolated backwards to the nucleus, their expected formation times coincide with maxima in the CN production rate. This confirms the results of Festou et al. (1990), who suggested an outburst to explain the bump in the column density profiles of December 4, 1985. All this indicates that a raise in the production rate finally results in expanding shell structures in the coma. Further detailed studies of the two-dimensional structures (jets and shells) in the CN coma, however, led to strong evidence for a connection between both structures and a complex formation mechanism for the shells from jets (Schulz and Schlosser, 1990). Nevertheless, it can be concluded that, whatever the formation mechanism of CN shells is like, it is in any case correlated to the activity of the nucleus.

REFERENCES

- A'Hearn, M. F., Hoban, S., Birch, P. V., Bowers, C., Martin, R. and Klingsmith III, D. A., 1986, *Nature* **324**, 649
- A'Hearn, M. F. and Vanysek, V., 1986, IHW Photometry And Polarimetry Net Letter, 3 February 1986
- A'Hearn and Vanysek, 1989, IHW-Archive of Observations of Comet P/Giacobini-Zinner, Ed.: Z. Sekanina, JPL
- Celnik, W. E., Koczet, P., Schlosser, W., Schulz, R., Svedja, P. and Weißbauer, K., 1988, *Astron. Astrophys. Suppl.* **72**, 89
- Festou, M. C., Tozzi, G. P., Smaldone, L. A., Felenbok, R., Falciani, R. and Zucconi, J.-M., 1990, *Astron. Astrophys.* **227**, 609
- Millis, R. L. and Schleicher, D. G., 1986, *Nature* **324**, 646
- Schlosser, W., Schulz, R., Koczet, P., 1986, *ESA SP-250*, Vol. III, 495
- Schulz, R. and Schlosser, W., 1989, *Astron. Astrophys.* **214**, 375 (Erratum: *Astron. Astrophys.* **222**, 367)
- Schulz, R. and Schlosser, W., 1990, *ESA SP-31S*, 121
- Schulz, R., 1991, Proc. 3rd ESO/ST-ECF Data Analysis Workshop, in press

AUTOMATED DETECTION OF ASTEROIDS IN REAL-TIME WITH THE SPACEWATCH TELESCOPE

J. V. Scotti, T. Gehrels, and D. L. Rabinowitz
Lunar and Planetary Laboratory, University of Arizona, Tucson, Arizona, 85721

Abstract

The Spacewatch telescope on Kitt Peak is being used to survey for near-earth asteroids using a Tektronix TK2048 CCD in scanning mode. We hope to identify suitable low Δv candidates amongst the near-earth asteroid population as possible exploration targets, to identify those objects which pose a danger to life on earth, and to study the physical properties of the objects in near-earth space. Between 1990 September and 1991 June, 14 new earth-approaching asteroids including 1 Aten, 9 Apollo, and 4 Amor type asteroids were detected by automated software and discriminated by their angular rates from the rest of the detected asteroids in near-real time by the observer. The average of about 1.5 earth-approaching asteroids per month is comparable to the total number found by all other observatories combined. One other Apollo type asteroid was detected by the observer as a long trailed image. The positions of this last object were measured and the object was tracked by the observer in real time. This object was determined to be a 5-10 meter diameter object which passed within 170 000 kilometers of earth. Of the 14 automatically detected earth-approaching asteroids, 10 have been found at distances in excess of 0.5 AU from earth. An average of more than 2000 asteroids are detected each month. Positions, angular rates, and brightnesses are determined for each of these asteroids in real-time.

REAL-TIME AUTOMATED DETECTION

We are surveying for near-earth asteroids with a TK2048 CCD operated in the scanning mode (Gehrels, *et al.*, 1991). We use the Spacewatch 0.91-meter Newtonian telescope of the Steward Observatory on Kitt Peak in Arizona during 18 nights centered on each new moon. The image data are read out of the CCD by a PC-AT compatible computer and immediately transferred into a Solbourne 5/600 "Sun" compatible multi-processor workstation located at the telescope. Software running on the Solbourne which we call the "Moving Object Detection Program," or MODP, employs the 3 Sparc CPU's to look for streaked images of nearby asteroids during the first 2 passes of a 3 pass scan set over the same area of sky. During the third pass, the software compares the locations of each star brighter than a selected threshold in all three scans to identify sets of images which display consistent motion. The locations of each of these candidates is marked for the observer in the scrolling image data. The motion vectors, positions, and brightnesses found for each object are displayed for the observer in real time in a separate text window (Rabinowitz, 1991a). Each month, in the course of our search for earth-approaching asteroids, we commonly identify several thousand other asteroids which, by their rate of motion, are most likely in the main belt. We verify each detection after discovery by visually inspecting the recorded images, but do not make follow-up observations unless the object has rates which make it a likely earth approacher suspect.

NEAR-EARTH ASTEROID IDENTIFICATION

After a night of observing, a review program collects snapshots 256x256 pixels on a side centered on the location of each of the candidates from all three scans of each survey region observed during the night. The observer then makes the final determination of which detections are of real asteroids and which are artifacts from the CCD or from the analysis by examining the character of all three images. As each real asteroid is selected by the observer, its rates of ecliptic motion are plotted in order to determine the object's probable orbit type (e.g. main belt, Hungaria, Trojan, or earth approacher) (Rabinowitz, *et al.*, 1990). Figure 1 shows the rate plot of all 2200 asteroids detected near opposition during the 1990 October observing run along with the rates of some of the 15 earth-approaching asteroids detected and discriminated by Spacewatch during the first 10 months of full time operation. These rate plots reveal distant earth-approaching asteroids with rates comparable to those of the main belt and smaller than the rates of some Hungaria and Phocaea type asteroids.

Figure 2 shows the rates of the 2200 asteroids detected in 1990 October, along with the rates of all the fast moving objects detected between 1981 and 1991 whose angular velocities fall within the plot. In the photographic surveys during those 10 years, most of the earth-approaching asteroids were discovered only when their rates of motion strongly differed from those of the background asteroid population.

DISCOVERY CIRCUMSTANCES FOR NEAR-EARTH ASTEROIDS

Figure 3 shows the discovery location and relative rates of motion for the earth-approaching asteroids detected between 1981 and 1991 exclusive of the Spacewatch discoveries. The majority of the

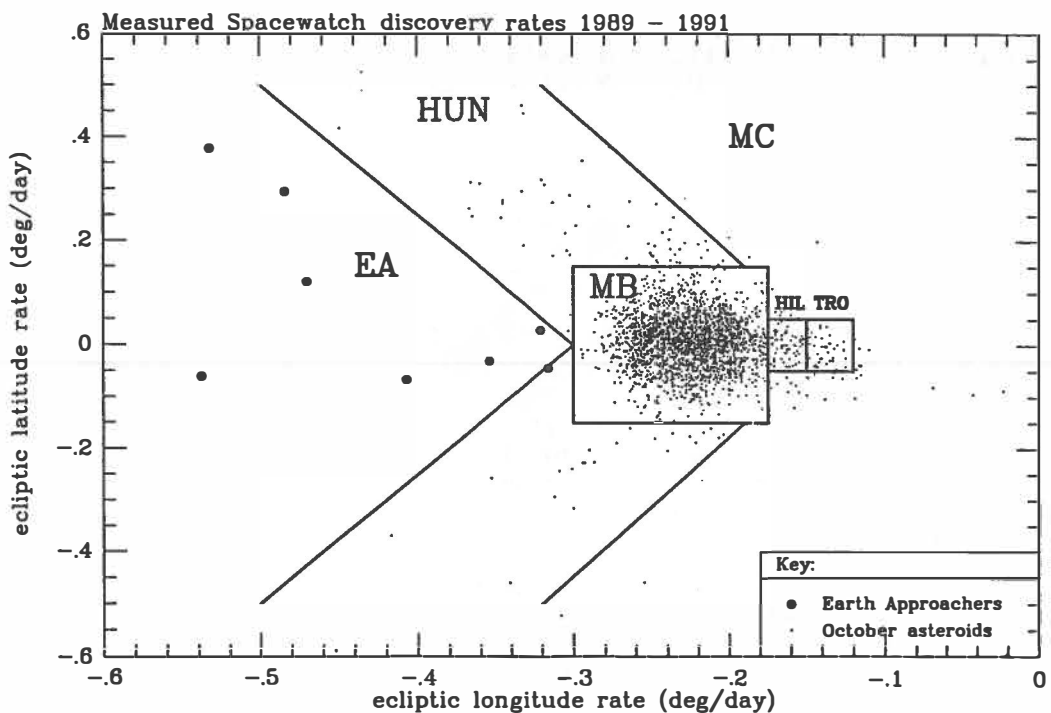


Figure 1 - The rate plot for the asteroids detected during the 1990 October observing run along with the rates of some of the earth-approaching asteroids detected and discriminated by Spacewatch during the first year.

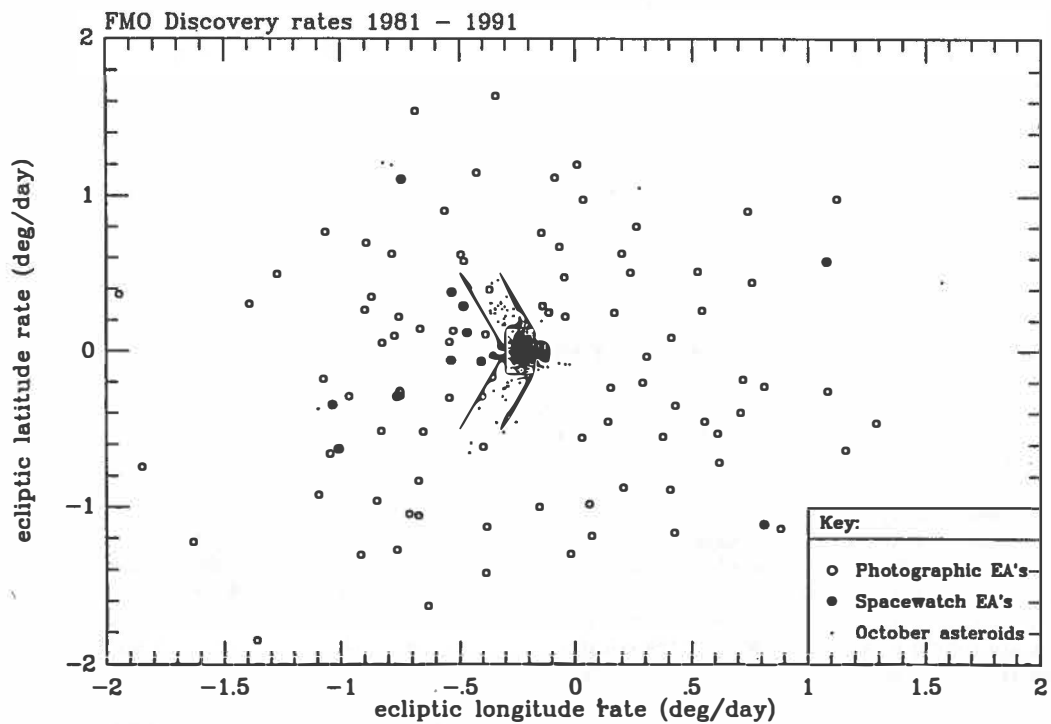


Figure 2 - The rate plot of Figure 1 along with the rates of all the fast moving objects detected between 1981 and 1991 whose rates fall within the limits of the plot.

photographic discoveries were made while the asteroid was well away from the opposition point. The discovery locations are nearly uniformly distributed in the region of opposition longitude ± 30 degrees and latitude 0 degrees to ± 20 degrees. This nearly uniform distribution can be accounted for by the method used to detect the majority of the earth-approaching asteroids. The systematic surveys have concentrated on the region of opposition, but have been able only to discriminate those asteroids which are near the

earth and moving fast. The observer had to be within the swarm in order to locate the earth-approaching asteroids. The bias towards the relative number of northern hemisphere observers is also apparent in the number of objects discovered north of the ecliptic compared to south of the ecliptic.

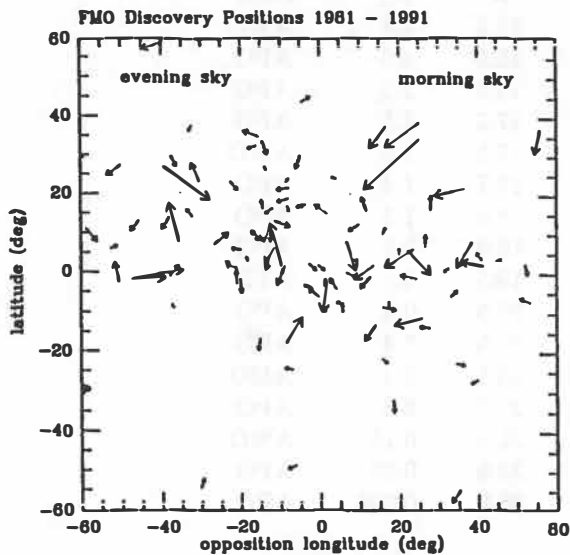


Figure 3 - The discovery location and angular motion vectors for the earth-approaching asteroids detected between 1981 and 1991 by observers other than Spacewatch.

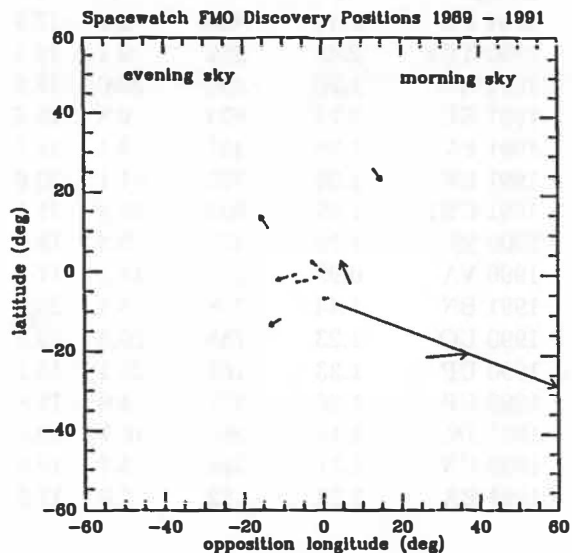


Figure 4 - The same plot as Figure 4, but for the earth-approaching asteroids discovered with the Spacewatch telescope. The long vector pointing towards the lower right is for 1991 BA.

Figure 4 shows the same plot for the Spacewatch discoveries. The majority of the Spacewatch discoveries have been made near the opposition point where the phase effect brightens the objects and where the rates can be used to discriminate the earth-approaching asteroids most effectively. Although the area within ± 30 degrees in longitude and ± 10 degrees in latitude has been the focus of the Spacewatch surveying, most of the discoveries have been made within $\sim 10^\circ$ of the opposition point.

THE SPACEWATCH NEAR-EARTH ASTEROIDS

Table 1 shows the 16 earth-approaching asteroids discovered by Spacewatch. The relative number of Apollo, Amor, and Aten type asteroids closely match those found by the photographic survey programs (Shoemaker, *et al.*, 1990). The types of orbits are also similar to those found in earlier surveys. The principle difference is in the geocentric distances of the asteroids at the time of their discovery. Of the 14 near-earth asteroids detected automatically, 10 were located while at geocentric distances of 0.5 AU or more. Objects whose absolute magnitude H is brighter than about 18.0 (about 1 kilometer diameter) are easily detected while they are within 1.0 AU of earth. Additionally, those objects located nearby include three of the smallest asteroids yet detected. Asteroid 1991 BA, for example, was found to have $H = 28.9$ which would correspond to a 5 to 10 meter diameter (Scotti, *et al.*, 1991). The population of these small objects, in the range of 5 to 10 meters up to about 150 meters, are a population of objects only observed previously by their passage through the atmosphere of the earth as meteors and fireballs. We have found that the estimated number of these small objects are enhanced when compared to the number extrapolated from our observations of larger near-earth asteroids (Rabinowitz, 1991b). Early detection and rapid follow-up with physical studies may aid in the comparison of the meteorite population with their parent bodies.

SUMMARY

The first 10 months of full time surveying with the Spacewatch telescope and automated CCD detection system has produced 15 new earth-approaching asteroids. We can detect earth-approaching asteroids when they are located in the inner half of the main belt of asteroids and are moving with rates comparable to the background asteroids. As with other photographic surveys, we can also detect the nearby objects. The higher quantum efficiency offered by CCD detectors allows us to detect smaller nearby objects, allowing study of meteoroid sized debris in the near-earth environment. With improved

Table 1 – Spacewatch Near Earth Asteroid Discoveries

Design.	<i>a</i>	<i>e</i>	<i>i</i>	1989 October – 1991 June				class
				<i>V</i>	Δ	H	D	
1991 FE	2.19	.455	3.9	17.9	1.509	14.9	4.8	AMO
1990 TG1	2.48	.692	9.1	19.1	1.900	15.0	4.6	APO
1991 AM	1.70	.695	30.0	18.6	0.913	16.5	2.3	APO
1991 EE	2.24	.624	9.8	19.4	0.888	17.5	1.5	APO
1991 FA	1.98	.447	3.1	18.7	0.830	17.5	1.5	AMO
1991 LH	1.35	.729	51.1	20.6	1.201	17.7	1.4	APO
1991 CB1	1.69	.622	15.8	21.1	1.552	18.0	1.3	APO
1990 SS	1.70	.475	19.4	18.9	0.623	19.0	0.9	APO
1990 VA	0.99	.279	14.2	17.9	0.229	19.5	0.6	ATE
1991 BN	1.44	.398	3.4	20.9	0.672	20.0	0.5	APO
1990 UO	1.23	.758	29.3	20.5	0.585	20.5	0.4	APO
1990 UP	1.33	.169	28.1	18.1	0.218	20.5	0.4	AMO
1989 UP	1.86	.473	3.9	15.8	0.061	20.7	0.3	APO
1991 JR	1.40	.260	10.1	19.5	0.090	22.5	0.15	AMO
1990 UN	1.71	.528	3.7	19.9	0.119	23.5	0.09	APO
1991 BA	2.24	.682	2.0	17.5	0.005	28.9	0.008	APO

Table 1 - The 16 earth-approaching asteroids detected by Spacewatch. Two, 1989 UP and 1991 BA, were detected by visual examination of the real-time display available at the telescope while the remaining 14 were detected automatically by MODP as either streaked images or by their consistent motion: *a* is the semimajor axis in AU, *e* is the orbital eccentricity, *i* is the orbital inclination in degrees, *V* is the observed brightness at discovery, Δ is the geocentric distance at the time of discovery in AU, *H* is the absolute magnitude, and *D* is the estimated diameter in kilometers using the mean of the diameters derived from assuming the mean albedoes of a C type and an S type asteroid.

detectors, larger telescopes and more of them, the population of earth-approaching asteroids can be surveyed much more rapidly and with a larger volume of spatial coverage.

REFERENCES

- Gehrels, T., McMillan, R. S., Scotti, J. V., and Perry, M. L. (1990) Drift scanning with a TK 2048 CCD, in CCD's in Astronomy, Vol 8, Astron. Soc. Pac. Conf. Series (G. H. Jacoby ed.), pp. 51-52. Brigham Young University, Provo, Utah.
- Rabinowitz, D. L. (1991a) Detection of Earth-approaching asteroids in near real time. Astron. J., **101**, 1518-1529.
- Rabinowitz, D. L. (1991b) The flux of small asteroids near the Earth, this volume.
- Rabinowitz, D. L., Scotti, J. V., Perry, M. L., Gehrels, T., and McMillan, R. S. (1990) Near real-time detection of Earth-approaching asteroids. Bull. Amer. Astron. Soc., **22**, 1117 (Abstract).
- Scotti, J. V., Rabinowitz, D. L., and Marsden, B. G. (1991) Near miss of the Earth by a small asteroid. Nature, in press.
- Shoemaker, E. M., Wolfe, R. F., Shoemaker, C. S. (1990) Asteroid and comet flux in the neighborhood of Earth, in Global catastrophes in Earth history, Geological Society of America special paper 247, pp. 155-170 (V. L. Sharpton and P. D. Ward, eds.).

SUBLIMATION RATES OF CARBON MONOXIDE AND CARBON DIOXIDE FROM COMETS AT LARGE HELIOCENTRIC DISTANCES

Zdenek Sekanina

*Jet Propulsion Laboratory, California Institute of Technology
Pasadena, California 91109, U.S.A.*

Using a simple model for outgassing from a small flat surface area, the sublimation rates of carbon monoxide and carbon dioxide, two species more volatile than water ice that are known to be present in comets, are calculated for a suddenly activated discrete source on the rotating nucleus. The instantaneous sublimation rate depends upon the comet's heliocentric distance and the Sun's zenith angle at the location of the source. The values are derived for the constants of CO and CO₂ in an expression that yields the local rotation-averaged sublimation rate as a function of the comet's spin parameters and the source's cometocentric latitude.

Numerous examples demonstrate that comets can flare up unpredictably at virtually any point of the orbit, including large heliocentric distances. An outburst of major proportions was recently experienced by Halley's comet at 14 AU from the Sun (West *et al.* 1991). While the actual cause of these unexpected events cannot be stated with certainty, one of the more attractive amongst the plausible scenarios is sudden activation of a discrete source of dust ejecta (that makes up the observed halo) driven by expanding gases much more volatile than water (that have no transitions in the observed optical region of the spectrum and thus remain undetected).

Judging from information based in part upon the results of experiments on board the spacecraft that intercepted Halley's comet, in part upon remote observations, carbon monoxide (e.g., Eberhardt *et al.* 1986, 1987, Woods *et al.* 1986, Krankowsky and Eberhardt 1990, Krankowsky 1991) and carbon dioxide (Krankowsky *et al.* 1986, Feldman *et al.* 1986, Combes *et al.* 1988, Krankowsky and Eberhardt 1990, Krankowsky 1991) are the most likely species potentially capable of instigating such eruptive events.

To facilitate studies of the production of these volatiles from an isolated source on the nucleus surface, it is necessary to determine the diurnal and seasonal variations in the sublimation rate, that is, its dependence upon the Sun's local zenith angle z and the comet's heliocentric distance r . A simple model for outgassing from a flat surface element, based upon the assumption that the absorbed solar energy is spent on sublimation and thermal reradiation (but not on heat conduction into the nucleus) and already employed in studies of the water production (Sekanina 1988), has now been applied to carbon monoxide and carbon dioxide. The dependence of the saturated vapor pressure p (in dyn/cm²) upon the temperature T (in °K) under equilibrium conditions has been expressed by

$$\log p = \mathcal{A} - \frac{\mathcal{B}}{T} + \mathcal{C} T, \quad (1)$$

where $\mathcal{A} = 10.11$, $\mathcal{B} = 334$, and $\mathcal{C} = 0$ have been adopted for CO to fit the data listed by Egerton and Edmondson (1928), while $\mathcal{A} = 11.4320$, $\mathcal{B} = 1275.62$, $\mathcal{C} = 0.006833$ for CO₂ have been taken from the same reference. The vapor pressures listed by Stull (1972) are generally in fair agreement with the adopted values of the coefficients, even though more elaborate formulas could be developed to improve the match. As in the case of water ice, solutions for the sublimation rate $Z(z, r)$ (measured in molecules/cm²/s) that was calculated from the equation of energy balance have been sought to satisfy a law

$$Z(z, r) = Z_0(r) \cdot \zeta(z, r), \quad (2)$$

where Z_0 is the sublimation rate at the subsolar point and $\zeta(z, r) \leq 1$ is the dimensionless relative sublimation rate at the Sun's zenith angle z , plotted for CO in Fig. 1 and for CO₂ in Fig. 2 at four different heliocentric distances. When almost all of the absorbed solar energy is spent on sublimation, the rate ζ varies essentially as $\cos z$. This is true up to a certain zenith distance of the Sun, beyond which ζ begins to drop more rapidly. The approximation introduced in Sekanina (1988) for the relative sublimation rate of water ice has also proven useful for CO and CO₂. Thus,

$$\begin{aligned}\zeta(z, r) &= \cos z - f(r) \cdot \sin^2 z && \text{for } 0 \leq z \leq z_c, \\ &= 0 && \text{for } z > z_c.\end{aligned}\quad (3)$$

Here $z_c = \arccos\{[1 + (2f)^{-2}]^{1/2} - (2f)^{-1}\}$ is the Sun's critical zenith angle, beyond which the sublimation rate is negligibly low compared with that at the subsolar point and $f(r)$ is a function of heliocentric distance that is discussed below. The optimum representations of the relative sublimation rates that were achieved by applying the approximation (3) are shown in Figs. 1 and 2 by dashed curves. This approach allows one to write the rotation-averaged sublimation rate (Z) at a given distance r (assumed constant during rotation) as

$$\langle Z \rangle = \frac{1}{2\pi} \int_{-\Theta_c}^{\Theta_c} Z(z) d\Theta = (Z_0/\pi) \cdot (a \Theta_c + b \sin \Theta_c + c \sin 2\Theta_c), \quad (4)$$

where $\Theta_c(r)$ is a critical hour angle of the Sun that depends upon z_c and the cometocentric latitudes of the active source, ϕ_{act} , and the subsolar point, ϕ_{ss} ,

$$\cos \Theta_c = \cos z_c \sec \phi_{act} \sec \phi_{ss} - \tan \phi_{act} \tan \phi_{ss}, \quad (5)$$

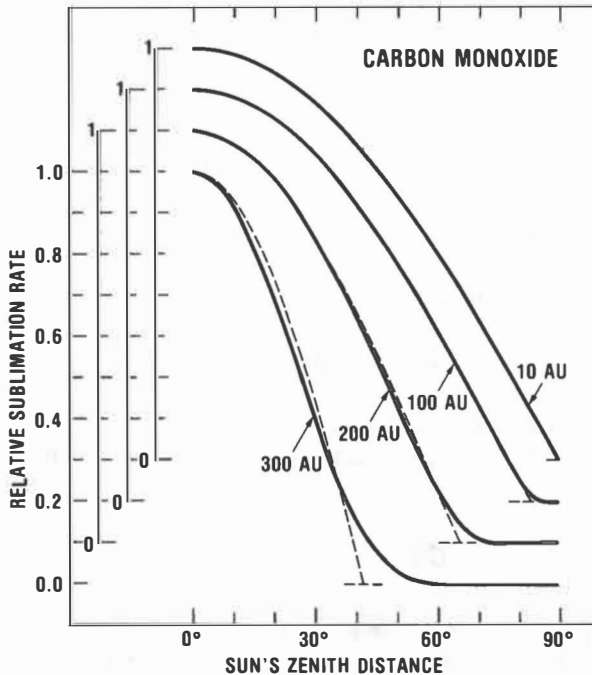


FIG. 1. Relative sublimation rate $\zeta(z, r)$ of carbon monoxide vs. the Sun's zenith angle at the location of the source as a function of heliocentric distance. The solid curves are the rates derived from the energy-balance equation. The broken curves are the least-squares solutions that accommodate the approximation (3). The curves have been shifted vertically for the sake of clarity.

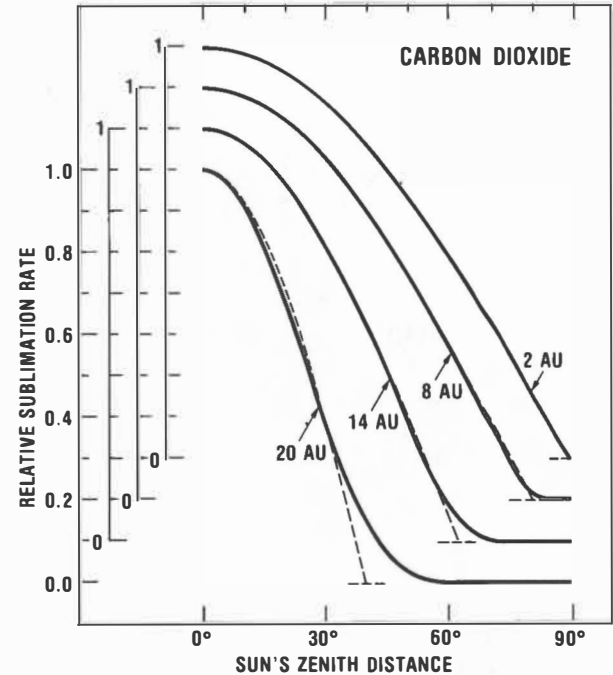


FIG. 2. Relative sublimation rate $\zeta(z, r)$ of carbon dioxide vs. the Sun's zenith angle at the location of the source as a function of heliocentric distance. The solid curves are the rates derived from the energy-balance equation. The broken curves are the least-squares solutions that accommodate the approximation (3). The curves have been shifted vertically for the sake of clarity.

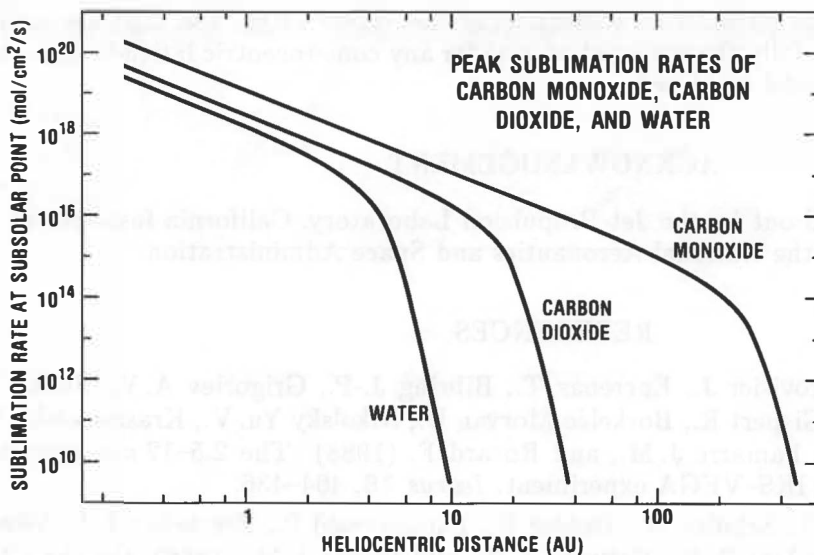


FIG. 3. The sublimation rate per unit outgassing area at the subsolar point as a function of heliocentric distance for carbon monoxide and carbon dioxide, compared with the sublimation rate for water ice.

and the coefficients a , b , and c are functions of ϕ_{act} , ϕ_{ss} , and $f(r)$:

$$\begin{aligned} a &= \sin \phi_{\text{act}} \sin \phi_{\text{ss}} - \frac{1}{2} f(1 + \sin^2 \phi_{\text{act}} \cos^2 \phi_{\text{ss}} + \cos 2\phi_{\text{act}} \sin^2 \phi_{\text{ss}}), \\ b &= \cos \phi_{\text{act}} \cos \phi_{\text{ss}} (1 + 2f \sin \phi_{\text{act}} \sin \phi_{\text{ss}}), \\ c &= \frac{1}{4} f \cos^2 \phi_{\text{act}} \cos^2 \phi_{\text{ss}}. \end{aligned} \quad (6)$$

The peak (subsolar-point) sublimation rate $Z_0(r)$ is expressed by a slightly generalized version of the formula used in Sekanina (1988) for water ice:

$$\log Z_0(r) = A + B \log(r/r_0) + C(r/r_0)^\beta + D \log[1 + (r/r_0)^\gamma], \quad (7)$$

where A , B , C , D , β , and γ are constants for the given ice and r_0 is a “normalizing” heliocentric distance that is related to the heat of sublimation L (crudely, $r_0 \propto 1/L^2$). Figure 3 compares the heliocentric variations in the sublimation rates of CO and CO₂ at the subsolar point with that of water ice. For CO the function $f(r)$ is fitted empirically by

$$f(r) = E(r/r_0)^2 [1 + F(r/r_0) + G(r/r_0)^2]. \quad (8)$$

For CO₂ this expression yields a fit that is somewhat inferior to that offered by a law

$$f(r) = \tilde{E}(r/r_0)^{7/4} \exp[\tilde{F}(r/r_0)^{\tilde{G}}]. \quad (9)$$

When r is in AU and $Z_0(r)$ in molecules/cm²/s, the coefficients have the numerical values listed in Table I for an assumed unit bolometric emissivity and an albedo of 4 percent. The coefficients A through γ provide an excellent fit up to $r \approx 500$ AU for CO and up to $r \approx 40$ AU for CO₂. The coefficients E through G offer a very good fit up to $r \approx 300$ AU for CO and the coefficients \tilde{E} through \tilde{G} are applicable up to $r \approx 20$ AU for CO₂.

TABLE I. Sublimation constants for carbon monoxide and carbon dioxide.

Species	r_0 (AU)	A	B	C	D	β	γ	E	F	G	\tilde{E}	\tilde{F}	\tilde{G}
CO	285	14.184	-2.00	-0.74	-0.63	2.09	14.95	1.386	-1.337	1.343
CO ₂	20.2	15.961	-1.95	-0.75	-1.74	1.50	8.55	1.882	-1.775	1.779	0.78	0.90	2.70

Once the nucleus rotation parameters (determining the values of Θ_c and ϕ_{ss}) are available, Eqs. (2) through (9) describe fully the sublimation rate for any cometocentric latitude ϕ_{act} , subject to the assumptions of the model employed.

ACKNOWLEDGEMENT

This research was carried out by the Jet Propulsion Laboratory, California Institute of Technology, under contract with the National Aeronautics and Space Administration.

REFERENCES

- Combes M., Moroz V.I., Crovisier J., Encrénaz T., Bibring J.-P., Grigoriev A.V., Sanko N.F., Coron N., Crifo J.F., Gispert R., Bockelée-Morvan D., Nikolsky Yu.V., Krasnopolsky V.A., Owen T., Emerich C., Lamarre J.M., and Rocard F. (1988) The 2.5–12 μm spectrum of comet Halley from the IKS-VEGA experiment. *Icarus* **76**, 404–436.
- Eberhardt P., Krankowsky D., Schulte W., Dolder U., Lämmerzahl P., Berthelier J.J., Woberies J., Stubbemann U., Hodges R.R., Hoffman J.H., and Illiano J.M. (1986) On the CO and N₂ abundance in comet Halley. In *Exploration of Halley's Comet*, ESA SP-250 (B. Battrick, E.J. Rolfe, and R. Reinhard, eds.), pp. 383–386. ESTEC, Noordwijk.
- Eberhardt P., Krankowsky D., Schulte W., Dolder U., Lämmerzahl P., Berthelier J.J., Woberies J., Stubbemann U., Hodges R.R., Hoffman J.H., and Illiano J.M. (1987) The CO and N₂ abundance in comet P/Halley. *Astron. Astrophys.* **187**, 481–484.
- Egerton A.C. and Edmondson W. (1928) Vapor pressure of chemical compounds in the crystalline state. In *International Critical Tables* (E.W. Washburn, ed.), vol. 3, pp. 207–209. McGraw-Hill, New York.
- Feldman P.D., A'Hearn M.F., Festou M.C., McFadden L.A., Weaver H.A., and Woods T.N. (1986) Is CO₂ responsible for the outbursts of comet Halley? *Nature* **324**, 433–436.
- Krankowsky D. (1991) The composition of comets. In *Comets in the Post-Halley Era* (R.L. Newburn, Jr., M. Neugebauer, and J. Rahe, eds.), pp. 855–877. Kluwer, Dordrecht.
- Krankowsky D. and Eberhardt P. (1990) Evidence for the composition of ices in the nucleus of comet Halley. In *Comet Halley: Investigations, Results, Interpretations* (J.W. Mason, ed.), vol. 1, pp. 273–289. Ellis Horwood, Chichester.
- Krankowsky D., Lämmerzahl P., Herrwerth I., Woberies J., Eberhardt P., Dolder U., Herrmann U., Schulte W., Berthelier J.J., Illiano J.M., Hodges R.R., and Hoffman J.H. (1986) *In situ* gas and ion measurements at comet Halley. *Nature* **321**, 326–329.
- Sekanina Z. (1988) Outgassing asymmetry of periodic comet Encke. I. Apparitions 1924–1984. *Astron. J.* **95**, 911–924, 970–971.
- Stull D.R. (1972) Vapor pressure. In *American Institute of Physics Handbook* (D.E. Gray, ed.), p. 4–313. McGraw-Hill, New York.
- West R.M., Hainaut O., and Smette A. (1991) Post-perihelion observations of P/Halley. III. An outburst at $r = 14.3$ AU. *Astron. Astrophys.* **246**, L77–L80.
- Woods T.N., Feldman P.D., Dymond K.F., and Sahnow D.J. (1986) Rocket ultraviolet spectroscopy of comet Halley and abundance of carbon monoxide and carbon. *Nature* **324**, 436–438.

INTERPRETING ASTEROID PHOTOMETRY AND POLARIMETRY USING A MODEL OF SHADOWING AND COHERENT BACKSCATTERING

Yu. G. Shkuratov † and K. Muinonen ‡

† Astronomical Observatory of Kharkov State Univ., Sumskaya Street 35, Kharkov 310022, Ukraine

‡ Lowell Observatory, 1400 West Mars Hill Road, Flagstaff, AZ 86001, U.S.A.

The shadow-hiding models for the opposition effect (Hapke 1966, Lumme and Bowell 1981) and negative polarization (Wolff 1975) of atmosphereless solar system bodies do not explain some experimental findings, such as the enhancing opposition effect and negative polarization with decreasing particle size down to wavelength scales. Figure 1 shows the enhancement for laboratory photometric and polarimetric data on artificial glass samples with different particle size (Shkuratov 1985, Shkuratov and Akimov 1987). These results are in agreement with the so-called coherent backscattering or interference mechanism proposed for the interpretation of the opposition effect and negative polarization by Shkuratov (1985) and Muinonen (1989).

We have developed two different approaches for describing the opposition effect and negative polarization produced by the shadow-interference mechanism. One is based on exact electromagnetic solutions for simple scattering systems that include dipole-dipole and dipole-surface coupling; surface-surface coupling was studied in the geometric optics approximation (Muinonen 1989 and 1990ab, Muinonen *et al.* 1990, Muinonen and Lumme 1991). The other is based on a point-scatterer approximation characterized by model photometric and polarimetric phase functions, and the mutual shadowing effect is derived using virtual volumes associated with the point-scatterers (Shkuratov 1988 and 1991, Shkuratov *et al.* 1989). Both approaches yield qualitatively similar results, although neither is entirely satisfactory. We regard them as prototypes for a future unified model of shadowing and coherent backscattering. The sharp opposition effect of 44 Nysa and the asteroid albedo-polarization rule are here explained using the point-scatterer approach.

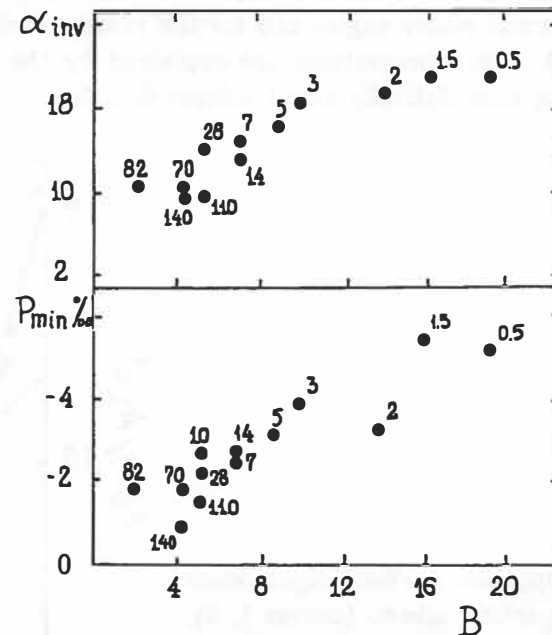


Fig. 1. Inversion phase angle α_{inv} and minimum P_{min} of linear polarization for artificial glass powders versus the opposition effect curvature $B = 10^3 \times [A(1^\circ 5) + A(12^\circ 5) - 2A(7^\circ)]/5^\circ 5$, where A is the bidirectional reflectance. Particle size is shown in microns for each data point.

OPPOSITION EFFECT OF 44 NYSA

Including the mutual shadowing and coherent backscattering effects but presently excluding rough surface shadowing, we describe the bidirectional reflectance by

$$A(\iota, \epsilon, \alpha) = \frac{\varpi}{4} \frac{\cos \iota \cos \epsilon}{\cos \iota + \cos \epsilon} [\chi(\alpha)T(\iota, \epsilon, \alpha) + D(\iota, \epsilon, \alpha)M(\iota, \epsilon, \alpha)], \quad (1)$$

where ϖ is the average single particle albedo, ι and ϵ are the angles of incidence and emergence, and α is the phase angle. Also, χ is the average single particle phase function, and T , D , and M are the mutual shadowing, coherent backscattering, and multiple scattering functions, respectively. Assuming an isotropic single-particle phase function, we obtain (Shkuratov *et al.* 1991)

$$\begin{aligned} T(\iota, \epsilon, \alpha) &= \sum_{n=0}^{\infty} \frac{(\cos \iota + \cos \epsilon)^{n+1}}{2^n \prod_{m=0}^n (\cos \iota + \cos \epsilon + mq \sin \alpha)}, \quad q = \frac{\xi}{1 - \xi} \\ M(\iota, \epsilon, \alpha) &= \left(\frac{1 + 2 \cos \iota}{1 + 2 \cos \iota \sqrt{1 - \varpi}} \right) \left(\frac{1 + 2 \cos \epsilon}{1 + 2 \cos \epsilon \sqrt{1 - \varpi}} \right) - 1 \\ D(\iota, \epsilon, \alpha) &= 1 + \frac{1}{\sqrt{1 + L^2[\sin^2 \iota + \sin^2 \epsilon + 2(\cos \iota \cos \epsilon - \cos \alpha)]}}, \quad L = \frac{4\pi r}{\lambda} (1 + \varpi) \sqrt{\frac{\varpi}{3(1 - \varpi)}}, \end{aligned} \quad (2)$$

where ξ is the volume density of the scattering medium and L is the average size of a 'flare spot' caused by multiple scattering within the surface. λ and r are the wavelength and the average particle radius. The present scattering model gives an enhancement of the opposition effect with increasing albedo due to the multiple scattering term $D(\iota, \epsilon, \alpha)M(\iota, \epsilon, \alpha)$. In Figure 2, this is illustrated for model parameters $\xi = 0.5$, $r/\lambda = 1$, $\varpi = 0.5$ (curve 1) and $\varpi = 0.85$ (curve 2), assuming that $\iota = 0^\circ$ and $\epsilon = \alpha$. Also, a slight wavelength dependence is predicted for the opposition effect in the case of spectrally neutral particulate media, illustrated by the ratio $A(\alpha; r/\lambda = 1.2)/A(\alpha; r/\lambda = 0.8)$ (curve 3).

Besides theoretical results, Figure 2 shows the observations by Harris *et al.* (1989) for the bright E-class asteroid 44 Nysa with geometric albedo about 45%. We emphasize that the asteroid data are disk-integrated, whereas the theoretical scattering law is for a local surface element. Thus, we treat 44 Nysa as if it were a planar disk, the normal of which points in the direction of the Sun. For small phase angles and for the present demonstration purposes, this simple assumption is justified. The observations are explained by the coherent backscattering mechanism without introducing unrealistically small volume densities.

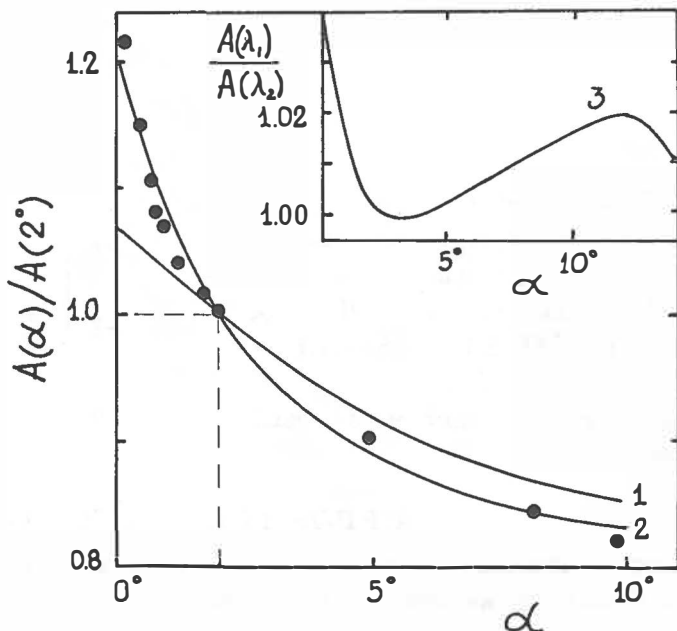


Fig. 2. Opposition effect dependence on single particle albedo (curves 1, 2), and on wavelength (curve 3). Observations by Harris *et al.* (1989) for 44 Nysa are explained by the coherent backscattering mechanism.

ALBEDO-POLARIZATION LAW

An approximate expression for the degree of linear polarization has been obtained by assuming an isotropic scattering phase function and a modified Rayleigh polarization $G \sin^2\alpha/(1 + \cos^2\alpha)$ (scale factor $0 < G \leq 1$) for single particles (Shkuratov 1991, Shkuratov and Melkumova 1991),

$$P(\alpha) = \frac{G}{18} (1 + 2\sqrt{1 - \omega})^2 \left\{ \sin^2\alpha + \frac{2\xi\omega[1 - \sqrt{1 + \rho^2 \sin^2\alpha}]^2}{\rho^2 \sin^2\alpha \sqrt{1 + \rho^2 \sin^2\alpha \ln(1 - \xi)}} \right\}, \quad \rho = \frac{8\pi r}{3\lambda \ln(1 - \xi)}. \quad (3)$$

We will now study the correlation of asteroid geometric albedos and polarization curves. The geometric albedos of dark asteroids, derived from thermal radiometry and polarimetry, differ from each other, as has been long known (Morrison 1977, Zellner *et al.* 1977). This difference occurs at low albedos in the dependence $\log p + k \log h = b$, where p is the geometric albedo, h is the polarization slope, and k and b are constants. No convincing explanation has been offered for this. Figure 3 shows our model dependencies $\log A(\alpha = 5^\circ) + k \log h = b$ for the parameters $r/\lambda = 0.5$, $\xi = 0.4$, and $G = 0.2$ (curve 1), $G = 0.9$ (curve 2). Thus, our albedo is the reflectance at the 5° phase angle, and this definition is used for both experimental and theoretical results. The filled circles present terrestrial samples (Zellner *et al.* 1977), and crosses are experimental data for mixtures of magnesium oxide and soot (Shkuratov and Akimov 1987). Laboratory measurements for mixtures of water-color pigments are also shown (dashed line).

Shkuratov (1980) attempted to interpret the experimentally verified saturation; using the present models this interpretation can be significantly improved. The theoretical curves consist of three major parts. The first high-albedo part, i.e. albedos larger than 10%, is approximately linear, undoubtedly according to the so-called Umov law. The second part, in the albedo range of 2–7%, results from a small contribution of multiple scattering. In the third part, for albedos smaller than 2%, the polarization slope flattens again: this derives from the decreasing amount of second-order scattering causing the negative polarization.

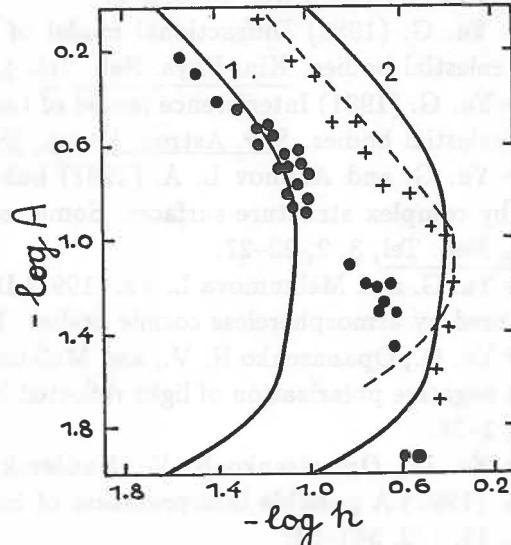


Fig. 3. Experimental and theoretical relations between albedo $A(\alpha = 5^\circ)$ and polarization slope h .

CONCLUSION

Three particular results for asteroids can be stated:

- The observed opposition effect and negative polarization require the existence of micron-scale fine structure in regolith particles. Although such small-scale structure has been widely assumed in the past, it is not predicted by previous theoretical models.

- A sharp and narrow opposition effect (the opposition spike) has recently been observed for some bright asteroids. In contrast, weak or non-existent opposition effects are exhibited by some dark asteroids. Such observations are explained by the coherent backscattering mechanism.
- The difference in radiometric and polarimetric albedos of dark asteroids is caused by the non-linearity of the relationship between geometric albedo and polarization slope.

References

- Hapke B. (1966) An improved lunar theoretical phase function. *Astron. J.*, **71**, 5, 333–339.
- Harris A. W., Young I. W., Contreiras L., Dockweiler T., Belkora L., Salo H., Harris W. D., Bowell E., Poutanen M., Binzel R. P., Tholen D. I., and Wang S. (1989) Phase relations of high-albedo asteroids: the unusual opposition brightening of 44 Nysa and 64 Angelina. *Icarus*, **81**, 356–374.
- Lumme K. and Bowell E. (1981) Radiative transfer in the surfaces of atmosphereless bodies. I. Theory. *Astron. J.*, **86**, 11, 1694–1704.
- Morrison D. (1977) Asteroid sizes and albedos. *Icarus*, **31**, 185–220.
- Muinonen K. (1989) Electromagnetic scattering by two interacting dipoles. Proc. 1989 URSI EM-Theory Symp. (Stockholm), 428–430.
- Muinonen K. (1990a) Ph.D. thesis, University of Helsinki.
- Muinonen K. (1990b) Scattering of light by solar system dust: the coherent backscatter phenomenon. 1990 Proc. Finnish Astron. Soc., 12–15.
- Muinonen K., Sihvola A. H., Lindell I. V., and Lumme K. (1991) Scattering by a small object close to an interface. II. Study of backscattering. *J. Opt. Soc. Am. A*, **8**, 477–482.
- Muinonen K. and Lumme K. (1991) Light scattering by solar system dust: the opposition effect and the reversal of linear polarization. In *IAU Colloquium 126, Origin and Evolution of Dust in the Solar System*, 159–162. Kluwer Academic Press.
- Shkuratov Yu. G. (1980) Albedo of asteroids. *Sov. Astron. J.*, **57**, 6, 1320–1322.
- Shkuratov Yu. G. (1985) On opposition brightness surge and light negative polarization of solid cosmic surfaces. *Astron. Circ.*, **1400**, 3–6.
- Shkuratov Yu. G. (1988) Diffractional model of the brightness surge of light scattered by solid surface of celestial bodies. *Kin. Phys. Neb. Tel.*, **4**, 4, 33–39.
- Shkuratov Yu. G. (1991) Interference model of the negative polarization of light scattered by solid surface of celestial bodies. *Sov. Astron. Vestn.*, **25**, 2, 152–161.
- Shkuratov Yu. G. and Akimov L. A. (1987) Laboratory studies of negative polarization of light scattered by complex structure surfaces. Some consequences for atmosphereless cosmic bodies. I. *Kin. Phys. Neb. Tel.*, **3**, 2, 22–27.
- Shkuratov Yu. G. and Melkunova L. Ya. (1991) Diffractional model of the negative polarization of light scattered by atmosphereless cosmic bodies. *Lunar and Planet. Sci. Conf. XXII*, 1243–1244.
- Shkuratov Yu. G., Opanasenko N. V., and Melkunova L. Ya. (1989) Interference surge of backscattering and negative polarization of light reflected by complex structure surfaces. Preprint 361, IRE AS USSR, 1–26.
- Shkuratov Yu. G., Opanasenko N. V., Basilevsky A. T., Zhukov B. S., Kreslavsky M. A., and Murchie S. (1991) A possible interpretation of bright features on the surface of Phobos. *Planet. Space Sci.*, **39**, 1/2, 341–347.
- Wolff M. (1975) The polarization of light reflected by rough planetary surface. *Appl. Opt.*, **14**, 6, 1395–1404.
- Zellner B., Leake M., Leberte T., Duseaux M., and Dollfus A. (1977) The asteroid albedo scale. I. Laboratory polarimetry of meteorites. Proc. 8th Lunar Sci. Conf., 1091–1110.

ON THE DISTRIBUTION OF MINOR PLANET INCLINATIONS

V.A.Shor, Institute of Theoretical Astronomy, USSR Academy of Sciences, E.I.Yagudina, Institute of Applied Astronomy, USSR Academy of Sciences

Abstract. The distribution of minor planet orbits with inclination to the ecliptic plane and with respect to the Jupiter orbit is studied. Position of the plane considered as the mean plane of the asteroid belt is determined.

Distribution of minor planets with inclination of their orbits to the ecliptic plane has been studied by many authors (see e.g. Chebotarev and Shor, 1978). In the present paper an attempt has been made to repeat some of the previously known results on the basis of essentially greater statistics. The minor planet orbits are taken from the year-book for 1991 (Batrakov, 1990). It contains the osculating elements of 4265 numbered planets.

The characteristic features of the distribution of minor planets with respect to inclination to ecliptic plane are well known. It is characterized by the sharp increase of the number of minor planets as the inclination increases from 0° towards the greater values of inclination and then, having reached the maximum it decreases more or less smoothly. Only rather small number of planets is inclined to the ecliptic plane at more than 30° . It can be said that the minor planet orbits 'tend to avoid' both very large and very small inclinations.

Certainly this distribution is influenced by the observational selection which, in particular leads to the excess of the planets with small inclinations to ecliptic plane among the newly discovered minor planets (Kiang, 1966).

On the other hand, the use of ecliptic plane as the main reference plane for description of the asteroid belt is not entirely justified. It might be expected that some peculiarities of distributions, especially in the domain of small inclinations, manifest themselves more clearly when the Jupiter orbital plane is used as the reference plane instead of ecliptic one. This idea is suggested by the fact that Jupiter exerts the main perturbing action on the majority of minor planets.

Aiming at the verification of this assumption we transformed the ecliptic elements of minor planets into the elements referred to the Jupiter orbital plane. Then we marked the poles of minor planet orbits on Jovicentric celestial sphere of a unit radius and found rectangular coordinates of their projections on Jupiter orbital plane. Fig.1 shows a picture of projections of minor planet poles on the X,Y plane, which coincides with Jupiter orbital plane. The pole of Jupiter orbital plane is situated in the center of the picture. The poles of those minor planets whose inclination to the Jupiter orbital plane is less than 2° are to be found inside the circle.

Just a glance at the picture shows some interesting regularities. The pole of Jupiter orbital plane is located in the center of deserted area. This area is surrounded by the belt of

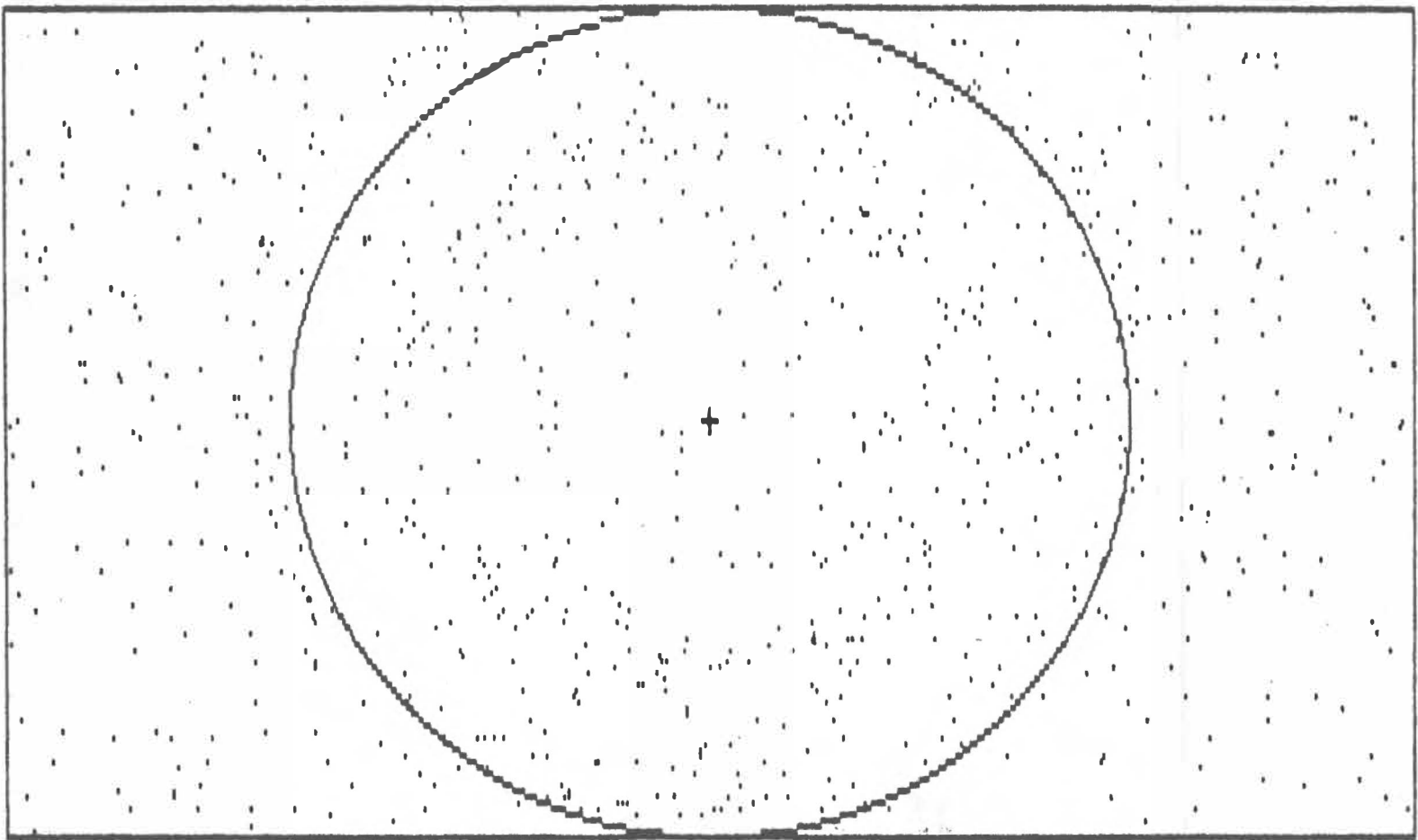


Fig.1. Positions of minor planet poles on Jupiter's orbit plane.
Circle radius is equal to 2° + - pole of Jupiter's plane

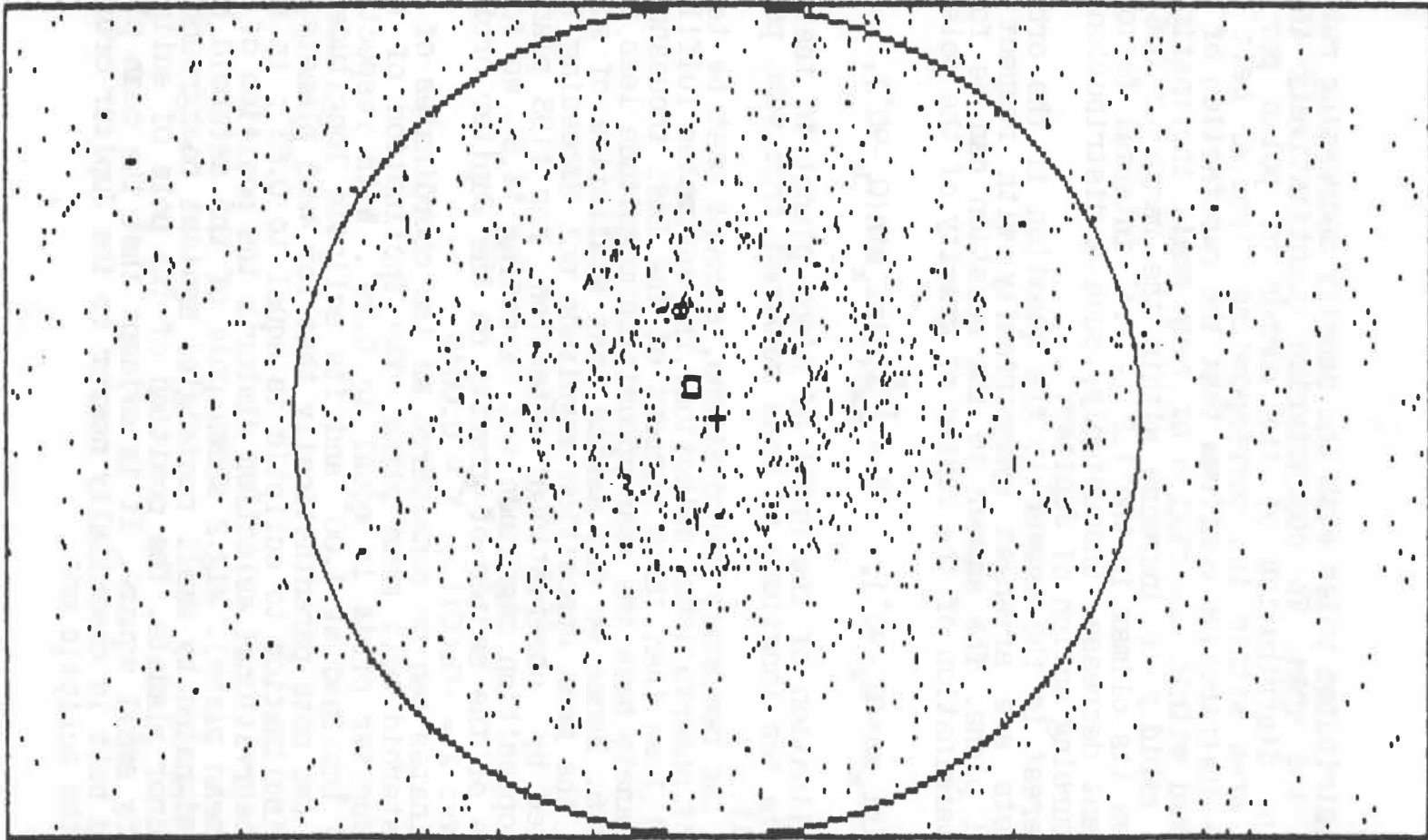


Fig.2. Positions of minor planet poles on Jupiter's orbit plane.

Circle radius is equal to 5°

- + - pole of Jupiter's plane
- - pole of minor planets mean plane
- - pole of ecliptic

more densely distributed poles with the density decreasing rather steady outside the area. To characterize quantitatively these observations the distribution of the number of poles per an arbitrary unit area within the corresponding circular belt was considered. The distribution confirms that the rarefaction of the poles is observed within the region of very small inclinations. Density begins rapidly to increase within the range of $0.6^\circ - 1.2^\circ$ and reaches its climax in the $1.2^\circ - 1.4^\circ$ interval followed by its subsequent decrease. Undoubtedly, such a distribution is due to the perturbing action of Jupiter.

Of some interest is the answer to the question if the orbits of minor planets are arranged symmetrically with respect to Jupiter orbital plane. The answer to the question can be found through the determination of the center of gravity of the poles:

$$X = \frac{1}{n} \sum_{nk=1}^n \sin \iota_k \cos(\Omega_k - 90^\circ), \quad Y = \frac{1}{n} \sum_{nk=1}^n \sin \iota_k \sin(\Omega_k - 90^\circ),$$

where ι is inclination of the orbit of minor planet to that of Jupiter and Ω is the longitude of node reckoned from some point of Jupiter orbit.

When making the necessary calculations, account must be taken of the effect of observational selection. The estimates fulfilled by us show that less than three percent of the last thousand of the numbered planets have the mean opposition magnitude less than or equal to 14.5. Hence we can assume that statistics of minor planets having the mean opposition magnitude not exceeding 14.5 is not distorted by observational selection. For 1193 planets with the mean opposition magnitude not exceeding 14.5 we found the coordinates of the center of gravity on the Jupiter orbital plane as follows: $X = -0.0011$, $Y = 0.0049$.

These coordinates can be considered as the coordinates of the pole of the asteroid belt mean plane. The inclination of this plane to the Jupiter orbit is equal to 0.29° . With respect to ecliptic it is inclined at 1.00° and its ecliptic longitude is equal to 96.4° (we note parenthetically that for 4265 planets the mean value of inclination to ecliptic is equal to 0.63° ; in such a manner the observational selection distorts the position of the asteroid belt mean plane). Fig.2 shows pole of the asteroid belt mean plane (designated by small rectangle) against background of the poles of minor planets. The position of the pole of ecliptic is designated by small square. It is evident that the mean plane of the asteroid belt is essentially nearer to the Jupiter orbital plane than to the ecliptic one.

References.

- Chebotarev G.A., Shor V.A. (1978) The structure of the asteroid belt. Fundamentals of Cosmic Physics, 3, 87-138.
 Batrakov Yu.V., ed. (1990) Ephemerides of Minor Planets for 1991. 'Nauka', Leningrad. 448 pp.
 Kiang T. 1966. Bias-free statistics of orbital elements of asteroids. Icarus, 5, 437-449.

DIURNAL VARIATION OF OVERDENSE METEOR ECHO DURATION AND OZONE

Miloš Šimek, Astronomical Institute of the Czechoslovak Academy of Sciences, 251 65 Ondřejov, Czechoslovakia.

Abstract

The diurnal variation of the median duration of overdense sporadic radar meteor echoes is examined. The meteors recorded in August, December and January by the Ondřejov meteor radar during the period 1958-1990 have been used for the analysis. A maximum median echo duration 1-3 hours after the time of local sunrise in the meteor region confirms the already known sunrise effect. Minimum echo duration occurring at the time of sunset seems to be the most important point of diurnal variation of the echo duration, when ozone is no longer dissociated by solar UV radiation. The effect of diurnal changes of the echo duration should be considered when the mass distribution of meteor showers is analysed.

1. Introduction

An enhancement of the proportion of long-duration radio echoes from Quadrantid meteors recorded after sunrise was found by Hughes and Baggaley (1972). The term "sunrise effect" was introduced by Nicholson and Poole (1974) from the analysis of Quadrantid shower echo rates but similar changes during non-shower period were not found.

McIntosh and Hajduk (1977) examined the occurrence of long-duration sporadic meteor echoes recorded by the Ottawa patrol radar in the period 1963-1967. They demonstrated an increase in the relative proportion of long-duration echoes during sunlit periods over comparable rates in the dark hours. The authors discussed the mechanism for effecting echo duration changes and noted that ozone concentration changes could play a significant role.

The influence of ozone to the duration of overdense radio meteor echo was described by Jones et al. (1990). This work is based on the theory of Baggaley and Cummack (1974) that the most effective process of free electron loss in a meteor trail results from reactions such as



where M^+ is the meteoric ion. Jones et al. pointed out the lack of a formula for determining the mass distribution index of meteoroids from the observationally-obtained duration distribution of overdense meteor echoes resulting from the fact that the concentration of O_3 versus altitude and its diurnal and seasonal variation are complicated and not well known.

It is possible, however, to examine the diurnal variation of median echo duration, which could reflect the influence of atmospheric chemical processes on the duration distribution.

2. Median echo duration

The number of echoes, N_C , with durations T or greater, is given in integral form as

$$(1) \quad \log N_C = -3/4 (s - 1) \log T + \text{const.},$$

where s is a distributive constant which is proportional to the slope of $\log N_C$ vs $\log T$ plot. Assuming s to be a function of T , McIntosh and Šimek (1974) derived a modification of Eq (1) in the form

$$(2) \quad \log N_C = -3/4 [s_0 - 1 + s_1(\log T) + s_2(\log T)^2] \log T + \text{const.},$$

where $s = s_0 + s_1 \log T + s_2 (\log T)^2$.

Providing s is a function of T one can associate values of s with the median and end points of the duration interval. Median duration \bar{T} corresponding with median value \bar{s} is then expressed as

$$(3) \log \bar{T} = - \frac{4 \log [0.5(T_A^{-3(sA-1)/4} + T_B^{-3(sB-1)/4})]}{3(\bar{s} - 1)}$$

where subscripts A and B designate values at the end points. If the duration interval is open, i.e. a count down to a limiting duration $T_A = 1$ s, then Eq (3) is modified as

$$(4) \log \bar{T} = - \frac{4 \log 2}{3(\bar{s} - 1)}$$

Whole range of echo durations $0.4 \leq T \leq 50$ s was divided into 16 classes to determine s and \bar{s} values. Eqs (2) and (5) were combined in an iterative process to calculate the final median duration \bar{T} .

Two periods of sporadic activity were examined. Due to diurnal echo rate variation and a lower number of observed periods between 15^h and 20^h LT, the number of echoes available was very low, and, though the data were collected over many years, it was necessary to combine December and January observations into one set of data. August sporadics represent the second investigated period. While the data from the December-January months consist of 77739 echoes (maximum number of 8626 at 3^h LT, minimum number of 206 at 19^h LT), the August period contains 47888 echoes (maximum of 3233 at 0^h LT, minimum of 654 at 18^h LT). Note that total observing time in particular hours is not equal.

3. Results and discussion

Values of \bar{T} are plotted in Fig. 1. Both curves show diurnal variation with significant comparable features.

- 1) The maximum value of \bar{T} occurs 1-3 hours after the time of local sunrise at a height of 93 km, an effect similar to that determined by McIntosh and Hajduk (1977).
- 2) Even when the August curve is so flat from 17^h to 21^h that there seems to be no clear minimum value of \bar{T} , the lowest point on the \bar{T} curve leads to the suggestion that the time of sunset is an important turning point in both examined periods.
- 3) Median echo durations are characterized by a slow rate of increase during the first hours of darkness-up to midnight.
- 4) A more rapid increase in the proportion of long-duration echoes starts about 5-6 hours before the time of the sunrise effect.
- 5) The decrease of \bar{T} from maximum to minimum takes place in about 8 hours. This period corresponds with daylight in December-January, while in the August results it extends only slightly past noon, with the remaining daylight hours showing only a slow variation and minor fluctuation.
- 6) The pronounced low value of \bar{T} at 6^h in August coincides with maximum elevation of the Apex of the Earth's way. A similar effect is possible, but not so definitive, in the December-January data when the Apex is lower.
- 7) Absolute values of \bar{T} are similar on both curves within the intervals 9^h - 12^h and 15^h - 19^h.

There are basically two different features of both curves in

Fig. 1 which should be considered:

a) the striking difference in the absolute values of \bar{T} at the time of the sunrise effect between the August data and the December-January data. \bar{T} is higher for the former by 0.73 ± 0.12 s than for the latter. Minimum \bar{T} values at the time of

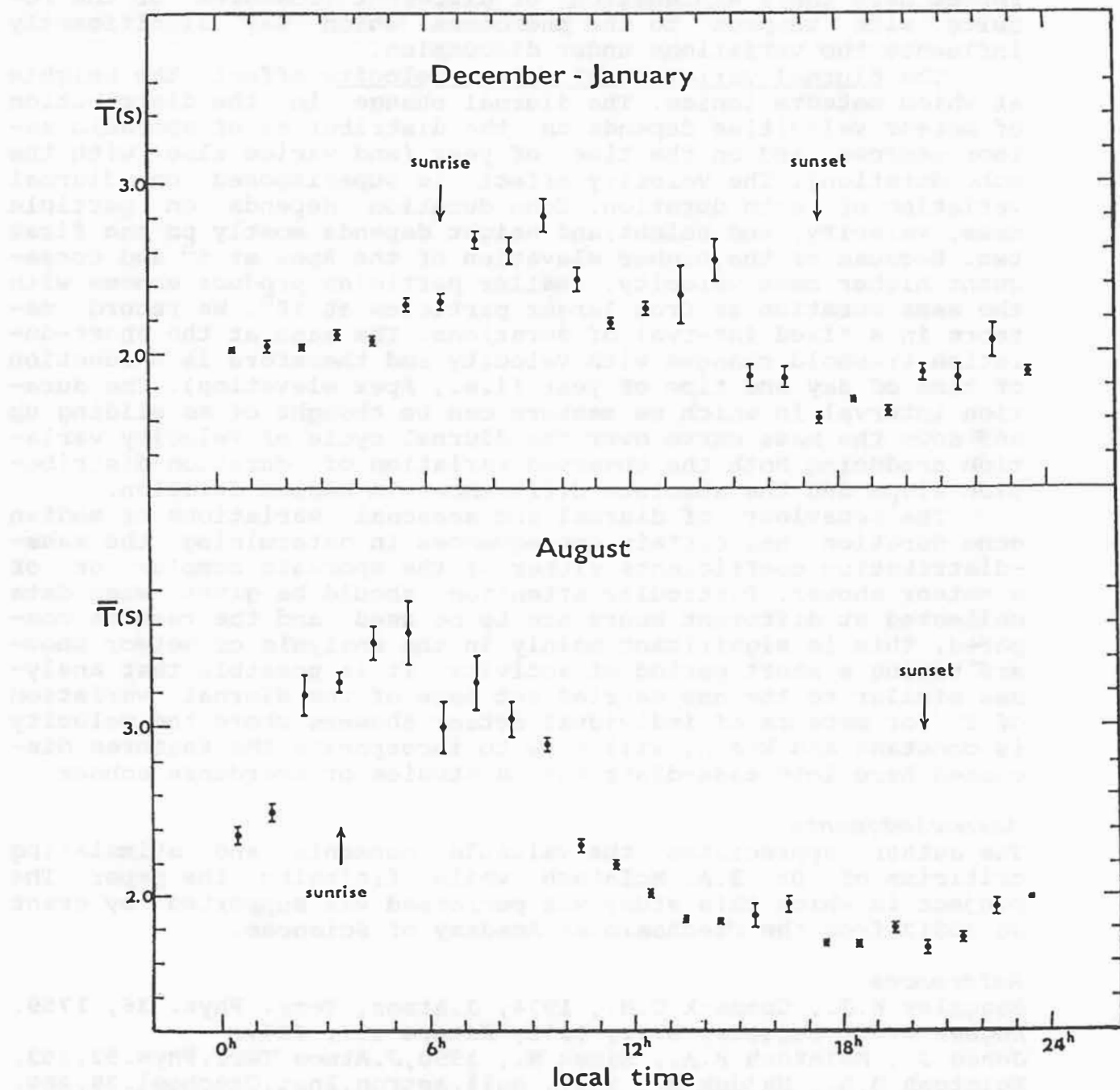


Fig.1. Median duration \bar{T} of sporadic meteor echoes with durations $T \geq 1$ s

sunset are in both periods practically the same;
 b) the secondary maximum of T in the December/January data between 12^h and 15^h is unusual and not understood.

McIntosh and Hajduk (1977) analyzed the rates of long-duration echoes recorded by the Ottawa patrol radar for the period 1963-1967. The results of their study and the work presented here are consistent and mutually confirming. We will not repeat here their explanation of different features of the results with respect to the phenomena which may significantly influence the variations under discussion.

The diurnal variation of meteor velocity affects the heights at which meteors ionize. The diurnal change in the distribution of meteor velocities depends on the distribution of sporadic meteor sources and on the time of year (and varies also with the echo duration). The velocity effect is superimposed on diurnal variation of echo duration. Echo duration depends on particle mass, velocity, and height; and height depends mostly on the first two. Because of the higher elevation of the Apex at 6^h and consequent higher mean velocity, smaller particles produce echoes with the same duration as from larger particles at 18^h. We record meteors in a fixed interval of durations. The mass at the short-duration threshold changes with velocity and therefore is a function of time of day and time of year (i.e., Apex elevation). The duration interval in which we measure can be thought of as sliding up and down the mass curve over the diurnal cycle of velocity variation producing both the observed variation of duration-distribution slope and the absolute differences in median duration.

The behaviour of diurnal and seasonal variations of median echo duration has certain consequences in determining the mass-distribution coefficients either of the sporadic complex or of a meteor shower. Particular attention should be given when data collected at different hours are to be used and the results compared. This is significant mainly in the analysis of meteor showers having a short period of activity. It is possible that analyses similar to the one carried out here of the diurnal variation of T for meteors of individual meteor showers where the velocity is constant and known, will show to incorporate the features discussed here into mass-distribution studies of overdense echoes.

Acknowledgments

The author appreciates the valuable comments and stimulating criticism of Dr. B.A. McIntosh while finishing the paper. The project in which this study was performed was supported by grant No 30312 from the Czechoslovak Academy of Sciences.

References

- Baggaley W.J., Cummack C.H., 1974, J. Atmos. Terr. Phys. 36, 1759.
- Hughes D.W., Baggaley W.J., 1972, Nature 237, 224.
- Jones J., McIntosh B.A., Šimek M., 1990, J. Atmos. Terr. Phys. 52, 253.
- McIntosh B.A., Hajduk A., 1977, Bull. Astron. Inst. Czechosl. 28, 280.
- McIntosh B.A., Šimek M., 1974, Bull. Astron. Inst. Czechosl. 25, 180.
- Nicholson T.F., Poole L.M.G., 1974, Planet. Space Sci. 22, 1669.

Melting, Vaporization, and Energy Partitioning for Impacts on Asteroidal and Planetary Objects

CATHERINE L. SMITHER AND THOMAS J. AHRENS

*Lindhurst Laboratory of Experimental Geophysics,
Seismological Laboratory 252-21, California Institute of Technology*

A three-dimensional smoothed particle hydrodynamics code was used to model normal and oblique impacts of silicate projectiles on asteroidal and planetary bodies. The energy of the system, initially in the kinetic energy of the impactor, is partitioned after impact into internal and kinetic energy of the impactor and the target body. These simulations show that, unlike the case of impacts onto a half-space, a significant amount of energy remains in the kinetic energy of the impacting body, as parts of it travel past the main planet and escape the system. This effect is greater for more oblique impacts, and for impacts onto the small planets. Melting and vaporization of both bodies were also examined. The amount of the target body melted was much greater in the case of smaller targets than for an impact of a similar scale on a larger body.

Smoothed particle hydrodynamics (SPH) [Monaghan & Gingold 1983, Benz et al 1986] is a technique which allows fully three-dimensional modeling of impact processes. In this study, we have used an SPH code developed at Caltech to examine the effects of impacts of silicate projectiles on planetary and asteroidal bodies to determine the extent of melting and vaporization of the impact, as well as the partitioning of energy in the system. The objects are modeled by a collection of particles, each representing a mass distribution in space, described as a function of a characteristic length scale. For each particle, the position, velocity, density, internal energy, pressure and bulk sound speed are calculated at each time step in the simulation. The system is self-gravitating, and energy and momentum are conserved throughout the run. The material properties are determined by an equation of state. For these simulations, we used the Tillotson equation of state [Tillotson 1962] for anorthosite [Ahrens & O'Keefe 1977a] for both the targets and the impactors.

We modeled impacts on two different target sizes: 1700 and 6400 km in radius, corresponding approximately to the size of the moon and the earth, respectively. Each target was hit with impactors of 40% and 60% of its radius (6% and 22% of its mass) at speeds of 10 and 20 km/s. In order to investigate the effects of oblique impacts, we varied the angle of incidence of the collision from 0° to 90°, where this angle is measured from the axis of the plane parallel to the impact trajectory to the line from the center of the target to the center of the impactor at the time of impact. Thus a normal impact corresponds to an angle of 0°, and a 90° impact is a glancing blow.

Initially, the energy of the system resides entirely in the kinetic energy of the impactor. Upon impact, some of the energy goes into ejection of material from the target, and some into heating (internal energy) of both bodies. Studies of impact onto a half-space [e.g. O'Keefe & Ahrens 1977a] show that little to none of the total energy remains in the kinetic energy of the impactor after the impact. This is as expected, since, for an impact onto a planet of effectively infinite radius, very little of the impactor material will be able to get past the target. However, for our cases of impacts on finite-sized bodies, we find that a significant portion of the total energy of the system remains in the kinetic energy of the impactor. This is especially pronounced in the more oblique, and higher velocity, collisions. Figure 1 shows the partitioning of energy for two cases of impacts on the 1700 km radius target body. The plot on the left shows the results of a 10 km/s normal impact of the smaller (40%) radius impactor. The energy is plotted normalized to the total initial energy of the system, and the time scale represents a normalized time, τ , such that $\tau = tU/r$, where U is the impact velocity, r the radius of the impactor, and t is the time in seconds. Most of the impactor is accreted to the target, so only a small fraction of the impactor material has any appreciable kinetic energy. Of the total system energy, 90% is in the internal energy of the target and the impactor. The plot on the right of figure 1 shows the results of an oblique (50°), 20 km/s collision of the larger (60%) impactor with the 1700 km target body. In this case, much of the impactor escapes the main object's gravity, and travels

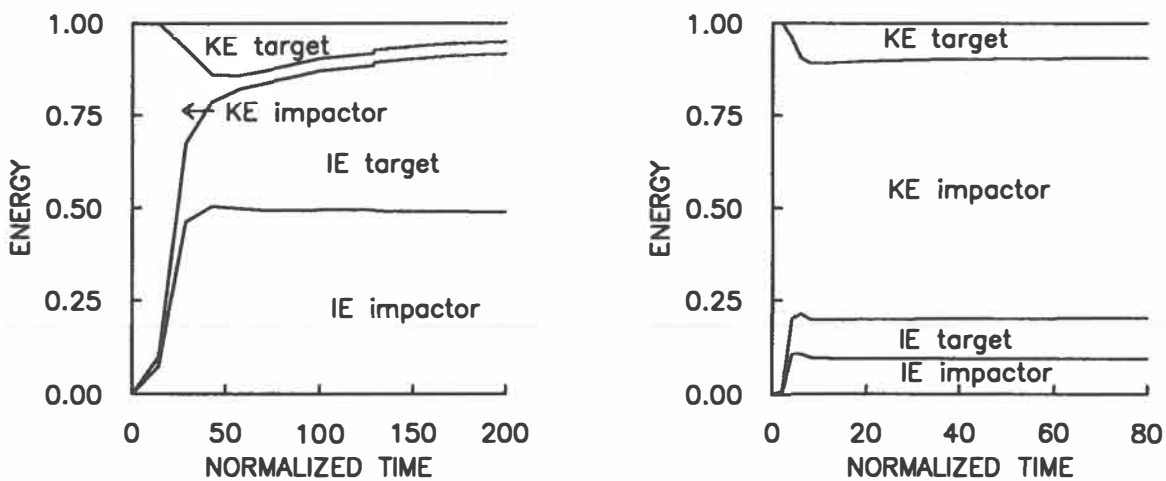


Figure 1: Partitioning of energy for two cases of impact on the 1700 km radius body. The figure on the left shows the results of a normal impact at 10 km/s with the smaller (40%) impactor. The figure on the right shows the case of an oblique (50°) collision with the larger impactor. Much of the energy of the system remains in the kinetic energy of the impactor in this case.

past it; thus, a significant amount (70%) of the total energy remains in the kinetic energy of this material. The corresponding cases for the larger target show that, in the case of a normal impact, 95% of the system energy is converted to internal energy; in the 50° impact at 20 km/s, 45% of the total energy remains in the kinetic energy of the impactor particles.

The impact causes melting of both the target and the impactor. For all but the most oblique collisions, all of the impactor is shocked to a state sufficient to cause complete melting. The smaller (1700 km) targets show much more melting than is seen in similar-sized impacts onto the 6400 km targets, as is shown in figure 2. The plots show the amount of mass of the target shocked to internal energies high enough to cause complete melting, calculated as the number of projectile masses melted, as a function of the impact angle. Normal impacts, which transfer more kinetic energy to the target, melt much more material than the oblique impacts do. The two plots show the melting of the 6400 km target (left) and the 1700 km target. The lines on each graph are labeled to identify the impact velocity in km/s and the relative size of the impactor and target (in percent). For normal and low-angle impacts, the smaller impactor melts less of the target, both in terms of the number of projectile masses and the total mass melted. The difference between the different cases is much less pronounced for more oblique impacts. Also shown in figure 2 is the amount of mass that was vaporized after the impact. The impacts onto the 6400 km target produced much more vaporization (.1 to .25 projectile masses for the 20 km/s, 40% impactor, .3 to .4 projectile masses for the 20 km/s, 60% impactor) than those onto the 1700 km targets (.1 to .2 projectile masses for the 20 km/s, 60% impactors).

The results shown above indicate that target size and impact parameter have a considerable effect on the amount of melting and vaporization and on the partitioning of energy. We also studied the formation of ejecta, material thrown off the target body at velocities greater than the escape velocity of the target, and the amount of impactor material accreted to the target. For all cases of impact onto the 6400 km body, very little material was ejected; only the 20 km/s collisions with the larger impactor were sufficient to propel material away from the target at more than the escape velocity, and the amount ejected ranged from 3 to 6% of the total mass of the target. The smaller targets lost much more mass. The larger and faster impacts at low angles were sufficient to cause catastrophic breakup of the target, where the largest fragment remaining has less than half the original mass of the target. The 10 km/s impacts with the larger impactor did not cause catastrophic breakup, but did cause 40% of the target to reach escape velocity in the case of normal impact, and 8% to escape in the 90° (glancing) impact. As was the case with the 6400 km target, collisions with the 40% impactor did not generate large quantities of ejecta. Normal impacts at 20 km/s caused 12%

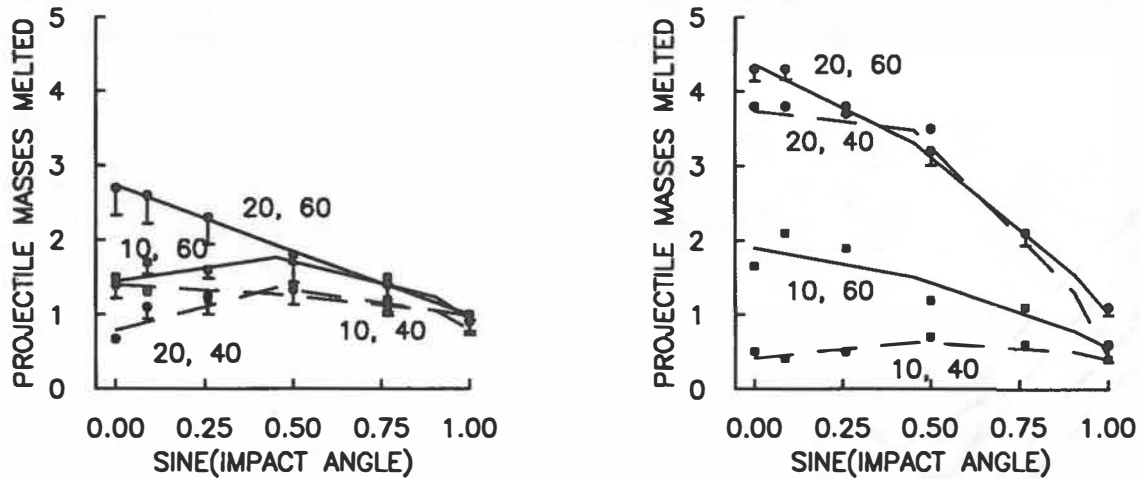


Figure 2: Melting of material on 6400 km (left) and 1700 km targets for the impacts described in the texts. The bars under some of the points show the amount of material vaporized. The smaller impacts generally show little to no vaporization. The four cases for each target are marked with two numbers, the first of which denotes the impact velocity in km/s, the second the relative size of the impactor.

of the target material to escape; 10 km/s impacts caused only 1 to 2% to escape.

For the larger targets, much of the impact mass was accreted. Except for the most oblique collisions, all of the smaller impactor remained with the target after impact. The 6400 km target, when hit by the 60% impactor at 10 km/s (a velocity lower than the escape velocity at its surface), caused 90 to 100% of the impactor material to be accreted. The only material from the impactor to escape was that which was on the side opposite the point of impact in the oblique cases. The higher velocity impacts accreted between 70 (normal impact) and 25% (90° impact) of the impactor material. The 1700 km targets, due to the lower escape velocity relative to the impact velocity, accreted much less of the impactor.

Figure 3 compares the SPH ejecta results with the two-dimensional normal-impact models of O'Keefe and Ahrens [1977b]. The curves are modified from their figure 2a, and show the amount of material, in terms of impactor masses, that reached escape velocity after impacts at 7.5, 15, 30, and 45 km/s. Our results for the two escape velocities 2.4 and 11 km/s are plotted as well. We plotted only the values from the normal and the most oblique (90°) impacts, as representative of the range of values. Only the 60% impactors are plotted, since the 40% impacts produced no measurable ejecta from the larger targets. (For this set of calculations, we cannot resolve material smaller than .018 projectile masses in the 40% case, and .005 projectile masses in the 60% case.) Our simulations of impacts of the 60% impactor produced more ejecta than predicted by the O'Keefe and Ahrens results. The normal impact onto our smaller target produced as much ejecta as would have been produced by an impact of twice the velocity onto the half-space. The ejecta predicted for the larger targets, while not as great in terms of total projectile masses as that of the smaller targets, was still much more than predicted by the half-space model. For clarity on this figure, we did not show the values for the amount of ejecta produced by the collision of the 40% impactor onto the smaller target. Normal impact caused .067 projectile masses to be ejected after the 10 km/s impact, and 2.0 projectile masses in the 20 km/s case. The corresponding values for the most oblique (90°) impact are .083 and .42 projectile masses for 10 and 20 km/s, respectively. The smaller normal impacts yield ejecta output much closer to that predicted by O'Keefe and Ahrens.

Our calculations show that the size of the target and the relative sizes of the target and the impactor are important parameters in the study of large impacts on planetary bodies. Impacts at the same specific energy (kinetic energy per unit mass) have significantly different effects on targets of different sizes. Future work will investigate this phenomenon in more detail by considering impacts onto other sizes of targets, at different velocities, for the same range of impact angles.

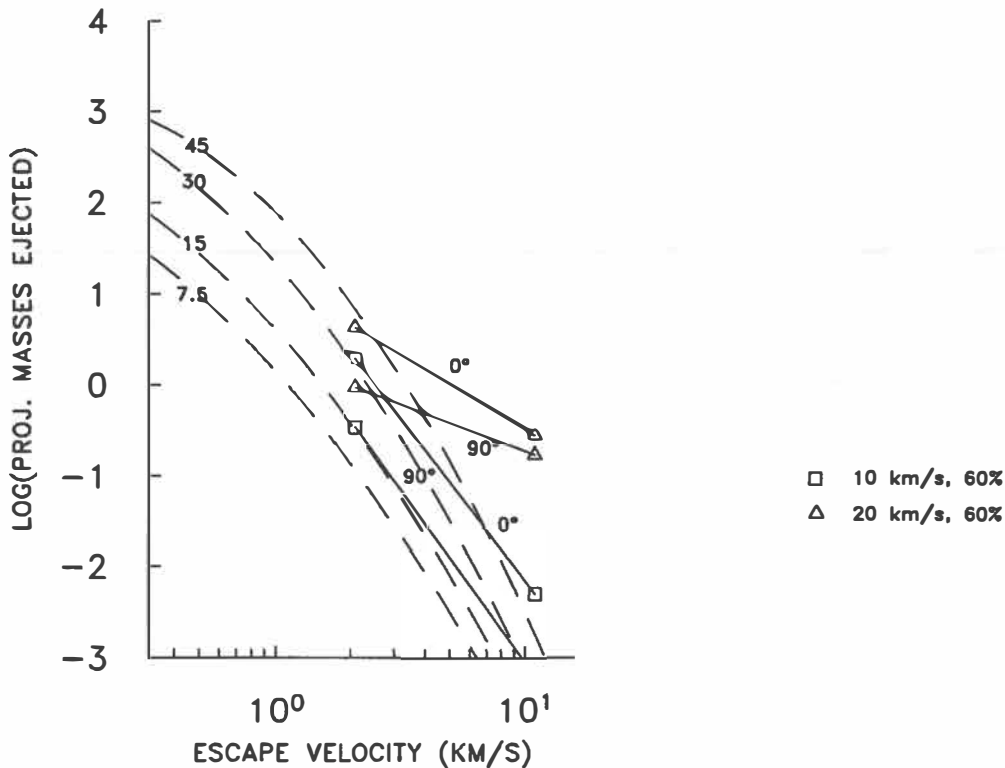


Figure 3: Mass of material ejected from the target, measured as multiples of the projectile mass. The dashed lines are modified from figure 2a of O'Keefe and Ahrens [1977b], and show the amount of ejecta produced by normal impacts at 7.5, 15, 30, and 45 km/s. The points plotted are from this study, and show the amount of ejecta from normal and glancing impacts of the larger projectile.

Acknowledgements. This research was supported by NASA. Contribution number 5074 of the Division of Geological and Planetary Sciences, California Institute of Technology.

REFERENCES

- Ahrens, T. J. and O'Keefe, J. D. Equations of state and impact-induced shock-wave attenuation on the moon, in *Impact and Explosion Cratering* 639-656 Pergamon Press, New York (1977).
- Benz, W. Slattery, W. L. and Cameron A. G. W. The origin of the moon and the single-impact hypothesis I, *Icarus* **66**, 515-535 (1986).
- Monaghan J. J. and Gingold R. A. Shock simulation by the particle method SPH, *J. Comput. Phys.* **52**, 374-389 (1983).
- O'Keefe J. D. and Ahrens T. J. Impact-induced energy partitioning, melting, and vaporization on terrestrial planets, *Proc. Lunar Sci. Conf. 8th*, 3357-3374 (1977a).
- O'Keefe J. D. and Ahrens T. J. Meteorite impact eject: Dependence of mass and energy lost on planetary escape velocity, *Science*, 1249-1251 (1977b).
- Tillotson J. H. Metallic equations of state for hypervelocity impact *General Atomic Report GA 3216* 139 pp. (1962).

3-D Orbital Evolution Model of Outer Asteroid Belt

Nina A. Solovaya¹, Igor A. Gerasimov¹, and Eduard M. Pittich²

¹Celestial Mechanics Department, Sternberg State Astronomical Institute
 119 889 Moscow, Russia

²Astronomical Institute, Slovak Academy of Sciences
 842 28 Bratislava, Czechoslovakia

The evolution of minor planets in the outer part of the asteroid belt is considered. In the framework of the semi-averaged elliptic restricted three-dimensional three-body model, the boundary of regions of the Hill's stability is found. As was shown in our work (Gerasimov and Solovaya, 1989) the Jacobian integral exists.

The equations of the motion in the rotating coordinate system have the form:

$$\begin{aligned}\ddot{\xi} - 2n\dot{\eta} &= [U'_\xi] \\ \ddot{\eta} + 2n\dot{\xi} &= [U'_\eta] \\ \ddot{\zeta} &= [U'_\zeta]\end{aligned}\tag{1}$$

$$[U] = \frac{n^2}{2}(\xi^2 + \eta^2) + \frac{k^2 m_1}{2\pi} \int_0^{2\pi} \frac{n}{r_1} dt + \frac{k^2 m_2}{2\pi} \int_0^{2\pi} \frac{n}{r_2} dt,\tag{2}$$

where

$$\frac{n dt}{2\pi} = \frac{dm_1}{m_1} = \frac{dm_2}{m_2}.$$

The Jacobian integral is

$$\frac{1}{2}(\dot{\xi}^2 + \dot{\eta}^2 + \dot{\zeta}^2) = [U] - C.$$

After averaging, the Jacobian integral in the Sun-centered siderical coordinates will have the following form:

$$C = \left(\frac{1}{2a} + \sqrt{\rho} \cos i \right) + \frac{1}{2} \mu^2 + \mu \left(\frac{2K(\kappa_2)}{\pi\nu} - x \right)\tag{3}$$

$$\nu^2 = (\rho^2 + 3\alpha^2)^2, \quad \alpha = (1 - \mu)e_j$$

$$x = R \cos \Theta, \quad \cos \Theta = \cos b \cos(l - l_j)$$

$$\cos \Theta_\pi = \cos \omega \cos l_{j\pi} + \sin \omega \sin l_{j\pi} \cos i.\tag{4}$$

We use a notation similar to the paper Gerasimov and Solovaya (1989), where R is the Sun-asteroid distance, ρ is the Jupiter-asteroid distance, Θ is the angle Jupiter-Sun-asteroid, μ is the ratio of Jupiter's mass to the sum of the masses of Sun and Jupiter, m_1 and m_2 are stationary masses on the rotating axes, e_j is the eccentricity of Jupiter's orbit, l and b are the longitude and latitude of an asteroid, l_j is the longitude of Jupiter, a, e, i and ω are the osculating elements

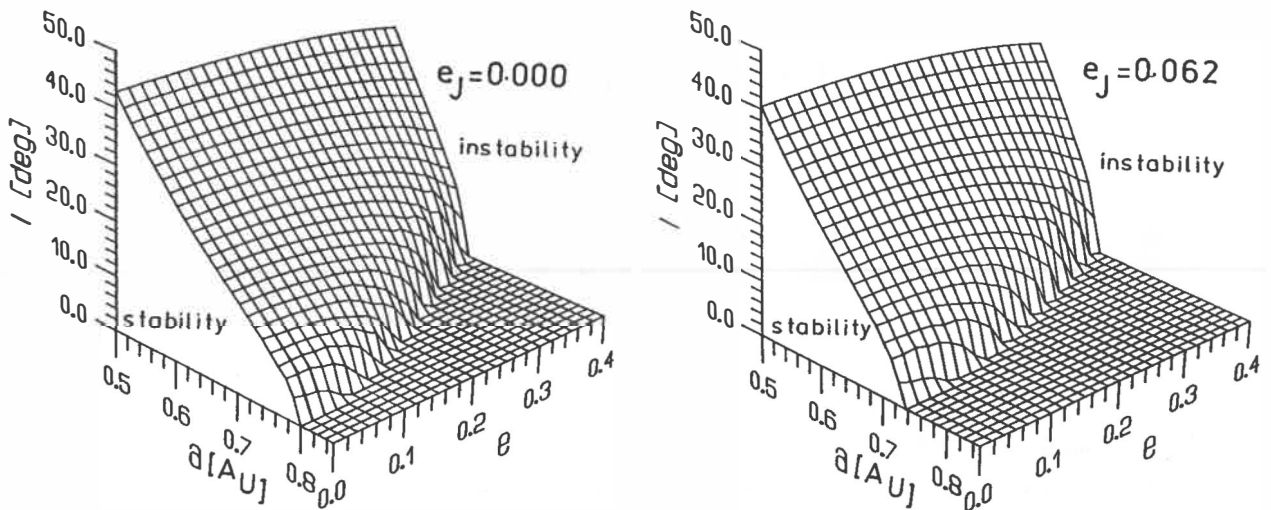


Figure 1. The regions of stability and instability of the motion.

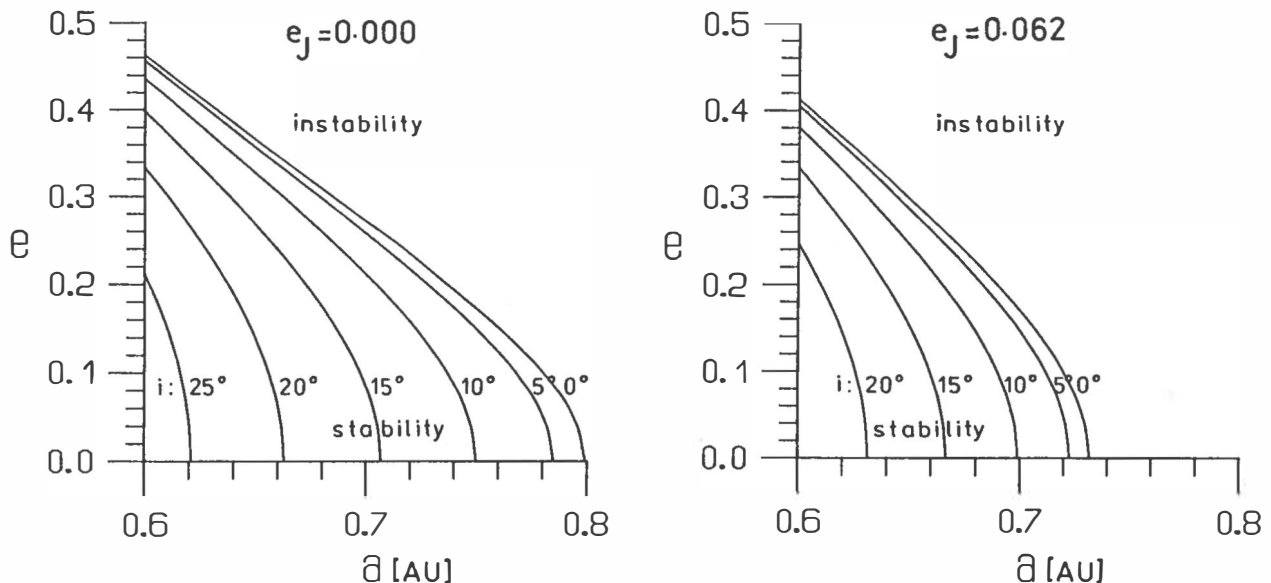


Figure 2. The regions of stability and instability of the motion projected to the (a,e) plane.

of an asteroid, and $K(\kappa_2)$ is the elliptic integral. When $e_J = 0$ then $K(\kappa_2) = \pi/2$. In our computation $\mu = 0.0009538$. We obtain the boundary of regions of possible stable motion from the equation (3) with a fixed value of C and changing elements of fictitious asteroids in the limits $0 \leq e \leq 0.4$ and $0^\circ \leq i \leq 40^\circ$.

For $e_J = 0$, the value of C is equal 1.51938 for the interior point L , for $e_J = 0.062$, $C = 1.538$, respectively. We decided to use the equation (3) for a model, in which the heliocentric elongation of an asteroid from Jupiter is equal 180° . The regions of the Hill's stability and instability are shown for the three-dimensional case in Figure 1. On the (a,e) plane these regions are plotted in Figure 2.

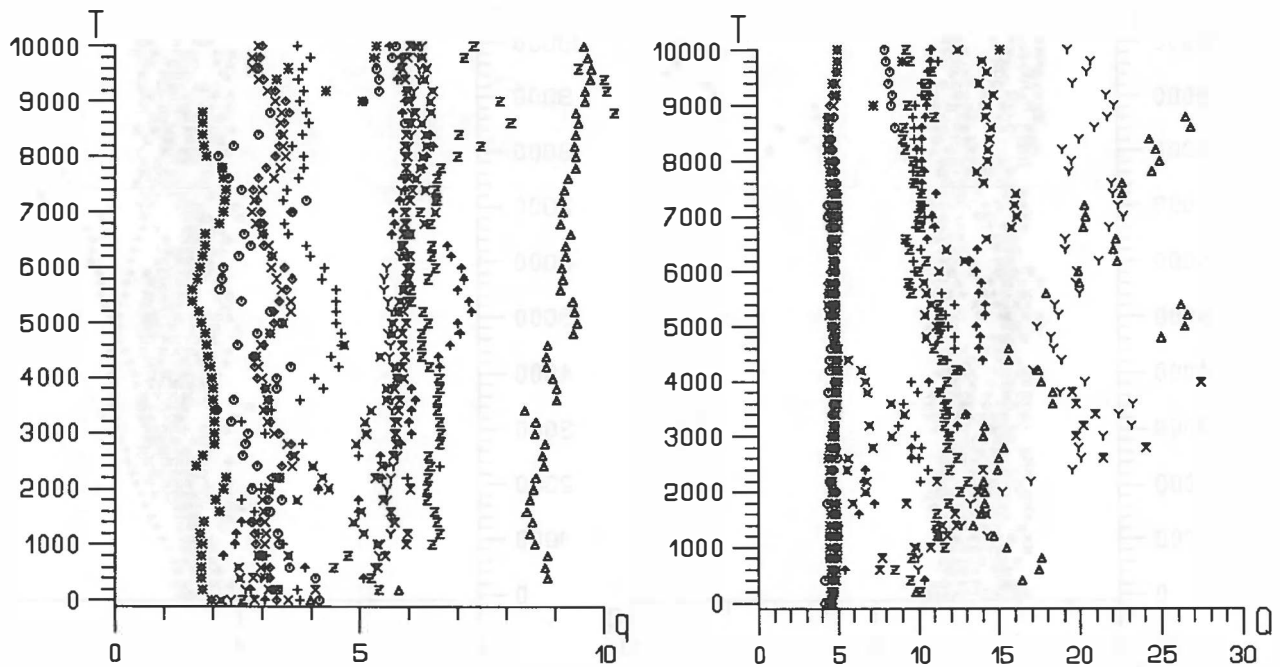


Figure 3. The evolution of the perihelion distance q [AU] and the aphelion distance Q [AU] of model asteroids within the period of 10 000 years for the first variant of e_j and the commencing asteroid inclination $i = 0^\circ$. Asteroids: \odot — 0.00 (the eccentricity), Δ — 0.04, $+$ — 0.08, \times — 0.12, \diamond — 0.16, \uparrow — 0.20, \square — 0.24, \swarrow — 0.28, Y — 0.32, \blacktriangleleft — 0.36, $*$ — 0.40.

In the outer part of the asteroid belt Hill's stable asteroid orbits cannot exist with high inclinations. Among real asteroids of the outer asteroidal belt we found only a few asteroids from Ephemerides of Minor Planets for 1991 (Batrakov, 1990), which were above the surface represented by Figure 1. They are asteroid 153 Hilda ($a = 0.766, e = 0.145, i = 7.85^\circ$), asteroid 361 Bononia ($a = 0.757, e = 0.125, i = 12^\circ.67$), asteroid 1212 Francette ($a = 0.760, e = 0.110, i = 7^\circ.58$), and asteroid 1529 Oterma ($a = 0.769, e = 0.190, i = 9^\circ.03$). According to Milani and Nobili (1985) and Schubart (1991) asteroids may exist within the outer asteroid belt if there are librations of the argument of perihelion. Then their aphelions will always remain far from Jupiter. Numerical investigations in the framework of the restricted three-body problem have been developed by many authors. They show that asteroids will be ejected by Jupiter in only a few thousand years, with the exception of the stable librators.

We took a dynamic model of the solar system, consisting of six major planets and eleven massless fictitious asteroids located at the similar to the four asteroids as mentioned above. We traced the orbital evolution of these asteroids using the numerical integration program with the integrator RA15 (Everhart, 1985). The input data a, e and i were taken from the equation (3) for the eccentricity of Jupiter $e_j = 0$ — the first variant, and $e_j = 0.062$ — the second variant. The starting value of the argument of perihelion was selected from the equation (4) at $\Theta = 180^\circ$. The starting epoch of the numerical integration is March 25, 1991 UT. The results obtained by the numerical integration for the groups of asteroids with started values of i equal 0° and 10° and for the same starting values of a and e are plotted in Figures 3–4.

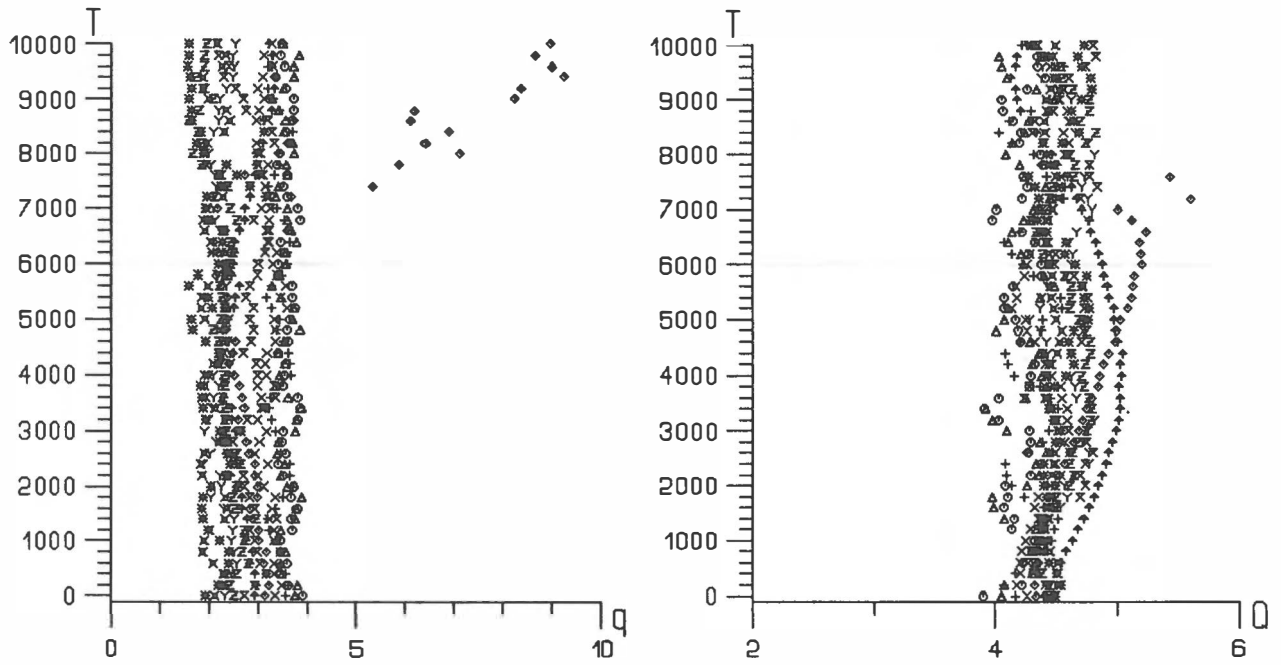


Figure 4. The evolution of the perihelion distance q [AU] and the aphelion distance Q [AU] of model asteroids within the period of 10 000 years for the first variant of e_j and the commencing asteroid inclination $i = 10^\circ$. Asteroids: \odot — 0.00 (the eccentricity), Δ — 0.04, $+$ — 0.08, \times — 0.12, \diamond — 0.16, \uparrow — 0.20, \boxtimes — 0.24, \geq — 0.28, Y — 0.32, \bowtie — 0.36, \ast — 0.40.

Asteroids with $i = 0^\circ$ are ejected to Saturn after close encounters with Jupiter. Asteroids having the inclination $\sim 10\text{--}20^\circ$ and the same commencing values of a and e as of the previous case are practically all stable. We see, that the inclination of orbits of asteroids from the outer belt has the same role in the three-dimensional model as the libration of the argument of perihelion in the two-dimensional model. When the inclinations of asteroids are $\sim 10\text{--}20^\circ$, aphelions of their orbits will always remain far from Jupiter.

References

- Batrakov Yu. V., ed. (1990) *Ephemerides of minor planets for 1991*, Nauka, Leningrad, 477 pp.
 Everhart E. (1985) An efficient integrator that used Gauss–Radau spacing. In *Dynamics of comets: their origin and evolution* (A. Carusi, G. B. Valsecchi, eds.), pp. 185–202. D. Reidel, Dordrecht.
 Gerasimov I. A. and Solovaya N. A. (1989) Evolution of the resonant group of minor planets of the outer part of the asteroidal belt. In *Asteroids Comets Meteors III*. (C.-I. Lagerkvist, H. Rickman, B. A. Lindblad, and M. Lindgren, eds.), pp. 91–94. Uppsala University, Uppsala.
 Milani A. and Nobili A. M. (1985) The depletion of the outer asteroid belt. *Astron. Astrophys.* **144**, 2, 261–274.
 Schubart J. (1991) Additional results of orbits of Hilda type asteroids. *Astron. Astrophys.* **241**, 2, 297–302.

THE TAPANUI REGION OF NEW ZEALAND : SITE OF A 'TUNGUSKA' AROUND 800 YEARS AGO?

Duncan Steel, *Anglo-Australian Observatory, Coonabarabran, NSW 2357, Australia*; and
Peter Snow, *Suffolk Street, Tapanui, Otago, New Zealand*.

Summary

We discuss the evidence that the wide-spread fires *ca.* 800 years ago which denuded the southern provinces of the South Island of New Zealand of the extensive forests present at that time were due to the entry of a large bolide into the atmosphere, the conflagration being ignited by the intense heat generated as this extraterrestrial projectile ablated/detonated in a similar manner to that of the Tunguska object of 1908. These fires led to the extinction of the giant terrestrial bird known as the Moa, and the end of the archaic epoch of Maori history known as the *Moa Hunter* period. This interpretation is well attested to in Maori myth and legend.

Introduction

The fact that the Earth is struck quite frequently by astronomical objects of substantial size is now well-established (*e.g.* Shoemaker, 1983). The last time that a large body was observed to intrude into the terrestrial environment was when a $\sim 10^{12}$ g object entered the atmosphere over the Tunguska region of Siberia in 1908, this apparently having been a part of the Taurid Complex (Kresák 1978; Steel *et al.*, 1991), whilst the expected 'annual event' (a ~ 20 kilotonne TNT-equivalent explosion) corresponds to an incoming mass of order 5×10^8 g (Table 2 of Ceplecha, 1992). The frequency of Earth-encounters with objects of such a size and energy as the Tunguska event progenitor (assuming that such events occur stochastically, which would not be the case if such objects are members of a coherent complex: Steel, 1991) is of the order of every few centuries or so (Shoemaker *et al.*, 1990). It is noteworthy that recent observations with the *Spacewatch* telescope (the first of ~ 10 –100 m-sized objects) indicate this size region to be rather more populous than previously thought (Rabinowitz, 1992), and those data have been used by Ceplecha (1992). Since mankind obviously has a vested interest in finding out more about the effects of such impacts (using that word advisedly since the Tunguska object detonated in the atmosphere and did not reach the surface: Krinov, 1963) it is of importance to identify other areas of our planet which have been subjected to such violations in the recent past (the last few millenia). In this paper it is suggested that the southern part of the South Island of New Zealand may have been the target of such a projectile about 800 years ago, so that a scientific study of the region is warranted.

New Zealand context

Near the town of Tapanui in the province of Otago is a structure known as the Landslip Crater or Landslip Hill (location $169^{\circ}09'$ East, $46^{\circ}04'$ South). This feature is an incomplete ovoid crater measuring 900 by 600 by 130 metres deep, which geological interpretation points to being a landslide (Lindqvist, 1990) and not a scar formed by an impact upon the Earth's surface of a large solid body, as such. Although this is apparently not an impact crater there exists *prima facie* evidence that links this site to a major cataclysm around 800 years ago. It is well-known that there were widespread fire(s) at about that time, possibly followed by a deluge, and this has usually been ascribed to the indigenous Maoris burning specific areas to drive the now-extinct Moas (*Dinornis*: a ratite) from the forests (Stevens *et al.*, 1988). Whilst in the North Island of New Zealand the forests at the time of the arrival of the first Polynesians (*ca.* 925 AD) were predominantly of broadleaf trees with few Moas present, in the South Island the forests were of podocarps which completely covered the island up to the treeline of the Southern Alps (Molloy *et al.*, 1963). In this environment the Moa flourished. Carbon dating of the charcoal which now pervades the soils

of the southern provinces (Southland, Otago and Canterbury) indicates that these fires occurred 600–1000 years ago with a clustering at ca. 800 years, although some burning may have occurred earlier, prior to the arrival of humans about a thousand years ago (Molloy *et al.*, 1963).

The 'conventional wisdom', then, says that the Moa was driven to extinction by the Maoris who hunted them by setting the fires: the Moa were deliberately driven with the flames into swamps, where many Moa remains are now found. If this is what actually happened then the newly-arrived Maori would have cut off one of their major sources of food, and ruined a stable environment (this area of New Zealand is now denuded of forests and is open hill-sheep country). Maori history is quite clearly divided into the early *Moa Hunter* or *Archaic* period, and the later *Classic Maori* period; the major inland Moa-hunting area covers the Tapanui region (Stevens *et al.*, 1988: p.117). Both archaeological evidence and spoken Maori history indicate that there were intermittent arrivals of peoples from Polynesia between 925 and 1150 AD. The 'Great Migration' which began ca. 1350 AD apparently (again from Maori legend) post-dates the extinction of the Moa.

However, there is some evidence that indicates a rather more coherent event than might be expected from gradual forest-burning. Snow (1983) states that the tree fall distribution from that period points radially away from the Tapanui site. Pajak (1989, 1990) claims that fallen trees are aligned radially *away* from this site out to a distance of 40–80 km, and then tend to point radially *inwards*, and suggests that this may be due to an explosion at Tapanui blasting the closer trees outwards, with the upwelling from a firestorm after the blast resulting in the inward falls. These suggestions require scientific study, and the dates of tree falls also require elucidation (it would seem remarkable if fallen trees from such antiquity still existed in large quantities).

Pajak (1989, 1990) also states that small globules of silicates which he terms *trinitites*, presumably taking their name from similar samples found around the Trinity (New Mexico) site after the first anthropomorphic nuclear explosion in 1945, are found thereabouts and that these are also evidence of a cataclysmic explosion, which he attributes to an extraterrestrial spacecraft. The conventional geological explanation would be that these are from some volcanic explosion, or are similar to tektites. There is also an abundance of *sarsens* or *Chinamen stones* spread across the vicinity, these being made of quartz sandstone. Pajak (1989, 1990) believes these to have been metamorphosed under high temperature and pressure conditions in his explosion as mentioned above, whilst Snow (1983) ascribes them to a bolide entering the atmosphere and breaking up, possibly after ejection from a lunar impact. Lindqvist (1990) identifies these as being made of fluvial quartz sandstone and conglomerates which have been silica-cemented, so that they are clearly produced by normal terrestrial processes, and apparently not related to the effects of an incoming asteroid or comet, if such did in fact occur.

Maori oral history

There is also the evidence of Maori myth, legend, poetry and song which speak of the falling of the skies, raging winds, upheaval of the Earth, and mysterious devastating fires from space. Many local place names may be translated in terms of a catastrophic event having occurred thereabouts, and *Tapanui* itself apparently means *The big explosion* or *The big devastating blow*: there is a Maori adage that "The history is in the names, and the names are in the land". Another nearby site is *Waipahi*, which may be taken to mean *The place of the exploding fire*. Other similar place names exist in abundance, and do not appear commonly elsewhere in New Zealand. Snow (1983) has listed many of these possible interpretations, and Maori mythology is rife with connections between these fires, the end of the Moas, and an object falling from the Moon or space. In fact the word *Moa* is relatively recent; in the early *Moa Hunter* epoch prior to the fires the animal was termed *Pouakai*, but afterwards it was remembered as *Manu Whakatau*, one translation of which is *The bird felled by strange fire*. Again, one Maori lament states that:

"Very calm and placid have become the raging billows,
That caused the total destruction of the Moa,
When the horns of the Moon fell from above down."

The idea that the Moa expired in some natural conflagration is not a new one. Hill (1913) argued for the North Island Moa being destroyed in the aftermath of a volcanic eruption or something similar, and quotes a conversation with an eighty-eight year old Maori chief: "The Moa disappeared after the coming of Tamaatea [a man/god] who set fire to the land. The fire was not the same as our fire but embers sent by Rongi [the sky]. The signs of the fires are still to be seen where red rocks like berries are found."

Since Maori legend unambiguously indicated the period at which the widespread fires occurred, and the time at which the Moa died out, and this oral tradition was later verified by modern Carbon-14 dating and botanical techniques, it would seem plausible that Maori myths may also contain at least their own interpretation of the origin of these fires. "It is my belief that hidden in Maori mythology there is also a message about the catastrophic nature of our past" (Snow, 1983).

Astronomical interpretation

As a baseline hypothesis, which in the best traditions of scientific practice requires a disproof, we adopt the idea that this structure at Tapanui is the scar produced by the detonation of a large bolide in the atmosphere *à la* Tunguska, and the forest fires were ignited by this cataclysmic event. How does this fit in with present-day ideas of terrestrial catastrophism?

One of the authors [D.S.], in collaboration with others, has advanced the hypothesis that in the present epoch the Earth is subject to episodes of substantial influx by macroscopic bodies, these being the debris produced by the break-up of a Giant Comet in the past 10,000–20,000 years. The various phenomena now seen (recurrent meteor showers, P/Comet Encke, several Apollo asteroids) are collectively termed the *Taurid Complex*. We believe that the core of this complex, under orbital precession, intersects our planet for four periods lasting a century or so, these four epochs being spread over a cycle time of a few thousand years (see Steel *et al.*, 1991). One such period was apparently at the start of the present millennium (Bailey *et al.*, 1990; Clube and Napier, 1990), and thus seems to correlate with the time of the entry of the bolide above New Zealand, if our hypothesis is correct. This also correlates with the putative time of the formation of the Giordano Bruno crater on the Moon (1178 AD: Hartung, 1976; Clube and Napier, 1990) which Snow (1983) linked into his baseline model of a large asteroidal impact; such an event within the last millennium seems to be an unlikely occurrence.

Yet another nearby place name is Otarehua, where 'Ota' means 'of the' and 'rehua' was the Maori name for Antares, the (northern) summer star. This may help to indicate the time of year at which the bolide entry occurred: perhaps near the northern mid-summer (austral mid-winter), when the daytime Taurid intersection with the Earth is most active and the Tunguska event occurred. Other place names may indicate the day in the lunar cycle when the New Zealand catastrophe happened, although without definite knowledge of the year this is not of use in fixing the date.

Whatever the source of the bolide which arrived in the atmosphere above the southern part of New Zealand about 800 years ago, if this is what actually occurred then the area would be of fundamental import in developing our understanding of the response of the Earth to such large insults. The purpose of this paper is to bring the site to the attention of scientists with expertise in the various areas which would be necessary for a rigorous study of the area, in order to show whether or not a Tunguska-type event did occur there around the twelfth century, and if so what may be learnt from it.

References

- Bailey, M.E., Clube, S.V.M. and Napier, W.M. (1990). The Origin of Comets, Pergamon Press, Oxford.
- Ceplecha, Z. (1992). Influx of interplanetary bodies onto the Earth. Astron. Astrophys. (in press).
- Clube, S.V.M. and Napier, W.M. (1990). The Cosmic Winter, Blackwells, Oxford.
- Hartung, J. (1976). Was the formation of a 20-km diameter impact crater on the Moon observed on June 18, 1178? Meteoritics, 11, 187–194.
- Hill, H. (1913). The Moa: Legendary, Historical, and Geological. Trans. N. Z. Inst., XLVI, 330.
- Kresák, L. (1978). The Tunguska object: A fragment of comet Encke? Bull. Astron. Inst. Czechoslov., 29, 129–134.
- Krinov, E.L. (1963). The Tunguska and Sikhote-Alin Meteorites. pp. 208–234 in The Moon, Meteorites and Comets, eds. B.M. Middlehurst and G.P. Kuiper, University of Chicago Press.
- Lindqvist, J.K. (1990). Deposition and diagenesis of Landslip Hill silcrete, Gore Lignite Measures (Miocene), New Zealand. New Zealand J. Geol. Geophys., 33, 137–150.
- Mollov, B.P.J., Burrows, C.J., Cox, J.E., Johnston, J.A. and Wardle, P. (1963). Distribution of Subfossil Forest Remains, Eastern South Island, New Zealand. New Zealand J. Botany, 1, 68–77.
- Pajak, J. (1989). Tapanui Cataclysm—An Explanation for the Mysterious Explosion in Otago, New Zealand, 1178 A.D., ISBN 0-9597698-7-0, 62 pp., privately printed by the author, 116 Rolla Street, NEV, Dunedin, New Zealand.
- Pajak, J. (1990). New Zealand's Tapanui Explosion. Ancient Skies, 17, #4, 1–4.
- Rabinowitz, D.L. (1992). The flux of small asteroids near the Earth. (These proceedings).
- Shoemaker, E.M. (1983). Asteroid and comet bombardment of the Earth. Ann. Rev. Earth Planet. Sci., 11, 461–494.
- Shoemaker, E.M., Wolfe, R.F. and Shoemaker, C.S. (1990). Asteroid and comet flux in the neighborhood of Earth. Geol. Soc. Amer. Spec. Pap., 247, 155–170.
- Snow, P.G. (1983). The Mystic Fires of Tamaatea, unpublished manuscript.
- Steel, D. (1991). Our asteroid-peled planet. Nature, 354, 265–267.
- Steel, D.I., Asher, D.J. and Clube, S.V.M. (1991). The structure and evolution of the Taurid Complex. Mon. Not. Roy. Astron. Soc., 251, 632–648.
- Stevens, G., McGlone, M., McCulloch, B. and Ward, V. (1988). Prehistoric New Zealand, Heinemann Reed, Auckland.

Acknowledgements: This work was supported by the Australian Research Council. A number of people have helped with discussions or correspondence on this topic, and in particular the interest and suggestions of the late Bob Williams of West Otago are remembered with gratitude.

Post-conference addition: After the presentation of this paper I [D.S.] was abashed to be informed by E.F. and R. Helin that a similar myth exists amongst the Australian aborigines of western New South Wales (E. Jones, The Story of the Falling Star, Aboriginal Studies Press, Canberra, 1989). This tells of a foretold falling star bringing fire and havoc as it shot through the skies, killing many people and depositing strange stones, again with a following deluge. The stones shown in that book are clearly non-meteoritic in origin (R.H. McNaught has visited the indicated site and found those rocks to be marble) but this may be due to confusion after centuries of story-telling.

1991 DA : AN ASTEROID IN A BIZARRE ORBIT

Duncan Steel and Robert H. McNaught,
Anglo-Australian Observatory,
Private Bag, Coonabarabran, NSW 2357, Australia; and

David Asher,
Department of Physics, University of Oxford,
Keble Road, Oxford, OX1 3RH, England, U.K.

Summary

Asteroidal object 1991 DA has an orbit of high inclination, crossing the planets from Mars to Uranus. This is unique for an asteroid, but not unusual for a comet of the Halley-type: it therefore seems likely that 1991 DA is an extinct or dormant comet. Previous CCD imaging has shown no indication of a coma; here we report spectroscopic observations of 1991 DA which lack any evidence of strong comet-like emissions. We also perform numerical integrations of the orbit of this object which show that it has been remarkably stable for the past $\sim 20,000$ yr, but chaotic before that. This may allow a new estimate to be made of the physical lifetimes of comets.

Introduction

The object denoted 1991 DA was discovered by the second-named author on a U.K. Schmidt Telescope plate exposed on 1991 February 18. It is estimated to be about 5 km in size. Astrometric observations soon showed it to have one of the most bizarre orbits known for any asteroid (Chapman, 1991): at 61.9° its inclination is the third highest of all known minor planets, and its eccentricity of 0.866 is also the third highest amongst asteroids. With a perihelion distance of 1.58 AU and aphelion at 22 AU, 1991 DA crosses the paths of Mars, Jupiter, Saturn and Uranus, and therefore would be expected to have a dynamical lifetime of at most $\sim 10^{5-6}$ years. CCD imaging of 1991 DA by English and Freeman (*IAU Circ.* 5199) and by West and by Ryder (*IAU Circ.* 5208) has shown no evidence of a coma despite the fact that the object was close to perihelion at the time. Here we report spectral observations with the Anglo-Australian Telescope which lack any comet-like emissions, backing up the conjecture that 1991 DA is asteroidal in nature. 1991 DA may therefore be a totally de-volatilized comet, or a comet which has formed an insulating crust.

Numerical integrations may indicate the path by which the present orbit of 1991 DA has come about, especially if non-gravitational forces have been negligible in the past. We have carried out such integrations extending over the last 50,000 yr and find that the orbit has been remarkably stable for at least the last $\sim 20,000$ yr, prior to which nodal crossings near Saturn lead to large changes in the orbit in close approaches to that planet. Before then the orbit is chaotic with longer integrations being of statistical interest only. A more detailed discussion of such integrations, over a longer time-base, is given by Hahn and Bailey (1991).

Spectroscopic Observations

We observed 1991 DA using the 3.9 m Anglo-Australian Telescope on the night of 1991 March 17. We had planned to obtain a high-dispersion spectrum covering the strong emissions from CN , CH , C_2 and C_3 in the range 380–520 nm manifested by many comets but an instrumental fault limited us to a spectrum from 530–1095 nm obtained with the Faint Object Red Spectrograph on the AAT. This is shown in Figure 1 after subtraction of the sky background and ratioing against the solar-analogue star 70 Virginis. There is no evidence for strong comet-like emissions in the spectrum, except possibly at 530–580 nm where C_2 emission may occur. Atmospheric absorption,

particularly near 760 nm, is evident (the star and asteroid were at rather different zenith angles) and longwards of 900 nm the atmospheric transmission was both low and variable, leading to the great scatter in this ratio spectrum (and the strong spike, absent in another spectrum). On this basis, therefore, we do not find any compelling evidence for cometary emissions from 1991 DA.

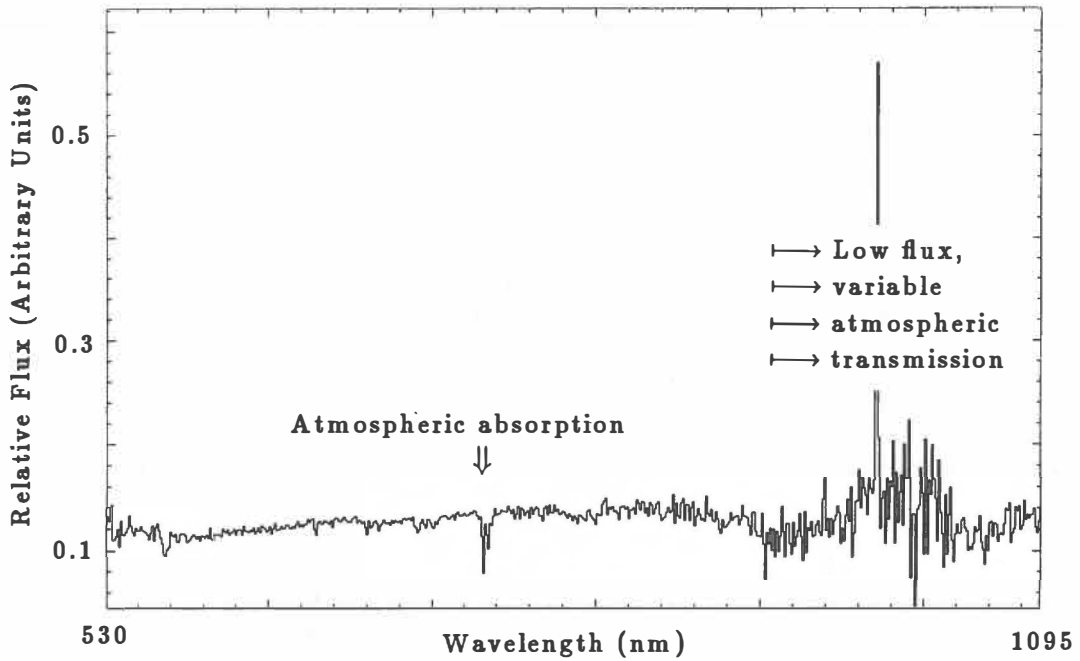


Figure 1: Ratio spectrum from 530–1095 nm for 1991 DA / 70 Virginis after subtraction of atmospheric background. No strong cometary emission lines are found. Above 900 nm the spectrum is noisy due to low signals and variable atmospheric transmission.

Numerical Integrations

We used a 7th order Runge-Kutta-Nyström integrator developed by Dormand and Prince (1978). It is a variable step-length method shown by Fox (1984) to be very efficient for high-eccentricity orbits. Fox (1984, personal communication) provided a Fortran subroutine implementing the method. Our steplengths ranging from a little below 0.1 yr at $r = 1.6$ AU to about 3 yr at $r = 22$ AU mean that we are not solving the equations of motion to anywhere near the limit of machine accuracy, but this is probably sufficient given the uncertainties in starting elements and the eventual chaotic nature of the orbit.

We included the six planets from Earth out to Neptune, updating their orbital elements every 500 yr using smoothed elements from Quinn (1991, personal communication) derived from the planetary integration of Quinn *et al.* (1991). Jupiter and Saturn dominate the effect on the secular change in elements of 1991 DA, and the long-term effect of precessing planetary elements is noticeable. The initial elements of 1991 DA were taken from MPC 18437: *viz.* $a = 11.8721271$ AU, $e = 0.8670227$, $i = 61.88558^\circ$, $\Omega = 313.40412^\circ$, $\omega = 191.25159^\circ$, $M = 8.95122^\circ$ at 1991.94.

In Figure 2 we show the history of the semi-major axis of 1991 DA for six different sets of starting elements; the topmost plot is with the elements just listed, and then descending we modify a by $+0.0001$ AU, e by $+0.000001$, and i , Ω and ω by $+0.001^\circ$ (one only of these changes in turn from the nominal orbit). These represent smaller uncertainties in the orbit than exist due to the short arc over which 1991 DA has been observed.

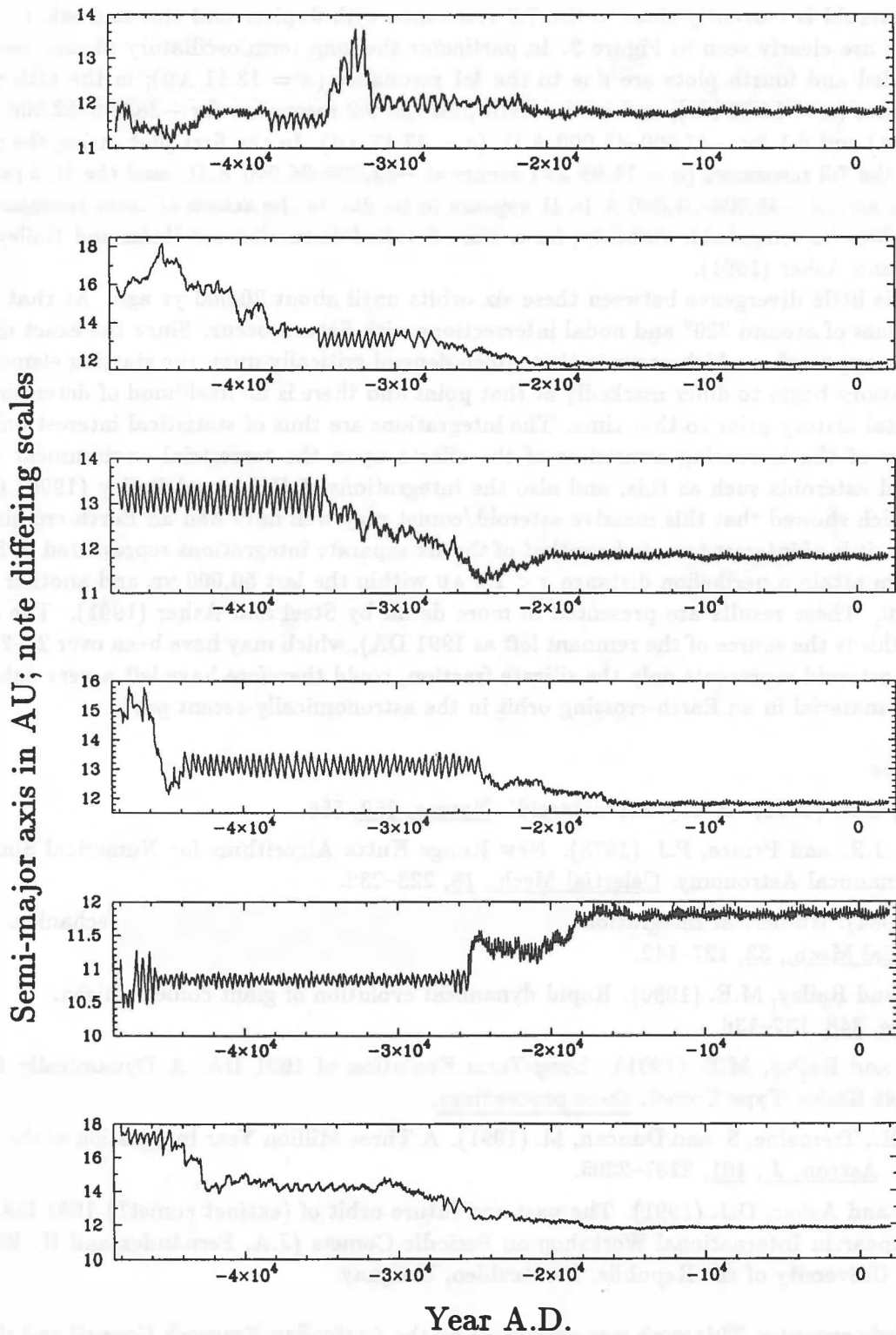


Figure 2: Results of numerical integrations of 1991 DA backwards over 50,000 yr from the present for slightly different starting parameters: for details see text. Only the semi-major axis for each of the six hypothetical orbits is shown. The plots do not start to diverge appreciably until $\sim 20,000$ yr ago when close approaches to Saturn become possible. The oscillatory parts of each plot are due to commensurabilities with Jupiter, which are described in the text.

The asteroid is currently close to the 7:2 resonance with Jupiter and this and other commensurabilities are clearly seen in Figure 2. In particular the long-term oscillatory phases seen in the second, third and fourth plots are due to the 4:1 resonance ($a = 13.11$ AU); in the fifth plot the 3:1 resonance ($a = 10.82$ AU); and in the sixth plot the 9:2 resonance for $-38,000$ – $32,000$ A.D. ($a = 14.18$ AU) and 6:1 for $-47,000$ – $45,000$ A.D. ($a = 17.17$ AU). In the first plot, using the nominal elements, the 7:2 resonance ($a = 11.99$ AU) occurs at $-32,000$ – $26,000$ A.D., and the 10:3 resonance ($a = 11.61$ AU) at $-38,000$ – $34,000$ A.D. It appears to be due to the action of these resonances that 1991 DA owes its remarkable stability; for a more detailed discussion see Hahn and Bailey (1991) and Steel and Asher (1991).

There is little divergence between these six orbits until about 20,000 yr ago. At that time, ω attains values of around 220° and nodal intersections with Saturn occur. Since the exact distances of the close approaches which occur in that epoch depend critically upon the starting elements, the six integrations begin to differ markedly at that point and there is no likelihood of determining the exact orbital history prior to that time. The integrations are thus of statistical interest only.

In view of the increasing awareness of the effects upon the terrestrial environment of large comets and asteroids such as this, and also the integrations of Hahn and Bailey (1990) for 2060 Chiron which showed that this massive asteroid/comet may well have had an Earth-crossing orbit in the past, it is of interest to note here that of the six separate integrations represented in Figure 2 two of them attain a perihelion distance $q < 1.0$ AU within the last 50,000 yr, and another reaches $q < 1.1$ AU. These results are presented in more detail by Steel and Asher (1991). The original comet (if this is the source of the remnant left as 1991 DA), which may have been over 20–25 km in size if the asteroid represents only the silicate fraction, could therefore have left a very substantial amount of material in an Earth-crossing orbit in the astronomically-recent past.

References

- Chapman, C.R. (1991). A way-out 'asteroid'. *Nature*, **350**, 556.
- Dormand, J.R. and Prince, P.J. (1978). New Runge-Kutta Algorithms for Numerical Simulation in Dynamical Astronomy. *Celestial Mech.*, **18**, 223–232.
- Fox, K. (1984). Numerical Integration of the Equations of Motion of Celestial Mechanics. *Celestial Mech.*, **33**, 127–142.
- Hahn, G. and Bailey, M.E. (1990). Rapid dynamical evolution of giant comet Chiron. *Nature*, **348**, 132–136.
- Hahn, G. and Bailey, M.E. (1991). Long-Term Evolution of 1991 DA: A Dynamically Evolved Extinct Halley-Type Comet, *these proceedings*.
- Quinn, T.R., Tremaine, S. and Duncan, M. (1991). A Three Million Year Integration of the Earth's Orbit. *Astron. J.*, **101**, 2287–2305.
- Steel, D.I. and Asher, D.J. (1991). The past and future orbit of (extinct comet?) 1991 DA. To appear in *International Workshop on Periodic Comets* (J.A. Fernández and H. Rickman, eds.), University of the Republic, Montevideo, Uruguay.

Acknowledgements: This work was supported by the Australian Research Council and the U.K. Science and Engineering Research Council. We thank the Director of the AAO, Russell Cannon, for the allocation of time on the AAT; Raylee Stathakis and Kevin Cooper for assistance in collecting the data; and David Allen for information on cometary spectra. Discussions with M.E. Bailey and G. Hahn on the numerical integrations were appreciated, as was a preprint of their paper.

A CCD Search for Distant Satellites of Asteroids 3 Juno and 146 Lucina

S. Alan Stern
Space Sciences Department
Southwest Research Institute
San Antonio, Texas

and

Edwin S. Barker
McDonald Observatory, University of Texas
Fort Davis, Texas

Abstract

We report the results of CCD searches for satellites of asteroids 146 Lucina and 3 Juno. Juno is one of the largest asteroids ($D=244$ km); no previous deep imaging search for satellites around it has been reported. A potential occultation detection of a small satellite orbiting 146 Lucina ($D=137$ km) km was reported by Arlot et al. (1985), but has not been confirmed. Using the 2.1m reflector at McDonald Observatory in 1990 and 1991 with a CCD camera equipped with a 2.7 arc-sec radius occulting disk, we were able to achieve limiting magnitudes of $m_R = 19.5$ and $m_R = 21.4$ around these two asteroids. This corresponds to objects of 1.6 km radius at Juno's albedo and distance, and 0.6 km radius at Lucina's albedo and distance. No satellite detections were made. Unless satellites were located behind our occultation mask, these two asteroids do not have satellites larger than the radii given above.

I. Introduction

The search for satellites of asteroids has been a topic of interest and discussion for some years. As described by Weidenshilling et al. (1989), evidence for asteroid satellites includes certain anomalously slow rotation rates, the shape of certain asteroid lightcurves, elongated asteroid images (e.g., 9 Metis) and the statistical frequency of doublet craters on the Earth and Moon (cf., the interesting recent work by Melosh and Stansberry 1991). Interest in binary asteroids has been further fueled by the discovery that Near-Earth Asteroid (NEA) 4769 Castalia (1989PB) is clearly bifurcated in radar images (Ostro et al. 1990).

In principle asteroid satellites could be created by several processes, including rotational fission, fragmentation followed by mutual capture, or as a result of ejecta from a low-speed collision. Theoretical results (Weidenshilling, et al. 1989; Chauvineau and Mignard 1990a,b) demonstrate that a range of long-term stable orbits exist, particularly for close binaries, even when solar and Jovian perturbations on the orbit are included.

The most immediate application of the discovery of an asteroid satellite would be the direct mass and density determination of the parent asteroid. Subsequent studies of the satellite's osculating elements would then permit information to be gleaned about the internal structure, tidal evolution, and lifetime of the parent-satellite system (particularly if the system has not reached tidal lock). The detection of asteroid satellites or orbiting debris would also (i) lead to new information on collision statistics in the parent-body orbit, and (ii) clearly be of interest to spacecraft mission designers. Yet another exciting

opportunity would be the potential for observations of mutual occultation events between the asteroid and its satellite, which could reveal important details about the individual radii, shapes, and surface markings of the parent asteroid and the satellite.

The general absence of *large* satellites around the brightest asteroids ($m_v < 16.5$) was noted almost 35 years ago (Kuiper et al. 1958). However, the presence of small satellites orbiting asteroids remains an open research topic. (e.g., van Flandern, Tedesco, and Binzel 1979; Weidenshilling, et al. 1989).

Two CCD imaging surveys for asteroid satellites have been reported in the past: Gehrels et al. (1987) and Gradie and Flynn (1988). Together these two groups searched the fields around 22 asteroids with detection limits of $m_v \sim 18 - 22$, which correspond to satellite diameters of a few km in most cases. No detections were made. Taken at face value, these searches indicate that less than $\sim 4\%$ of all asteroids have faint companions. In fact, owing to the concentration on relatively large asteroids and distant-satellite orbits, the actual satellite-occurrence statistics for the asteroid population as a whole could be quite different.

We report here the results of a project we undertook in preparation for a new satellite search around ~ 50 asteroids. In this pilot project, we made searches around two new objects: 3 Juno and 146 Lucina.

II. 3 Juno

The search for objects orbiting the S type 3 Juno was made on 7 May 1990 UT. Juno was near aphelion at a heliocentric distance of 3.34 AU, a geocentric distance of 2.36 AU, and less than 72 hours from opposition.

To conduct this search, we employed the 2.1m Struve reflector at McDonald Observatory, equipped with a focal reducing camera (FRC). The FRC employs a Tektronix 512x512 CCD with $15e^-$ readout noise. The FRC optical train was configured with an RG5 filter to reduce Rayleigh scattered moonlight, and a 5.4 arcsec diameter occulting disk to block the light of Juno itself. This configuration allowed us to search the entire region beyond ≈ 10 arcsec from Juno with the scattered light nearly-eliminated. In the region between 6 and 10 arcsec from Juno, which is outside the occulting mask but inside the region where diffraction, seeing, and finite pixel size effects contribute to scattered light, we found the scattered/diffracted light PSF to be angularly symmetric. This allowed us to search this region for discrete photometric peaks which might represent a close-in satellite. However, scattered/diffracted light statistics caused our detection limits in the 6-10 arcsec region to be ≈ 2 magnitudes less constraining than those beyond 10 arcsec. Calibration images of Juno itself were made in order to obtain a magnitude standard for this run.

The plate scale of the FRC was measured to be 1.01 arcsec/pixel. The clear field of the filter was 265 arcsec across. We estimate the size of Juno's sphere of influence, according to Szebehely's tidal stability criterion (Szebehely 1967), as:

$$R_{stab} = a_J(1 - e_J) \left(\frac{\mu}{81} \right)^{1/3} \quad (1)$$

where a_J is Juno's semi-major axis, e_J is Juno's orbital eccentricity, and μ is the ratio of Juno's mass to the solar mass. Taking Juno's radius to be 122 km (Tedesco et al. 1989) and adopting a density of 3 g cm^{-3} , we find $\mu = 1.14 \times 10^{-11}$ and $R_{stab} = 1.56 \times 10^4 \text{ km}$. At the 2.36 AU geocentric distance on the night observed, this corresponds to a stability

radius of 128 Juno radii or ≈ 9 arcsec on the sky. Given Juno's geocentric distance on the night observed, the 5.4" occulting disk prevented us from observing objects within ≈ 38 Juno radii of the asteroid, or 15% of the projected stability field. Assuming a bulk density of $\rho_{juno} = 3 \text{ g cm}^{-3}$, a satellite orbiting synchronously with Juno would lie near $2.4R_{juno}$.

We guided the image on Juno while imaging the surrounding field in a series of deep CCD exposures. Over a period of an hour, we made eight CCD exposures of the field surrounding Juno. Juno's sky motion during our observations was 33 arcsec/hr. This rapid motion ensured that any suspect satellites could easily be seen to move with Juno against the fixed background star field. Assuming Juno's density is near 3 gm cm^{-3} , an object with a semi-major axis at the edge of the stability region defined by Szebehely's criterion would have a period of 115 days. An object orbiting at the edge of our occulting disk would have a period of 18.6 days. Therefore, any satellite of Juno would be seen to move across the background star field very nearly in concert with, and in an essentially fixed relation to Juno.

The seeing in the Juno field images was typically 2-2.3 arcsec FWHM during our observations. This necessitated the use of a rather wide, 5.4" occulting disk. Eleven images of the field surrounding Juno were obtained, with exposure times ranging from 100 to 600 seconds. Seven of these images had 300 second exposure times.

The Juno field images were processed using IRAF and then looped on an image display device to search for co-moving companions. Different scaling and image processing methods (e.g., histogram equalization, smoothing, and removal of background stars) were used to assist in the satellite search. No co-moving object detections were made.

To determine the limiting magnitudes of the search, the DAOPHOT routine ADDSTAR (Stetson 1987) was used to create artificial stars on representative CCD images. A total of 1000 artificial stars were used to determine limiting magnitudes. These artificial stars were created spanning a range of magnitudes as low as 26, using an as-measured point-spread-function (PSF) of Juno; appropriate counting statistics were added to each artificial PSF. These artificial images were then examined visually in the same manner as the program images to find the number of stars detected as a function of magnitude. To convert instrumental magnitudes to observed magnitudes, the DAOPHOT routine PHOTOMETRY was used to measure the magnitudes of 3 Juno in our magnitude-reference frame. The differences between these instrumental magnitudes and their true observational magnitudes were used to scale the measurements of the artificial stars. Using these techniques we found the Juno images allowed us to detect co-moving objects as faint as $m_R = 19.5$ in the region beyond 10 arcsec from Juno and $m_R = 17.6$ in the region between 6 and 10 arcsec from Juno.

Juno's V magnitude on 7 May 1990 was 10.1. Based on the limiting R magnitude of 19.5 in our search, we conclude that no objects larger than $\approx 3.3\sqrt{\alpha}$ km were orbiting Juno beyond $37R_{juno}$, at the time of our observations, where α is the albedo ratio of a prospective satellite to Juno.

III. 146 Lucina

On UT 5 and 6 May 1991 we observed the field around the C type 146 Lucina using the same instrument and observing protocols as the 3 Juno observations conducted in 1990. Taking Lucina's radius to be 68.5 km (Tedesco et al. 1989) and adopting a density of 3 g cm^{-3} , we find $\mu = 2.03 \times 10^{-12}$ and $R_{max} = 1.08 \times 10^4$ km. At the 1.73 AU geocentric

distance observed, this corresponds to 100 Lucina radii or ≈ 86 arcsec on the sky.

On 5 May 1991 we obtained seven 600 second integrations on the field surrounding 146 Lucina using the same occulting disk as in the Juno work. On 6 May 1991 we obtained an additional 3 exposures of the surrounding field, two of which were 1800 sec in length; a third, 600 second exposure was also obtained. Given the 1.73 AU geocentric distance of Lucina on the two nights observed, the occulting disk prevented us from detecting any objects located within ≈ 3400 km of the asteroid (50 Lucina radii; period=28 days); this distance corresponds to about 32% of size of the projected stability field (this constraint unfortunately does not include the 1600 km projected distance at which Arlot et al. (1985) made the photoelectric detection of a putative satellite during a stellar occultation even; see below). Assuming a bulk density of $\rho_{lucina} = 3 \text{ g cm}^{-3}$ a satellite at the synchronous point would lie near $4.6R_{lucina}$.

Using the same analysis techniques as with Juno, a careful search of the images revealed no objects travelling with Lucina. In the 600 second CCD images we obtained a limiting magnitude of 21.4 for objects > 10 arcsec from Lucina, and 19.7 for objects 6-10 arcsec from Lucina. The 1800 sec exposures yielded a limiting magnitude of 22.6 for objects > 10 arcsec from Lucina, and 20.5 for objects 6-10 arcsec from Lucina. (The limiting magnitudes in this run were deeper relative to the 1990 Juno run than increased exposure time alone would imply; this is because, unlike the Juno run, moonlight was not a factor.)

Lucina's V magnitude on 5 and 6 May 1991 was 12.3. Based on the limiting magnitude of our search, we conclude that no objects with albedo equal to Lucina's larger than ≈ 0.6 km were orbiting Lucina beyond 50 R_{lucina} . Because the satellite detection claimed by Arlot et al. (1985) occurred at $\approx 23R_{lucina}$, our results unfortunately cannot directly rule out (or confirm) theirs. We can, however, conclude that more distant satellites larger than our detection limit are unlikely (admitting the possibility of a satellite having been under the occulting disk). We further conclude that if the Arlot et al. "satellite" is real, it is likely in an orbit with $e < 0.5$ and $a < 5 \times 10^3$ km.

IV. Outlook

Our detection limits set new constraints on the probability of satellites around two asteroids not previously searched by imaging techniques. Unless by chance a satellite was hidden behind our occulting disk during our runs, neither 3 Juno nor 146 Lucina appear to have satellites > 1.6 and > 0.6 km in radius orbiting them at > 40 and > 50 parent-asteroid radii, respectively.

We point out that groundbased coronographic searches for asteroid satellites in the main belt cannot escape the catch-22 imposed by seeing, which necessitates using an occulting disk larger than the apparent size of the synchronous orbit where tidal forces could be expected to bring debris after a collision. Therefore, although deep searches such as ours can make progress in the more distant regions of asteroid stability fields, either Space Telescope or groundbased speckle techniques would be expected to yield the best results for searches in the prime, inner region near each parent asteroid. However, for NEAs, deep coronographic searches like ours (which probe to much fainter magnitudes than speckle techniques) *can* often probe inside the synchronous point, making such targets attractive future search candidates.

These findings constitute the first results of a planned McDonald CCD satellite-search

campaign intended to triple the total number of asteroids surveyed for satellites by direct imaging techniques. We hope to survey several dozen asteroids (including many NEAs). Operating during dark time and with 1-1.5" seeing, we expect to routinely reach a limiting magnitude near $m_R = 23.5$ at 1-2 arcsec from our search targets.

Acknowledgments

Alan Harris and Tom Gehrels provided valuable critiques of this manuscript. This research was partially supported by a NASA operating grant to McDonald Observatory.

References

- Arlot, J., Lecacheux, J., Richardson, C., and Thuillot, W. 1985. A possible satellite of (146) Lucina. *Icarus*, **61**, 224.
- Chauvineau, B., and F. Mignard, 1990a. Dynamics of Binary Asteroids I. Hill's Case. *Icarus*, **83**, 360.
- Chauvineau, B., and F. Mignard, 1990b. Dynamics of Binary Asteroids II. Jovian Perturbations. *Icarus*, **87**, 377.
- Gehrels, T., Drummond, J.D., and N.A. Levenson (1987). The absence of satellites of asteroids. *Icarus*, **70**, 257.
- Gradie, J. and L. Flynn (1988). A search for satellites and dust shells around asteroids: negative results. *Lunar Planet. Sci.*, **XIX**, 405. (abstract).
- Kuiper, G.P., Fujita, Y., Gehrels, T., Groeneveld, I., Kent, J., Van Biesbroek, G., and J. van Houten, 1958. Survey of asteroids. *Astrophys. J. Suppl.*, **3**, 799.
- Melosh, H.J., and J.A. Stansberry, 1991. Doublet craters and the tidal disruption of binary asteroids. *Icarus*, **94**, 171.
- Ostro, S.J. et al., 1990. Radar observations of asteroid 1989PB. *Science*, **248**, 1523.
- Szebehely, V., 1967. *The Theory of Orbits: The Restricted Problem of Three Bodies*, Academic Press, New York, 668pp.
- Stetson, P.B., 1987. DAOPHOT: A Computer Program for Crowded-Field Stellar Photometry. *PASP*, **99**, 191.
- Tedesco, E., 1989. Asteroid Colors, Magnitudes, and Diameters. In *Asteroids II* (R.P. Binzel, T. Gehrels, and M.S. Matthews, eds.). U. Az. Press, Tucson. pp. 1090.
- Van Flandern, T.C., Tedesco, E.F., and R.P. Binzel (1979). Satellites of Asteroids. In *Asteroids* (T. Gehrels, ed.). U. Az. Press, Tucson, 443.
- Weidenshilling, S.W., Paolicchi, P., and V. Zappalà (1989). Do asteroids have satellites? In *Asteroids II* (R.P. Binzel, T. Gehrels, and M.S. Matthews, eds.). U. Az. Press, Tucson. 643.

CARTOGRAPHY OF ASTEROIDS AND COMET NUCLEI FROM LOW RESOLUTION DATA

Philip J. Stooke

Department of Geography, University of Western Ontario
London, Ontario, Canada N6A 5C2 (Stooke@vaxr.sscl.uwo.ca).

High resolution images of non-spherical objects, such as Viking images of Phobos and the anticipated Galileo images of Gaspra, lend themselves to conventional planetary cartographic procedures: control network analysis, stereophotogrammetry, image mosaicking in 2D or 3D and airbrush mapping (1). There remains the problem of a suitable map projection for bodies which are extremely elongated or irregular in shape. Many bodies will soon be seen at lower resolution (5 - 30 pixels across the disk) in images from speckle interferometry, the Hubble Space Telescope (even after repair), ground-based radar, distant spacecraft encounters and closer images degraded by smear. Different data with similar effective resolutions are available from stellar occultations, radar or lightcurve convex hulls, lightcurve modelling of albedo variations and cometary jet modelling. With such low resolution, conventional methods of shape determination will be less useful or will fail altogether, leaving limb and terminator topography as the principal sources of topographic information.

I have developed a method for shape determination based on limb and terminator topography (2,3,4,5). It has been applied to the nucleus of Comet Halley (6) and the jovian satellite Amalthea (7). The Halley map will be repeated now that a new consensus appears to be emerging on the nucleus rotation state. The Amalthea results are described here to give an example of the cartographic possibilities and problems of anticipated data sets.

Voyager images of Amalthea were decompressed from PDS CD-ROMs, outlines digitized and coordinates converted to kilometres in the image plane. An initial triaxial ellipsoid model was registered with the digitized outlines and iteratively modified by locally increasing or decreasing radii until the model successfully duplicated all limbs and terminators in the eight images used for modelling. Topography of major craters and ridges was estimated but is very poorly constrained by the data. For instance, the depths of the two largest craters on Amalthea are virtually unknown. The model is illustrated with graticules depicting Voyager images (Figure 1), and views from mutually perpendicular directions including the polar view not seen by Voyager (Figure 2).

The origin of the planetocentric coordinate system is the assumed centre of mass, tested by comparing volumes on either side of three mutually perpendicular planes during modelling. The centre of mass is probably within about 5 km of the position assumed here, assuming uniform or radially symmetrical internal mass distribution. The model has a volume of 2.5 ± 0.5 million cubic km. Radii are typically uncertain by about 2 pixels (10 to 20 km) near limbs and terminators (less where several intersect), but are very poorly constrained elsewhere. Although limbs can be located to within a pixel on most Voyager images, their geographic locations on the model are uncertain by many degrees, a major source of uncertainty in the model and very difficult to quantify.

Cartographic options for non-spherical worlds have until recently been very limited. The first such maps (e.g. 8,9), rough sketches on unmodified cylindrical projections of a sphere, inevitably contain enormous distortions. More sophisticated approaches include a modified cylindrical (Mercator-like) projection developed by John Snyder (10) and so far used only for a Soviet map of Phobos, and the use of mutually perpendicular orthographic views of a 3-D digital photomosaic (11). These suffer from other problems. The cylindrical projections give a good representation of the circumequatorial regions with relatively minor distortions if the body is well approximated by a triaxial ellipsoid. They will contain massive distortions if the shape is more complex and do nothing to indicate the true shape of the body. The orthographic approach suffers mainly from excessive redundancy since six orthogonal views are needed for good surface coverage. That number could increase for bizarre shapes such as toroidal or pretzel-like pierced forms which might result from prolonged deepening of active vents on comet nuclei. Bodies with a distinctly faceted shape, with roughly planar faces forming a shape more like a pyramid than a cube, might suffer from this approach if axis-fixed orthogonal views were always significantly oblique to one or more faces.

I have described a map projection system based on azimuthal projections in which the radius constant of the spherical projection is replaced with the local radius of the surface to be projected (2,3,4,5), ultimately inspired by the work of Ralph Turner (12). Any azimuthal projection can be modified in this way, giving as a minimum equal area, equidistant and conformal versions (Figure 3). The conformal version is the equivalent of the familiar Stereographic projection. For maps of a body divided into two 'hemispheres' the boundary of each half exactly reproduces the cross-sectional shape in the dividing plane, giving a good idea of the true shape and positions of features relative to that shape. Parallels and meridians follow topography and act as 'form lines', enhancing shape visualization. Because of these qualities this class of projection is called **morphographic**. Distortions are very much less severe in these maps than in unmodified cylindrical projections (4,5) and are minimized for an elongated object if maps of opposite 'hemispheres' are centred on the shorter axes rather than the longest.

In work undertaken to date (6,7) the projection has been applied to the actual shape of the body, so far as it can be determined by the modelling approach described above. This works well for bodies which correspond

reasonably well to a triaxial ellipsoid shape, with small craters or hills but no massive deviations from the smooth surface. It is less satisfactory in cases where a major concavity exists, such as the south polar 'saddle' of Deimos or the large and deep craters Pan and Gaea on Amalthea. The principal problem is that these projections are not 'unique'. A point's location is determined both by its angular distance from the origin of the projection and by the radius at that point. Along a single azimuth from the origin, two points with certain combinations of radius and angular distance may coincide. This is most severe when areas of high local relief occur near the boundary of the 'hemisphere'. A high ridge or crater wall may be projected outwards from the centre of the map to overlie a more distant depression, a phenomenon resembling layover in synthetic aperture radar (SAR) images. In lower relief areas crater bottoms are displaced towards the centre of the map by an amount related to angular distance from the centre of the map, and hilltops are displaced outwards, again similar to distortions in SAR images.

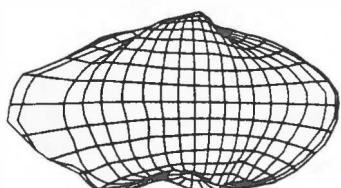
The 'layover' problem can be reduced by selecting a different morphographic projection. The conformal projection expands the outer part of each 'hemisphere' more than the equal area version, and reduces the effect, but this limits choice of projection. It is preferable to apply the desired projection to a different surface than the actual topography of the body. There are several possibilities. The simplest is to use the best fit triaxial ellipsoid as a projection surface. Topography is projected onto the triaxial ellipsoid along ellipsoid radii, and the ellipsoid is then projected according to the morphographic equations. This works well to give an impression of the degree of elongation of the body and the positions of features relative to the overall shape. Where the shape is poorly determined (e.g. speckle or HST images of asteroids with about 10 pixels across the disk) but substantial elongation is apparent this is probably the most desirable form of the projection to use. A better indication of overall shape can be obtained by using the three dimensional convex hull of the body as a projection surface. The global shape will be still better depicted if the projection is applied to the surface on which craters and steep hills or ridges are superimposed. This is obtained by extending the local surface across craters to roughly duplicate the pre-impact topography of the region, and by removing the most prominent hills and ridges. The largest concavities (e.g. south polar saddle of Deimos) would remain, but localized high relief would be smoothed over on the projected surface. The relief is removed from the surface which controls the projection, but would be portrayed on the map as a photomosaic or by contouring or relief shading. Various versions of a map grid for Amalthea illustrate this (Figure 4). The triaxial ellipsoid model is composite: the longest semi-axes are 150 km away from Jupiter and 120 km towards Jupiter. The b and c semi-axes are 75 and 70 km respectively. All grids in Figure 4 are conformal.

The shape-modelling method described above can be applied to any object for which low resolution data are acquired. The morphographic map projections are suitable for all non-spherical bodies including those whose shapes are more precisely known. Particularly significant uses include registering data obtained by different techniques (e.g. HST images and a radar convex hull) or at different oppositions (e.g. HST images of an asteroid centred at two different latitudes), and estimating local slopes to help interpret disk-resolved photometry. The results can be portrayed graphically as shown here, giving base maps for geological interpretation and aids to visualization of the object itself. To illustrate mapping options I present a shaded relief map of Amalthea with local radius contours (Figure 5) and an albedo province map of asteroid (4) Vesta (Figure 6). The Vesta map assumes the triaxial ellipsoid shape described by Drummond et al. (13), though a spherical form is probably preferable. The projection gives an equal area map of the triaxial ellipsoid. The albedo patterns are a composite of speckle images (13), lightcurve modelling (14) and rotational spectral variations (15). The letter labels are from ref. (13). This map is intended only to illustrate the projection and should not be interpreted as a definitive model of the albedo distribution on (4) Vesta.

- REFERENCES: (1) Greeley R., Batson R.M., eds (1990) Planetary Mapping. Cambridge University Press. (2) Stooke P.J. (1986) Automated cartography of non-spherical worlds. Proc. 2nd Internat. Symp. Spatial Data Handling, pp. 523-536. (3) Stooke P.J., Keller C.P. (1987) Morphographic projections for maps of non-spherical worlds. Lunar Planet. Sci. XVIII, pp. 956-957. Lunar and Planetary Institute, Houston. (4) Stooke P.J. (1988) Cartography of Non-Spherical Worlds. Ph.D. Diss., Univ. of Victoria. 169 pp. (5) Stooke P.J., Keller C.P. (1990) Map projections for non-spherical worlds - the variable radius projections. Cartographica 27 (2), 82-100. (6) Stooke P.J., Abergel A. (1991) Morphology of the nucleus of comet P/Halley. Astron. Astrophys. (in press). (7) Stooke P.J. (1991) A model and map of Amalthea. Earth, Moon, Planets (in press). (8) Duxbury T.C. (1974) Phobos: control network analysis. Icarus 23, 290-299. (9) Veverka J., Thomas P., Davies M., Morrison D. (1981) Amalthea: Voyager imaging results. Journ. Geophys. Res. 86, 8675-8692. (10) Snyder J.P. (1985) Conformal mapping of the triaxial ellipsoid. Survey Review 28, 130-148. (11) Planetary Cartography Working Group (1984) Planetary Cartography in the Next Decade (1984-1994). NASA SP-475, National Aeronautics and Space Administration, Washington D.C. (12) Turner R. (1978) A model of Phobos. Icarus 33, 116-140. (13) Drummond J., Eckart A., Hege E.K. (1988) Speckle interferometry of asteroids. IV. Reconstructed images of 4 Vesta. Icarus 73, 1-14. (14) Cellino A., Zappala V., Di Martino M., Farinella P., Paolicchi P. (1987) Flattening, pole, and albedo features of 4 Vesta from photometric data. Icarus 70, 546-565. (15) Gaffey M.J. (1983) The asteroid (4) Vesta: rotational spectral variations, surface material heterogeneity, and implications for the origins of the basaltic achondrites. Lunar Planet. Sci. XIV, pp. 231-232. Lunar and Planetary Institute, Houston.

Figure 1.
Amalthea model, orthographic views matching Voyager images.

Voyager 1 FDS 16377.32



Voyager 1 FDS 16381.47

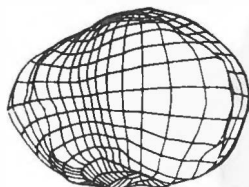
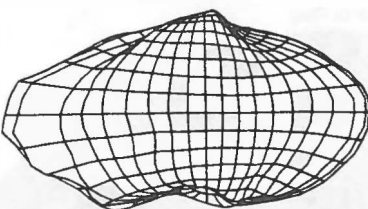


Figure 2.
Orthographic orthogonal views of the Amalthea model.
lat. 0° long. 90°



lat. 0° long. 0°

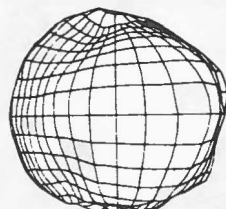


Figure 3.
Equal area (top) and conformal map grids for Amalthea.

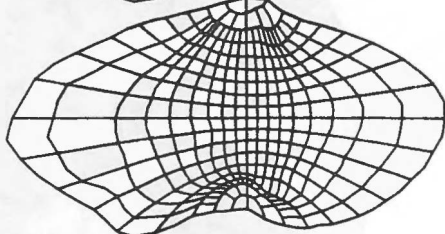
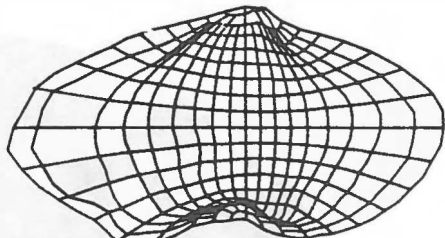


Figure 4.
Conformal map grids for one side of Amalthea, based on the best-fit triaxial ellipsoid model (see text) (left), convex hull of the topographic model (centre) and full topographic model (right). Grid on left is distorted by mismatch of true and model shape, grid on right by 'layover' on the rim of crater Gaea at the south pole.

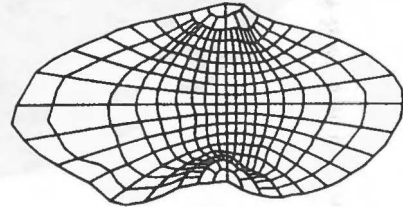
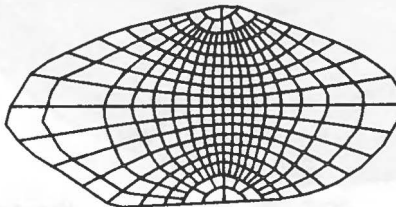
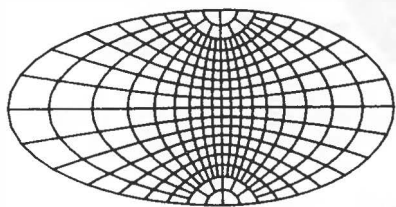


Figure 5.
Shaded relief map of Amalthea, morphographic conformal projection, with radius contours at 10 km intervals.

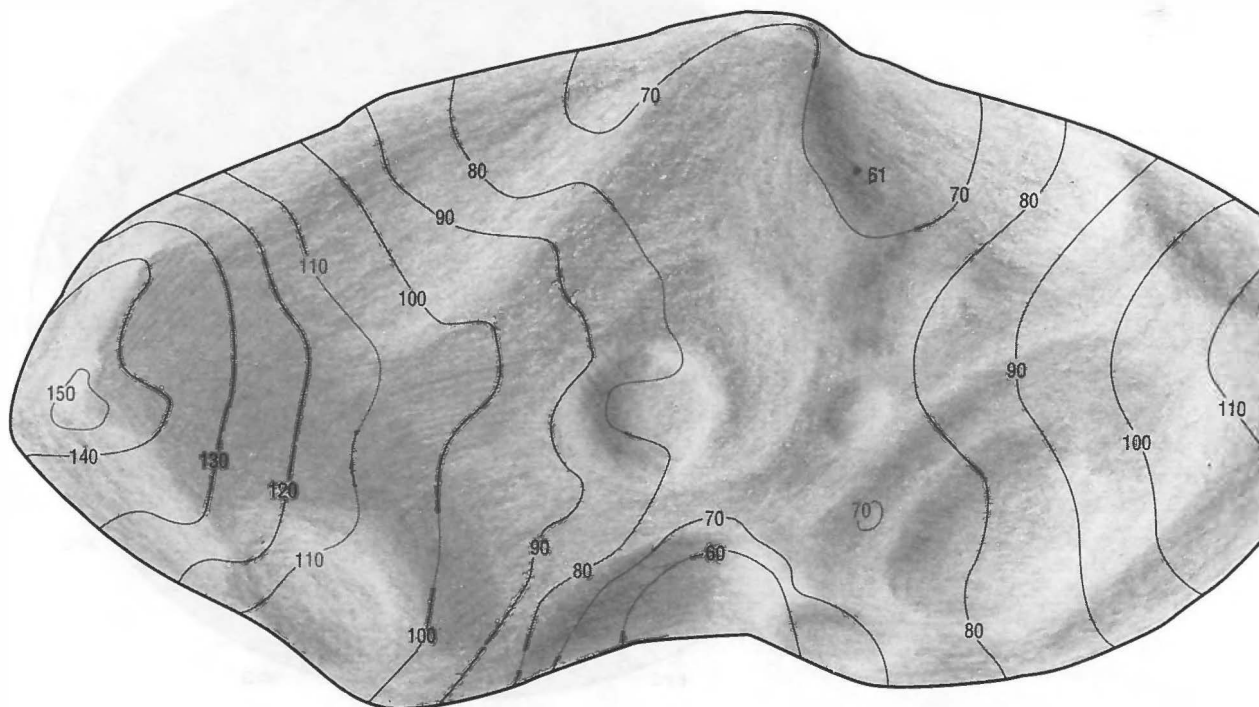
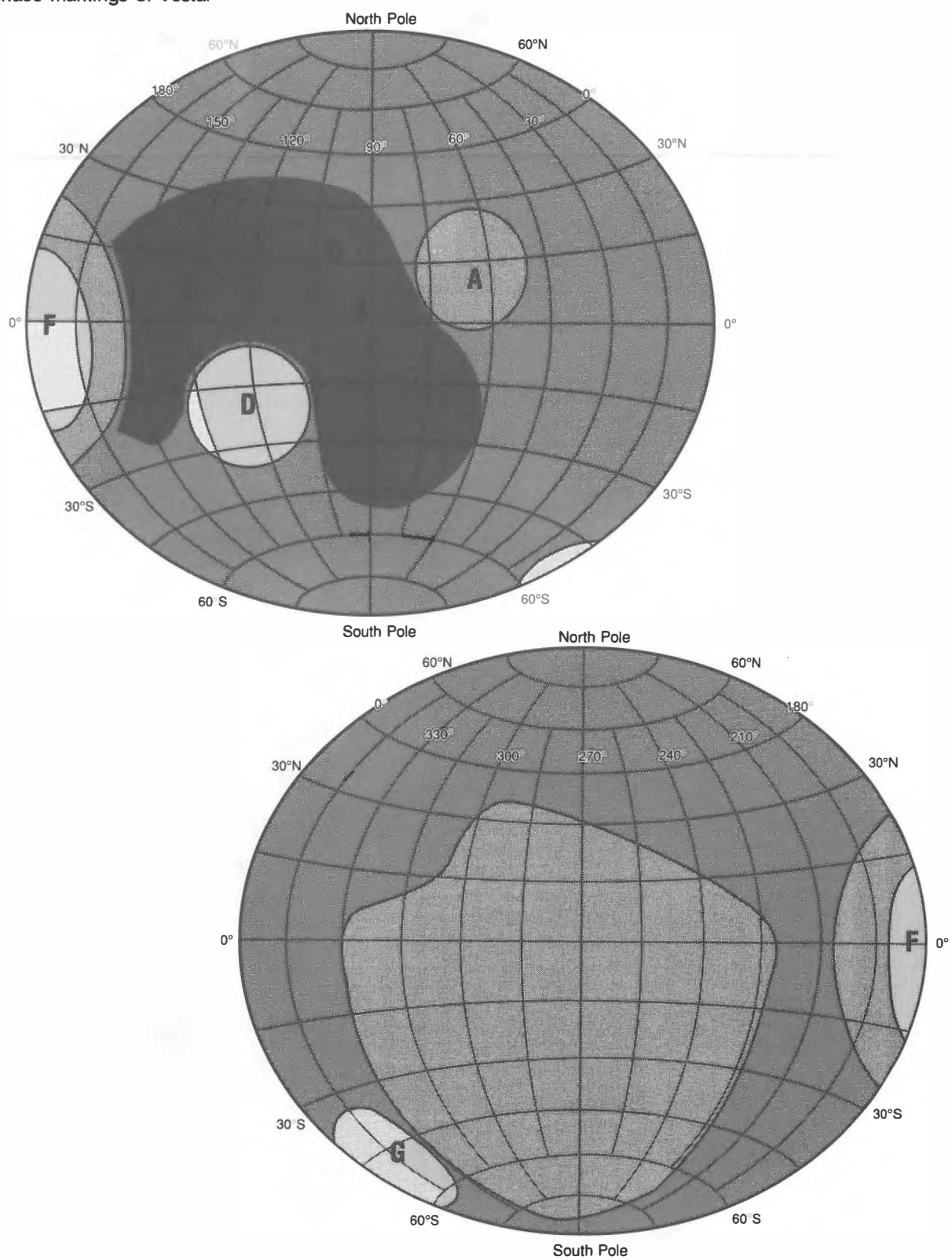


Figure 6.

Albedo provinces on asteroid (4) Vesta based on refs. 13,14,15. This is intended only to illustrate the projection, an equal area map of a triaxial ellipsoid (dimensions from ref. 13), not to be a definitive model of the shape or surface markings of Vesta.



THE NATURE OF COMET NUCLEI

Mark V. Sykes

Steward Observatory

University of Arizona

Tucson AZ 85721

Russell G. Walker

Jamieson Science and Engineering

5321 Scotts Valley Drive, Suite 204

Scotts Valley CA 95066

The icy-conglomerate model of comet nuclei has dominated all others since its introduction by Whipple (1950). It provided a basis for understanding the non-gravitational motions of comets which had perplexed dynamicists up to that time, and provided a focus for understanding cometary composition and origin. The image of comets as "dirty snowballs" was quickly adopted. Such images carried with it the notion that cometary surfaces must have high albedos, much like a snow-covered field in winter. This view began changing as it was realized that (1) comets were primitive bodies, (2) the most primitive meteoritic material, though most likely deriving from asteroids, was carbonaceous and dark, and (3) it only took a small amount of dark material to significantly reduce the albedo of ice (Clark 1982). Groundbased observations also suggested that comets might actually be dark objects (Hartmann *et al.* 1982; Cruikshank *et al.* 1985). This was dramatically confirmed when the *Giotto* and *Vega* spacecraft flew past the nucleus of Halley's comet in 1986. The nucleus was found to be so dark that it reflected only about 5% of the incident sunlight (Keller *et al.* 1986; Sagdeev *et al.* 1986).

So, how much of the dirty snowball is actually dirt?

Estimates based on mass-loss rates determined from gas and dust emissions observed from the Earth tended to place the refractory to volatile mass ratio between 0.1 and 1 (Greenberg 1982; Delsemme 1982). Thus, comets were primarily ice, both by mass and volume. The dust impact experiment on *Giotto* determined that there was a greater population of large particles than had been previously assumed - particles not easily seen at visual wavelengths from the ground. Based on these measurements it was estimated that Halley had a refractory to volatile mass ratio of 2 (McDonnell *et al.* 1991).

Recent analysis of comet dust trails, a phenomenon discovered by the *Infrared Astronomical Satellite* (Sykes *et al.* 1986a), suggests that the refractory to volatile mass ratio for short-period comets should be around 3 (Sykes and Walker 1991). Thus, a comet would be around 50% refractory material by volume (compressed) and 75% by weight. Such a mixture at outer-solar system temperatures would be best described as a frozen mudball.

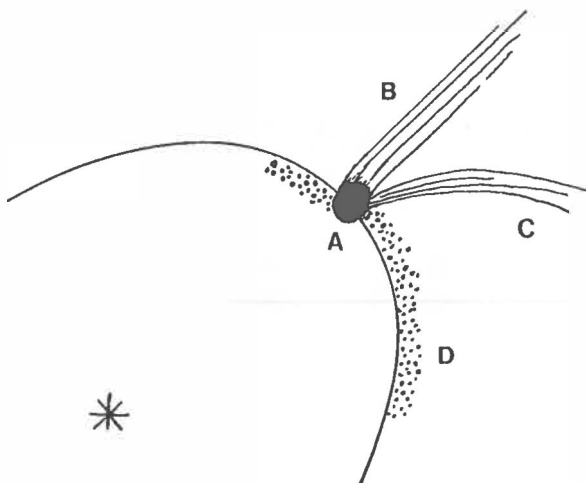


Figure 1. Comets generally exhibit a variety of phenomena at visual wavelengths including (a) the coma, (b) an ion tail, and (c) a dust tail. The *Infrared Astronomical Satellite* was the first to detect the comet dust trail (d) consisting of large particles moving slowly away from the nucleus along orbital paths very close to that of the parent comet (from Sykes and Walker 1991).

Trails are not to be confused with either cometary comae or tails (Fig. 1). They consist of large - mm to cm size - particles moving at velocities of meters/sec relative to their parent comet (Sykes *et al.* 1986b). Because of these low velocities and their relative insensitivity to radiation pressure, trails are found very close to the orbital path of their parent comet. They extend over only a portion of their parent orbit, always connected to the orbital position of the nucleus, and their lengths limited by the effects of gravitational perturbations (which can result in relatively sudden shifts in orbits independently for the parent comet and trail particles).

On the basis of an exhaustive survey of the IRAS data, giving consideration to observational selection effects in that data, we inferred that all short period comets have trails - though only 8 were detected at the time of the IRAS mission. The generality of the trail phenomenon is important, because what we learn about the specific trails observed may then be extended to the rest of the short-period comet population.

Mass loss rates have been calculated for trail particles and compared to total mass loss rates for the same comets on the basis of visual wavelength observations (Kresák and Kresáková 1987). These latter calculations assume a refractory/volatile mass ratio of 0.33, and consider the detailed orbital evolution of these comets over the past 100 years. They are compared to the trail mass loss rates in Figure 2. In each case it is found that the trail mass loss rates exceed those based on estimates of gas production and small dust particles. This suggests that trails are a significant if not principal mechanism of mass loss in short-period comets (Sykes and Walker 1991).

Trail particles are quickly devolatilized in the inner solar system (Lien 1990) and therefore consist of purely refractory particles. Such large mass loss rates in refractory particles implies a much larger fraction of the nucleus consists of refractory material than

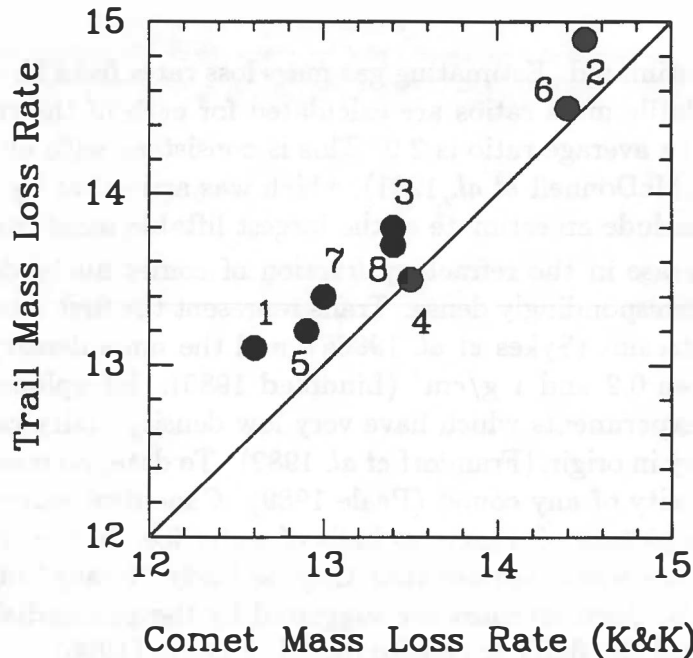


Figure 2. Trail mass loss rates determined by Sykes and Walker (1991) compared to total comet mass loss rates as determined by Kresak and Kresakova (1987) for (1) Churyumov-Gerasimenko, (2) Encke, (3) Gunn, (4) Kopff, (5) Pons-Winnecke, (6) Schwassmann-Wachmann 1, (7) Tempel 1, and (8) Tempel 2. Units are in Log (grams/century).

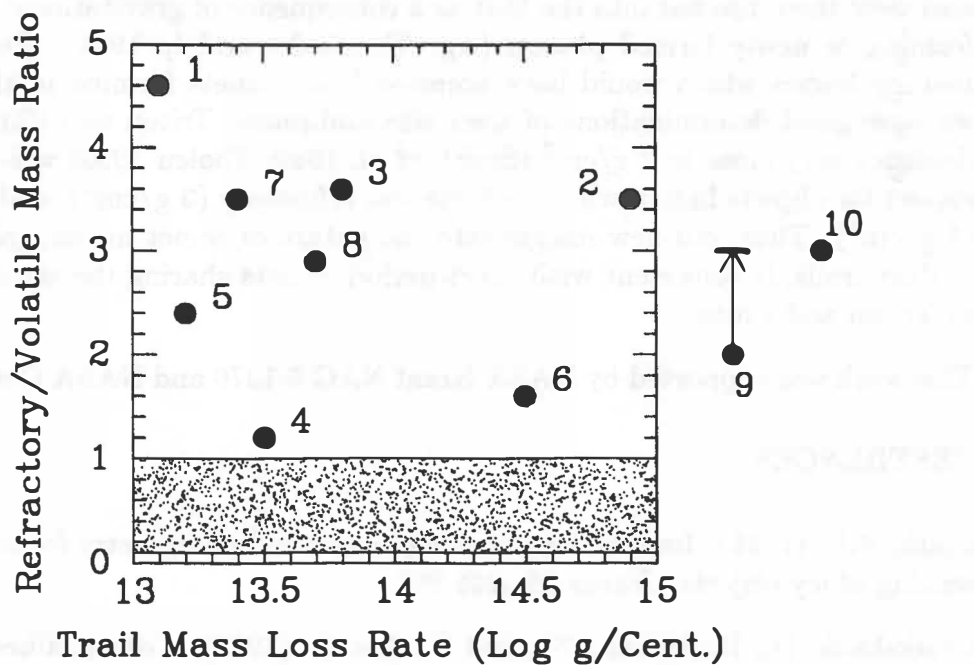


Figure 3. Refractory to volatile mass ratios are shown for trail comets as enumerated above. For comparison, values are shown for (9) Halley (McDonnell *et al.* 1991) and (10) Pluto and Triton (see text). The shaded area spans the canonical ratios between 0.1 and 1.

had previously been estimated. Estimating gas mass loss rates from Kresák and Kresáková (1987), refractory/volatile mass ratios are calculated for each of the trail comets and are shown in Figure 3. The average ratio is 2.9. This is consistent with an upper limit of ~ 3 estimated for Halley (McDonnell *et al.* 1991), which was arrived at by extrapolating their size distributions to include an estimate of the largest liftable mass from the surface.

Such a large increase in the refractory fraction of comet nuclei does not necessarily mean that they are correspondingly dense. Trails represent the first stage in the dynamical evolution of meteor streams (Sykes *et al.* 1986a), and the mass density of meteor stream particles range between 0.2 and 1 g/cm³ (Lindblad 1986). Interplanetary dust particles collected by aircraft experiments which have very low density "fairy-castle" structure are thought to be cometary in origin (Frandorf *et al.* 1982). To date, no meaningful constraints exist for the mass density of any comet (Peale 1989). Canonical values of ~ 1 g/cm³ are based on the intuitive picture of comets as balls of water ice. In the case of comets being "mudballs" low densities would require that they be fairly "foamy" objects with a lot of interior spaces or voids. Such interiors are suggested by the primordial rubble pile model of Weissman (1986) and the fluffy aggregate model of Donn (1990).

A large refractory/volatile ratio reinforces current ideas about the formation location of short-period comets. Dynamical studies (Duncan *et al.* 1988) suggest that short-period comets come from the Kuiper Belt which is hypothesized as a disk of comets extending from about 30 to over 100 AU from the Sun. The Kuiper Belt itself is thought to have been populated primarily by comets which formed in the region of Uranus and Neptune and were then injected into the Belt as a consequence of gravitational encounters with the forming or newly formed planets (e.g. Fernández and Ip 1981). Fortunately, there are two icy bodies which would have accreted from comets forming in this region for which we have good determinations of their size and mass: Triton and Pluto. Both have mass densities very close to 2 g/cm³ (Smith *et al.* 1989; Tholen 1990) which is what we would expect for objects half of whose volume was refractory (3 g/cm³), and the other half is ice (1 g/cm³). Thus, our new insight into the nature of comet nuclei, gained from the study of dust trails, is consistent with short-period comets sharing the same formation location as Triton and Pluto.

This work was supported by NASA Grant NAG 5-1370 and NASA Contract NAS 5-30772.

REFERENCES

- Clark, R.N. (1982). Implications of using broadband photometry for compositional remote sensing of icy objects. *Icarus* **49**, 244-257.
- Cruikshank, D., Hartmann, W., and Tholen, D. (1985). Colour, albedo, and nucleus size of Halley's comet. *Nature* **315**, 122-124.
- Delsemme, A. (1982). Chemical composition of cometary nuclei. In *Comets* (L. Wilkening, ed.), pp. 85-130. University of Arizona Press, Tucson.
- Donn, B. (1990). The formation and structure of fluffy cometary nuclei from random accumulation of grains. *Astron. Astroph.* **235**, 441-446.

- Duncan, M., Quinn, T., and Tremaine, S. (1988). The origin of short-period comets. *Astroph. J.* **328**, L69-L73.
- Fernández, J.A. and Ip, W.-H. (1981). Dynamical evolution of a cometary swarm in the outer planetary region. *Icarus* **47**, 470-470.
- Fraundorf, P., Brownlee, D., and Walker, J. (1982). Laboratory studies of interplanetary dust. In *Comets* (L. Wilkenning, ed.), pp. 383-409. University of Arizona Press, Tucson.
- Greenberg, J. (1982). What are comets made of? A model based on interstellar dust. In *Comets* (L. Wilkenning, ed.), pp. 131-143. University of Arizona Press, Tucson.
- Hartmann, W., Cruikshank, D., and Degewij, J. (1982). Remote comets and related bodies: VJHK colorimetry and surface materials. *Icarus* **52**, 377-408.
- Keller, H. (16 Co-authors) (1986) First Halley Multicolour Camera imaging results from Giotto. *Nature* **321**, 320-325.
- Kresák, L. and Kresáková, M. (1987). The mass loss rates of periodic comets. In *Symposium on the Diversity and Similarity of Comets*, pp. 739-744. ESA SP-278.
- Lien, D. (1990). Dust in comets I. Thermal properties of homogeneous and heterogeneous grains. *Astroph. J.* **335**, 680-692.
- Lindblad, B.A. (1976). Meteoroid densities. In *Interplanetary Dust and Zodiacal Light* (H. Elsasser and H. Fechtig, eds.), pp. 373-378, Springer-Verlag, New York.
- McDonnell, J.A.M., Lamy, P., and Pankiewicz, G. 1991. Physical properties of cometary dust. In *Comets in the Post-Halley Era* (R. Newburn, ed.), pp. 1013-1043. Kluwer, Dordrecht.
- Peale, S.J. (1989). On the density of Halley's comet. *Icarus* **82**, 36-49.
- Sagdeev, R. (6 Co-authors) (1986) Television observations of comet Halley from Vega spacecraft. *Nature* **321**, 262-266.
- Smith, B. (64 Co-authors) (1989). Voyager 2 at Neptune: Image science results. *Science* **246**, 1422-1449.
- Sykes, M. and Walker, R. (1991). Cometary dust trails I. Survey. Submitted to *Icarus*.
- Sykes, M., Lebofsky, L., Hunten, D., and Low, F. (1986a). The discovery of dust trails in the orbits of periodic comets. *Science* **232**, 1115-1117.
- Sykes, M., Hunten, D. and Low, F. (1986b). Preliminary analysis of cometary dust trails. *Adv. Sp. Res.* **6**, 67-78.
- Tholen, D. (1990). Further analysis of Pluto-Charon mutual event observations - 1990. *Bull. Am. Astr. Soc.* **22**, 1129.
- Weissman, P. (1986). Are cometary nuclei primordial rubble piles? *Nature* **320**, 242-244.
- Whipple, F. (1950). A comet model I. The acceleration of comet Encke. *Astrophys. J.* **111**, 375-394.

FORCED PRECESSION OF THE COMETARY NUCLEUS WITH RANDOMLY PLACED ACTIVE REGIONS

Sławomira Szutowicz

Space Research Centre, Bartycka 18, 00-716 Warszawa, Poland

ABSTRACT

The cometary nucleus is assumed to be triaxial or axisymmetric spheroid rotating about its axis of maximum moment of inertia and is forced to precess due to jets of ejected material. Randomly placed regions of exposed ice on the surface of the nucleus are assumed to produce gas and dust. The solution of the heat conduction equation for each active region is used to find the gas sublimation rate and the jet acceleration. Precession of the comet nucleus is followed numerically using a phase-averaged system of equations. The gas production curves and the variation of the spin axis during the orbital motion of the comet are presented.

MODEL

The cometary nucleus is modelled as a rotating, triaxial or axisymmetric ellipsoid that precesses under the torque from gas and dust jets escaping from active spots on its surface. The activity of these regions is controlled by time dependent insolation which is a function of the zenith angle of the Sun (changing due to the nucleus rotation) and the heliocentric distance of the comet nucleus. The insolation function describes the solar energy influx and is included in the energy balance equation on the nucleus surface as one of the boundary condition for the heat conduction equation. The heat conduction equation is solved for each active region. The obtained solution i.e. the surface temperature distribution is then used to calculate the sublimation flux of H₂O molecules and the jet acceleration. The jet acceleration from the outgassing acting on the nonspherical nucleus produces the torque. The nucleus rotates about its axis of maximum moment of inertia (C) and its rotational axis is forced to precess. The precession of the spin axis produces changes in the pattern of the insolation of any region on the nucleus surface which, in turn affect the magnitude of the torque. To describe the precessing motion of the nucleus a phase-averaged system of equation is used (Julian, 1988) in which the torque is averaged over a rotation and a nutation is suppressed. Then the rate of change of averaged angular momentum is of the form:

$$C\omega \frac{d\mathbf{u}}{dt} = l(\mu)\mathbf{u} \times \mathbf{F}$$

where: ω is the angular velocity magnitude, \mathbf{u} is the unit vector in the direction of the rotation axis, $l(\mu)$ is function of cometographic latitude (μ) of point of integrated outgassing and \mathbf{F} is the reaction force of the jet. The phase averaging allows to extend the precession model of Whipple-Sekanina (1979) as applied to an oblate comet nucleus on the prolate and triaxial ones.

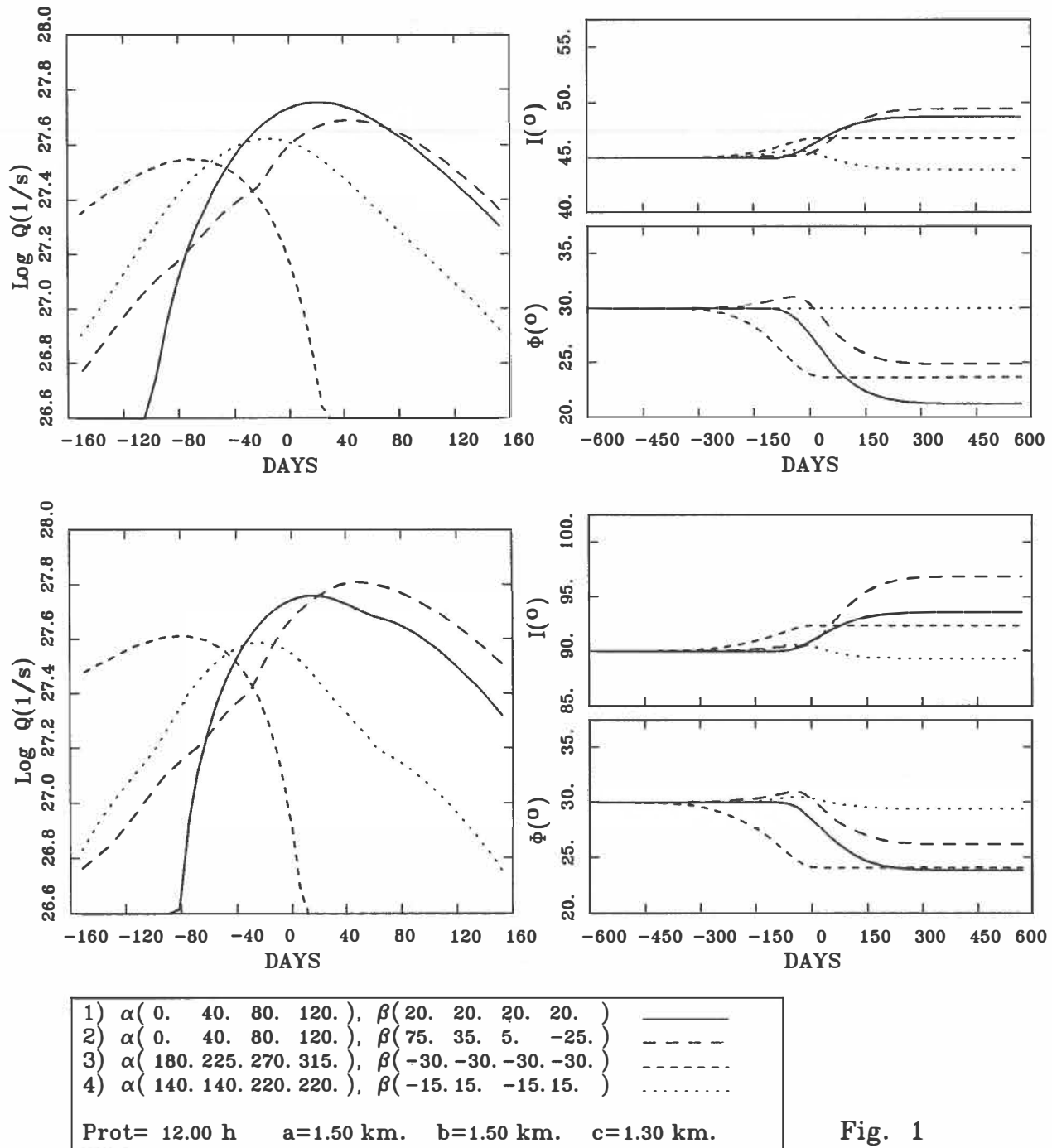


Fig. 1

Figs. 1, 2, 3, 4. The gas production rate (Q) and the orientation of the spin axis (I, Φ) with respect to the orbital plane as a function of time (relative to perihelion passage). Each curve shows the results for the comet nucleus with 4 active regions which positions are prescribed by cometocentric longitude α and latitude β . The rotational period P_{rot} and the size (a, b, c) of the comet nucleus are given.

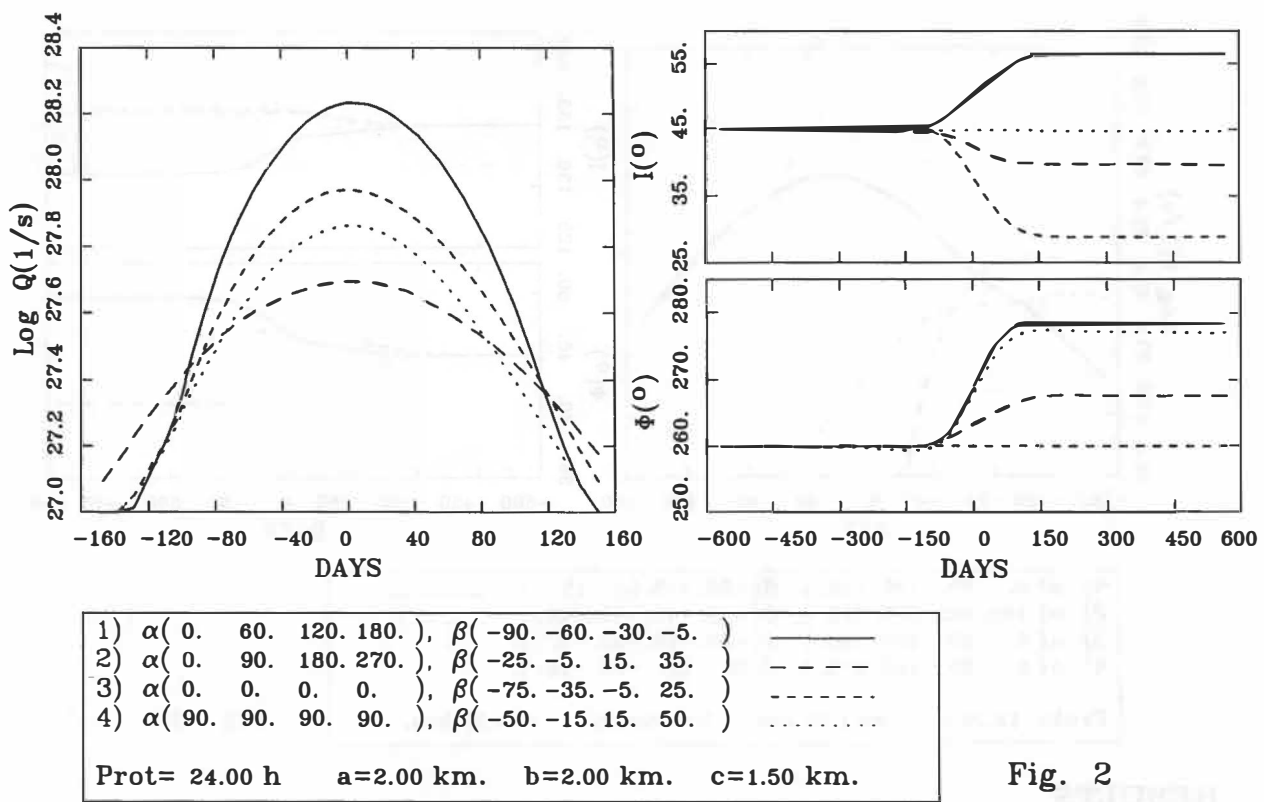


Fig. 2

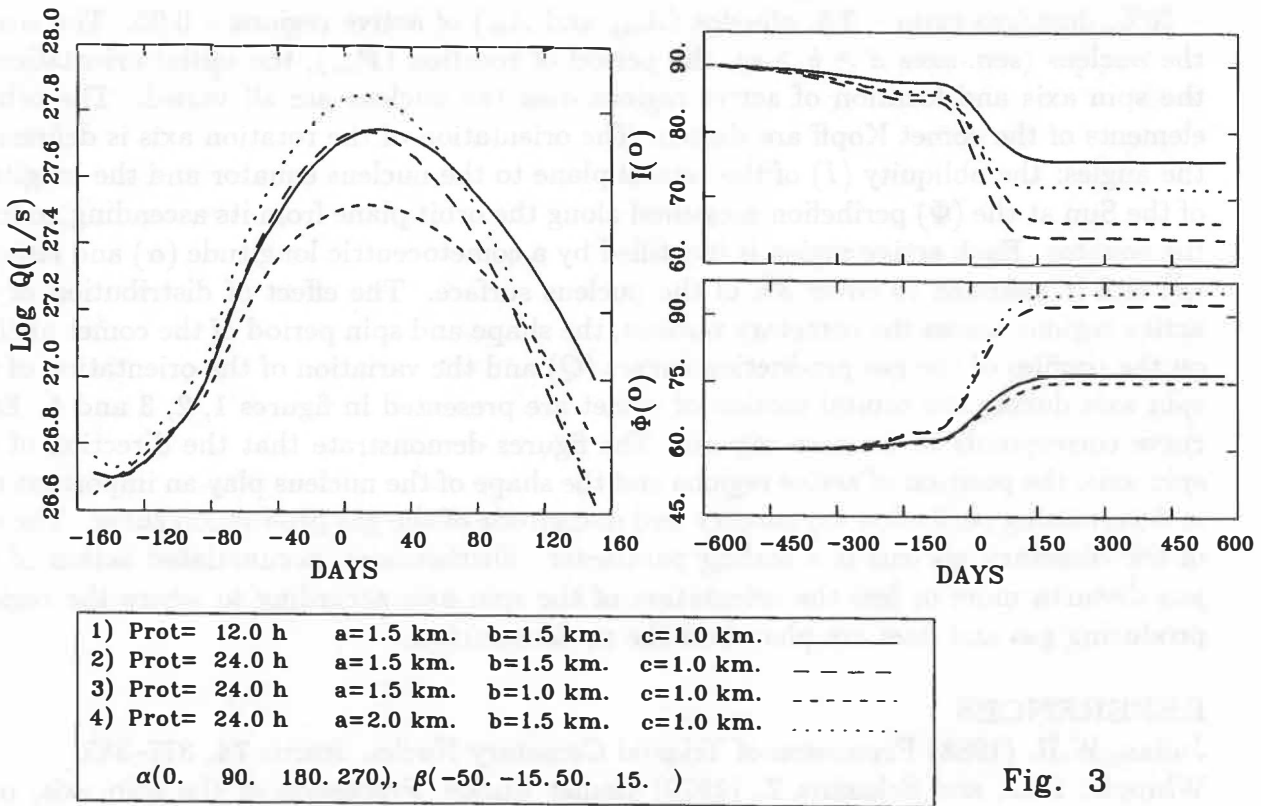


Fig. 3

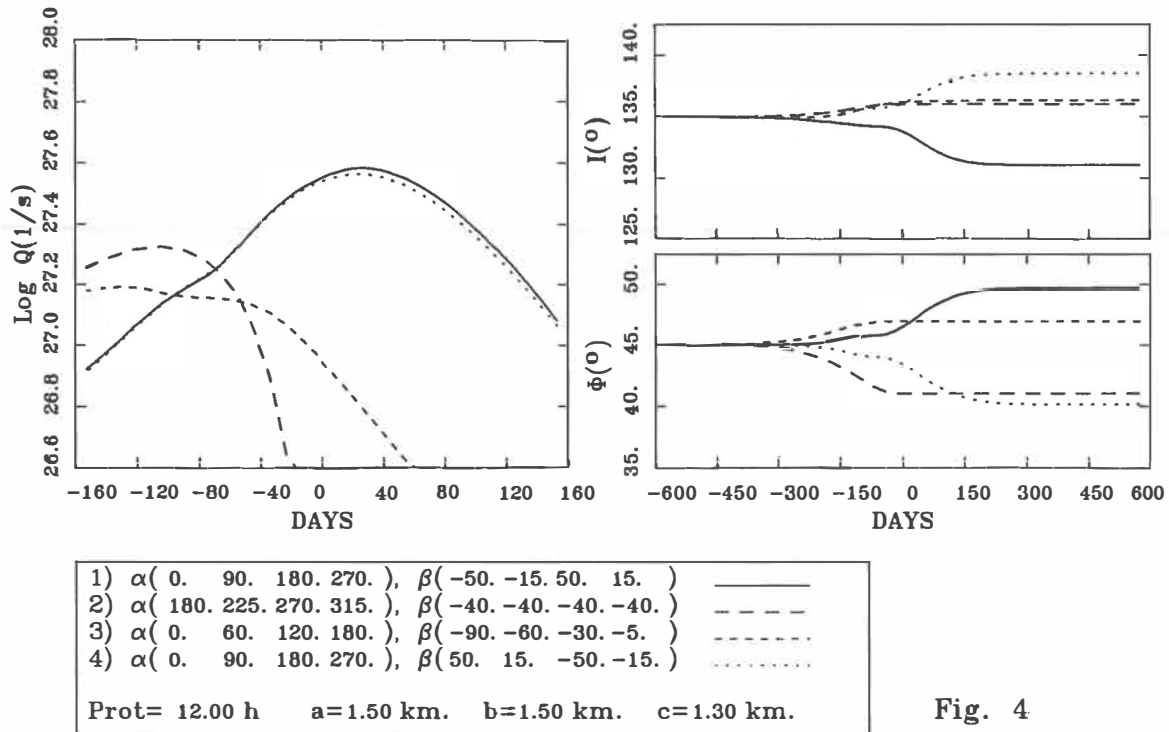


Fig. 4

RESULTS

Obtained results are based on models computed with the following physical parameters of the nucleus: density $\rho = 0.6 \text{ g/cm}^3$, thermal inertia $I_t = 1000 \text{ W s}^{1/2} \text{ m}^{-2} \text{ K}^{-1}$, CO contents – 10%, dust/gas ratio – 0.5, albedos (A_{vis} and A_{ir}) of active regions – 0.05. The size of the nucleus (semiaxes $a \geq b \geq c$), the period of rotation (P_{rot}), the initial orientation of the spin axis and location of active regions over the nucleus are all varied. The orbital elements of the comet Kopff are chosen. The orientation of the rotation axis is defined by the angles: the obliquity (I) of the orbital plane to the nucleus equator and the longitude of the Sun at the (Φ) perihelion measured along the orbit plane from its ascending node on the equator. Each active region is identified by a cometocentric longitude (α) and latitude (β) and is assumed to cover 3% of the nucleus surface. The effect of distribution of the active regions across the cometary nucleus, the shape and spin period of the comet nucleus on the profiles of the gas production curves (Q) and the variation of the orientation of the spin axis during the orbital motion of comet are presented in figures 1, 2, 3 and 4. Each curve corresponds to 4 active regions. The figures demonstrate that the direction of the spin axis, the position of active regions and the shape of the nucleus play an important role in determining perihelion asymmetry and magnitude of the gas production curve. The size of the cometary nucleus is a scaling parameter. Furthermore, accumulated action of the jets disturbs more or less the orientation of the spin axis according to where the regions producing gas and dust are placed on the nucleus surface.

REFERENCES

- Julian, W.H. (1988) Precession of Triaxial Cometary Nuclei. *Icarus* **74**, 377–382.
 Whipple, F.L., and Sekanina Z. (1979) Comet Encke: Precession of the spin axis, non-gravitational motion, and sublimation. *Astron. J.* **84**, 1894–1909.

VELOCITY DISTRIBUTION OF FRAGMENTS OF CATASTROPHIC IMPACTS

Yasuhiko Takagi
Toho Gakuen Junior College
Manabu Kato
Nagoya University
Hitoshi Mizutani
Institute of Space and Astronautical Science

ABSTRACT

Three dimensional velocities of fragments produced by laboratory impact experiments were measured for basalts and pyrophyllites. The velocity distribution of fragments obtained shows that the velocity range of the major fragments is rather narrow, at most within a factor of 3 and that no clear dependence of velocity on the fragment mass is observed. The NonDimensional Impact Stress (NDIS) defined by Mizutani et al. (1990) is found to be an appropriate scaling parameter to describe the overall fragment velocity as well as the antipodal velocity.

INTRODUCTION

Size distribution, velocity distribution, and energy partition of fragments produced by catastrophic collision are important for understanding process of planetary growth. The experimental data relevant to this problem, however, is not sufficient due to some experimental difficulties. Recently Nakamura and Fujiwara (1991) determined three dimensional velocities of some tens of fragments produced by a catastrophic impact experiments. Their result shows that the fragment velocities are proportional to $m^{-1/6}$, where m is the fragment mass. The present study reports results of our new impact experiments where the impact velocities are set to be lower than those in Nakamura and Fujiwara (1990).

EXPERIMENTAL METHODS

Impact experiments were performed by a single-stage powder gun at Nagoya University. Projectiles of cylindrical aluminums 1.0 cm in diameter and length were impacted to targets of cubic basalts and pyrophyllites. The experimental conditions are listed in Table 1.

Table 1. Experimental Conditions

Target	Material	v^* (m/s)	Mass (g)	Projectile Mass (g)	Impact Velocity (m/s)	Impact Energy (J)	Impact		
							NDIS	m_L/M_t	$\Sigma m/M_t$
# 1	Basalt	33.8	50.71	7.56	143	77.3	0.333	0.131	0.737
# 2	Basalt	33.8	139.8	7.59	140	74.4	0.119	0.825	0.940
# 3	Pyrophyllite	8.98	323.7	2.23	413	190.2	0.216	0.296	0.978
# 4	Pyrophyllite	8.98	339.1	2.25	653	479.7	0.344	0.141	0.809

v^* : characteristic velocity of target material (see text), m_L : largest fragment mass, M_t : target mass, Σm : total mass of fragment whose velocity could be measured.

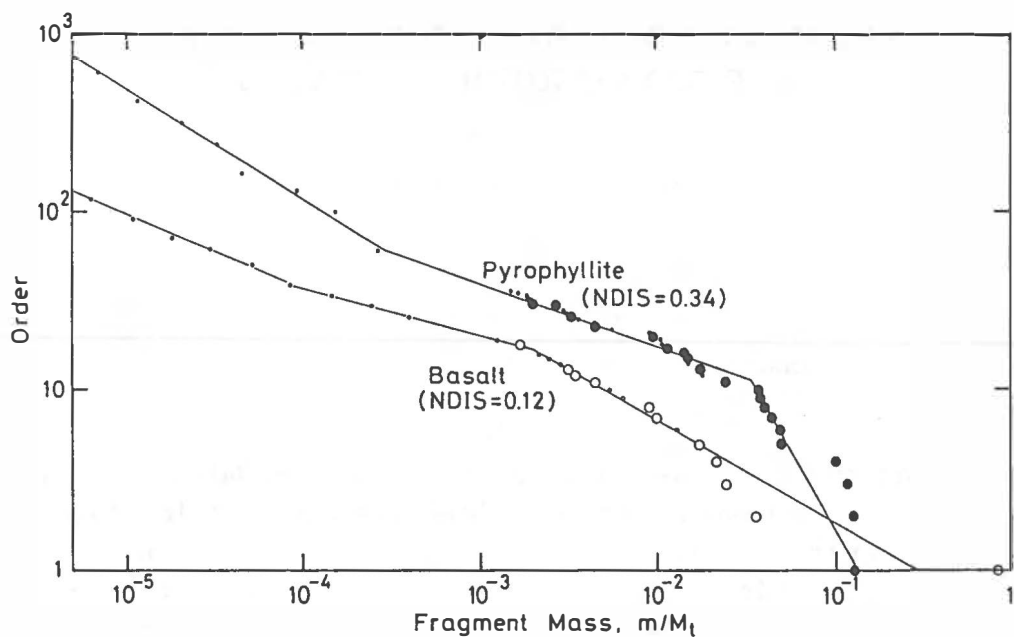


Fig. 1. The relation of the fragment mass normalized by the original target mass and the fragment order in size (= the cumulative number of fragments heavier than the mass). The large marks indicate fragments whose velocities could be measured.

Motions of fragments were recorded by a high-speed motion camera in 1500 to 3000 frame/sec. Four mirrors were set in front of the lens in order to obtain the stereographic picture of the fragment motions. Three dimensional position of fragments were obtained from the stereographic picture for each frame of the motion pictures and the velocity of fragment were determined by the least-squares fitting of the position-time data. The estimated error of the velocity determination is within 17 % of the determined velocity. Fragments containing more than 97.5 % of the mass of the target were recovered after the experiment and the mass of each fragment larger than 4 mm was measured to determine the size distribution of the fragments.

RESULTS

Figure 1 shows size distributions of fragments obtained in the present two experiments. As described in our earlier papers (Takagi *et al.*, 1984; Mizutani *et al.*, 1990), the size distribution curves are divided into three regimes. The large marks in the figure indicate fragments whose velocities could be measured. Almost all the velocities of fragments in the regime I were measured. The total mass of fragments whose velocities could be measured is 74 to 98 percent of the initial target mass.

Figure 2 shows the velocity of each fragment as a function of its mass. In this figure, fragment velocities are normalized by the characteristic velocity of the target material (Mizutani *et al.*, 1990), $v^* = Y/C_0 \rho$, where Y , C_0 , and ρ are the strength, bulk sound velocity, and density of the target, respectively. Fragment masses are also normalized by the original target mass, M_t .

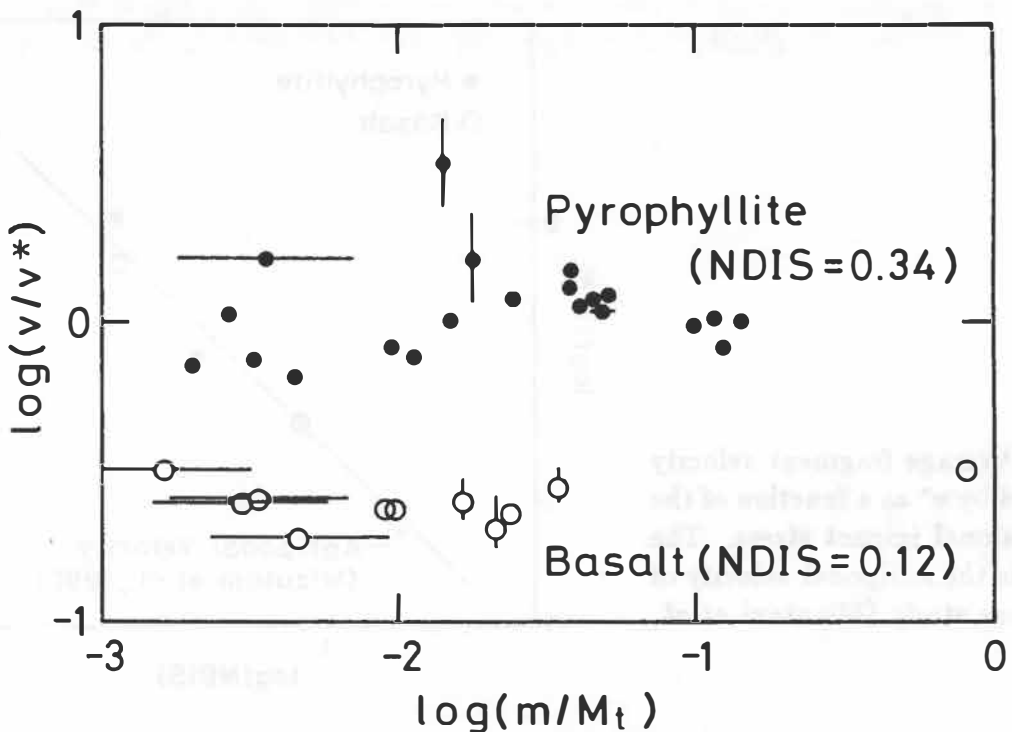


Fig. 2. Mass-velocity relations of fragments. Circles with horizontal error-bar show the data on images which were not identified with recovered fragments. The masses of these fragments were estimated from the projected areas on the film.

It is the most remarkable in Fig. 2 that the velocity range of fragments is rather narrow, at most within a factor of 3. This result is contradictory to Nakamura and Fujiwara's result, where they found the fragment velocity correlates with the mass as a manner of $v \propto m^{-1/6}$. Although we need further research to understand why we obtained different results from Nakamura and Fujiwara's result, possible sources of the difference must be sought for different experimental condition, i.e. impact velocity, size range of fragments, and others.

Figure 3 shows the average (weighted by the mass) fragment velocity normalized by the characteristic velocity, v^* . The result suggests that the $v/v^* - \text{NDIS}$ relation is an appropriate scaling law to describe the overall fragment velocity as well as the antipodal velocity. On the other hand, this result shows that the energy partition to kinetic energy of basalt fragments is an order of magnitude larger than that of pyrophyllite fragments, because the normalizing velocity, v^* , of basalt is four times larger than that of pyrophyllite.

SUMMARY

The present results show that the fragment velocity is controlled by our scaling parameter of NDIS. The observation in turn suggests fragment velocity is not simply controlled by surface energy as discussed by Nakamura and Fujiwara (1991) but is controlled by impact shock strength and physical properties of the target (Mizutani *et al.*, 1990). At any rate, further experimental studies are necessary for better understanding impact

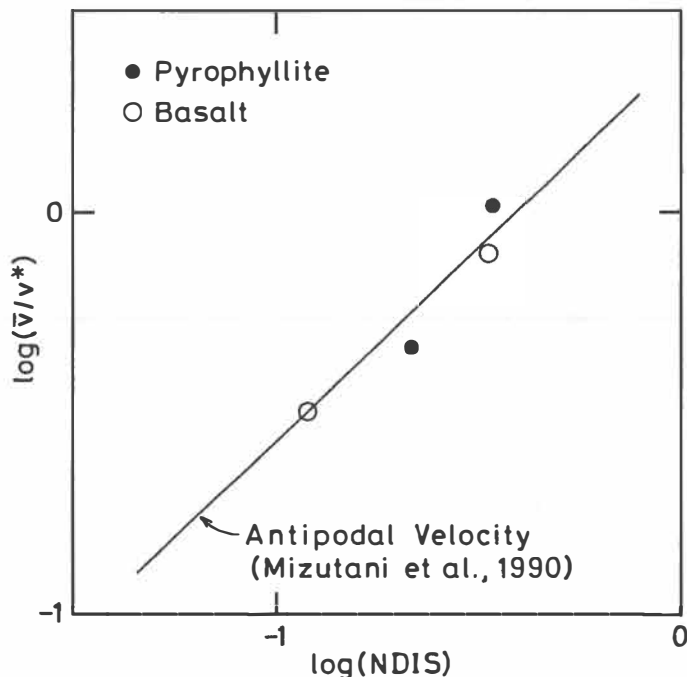


Fig. 3. Average fragment velocity normalized by v^* as a function of the nondimensional impact stress. The solid line is the antipodal velocity of the previous study (Mizutani *et al.*, 1990).

fragmentation process. The present method using a stereographic high-speed camera will provide a useful and power means for this purpose.

Acknowledgment

This study was supported by Grant-in-Aid for General Scientific Research (No. 03640364) and for Scientific Research on Priority Areas (No. 03232207) from the Ministry of Education, Science, and Culture, Japan.

References

- Mizutani H., Takagi Y., and Kawakami S. (1990) New scaling law on impact fragmentation, *Icarus*, 87, 307–326.
- Nakamura A. and Fujiwara A. (1991) Velocity distribution of fragments formed in simulated collisional disruption, *Icarus*, 92, 132–146.
- Takagi, Y., Mizutani H., and Kawakami S. (1984) Impact fragmentation experiments of basalts and pyrophyllites *Icarus*, 59, 462–477.

The vicinity of Jupiter : a region to look for comets

G. Tancredi ^{1,2} and M. Lindgren ¹

¹ Astronomiska Observatoriet, Box 515, S-75120 Uppsala, Sweden

² Dept. Astronomía, Fac. de Ciencias, Montevideo, Uruguay

ABSTRACT

Low-relative velocity and long-lasting encounters can dramatically change the orbital elements of a comet; the object could be temporarily bound to Jupiter for a period of several years.

It is well stated that most of the discoveries of comets occurred just after a close encounter with the planet and a decrease of the perihelion distance of the comet. So, why don't we look for comets during close encounters with Jupiter rather than wait to find them afterwards? To estimate the feasibility of this proposal we have made dynamical computations and observational analysis of the Jupiter family of comets. A criterion to distinguish comets during an encounter from other moving objects in the field is discussed.

THE SPACE DISTRIBUTION OF JUPITER-FAMILY COMETS

Kresák (1979) made a first attempt to look at the space distribution of asteroids and comets and found a few interesting patterns not observed in the usual orbital elements phase-space where we study these objects. We made numerical integrations of the whole sample of Jupiter family (hereafter JF) comets (143 short-period comets with $P < 20$ yr) to have a new look into the problem and in particular to analyze the distribution of objects on different regions of the Solar System. We integrated each comet and the nine planets at a time, starting at J.D. 2448000.5 for 200 yr into the past (for more details about the integration method see Tancredi and Rickman 1991, hereafter TR). At every 500 days the heliocentric positions and velocities of the objects were stored.

We were interested in the positional distribution of comets at any time. As JF comets have low inclinations, we took the ecliptic plane as the reference plane and divided the plane into square boxes of 1 AU. Cubes of 1 AU centered on these boxes were considered to compute the mean number of comets inside each cube at any time. In Fig. 1 we present a grey-scale picture of the observed distribution, where the darkest point corresponds to a density of 1 obj/AU³. The orbit of Jupiter with its perihelia and apsidal lines is superposed. We can see a "crater-like" structure, with a slight increase of the density of comets towards the orbit of Jupiter. This is naturally explained considering that JF comets tend to have their aphelia in the range 5 to 7 AU where they spend most of their time.

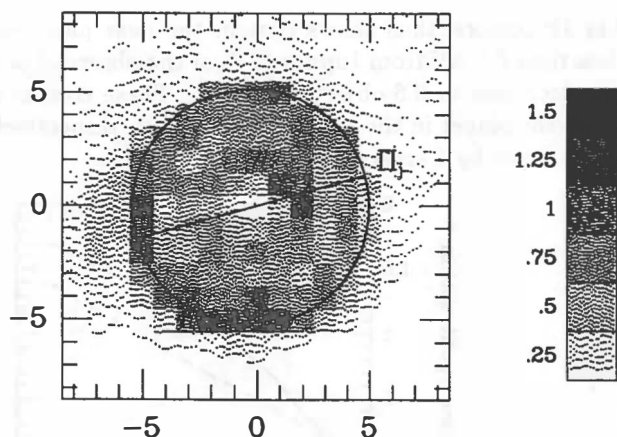


Fig. 1. Grey-scale picture of the positional distribution of observed short-period comets at any time in ecliptic-fixed frame. The orbit of Jupiter with its perihelion and apsidal line is superposed.

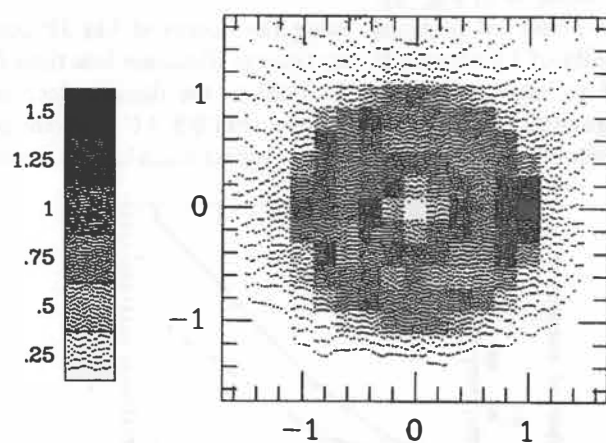


Fig. 2. Grey-scale picture of the positional distribution of observed short-period comets at any time in a rotating-pulsating frame with Jupiter fixed (unit distance = distance Jupiter-Sun).

As Jupiter is the main body responsible for shaping the distribution of JF comets, we plotted the distribution of objects in a more appropriate frame : a rotating-pulsating frame, with the instantaneous distance Jupiter-Sun as unit distance and the instantaneous Jupiter's angular velocity as the rotating velocity. In this frame the Sun is at the centre and Jupiter is always at $x = 1$, $y = 0$. Fig. 2 shows a grey-scale picture of the space distribution. The "crater rim" observed in Fig. 1 almost shrinks to a point, i.e. Jupiter's position; where the density reaches a value of 1.4 obj/AU³.

The importance of this finding is that we do not only constrain the position where comets tend to concentrate but we also constrain their velocities, because, as we will show later, the relative velocities to Jupiter are generally low.

The previous density values give only a rough estimate of the number of comets close to Jupiter at any time, computed by making an average over the last 200 yr. Most comets have been discovered just after a close encounter with Jupiter (Karm and Rickman 1982, TR), when their perihelion distance decreased. In addition to this point, when we plot the distribution of number of encounters at distances < 0.5 AU from Jupiter during the past and future 1000 yr for the whole sample of observed JF comets (TR), we see a peak at the present time (Fig. 3).

It is obvious that the observed JF comets is a biased sample of the whole population in the sense that we have a preponderance of comets that have experienced a close encounter in the near past. Due to the chaotic behaviour of the majority of short-period comets orbits, if we integrate the observed population for a long enough period of time, the successive encounters with Jupiter will randomize the orbital distribution and we would obtain a closer representation of the whole sample. We will compare the figures obtained averaging over the last 1000 yr and the ones obtained for the last 40 yr (when the discovery rate of JF comets has had a dramatic increase, TR).

In Fig. 4 we plot the number of comets at any time within a certain distance D to Jupiter as a function of this distance (the full-line corresponds to the average over the last 40 yr, the dashed-line over the last 1000 yr). Although at greater minimum distances to the planet the number of encounters increases, the duration of these encounters does not have a steep increase. This fact is shown in Fig. 5, where we plot the time a comet spends within a certain distance D to Jupiter as a function of this distance (full and dashed-lines are the same as in Fig. 4).

These calculations, using the observed 143 JF comets, then shows that in the near past there was a density of 1.5 objects at any time at distances less than 0.5 AU from Jupiter (1 % of the observed population) and averaging over the last 1000 yr the density decreases to 0.6 objects (0.4 %). These comets spend an average time of 1.1 and 0.7 yr within 0.5 AU from the planet in the last 40 and 1000 yr, respectively. These numbers agree quite well with similar calculations made by Carusi et al. (1985).

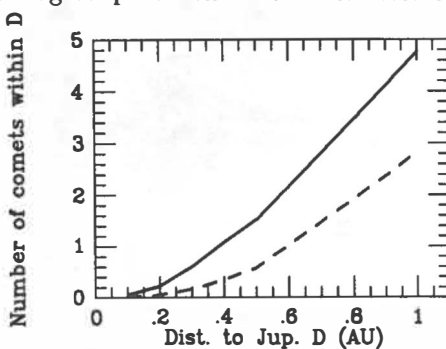


Fig. 4. Number of comets at any time within a certain distance D to Jupiter as a function of this distance (full-line : average over the last 40 years, dashed-line : average over last 1000 years).

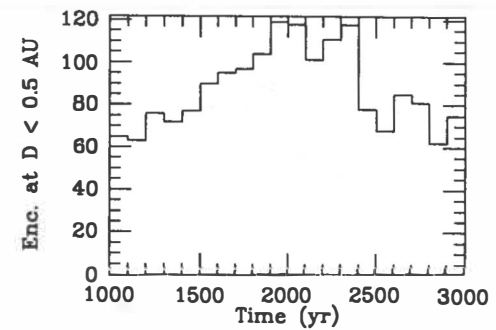


Fig. 3. Distribution of the number of encounters with minimum distance $D < 0.5$ AU for 2000 years centered in the present epoch.

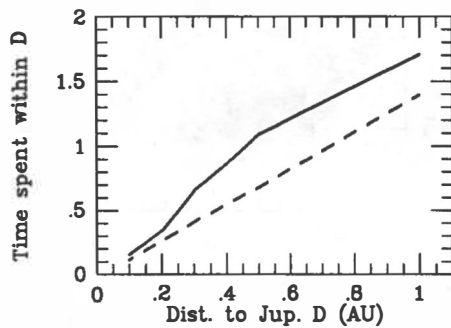


Fig. 5. Time spent within a certain distance D to Jupiter as a function of this distance (full and dashed-lines same as in Fig. 4).

A SEARCH FOR COMETS AT CLOSE ENCOUNTERS

If comets are usually discovered after a close encounter with Jupiter and the actual density of observed JF comets around Jupiter is greater by a factor of 2 or 3 compared to any other place in the Solar System, we may ask why we do not look for comets around Jupiter. Below, we will identify the problems and define an observational strategy to do such a search.

a) The identification problem

At Jupiter's opposition, a distance of 0.5 AU from the planet corresponds to a projected angular distance in the sky plane of 7° . A Schmidt telescope with a plate size on the order of $5^\circ \times 5^\circ$ is the most suitable instrument to cover such a big region of the sky.

If we take a plate of an ecliptic region we would find from 200 up to 400 asteroids down to 20 mag. in a $5^\circ \times 5^\circ$ field (van Houten et al. 1970). We may also find a few comets that are not undergoing a close encounter with Jupiter. How could we distinguish those objects from comets at close encounters? At Jupiter's distance to the Sun, we expect that comets would not show any trace of activity, making almost impossible any observational distinction from asteroids. Therefore, if we do not have clear physical differences we have to look for a dynamical criterion to separate these two samples.

The distribution of Tisserand parameters (T) for JF comets shows a concentration towards 3, and values generally greater than 2.5 (TR). Remembering that the encounter velocity with Jupiter (expressed in terms of the planet's orbital velocity) is given by $U^2 = 3 - T$, we concluded that JF comets tend to have low velocity encounters with Jupiter and their heliocentric orbital velocity is similar to that of Jupiter at the time of the encounter. If we make the observations close to Jupiter's opposition, the vast majority of the field asteroids will move with typical retrograde velocities of main belt objects, while the comets that are experiencing a close encounter will have a slower motion, similar to that of Jupiter.

Fig. 6 shows the hourly motion in α and δ of all numbered asteroids with angular separation from Jupiter less than 10° (small dots) and the planet for the 1992 opposition (29/2/1992). We computed the mean relative velocities during the encounters for different JF comets that experienced encounters in the last 40 yr. For comets with a minimum distance to Jupiter < 0.5 AU, we found that the mean relative velocity had a median value of 6 km/s. As the previous value corresponds to a relative velocity in any direction, we calculated the projected median velocity on the sky plane averaging over all possible directions (a factor of $\frac{\pi}{4}$ times the velocity). In Fig. 6 we drew a full circle with radius corresponding to this projected median velocity ($5''/\text{hr}$ in the sky plane) and dashed lines corresponding to the upper and lower quartiles. Tracking the telescope on Jupiter we would find that asteroids should show a trail on the order of $17''$ in one hour exposure (0.25 mm with a plate-scale of $67.5''/\text{mm}$), while comets should be more like point-sources. The stars will appear as trails of $19''.7$ (0.29 mm with the same scale-plate) but in opposite direction compared to asteroids. Therefore, if we make the observations close to Jupiter's opposition and track the telescope on the planet, we would be able to pinpoint very easily comets at close encounters.

b) The magnitude problem

The heliocentric distance of Jupiter ranges between 4.9 and 5.5 AU. The correction that we have to introduce to the absolute magnitude to obtain the apparent magnitude depends on the particular circumstances of the opposition. We make our calculations for the 1992 opposition, when Jupiter will have an heliocentric distance $r_j = 5.4$ AU and geocentric distance $\rho_j = 4.4$ AU. Assuming that at Jupiter's distance from the Sun, the comet would look like a bare nucleus, we express the difference between apparent and absolute nuclear magnitude $\Delta m = 5 \log(r\rho)$. For comets at close encounters we obtain a mean value of

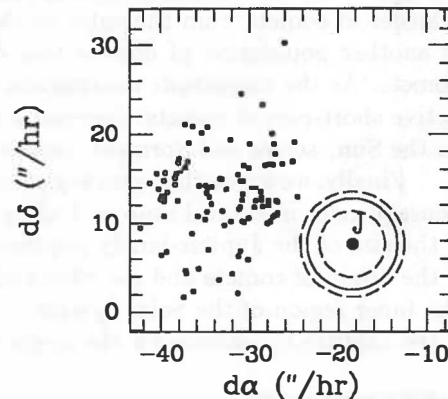


Fig. 6. Hourly motion in α and δ of all numbered asteroids (small dots) and Jupiter for 28/2/1992. Circles centered in Jupiter with radius corresponding to different projected relative velocities are superposed (see text).

$\Delta m = 7$. If the telescope has a limiting magnitude of 21 - 23 in a 1-2 hours exposure, we could detect comets brighter than absolute nuclear $H_n(1,0) \approx 14 - 16$.

Based on nucelar photographic magnitude determinations made by Roemer during 1960's and cratering rates on Galilean satellites, Shoemaker and Wolfe (1982) developed an expression for the power law distribution of number of comets (N) with brightness (H_n)

$$\frac{N(H_n + \Delta H_n)}{N(H_n)} = 10^{0.4\Delta H_n} \quad (1)$$

The size of the JF population is unknown and in fact, a search like the one proposed here could give a better estimation of the number of JF comets. Previous estimations of the population size range from one thousand (Shoemaker and Wolfe 1982) to a few (3-4) thousand objects (Fernández et al. 1991) down to nuclear magnitude $H_n(1,0) = 17.5$ and perihelion distance $q < 5.5$. Using eq. (1), the total number of comets in the range of detectable nuclear magnitudes (14-16) could then range from 60 to 170 for $H_n(1,0) < 14$ and 360 to 1000 for $H_n(1,0) < 16$.

If we take plates covering a region out to a distance of 0.7 AU from Jupiter (a field of $20^\circ \times 20^\circ$ centered on Jupiter) and consider the values of the density of comets around Jupiter found before, we would expect to find a comet with a probability of 60 % in the worst case (e.g. density of 0.6 comets at distances less than 0.5 AU, smallest population and observed limiting magnitude 21) up to 20 comets in the best alternative (e.g density of 1.5, largest population and mag. 23).

The values of the number of comets at close encounters obtained before are only a lower limit to the values that we would obtain during the observations because we are neglecting two other sources of encountering objects. When we consider the observed population, we are taking into account very few cases of comets moving between Jupiter and Saturn. This population of objects could contribute a lot to the number of encounters, and we would expect a large number of objects belonging to this sample if a gradual transfer of comets from the outer to the inner regions of the Solar System is assumed. Furthermore, there is another population of objects that could increase the number of objects at close encounters: dormant comets. As the magnitude distribution and the estimates of the population size were based on the observed active short-period comets, dormant comets are not included in our estimations, and at Jupiter's distance to the Sun, active and dormant comets would have a similar appearance.

Finally, we argue that a survey of comets during their close encounters with Jupiter could have important consequences in several aspects dealing with the evolution of small bodies of the Solar System; e.g.:

- * the size of the Jupiter-family population of comets
- * the origin of comets and the effects of encounters with Jupiter in the transfer of comets from the outer to the inner region of the Solar System
- * the capture-hypothesis for the origin of the outer satellites of the outer planets.

REFERENCES

- Carusi, A.; Kresák, L.; Perozzi, E. and Valsecchi, G.B. (1985) First Results of the integration of motion of short-period comets over 800 years. In Dynamics of comets : their origins and evolution (A. Carusi and G.B. Valsecchi eds.), p. 319-340, Reidel Pub. Co..
- Fernández, J.A., Kamél, L. and Rickman, H. (1991) The distribution of perihelion distance and population size of the short-period comet family. Submitted to International Workshop on Periodic Comets (J.A. Fernández and H. Rickman, eds.). Univ. de la República, Montevideo, Uruguay.
- van Houten, C.J., van Houten-Groeneweld, I., Herget, P. and Gehrels, T. (1970) The Palomar-Leiden survey of faint minor planets. Astr. Astrophys. Suppl., **2**, 339-448.
- Karm, J. and Rickman, H. (1982) Pre-discovery encounters between short-period comets and Jupiter estimated by a keplerian approximation, Bull Astron. Inst. Czechosl., **33**, p.359-370.
- Kresák, L. (1979) Three-dimensional distribution of minor planets and comets. In Dynamics of the Solar System (R. Duncombe, ed.), p. 239-244, Reidel Pub. Co..
- Shoemaker, E. M. and Wolfe, R.F. (1982) Cratering time scales for the galilean satellites. In Satellites of Jupiter (D. Morrison, ed.), p. 277-339, Univ. of Arizona Press, Tucson, Arizona.
- Tancredi, G. and Rickman, H. (1991) The evolution of short-period comets for 2000 years. Submitted to Chaos, Resonances and Collective Phenomena in the Solar System (S. Ferraz Mello, ed.), Reidel Pub. Co..

DETERMINATION OF ORBITS OF COMETS: P/KEARNS-KWEE, P/GUNN, INCLUDING NONGRAVITATIONAL EFFECTS IN THE COMETS' MOTION

B. Todorovic-Juchniewicz, G. Sitarski

Space Research Centre, Bartycka 18, 00–716 Warszawa, Poland

ABSTRACT

To improve the orbits we collected all the positional observations of the comets. The observations were selected and weighted according to objective mathematical criteria and the mean residuals *a priori* were calculated for both comets. We took into account nongravitational effects in the comets' motion using the Marsden's method applied in two ways: either determining the three constant parameters A_1, A_2, A_3 or the four parameters A, η, I, ϕ connected with the rotating nucleus of the comet. To link successfully all the observations we had to assume for both comets that $A(t) = A_0 \exp(-B \cdot t)$ where B was an additional nongravitational parameter.

METHOD FOR NONGRAVITATIONAL EFFECTS

According to the known Marsden's method a nongravitational force acting on a comet is defined by its three components in orbital coordinates: F_1 – the radial component, F_2 – the transverse component in the orbit plane, F_3 – the component normal to the orbit plane (Marsden 1969). It is assumed that $F_i = A_i g(r)$, and the nongravitational parameters A_i , $i = 1, 2, 3$ are to be determined as constant quantities from observations for an individual comet; the analytical form of the function $g(r)$ is known (Marsden *et al.* 1973).

If the nongravitational force acts on the comet owing to the rocket effect of ejection of material from the rotating comet's nucleus, then:

$$A_i = AC_i(\eta, I, \lambda = v + \phi)$$

where $A = (A_1^2 + A_2^2 + A_3^2)^{1/2}$, η is the lag angle, I – the equatorial obliquity, v – the true anomaly of the comet, ϕ – the cometocentric solar longitude at perihelion; the direction cosines C_i have the following form:

$$\begin{aligned}C_1 &= \cos \eta + (1 - \cos \eta) \sin^2 I \sin^2 \lambda \\C_2 &= \sin \eta \cos I + (1 - \cos \eta) \sin^2 I \sin \lambda \cos \lambda \\C_3 &= -[\sin \eta \cos \lambda - (1 - \cos \eta) \cos I \sin \lambda] \sin I\end{aligned}$$

It appears that A, η, I, ϕ can be determined from observations by the least squares method (Sitarski 1990). To link successfully all the observations of P/Kearns-Kwée and of P/Gunn as well, we had to assume that the nongravitational parameter A depended on time. We accepted that $A(t) = A_0 \exp(-B \cdot t)$ where t was counted in days from the epoch of osculation. Thus the five nongravitational parameters: A_0, B, η, I, ϕ have been determined from observations along with corrections to the six orbital elements.

OBSERVATIONAL MATERIAL

Observations of the comets were selected and weighted (each apparition separately) according to objective mathematical criteria (Bielicki 1972). A mean residual *a priori* was calculated as follows: mean residual = $[\sum_j^k n_j w_j \mu_j^2 / \sum_j^k n_j]^1/2$ where k —number of apparitions, n_j —number of residuals of the j -th apparition, w_j —weight of the j -th apparition, μ_j —value of the mean residual of the j -th apparition.

Characteristics of observations of Comet P/Kearns-Kwee:

Apparition	Number of observations	Number of residuals	Mean residual	Weight of apparition
1963.08.17 – 1965.04.24	60	115	1."33	0.64
1971.07.26 – 1973.04.04	96	188	1.26	0.71
1981.06.29 – 1982.02.26	46	83	1.41	0.56
1989.09.10 – 1991.03.21	64	123	0.74	2.07

Observation interval: 1963 Aug. 17 – 1991 Mar. 21

Number of observations: 266

Number of residuals used for the orbit improvement: 509

Mean residual *a priori*: 1."06

In case of Comet P/Kearns-Kwee we detected a displacement of the photometric center from the center of mass of the comet's nucleus (Sitarski 1984). We assume that the displacement of both centers along the radius-vector r is expressed by $\Delta r = Dr^{-3} \exp(-r^2/2)$ where the value of D is to be determined from the observational equations by the least squares method along with other parameters of the comet's motion.

Characteristics of observations of Comet P/Gunn:

Interval	Number of observations	Number of residuals	Mean residual	Weight of interval
1954.08.08 – 1954.08.08	2	4	–	1.00
1970.10.27 – 1971.11.18	13	26	0."74	0.98
1972.12.03 – 1975.07.03	42	83	1.07	0.46
1976.04.24 – 1978.10.28	24	46	1.04	0.49
1980.12.07 – 1983.09.28	20	40	0.81	0.81
1984.08.24 – 1987.01.04	20	38	0.39	3.50
1988.01.15 – 1990.09.24	78	153	0.78	0.88

Observation interval: 1970 Oct. 27 – 1990 Sep. 24

Number of observations: 197

Number of residuals used for the orbit improvement: 386

Mean residual *a priori*: 0."73

RESULTS

Orbit of Comet P/Kearns-Kwee:

(Epoch of osculation: 1963 Nov. 27.0 ET, Equinox: 1950.0)

- With nongravitational parameters A_1, A_2, A_3 :

$$\begin{aligned} T &= 1963 \text{ Dec. } 7.00738 \text{ ET} & \omega &= 131^\circ 19146 \\ q &= 2.21317774 \text{ a.u.} & \Omega &= 315.43935 \\ e &= 0.48653298 & i &= 8.99170 \\ A_1 &= (+0.59457 \pm 0.13152) \times 10^{-8} \\ A_2 &= (-0.38585 \pm 0.00154) \times 10^{-8} \\ A_3 &= (-0.15898 \pm 0.20130) \times 10^{-8} \\ D &= (+0.95212 \pm 0.17450) \times 10^{-2} \end{aligned}$$

Mean residual *a posteriori*: 4".67

- With $A = A_0 e^{-B \cdot t}$ and angular parameters η, I, ϕ :

$$\begin{aligned} T &= 1963 \text{ Dec. } 7.00735 \text{ ET} & \omega &= 131^\circ 19250 \\ q &= 2.21318442 \text{ a.u.} & \Omega &= 315.43918 \\ e &= 0.48653473 & i &= 8.99151 \\ A_0 &= (+1.47950 \pm 0.06238) \times 10^{-8} \\ B &= (+0.11971 \pm 0.00151) \times 10^{-3}/\text{day} \\ \eta &= 33^\circ 30 \pm 2^\circ 68 \\ I &= 143.22 \pm 8.55 \\ \phi &= 334.45 \pm 17.01 \\ D &= (+0.36178 \pm 0.04559) \times 10^{-2} \end{aligned}$$

Mean residual *a posteriori*: 1".24

Before the discovery of P/Kearns-Kwee a close approach of the comet to Jupiter to within 0.033 a.u. occurred in November 1961. That approach considerably changed the comet's orbit (before the approach: $q = 4.302$, $e = 0.691$, $i = 2^\circ 88$).

Orbit of Comet P/Gunn:

(Epoch of osculation: 1989 Oct. 1.0 ET, Equinox: 1950.0)

- With nongravitational parameters A_1, A_2, A_3 :

$$\begin{aligned} T &= 1989 \text{ Sep. } 24.96595 \text{ ET} & \omega &= 196^\circ 93927 \\ q &= 2.47155291 \text{ a.u.} & \Omega &= 67.86640 \\ e &= 0.31439342 & i &= 10.37272 \\ A_1 &= (+2.52440 \pm 0.00545) \times 10^{-8} \\ A_2 &= (+0.50284 \pm 0.00050) \times 10^{-8} \\ A_3 &= (-0.14875 \pm 0.15015) \times 10^{-8} \end{aligned}$$

Mean residual *a posteriori*: 1".52

2. With $A = A_0 e^{-B \cdot t}$ and the angular parameters η, I, ϕ :

$$\begin{aligned}
 T &= 1989 \text{ Sep. } 24.97004 \text{ ET} & \omega &= 196^\circ 94062 \\
 q &= 2.47155081 \text{ a.u.} & \Omega &= 67.86623 \\
 e &= 0.31439419 & i &= 10.37270 \\
 A_0 &= (+1.15530 \pm 0.07298) \times 10^{-8} \\
 B &= (+0.12002 \pm 0.00751) \times 10^{-3} / \text{day} \\
 \eta &= 53^\circ 45 \pm 12^\circ 91 \\
 I &= 73.29 \pm 3.67 \\
 \phi &= 84.84 \pm 4.37
 \end{aligned}$$

Mean residual *a posteriori*: 1".15

Comet P/Gunn approached Jupiter to within 0.353 a.u. in July 1965, and it changed the comet's orbit (before the approach: $q = 3.290$, $e = 0.178$, $i = 10^\circ 87$).

CONCLUSIONS

We can see that accepting the constant nongravitational parameters A_1, A_2, A_3 it was impossible to find resonable solutions for orbits of the considered comets: the mean residuals *a posteriori* were much greater than those *a priori* (especially for P/Kearns-Kwee). Assuming an expotential time dependence for the nongravitational parameter $A(t)$ we got the acceptable solutions for both comets.

Both comets approached Jupiter, and the approaches changed the comets' orbits in the same manner: perihelion distances diminished. The expotential decreasing of non-gravitational effects, as detected in the motion of both comets (the positive values of the parameter B), can be explained by the diminishing of the comets' activity with time after a rapid increase of activity caused by the changes of orbits due to approaches of the comets to Jupiter.

REFERENCES

- Bielicki, M., 1972, in: *The motion, evolution of orbits, and origin of comets*, D.Reidel, Dordrecht, 112.
 Marsden, B.G., 1969, *Astron. J.*, **74**, 720.
 Marsden, B.G., Sekanina, Z., and Yeomans, D.K., 1973, *Astron. J.*, **78**, 211.
 Sitarski, G., 1984, *Acta Astr.*, **34**, 269.
 Sitarski, G., 1990, *Acta Astr.*, **40**, 405.

MINOR SATELLITES AND THE GASGRA ENCOUNTER

Tom Van Flandern
Meta Research / Washington, DC

Abstract. Observational evidence, especially from occultations and radar, indicate that satellites of minor planets are numerous and commonplace. This leads to the prediction that the Galileo spacecraft will find many such "minor satellites" at the upcoming close encounter with minor planet 951 Gaspra.¹ If such objects are found, this argues strongly against the current theory of minor planet origin from the primeval solar nebula.

Introduction. On October 29, 1991 the Galileo spacecraft will encounter the minor planet 951 Gaspra. This will be our first close up view of a minor planet. However if the spacecraft high-gain antenna remains undeployed, the results will not be known until the spacecraft approaches Earth again in December, 1992. On that occasion, we should learn a great deal about the nature and the origin of minor planets. The encounter provides a crucial test of the prevailing theory of origin of minor planets: a test which the theory might not pass!

Most planetary astronomers believe that each minor planet consists of a single, isolated rocky body which, except for collisional fragmentation, should have remained substantially unchanged since it condensed from the primeval solar nebula 4.6 billion years ago. The chief challenger to this model is the view that each minor planet consists of a rocky nucleus, surrounded by a cloud of orbiting debris. The debris would contain rocky fragments of a variety of sizes, from many kilometers in diameter down to dust size. Such abundant orbiting debris fragments have too much angular momentum to have originated in collisional events. If they exist, origin in a planetary breakup event is indicated.

History. The United States spacecraft Galileo, launched October 18, 1989, is on an extended 6-year mission to the planet Jupiter. The spacecraft trajectory cuts through the asteroid belt twice. Between these passages the spacecraft comes back near the Earth for a gravity assist. During its first excursion of the asteroid belt, the Galileo spacecraft will pass close to the minor planet 951 Gaspra. Pre-encounter, we know the following about Gaspra: diameter, roughly 16 km; rotation, 7.03 hours; amplitude of light variation, 0.8 magnitudes (Binzel R.P., 1991, private communication); "unusual" type S asteroid.

¹Note added in proof: This paper is presented exactly as originally submitted to preserve the integrity of its prediction. One picture of Gaspra from the Galileo encounter has since been transmitted to Earth, in which no satellites are seen. The downloaded image frame reveals only 0.001 of the volume of space within which Gaspra might have stable moons. Images still on-board the spacecraft will tell us more about the remaining space. However the synchronous orbit, at about 3-4 radii from Gaspra's center, is the most stable orbit for satellites; and the absence of large moons in the portion of it which can be seen does significantly lower the probability of finding moons in the rest of the volume.

Observations. As a result of predictions made chiefly by D.W. Dunham, several dozen occultations of stars by minor planets have been successfully observed over the past 15 years. On the majority of occasions when multiple observers were involved, secondary occultations have been reported as well (Binzel & Van Flandern, 1979). Although the nature of these secondary occultations is ambiguous in some cases, in others it is not. Cases where the light drops by several magnitudes, but where the minor planet remains faintly visible to the observer after the star has disappeared, cannot be due to causes in the observer's environment or near the Earth. In two cases, such secondary occultations were confirmed by a second, independent observer. The only plausible explanation is that additional bodies in the immediate environment of the minor planet occulted the star (Van Flandern, 1980).

There is also asteroid lightcurve evidence of multiplicity (Van Flandern, Tedesco, & Binzel, 1979); doublet craters and crater chains evidence on many planetary surfaces; and the suggestion that meteorites often "break up" at altitudes over 100 km above the Earth's surface, where the atmospheric shearing forces are still negligible (Wetherill & Revelle, 1982). All of this supports the multiple-body nature of at least some minor planets.

One other line of direct evidence involves radar ranging to Apollo asteroids passing quite close to the Earth. Although such events are rare, in two of the nine asteroids targeted to date (the two with the highest available resolution: 1627 Ivar and 1989 PB), more than one radar echo in the image was seen. In the latest passage, asteroid 1989 PB was found to be at least a contact binary asteroid by means of radar echoes (Ostro et al., 1990).

Since so few minor planets have occulted stars or been observed by radar, yet so many of these few have shown evidence of companions (dubbed "minor satellites"), the author has concluded that minor satellites are numerous and commonplace. There is evidence that minor planets are surrounded by debris clouds containing a range of bodies from kilometer size down to dust size. E.g. a few minor planets have shown "halos" on long exposure photos. And during occultations of stars by minor planets, unusual scintillation of the starlight for brief periods has twice been seen visually, and once recorded photoelectrically (Van Flandern, Tedesco, & Binzel, 1979). The apparent explanation is partial occultations of the starlight by numerous bodies near the minor planet too small to produce total occultations.

Prediction. The radius of the gravitational sphere of influence, within which satellites are dynamically stable against the force of the Sun, is approximately given by 100 times the perihelion distance in astronomical units (au) times the diameter of the parent minor planet (Van Flandern, Tedesco, & Binzel, 1979). For example, a 50 km minor planet which reaches perihelion at 2 au from the Sun has a sphere of influence extending out to about 10,000 km. All of the minor satellite detections to date have been far inside of the theoretical sphere of influence for their parent.

Gaspra's calculated sphere of influence extends to approximately 3000 km. The Galileo spacecraft is targeted to approach the minor planet to within about 1600 km. But since tidal forces are significant for evolving the orbits of minor satellites, it is expected that long-term stable orbits will lie mostly within about 1/3 of the theoretical radius of the sphere of influence. Objects farther out will evolve outward under tidal forces until they escape into the minor planet's solar orbit. So these outer regions should only be populated sparsely by objects in transition to escape from the minor planet. And the collision hazard should be only a small fraction of what it would be farther in. But note that, at the 8 km/s relative speed between spacecraft and asteroid, collisions with even dust particles can do extensive damage.

From observational and theoretical considerations, we expect that Galileo will photograph a Gaspra surrounded by a cloud of debris ranging in size from kilometers down to dust. From a distance, this debris cloud may resemble a faint comet coma. Gaspra should have several satellites plainly visible to Galileo when it arrives. The only reservation about this prediction is that if Gaspra was involved in a major collision, all its satellites could have been stripped off. But in any case, if the model is correct, the nucleus of Gaspra should still show the accretion of several tidally-decayed former minor satellites. And whether Gaspra does or does not exhibit orbiting satellites, observations with the Hubble Space Telescope will soon prove whether the minor satellite phenomenon is commonplace or rare.

Origins. Planetary astronomers have been reluctant to accept the observational evidence for minor satellites. In the prevailing viewpoint, minor planets condensed from a primeval solar nebula 4.6 billion years ago, and have remained much the same ever since, except for collisional evolution. Present-day satellites could only arise through collisional fragmentation. But since the mean velocity between asteroids is about 5 km/s, collisions are generally violent and highly destructive affairs, unlikely to leave behind stable satellites. And if any did somehow form, they would be soon removed by tidal forces and subsequent collisions.

The laws of gravitation forbid permanent capture of satellites by gravitational forces alone. Capture needs the assistance of non-gravitational forces; for example, tidal forces, collisions, drag, or solar radiation pressure. Of these, only collisions are strong enough to affect kilometer-sized bodies significantly. The other forces are so slight that they have an insignificant effect during the short time intervals when capture conditions might be operative. Capture could occur from these other forces only under the rarest and most improbable of circumstances.

Even with collisions, stable satellite survival must be quite rare. A collisional fragment which does not have escape velocity enters an elliptical orbit which intersects the surface from which it came; so it just falls back. Even if secondary collisions alter its orbit a bit, tidal forces soon bring it back down. Attaining

a stable orbit requires that the satellite be supplied with ample orbital angular momentum. But it is precisely orbital angular momentum which is absent from fragments when two minor planets collide. Hence collisional processes cannot lead to the formation of abundant stable satellites under plausible circumstances. It is for this reason that the credibility of the observational evidence suggesting that minor satellites may be abundant has been attacked so tenaciously (Reitsema, 1981; note reply by Van Flandern, 1981).

We therefore conclude that, if minor satellites are found to be numerous and commonplace (as would be strongly suggested if Gaspra, a randomly-selected asteroid for this purpose, is found to possess numerous minor satellites and a debris cloud), the origin of these satellites and debris clouds must date from the origin of the minor planets themselves. For example, if all minor planets originated from the disintegration of a much larger body, then each would trap some escaping debris and fragments within its own sphere of influence once it escaped the gravitational sphere of influence of the disintegrated parent body. Any such formation event must have been astronomically recent because collisions over 4.6 billion years would eliminate most minor satellites. But other evidence already exists to support this hypothesis (Van Flandern, 1978).

Conclusions. Gaspra and the Hubble Space Telescope will determine whether minor satellites are abundant or rare. This in turn will provide a test of the prevailing model that asteroids originated as small bodies from the primeval solar nebula 4.6 billion years ago, and have undergone only collisional evolution since then. If the observational evidence for abundant minor satellites from occultations of stars by asteroids, lightcurves, and radar ranging is enhanced by finding minor satellites in this encounter, the theory of origin of minor planets which has prevailed over most of the past two centuries will be dealt a severe blow to its continued credibility. Luckily, we don't have long to wait to find out!

References.

- Binzel R.P. and Van Flandern T.C. (1979) Minor planets: the discovery of minor satellites. Science, 203, 903-905.
Ostro S.J., Chandler J.F., Hine A.A., Rosema K.D., Shapiro I.I., and Yeomans D.K. (1990) Radar images of asteroid 1989 PB. Science, 248, 1523-1528.
Reitsema H. (1981) Minor planet satellites. Science, 211, 297.
Van Flandern T.C. (1978) A former asteroidal planet as the origin of comets. Icarus, 36, 51-74.
Van Flandern T.C. (1980) Satellites of minor planets: a new frontier for celestial mechanics. Celest.Mech., 22, 79-80.
Van Flandern T.C. (1981) Minor satellites. Science, 211, 297-298.
Van Flandern T.C., Tedesco E.F., and Binzel R.P. (1979) Satellites of asteroids. In Asteroids (T. Gehrels, ed.), pp. 443-465. U. of Ariz. Press, Tucson.
Wetherill G.W. and Revelle D.O. (1982) Relationships between comets, large meteors, and meteorites. In Comets (L.L. Wilkening, ed.), pp. 297-319. U. of Ariz. Press, Tucson.

THE ROLE OF ORGANIC POLYMERS IN THE STRUCTURE OF COMETARY DUST

V. Vanysek¹, H. Boehnhardt², and H. Fechtig³

¹ Institute of Astronomy, Charles University, Prague, Czechoslovakia

² MBP Software & Systems ESOC, Dortmund, and Dr.-Remeis-Sternwarte, Bamberg, FRG

³ Max-Planck-Institute fuer Kernphysik, Heidelberg, FRG

Abstract

Several phenomena observed in P/Halley and other comets indicate additional fragmentation of dust particles or dust aggregates in cometary atmospheres. The disintegration of dust aggregates may be explained by sublimation of polymerized formaldehyde - POM - which play a role as binding material between submicron individual particles.

Introduction

In situ obtained data concerning the size and composition of the dust in Comet Halley indicate that a high percentage of the dust particles are composite grains containing organic species among the may be also polymerized molecules. One of the very first proposed candidate for polymers in cometary material was formaldehyde in form of polyoxymethylene or POM (Vanysek and Wickramasinghe 1975). After the discovery of repeating mass spectral pattern at 45, 61, 75, 91 and 105 amu in inner coma of comet Halley by the PICCA experiment on board of the space craft GIOTTO (Mitchell *et al.* 1986, 1987) the possible presence of POM or similar compounds in comets was widely discussed (Huebner 1987, Huebner *et al.* 1989 and reference therein). Also within the frame of the model of agglomerated grains for cometary dust the possible role of organic polymers as gluing material between the individual building blocks of submicron size was outlined (Boehnhardt *et al.* 1990). In here outlined study this problem is newly reviewed in regard to some recently published laboratory results.

Fragmentation process

The fragmentation of polyoxymethylene has been studied experimentally by mass spectrometry of sublimated POM (Möller and Jackson 1990) and by mass spectroscopy of sputtered POM by protons (Moore and Tanabé 1990). These experiments show that polymeric forms can be produced from the pure solid by sublimation or by bombardment of POM or a silicate-POM composite by protons of several hundreds keV energy. The mass distribution of fragments corresponds with the spectrum obtained by space experiment. The intensity of peaks on the laboratory spectrograms (Moore and Tanabé 1990), decreases with increasing mass as does the PICCA data. Typical masses of fragments produced by laboratory experiments are summarized in Table 1. However, the sputtering mechanism initiated by energetic protons seems to be much less effective in the interplanetary environment and the yield may be 10^{-3} smaller as requires the estimated number density of formaldehyde monomers in the inner coma of P/Halley at the time of GIOTTO space craft fly-by (Mitchell *et al.* 1987). Thus, the only acceptable process remains the sublimation from solids.

Table 1 Mass of fragmented $(H_2CO)_n X$

amu	n	X	amu	n	X
30	1		90	3	
47	1	OH	91	3	H
60	2		105	3	CH ₃
61	2	H	119	3	HCO
73	2	CH	121	4	H
74	2	CH ₂	131	3	C0...CH
75	2	CH ₃	133	4	CH
89	2	HCO	135	4	CH ₄

POM may grow into long chains resulting in relatively stable solids with melting point about 400 to 500 K. Nevertheless, the growing process is terminated by the saturation. If we assume, that equilibrium state could be reached in the interstellar dense clouds as well in the primordial solar nebula about the mass between 120 to 150 amu, i.e approximately with mass \approx monomer mass $\times n$, where $n = 4$ to 5, then such a compound must be regarded rather as a heavy molecule than as solids. But in such a state can be accreted and preserved in the CHON particles. On the other hand, the formaldehyde monomers easily polymerize on the silicate solids and form the silicate-POM composite, which may serve as a binding material between individual submicron particles in fluffy dust grains. The disintegration of such a structures by heating may be very efficient, because at heliocentric distances about 0.5 AU the submicrons grains achieve temperatures above the melting point for POM. Very small fragments of POM may be heated by absorption of UV photons by thermal impulse up to 1000 K and disintegrated immediately to monomers of completely dissociated. However, at low temperatures only few POM binding "bridges" between individual particles may contribute to the stability of dust aggregates. For fragile dust aggregates, where there are only few bridges, the estimated tensile strength should be in range 10^4 to 10^5 dyn cm⁻², which is the lower limit for submicron particles which may withstand the fragmentation by electrostatic charging in the cometary plasma (Boehnhardt 1986, Boehnhardt and Fechtig 1987). The disappearance of the POM binding bridges is followed by disintegration of the dust aggregates and increasing number density of submicron particles in larger distances from the cometary nucleus. There are many phenomena which indicate the fragmentation of cometary dust. Boehnhardt *et al.* (1990) discussed in regard to the POM role following of them: Changes of mass distribution of dust with the nuclear distance, identical boundaries of particles with very different masses, appearance of clusters and packets of dust grains in coma, missing smallest grains in the dust jet while high count rates of these particles in general coma background, and production of CHON particles in coma. The sublimation of "gluing" material of POM type between individual submicron particles may be able to explain both the fragmentation of particle aggregates and additional gas production in the coma of P/Halley. From the CHON particles may be also released polymerized molecules, which however occurred only in shorter chains.

- Boehnhardt H. (1986) ESA SP-250 Vol.II. pp 207
- Boehnhardt H., and Fechtig, H. (1987) Astron. Astrophys. 187, 827
- Boehnhardt H. Fechtig H. and Vanysek V. (1990) Astron. Astrophys., 231, 543
- Huebner W.F.(1987) Science 237, 628
- Huebner W.F.Boice D.C. and Korth A. (1989) Adv. Space Res. 9(2), 29
- Mitchell D.L., Lin R.P., Anderson K.A., Carlson C.W., Curtis D.W. Korth A., Richter A.K., Reme H., Sauvaud J.A., d'Uston C., Mendis D.A. (1986) ESA SP-250, Vol I. , 203 pp.
- Mitchell D.L., Lin R.P., Anderson K.A., Carlson C.W., Curtis D.W. Korth A., Richter A.K., Reme H., Sauvaud J.A., d'Uston C., Mendis D.A. (1987) Science, 273, 626
- Moore M.H. and Tanabé T. (1990) Astrophys. J. 365, L39
- Möller D.L., and Jackson,W.M.(1990) Icarus 86, 189
- Vanysek V. and Wickramasinghe N.C. (1975) Ap. Space Sci. 33. L19

HIGH RESOLUTION IMAGES OF P/TEMPEL 1 AND P/TEMPEL 2 CONSTRUCTED FROM IRAS SURVEY DATA

Russell G. Walker¹, Humberto Campins², and Martin Schlapfer¹
1. Jamieson Science and Engineering 2. University of Florida

ABSTRACT

Infrared images of P/Tempel 1 and P/Tempel 2 have been constructed from IRAS survey data using a computer algorithm based on the Maximum Correlation Method for Image Construction (Aumann et al, 1990). The resulting images are of sufficiently high quality and resolution to delineate coma and tail morphology, and permit accurate photometry of the total dust complex. Comparisons of the infrared colors and photometric profiles of Tempel 1 and Tempel 2 at similar heliocentric distances, show that the grains produced by the two comets are quite similar in radiometric and dynamic properties. Tempel 1 is found to produce about 30% more dust in its coma and tail than Tempel 2. The comae of Tempel 1 and Tempel 2 are expanding with mean velocities of 5.8 ± 0.07 and 6.1 ± 0.17 m/sec respectively, indicative of the ejection of large grains. The IRAS catalogued infrared fluxes (Walker, 1986) are found to be underestimated by as much as a factor of three for the comets. Therefore, it is essential to create images of the comets to obtain meaningful IRAS photometry.

I. INTRODUCTION

The Infrared Astronomical Satellite (IRAS) sky survey produced 122 highly reliable detections of 24 comets (Walker, et al, 1987). These were the basis for a preliminary estimate of dust production rates for 12 of the comets (Walker and Aumann, 1984), and limited discussion of the physical and thermal properties of their grains (Walker, 1986). It was clear that the survey fluxes were corrupted by the spatial frequency response of the IRAS point source filter. Extended portions of the coma were attenuated, and the response heavily weighted by the intensity gradient in the central region. Thus the observed response was dependent upon the spatial asymmetry of the comet's emission relative to the direction scanned. In addition, it was not possible to obtain reliable infrared colors due to the variation with spectral band of the size of the field viewed. For these reasons we undertook a program to construct comet images from the IRAS survey data that are free from such instrumental effects, and that will permit an accurate measure of the infrared flux, colors, and morphology.

II. THE IMAGES

Infrared images of P/Tempel 1 (T1) and P/Tempel 2 (T2) have been constructed from IRAS survey data using a computer algorithm based on the Maximum Correlation Method for Image Construction (MCM) (Aumann, et al, 1990). Previous images of IRAS comet observations were from raster scans taken in the IRAS "pointed observation" mode (Walker et al, 1984; Walker and Aumann, 1990; Campins, et al, 1990), and motion of the comet during the few minutes required to complete the raster was small compared to the spatial resolution in the image. Image construction from survey data requires the use of scans that span relatively large time intervals (8 to 23 hours for the images of Tempel 1 and Tempel 2) during which the motion of the comet cannot be ignored (10 to 20 resolution elements). Thus our image construction was performed in a moving Sun-referenced coordinate system with the comet at the origin.

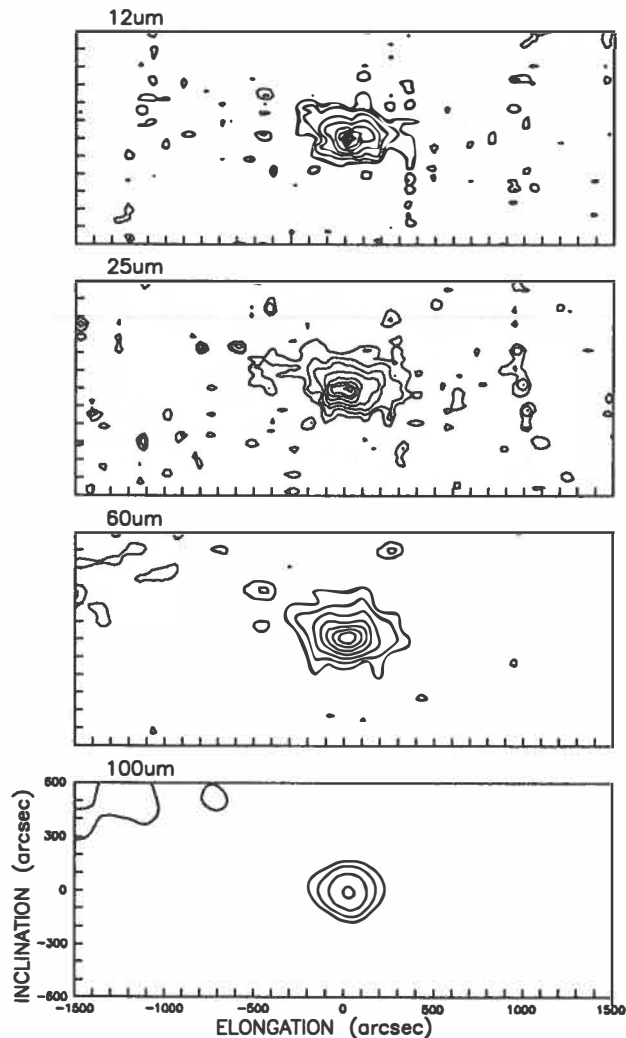


Figure 1. P/Tempel 1

In both figures the field displayed is $20' \times 50'$ with a $24''$ pixel size. Contours start at a signal to noise ratio of 3, and increase in steps of a factor of 2.

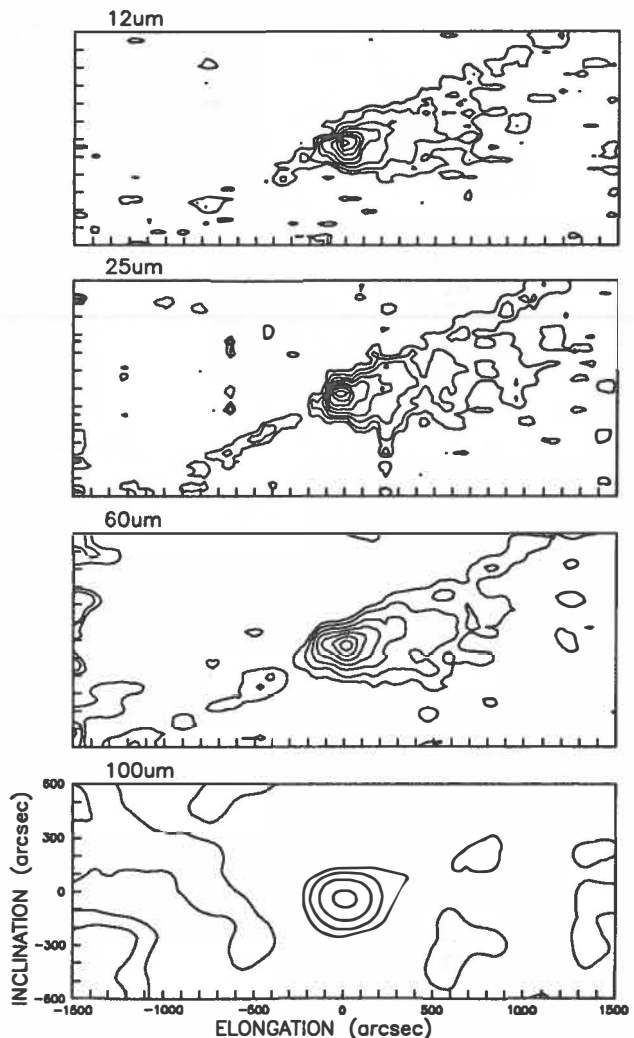


Figure 2. P/Tempel 2

Motion of the comet relative to the IRAS survey progression limits the number of scans that cross the comet image, and thus determines the effective spatial resolution achievable by the moving MCM. Typically, 6 to 9 survey scans are used to build each image. The resolution improvement over a single survey scan is a factor of 1.1, 1.1, 1.6, and 2.2 in the in-scan direction, and 6.6, 6.6, 5.0, and 3.7 in the cross-scan direction for the 12, 25, 60, and 100 μm bands respectively. The best spatial resolution achieved in this case was about 41, 41, 57, and 81 arcsec respectively.

Five sets of images were constructed of T1 at 12, 25, 60 and 100 μm . These span the period from 4.6 days to 81 days after perihelion passage. Similarly, four sets of images were produced of T2 that span from 46 to 97 days past perihelion. Figures 1 and 2 show a typical set of images of T1 and T2. The heliocentric and geocentric distances are 1.49 AU and 0.98 AU respectively for T1 and 1.71 AU and 1.01 AU for T2. T1 is 4.5 days past perihelion, while T2 is 97 days past perihelion. The T2 debris trail is prominent in Figure 2.

III. RESULTS

Four sets of T1 and 3 sets of T2 images have been subject to photometry through a series of circular apertures centered on the comet nucleus and extending to 10' radius. Entries in the first four lines of Table 1 define the circumstances of the observations. ρ is the heliocentric distance, Δ is the geocentric distance, ϕ is the phase angle, and Δt is the time (days) since perihelion passage. $R(12)$ and $R(25)$ are the radii of the apertures (km) that contain 1/2 of the total flux measured at 12 μm and 25 μm , and are a measure of the radius of the dust coma. A plot of $R(12)$ and $R(25)$ versus Δt yields a linear relation for both comets with a mean expansion velocity of 5.8 ± 0.07 m/sec for T1 and 6.1 ± 0.17 m/sec for T2.

The total coma fluxes measured in the 12 μm band are given by F12. The total flux ratios F12/F25 and F25/F60 do not vary significantly between these comets at comparable heliocentric distances. This indicates that the thermal properties of the grains are similar in both comets. The F60/F100 ratio shows more variation but is a less reliable measure due to the variable infrared background cirrus.

Table 1. A Photometric Comparison of Tempel 1 and Tempel 2.

Parameter	T1	T2	T1	T1	T2	T1	T2
ρ	1.49	1.47	1.52	1.50	1.51	1.56	1.56 au
Δ	0.98	1.11	1.14	1.06	1.09	1.27	1.06 au
ϕ	42.5	43.7	41.7	42.4	42.2	40.2	39.9 °
Δt	4.49	46.36	29.96	19.16	56.12	45.82	69.44 d
$R(12)$	55200	54500	63900	55800	62200	75300	70200 km
$R(25)$	54800	58200	69200	58500	54000	74200	66200 km
F12	28.8	16.4	21.6	24.0	16.9	18.5	19.5 Jy
F12/F25	0.46	0.44	0.48	0.43	0.40	0.43	0.46 ± 0.03
F25/F60	2.67	2.55	2.43	2.67	2.72	----	---- ± 0.14
F60/F100	3.31	(1.7)	2.24	2.43	2.79	----	---- ± 0.28
$\Delta^2 F_{12}$	27.7	20.2	28.0	26.9	20.1	29.8	21.9
$\Delta^2 F_{25}$	59.5	46.0	58.4	63.1	50.2	69.4	47.6
$\Delta^2 F_{60}$	22.3	18.0	24.2	23.6	18.4	----	----

The quantity $\Delta^2 F(\text{band})$, is measure of the total number of emitting grains in the coma. The number of grains in the coma of T1 is about 1.3 times the number in the coma of T2. This ratio is essentially independent of the wavelength, further indication that the two size distributions are similar.

IV. CONCLUSIONS

Image construction by MCM has proven to be a reliable and effective technique to produce comet images from IRAS survey data. We now have the capability to observe the large scale coma and tail emission using the IRAS survey scans.

Table 2 compares the fluxes derived from the images with the catalogued point source fluxes of the same observation. The catalogued infrared fluxes are underestimated by as much as a factor of three for T1 and T2. These factors

could be greater for other comets. It is essential to create images of the comets to obtain a meaningful measure of their infrared properties.

The infrared flux ratios are similar for the two comets indicating that the grain composition and size distribution are also similar for the two. The F(12)/F(25) flux ratios are only slightly greater than those expected for a blackbody at the same heliocentric distance, while the F(25)/F(60) ratios are significantly larger. This indicates that the infrared emission from the dust coma is dominated by grains smaller than 60 μm , and smaller than those observed in the debris trail of either comet (Sykes and Walker, 1991). This result is in apparent conflict with the low velocities found for the coma expansion, which are characteristic of large particles (on the order of 1 cm radius, assuming a density of 1 g/cm³). Possible mechanisms to resolve this apparent conflict include fragmentation of grains in the coma and/or the existence of fluffy grains that can behave thermally as small particles.

Table 2. Ratio of the Total Flux in the Image to the Cataloged Point Source Flux (Obs. is an image identifier).

	Tempel 1				Tempel 2				
Obs.	12 μm	25 μm	60 μm	100 μm	Obs.	12 μm	25 μm	60 μm	100 μm
339	2.39	2.91	1.50	0.99	346	1.53	1.89	1.48	1.60
368	2.52	3.19	1.68	1.56	365	1.68	2.29	1.43	1.15
389	2.74	3.00	1.99	2.06	392	2.58	2.56	----	----
421	3.03	3.58	----	----	448	3.63	3.54	2.29	2.61
Mean	2.67	3.17	1.72	1.54	Mean	2.36	2.57	1.73	1.79

This work was supported by NASA Contract NAS5-30772 and NASA Grant NAGW-1821.

V. REFERENCES

- Aumann, H.H., Fowler, J.W., and Melnyk, M.(1990) A Maximum Correlation Method for Image Construction of IRAS Survey Data, Astron. J. 99, 1674-1681.
- Campins, H., Walker, R.G., and Lien, D.J. (1990) IRAS Images of Comet Tempel 2. ICARUS, 86, 228-235
- Sykes, M. V. and Walker, R.G.(1991) Cometary Dust Trails I. Survey, Submitted to ICARUS.
- Walker, R.G., Aumann, H.H., (1984) IRAS Observations of Cometary Dust, Advances in Space Research, 4, 197-201
- Walker, R.G., and Aumann, H.H., (1990) IRAS Comet Observations - The Continuing Saga, Adv. Space Res., 10, 151-158
- Walker, R.G., Matson, D.L., and Veeder, G.J.(1987) IRAS Observations of Comets. Advances in Space Research, 6, 57-66.
- Walker, R.G.(1986) IRAS Comets. In Infrared Astronomical Satellite Asteroid and Comet Survey, (D.L. Matson, ed.), Chap.3, pp. 1-22. JPL D-3698, Jet Propulsion Laboratory, Pasadena
- Walker, R.G. et al, (1984) Observations of Comet IRAS-Araki-Alcock, 1983d, Astrophys. J., 278, L11-L14

ROTATION OF SPLIT COMETARY NUCLEI

Jun-ichi WATANABE

National Astronomical Observatory of Japan, Osawa, Mitaka, 181 Tokyo, JAPAN

Abstract

A simple model for the rotational motion of split cometary nuclei is studied. A large-amplitude precession is easily excited due to the change of the moments of inertia even if the perturbation is small at the splitting. The damping timescale of the excited precession is widely ranged because of the uncertainty of the physical parameter of cometary nuclei. We also discuss another possibility for clarifying the evolution of the short period comets by studying the split cometary nuclei.

1 Introduction

The rotation of split cometary nuclei is important for studying the internal structure of nuclei. The split nuclei may experience two phases; excitation of the precession, and its damping. The precession may be excited due to the change of the moments of inertia, or to mechanical forces in the splitting, or to the torque caused by the repulsive forces of jets from newborn active regions. Because the situation is too complicated to be modeled, no theoretical work has been done for the rotation of the split cometary nuclei. We model the excitation of the precession by considering only the change of the moments of inertia in this paper, and show high probability of the large precession. The damping of this precession is also discussed in this paper.

2 Excitation of the Precession

We consider a simple model for studying the effect of the change of the moments of inertia at the splitting, assuming a small perturbation. Considering that a nucleus of the axial ratio $1 : b : c$ with a homogeneous density ρ splits by a plane at the position P in the x -axis, new moments of inertia of the split nucleus are

$$I_x = K(b^2 + c^2)(8 - 15P + 10P^3 - 3P^5), \quad (1)$$

$$I_y = K[8(1 + c^2) - 15c^2P - 10(2 - c^2)P^3 + 3(4 - c^2)P^5] - M\delta x, \quad (2)$$

$$I_z = K[8(1 + b^2) - 15b^2P - 10(2 - b^2)P^3 + 3(4 - b^2)P^5] - M\delta x, \quad (3)$$

where $K = \rho\pi bc/60$, M is the mass of the fragment as $\rho\pi bc(1 - P)^2(2 + P)/3$, and δ is the distance between the new and old centers of gravity as $\delta x = 3(1 + P)^2/4(2 + P)$. According to the observational suggestion (Sekanina 1982), we take the parameter P so that the mass ratio does not exceed 0.05.

2.1 Spherical Nucleus($b = c = 1$): The split makes drastic change in the moments of inertia. For example, the fragment mass ratio 0.05 gives $P = 0.7$, and the resulted ratio of the moments of inertia is 1.0:0.9:0.9. The trace of the angular momentum on the nucleus is shown in figure 2. The bold arrow is the original direction of the angular momentum vector, and the circular curves indicate the traces on which the angular momentum vector moves along. Because the angular momentum vector is constant in the inertia space, the nucleus could be up-side-down. This means the large amplitude precession. It should be noted that all the cases in the spherical nucleus is the same situation even if the fragment is small.

2.2 Prolate Nucleus($b = c$): The original nucleus has a tendency to be precessing in a large amplitude. In case of Comet P/Halley, the trace of the angular momentum is long and slender, then we have a relation indicating that a small perturbation causes the large amplitude precession(Watanabe 1989). Because this characteristic holds generally after splitting in the prolate nucleus, the large amplitude precession is easily excited.

2.3 Oblate Nucleus($b = 1$): The nucleus with higher oblateness such like Comet P/Tempel 2(Sekanina 1987) is more stable for the precession. In the low oblateness nucleus like Comet P/Encke (Whipple and Sekanina 1979), the precession is easily excited.

Even if we consider the effect of the change of the moments of inertia only, the first conclusion is that split nuclei would have a large precession unless it was highly oblate one. It should be noted that the particular precession states are entirely dependent on the particular assumption allowing this calculation. Other effects at the splitting would increase the possibility of the large precession.

3 Damping of the Precession

The damping timescale τ is derived by considering the internal energy dissipation (Burns and Safronov 1973) as $\tau \sim k\mu Q/\rho R^2 \omega^3$, where μ is the shear modulus, Q the quality factor, R the radius, ω the rotation angular velocity, and k is the shape factor of $O(10)$. The damping time scale depends on the internal physical condition. Although we do not know such information, some experimental data on the ice are used for this estimate. However, the published data for shear modulus and the quality factor are widely ranged(Peale and Lissauer 1989). The damping timescale ranges several 10^4 ($Q \sim 10, \mu \sim 10^{11}$), up to 10^7 ($Q \sim 10^3, \mu \sim 10^{12}$) yrs. Therefore, it is reasonable that split cometary nuclei are in the precession states.

In this point of view, we observed Comet P/Taylor, which is one of survived split cometary nuclei, during the apparition of 1990-1991 by using the CCD direct imaging technique. Preliminary result for the light curve is, however, too sparse to say anything about the rotational state because of the poor observational condition.

4 Discussion

There are some further possibilities for the nucleus rotation of the split cometary nuclei. If the damping time scale is not short, it may give information not only on the internal structure, but also the evolution of the short period comets. If other short period comets have precession as same as the known split nuclei, then there may be a possibility that short period comets comes from the split origin(Clube and Napier 1984). Otherwise, it means that the split evolution may be impossible, and we need other model, for example, the inner Oort cloud or Kuiper belt(Weissman 1991), to explain the unbalance of the number flux between the short and long period comets. It should be noted that this argument is not so strong because we must study the effect of the torque originated from jets, which is neglected in this paper(Belton 1991).

REFERENCES

- Belton M.J.S.(1991) Characterization of the rotation of cometary nuclei.
In Comets in the Post Halley Era(R.L.Newburn Jr., M.Neugebauer, and J.Rahe, eds.), Vol. 2, pp.691-721. Kluwer Academic Pub., Dordrecht.
- Burns J.A. and Safronov V.S.(1973) Asteroid nutation angles.
Mon.Not. R. astr. Soc.,165, 403-411.
- Clube S.V.M., and Napier W.M.(1984) The microstructure of terrestrial catastrophism.
Mon.Not. R. astr. Soc.,211, 953-968.
- Peale S.J., and Lissauer, J.J.(1989) Rotation of Halley's comet. Icarus,79, 396-430.
- Sekanina Z.(1982) The problem of split comet in review.
In Comets(L.L. Wilkening eds.),pp.251-287, University of Arizona Press, Tucson.
- Sekanina Z.(1987) Anisotropic emission from comets: Fans versus jets. II. Periodic comet Tempel 2. In Diversity and Similarity of Comets(E.J. Rolfe, and B. Battrick, eds),ESA SP-278, pp.323-336, ESTEC, Noordwijk.
- Watanabe J.(1989) Rotational motion of the nucleus of comet P/Halley.
Pub. Astron. Soc. Japan, 41, 897-918.
- Weissman P.R.(1991) Dynamical history of the Oort cloud.
In Comets in the Post Halley Era (R.L.Newburn Jr., M.Neugebauer, and J.Rahe, eds.), Vol. 1, pp.463-486. Kluwer Academic Pub., Dordrecht.
- Whipple F.L., and Sekanina Z.(1979) Comet Encke:Precession of the spin axis, nongravitational motion, and sublimation. Astron.J., 84, 1894-1909.

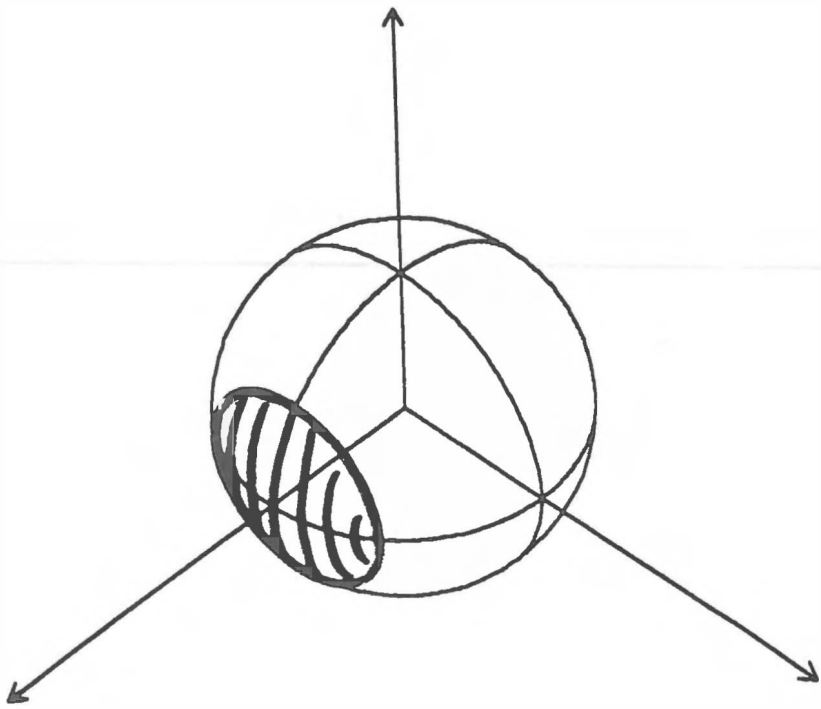
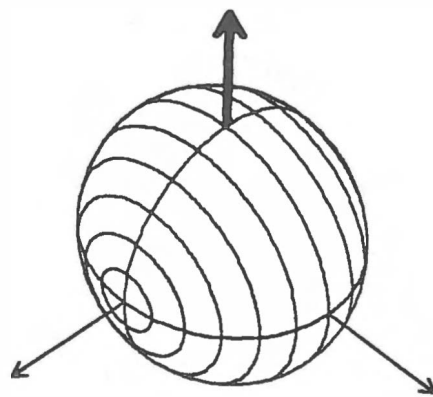


Figure 1: Split model of the spherical nucleus in case of the mass ratio 0.05

Figure 2: Traces of the angular momentum vector on the remnant nucleus of splitting in figure 1. The traces are concentric circles. Note the original angular momentum vector(bold arrow) become unstable for the perturbation.



METEOR RADIANT MAPPING WITH MU RADAR

J. WATANABE¹, T. NAKAMURA², T. TSUDA², M. TSUTSUMI², A. MIYASHITA¹,
and M. YOSHIKAWA³

1:National Astronomical Observatory of Japan

2:Radio Atmospheric Science Center, Kyoto University

3:Communications Research Laboratory

Abstract

We carried out the radiant point mapping of meteor showers with the MU radar by using a modified mapping method originally proposed by Morton and Jones(1982). The modification is that we weighted each meteor echo by using the beam pattern of the radar system. In this paper, we present a preliminary result of the radiant point mapping of the Geminids meteor shower in 1989.

1 Introduction

It is important to monitor the annual activities of meteor showers in order to know the structure and evolution of meteor streams. There are two merits to utilize radar systems for this purpose. One is that the radar observations realize the uniform and stationary observational conditions, which is the most important for monitoring. The other merit is that the radar observes generally fainter meteors, that is, smaller particles than usual optical methods. Because both the radiation pressure and the Poynting-Robertson effect cause the mass segregation in the streams, the radiant point determined by the optical observations may differ from that in the radar method. Therefore, the radiant point mapping by the radar observations is useful for knowing the evolutionary stage of each meteor stream. The mapping method for the radiant points of meteor showers with an all sky radar systems was proposed by Morton and Jones(1982), and its application to some major showers has been carried out by Poole and Roux(1989). In this paper, we present the modified mapping method along with the result of its application to the 1989 Geminids meteor shower.

2 MU Radar

The MU radar located at Shigaraki, Japan(34.85°N , 136.10°E), is a Mesosphere Stratosphere and Troposphere radar with the frequency and the peak power of 46.5MHz and 1MW , respectively, which was mainly designed to observe atmospheric dynamics of the middle and upper atmosphere(Fukao et al. 1985a,b). One of the characteristics of this radar is the fast beam steering by means of the active phased array antenna, which enables us to investigate the tridimensional structure of the atmospheric motions with a high resolution.

This radar is also characterized by the versatility of the antenna array. By using four antennas out of 475 Yagi arrays and four receiver channels, more than several hundred echoes from the ionized meteor trails can be received efficiently(Nakamura et al. 1991). The beam pattern of the MU radar has been measured. This gives us a useful information for correcting the meteor echo counting.

3 Radiant Point Mapping of Meteor Showers

The principle of our mapping method is the same as Morton and Jones(1982). The radar echo comes from a meteor trail which is perpendicular to the MU radar. The radiant point of each meteor exists upon the great circle of which the pole is the direction of the echo. Because of the uncertainty of the echo direction, we must think a band region of the possible radiant point for each meteor. Piling up each band region, we obtain the position of the radiant point statistically. Figure 1 is the radiant point mapping for the 1989 Geminids with the correction of the beam pattern. The principle of this correction is that the echoes from the position of the larger zenith angle should be counted more than 1.0. The band region of the possible radiant point has generally a higher value with the larger zenith angle. The weight for the echo in the zenith angle Z is given by $W = 1.0/L$, where L is the loss of the antenna, and depends on the zenith angle as $L = K - Gt(Z) - Gr(Z)$, where Gt and Gr are the Gain of *TX* and *RX* antenna, respectively, and K is a constant of the system(-74.414dB). The zenith angle dependence of the weight is shown in figure 2. The height of the radiant point contour level becomes larger than the original mapping method. This means that the correction of the beam pattern is effective for such radiant point mapping, especially in the case of the minor meteor showers. Analyzing the data obtained in the 1989 Geminids, we found the daily motion of the radiant point toward the east(P.A.= $70^\circ \pm 10^\circ$). Although we changed the beam pattern as an experiment for the atmospheric observations, this motion is recognized. The motion is more than 2 degrees per day, which is larger than usual value in the optical observation. The main reason of this difference is not clear.

We are planning to monitor the activities of the Leonids until 1999.

REFERENCES

- Fukao S., Sato T., Tsuda T., Kato S., Wakasugi K., and Makihira T.(1985a) The MU radar with an active phased array system, 1. Antenna and power amplifiers. *Radio Sci.*, **20**, 1155–1168.
- Fukao S., Tsuda T., Sato T., Kato S., Wakasugi K., and Makihira T.(1985b) The MU radar with an active phased array system, 2. In-house equipment. *Radio Sci.*, **20**, 1169–1176.
- Morton J.D., and Jones J.(1982) A method for imaging radio meteor radiant distributions. *Mon. Not. R. astr. Soc.*, **198**, 737–746.

Nakamura T., Tsuda T., Tsutsumi M., Kita K., Uehara T., Kato S., and Fukao S.(1991) Meteor wind observations with the MU radar. Radio Sci.,26, 857-869.

Pool L.M.G., and Roux D.G.(1989) Meteor radiant mapping with an all-sky radar. Mon. Not. R. astr. Soc.,236, 645-652.

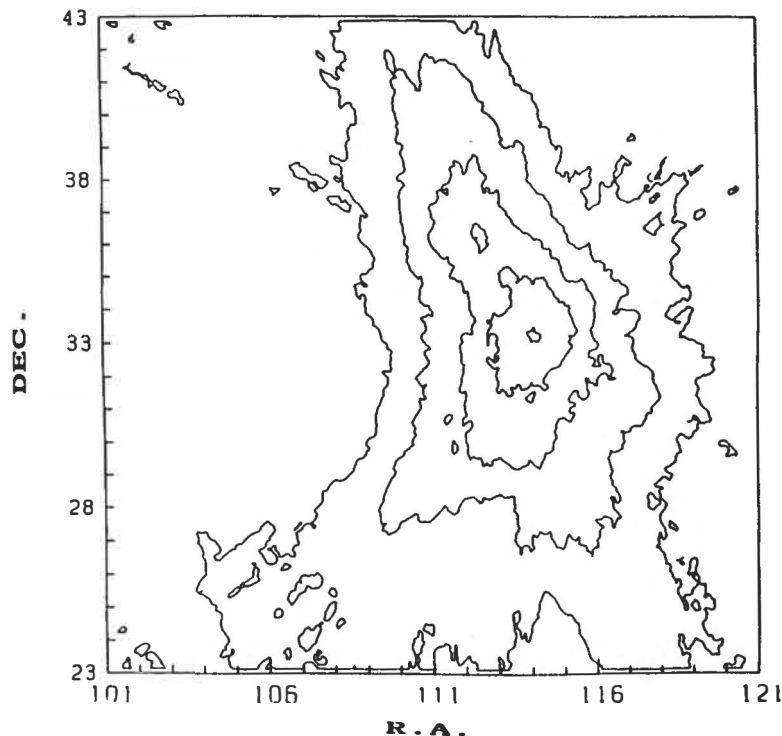
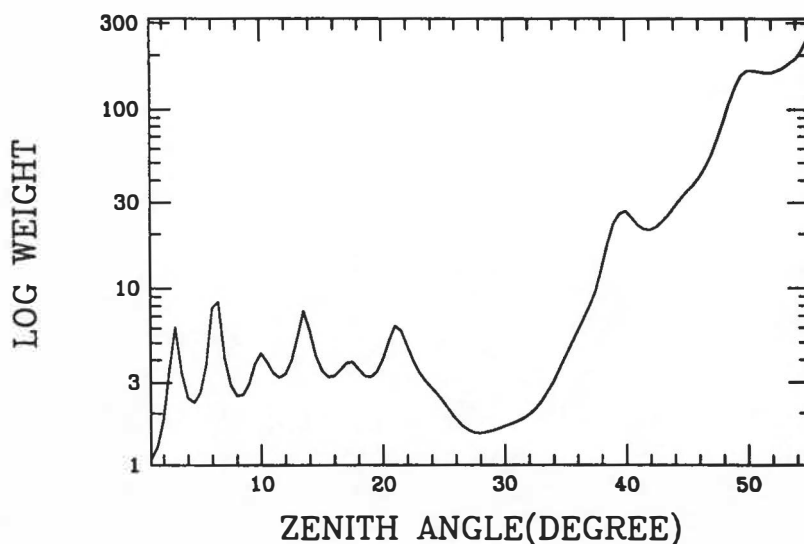


Figure 1: Radiant point mapping of the Geminids on December 12 1989.

Figure 2: The zenith angle dependence of the weight for an echo W for the correction of the beam pattern.



THE COMET RENDEZVOUS ASTEROID FLYBY MISSION: A STATUS REPORT

Paul Weissman and Marcia Neugebauer, Jet Propulsion Laboratory, Pasadena, CA 91109

The Comet Rendezvous Asteroid Flyby (CRAF) mission was approved for a New Start by the United States Congress in 1989. CRAF will be developed in parallel with the Cassini (Saturn orbiter/ Titan probe) mission. The two missions have been combined into a joint program because of the substantial cost savings (~\$500M, or > 25%) which can be realized by using a common spacecraft design, several identical science instruments, a single management team, and a joint ground operations and data handling system for the two missions. CRAF and Cassini will be the first users of the new Mariner Mark II spacecraft which has been designed to carry out the next generation of planetary missions to the outer planets and to small bodies.

CRAF is a joint mission between the United States, Germany, and Italy. Each partner will provide both engineering hardware and science experiments. Cassini is a joint mission between the United States, Germany, Italy, and the European Space Agency (ESA), with ESA providing the Titan atmospheric entry probe, called Huygens.

Mission Profile. The ultra-fast Halley flyby missions in 1986 gave us a first, quick glimpse of a comet nucleus and the first *in situ* measurements of cometary gas and dust. Plasma measurements were carried out on both the 1985 ICE flyby of comet Giacobini-Zinner and the Halley flybys. These missions confirmed many of our basic ideas about comets and raised many interesting questions for further research. It was learned, for example, that comets contain a large amount of organic material, but the molecular composition of this material could not be uniquely determined. The nucleus of comet Halley was found to be dark and irregularly shaped, but very little was learned about the physical state and structure of the ices and grains within the nucleus.

The most important difference between CRAF and the earlier comet flyby missions is that CRAF will be a rendezvous mission, which means that the spacecraft will be maneuvered to follow an orbit around the Sun that precisely matches the comet's orbit. With a rendezvous, it will be possible to orbit the nucleus at an altitude of 10 - 100 km, to observe the comet over several years as its activity grows and wanes, to accurately measure the nucleus' mass and density, to move from place to place in the coma and tail of the active comet, to collect and study relatively undamaged cometary material, and to carry out a program of adaptive exploration using early results to plan later measurements.

CRAF's target is the short-period comet Kopff, which has been observed on 13 perihelion passages since its discovery in 1906 and is one of the most active of the comets that can be reached with a rendezvous mission. An active comet is highly preferred over one that has largely exhausted its supply of volatiles. Kopff has a perihelion distance of 1.58 AU.

The CRAF trajectory to Kopff is shown in Figure 1. Following launch on a Titan 4/Centaur expendable vehicle in April 1997, the spacecraft will perform a gravity assist flyby of Mars and two gravity assists at the Earth to fling it out toward the orbit of Jupiter. Between the two Earth flybys, the spacecraft will fly by the asteroids 88 Thisbe in June 2001, and 19 Fortuna in October 2002. A third asteroid flyby may also be possible en route to Kopff, following the second Earth flyby. In January 2006, the CRAF spacecraft will rendezvous with comet Kopff at a heliocentric distance of 5.3 AU, when the comet will be near its aphelion and in a state of low activity.

Comet Observations. The investigations tentatively selected for CRAF are listed in Table 1. A guest investigator program is planned to increase participation in the mission after launch.

The first order of business after arrival at comet Kopff will be to determine the mass of the nucleus by careful radio tracking during a series of increasingly close, slow flybys. Once the mass is known, the spacecraft will be maneuvered into orbit about the nucleus. If the comet nucleus has an average radius of 4 km and an average density of 0.8 g/cm³, a nominal orbit would have a radius of 79 km and a period of 14 days. The semimajor axis, eccentricity, and inclination of the spacecraft's orbit can be easily changed with very little expenditure of fuel.

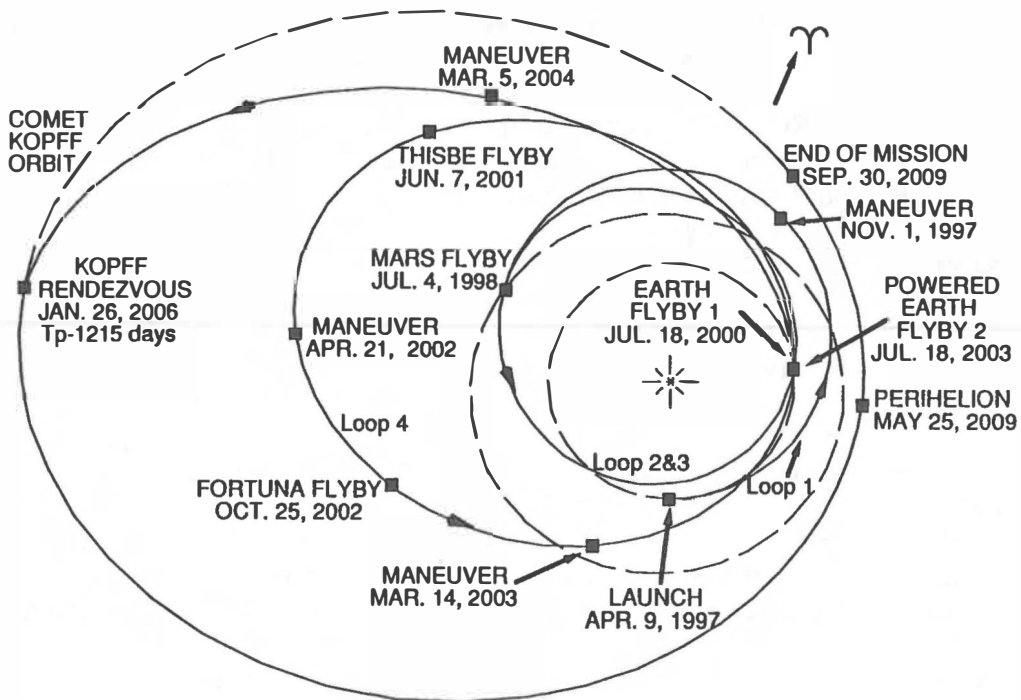


Figure 1. The interplanetary trajectory of the CRAF spacecraft, projected onto the ecliptic plane.

The initial flybys and orbits will also be devoted to mapping the nucleus and studying it to understand its physical properties. CRAF will carry two wide angle cameras and a narrow angle camera, each with 1024x1024 CCD detectors and an array of different filters. From a 79-km orbit, the spatial resolution of the narrow angle camera will be 0.95 meters/line-pair; as compared to the ~80 meters/line-pair resolution of the final picture of the nucleus of comet Halley by Giotto.

The visual/infrared mapping spectrometer (VIMS) will image the nucleus at visual and near-IR wavelengths in each of 352 spectral channels between 0.35 and 5.1 μm , with an angular resolution of 0.5 mrad/pixel (surface resolution of 40 m from a 79 km orbit). VIMS uses cooled CCD and InSb detectors. Surface materials that can be identified by VIMS include: silicates, ices, organics, oxides, salts, metals, emitting ions, and water in clays. When the comet is active, VIMS can also be used to map the distribution of many of the important molecules in the coma.

The third remote sensing instrument is the thermal infrared radiometer (TIREX) which will map the nucleus surface temperature distribution to determine thermo-physical properties and energy balance as well as to aid in the identification of surface materials. TIREX has one visual channel and 18 infrared channels between 5 and >50 μm . Its field of view is 1.5 mrad (118 m from a 79 km orbit). TIREX will be helpful in identifying regions where ices may be close to the surface of the nucleus and thus be possible sites of future activity.

Continued radio tracking of the spacecraft, including some data from very low orbits (< 5 nucleus radii, or ~20 km), will yield measurement of the comet's mass to an accuracy better than 0.1%, as well as information about the mass distribution within the nucleus. The resulting value of bulk density will shed light on how the comet nucleus may have been accreted in the primordial solar nebula and what processing it might have undergone since its formation.

As it approaches the Sun, the comet will become more active and the spacecraft will move in and out through the cometary coma, measuring the properties of the gas and plasma and collecting dust for onboard analysis. The Cometary Matter Analyzer experiment will use secondary ion mass spectroscopy (SIMS) for analysis of collected samples of dust and gas. The very high mass resolution (>3000) of this instrument will allow the identification of different molecules with the

Table 1. CRAF Science Payload, Principal Investigators/Team Leaders, and Home Institutions

ISS	Imaging Science (facility)	Joseph Veverka	Cornell University
VIMS	Visual and Infrared Mapping Spectrometer (facility)	Thomas B. McCord	University of Hawaii
TIREX	Thermal Infrared Experiment	Francisco Valero	NASA Ames Research Center
CoMA	Cometary Matter Analyzer	Jochen Kissel	Max-Planck-Institut, Heidelberg
CIDEX	Cometary Ice and Dust Experiment	Glenn C. Carle	NASA Ames Research Center
CODEM	Comet Dust Environment Monitor	W. Merle Alexander	Baylor University
NGIMS	Neutral Gas and Ion Mass Spectrometer	Hasso B. Niemann	NASA Goddard Space Flight Center
CRIMS	Cometary Retarding Ion Mass Spectrometer	Thomas E. Moore	NASA Marshall Space Flight Center
SPICE	Suprathermal Plasma Investigation of Cometary Environments	James L. Burch	Southwest Research Institute
MAG	Magnetometer	Bruce T. Tsurutani	Jet Propulsion Laboratory
CREWE	Coordinated Radio, Electron, and Wave Experiment	Jack D. Scudder	NASA Goddard Space Flight Center
RSS	Radio Science (facility)	Donald K. Yeomans	Jet Propulsion Laboratory

same molecular weight (e.g., CH versus ^{13}C , or CO versus N₂). The CIDEX experiment will analyze bulk samples of collected dust and ice by alternating x-ray fluorescence measurements with pyrolysis and gas chromatography of the evolved gases.

A dust environment monitor, CODEM, will continuously measure the flux of particles as a function of particle momentum. If a grain is sufficiently electrically charged, it will also be possible to measure its vector velocity, and hence, its mass. The count rates from the momentum sensor will be made available to the spacecraft and to other science instruments in real time to allow them to close protective shutters or take other actions based on the dust flux.

CRAF will also carry a mass spectrometer, NGIMS, for the analysis of coma gases. Its electric quadrupole analyzer can analyze species from any of four sources: 1) an open or fly-through source for the analysis of highly reactive species, 2) a closed source which allows concentration of non-reactive species, 3) a thermal ion source, and 4) a SIMS source for concentrating heavy organic species.

There are two instruments for the study of the mass spectra and velocity distributions of ions. CRIMS can measure thermal ions with temperatures as low as 25 K while SPICE is sensitive to cometary ions which have been picked up by the solar wind. Finally, CRAF carries dual 3-axis vector magnetometers, electron spectrometers for electron energies up to 30 keV, and sensors for measurements of hydromagnetic and plasma waves. The electric wave detector can also operate as a plasma sounder to study electron distributions with temperatures as low as 100 K. With this comprehensive array of plasma detectors, CRAF will address many of the questions left unanswered by the earlier comet flybys; a principal advantage is the ability to study the interaction of a comet with the solar wind over broad ranges of solar wind conditions and levels of cometary activity.

Asteroid Observations. En route to Kopff, CRAF will fly by two main belt asteroids: 88 Thisbe which has a diameter of 232 km, and 19 Fortuna which is 200 km in diameter. Both are primitive type asteroids with surface compositions believed to be similar to carbonaceous chondrite meteorites. CRAF will approach Thisbe from the sunlit side and Fortuna from the night side, at flyby speeds of 5.2 and 12.6 km/sec, respectively. The closest approach will be targeted for a distance of ~80 asteroid radii, which will allow each asteroid's mass and density to be determined to an accuracy of better than 10%, while still keeping the spacecraft beyond the range of any debris which might be trapped in orbit about the asteroid. All the remote sensing instruments described above will observe during the flybys. The spatial resolution at closest approach at Thisbe will be

112 meters/line-pair for the narrow angle camera, 4.6 km/pixel for VIMS, and 13.9 km/pixel for TIREX; resolution at Fortuna will be about 10% better. Observations with these instruments will allow determination of each asteroid's shape, surface topography, mean density, and rotation vector as well as the distribution of different material types on their surfaces. The gas and plasma detectors will search for any residual comet-like emissions from the asteroids, while CODEM will measure the properties of any fine debris in orbit around the asteroids. One of the key results will be comparison of the properties of the carbonaceous asteroids observed by CRAF with the stony asteroids observed by the Galileo spacecraft, addressing questions about the compositional heterogeneity and evolution of asteroids.

The Spacecraft. A computer-drawn picture of the CRAF spacecraft is shown in Figure 2. CRAF is 3-axis stabilized and will usually keep its 4-meter diameter high gain antenna pointed toward the Earth. Most of the experiments are mounted on one or the other of the articulated scan platforms shown in the Figure, or on the magnetometer boom. The same spacecraft will be used for the Cassini mission, with a different set of instruments mounted on the high-precision scan platform and with an instrumented turntable replacing the low-precision pointing platform. The Titan atmospheric entry probe will be mounted on the side of the spacecraft.

Options under study for future Mariner Mark II missions include a Neptune orbiter, a Pluto flyby, and a joint US-ESA mission to return a sample of a comet nucleus to Earth.

Current Status. Congressional action on the 1992 NASA budget provided less than full funding for CRAF/Cassini, leading to a slip to the 1997 launch to comet Kopff, from the previously planned 1996 mission to comet Tempel 2. Spacecraft and instrument development is continuing.

The work reported here was performed at the Jet Propulsion Laboratory
under a contract with the National Aeronautics and Space Administration.

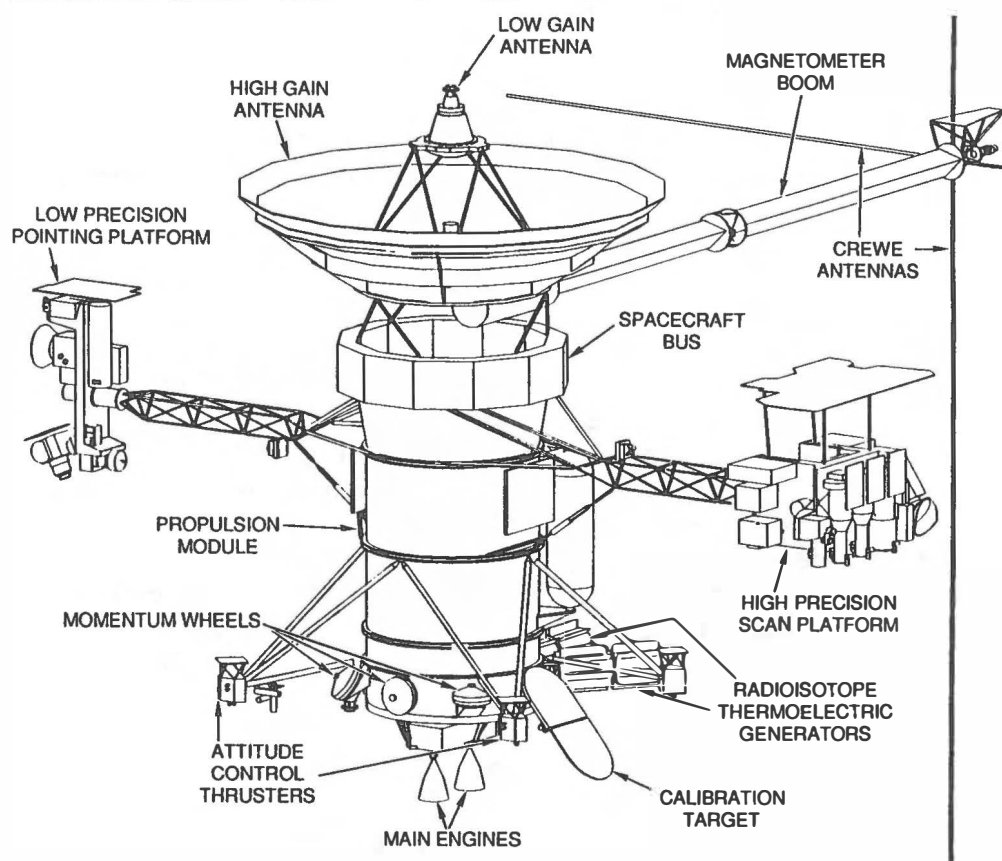


Figure 2. Computer-generated drawing of the Mariner Mark II spacecraft in CRAF configuration.

A NEW ACTIVITY INDEX FOR COMETS

by Fred L. Whipple
Smithsonian Astrophysical Observatory

Summary

An activity index, AI, is derived from observational data to measure the increase of activity in magnitudes for comets when brightest near perihelion as compared to their inactive reflective brightnesses at great solar distances. Because the observational data are still instrumentally limited in the latter case and because many comets carry particulate clouds about them at great solar distances, the application of the activity index is still limited. A tentative application is made for the comets observed by Max Beyer over a period of nearly 40 years, providing a uniform magnitude system for the near-perihelion observations.

In all, 32 determinations are made for long-period (L-P) comets and 15 for short-period (S-P). Although the correlations are scarcely definitive, the data suggest that the faintest comets are just as active as the brightest and that the S-P comets are almost as active as those with periods (P) exceeding 10^4 years or those with orbital inclinations of $i < 120^\circ$. Comets in the range $10^2 < P < 10^4$ yr. or with $i > 120^\circ$ appear to be somewhat more active than the others.

There is no evidence to suggest aging among the L-P comets or to suggest other than a common nature for comets generally.

Introduction

The physical characteristics of comets have been measured in many ways, including integrated or nuclear magnitudes and colors, coma and tail dimensions, polarizations and orientations, spectral characteristics of the various components and variations of all of these measured quantities. Few of these measures, however, provide classification criteria comparable to or correlated strongly with the criteria of orbital period and orientation. For example, the dust-to-gas ratio (D/G) in the coma spectra of comets is highly dependent upon solar distance, r . In a thorough statistical study, Donn (1977) could find no significant difference between "new" and "evolved" comets as measured by the D/G ratio, although comets show a wide diversity in this ratio at relatively small solar distances. By "evolved" comets, Donn refers, of course, to short-period comets as compared to "new" comets, defined by Oort (1950) as having extremely long periods, or extremely small values of the inverse semimajor axis, a .

Kresák (1973) used the extreme solar distances, r_o , to which short-period comets had been observed as a criterion for the state of activity of their nuclei. Again (1977) he compared properties of old and new comets, finding few correlations. Rickman et al. (1987), in estimating the masses, volumes and densities of short-period comet nuclei, introduce a quantity, S_f , to represent the active area of a comet (in km^2) at the time of maximum brightness.

Meech (1990) has made a most valuable summation of evidence and criteria for differentiating old from new comets and for the aging of comets. A major effect is that many new comets are brighter and relatively more active before perihelion than after, as compared to short-period (S-P) comets where the reverse is frequently true. Meech's comparison, showing that new comets are systematically observed to greater solar distances than S-P comets, includes a number with very large values of the perihelion distance. Clearly for this criterion to be more significant, intrinsic brightness (physical dimensions?) should be allowed for in the comparisons.

As a consequence of such considerations, I have attempted to devise an observational measure for the comparative activity of a comet between maximum near perihelion, q , and minimum at great solar distances. Clearly such a criterion or activity index, AI, must be highly dependent upon the value of q so that the characteristics of an individual comet will depend on the deviation of its AI from the average at the individual comet's perihelion distance.

The Activity Index

The classical absolute magnitude of a comet, $H - y$, is defined (e.g. Vsekhsvyatskii, 1964) by

$$H - y = m - 5 \log \Delta - y \log r$$

1

where m is the observed magnitude, Δ and r the geocentric and heliocentric distances, respectively, measured in AU, and $y = 2.5n$, with n being the inverse power of r in the luminosity equation.

For typical comets, $n \sim 4$ ($y \sim 10$) when they are active near perihelion, ideally decreasing to $n = 2$ ($y = 5$) at large r when, theoretically, the comets are reflecting sunlight as inert bodies. Thus H_{10} is often found to be appropriate near perihelion although y may be found to assume a wide range of values.

The basic objective of the activity index is to evaluate the absolute magnitude change of a comet from near perihelion to the extreme observed value of r_o and H_5 . The extreme value of H_5 should be corrected to its opposition value by the addition of the term $-2.5 \log \phi(\alpha)$ where $\phi(\alpha)$ is a function of the phase angle, α , measured at the comet between the Earth and the Sun. The phase-angle correction is yet to be well measured for comets so the correction here will be approximated by $-0^m.03\alpha$, where α is measured in degrees and is generally small (see e.g. Kresak, 1973). Hence the extreme absolute magnitude is here defined as

$$h_o = H_5 - 0.03\alpha,$$

2

evaluated near the maximum observed solar distance, r_o .

For comparison, the perihelion (q) value of the magnitude is taken as H_y , the absolute magnitude near perihelion later corrected to $r = q$ with ($y = 2.5n$), the correction term $+y \log q$, where q is measured in AU.

The Activity Index, AI, is then determined by the difference between these two magnitudes, h_o and H_y , both evaluated at $r = q$ as:

$$AI = h_o - H_y + (5 - y) \log q.$$

3

The activity index is thus ideally the magnitude difference between the comet as seen when inactive and when most active. In fact, of course, this ideal is not always reached because few comets are observed to great enough distances for their light curves to follow a simple $1/r^2$ law and because, as Meech's (1990) Table 1 testifies, most comets have still remained diffuse when last observed. In addition minor corrections to h_o may be needed because of magnitude variations caused by rotation of the nucleus while, h_o and H_y may not be exactly comparable because of unknown phase-angle effects.

The probable differences between the faint and bright magnitude systems may not seriously denigrate the AI values because their absolute values are not their principle merit. They are most valuable in comparing different classes of comets. The vital consideration in such studies is thus to assure consistency within each magnitude system.

A Tentative Application of the Activity Index

A very serious problem in making practical use of the activity index is simply illustrated by comparing two extensive tables of H_{10} for periodic comets by Kresák and Kresáková (1987) and Hughes (1987). For 48 comets the mean difference in the tabulated values is $3^m.06$ with $\sigma = 1^m.34$, for a single difference, the Hughes' values being the larger (*i.e.*, fainter in luminosity). In spite of such a systematic difference, the two studies agree that the comets of intermediate period (15 or 20 to 200 years) differ significantly in their logarithmic cumulative H_{10} distributions from the S-P and L-P groups. On the other hand, Hughes finds that the S-P and L-P comets have similar distribution slopes in the $H_{10} \log(\text{number})$ cumulative diagram while Kresák and Kresáková conclude that the three groups are all different in this respect.

Because of such magnitude calibration problems, this tentative study with the activity index is limited to brighter comets observed by Max Beyer over more than four decades and listed in some 42 articles (see Beyer, 1969, for these references) including 17 major compilations of physical observations of comets. This remarkable observation set is unparalleled and can provide a test base leading to further studies with more recent observations, particularly those involving fainter limiting magnitudes for extreme values of r_o .

During the period of Beyer's observations, the limiting magnitudes increased a bit as observing techniques improved. Major contributors were Hamilton M. Jeffers and Elizabeth Roemer with their associates, and the perennial George Van Biesbroeck, though the latter tended to be less meticulous in his magnitude system than the former. Also Jeffers and Roemer frequently evaluated the nuclear magnitude, a practice that is important in this study because a majority of comets maintain a particulate coma at great solar distances, as mentioned earlier.

The basic data for long-period comets are listed in Table Ia and for short-period comets in Table Ib. The successive columns contain:

1. Comet name to 14 spaces.
2. The comet's Roman numeral designation.
3. q : Perihelion distance in AU.

4. i : Orbital inclination to the ecliptic.
 5. Orbital $1/a(\text{AU})^{-1}$ original (Marsden, 1989, Tab. 3) or Period in years.
 6. H_g : the absolute magnitude ($\Delta = 1$) derived by M. Beyer (1969 references).
 7. $y = 2.5n$, where n is Beyer's value.
 8. Obs: Observer of comet (m_o) at great $r = r_o$; VB: van Biesbroeck; J: Jeffers; H: Hirose; C: L. Cunningham; JVR: Jeffers, S. Vasilevskis and Roemer; JK: Jeffers and Klemola; JS: Jeffers and Stephenson; R: Roemer; RTL: Roemer, Thomas and Lloyd; WP: West and Pedersen.
 9. m_o : observed magnitude at $r = r_o$.
 10. r_o : great solar distance.
 11. h_o : H_5 at r_o corrected by -0.3α (Eq. 2).
 12. AI: Activity Index (see Eq. 3, above).
 13. ΔAI : Mean residual Eq. 4 and Eq. 5 plus corr. Eq. 6 below.
 14. (In Table Ib only) year of m_o measure.

Table Ia: Data for Long-Period Comets

Name	No.	q	i	$1/a$ orig	H_g	y	Obs	m_o ^a	r_o ^a	h_o	AI	ΔAI
Pelt.-Whip.	1932 V	1.037	71°7	22945	7.42	32.0	VB	17	1.59	13.7	5.8	-0.2
Dod.-Forb.	1932 X	1.131	24.5	24562	7.7	16.4	J	17.5	2.02	13.5	5.2	-0.5
Fri.-Ree.-Hon.	1941 II	0.942	26.3	19938	10.9	5.4	H	>17 ^(b)	1.36	17.0	(6.2)	(-0.8)
deKock-Paraskev.	1941 IV	0.790	168.2	2029	5.77	5.0	J	17	3.54	12.0	6.2	-0.5
Whip.-Fedt.-Tev.	1943 I	1.354	19.7	7352	4.17	10.3	VB	16.5	2.74	11.6	6.7	+1.4
Bester	1947 I	2.408	108.2	-1	3.12	14.3	J	18.7	5.8	10.9	4.2	+0.3
Bester	1948 I	0.748	140.6	24	6.31	7.4	J	17.7	4.0	11.2	5.2	-1.7
Pa.-Mrkos	1948 V	2.107	92.9	34	4.37	11.1	J	19.2	6.6	10.8	4.4	+0.1
Bap.-Bok-New.	1949 IV	2.058	105.8	735	5.59	13.8	C	19.0	5.5	11.6	3.3	-1.2
Minkowski	1951 I	2.572	144.2	37	7.15	3.8	C	19.0	6.4	10.6	4.0	+0.2
Mrkos	1952 V	1.283	112.0	14220	5.81	29.3	B	>17.5	1.9	13.8	>5.4	>-0.7
Peltier	1952 VI	1.202	45.6	+2	8.87	14.2	JVR	18	2.2	14.4	4.8	-1.5
Mrkos-Honda	1953 III	1.022	93.9	2983	7.48	30.5	R	19.3	3.3	14.6	7.1	+0.3
Abell	1954 X	0.970	53.2	70	5.86	9.1	R	>18	5.0	11.0	>5.2	>-1.2
Mrkos	1955 III	0.534	86.5	20013	6.85	13.0	J	18 ^(c)	2.0	13.9	9.2	+0.8
Bak.-Mac.-Kri.	1955 IV	1.427	50.0	4353	4.79	18.1	R	18	2.4	13.8	7.0	+1.1
Honda ^(d)	1955 V	0.885	107.5	-727	6.85	11.7	VB	16 ^(d)	1.9	12.1	(5.6)	(-1.3)
Baade	1955 VI	3.870	100.4	+42	3.05	10.8	JK	19.5	7.7	10.6	4.1	+1.1
Mrkos	1956 III	0.842	147.5	Par.	10.8 ^(d)	5	VB	18	0.9	16.1	(5.3)	(-2.3)
Arend-Roland	1957 III	0.316	119.9	-98	5.15	10.9	R	18.8	5.4	13.4	11.1	+1.5
Mrkos	1957 V	0.355	93.9	2001	3.63	5.5	R	19.0	5.0	12.0	8.6	-0.5
Burnham	1958 III	1.323	15.8	256	6.75	18.1	RTL	19.0	2.5	14.2	5.8	-0.4
Burn.-Slau.	1959 I	1.628	61.3	76	7.10	12.2	RTL	19.6	4.1	13.6 ^(e)	5.0	-0.7
Burnham	1960 II	0.504	159.6	-135	7.78	9.5	RTL	17.5 ^(c)	1.5	14.9 ^(e)	8.4	-0.4
Seki-Lines	1962 III	0.03138	65.0	25	5.12 ^(f)	8.9	R	20.4	4.9	14.0	(14.7)	(-0.8)
Honda	1962 IV	0.653	72.9	Par.	10.47	13.0	R	20.5 ^(g)	1.5	19.2	(10.2)	(-1.4)
Humason	1962 VIII	2.133	153.3	4935	2.14	8.7	R	17.8	5.7	17.8	6.8	+1.1
Ikeya	1963 I	0.632	160.6	11389	5.18	12.0	R	19.2	3.4	13.4	9.6	+1.5
Everhart	1964 IX	1.259	68.0	2721	6.39	15.1	R	19.5	2.9	14.2	6.8	+0.2
Ikeya-Seki	1968 I	1.697	129.3	842	3.12	14.6	R	21.5	6.7	13.4	8.0	+2.2
Tago-Hon.-Yam.	1968 IV	0.680	102.2	6492	10.28	13.9	R	>20	1.6	>16.5	>7.7	>-0.8
Bally-Clay.	1968 VII	1.771	93.2	Par.	8.08	6.8	R	17	1.9	13.1	4.6	(-1.1)
Tag.-Sat.-Kos.	1969 IX	0.473	75.8	507	6.39	7.6	R	18.1	2.5	13.2	7.7	-1.3
Bennett	1970 II	0.538	90.0	7334	3.45	11.1	R	18.9	4.5	12.0	10.2	+1.7
Abe	1970 XV	1.113	126.7	283	5.56	6.5	R	16.9	2.6	13.6	7.9	+0.9

Table Ib: Data for Short-Period Comets

Name	No.	<i>q</i>	i	Per.	H_y	<i>y</i>	Obs	m_o ^a	r_o ^a	h_o	AI	ΔAI
Arend-Rigaux	1957 VII	1.386	17°2	6y7	8 ^m .87	21.5	R	20 ^m .5	3.0	16 ^m .4	5 ^m .3	-1 ^m .5
Ash.-Jack.	1956 II	2.325	12.5	7.5	8.73	5.0	R	20.0	3.8	14.9	6.1	+0.9
Encke	1953 ^b	0.338	12.4	3.3	10.14 ^b	11.7 ^b	R	20.2	3.3	16.0	9.0	-1.0
Faye	1969 VI	1.616	9.1	7.4	10.20	6.4	R	20.9	3.4	15.6	5.1	-1.0
Giac.-Zinn.	1959 VIII	0.936	30.9	6.4	10.18	23.6	WP	25.0	4.8	17.8	8.3	-0.2
Hon.-MrK.-Paj.	1954 III	0.556	13.2	5.2	12.78	15.2	JS	19.5	1.6	17.6	7.4	-2.5
Kearns Kwee	1963 VIII	2.213	9.0	9.0	9.23	5.0	RL	20.1	4.0	14.6	5.4	+0.1
Olbers	1956 IV	1.178	44.6	69.6	5.02	9.8	R	18.8	4.3	12.8	7.4	+1.1
Pons-Brook	1954 VII	0.774	74.2	70.9	4.66	10.8	J	18.0	4.3	11.5	7.5	+0.5
Pons-Win.	1951 VI	1.160	21.7	6.2	11.4	5.0	R	18.1	1.5	16.8	5.4	-1.9
Reinmuth2	1954 VI	1.686	7.1	6.6	10.82	7.6	R	20.5	3.2	16.2	4.6	-1.8
Schajn-Schad.	1971 IX	2.227	6.2	7.3	9.5	5.0	R	19.8	1.8	17.0	7.5	+1.7
Schw-Wach.2	1961 VII	2.157	3.7	6.5	8.47	10.0	R	>20.0	3.0	14.8	4.7	-0.6
Schaumasse	1960 III	1.196	12.0	8.2	7.6 ⁱ	21.4 ⁱ	RTL	19.0	2.1	16.5	7.7	+0.8
Tut.-Gia.-Kre.	1962 V	1.123	13.8	5.5	10.77 ⁱ	26.8 ⁱ	RL	21.0	2.0	19.1	7.3	-0.6

Notes to Table Ia and Ib:

- a) Many of the references to these observations are contained in the tabulations by Svoren (1984 and 1985) and by Kamél (1991).
- b) Based in "not seen" observation.
- c) Became brighter later.
- d) Split.
- e) Poorly observed.
- f) Not observed near *q*.
- g) Faded rapidly and may have disappeared. No nucleus seen.
- h) Mean of 5 dates and measures.
- i) Mean of 2 measures.

Discussion: L-P Comets

Table I shows, as expected, a strong dependence of AI on the perihelion distance. From the data for the L-P comets in Table Ia, two least-square solutions for this dependence were calculated. The first included a term proportional to the date, $\Delta t = (19xx - 1900)/100$, yielding:

$$(3.19 \pm 1.15) + (6.41 \pm 2.04)\Delta t - (5.41 \pm 0.78)\log q = AI \quad (4)$$

where values of standard deviations are included.

A second solution was made, not including a time variation viz.:

$$(6.76 \pm 0.23) - (5.88 \pm 0.88)\log q = AI. \quad (5)$$

The solution with Δt (Eq. 4) represents the observations slightly better than that with only the $\log q$ -term, $\sigma = 1^m.06$ vs. $1^m.26$ for a single AI. The dependence *q* in AI is $1/q^{2.2}$ for Eq. 4 and $1/q^{2.4}$ for Eq. 5, perhaps not as high a power as might have been expected.

There appeared to be some dependence of the AI residuals on h_o , the absolute magnitude at great distance. A solution shows that AI residuals systematically increased with the value of h_o , leading to a correction to the AI residuals of

$$\text{Correction } (\Delta AI) = 0^m.145(13^m.43 - h_o). \quad (6)$$

The question as to whether Eq. 4 or Eq. 5 is superior in seeking correlations with other physical or orbital characteristics of comets has no clearcut answer. The residuals from Eq. 4 shows a rather large dependence

Table II
Values of ΔAI for L-P Comets (Table Ia)

$\frac{1}{a} \times 10^6 \text{ AU}^{-1}$	< 22	22-100	100-464	464-2154	2154-10 ⁴	10 ⁴ -46416
Per.(yr.)	> 10 ⁷	10 ⁶ – 10 ⁷	10 ⁵ – 10 ⁶	10 ⁴ – 10 ⁵	10 ³ – 10 ⁴	10 ² – 10 ³
	m	m	m	m	m	m
ΔAI	+0.3	-1.7	-0.4	-0.5	+1.4	-0.2
ΔAI	-1.5	+0.1	+0.9	-1.2	+0.3	-0.5
ΔAI	(-1.3)	+0.2		-0.5	+1.1	(-0.8)
ΔAI	+1.5	-1.2		+2.2	+1.1	-0.7
ΔAI	-0.4	+1.1		-1.3	+0.2	+0.8
ΔAI		-0.7			-0.8	+1.5
ΔAI		(-0.8)			+1.7	
Mean	-0.28	-0.43	+0.25	-0.26	+0.71	+0.02

Table III
Gas/Dust Ratios (L-P Comets)

Comet	<u>High</u>		<u>Low-Medium</u>		
	q	ΔAI	Comet	q	ΔAI
	AU	m		AU	m
1957III	0.32	+1.5	1948I	0.75	-1.7
1957V	0.36	-0.5	1955V	0.88	-1.3
1962III	0.03	-0.8	1960II	0.50	-0.4
1970II	0.54	+1.7	1969IX	0.47	-1.3

on date while Eq. 5 clearly errs for the earliest comets. To avoid a possible fruitless discussion, I will list the mean residual of Eq. 4 and Eq. 5 corrected by Eq. 6 for such comparisons (ΔAI). The residuals in parenthesis will be included because they seem to be consistent with the others and because the data sample is so small. Thus, Table II lists these mean residuals for the orbital classes grouped in decades of periods.

With the limited data set of Table II, the comets with periods $> 10^4$ yr. appear to be slightly less active than those in the range $10^4 > P > 10^2$ yr. The difference is $-0^m.27 \pm 0.25$ (19 comets), compared to $0^m.39 \pm 0.26$ (13 comets) or $0^m.66$ in total at roughly the 2σ level. The difference is even stronger between the comets in the group $10^4 > P > 10^3$ yr. and the remainder, both of longer and shorter period. Because the difference in activity level of comets with periods exceeding 10^4 yr. is only about half that of the shorter-period L-P comets, there seems to be little cause to attach much importance to the result. If it is later sustained by much more data, it may become of real physical interest.

Table II, however, definitely does not support any theory of decreasing activity with aging among L-P comets. Highly retrograde L-P comets with $i > 110^\circ$ do, on the other hand, appear to be more active than those with $i < 110^\circ$: Mean $\Delta AI = +0^m.41 \pm 0^m.39$ for 10 comets ($i > 110^\circ$) vs. $-0^m.19 \pm 0^m.20$ for 22 comets ($i < 110^\circ$), neglecting the three poorly observed parabolic comets. This difference, in each case at the 1σ level, is scarcely definitive, but is suggestive.

Similarly an increase in the Dust/Gas (D/G) ratio with ΔAI is suggested by eight comets with $q < 1 \text{ AU}$ in Table III, where the ratio is taken from the compilation by Donn (1977). The mean ΔAI for four comets with high D/G is +0.5 and -1.2 for the four with low and medium values of D/G. It seems quite logical that dusty comets should appear to brighten more than "gassy" comets, simply because the dust is ejected through the coma more slowly than the gas.

No other suggestive correlations of ΔIA with observed characteristics of L-P comets were found. Gener-

Table IV
Comparison of AI with Sf

Comet	$h_o - AI$	$2.5 \log Sf$	Δ
A-J	8 ^m .7	2 ^m .07	+0 ^m .52
E	7.0	0.25	(-2.88)
F	10.5	0.41	+0.36
GZ	9.6	0.94	+0.01
HMP	10.2	0.11	-0.20
KK	9.2	0.10	-1.09
O	5.6	4.92	+0.56
PB	4.0	5.11	-0.66
SW2	10.1	1.02	+0.62
Sch	8.8	2.15	+0.60
TGK	12.4	-1.80	-0.70

ally, through the comets with large values of ΔIA seemed to include the more interesting or individualistic ones.

As a concluding remark about the L-P comets, the scatter in ΔIA seems remarkably small ($\sigma = \pm 1^m.06$) implying a mean range of only a factor of 7.0, or only a factor of 2.7 from the mean for the variations in brightness increase from "inactively" to maximum, evaluated near the proper perihelion for each comet. The total range derived is 3^m.9 or a factor of 36. On the other hand, the range in h_o , presumably a measure of cometary area (for a fixed albedo), is 7.^m2 or a factor of 759. This implies a range of 28 in radius or 2×10^4 in volume (or mass, if of constant density). In other words, the smallest comet nuclei appear to behave remarkably like the largest over four orders of magnitude in volume. Equation 6, relating ΔIA to h_o , suggests that small nuclei may, indeed, be relatively more active than larger ones. The effect, however, may be only a magnitude-system defect.

Discussion: S-P Comets

For the short-period comets, Beyer's data are rather limited, including only 15 good cases (Table Ia). This scatter in activity is only slightly larger than for the L-P comets ($\pm 1^m.24$ in σ of ΔIA vs. $\pm 1^m.06$). The S-P comets are systematically less active than the S-P comets by $0^m.40 \pm 0^m.37$ or 1σ , making them almost as active as the comets with $P > 10^4$ yr. (Table II) and the L-P comets of $i < 110^\circ$. No correlation indicating an increase of ΔIA with high vs. low-medium dust appears among the 7 S-P comets of Table Ia included in Donn's (1977) list.

If the present calculations of cometary activity are valid, they should demonstrate a positive correlation with the active areas calculated by Rickman et al. (1987) designated as Sf . Such values are listed for the 11 common comets in Table IV. Activity near perihelion is indicated in magnitudes by $h_o - AI$ (Col. 2 of Table IV) and should correlate with $2.5 \log Sf$ (Col. 3), where Sf is the active area in km, for the comets identified by 1 to 3 letters in Col. 1 of Table IV. A least-squares solution yields the result, omitting P/Encke which fits poorly:

$$(9^m.30 \pm 0.88) - (0^m.88 \pm 0.10)(h_o - AI) = 2.5 \log Sf \quad (6)$$

The residuals from Eq. 6 are listed (O-C) in the fourth column of Table IV, in magnitudes, with $\sigma = \pm 0^m.62$. Considering the differences in methodology between the analysis by Rickman et al. and that of the present paper, a mean error of only $\pm 0^m.62$ over a range of 7^m to 8^m indicates reasonable consistency between the two and implies that both have physical significance.

In the present study, values of h_o for S-P comets were obtained from data similar to those for h_o in Tables Ia and b, but for which H_{10} or similar near-perihelion data were not available from observations by Beyer. From 14 comparisons of H_{10} by Kresák and Kresáková (KK, 1987) with Beyer's results, a correction of $-1^m.1 \pm 0^m.2$ to KK's H_{10} leads to a mean agreement with Beyer's values at perihelion. In all, values of

ΔI and ΔAI have been obtained for 36 S-P comets in this fashion. The value of ΔAI averages $0^m.07$ smaller than for the 15 S-P comets of Table Ib. The comparison of 13 in common with the S_f values of Rickmann et al. lead to results much like those of Eq. 6 and Table IV although the scatter is much larger ($\sigma = 1^m.73$ vs. $\pm 0^m.62$). For that reason no listing of these calculations are included. The mean value of h_o for these 36 S-P comets is $2^m.6$ fainter than for the 15 represented by Beyer magnitudes. The difference in the mean value of ΔAI from that of Beyer S-P comets is more than explained by the corrections of Eq. 5 for h_o magnitudes. No conclusion about the mean relative activity of these fainter comets appears valid.

Discussion: General Comments

In recent years observers have directed much effort in an attempt to distinguish significant systematic differences in the spectra and other properties of L-P and S-P comets. After several studies of cometary spectra including Cochran (1987), Cochran et al. (1989) state "Overall, however, we must now conclude that there is no obvious differences between low activity comets and the "normal" comets and that all of the studied comets appear fairly homogeneous." From IUE observations of faint comets, Weaver et al. (1981) reach the same conclusion: "All of the cometary spectra are remarkably similar which suggests that these comets may have a common composition and origin." These statements seem also to represent the results of the present paper concerning the activity level of L-P and S-P comets.

Some differences in the spectra of individual comets are, however, evident, such as noted in the review of comets observed by the IUE satellite by A'Hearn (1989), from spectra of seventeen comets by Newburn and Spinrad (1984, 1985, 1989) and earlier from abundance measures by A'Hearn and Millis (1980). In a summary of calculations and estimates of cometary albedos, Hartmann et al. (1987) find a considerable range; the lower values, incidentally, correlate somewhat with negative values of ΔAI . Dust-to-gas ratios also vary greatly from comet to comet. To what extent these differences were induced by different environments and aging, and to what extent they represent localized differences in the nuclei induced by the falling together of components of somewhat different properties produced in a common original environment is difficult to ascertain.

In general, however, the accumulating evidence does little to suggest a drastically different environment for the origin of L-P vs. S-P comets, or for large subgroups among them.

This study was supported by NASA Grant NSG-7082. I am particularly grateful to Brian G. Marsden for a computer disc of his comet-orbit catalogue and for use of several of his programs.

References

- A'Hearn, M.F. 19889 "Comets" *A Decade of UV Astronomy using IUE*, Eur. Sp. Agency SP-281, 47-58.
- A'Hearn, M.F. and Millis, R.L. 1980, *Astron. J.*, **85**, 1528-1537.
- Beyer, M. 1969, *Astr. Nach.*, **291**, 257-264.
- Cochran, A.L. 1987, *Astron. J.*, **92**, 231-243.
- Cochran, A.L., Green, J.R., and Barker, S. 1989, *Icarus*, **79**, 125-144.
- Donn, B. 1977, *Comets, Asteroids, Meteroites*, ed. A.H. Delsemme, Univ. Toledo, 15-23.
- Hartmann, W.K., Tholen, D.J., and Cruikshank, D.P. 1987, *Icarus*, **69**, 33-50.
- Hughes, D.W. 1987, *Symposium on the Diversity and Similarity of Comets*, Brussels, Eur. Sp. Agency, Sp-278, 43-48.
- Kamél, L. 1991, "The Structure of Comets as Evidenced by Their Light Curves". Uppsala Univ. Thesis.
- Kresák, L. 1973, *Bull. Astr. Inst. Czech.*, **24**, 264-283.
- Kresák, L. 1977, *Bull. Astr. Inst. Czech.*, **28**, 346-355.
- Kresák, L. and Kresáková, M. 1987, *Symposium on the diversity and Similarity of Comets*, Brussels, Eur. Sp. Agency, Sp-278, 37-42.
- Marsden, B.G. 1989, *Catalogue of Cometary Orbits* 5th ed., Smithsonian Astrophysical Observatory.
- Meech, K.J. 1990, *Comets in the Post-Halley Era*, IAU Colloquium 116, Bamberg, FRG, in press.
- Newburn, R.L. and Spinrad, H.S. 1984, *Astron. J.*, **89**, 289-309.
- Newburn, R.L. and Spinrad, H.S. 1985, *Astron. J.*, **90**, 2591-2608.
- Newburn, R.L. and Spinrad, H.S. 1989, *Astron. J.*, **97**, 552-569.
- Oort, J.H. 1950, *Bull. Astr. Inst. Neth.*, **11**, 91-110.

- Rickman, H., Kamél, L., Festou, M.C., and Froeschlé 1987, *Symposium on the Diversity and Similarity of Comets*, Brussels, Eur. Sp. Agency, Sp-278, 471-481.
- Svoren, J. 1985, *Contr. Astron. Obs. Skalnaté Pleso*, **13**, 93-125.
- Svoren, J. 1984, *Contr. Astron. Obs. Skalnaté Pleso*, **12**, 7-44.
- Vsekhsvyatskii, S.K. 1964, *Physical Characteristics of Comets*, Jerusalem.
- Weaver, H.A., Feldman, P.D., Festou, M.C., A'Hearn, M.F., and Keller, H.U. 1981, *Icarus*, **47**, 449-463.

THE MASS OF (1) CERES FROM PERTURBATIONS ON (348) MAY

Gareth V. Williams

Harvard-Smithsonian Center for Astrophysics, Cambridge, MA 02138, U.S.A.

ABSTRACT

The most promising ground-based technique for determining the mass of a minor planet is the observation of the perturbations it induces in the motion of another minor planet. This method requires careful observation of both minor planets over extended periods of time. The mass of (1) Ceres has been determined from the perturbations on (348) May, which made three close approaches to Ceres at intervals of 46 years between 1891 and 1984. The motion of May is clearly influenced by Ceres, and by using different test masses for Ceres, a search has been made to determine the mass of Ceres that minimizes the residuals in the observations of May.

Introduction

The masses of the largest minor planets are rather poorly known. Traditionally, the masses of the major planets were obtained by observing their mutual perturbations or by observing their satellite systems. These methods are not easily applicable to minor planets: no minor planets are known to have satellites; the minor-planet perturbations on any of the major planets are negligible (from a ground-based viewpoint, except by tracking spacecraft); and the mutual minor-planet perturbations generally are small. However, the mutual-perturbation method, when applied to suitable objects, is the best ground-based method currently available for determining minor-planet masses. The best circumstances for using this method occur when one of the minor planets is large compared to the other, when the two objects make close, periodic approaches to each other, and when both have long observational histories.

A suitable pair of objects with long observational histories that make periodic close approaches to one another are (1) Ceres and (348) May: to 0.0816 AU in April 1938 and to 0.0424 AU in September 1984 (a moderately close-approach to 0.2006 AU occurred in December 1891, just prior to May's discovery). The orbital inclinations and nodal longitudes of Ceres and May are broadly similar, and since both orbits are of low eccentricity with semi-major axes differing by only 0.2 AU, encounters between the two tend to be quite prolonged: during the 1938 encounter May was within 0.1 AU of Ceres from December 1937 until July 1938; in 1984 the corresponding dates are February 1984 and March 1985. In addition, May is so small that its perturbing effect on Ceres can be neglected.

The first direct measurement of the mass of a minor planet was made by Hertz (1966), who, noting that (4) Vesta and (197) Arete approached each other to within a few hundredths of an AU every 18 years, determined the mass of Vesta to be $(1.17 \pm 0.10) \times 10^{-10} M_{\odot}$. This value was later revised to $(1.20 \pm 0.08) \times 10^{-10} M_{\odot}$ (Hertz, 1968). Prior to this determination, the masses of minor planets were estimated on the basis of measured or presumed diameters and presumed densities.

The suggestion that the mass of Ceres, M_c , might be determined from the perturbations it induced in the motion of a smaller body was made by Gauss. In 1802, shortly after the discovery of Pallas, he noted the close approach of the orbits of Ceres and Pallas at the descending node of the latter, and expressed the hope that the masses of both bodies might be determined from their gravitational influences on each other.

From consideration of the perturbations on Pallas by Ceres, Schubart (1970) derived $M_c = (6.7 \pm 0.4) \times 10^{-10} M_{\odot}$. From the perturbations by Ceres on Vesta, Schubart (1971) derived $M_c = 5.1 \times 10^{-10} M_{\odot}$, and combined this result and his 1970 value to obtain $M_c = (6.0 \pm 0.7) \times 10^{-10} M_{\odot}$. Schubart (1974), using a slightly different set of Pallas observations, refined this value to $M_c = (5.9 \pm 0.3) \times 10^{-10} M_{\odot}$. Landgraf (1988), again considering perturbations on Pallas, found $M_c = (5.0 \pm 0.3) \times 10^{-10} M_{\odot}$. Standish and Hellings (1989), considering the perturbations on Mars determined from the highly accurate ranging data from the Viking landers, found $M_c = (5.0 \pm 0.2) \times 10^{-10} M_{\odot}$.

For some time, E. Bowell, Lowell Observatory, has been recalculating the orbits of the old numbered minor planets on a regular basis. Bowell was unsuccessful in his attempt to represent the motion of May by considering perturbations by Mercury to Pluto, and he brought the matter to the attention of the author at the Minor Planet Center (hereafter referred to as MPC). After several attempts to obtain a reasonable orbit failed, the author realized that Ceres might be perturbing May significantly. Since the presumed effect of

Ceres was quite large (more than 100" in right ascension between 1892 and 1989), it was reasoned that the perturbations on May might be a rather sensitive indicator of the mass of Ceres. This hypothesis could not be tested until development versions of perturbation programs designed to work in the J2000.0 system were completed in late 1990, as the B1950.0 versions in use previously at the MPC were not designed to handle Ceres as a perturbing body.

The Observations

(348) May was discovered by A. Charlois in Nice on November 18, 1892. It was followed until January 1893 and was recovered by J. Palisa in Vienna in March 1894. It was followed there and at Nice for a month, but was not observed again until 1905. Observations seem to have been made at almost every opposition subsequent to 1910.

It is known that the archive of minor-planet observations at the MPC is fragmentary for observations made before 1939. A project to include more pre-1939 material in the archive is progressing. Efforts are also being made to encourage the remeasurement of plates for which only approximate positions have been previously reported.

A literature search was undertaken to obtain pre-1939 observations of May, so the observed arc could be extended back to the discovery opposition. Good series of observations made at Algiers were located. It was possible to rereduce the micrometric observations using the planet-minus-comparison offsets as given in the original publication and modern comparison-star positions. The rereduction of micrometer measures is a tedious task to do by hand, so the process was automated. The program that was written to accomplish this task, COMPSTAR, will also be used to handle the automatic rereduction of micrometric measures that are encountered in the course of the long-term project to expand the MPC archives.

A number of positions of (348) May in the MPC archive were approximate positions. Such positions are useless for orbit determination, and their only purpose is to show that there is a plate available for remeasurement. Precise measurements were desired for the series of approximate positions obtained at the Goethe Link Observatory, Indiana, and Turku, Finland. The plates taken in Indiana are now archived at the Lowell Observatory. The Indiana plates containing images of May were remeasured by B. A. Skiff, following a request to E. Bowell, and the relevant Turku plates were remeasured by A. Niemi, following a request to L. Oterma. A search of the Harvard plate-archives by C. Y. Shao led to the identification of a number of images of May from the 1920s and 1930s, and measurement of these images was undertaken by A. J. Noymer.

At the request of the author May was put on the observing program of the Oak Ridge Observatory. A number of observations at the 1991 opposition were obtained, extending over an arc of three months. A new orbit for May, computed in the J2000.0 system, published recently in the *Minor Planet Circulars* (Williams, 1991) includes these new observations.

The Orbits

A number of different orbits were calculated for May, considering the perturbations by Mercury to Neptune plus Ceres, using a different mass for Ceres in each orbit. The same observations were used in each calculation: 75 observations at 29 oppositions, 1892-1991. These observations showed reasonable residuals from a preliminary orbit calculation.

The first mass used was the 1976 IAU-recommended value, $5.9 \times 10^{-10} M_{\odot}$. Solutions were also done using masses ranging from (in units of $10^{-10} M_{\odot}$) 4.0 to 5.6. The r.m.s. residuals for each orbit solution are given below:

Mass ($\times 10^{-10} M_{\odot}$)	0	4.0	4.2	4.4	4.6	4.7	4.8	4.9	5.0
r.m.s. residual ("")	2.97	1.23	1.19	1.16	1.15	1.14	1.14	1.14	1.15
Mass ($\times 10^{-10} M_{\odot}$)	5.2	5.4	5.6	5.9					
r.m.s. residual ("")	1.16	1.19	1.23	1.31					

It can be seen from the table that the IAU-recommended value is too large. The mass of Ceres and its mean error were determined by the method of Herget (1972): this gave $(4.80 \pm 0.22) \times 10^{-10} M_{\odot}$.

As a test to see whether the motion of May was affected by any large minor planet other than Ceres, the influence of (511) Davida was examined (May and Davida can approach to within 0.05 AU). Assuming that Ceres and Davida have the same density, and using the diameters given by Tedesco (1989), a reasonable estimate for the mass of Davida was $3 \times 10^{-11} M_{\odot}$. The orbit of May was recalculated twice: once considering

perturbations by Venus to Neptune plus Ceres; and once including perturbations by Davida. Comparison of the residuals of both solutions showed small differences of $\sim 0''4$ in right ascension by 1892. This is only 0.4% of the difference caused by Ceres and does not significantly alter the estimate of the error of the derived mass of Ceres.

Preliminary Conclusions and Further Work

A preliminary determination of the mass of (1) Ceres, deduced from the perturbations on (348) May, is $(4.80 \pm 0.22) \times 10^{-10} M_{\odot}$.

A request has been made to L. D. Schmadel and S. Röser of the Astronomisches Rechen-Institut, Heidelberg, to secure the remeasurement of the relevant plates taken by Wolf and Reinmuth.

A search has also been made to locate other minor planets that approach Ceres periodically. Many objects were found to have orbits that approach Ceres very closely. This extensive list can be shortened by considering the observed arc of each object, whether there are any approaches to Ceres during the observed arc and, if there are, the number and duration of these approaches. Although this is quite time-consuming, several promising candidates have been identified, and study of the motion of these objects may help to constrain the mass of Ceres further.

A recent independent study of the motion of (203) Pompeja (Goffin, 1991) determined the mass of Ceres to be $(4.7 \pm 0.3) \times 10^{-10} M_{\odot}$. Although it has been clear for some time that the influence of Pluto is negligible on the motion of most minor planets and that Ceres should be included as a perturbing body when orbits are computed with full perturbations, it is important that all orbit computations are done using a standard value for the mass of Ceres. Commission 20 of the IAU, at a session at the 1991 IAU General Assembly in Buenos Aires, suggested the use of $5.0 \times 10^{-10} M_{\odot}$ as the mass of Ceres. This is the value that is now in use at the MPC.

References

- Goffin E. (1991) *Astron. & Astrophys.*, **249**, 563.
- Herget P. (1972) On The Determination of Planetary Masses. In *IAU Symp. No. 45: The Motion, Evolution of Orbits, and Origin of Comets* (G. A. Chebotarev, E. I. Kazimirchak-Polonskaya and B. G. Marsden, eds.), pp. 244-245.
- Hertz H. G. (1966) *IAU Circular* 1983.
- Hertz H. G. (1968) *Science*, **160**, 299.
- Landgraf W. (1988) *Astron. & Astrophys.*, **191**, 161.
- Schubart J. (1970) *IAU Circular* 2268.
- Schubart J. (1971) Asteroid Masses and Densities. In *Physical Studies of Minor Planets* (T. Gehrels, ed.), pp. 33-39.
- Schubart J. (1974) *Astron. & Astrophys.*, **30**, 289.
- Standish E. M. and Hellings R. W. (1989) *Icarus*, **80**, 326.
- Tedesco E. F. (1989) Asteroid Magnitudes, UBV Colors, and IRAS Albedos and Diameters. In *Asteroids II* (R. P. Binzel, T. Gehrels, M. S. Matthews, eds.), 1090-1138.
- Williams G. V. (1991) *Minor Planet Circular* 19274.

Object	Date of approach	Δ_{\min} (AU)
(32) Pomona	1975 Nov.	0.0250
(58) Concordia	1929 Sept.	0.0408
(84) Klio	1990 Mar.	0.0417
(91) Aegina	1973 Sept.	0.0332
(135) Hertha	1907 Feb.	0.0529
(165) Loreley	1909 May	0.0824
	1937 Jan.	0.0387
	1964 Sept.	0.0966
(203) Pompeja	1948 Aug.	0.0165
	1969 Feb.	0.0781
(255) Oppavia	1955 Nov.	0.0804
	1958 Apr.	0.0418
(324) Bambergia	1944 Mar.	0.0207

GASPERA AND IDA IN FAMILIES

James G. Williams
Jet Propulsion Laboratory, Calif. Institute
of Technology, Pasadena, CA 91109

The Galileo flyby candidates 951 Gaspra and 243 Ida are both in families. The former is in a complex of families associated with 8 Flora and the latter is in the Koronis family.

Fig. 1 shows a proper $a \sin i$ projection of part of the Flora region near 8 Flora. The proper elements are from Williams and Hierath (1987) and Williams (1989). Only part of the Flora region is shown. The Flora region is a very complex region of the belt, consisting of adjacent and overlapping families (Williams 1991). 8 Flora is a 141 km diameter S (Tedesco et al. 1989) and the remaining asteroids in the figure are all small (<25 km). The cluster to the lower left of 8 Flora is family 189 which probably results from a cratering event. Cratering is suggested because 8 Flora is at the edge of the cluster (the material came off one side) and the small fragments are less than 25 km in diameter. The cluster to the upper right, actually two clumps, is family 183, probably another (or two) cratering event. The material to the lower right is thought to be overlapping families. Gaspra has been assigned to family 189 because it is close to the cluster, but as can be seen it is in a less dense zone between clusters and, due to the complexity of the region, cannot be guaranteed to have arisen from the same cratering event. Barucci et al. (1987) and Tholen (1989) classify Gaspra and Flora as Ss. Because the spectrum of Gaspra is similar to Flora (Zellner et al. 1985) and because Gaspra is near to Flora in a region dominated by small bodies which are thought to have come from Flora, Gaspra is almost certainly a piece of 8 Flora. The most likely alternative to

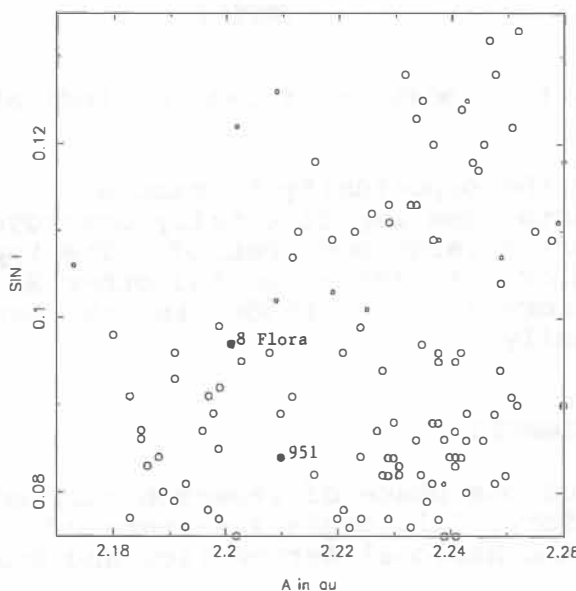


Fig. 1 Region near 8 Flora which contains 951 Gaspra.

cratering is the subsequent breakup of a larger fragment blasted off of 8 Flora. The event which created family 189 deposited part of the material in shallow Mars crossing orbits and there may be meteorite samples of Flora which are similar to Gaspra. Tedesco (1979) has done a study of asteroids in the Flora region. The Flora region and its proximity to Mars crossing are discussed further in Williams (1991).

243 Ida belongs to the Koronis family. The Koronis family (Fig. 2) consists of a dense core with surrounding material. 243 Ida is located in the dense core of the Koronis family as shown in the figure. The Koronis family results from the total breakup of its parent body. Ida is an S (Barucci 1987, Tholen 1989) like other Koronis family members (Gradie et al. 1979, Zellner et al. 1985, Bell 1989). Spectra are available (Chapman and Gaffey 1979, Zellner et al. 1985). The Koronis family is discussed further in Williams (1991).

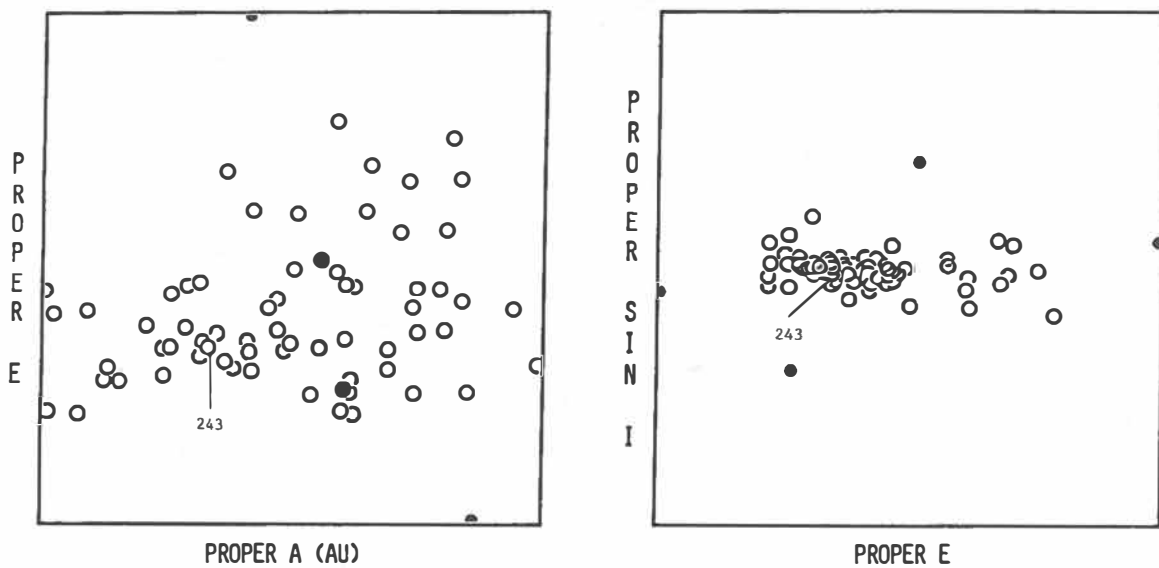


Fig. 2. The Koronis family with the location of 243 Ida indicated.

The Galileo spacecraft will have the opportunity to sample fragments from two types of impacts; one impact totally destroyed the parent body and the other left a large body behind. The types of Ss are also different, the colors of Gaspra and the other Ss in the complex of families near 8 Flora are much redder in U-V than Ida and the Ss of the Koronis family.

ACKNOWLEDGMENT

This paper presents the results of one phase of research carried out at the Jet Propulsion Laboratory, California Institute of Technology, under contract with the National Aeronautics and Space Administration.

REFERENCES

- Barucci M. A., Capria M. T., Coradini A., and Fulchignoni M. (1987) Classification of asteroids using G-mode analysis. *Icarus*, 72, 304-324.
- Bell J. F. (1989) Minearalogical clues to the origins of asteroid dynamical families. *Icarus*, 78, 426-440.
- Chapman C. R., and Gaffey M. J. (1979) Reflectance spectra for 277 asteroids. In *Asteroids* (T. Gehrels, ed.), pp. 655-687. Univ. of Arizona Press.
- Gradie J. C., Chapman C. R., and Williams J. G. (1979) Families of minor planets. In *Asteroids* (T. Gehrels, ed.), pp. 359-390, Univ. of Arizona Press, Tucson.
- Tedesco E. F. (1979) The origin of the Flora family. *Icarus*, 40, 375-382.
- Tedesco E. F., Williams J. G., Matson D. L., Veeder G. J., Gradie J. C., and Lebofsky L. A. (1989) Three-parameter asteroid taxonomy classifications. In *Asteroids II* (R. P. Binzel, T. Gehrels, and M. S. Matthews, eds.), pp. 1151-1161. Univ. Arizona Press, Tucson.
- Tholen D. J. (1989) Asteroid taxonomic classificaitons. In *Asteroids II* (R. P. Binzel, T. Gehrels, and M. S. Matthews, eds.), pp. 1139-1150. Univ. Arizona Press, Tucson.
- Williams J. G. (1989) Asteroid family identifications and proper elements. In *Asteroids II* (R. P. Binzel, T. Gehrels, and M. S. Matthews, eds.), pp. 1034-1072. Univ. Arizona Press, Tucson.
- Williams J. G. (1991) Asteroid families - an initial search. *Icarus*, in press.
- Williams J. G. and Hierath J. E. (1987) Palomar-Leiden minor planets: proper elements, frequency distributions, belt boundaries, and family memberships. *Icarus*, 72, 276-303.
- Zellner B., Tholen D. J., and Tedesco E. F. (1985) The eight-color asteroid survey: results for 589 minor planets. *Icarus*, 61, 355-416.

WHAT MAKES A FAMILY RELIABLE?

James G. Williams

Jet Propulsion Laboratory, Calif. Inst. of Tech., Pasadena, CA 91109

Asteroid families are clusters of asteroids in proper element space which are thought to be fragments from former collisions. Studies of families promise to improve understanding of large collision events and a large event can open up the interior of a former parent body to view. While a variety of searches for families have found the same heavily populated families, and some searches have found the same families of lower population, there is much apparent disagreement between proposed families of lower population of different investigations (Carusi and Valsecchi 1982). Indicators of reliability, factors compromising reliability, an illustration of the influence of different data samples, and a discussion of how several investigations perceived families in the same region of proper element space are given.

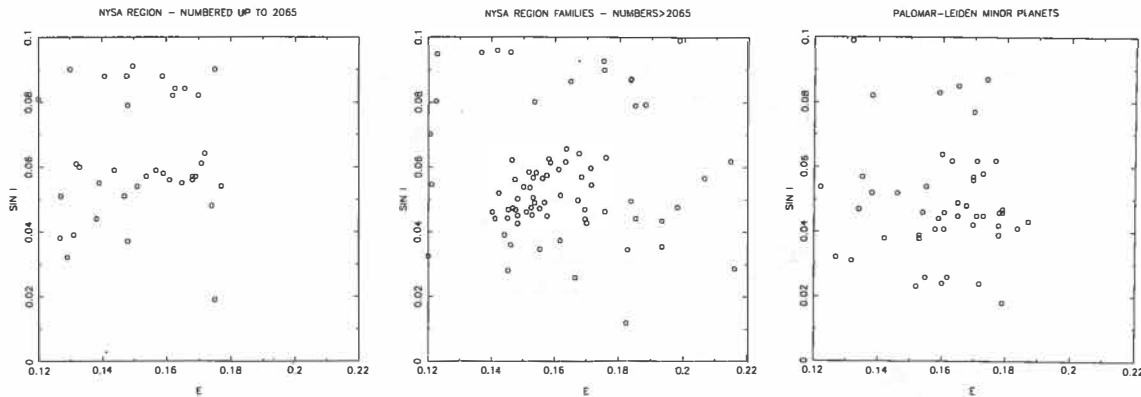
Ideally, the asteroids which cluster together to form a proposed family should all come from the same impact event. But the match between the memberships of the proposed family and the surviving fragments of a single impact event may be imperfect and the reliability of a family must be judged by the available data. Several factors contribute to the perception of a family's reliability. Included are high population, a compact size in proper element space, high density, a low background of neighboring objects, neighboring families clearly separate, and reasonable geometry (no pretzels). If available, albedos, colors, spectra, and taxonomic classifications are important, particularly if the family's properties are in contrast to the background. The addition of newly discovered, higher numbered asteroids is an indicator of reliability as is the presence of the family in other data samples, e. g., the Palomar-Leiden (van Houten et al. 1970) or UCAS surveys. The discovery of the same family by different investigators gives further confidence.

Seldom does a family satisfy all of the above properties. Many factors work against reliability. There are more families of low population than high population and low population families are more vulnerable. Some families have larger extent than others and if they are not well populated they will be less evident because of low density. The mapping of the velocities of dispersion from the impact into the scatter of the three proper elements (a , e , $\sin i$) depends upon the unknown location in the orbit at the time of breakup. Thus, families may be elongated or tilted in unpredictable ways which complicates the search procedure. There are examples of crowded or overlapping families. Likely examples of multiple families from a single parent body are known. The background density of asteroids is different in different parts of the belt so that uniform criteria for picking out families need not be optimum criteria. Some considerations depend on properties of families that are not yet well understood. The taxonomy may not be homogeneous in some families because the parent body was differentiated so that interpretation of the taxonomy enters judgement of reliability. A family with a steep size distribution has more members to discover, but there appear to be genuine

families with shallow size distributions which do not add many high numbered objects. The background asteroids may not be isolated, they may form low population clumps (unrecognized families) so that it is possible to mistakenly combine disparate clumps into one "family". Structure is common in the well populated families (commonly asymmetries and denser cores) and it cannot be assumed that the less populated families lack structure. Among the less reliable families, additional data will establish reliability or require reconsideration, but some cases, such as overlapping families, will always prove difficult.

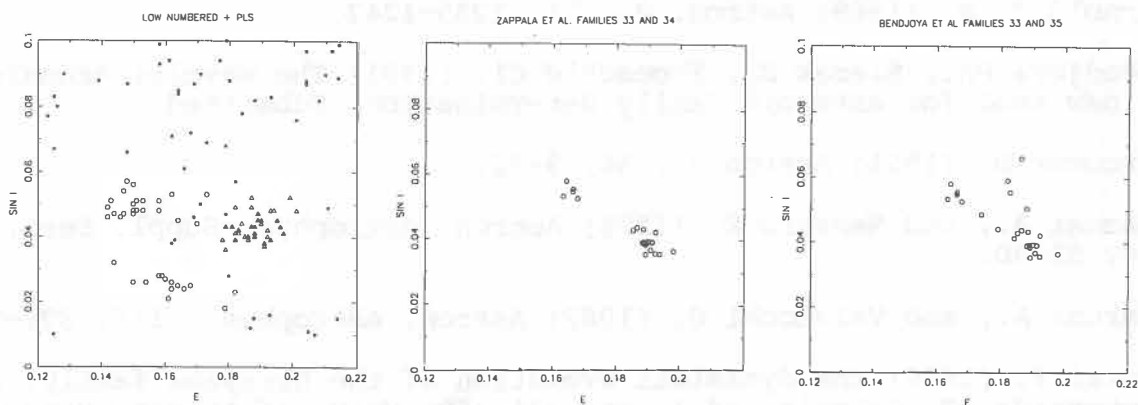
A study of about 1% of the belt's phase space (2.34–2.49 AU, modest e , low $\sin i$) was undertaken to understand why different investigators have proposed different families and to examine how the data sample influences the detection of families. This region includes four major families and two slices, divided at 2.415 AU, were considered. Each slice contains two major families: Mildred and Jutta for the inner slice and Nysa and Hertha for the outer slice. The family names used here will follow Williams (1991).

Three data samples were picked: asteroids with numbers up to 2065, higher numbered objects, and Palomar-Leiden (PLS) objects. These samples are progressively fainter. For the 2.34–2.415 AU slice, the Jutta and Mildred families have a few members among the lower numbered asteroids and they are quite well populated among both samples of fainter asteroids. This is what one might expect for reliable families. The slice from 2.415–2.49 AU is more surprising and is illustrated in Fig. 1. The densest cluster of asteroids for each data sample is in a different location. For the lower numbered asteroids, the cluster slightly to the upper left of center is the Nysa family. The PLS sample shows some Nysa family members, but the Hertha family just below center is more prominent. This is understandable if the size distributions of the two families are different. The plot of higher numbered objects shows a few objects at the location of the Hertha family, a considerable number of objects at the location of the previously recognized Nysa family, and a dense cluster to the left of the former family and below the latter family. I suspect that this cluster is yet another major family, but it is crowded against the Nysa and Hertha families and the figure illustrates that it can be difficult to make a unique division between crowded families. It is evident that the data sample can influence the recognition of families. Brouwer (1951), Arnold (1969), and Williams (1991) did not use the higher numbered



sample and found virtually the same Nysa family. Bendjoya et al. (1991) included part of that Nysa family with the new cluster in a single family. Both Zappala et al. (1990) and Bendjoya et al. also picked out a dense portion within the right side of the Nysa family of Brouwer, Arnold, and Williams as a separate family.

Fig. 2 shows the slice from 2.34–2.415 AU. The first frame shows the lower numbered and PLS asteroids with larger symbols used for the Jutta, Mildred, and Massalia family members given in Williams and Hierath (1987) and Williams (1989). The Jutta family is to the left of center, Mildred family members to the lower right of center are shown with triangles, and the Massalia family lies at low inclination. The second and third frames show the family members proposed by Zappala et al. and Bendjoya et al., but background objects are not shown. Both investigations found a cluster of five members at the right side of the Jutta family (which they both call the Leonce family) and both discover a well populated cluster corresponding to the Mildred family. Most of the family members in the first frame are PLS objects, while most of the family members in the second and third frames are high numbered asteroids so the families have been recognized in different data samples. Bendjoya et al. also include as Mildred family members objects which are well beyond the family boundaries of the other two investigations.



Without higher numbered or PLS asteroids Hirayama, Brouwer, and Arnold could not find the Mildred and Jutta families. Van Houten et al. (1970) put the Nysa, Hertha, Jutta, and Mildred families together into a single "Nysa" family. Lindblad and Southworth (1971), when using a distance criteria intended to match van Houten et al., combined these four families plus the Massalia family into one. For other earlier investigators, table 6 of Carusi and Valsecchi (1982) is useful. Carusi and Massaro's (1978) Nysa family includes parts of the four major families. Kozai's (1979) family 5 has the Jutta family as a major component and his family 15 includes the Nysa family and a considerable amount of other material. Thus we see that some investigations have made families of larger extent by combining, what are considered here to be, several individual families. Thus, different investigators may find the same broad structures, but may partition them into families differently depending on their individual criteria.

The conclusions may be summarized. 1) Many factors influence a family's discovery and the assessment of its reliability. 2) The mean magnitude of different asteroid samples influences the relative prominence of different families and influences which families are found. 3) The criteria of different investigations influences the proposed families and can strongly influence the size of the proposed family in proper element space. 4) Even when different investigations produce very different lists of families, the differences may be understandable as smaller pieces of families or combinations of adjacent families. The proposed families are correlated, not random. 5) Both statistics and geometry are valuable for assessing family reliability. 6) Real asteroid families, meaning collections of fragments from impacts, exist.

ACKNOWLEDGMENTS

Proper elements were provided by R. Wolfe and E. Shoemaker for the middle frame of Fig. 1 and by A. Milani and Z. Knezevic (version 4.2) for the two right-hand frames of Fig. 2. This paper presents the results of one phase of research carried out at the Jet Propulsion Laboratory, California Institute of Technology, under contract with the National Aeronautics and Space Administration.

REFERENCES

- Arnold J. R. (1969) *Astron. J.*, 74, 1235-1242.
- Bendjoya Ph., Slezak E., Froeschle Cl. (1991) The wavelet transform: a new tool for asteroid family determination. Submitted.
- Brouwer D. (1951) *Astron. J.*, 56, 9-32.
- Carusi A., and Massaro E. (1978) *Astron. Astrophys. Suppl. Ser.*, 34, 81-90.
- Carusi A., and Valsecchi G. (1982) *Astron. Astrophys.*, 115, 327-335.
- Kozai Y. (1979) The dynamical evolution of the Hirayama family. In *Asteroids* (T. Gehrels, ed.), pp. 334-358. Univ. of Arizona Press.
- Lindblad B. A., and Southworth R. B. (1971) In *Physical Studies of Minor Planets* (T. Gehrels, ed.), pp. 337-352. NASA SP-267, U. S. Government Printing Office, Washington, D. C.
- van Houten C. J., van Houten-Groeneveld I., Herget P., and Gehrels T. (1970) *Astron. Astrophys. Suppl. Ser.*, 2, 339-348.
- Williams J. G. (1989) In *Asteroids II* (R. P. Binzel, T. Gehrels, and M. S. Matthews, eds.), pp. 1034-1072. Univ. Arizona Press, Tucson.
- Williams J. G. (1991) Asteroid families - an initial search. *Icarus*, in press.
- Williams J. G. and Hierath J. E. (1987) *Icarus*, 72, 276-303.
- Zappala V., Cellino A., Farinella P., and Knezevic Z. (1990) Asteroid families. I. *Astron. J.*, 100, 2030-2046.

THE UNUSUAL LIGHTCURVE OF 1990 TR

Wieslaw Z. Wisniewski, Space Sciences Bld. Lunar and Planetary Laboratory,
University of Arizona, Tucson, Arizona 85721, USA

ABSTRACT

Amor asteroid 1990 TR was monitored during three nights shortly after discovery. Obtained lightcurves did not reveal a repeatable curve with two maxima and two minima. However, some features suggest periodicity, and a synodic rotational period $P = 6.25$ hours was determined. Individual and composite lightcurves are presented. The colors are best represented by the class S.

INTRODUCTION

When monitoring lightcurves of asteroids we usually expect to observe two maxima and two minima, reflecting an elongated shape for the observed object. There are just a few known objects, e.g. 29 Amphitrite, 51 Namausa, 75 Euridike, 287 Neptys, and 471 Papagena which show 3 maxima and 3 minima in their lightcurves. 471 Papagena had been extensively studied by several researches with unambiguous results. (Lustig 1977, Scaltriti and Zappala 1978, Surdej and Surdej 1977, Di Martino and Cacciatori 1984). Such lightcurves with multiple extrema are interpreted as caused by irregular shapes and/or by albedo spots on the objects surface. To this list we may add Earth Approaching asteroid 1990 TR.

Asteroid 1990 TR was discovered by S. Ueda and H. Kaneda (IAU Circ. #5121) and independently by A. V. Tarasova and L. I. Chernykh (IAU Circ. #5137). The ephemeris based on the discovery predicted the object to be as bright as 12.9 magnitude in Oct 1990 and still as bright as 14.4 at the end of November.

OBSERVATIONS AND RESULTS

Amor asteroid 1990 TR was monitored during the nights of Nov 13 and 18, 1990. Color measurements were obtained during the night of Nov 19. The data presented here were obtained with a photoelectric photometer equipped with a Hamamatsu photomultiplier R943-02 on the 1.5 meter telescope at the University of Arizona Observatory on Mt. Lemmon in the Catalina Mountain range of Tucson. When monitoring visual lightcurves, two comparison stars in the vicinity of the asteroid were measured regularly. The ubvwx "subset" filters of the eight-color asteroid filters (Tedesco et al. 1982) were used. Comparison stars' standardization and color transformation was done during the night of Nov 19. The aspect data and physical parameters are presented in Table I and Table II respectively.

Unexpectedly, the observations turned out to be quite challenging, as 1990 TR appeared to be about 1.5 mag fainter ($V = 15.2$ at maximum) than predicted by the initial ephemeris. The 5.5 hours of monitoring during the first night revealed a complex lightcurve with two maxima and two minima followed by a semi-plateau (Fig. 1). To be certain that the lightcurve is not modulated by faint stars, the asteroid path was checked against a Hubble Telescope Guide Star plate. The path seems to be clear to the best of my knowledge. On Nov 18 a plateau was observed again (Fig. 2). Assuming that this is the same as the one from Nov 13, the composite lightcurve was plotted as seen in Fig. 3, from which a synodic period of rotation $P = 6\text{hr } 15\text{m}$ was determined. However a period of $7\text{hr } 54\text{min}$ will match both lightcurves and single measurements from the night of Nov 19 as well.

At present there is not enough data to differentiate between the interpretations of irregular shape or albedo spots. Perhaps a local topography like craters and flat areas should be taken into consideration. There are small asteroids with lightcurves having "bump" visible only on occasion. Fig. 4 shows such lightcurve for 1917 Cuyo observed in Oct 1989. Similarly, Fig. 5 shows two pronounced bumps for 3908 1980 PA. A well known asteroid with three maxima, 1580 Betulia, has at times a "normal" two maxima lightcurve as observed in May 1989 (Fig. 6). There is just a hint of maximum splitting. If this were the only observation of Betulia we would treat it as a typical asteroid.

As 1990 TR appears to be an interesting candidate for future studies, I calculated its ephemeris for the next 10 years. In Table III the favorable oppositions are listed. The +1.5 mag correction to the V magnitude was applied. At its best, the object may be observed from the southern hemisphere, being 17.1 magnitude at its brightest. This calls for a CCD camera and a telescope larger than 1 meter.

With so much successful activity in discoveries of Earth Approaching asteroids, reaching to fainter and fainter ones - read shorter and shorter observability windows - the follow up is falling behind. A much better organized, concentrated, effort is needed. This doesn't mean necessarily an increase in current total observing time. One or two nights of observations from telescopes well spaced in longitude will produce by far more complete data than hundreds of hours of observing at one site (weather permitting such a long run). This is particularly true if an object turns out to be a slow rotator, with a period of several days.

ACKNOWLEDGMENTS

Support by Space Engineering Research Center at the University of Arizona and by NASA Grant NAGW-716 is gratefully acknowledged.

TABLE I
Aspect data for 1990 TR

Date UT yr/mo/day	RA h m	Dec (1950)	Long (1950)	Lat (1950)	r (AU)	Δ	Phase
90/11/13	01 56	26 47	36.55	13.91	1.405	0.432	13.4
90/11/18	01 55	27 03	36.45	14.25	1.429	0.467	15.9
90/11/19	01 55	27 06	36 45	14.26	1.434	0.474	16.1

TABLE II
Physical Parameters for 1990 TR

Date	u-v	b-v	v	v-w	v-x	Period	amp.	H	CLASS
90/11/19	m 0.81	m 0.12	m 15.22	m 0.13	m 0.07	h 6.15	m 0.19	m 16.05	S

TABLE III
Favorable oppositions for 1990 TR

Date	Dec	V mag.
1993 May-Aug	-40	17.1 - 18
1996 Apr-Jun	-25	18.3 - 19

REFERENCES

- Di Martino M., and Caciatori S. (1984) Photoelectric Photometry of 14 Asteroids. *Icarus*, **60**, 75-82.
- Lustig G. (1977) Die Rotations Periode und die Photoelektrische Lichtkurve des Planetoiden 471 Papagena. *Astron. & Astrophys. Suppl.*, **30**, 117-119
- Scaltriti F. and Zapalla V. (1978) Photoelectric Photometry of Asteroids 37, 80, 97, 216, 270, 313 and 471. *Icarus*, **34**, 428-435.
- Surdej A. and Surdej J. (1977) Rotation Period and Photoelectric Lightcurves of Asteroid 471 Papagena. *Astron. & Astrophys. Suppl.*, **30**, 121-124.
- Tarasova A. V. and Chernykh L. I. (1990) 1990 TR. *IAU Circ.* #5137.
- Tedesco E. F., Tholen D. J., and Zellner B. (1982) The Eight Color Survey: Standard Stars. *Astron. J.*, **87**, 1585-1592.
- Ueda S., and Kaneda H. (1990) 1990 TR. *IAU Circ.* #5121.

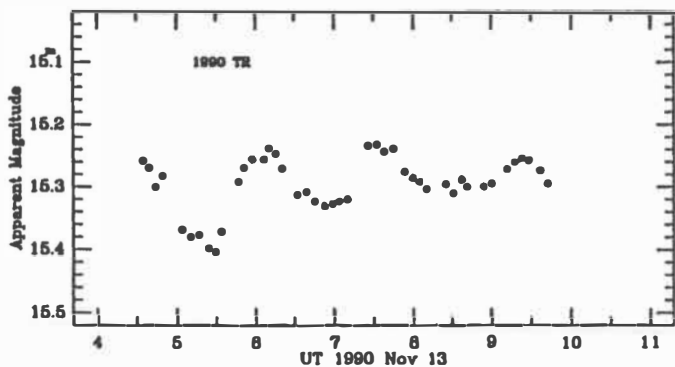


Fig. 1. Lightcurve of 1990 TR obtained on Nov 13, 1990.

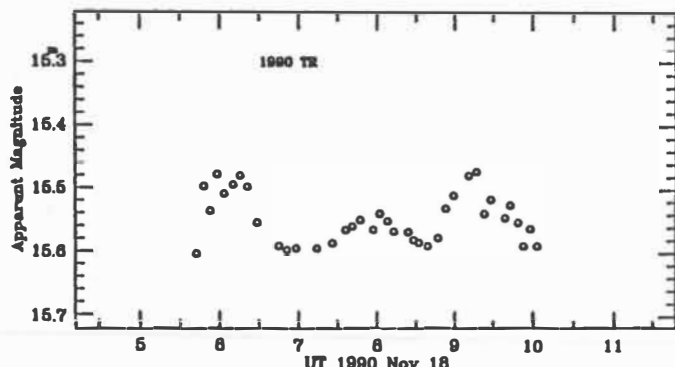


Fig. 2. Lightcurve of 1990 TR obtained on Nov 18, 1990.

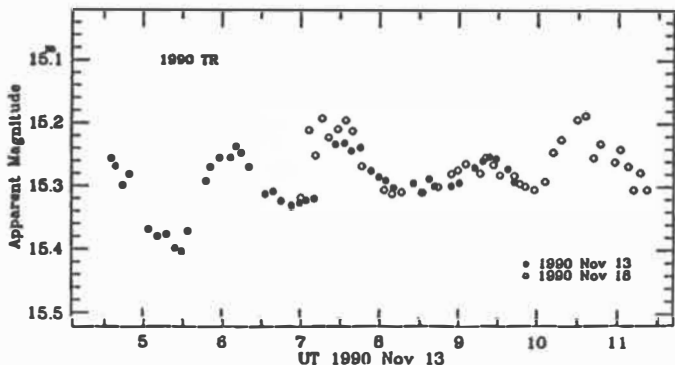


Fig. 3. Composite lightcurve of 1990 TR.

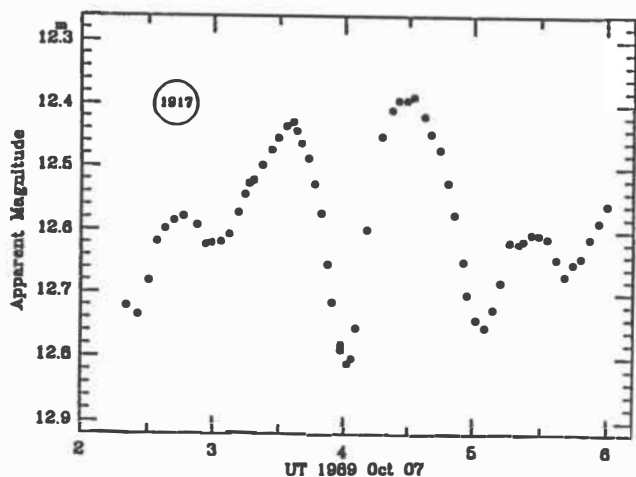


Fig. 4. Lightcurve of 1917 Cuyo obtained on Oct 7, 1989.

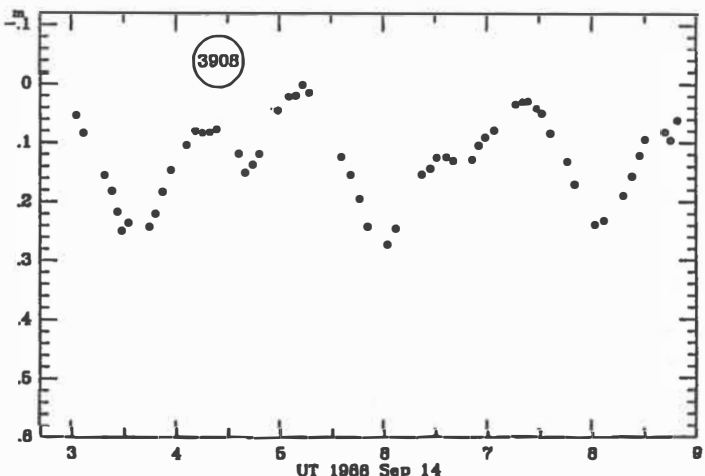


Fig. 5. Lightcurve of 3908 (1980 PA) obtained on Sep 14, 1988.

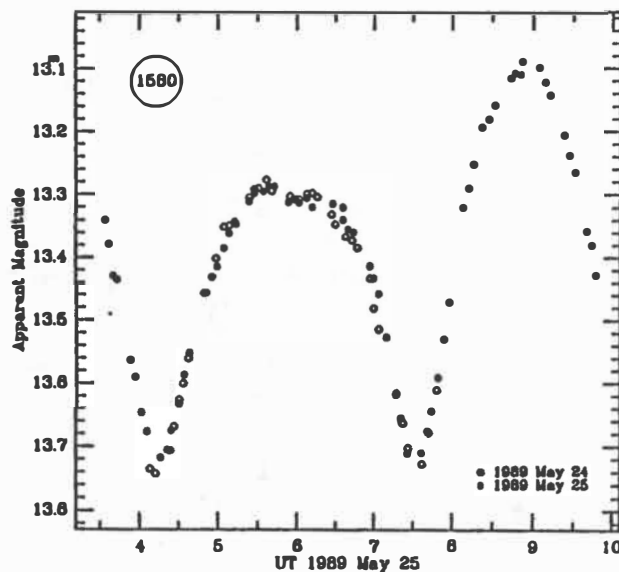


Fig. 6. Lightcurve of 1580 Betulia obtained on May 24-25, 1989.

VELOCITY DISTRIBUTIONS OF H AND OH PRODUCED THROUGH SOLAR PHOTODISSOCIATION OF H₂O

C. Y. Robert Wu, F. Z. Chen, and D. L. Judge
Space Sciences Center and Department of Physics
University of Southern California
Los Angeles, CA 90089-1341

The calculated velocity distributions of atomic hydrogen and hydroxyl radicals produced through solar photodissociation of gaseous water molecules are presented. Under collisionless conditions, the calculation has been carried out using the most recent available data for the production of H and OH through photodissociation of H₂O from its dissociation onset throughout the EUV region. Because the lack of data in certain spectral regions, we can only obtain an upper and lower bounds to the velocity distributions. The results show that the H atoms and OH radicals produced exhibit multiple velocity groups. Since most of the current cometary modeling uses a single velocity of 20 km/s associated with the photodissociation of H₂O, the present results may be useful in interpreting the *many peaks* observed in the velocity distributions of cometary atomic hydrogen.

INTRODUCTION

H₂O is a major constituent of the atmospheres of comets, satellites of the outer solar system, and is also a major constituent of the atmosphere of the Earth. A major feature of comets is the extended atomic hydrogen coma which can reach tens of gigameters (10⁶ km) from the nucleus. Observations of atomic hydrogen emission lines (Ly- α ; Ly- β ; and H α) yield information about the heliocentric variation of the total gas production rate, since H₂O is apparently the ultimate parent of H. Such data also provide information about the hydrogen velocity distribution, the lifetime of atoms against solar wind charge exchange and photoionization loss, and the solar Ly- α radiation pressure. Similarly, observations of the 18-cm OH line profiles have yielded information on the velocity distributions of the ejected OH and on the expanding cometary H₂O.

The hydrogen Ly- α isophotes in the outer region observed in several comets can be reproduced by a theoretical model assuming a two-component (20 and 8 km/s) Maxwellian velocity distribution of H atoms with equal production rates. It has been suggested that the high-velocity component arises from photodissociation of H₂O and the low-velocity component from photodissociation of OH. A better knowledge about the velocity distribution of H atoms and OH radicals produced through photodissociation of H₂O can be obtained in a more rigorous treatment of this important problem. Such a velocity distribution can in principle be determined if the partial cross sections of *all* the possible photodissociation processes are known.

The relevant processes that produce H and OH photofragments in the ground and excited states are:



In his pioneering work, *Festou* [1981] only treated process (1) and only considered the first absorption band of H₂O in the 1360-1860 Å region and the absorption at the H Ly- α line. Recently, *Crovisier* [1989] improved the model calculation by including the vibrational energy distributions of the ground state OH fragment and obtained an averaged OH velocity of 1.05 km/s (the corresponding H velocity is 17.85 km/s). This velocity is 10% smaller than that derived by neglecting the internal vibrational energy of OH(X² Π) photofragments. In the present work we have extended the photon wavelength from 1860 Å throughout the EUV region and have also included the six photodissociation processes listed above.

TOTAL AND PARTIAL PHOTOEXCITATION CROSS SECTIONS OF H₂O

The photoexcitation processes of H₂O in the VUV-EUV region have been extensively studied both experimentally and theoretically [*Dutuit et al.*, 1985; *Wu and Judge*, 1988; 1991] and the photoabsorption and photoionization cross section data are well known. However, only limited photodissociation data are available at a few incident photon wavelengths [*Berkowitz* 1979].

It is well known that photoexcitation of the H₂O molecule rarely results in fluorescence from excited states of the neutral H₂O molecule and parent H₂O⁺ ion. In contrast with these, the fluorescence from excited H^{*} and OH^{*} photofragments is intense, with a maximum quantum yield of 0.12 and 0.1, respectively. In addition to the excited photofragments, the other neutral products may include the parent molecule and neutral photofragments which are in the ground and metastable states. The maximum quantum yields for producing the neutral products [*Wu and Judge* 1988] are 1.0, ~0.6, and ~0.3 for the wavelength ranges >984, 800-984, and 600-800 Å, respectively. By subtracting the partial cross sections for producing the excited photofragments from that of the total neutral products, the remaining cross sections are the cross sections for producing the *undetected neutral products*. The quantum yield for the undetected neutral products can be as high as 0.43 at 810 Å [*Wu and Judge*, 1988; 1991]. In the present work, a lower bound is set for the case that all the *undetected neutral products* are something other than H and OH fragments. An upper bound is set by assuming the *undetected neutral products* are all H and OH fragments. As a result, an upper and lower bounds of velocity distributions are calculated. The *real* distributions will probably lie in between these two extremes.

VELOCITY DISTRIBUTIONS OF DISSOCIATION FRAGMENTS

The excess excitation energy ΔE is defined as the difference between the incident photon energy $h\nu$ and the threshold energy $E_0(\Lambda)$ for the dissociation process of interest at a given temperature, less the internal energy $E(v,J)$, i.e., the vibrational and rotational energies, of the photofragments. This can be expressed as $\Delta E = h\nu - E_0(\Lambda) - E(v,J)$, where Λ is the specific electronic state of the parent molecule involved in the dissociation channel of interest. The v and J are the vibrational and rotational quantum numbers, respectively. From the conservation of energy and momentum the excess energy is converted into kinetic energy of the H and OH fragments in the dissociation of H₂O. The kinetic energy of the respective H and OH fragments is $(17/18)\Delta E$ and $(1/18)\Delta E$. Thus, the velocity of the respective H and OH is $13.44(\Delta E)^{1/2}$ and $0.796(\Delta E)^{1/2}$ km/s with ΔE in units of eV.

The production rate of a specific photofragment is $A(\lambda) = F_{\odot\lambda}\eta_\lambda(1 - e^{-n\ell})$, where $F_{\odot\lambda}$ is the solar flux at λ , η_λ is the quantum yield for producing the specific photofragments, $n\ell$ is the column density, and σ_λ is the photoabsorption cross section at λ .

The calculation has been carried out using (a) the most recent available absolute absorption cross section of H₂O and the quantum yields for the production of H and OH through photodissociation of H₂O from its absorption onset throughout the EUV region [*Judge and Wu*,

1990; Lee and Suto, 1986; Wu and Judge, 1988; 1991], (b) the newly available vibrational and rotational energy distributions of both the excited [Lee et al., 1978; Wu and Judge, 1991] and the ground state [Engel et al., 1988] OH photofragments, and (c) the integrated solar flux in 10 Å increments from 500 to 1860 Å in the *continuum* regions [Lean, 1987; Mount and Rottman, 1983a; 1983b; Valley, 1966] and the specific wavelength and flux at the bright solar lines [Valley, 1966], e.g., the H Ly- α , - β , - γ , O VI, C III, He I, etc.

The calculated upper and lower bound results are shown in Figs. 1 and 2. For the upper bound case, the H atoms produced exhibit multiple velocity groups centered at 11.3, 14.1, 18.4, 30.5, 35.6, 37.2, and 39.8 km/s, see the dotted curve in Fig. 1, while the OH radicals produced can have a velocity group as high as 2.34 km/s, as shown by the dotted curve in Fig. 2. The averaged values of the upper and lower bound velocity distributions of H photofragments are 19.79 and 22.53 km/s, respectively. The corresponding values of the OH radicals are 1.09 and 1.05 km/s, respectively. Our lower bound value is in excellent agreement with that reported by Crovisier [1989]. However, the shape of his OH distribution is different from ours. As can be seen from Fig. 2 the calculated shape centered at 1.0 km/s shows high intensity at low OH velocity and gradually decreases toward the high velocity end. The many peaks obtained in the present work may be useful in interpreting the *many peaks* observed in the velocity distributions of the H Ly- α and H α of comets.

Acknowledgments

This material is based upon work supported by the National Aeronautics and Space Administration under Grant No. NAGW-1924 and by the National Science Foundation under Grant No. ATM-8722482. We are grateful to the staff of the Synchrotron Radiation Center of the University of Wisconsin, particularly E.M. Rowe and R. Otte. The Synchrotron Radiation Center is supported by the National Science Foundation under Grant No. DMR-8821625.

References

- Berkowitz, J. (1979) Photoabsorption, Photoionization, and Photoelectron Spectroscopy. Academic Press, New York. pp239-247.
- Crovisier, J. (1989) The photodissociation of water in cometary atmospheres, Astron. Astrophys. **213**, 459-464.
- Dutuit, O., Tabche-Fouhaile, A., Nenner, I., Frohlich, H., Guyon, P.M. (1985) Photodissociation processes of water vapor below and above the ionization potential, J. Chem. Phys., **83**, 584-596.
- Engel, V., Schinke, R., Staemmler, V. (1988) Photodissociation dynamics of H₂O and D₂O in the first absorption band: A complete ab initio treatment, J. Chem. Phys., **88**, 129-148.
- Festou, M.C. (1981) The density distribution of neutral compounds in cometary atmospheres, Astron. Astrophys., **95**, 69-79, and **96**, 52-57.
- Judge, D.L., Wu, C.Y.R. (1990) Absolute vacuum ultraviolet photoabsorption cross section studies of atomic and molecular species: Techniques and observational data, NASA Conf. Publ., **3077**, 93-113.
- Lean, J.L. (1987) Solar ultraviolet irradiance variations: A review, J. Geophys. Res., **92**, 839-868.
- Lee, L.C., Oren, L., Phillips, E., Judge, D.L. (1978) Cross sections for production of the OH(A-X) fluorescence by photodissociation of H₂O vapor, J. Phys., **B11**, 47-54.
- Lee, L.C., Suto, M. (1986) Quantitative photoabsorption and fluorescence study of H₂O and D₂O at 50-190 nm, Chem. Phys., **110**, 161-169.
- Mount, G.H., and Rottman, G.J. (1983a) The solar absolute spectral irradiance 1150-3171 Å: May 17, 1982, J. Geophys. Res., **88**, 5403-5410.
- Mount, G.H., and Rottman, G.J. (1983b) The solar absolute spectral irradiance at 1216 Å and 1800-

- 3171 Å: January 12, 1983, *J. Geophys. Res.*, **88**, 6807-6811.
 Valley, S.L. (1966) ed. *Handbook of Geophysics and Space Environments* (McGraw-Hill, N.Y.), Chapter 16.
 Wu, C.Y.R., Judge, D.L. (1988) Multichannel processes of H₂O in the 18 eV region, *J. Chem. Phys.*, **89**, 6275-6282.
 Wu, C.Y.R., Judge, D.L. (1991) Multichannel processes in the vacuum ultraviolet photon excitation of molecular systems, *Trends in Chem. Phys.*, (in press).

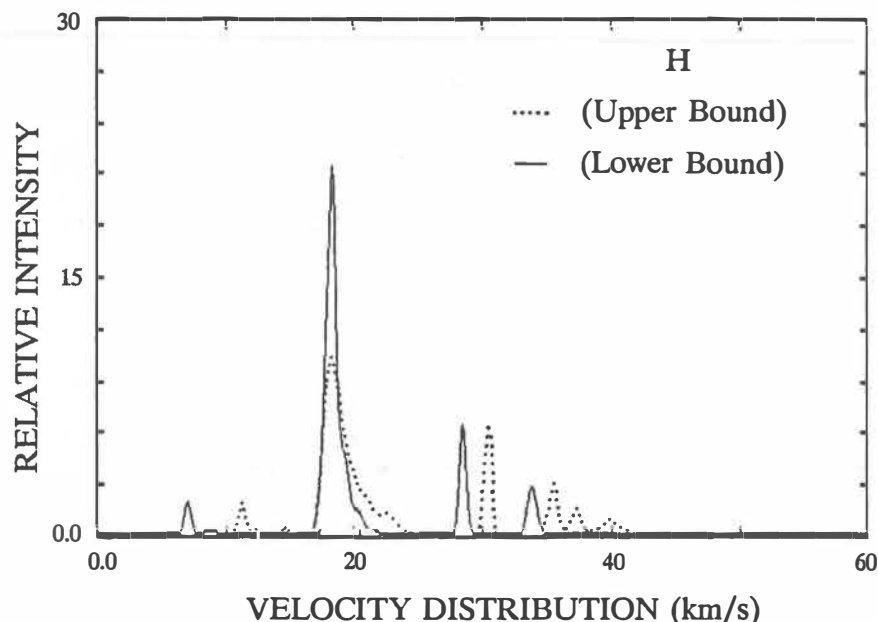


Fig. 1 The velocity distribution of H photofragments produced through solar photodissociation of H₂O. The dashed and solid curves represent the upper and lower bound cases, respectively. See the text for further detail.

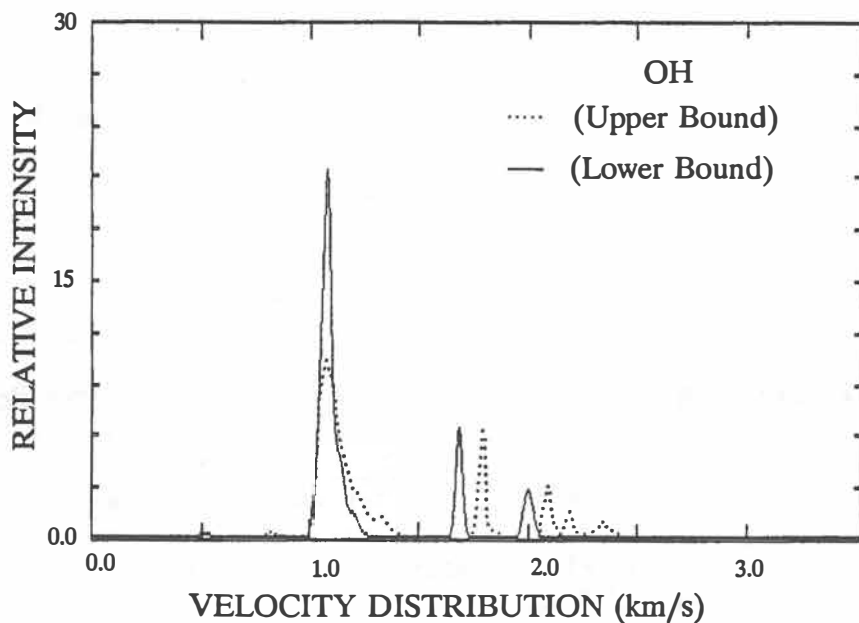


Fig. 2. Same as Fig. 1 except that this is for the velocity distribution of OH photofragments.

Formation of the Leonid Meteor Stream and Storm

Zidian Wu and I. P. Williams

Astronomy Unit, Queen Mary and Westfield College, University of London,
Mile End Road, London E1 4NS, UK

Abstract

It is well known that some meteor showers display a very high level of activity at certain times, the most famous being the Leonid shower with very spectacular displays at roughly 33 year intervals. This period being also the period of the parent comet of the stream, Comet Tempel-Tuttle. An investigation of the geometry of the comet and the Earth at the time of each high activity occurrence by Yeomans (1981) suggests that most of the meteoroids are found outside the cometary orbit and lagging the comet.

In this paper we simulate the formation process of such a stream by numerically integrating the orbits of dust particles ejected from the comet and moving under the influence of gravity and radiation pressure. The intersection of these dust particles with the Earth is also considered and it is concluded that about 12% of the ejected particles may be observed and that of those observable, 63% will be outside the cometary orbit and behind the comet.

1. Introduction

The Leonid meteor shower is one of the most famous meteor showers because of its very spectacular appearance, at periodic intervals, especially in 1799 and 1833. Newton (1863,1864) and Adams (1866) suggested that the orbital period of whatever phenomenon was responsible could be about 33.25 years. Comet P/Tempel-Tuttle (or 1866 I) was discovered by both Tempel and Tuttle in 1866, and, because of its orbital similarity to the Leonids, is considered the parent comet of the stream (eg. Schiaparelli, 1867). The period of comet Tempel-Tuttle is 33.3 years. After its 1866 discovery, two returns were not seen, but on June 30, 1965, the comet was recovered by Schubart (1965). By using Whipple's model for the ejection of dust from comets (Whipple, 1951) McIntosh (1973) investigated the orbital evolution of particles in three mass intervals, at 1g, 0.1g and 0.01g. and compared the results with radar observations of the stream over a 10 year interval. Yeomans (1981) showed the empirical distribution of dust surrounding Comet P/Tempel-Tuttle by analyzing the associated Leonid meteor shower data over the interval 902-1969. He found that the majority of the particles observed were located at a position outside the comet and lagging behind it. Essentially, this information concerning the location of the meteoroids is given as Fig.1. It should be stressed that this gives information on where the Earth was when stream activity was detected. It says nothing about the situation where the Earth has not been.

The non-gravitational effects required to explain the deviation of comet Tempel-Tuttle from pure gravitational motion implies a preferential ejection of gas and dust in the solar direction, resulting in the particles subsequently being found inside the original orbit and ahead of the comet. Yeomans therefore concluded that radiation pressure and planetary perturbation, must play an important part in the dynamic evolution of the Leonid meteoroids and it is interesting to enquire how these effects of planetary perturbations and radiation pressure affect the orbital motion so as to place the meteoroids in locations opposite to what was expected. We will also discuss the selectivity of the observation (Babadzhanov and Obrubov, 1987).

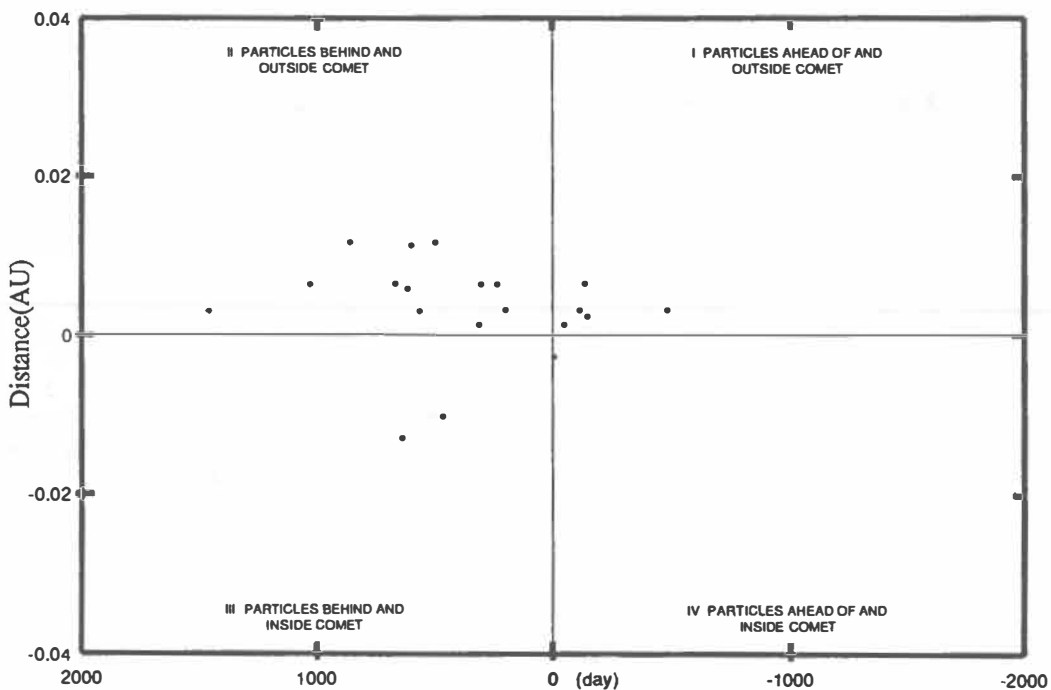


Figure 1 Meteor particles surrounding the comet

2. The Model

In our model, we assume that meteoroids are ejected from the cometary nucleus in directions which makes angles of 0° , in steps of 30° up to 330° with the direction of motion of the comet. For simplicity, all ejection is assumed to be in the orbital plane of the comet. Three different masses are taken for the meteoroids, 0.01g, 0.1g and 1g. The ejection speed is given by Whipple (1951). The meteoroids move under the gravitational field of the sun, weakened by radiation pressure. The effect of such weakening is to increase the dimensions of the meteoroid orbit as was first pointed out by Kresakova (1974). The ratio of the magnitude of the solar force due to radiation and gravity on the particle is 5.74×10^{-5} /sp (in cgs systems). Perturbations due to Jupiter, Earth, Saturn and Uranus are included, those due to the other planets being insignificant. As the orbit of the comet in 1699 was integrated backward numerically by a single orbit generated from observations in 1965 and 1866 (Yeomans, 1981), we chose 1699 as the epoch of simulation. The initial positions of the planets are determined by empirical formula (Escobal, 1968). The equations of motion of each of the meteoroids were numerically integrated using an improved Runge-Kutta-Nystrom method (Dormand et al, 1987) and integration was performed over an interval of 266 years, or eight cycles of the Comet Tempel-Tuttle.

3. Results

3.1 Initial distribution.

The principal phenomena of interest in this paper is the distribution of meteoroids in relation to the comet, particularly when the comet is close to the the descending node, since this is when the meteors are seen, and, in order to compare with observations we require the time difference at nodal passage and the heliocentric distances at this epoch. From the model, we find for small particles with mass 0.01g, radiation pressure plays an important initial role, making the semi-major axis 2.5% larger and introduces a delay of about 490 days in the nodal passage time after one orbital period. In contrast, for the

largest meteoroid size investigated, the increase in semi-major axis is only about 0.23% and results in a nodal passage delay of only about 43 days.

3.2 The final distribution

After the meteoroids are ejected, their evolution is affected by planetary perturbations. The effects of perturbations are harder to predict in a simple way and can only be determined from the numerical integration. It is also hard to disentangle the perturbational effects from that of the initial conditions, since both are present in the final distribution. However, some insight can be gained by comparing the initial and final distribution for a given meteoroid size and by comparing the final distribution for different meteoroid sizes. Fig 2 gives the final distribution in terms of the distance from the meteoroid to the comet and the time difference between particles and the comet at node for the larger meteoroids.

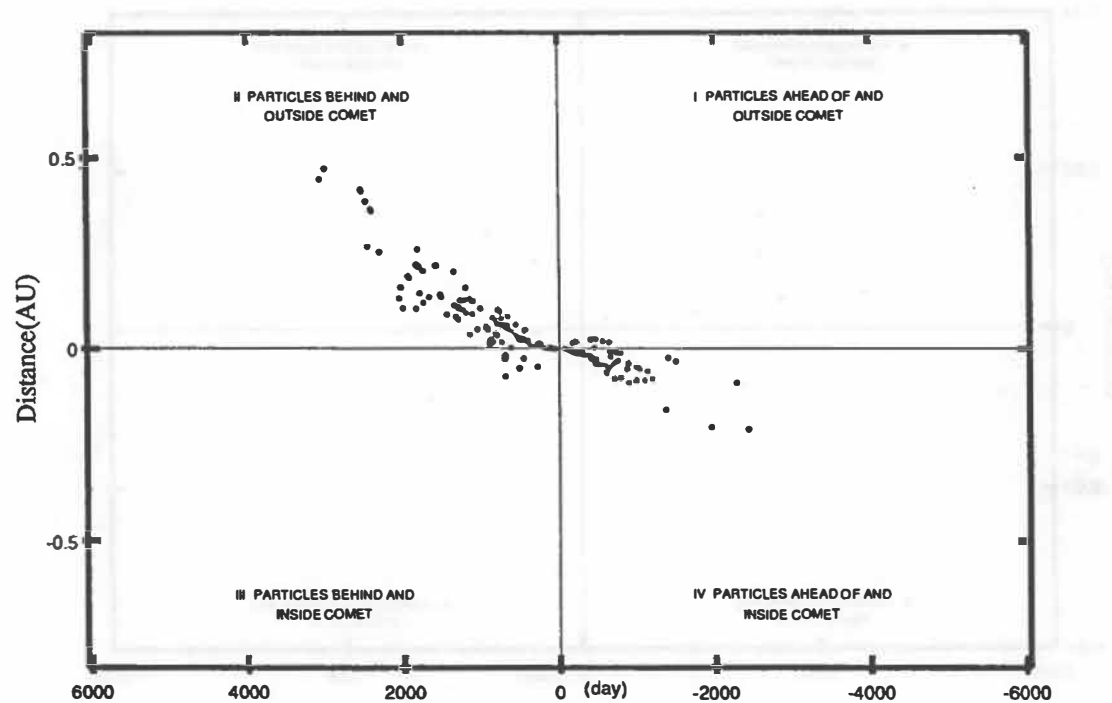


Figure 2 Final distribution of the particles surrounding the comet after the perturbation

From the computational results, which for brevity are not given here, the following general conclusions can be reached:

- 1° All meteoroids found in Quadrant I and III (ahead and outside or behind and inside, see Fig 2) are there because of the effects of planetary perturbations;
- 2° Though individual meteoroids may deviate by a largely amount from the initial configuration through the effects of planetary perturbation, the majority remain concentrated near the comet. The general shape of the stream does not appear modified;
- 3° At the descending node, the width of the meteor stream outside the cometary orbit is about twice that inside it ;
- 4° If, for an event such as the 1799 or 1833 storms, we arbitrarily assume that the distance between the particle and the Earth, D_{PE} , is less than 0.05 AU and the distance between the particle and the comet, D_{PC} , satisfies $-0.015 \leq D_{PC} \leq 0.020$ (AU), then the

storm particles represent about 12% of the total particles ejected while 63% of these particles are situated in Quadrant II, a storm is more likely when the Earth is behind and outside the comet. Fig.3 is a plot of the "meteor storm" from the simulation and should be compared with the observations in Fig 1.

4 Selectivity of the Observation

In order for meteors to be seen on Earth, it is necessary that the nodal distance of the orbit is 1AU. In addition, for streams such as the Leonids, where the meteoroids are not distributed uniformly around the orbit, meteors will only be seen periodically. However, for the first condition to be satisfied, it is the nodal distance of the actual meteoroid, not that of the mean stream that has to be 1AU, so that the width of the stream is an important consideration for the observation of the meteors.

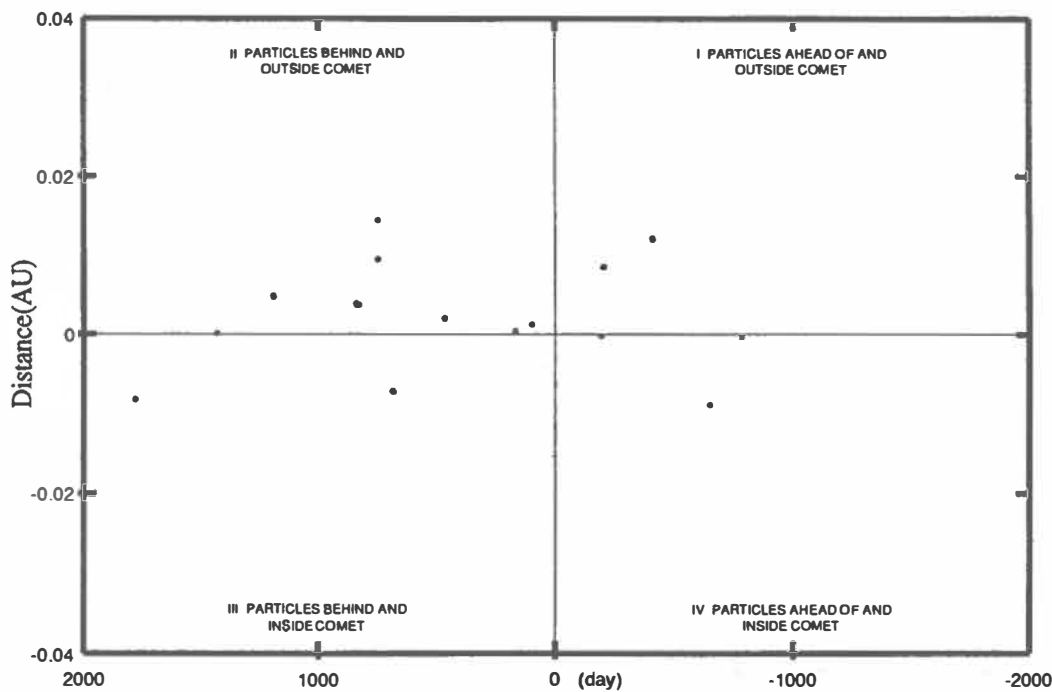


Figure 3 "Observed" model particles surrounding the comet

From our simulation, the width of the meteoroid stream outside the cometary orbit is about 0.039 AU while the inner width is only 0.016 AU. For the largest meteoroids only, where ejection speed and the effects of radiation pressure are both less, the outside width is only 0.015 AU and is illustrated in Fig 4.

At the descending node, the heliocentric distance of Comet P/Tempel-Tuttle is less than 1 AU, but with heliocentric distance increasing. Consequently, for the dense part of the meteor stream the outer part is closer to the ecliptic as the comet moves from the node than the inner part (see Fig.4). For the outer part, the closest distance is only about 0.008 AU or less, while the inside portion is about 0.023 AU from the ecliptic. As the observation events will occur only when the Earth-meteoroid distance is less than some value (eg. 0.015 AU, see Yeomans 1981), the inside meteoroids have little chance of being observed. This effect, together with the greater width of the outer portion, makes it much more likely that the storms are seen when the Earth is outside and behind the comet, as is observed.

5. Conclusions

By numerical integrating our model the rough shape of the stream at the descending node is obtained and the conditions under which a meteor storm will occur have been discussed. We conclude that most meteor storm will occur when the Earth is behind and outside the comet for the following reasons.

1° At the descending node, the width of the part of the stream outside the cometary orbit is about twice the inside part;

2° The distance between the Earth and the meteoroids in the outer part is less than that to the inner part.

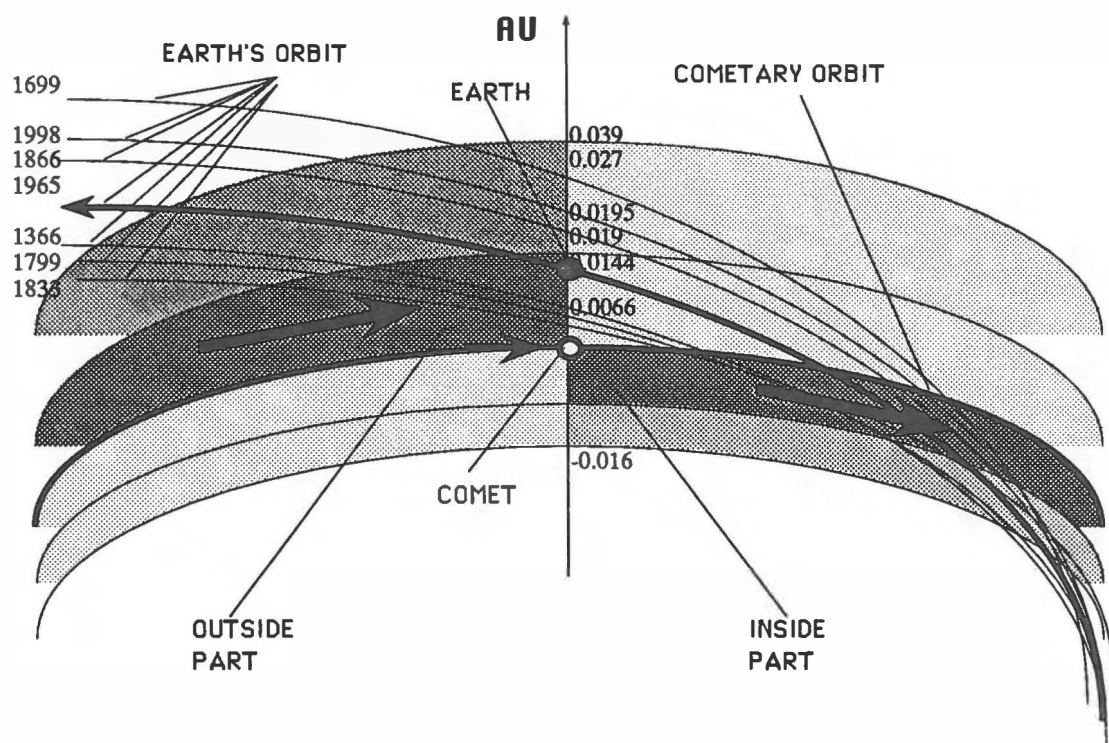


Figure 4 Position of the Earth, Comet Tempel-Tuttle & the Leonids

References

- Adams, J. C., 1866. *Mon. Not. Roy. Astron. Soc.* **27**, 247;
 Babadzhyan, P. B. and Obrubov, Yu. V., 1987. *Evolution of meteoroid stream*, In Proceeding of X Eur. Astro. meeting of IAU;
 Dormand, J. R., El-Mikkawy, M. E. A. and Prince, P. J., 1987, *IMA J. Numer. Anal.*, **7**, 423;
 Escobal, P. R., 1968. *Methods of Astrodynamics*, John Wiley & Sons, Inc. New York, London, Sydney;
 Kresakova, M., 1974. *Bull. Astron. Inst. Czech.*, **25**, 20;
 McIntosh, B. A., 1973. Origin and evolution of recent Leonid meteor showers. In *Evolutionary and Physical Properties of Meteoroids*, NASA SP-319, pp. 193-197;
 Newton, H. A., 1863. *Amer. J. Sci. Arts* (2nd series), **36**, 145 - 149;
 Newton, H. A., 1864. *Amer. J. Sci. Arts* (2nd series), **38**, 53 - 61;
 Schiaparelli, G.V., 1867. *Astron. Nach.* **68**, 331;
 Schubart, J., 1965. IAU Circular No. 1907;
 Whipple, F. L., 1951. *Astrophys. J.*, **113**, 464 - 474;
 Yeomans, D. K., 1981. *ICARUS* **47**, 492 - 499.

The Contribution of Electron Collisions to Rotational Excitations of Cometary Water

X. Xie* and M. J. Mumma† Laboratory for Extraterrestrial Physics,
Code 693, NASA Goddard Space Flight Center, Greenbelt, MD 20771

Abstract

The e- H_2O collisional rate for exciting rotational transitions in cometary water is evaluated for conditions found in comet Halley during the Giotto spacecraft encounter. In the case of the $0_{00} \rightarrow 1_{11}$ rotational transition, the e- H_2O collisional rate exceeds that for excitation by neutral-neutral collisions at distances exceeding 3000 km from the cometary nucleus. Thus, the rotational temperature of the water molecule in the intermediate coma may be controlled by collisions with electrons rather than with neutral collisions, and the rotational temperature retrieved from high resolution infrared spectra of water in comet Halley may reflect electron temperatures rather than neutral gas temperature in the intermediate coma.

1 Introduction

The encounters of the Giotto and Vega spacecraft with comet Halley, and observations with space-based (IUE), airborne (KAO), and ground-based telescopes, during Halley's last apparition resulted in major advances in our understanding of its chemical composition and of the physical conditions and physical processes in the cometary coma. While *in situ* measurements provided direct information on conditions in the intermediate coma during the spacecraft encounters, it is the earth-based spectroscopy of parent molecules, especially water vapor (the dominant volatile species in the comet), that offers a remote but direct probe of physical conditions there. However, these conditions may only be retrieved from spectral data if the processes that control rotational populations and spectral line formation are well understood. The theoretical studies by Bockelee-Morvan (1987) and Storrs and Mumma (1991) achieved satisfactory fits to the line-by-line intensities revealed in infrared spectra of the ν_3 -band of water in comet Halley acquired on the Kuiper Airborne Observatory (KAO) (Mumma et al. 1986 and Weaver et al. 1987). However, the use of a cross-section of $5 \times 10^{-14} \text{ cm}^2$ or larger is questionable. Storrs and Mumma (1991) suggested the need for such a large cross-section could indicate that other processes, such as electron or ion collisions, were affecting rotational excitations. High electron density deduced from Giotto and Vega measurements (Ip and Axford 1990, Pedersen et al. 1987) and low electron temperature in the inner coma from the ionosphere model (Körömezey et al. 1987) could make electron collisions non-negligible in exciting water rotational transitions.

2 Collisional cross-sections for water rotational transitions

Itikawa (1972) used the Born approximation to calculate the cross-section for rotational transitions by $e - H_2O$ collisions, which cross-section is formulated as follows

$$\sigma_{J_{K_a K_c} \rightarrow J'_{K'_a K'_c}} = \frac{8\pi}{3k^2} \frac{D^2}{2J+1} S_{J'_{K'_a K'_c} J_{K_a K_c}} \ln \frac{k+k'}{k-k'}, \quad (1)$$

where D=1.85 Debye is the permanent dipole moment of the water molecule; J , K_a and K_c are quantum numbers for the initial state of the transition and J' , K'_a and K'_c for the final state; and k and k' are the

*also Astronomy Department, University of Pennsylvania, Philadelphia, PA 19104.

†Chief Scientist, Planetary and Astrophysical Sciences.

initial and final wave numbers of the electron. The line strength $S_{J'_{K'_0} K'_c} J_{K_a K_c}$ is given in Schwendeman and Laurie (1958). In the paper by Xie and Mumma (1992), it is shown that the calculated cross-sections from Eq (1) are consistent with the total cross-section measurements from the electron scattering experiments at low impact energy by Sokolov and Sokolova (1982), and the effective $H_2O - H_2O$ cross-section is probably far smaller than $5 \times 10^{-14} cm^2$ currently used in the literature. In our evaluation, the H_2O -neutral gas cross-section is taken to be $5 \times 10^{-14} cm^2$, which is the upper limit.

3 Collisional rate for the $0_{00} \rightarrow 1_{11}$ rotational transition

The electron temperature is relatively low with $T_e < 300K$ and follows the neutral gas temperature inside the contact surface (Körömezey et al. 1987), it increases with cometocentric distance outside the contact surface (Gan and Cravens 1990), where electron heat conduction becomes important. In our evaluation, the electron temperature in the cometary coma is taken to be approximately equal to the ion temperature measured from Giotto (Lämmenzahl et al. 1987).

$$T_e = \begin{cases} 200 \text{ K} & r < 4500 \text{ km} \\ 2000 \text{ K} & 4500 \text{ km} < r < 7280 \text{ km} \\ 5000 \text{ K} & 7280 \text{ km} < r < 1.25 \times 10^4 \text{ km} \\ 10000 \text{ K} & 1.25 \times 10^4 \text{ km} < r < 2 \times 10^5 \text{ km} \end{cases} \quad (2)$$

The electron density is assumed to be equal to the total ion density from Giotto measurements (after Ip and Axford 1990) as follows

$$n_e = \begin{cases} \frac{1.3 \times 10^7}{r} \text{ cm}^{-3} & r < 7280 \text{ km} \\ 1.7 \times 10^{-2} r^{1.3} \text{ cm}^{-3} & 7280 \text{ km} < r < 1.25 \times 10^4 \text{ km} \\ 5.6 \times 10^3 (\frac{10^4}{r})^2 \text{ cm}^{-3} & 1.25 \times 10^4 \text{ km} < r < 2.0 \times 10^5 \text{ km}, \end{cases} \quad (3)$$

where r is the cometocentric distance in km. The corresponding H_2O production rate at the Giotto encounter was about 5×10^{29} molecules/sec (Krankowsky et al. 1986). The collisional excitation rate (s^{-1}) for the rotational transition $0_{00} \rightarrow 1_{11}$ is given in the following form

$$\nu_{e-H_2O} = \begin{cases} \frac{20}{r} s^{-1} & r < 4500 \text{ km} \\ \frac{1.8}{r} s^{-1} & 4500 \text{ km} < r < 7280 \text{ km} \\ 1.7 \times 10^{-8} r^{1.3} s^{-1} & 7280 \text{ km} < r < 1.25 \times 10^4 \text{ km} \\ 45 \times (\frac{10^4}{r})^2 s^{-1} & 1.25 \times 10^4 \text{ km} < r. \end{cases} \quad (4)$$

The corresponding water-neutral gas collision frequency at cometocentric radius r is given by

$$\nu_{H_2O-H_2O} = \frac{7.5 \times 10^4}{r^2} s^{-1}. \quad (5)$$

Here the expansion velocity of the neutral gas is taken as 1.0 km/s and kinetic temperature of water molecules is 60 K in the coma a few thousand kilometers away from the nucleus.

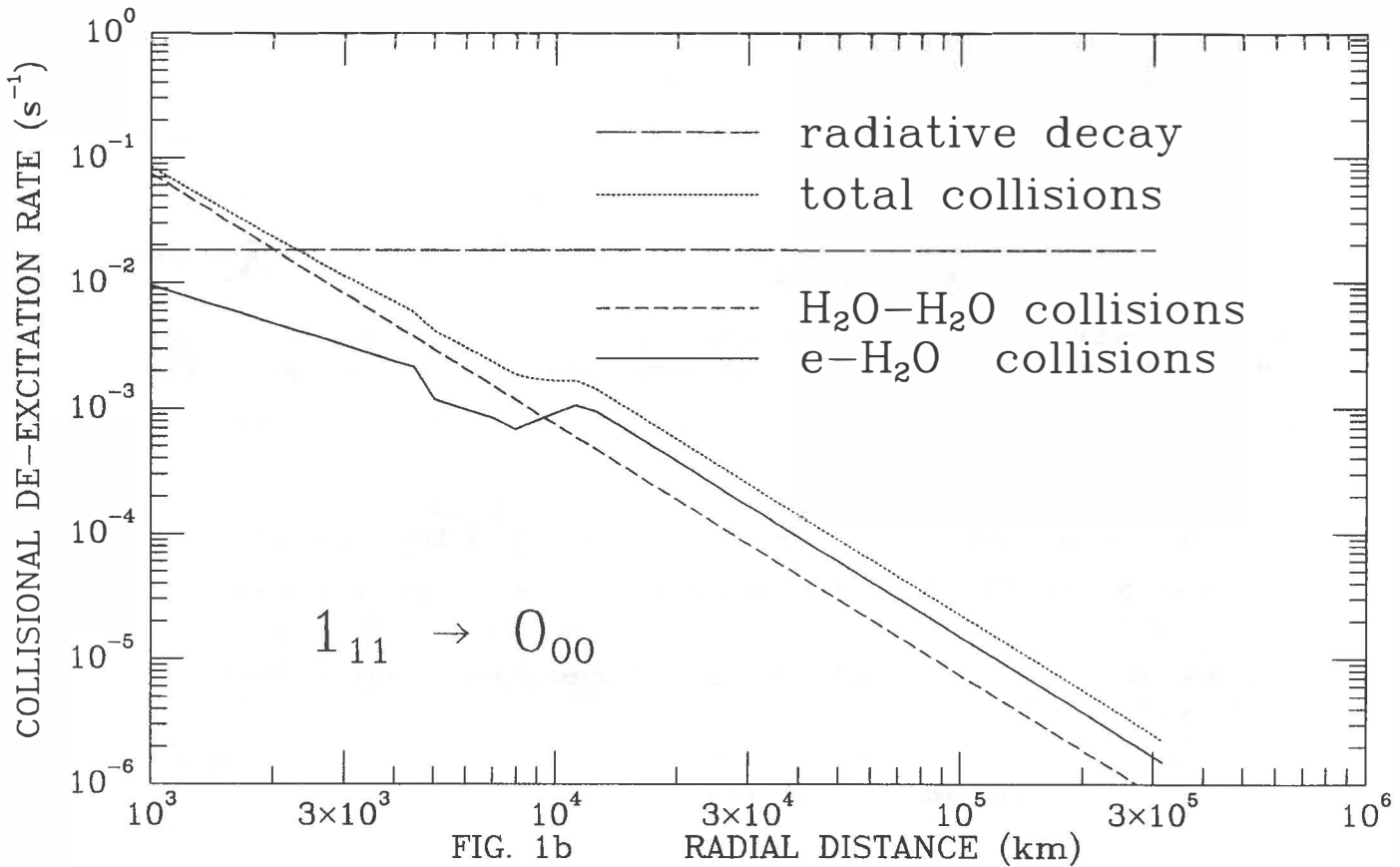
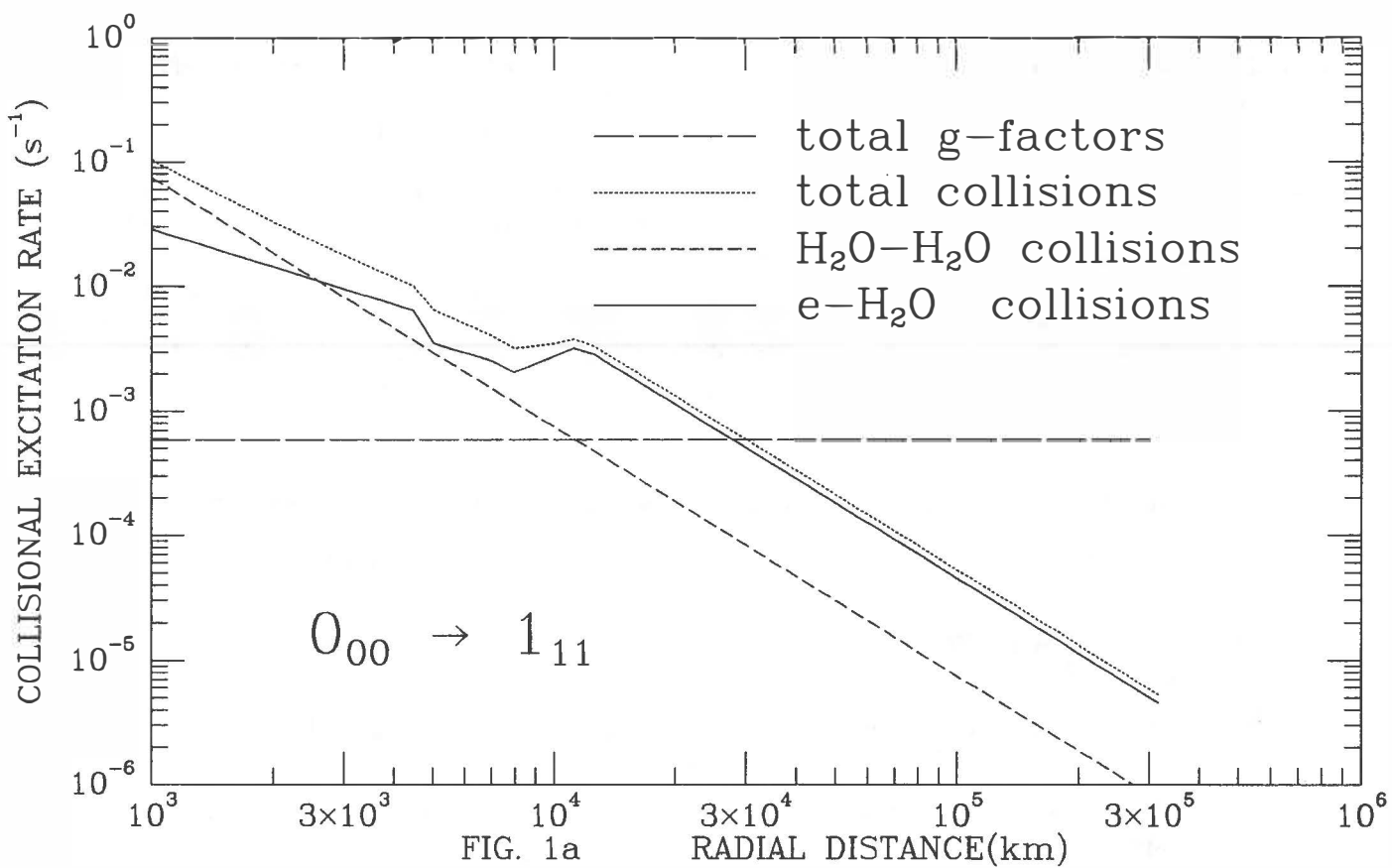
4 Rotational populations of water molecule in Comet Halley

The excitation rate for the $0_{00} \rightarrow 1_{11}$ transition is shown in Fig. 1a. It is clear that for the $0_{00} \rightarrow 1_{11}$ transition the $e - H_2O$ collisional excitation rate will be equal to that of $H_2O - H_2O$ collisions somewhere around $10^3 - 10^4 \text{ km}$ and will exceed the latter in the more distant region. The excitation rate due to vibrational infrared fluorescence (at 0.9 AU) is also plotted in Fig. 1a. Clearly infrared resonance fluorescence dominates rotational pumping only in the outer coma. De-excitational rates for the $0_{00} \rightarrow 1_{11}$ rotational transition are shown in Fig. 1b, where the rates for relaxation by $e - H_2O$ and $H_2O - H_2O$ collisions are compared with radiative relaxation in the optically thin case. In the optically thick coma,

optical trapping leads to an efficient reduction in the Einstein-A coefficient and enhances the effect of collisions (Xie and Mumma 1992). For the active comet with a gas production rate of $5 \times 10^{29} \text{ mol/s}$, the critical radius corresponding to $\tau_c = 1.0$ is about $1 \times 10^5 \text{ km}$ for the $0_{00} \rightarrow 1_{11}$ rotational transition. The intermediate coma ($r \leq \sim 1 \times 10^4 \text{ km}$) sampled by the KAO observations is optically thick for the $0_{00} \rightarrow 1_{11}$ rotational transition. As the result of optical trapping, there is a more extended inner coma, where collisional relaxation dominates and rotational excitation for cometary water is controlled by collisional effects, not by fluorescence. In the region where the electron collisional rate is comparable to or larger than that of neutral gas collisions, electron collisions will affect the rotational population. Therefore, the temperature measured for the rotational states will be a measure of the electron or neutral kinetic temperatures, depending on cometocentric distance. In the intermediate region, where electron collisions dominate, the rotational temperature is undoubtedly controlled by electrons.

References

- Bockelee-Morvan D. (1987) A model of the excitation of water in Comets. *Astr. Ap.*, **181**, 169–181.
- Gan L. and Cravens T.E. (1990) Electron energetics in the inner coma of Comet Halley. *J. Geophys. Res.*, **95**, 6285–6303.
- Ip W.H. and Axford W.I. (1990) Chapter 5. The Plasma. in **Physics and Chemistry of Comets** (Huebner F. Eds), pp. 177.
- Itikawa Y. (1972) Rotational transitions of an asymmetric-top molecule by electron collision: Application to H_2O and H_2CO . *J. of Phys. Soc. of Japan*, **32**, 217–226.
- Körösmezey A., Cravens T.E., Gombosi T.I., Nagy A.F., Mendis D.A., Szegő K., Gribov B.E., Sagdeev R.Z., Shapiro V.D. Shevchenko V.I. (1987) *J. of Geophys. Res.*, **92**, 7331–7340.
- Krankowsky D., Lämmenzahl P., Herrwerth I., Woweries J., Eberhardt P., Dolder P., Herrmann U., Schulte W., Berthelier J.J., Illiano J.M., Hodges R.R., and Hoffman, J. H. (1986) *In situ* gas and ion measurements at comet Halley. *Nature*, **321**, 327–329.
- Lämmenzahl P., Krankowsky D., Hodges R.R., Stubbemann U., Woweries J., Herrwerth I., Berthelier J.J., Illiano J.M., Eberhardt P., Dolder U., Schulte W., and Hoffman J. H. (1987) Expansion velocity and temperatures of gas and ions measured in the coma of comet P/Halley. *Astr. Ap.*, **187**, 169–173.
- Mumma M.J., Weaver H.A., Larson H.P., Davis D.S. and Williams M. (1986) Detection of water vapor in Halley's comet. *Science*, **232**, 1523–1528.
- Pedersen A., Grard R., Trotignon J.G., Beghin C., Mikhailov Y. and Mogilevsky M. (1987) Measurements of low energy electrons and spacecraft potentials near comet P/Halley. *Astr. Ap.*, **187**, 297–303.
- Schwendeman and Laurie (1958) **Tables of Line Strengths for Rotational Transitions of Asymmetric Rotor Molecules**, Pergamon Press.
- Sokolov V.F. and Sokolova Y.A. (1982) Total cross sections for electron scattering by H_2S , SO_2 and H_2O molecules at electron energies in the range 0–10 ev. *Sov. Tech. Phys. Lett.*, **7**, 268–269.
- Storrs A.D. and Mumma M.J. (1991) Modeling optically thick lines in cometary comae. Preprint submitted to *Icarus*.
- Weaver H.A., Mumma M.J., Larson H.P. (1987) Infrared investigation of water in Comet P/Halley. *Astr. Ap.*, **187**, 411–418.
- Xie X. and Mumma M.J. (1992) The Effect of Electron Collisions on Rotational Populations of Cometary Water. *Ap. J.* to be published in February, 1992.



ON THE DYNAMICAL STRUCTURE OF THE TROJAN GROUP OF ASTEROIDS

R.V.Zagretdinov*, I.P.Williams,
Queen Mary and Westfield College, London, U.K.
M.Yoshikawa,
National Astronomical Observatory, Tokyo, Japan

Abstract

Using a semi-analytical approach, domains of possible motion for Trojan asteroids have been established. It is shown that stable librating motion is possible for both high inclination and high eccentricity. frequency distributions have also been produced for real Trojan asteroids, against differing libration amplitudes and libration periods.

Using a semi-analytical model described by Yoshikawa (1990), we consider the possible motion of massless Trojan asteroids, that is asteroids situated close to the 1:1 resonance region with Jupiter, which is assumed to be moving on its actual elliptic orbit. The asteroids are allowed to move on non-circular orbits in three dimensions. For convenience we define the critical argument, σ^* , to be the mean longitude of Jupiter minus that of asteroid, and denote the longitude of perihelion of an asteroid minus that of Jupiter by $(\omega - \omega_J)^*$. The variation of a^* , the semi-major axis of an asteroid orbit as a function of σ^* are obtained for specified values of the other parameters of the test orbit, namely the proper eccentricity, e^* , the proper inclination, i^* , and $(\omega - \omega_J)^*$. Figure 1 shows the resulting twenty five plots when i^* is zero with five different values of $(\omega - \omega_J)^*$, $0^\circ, 90^\circ, 180^\circ, 270^\circ$ and 360° and five different values of e^* , 0.02, 0.05, 0.10, 0.15 and 0.20. By inspecting these plots, it is evident that stable libration motion is possible in all cases provided the libration angle (maximum - minimum value of σ^*), D , is less than about 50° . The results do not appear to be particularly dependent on either the value of e^* or on $(\omega - \omega_J)^*$ throughout the ranges investigated. In Figure 2, the value of the proper inclination, i^* , was increased to about 20° , with minor variations about this value, the other parameters taking the same values as in Figure 1. As can be seen, the domain for stable libration is now generally larger than in Figure 1, especially at low values of the proper eccentricity and sometimes even horseshoe orbits are found (for example at $e^* = 0.1$ and $(\omega - \omega_J)^* = 90^\circ$). It is also interesting to note that the size of the stable libration region is larger when $e^*=0.2$ than when $e^*=0.02$ and that some displacement of the libration centre from the Lagrangian equilibrium points ($\sigma^*=60^\circ$ and 300°) has occurred. Space does not permit the inclusion of diagrams indicating areas of possible libration for all sets of parameters investigated, however, even when the proper inclination, i^* is increased to 50° , large domains of stable librating motion still remain, though in this case, zones are more sensitive to the value of $(\omega - \omega_J)^*$. The

* Permanent address: Kazan State University, Kazan, U.S.S.R.

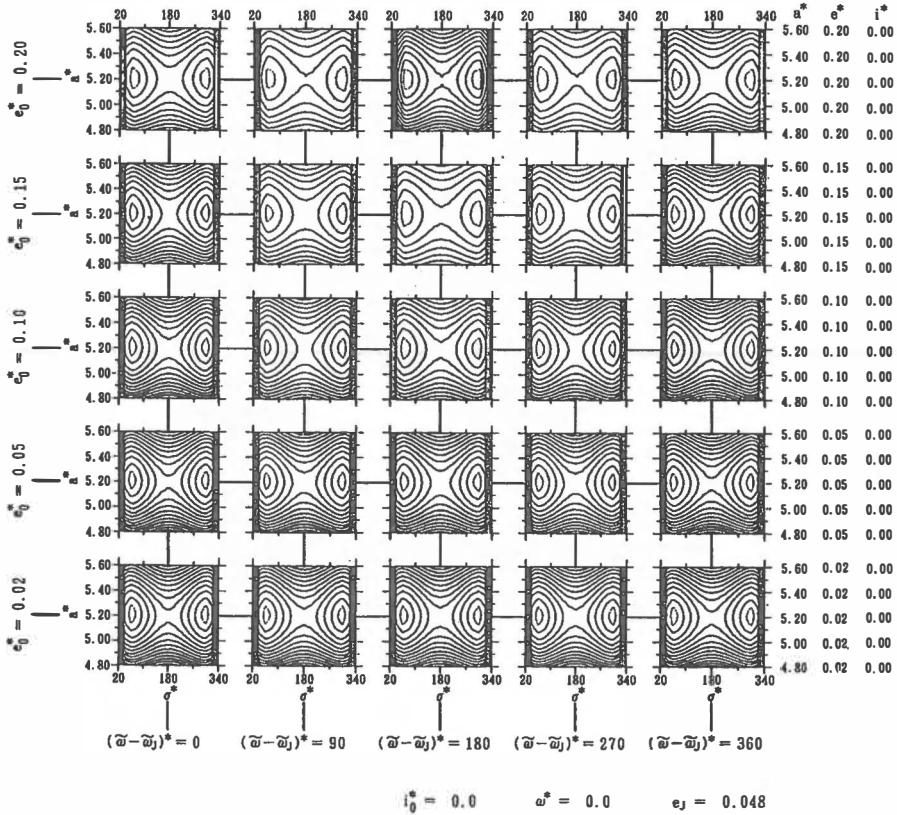


FIG.1. The 1:1 resonance. Model A for $ej = 0.048$ and $i^*=0^\circ$. On the right side, the values of e^* and i^* are shown as a function of a^* .

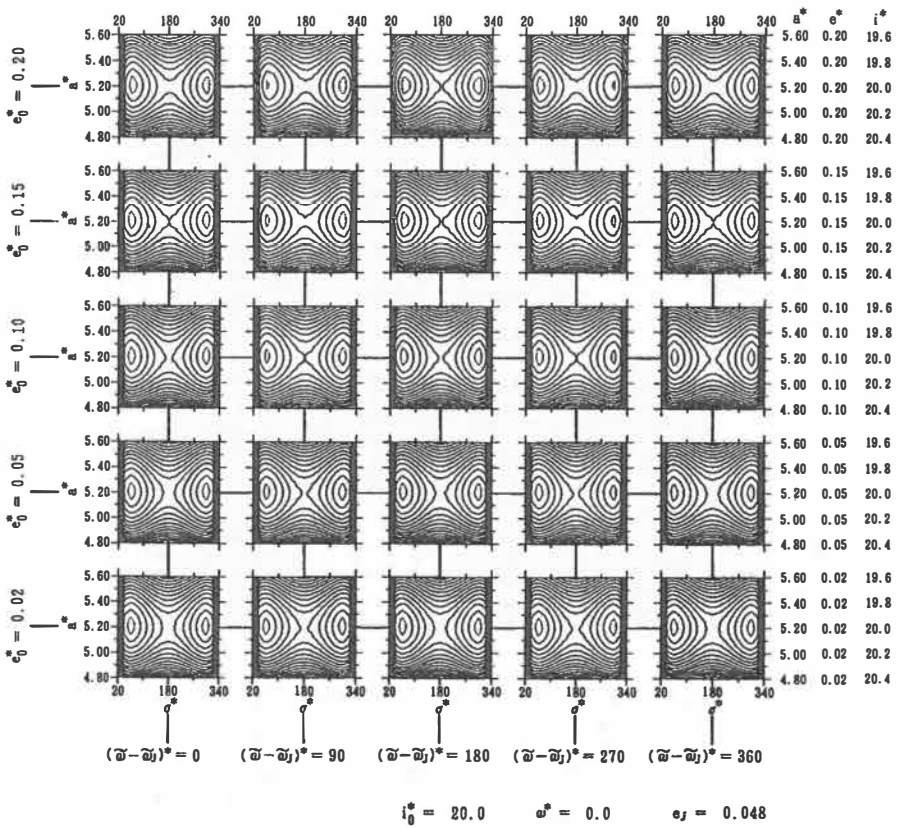


FIG.2. Model A for $\omega^*=0^\circ$ and $i^*=20^\circ$.

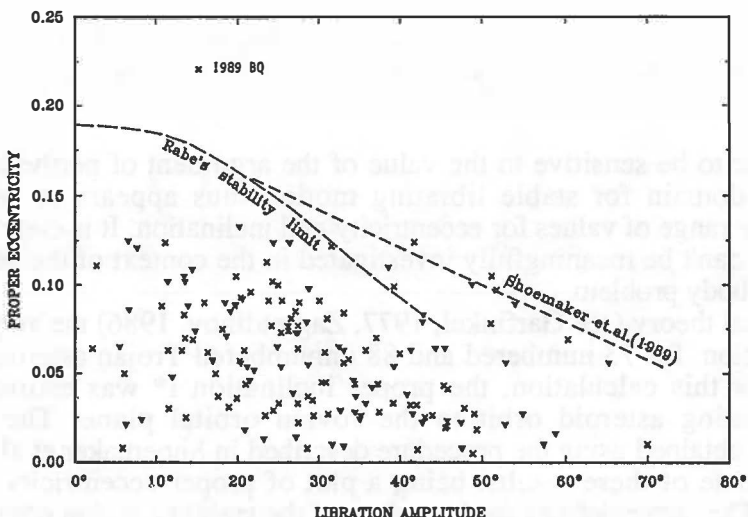


FIG. 3. Distribution of proper eccentricity (e^*) vs libration amplitude (D) for 73 numbered (v) and 88 unnumbered (x) Trojans.

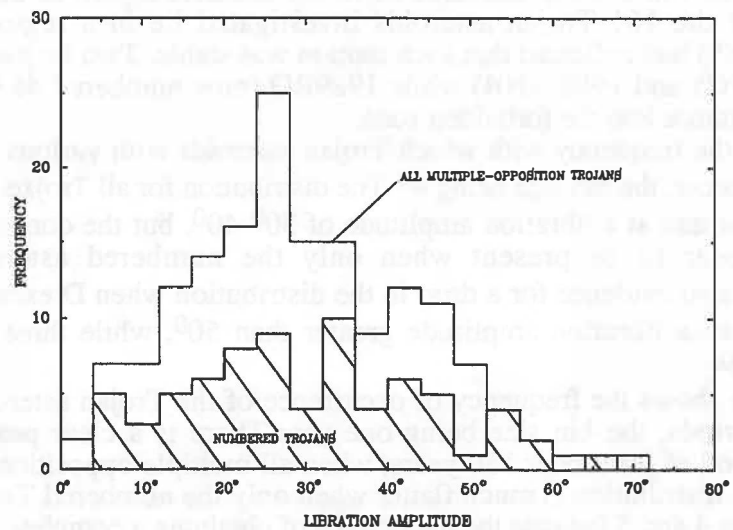


FIG. 4. Frequency distribution of libration amplitude (D) of Trojans.

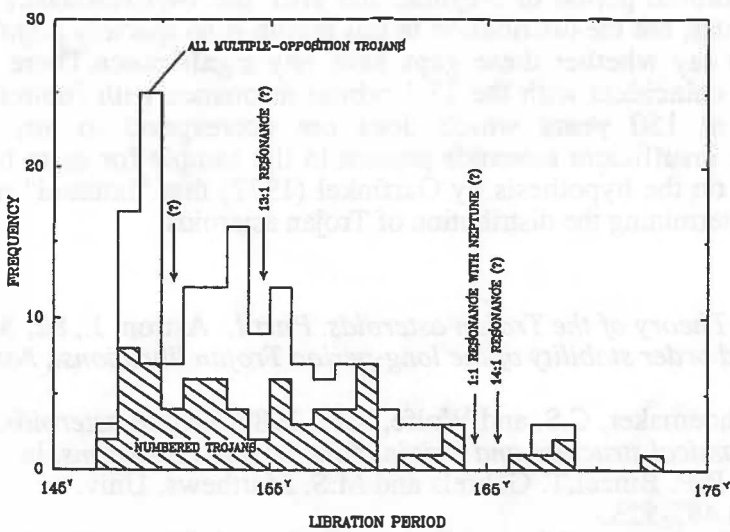


FIG. 5. Frequency distribution of libration period of Trojans.

results do not appear to be sensitive to the value of the argument of perihelion. The dimensions of the domain for stable librating motion thus appears to be large, encompassing a wide range of values for eccentricity and inclination. It is clear that the real Trojan problem can't be meaningfully investigated in the context of the restricted circular planar three body problem.

Using an analytical theory (see Garfinkel, 1977, Zagretdinov, 1986) the amplitudes and periods of libration for 73 numbered and 88 unnumbered Trojan asteroids have been calculated. For this calculation, the proper inclination i^* was estimated by referring the osculating asteroid orbit to the Jovian orbital plane. The proper eccentricity, e^* , was obtained using the procedure described in Shoemaker et al (1989). Figure 3 displays some of these results, being a plot of proper eccentricity against libration amplitude. The curve defines the boundary of the stability region obtained by Shoemaker et al (1989). Also shown is an earlier limit to stability obtained by Rabe (1967). It is seen than while many asteroids lie in the unstable region as defined by Rabe, almost all of the 161 Trojan asteroids investigated lie in a region where Shoemaker et al (1989) had indicated that such motion was stable. Two lie just outside this region, (1989 UC5 and 1988 RNB) while 1989BQ (now numbered 4835) lies a very considerable distance into the forbidden zone.

Figure 4 shows the frequency with which Trojan asteroids with various libration amplitudes actually occur, the bin size being 40° . The distribution for all Trojan asteroids shows a strong maximum at a libration amplitude of 300° - 40° , but the corresponding peak does not appear to be present when only the numbered asteroids are considered. There is also evidence for a drop in the distribution when D exceeds 50° . Eleven asteroids have a libration amplitude greater than 50° , while three have an amplitude of over 60° .

Finally, Figure 5 shows the frequency of occurrence of the Trojan asteroids with various libration periods, the bin size being one year. There is a clear peak in the distribution at a period of just under 150 years, when all multiple opposition Trojans are included, but the distribution is much flatter when only the numbered Trojans are included. Both figures 4 and 5 indicate the importance of obtaining a complete sample of Trojans as soon as possible. There are gaps in the distribution corresponding to a 1:1 resonance with the orbital period of Neptune and also the 14:1 resonance with the orbital period of Jupiter, but the distribution in this region is so sparsely populated that it is not possible to say whether these gaps have any significance. There is also a suggestion of a gap coincident with the 13:1 orbital resonance with Jupiter, while a strong gap exists at 150 years which does not correspond to any obvious resonance. There are insufficient asteroids present in the sample for us to be able to comment positively on the hypothesis by Garfinkel (1977) that "internal" resonance may play a role in determining the distribution of Trojan asteroids.

References

- Garfinkel, B., 1977, *Theory of the Trojan asteroids. Part I*, Astron. J., **82**, 368-379.
- Rabe, E., 1967, *Third order stability of the long-period Trojan librations.*, Astron. J., **72**, 10-17.
- Shoemaker, E.M., Shoemaker, C.S. and Wolfe, R.F., 1989, *Trojan asteroids: Populations, Dynamical structure and Origin of the L4 and L5 swarms*, In *Asteroids II*, eds. R.P. Binzel, T. Gehrels and M.S. Matthews, Univ. of Arizona Press, pp 487-523.
- Yoshikawa, M., 1990, *Motions of Asteroids at the Kirkwood Gaps. I. On the 3:1 resonance with Jupiter.*, Icarus, **87**, 78-102.
- Zagretdinov, R.V., 1986, *On the theory of Trojan asteroids motion.*, Kinem. Phys. Neb. Tel. 2, **3**, 68-74 (in Russian).

A COMPARISON BETWEEN FAMILIES OBTAINED FROM DIFFERENT PROPER ELEMENTS

V. Zappalà¹, A. Cellino¹, P. Farinella²

¹ Osservatorio Astronomico di Torino, Italy

² Dipartimento di Matematica, Università di Pisa, Italy

Abstract. Using the hierarchical method of family identification developed by Zappalà et al. [Astron. J., 100, 2030 (1990)] we compare the results coming from the data set of proper elements computed by Williams (about 2100 numbered + about 1200 PLS II asteroids) and by Milani and Knežević (5.7 version, about 4200 asteroids). Apart from some expected discrepancies due to the different data sets and/or low accuracy of proper elements computed in peculiar dynamical zones, a good agreement was found in several cases. It follows that these high reliability families represent a sample which can be considered independent on the methods used for their proper elements computation. Therefore, they should be considered as the best candidates for detailed physical studies.

It is well known that asteroid dynamical families are a fascinating, but until recently puzzling subject. In fact, in spite of a noticeable effort carried out for several years by many authors, it has not long been possible to achieve a satisfactory agreement among the different proposed family lists. In particular, substantial disagreement exists for what concerns both the amount of existing families and the number and identity of their members. A detailed review of this subject can be found in Valsecchi et al. (1989).

Moreover, a review by Chapman et al. (1989) emphasizes another difficulty, in a physical sense, affecting many of the proposed families: in particular, only a few of them (mainly the most populous ones) are self-consistent from a cosmochemical point of view. In other words, most of the smaller clusterings identified in the space of proper elements by different authors, are composed by asteroids whose taxonomic types conflict with each other, in the sense that no plausible process of collisional origin from a single plausible parent body could explain the observed variety of taxonomic types of their supposed members.

On the other hand, the most recent advances in the studies of the overall collisional evolution of the asteroid belt (see, for a review, Davis et al., 1989) require some reliable estimates of the number and physical properties of the presently existing dynamical families, since they can provide some crucial constraints for the general evolutionary models proposed. At the same time, a knowledge of the main physical properties of the family members could shed some light on the general problem of the physics of catastrophic impacts and their collisional outcomes.

There are many reasons for the inconsistencies found in the past among the different proposed family lists. The main reasons are: different data sets used; different adopted methods of proper element computations; different procedures for clustering identification.

Recently, Zappalà et al. (1990) have carried out a new analysis, in which they used the biggest data set (about 4100 objects) ever analyzed for family identification purposes, as well as a new identification method. For what concerns the adopted proper elements, they used those computed by Milani and Knežević (1990), on the basis of a second-order, forth degree secular perturbation theory.

The new identification method is based on hierarchical clustering techniques of multivariate data analysis. The basic idea is to compute all the mutual distances among the analyzed objects, on the basis of some definition of a metric in the proper elements space (in particular, the adopted distance definition is related to the incremental velocity needed for orbital change after ejection from a fragmented parent body). In this way, it is possible to build some *dendograms*, containing all necessary information about the existing clusterings of objects, having mutual distances smaller than any given value d . They are then compared with analogous dendograms obtained for fictitious populations of quasi-randomly generated objects, in order to find a critical value of distance ("quasi-random level") for which the clusterings found cannot be due to pure chance. These clusterings are defined as asteroid families in the Zappalà et al. (1990) paper.

In this way a new list of 21 families has been obtained, which includes, in addition to the well known and already firmly established Eos, Themis and Koronis families, at least 12 other families which appear to be highly reliable. These results must be compared with those obtained by other studies on the same subject available in the literature. In particular, one of the outstanding previous analyses is that carried out by Williams (1979), who used his own theory of proper elements computation (Williams 1969), and analyzed a large data set of 1796 numbered objects, in addition to a sample of the best orbits from the PLS survey. By applying a subjective method of clustering identification, Williams recognized 104 families. More recently, Williams (1989) has redone his analysis including a larger sample of numbered asteroids (2065), and found again a large number of families: 117.

It is interesting to infer whether the discrepancies between the Williams (1979, 1989) and the Zappalà et al. (1990) family lists are mostly due to the different identification methods used, or to the different sets of adopted proper elements.

An obvious procedure to discriminate among these two possibilities is to apply the same method of clustering identification to the two different samples of asteroid proper elements. In this paper, we present the results of such an exercise, in which the Zappalà et al. (1990) identification method has been applied separately to the extended data set (4258 objects) of the 5.7 version of asteroid proper elements by Milani and Knežević, as well as to the Williams (1989) proper elements lists, including 1968 numbered objects and 1227 PLSs.

The overall results of the present analysis are shown in Table 1, which shows, respectively, the number of resulting clusterings found using the Williams data set, the corresponding number of clusterings coming from the Milani and Knežević data set, and the number of "intersection clusterings", i.e., those who are found to be composed (at least partially) by the same objects in both the samples. Table 1 shows separately the cases corresponding to clusterings composed by a number $N \geq 5$ and $N \geq 10$ of objects. As can be seen, the agreement is quite good, mainly in the case of the most populous ($N \geq 10$) groupings. This can indicate that the global differences between the Williams (1979, 1989) and the Zappalà et al. (1990) classifications are probably mostly due to the different adopted methods of clustering identification, than to a substantial difference of the proper elements data sets.

Table 2 shows in a more detailed way the results of the present analysis for what concerns the clusterings having $N \geq 10$ members. In particular, for each of them, the number of Williams numbered objects (complete down to the number 2065), the number of PLS objects in the Williams data set, the number of the corresponding Milani and Knežević numbered asteroids (i.e., those having number ≤ 2065), and the Milani and Knežević numbered objects beyond the 2065 are shown, respectively, as well as the number of common objects present in both classifications. It is evident that the agreement can be considered quite good, in the sense that for these clusterings the intersection is generally very close to the number of common objects having number ≤ 2065 , which is the maximum possible intersection of the two data sets. The next step of this analysis will be obviously to compute Milani and Knežević proper elements for the PLS asteroids having the best determined osculating elements, and to use them

Table I

	Williams	MK57	Intersection
$N \geq 5$	26	20	16
$N \geq 10$	15	14	14

Table II

Family [Zappalà et al. (1990)] list	Williams Num.	PLS	MK 57		Intersection	remarks
			Num	H.Num.		
31 + 35	4	5	5	12	4	Vesta
32	5	3	9	32	5	F-type
33	4	29	2	21	2	
41	17	9	25	77	16	Eunomia
44	8	7	8	12	7	Adeona (Alexandra)
45	14	2	17	21	13	Maria
46	7	5	6	14	6	
48	5	5	3	20	3	
51	54	29	54	101	54	Koronis
61	89	9	80	127	79	Eos
71	75	38	72	165	71	Themis
1183 (*)	3	10	2	12	1	
135 (*)	1	18	1	16	1	Hertha
808 (*)	4	7	3	4	3	

(*) Families not found in the Zappalà et al. (1990) paper, due to the smaller data set used with respect to the present analysis. Here, they are identified by their least-numbered asteroid.

for carrying out a new updated list of asteroid dynamical families (Zappalà et al., in preparation).

Table 1 shows that the method for clustering identification by Zappalà et al. (1990), even in the case of smaller permitted clusterings, can allow us to identify less than 30 "families" by making use of the Williams' data set. This number has to be compared with the high number of families found by Williams (117) using the same data set. This discrepancy can be explained, in our opinion, if we admit that the Williams' criterion of family identification was too liberal.

Figure 1 shows a general tentative classification of asteroid families; for a specific discussion of this subject, see the Farinella et al. paper published elsewhere in the present book. The figure shows a typical *stalactite diagram* for the asteroids having proper orbital semiaxes ranging between 2.500 and 2.825 AU (corresponding, respectively, to the 1/3 and the 2/5 mean motion resonances with Jupiter). The stalactite diagram shows, for different levels of the distance, the resulting clusterings of objects. The width of a stalactite at each level is given by the number of objects belonging to the clustering at that distance level. The dashed level is the "quasi-random level", or the distance level under which no clusterings are found in the case of fictitious populations of quasi-randomly generated objects (for a detailed explanation of this, see the Zappalà et al., 1990 paper).

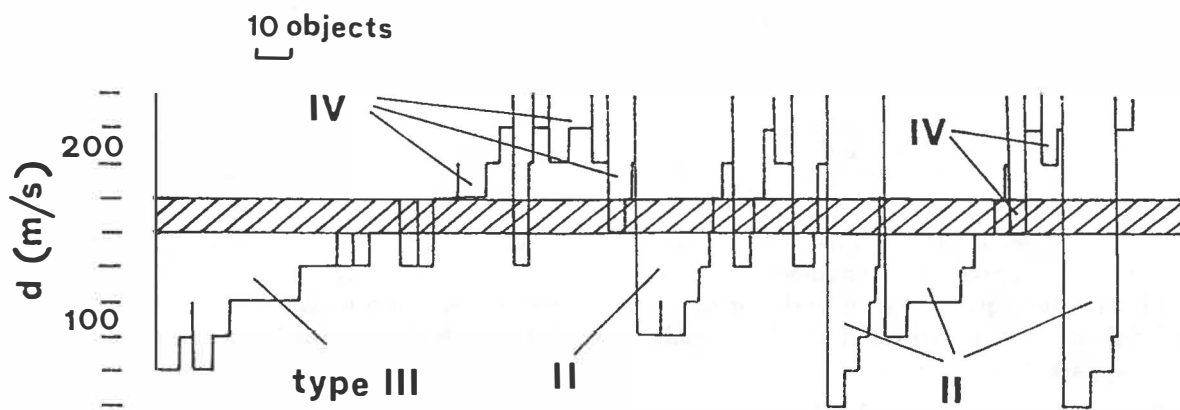
As can be seen in the Figure, there are fundamentally three kinds of stalactites. The type II is sharp and deep, and corresponds to the families which are well defined and have been found by both Williams (1979, 1989) and Zappalà et al. (1990), with a large intersection of common objects. Type III are less sharp, and their members grow gradually as long as the distance level increases, so that the level at which one "cuts" the stalactite in order to define the family membership is crucial. Numerical simulations (see Bendjoya et al. in this book) show that in such cases one has to make a choice between two main possibilities: (1) to cut the stalactite at a low level, losing probably a significant amount of family members; this is in general the choice performed in the Zappalà et al. (1990) paper. (2) to be "liberal", cutting the

stalactite at higher levels, but taking into account that in this way a very large percentage of interlopers can be included in the assumed family; this has been generally done by Williams (1979, 1989). Finally, type IV stalactites are those that do not reach at present the rank of possible families on the basis of the Zappalà et al. (1990) criterion. Instead, they have often been considered as real families by Williams (1979, 1989).

References.

- Chapman C. R., Paolicchi P., Zappalà V., Binzel R. P., and Bell J. F. (1989) Asteroids families: physical properties and evolution. In Asteroids II (R. P. Binzel, T. Gehrels, and M. Shapley Matthews, eds.), pp. 386-415. University of Arizona Press, Tucson.
- Davis D. R., Weidenschilling S. J., Farinella P., Paolicchi P., and Binzel R. P. (1989) Asteroids collisional history: effects on sizes and spins. In Asteroids II (R. P. Binzel, T. Gehrels, and M. Shapley Matthews, eds.), pp. 805-826. University of Arizona Press, Tucson.
- Milani A., and Knežević Z. (1990) Secular perturbation theory and computation of asteroid proper elements. Celestial Mechanics, **49**, 247-411.
- Valsecchi G., Carusi A., Knežević Z., Kresák Ľ, and Williams J. G. (1989) Identification of asteroid dynamical families. In Asteroids II (R. P. Binzel, T. Gehrels, and M. Shapley Matthews, eds.), pp. 368-385. University of Arizona Press, Tucson.
- Williams J. G. (1969) Secular perturbation in the Solar System. Ph. D. Thesis, University of California, Los Angeles.
- Williams J. G. (1979) Proper elements and family memberships of the asteroids. In Asteroids (T. Gehrels, ed.), pp. 1040-1063. University of Arizona Press, Tucson.
- Williams J. G. (1989) Proper elements and family memberships. In Asteroids II (R. P. Binzel, T. Gehrels, and M. Shapley Matthews, eds.), pp. 1034-1072. University of Arizona Press, Tucson.
- Zappalà V., Cellino A., Farinella P., and Knežević Z. (1990) Asteroid families. I. Identification by hierarchical clustering and reliability assessment. Astron. J., **100**, 2030-2046.

Figure 1



A CANDIDATE FOR THE PARENT BODY OF THE TAURID COMPLEX AND ITS SEARCH EPHEMERIS

K. Ziolkowski

Space Research Centre, Bartycka 18, 00-716 Warsaw, Poland

ABSTRACT

Unusual asteroid 5025 P-L, which its perihelion close to the orbit of Mercury and its aphelion between the orbits of Jupiter and Saturn, seems to be a good candidate for the parent body of the Taurid complex of small interplanetary objects. Evidences that this asteroid is a major source of meteoroids as well as an analysis of the orbits of asteroidal and cometary members of the Taurid complex presented in the paper, lead to conclusion that 5025 P-L might be regarded as a remnant of a giant comet which was a progenitor of the overall complex according to the hypothesis of Clube and Napier. Unfortunately, the orbit of 5025 P-L is very poorly determined because the computations were based upon only three positional observations over an arc of only four days in October 1960. Any further research on the problem of origin and evolution of the Taurid complex needs better determined orbit of this key asteroid. Therefore its new positions are necessary. In order to enable the search of eventual trails of 5025 P-L on plates which can be found in archives, its ephemeris for the opposition in 1960, when the asteroid passed about 0.5 AU from the Earth, is presented.

GENERAL REMARKS

Among the asteroidal members of the Taurid complex of small interplanetary bodies in high-eccentricity, low-inclination and short-period orbits, the minor planet 5025 P-L seems to be especially interesting because its orbit may be considered in some measure as a transitional one between orbits of the two cometary members of this complex. The membership of short period comet Encke in the Taurid complex is undisputable. There are also evidences that comet 1967 II Rudnicki belongs to the Taurid complex (Olson-Steel 1987, Ziolkowski 1988, 1990) although its long period orbit creates some difficulties in the understanding of this connection. According to the hypothesis of Clube and Napier (1984) the Taurid complex has originated from a giant comet which arrived in an Earth-crossing orbit and broke up some 10^4 - 10^5 years ago. Let us consider an object which moves along the orbit similar to the orbit of asteroid 5025 P-L. It is easy to show that the 2-3 percent changes of its velocity in perihelion can transfer this object on the orbit similar to the short-period orbit of comet Encke as well as to the long-period orbit of comet Rudnicki. In particular the decrease of the velocity of 5025 P-L by 1.4 km/s gives the orbit which shape is similar to the orbit of comet Encke and the increase by 1.7 km/s gives the orbit which shape is similar to the original orbit of comet Rudnicki. According to investigations of Clube and Napier (1984) those values of the velocity changes seem to be acceptable. This estimation, together with the evidence that asteroid 5025 P-L is a major source of meteoroids (Olson-Steel 1988), leads to the conclusion that this unusual object might be regarded as a remnant of a giant comet which was a progenitor of the overall Taurid

complex. Therefore any further researches on the problem of origin and evolution of the complex need a good knowledge of the motion of 5025 P-L. Unfortunately its orbit is very poorly determined because the computations were based upon only three positional observations made on October 22, 25 and 26, 1960 in the frame of the Palomar-Leiden Survey of faint minor planets (Van Houten et al. 1984). If the elements obtained by this way can be reliable, the object would have its perihelion close to the orbit of Mercury and its aphelion between the orbits of Jupiter and Saturn. It may be well to add that the orbit of such a body is dynamically unstable due its possibilities of approaches to the major planets. An absolute magnitude of the object was estimated as 16.9 mag. which indicates that it is likely a large body.

REQUEST TO OBSERVERS

The new positions of asteroid 5025 P-L are urgently needed. In a search for eventual trails of this object on plates exposed in 1960-1961, which can be found in archives, you can make use of the ephemeris given in Table 1 (α, δ – right ascension and declination of the object; D, R – distances from the Earth and Sun; mag. = $16.9 + 5 \log D + 5 \log R$; $\Delta\alpha, \Delta\delta$ – changes in α and δ when the perihelion time is changed by 1 day: T+1, and the semimajor axis is changed by 0.01 AU: $a + 0.01$).

The ephemeris was computed on the basis of the following values of orbital elements of asteroid 5025 P-L (Van Houten et al. 1984):

T = 1961 Jan. 18.6604 ET EPOCH = 1960 Sep. 23.0 ET

$$\left. \begin{array}{l} \omega = 149.^{\circ}9300 \\ \Omega = 355.^{\circ}9100 \\ i = 6.^{\circ}2000 \\ q = 0.439383 \text{ AU} \end{array} \right\} 1950.0 \quad \begin{array}{l} e = 0.895400 \\ a = 4.200600 \text{ AU} \\ n = 0.^{\circ}1144820 \\ P = 8.609 \text{ years} \end{array}$$

REFERENCES

- Clube S.V.M., Napier W.M., 1984, *Mon.Not.R.astr.Soc.* **211**, 953.
 Olsson-Steel D., 1987, *The Observatory* **107**, 157.
 Olsson-Steel D., 1988, *Icarus* **75**, 64.
 Van Houten C.J., Herget P., Marsden B.G., 1984, *Icarus* **59**, 1.
 Ziolkowski K., 1988, *The Observatory* **108**, 182.
 Ziolkowski K., 1990, *Acta Astronomica* **40**, 397.

Table 1

Ephemeris for asteroid 5025 P-L

DATE (E.T.)	$\alpha'_{1950.0}$	$\delta'_{1950.0}$	D	R	mag.	T+1		a + 0.01	
			h m	$^{\circ} /$		$\Delta\alpha$	$\Delta\delta$	$\Delta\alpha$	$\Delta\delta$
1960 Sep. 23	1 28.62	+12 58.1	1.148	2.098	18.8	-1.78	-13. ⁶	+0.57	+4. ³
28	1 21.87	+12 42.8	1.062	2.035					
Oct. 3	1 13.59	+12 20.0	0.983	1.971	18.3	-1.91	-16.0	+0.65	+5.0
8	1 03.69	+11 48.7	0.910	1.906					
13	0 52.13	+11 08.0	0.844	1.839	17.9	-1.89	-18.2	+0.72	+5.8
18	0 38.98	+10 17.1	0.787	1.772					
23	0 24.42	+ 9 16.1	0.737	1.703	17.4	-1.52	-19.2	+0.76	+6.7
28	0 08.77	+ 8 06.0	0.695	1.633					
Nov. 2	23 52.41	+ 6 48.5	0.661	1.562	17.0	-0.78	-17.8	+0.73	+7.1
7	23 35.79	+ 5 26.2	0.633	1.489					
12	23 19.31	+ 4 01.8	0.612	1.415	16.6	+0.34	-13.5	+0.62	+6.9
13	23 16.07	+ 3 44.9	0.608	1.400					
14	23 12.85	+ 3 28.1	0.604	1.385	16.5	+0.60	-12.3	+0.59	+6.8
15	23 09.65	+ 3 11.4	0.601	1.370					
16	23 06.48	+ 2 54.7	0.597	1.355	16.4	+0.88	-11.0	+0.57	+6.7
17	23 03.34	+ 2 38.2	0.594	1.339					
18	23 00.23	+ 2 21.8	0.591	1.324	16.4	+1.16	-9.8	+0.54	+6.4
19	22 57.16	+ 2 05.5	0.588	1.309					
20	22 54.11	+ 1 49.3	0.585	1.293	16.3	+1.44	-8.3	+0.50	+6.4
21	22 51.09	+ 1 33.4	0.583	1.278					
22	22 48.11	+ 1 17.5	0.580	1.262	16.2	+1.74	-6.8	+0.47	+6.2
23	22 45.15	+ 1 01.8	0.577	1.247					
24	22 42.23	+ 0 46.3	0.575	1.231	16.1	+2.05	-5.2	+0.43	+6.0
25	22 39.34	+ 0 31.0	0.572	1.215					
26	22 36.47	+ 0 15.8	0.570	1.199	16.1	+2.37	-3.6	+0.40	+5.8
27	22 33.63	+ 0 00.8	0.567	1.183					
28	22 30.81	- 0 14.1	0.565	1.167	16.0	+2.71	-1.9	+0.36	+5.6
29	22 28.01	- 0 28.8	0.562	1.151					
30	22 25.23	- 0 43.4	0.560	1.135	15.9	+3.06	-0.2	+0.32	+5.3
Dec. 1	22 22.46	- 0 57.9	0.558	1.119					
2	22 19.71	- 1 12.3	0.555	1.103	15.8	+3.43	+1.7	+0.28	+5.1
3	22 16.96	- 1 26.6	0.552	1.087					
4	22 14.21	- 1 40.9	0.550	1.070	15.7	+3.82	+3.7	+0.25	+4.8
5	22 11.47	- 1 55.1	0.547	1.054					
6	22 08.71	- 2 09.4	0.544	1.038	15.7	+4.23	+5.8	+0.21	+4.6
7	22 05.95	- 2 23.6	0.542	1.021					
8	22 03.16	- 2 37.9	0.539	1.004	15.6	+4.67	+8.0	+0.17	+4.3
9	22 00.35	- 2 52.3	0.536	0.988					
10	21 57.51	- 3 06.9	0.533	0.971	15.5	+5.14	+10.5	+0.12	+4.1
11	21 54.63	- 3 21.6	0.530	0.955					
12	21 51.70	- 3 36.5	0.527	0.938	15.4	+5.65	+13.1	+0.08	+3.9
13	21 48.72	- 3 51.6	0.523	0.921					
14	21 45.67	- 4 07.1	0.520	0.904	15.3	+6.21	+15.8	+0.04	+3.5
15	21 42.56	- 4 23.0	0.517	0.887					
16	21 39.35	- 4 39.3	0.513	0.871	15.2	+6.81	+19.0	-0.01	+3.2
17	21 36.06	- 4 56.1	0.510	0.854					
18	21 32.65	- 5 13.4	0.506	0.837	15.0	+7.47	+22.3	-0.06	+2.9
19	21 29.13	- 5 31.3	0.503	0.820					
20	21 25.48	- 5 50.0	0.499	0.803	14.9	+8.19	+26.0	-0.11	+2.6
21	21 21.68	- 6 09.4	0.496	0.786					
22	21 17.73	- 6 29.7	0.492	0.769	14.8	+8.97	+29.9	-0.16	+2.3
23	21 13.61	- 6 50.9	0.489	0.753					
24	21 09.30	- 7 13.2	0.485	0.736	14.7	+9.81	+34.2	-0.22	+2.0
25	21 04.79	- 7 36.5	0.482	0.719					
26	21 00.06	- 8 01.0	0.479	0.703	14.5	+10.73	+38.7	-0.27	+1.6
27	20 55.12	- 8 26.7	0.476	0.686					
28	20 49.94	- 8 53.7	0.474	0.670	14.4	+11.68	+43.3	-0.32	+1.2
29	20 44.52	- 9 22.0	0.472	0.654					
1961 Feb. 10	18 59.44	-25 29.1	1.101	0.681	16.3	+0.86	+6.7	-0.26	-0.2
15	19 11.62	-25 41.2	1.184	0.764					
20	19 23.47	-25 45.5	1.256	0.848	17.0	+0.36	+3.5	-0.28	-0.5
25	19 34.68	-25 44.4	1.319	0.932					
Mar. 2	19 45.12	-25 39.8	1.373	1.016	17.6	+0.22	+1.9	-0.28	-0.8
7	19 54.75	-25 33.4	1.419	1.098					
12	20 03.56	-25 26.1	1.458	1.178	18.1	+0.18	+1.0	-0.29	-1.0
17	20 11.53	-25 18.8	1.490	1.257					

COMA - A HIGH RESOLUTION TIME-OF-FLIGHT SECONDARY ION MASS SPECTROMETER (TOF-SIMS) FOR IN SITU ANALYSIS OF COMETARY MATTER

H. Zscheeg, J. Kissel, Gh. Natour
Max-Planck-Institut für Kernphysik, 6900 Heidelberg, FRG

A lot of clues concerning the origin of the solar system can be found by sending an exploring spacecraft to a rendezvous with a comet. Here we describe the space experiment CoMA, which will measure the elemental, isotopic and molecular composition of cometary dust grains. It will be flown on NASA's mission CRAF.

The motivation to build a sophisticated space probe experiment

One way to achieve a more profound understanding of the origin and the formation of the solar system is to have a close look at the refrigerated messengers from those times - the comets. Too small to undergo geological processing and too cold to be subject to major chemical changes, cometary nuclei consist of pristine material. Only their surface may have been processed by cosmic rays and electromagnetic radiation to higher complex (e. g. polymerized) molecules /1/.

This is one of the main motivations of NASA's cometary rendezvous and asteroid flyby mission (CRAF). Lasting about nine years, it is to perform a detailed in situ analysis of a comet and its surroundings. On the way out it also will examine an asteroid during flyby.

One of the experiments on board - contributed by the Federal Republic of Germany - is the cometary matter analyzer (CoMA). This is a time-of-flight secondary ion mass spectrometer. CoMA will shed some light on the elemental, isotopic and molecular composition of solid and gaseous cometary matter. It will give information about the organic inventory /2/, the gas-dust-interaction and the activity of the nucleus in different parts of the cometary orbit. All this will be achieved by examining dust grains and gas originating from a comet, probably p/Kopff.

A peek at the principles of time-of-flight secondary ion mass spectrometry

Primary ions impinging on a target surface produce - besides sputtered neutral target atoms and molecules - positively and negatively charged secondary ions. Those can be mass analyzed. In case of a time-of-flight mass spectrometer they are extracted with a fixed initial kinetic energy (keV-range) and fed into a drift space. Different ion masses translate into different times of flight to the detector which is located at the end of the drift space. A clock is set running when the primary ions impinge on the target surface and the secondary ions leave. To precisely pin down the starting moment, a primary ion pulse which is as short as possible must be used. But it still has to contain enough ions to sputter a sufficient number of secondary particles.

The goals of the cometary matter analyzer

CoMA will perform the analysis of cometary samples with a mass resolution unprecedented by a space instrument.

It will yield the abundances of all elements, except U and the noble gases. Thus it will be possible to better characterize their role in solar system chemistry.

Furthermore it will be able to separate the isotopes of a number of light elements (C, N, O, Mg). Due to the high mass resolution, interferences by isobaric molecules are reduced. For example, distinguishing between ^{12}CH and ^{13}C gives access to the presolar records of possibly stellar condensates. Determination of the isotopy of above mentioned key elements will set stringent constraints on the boundary conditions of models describing origin and evolution of comets.

In its extended operation mode CoMA will comprise a mass range up to 3000 da. This enables a detailed analysis of organic cometary constituents and will probably give insight into their formation processes. Perhaps even some questions concerning the origin of life on Earth will be answered.

The three parts of sophistication - CoMA's subunits

The cometary matter analyzer consists of three basic units: the dust collector subsystem, the primary ion gun and the time-of-flight mass spectrometer. CoMA's mass will be about 16 kg and the power consumption will be around 22 W.

First part - the dust collector subsystem

Task of this subsystem is to handle the targets which collect cometary dust particles.

It accommodates around 100 targets located in a target wheel. They are individually selectable to meet the demands of the differing features of the particles to be collected. The system mechanically moves the targets from the store- to the collect-, clean- and analyze-positions. It also adds a mechanical scan capability (about 1 cm^2) and exact positioning to the electric scan capability of the primary ion beam.

The targets are optimized to softly collect cometary dust grains of different sizes and velocities or to adsorb cometary gases effectively. Foils coated with highly porous metal blacks are the best choice for this. For high velocity particles ($> 100 \text{ m/s}$), platinum black structures will be used. Fluffy-brITTLE particles of low velocity ($< 100 \text{ m/s}$) will be collected by ruthenium black covered targets. Palladium black is suited best for collecting compact, low velocity grains.

Each target has markers on it. Thus a reference system is established and collected particles can be found repeatedly.

In front of the entrance aperture a concentrator is located. It increases the effective aperture and so the number of collected particles will be higher by an order of magnitude.

Second part - the primary ion gun

Instead of using one of the widespread electron impact ion sources, a liquid metal ion source (LMIS) has been chosen for CoMA. Its mechanical setup is much simpler. Basically it consists of a heatable reservoir containing the metal, a needle which is wetted by the molten metal and an extraction electrode. The ion beam is emitted from a liquid metal protrusion near the needle tip/3/. This kind of source doesn't need any voluminous gas containers and sophisticated valves. Liquid metal ion sources also feature a high brightness.

Because of the small ion emission volume, those sources are well suited for microfocus applications. As a metal, isotopically pure ^{115}In is used. So there is no need for mass separation of the primary ion beam. Indium is advantageous to Gallium, because under normal conditions it is solid. The divergent 10 keV ion beam (some uA) is transformed to a parallel beam with an extraction lens. Afterwards it is scanned across an aperture. This results in a 100 ns pulse, which is subsequently further compressed to less than 2 ns by a bunching sequence. Latter has to time focus ions with different starting times and also different starting energies (energy spread of ion source). The ion pulse is forwarded through a focusing lens into a 40 um spot (high resolution mode)on the sample. Inside the acceptance area of the spectrometer's extraction lens (+ - 0.2 mm) electrical scanning can be performed. For erosion and cleaning purposes a DC-mode is implemented also.

The operation time of the gun will be at least 5000 h /4/.

The attached electronics mainly consists of a timing controller for the various voltage pulses.

Third part - the time of flight mass spectrometer

Secondary ions starting from the analyzed spot first are accelerated into the extraction lens and then move through the flight tube into the reflector /5, 6/. It sends them back to the additional ion mirror located on the baseplate. This unit mirrors them into the reflector, where they turn around once more. Finally they are sensed from a detector also sitting on the baseplate.

The asymmetric extraction lens features a wide acceptance angle at low chromatic and spherical aberration at a great focal length.

Using a two stage reflector high mass resolution as well as second order energy compensation are achieved. The two areas of different electric fields inside the stack of equipotential rings are separated by meshes of high transmission. This improves the spectrometer's acceptance.

Mechanical changes (i.e. due to temperature variations) can be made up for in wide ranges by adjusting the reflector voltages.

The additional ion mirror doubles ion flight times at constant geometric dimensions by folding once the flight path (3 m) of the ion beam.

Secondary ions are detected by a two stage channelplate with integrated nonlinear preamplifier.

Overall transmission will be 0.35, mass resolution about 13000. Both positive and negative ions can be analyzed.

Instrument electronics consists of three parts. The fast data acquisition system has a measuring range of about 400 us with an accuracy of 1 ns. Data preprocessing will allow to set time windows within the measur-

ing range as well as the variation of time resolution. The spectrum data accumulation will perform a summation of spectrum events.

Putting the parts together - the setup as a whole

The dust collector subsystem is connected to the baseplate of the time-of-flight mass spectrometer. On this baseplate the secondary ion extraction lens, the hard mirror and the detector assembly are mounted. To the other side follows the flight tube and a second plate. This one connects the tube to the reflector.

Between both plates there is space for the primary ion gun and electronic boards (FIGURE 1). The remainder of the electronics is housed in an electronic box.

The CoMA instrument is managed by a processor system.

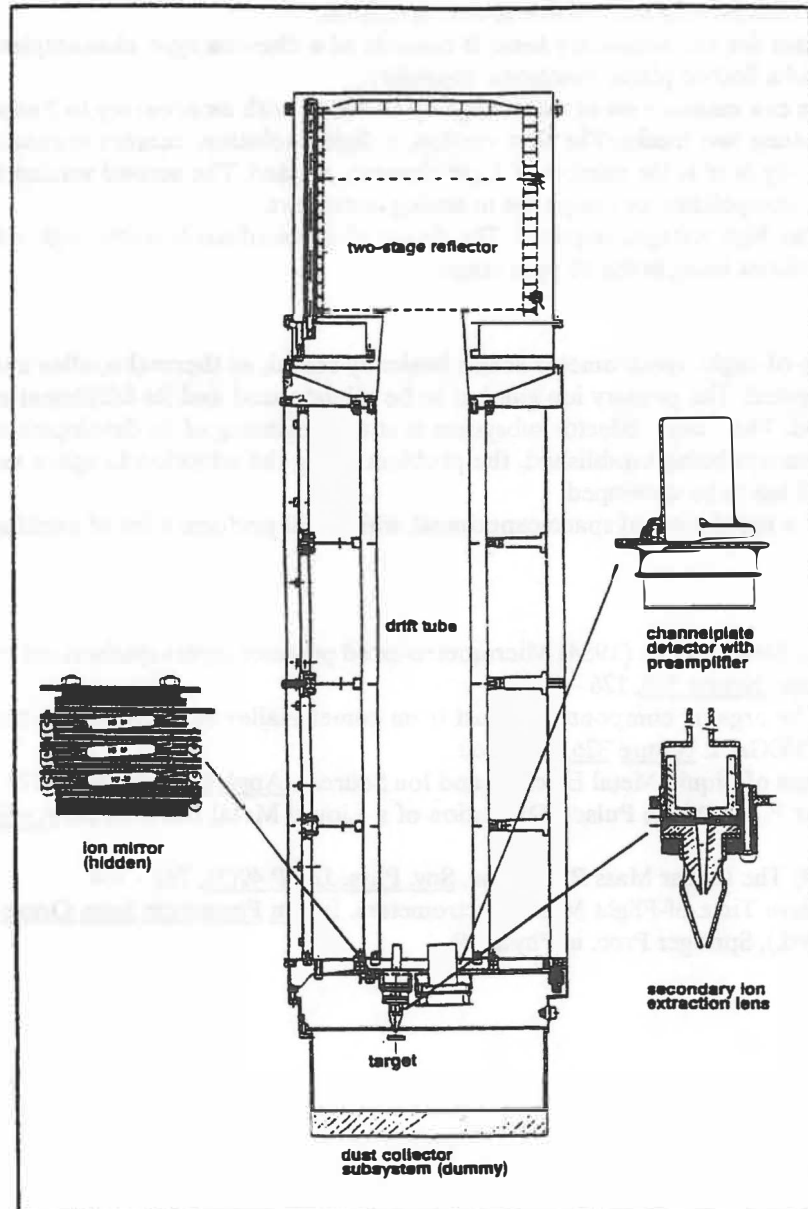


FIGURE 1

The present sophisticated setup of CoMA. Shown is a cut view of the hardware of the time-of-flight mass spectrometer. This mechanical design is very similar to the final space design. Some of the elements are additionally shown magnified. Length is about 780mm, diameter about 170mm.

Present status of CoMA

The feasibility of the spectrometer design containing the additional ion mirror was verified. This first model utilized components of standard mechanical precision. A 3 ns pulse N₂-Laser generated the secondary ions from the target. The next step consisted of measurements with a more sophisticated model, which basically

resembled the flight unit. In those successful measurements secondary ion extraction lens, additional ion mirror and detector could be externally adjusted. The channelplate detector had a fluorescent screen, so that position and shape of the secondary ion beam could be evaluated.

In all those measurements the mass resolution was limited by the duration of the secondary ion formation process and not yet by the spectrometer design.

With a similar model, vibration tests were undertaken.

The primary ion gun in its present state can deliver ion pulses of 2.8 ns duration. They are generated by a combination of scanning the DC-beam across an aperture and subsequently bunching the emerging pulses. Specially designed HV-switches produce voltage pulses of high amplitude (500 V) and short risetimes (some ns). The ion source is a commercial one. Its small reservoir is directly heated.

Development of an ion source containing about 5 g of ^{115}In in an indirectly heated ceramic reservoir is under way to meet the demand of an unusual long and reliable source operation.

Also progress is made with a detector for the secondary ions. It consists of a chevron type channelplate assembly with integrated amplifier and a limited planar resolution capability.

The fast data acquisition electronics can measure events in a range up to 400 us with an accuracy to 2 ns at present. The development evolves along two tracks. The first version, a digital solution, centers around a tapped transmission line. Main difficulty here is the number of logic elements needed. The second version is an analog one. It performs an analog interpolation by ramp time to analog converters.

Especially critical is the stability of the high voltages required. The design of extraordinarily stable high voltage converters has been finished, stabilities being in the 10 ppm range.

Outlook

The mechanical concept of the time-of-flight spectrometer seems basically sound, as thermal studies and mechanical tests up to now demonstrated. The primary ion gun has to be miniaturized and its fulfillment of the requirements must still be verified. The dust collector subsystem is at the beginning of its development. Electronics is well on its way, the concept being established, the problem being the adaption to space requirements. Also a lot of software still has to be developed.

So in the near future there will exist a sophisticated space experiment which will perform a lot of exciting analyses on cometary matter.

References:

- /1 Foti G., Calcagno L., Sheng K. L., Strazzulla G. (1984) Micrometre-sized polymer layers synthesized by MeV ions impinging on frozen methane. *Nature* **310**, 126 - 128
- /2 Kissel J., Krueger F. R. (1987) The organic component in dust from comet Halley as measured by the PUMA mass spectrometer on board VEGA 1. *Nature* **326**, 755 - 760
- /3 Gomer R. (1979) On the Mechanism of Liquid Metal Electron and Ion Sources. *Appl. Phys.* **19**, 365 - 379
- /4 Kissel J., Zscheeg H., Rüdenauer F. G. (1988) Pulsed Operation of a Liquid Metal Ion Source. *Appl. Phys. A47*, 167 - 169
- /5 Mamyrin B. A., Smikh D. V. (1979) The Linear Mass Reflectron. *Sov. Phys. JETP* **49**(5), 762 - 764
- /6 Wollnik, H. (1986) Design of Modern Time-of-Flight Mass Spectrometers. In Ion Formation from Organic Solids IFOS III (A. Benninghoven ed.), Springer Proc. in Physics 9

Indexes

Author Index

A'Hearn M. F.	177, 443	Di Martino M.	157, 421	Jones J.	269, 273, 277
Ahrens T. J.	561	DiSanti M. A.	187	Jones W.	269, 277, 281
Akisawa H.	1	Dovgopol A. N.	45	Jorda L.	285
Andreev V. V.	5, 9, 17	Durda D. D.	153, 161, 223	Judge D. L.	657
Aoki T.	529				
Asher D.	573	Farinella P.	113, 165, 167, 675	Kaasalainen M.	289
Babadzhanov P. B.	23, 27	Fechtig H.	613	Kaiser R. I.	293
Baggaley W. J.	33, 37	Feldman P. D.	171, 177	Kamél L.	509
Bailey M. E.	227	Festou M. C.	171, 175, 177, 345, 509	Kato M.	597
Bao Y.	253			Keay C.	297
Bär A.	77	Filimonova T. K.	17	Kingsley S. P.	281
Baratta G. A.	41	Filonenko V. S.	121	Kissel J.	683
Barbieri C.	345	Fink U.	183, 187, 215	Klačka J.	301
Barker E. S.	577	Fitzsimmons A.	191	Knežević Z.	305
Barucci M. A.	379	Flynn G. J.	195	Kochan H.	313, 497
Belkovich O. I.	9, 17	Fomenkova M. N.	65	Kochetova O. M.	309
Belskaya I. N.	45	Froeschlé C.	201, 439	Koczet P.	537
Belton M. J. S.	49	Froeschlé Ch.	167, 205	Kölzer G.	313
Bendjoya Ph.	57, 61	Froeschlé Cl.	57, 61, 167	Kömle N. I.	317
Benedix G. K.	65	Fulchignoni M.	379	Konno I.	85, 321, 329, 529
Benest D.	69			Koschack R.	501
Bénit J.	521	Ge W.	533	Kotsarenko N. Ya.	125
Bhargavi S. G.	487	Geballe T. R.	211	Kouchi A.	325
Birch P. V.	443	Gehrels T.	541	Kozuka Y.	321, 329, 529
Birkle K.	81	Gérard E.	73	Kwiatkowski T.	333
Bockelée-Morvan D.	73, 133	Gerasimov I. A.	565		
Boehnhardt H.	77, 81, 613	Geyer E. H.	257, 265, 477	Lagerkvist C.-I.	145, 191, 379
Boice D. C.	85	Gomes R. S.	153	Lamberg L.	289
Bois E.	439	Gonano-Beurer M.	157, 421	Larson S. M.	337
Bonev T.	257, 261	Gonczi R.	69, 167	Lazzarin M.	345
Boswell J.	89	Gosine J.	253	Levasseur-Regourd A. Ch.	349
Bourgois G.	73	Green D. W. E.	285	Levison H. F.	353
Bowell E.	429	Green S. F.	211	Lien D. J.	359
Brandt J. C.	93, 493	Greenberg J. M.	325	Lindblad B. A.	363, 367
Brooke T.	211	Grün E.	223	Lindgren M.	371, 601
Brown M. E.	97	Grundy W. M.	215	Lizunov G. V.	125
Burns J. A.	101	Gustafson B. Å. S.	153, 161, 219, 223	Lu C.	253
Campins H.	617			Lumme K.	289
Capria M. T.	379	Hadamcik E.	349	Lundström M.	145
Cellino A.	57, 165, 675	Hahn G.	145, 227	Luu J. X.	375
Celnik W. E.	537	Hamabe M.	529		
Cephecha Z.	109	Hamilton D. P.	101	Mack P.	237
Chamberlin A. B.	413	Hasegawa H.	231	Magnusson P.	191, 379
Chauvineau B.	113	Hawkes R. L.	517	Manara A.	381
Chen F. Z.	657	Helin E. F.	235	Mardon A. A.	385
Chorney G. F.	117	Heyd R.	237, 505	Mardon E. G.	385
Churyumov K. I.	117, 121, 125	Hicks M.	183	Marsden B. G.	395
Clairemidi J.	129, 525	Hoffmann H.	421	Massonne L.	77
Colom P.	73, 133	Hopp U.	81	Matese J. J.	399
Combi M.	187	Huebner W. F.	85	McBride N.	403
Crovisier J.	73, 133, 137, 285	Hughes D. W.	89, 403	McCrosky R. E.	109
Cunningham C. J.	141	Ibadov S.	241	McDonnell J. A. M.	407
Dahlgren M.	145, 191, 379	Ipatov S. I.	245	McFadden L. A.	65, 413
Davies J. K.	211	Isobe S.	529	McNaught R. H.	573
Davis D. R.	165	Ivanova V.	261	Meisser W.	537
Delamere A.	49	Jackson W. M.	249, 253	Michałowski T.	333, 417
Delva M.	149	Jayaraman S.	153	Mignard F.	113
Dermott S. F.	153, 161, 223	Jockers K.	257, 261, 265, 477	Milani A.	305
Despois D.	133			Millis R. L.	443
				Minami S.	529
				Miyashita A.	625
				Mizutani H.	597

Moreels G.	129, 525	Snow M.	93, 493	Zagretdinov R. V.	671
Morrow E. M.	65	Snow P.	569	Zappalá V.	57, 165, 675
Mottola S.	157, 421	Solovaya N. A.	565	Ziólkowski K.	679
Mueller B. E. A.	425	Song X.	253	Zscheeg H.	683
Muinonen K.	429, 549	Spinrad H.	97		
Mukai T.	325	Stathakis R.	505		
Mumma M. J.	667	Steel D.	569, 573		
		Steel D. I.	37		
Nakamura A.	1	Steiner G.	317		
Nakamura T.	433, 625	Stern S. A.	85, 577		
Natour Gh.	683	Štöhl J.	469, 473		
Neugebauer M.	629	Stooke P. J.	583		
Neukum G.	157, 421	Strazzulla G.	41		
Nicholson P. D.	153	Sykes M. V.	587		
Nishioka K.	321	Szutowicz S.	593		
Numazawa S.	329				
		Takagi Y.	597		
Oberti P.	439	Takahashi T.	321		
Obrubov Yu. V.	27	Takeuchi H.	529		
Okamura S.	529	Tancredi G.	509, 601		
Osip D. J.	443	Taylor A. D.	33, 37		
Ostro S. J.	447	Tegler S. C.	505		
		Thiel K.	313		
Paubert G.	133	Thomas H.	497		
Pauwels Th.	451, 455	Todorovic-Juchniewicz B.	605		
Peale S. J.	459	Tokunaga A. T.	211		
Petit J.-M.	201	Tozzi G. P.	345		
Pittich E. M.	565	Tsuda T.	625		
Porubčan V.	367, 469, 473	Tsumura M.	1		
Prasad C. D.	265, 477	Tsutsumi M.	625		
Rabinowitz D. L.	481, 541	Urdahl R. S.	253		
Rajamohan R.	487				
Ramsay D. A.	505	Valsecchi G. B.	381		
Randall C. E.	93, 493	Vaňa R.	473		
Ratcliff P. R.	407	Van Flandern T.	609		
Ratke L.	497	Vanysek V.	81, 613		
Rauer H.	261, 265, 477	Verkhoglyadova O. P.	125		
Renard J. B.	349	Vernotte F.	129, 525		
Rendtel J.	501				
Rettig T. W.	505	Walker R. G.	587, 617		
Rickman H.	509	Watanabe J.	1, 231, 621, 625		
Rietmeijer F. J. M.	513	Webster A. R.	273		
Robertson M. C.	517	Wehinger P.	237		
Roessler K.	293, 521	Weissman P.	629		
Rousselot P.	129, 525	Whipple F. A.	633		
		Whitman P. G.	399		
Saito M.	321	Whitmire D. P.	399		
Saito T.	321, 329, 529	Williams G. V.	641		
Sauer M.	521	Williams I. P.	191, 219, 661, 671		
Schlaperf M.	617	Williams J.	385		
Schleicher D. G.	443	Williams J. G.	645, 649		
Schloerb F. P.	533	Wisniewski W. Z.	447, 653		
Schlosser W.	537	Wu C. Y. R.	657		
Scholl H.	205	Wu Z.	661		
Schulz R.	537	Wyckoff S.	237, 505		
Schwingenschuh K.	149				
Scotti J. V.	541				
Sekanina Z.	545				
Shkuratov Yu. G.	549	Xie X.	667		
Shor V. A.	309, 553	Xing Z. F.	325		
Sidorov V. V.	17	Xu Y. L.	153		
Simek M.	557				
SitarSKI G.	605	Yagudina E. I.	553		
Slaughter C. D.	337	Yamamoto T.	325		
Slezak E.	61	Yi Y.	93, 493		
Smithers C. L.	561	Yoshikawa M.	433, 625, 671		

Subject Index*

Asteroids

Albedo	289, 549, 583	Orbits, error analysis	429
Amalthea (satellite of Jupiter)	583	Origin	227, 573, 645
Minor asteroids	<i>see</i> Near-Earth Asteroids	Parent bodies	165, 645, 649, 679
Apollo asteroids	<i>see</i> Near-Earth Asteroids	Phase relations	45, 549
Astrometry	235, 395, 429, 455, 481, 541, 641	Phobos (satellite of Mars)	9, 583
Aten asteroids	<i>see</i> Near-Earth Asteroids	Photometry	45, 157, 289, 309, 333, 379, 417, 421, 447, 549, 653
Bias effects, observational	65	PLS survey	649
Binary asteroids	101, 113, 577	Polarimetry	549
CCD observations	157, 215, 235, 421, 447, 487, 541, 573, 577	Pole orientations	45, 289, 333, 417, 447
Chaotic orbits	145, 167, 201, 205, 227, 245, 565, 573	Proper elements	57, 61, 165, 363, 645, 649, 675
Cluster analysis	57, 61, 165, 363, 649, 675	Radar observations	447
Collisional processes	101, 113, 161, 167, 561, 597, 645, 649	Recovery	395
Composition	191, 215, 413	Regolith	549
Cratering	561, 583, 645	Relation to comets	85, 219, 227, 481, 487, 573
Cybele asteroids	157	Relation to meteoroids	23, 37, 109, 153, 161, 167, 195, 205, 219, 223, 407, 413, 473, 481, 679
Databases	309, 379, 395, 481	Resonances	145, 167, 205, 227, 245, 573, 671
Deimos (satellite of Mars)	9, 215, 583	Rotation	45, 157, 417, 447, 653
Density (mass)	641	Light scattering	549
Discovery surveys	65, 235, 395, 481, 541, 649	Shape	45, 157, 289, 333, 417, 421, 447, 583, 653
Earth-crossing asteroids	<i>see</i> Near-Earth asteroids	Size distribution	481, 649
Families	57, 61, 161, 165, 363, 597, 645, 649, 675	Spectral observations	191, 215, 413, 421, 487, 573
Flora asteroids	165, 645	Trojan asteroids	157, 191, 671
Galileo mission	645	UCAS survey	649
Gas emission	85, 573	Väisälä orbit	395
Hilda asteroids	157		
Hirayama families	<i>see</i> Families		
History	141		
Kirkwood gaps	145, 245		
Lightcurves	<i>see</i> Photometry		
Magnitudes	309		
Mars-crossing asteroids	145, 245, 481, 541, 645		
Martian satellites	9, 215, 583		
Mass (density)	641		
Near-Earth asteroids (NEAs)	49, 65, 145, 205, 227, 235, 245, 395, 447, 473, 481, 541, 653		
Orbit determination	309, 395, 429, 553, 641, 679		
Orbital dynamics/evolution	101, 145, 167, 201, 205, 219, 227, 245, 553, 565, 573, 671		
Orbital elements	309, 553		
Orbital stability	<i>see</i> Orbital dynamics/evolution, Chaotic orbits		

Specific Asteroids

1 Ceres	141, 641
3 Juno	577
4 Vesta	583
14 Irene	45
16 Psyche	289
17 Thetis	413
21 Lutetia	417
39 Laetitia	289
43 Ariadne	413
46 Hestia	413
51 Nemausa	45
119 Althaea	413
138 Tolosa	413
146 Lucina	577
153 Hilda	565
243 Ida	645
250 Bettina	417
335 Roberta	413
337 Devosa	417

* Page numbers refer to the first page of an article in which a term is discussed.

348 May	641	CCD observations	81, 89, 183, 187, 257, 265, 337, 345, 349, 353, 451, 529
361 Bononia	565	Chaotic orbits	<i>see Orbital dynamics/ evolution</i>
386 Siegena	413	CHON	<i>see Organic compounds</i>
391 Ingeborg	413	Collisional processes	399
413 Edburga	413	Comae	1, 73, 77, 81, 85, 89, 97, 133, 137, 177, 187, 237, 241, 249, 253, 257, 337, 345, 477, 505, 525, 537
487 Venetia	413	Composition	41, 133, 137, 171, 183, 211, 237, 241, 293, 443, 477, 505, 521, 533, 587, 613, 657, 683
532 Herculina	333	Cosmic ray interaction	293
678 Fredegundis	413	CRAF mission	1, 171, 183, 629, 683
695 Bella	413	Crust formation	<i>see Mantle</i>
804 Hispania	417	Databases	443
951 Gaspra	101, 421, 583, 645	Density	509
1212 Francette	565	Disconnection events	93, 149, 257, 321, 493
1403 Idelsonia =		Discovery surveys	353
1935 QA	395	Dust	81, 85, 129, 227, 241, 249, 313, 349, 359, 403, 513, 613, 617, 683
1529 Oterma	565	Dust/gas ratio	171, 177, 183, 443, 587
1580 Betulia	653	Gas	<i>see Production rates</i>
1627 Ivar	235	Giotto mission	241
1917 Cuyo	447, 653	H/ OH cloud	73, 97, 257, 657, 667
2060 Chiron	573	Historical observations	385
3200 Phaethon	481	Image processing	337
3288 Seleucus	145	IRAS observations	587, 617
3551 1983 RD	145	IUE observations	171, 345
3908 1980 PA	653	Jets	81, 89, 249
4276 Clifford	145	Jupiter family	371, 601
4953 1990 MU	395	Kuiper belt	353
4954 Eric	235	Laboratory experiments	253, 293, 313, 497, 521
1973 NA	227	Lightcurves	1, 121, 177, 231, 285, 509
1981 EJ ₃₀	145	Long-period comets	399, 633
1982 YA	227	Magnetic field	73, 93, 149, 257, 321, 329, 493, 529
1983 RJ ₄	145	Magnitudes	121, 285, 509, 633
1985 FZ	395	Mantle	41, 231, 249, 317, 399, 497, 521, 573
1986 RM ₂	145	Nongravitational forces	399, 459, 509, 605
1987 DA ₇	145	Nuclei	41, 261, 293, 313, 317, 325, 439, 497, 509, 521, 545, 587, 621, 633
1987 UV ₁	145	Orbit determination	399, 605
1989 UK ₂	145	Orbital dynamics/ evolution	69, 227, 353, 371, 381, 433, 573, 601, 605
1989 UP	541	Organic compounds	41, 117, 133, 137, 187, 237, 253, 261, 293, 345, 505, 513, 521, 533, 537, 545, 613, 683
1990 SS	541	Origin	227, 353, 573
1990 TG ₁	541		
1990 TR	653		
1990 UN	481, 541		
1990 UP	541		
1990 VA	541		
1991 AM	541		
1991 BA	235, 481, 541		
1991 BN	541		
1991 CB ₁	541		
1991 DA	227, 235		
1991 EE	541		
1991 FA	541		
1991 FE	541		
1991 JR	481, 541		
1991 JW	395		
1991 LH	541		
1991 UO	541		
1991 VG	235		
5481 T-2	145		

Comets

Active areas	77, 375, 509, 545, 593, 633
Aging	313, 521, 573, 633
Astrometry	451
Carbon compounds	<i>see Organic compounds</i>
Cartography	583

Parent molecules	133, 137, 187, 253, 261, 293, 477, 505, 533, 613, 667
Photometry	261, 425, 443, 657
Plasma dynamics	93, 149, 257, 265, 321, 329, 493, 529
Polarimetry	349
Production rates	171, 177, 183, 187, 285, 345, 359, 443, 525, 537, 545, 657
Radio observations	73, 133, 137, 285, 533
Relation to asteroids	85, 219, 227, 481, 487, 573
Relation to meteoroids	5, 23, 27, 33, 37, 153, 195, 269, 367, 403, 407, 469, 587, 661
Resonances	<i>see</i> Orbital dynamics/evolution
Rotation	81, 89, 425, 439, 459, 545, 593, 621
Shape	425, 583
Short-period comets	261, 353, 371, 381, 433, 601, 633
Solar activity	121, 293, 321, 329
Spacecraft observations	49, 683
Spectral observations	73, 97, 117, 133, 183, 187, 211, 237, 241, 253, 265, 345, 505, 667
Sublimation	<i>see</i> Production rates
Sungrazing comets	5, 227
Tails	93, 149, 237, 257, 261, 265, 321, 329, 493, 529
Thermal models	317, 325, 497
Vega missions	129, 149, 241, 525

Specific Comets

Aarseth-Brewington (1989 XXII)	137
Austin (1990 V)	97, 133, 137, 211, 231, 237
Bradfield (1987 XXIX)	171
P/Brorsen-Metcalf	81, 133, 137, 321
P/Churyumov-Gerasimenko	121
P/d'Arrest	177
P/Encke	481
P/Gunn	605
P/Halley	89, 93, 121, 171, 187, 227, 241, 359, 459, 477, 493, 505, 537, 583, 667
P/Hartley-IRAS	227
P/Kearns-Kwee	605
P/Kopff	171
Levy (1990XX)	73, 97, 133, 137, 265, 477, 533
P/Machholz	27, 227
Nishikawa-Takamigawa-Tago (1987 III)	505

Okasakii-Levy-Rudenko (1989 XIX)	137, 321
P/Schwassmann-Wachmann 1	261
Skorichenko-George (1990 VI)	117
P/Slaughter-Burnham	69
Sorrels (1987 II)	451
P/Tempel 1	171
P/Tempel 2	171, 183, 509
P/Thatcher	469
Wilson (1987 VII)	171, 505

Meteors and Interplanetary Dust

Atmospheric detonation	569
Atmospheric entry	23, 109, 195, 277, 281, 517, 557
Bolides	297
Collisional evolution	101, 161, 223
Density	23, 109
Diffusion heights	281
Dust	33, 161, 223, 407
Echo duration	557
Electrophonic sounds	297
Fireballs	297
Fluxes	9, 17
Fragmentation	23, 109, 517
Grain size	223, 517
Meteorites	513, 645
Orbits and orbital evolution	27, 37, 101, 223, 269, 661
Production	<i>see</i> Sources, Relation to Asteroids, Relation to comets
Radar observations	5, 17, 33, 37, 273, 277, 281, 557, 625
Relation to asteroids	23, 37, 109, 153, 161, 167, 195, 205, 219, 223, 407, 413, 473, 481, 679
Relation to comets	5, 23, 27, 33, 37, 153, 195, 269, 367, 403, 407, 469, 587, 661
Shower bursts	367, 469, 661
Showers	<i>see</i> Streams
Size distributions	223, 281, 313, 367, 469
Sources	5, 9, 161, 195, 223, <i>see also</i> Relation to asteroids, Relation to comets
Sporadic meteors	5, 517, 557
Storms	367, 469, 661
Streams	17, 23, 27, 33, 109, 269, 273, 367, 403, 469, 473, 501, 625, 661, 679
Tunguska-like event	569
Television observations	517

Trains	277
Visual observations	367, 501
Wake	517
Zodiacal cloud	153, 161, 195, 223, 241
Zodiacal dust bands	153, 161

Specific Meteor Streams

δ Aquarid	273
Geminid	281, 481, 625
Leonid	469, 661
Lyrid	367, 469
Phi Boötis	481
Quadrantid	27, 269
Taurid	569